

GEOPHYSICAL MONOGRAPH SERIES

AGU
ADVANCING EARTH
AND SPACE SCIENCE

Mantle Convection and Surface Expressions

Editors

Hauke Marquardt
Maxim Ballmer
Sanne Cottaar
Jasper Konter

WILEY

GEOPHYSICAL MONOGRAPH SERIES

Mantle Convection and Surface Expressions

Hauke Marquardt, University of Oxford, UK

Maxim Ballmer, University College London, UK

Sanne Cottaar, University of Cambridge, UK

Jasper Konter, University of Hawaii at Mānoa, USA



The convective motion of material in Earth's mantle, powered by heat from the deep interior of our planet, drives plate tectonics at the surface, generating earthquakes and volcanic activity. It shapes our familiar surface landscapes, and also stabilizes the oceans and atmosphere on geologic timescales.

Mantle Convection and Surface Expressions brings together perspectives from observational geophysics, numerical modelling, geochemistry, and mineral physics to build a holistic picture of the deep Earth. It explores the dynamic processes occurring in the mantle as well as the associated heat and material cycles.

Volume highlights include:

- Perspectives from different scientific disciplines with an emphasis on exploring synergies
- Current state of the mantle, its physical properties, compositional structure, and dynamic evolution
- Transport of heat and material through the mantle as constrained by geophysical observations, geochemical data and geodynamic model predictions
- Surface expressions of mantle dynamics and its control on planetary evolution and habitability

The American Geophysical Union promotes discovery in Earth and space science for the benefit of humanity. Its publications disseminate scientific knowledge and provide resources for researchers, students, and professionals.


Cover Design: Wiley

Cover Image: Synchrotron X-ray diffraction image collected in a high-pressure/-temperature diamond-anvil cell experiment to determine the deformation behavior of (Mg,Fe)O ferropericlase;

© Courtesy of Hauke Marquardt

www.wiley.com

WILEY

 Also available
as an e-book

AGU ADVANCING
EARTH AND
SPACE SCIENCE

ISBN 978-1-119-52861-6



9 781119 528616

Geophysical Monograph Series

Geophysical Monograph Series

- 212 **The Early Earth: Accretion and Differentiation** *James Badro and Michael Walter (Eds.)*
- 213 **Global Vegetation Dynamics: Concepts and Applications in the MC1 Model** *Dominique Bachelet and David Turner (Eds.)*
- 214 **Extreme Events: Observations, Modeling and Economics** *Mario Chavez, Michael Ghil, and Jaime Urrutia-Fucugauchi (Eds.)*
- 215 **Auroral Dynamics and Space Weather** *Yongliang Zhang and Larry Paxton (Eds.)*
- 216 **Low-Frequency Waves in Space Plasmas** *Andreas Keiling, Dong-Hun Lee, and Valery Nakariakov (Eds.)*
- 217 **Deep Earth: Physics and Chemistry of the Lower Mantle and Core** *Hidenori Terasaki and Rebecca A. Fischer (Eds.)*
- 218 **Integrated Imaging of the Earth: Theory and Applications** *Max Moorkamp, Peter G. Lelievre, Niklas Linde, and Amir Khan (Eds.)*
- 219 **Plate Boundaries and Natural Hazards** *Joao Duarte and Wouter Schellart (Eds.)*
- 220 **Ionospheric Space Weather: Longitude and Hemispheric Dependences and Lower Atmosphere Forcing** *Timothy Fuller-Rowell, Endawoke Yizengaw, Patricia H. Doherty, and Sunanda Basu (Eds.)*
- 221 **Terrestrial Water Cycle and Climate Change Natural and Human-Induced Impacts** *Qihong Tang and Taikan Oki (Eds.)*
- 222 **Magnetosphere-Ionosphere Coupling in the Solar System** *Charles R. Chappell, Robert W. Schunk, Peter M. Banks, James L. Burch, and Richard M. Thorne (Eds.)*
- 223 **Natural Hazard Uncertainty Assessment: Modeling and Decision Support** *Karin Riley, Peter Webley, and Matthew Thompson (Eds.)*
- 224 **Hydrodynamics of Time-Periodic Groundwater Flow: Diffusion Waves in Porous Media** *Joe S. Depner and Todd C. Rasmussen (Auth.)*
- 225 **Active Global Seismology** *Ibrahim Cemen and Yucel Yilmaz (Eds.)*
- 226 **Climate Extremes** *Simon Wang (Ed.)*
- 227 **Fault Zone Dynamic Processes** *Marion Thomas (Ed.)*
- 228 **Flood Damage Survey and Assessment: New Insights from Research and Practice** *Daniela Molinari, Scira Menoni, and Francesco Ballio (Eds.)*
- 229 **Water-Energy-Food Nexus – Principles and Practices** *P. Abdul Salam, Sangam Shrestha, Vishnu Prasad Pandey, and Anil K Anal (Eds.)*
- 230 **Dawn–Dusk Asymmetries in Planetary Plasma Environments** *Stein Haaland, Andrei Rounov, and Colin Forsyth (Eds.)*
- 231 **Bioenergy and Land Use Change** *Zhangcai Qin, Umakant Mishra, and Astley Hastings (Eds.)*
- 232 **Microstructural Geochronology: Planetary Records Down to Atom Scale** *Desmond Moser, Fernando Corfu, James Darling, Steven Reddy, and Kimberly Tait (Eds.)*
- 233 **Global Flood Hazard: Applications in Modeling, Mapping and Forecasting** *Guy Schumann, Paul D. Bates, Giuseppe T. Aronica, and Heiko Apel (Eds.)*
- 234 **Pre-Earthquake Processes: A Multidisciplinary Approach to Earthquake Prediction Studies** *Dimitar Ouzounov, Sergey Pulinet, Katsumi Hattori, and Patrick Taylor (Eds.)*
- 235 **Electric Currents in Geospace and Beyond** *Andreas Keiling, Octav Marghitu, and Michael Wheatland (Eds.)*
- 236 **Quantifying Uncertainty in Subsurface Systems** *Celine Scheidt, Lewis Li, and Jef Caers (Eds.)*
- 237 **Petroleum Engineering** *Moshood Sanni (Ed.)*
- 238 **Geological Carbon Storage: Subsurface Seals and Caprock Integrity** *Stephanie Vialle, Jonathan Ajo-Franklin, and J. William Carey (Eds.)*
- 239 **Lithospheric Discontinuities** *Huaiyu Yuan and Barbara Romanowicz (Eds.)*
- 240 **Chemostratigraphy Across Major Chronological Eras** *Alcides N. Sial, Claudio Gaucher, Muthuvairavasamy Ramkumar, and Valderez Pinto Ferreira (Eds.)*
- 241 **Mathematical Geoenergy: Discovery, Depletion, and Renewal** *Paul Pukite, Dennis Coyne, and Daniel Challou (Eds.)*
- 242 **Ore Deposits: Origin, Exploration, and Exploitation** *Sophie Decree and Laurence Robb (Eds.)*
- 243 **Kuroshio Current: Physical, Biogeochemical and Ecosystem Dynamics** *Takeyoshi Nagai, Hiroaki Saito, Koji Suzuki, and Motomitsu Takahashi (Eds.)*
- 244 **Geomagnetically Induced Currents from the Sun to the Power Grid** *Jennifer L. Gannon, Andrei Swidinsky, and Zhonghua Xu (Eds.)*
- 245 **Shale: Subsurface Science and Engineering** *Thomas Dewers, Jason Heath, and Marcelo Sánchez (Eds.)*
- 246 **Submarine Landslides: Subaqueous Mass Transport Deposits From Outcrops to Seismic Profiles** *Kei Ogata, Andrea Festa, and Gian Andrea Pini (Eds.)*
- 247 **Iceland: Tectonics, Volcanics, and Glacial Features** *Tamie J. Jovanelly*
- 248 **Dayside Magnetosphere Interactions** *Qiugang Zong, Philippe Escoubet, David Sibeck, Guan Le, and Hui Zhang (Eds.)*
- 249 **Carbon in Earth's Interior** *Craig E. Manning, Jung-Fu Lin, and Wendy L. Mao (Eds.)*
- 250 **Nitrogen Overload: Environmental Degradation, Ramifications, and Economic Costs** *Brian G. Katz*
- 251 **Biogeochemical Cycles: Ecological Drivers and Environmental Impact** *Katerina Dontsova, Zsuzsanna Balogh-Brunstad, and Gaël Le Roux (Eds.)*
- 252 **Seismoelectric Exploration: Theory, Experiments, and Applications** *Niels Grobbe, André Revil, Zhenya Zhu, and Evert Slob (Eds.)*
- 253 **El Niño Southern Oscillation in a Changing Climate** *Michael J. McPhaden, Agus Santoso, and Wenju Cai (Eds.)*
- 254 **Dynamic Magma Evolution** *Francesco Vetere (Ed.)*
- 255 **Large Igneous Provinces: A Driver of Global Environmental and Biotic Changes** *Richard. E. Ernst, Alexander J. Dickson, and Andrey Bekker (Eds.)*
- 256 **Coastal Ecosystems in Transition: A Comparative Analysis of the Northern Adriatic and Chesapeake Bay** *Thomas C. Malone, Alenka Malej, and Jadran Faganeli (Eds.)*
- 257 **Hydrogeology, Chemical Weathering, and Soil Formation** *Allen Hunt, Markus Egli, and Boris Faybishenko (Eds.)*
- 258 **Solar Physics and Solar Wind** *Nour E. Raouafi and Angelos Vourlidas (Eds.)*
- 259 **Magnetospheres in the Solar System** *Romain Maggiolo, Nicolas André, Hiroshi Hasegawa, and Daniel T. Welling (Eds.)*
- 260 **Ionosphere Dynamics and Applications** *Chaosong Huang and Gang Lu (Eds.)*
- 261 **Upper Atmosphere Dynamics and Energetics** *Wenbin Wang and Yongliang Zhang (Eds.)*
- 262 **Space Weather Effects and Applications** *Anthea J. Coster Philip J. Erickson, and Louis J. Lanzerotti (Eds.)*

Geophysical Monograph 263

Mantle Convection and Surface Expressions

Hauke Marquardt
Maxim Ballmer
Sanne Cottaar
Jasper Konter
Editors

This Work is a co-publication of the American Geophysical Union and John Wiley and Sons, Inc.



WILEY

This edition first published 2021
© 2021 American Geophysical Union

All rights reserved. No part of this publication may be reproduced, stored in a retrieval system, or transmitted, in any form or by any means, electronic, mechanical, photocopying, recording or otherwise, except as permitted by law. Advice on how to obtain permission to reuse material from this title is available at <http://www.wiley.com/go/permissions>.

The right of Hauke Marquardt, Maxim Ballmer, Sanne Cottaar, and Jasper Konter to be identified as the editors of this work has been asserted in accordance with law.

Published under the aegis of the AGU Publications Committee

Brooks Hanson, Executive Vice President, Science
Carol Frost, Chair, Publications Committee
For details about the American Geophysical Union visit us at www.agu.org.

Registered Office

John Wiley & Sons, Inc., 111 River Street, Hoboken, NJ 07030, USA

Editorial Office

111 River Street, Hoboken, NJ 07030, USA

For details of our global editorial offices, customer services, and more information about Wiley products visit us at www.wiley.com.

Wiley also publishes its books in a variety of electronic formats and by print-on-demand. Some content that appears in standard print versions of this book may not be available in other formats.

Limit of Liability/Disclaimer of Warranty

While the publisher and authors have used their best efforts in preparing this work, they make no representations or warranties with respect to the accuracy or completeness of the contents of this work and specifically disclaim all warranties, including without limitation any implied warranties of merchantability or fitness for a particular purpose. No warranty may be created or extended by sales representatives, written sales materials or promotional statements for this work. The fact that an organization, website, or product is referred to in this work as a citation and/or potential source of further information does not mean that the publisher and authors endorse the information or services the organization, website, or product may provide or recommendations it may make. This work is sold with the understanding that the publisher is not engaged in rendering professional services. The advice and strategies contained herein may not be suitable for your situation. You should consult with a specialist where appropriate. Further, readers should be aware that websites listed in this work may have changed or disappeared between when this work was written and when it is read. Neither the publisher nor authors shall be liable for any loss of profit or any other commercial damages, including but not limited to special, incidental, consequential, or other damages.

Library of Congress Cataloging-in-Publication Data

Names: Marquardt, Hauke, editor. | Ballmer, Maxim D., editor. | Cottaar, Sanne, editor. | Konter, Jasper, editor.
Title: Mantle convection and surface expressions / Hauke Marquardt, Maxim Ballmer, Sanne Cottaar, Jasper Konter, editors.
Description: Hoboken, NJ : Wiley, [2021] | Includes index.
Identifiers: LCCN 2021001626 (print) | LCCN 2021001627 (ebook) | ISBN 9781119528616 (cloth) | ISBN 9781119528586 (adobe pdf) | ISBN 9781119528593 (epub)
Subjects: LCSH: Heat-Convection, Natural. | Mantle plumes. | Surface fault ruptures. | Geodynamics. | Earth (Planet)-Mantle. | Earth (Planet)-Crust.
Classification: LCC QE509.4 .M358 2021 (print) | LCC QE509.4 (ebook) | DDC 511.1/16-dc23
LC record available at <https://lcn.loc.gov/2021001626>
LC ebook record available at <https://lcn.loc.gov/2021001627>

Cover Design: Wiley

Cover Image: Synchrotron X-ray diffraction image collected in a high-pressure/-temperature diamond-anvil cell experiment to determine the deformation behavior of (Mg,Fe)O ferropericlasite; © Courtesy of Hauke Marquardt

Set in 10/12pt Times New Roman by Straive, Pondicherry, India

We truly hope the multidisciplinary research in this book represents the philosophy and spirit of her science, and believe that the research compiled here builds on her broad contributions to the understanding of mantle convection over the last decades.

Dedication

We would like to dedicate this book to Louise Kellogg (1959–2019).

CONTENTS

List of Contributors ix

Preface xiii

Part I: State of the Mantle: Properties and Dynamic Evolution

- 1 Long-Wavelength Mantle Structure: Geophysical Constraints and Dynamical Models**
Maxwell L. Rudolph, Diogo L. Lourenço, Pritwiraj Moulik, and Vedran Lekić 3
- 2 Experimental Deformation of Lower Mantle Rocks and Minerals**
Lowell Miyagi 21
- 3 Seismic Wave Velocities in Earth's Mantle from Mineral Elasticity**
Johannes Buchen 51
- 4 From Mantle Convection to Seismic Observations: Quantifying the Uncertainties Related to Anelasticity**
Bernhard S. A. Schuberth and Tobias Bigalke 97
- 5 Geochemical Diversity in the Mantle**
Takeshi Hanyu and Li-Hui Chen 121
- 6 Tracking the Evolution of Magmas from Heterogeneous Mantle Sources to Eruption**
Ananya Mallik, Sarah Lambart, and Emily J. Chin 151
- 7 Super-Deep Diamonds: Emerging Deep Mantle Insights from the Past Decade**
Evan M. Smith and Fabrizio Nestola 179
- 8 Seismic and Mineral Physics Constraints on the D" Layer**
Jennifer M. Jackson and Christine Thomas 193
- 9 Toward Consistent Seismological Models of the Core–Mantle Boundary Landscape**
Paula Koelemeijer 229

Part II: Material Transport Across the Mantle: Geophysical Observations and Geodynamic Predictions

- 10 Dynamics of the Upper Mantle in Light of Seismic Anisotropy**
Thorsten W. Becker and Sergei Lebedev 259
- 11 Mantle Convection in Subduction Zones: Insights from Seismic Anisotropy Tomography**
Zhouchuan Huang and Dapeng Zhao 283
- 12 The Cycling of Subducted Oceanic Crust in the Earth's Deep Mantle**
Mingming Li 303
- 13 Toward Imaging Flow at the Base of the Mantle with Seismic, Mineral Physics, and Geodynamic Constraints**
Andy Nowacki and Sanne Cottaar 329
- 14 Seismic Imaging of Deep Mantle Plumes**
Jeroen Ritsema, Ross Maguire, Laura Cobden, and Saskia Goes 353

Part III: Surface Expressions: Mantle Controls on Planetary Evolution and Habitability

15 Observational Estimates of Dynamic Topography Through Space and Time
Mark Hoggard, Jacqueline Austermann, Cody Randel, and Simon Stephenson 373

16 Connecting the Deep Earth and the Atmosphere
Trond H. Torsvik, Henrik H. Svensen, Bernhard Steinberger, Dana L. Royer, Dougal A. Jerram, Morgan T. Jones, and Mathew Domeier 413

17 Mercury, Moon, Mars: Surface Expressions of Mantle Convection and Interior Evolution of Stagnant-Lid Bodies
Nicola Tosi and Sebastiano Padovan 455

Index 491

LIST OF CONTRIBUTORS

Jacqueline Austermann

Lamont-Doherty Earth Observatory
Columbia University
New York, NY, USA

Thorsten W. Becker

Institute for Geophysics
Jackson School of Geosciences
The University of Texas at Austin
Austin, TX, USA;

and

Department of Geological Sciences
Jackson School of Geosciences
The University of Texas at Austin
Austin, TX, USA

Tobias Bigalke

Department of Earth and Environmental Sciences
Ludwig-Maximilians-Universität München
Munich, Germany

Johannes Buchen

Seismological Laboratory
California Institute of Technology
Pasadena, CA, USA

Li-Hui Chen

Department of Geology
Northwest University
Xian, China

Emily J. Chin

Scripps Institution of Oceanography
University of California San Diego
La Jolla, CA, USA

Laura Cobden

Department of Earth Sciences
Utrecht University
Utrecht, The Netherlands

Sanne Cottaar

Department of Earth Sciences
University of Cambridge
Cambridge, UK

Mathew Domeier

Centre for Earth Evolution and Dynamics
University of Oslo
Oslo, Norway

Saskia Goes

Department of Earth Science and Engineering
Imperial College London
London, UK

Takeshi Hanyu

Research Institute for Marine Geodynamics
Japan Agency for Marine-Earth Science and Technology
Yokosuka, Japan

Mark Hoggard

Department of Earth & Planetary Sciences
Harvard University
Cambridge, MA, USA;

and

Lamont-Doherty Earth Observatory
Columbia University
New York, NY, USA

Zhouchuan Huang

School of Earth Sciences and Engineering
Nanjing University
Nanjing, China

Jennifer M. Jackson

Seismological Laboratory
California Institute of Technology
Pasadena, CA, USA

Dougal A. Jerram

Centre for Earth Evolution and Dynamics
University of Oslo
Oslo, Norway;

and

DougalEARTH Ltd.

Solihull, UK;

and

Earth, Environmental and Biological Sciences
Queensland University of Technology
Brisbane, Queensland, Australia

Morgan T. Jones

Centre for Earth Evolution and Dynamics
University of Oslo
Oslo, Norway

Paula Koelemeijer

Department of Earth Sciences
Royal Holloway University of London
Egham, UK;
and

Department of Earth Sciences
University College London
London, UK

Sarah Lambart

Department of Geology and Geophysics
University of Utah
Salt Lake City, UT, USA

Sergei Lebedev

Dublin Institute for Advanced Studies
Dublin, Ireland

Vedran Lekić

Department of Geology
University of Maryland
College Park, MD, USA

Mingming Li

School of Earth and Space Exploration
Arizona State University
Tempe, AZ, USA

Diogo L. Lourenço

Department of Earth and Planetary Sciences
University of California
Davis, CA, USA

Ross Maguire

Department of Geology
University of Maryland
College Park, MD, USA

Ananya Mallik

Department of Geosciences
University of Arizona
Tucson, AZ, USA

Lowell Miyagi

Geology and Geophysics
University of Utah
Salt Lake City, UT, USA

Pritwiraj Moulik

Department of Geology
University of Maryland
College Park, MD, USA

Fabrizio Nestola

Department of Geosciences
University of Padova
Padua, Italy

Andy Nowacki

School of Earth and Environment
University of Leeds
Leeds, UK

Sebastiano Padovan

Deutsches Zentrum für Luft- und Raumfahrt
Institute of Planetary Research
Berlin, Germany;
and
WGS, Flight Dynamics
EUMETSAT
Darmstadt, Germany

Cody Randel

Lamont-Doherty Earth Observatory
Columbia University
New York, NY, USA

Jeroen Ritsema

Department of Earth and Environmental Sciences
University of Michigan
Ann Arbor, MI, USA

Dana L. Royer

Department of Earth and Environmental Sciences
Wesleyan University
Middletown, CT, USA

Maxwell L. Rudolph

Department of Earth and Planetary Sciences
University of California, Davis
Davis, CA, USA

Bernhard S. A. Schubert

Department of Earth and Environmental Sciences
Ludwig-Maximilians-Universität München
Munich, Germany

Evan M. Smith

Gemological Institute of America
New York, NY, USA

Bernhard Steinberger

Helmholtz Centre Potsdam
GFZ German Research Centre for Geosciences
Potsdam, Germany;

and

Centre for Earth Evolution and Dynamics
University of Oslo
Oslo, Norway

Simon Stephenson

Department of Earth Sciences
University of Oxford
Oxford, UK

Henrik H. Svensen

Centre for Earth Evolution and Dynamics
University of Oslo
Oslo, Norway

Christine Thomas

Institut für Geophysik
Westfälische Wilhelms-Universität
Münster, Germany

Trond H. Torsvik

Centre for Earth Evolution and Dynamics
University of Oslo
Oslo, Norway;
and
School of Geosciences
University of Witwatersrand
Johannesburg, South Africa

Nicola Tosi

Deutsches Zentrum für Luft- und Raumfahrt
Institute of Planetary Research
Berlin, Germany

Dapeng Zhao

Department of Geophysics
Tohoku University
Sendai, Japan

PREFACE

Convection in Earth's mantle is linked to plate tectonic processes and controls the fluxes of heat and material between deep mantle reservoirs, the surface, and the atmosphere over billions of years. A better understanding of these mantle material cycles and their impact on the long-term evolution of our planet, as well as their potential role on other planetary bodies, requires integrated approaches that involve all disciplines studying the solid Earth.

Over the past decades, the rise in geophysical data has provided increasingly sharp images of the deep mantle, including direct images of sinking slabs and rising plumes. Increasingly accurate and novel types of geochemical data of hotspot lavas provide a detailed account of the spectrum and origin of mantle heterogeneity. Models of mantle convection make predictions on the distribution of this heterogeneity through time, and on the evolution of our planet from accretion to the present-day. In turn, mineral physics provides increasingly realistic material properties needed to interpret the geophysical observables and constrain geodynamic models. This profound progress in the deep Earth Sciences has even advanced neighboring fields such as Planetary Sciences, Cosmochemistry, and Astrobiology, for example by providing insight into the conditions for habitability on the timescales of biological evolution, and thus, for the sustainability of higher life.

This AGU book unifies researchers with an expertise in different solid Earth disciplines, including observational geophysics, numerical modelling, geochemistry and mineral physics, to outline current concepts on dynamic processes occurring in the mantle and associated material cycles. Since each sub-discipline is restricted by fundamental uncertainties, true progress is increasingly made at the intersection between different sub-disciplines. The present book is hence devoted to synergetic multi-disciplinary work, motivated by the vision of a holistic picture of the deep Earth.

Despite the common call for trans-disciplinary research, only limited work has been done that truly and quantitatively integrates different approaches. Sometimes, just the lack of a common language, with different jargon across discipline boundaries, prevents any directed and sustainable progress. It is our hope that this AGU book can help to bridge the gaps between different Earth Science communities, resolve some semantic issues, and foster future collaborations. We attempted to ensure that chapters are written in a style accessible for researchers

from all sub-disciplines. It is up to the reader to decide if we succeeded.

This book does not aim to provide a comprehensive overview of all relevant research strands. Instead, we aim to cover a wide range of relevant topics and emphasize the interdisciplinary connection between them. As the overarching idea of the book is to bridge between the disciplines, the subsections of the book are not sorted by discipline, but instead by guiding research questions.

The first part of the book summarizes the current state of the mantle, its properties and dynamic evolution. This is followed by part two, which discusses the transport of heat and material through the mantle, as constrained by geophysical observations and geodynamic model predictions. The final part of the book focuses on the surface expressions of mantle dynamics and its control on planetary evolution and habitability.

PART I: STATE OF THE MANTLE: PROPERTIES AND DYNAMIC EVOLUTION

The viscosity of the mantle governs large-scale material flow within our planet and ultimately dictates the interaction between Earth's deep interior and surface geology. The first chapter of this book, contributed by **Maxwell Rudolph et al.**, focuses on the viscosity profile of the mid- and lower mantle and examines its connection to mantle dynamics. Based on analysis of the geoid and seismic tomographic models, the authors favor the presence of a low-viscosity channel in the mid-mantle.

Mantle dynamic processes and relevant properties, including mantle viscosity, are governed by the physical behavior of mantle minerals and rocks. **Lowell Miyagi** reviews the progress made in the experimental study of the plastic behavior of lower mantle materials at high pressures and temperatures. While the overwhelming amount of past experiments on lower-mantle deformation has been performed on mono-mineralic samples, he emphasizes the importance of understanding the effective rheology of rocks, which may behave dramatically different than the sum of their parts as a result of strain-partitioning between the minerals.

The interpretation of seismic observations always critically relies on our knowledge about the elastic properties of Earth's mantle materials at the conditions expected at depth. This information is largely derived from

high-pressure/-temperature experiments as well as computations. **Johannes Buchen** reviews the current state of high-pressure/-temperature elasticity measurements and outlines future directions. Exemplarily, he discusses the possible effect of the iron spin transition in ferropericlase, and evaluates the potential to resolve compositional variations in the mantle from seismic observations.

Geophysical observations, and their interpretation, can only provide a snapshot of the current state of Earth's mantle, but do not directly constrain the causative history of mantle-dynamic processes. **Bernhard Schuberth and Tobias Bigalke** review approaches to quantitatively link predictions from dynamic mantle evolution models to present-day seismological observations. After providing a general overview of past works, they focus on the importance of better constraining anelastic effects and their uncertainties to interpret seismic observations, as may be constrained by future mineral physics work.

Complementary constraints on compositional heterogeneity within the Earth's mantle, and thus on mantle convection and material cycles between the surface and the mantle, are provided through the analysis of trace elements and isotope ratios in various basaltic rocks exposed on Earth's surface. **Takeshi Hanyu and Li-Hui Chen** review our current understanding of chemical diversity in the mantle, as derived from the composition of surface basalts. They highlight some recent alternative models, and discuss implications for the deep cycling of volatile elements.

Part of the geochemical variation described in the chapter on isotopic data could result from selective sampling of the mantle through melting of different source lithologies as a function of pressure and temperature. **Ananya Mallik et al.** examine the role of melting a mantle assemblage of different lithologies, melt-rock reaction, and magma differentiation for the genesis of mid-ocean ridge basalts (MORB), ocean island basalts (OIB), and volcanic arcs.

Diamonds provide complementary information on the composition and mineralogy of the deep mantle. Tiny mineral and glass inclusions in diamonds directly sample the petrology of the deep Earth, providing constraints on its chemistry and mineralogy beyond those derived through the interpretation of geophysical observations and geochemical analyses of surface volcanic rocks. **Evan Smith and Fabrizio Nestola** summarize the progress in this field during the last decade, focusing on findings of major relevance to our understanding of deep Earth material and volatile cycles.

The D" layer in the lowermost mantle is characterized by several unique geophysical features that are distinct from the bulk of the lower mantle, including ultralow velocity zones, ULVZ. **Jennifer Jackson and Christine Thomas** contribute a review of seismic observables and

their possible interpretations based on mineral-physics data, and present a case study focusing on the deep mantle below the Bering Sea and Alaska.

Paula Koelemeijer discusses the challenges involved in determining the topography of the core–mantle boundary (CMB) from geodynamic and seismic constraints. She highlights the close correlation with the density structure in the lowermost mantle and its association with the observed large low shear velocity provinces (LLSVP) as are observed under Africa and the Pacific. She concludes that more work is needed to better constrain CMB topography, which would be a critical step toward understanding the nature of LLSVPs and their relationship to mantle dynamics.

PART II: MATERIAL TRANSPORT ACROSS THE MANTLE: GEOPHYSICAL OBSERVATIONS AND GEODYNAMIC PREDICTIONS

When combined with mineral physics constraints, observations of seismic anisotropy in Earth's mantle can be used to infer mantle flow patterns and understand material transport through the mantle. **Thorsten Becker and Sergei Lebedev** summarize seismic anisotropy observations made in the upper mantle and discuss their relation to laboratory measurements. It is shown that regional convection patterns can be resolved using anisotropy observations, but uncertainties remain and systematic relationships need to be further refined and established.

An essential regional component of mantle convection is the subduction and deep cycling of oceanic lithosphere. Indeed, the sinking of subducted slabs through the mantle is a key driver of mantle circulation and plate tectonics. **Zhouchuan Huang and Dapeng Zhao** discuss the analysis of seismic anisotropy in subduction zone settings that is used to infer deformation and flow patterns around subducting slabs in the upper mantle.

Subducted oceanic crust often descends deep into the mantle, commonly reaching the core–mantle boundary. Understanding the fate of subducted material and its chemical interaction with the surrounding mantle is pivotal to our understanding of deep Earth material cycles, the interpretation of geophysical heterogeneity, and the diversity of geochemical signatures found in surface rocks. **Mingming Li** reviews our understanding of the distribution, physical behavior and chemical interaction of subducted oceanic crust in the deep mantle that emerges by integrating evidence from different disciplines.

In regions where subducting slabs reach the core–mantle boundary, they may cause deformation strong enough to induce seismic anisotropy, in a similar way as discussed above for the upper mantle. **Andy Nowacki and Sanne Cottaar** explore the potential and limitations

of multidisciplinary approaches to infer deep mantle flow from recent observations of lowermost mantle seismic anisotropy.

While the downwelling limbs of mantle convection are commonly observed in seismic images, at least in some cases from the surface to the core–mantle boundary (see above), the nature of upwellings remains more under-resolved and uncertain. However, while their existence has been highly debated for a long time, researchers now converge towards a consensus in terms of the sheer existence and nature of plume-like upwellings. **Jeroen Ritsema et al.** report on the challenges involved in imaging mantle plumes by seismic methods. They conclude that the deployment of seismic receivers on the ocean floors would lead to a significant advancement in our ability to image the interior of our planet in general, and mantle plumes in particular.

PART III: SURFACE EXPRESSIONS: MANTLE CONTROLS ON PLANETARY EVOLUTION AND HABITABILITY

An important surface expression of mantle dynamics is dynamic topography. Dynamic topography arises directly from mantle flow and the related stresses at the base of the lithosphere. It thus contains information about the density structure of the mantle. The study of dynamic topography can potentially provide a picture of Earth's mantle flow and structure through time, when coupled with geological constraints of subsidence and uplift. **Mark Hoggard et al.** review the progress made in quantifying dynamic topography, summarize the inherent limitations, and point out future research directions.

Trond Torsvik et al. bring together the main topics discussed in this book in a single chapter. They discuss the

role of mantle upwellings (plumes) and downwellings (slabs) on atmospheric evolution and climate. Plume heads may rise from the margins of LLSVPs and sustain flood-basalt volcanism, outgassing and silicate weathering at the surface. Slab subduction and related arc volcanism, in turn, control the ingassing of atmospheric species, including greenhouse gases. Together, these key ingredients of mantle convection stabilize Earth's long-term atmospheric conditions, climate, and habitability.

While Earth's surface is currently reshaped by plate tectonic processes that are intimately linked to mantle convection, other terrestrial bodies in the solar system display a stagnant lid that does not participate in underlying mantle convection. In other words, the surfaces of these planets consist of just one single plate with very restricted surface deformation. **Nicola Tosi and Sebastiano Padovan** present key processes and observations to understand mantle convection in the stagnant-lid regime, which is much more common in our solar system, and most probably throughout the universe, than the plate-tectonic regime. The comparison of mantle convection styles in both these regimes leads to a more coherent picture of planetary interior dynamics and evolution.

Hauke Marquardt

University of Oxford, UK

Maxim Ballmer

University College London, UK

Sanne Cottaar

University of Cambridge, UK

Jasper Konter

University of Hawaii at Mānoa, USA

Part I

State of the Mantle: Properties and Dynamic Evolution

Long-Wavelength Mantle Structure: Geophysical Constraints and Dynamical Models

Maxwell L. Rudolph¹, Diogo L. Lourenço¹, Pritwiraj Moulik², and Vedran Lekić²

ABSTRACT

The viscosity of the mantle affects every aspect of the thermal and compositional evolution of Earth's interior. Radial variations in viscosity can affect the sinking of slabs, the morphology of plumes, and the rate of convective heat transport and thermal evolution. Below the mantle transition zone, we detect changes in the long-wavelength pattern of lateral heterogeneity in global tomographic models, a peak in the the depth-distribution of seismic scatterers, and changes in the dynamics plumes and slabs, which may be associated with a change in viscosity. We analyze the long-wavelength structures, radial correlation functions, and spectra of four recent global tomographic models and a suite of geodynamic models. We find that the depth-variations of the spectral slope in tomographic models are most consistent with a geodynamic model that contains both a dynamically significant phase transition and a reduced-viscosity region at the top of the lower mantle. We present new inferences of the mantle radial viscosity profile that are consistent with the presence of such a feature.

1.1. INTRODUCTION

Heterogeneity in Earth's mantle is dominated by its very long-wavelength components in the upper mantle, transition zone, and the lowermost mantle. Such long-wavelength variations reflect the distribution of the continents and the ocean basins in the uppermost mantle, subducted slabs in the transition zone and the degree-2 dominant continent-sized large low shear velocity provinces (LLSVPs) in the lowermost mantle. The long-wavelength structure of the upper mantle is positively correlated with the lowermost mantle structure (Figure 1.1),

supporting the well-established idea that the lower mantle and lithospheric plate systems mutually interact through subduction and upwelling to produce related large-scale structures. However, the transition zone and shallow lower mantle contain large-scale heterogeneity that is weakly anticorrelated with the upper mantle and lowermost mantle. Observations of deflected upwellings, slab stagnation above and below the 650 km phase transition, the presence of seismic scatterers, and changes in the large-scale pattern of mantle structure suggest the possibility of changes in mantle properties across this region that lack a single agreed-upon explanation.

The presence of faster-than-average material surrounding the pair of LLSVPs in the lowermost mantle can be explained well by models of slab sinking constrained by subduction history, assuming that slabs sink vertically from the trench (Ricard et al., 1993), even when using only the most recent 200 Myr of subduction history. Although

¹Department of Earth and Planetary Sciences, University of California, Davis, CA, USA

²Department of Geology, University of Maryland, College Park, MD, USA

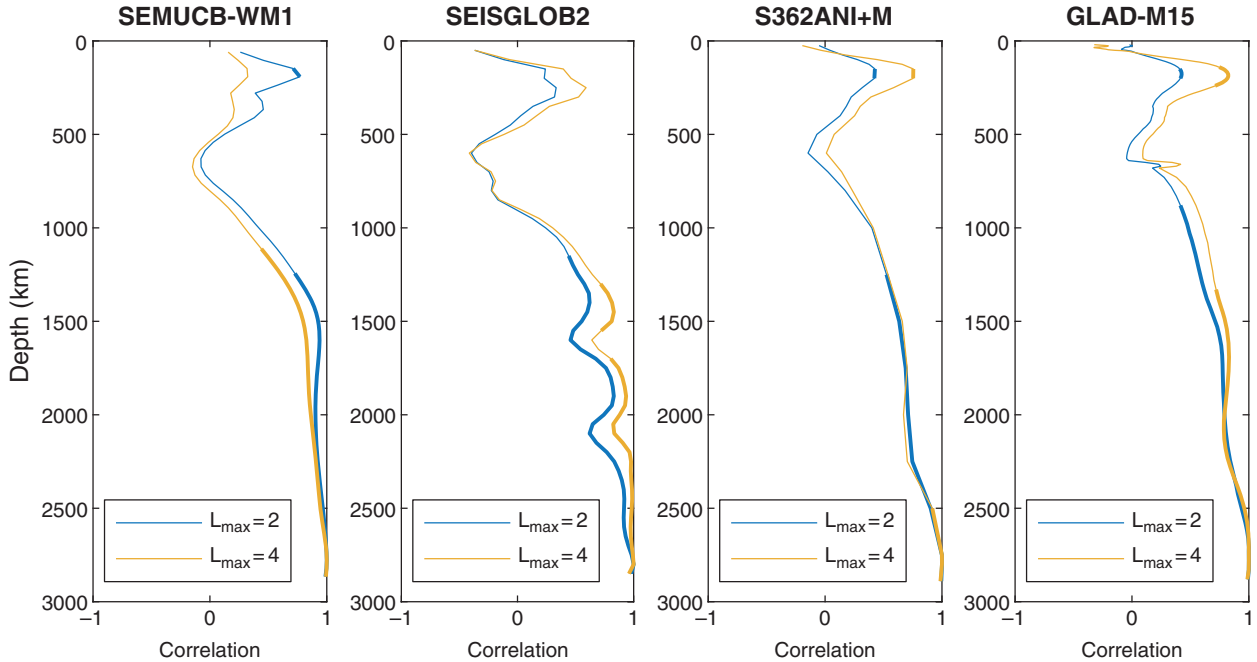


Figure 1.1 Correlation between structure at 2800 km depth and other mantle depths for each of four tomographic models. Correlations for spherical harmonic degrees 1–2 are shown in blue and degrees 1–4 are shown in yellow. Where the curves are thicker, the correlation is significant at the $p = 0.05$ level.

the thermochemical nature of LLSVPs is sometimes debated (e.g., Davies et al., 2015), several lines of evidence now suggest that the LLSVPs are both warmer and compositionally distinct from the surrounding lower mantle. The anti-correlation of shear- and bulk sound speed (Su and Dziewonski, 1997; Masters et al., 2000), sharp boundaries imaged by detailed waveform modeling (e.g., He and Wen, 2009; Wang and Wen, 2007), tidal constraints (Lau et al., 2017), and inferences of density from full-spectrum tomography (e.g., Moulik and Ekström, 2016) are all consistent with a thermochemical rather than purely thermal origin of the LLSVPs. Additional evidence for a thermochemical origin is provided by the distribution of present day hotspots near the interiors and margins of the LLSVPs (Thorne et al., 2004; Burke et al., 2008; Austermann et al., 2014), expected on the basis of laboratory analogue experiments and numerical simulations (Davaille et al., 2002; Jellinek and Manga, 2002), as well as the observation that primitive helium isotope ratios in ocean island basalts are associated with mantle plumes rooted in the LLSVPs (e.g., Williams et al., 2019). The reconstructed eruption locations of large igneous provinces also fall near the present-day boundaries of the LLSVPs (Burke and Torsvik, 2004; Torsvik et al., 2006), which supports the idea that the LLSVPs have been relatively stable over at least the past 200 Myr. Geodynamic models that impose time-dependent, paleogeographically constrained plate motions can produce

chemical piles whose large-scale features are consistent with the morphology of the LLSVPs (e.g., McNamara and Zhong, 2005; Bower et al., 2013; Rudolph and Zhong, 2014).

All recent global tomographic models are generally in very good agreement at long wavelengths in the lowermost mantle (e.g., Becker and Boschi, 2002; Cottaar and Lekic, 2016). The long-wavelength structure, comprising spherical harmonic degrees 1–4, is consistent in the upper and lowermost mantle across four recent global V_S tomographic models (Figure 1.2). However, shear velocity variations across the mantle transition zone and shallow lower mantle appear to shift to a pattern that is weakly anticorrelated with structure in both the asthenosphere and lowermost mantle. This change in large-scale structure, evident in the global maps of V_S variations (Figure 1.2), is also captured by the mantle radial correlation function (RCF), shown in Figure 1.3 (e.g., Jordan et al., 1993; Puster and Jordan, 1994), which measures the similarity of the pattern of structures between every pair of depths in the mantle. Radial correlation analyses of global tomographic models reveal a zone of decorrelation across the transition zone and shallow lower mantle. Some (but not all) recent global shear-wave (e.g., French and Romanowicz, 2014; Durand et al., 2017) and P wave (Fukao and Obayashi, 2013; Obayashi et al., 2013) tomographic models show a dramatic change in the radial correlation structure near

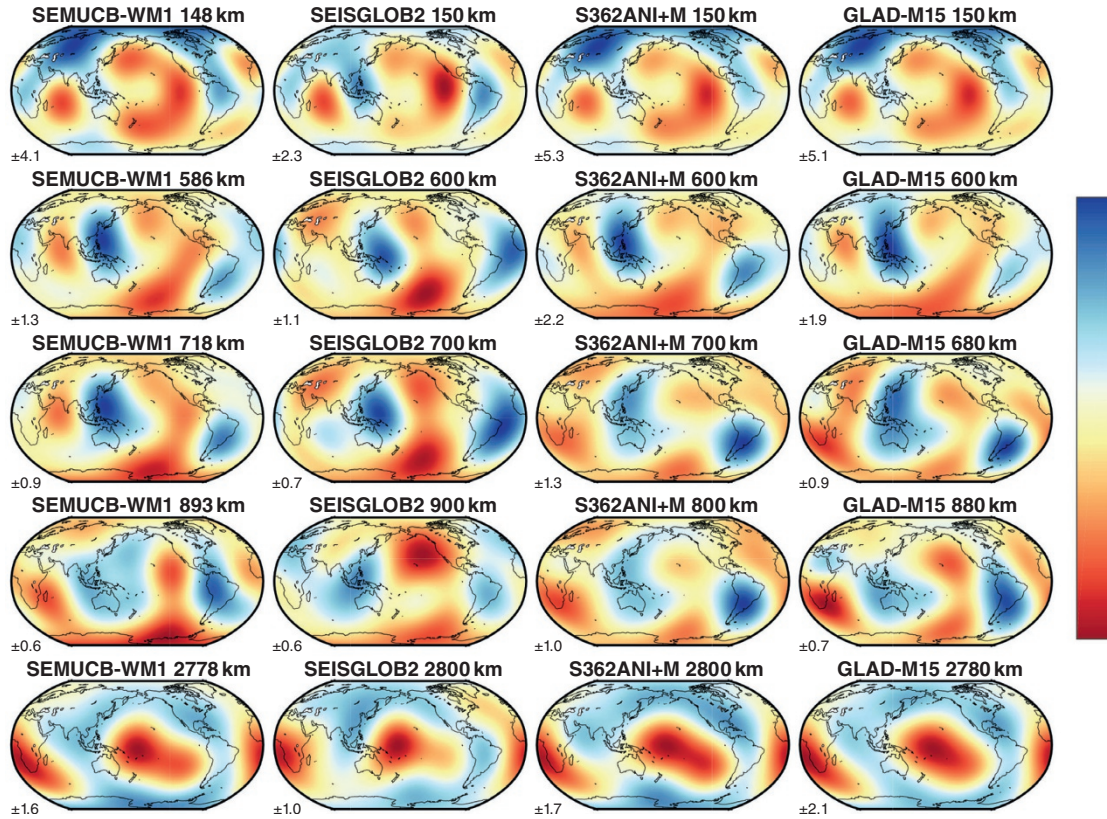


Figure 1.2 Shown here are plots of Voigt V_S variations at spherical harmonic degrees 1–4 from four recent tomographic models at selected depths across the transition zone and shallow lower mantle and within the lowermost mantle and the lithosphere. In each subpanel, the amplitude of the color scale is indicated in percent.

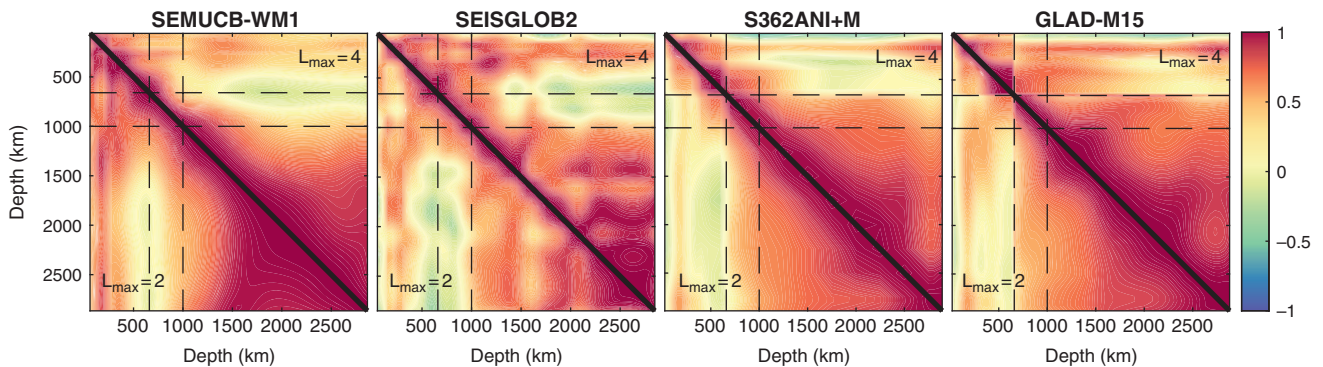


Figure 1.3 Radial correlation functions computed for four recent global tomographic models. The color scale indicates the value of the correlation between structures at different mantle depths. In each panel, the lower-left triangle is the RCF for only spherical harmonic degrees 1–2, while the upper right triangle shows the RCF for degrees 1–4.

1,000 km depth. While the precise depth of the change in the long-wavelength correlation is affected by the data constraints and model parameterization choices of the tomographic models (discussed later), it appears to coincide with other shorter-wavelength features such as

scatterers and deflected plumes, suggesting that they may share a common dynamical origin.

Changes in the continuity and shape of upwelling and downwelling features have been identified in both global and regional tomographic models. The

whole-mantle waveform tomographic model SEMUCB-WM1 (French and Romanowicz, 2014) reveals striking lateral deflections of upwellings beneath several active hotspots. In particular, the imaged plume conduit beneath St. Helena appears to be deflected 1,000–650 km, in contrast to its more vertical shape in the lower mantle below 1,000 km and in the upper mantle and transition zone (French and Romanowicz, 2015). While St. Helena provides perhaps the most striking example, there are also possible deflections near 1,000 km beneath the Canaries and Macdonald (French and Romanowicz, 2015). Regional tomography of the North Atlantic shows some evidence of deflection of the Iceland plume above 1,000 km depth (Rickers et al., 2013), though this is not seen in all regional and global models (French and Romanowicz, 2015; Yuan and Romanowicz, 2017). Regional tomography indicates that the Yellowstone plume is laterally shifted near 1,000 km (Nelson and Grand, 2018). Slabs imaged in the global P wave model GAP-P4 (Obayashi et al., 2013; Fukao and Obayashi, 2013) appear to stagnate within or below the mantle transition zone. The Northern Mariana slab is imaged as a nearly horizontal feature above 1,000 km, the Java slab is stagnant or less steeply inclined above 1,000 km, and the Tonga slab is imaged as a horizontal fast anomaly above 1,000 km (Fukao and Obayashi, 2013). This behavior is not universal; in Central America, there is no evidence for slab ponding or stagnation, and many slabs in the Western Pacific and South America are imaged above 650 km depth.

Seismic scatterers have been identified in the mid-mantle, and their depth-distribution peaks near 1,000 km. Using P -to- S receiver function stacks, Jenkins et al. (2016) located scatterers beneath Europe, Iceland, and Greenland. The scatterers are distributed at depths of ~ 800 –1400 km, with a peak near 1,000 km. In global surveys of seismic reflectors, scatterers are observed in all regions with data coverage, and with no clear association to tectonic province or subduction history (Waszek et al., 2018; Frost et al., 2018). The global distribution of reflectors imaged by Waszek et al. (2018) is quite broadly distributed across the depth range of 850–1300 km with a peak close to 875 km depth. Changes in the distribution of small-scale heterogeneity are also supported by analyses of the spectra of tomographic models. A decrease in the redness in mantle tomographic models occurs below 650 km, coincident with the observations of short-wavelength scattering features, stagnant slabs, and deflected upwellings.

The observational evidence for changes in mantle structure from long-wavelength radial correlation, the behavior of upwellings and downwellings, and the depth- and lateral-distribution of short wavelength scattering features suggests the possibility of changes in mantle

properties and processes in the mid mantle. Several mechanisms have been proposed for such a change, including a change in viscosity (Rudolph et al., 2015) or a change in composition (Ballmer et al., 2015). In the remainder of this chapter, we present new analyses of mantle tomographic models with an eye toward understanding which features in the tomographic models give rise to the changes in the long-wavelength radial correlation structure. Next, we use 3D spherical geometry mantle convection models to assess the implications of different mantle viscosity structures for the development of large-scale structure. Finally, we examine previous and new inferences of the mantle viscosity profile, constrained by the long-wavelength geoid.

1.2. METHODS

1.2.1. Mantle Tomography

We compare the results of the geodynamic modeling with the characteristics of four recent global tomographic V_S models that differ in data selection, theoretical framework, and model parameterization and regularization choices. SEMUCB-WM1 (French and Romanowicz, 2014) is a global anisotropic shear-wave tomographic model based on full-waveform inversion of three-component long-period seismograms, divided into wave-packets containing body waves and surface waves including overtones. Accurate waveform forward modeling is achieved using the spectral element method (Capdeville et al., 2005), 2D finite frequency kernels are computed using nonlinear asymptotic coupling theory (Li and Romanowicz, 1995), and the tomographic model is constructed by iterating using the quasi-Newton method. SEISGLOB2 (Durand et al., 2017) is an isotropic shear-wave model constrained by data sensitive primarily to V_{SV} structure—spheroidal mode splitting functions, Rayleigh wave phase velocity maps, and body wave travel-times. The inverse problem is fully linearized, with sensitivity of normal mode and Rayleigh wave data computed using first order normal mode perturbation theory, and traveltimes data using ray theory, both computed in a reference spherically symmetric model. GLAD-M15 (Bozdağ et al., 2016) is a global tomographic model that, like SEMUCB-WM1, aims to fit full, three-component seismic waveforms. Once again, the spectral element method (Komatitsch and Tromp, 2002) enables accurate forward modeling, while 3D finite frequency kernels are computed using the adjoint method at each iteration. GLAD-M15 uses S362ANI (Kustowski et al., 2008) as a starting model and carries out an iterative conjugate gradient refinement of the 3D velocity structure to match observations while accounting for the full nonlinearity

of the sensitivity of the misfit function to earth structure. The fourth model, S362ANI+M (Moulik and Ekström, 2014), is a global model based on full-spectrum tomography, which employs seismic waveforms and derived measurements of body waves (~ 1 –20s), surface waves (Love and Rayleigh, ~ 20 –300s), and normal modes (~ 250 –3300s) to constrain physical properties – seismic velocity, anisotropy, density, and the topography of discontinuities – at variable spatial resolution. The inverse problem is solved iteratively and jointly with seismic source mechanisms, using sensitivity kernels that account for finite-frequency effects for the long-period normal modes, along-branch coupling for waveforms and ray theory for body-wave travel times and surface-wave dispersion. Model SEISGLOB2 was obtained as spatial expansions of Voigt V_S in netcdf format from the IRIS Data Management Center ([http://ds.iris.edu/ds/products/emc-earthmodels/](http://ds.iris.edu/ds/products/emc-earthmodels/http://ds.iris.edu/ds/products/emc-earthmodels/)). S362ANI+M was provided in netcdf format on a two-degree grid and at 25 depths. GLAD-M15 was provided on a degree-by-degree grid and at 132 depths by the authors (Bozdağ, *pers. comm.*). Model SEMUCB-WM1 was obtained from the authors' web page and evaluated using the model evaluation tool `a3d` on a degree-by-degree grid at 65 depths.

The tomographic models were expanded into spherical harmonics to calculate power spectra and to facilitate wavelength-dependent comparisons among models. First, at each depth, models were resampled using linear interpolation onto 40,962 equispaced nodes, providing a uniform resolution equivalent to 1×1 equatorial degree. Spherical harmonic expansions were carried out using the *slepian* MATLAB routines (Simons et al., 2006). Spherical harmonic coefficients were computed using the 4π -normalized convention, such that the spherical harmonic basis functions Y_{lm} satisfy $\int_{\Omega} Y_{lm} Y_{l'm'} d\Omega = 4\pi \delta_{ll'} \delta_{mm'}$ where Ω is the unit sphere. The power per degree and per unit area σ_l^2 was computed as

$$\sigma_l^2 = \sum_{m=0}^{l_{\max}} (a_{lm}^2 + b_{lm}^2), \quad (1.1)$$

where a_{lm} and b_{lm} are real spherical harmonic coefficients (and $b_{l0} = 0$ for all l). We note that Equation (1.1) is a measure of power per unit area per spherical harmonic degree, and not per spherical harmonic coefficient. This choice differs by a factor of $1/(2l+1)$ from the definitions adopted in Dahlen and Tromp (1998) and used in Becker and Boschi (2002), and our definition omitting the multiplicative prefactor gives the appearance of a flatter power spectrum. Because we use this convention uniformly here, the choice of convention for the normalization of power does not affect our interpretations. From the spherical harmonic power spectra, we computed a spectral slope,

which contains information about the relative amounts of power present at different wavelengths. Multiple definitions of spectral slope have been used with spherical harmonic functions, depending on whether spectral fitting is carried out in log-log or log-linear space. Here, the spectral slope is defined based on a straight-line fit to σ_l^2 vs. l in log-log coordinates, for spherical harmonic degrees 2–20. A slope of zero would indicate uniform power at all spherical harmonic degrees (the power spectrum of a delta function on the sphere (e.g., Dahlen and Tromp, 1998)), and increasingly negative slopes indicate more rapidly decreasing power at shorter wavelengths.

Radial correlation functions (Jordan et al., 1993; Puster and Jordan, 1994; Puster et al., 1995) were calculated from the spherical harmonic expansions. The RCF measures the similarity of δ_V structures at depths z and z' as

$$R_{\delta_V}(z, z') = \frac{\int_{\Omega} \delta_V(z, \theta, \phi) \delta_V(z', \theta, \phi) d\Omega}{\sqrt{\int_{\Omega} \delta_V(z, \theta, \phi)^2 d\Omega} \sqrt{\int_{\Omega} \delta_V(z', \theta, \phi)^2 d\Omega}}. \quad (1.2)$$

where θ and ϕ denote the polar angle and azimuthal angle and Ω refers to integration over θ and ϕ . When working with normalized spherical harmonic functions, the above expression is equivalent to the linear correlation coefficient of vectors of spherical harmonic coefficients representing the velocity variations. Because the denominator of the expression for radial correlation normalizes by the standard deviations of the fields at both depths, the RCF is sensitive only to the pattern and not to the amplitude of velocity variations.

1.2.2. Mantle Circulation Models

We carried out a suite of 3D geodynamic models in spherical geometry using CitcomS version 3.1.1 (Zhong et al., 2000, 2008) with modifications to impose time-dependent plate motions as a surface boundary condition (Zhang et al., 2010). CitcomS solves the equations of mass, momentum, and energy conservation for incompressible creeping (zero Reynolds number) flow under the Boussinesq approximation in 3D spherical shell geometry. All of the models include a compositionally distinct layer (advected using tracers), meant to be analogous to the LLSVP material, which is assigned an excess density of 3.75%, equivalent to a buoyancy ratio of $B = 0.5$. The intrinsic density difference adopted here is chosen such that the compositionally distinct material remains stable against entrainment and is consistent with other geodynamic modeling studies (Mc-Namara and Zhong, 2004, 2005), leading to a net buoyancy compatible with the available constraints from normal modes and solid earth tides Moulik and Ekström (2016); Lau et al. (2017). The compositionally distinct material is initially

present as a uniform layer of 250 km thickness. All of the models include time-dependent prescribed surface plate motions, which shape the large-scale structure of mantle flow. We adopt plate motions from a recent paleogeographic reconstruction by Matthews et al. (2016), which spans 410 Ma-present, although some of the calculations do not include the entire plate motion history. All of the models except Case 40 (Table 1.1) impose the initial plate motions for a period of 150 Myr to spin-up the model and initialize large-scale structure following Zhang et al. (2010). The mechanical boundary conditions at the core-mantle boundary are free-slip, and the temperature boundary conditions are isothermal with a nondimensional temperature of 0 at the surface and 1 at the core-mantle boundary. We use a temperature- and depth-dependent viscosity with the form $\eta(z) = \eta_z(z) \exp[E(0.5 - T)]$, where $\eta_z(z)$ is a depth-dependent viscosity prefactor and $E = 9.21$ is a dimensionless activation energy, which gives rise to relative viscosity variations of 10^4 due to temperature variations. The models are heated by a combination of basal and internal heating, with a dimensionless internal heating rate $Q = 100$.

We include the effects of a phase transition at 660 km depth in some of the models. Phase transitions are implemented in CitcomS using a phase function approach (Christensen and Yuen, 1985). We adopt a density increase across 660 km of 8%, a reference depth of 660 km, a reference temperature of 1573 K, and a phase change width of 40 km. We assume a Clapeyron slope of -2 MPa/K. Recent experimental work favors a range of -2 to -0.4 MPa/K (Fei et al., 2004; Katsura et al., 2003), considerably less negative than values employed in earlier geodynamical modeling studies that produced layered convection (Christensen and Yuen, 1985). The models shown in the present work are a subset of a more exhaustive suite of models from Lourenço and Rudolph (in review), which consider a broader range of convective vigor and additional viscosity structures. We list the parameters that are varied between the five models in Table 1.1 and the radial viscosity profiles used in all of the models are shown in Figure 1.4.

1.2.3. Inversions for Viscosity

We carried out inversions for the mantle viscosity profile constrained by the long-wavelength nonhydrostatic geoid. The amplitude and sign of geoid anomalies depend on the internal mantle buoyancy structure as well as the deflection of the free surface and core-mantle boundary, which, in turn, are sensitive to the relative viscosity variations with depth (Richards and Hager, 1984; Hager et al., 1985). Because the long-wavelength geoid is not very sensitive to lateral viscosity variations (e.g., Richards and Hager, 1989; Ghosh et al., 2010), we neglect these, solving only for the radial viscosity profile. The geoid is not sensitive to absolute variations in viscosity, so the profiles determined here show only relative variations in viscosity, and absolute viscosities could be constrained using a joint inversion that includes additional constraints such as those offered by observations related to glacial isostatic adjustment. In order to estimate the viscosity profile, we first convert buoyancy anomalies from mantle tomographic models into density anomalies and then carry out a forward model to generate model geoid coefficients. We then compare the modeled and observed geoids using the Mahalanobis distance

$$\Phi(\underline{m}) = (\underline{N}_{\text{model}}(\underline{m}) - \underline{N}_{\text{obs}})^{\top} \underline{\underline{C}}_D^{-1} (\underline{N}_{\text{model}}(\underline{m}) - \underline{N}_{\text{obs}}), \quad (1.3)$$

where \underline{N} denotes a vector of geoid spherical harmonic coefficients calculated from the viscosity model with parameters \underline{m} , $\underline{\underline{C}}_D$ is the data-plus-forward-modeling covariance matrix. The Mahalanobis distance is an L_2 -norm weighted by an estimate of data+forward modeling uncertainty, and is sensitive to both the pattern and amplitude of misfit.

We used geoid coefficients from the GRACE geoid model GGM05 (Ries et al., 2016) and the hydrostatic correction from Chambat et al. (2010). We use a transdimensional, hierarchical, Bayesian approach to the inverse problem (e.g., Sambridge et al., 2013), based on the methodology described in (Rudolph et al., 2015). We carry out

Table 1.1 Summary of parameters used in geodynamic models. z_{lm} denotes the depth of the viscosity increase between the upper and lower mantle and $\Delta\eta_{lm}$ is the magnitude of the viscosity increase at this depth. LVC indicates whether the model includes a low-viscosity channel below 660 km. Spinup time is the duration for which the initial plate motions are imposed prior to the start of the time-dependent plate model. We indicate whether the model includes the endothermic phase transition, which always occurs at a depth of 660 km and with Clapeyron slope -2 MPa/K.

Case	z_{lm}	$\Delta\eta_{lm}$	LVC?	Spinup time	Phase transition?	Start time
Case 8	660 km	100	No	150 Myr	No	400 Ma
Case 9	660 km	30	No	150 Myr	No	400 Ma
Case 18	1000 km	100	No	150 Myr	Yes	400 Ma
Case 32	660 km	100	No	150 Myr	Yes	400 Ma
Case 40	660 km	100	Yes	0 Myr	Yes	250 Ma

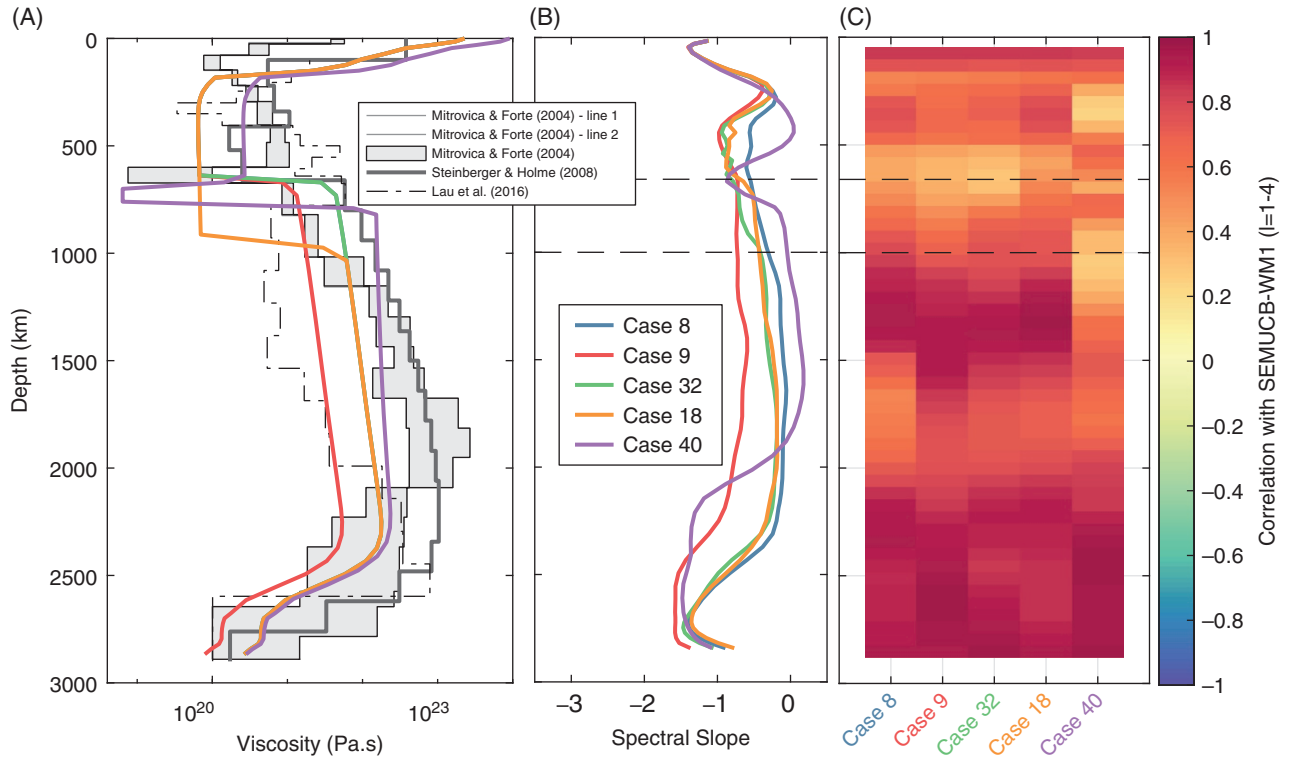


Figure 1.4 (A) Viscosity profiles used in our geodynamic models. For comparison, we also show viscosity profiles obtained in a joint inversion constrained by glacial isostatic adjustment (GIA) and convection-related observables (Mitrovia and Forte (2004) Figure 1.4B), a combination of geoid, GIA, geodynamic constraints (Case C from Steinberger and Holme (2008)) and a joint inversion of GIA data including the Fennoscandian relaxation spectrum (Fig. 12 from Lau et al. (2016)). (B) Spectral slope vs. depth computed from the dimensionless temperature field of the geodynamic models. (C) Correlation at spherical harmonic degrees 1–4 between each of the geodynamic models and SEMUCB-WM1.

forward models of the geoid using the propagator matrix code HC (Hager and O’Connell, 1981; Becker et al., 2014). Relative to our previous related work (Rudolph et al., 2015), the inversions presented here differ in their treatment of uncertainty, scaling of velocity to density variations, and parameterization of radial viscosity variations.

We inferred density anomalies from two different tomographic models. First, we used SEMUCB-WM1 and scaled Voigt V_S anomalies to density using a depth-dependent scaling factor for a pyrolitic mantle composition along a 1600 K mantle adiabat, calculated from thermodynamic principles using HeFESTo Stixrude and Lithgow-Bertelloni, 2011). Second, we used a whole-mantle model of density variations constrained by full-spectrum tomography (Moulik and Ekström, 2016). This model, hereafter referred to as ME16-160, imposes a best data-fitting scaling factor between density and V_S variations of $d \ln \rho / d \ln V_S = 0.3$ throughout the mantle. We note that Moulik and Ekström (2016) present a suite of

models with different choices for data weighting and preferred correlation between density variations and V_S variations in the lowermost mantle. The specific model used here ignores sensitivity to the density-sensitive normal modes (data weight $w_{0,S_2} = 0$) and imposes strong $V_S - \rho$ correlation in the lowermost mantle ($\gamma_\rho^{D''} = 10^{11}$). While this model is not preferred by seismic data, these choices produce a density model that closely resembles a scaled V_S model in the lowermost mantle. We note that the assumption of purely thermal contributions to density is unlikely to be correct in the lowermost mantle, where temperature and compositional variations both contribute to density variations. However, this assumption should not affect our inferences of viscosity, for two reasons. First, previous viscosity inversions found that removing all buoyancy structure from the bottom 1,000 km of the mantle did not significantly influence the retrieved viscosity profile (Rudolph et al., 2015). This is confirmed by inversions for a four-layer viscosity structure constrained by thermal vs. thermochemical mantle buoyancy Liu and Zhong

(2016). Second, geodynamic models of thermochemical convection suggest that the thermal buoyancy above the LLSVPs counteracts the thermal and chemical buoyancy of the compositionally distinct LLSVPs, resulting in only a very small net contribution to the long-wavelength geoid from the bottom 1,000 km of the mantle (Liu and Zhong, 2015).

In the inversions using SEMUCB-WM1, we assume a diagonal covariance matrix to describe the data and forward modeling uncertainty on geoid coefficients, i.e., uncorrelated errors and uniform error variance at all spherical harmonic degrees (because the corresponding posterior covariance matrix is not available). For the inversions using ME16-160, we first sample the *a posteriori* covariance matrix of the tomographic model, generating a collection of 10^5 whole-mantle models of density and wavespeed variations. For each of these models, we calculate a synthetic geoid assuming a reference viscosity profile (Model C from *Steinberger and Holme (2008)*). This procedure yields a sample of synthetic geoids from which we calculate a sample covariance matrix that is used to compute the Mahalanobis distance as a measure of viscosity model misfit.

In all of the inversions shown in this chapter, we include a hierarchical hyperparameter that scales the covariance matrix. This parameter has the effect of smoothing the misfit function in model space, and the value of the hyperparameter is retrieved during the inversion, along with the other model parameters. The inversion methodology, described completely in Rudolph et al. (2015), uses a reversible-jump Markov-Chain Monte Carlo (rjMCMC) method (Green, 1995) to determine the model parameters (the depths and viscosity values of control points

describing the piecewise-linear viscosity profile) and the noise hyperparameter (Malinverno, 2002; Malinverno and Briggs, 2004). The rjMCMC method inherently includes an Occam factor, which penalizes overparameterization. Adding model parameters must be justified by a significant reduction in misfit. The result is a parsimonious parameterization of viscosity that balances data fit against model complexity. In general, incorporating additional data constraints or *a priori* information about mantle properties could lead to more complex solutions.

1.3. RESULTS

The power spectra of four recent global tomographic models are shown in Figure 1.5. While S362ANI+M contains little power above spherical harmonic degree 20 due to its long-wavelength lateral parameterization with 362 evenly spaced spline knots, the other models contain significant power at shorter wavelengths that are beyond the scope of this study. In general, the models are dominated by longer wavelengths at all depths. The spectral slope for each model (up to degree 20) is shown in the rightmost panel of Figure 1.5. Increasingly negative spectral slopes indicate that heterogeneity is dominated by long-wavelength features. All of the models generally show a more negative spectral slope in the transition zone than in the upper mantle or the shallow lower mantle, indicating the presence of more long-wavelength V_S heterogeneity within the transition zone and just below the 650 km discontinuity, which we attribute to the lateral deflection of slabs.

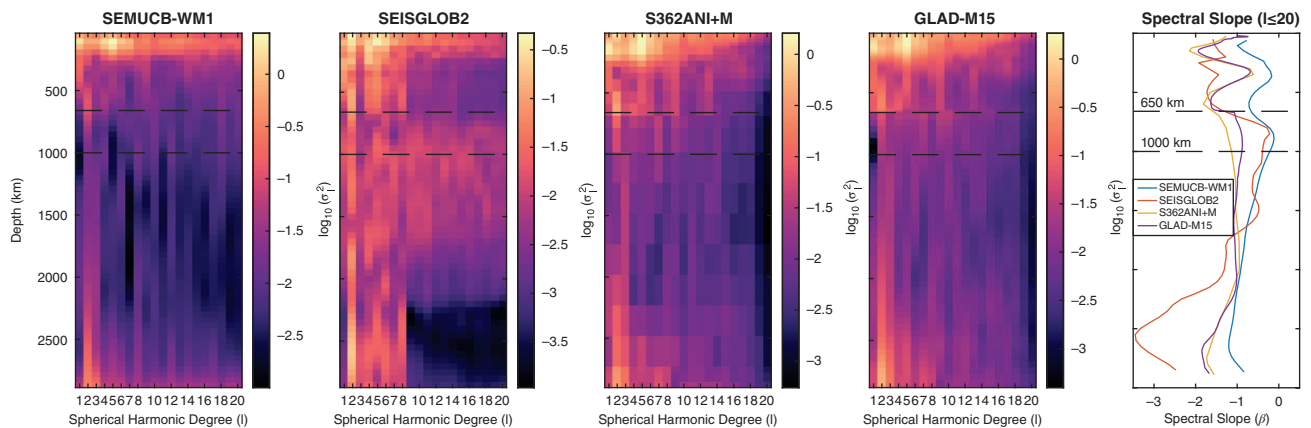


Figure 1.5 Power spectra of four recent global V_S tomographic models. Because our focus is on long-wavelength structure, and to ensure a more equitable comparison, we show only spherical harmonic degrees 1–20, though SEMUCB-WM1, SEISGLOB2, and GLAD-M15 contain significant power at shorter wavelengths. At the right, we show spectral slopes (defined in the text) for the four models. Here, increasingly negative values indicate a concentration of power in longer wavelengths/lower spherical harmonic degrees.

Figure 1.3 shows radial correlation plots for the four tomographic models. Here, the spherical harmonic expansions are truncated at degrees 2 (lower left triangle) and 4 (upper right triangle). At degrees 1–2 and 1–4, both SEMUCB-WM1 and SEISGLOB2 show a clear change in the correlation structure near 1,000 km depth. On the other hand, S362ANI+M and GLAD-M15 both show a change in correlation structure at 650 km.

We compared the character of heterogeneity in the geodynamic models with mantle tomography by calculating the power spectrum and spectral slope of each of the five geodynamic models. Because the depth-variation of power in the geodynamic models does not have as straightforward an interpretation as the V_S power spectra shown for tomographic models, we focus on the spectral slope of the geodynamic models, shown in Figure 1.4. We computed correlation coefficients between each of the geodynamic models and SEMUCB-WM1, shown in Figure 1.4C.

For both of the tomographic models used to infer mantle viscosity, we carried out viscosity inversions (Figure 1.6) constrained by spherical harmonic degree 2 only, degrees 2 and 4 only, and degrees 2–7. The viscosity profiles are quite similar, regardless of which spherical harmonic degrees are used to constrain the inversion. However, we observe an increase in the overall

complexity of the viscosity profile as more spherical harmonic degrees are included, as well as a tendency towards developing a low-viscosity region below the 650 km discontinuity (red curves in Figure 1.6), considered in the context of parsimonious inversions, this tendency toward increased complexity can be attributed to the progressively greater information content of the data. The posterior ensembles from the viscosity inversions contain significant variability among accepted solutions, and the solid lines in Figure 1.6 indicate the log-mean value of viscosity present in the ensemble at each depth while the shaded regions enclose 90% of the posterior solutions. We note that while the individual solutions in the posterior ensemble produce an acceptable misfit to the geoid, the ensemble mean itself may not. Therefore, potential applications in the future need to account for all samples of viscosity models in our ensemble rather than employ or evaluate the ensemble mean in isolation.

1.4. DISCUSSION

The recent tomographic models considered here show substantial discrepancies in the large-scale variations within the mid mantle. The low overall RMS of heterogeneity (with the consequent small contribution to data

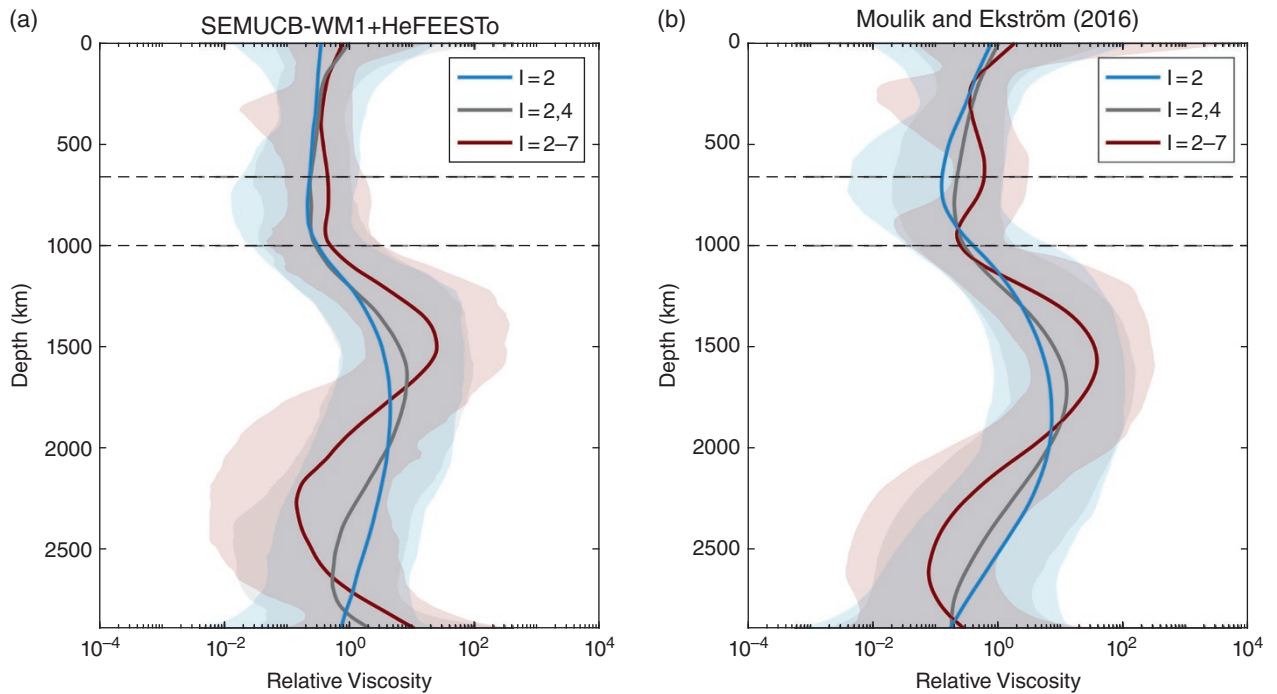


Figure 1.6 Results from transdimensional, hierarchical, Bayesian inversions for the mantle viscosity profile, using two different models for density. (a) Density was scaled from Voigt V_S variations in SEMUCB-WM1 using a depth-dependent scaling factor computed using HeFEESTo (Stixrude and Lithgow-Bertelloni, 2011). (b) Density variations from a joint, whole-model mantle of density and seismic velocities (Moulik and Ekström, 2016)

variance) and a reduction in data constraints at these depths (e.g., normal modes, overtone waveforms) exacerbates the relative importance of *a priori* information (e.g., damping) in some tomographic models. The RCF plots shown in Figure 1.3 show that even at the very long wavelengths characterized by spherical harmonic degrees 1–2 and 1–4, there is rapid change in the RCF near 1,000 km in SEMUCB-WM1 and SEISGLOB2. On the other hand, S362ANI+M and GLAD-M15 both show more evidence for a change in structure near 1,000 km at degrees 1–2 but closer to the 650 km discontinuity for degrees up to 4. In order to understand the changes in the RCF, spatial expansions of the structures in the four tomographic models are shown for degrees 1–4 and at depths within the lithosphere, transition zone, and lowermost mantle are shown in Figure 1.2. We previously examined the long-wavelength structure of SEMUCB-WM1 and suggested that the changes in its RCF at 1,000 km depth are driven primarily by the accumulation of slabs in and below the transition zone in the Western Pacific (Lourenço and Rudolph, in review).

The shift in pattern of mantle heterogeneity within and below the transition zone is influenced by changes in the large-scale structure of plate motions. In Figure 1.7, we show the long-wavelength structure of plate motions at 0, 100, and 200 Ma. We expanded the divergence component of the plate motion model by Matthews et al. (2016) using spherical harmonics and show only the longest-wavelength components of the plate motions. This analysis is similar in concept to the multipole expansion carried out by Conrad et al. (2013) to assess the stability of long-wavelength centers of upwelling, as a proxy for the long-term stability of the LLSVPs. These long-wavelength characteristics of the plate motions need to be interpreted with some caution because the power spectrum of the divergence of plate motions is not always dominated by long-wavelength power, and power at higher degrees may locally erase some of the structure that overlaps with low spherical harmonic degrees (Rudolph and Zhong, 2013). However, for the present day (Figure 1.7, right column), the long-wavelength divergence field does show a pattern of flow with centers of long-wavelength

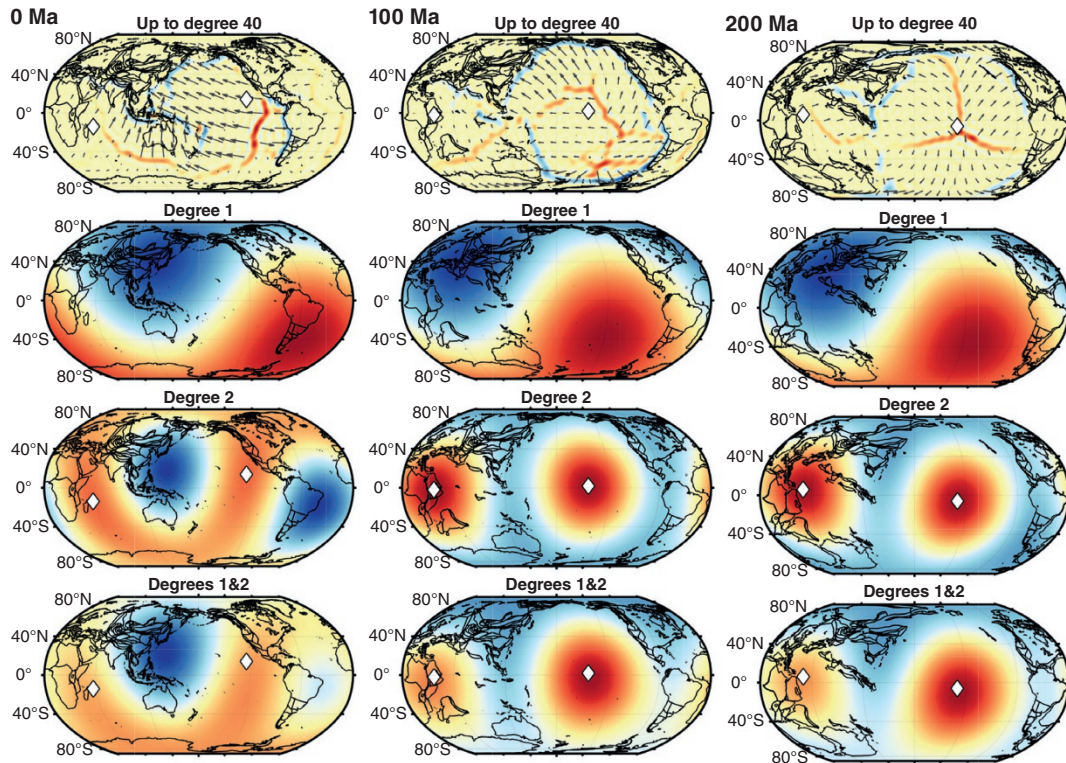


Figure 1.7 Divergence component of plate motions computed for 0, 100, and 200 Ma. In the top row, we show the divergence field up to spherical harmonic degree 40. Red colors indicate positive divergence (spreading) while blue colors indicate convergence. The second row shows only the spherical harmonic degree-1 component of the divergence field, which represents the net motion of the plates between antipodal centers of long-wavelength convergence and divergence. The third row shows the spherical harmonic degree-2 component of the divergence, and the bottom row shows the sum of degrees 1 and 2. The white diamonds in the bottom two rows indicate the locations of the degree-2 divergence maxima (i.e., centers of degree-2 spreading).

convergence centered beneath the Western Pacific and beneath South America, where most of the net convergence is occurring. On the other hand, at 100 and 200 Ma, the pattern of long-wavelength divergence is dominated by antipodal centers of divergence, ringed by convergence. The mid-mantle structures seen in global tomographic models (Figure 1.2) closely resemble the long-wavelength divergence field for 0 Ma, while the lowermost mantle structure is most correlated with the divergence field from 100 and 200 Ma (Figure 1.7). This analysis of the long wavelength components of convergence/divergence and the long-wavelength mantle structure is consistent with analyses of the correlation between subduction history with mantle structure that include shorter wavelength structures (Wen and Anderson, 1995; Domeier et al., 2016). In particular, Domeier et al. (2016) found that the pattern of structure at 600–800 km depth is highly correlated with the pattern of subduction at 20–80 Ma. This suggests a straightforward interpretation of the changes in very long wavelength mantle structure, and the associated RCF, because the present-day convergence has a distinctly different long-wavelength pattern from the configuration of convergence at 50–100 Ma, and the mid-mantle structure is dominated by the more recently subducted material. We note, however, that this explanation addresses only the seismically fast features and does not capture additional complexity associated with active upwellings.

The power spectra of mantle tomographic models contain information about the distribution of the spatial scales of velocity heterogeneity in the mantle, and this can be compared with the power spectra of geodynamic models. Interpreting the relative amounts of power at different wavelength but at a constant depth is more straightforward than the interpretation of depth-variations in power spectral density. In mantle tomography, decreasing resolution with depth as well as the different depth-sensitivities of the seismological observations such as surface wave dispersion, body wave travel times, and normal modes used to constrain tomographic models can lead to changes in power with depth that may not be able to accurately reflect the *true* spectrum of mantle heterogeneity. The geodynamic models presented here have only two chemical components – ambient mantle and compositionally dense pile material. The models are carried out under the Boussinesq approximation, so there is no adiabatic increase in temperature with depth, and the governing equations are solved in nondimensional form. Therefore, to make a direct comparison of predicted and observed shear velocity heterogeneity, many additional assumptions are necessary to map dimensionless temperature variations into wavespeed variations. The effective value of $d \ln V_S / d \ln T$ at constant pressure is depth-dependent, with values decreasing by more than a factor of two from

the asthenosphere to 800 km depth (e.g., Cammarano et al., 2003), and compositional effects become as important as temperature in the lowermost mantle (Karato and Karki, 2001). Here, we compare the temperature spectrum of geodynamic models with the δV_S spectrum in tomographic models, and this is most appropriate at depths where long-wavelength V_S variations are primarily controlled by temperature. For all of the mantle tomographic models considered, there is a local minimum in spectral slope centered on (or slightly above for SEMUCB-WM1) 650 km, reflecting the dominance of long-wavelength structures noted above. Below the base of the transition zone, the spectral slope increases, suggesting the presence of shorter-wavelength velocity heterogeneity. In the lowermost mantle, all of the tomographic models are again dominated by very long-wavelength structures, indicated by a decrease in the power spectral slope. We note that the slope for SEISGLOB2 is quite different from the other models due to the limited power at spherical harmonic degrees above 8 in this model, which may be due to regularization choices and limited sensitivity of their data to short-wavelength structure.

In analyzing the changes in spectral content of tomographic models, we assume that the model spectral content is an accurate reflection of the true spectrum of mantle heterogeneity. A geodynamic study has suggested that there could be substantial aliasing from shorter to longer wavelengths due to model regularization, limited data sensitivities and theoretical assumptions (Schuberth et al., 2009), potentially influencing our inferences of spectral slopes in the transition zone. However, aliasing is likely to be very limited at the wavelengths considered here for three reasons. First, aliasing is expected to be small if the model parameterization is truncated at a spherical harmonic degree where the power spectrum has a rapid falloff with degree (e.g., Mégnin et al., 1997; Boschi and Dziewonski, 1999). Second, a recent model like S362ANI+M uses diverse observations – normal modes, body waves (S, SS, SS precursors), long-period surface waves, and overtone waveforms – whose data variance are dominated by the longest wavelength components and show a clear falloff in power above a corner wave number (e.g., Su and Dziewonski, 1991, 1992; Masters et al., 1996). Third, we note that the spectral slope minimum in the lower part of the transition zone is recovered with models that employ various theoretical approximations.

The geodynamic models all produce long-wavelength structures that are quite similar to tomographic models at the surface and in the lowermost mantle, but there are some distinct differences in the mid-mantle that arise from differences in the viscosity profiles and inclusion or omission of phase transitions. In Figure 1.4c, we show the correlation between each of the convection models and SEMUCB-WM1 as a function of depth, for spherical

harmonic degrees 1-4. All of the models produce structures that are highly correlated with SEMUCB-WM1 in the lithosphere and and lowermost mantle. The former is entirely expected because the lithospheric temperature structure is entirely determined by plate cooling in response to the imposed plate motions, which are well-constrained for the recent past. Similar models have successfully predicted the long-wavelength lowermost mantle structure, which is shaped largely by subduction history (e.g., McNamara and Zhong, 2005; Zhang et al., 2010). Recently, Mao and Zhong (2018; 2019) demonstrated that the inclusion of an endothermic phase transition at 660 km in combination with a low viscosity channel below the transition zone can produce slab behaviors consistent with tomographically imaged structures beneath many subduction zones.

Our Case 40 includes a low-viscosity channel below 660 km and a phase transition but differs from the models shown in Mao and Zhong (2018) in that we use a longer plate motion history and a different plate reconstruction. We find that relative to the other models considered, this model produces the best correlation in long-wavelength structure within and immediately below the mantle transition zone (Figure 1.4c), but poorer overall correlation between c. 800–1,000 km than the other models considered. Intriguingly, the power spectral slope in Case 40 is more similar to the pattern seen in the tomographic models (Figure 1.5) than any of the other cases, showing an increase in the slope of the power spectrum below the base of the transition zone, similar to the feature observed in SEISGLOB2 (Durand et al., 2017). The key parameter that distinguishes this model from the others is the inclusion of the low-viscosity channel, which can have a “lubrication” effect on slabs, allowing them to move laterally below the base of the transition zone. Among the other cases, we can see that there is limited sensitivity of the power spectral slope to whether viscosity is increased at 660 km or 1,000 km depth. Indeed, in Cases 18 (viscosity increase at 1,000 km) and 9 (viscosity increase at 660 km depth), the most significant change in spectral slope is at a depth of 660 km, coincident with the included phase transition. We note that Case 9 has the best overall correlation with the tomographic model due to high values of correlation throughout much of the lower mantle, but does not reproduce structure in the transition zone or shallow lower mantle as well as some of the other models.

In previous work (Rudolph et al., 2015), we presented evidence for an increase in viscosity in the mid-mantle based on inversions constrained by the long-wavelength geoid. The viscosity inversions shown in Figure 1.6 are quite similar to what we found previously, despite different choices in parameterization (piecewise linear variation of viscosity vs. piecewise constant), and the use of a different tomographic model (the density model ME16-160, for

which results are shown in Figure 1.6b). There are key differences in the parameterizations of SEMUCB-WM1 versus the density model ME16-160, especially near the transition zone. SEMUCB-WM1 uses a continuous parameterization in the radial direction using splines, whereas ME16-160, which adopts the same radial parameterization as S362ANI and S362ANI+M (e.g., Kustowski et al., 2008; Moulik and Ekström, 2014), allows a discontinuity in the parameterization at 650 km depth. Moreover, S362ANI+M includes data particularly sensitive to these depths such as normal modes and the precursors to the body wave phase *SS* that reflect off transition-zone discontinuities. As a result, the change in the pattern of heterogeneity from the transition zone to the lower mantle across the 650-km discontinuity is more abrupt in ME16-160 compared to SEMUCB-WM1. The depth and abruptness of changes in structure are exactly the features reflected in the plots of the radial correlation function in Figure 1.3. SEMUCB-WM1 shows a clear decorrelation at 1,000 km depth and a minimum in correlation length at 650 km. On the other hand, S362ANI+M and GLAD-M15 show the most substantial change in correlation structure at 650 km depth and a minimum in correlation at shallower depths in the upper mantle. Given the differences in the depths at which major changes in lateral structure occur in SEMUCB-WM1 vs. ME16-160, one might expect to recover a somewhat different preferred depth of viscosity increase between the upper mantle and lower mantle, because the preferred depth of the viscosity increase is typically very close to the crossover depth from positive to negative sensitivity in the geoid kernel. The fact that viscosity inversions with both tomographic models yield a viscosity increase substantially deeper than 650 km and closer to 1,000 km may therefore be significant.

Some of the inferred viscosity profiles contain a region with reduced viscosity below the 650 km phase transition (Figure 1.6b). The low-viscosity channel emerges as a feature in our ensemble solutions as additional data constraints are added to the inversion, justifying more complex solutions. The low-viscosity region is a pronounced feature in the viscosity profiles based on ME16-160 and there also appears to be a more subtle expression of this feature in the viscosity profiles based on SEMUCB-WM1. Such a feature has been suggested on the basis of several lines of evidence. First, the transition from ringwoodite to bridgmanite plus ferropericlase involves complete recrystallization of the dominant phases present, and multiple mechanisms associated with the phase transition could modify the viscosity. In convective downwellings, the phase transition could be accompanied by a dramatic reduction in grain size to $\sim\mu\text{m}$ size (Solomatov and Reese, 2008). On theoretical grounds, it might be expected that transformational superplasticity could reduce viscosity

by two to three orders of magnitude within 1.5 km of the 650 km phase transition (Panasyuk and Hager, 1998). Second, inversions for the viscosity profile constrained by the global long-wavelength geoid allowed for the presence of a low-viscosity channel at the base of the upper mantle (Forte et al., 1993), and a similar “second asthenosphere” was recovered in inversions constrained by regional (oceanic) geoid anomalies (Kido et al., 1998). The effect of the low-viscosity channel can modify predictions associated with GIA observables Milne et al. (1998), and in joint inversions of GIA, misfits can be significantly reduced for models that include such a low-viscosity notch (Mitrovica and Forte, 2004). Finally, in global geodynamic models with prescribed plate motions, the behavior of slabs is broadly consistent with observations of stagnation when such a feature is included (Mao and Zhong, 2018; Lourenço and Rudolph, in review).

An increase in viscosity in the mid-mantle or viscosity “hill,” which is a feature common to all of our viscosity inversions, has been suggested on the basis of geophysical inversions, and several potential mechanisms exist to explain such a feature. An increase in viscosity below 650 km depth has been recovered in many inversions constrained by the long wavelength geoid and GIA observables (e.g., King and Masters, 1992; Mitrovica and Forte, 1997; Forte and Mitrovica, 2001; Rudolph et al., 2015). An increase in viscosity would be expected to slow sinking slabs (Morra et al., 2010) and affect the dynamics of plumes. The correlation between subduction history and tomographic models has been used to test whether slabs sink at a uniform rate in the lower mantle. A recent study of the similarity between convergence patterns in plate reconstructions and patterns of mantle lateral heterogeneity from an average of V_S tomographic models suggests that the data can neither confirm nor reject the possibility of a change in viscosity below 600 km (Domeier et al., 2016). On the other hand, an analysis of a catalog that relates imaged fast anomalies to specific subduction events does find evidence that the rate of slab sinking decreases across a “slab deceleration zone” between 650–1500 km (van der Meer et al., 2018); one explanation for such a deceleration zone is the increase in viscosity in the shallow lower mantle seen in all of our inverted viscosity profiles.

Several mechanisms exist that could produce an increase in viscosity in the mid-mantle. Marquardt and Miyagi (2015) measured the strength of ferropericlasts at pressures of 20–60 GPa (600–1,000 km) and observed an increase in strength across this range of pressures. Though ferropericlasts are a minor modal component of the lower mantle, it could become rheologically limiting if organized into sheets within rapidly deforming regions, an idea supported by experiments with two-phase analog materials (Kaercher et al., 2016) and with bridgmanite-

magnesiowüstite mixtures (Girard et al., 2016). If the lower mantle rheology is determined by the arrangement of distinct mineral phases, we expect history-dependence and anisotropy of viscosity (Thielmann et al., 2020), further confounding our interpretations of viscosity in inversions. An increase in the viscosity of ferropericlasts is also supported by experimental determinations of the melting temperature at mantle pressures (Deng and Lee, 2017), which show a local maximum in melting temperature for pressures near 40 GPa (1,000 km). Changes in the proportionation of iron could also alter the viscosity of bridgmanite across a depth range consistent with the inferred mid-mantle viscosity increase. Shim et al. (2017) suggested that at depths of 1,100–1,700 km, an increase in the proportionation of iron into ferropericlasts could depress the melting point of bridgmanite, increasing the viscosity predicted using homologous temperature scaling. These various mechanisms are not mutually exclusive and could operate in concert to produce an increase in viscosity near 1,000 km. Finally, we note that the deformation mechanisms of even single phases within the lower mantle remain uncertain. While the lower mantle has long been thought to deform by diffusion creep due to absence of seismic anisotropy at most lower mantle depths, recent calculations suggest that another deformation mechanism – pure climb creep, which is insensitive to grain size and produces no seismic anisotropy – may be active in bridgmanite at lower mantle conditions (Boioli et al., 2017).

1.5. CONCLUSIONS

We analyzed the long-wavelength structure of four recent global tomographic models and compared the features of these models with predicted structures in five geodynamic models that incorporate surface velocity constraints from plate reconstructions. The long-wavelength radial correlation functions of SEMUCB-WM1 and SEISGLOB2 show strong evidence for a change in radial correlation structure near 1,000 km depth, whereas the most abrupt change in the RCFs for S362ANI+M and GLAD-M15 occur at 650 km depth. The change in the RCF reflects a change in the pattern of long-wavelength structure between the lower mantle and transition zone. The transition zone structure is correlated with more recent subduction history, whereas the long-wavelength, lower-mantle structure is more similar to ancient subduction history, in agreement with previous work. The long-wavelength transition zone structure is dominated by seismically fast anomalies in the Western Pacific, and especially beneath the Philippine Sea Plate. This suggests that the change in the pattern of long-wavelength heterogeneity in the transition zone and shallow lower mantle is

controlled by subduction history and by the interaction of slabs with mantle phase transitions and rheological changes. The depth of changes in the pattern of heterogeneity in the models (and the associated RCFs) is sensitive to the data used to constrain the inversions and the radial parameterizations. Future studies that investigate whether these changes in long-wavelength structure occur at 650 km depth or somewhat deeper within the lower mantle will have important implications for our understanding of mantle structure and dynamics. All of the tomographic models show a local minimum in the spectral slope at or slightly above 650 km, indicating concentration of power at longer wavelengths within the transition zone. This feature is most consistent with a global geodynamic model that includes a weakly endothermic (-2 MPa/K) phase transition at 660 km depth and a low viscosity channel below 660 km and a viscosity increase in the shallow lower mantle. New inferences of the viscosity profile (Figure 1.6) using both a whole-mantle density model from full-spectrum tomography (Moulik and Ekström, 2016) and a scaled V_S model (SEMUCB-WM1, French and Romanowicz (2014)), recover viscosity profiles that are compatible with the presence of a low-viscosity channel below 660 km depth and a viscosity maximum in the mid-mantle.

ACKNOWLEDGMENTS

The authors thank John Hernlund and Fred Richards for their reviews, which improved the quality and clarity of the manuscript. The authors thank Ebru Bozdağ for providing the GLAD-M15 tomographic model and for helpful discussions about this model. All of the authors acknowledge support from the National Science Foundation through NSF Geophysics grant EAR-1825104, and MLR acknowledges NSF CSEDI grant EAR-1800450. Computational resources were provided through NSF Major Research Instrumentation grant DMS-1624776 to Portland State University and by UC Davis. VL acknowledges support from the Packard Foundation.

REFERENCES

- Austermann, J., B. T. Kaye, J. X. Mitrovica, & P. Huybers (2014). A statistical analysis of the correlation between large igneous provinces and lower mantle seismic structure. *Geophysical Journal International*, *197*(1), 1–9, doi:10.1093/gji/ggt500.
- Ballmer, M. D., N. C. Schmerr, T. Nakagawa, & J. Ritsema (2015). Compositional mantle layering revealed by slab stagnation at ~ 1000 -km depth. *Science Advances*, *1*(11), e1500815, doi:10.1126/sciadv.1500815.
- Becker, T. W., & L. Boschi (2002). A comparison of tomographic and geodynamic mantle models. *Geochemistry, Geophysics, Geosystems*, *3*(1), 1003–n/a, doi:10.1029/2001GC000168.
- Becker, T. W., C. O'Neill, & B. Steinberger (2014). HC, a global mantle circulation solver.
- Boioli, F., P. Carrez, P. Cordier, B. Devincere, K. Gouriet, P. Hirel, A. Kraych, & S. Ritterbex (2017). Pure climb creep mechanism drives flow in Earth's lower mantle. *Science Advances*, *3*(3), e1601958, doi:10.1126/sciadv.1601958.
- Boschi, L., & A. M. Dziewonski (1999). High- and low-resolution images of the Earth's mantle: Implications of different approaches to tomographic modeling. *Journal of Geophysical Research: Solid Earth*, *104*(B11), 25,567–25,594, doi:10.1029/1999JB900166.
- Bower, D. J., M. Gurnis, & M. Seton (2013). Lower mantle structure from paleogeographically constrained dynamic Earth models. *Geochemistry, Geophysics, Geosystems*, *14*(1), 44–63, doi:10.1029/2012GC004267.
- Bozdağ, E., D. Peter, M. Lefebvre, D. Komatitsch, J. Tromp, J. Hill, N. Podhorszki, & D. Pugmire (2016). Global adjoint tomography: first-generation model. *Geophysical Journal International*, *207*(3), 1739–1766, doi:10.1093/gji/ggw356.
- Burke, K., & T. H. Torsvik (2004). Derivation of Large Igneous Provinces of the past 200 million years from long-term heterogeneities in the deep mantle. *Earth and Planetary Science Letters*, *227*(3–4), 531–538.
- Burke, K., B. Steinberger, T. H. Torsvik, & M. A. Smethurst (2008). Plume Generation Zones at the margins of Large Low Shear Velocity Provinces on the core–mantle boundary. *Earth and Planetary Science Letters*, *265*(1–2), 49–60, doi:10.1016/j.epsl.2007.09.042.
- Cammarano, F., S. Goes, P. Vacher, & D. Giardini (2003). Inferring upper-mantle temperatures from seismic velocities. *Physics of the Earth and Planetary Interiors*, *138*(3), 197–222, doi:10.1016/S0031-9201(03)00156-0.
- Capdeville, Y., Y. Gung, & B. Romanowicz (2005). Towards global earth tomography using the spectral element method: a technique based on source stacking. *Geophysical Journal International*, *162*(2), 541–554, doi:10.1111/j.1365-246X.2005.02689.x.
- Chambat, F., Y. Ricard, & B. Valette (2010). Flattening of the Earth: further from hydrostaticity than previously estimated. *Geophysical Journal International*, *183*(2), 727–732, doi:10.1111/j.1365-246X.2010.04771.x.
- Christensen, U. R., & D. A. Yuen (1985). Layered convection induced by phase transitions. *Journal of Geophysical Research: Solid Earth*, *90*(B12), 10,291–10,300, doi:10.1029/JB090iB12p10291.
- Conrad, C. P., B. Steinberger, & T. H. Torsvik (2013). Stability of active mantle upwelling revealed by net characteristics of plate tectonics. *Nature*, *498*(7455), 479–482, doi:10.1038/nature12203.
- Cottaar, S., & V. Lekic (2016). Morphology of seismically slow lower-mantle structures. *Geophysical Journal International*, *207*(2), 1122–1136, doi:10.1093/gji/ggw324.
- Dahlen, F. A., & J. Tromp (1998). *Theoretical Global Seismology*, Princeton University Press.

- Davaille, A., F. Girard, & M. Le Bars (2002), How to anchor hotspots in a convecting mantle? *Earth and Planetary Science Letters*, 203(2), 621–634, doi:10.1016/S0012-821X(02)00897-X.
- Davies, D. R., S. Goes, & H. C. P. Lau (2015), Thermally Dominated Deep Mantle LLSVPs: A Review. In A. Khan and F. Deschamps (Eds.), *The Earth's Heterogeneous Mantle: A Geophysical, Geodynamical, and Geochemical Perspective*, pp. 441–477, Springer International Publishing, Cham, doi:10.1007/978-3-319-15627-9_14.
- Deng, J., & K. K. M. Lee (2017), Viscosity jump in the lower mantle inferred from melting curves of ferropicriolite. *Nature Communications*, 8(1), 1997, doi:10.1038/s41467-017-02263-z.
- Domeier, M., P. V. Doubrovine, T. H. Torsvik, W. Spakman, & A. L. Bull (2016), Global correlation of lower mantle structure and past subduction. *Geophysical Research Letters*, 43(10), 4945–4953, doi:10.1002/2016GL068827.
- Durand, S., E. Debayle, Y. Ricard, C. Zaroli, & S. Lambotte (2017), Confirmation of a change in the global shear velocity pattern at around 1000 km depth. *Geophysical Journal International*, 211(3), 1628–1639, doi:10.1093/gji/ggx405.
- Fei, Y., J. Van Orman, J. Li, W. van Westrenen, C. Sanloup, W. Minarik, K. Hirose, T. Komabayashi, M. Walter, & K. Funakoshi (2004), Experimentally determined postspinel transformation boundary in Mg₂SiO₄ using MgO as an internal pressure standard and its geophysical implications. *Journal of Geophysical Research: Solid Earth (1978–2012)*, 109(B2).
- Forte, A. M., & J. X. Mitrovica (2001), Deep-mantle high-viscosity flow and thermochemical structure inferred from seismic and geodynamic data. *Nature*, 410, 1049–1056.
- Forte, A. M., A. M. Dziewonski, & R. L. Woodward (1993), Aspherical Structure of the Mantle, Tectonic Plate Motions, Nonhydrostatic Geoid, and Topography of the Core-Mantle Boundary. In *Dynamics of Earth's Deep Interior and Earth Rotation*, pp. 135–166, American Geophysical Union (AGU), doi:10.1029/GM072p0135.
- French, S. W., & B. Romanowicz (2015), Broad plumes rooted at the base of the Earth's mantle beneath major hotspots. *Nature*, 525(7567), 95–99, doi:10.1038/nature14876.
- French, S. W., & B. A. Romanowicz (2014), Whole-mantle radially anisotropic shear velocity structure from spectral-element waveform tomography. *Geophysical Journal International*, 199(3), 1303–1327, doi:10.1093/gji/ggu334.
- Frost, D. A., E. J. Garnero, & S. Rost (2018), Dynamical links between small- and large-scale mantle heterogeneity: Seismological evidence. *Earth and Planetary Science Letters*, 482, 135–146, doi:10.1016/j.epsl.2017.10.058.
- Fukao, Y., & M. Obayashi (2013), Subducted slabs stagnant above, penetrating through, and trapped below the 660 km discontinuity. *Journal of Geophysical Research (Solid Earth)*, 118(11), 2013JB010466–5938, doi:10.1002/2013JB010466.
- Ghosh, A., T. W. Becker, & S. J. Zhong (2010), Effects of lateral viscosity variations on the geoid. *Geophysical Research Letters*, 37(1), 01301, doi:10.1029/2009GL040426.
- Girard, J., G. Amulele, R. Farla, A. Mohiuddin, and S.-i. Karato (2016), Shear deformation of bridgmanite and magnesiowüstite aggregates at lower mantle conditions. *Science*, 351(6269), 144–147, doi:10.1126/science.aad3113.
- Green, P. J. (1995), Reversible jump Markov chain Monte Carlo computation and Bayesian model determination. *Biometrika*, 82(4), 711–732, doi:10.1093/biomet/82.4.711.
- Hager, B. H., & R. J. O'Connell (1981), A simple global model of plate dynamics and mantle convection. *Journal of Geophysical Research*, 86(B), 4843–4867, doi:10.1029/JB086iB06p04843.
- Hager, B. H., R. W. Clayton, M. A. Richards, R. P. Comer, & A. M. Dziewonski (1985), Lower mantle heterogeneity, dynamic topography and the geoid. *Nature*, 313(6003), 541–545, doi:10.1038/314752a0.
- He, Y., & L. Wen (2009), Structural features and shear-velocity structure of the “Pacific Anomaly.” *J. Geophys. Res.*, 114(B2), B02309, doi:10.1029/2008JB005814.
- Jellinek, A. M., & M. Manga (2002), The influence of a chemical boundary layer on the fixity, spacing and lifetime of mantle plumes. *Nature*, 418(6899), 760–763, doi:10.1038/nature00979.
- Jenkins, J., A. Deuss, & S. Cottaar (2016), Converted phases from sharp 1000 km depth mid-mantle heterogeneity beneath Western Europe. *Earth and Planetary Science Letters*, 459, 196–207, doi:10.1016/j.epsl.2016.11.031.
- Jordan, T. H., P. Puster, & G. A. Glatzmaier (1993), Comparisons between seismic Earth structures and mantle flow models based on radial correlation functions. *Science*, 261, 1427–1431.
- Kaercher, P., L. Miyagi, W. Kaniitpanyacharoen, E. Zepeda-Alarcon, Y. Wang, D. Parkinson, R. A. Lebensohn, F. De Carlo, & H.-R. Wenk (2016), Two-phase deformation of lower mantle mineral analogs. *Earth and Planetary Science Letters*, 456, 134–145, doi:10.1016/j.epsl.2016.09.030.
- Karato, S.-i., & B. B. Karki (2001), Origin of lateral variation of seismic wave velocities and density in the deep mantle. *Journal of Geophysical Research: Solid Earth*, 106(B10), 21,771–21,783, doi:10.1029/2001JB000214.
- Katsura, T., H. Yamada, T. Shinmei, A. Kubo, S. Ono, M. Kanzaki, A. Yoneda, M. J. Walter, E. Ito, S. Urakawa, K. Funakoshi, & W. Utsumi (2003), Post-spinel transition in Mg₂SiO₄ determined by high P–T in situ X-ray diffractometry. *Physics of the Earth and Planetary Interiors*, 136(1–2), 11–24.
- Kido, M., D. A. Yuen, O. Čadež, & T. Nakakuki (1998), Mantle viscosity derived by genetic algorithm using oceanic geoid and seismic tomography for whole-mantle versus blocked-flow situations. *Physics of the Earth and Planetary Interiors*, 107(4), 307–326.
- King, S. D., & G. Masters (1992), An inversion for radial viscosity structure using seismic tomography. *Geophysical Research Letters*, 19(15), 1551–1554, doi:10.1029/92GL01700.
- Komatitsch, D., & J. Tromp (2002), Spectral-element simulations of global seismic wave propagation—I. Validation. *Geophysical Journal International*, 149(2), 390–412, doi:10.1046/j.1365-246X.2002.01653.x.
- Kustowski, B., G. Ekström, & A. M. Dziewoński (2008), Anisotropic shear-wave velocity structure of the Earth's mantle: A global model. *Journal of Geophysical Research: Solid Earth*, 113(B6), doi:10.1029/2007JB005169.
- Lau, H. C. P., J. X. Mitrovica, J. Austermann, O. Crawford, D. Al-Attar, & K. Letychev (2016), Inferences of mantle viscosity based on ice age data sets: Radial structure. *Journal of*

- Geophysical Research*, 123, 7237–7252, doi:https://doi.org/10.1029/2018JB015740.
- Lau, H. C. P., J. X. Mitrovica, J. L. Davis, J. Tromp, H.-Y. Yang, & D. Al-Attar (2017). Tidal tomography constrains Earth's deep-mantle buoyancy. *Nature*, 551, 321–326, doi:10.1038/nature24452.
- Li, X.-D., & B. Romanowicz (1995). Comparison of global waveform inversions with and without considering cross-branch modal coupling. *Geophysical Journal International*, 121(3), 695–709, doi:10.1111/j.1365-246X.1995.tb06432.x.
- Liu, X., & S. Zhong (2015). The long-wavelength geoid from three-dimensional spherical models of thermal and thermochemical mantle convection. *Journal of Geophysical Research: Solid Earth*, 120(6), 4572–4596, doi:10.1002/2015JB012016.
- Liu, X., & S. Zhong (2016). Constraining mantle viscosity structure for a thermochemical mantle using the geoid observation. *Geochemistry, Geophysics, Geosystems*, 17(3), 895–913, doi:10.1002/2015GC006161.
- Lourenço, D. L., & M. L. Rudolph (in review). Shallow lower mantle viscosity modulates the pattern of mantle structure, in review at *Proceedings of the National Academy of Sciences*.
- Malinverno, A. (2002). Parsimonious Bayesian Markov chain Monte Carlo inversion in a nonlinear geophysical problem. *Geophysical Journal International*, 151(3), 675–688, doi:10.1046/j.1365-246X.2002.01847.x.
- Malinverno, A., & V. A. Briggs (2004). Expanded uncertainty quantification in inverse problems: Hierarchical Bayes and empirical Bayes. *Geophysics*, 69(4), 1005–1016, doi:10.1190/1.1778243.
- Mao, W., & S. Zhong (2018). Slab stagnation due to a reduced viscosity layer beneath the mantle transition zone. *Nature Geoscience*, 11(11), 876, doi:10.1038/s41561-018-0225-2.
- Mao, W., & S. Zhong (2019). Controls on global mantle convective structures and their comparison with seismic models. *Journal of Geophysical Research: Solid Earth*, doi:10.1029/2019JB017918.
- Marquardt, H., & L. Miyagi (2015). Slab stagnation in the shallow lower mantle linked to an increase in mantle viscosity. *Nature Geoscience*, 8(4), 311–314, doi:10.1038/ngeo2393.
- Masters, G., S. Johnson, G. Laske, H. Bolton, & J. H. Davies (1996). A Shear-Velocity Model of the Mantle [and Discussion]. *Philosophical Transactions of the Royal Society of London. Series A: Mathematical, Physical and Engineering Sciences*, 354(1711), 1385–1411, doi:10.1098/rsta.1996.0054.
- Masters, G., G. Laske, H. Bolton, & A. Dziewonski (2000). The Relative Behavior of Shear Velocity, Bulk Sound Speed, and Compressional Velocity in the Mantle: Implications for Chemical and Thermal Structure. In *Earth's Deep Interior: Mineral Physics and Tomography From the Atomic to the Global Scale*, vol. 117, edited by S.-i. Karato, A. M. Forte, R. Lieberman, G. Masters, & L. Stixrude, pp. 63–87, American Geophysical Union, Washington, D. C.
- Matthews, K. J., K. T. Maloney, S. Zahirovic, S. E. Williams, M. Seton, & R. D. Müller (2016). Global plate boundary evolution and kinematics since the late Paleozoic. *Global and Planetary Change*, 146, 226–250, doi:10.1016/j.gloplacha.2016.10.002.
- McNamara, A. K., & S. Zhong (2004). Thermochemical structures within a spherical mantle: Superplumes or piles? *J. Geophys. Res.*, 109(B7), B07402, doi:10.1029/2003JB002847.
- McNamara, A. K., & S. Zhong (2005). Thermochemical structures beneath Africa and the Pacific Ocean. *Nature*, 437(7062), 1136–1139, doi:10.1038/nature04066.
- Milne, G. A., J. X. Mitrovica, & A. M. Forte (1998). The sensitivity of glacial isostatic adjustment predictions to a low-viscosity layer at the base of the upper mantle. *Earth and Planetary Science Letters*, 154(1), 265–278, doi:10.1016/S0012-821X(97)00191-X.
- Mitrovica, J. X., & A. M. Forte (1997). Radial profile of mantle viscosity: Results from the joint inversion of convection and postglacial rebound observables. *Journal of Geophysical Research: Solid Earth*, 102(B2), 2751–2769, doi:10.1029/96JB03175.
- Mitrovica, J. X., & A. M. Forte (2004). A new inference of mantle viscosity based upon joint inversion of convection and glacial isostatic adjustment data. *Earth and Planetary Science Letters*, 225(1–2), 177–189, doi:10.1016/j.epsl.2004.06.005.
- Morra, G., D. A. Yuen, L. Boschi, P. Chatelain, P. Koumoutsakos, & P. J. Tackley (2010). The fate of the slabs interacting with a density/viscosity hill in the mid-mantle. *Physics of the Earth and Planetary Interiors*, 180(3–4), 271–282, doi:10.1016/j.pepi.2010.04.001.
- Moulik, P., & G. Ekström (2014). An anisotropic shear velocity model of the Earth's mantle using normal modes, body waves, surface waves and long-period waveforms. *Geophysical Journal International*, 199(3), 1713–1738, doi:10.1093/gji/ggu356.
- Moulik, P., & G. Ekström (2016). The relationships between large-scale variations in shear velocity, density, and compressional velocity in the Earth's mantle. *Journal of Geophysical Research (Solid Earth)*, 121(4), 2737–2771, doi:10.1002/2015JB012679.
- Mégnin, C., H.-P. Bunge, B. Romanowicz, & M. A. Richards (1997). Imaging 3-D spherical convection models: What can seismic tomography tell us about mantle dynamics? *Geophysical Research Letters*, 24(11), 1299–1302, doi:10.1029/97GL01256.
- Nelson, P. L., & S. P. Grand (2018). Lower-mantle plume beneath the Yellowstone hotspot revealed by core waves. *Nature Geoscience*, 11(4), 280–284, doi:10.1038/s41561-018-0075-y.
- Obayashi, M., J. Yoshimitsu, G. Nolet, Y. Fukao, H. Shiobara, H. Sugioka, H. Miyamachi, & Y. Gao (2013). Finite frequency whole mantle *P* wave tomography: Improvement of subducted slab images. *Geophysical Research Letters*, 40(21), 2013GL057401–5657, doi:10.1002/2013GL057401.
- Panasjuk, S. V., & B. H. Hager (1998). A model of transformational superplasticity in the upper mantle. *Geophysical Journal International*, 133(3), 741–755, doi:10.1046/j.1365-246X.1998.00539.x.
- Puster, P., & T. H. Jordan (1994). Stochastic analysis of mantle convection experiments using two-point correlation functions. *Geophysical Research Letters*, 21(4), 305–308, doi:10.1029/93GL02934.
- Puster, P., T. H. Jordan, & B. H. Hager (1995). Characterization of mantle convection experiments using two-point correlation

- functions. *Journal of Geophysical Research: Solid Earth*, 100 (B4), 6351–6365, doi:10.1029/94JB03268.
- Ricard, Y., M. Richards, C. Lithgow-Bertelloni, & Y. Le Stunff (1993). A geodynamic model of mantle density heterogeneity. *J. Geophys. Res.*, 98(B12), 21,895, doi:10.1029/93JB02216.
- Richards, M. A., & B. H. Hager (1984). Geoid anomalies in a dynamic Earth. *Journal of Geophysical Research: Solid Earth*, 89(B7), 5987–6002, doi:10.1029/JB089iB07p05987.
- Richards, M. A., & B. H. Hager (1989). Effects of lateral viscosity variations on long-wavelength geoid anomalies and topography. *J. Geophys. Res.*, 94(B8), 10,299, doi:10.1029/JB094iB08p10299.
- Rickers, F., A. Fichtner, & J. Trampert (2013). The Iceland-Jan Mayen plume system and its impact on mantle dynamics in the North Atlantic region: Evidence from full-waveform inversion. *Earth and Planetary Science Letters*, 367, 39–51.
- Ries, J., S. Bettadpur, R. Eanes, Z. Kang, U. Ko, C. McCullough, P. Nagel, N. Pie, S. Poole, T. Richter, H. Save, & B. Tapley (2016). Development and Evaluation of the Global Gravity Model GGM05. *Tech. Rep. CSR-16-02*, The University of Texas at Austin, Center for Space Research.
- Rudolph, M. L., & S. Zhong (2013). Does quadrupole stability imply LLSVP fixity? *Nature*, 503(7477), E3–E4, doi:doi:10.1038/nature12792.
- Rudolph, M. L., & S. J. Zhong (2014). History and dynamics of net rotation of the mantle and lithosphere. *Geochemistry, Geophysics, Geosystems*, 15(9), 3645–3657.
- Rudolph, M. L., V. Lekic, & C. Lithgow-Bertelloni (2015). Viscosity jump in Earth's mid-mantle. *Science*, 350(6266), 1349–1352, doi:10.1126/science.aad1929.
- Sambridge, M., T. Bodin, K. Gallagher, & H. Tkalcic (2013). Transdimensional inference in the geosciences. *Philosophical Transactions of the Royal Society A: Mathematical, Physical and Engineering Sciences*, 371, 20110,547, doi:10.1111/j.1365-246X.1990.tb04588.x.
- Schuberth, B. S. A., H.-P. Bunge, & J. Ritsema (2009). Tomographic filtering of high-resolution mantle circulation models: Can seismic heterogeneity be explained by temperature alone? *Geochemistry, Geophysics, Geosystems*, 10(5), doi:10.1029/2009GC002401.
- Shim, S.-H., B. Grocholski, Y. Ye, E. E. Alp, S. Xu, D. Morgan, Y. Meng, & V. B. Prakapenka (2017). Stability of ferrous-iron-rich bridgmanite under reducing midmantle conditions. *Proceedings of the National Academy of Sciences*, 114(25), 6468–6473, doi:10.1073/pnas.1614036114.
- Simons, F., F. Dahlen, & M. Wieczorek (2006). Spatiospectral Concentration on a Sphere. *SIAM Review*, 48(3), 504–536, doi:10.1137/S0036144504445765.
- Solomatov, V. S., & C. C. Reese (2008). Grain size variations in the Earth's mantle and the evolution of primordial chemical heterogeneities. *Journal of Geophysical Research: Solid Earth*, 113(B7), doi:10.1029/2007JB005319.
- Steinberger, B., & R. Holme (2008). Mantle flow models with core-mantle boundary constraints and chemical heterogeneities in the lowermost mantle. *Journal of Geophysical Research: Solid Earth*, 113(B5), doi:10.1029/2007JB005080.
- Stixrude, L., & C. Lithgow-Bertelloni (2011). Thermodynamics of mantle minerals - II. Phase equilibria. *Geophysical Journal International*, 184(3), 1180–1213, doi:10.1111/j.1365-246X.2010.04890.x.
- Su, W.-j., & A. M. Dziewonski (1991). Predominance of long-wavelength heterogeneity in the mantle. *Nature*, 352(6331), 121–126, doi:10.1038/352121a0.
- Su, W.-j., & A. M. Dziewonski (1992). On the scale of mantle heterogeneity. *Physics of the Earth and Planetary Interiors*, 74(1), 29–54, doi:10.1016/0031-9201(92)90066-5.
- Su, W.-j., & A. M. Dziewonski (1997). Simultaneous inversion for 3-D variations in shear and bulk velocity in the mantle. *Physics of the Earth and Planetary Interiors*, 100(1–4), 135–156.
- Thielmann, M., G. J. Golabek, & H. Marquardt (2020). Ferropericline control of lower mantle rheology: Impact of phase morphology. *Geochemistry, Geophysics, Geosystems*, (n/a), doi:10.1029/2019GC008688.
- Thorne, M. S., E. J. Garnero, & S. P. Grand (2004). Geographic correlation between hot spots and deep mantle lateral shear-wave velocity gradients. *Physics of the Earth and Planetary Interiors*, 146(1–2), 47–63, doi:10.1016/j.pepi.2003.09.026.
- Torsvik, T. H., M. A. Smethurst, K. Burke, & B. Steinberger (2006). Large igneous provinces generated from the margins of the large low-velocity provinces in the deep mantle. *Geophysical Journal International*, 167(3), 1447–1460, doi:10.1111/j.1365-246X.2006.03158.x.
- van der Meer, D. G., D. J. J. van Hinsbergen, & W. Spakman (2018). Atlas of the underworld: Slab remnants in the mantle, their sinking history, and a new outlook on lower mantle viscosity. *Tectonophysics*, 723, 309–448, doi:10.1016/j.tecto.2017.10.004.
- Wang, Y., & L. Wen (2007). Geometry and P and S velocity structure of the “African Anomaly.” *J. Geophys. Res.*, 112(B5), B05,313, doi:10.1029/2006JB004483.
- Waszek, L., N. C. Schmerr, & M. D. Ballmer (2018). Global observations of reflectors in the mid-mantle with implications for mantle structure and dynamics. *Nature Communications*, 9(1), 1–13, doi:10.1038/s41467-017-02709-4.
- Wen, L., & D. L. Anderson (1995). The fate of slabs inferred from seismic tomography and 130 million years of subduction. *Earth and Planetary Science Letters*, 133(1), 185–198, doi:10.1016/0012-821X(95)00064-J.
- Williams, C. D., S. Mukhopadhyay, M. L. Rudolph, & B. Romanowicz (2019). Primitive Helium is Sourced from Seismically Slow Regions in the Lowermost Mantle. *Geochemistry, Geophysics, Geosystems*, 20(8), 4130–4145, doi:10.1029/2019GC008437.
- Yuan, K., & B. Romanowicz (2017). Seismic evidence for partial melting at the root of major hot spot plumes. *Science*, 357(6349), 393–397, doi:10.1126/science.aan0760.
- Zhang, N., S. Zhong, W. Leng, & Z.-X. Li (2010). A model for the evolution of the Earth's mantle structure since the Early Paleozoic. *J. Geophys. Res.*, 115(B6), B06,401, doi:10.1029/2009JB006896.
- Zhong, S., M. T. Zuber, L. Moresi, & M. Gurnis (2000). Role of temperature-dependent viscosity and surface plates in spherical shell models of mantle convection. *J. Geophys. Res.*, 105(B5), 11,063–11,082, doi:10.1029/2000JB900003.
- Zhong, S., A. McNamara, E. Tan, L. Moresi, & M. Gurnis (2008). A benchmark study on mantle convection in a 3-D spherical shell using CitcomS. *Geochemistry, Geophysics, Geosystems*, 9(10), Q10,017.

2

Experimental Deformation of Lower Mantle Rocks and Minerals

Lowell Miyagi

ABSTRACT

Plastic deformation of rocks and mineral phases in the Earth's interior plays a primary role in controlling large-scale dynamic processes such as mantle convection and associated plate tectonics. Volumetrically, the lower mantle is the largest region of the Earth, and thus great effort has been made to study the deformation behavior of the mineral phases that comprise the lower mantle. Plastic deformation of these rocks and mineral phases can also lead to preferred orientation development (texture), which, in turn, can result in anisotropic physical properties. Many regions of the Earth's interior exhibit seismic anisotropy, and thus, considerable effort has been made to understand the processes leading to texture and anisotropy development in deep Earth phases. Studying deformation of lower mantle materials is technically challenging due to the extreme pressures and temperatures experienced by materials in the deep Earth. However, recent technological advances have allowed significant progress to be made toward understanding the deformation behavior of lower mantle phases. This chapter provides an overview of deformation mechanisms in lower mantle materials and the current state of experimental deformation studies on lower mantle mineral phases and polyphase aggregates of materials relevant to the lower mantle.

2.1. INTRODUCTION

Large-scale geodynamic phenomena such as post-glacial rebound, mantle convection, slab subduction, and plate motion are intimately linked to plastic deformation of minerals and rocks in the Earth's deep interior. The lower mantle, which ranges from the 660 km seismic discontinuity and continues to the core mantle boundary (CMB) at ~2900 km depth, constitutes ~55% of the Earth by volume, and thus lower mantle properties play a fundamental role in controlling much of Earth's dynamic behavior. As such, considerable effort has been directed at parameterizing rheological behavior of mantle rocks and minerals at high pressure and temperature conditions.

For studying geodynamic behavior, the goal is generally to understand the stress-strain rate response of rocks and minerals in order to characterize viscosity of mantle materials. This behavior can change dramatically with changes in pressure, temperature, composition, and grain size (Cordier & Goryaeva, 2018; Frost & Ashby, 1982; Karato, 2010; Marquardt & Miyagi, 2015). Thus, a major area of research is to determine and quantify variations in stress-strain rate response of these materials as a function of these conditions. In addition to flow laws, great interest has been generated in understanding the relationship between deformation and anisotropy in mantle rocks. Seismic anisotropy is observed in many regions of the Earth's interior and is widely believed to be due to deformation-induced texture (crystallographic preferred orientation) of constituent mineral phases in the Earth's interior (Karato, 1998; Karato et al., 2007; Long &

Geology and Geophysics, University of Utah, Salt Lake City, UT, USA

Mantle Convection and Surface Expressions, Geophysical Monograph 263, First Edition.
Edited by Hauke Marquardt, Maxim Ballmer, Sanne Cottaar, and Jasper Konter.
© 2021 American Geophysical Union. Published 2021 by John Wiley & Sons, Inc.
DOI: 10.1002/9781119528609.ch2

Becker, 2010; Romanowicz & Wenk, 2017). If one has a detailed understanding of the mechanisms of texture development and the relationship between deformation, texture, and anisotropy, then one can use observations of seismic anisotropy to infer mantle flow patterns in the deep Earth (Chandler et al., 2018; Cottaar et al., 2014; Long & Becker, 2010; Nowacki et al., 2010, 2011; Tommasi et al., 2018; Walker et al., 2011, 2018).

Although the exact mineralogy and chemistry of the lower mantle is still debated, seismic velocities and densities of the lower mantle are consistent with a mineralogy composed predominantly (65% to 85% by volume) of (Mg,Fe)(Si,Al,Fe)O₃ bridgmanite (Brg) with (Mg,Fe)O ferropericlasite (Fp) as the second-most abundant phase, and a few percent of CaSiO₃ perovskite (Ca-Pv) (e.g., Kuronov et al., 2017; Matas et al., 2007; Mattern et al., 2005). At conditions similar to those of the D'' (~2700 km), Brg undergoes a solid-solid phase transformation to a post-perovskite structured phase (pPv) (Murakami et al., 2004; Oganov & Ono, 2004; Shim et al., 2004). The stability and depth of this phase transition varies considerably depending on chemical composition (Grocholski et al., 2012), but pPv is likely to be a major phase at least in localized regions above the CMB. Iron content in the lower mantle is likely to be in the 10 mole % range (Matas et al., 2007) but the partitioning of iron between Fp, Brg, and pPv is not fully constrained (e.g., Piet et al., 2016). This chapter will focus on reviewing the current state of deformation experiments on the major lower mantle phases (Brg, Ca-Pv, pPv, and Fp) with a discussion of the current knowledge of deformation mechanisms in these phases and the potential for interactions between phases when deformed in a polyphase rock.

2.2. BACKGROUND

In high-pressure laboratory experiments, minerals deform by several mechanisms. At high temperatures and low stress, crystals deform by motion of point defects through grains and/or along grain boundaries. These types of diffusion creep are typically referred to as Nabarro-Herring Creep (Herring, 1950; Nabarro, 1948) and Coble Creep (Coble, 1963), respectively. While there are some subtle rheological differences between flow dominated by each of these mechanisms, generally speaking, diffusion creep leads to a Newtonian rheology – that is, a linear stress–strain rate relationship. Strain rate ($\dot{\epsilon}$) in the diffusion creep regime is generally written in the following form:

$$\dot{\epsilon} = \frac{\alpha D \sigma \Omega}{h^m RT}$$

where α is a parameter that describes the contribution of grain boundary sliding, D is the diffusion coefficient, σ is

stress, Ω is atomic volume, h is grain size, m is 2–3, R is the gas constant (8.314510 J/mol·K), and T is temperature. Grain size dependence comes about because efficiency of diffusion is strongly dependent on length scale ($D \approx l^2/t$) and thus diffusion creep is efficient only over short lengths, i.e., small grain sizes. Diffusion coefficients have an Arrhenius type relationship with temperature (Arrhenius, 1889; van't Hoff, 1884). The effect of pressure can also be included, leading to a temperature and pressure dependence of the diffusion coefficient, which is given by

$$D = D_0 \exp\left(-\frac{E_a + PV_a}{RT}\right)$$

where D_0 is termed the frequency factor, E_a is activation energy and V_a is the activation volume (e.g., Poirier, 1985). Thus, high temperature increases the efficiency of diffusion creep while pressure lowers efficacy. Thus, viscosity of a mineral will generally decrease with temperature and increase with pressure.

On the other end of the spectrum, at high stress and low temperatures, plasticity occurs by dislocation glide. Dislocations accommodate strain through the propagation of linear defects through a crystal. Dislocations occur on a slip system that is characterized by a plane (hkl) and a direction $\langle uvw \rangle$. Shearing along the slip plane in the slip direction results in an offset in the crystal lattice thus accommodating shear strain. Resistance to glide is controlled by the Peierls stress (Nabarro, 1947; Peierls, 1940). For a monoatomic lattice, the Peierls stress (σ_p) is given by

$$\sigma_p = \frac{2G}{w} \exp\left(-\frac{2\pi d_{hkl}}{w \bar{b}}\right)$$

where G is the shear modulus, w is a term that depends on the dislocation character (screw vs. edge), d_{hkl} is the lattice spacing of the glide plane and \bar{b} is the Burgers vector. The Burgers vector gives the magnitude and direction of lattice distortion resulting from a dislocation. A few general trends can be seen from this formulation. If G is large, then $\sigma_p \propto$ elastic properties. Since G in minerals is strongly dependent on pressure, the strength of minerals, likewise, is strongly dependent on pressure. The term $\frac{d_{hkl}}{\bar{b}}$ is sometimes used to predict which glide plane should be favored as a large d_{hkl} and short \bar{b} should result in a lower Peierls stress. However, caution should be used when applying this to minerals, as the above formulation is derived for a monoatomic lattice. Minerals, in contrast, have mixed bond strength and often do not follow this rule. Recent developments have allowed calculation of lattice friction for minerals over a wide range of conditions using the Peierls-Nabarro model (e.g., Carrez et al., 2007a; Cordier & Goryaeva, 2018). Of particular importance, to

the following discussion is that dislocation activity leads to grain rotation, which results in texture. Texture frequently leads to anisotropic bulk physical properties of polycrystals.

At stress conditions, intermediate to dislocation glide and diffusion creep, deformation is dominated by dislocation creep, i.e., glide accommodated by climb via diffusion. When dislocation glide alone is active, dislocations can interact and encounter obstacles to dislocation motion, which results in hardening. When stresses are low (typically due to high temperature and/or slow strain rates), dislocations can climb (diffuse) out of plane to bypass obstacles. Depending on ease of climb, various forms of constitutive laws can be written (Weertman, 1970; Weertman & Weertman, 1975). These lead to a non-linear stress-strain rate relationship where $\dot{\epsilon} \propto \sigma^n$ and $n = 3-5$. Notably, there is no grain size dependence.

Frequently a general constitutive equation is used that can capture both diffusion and dislocation creep (Hirth & Kohlstedt, 2003):

$$\dot{\epsilon} = A\sigma^n h^{-m} \exp\left(-\frac{E_a + PV_a}{RT}\right)$$

where A is an empirically determined pre-exponential factor. For diffusion creep, n is 1 and m is 2–3, and for dislocation creep n is typically 3–5 and $m = 0$.

While it is relatively straightforward to determine deformation mechanisms in the laboratory, it is much harder to determine operative mechanisms in the deep Earth. For crustal and upper mantle rocks, microstructural signatures of deformation can be observed and provide constraints on active deformation mechanisms (e.g., Knipe, 1989; Park & Jung, 2017; Passchier & Trouw, 2005). However, for the lower mantle natural samples of sufficient size to study and determine deformation mechanisms are not available, and deformation mechanisms must be inferred indirectly. Seismic observations are one of the few methods to image the Earth's deep interior, and seismic anisotropy can provide clues to deformation mechanisms in the deep Earth. Seismic anisotropy is generally attributed to texture development due to plastic deformation by dislocation creep. It is generally assumed that if there is no anisotropy, diffusion creep is operative, as in most case diffusion creep does not induce texture. Conversely, the general assumption is that if seismic anisotropy is observed, dislocation creep is likely (see Karato (2010) for a discussion of potential deformation mechanism in the mantle).

Note that a few cases have been observed where texture does develop in minerals deformed in diffusion creep, as defined by Newtonian rheology ($n = 1$). These are generally samples that have been deformed near the transition between diffusion creep and dislocation creep (e.g., Barreiro et al., 2007), unusual cases in the presence

of fluid/melt (Bons & den Brok, 2000), or due to strongly anisotropic grain shapes (Miyazaki et al., 2013; Yoshizawa et al., 2004). One should also recognize that deformation by diffusion and dislocations are competing processes and that both diffusion creep and dislocation creep can operate simultaneously in the same sample.

In the lower mantle, seismic anisotropy is observed at the top of the lower mantle near subducting slabs (Ferreira et al., 2019; Lynner & Long, 2015; Mohiuddin et al., 2015; Wookey et al., 2002) and also at the base of the mantle in the D'' region (for recent summaries of D'' anisotropy, see Creasy et al., 2019 and Romanowicz & Wenk, 2017). In contrast to these regions, the bulk of the mantle appears to be seismically isotropic. This has led to the suggestion that the bulk of the mantle deforms by diffusion creep (Karato et al., 1995), whereas regions of high strain near subducting slabs and at boundary layers such as near the CMB undergo deformation by dislocation creep (McNamara et al., 2002). However, others have suggested that isotropy might be due to patterns of anisotropy for Brg and Fp that cancel each other leading to an isotropic aggregate (Wenk, Speziale, et al., 2006). In any case, it appears that dislocation creep is active in at least some regions of the lower mantle, but it might also be likely that the mantle is close to the transition between diffusion creep and dislocation creep. As such, strain rate gradients in the mantle may result in transitions between diffusion-dominated and dislocation-dominated regimes.

2.3. METHODS: EXPERIMENTAL DEFORMATION OF LOWER MANTLE MINERALS

Deformation studies of lower mantle phases are complicated by the fact that many phases are unstable (Brg) or unquenchable (Ca-Pv and pPv) to ambient conditions. Both Ca-Pv and pPv become amorphous during pressure release and cannot be preserved to ambient pressures. Thus study of recovered samples (from high pressure and/or temperature experiments) is difficult or impossible, necessitating *in-situ* analysis. A technique that has led to significant advances in deformation studies of these phases is the use of synchrotron x-ray diffraction in conjunction with high pressure and temperature deformation devices.

2.3.1. The Diamond Anvil Cell as a Deformation Device

The diamond anvil cell (DAC) uses two gem-quality diamonds with flat tips (culets) in opposed anvil geometry to generate high confining pressure (e.g., Jayaraman, 1983). In DAC experiments, a tiny sample (< 0.1 mm) is confined within a gasket and the anvils impose pressure

and stress on the sample. The DAC is capable of generating pressures in excess of those experienced at the center of the Earth. Most commonly, the DAC is used in axial diffraction geometry where the x-ray beam is parallel to the compression axis. This is advantageous as the diamonds are nearly x-ray transparent. In these types of experiments the sample is typically surrounded by a soft pressure medium to reduce differential stress to near hydrostatic conditions. This type of experiment has been highly successful for studying phase equilibria and equations of state at high pressure and temperature. The DAC has also been used in axial geometry without a pressure medium to infer yield strength from radial pressure gradients (e.g., Meade & Jeanloz, 1988).

The DAC may also be used in radial geometry to study deformation properties at high pressures. In radial diffraction, the x-ray beam is directed through the gasket, orthogonal to the compression direction. For these experiments, no pressure medium is used so that the diamonds impose pressure and deviatoric stress to deform the material elastically and plastically. This geometry requires x-ray transparent gaskets such as beryllium or amorphous boron (Hemley et al., 1997; Merkel & Yagi, 2005) to allow passage of the x-ray beam across the sample. Radial diffraction technique and the DAC has now been used for around two decades to make *in-situ* measurement of lattice strains and texture development at high pressure (Hemley et al., 1997; Wenk et al., 2000).

Although the DAC reaches the highest pressure range of all the deformation devices, it has many limitations.

Generating high temperatures during DAC deformation is technically challenging; most DAC deformation experiments are room temperature. High temperatures are generated in the DAC through the use of electrical resistive heating or by focusing an infrared laser beam through the diamonds and onto the sample. Resistive heating produces relatively uniform temperatures within the sample, but temperatures are significantly lower than those that can be achieved through laser heating (Figure 2.1). For radial diffraction resistive heating is also complicated by the fact that any heater surrounding the sample must allow passage of x-rays in the radial direction. A graphite resistive heater has been developed for radial geometry (Liermann et al., 2009; Petitgirard et al., 2009) and has been used statically (without active compression) to generate temperatures as high as 1785 K at 40 GPa (Miyagi et al., 2013). More recently, Immoor et al. (2018) used this technique to deform a sample of Fp along a 1400 K isotherm to ~ 70 GPa (Figure 2.1).

Laser heating can reach temperatures as high as ~ 6000 K (Boehler, 2000) but generally has large axial and radial temperature gradients (Boehler, 2000; Manga & Jeanloz, 1996). Axial gradients can result due to the high thermal conductivity of the diamond anvils, creating lower temperatures near the diamonds. Radial temperature gradients are more problematic for radial diffraction and arise because the laser hotspot is typically smaller than the sample dimensions. Gasket material may also conduct heat away from the edges of the sample. Additionally, temperatures may not be uniform throughout the laser hotspot.

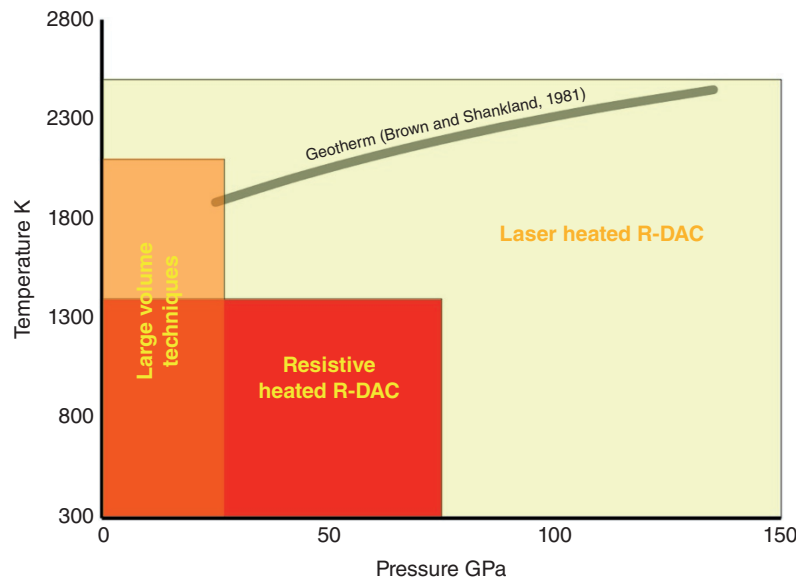


Figure 2.1 Approximate pressure and temperature capabilities of various deformation devices including both large volume techniques and the radial diffraction diamond anvil cell (R-DAC). Also plotted for reference is a “cold” mantle geotherm (Brown and Shankland, 1981).

Advances such as double-sided heating (Shen et al., 2001) and beam shaping (Prakapenka et al., 2008) have significantly reduced temperature gradients in the DAC. Surrounding the sample in an insulating material serves to both increase heating efficiency and reduce thermal gradients by reducing heat conduction away from the hotspot. However, for deformation experiments in radial geometry, this can be problematic. In addition to extra diffraction peaks from the insulating material, which complicates lattice strain and texture analysis, the insulation material must also be strong enough to impose deformation on the sample. If the insulation material is weak, strain will partition into the insulation material and the harder phase will remain relatively undeformed. As most lower mantle phases have high strength, this significantly limits the choice of insulation material, and in practice most radial diffraction measurements with laser heating do not use an insulating material. Additionally, laser heating in radial geometry is challenging, as most synchrotron beamlines are set up for laser heating in axial geometry, and reconfiguring the laser system for heating in radial geometry is difficult and time consuming (Kunz et al., 2007). Thus, only a few studies have performed radial diffraction experiments coupled with laser heating (Kunz et al., 2007; Merkel et al., 2004; Miyagi et al., 2013; Miyagi, Kunz, et al., 2008; Wu et al., 2017). The highest pressures and temperatures reached for radial diffraction and laser heating in the DAC are $\sim 2500\text{K}$ and 150 GPa (Figure 2.1; Wu et al., 2017).

In compression, experiments, diamonds induce both pressure and deviatoric stress on the sample, and these cannot be easily decoupled. Thus, studying deformation properties at a fixed confining pressure in the DAC is currently not possible. This means that flow stresses estimated from DAC experiments convolute strengthening due to pressure and strain hardening. Controlling strain rates is difficult in the DAC. Often, deformation is controlled through manual increase of pressure/stress through turning load screws. Not only does this result in a discontinuous increase in stress and strain, but it is incompatible with simultaneous heating and deformation. Furthermore, the small sample size makes it difficult to measure sample dimensions during experiments, and commonly strain (and thus strain rate) cannot be measured. The use of a gas membrane has somewhat improved on this, as compression is smoother than with screws. The DAC can also be used with a piezoelectric actuator, which can provide a more controlled compression than a membrane-driven DAC (Evans et al., 2007; Jenei et al., 2019). The dynamic DAC has recently been combined with high-resolution radiography to successfully measure small strains in an iron sample at high pressure (Hunt et al., 2018). Estimated total strains for compression in the DAC are ~ 0.3 (30%) and strain rates (albeit discontinuous) are on the order of 10^{-4}s^{-1} (Marquardt & Miyagi,

2015). Recently, rotational DACs have been developed that allow large shear strains to be imposed at pressures in excess of 100 GPa (Azuma et al., 2018; Nomura et al., 2017).

Small sample sizes in the DAC further limit its capabilities as a deformation device. Sample sizes are quite small in the DAC, generally $0.03\text{--}0.05\text{ mm}$ thick at the start of an experiment and on the order of a few hundredths of a millimeter to a few tenths of a millimeter in diameter. This yields corresponding sample volumes of $\sim 10^{-2}\text{ mm}^3$ to 10^{-5} mm^3 , but volumes become significantly reduced at high pressures. As a sufficient number of grains must be sampled to obtain statistically representative information, the upper limit of grain sizes feasible in the DAC is quite low. This makes studying the effect of changing grain size on rheology problematic in the DAC. One technique that has been recently developed that somewhat alleviates this problem is the use of multigrain crystallography, which allows the use of coarse-grained samples (Nisr et al., 2012). In spite of its many limitations, the DAC remains the only deformation device that can reach pressures covering the entire range of the lower mantle (Figure 2.1).

2.3.2. Large-Volume Deformation Devices

These devices cover a more limited pressure and temperature range than the DAC (Figure 2.1) but have the advantage of allowing larger volume samples (on the order of a few mm^3), longer and more stable heating (via resistive heating), measurement of strain and strain rate, greater variation of grain size, and better control of the stress state (Karato & Weidner, 2008). The D-DIA is a six-ram cubic type multianvil press. In this configuration, the top and bottom rams are differential, meaning that they can be moved independently of the other four rams (Y. Wang et al., 2003). This allows the user to advance all six rams simultaneously to increase pressure quasi-hydrostatically. Additionally, by cycling the differential rams, the user can impose differential stress to shorten or lengthen the sample at a near fixed confining pressure. This allows better control of stress state and to some degree allows the user to decouple hydrostatic and deviatoric stresses. The D-DIA generally operates up to $\sim 10\text{ GPa}$ at 1600 K , but recent efforts using a D-DIA with a multianvil 6-6 assembly (a second stage of six anvils in a cubic geometry) has reached conditions as high as 20 GPa and 2000 K (Kawazoe et al., 2010). Tsujino et al. (2016) used a cubic press with a 6-8 (a second stage of 8 anvils in octahedral geometry) assembly to deform a Brg sample to 25 GPa and 1873 K , by using pistons cut at 45° to induce shear strain. Another approach using the multianvil type apparatus that has proven successful is a 6-8 Kawai type multianvil assembly that has

been modified with a pair of differential rams and is called the differential T-CUP or DT-CUP (Hunt et al., 2014). The 6-8 multianvil design compresses an octahedral sample assembly and due to better support of the anvils can reach significantly higher pressures than a cubic (DIA) type press. Using a so-called broken anvil design, the DT-CUP has been used to successfully perform deformation experiments to 24 GPa and ~1800 K (Hunt & Dobson, 2017).

The Rotational Drickamer Apparatus (RDA) is an opposed anvil device, where one anvil has the capability to rotate. Pressure and compressive stress are increased by advancing the anvils. When the desired pressure is reached, large shear strain can be induced by rotation of the anvil (Yamazaki & Karato, 2001a). The RDA can reach P-T conditions of the upper lower mantle ~27 GPa at ~2100 K (Girard et al., 2016). The main advantages of the RDA are that it can reach higher pressures than other large-volume techniques and can reach high shear strains. However, the RDA is limited to smaller samples than the above multianvil techniques and also has larger temperature and pressure gradients. Due to the fact that deformation is induced by rotation of the anvils, the RDA also has large strain gradients across the sample, though this is somewhat alleviated by using a doughnut-shaped sample. Generally speaking, the large volume apparatuses are far superior to the DAC in terms of measuring rheological properties but lack the pressure range available in the DAC, and thus, currently these two types of techniques are complementary for understanding deformation of lower mantle phases.

2.3.3. Texture and Strength Measurements in High-Pressure Experiments

For samples deformed in axial compression, lattice planes perpendicular to compression are more reduced in spacing relative to planes perpendicular to the radial direction (Singh, 1993; Singh et al., 1998). This is due to elastic strain imposed by the deformation device. If single crystal elastic properties are known, differential stress supported by the sample can be calculated from measured lattice strains (Singh, 1993; Singh et al., 1998). Stresses measured during these experiments can provide a lower bounds estimate for the flow strength of the material (Kavner & Duffy, 2001; Merkel et al., 2002). During plastic deformation, lattice strains may become systematically larger or smaller on various crystallographic planes, as stress is anisotropically relieved by dislocation motion. Frequently, in high-pressure experiments, aggregate flow strength is taken to be an arithmetic mean of stresses calculated on the measured lattice plane. This method can be biased, depending on which lattices planes are measured. Lattice strain anisotropy does provide information on

active deformation mechanisms and can be used to constrain slip system activities (Karato, 2009; Turner & Tomé, 1994). Texture development is an expression of plastic deformation and results from dislocation glide/creep and/or mechanical twinning. Texture is easily observed with radial x-ray diffraction as systematic intensity variations along diffraction rings. By deconvoluting these intensity variations, textures can be measured in-situ in DACs or large volume deformation devices (Wenk, Lonardelli, et al., 2006). For an example methodology of texture analysis from radial x-ray diffraction the reader is referred to Wenk et al. (2014).

Deformation mechanisms can be inferred from high-pressure experiments by forward modeling texture development and/or lattice strain evolution with polycrystal plasticity codes. Although full field methods such as finite elements (Castelnau et al., 2008) or Fast Fourier Transform methods (Kaercher et al., 2016) can be used to model deformation behavior, homogenization schemes such as the self-consistent method are more common (Merkel et al., 2009; Wenk, Lonardelli, et al., 2006). This is due to the high degree of efficacy coupled with considerably reduced computational expense for self-consistent methods. The most commonly used method is the Visco Plastic Self-Consistent (VPSC) code (Lebensohn & Tomé, 1993), which simulates texture development as a function of slip system activities. The VPSC method has been further modified to account for the effects of recrystallization (e.g., Wenk et al., 1997). Although VPSC can account for large strains and rate sensitive deformation, it neglects elastic deformation. As such, it does not account for hydrostatic pressure and cannot be used to model lattice strains. On the other hand, the Elasto-Plastic Self Consistent (EPSC) method (Turner & Tomé, 1994) can be used to model slip system activities as a function of lattice strain evolution. However, strictly speaking, the strain formulation used in EPSC is applicable to small strains and does not include rate-sensitive deformation. Early implementations of EPSC did not account for texture development due to slip and twinning or grain shape evolution. The EPSC method has been extended to include grain reorientation and stress relaxation due to twinning (Clausen et al., 2008) and then further modified to approximately account for large strains, ridged body rotation, texture, and grain shape evolution (Neil et al., 2010). This version of EPSC has been used to model texture and lattice strain evolution in high-pressure experiments (e.g., Li & Weidner, 2015; Merkel et al., 2012; Raterron et al., 2013). Most recently, a fully general, rate sensitive, large-strain Elasto-Visco Plastic Self-Consistent (EVPSC) method was developed (H. Wang et al., 2010) and applied to high-pressure deformation (F. Lin et al., 2017) to simultaneously model lattice strain and texture evolution. One advantage of EVPSC is that it can effectively simulate large strain

texture and lattice strain development to provide quantitative values for polycrystal critical resolved shear stresses (CRSS) and to constrain secondary slip systems (F. Lin et al., 2017).

In self-consistent codes, each grain is treated as an inclusion in an anisotropic, homogeneous medium that has the average properties of the polycrystal. In VPSC and EVPSC, rate sensitivity of slip systems is included as a power law behavior. As deformation proceeds, crystals deform and rotate to generate texture. The resulting texture depends on the active slip systems and deformation geometry. Slip system activity depends on the stress resolved onto the slip systems and the critical resolved shear stress (CRSS) needed to activate the slip system. Applying different CRSS values favors one slip system over others. Different dominant slip systems result in different texture types and different lattice strain anisotropies. By determining which simulated texture and lattice strain evolution most closely resembles experiments, deformation mechanism can be inferred.

2.3.4. A Note on Scaling Experiments to the Lower Mantle

Caution should be exercised when extrapolating laboratory results to the deep Earth. First and foremost, laboratory strain rates are many orders of magnitude faster than natural strain rates. Laboratory strain rates for deformation of lower mantle phases are typically on the order of 10^{-4} s^{-1} to 10^{-7} s^{-1} . In contrast, strain rates in the Earth are likely on the order of 10^{-12} s^{-1} to 10^{-16} s^{-1} . Given the large difference in the human time scale and geologic time this discrepancy cannot be addressed directly by laboratory studies and systematic trends from laboratory experiments must be extrapolated to conditions of the Earth. One potential pitfall with this is the underlying assumption that no unknown deformation mechanism exists that operates at mantle conditions but is not operative in the laboratory (Boioli et al., 2017). Unlike the crust and upper mantle, natural samples that can provide evidence of operative deformation mechanisms do not exist and thus one is left to use the best data from the laboratory and from theory.

Total strain achieved in experiments can also be quite different than those in nature. While some devices can achieve large strains, for example the RDA has been used to achieve shear strains of ~ 2 (200%) (Y. Xu et al., 2005) and the rotational DAC has been used to deform samples to shear strains of ~ 4 (400%) (Nomura et al., 2017), compression studies typically attain strains of ~ 0.3 strain (30%) (e.g., Marquardt & Miyagi, 2015; Y. Wang et al., 2003). In contrast, slabs subducted into the lowermost mantle likely experience much larger shear strains on the order of 6–10 (e.g., Allègre & Turcotte, 1986; Tommasi et al., 2018; Wenk et al., 2011).

High pressures and temperatures of the full range of the lower mantle are also difficult to achieve in deformation experiments, and, thus, deformation experiments have been limited to lower pressures and high temperatures or high pressures and low temperatures. Unfortunately, deformation mechanisms in lower mantle phases can change with temperature (e.g., Immoor et al., 2018) and also with pressure (Marquardt & Miyagi, 2015), and thus direct extrapolation of lower-pressure, high-temperature studies or high-pressure, low-temperature studies may not represent the behavior in the deep Earth. However, with appropriate caution, some constraints on the deformation mechanisms and general rheology of the lower mantle can be obtained.

2.4. DEFORMATION STUDIES OF LOWER MANTLE PHASES

Most deformation experiments have focused on slip systems and texture development in lower mantle phase (Immoor et al., 2018; Merkel et al., 2007; Miyagi et al., 2010; Miyagi & Wenk, 2016), and only a few experiments have studied rheological properties (e.g., Girard et al., 2016). This is largely due to experimental difficulties related to measurement of rheological properties under controlled strain rate conditions and also due to intense interest in the relationship between texture and anisotropy in the lower mantle. Texture measurements have largely been performed at uncontrolled strain rates and in most cases at room temperature in the DAC. In contrast, measurements of rheological properties require precise control of strain rates and temperature in order to access and characterize stress–strain rate relationships for various deformation regimes. Most deformation experiments have been performed in the dislocation glide regime or in dislocation creep regime with no experimental studies on diffusion creep at lower mantle pressures and temperatures. Typically, diffusion creep rheology has been estimated based on measured or calculated diffusion coefficients and estimates of mantle grain size combined with the diffusion creep equation (e.g., Ammann et al., 2010; Deng & Lee, 2017; Van Orman et al., 2003; J. Xu et al., 2011; Yamazaki et al., 2000; Yamazaki & Karato, 2001b). A few diffusion creep studies have been performed on lower mantle analog materials (Karato et al., 1995).

The following discussion primarily focuses on experimental studies that achieve pressures in excess of ~ 20 GPa. These measurements were performed either in the dislocation glide or in dislocation creep regime. In the following sections, I will first discuss studies on mineral strengths and then will discuss texture measurements and slip system activities.

2.4.1. Differential Stress Measurements in Lower Mantle Phases

Radial diffraction experiments can provide information on flow stress of materials. Lattice strains measured during deformation experiments can be used to calculate differential stresses supported by each lattice plane sampled by diffraction. If plastic flow has been achieved, then these stresses represent the flow strength of the material. Note that particularly in DAC experiments, the measured differential stress value is unlikely to correspond to the yield strength/stress at pressure as the material undergoes strain hardening. Thus, if plasticity has occurred, these values are representative of the flow strength as opposed to the yield strength. In some studies, it is not clear that flow stress has been achieved, and thus these measurements can only provide a lower bounds for the flow stress. If significant texture evolution is observed, then one may be able to assume that the flow stress has been reached. However, more sophisticated modeling using, for example, EPSC (Clausen et al., 2008; Neil et al., 2010; Turner & Tomé, 1994) or EVPSC (H. Wang et al., 2010), methods can provide a more robust estimate of the flow strength (Burnley & Zhang, 2008; L. Li et al., 2004; F. Lin et al., 2017; Merkel et al., 2009; Raterron et al., 2013).

Methodologies used to calculate stresses in these types of experiments can result in discrepancies between measurements. Calculation of stresses not only requires knowledge of the elastic properties of the materials but also the assumption of an appropriate micromechanical model. Generally, some sort of Reuss-Voigt-Hill approximation is used to calculate stress from individual lattice strains using the method outlined in Singh (1993) and Singh et al. (1998). Alternately, some studies have used the moment pole stress model (Matthies & Humbert, 1993) and the bulk path geometric mean (Matthies et al., 2001) to calculate stress. Generally, elastic properties calculated with a Reuss-Voigt-Hill average and the geometric mean are quite close (Mainprice et al., 2000). However, differences can arise between these methodologies because the moment pole stress model typically assigns a single stress value based only on elastic anisotropy. As this does not account for plastic anisotropy, this may result in systematic deviations from the true stress. On the other hand, using the method of Singh (1993) and Singh et al. (1998) allows one to calculate a stress on each plane. This is particularly useful where large plastic anisotropy is observed. However, one is still left with the problem of deciding the appropriate way to average stresses measured on individual planes to get a “bulk stress”. The general practice is to take a simple arithmetic mean of the measured lattice planes on all planes and use the deviation in the values to calculate an error on the

measurement. Because limited diffraction planes are sampled in experiments, sampling bias may result in systematically over- or underestimating the bulk stress. Again, more sophisticated modeling using the EPSC method (Clausen et al., 2008; Neil et al., 2010; Turner & Tomé, 1994) or EVPSC method (H. Wang et al., 2010) can alleviate issues with sampling bias (e.g., Burnley & Kaboli, 2019; Burnley & Zhang, 2008; Li et al., 2004; Li & Weidner, 2015; F. Lin et al., 2017; Merkel et al., 2009, 2012; Raterron et al., 2013). Another issue with flow strength measurement in the DAC, which is exacerbated at high temperatures is that strain rates are typically unconstrained, which is problematic for minerals that are generally rate sensitive. In the following discussion, the majority of the deformation studies, particularly in the DAC, are at uncontrolled strain rates. Finally, the effects of grain size strengthening (particularly in room temperature experiments) through the well-known Hall-Petch effect, where grain boundaries as barriers to dislocation motion, are typically poorly constrained. Frequently, grain size and microstructure are not documented in DAC studies.

Ferropicliase. Figure 2.2 shows a summary of periclase (Per) and Fp stress measurements for studies that exceed ~ 20 GPa. All of these measurements have been made in the DAC with the exception of the measurements of Girard et al. (2016). Of these, the measurements of Girard et al. (2016) and those of Miyagi & Wenk (2016) were made on a two-phase mixture of Brg and Fp. A few trends are clear in the data. At lower pressures and room temperature pure Per (Figure 2.2, black symbols) appears to support higher differential stresses than Fp compositions (Merkel et al., 2002; Singh et al., 2004). In all Fp measurements except those of J.-F. Lin et al. (2009) Fp exhibits a steep rise in differential stress with pressure as noted by Marquardt & Miyagi (2015). The reason for the discrepancy between the data of J.-F. Lin et al. (2009) and the other measurements is not clear. There is one very low data point (brown cross) from Miyagi & Wenk (2016). This data point was collected immediately after conversion to Brg + Fp, and as the sample has not yet been deformed, this point is not reflective of a flow stress. By ~ 60 GPa differential stress values in Fp achieves similar values to those of Per. It is possible that differences between Per and Fp may be due to composition, but the effects of grain size on the yield strength should be explored. Singh et al. (2004) suggest a significant effect of grain size on the strength of Per but the difference in grain size – for example between Singh et al. (2004) and Marquardt & Miyagi (2015) – is not known, as recovered samples were not studied for microstructure (in the latter case, due to anvil failure).

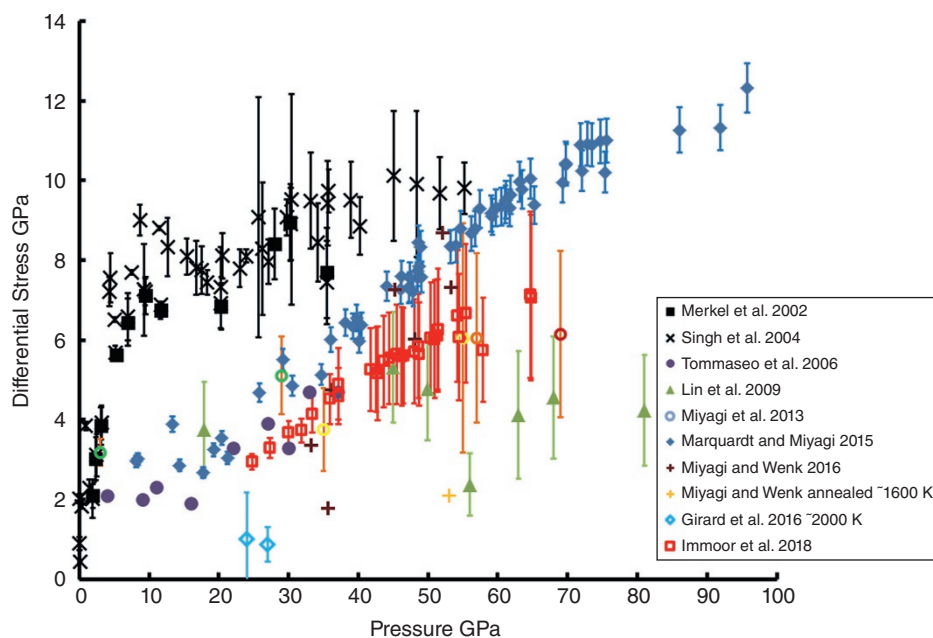


Figure 2.2 Summary of high-pressure differential stress measurements on periclase and ferropericlase. Measurements in periclase are in black and ferropericlase are in colored symbols.

During higher-temperature deformation at 1400 K (Figure 2.2, red open squares), the results of Immoor et al. (2018) show a similar steep trend with pressure, but the magnitude is lower than the room temperature experiments of Marquardt & Miyagi (2015). The results of Immoor et al. (2018) are also generally consistent with the results from Miyagi et al. (2013) (Figure 2.2, open circles), which used resistive heating and laser + resistive heating to achieve high temperatures in the DAC. Notably, all three of these studies used the same Fp sample. Data points from Miyagi et al. (2013) at ~ 775 K (Figure 2.2, yellow open circles) and ~ 1000 K (Figure 2.2, orange open circles) using resistive heating are very close to the values of Immoor et al. (2018). The ~ 2300 K data point using resistive + laser heating (Figure 2.2, red open circle) is slightly below the data of Immoor et al. (2018), but with overlapping error bars. One should note that the error bars on these data sets represent the range of lattice strains measured on various lattice planes, and large error bars are associated with the large plastic anisotropy of this phase.

The data points of Girard et al. (2016) at ~ 2000 K (Figure 2.2, blue open diamonds) represent the only large volume experiment at these pressures. Only data collected after $\sim 20\%$ strain was used for these data points, as this is where steady state stress levels are achieved. These data points lie far below the DAC measurements, and also have a greater separation from the measurements of Marquardt & Miyagi (2015) than the ~ 2300 K measurement of Miyagi et al. (2013). This difference may be due to lower

strain rates in RDA, but may also be due to grain size and the fact that this sample was deformed as part of a two-phase assemblage. There is additionally another low data point from Miyagi & Wenk (2016) that was annealed at ~ 1600 K for ~ 30 minutes (Figure 2.2, yellow cross). It is unsurprising that this point is low, as this is essentially a stress relaxation experiment.

When comparing DAC experiments to DAC experiments, the results on Per (Merkel et al., 2002; Singh et al., 2004) are quite consistent. Aside from the data of J.-F. Lin et al. (2009), room-temperature results of Marquardt & Miyagi (2015), Miyagi et al. (2013) Miyagi & Wenk (2016), and Tommaseo et al. (2006) are all quite similar, particularly when considering compositional variations between these experiments. There is not an obvious trend for strength and composition. However, a low-pressure deformation study by Long et al. (2006) found that Fp samples with high Fe contents ($>50\%$) develop texture faster than samples with low Fe contents, indicating a weakening with high Fe content. The effects of Fe content, grain size, strain rate, and temperature still need to be systematically explored for Fp at mantle conditions.

CaSi₃ Perovskite. Flow strength measurements on major mantle silicates are even more limited than measurements on Fp. Two differential stress measurements in the DAC exist for Ca-Pv. Shieh et al. (2004) used energy dispersive x-ray diffraction to measure differential stress

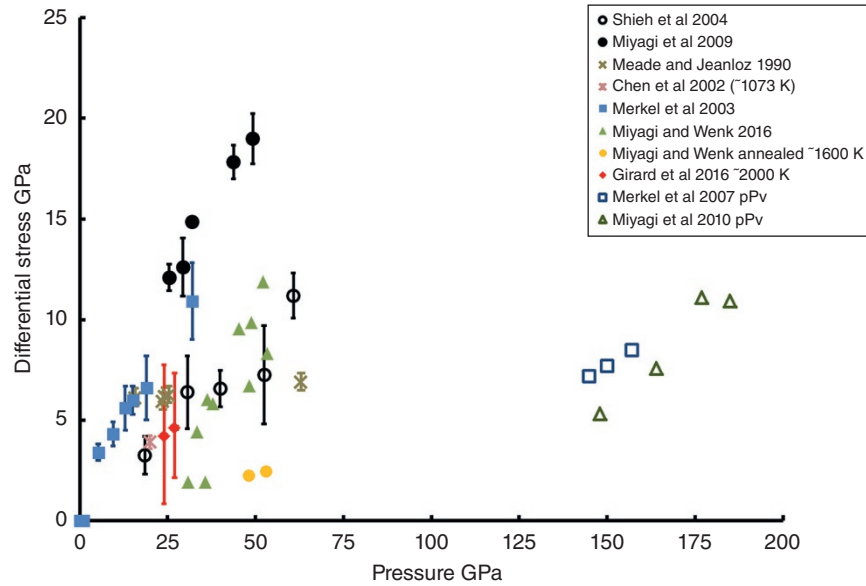


Figure 2.3 Summary of high-pressure differential stress measurement on CaSiO_3 perovskite, bridgmanite and MgSiO_3 post-perovskite. Measurements on CaSiO_3 perovskite are shown in black symbols, measurements on bridgmanite are shown in closed colored symbols, and measurements on MgSiO_3 post-perovskite are shown with open colored symbols.

in Ca-Pv to ~60 GPa (Figure 2.3, black open circles). Miyagi et al. (2009) used angle dispersive x-ray diffraction to measure differential stresses to 49 GPa (Figure 2.3, black closed circles). There is a large discrepancy between these measurements, with the values of Miyagi et al. (2009) about twice as large as those of Shieh et al. (2004). In addition to potential differences in grain size, there are a couple possibilities for differences in strength measurements. Shieh et al. (2004) used a natural sample (unspecified composition), while Miyagi et al. (2009) used a synthetic starting material; thus, starting material composition could play a role. Perhaps a more likely explanation is the use of laser absorbers in these experiments. In the work of Shieh et al. (2004), Pt was mixed in the sample to use as a laser absorber. In contrast, in the work of Miyagi et al. (2009), amorphous boron was mixed with the sample. It is possible that presence of boron can artificially raise the strength of the sample through doping or pinning at grain boundaries. In any case, if the values of Miyagi et al. (2009) are reflective of flow strength, then Ca-Pv would have the highest room temperature flow strength of the major mantle silicates. However, if the measurements of Shieh et al. (2004) represent the true room temperature flow strength, then Ca-Pv has a similar room temperature flow strength to Brg.

Bridgmanite. Of the measurements on Brg, one measurement was made in the DAC on a presynthesized sample using ruby fluorescence and the pressure gradient technique (Meade & Jeanloz, 1990). Two measurements

have been made in the DAC with angle dispersive diffraction on a presynthesized sample (Merkel et al., 2003) or samples synthesized *in-situ* from enstatite, olivine, and ringwoodite (Miyagi & Wenk, 2016). All of these DAC experiments were performed at room temperature, aside from two data points from Miyagi & Wenk (2016) where samples were annealing at ~1600K for 30 minutes. Two studies using large volume apparatus have also been performed. Chen et al. (2002) performed stress relaxation experiments using a DIA type apparatus and determined stress levels from x-ray line broadening. More recently, Girard et al. (2016) performed high shear strain experiments using the RDA in conjunction with energy dispersive x-ray diffraction to determine stress levels in a two-phase aggregate of Brg and Fp. This is to date the only high pressure and high temperature controlled strain rate deformation experiment on Brg. For the differential stresses plotted in Figure 2.3 for Girard et al. (2016), only data collected after ~20% strain was used, as this is where steady-state stress levels are achieved. One should note that in Miyagi & Wenk (2016), a moment pole stress model was used to fit lattice strains, and standard deviations from this model (smaller than the symbols in Figure 2.2) represent errors in fitting and likely underestimate errors in the measurement and those due to plastic anisotropy. Thus, this study has smaller error bars than other measurements.

When looking at differential stress measurements on Brg, the slope of differential stress versus pressure is steep, with the exception of the data of Meade & Jeanloz (1990),

which is much flatter (Figure 2.3, green Xs). Stresses are highest in the experiment of Merkel et al. (2003) (Figure 2.3, blue squares). This sample, like Meade & Jeanloz (1990), was mostly compressed outside of the Brg stability field ($P < \sim 23$ GPa), and it is unclear if this may affect the flow strength of the material. The slope of the room temperature data of Miyagi & Wenk (2016) is the steepest but data points at ~ 30 GPa are immediately after synthesis and prior to deformation (Figure 2.3, green triangles) so are not reflective of the materials flow strength. If we assume that the highest measured stresses in the DAC are reflective of the room temperature flow strength, then Brg is significantly stronger than Fp, particularly at lower pressures. However Fp becomes much closer in strength to Brg at higher pressures (Figure 2.2, 3). Differential stresses measured in Brg in the large-volume apparatus at high temperature are lower than room temperature DAC experiments (Figure 2.3). Stress levels measured in Chen et al. (2002) (Figure 2.3, light red X) and Girard et al. (2016) (Figure 2.3, red diamonds) are 2–3 GPa lower than measurements of Meade & Jeanloz (1990) and Merkel et al. (2003) at similar pressures, though the large error bars of Girard et al. (2016) do overlap with the DAC data. Interestingly, the stress levels measured in the study of Chen et al. (2002) at 1073 K are very similar to those of Girard et al. (2016) at ~ 2000 K. It is unsurprising that stress relaxation provides a lower value than steady state measurements. Likewise, the DAC annealing points of Miyagi & Wenk (2016) at ~ 50 GPa are quite low. Recently Kraych et al. (2016) used molecular dynamics simulations to study temperature dependence of the strength of Brg. At 30 GPa, the calculations of Kraych et al. (2016) show reasonable good agreement with both room temperature DAC measurements and the high-temperature measurements of Girard et al. (2016), showing the great potential for theory to link room-temperature measurement to high-temperature measurements and also the potential to link laboratory strain rates to mantle strain rates.

Post-Perovskite. For MgSiO_3 pPv only two studies report differential stress as a function of pressure (Merkel et al., 2007; Miyagi et al., 2010). A third high-temperature study reported a differential stress of 0.25–1.5 GPa at a pressure range of 130–156 GPa and 2500–3000 K (Wu et al., 2017), however, in this study the MgSiO_3 pPv samples were sandwiched between layers of either NaCl or KCl and so it is likely that the measured stress levels reflect the flow strength of the NaCl or KCl pressure medium rather than that of MgSiO_3 pPv.

There is a large pressure gap between the highest-pressure measurements on Brg at ~ 60 GPa and strength measurements on MgSiO_3 pPv at pressures > 130 GPa (Figure 2.3). The two measurements on MgSiO_3 pPv

are similar though those of Merkel et al. (2007) (Figure 2.3, blue open squares) are higher than those of Miyagi et al. (2010) (Figure 2.3, green open triangles). For these measurements, Miyagi et al. (2010) used a moment pole stress model and as discussed above the small error bars (smaller than the symbols) only represent fitting errors. In contrast, the study of Merkel et al. (2007) has small errors (smaller than the symbols) but uses the method of Singh et al. (1998). The small error bars in this study are due to that fact that there are only small variations in stresses calculated on different lattice planes.

Differences in differential stress measurements between Miyagi et al. (2010) and Merkel et al. (2007) could be due to composition. A natural enstatite was used for synthesis in Merkel et al. (2007), whereas a synthetic MgSiO_3 glass was used as starting material in Miyagi et al. (2010). Another possibility is grain size. Visual comparison of raw diffraction images in these two studies shows spottier diffraction rings in Miyagi et al. (2010), which qualitatively indicates larger grain size, and may result in lower flow strength. Interestingly, if room temperature flow strength measurements on Brg are compared to pPv, the highest value measured in Brg is 11.9 GPa at a pressure of 52 GPa (Miyagi & Wenk, 2016). In pPv the highest differential stress value is 11.1 GPa at 177 GPa (Miyagi et al., 2010). If one assumes that pressure increases the flow strength of Brg (as would be expected), then at room temperature pPv may be significantly weaker than Brg. A theoretical study by Ammann et al. (2010) suggests that high-temperature strength of MgSiO_3 pPv may be much lower than Brg based on calculated diffusion coefficients. Likewise, experimental work on pPv analogs found that during high temperature deformation the pPv phase is ~ 5 – 10 time weaker than the perovskite (Pv) phase (Dobson et al., 2012; Hunt et al., 2009). If room temperature flow strength is lower and if diffusion is faster in MgSiO_3 pPv, there is a high likelihood that Brg is significantly stronger than MgSiO_3 pPv over a range of pressure and temperature conditions. If the strength contrast between Brg and pPv is as large as the analog studies indicate then pPv may be similar or even weaker than Fp.

2.4.2. Textures and Slip Systems in Lower Mantle Phases

Recently, Merkel & Cordier (2016) reviewed slip systems in lower mantle and core phases. As such the following discussion will briefly review textures and slip systems in lower mantle phase but will mostly focus on more recent developments. For a more detailed discussion of studies on slip systems prior to 2016 and for a figure showing the relationship between crystal structures and slip systems, the reader is referred to the review by Merkel & Cordier (2016). A summary of experimentally

Table 2.1 Summary of inferred slip systems in the major lower mantle phases and the conditions under which they are expected to dominate based on experimental data. See text for details of the experiments.

Mantle phase	Slip system	P-T conditions
Ferropericlase	{110}<1- $\bar{1}0$ > {100}<011>	High P, low T High P, high T
Ca-Perovskite	{110}<1-10>	High P low T
Bridgmanite	(001) in [100], [010] or <110> (100)[010] (100){001}	P < ~55 GPa, low T P > ~55 GPa, low T High P, high T
Post-Perovskite	(001)[100] (010)[100] and (010)<u0w>	High P, low T and high P, high T CalrO ₃ , high P, low T, and high P, high T

inferred slip systems of lower mantle phases is given in Table 2.1.

In compression studies texture development is typically represented by inverse pole figures (IPFs) of the compression direction (Figures 2.4–2.5). IPFs show the probability of finding the pole to a lattice plane in the compression direction (i.e., the relationship between one sample direction and all crystallographic plane normals). Texture intensity is typically given in multiples of random distribution (m.r.d.) or multiples of uniform distributions (m.u.d.) where an m.r.d. or an m.u.d. of 1 is random and a higher or lower number represents a greater or fewer number of orientations, respectively. In cases where the deformation geometry is more complex than compression (e.g., simple shear), it is common to represent textures with pole figures (Figure 2.4g). Pole figures show the orientation of a specific lattice plane normal to the sample coordinate system (i.e., one or a few specific lattice planes to all sample directions).

Ferropericlase. Perhaps due to their stability at ambient conditions Per and Fp are most studied of the mantle phases (Heidelbach et al., 2003; Immoor et al., 2018; F. Lin et al., 2017; Long et al., 2006; Merkel et al., 2002; Stretton et al., 2001; Uchida et al., 2004; Yamazaki & Karato, 2002). For a detailed review of deformation mechanisms in Per the reader is referred to (Amodeo et al., 2018). Slip in Per and Fp occurs in the $\langle 110 \rangle$ direction on {110}, {100} and {111} planes (Amodeo et al., 2018). In both Per and Fp low temperature deformation is by dominant slip on {110}<1 $\bar{1}0$ > over a wide range of pressures (Table 2.1; F. Lin et al., 2017; J.-F. Lin et al., 2009; Merkel et al., 2002; Paterson & Weaver, 1970; Tommaseo et al., 2006). High pressure compression studies at low temperatures show textures characterized by {100} at high angles to compression which is attributed to slip on {110}<1 $\bar{1}0$ > (Figure 2.4a, Table 2.1; Immoor et al., 2018; J.-F. Lin et al., 2009; Marquardt & Miyagi, 2015; Merkel et al., 2002; Tommaseo et al., 2006). High-temperature studies on Per show increased activity of the {100}<011> slip system with

elevated temperature (Appel & Wielke, 1985; Copley & Pask, 1965; Hulse et al., 1963; Paterson & Weaver, 1970; Sato & Sumino, 1980).

Theoretical calculations (Amodeo et al., 2012, 2016) and single crystal deformation experiments on Per to 8 GPa (Girard et al., 2012) suggest a possible transition to {100}<011> slip at pressure somewhere between 23 and 40 GPa. High pressure DAC measurement on Fp documented an abrupt increase in yield strength between 20 and 60 GPa, which may be associated with this slip system transition (Marquardt & Miyagi, 2015). However for a transition from {110}<1 $\bar{1}0$ > slip to {100}<011> one would expect a texture change from {100} planes oriented at high angles to compression to {110} planes at high angle to compression (Figure 2.4a, b). Texture changes associated with a pressure induced slip system changes have not been documented and this may be due to difficulty in overprinting the lower pressure textures (Amodeo et al., 2016).

In Fp, Fe content may play a role in controlling deformation mechanisms. Subtle change in textures observed in room temperature DAC experiments may be linked to reduced activity of {110}<1 $\bar{1}0$ > (Tommaseo et al., 2006). In low pressure, high-temperature shear experiments (300 MPa and up to 1473K), changes in deformation mechanisms appear to be most pronounced in samples with Fe contents in excess of 50% (Long et al., 2006). During high-temperature deformation of Fp to high shear strains, {111}<1 $\bar{1}0$ > slip may also be activated (Heidelbach et al., 2003; Long et al., 2006; Yamazaki & Karato, 2002). Recent resistive heated DAC experiments on Fp show a transition to a {110} maximum in IPFs of the compression direction (Figure 2.4b), and this is attributed to increased activity of {100}<011> slip with temperature at mantle pressures (Table 1). At ~1400K and pressures of 30–60 GPa both {110}<1 $\bar{1}0$ > and {100}<011> slip systems are ~equally active (Immoor et al., 2018). Based on current experimental data, it appears that {110}<1 $\bar{1}0$ > is typically dominant in Fp at lower pressure and temperature and at high pressure and temperature {100}<011> becomes increasingly dominant (Table 2.1).

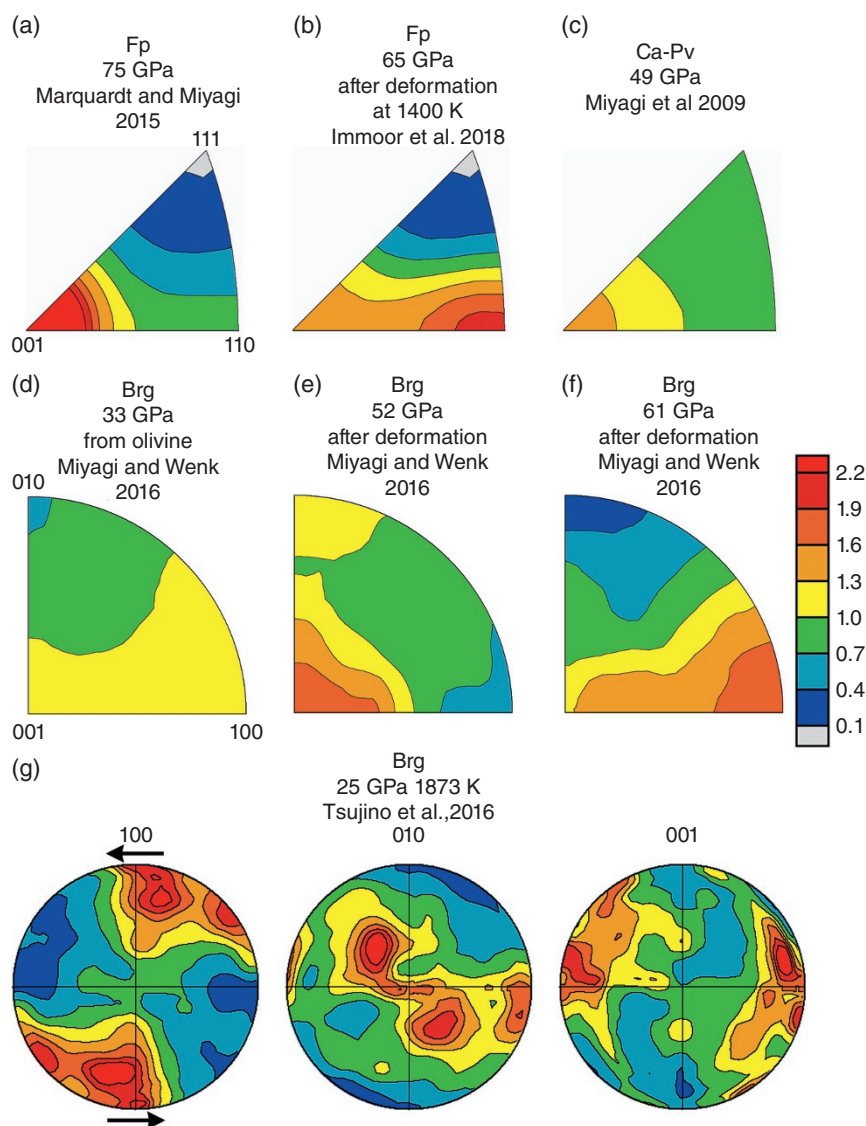


Figure 2.4 Summary of textures observed in ferropericlase (a) and (b), CaSiO_3 perovskite (c), and in bridgmanite (d–g). Textures are shown as equal area, upper hemisphere, projection inverse pole figures of the compression direction for (a–f). Due to the lower symmetry deformation geometry (shear) the texture data of Tsujino et al. (2016) are represented as pole figures of (100) (010), and (001). Black arrows indicate the sense of shear. The textures plotted in g) are those from the extended data figure 7 of Tsujino et al. (2016) which were obtained using the Materials Analysis Using Diffraction program (Lutterotti et al., 1997). Scale bar is in multiples of random distribution.

CaSiO_3 Perovskite. There is only one room temperature deformation experiment measuring texture development in Ca-Pv (Miyagi et al., 2009). This experiment measured texture development at ~ 25 – 50 GPa and found a $\{100\}$ compression texture (Figure 2.4c) consistent with deformation on the $\{110\}\{1\bar{1}0\}$ slip system (Table 2.1; pseudo cubic reference). This is consistent with computational work (Ferré et al., 2009). One should note that Ca-Pv deviates from the cubic symmetry but the structure is poorly constrained due to the small deviations from cubic

symmetry. Several potential lower symmetry structures have been proposed (Shim et al., 2002).

Deformation of Bridgmanite. A few deformation studies exist on Brg, using the DAC (Meade et al., 1995; Meade & Jeanloz, 1990; Merkel et al., 2003; Miyagi & Wenk, 2016; Wenk et al., 2004; Wenk, Lonardelli, et al., 2006), a modified large-volume press assembly (Chen et al., 2002; Cordier et al., 2004; Tsujino et al., 2016), and the RDA (Girard et al., 2016). Early DAC

deformation studies of Brg found no evidence for texture development in decompressed samples (Meade et al., 1995) or in *in-situ* measurements of samples deformed outside the Brg stability field (Merkel et al., 2003). In contrast, Wenk et al. (2004) and Wenk, Lonardelli, et al. (2006) reported significant texture development in Brg and Brg + Fp aggregates synthesized *in-situ* in the DAC from different starting materials. Different textures were observed, depending on starting material, and it was suggested that textures could be explained by slip on (010)[100], (100)[010], and (001)(110). Twinning on (110) was also suggested as a mechanism for texture development (Wenk et al., 2004). However, subsequent measurements by Miyagi & Wenk (2016) showed that the wide range of textures observed in Wenk et al. (2004) were likely due to the phase transformation from varied starting materials. Synthesis of bridgmanite from enstatite results in a strong (001) transformation texture while synthesis from olivine or ringwoodite results in a weak (100) transformation texture (e.g., Figure 2.4d; Miyagi & Wenk, 2016).

Twinning has been documented in Brg and is associated with the phase transformation to Brg but also has been observed in stress relaxation experiments. TEM studies of recovered samples from high-pressure experiments documented reflection twins on (110) and (112) (Martinez et al., 1997; Y. Wang et al., 1990, 1992). *In-situ* stress relaxation measurements at 20 GPa and 1073 K using the LVP and also found evidence for activity of (110) twinning (Chen et al., 2002).

Experimental evidence for slip systems in Brg generally shows either deformation on (001) planes or (100) planes. Several studies have documented texture, line broadening, or TEM observations consistent with slip on (001) planes. Cordier et al. (2004) suggested (001)[100] and (001)[010] dislocations based on x-ray line broadening analysis of samples recovered from a large-volume press deformation experiment at 25 GPa and 1700 K. A TEM study by Miyajima et al. (2009) documented $\langle 110 \rangle$ Burgers vectors, indicating that the likely slip plane is (001). Room-temperature DAC experiments observed a (001) maximum at pressures < 55 GPa and room temperature (Figure 2.4e), consistent with dominant (001) slip, with some combination of slip in [100], [010], and $\langle 110 \rangle$ directions (Miyagi & Wenk, 2016). However, after laser annealing and compression above 55 GPa, Miyagi & Wenk (2016) observed a (100) texture maximum (Figure 2.4f) consistent with slip on (100). Interestingly, numerical modeling using first principles and the Peierls-Nabarro model suggests that at pressures < 30GPa, slip on (001)(110) is dominant, but at higher pressures (100)[010] slip is more active in Brg (Mainprice et al., 2008). Recent shear deformation

experiments to 80% strain at 25 GPa and 1873 K in the D-DIA with a Kawai type assembly showed textures consistent with slip on (100)[001] (Figure 2.2g; Tsujino et al., 2016).

Generally, numerical models to evaluated slip system strengths find that (010)[100] and (100)[010] should be the easiest slip systems (Ferré et al., 2007; Gouriet et al., 2014; Hirel et al., 2014). So far, experiments have not documented evidence for (010) slip. One should note, however, that due to geometric constraints and the number of symmetric variants, the easiest slip systems is not always most active during deformation (Mainprice et al., 2008). Based on experiments, it appears that at lower pressures and room temperature, slip on (001) dominates, but at higher pressure and at higher temperature (100), slip appears to be active (Table 2.1). However, systematic studies of slip system changes in Brg as a function of temperature, pressure, strain rate, and composition have not been performed and remain technically challenging. Furthermore, numerical simulations indicate that in the lower mantle, pure-climb creep (Nabarro, 1967) may be the dominant deformation mechanism (Boioli et al., 2017; Cordier & Goryaeva, 2018; Reali et al., 2019), but due to experimental limitations, this deformation regime has yet to be explored in bridgmanite.

2.4.3. Post-Perovskite

Although many studies have focused on slip systems and texture development in MgSiO_3 pPv and pPv analogs, the dominant slip systems are still debated. In general, the slip plane tends to be better constrained than slip direction. Nonetheless, three sets of dominant slip systems have been proposed for pPv. These are slip on (010) planes, slip on (100), and/ or $\{110\}\langle 1\bar{1}0 \rangle$, and finally slip on the (001) plane.

Early studies proposed that slip should occur on the (010) plane based on the fact that this coincides with the layering of the SiO_6 octahedra in the pPv structure (Iitaka et al., 2004; Murakami et al., 2004; Oganov & Ono, 2004). Several theoretical calculations have also supported slip on (010) in pPv or pPv analog materials (Carrez et al., 2007b, 2007a; Goryaeva et al., 2015a, 2015b, 2016, 2017; Metsue et al., 2009). Experimental evidence for slip on the (010) plane in pPv is limited to the CaIrO_3 analog. Due to the fact that it is stable in the pPv structure at ambient or near-ambient conditions (Rodi & Babel, 1965), CaIrO_3 has been the most studied for deformation mechanisms of the pPv structured compounds. In compression studies, CaIrO_3 develops a maximum at (010) in the IPF (Figure 2.5a; Hunt et al., 2016; Miyagi, Nishiyama, et al., 2008; Niwa et al., 2007). A wide range of experiments using the DAC, D-DIA, and other large volume apparatus at

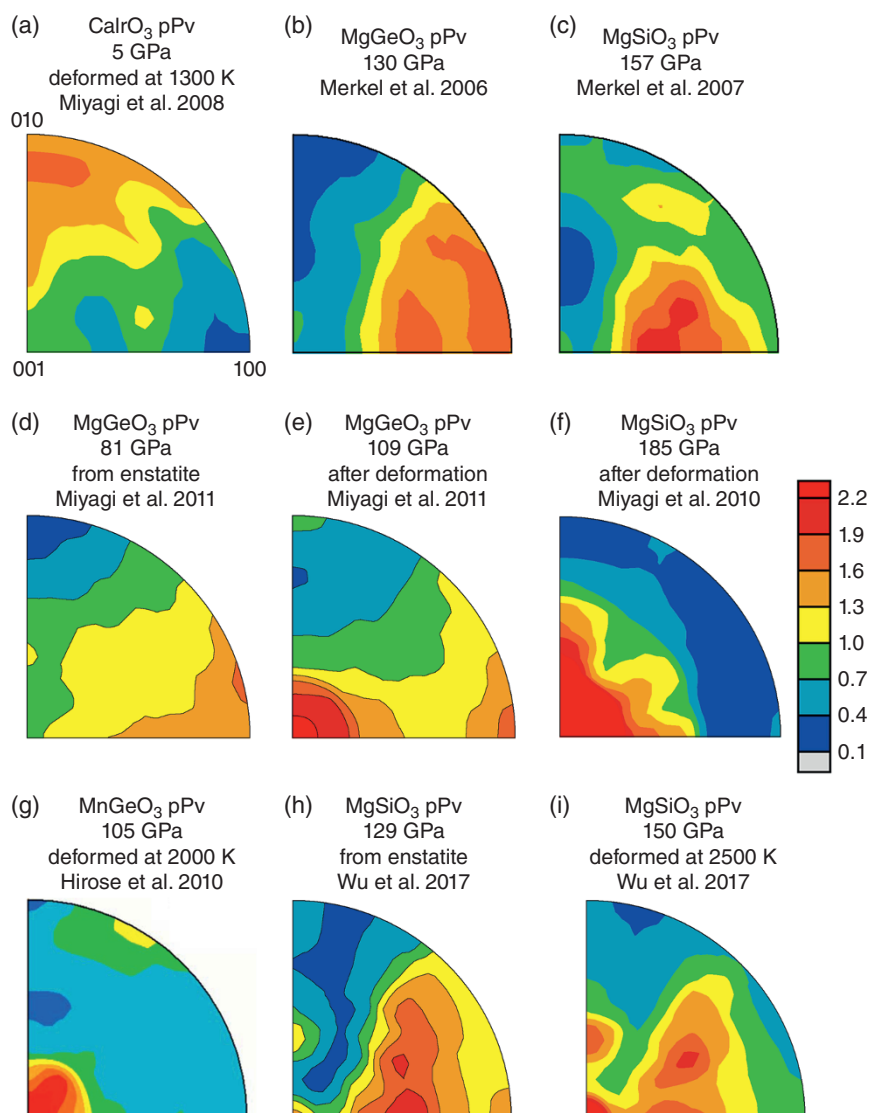


Figure 2.5 Summary of the various texture types observed in post-perovskite structured compounds over a range of pressure and temperature conditions. Textures are represented as equal area, upper hemisphere projection, inverse pole figures of the compression direction. Scale bar is in multiples of random distribution.

pressure and temperature condition up to 6 GPa and 1300 K over a range of strain rates all find dominant slip on (010) [100] and (010) $\langle u0w \rangle$ (Table 2.1; Hunt et al., 2016; Miyagi, Nishiyama, et al., 2008; Miyajima et al., 2006; Miyajima & Walte, 2009; Niwa et al., 2007; Walte et al., 2007, 2009; Yamazaki et al., 2006).

Evidence for (100) or and/ or $\{110\}\langle 1\bar{1}0 \rangle$ comes from theoretical calculations and two early DAC studies. First-principles metadynamics and energetics of stacking faults predicted slip on $\{110\}\langle 1\bar{1}0 \rangle$ during the phase transformation from Brg to pPv (Oganov et al., 2005). Shortly thereafter, room temperature radial diffraction DAC experiments on MgGeO_3 pPv and MgSiO_3 pPv found

textures characterized by (100) planes at high angles to compression (Figure 2.5b, c). Polycrystal plasticity modeling showed that these texture could be explained by slip on $\{110\}\langle 1\bar{1}0 \rangle$ and (100) planes (Merkel et al., 2006, 2007). It is important to note that both Merkel et al. (2006) and Merkel et al. (2007) converted to the pPv phase directly from the enstatite phase, and no change in texture was observed upon further pressure increase. Subsequent studies on MgGeO_3 pPv in the DAC using axial diffraction geometry (Okada et al., 2010) and radial diffraction geometry (Miyagi et al., 2011) found that alignment of (100) planes at high angles to compression resulted from the phase transformation

from an enstatite starting material (Figure 2.5d). Further compression showed that the initial (100) transformation texture shifted to (001) (Figure 2.5e) upon deformation consistent with dominant slip on (001)[100] (Table 1; Miyagi et al., 2011; Okada et al., 2010).

Slip on (001) planes in the pPv structure is supported by several DAC experiments both at ambient conditions (Miyagi et al., 2010, 2011; Okada et al., 2010) and high temperature (Hirose et al., 2010; Wu et al., 2017). Miyagi et al. (2010) found in pPv synthesized from MgSiO₃ glass that an initial (001) texture was observed after conversion at 148 GPa. Upon compression to 185 GPa this texture doubled in strength, consistent with slip on the (001) plane (Table 2.1; Figure 2.5f). High-temperature deformation experiments on MnGeO₃ pPv documented the development of a (001) texture during compression from 63 GPa to 105 GPa at 2000 K (Figure 2.5g; Hirose et al., 2010). Deformation textures consistent with (001) slip have also been documented in MgGeO₃ pPv (Figure 2.5e; Miyagi et al., 2011; Okada et al., 2010). More recently, Wu et al. (2017) observed in MgSiO₃ pPv a similar transformation texture to that of Merkel et al. (2007) (Figure 2.5h) followed by the development of a (001) texture during compression to 150 GPa at 2500 K (Figure 2.5i).

Experimental deformation of MnGeO₃ pPv, MgGeO₃ pPv, and MgSiO₃ pPv are all consistent with slip on (001) (Table 2.1; Figure 2.5e, f, g, i). There is no clear experimental evidence to support deformation on (100) or {110}{1 $\bar{1}$ 0}. Textures previously attributed to slip on (100) and {110}{1 $\bar{1}$ 0} have been shown to be due to the transformation from enstatite to pPv (Figure 2.5d, h). The evidence that slip on (010)[100] is the dominant system in CaIrO₃ is clearly robust based on the large number of independent and consistent experimental results (Hunt et al., 2016; Miyajima et al., 2006; Miyajima & Walte, 2009; Niwa et al., 2007; Walte et al., 2007, 2009; Yamazaki et al., 2006). CaIrO₃ pPv has very different structural parameters than MgSiO₃ pPv, in terms of bond lengths, bond angles, and octahedral distortions (Kubo et al., 2008). Raman spectroscopy measurements have also indicated that bonding in CaIrO₃ pPv is different from other pPv structured compounds (Hustoft et al., 2008). First-principles computations find CaIrO₃ pPv to have elastic properties and an electronic structure that are inconsistent with MgSiO₃ pPv (Tsuchiya & Tsuchiya, 2007). Finally, first-principles calculations based on the Peierls-Nabarro model indicate that MgSiO₃, MgGeO₃, and CaIrO₃ exhibit considerable variations in dislocation mobilities (Metsue et al., 2009). Thus, it is perhaps unsurprising that CaIrO₃ pPv appears to be a poor analog for the deformation behavior of MgSiO₃ pPv. This is unfortunate, as CaIrO₃ pPv is the only pPv to be systematically studied at high temperature and varied strain rates.

2.5. POLYPHASE DEFORMATION

Nearly all deformation experiments on lower mantle phases have been performed on single-phase materials. Some notable exceptions are DAC texture measurements on Brg and Fp mixtures (Miyagi & Wenk, 2016; Wenk et al., 2004; Wenk, Lonardelli, et al., 2006), differential stress measurements on Brg and Fp mixtures using the DAC (Miyagi & Wenk, 2016), and high shear strain steady state deformation using the RDA (Girard et al., 2016).

2.5.1. Stress and Strain Partitioning in Polyphase Aggregates

Several challenges exist for studying deformation of polyphase aggregates. Of primary importance is understanding stress and strain or strain rate partitioning between phases. This can affect both the interpretation of stress levels measured in the individual phases as well as attempts to estimate the bulk mechanical properties of the aggregate. Based on observations of naturally deformed crustal rocks and analogs deformed in laboratory experiments, Handy (1990, 1994) outlined a method to place bounds on the mechanical properties of a two-phase aggregate with non-Newtonian rheology and a strength contrast. Others have also outlined methods to study two-phase deformation either analytically (e.g., Takeda (1998) for Newtonian rheology) or numerically (e.g., Jessell et al., 2009; Takeda & Griera, 2006; Treagus, 2002; Tullis et al., 1991). However Handy's phenomenological description remains a useful approach to addressing the problem of polyphase deformation. Handy's description will be briefly summarized below.

In Handy's formulation the strength of a two-phase mixture depends not only on the rheological properties of the individual phases but also on the microstructure and phase proportions. In Handy's formalism bounds can be placed on the mechanical behavior of a two phase aggregate as the bulk properties lie between two end members. These end members are based on the degree of interconnectivity of the weaker or the stronger phase. If the weak phase is interconnected, the microstructure is termed an interconnected weak layer (IWL) (Figure 2.6a), and if the strong phase is connected, it is termed a load-bearing framework (LBF) (Figure 2.6b).

In the case of an IWL microstructure, the aggregate approaches an iso-stress state. That is to say that both phases experience similar stress levels but strain at very different rates. For a pure iso-stress condition, the soft phase modulates the stress levels and strain is partitioned into the weak phase (Figure 2.6c). Thus, the bulk properties of the aggregate approach those of the softer phase. In cases where yield strength contrast is large, stress levels in

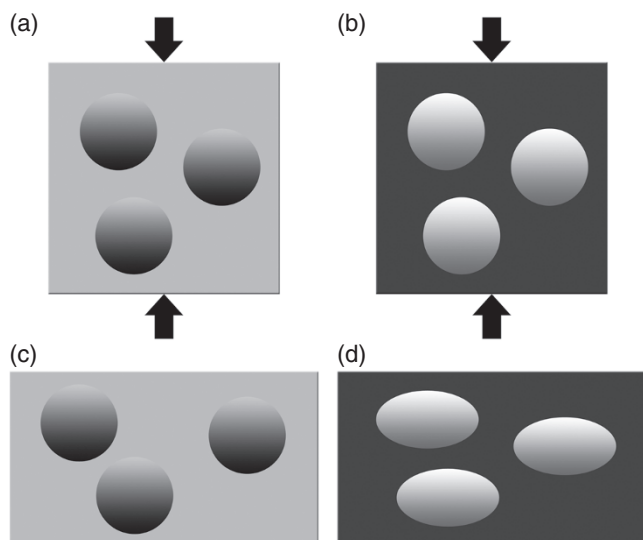


Figure 2.6 Schematic of (a) interconnected weak layer and (b) load-bearing framework microstructures. Light gray indicates the weaker phase and dark gray/black indicates the stronger phase. During deformation of the interconnected weak layer microstructure (c), strain is partitioned into the weaker phase and strong inclusions remain relatively undeformed. Stresses in the two phases will be similar but large strain heterogeneity is induced in the weak phase as the weaker material must flow around the rigid inclusions. During deformation of the load-bearing framework microstructure (d) strain is distributed ~homogeneously as the strong matrix imposes its strain and strain rate on the weaker inclusions. Stresses will be lower in the weaker phase as it flows at lower stress than the stronger matrix.

the hard phase may be too low to result in yielding as stress levels in the strong phase are limited by yielding of the soft phase. Although IWL approaches that of an iso-stress state, these are not identical and there are several important differences. For IWL deformation, if the aggregate is composed of small to moderate amounts of the weak phase and/or the strong phase has a significantly higher stress exponent than the weak phase, then the weak phase will deform at higher stresses and strain rates than the iso-stress condition and the stronger phase will deform at lower stress and strain rate than the iso-stress condition. However, if there are large proportions of the softer phase and/or the stress exponent of the harder phase is similar or smaller than the soft phase, then stress levels in the harder phase will exceed the soft phase.

In contrast, when a LBF microstructure exists, the soft phase is not interconnected and the rheology of the aggregate is controlled by the harder phase. Stress is supported primarily by the stronger phase and the stronger phase imposes its strain rate on the softer phase (Figure 2.6d). In this case, stress levels in the two phases diverge. Although local heterogeneous strain rate occurs at phase

boundaries, the aggregate as a whole behaves in a manner very close uniform strain rate in the two phases.

Determining conditions where IWL versus LBF are stable depends on phase proportions, strength contrast and total strain. Strength contrast will be determined by the contrast in parameters in the flow laws for the phases (e.g., activation energy and volume and stress exponent). Larger strength contrasts between the phases and a lower volume fraction of the softer phase promotes stability of a LBF. Generally speaking IWL dominates when the volume fraction of the weak phase exceeds ~30–40% (i.e., percolation threshold). However, large strains also tend to favor IWL microstructures as the weaker inclusions coalesce to form interconnected microstructures resulting in a transition from LBF to IWL behavior (Handy, 1990, 1994).

2.5.2. Differential Stresses in High Pressure Studies of Polyphase Aggregates

Given the discussion above, the difficulty in interpreting stress data from high pressure experiments on polyphase materials becomes clear. Unless one knows if a material deforms in an IWL or LBF style, interpretation of stresses measured in individual phases becomes problematic. In high-pressure experiments that use lattice strain to calculate stresses, the stresses are measured in the individual phases and there is not currently a technique that is used to independently measure the bulk strength of the material. Looking at the two deformation experiments on Brg and Fp that are shown in Figures 2.2 and 2.3, a large discrepancy is observed. Miyagi & Wenk (2016) find room-temperature strength of Brg to be ~1.4 times that of Fp, while in contrast Girard et al. (2016) find Brg to be about four times stronger. Notable differences exist between these two experiments, primarily that the work of Girard et al. (2016) is performed at high temperature and under steady-state conditions. Computations by Kraych et al. (2016) find the strength contrast to be ~4 at 30 GPa and room temperature, but find that this decreases at high temperatures. Although the calculated strength of Brg in this study is similar to those of experiments at room temperature and high temperature, the strength contrast trend is inconsistent with the two-phase experiments. However, in the experiments this may be due to microstructure and the effect of IWL versus LBF-style deformation. Miyagi & Wenk (2016) did not recover samples for microstructural analysis; however, the larger sample in Girard et al. (2016) is amenable to documentation of microstructure. Microstructural analysis from this experiment seems to indicate that although Brg appears to be interconnected, as would be expected for LBF behavior, strain seems to be largely partitioned into the softer Fp, which is expected for IWL behavior.

Based on the description of Handy, an LBF should result in large differences in stresses measured in each phase whereas the stresses measured in each phase for IWL should be close. One possibility for this discrepancy is that the samples in Girard et al. (2016) are transitioning between LBF and IWL, and if this is the case this transition would occur at strains greater than 60–70%. Indeed, this study concluded that at high strains shear weakening and strain localization is expected to occur. In contrast to Girard et al. (2016), a study on 72% CaGeO₃ Pv + 28% MgO as an analog for Brg + Fp found a strength contrast of ~2 and found that the stresses in CaGeO₃ in the two-phase experiments were higher than in single-phase experiments. Based on this, it was concluded that a LBF behavior dominates (Y. Wang et al., 2013). Another analog study on NaMgF₃ Pv + NaCl analogs with a strength contrast of ~10 found systematically lower stresses in NaMgF₃ with the addition of 15–70% NaCl (Kaercher et al., 2016). In contrast to NaMgF₃, stress levels remained ~ constant in NaCl independent of volume fraction. Deformation behavior of samples with volume fractions of NaCl > 50% were consistent with an IWL. Samples with less than 50% NaCl were not consistent with either an IWL or an LBF and it was concluded that the behavior of the samples were somewhere intermediate to IWL and LBF.

There are several reasons why high-pressure experiments may not match stress levels expected for either IWL or LBF microstructures. IWL and LBF are bounds on stress and strain partitioning, so it is not surprising that experiments may deviate from these two end-member behaviors. In Handy's formulation, constant volume deformation is assumed, and this may not necessarily be the case for high pressure (and high temperature) experiments, particularly if pressure or temperature changes occur during deformation, such as in DAC experiments and to a lesser extent in large volume deformation. Although nonlinearity of deformation is accounted for, the behavior predicted by Handy (1990, 1994) assumes plastically isotropic phases. This is not strictly true for most minerals particularly those deforming via dislocations. Finally, given that the percolation threshold for a phase is ~30–40% by volume, there is a range of phase proportions where interconnectedness of both phases occurs. Although simultaneous interconnectedness of phases may not be stable to higher strains, it may be stable over relatively small strains experienced in experiments, and one would expect that this would result in stress and strain partitioning that is intermediate to IWL and LBF end members.

2.5.3. Texture Development in Polyphase Materials

Texture development in polyphase materials is also complex. Experimental texture studies in polyphase earth

materials are fairly limited, however, in material science deformation and texture development in composites has been studied more extensively. The following discussion will focus on composites with large strength contrasts, as this is more relevant to the discussion of lower mantle aggregates. One class of materials that have a large strength contrast is metal matrix composites. These materials are composed of a ductile metal matrix that has been reinforced with hard carbides, borates, or oxides and thus present a composite with a large strength contrast. It is commonly observed that the inclusion of hard particles results in modification of texture type or a reduction in texture strength in the metal matrix (e.g., Garcés et al., 2005, 2006; Poudens et al., 1995; S. C. Xu et al., 2011; Zhang et al., 2004). In these materials, high strength particles induce complex strain fields around these nearly undeformed inclusions, resulting in texture strength reduction in the metal matrix. In Al+SiC composites, SiC concentrations >10% show decreased texture strength in the Al matrix (Poudens et al., 1995; Zhang et al., 2004). Likewise Garcés et al. (2006) found that in Mg+Y₂O₃ composites, the addition of yttria particles lowers texture strength in the softer Mg phase due to complex deformation patterns around the hard ceramic particles. In aluminum borate reinforced 6061 aluminum alloy, texture development in the aluminum matrix is quite different when compared to pure phase 6061 alloys (S. C. Xu et al., 2011). These cases are extreme examples where the hard phase does not deform and so the matrix must flow around the particles. A less extreme example is a study on extrusion of Al-Pb composites containing 20%, 40%, 60%, and 80% volume fractions of Al (Brokmeier et al., 1988). This study found that in both phases, increasing the volume fraction of a phase resulted in a decrease in texture strength of the other phase. The texture decrease in the harder Al phase is attributed to increased strain partitioning into the softer phase (i.e., there is less internal deformation of Al grains as the volume fraction of Pb increases). In the softer Pb phase, the decrease in texture strength with addition of Al is attributed to heterogeneous strain induced in the Pb phase by the hard Al grains. The authors term this effect “turbulence of flow” (Brokmeier et al., 1988). These studies consistently show that in composites with large strength contrast, texture reduction, or significant texture modification in the softer phase is linked to deformation heterogeneity in regions adjacent to the harder phase. In particular, stronger particles generate complex deformation geometries in surrounding regions, disrupting coherent texture formation in the softer phase.

In earth science, crustal and upper mantle materials can exhibit similar behaviors. Handy (1994) notes in his discussion of IWL behavior that there is large stress, strain, and strain rate heterogeneity in regions surrounding hard feldspar grains in naturally deformed quartz feldspar

mylonites, but texture measurements were not reported. In quartz + mica aggregates, the addition of rigid micas has been shown to reduce texture strength in the quartz phase both in simulations and experiments (Canova et al., 1992; J. Tullis & Wenk, 1994). Bystricky et al. (2006) studied deformation of olivine + $(\text{Mg}_{0.7}\text{Fe}_{0.3})\text{O}$ as an analog for polyphase mantle rock. This sample contained 20% olivine and was deformed in dislocation creep to very high shear strains of $\gamma \sim 15$ in a gas media apparatus. In these experiments, the majority of the strain was partitioned into the Fp matrix but olivine grains did deform and developed texture. Although the Fp phase did texture, the texture patterns of the Fp differed significantly from previous single phase experiments (Heidelbach et al., 2003; Yamazaki & Karato, 2002). These anomalous textures were attributed to local heterogeneity in flow geometry adjacent to the olivine clasts (Bystricky et al., 2006). Similar to the behavior of metal composites, these studies show that large differences in rheological properties between two phases in an aggregate can result in heterogeneous deformation even with relatively small amounts of the harder phase. Likewise, in earth materials heterogeneous deformation of the softer phase can result in significantly modified textures and/or randomization of the softer phase.

2.5.4. Texture Development in High Pressure Studies of Polyphase Aggregates

Similar trends in polyphase texture development are also observed in high-pressure studies. When Brg + Fp are deformed together in the DAC, Fp does not develop significant texture (Miyagi & Wenk, 2016; Wenk et al., 2004; Wenk, Lonardelli, et al., 2006) (Figure 2.7). In these materials, weaker Fp is expected to accommodate the majority of strain (Girard et al., 2016), but in contrast to metal matrix composites and studies on quartz + mica and olivine + Fp aggregates the harder bridgmanite phase is volumetrically dominant. This behavior is similar however to Al+Pb where textures in Pb become nearly random at larger volume fractions of Al (Brokmeier et al., 1988). Similarly, in two-phase aggregates of NaMgF_3 Pv + NaCl deformed in the D-DIA at a range of strain rates, temperatures and phase proportions, NaCl does not develop significant texture while the stronger NaMgF_3 phase does (Kaercher et al., 2016). These materials have large strength contrasts of ~ 10 and this behavior is observed over a wide range of phase proportions (NaCl = 15–70%). Microstructural analysis using synchrotron tomography and scanning electron microscopy shows that although texture development in this phase is weak, the majority of the strain partitions into NaCl. Plasticity modeling indicates that local stress–strain heterogeneities caused by grain-to-grain interactions between the Pv phase

and the NaCl phase result in a randomization of the NaCl phase (Kaercher et al., 2016), consistent with polyphase texture studies at lower pressures (Brokmeier et al., 1988; Canova et al., 1992; Garcés et al., 2006; Poudens et al., 1995; J. Tullis & Wenk, 1994).

In contrast to experiments on Brg + Fp in the DAC and NaMgF_3 + NaCl aggregates in the D-DIA, D-DIA deformation experiments on CaGeO_3 + MgO do observe texture development in MgO (Y. Wang et al., 2013). Notably the strength contrast between CaGeO_3 and MgO (~ 2) is significantly lower than NaMgF_3 and NaCl (~ 10) and similar or lower than Brg and Fp (~ 1.4 – 4). This discrepancy may be due to strength contrast but also to the degree of anisotropy of the Pv phase. Both Brg and NaMgF_3 are orthorhombic and exhibit a dominant slip plane that has no additional symmetric variants (of the plane). In Brg the dominant slip plane at room temperature appears to be (001) (e.g., Cordier et al., 2004; Miyagi & Wenk, 2016; Miyajima et al., 2009) or (100) at higher temperatures (Tsujino et al., 2016). In NaMgF_3 Pv the dominant slip plane appears to be (100) (Kaercher et al., 2016). Thus, plastic anisotropy of these phases is relatively high. In contrast, CaGeO_3 is close to cubic (pseudo-cubic) and deforms predominantly on the $\{110\}\langle 1\bar{1}0 \rangle$ slip system. This slip system has six symmetric variants and so plastic anisotropy is much lower than for Brg and NaMgF_3 Pv. Thus, it is likely that the degree of plastic anisotropy of the harder phase plays an important role in controlling texture development in the softer phase. The modeling of Kaercher et al. (2016) shows that highly anisotropic NaMgF_3 Pv grains impinge on NaCl grains and cause heterogeneous local stress–strain fields around the soft NaCl grains. This causes the local stress–strain field to deviate from the macroscopic field, and since this varies from grain to grain, the NaCl phase does not develop “coherent” texture.

In contrast to Brg + Fp and their analogs, deformation studies on pPv + Fp have not been performed either on the silicate system or in analog materials. Since Mg-pPv is orthorhombic and appears to exhibit dominant slip on the (001) plane (Miyagi et al., 2010) one might expect that Fp deformed with Mg-pPv may not develop texture due to high plastic anisotropy of the Mg-pPv. However, a theoretical study by Ammann et al. (2010) suggests that Mg-pPv may be considerably weaker than Brg. Experimental work on CaIrO_3 Pv and pPv found that the pPv phase is ~ 5 times weaker than the Pv phase (Hunt et al., 2009), and in NaCoF_3 the pPv phase is 5–10 times weaker than the Pv phase (Dobson et al., 2012). This strength difference is similar to or larger than proposed strength differences between Brg and Fp (Girard et al., 2016; Kraych et al., 2016; Miyagi & Wenk, 2016) and it is possible that MgSiO_3 pPv is similar in strength or even weaker than Fp. If MgSiO_3 pPv is significantly weaker than Brg, then

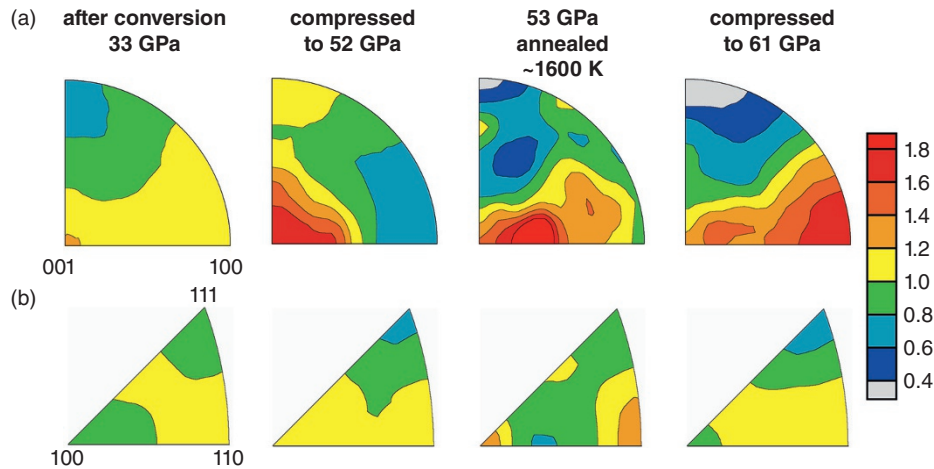


Figure 2.7 Texture development during diamond anvil cell deformation of bridgmanite + ferropericlae synthesized from San Carlos olivine. Inverse pole figures for bridgmanite are shown in (a) and inverse pole figures for ferropericlae are shown in (b). Surprisingly, ferropericlae, which is the weaker phase, does not develop texture while bridgmanite does. Source: Miyagi & Wenk (2016).

the strength contrast between MgSiO_3 pPv and Fp may be low enough that the polyphase behavior is significantly different than in Brg + Fp aggregates and it is not clear how texture may develop in the individual phases. Additionally experiments suggest coexistence of Brg and MgSiO_3 pPv in many regions above the CMB (Andraut et al., 2010; Grocholski et al., 2012). Thus the deformation behavior of MgSiO_3 pPv + Brg and MgSiO_3 pPv + Brg + Fp aggregates will also be important in the lowermost mantle.

Clearly, large differences in rheological properties between two phases in an aggregate can result in heterogeneous deformation, even with relatively small amounts of the harder phase. Heterogeneous deformation of the softer phase can result in randomization of the softer phase. While many examples on metals and crustal rocks are aggregates where the soft phase is volumetrically dominant, in high-pressure phases it appears that low-symmetry hard phases that are volumetrically dominant can disrupt texture formation in the soft phase. However, systematic study of this phenomenon as a function of plastic anisotropy, microstructure, phase fractions, and strength contrast has not yet been undertaken.

2.6. IMPLICATIONS

In polyphase mantle rock, complex interactions with respect to bulk strength are likely. At this point, it seems well established that Fp is weaker than Brg but the degree of this strength contrast is not fully constrained (Girard et al., 2016; Kraych et al., 2016; Miyagi & Wenk, 2016; Yamazaki & Karato, 2001b). Depending on the amount

of Fp and the microstructure of the mantle and IWL type, microstructure may be relevant and Fp would control the strength of the aggregate. Given that estimates of the volume fraction of Fp are likely to be less than 30%, stability of an IWL microstructure should be largely dependent on the total strain experienced by the aggregate. High-strain torsion experiments on a calcite + anhydrite mixture to shear strains of 57 at 1.5 GPa show extensive phase segregation that results in compositional layering similar to crustal mylonites (Cross & Skemer, 2017). If such phase segregation and compositional layering occurs in the lower mantle, it is likely that shear strain would be largely partitioned into the softer ferropericlae. Thus, in regions of high strain, such as in and around slabs, Fp is likely to control the strength of the mantle. If Fp in the mantle experiences a large increase in strength (Deng & Lee, 2017; Marquardt & Miyagi, 2015), this could lead to a mid-mantle increase in viscosity consistent with geophysical observations (Mitrovica & Forte, 2004; Rudolph et al., 2015). This strengthening and consequent viscosity increase could explain observations of mid mantle slab stagnation (Fukao & Obayashi, 2013; C. Li et al., 2008) and plume broadening (French & Romanowicz, 2015).

Ca-Pv, which is a relatively minor phase in the bulk of the lower mantle, can reach up 30% by volume in Mid-Ocean Ridge Basalts (MORB) subducted into the lower mantle (Hirose et al., 2005; Ricolleau et al., 2010). As such, it is important to understand the rheological behavior of this mineral in the lower mantle and to resolve the discrepancies between the current measurements of Shieh et al. (2004) and Miyagi et al. (2009). One potential implication of a strong Ca-Pv as suggested by the

measurements of Miyagi et al. (2009) is that it could act to strengthen the slab, and it may behave similarly to carbide or ceramic particles in metal matrix composites, reducing texture development in the other phases. This could lead to reduced anisotropy in MORB rich regions of the slab. However if the strength Ca-Pv is similar to the other phases then it will play a less profound role in controlling slab strength and anisotropy.

In deeper regions of the mantle, MgSiO₃ pPv is likely the dominant phase in regions above the CMB. Although a direct comparison of experiments is difficult, as pressures do not overlap, pPv appears to be weaker than Brg in DAC experiments. Given that theoretical calculations of diffusion coefficients also indicate that pPv is significantly weaker than Brg (Ammann et al., 2010) and that analog materials show the pPv phase to be 5–10 times weaker than Pv (Dobson et al., 2012; Hunt et al., 2009), it is reasonable to expect that pPv is likely to be one of the weaker phases in the lower mantle. Interestingly the strength contrast between Pv and pPv analogs is as large or larger than that predicted for Brg and Fp (Kraych et al., 2016); thus, Fp and pPv may have similar strengths. If this is the case, aggregates of pPv + Fp would be considerably weaker than the rest of the mantle, and this would lead to shear localization in the D'' layer. Shear localization above the CMB and resultant large strains and high strain rates could result in increased dislocation activity, consistent with presence of wide spread anisotropy in this region. Geodynamic models have also shown that a weak pPv layer will have important geodynamic implications for mantle convection in terms of heat transfer and temperature gradients, viscosity, and flow velocity (Nakagawa & Tackley, 2011; Samuel & Tosi, 2012).

Slip system activities and texture development in lower mantle phases have important implications for interpretation of seismic anisotropy. For a recent review of seismic anisotropy in the deep earth and methods to interpret anisotropy, see Romanowicz & Wenk (2017). The methodology that is typical used to relate slip systems to anisotropy has been to use a flow model combined with plasticity modeling to predict texture development in the deep earth. Single crystal elastic properties are then averaged over these textures to obtain polycrystal elastic properties. These combined with density can be used to calculate seismic properties. In the lower mantle, these properties are typically compared to shear wave splitting to assess the viability of that phase and deformation state to explain observed anisotropy. Flow models to calculate anisotropy may be obtained from convection simulations (Chandler et al., 2018; Cottaar et al., 2014; Immoor et al., 2018; Merkel et al., 2007; Miyagi et al., 2010; Wenk et al., 2011; Wu et al., 2017) or from instantaneous global flow models based on tomographic inversions (Ford & Long, 2015; Nowacki et al., 2013; Walker et al., 2011, 2018). Others

have directly compared results from shear experiments to the mantle (e.g., Tsujino et al., 2016; Yamazaki et al., 2006) or from simple shear simulations as an approximation for mantle deformation (Merkel et al., 2006; Tommasi et al., 2018).

In the top of the lower mantle, single crystal elastic properties of ferropericlase are nearly isotropic (Marquardt et al., 2009). Furthermore, experiments seem to indicate that in the presence of Brg, Fp will not develop significant texture (Kaercher et al., 2016; Miyagi & Wenk, 2016; Wenk, Lonardelli, et al., 2006), and thus ferropericlase is unlikely to be a source of anisotropy in the top of the lower mantle. Ca-Pv can have large single crystal elastic anisotropy at the top of the lower mantle (Karki & Crain, 1998), but its contribution to anisotropy has not been explored. Recent shear experiments on Brg show texture and anisotropy development that is qualitatively consistent with observations of seismic anisotropy in the top of the lower mantle (Tsujino et al., 2016). Thus, Brg with slip on (100)[001] appears to be the most likely candidate to explain anisotropy in this region.

In the lowermost mantle simulations of D'' anisotropy do not provide a clear consensus on which phases and slip systems provide the best match. Studies by Chandler et al. (2018), Cottaar et al. (2014), and Wenk et al. (2011) find that pPv with slip on (001) planes provides the best match to anisotropy in the circum-pacific region. In contrast, Nowacki et al. (2013) and Walker et al. (2011) found that pPv with slip on (010) provides the best match to global observations. Interestingly these results are most strongly correlated in regions of Large Low Shear Velocity Provinces (LLSVPs), where it is unclear if pPv is stable (e.g., Grocholski et al., 2012). Ford and Long (2015) tested the predictions of Walker et al. (2011) against their measurements of shear wave splitting at the eastern edge of the African LLSVP and found a large misfit between the model and observations. However, if constraints on the direction of the flow field were relaxed, pPv with slip on (010) provided the best match. Most recently, models including the effects of the Brg to pPv phase transition on texture development have been performed using flow models from convection simulations (Chandler et al., 2018) and from instantaneous flow field models (Walker et al., 2018). Both of these studies find the best fit to global anisotropy with pPv deformed by dominant slip on (001) planes. A recent study on Fp at high pressure and temperatures found that slip on {100}<011> could explain complex and laterally varying anisotropy near the edges of LLSVPs (Immoor et al., 2018).

In the mantle, polyphase interactions could play an important role in texture development however; to date most models of anisotropy are based on single phase experimental results. Additionally, most simulate deformation of single phases rather than deformation of a

polyphase aggregate. The exceptions are the simulations of Cottaar et al. (2014), which contain Brg/pPv 75% and Fp 25%, Chandler et al. (2018), which uses an aggregate of Brg/pPv 60%, Fp 20%, and CaPv 20%, and Tommasi et al. (2018), which uses an aggregate of pPv 70% and Fp 25%. However, all of these studies use VPSC to simulate texture development. As a homogenization scheme (as opposed to full field methods), VPSC does not account for microstructural effects other than phase proportion, grain shape evolution, and grain orientation. Thus, VPSC cannot track spatial relationships between grains and phases and cannot distinguish between IWL or LBF microstructures and also cannot account for local variations in the stress–strain field. If Fp in the lower mantle does not develop texture when deformed with bridgmanite then any anisotropy observed in the bulk of the lower mantle is likely due to bridgmanite. This would also imply that the observation of isotropy in the bulk of the lower mantle is likely due to a lack of texture development in all the phases, e.g., due to diffusion creep (Karato et al., 1995) and/or pure climb creep (Boioli et al., 2017; Cordier & Goryaeva, 2018; Reali et al., 2019), rather than texturing where anisotropy patterns of the individual phases cancel each other (Wenk, Speziale, et al., 2006). It remains to be seen how texture develops in aggregates of pPv + Fp of Brg+pPv+Fp, but this will have important consequences for sources of anisotropy in the lowermost mantle.

2.7. CONCLUSIONS

Although considerable progress has been made toward rheology studies of lower mantle phases, high pressure and temperature deformation studies particularly at steady state deformation conditions remain sparse. Significant advances have been made in documenting texture development and slip system activities in lower mantle phases and some general trends are observed with respect to differential stress measurements in these phases. Based on the experimental body as a whole, at mantle pressure Fp appears to be significantly weaker than Brg; however, the strength contrast as a function of pressure, temperature, and strain remains poorly constrained. As would be expected the strength of both of these phases decreases with increased temperature and with decreased strain rates. Room-temperature strengths of Brg and MgSiO₃ pPv seem to indicate that MgSiO₃ pPv is weaker than Brg, but there is a large pressure gap between measurements in these two phases. Texture development in two-phase aggregates also exhibits complex behavior with high plastic anisotropy hard phases disrupting texture development in softer more highly strained phases. Bulk behavior of lower mantle polyphase aggregates (i.e., rocks) remains relatively unstudied but has important

implications for mechanical properties and anisotropy development in the deep Earth. Challenges exist both to interpretation of bulk rheology of these materials and texture development in the various phases. Systematic studies of polyphase deformation documenting the effects of strength contrast, plastic anisotropy, and microstructure will be vital moving forward. Additional complications may occur at high temperatures where possibilities exist for phases to deform by different deformation mechanisms. Recent technical advances in experimental deformation as well as theoretical developments have provided new capabilities to tackle these problems in the near future.

ACKNOWLEDGMENTS

LM acknowledges support from the National Science Foundation through EAR-1654687 and from the Capitol DOE Alliance Center (CDAC). LM would also like to thank two anonymous reviewers and editor H. Marquardt, whose comments greatly improved the manuscript.

REFERENCES

- Allègre, C. J., & Turcotte, D. L. (1986). Implications of a two-component marble-cake mantle. *Nature*, 323(6084), 123–127. <https://doi.org/10.1038/323123a0>
- Ammann, M. W., Brodholt, J. P., Wookey, J., & Dobson, D. P. (2010). First-principles constraints on diffusion in lower-mantle minerals and a weak D'' layer. *Nature*, 465(7297), 462–465. <https://doi.org/10.1038/nature09052>
- Amodeo, J., Carrez, P., & Cordier, P. (2012). Modelling the effect of pressure on the critical shear stress of MgO single crystals. *Philosophical Magazine*, 92(12), 1523–1541. <https://doi.org/10.1080/14786435.2011.652689>
- Amodeo, J., Dancette, S., & Delannay, L. (2016). Atomistically-informed crystal plasticity in MgO polycrystals under pressure. *International Journal of Plasticity*, 82(March), 177–191. <https://doi.org/10.1016/j.ijplas.2016.03.004>
- Amodeo, J., Merkel, S., Tromas, C., Carrez, P., Korte-Kerzel, S., Cordier, P., et al. (2018). Dislocations and Plastic Deformation in MgO Crystals: A Review. *Crystals*, 8(6), 240. <https://doi.org/10.3390/cryst8060240>
- Andrault, D., Muñoz, M., Bolfan-Casanova, N., Guignot, N., Perrillat, J. P., Aquilanti, G., & Pascarelli, S. (2010). Experimental evidence for perovskite and post-perovskite coexistence throughout the whole D' region. *Earth and Planetary Science Letters*, 293(1–2), 90–96. <https://doi.org/10.1016/j.epsl.2010.02.026>
- Appel, F., & Wielke, B. (1985). Low temperature deformation of impure MgO single crystals. *Materials Science and Engineering*, 73, 97–103. [https://doi.org/10.1016/0025-5416\(85\)90299-X](https://doi.org/10.1016/0025-5416(85)90299-X)
- Arrhenius, S. (1889). Über die Reaktionsgeschwindigkeit bei der Inversion von Rohrzucker durch Säuren. *Zeitschrift Für*

- Physikalische Chemie*, 4(1), 226–248. <https://doi.org/10.1515/zpch-1889-0416>
- Azuma, S., Nomura, R., Uesugi, K., Nakashima, Y., Kojima, Y., Doi, S., & Kakizawa, S. (2018). Anvil design for slip-free high pressure deformation experiments in a rotational diamond anvil cell. *High Pressure Research*, 38(1), 23–31. <https://doi.org/10.1080/08957959.2017.1396327>
- Barreiro, J. G., Lonardelli, I., Wenk, H. R., Dresen, G., Rybacki, E., Ren, Y., & Tomé, C. N. (2007). Preferred orientation of anorthite deformed experimentally in Newtonian creep. *Earth and Planetary Science Letters*, 264(1–2), 188–207. <https://doi.org/10.1016/j.epsl.2007.09.018>
- Boehler, R. (2000). Laser heating in the diamond cell: techniques and applications. *Hyperfine Interactions*, 128(1/3), 307–321. <https://doi.org/10.1023/A:1012648019016>
- Boioli, F., Carrez, P., Cordier, P., Devincre, B., Gouriet, K., Hirel, P., et al. (2017). Pure climb creep mechanism drives flow in Earth's lower mantle. *Science Advances*, 3(3), e1601958. <https://doi.org/10.1126/sciadv.1601958>
- Bons, P. D., & den Brok, B. (2000). Crystallographic preferred orientation development by dissolution–precipitation creep. *Journal of Structural Geology*, 22(11–12), 1713–1722. [https://doi.org/10.1016/S0191-8141\(00\)00075-4](https://doi.org/10.1016/S0191-8141(00)00075-4)
- Brokmeier, H. G., Böcker, W., & Bunge, H. J. (1988). Neutron Diffraction Texture Analysis in Extruded Al-Pb Composites. *Textures and Microstructures*, 8, 429–441. <https://doi.org/10.1155/TSM.8-9.429>
- Brown, J. M., & Shankland, T. J. (1981). Thermodynamic parameters in the Earth as determined from seismic profiles. *Geophysical Journal International*, 66(3), 579–596. <https://doi.org/10.1111/j.1365-246X.1981.tb04891.x>
- Burnley, P. C., & Kaboli, S. (2019). Elastic plastic self-consistent (EPSC) modeling of San Carlos olivine deformed in a D-DIA apparatus. *American Mineralogist*, 104(2), 276–281. <https://doi.org/10.2138/am-2019-6666>
- Burnley, P. C., & Zhang, D. (2008). Interpreting in situ x-ray diffraction data from high pressure deformation experiments using elastic–plastic self-consistent models: an example using quartz. *Journal of Physics: Condensed Matter*, 20(28), 285201. <https://doi.org/10.1088/0953-8984/20/28/285201>
- Bystricky, M., Heidelbach, F., & Mackwell, S. (2006). Large-strain deformation and strain partitioning in polyphase rocks: Dislocation creep of olivine–magnesiowüstite aggregates. *Tectonophysics*, 427(1–4), 115–132. <https://doi.org/10.1016/J.TECTO.2006.05.025>
- Canova, G. R., Wenk, H. R., & Molinari, A. (1992). Deformation modelling of multi-phase polycrystals: case of a quartz-mica aggregate. *Acta Metallurgica Et Materialia*, 40(7), 1519–1530. [https://doi.org/10.1016/0956-7151\(92\)90095-V](https://doi.org/10.1016/0956-7151(92)90095-V)
- Carrez, P., Ferré, D., & Cordier, P. (2007a). Implications for plastic flow in the deep mantle from modelling dislocations in MgSiO₃ minerals. *Nature*, 446(7131), 68–70. <https://doi.org/10.1038/nature05593>
- Carrez, P., Ferré, D., & Cordier, P. (2007b). Peierls-Nabarro model for dislocations in MgSiO₃ post-perovskite calculated at 120 GPa from first principles. *Philosophical Magazine*, 87(22), 3229–3247. <https://doi.org/10.1080/14786430701268914>
- Castelnau, O., Blackman, D. K., Lebensohn, R. A., & Ponte Castañeda, P. (2008). Micromechanical modeling of the viscoplastic behavior of olivine. *Journal of Geophysical Research*, 113(B9), B09202. <https://doi.org/10.1029/2007JB005444>
- Chandler, B. C., Yuan, K., Li, M., Cottaar, S., Romanowicz, B., Tomé, C. N., & Wenk, H. R. (2018). A Refined Approach to Model Anisotropy in the Lowermost Mantle. *IOP Conference Series: Materials Science and Engineering*, 375(1), 012002. <https://doi.org/10.1088/1757-899X/375/1/012002>
- Chen, J., Weidner, D. J., & Vaughan, M. T. (2002). The strength of Mg_{0.9}Fe_{0.1}SiO₃ perovskite at high pressure and temperature. *Nature*, 419(6909), 824–826. <https://doi.org/10.1038/nature01130>
- Clausen, B., Tomé, C. N., Brown, D. W., & Agnew, S. R. (2008). Reorientation and stress relaxation due to twinning: Modeling and experimental characterization for Mg. *Acta Materialia*, 56(11), 2456–2468. <https://doi.org/10.1016/J.ACTAMAT.2008.01.057>
- Coble, R. L. (1963). A Model for Boundary Diffusion Controlled Creep in Polycrystalline Materials. *Journal of Applied Physics*, 34(6), 1679–1682. <https://doi.org/10.1063/1.1702656>
- Copley, S. M., & Pask, J. A. (1965). Plastic Deformation of MgO Single Crystals up to 1600°C. *Journal of the American Ceramic Society*, 48(3), 139–146. <https://doi.org/10.1111/j.1151-2916.1965.tb16050.x>
- Cordier, P., & Goryaeva, A. (Eds.). (2018). Multiscale modeling of the mantle rheology : the RheoMan project. European research council. Retrieved from https://books.google.com/books?id=8bTRvQEACAAJ&dq=Multiscale+Modeling+of+the+Mantle+Rheology&hl=en&sa=X&ved=0ahUKewix9_zn9trjAhWBtp4KHVcOAZ0Q6AEIKjAA
- Cordier, P., Ungár, T., Zsoldos, L., & Tichy, G. (2004). Dislocation creep in MgSiO₃ perovskite at conditions of the Earth's uppermost lower mantle. *Nature*, 428(6985), 837–840. <https://doi.org/10.1038/nature02472>
- Cottaar, S., Li, M., McNamara, A. K., Romanowicz, B., & Wenk, H. R. (2014). Synthetic seismic anisotropy models within a slab impinging on the core-mantle boundary. *Geophysical Journal International*, 199(1), 164–177. <https://doi.org/10.1093/gji/ggu244>
- Creasy, N., Pisconti, A., Long, M. D., Thomas, C., & Wookey, J. (2019). Constraining lowermost mantle anisotropy with body waves: a synthetic modelling study. *Geophysical Journal International*, 217(2), 766–783. <https://doi.org/10.1093/gji/ggz049>
- Cross, A. J., & Skemer, P. (2017). Ultramylonite generation via phase mixing in high-strain experiments. *Journal of Geophysical Research: Solid Earth*, 122(3), 1744–1759. <https://doi.org/10.1002/2016JB013801>
- Deng, J., & Lee, K. K. M. (2017). Viscosity jump in the lower mantle inferred from melting curves of ferropericlase. *Nature Communications*, 8(1), 1997. <https://doi.org/10.1038/s41467-017-02263-z>
- Dobson, D. P., McCormack, R., Hunt, S. A., Ammann, M. W., Weidner, D., Li, L., & Wang, L. (2012). The relative strength of perovskite and post-perovskite NaCoF₃. *Mineralogical Magazine*, 76(04), 925–932. <https://doi.org/10.1180/minmag.2012.076.4.09>
- Evans, W. J., Yoo, C.-S., Lee, G. W., Cynn, H., Lipp, M. J., & Visbeck, K. (2007). Dynamic diamond anvil cell (dDAC):

- A novel device for studying the dynamic-pressure properties of materials. *Review of Scientific Instruments*, 78(7), 073904. <https://doi.org/10.1063/1.2751409>
- Ferré, D., Carrez, P., & Cordier, P. (2007). First principles determination of dislocations properties of MgSiO₃ perovskite at 30 GPa based on the Peierls-Nabarro model. *Physics of the Earth and Planetary Interiors*, 163(1–4), 283–291. <https://doi.org/10.1016/j.pepi.2007.05.011>
- Ferré, D., Cordier, P., & Carrez, P. (2009). Dislocation modeling in calcium silicate perovskite based on the Peierls-Nabarro model. *American Mineralogist*, 94(1), 135–142. <https://doi.org/10.2138/am.2009.3003>
- Ferreira, A. M. G., Faccenda, M., Sturgeon, W., Chang, S.-J., & Scharndong, L. (2019). Ubiquitous lower-mantle anisotropy beneath subduction zones. *Nature Geoscience*, 12(4), 301–306. <https://doi.org/10.1038/s41561-019-0325-7>
- Ford, H. A., & Long, M. D. (2015). A regional test of global models for flow, rheology, and seismic anisotropy at the base of the mantle. *Physics of the Earth and Planetary Interiors*, 245, 71–75. <https://doi.org/10.1016/J.PEPI.2015.05.004>
- French, S. W., & Romanowicz, B. (2015). Broad plumes rooted at the base of the Earth's mantle beneath major hotspots. *Nature*, 525(7567), 95–99. <https://doi.org/10.1038/nature14876>
- Frost, H. J., & Ashby, M. F. (1982). *Deformation mechanism maps: the plasticity and creep of metals and ceramics*. Pergamon Press. Retrieved from <http://publications.eng.cam.ac.uk/372960/>
- Fukao, Y., & Obayashi, M. (2013). Subducted slabs stagnant above, penetrating through, and trapped below the 660 km discontinuity. *Journal of Geophysical Research: Solid Earth*, 118(11), 5920–5938. <https://doi.org/10.1002/2013JB010466>
- Garcés, G., Pérez, P., & Adeva, P. (2005). Effect of the extrusion texture on the mechanical behaviour of Mg–SiCp composites. *Scripta Materialia*, 52(7), 615–619. <https://doi.org/10.1016/J.SCRIPMAT.2004.11.024>
- Garcés, G., Rodríguez, M., Pérez, P., & Adeva, P. (2006). Effect of volume fraction and particle size on the microstructure and plastic deformation of Mg–Y₂O₃ composites. *Materials Science and Engineering: A*, 419(1–2), 357–364. <https://doi.org/10.1016/J.MSEA.2006.01.026>
- Girard, J., Chen, J., & Raterron, P. (2012). Deformation of periclase single crystals at high pressure and temperature: Quantification of the effect of pressure on slip-system activities. *Journal of Applied Physics*, 111(11). <https://doi.org/10.1063/1.4726200>
- Girard, J., Amulele, G., Farla, R., Mohiuddin, A., & Karato, S. (2016). Shear deformation of bridgmanite and magnesiowüstite aggregates at lower mantle conditions. *Science (New York, N. Y.)*, 351(6269), 144–7. <https://doi.org/10.1126/science.aad3113>
- Goryaeva, A. M., Carrez, P., & Cordier, P. (2015a). Modeling defects and plasticity in MgSiO₃ post-perovskite: Part 1—generalized stacking faults. *Physics and Chemistry of Minerals*, 42(10), 781–792. <https://doi.org/10.1007/s00269-015-0762-9>
- Goryaeva, A. M., Carrez, P., & Cordier, P. (2015b). Modeling defects and plasticity in MgSiO₃ post-perovskite: Part 2—screw and edge [100] dislocations. *Physics and Chemistry of Minerals*, 42(10), 793–803. <https://doi.org/10.1007/s00269-015-0763-8>
- Goryaeva, A. M., Carrez, P., & Cordier, P. (2016). Low viscosity and high attenuation in MgSiO₃ post-perovskite inferred from atomic-scale calculations. *Scientific Reports*, 6(1), 34771. <https://doi.org/10.1038/srep34771>
- Goryaeva, A. M., Carrez, P., & Cordier, P. (2017). Modeling defects and plasticity in MgSiO₃ post-perovskite: Part 3—Screw and edge [001] dislocations. *Physics and Chemistry of Minerals*, 44(7), 521–533. <https://doi.org/10.1007/s00269-017-0879-0>
- Gouriet, K., Carrez, P., & Cordier, P. (2014). Modelling [1 0 0] and [0 1 0] screw dislocations in MgSiO₃ perovskite based on the Peierls–Nabarro–Galerkin model. *Modelling and Simulation in Materials Science and Engineering*, 22(2), 025020. <https://doi.org/10.1088/0965-0393/22/2/025020>
- Grocholski, B., Catalli, K., Shim, S.-H., & Prakapenka, V. (2012). Mineralogical effects on the detectability of the post-perovskite boundary. *Proceedings of the National Academy of Sciences*, 109(7), 2275–2279. <https://doi.org/10.1073/pnas.1109204109>
- Handy, M. R. (1990). The solid-state flow of polymineralic rocks. *Journal of Geophysical Research*, 95(B6), 8647. <https://doi.org/10.1029/JB095iB06p08647>
- Handy, M. R. (1994). Flow laws for rocks containing two non-linear viscous phases: A phenomenological approach. *Journal of Structural Geology*, 16(3), 287–301. [https://doi.org/10.1016/0191-8141\(94\)90035-3](https://doi.org/10.1016/0191-8141(94)90035-3)
- Heidelbach, F., Stretton, I., Langenhorst, F., & Mackwell, S. (2003). Fabric evolution during high shear strain deformation of magnesiowüstite (Mg_{0.8}Fe_{0.2}O). *Journal of Geophysical Research: Solid Earth*, 108(B3). <https://doi.org/10.1029/2001JB001632>
- Hemley, R. J., Mao, H., Shen, G., Badro, J., Gillet, P., Hanfland, M., & Häusermann, D. (1997). X-ray Imaging of Stress and Strain of Diamond, Iron, and Tungsten at Megabar Pressures. *Science*, 276(5316), 1242–1245. <https://doi.org/10.1126/science.276.5316.1242>
- Herring, C. (1950). Diffusional Viscosity of a Polycrystalline Solid. *Journal of Applied Physics*, 21(5), 437–445. <https://doi.org/10.1063/1.1699681>
- Hirel, P., Krach, A., Carrez, P., & Cordier, P. (2014). Atomic core structure and mobility of [1 0 0](0 1 0) and [0 1 0](1 0 0) dislocations in MgSiO₃ perovskite. *Acta Materialia*, 79, 117–125. <https://doi.org/10.1016/j.actamat.2014.07.001>
- Hirose, K., Takafuji, N., Sata, N., & Ohishi, Y. (2005). Phase transition and density of subducted MORB crust in the lower mantle. *Earth and Planetary Science Letters*, 237(1–2), 239–251. <https://doi.org/10.1016/j.epsl.2005.06.035>
- Hirose, K., Nagaya, Y., Merkel, S., & Ohishi, Y. (2010). Deformation of MnGeO₃ post-perovskite at lower mantle pressure and temperature. *Geophysical Research Letters*, 37(L20302). <https://doi.org/10.1029/2010gl044977>
- Hirth, G., & Kohlstedt, D. (2003). Rheology of the upper mantle and the mantle wedge: A view from the experimentalists (pp. 83–105). American Geophysical Union (AGU). <https://doi.org/10.1029/138GM06>

- Hulse, C. O., Copley, S. M., & Pask, J. A. (1963). Effect of Crystal Orientation on Plastic Deformation of Magnesium Oxide. *Journal of the American Ceramic Society*, 46(7), 317–323. <https://doi.org/10.1111/j.1151-2916.1963.tb11738.x>
- Hunt, S. A., & Dobson, D. P. (2017). Note: Modified anvil design for improved reliability in DT-Cup experiments. *Review of Scientific Instruments*, 88(12), 126106. <https://doi.org/10.1063/1.5005885>
- Hunt, S. A., Weidner, D. J., Li, L., Wang, L., Walte, N. P., Brodholt, J. P., & Dobson, D. P. (2009). Weakening of calcium iridate during its transformation from perovskite to post-perovskite. *Nature Geoscience*, 2(11), 794–797. <https://doi.org/10.1038/ngeo663>
- Hunt, S. A., Weidner, D. J., McCormack, R. J., Whitaker, M. L., Bailey, E., Li, L., et al. (2014). Deformation T-Cup: A new multi-anvil apparatus for controlled strain-rate deformation experiments at pressures above 18 GPa. *Review of Scientific Instruments*, 85(8), 085103. <https://doi.org/10.1063/1.4891338>
- Hunt, S. A., Walker, A. M., & Mariani, E. (2016). In-situ measurement of texture development rate in CaIrO₃ post-perovskite. *Physics of the Earth and Planetary Interiors*, 257, 91–104. <https://doi.org/10.1016/j.pepi.2016.05.007>
- Hunt, S. A., Fenech, D. M., Lord, O. T., Redfern, S. A. T., & Smith, J. S. (2018). Anelasticity of HCP-Fe up to 70 GPa by overcoming X-ray diffraction sampling limitations. In *2018 AGU Fall Meeting, Washington, D.C.* (p. Abstract MR14A-02).
- Hustoft, J., Shim, S.-H., Kubo, A., & Nishiyama, N. (2008). Raman spectroscopy of CaIrO₃ postperovskite up to 30 GPa. *American Mineralogist*, 93(10), 1654–1658. <https://doi.org/10.2138/am.2008.2938>
- Iitaka, T., Hirose, K., Kawamura, K., & Murakami, M. (2004). The elasticity of the {MgSiO₃} post-perovskite phase in the lowermost mantle. *Nature*, 430(July), 442–445.
- Immoor, J., Marquardt, H., Miyagi, L., Lin, F., Speziale, S., Merkel, S., et al. (2018). Evidence for {100}<011> slip in ferropericlase in Earth's lower mantle from high-pressure/high-temperature experiments. *Earth and Planetary Science Letters*, 489, 251–257. <https://doi.org/10.1016/j.epsl.2018.02.045>
- Jayaraman, A. (1983). Diamond anvil cell and high-pressure physical investigations. *Reviews of Modern Physics*, 55(1), 65–108. <https://doi.org/10.1103/RevModPhys.55.65>
- Jenei, Z., Liermann, H. P., Husband, R., Méndez, A. S. J., Pennicard, D., Marquardt, H., et al. (2019). New dynamic diamond anvil cells for tera-pascal per second fast compression x-ray diffraction experiments. *Review of Scientific Instruments*, 90(6), 065114. <https://doi.org/10.1063/1.5098993>
- Jessell, M. W., Bons, P. D., Griera, A., Evans, L. A., & Wilson, C. J. L. (2009). A tale of two viscosities. *Journal of Structural Geology*, 31(7), 719–736. <https://doi.org/10.1016/j.jsg.2009.04.010>
- Kaercher, P., Miyagi, L., Kanitpanyacharoen, W., Zepeda-Alarcon, E., Wang, Y., Parkinson, D., et al. (2016). Two-phase deformation of lower mantle mineral analogs. *Earth and Planetary Science Letters*, 456, 134–145. <https://doi.org/10.1016/j.epsl.2016.09.030>
- Karato, S. I. (1998). Some remarks on the origin of seismic anisotropy in the D'' layer. *Earth, Planets and Space*, 50(11–12), 1019–1028. <https://doi.org/10.1186/BF03352196>
- Karato, S. I. (2009). Theory of lattice strain in a material undergoing plastic deformation: Basic formulation and applications to a cubic crystal. *Physical Review B - Condensed Matter and Materials Physics*, 79(21), 214106. <https://doi.org/10.1103/PhysRevB.79.214106>
- Karato, S. I. (2010). Rheology of the Earth's mantle: A historical review. *Gondwana Research*, 18(1), 17–45. <https://doi.org/10.1016/J.GR.2010.03.004>
- Karato, S. I., & Weidner, D. J. (2008). Laboratory Studies of Rheological Properties of Minerals Under Deep Mantle Conditions. *Elements*, 4, 191–196. <https://doi.org/10.2113/GSELEMENTS.4.3.191>
- Karato, S. I., Zhang, S., & Wenk, H. R. (1995). Superplasticity in earth's lower mantle: Evidence from seismic anisotropy and rock physics. *Science*, 270(5235), 458–461. <https://doi.org/10.1126/science.270.5235.458>
- Karato, S. I., Jung, H., Katayama, I., & Skemer, P. (2007). Geodynamic Significance of Seismic Anisotropy of the Upper Mantle: New Insights from Laboratory Studies. *Annual Review of Earth and Planetary Sciences*, 36(1), 59–95. <https://doi.org/10.1146/annurev.earth.36.031207.124120>
- Karki, B. B., & Crain, J. (1998). First-principles determination of elastic properties of CaSiO₃ perovskite at lower mantle pressures. *Elastic Moduli and Anisotropy*, 25(14), 2741–2744.
- Kavner, A., & Duffy, T. S. (2001). Strength and elasticity of ringwoodite at upper mantle pressures. *Geophysical Research Letters*. <https://doi.org/10.1029/2000GL012671>
- Kawazoe, T., Ohuchi, T., Nishiyama, N., Nishihara, Y., & Iri-fune, T. (2010). Preliminary deformation experiment of ringwoodite at 20 GPa and 1 700 K using a D-DIA apparatus. *Journal of Earth Science*, 21(5), 517–522. <https://doi.org/10.1007/s12583-010-0120-2>
- Knipe, R. (1989). Deformation mechanisms — recognition from natural tectonites. *Journal of Structural Geology*, 11(1–2), 127–146. [https://doi.org/10.1016/0191-8141\(89\)90039-4](https://doi.org/10.1016/0191-8141(89)90039-4)
- Kraych, A., Carrez, P., Hirel, P., Clouet, E., & Cordier, P. (2016). Peierls potential and kink-pair mechanism in high-pressure MgSiO₃ perovskite: An atomic scale study. *Physical Review B*, 93(1), 1–9. <https://doi.org/10.1103/PhysRevB.93.014103>
- Kubo, A., Kiefer, B., Shim, S.-H., Shen, G., Prakapenka, V. B., & Duffy, T. S. (2008). Rietveld structure refinement of MgGeO₃ post-perovskite phase to 1 Mbar. *American Mineralogist*, 93(7), 965–976. <https://doi.org/10.2138/am.2008.2691>
- Kunz, M., Caldwell, W. A., Miyagi, L., & Wenk, H. R. (2007). In situ laser heating and radial synchrotron x-ray diffraction in a diamond anvil cell. *Review of Scientific Instruments*, 78(6). <https://doi.org/10.1063/1.2749443>
- Kurnosov, A., Marquardt, H., Frost, D. J., Ballaran, T. B., & Ziberna, L. (2017). Evidence for a Fe³⁺-rich pyrolytic lower mantle from (Al,Fe)-bearing bridgmanite elasticity data. *Nature*, 543(7646), 543–546. <https://doi.org/10.1038/nature21390>
- Lebensohn, R. A., & Tomé, C. N. (1993). A self-consistent anisotropic approach for the simulation of plastic deformation and texture development of polycrystals: Application to zirconium alloys. *Acta Metallurgica Et Materialia*, 41(9), 2611–2624. [https://doi.org/10.1016/0956-7151\(93\)90130-K](https://doi.org/10.1016/0956-7151(93)90130-K)

- Li, C., van der Hilst, R. D., Engdahl, E. R., & Burdick, S. (2008). A new global model for *P* wave speed variations in Earth's mantle. *Geochemistry, Geophysics, Geosystems*, 9(5), n/a-n/a. <https://doi.org/10.1029/2007GC001806>
- Li, L., & Weidner, D. J. (2015). *In situ* analysis of texture development from sinusoidal stress at high pressure and temperature. *Review of Scientific Instruments*, 86(12), 125106. <https://doi.org/10.1063/1.4937398>
- Li, L., Weidner, D. J., Chen, J., Vaughan, M. T., Davis, M., & Durham, W. B. (2004). X-ray strain analysis at high pressure: Effect of plastic deformation in MgO. *Journal of Applied Physics*, 95(12), 8357–8365. <https://doi.org/10.1063/1.1738532>
- Liermann, H. P., Merkel, S., Miyagi, L., Wenk, H. R., Shen, G., Cynn, H., & Evans, W. J. (2009). Experimental method for *in situ* determination of material textures at simultaneous high pressure and high temperature by means of radial diffraction in the diamond anvil cell. *Review of Scientific Instruments*, 80(10), 1–8. <https://doi.org/10.1063/1.3236365>
- Lin, F., Hilalret, N., Raterron, P., Addad, A., Immoor, J., Marquardt, H., et al. (2017). Elasto-viscoplastic self consistent modeling of the ambient temperature plastic behavior of periclase deformed up to 5.4 GPa. *Journal of Applied Physics*, 122(20). <https://doi.org/10.1063/1.4999951>
- Lin, J.-F., Wenk, H.-R., Voltolini, M., Speziale, S., Shu, J., & Duffy, T. S. (2009). Deformation of lower-mantle ferropericlase (Mg,Fe)O across the electronic spin transition. *Physics and Chemistry of Minerals*, 36(10), 585–592. <https://doi.org/10.1007/s00269-009-0303-5>
- Long, M. D., & Becker, T. W. (2010). Mantle dynamics and seismic anisotropy. *Earth and Planetary Science Letters*, 297(3–4), 341–354. <https://doi.org/10.1016/J.EPSL.2010.06.036>
- Long, M. D., Xiao, X., Jiang, Z., Evans, B., & Karato, S. ichiro. (2006). Lattice preferred orientation in deformed polycrystalline (Mg,Fe)O and implications for seismic anisotropy in *D''*. *Physics of the Earth and Planetary Interiors*, 156(1–2), 75–88. <https://doi.org/10.1016/j.pepi.2006.02.006>
- Lutterotti, L., Matthies, S., Wenk, H. R., Schultz, A. S., & Richardson, J. W. (1997). Combined texture and structure analysis of deformed limestone from time-of-flight neutron diffraction spectra. *Journal of Applied Physics*, 81(2), 594–600. <https://doi.org/10.1063/1.364220>
- Lynner, C., & Long, M. D. (2015). Heterogeneous seismic anisotropy in the transition zone and uppermost lower mantle: evidence from South America, Izu-Bonin and Japan. *Geophysical Journal International*, 201(3), 1545–1552. <https://doi.org/10.1093/gji/ggv099>
- Mainprice, D., Barruol, G., & Ben Ismail, W. (2000). The seismic anisotropy of the earth's mantle: From single crystal to polycrystal. *Geophysical Monograph Series*, 117, 237–264. <https://doi.org/10.1029/GM117p0237>
- Mainprice, D., Tommasi, A., Ferré, D., Carrez, P., & Cordier, P. (2008). Predicted glide systems and crystal preferred orientations of polycrystalline silicate Mg-Perovskite at high pressure: Implications for the seismic anisotropy in the lower mantle. *Earth and Planetary Science Letters*, 271(1–4), 135–144. <https://doi.org/10.1016/j.epsl.2008.03.058>
- Manga, M., & Jeanloz, R. (1996). Axial temperature gradients in dielectric samples in the laser-heated diamond cell. *Geophysical Research Letters*. <https://doi.org/10.1029/96GL01602>
- Marquardt, H., & Miyagi, L. (2015). Slab stagnation in the shallow lower mantle linked to an increase in mantle viscosity. *Nature Geoscience*, 8(4), 311–314. <https://doi.org/10.1038/ngeo2393>
- Marquardt, H., Speziale, S., Reichmann, H. J., Frost, D. J., Schilling, F. R., & Garnero, E. J. (2009). Elastic shear anisotropy of ferropericlase in earth's lower mantle. *Science*, 324(5924), 224–226. <https://doi.org/10.1126/science.1169365>
- Martinez, I., Wang, Y., Guyot, F., Liebermann, R. C., & Doukham, J.-C. (1997). Microstructures and iron partitioning in (Mg,Fe)SiO₃ perovskite- (Mg,Fe)O magnesiowustite assemblages: An analytical transmission electron microscopy study. *Journal of Geophysical Research*, 102(B3), 5265–5280. <https://doi.org/10.1029/96JB03188>
- Matas, J., Bass, J., Ricard, Y., Mattern, E., & Bukowinski, M. S. T. (2007). On the bulk composition of the lower mantle: Predictions and limitations from generalized inversion of radial seismic profiles. *Geophysical Journal International*, 170(2), 764–780. <https://doi.org/10.1111/j.1365-246X.2007.03454.x>
- Mattern, E., Matas, J., Ricard, Y., & Bass, J. (2005). Lower mantle composition and temperature from mineral physics and thermodynamic modelling. *Geophysical Journal International*, 160(3), 973–990. <https://doi.org/10.1111/j.1365-246X.2004.02549.x>
- Matthies, S., & Humbert, M. (1993). The Realization of the Concept of a Geometric Mean for Calculating Physical Constants of Polycrystalline Materials. *Physica Status Solidi (B)*, 177(2), K47–K50. <https://doi.org/10.1002/pssb.2221770231>
- Matthies, S., Priesmeyer, H. G., & Daymond, M. R. (2001). On the diffractive determination of single-crystal elastic constants using polycrystalline samples. *Journal of Applied Crystallography*, 34(5), 585–601. <https://doi.org/10.1107/S0021889801010482>
- McNamara, A. K., Van, P. E., & Karato, S. (2002). Development of anisotropic structure in the Earth's lower mantle by solid-state convection Is there evidence for the localization of dislocation creep in the lowermost mantle ?, 416(March), 310–314.
- Meade, C., & Jeanloz, R. (1988). Yield strength of MgO to 40 GPa. *Journal of Geophysical Research*, 93(B4), 3261. <https://doi.org/10.1029/JB093iB04p03261>
- Meade, C., & Jeanloz, R. (1990). The strength of mantle silicates at high pressures and room temperature: implications for the viscosity of the mantle. *Nature*, 348(6301), 533–535. <https://doi.org/10.1038/348533a0>
- Meade, C., Silver, P. G., & Kaneshima, S. (1995). Laboratory and seismological observations of lower mantle isotropy. *Geophysical Research Letters*, 22(10), 1293–1296. <https://doi.org/10.1029/95GL01091>
- Merkel, S., & Cordier, P. (2016). Deformation of Core and Lower Mantle Materials (pp. 89–99). American Geophysical Union (AGU). <https://doi.org/10.1002/9781118992487.ch7>
- Merkel, S., & Yagi, T. (2005). X-ray transparent gasket for diamond anvil cell high pressure experiments. *Review of Scientific Instruments*, 76(4), 2004–2006. <https://doi.org/10.1063/1.1884195>
- Merkel, S., Wenk, H. R., Shu, J., Shen, G., Gillet, P., Mao, H., & Hemley, R. J. (2002). Deformation of polycrystalline MgO at pressures of the lower mantle. *Journal of Geophysical*

- Research: Solid Earth*, 107(B11), ECV 3-1-ECV 3-17. <https://doi.org/10.1029/2001JB000920>
- Merkel, S., Wenk, H. R., Badro, J., Montagnac, G., Gillet, P., Mao, H. K., & Hemley, R. J. (2003). Deformation of (Mg_{0.9},Fe_{0.1})SiO₃ Perovskite aggregates up to 32 GPa. *Earth and Planetary Science Letters*, 209(3–4), 351–360. [https://doi.org/10.1016/S0012-821X\(03\)00098-0](https://doi.org/10.1016/S0012-821X(03)00098-0)
- Merkel, S., Wenk, H. R., Gillet, P., Mao, H. K., & Hemley, R. J. (2004). Deformation of polycrystalline iron up to 30 GPa and 1000 K. *Physics of the Earth and Planetary Interiors*, 145(1–4), 239–251. <https://doi.org/10.1016/j.pepi.2004.04.001>
- Merkel, S., Kubo, A., Miyagi, L., Speziale, S., Duffy, T. S., Mao, H. K., & Wenk, H. R. (2006). Plastic deformation of MgGeO₃ post-perovskite at lower mantle pressures. *Science*, 311(5761), 644–646. <https://doi.org/10.1126/science.1121808>
- Merkel, S., McNamara, A. K., Kubo, A., Speziale, S., Miyagi, L., Meng, Y., et al. (2007). Deformation of (Mg,Fe)SiO₃ post-perovskite and D'' anisotropy. *Science*, 316(5832), 1729–1732. <https://doi.org/10.1126/science.1140609>
- Merkel, S., Tomé, C., & Wenk, H. R. (2009). Modeling analysis of the influence of plasticity on high pressure deformation of hcp-Co. *Physical Review B - Condensed Matter and Materials Physics*, 79(6), 1–13. <https://doi.org/10.1103/PhysRevB.79.064110>
- Merkel, S., Gruson, M., Wang, Y., Nishiyama, N., & Tomé, C. N. (2012). Texture and elastic strains in hcp-iron plastically deformed up to 17.5 GPa and 600 K: experiment and model. *Modelling and Simulation in Materials Science and Engineering*, 20(2), 024005. <https://doi.org/10.1088/0965-0393/20/2/024005>
- Metsue, A., Carrez, P., Mainprice, D., & Cordier, P. (2009). Numerical modelling of dislocations and deformation mechanisms in CaIrO₃ and MgGeO₃ post-perovskites—Comparison with MgSiO₃ post-perovskite. *Physics of the Earth and Planetary Interiors*, 174(1–4), 165–173. <https://doi.org/10.1016/j.pepi.2008.04.003>
- Mitrović, J. X., & Forte, A. M. (2004). A new inference of mantle viscosity based upon joint inversion of convection and glacial isostatic adjustment data. *Earth and Planetary Science Letters*, 225(1–2), 177–189. <https://doi.org/10.1016/J.EPSL.2004.06.005>
- Miyagi, L., & Wenk, H.-R. (2016). Texture development and slip systems in bridgmanite and bridgmanite + ferropericlasite aggregates. *Physics and Chemistry of Minerals*, 43(8), 597–613. <https://doi.org/10.1007/s00269-016-0820-y>
- Miyagi, L., Nishiyama, N., Wang, Y., Kubo, A., West, D. V., Cava, R. J., et al. (2008). Deformation and texture development in CaIrO₃ post-perovskite phase up to 6 GPa and 1300 K. *Earth and Planetary Science Letters*, 268(3–4), 515–525. <https://doi.org/10.1016/j.epsl.2008.02.005>
- Miyagi, L., Kunz, M., Knight, J., Nasiatka, J., Voltolini, M., & Wenk, H.-R. (2008). *In situ* phase transformation and deformation of iron at high pressure and temperature. *Journal of Applied Physics*, 104(10), 103510. <https://doi.org/10.1063/1.3008035>
- Miyagi, L., Merkel, S., Yagi, T., Sata, N., Ohishi, Y., & Wenk, H. R. (2009). Diamond anvil cell deformation of CaSiO₃ perovskite up to 49 GPa. *Physics of the Earth and Planetary Interiors*, 174(1–4), 159–164. <https://doi.org/10.1016/j.pepi.2008.05.018>
- Miyagi, L., Kanitpanyacharoen, W., Kaercher, P., Lee, K. K. M., & Wenk, H.-R. (2010). Slip Systems in MgSiO₃ Post-Perovskite: Implications for D'' Anisotropy. *Science*, 329(5999), 1639–1641. <https://doi.org/10.1126/science.1192465>
- Miyagi, L., Kanitpanyacharoen, W., Stackhouse, S., Militzer, B., & Wenk, H. R. (2011). The enigma of post-perovskite anisotropy: Deformation versus transformation textures. *Physics and Chemistry of Minerals*, 38(9), 665–678. <https://doi.org/10.1007/s00269-011-0439-y>
- Miyagi, L., Kanitpanyacharoen, W., Raju, S. V., Kaercher, P., Knight, J., MacDowell, A., et al. (2013). Combined resistive and laser heating technique for in situ radial X-ray diffraction in the diamond anvil cell at high pressure and temperature. *In Review of Scientific Instruments* (Vol. 84). <https://doi.org/10.1063/1.4793398>
- Miyajima, N., & Walte, N. (2009). Burgers vector determination in deformed perovskite and post-perovskite of CaIrO₃ using thickness fringes in weak-beam dark-field images. *Ultramicroscopy*, 109(6), 683–692. <https://doi.org/10.1016/j.ultramicro.2009.01.010>
- Miyajima, N., Ohgushi, K., Ichihara, M., & Yagi, T. (2006). Crystal morphology and dislocation microstructures of CaIrO₃: A TEM study of an analogue of the MgSiO₃ post-perovskite phase. *Geophysical Research Letters*, 33(12), 1–4. <https://doi.org/10.1029/2005GL025001>
- Miyajima, N., Yagi, T., & Ichihara, M. (2009). Dislocation microstructures of MgSiO₃ perovskite at a high pressure and temperature condition. *Physics of the Earth and Planetary Interiors*, 174(1–4), 153–158. <https://doi.org/10.1016/j.pepi.2008.04.004>
- Miyazaki, T., Sueyoshi, K., & Hiraga, T. (2013). Olivine crystals align during diffusion creep of Earth's upper mantle. *Nature*, 502(7471), 321–326. <https://doi.org/10.1038/nature12570>
- Mohiuddin, A., Long, M. D., & Lynner, C. (2015). Mid-mantle seismic anisotropy beneath southwestern Pacific subduction systems and implications for mid-mantle deformation. *Physics of the Earth and Planetary Interiors*, 245, 1–14. <https://doi.org/10.1016/J.PEPI.2015.05.003>
- Murakami, M., Hirose, K., Kawamura, K., Sata, N., & Ohishi, Y. (2004). Post-perovskite phase transition in MgSiO₃. *Science*, 304(5672), 855–8. <https://doi.org/10.1126/science.1095932>
- Nabarro, F. R. N. (1947). Dislocations in a simple cubic lattice. *Proceedings of the Physical Society*, 59(2), 256–272. <https://doi.org/10.1088/0959-5309/59/2/309>
- Nabarro, F. R. N. (1948). Deformation of crystals by the motion of single atoms. In *Report on a Conference on Strength of Solids* (pp. 75–90). London: Physical Society.
- Nabarro, F. R. N. (1967). Steady-state diffusional creep. *Philosophical Magazine*, 16(140), 231–237. <https://doi.org/10.1080/14786436708229736>
- Nakagawa, T., & Tackley, P. J. (2011). Effects of low-viscosity post-perovskite on thermo-chemical mantle convection in a 3-D spherical shell. *Geophysical Research Letters*, 38(4), L04309. <https://doi.org/10.1029/2010GL046494>

- Neil, C. J., Wollmershauser, J. A., Clausen, B., Tomé, C. N., & Agnew, S. R. (2010). Modeling lattice strain evolution at finite strains and experimental verification for copper and stainless steel using in situ neutron diffraction. *International Journal of Plasticity*, 26(12), 1772–1791. <https://doi.org/10.1016/J.IJPLAS.2010.03.005>
- Nisr, C., Ribárik, G., Ungár, T., Vaughan, G. B. M., Cordier, P., & Merkel, S. (2012). High resolution three-dimensional X-ray diffraction study of dislocations in grains of MgGeO₃ post-perovskite at 90 GPa. *Journal of Geophysical Research: Solid Earth*, 117(B3). <https://doi.org/10.1029/2011JB008401>
- Niwa, K., Yagi, T., Ohgushi, K., Merkel, S., Miyajima, N., & Kikegawa, T. (2007). Lattice preferred orientation in CaIrO₃ perovskite and post-perovskite formed by plastic deformation under pressure. *Physics and Chemistry of Minerals*, 34(9), 679–686. <https://doi.org/10.1007/s00269-007-0182-6>
- Nomura, R., Azuma, S., Uesugi, K., Nakashima, Y., Irifune, T., Shinmei, T., et al. (2017). High-pressure rotational deformation apparatus to 135 GPa. *Review of Scientific Instruments*, 88(4), 044501. <https://doi.org/10.1063/1.4979562>
- Nowacki, A., Wookey, J., & Kendall, J. M. (2010). Deformation of the lowermost mantle from seismic anisotropy. *Nature*, 467(7319), 1091–1094. <https://doi.org/10.1038/nature09507>
- Nowacki, A., Wookey, J., & Kendall, J. M. (2011). New advances in using seismic anisotropy, mineral physics and geodynamics to understand deformation in the lowermost mantle. *Journal of Geodynamics*, 52(3–4), 205–228. <https://doi.org/10.1016/j.jog.2011.04.003>
- Nowacki, A., Walker, A. M., Wookey, J., & Kendall, J.-M. (2013). Evaluating post-perovskite as a cause of D' anisotropy in regions of palaeosubduction. *Geophysical Journal International*, 192(3), 1085–1090. <https://doi.org/10.1093/gji/ggs068>
- Oganov, A. R., & Ono, S. (2004). Theoretical and experimental evidence for a post-perovskite phase of MgSiO₃ in Earth's D' layer. *Nature*, 430(6998), 445–448. <https://doi.org/10.1038/nature02701>
- Oganov, A. R., Martoňák, R., Laio, A., Raiteri, P., & Parrinello, M. (2005). Anisotropy of earth's D' layer and stacking faults in the MgSiO₃ post-perovskite phase. *Nature*, 438(7071), 1142–1144. <https://doi.org/10.1038/nature04439>
- Okada, T., Yagi, T., Niwa, K., & Kikegawa, T. (2010). Lattice-preferred orientations in post-perovskite-type MgGeO₃ formed by transformations from different pre-phases. *Physics of the Earth and Planetary Interiors*, 180(3–4), 195–202. <https://doi.org/10.1016/J.PEPI.2009.08.002>
- Van Orman, J. A., Fei, Y., Hauri, E. H., & Wang, J. (2003). Diffusion in MgO at high pressures: Constraints on deformation mechanisms and chemical transport at the core-mantle boundary. *Geophysical Research Letters*, 30(2), 26–29. <https://doi.org/10.1029/2002GL016343>
- Park, M., & Jung, H. (2017). Microstructural evolution of the Yugu peridotites in the Gyeonggi Massif, Korea: Implications for olivine fabric transition in mantle shear zones. *Tectonophysics*, 709, 55–68. <https://doi.org/10.1016/J.TECTO.2017.04.017>
- Passchier, C. W. (Cees W.), & Trouw, R. A. J. (Rudolph A. J. (2005). *Microtectonics*. Springer.
- Paterson, M. S., & Weaver, C. W. (1970). Deformation of Polycrystalline Under Pressure. *Journal of the American Ceramic Society*, 53(8), 463–471.
- Peierls, R. (1940). The size of a dislocation. *Proceedings of the Physical Society*, 52(1), 34–37. <https://doi.org/10.1088/0959-5309/52/1/305>
- Petitgirard, S., Daniel, I., Dabin, Y., Cardon, H., Tucoulou, R., & Susini, J. (2009). A diamond anvil cell for x-ray fluorescence measurements of trace elements in fluids at high pressure and high temperature. *Review of Scientific Instruments*, 80(3), 033906. <https://doi.org/10.1063/1.3100202>
- Piet, H., Badro, J., Nabiei, F., Dennenwaldt, T., Shim, S.-H., Cantoni, M., et al. (2016). Spin and valence dependence of iron partitioning in Earth's deep mantle. *Proceedings of the National Academy of Sciences*, 113(40), 11127–11130. <https://doi.org/10.1073/PNAS.1605290113>
- Poirier, J.-P. (1985). *Creep of crystals : high-temperature deformation processes in metals, ceramics, and minerals*. Cambridge University Press.
- Poudens, A., Bacroix, B., & Bretheau, T. (1995). Influence of microstructures and particle concentrations on the development of extrusion textures in metal matrix composites. *Materials Science and Engineering: A*, 196(1–2), 219–228. [https://doi.org/10.1016/0921-5093\(94\)09703-8](https://doi.org/10.1016/0921-5093(94)09703-8)
- Prakapenka, V. B., Kubo, A., Kuznetsov, A., Laskin, A., Shkurikhin, O., Dera, P., et al. (2008). Advanced flat top laser heating system for high pressure research at GSECARS: application to the melting behavior of germanium. *High Pressure Research*, 28(3), 225–235. <https://doi.org/10.1080/08957950802050718>
- Raterron, P., Merkel, S., & III, C. W. H. (2013). Axial temperature gradient and stress measurements in the deformation-DIA cell using alumina pistons. *Review of Scientific Instruments*, 84(4), 043906. <https://doi.org/10.1063/1.4801956>
- Reali, R., Van Orman, J. A., Pigott, J. S., Jackson, J. M., Boioli, F., Carrez, P., & Cordier, P. (2019). The role of diffusion-driven pure climb creep on the rheology of bridgmanite under lower mantle conditions. *Scientific Reports*, 9(1), 2053. <https://doi.org/10.1038/s41598-018-38449-8>
- Ricolleau, A., Perrillat, J.-P., Fiquet, G., Daniel, I., Matas, J., Addad, A., et al. (2010). Phase relations and equation of state of a natural MORB: Implications for the density profile of subducted oceanic crust in the Earth's lower mantle. *Journal of Geophysical Research*, 115(B8), B08202. <https://doi.org/10.1029/2009JB006709>
- Rodi, F., & Babel, D. (1965). Ternare Oxide der Übergangsmetalle. IV. Erdalkaliiridium(IV)-oxide: Kristallstruktur von CaIrO₃. *Zeitschrift Fur Anorganische Und Allgemeine Chemie*, 336(1–2), 17–23. <https://doi.org/10.1002/zaac.19653360104>
- Romanowicz, B., & Wenk, H. R. (2017). Anisotropy in the deep Earth. *Physics of the Earth and Planetary Interiors*, 269(May), 58–90. <https://doi.org/10.1016/j.pepi.2017.05.005>
- Rudolph, M. L., Lekić, V., & Lithgow-Bertelloni, C. (2015). Viscosity jump in Earth's mid-mantle. *Science (New York, N. Y.)*, 350(6266), 1349–52. <https://doi.org/10.1126/science.aad1929>
- Samuel, H., & Tosi, N. (2012). The influence of post-perovskite strength on the Earth's mantle thermal and chemical

- evolution. *Earth and Planetary Science Letters*, 323–324, 50–59. <https://doi.org/10.1016/J.EPSL.2012.01.024>
- Sato, F., & Sumino, K. (1980). The yield strength and dynamic behaviour of dislocations in MgO crystals at high temperatures. *Journal of Materials Science*, 15(7), 1625–1634. <https://doi.org/10.1007/BF00550578>
- Shen, G., Rivers, M. L., Wang, Y., & Sutton, S. R. (2001). Laser heated diamond cell system at the advanced photon source for in situ x-ray measurements at high pressure and temperature. *Review of Scientific Instruments*, 72(2), 1273–1282. <https://doi.org/10.1063/1.1343867>
- Shieh, S. R., Duffy, T. S., & Shen, G. (2004). Elasticity and strength of calcium silicate perovskite at lower mantle pressures. *Physics of the Earth and Planetary Interiors*, 143(1–2), 93–105. <https://doi.org/10.1016/j.pepi.2003.10.006>
- Shim, S.-H., Jeanloz, R., & Duffy, T. S. (2002). Tetragonal structure of CaSiO₃ perovskite above 20 GPa. *Geophysical Research Letters*, 29(24), 2166. <https://doi.org/10.1029/2002GL016148>
- Shim, S.-H., Duffy, T. S., Jeanloz, R., & Shen, G. (2004). Stability and crystal structure of MgSiO₃ perovskite to the core-mantle boundary. *Geophysical Research Letters*, 31(10). <https://doi.org/10.1029/2004GL019639>
- Singh, A. K. (1993). The lattice strains in a specimen (cubic system) compressed nonhydrostatically in an opposed anvil device. *Journal of Applied Physics*, 73(9), 4278–4286. <https://doi.org/10.1063/1.352809>
- Singh, A. K., Mao, H., Shu, J., & Hemley, R. J. (1998). Estimation of Single-Crystal Elastic Moduli from Polycrystalline X-Ray Diffraction at High Pressure: Application to FeO and Iron. *Physical Review Letters*, 80(10), 2157–2160. <https://doi.org/10.1103/PhysRevLett.80.2157>
- Singh, A. K., Liermann, H. P., & Saxena, S. K. (2004). Strength of magnesium oxide under high pressure: Evidence for the grain-size dependence. *Solid State Communications*, 132(11), 795–798. <https://doi.org/10.1016/j.ssc.2004.09.050>
- Stretton, I., Heidelbach, F., Mackwell, S., & Langenhorst, F. (2001). Dislocation creep of magnesiowüstite (Mg_{0.8}Fe_{0.2}O). *Earth and Planetary Science Letters*, 194, 229–240.
- Takeda, Y.-T. (1998). Flow in rocks modelled as multiphase continua: Application to polymineralic rocks. *Journal of Structural Geology*, 20(11), 1569–1578. [https://doi.org/10.1016/S0191-8141\(98\)00043-1](https://doi.org/10.1016/S0191-8141(98)00043-1)
- Takeda, Y.-T., & Griera, A. (2006). Rheological and kinematical responses to flow of two-phase rocks. *Tectonophysics*, 427(1–4), 95–113. <https://doi.org/10.1016/J.TECTO.2006.03.050>
- Tommaseo, C. E., Devine, J., Merkel, S., Speziale, S., & Wenk, H. R. (2006). Texture development and elastic stresses in magnesiowüstite at high pressure. *Physics and Chemistry of Minerals*, 33(2), 84–97. <https://doi.org/10.1007/s00269-005-0054-x>
- Tommasi, A., Goryaeva, A., Carrez, P., Cordier, P., & Mainprice, D. (2018). Deformation, crystal preferred orientations, and seismic anisotropy in the Earth's D'' layer. *Earth and Planetary Science Letters*, 492, 35–46. <https://doi.org/10.1016/J.EPSL.2018.03.032>
- Treagus, S. H. (2002). Modelling the bulk viscosity of two-phase mixtures in terms of clast shape. *Journal of Structural Geology*, 24(1), 57–76. [https://doi.org/10.1016/S0191-8141\(01\)00049-9](https://doi.org/10.1016/S0191-8141(01)00049-9)
- Tsuchiya, T., & Tsuchiya, J. (2007). Structure and elasticity of Cmc₂ CaIrO₃ and their pressure dependences: Ab initio calculations. *Physical Review B - Condensed Matter and Materials Physics*, 76(14), 2–5. <https://doi.org/10.1103/PhysRevB.76.144119>
- Tsujino, N., Nishihara, Y., Yamazaki, D., Seto, Y., Higo, Y., & Takahashi, E. (2016). Mantle dynamics inferred from the crystallographic preferred orientation of bridgmanite. *Nature*, 539(7627), 81–84. <https://doi.org/10.1038/nature19777>
- Tullis, J., & Wenk, H.-R. (1994). Effect of muscovite on the strength and lattice preferred orientations of experimentally deformed quartz aggregates. *Materials Science and Engineering: A*, 175(1–2), 209–220. [https://doi.org/10.1016/0921-5093\(94\)91060-X](https://doi.org/10.1016/0921-5093(94)91060-X)
- Tullis, T. E., Horowitz, F. G., & Tullis, J. (1991). Flow laws of polyphase aggregates from end-member flow laws. *Journal of Geophysical Research*, 96(B5), 8081. <https://doi.org/10.1029/90JB02491>
- Turner, P. A., & Tomé, C. N. (1994). A study of residual stresses in Zircaloy-2 with rod texture. *Acta Metallurgica et Materialia*, 42(12), 4143–4153. [https://doi.org/10.1016/0956-7151\(94\)90191-0](https://doi.org/10.1016/0956-7151(94)90191-0)
- Uchida, T., Wang, Y., Rivers, M. L., & Sutton, S. R. (2004). Yield strength and strain hardening of MgO up to 8 GPa measured in the deformation-DIA with monochromatic X-ray diffraction. *Earth and Planetary Science Letters*, 226(1–2), 117–126. <https://doi.org/10.1016/j.epsl.2004.07.023>
- van't Hoff, M. J. H. (1884). *Etudes de dynamique chimique*. Amsterdam: Fredrick Muller and Company. <https://doi.org/10.1002/recl.18840031003>
- Walker, A. M., Forte, A. M., Wookey, J., Nowacki, A., & Kendall, J. M. (2011). Elastic anisotropy of D'' predicted from global models of mantle flow. *Geochemistry, Geophysics, Geosystems*, 12(10), 1–22. <https://doi.org/10.1029/2011GC003732>
- Walker, A. M., Dobson, D. P., Wookey, J., Nowacki, A., & Forte, A. M. (2018). The anisotropic signal of topotaxy during phase transitions in D''. *Physics of the Earth and Planetary Interiors*, 276, 159–171. <https://doi.org/10.1016/j.pepi.2017.05.013>
- Walte, N. P., Heidelbach, F., Miyajima, N., & Frost, D. (2007). Texture development and TEM analysis of deformed CaIrO₃: Implications for the D'' layer at the core-mantle boundary. *Geophysical Research Letters*, 34(8), 1–5. <https://doi.org/10.1029/2007GL029407>
- Walte, N. P., Heidelbach, F., Miyajima, N., Frost, D. J., Rubie, D. C., & Dobson, D. P. (2009). Transformation textures in post-perovskite: Understanding mantle flow in the D' layer of the earth. *Geophysical Research Letters*, 36(4), 0–4. <https://doi.org/10.1029/2008GL036840>
- Wang, H., Wu, P. D., Tomé, C. N., & Huang, Y. (2010). A finite strain elastic-viscoplastic self-consistent model for polycrystalline materials. *Journal of the Mechanics and Physics of Solids*, 58(4), 594–612. <https://doi.org/10.1016/j.jmps.2010.01.004>
- Wang, Y., Guyot, F., Yeganeh-Haeri, A., & Liebermann, R. C. (1990). Twinning in MgSiO₃ perovskite. *Science*, 248(4954), 468–471. <https://doi.org/10.1126/science.248.4954.468>

- Wang, Y., Guyot, F., & Liebermann, R. C. (1992). Electron microscopy of (Mg, Fe)SiO₃ Perovskite: Evidence for structural phase transitions and implications for the lower mantle. *Journal of Geophysical Research*, 97(B9), 12327. <https://doi.org/10.1029/92JB00870>
- Wang, Y., Durham, W. B., Getting, I. C., & Weidner, D. J. (2003). The deformation-DIA: A new apparatus for high temperature triaxial deformation to pressures up to 15 GPa. *Review of Scientific Instruments*, 74(6), 3002–3011. <https://doi.org/10.1063/1.1570948>
- Wang, Y., Hilairat, N., Nishiyama, N., Yahata, N., Tsuchiya, T., Morard, G., & Fiquet, G. (2013). High-pressure, high-temperature deformation of CaGeO₃ (perovskite)±MgO aggregates: Implications for multiphase rheology of the lower mantle. *Geochemistry, Geophysics, Geosystems*, 14(9), 3389–3408. <https://doi.org/10.1002/ggge.20200>
- Weertman, J. (1970). The creep strength of the Earth's mantle. *Reviews of Geophysics*, 8(1), 145. <https://doi.org/10.1029/RG008i001p00145>
- Weertman, Johannes, & Weertman, J. R. (1975). High Temperature Creep of Rock and Mantle Viscosity. *Annual Review of Earth and Planetary Sciences*, 3(1), 293–315. <https://doi.org/10.1146/annurev.ea.03.050175.001453>
- Wenk, H.-R., Canova, G., Bréchet, Y., & Flandin, L. (1997). A deformation-based model for recrystallization of anisotropic materials. *Acta Materialia*, 45(8), 3283–3296. [https://doi.org/10.1016/S1359-6454\(96\)00409-0](https://doi.org/10.1016/S1359-6454(96)00409-0)
- Wenk, H.-R., Matthies, S., Hemley, R. J., Mao, H. K., & Shu, J. (2000). The plastic deformation of iron at pressures of the Earth's inner core. *Nature*, 405(6790), 1044–1047. <https://doi.org/10.1038/35016558>
- Wenk, H.-R., Lonardelli, I., Pehl, J., Devine, J., Prakapenka, V., Shen, G., & Mao, H. K. (2004). In situ observation of texture development in olivine, ringwoodite, magnesio-wüstite and silicate perovskite at high pressure. *Earth and Planetary Science Letters*, 226(3–4), 507–519. <https://doi.org/10.1016/j.epsl.2004.07.033>
- Wenk, H.-R., Lonardelli, I., Merkel, S., Miyagi, L., Pehl, J., Speziale, S., & Tommaseo, C. E. (2006). Deformation textures produced in diamond anvil experiments, analysed in radial diffraction geometry. *Journal of Physics Condensed Matter*, 18(25). <https://doi.org/10.1088/0953-8984/18/25/S02>
- Wenk, H.-R., Speziale, S., McNamara, A. K., & Garnero, E. J. (2006). Modeling lower mantle anisotropy development in a subducting slab. *Earth and Planetary Science Letters*, 245(1–2), 302–314. <https://doi.org/10.1016/j.epsl.2006.02.028>
- Wenk, H.-R., Cottaar, S., Tomé, C. N., McNamara, A., & Romanowicz, B. (2011). Deformation in the lowermost mantle: From polycrystal plasticity to seismic anisotropy. *Earth and Planetary Science Letters*, 306(1–2), 33–45. <https://doi.org/10.1016/J.EPSL.2011.03.021>
- Wenk, H.-R., Lutterotti, L., Kaercher, P., Kanitpanyacharoen, W., Miyagi, L., & Vasin, R. (2014). Rietveld texture analysis from synchrotron diffraction images. II. Complex multiphase materials and diamond anvil cell experiments. *Powder Diffraction*, 29(3). <https://doi.org/10.1017/S0885715614000360>
- Wookey, J., Kendall, J.-M., & Barruol, G. (2002). Mid-mantle deformation inferred from seismic anisotropy. *Nature*, 415(6873), 777–780. <https://doi.org/10.1038/415777a>
- Wu, X., Lin, J. F., Kaercher, P., Mao, Z., Liu, J., Wenk, H. R., & Prakapenka, V. B. (2017). Seismic anisotropy of the D'' layer induced by (001) deformation of post-perovskite. *Nature Communications*, 8, 1–6. <https://doi.org/10.1038/ncomms14669>
- Xu, J., Yamazaki, D., Katsura, T., Wu, X., Remmert, P., Yurimoto, H., & Chakraborty, S. (2011). Silicon and magnesium diffusion in a single crystal of MgSiO₃ perovskite. *Journal of Geophysical Research*, 116(B12), B12205. <https://doi.org/10.1029/2011JB008444>
- Xu, S. C., Wang, L. D., Zhao, P. T., Li, W. L., Xue, Z. W., & Fei, W. D. (2011). Evolution of texture during hot rolling of aluminum borate whisker-reinforced 6061 aluminum alloy composite. *Materials Science and Engineering: A*, 528(7–8), 3243–3248. <https://doi.org/10.1016/J.MSEA.2010.12.103>
- Xu, Y., Nishihara, Y., & Karato, S. (2005). Development of a rotational Drickamer apparatus for large-strain deformation experiments at deep Earth conditions. *Advances in High-Pressure Technology for Geophysical Applications*, 167–182. <https://doi.org/10.1016/B978-044451979-5.50010-7>
- Yamazaki, D., & Karato, S. I. (2001a). High-pressure rotational deformation apparatus to 15 GPa. *Review of Scientific Instruments*, 72(11), 4207–4211. <https://doi.org/10.1063/1.1412858>
- Yamazaki, D., & Karato, S. I. (2001b). Some mineral physics constraints on the rheology and geothermal structure of Earth's lower mantle. *American Mineralogist*, 86(4), 385–391. <https://doi.org/10.2138/am-2001-0401>
- Yamazaki, D., & Karato, S. I. (2002). Fabric development in (Mg,Fe)O during large strain, shear deformation: Implications for seismic anisotropy in Earth's lower mantle. *Physics of the Earth and Planetary Interiors*, 131(3–4), 251–267. [https://doi.org/10.1016/S0031-9201\(02\)00037-7](https://doi.org/10.1016/S0031-9201(02)00037-7)
- Yamazaki, D., Kato, T., Yurimoto, H., Ohtani, E., & Toriumi, M. (2000). Silicon self-diffusion in MgSiO₃ perovskite at 25 GPa. *Physics of the Earth and Planetary Interiors*, 119(3–4), 299–309. [https://doi.org/10.1016/S0031-9201\(00\)00135-7](https://doi.org/10.1016/S0031-9201(00)00135-7)
- Yamazaki, D., Yoshino, T., Ohfuji, H., Ando, J. ichi, & Yoneda, A. (2006). Origin of seismic anisotropy in the D'' layer inferred from shear deformation experiments on post-perovskite phase. *Earth and Planetary Science Letters*, 252(3–4), 372–378. <https://doi.org/10.1016/j.epsl.2006.10.004>
- Yoshizawa, Y., Toriyama, M., & Kanzaki, S. (2004). Fabrication of Textured Alumina by High-Temperature Deformation. *Journal of the American Ceramic Society*, 84(6), 1392–1394. <https://doi.org/10.1111/j.1151-2916.2001.tb00848.x>
- Zhang, W. L., Gu, M. Y., Wang, D. Z., & Yao, Z. K. (2004). Rolling and annealing textures of a SiCw/Al composite. *Materials Letters*, 58(27–28), 3414–3418. <https://doi.org/10.1016/J.MATLET.2004.05.065>

3

Seismic Wave Velocities in Earth's Mantle from Mineral Elasticity

Johannes Buchen

ABSTRACT

The propagation of seismic waves through Earth's mantle is controlled by the elastic properties of the minerals that form mantle rocks. Changes in pressure, temperature, and chemical composition of the mantle as well as phase transitions affect seismic wave speeds through their impact on mineral elasticity. The elastic properties of minerals can be determined in experiments and by first-principle computations and be combined to model the elastic wave speeds of mantle rocks. Based on recent advances, I evaluate the uncertainties on modeled elastic wave speeds and explore their sensitivity to physical and chemical key parameters. I discuss the elastic properties of solid solutions and elastic anomalies that arise from continuous phase transitions, such as spin transitions and ferroelastic phase transitions. Models for rocks of Earth's lower mantle indicate that continuous phase transitions and Fe-Mg exchange between major mantle minerals can have significant impacts on elastic wave speeds. When viewed in context with other constraints on the structure and dynamics of the lower mantle, mineral-physical models for the elastic wave speeds of mantle rocks can help to separate thermal from compositional signals in the seismic record and to identify patterns of material transport through Earth's deep interior.

3.1. INTRODUCTION

Seismic waves irradiated from intense earthquakes propagate through Earth's interior and probe the physical properties of materials that constitute Earth's mantle. Analyzing travel times and wave forms of seismic signals allows reconstructing the propagation velocities of seismic waves in Earth's interior. With the fast-growing body of seismic data and improvements in seismological methods, such reconstructions reveal more and more details about Earth's deep seismic structure. The propagation velocities of body waves, i.e., compressional (P) and shear (S)

waves, are mainly controlled by the elastic properties of the mantle. The interpretation of seismic observations therefore requires a profound understanding of how pressure, temperature, and chemical composition affect the elastic properties of candidate materials. High-pressure experiments and quantum-mechanical calculations have been devised to sample thermodynamic and elastic properties of deep-earth materials by simulating the extreme conditions deep within Earth's mantle. Their results serve as anchor points for thermodynamic models that allow predicting the elastic properties of mantle rocks for comparison with seismic observations.

The task of assessing the composition of Earth's interior by comparing seismic velocities with elastic properties of candidate materials was pioneered by Francis

Seismological Laboratory, California Institute of Technology, Pasadena, CA, USA

Birch (Birch, 1964, 1952). Building on the work of Murnaghan (Murnaghan, 1937), Birch was also among the first to advance finite-strain theory for describing the elastic properties of materials subjected to strong compressions (Birch, 1947, 1939, 1938). Further extensions and generalizations of finite-strain formulations (Davies, 1974; Thomsen, 1972a) lead to widespread and successful applications of finite-strain theory in modeling seismic properties of mantle materials (Bass & Anderson, 1984; Cammarano et al., 2003; Cobden et al., 2009; Davies and Dziewonski, 1975; Duffy & Anderson, 1989; Ita & Stixrude, 1992; Jackson, 1998; Stixrude & Lithgow-Bertelloni, 2005). Today, compilations of finite-strain and thermodynamic parameters for mantle minerals and dedicated software tools allow computing phase diagrams for typical rock compositions together with elastic properties (Chust et al., 2017; Connolly, 2005; Holland et al., 2013; Stixrude & Lithgow-Bertelloni, 2011). Mineral-physical databases have proven particularly useful in modeling the seismic properties of Earth's mantle to depths of about 900 km (Cammarano et al., 2009; Cobden et al., 2008; Xu et al., 2008). To some extent, this success reflects current capabilities of high-pressure experiments as most major minerals of the upper mantle and transition zone can be synthesized and their elastic properties be determined for relevant compositions and at realistic pressures and temperatures, limiting the need for far extrapolations.

For the lower mantle, however, the situation is different as information on the elastic properties of minerals and rocks at pressures and temperatures spanning those of Earth's lower mantle is more challenging to retrieve, both from experiments and computations. This might be one reason why attempts to interpret the seismic structure of the lower mantle based on incomplete mineral-physical data have led to contradicting conclusions about the composition and temperature profile of the lower mantle (Cobden et al., 2009; Khan et al., 2008; Matas et al., 2007; Mattern et al., 2005). In recent years, however, important progress has been made in constraining the elastic properties of lower-mantle minerals at high pressures and high temperatures, as for instance by experimental measurements on different bridgmanite compositions (Fu et al., 2018; Kurnosov et al., 2017; Murakami et al., 2012), on unquenchable cubic calcium-silicate perovskite (Gréaux et al., 2019; Thomson et al., 2019), and on the calcium-ferrite structured phase (Dai et al., 2013), as well as by better constraining thermoelastic parameters through experiments and computations (Gréaux et al., 2016; Murakami et al., 2012; Yang et al., 2016; Zhang et al., 2013). Similarly, experiments on single crystals (Antonangeli et al., 2011; Crowhurst et al., 2008; Marquardt et al., 2009c, 2009b; Yang

et al., 2015), improved computational methods (Wu et al., 2013; Wu and Wentzcovitch, 2014), and measurements at seismic frequencies (Marquardt et al., 2018) have advanced our understanding of how the spin transition of ferrous iron affects the elastic properties of ferropericlase. Many of these and other achievements have not yet been incorporated into mineral-physical databases, and the effects of spin transitions on mineral elasticity are not accounted for by commonly applied finite-strain formalisms.

This chapter aims to review recent advancements in experimental and computational mineral physics on the elastic properties of mantle minerals. A brief introduction to finite-strain theory and to the elastic properties of minerals and rocks is followed by an overview of experimental and computational methods used to determine elastic properties of minerals at pressures and temperatures of Earth's mantle. To assess the resilience and reliability of mineral-physical models and their potential to explain seismic observations, I systematically evaluate how uncertainties on individual finite-strain parameters impact computed elastic wave velocities for major mantle minerals and address the effect of inter- and extrapolating elastic properties across complex solid solutions. This analysis aims at revealing the leverages of finite-strain parameters and extrapolations in chemical compositions on elastic wave velocities in order to guide future efforts to improve mineral-physical models by reducing uncertainties on key parameters and compositions. With a particular focus on minerals of the lower mantle, I discuss the effect of continuous phase transitions on elastic properties, including ferroelastic phase transitions and spin transitions. A volume-dependent formulation for spin transitions is proposed that is readily combined with existing finite-strain formalisms. To provide an up-to-date perspective on the elastic properties of Earth's lower mantle, I combine most recent elasticity data and derive elastic wave velocities for a selection of potential mantle rocks, taking into account spin transitions in ferrous and ferric iron and the ferroelastic phase transition in stishovite. A comparison of scenarios for different assumptions about compositional parameters reveals persisting challenges in the mineral physics of the lower mantle.

3.2. ELASTIC PROPERTIES

When a seismic wave passes through a rock, the wave imposes stresses and strains on the rock and on the individual mineral grains that compose the rock. In Earth's mantle, these stresses and strains are much smaller than

those that arise from compression and heating of the rock to pressures and temperatures in the mantle. The mineral grains or crystals react to compression and heating as well as to seismic waves mainly by reversible elastic deformation. For each crystal grain in the rock, the small stresses and strains imposed by a seismic wave can be assumed to obey a linear relationship between the stress tensor σ_{ij} and the infinitesimal strain tensor e_{ij} (Haussühl, 2007; Nye, 1985):

$$\sigma_{ij} = c_{ijkl}e_{kl}$$

$$e_{ij} = s_{ijkl}\sigma_{kl}$$

with the components of the elastic stiffness tensor c_{ijkl} and the elastic compliance tensor s_{ijkl} of the crystal.

Large strains that arise from compression and thermal expansion can be described by the Eulerian finite-strain tensor E_{ij} (Birch, 1947; Davies, 1974; Stixrude & Lithgow-Bertelloni, 2005). For hydrostatic compression and heating, the resulting finite strain is dominated by volume strain and can be approximated by an isotropic tensor with $E_{ij} = -f\delta_{ij}$ where $f = [(V_0/V)^{2/3} - 1]/2$. V_0/V is the ratio of the volume V_0 of the crystal at the reference state to the volume V in the compressed and hot state. In principle, the definition of the reference state is arbitrary. From an experimental point of view, it is convenient to define the reference state to be the state of the mineral at ambient pressure and temperature, i.e., $P_0 = 1 \times 10^{-4}$ GPa and $T_0 = 298$ K. Based on an expansion of the Helmholtz free energy F in finite strain, physical properties, including pressure and elastic stiffnesses, can be described as a function of volume and temperature (Birch, 1947; Davies, 1974; Thomsen, 1972a). Throughout this chapter, I will use the self-consistent formalism presented by Stixrude and Lithgow-Bertelloni (2005) that combines finite-strain theory with a quasi-harmonic Debye model for thermal contributions to calculate pressure and elastic properties (Ita & Stixrude, 1992; Stixrude & Lithgow-Bertelloni, 2005).

For a truncation of the Helmholtz free energy after the fourth-order term in finite strain, the components of the isentropic elastic stiffness tensor are given by (Davies, 1974; Stixrude & Lithgow-Bertelloni, 2005):

$$\begin{aligned} c_{ijkl} = & (1 + 2f)^{5/2} \left(c_{ijkl0} + \left(3K_0 c'_{ijkl0} - 5c_{ijkl0} \right) f \right. \\ & + \left[6K_0 c'_{ijkl0} - 14c_{ijkl0} - \frac{3}{2} K_0 \delta_{kl}^{ij} (3K'_0 - 16) \right] f^2 \\ & + \frac{1}{2} \left[9K_0^2 c''_{ijkl0} + 3K_0 \left(c'_{ijkl0} + \delta_{kl}^{ij} \right) (3K'_0 - 16) \right. \\ & \left. \left. + 63c_{ijkl0} \right] (1 + 2f) f^2 \right) \end{aligned}$$

$$\begin{aligned} & - \frac{9}{2} K_0 \delta_{kl}^{ij} \left[K_0 K''_0 + K'_0 (K'_0 - 7) + \frac{143}{9} \right] f^3 \Big) \\ & + \left[\gamma_{ij} \gamma_{kl} + \frac{1}{2} (\gamma_{ij} \delta_{kl} + \gamma_{kl} \delta_{ij}) - \eta_{ijkl} \right] \frac{\Delta_{\text{TH}} U}{V} \\ & - \gamma_{ij} \gamma_{kl} \frac{\Delta_{\text{TH}}(C_V T)}{V} + \gamma_{ij} \gamma_{kl} \frac{C_V T}{V} \end{aligned}$$

where $\delta_{kl}^{ij} = -\delta_{ij} \delta_{kl} - \delta_{il} \delta_{jk} - \delta_{jl} \delta_{ik}$. The parameters of the cold part (lines 1–5) of this expression are the components of the isothermal elastic stiffness tensor c_{ijkl0} at the reference state and their first and second pressure derivatives c'_{ijkl0} and c''_{ijkl0} , respectively. They combine to the isothermal bulk modulus K_0 at the reference state as:

$$K_0 = c_{ijkl0} \delta_{ij} \delta_{kl} / 9$$

In an analogous way, the first and second pressure derivatives of the components of the elastic stiffness tensor combine to the first and second pressure derivatives of the bulk modulus K'_0 and K''_0 , respectively. The number of independent components of the elastic stiffness tensor depends on the crystal symmetry of the mineral and ranges from 21 for monoclinic (lowest) symmetry to 2 for an elastically isotropic material (Haussühl, 2007; Nye, 1985). Many mantle minerals, including olivine, wadsleyite, and bridgmanite, display orthorhombic crystal symmetry with 9 independent components of the elasticity tensors. For minerals with cubic crystal symmetry, such as ringwoodite, most garnets, and ferropiclasite, the number of independent components is reduced to 3.

The thermal contribution (lines 6–7) includes the changes in internal energy $\Delta_{\text{TH}} U$ and in the product of isochoric heat capacity C_V and temperature T , $\Delta_{\text{TH}}(C_V T)$, that result from heating the mineral at constant volume V from the reference temperature T_0 to the temperature T . The internal energy U is computed from a Debye model (Ita & Stixrude, 1992) based on an expansion of the Debye temperature θ in finite strain (Stixrude & Lithgow-Bertelloni, 2005). The Grüneisen tensor is then defined as:

$$\gamma_{ij} = - \frac{1}{\theta} \frac{\partial \theta}{\partial e_{ij}}$$

and the strain derivative of the Grüneisen tensor as:

$$\eta_{ijkl} = \frac{\partial \gamma_{ij}}{\partial e_{kl}}$$

The Grüneisen tensor and the tensor η_{ijkl} are functions of finite strain themselves that are parameterized using their values at ambient conditions, i.e., γ_{ij0} and η_{ijkl0} (Stixrude & Lithgow-Bertelloni, 2005).

Seismic waves travel with wavelengths on the order of kilometers that by far exceed the grain sizes of mantle rocks. Seismic waves thus probe the elastic response of a collection or an aggregate of mineral grains. In the simplest case of a monomineralic aggregate, all grains are crystals of the same mineral. The crystals can be randomly oriented or aligned to form a crystallographic preferred orientation (CPO). CPO can result from deformation or from crystallization of mineral grains under the action of an anisotropic external field (Karato, 2008). In general, crystals are elastically anisotropic, and any preferred orientation of crystals will partly transfer the elastic anisotropy of individual crystals to the aggregate (Mainprice, 2015; Mainprice et al., 2000).

When combining the elastic properties of individual crystals to those of the aggregate, we further have to take into account that stresses and strains may not be distributed homogeneously throughout the aggregate as some crystals may behave stiffer and deform less than others. The effective stiffness of a crystal depends on the orientation of the crystal with respect to the imposed stress and strain fields. Crystals may also be clamped between neighboring grains and be forced into a strain state that may not correspond to a state of unconstrained mechanical equilibrium with the imposed external stress field. Approximations and bounds to the complex elastic behavior of crystalline aggregates have been reviewed by Watt et al. (1976). Here, I adopt the simplest bounding scheme based on the Voigt and Reuss bounds (Reuss, 1929; Voigt, 1928; Watt et al., 1976) and assume a random orientation of crystals.

The Voigt bound is based on the assumption that the strain is homogeneous throughout the aggregate (Reuss, 1929; Watt et al., 1976). Regardless of its orientation, each crystal in the aggregate is deformed according to the external strain field imposed, for example, by a seismic wave. Because the resulting stresses are calculated from the strains using the elastic stiffnesses, we need to average the components of the elastic stiffness tensor c_{ijkl} over all orientations. For a monomineralic aggregate, this leads to the following expressions for the isotropic bulk modulus K and the isotropic shear modulus G (Hill, 1952; Watt et al., 1976):

$$K^V = [c_{1111} + c_{2222} + c_{3333} + 2(c_{1122} + c_{1133} + c_{2233})]/9$$

$$G^V = [c_{1111} + c_{2222} + c_{3333} + 3(c_{2323} + c_{1313} + c_{1212}) - (c_{1122} + c_{1133} + c_{2233})]/15$$

The Reuss bound assumes that the imposed external stress field is homogeneous throughout the aggregate (Reuss, 1929; Watt et al., 1976). In this case, the strains

are calculated from the stresses using the components of the elastic compliance tensor s_{ijkl} . The isotropic bulk and shear moduli of a monomineralic aggregate of randomly oriented crystals are then (Hill, 1952; Watt et al., 1976):

$$K^R = 1/[s_{1111} + s_{2222} + s_{3333} + 2(s_{1122} + s_{1133} + s_{2233})]$$

$$G^R = 15/[4(s_{1111} + s_{2222} + s_{3333}) + 3(s_{2323} + s_{1313} + s_{1212}) - 4(s_{1122} + s_{1133} + s_{2233})]$$

Most mantle rocks are composed of several mineral phases, each of which has different elastic properties. For a polymineralic rock composed of different mineral phases with volume fractions v_i , the bulk and shear moduli M_i of individual mineral phases are then combined to the Voigt bound as (Watt et al., 1976):

$$M^V = \sum_i v_i M_i$$

and to the Reuss bound as (Watt et al., 1976):

$$M^R = 1/\sum_i \frac{v_i}{M_i}$$

While the Voigt and Reuss averages provide bounds to the elastic behavior of a crystalline aggregate, the Voigt-Reuss-Hill averages are often used as an approximation to the actual elastic response (Chung & Buessem, 1967; Hill, 1952; Thomsen, 1972b):

$$K^{VRH} = (K^V + K^R)/2$$

$$G^{VRH} = (G^V + G^R)/2$$

Note that the calculation of the Voigt and Reuss bounds in their strictest sense would require the elastic stiffness and compliance tensors of all minerals in the rock at the respective pressure and temperature. For many minerals, however, bulk and shear moduli have so far only been determined on polycrystalline aggregates and are themselves averages over the elastic properties of many individual crystals. For polycrystalline aggregates, the changes of the aggregate bulk and shear moduli of a mineral that result from compression and heating can be described by combining the finite-strain expressions for individual components c_{ijkl} to finite-strain expressions for the isotropic bulk and shear moduli (Birch, 1947; Davies, 1974; Stixrude & Lithgow-Bertelloni, 2005). Under the assumption of isotropic finite strain, the expressions would resemble those for the Voigt bound. In analogy to the elastic moduli, the components of the tensor η_{ijkl} are combined to the isotropic parameters η_V and η_S with respect to volume and shear strain, respectively (Stixrude & Lithgow-Bertelloni, 2005). When determined on a polycrystalline sample,

however, aggregate moduli are not readily identified with either of the bounds or with a simple average as the elastic response of the aggregate falls somewhere in between the Voigt and Reuss bounds and may even fall outside the bounds if a CPO is present.

Once the elastic properties of individual minerals have been combined to bulk and shear moduli of an isotropic polycrystalline rock, the propagation velocities v of longitudinal waves (P) and transverse or shear waves (S) can be calculated by:

$$v_P = \sqrt{\frac{K + 4G/3}{\rho}}$$

$$v_S = \sqrt{G/\rho}$$

The density ρ of the rock is computed by combining the molar masses and volumes of all minerals according to their abundances. Note that wave velocities discussed throughout this chapter are based on the elastic response of minerals and rocks only and do not include corrections for anelastic behavior that might affect wave velocities at seismic frequencies and at high temperatures (Jackson, 2015; Karato, 1993).

3.3. EXPERIMENTS

Finite-strain theory describes the elastic stiffnesses or moduli as functions of volume and temperature. The parameters needed for this description are therefore best determined from data sets that relate elastic stiffnesses or moduli with the corresponding volume (or density) and temperature. Since sound wave velocities are combinations of elastic moduli and density, they contain information on the elastic properties that is best retrieved when volume and temperature are determined along with sound wave velocities. Alternatively, volume can be inferred from pressure measurements via an equation of state (EOS) that relates pressure to volume and temperature. More information on theoretical and experimental aspects of high-pressure equations of state for solids has been summarized in recent review articles (Angel, 2000; Angel et al., 2014; Holzapfel, 2009; Stacey & Davis, 2004). Here, I give a brief overview of methods that constrain elastic properties other than the EOS. More detailed introductions into these and other methods to characterize the elastic properties of minerals can be found in Schreuer and Haussühl (2005) and in Angel et al. (2009).

The elastic stiffness tensor completely describes the elastic anisotropy of a crystal and hence also determines the velocities of sound waves travelling in different crystallographic directions. The components of the elastic stiffness tensor can therefore be derived by measuring the velocities

of sound waves that propagate through a single crystal along a set of different directions selected so as to adequately sample the elastic anisotropy of the crystal. The minimum number of individual measurements depends on the number of independent components c_{ijkl} and hence on the crystal symmetry. At high pressures, sound wave velocities can be determined using light scattering techniques on single crystals contained in diamond anvil cells (DAC). Both Brillouin spectroscopy and impulsive stimulated scattering (ISS) are based on inelastic scattering of light by sound waves (Cummins & Schoen, 1972; Dil, 1982; Fayer, 1982). The applications of Brillouin spectroscopy and ISS to determine elastic properties at high pressures have been reviewed by Speziale et al. (2014) and by Abramson et al. (1999), respectively. Light scattering experiments on single crystals compressed in DACs have proven successful in deriving full elastic stiffness tensors of mantle minerals up to pressures of the lower mantle (Crowhurst et al., 2008; Kurnosov et al., 2017; Marquardt et al., 2009c; Yang et al., 2015; Zhang et al., 2021). At combined high pressures and high temperatures, elastic stiffness tensors have been determined using Brillouin spectroscopy by heating single crystals inside DACs using resistive heaters or infrared lasers (Li et al., 2016; Mao et al., 2015; Yang et al., 2016; Zhang & Bass, 2016).

Resistive heaters for DACs commonly consist of platinum wires coiled on a ceramic ring that is placed around the opposing diamond anvils with the pressure chamber between their tips (Kantor et al., 2012; Sinogeikin et al., 2006). With this configuration, the pressure chamber containing the sample is heated from the outside together with the diamond anvils and the gasket. Heating and oxidation of diamond anvils and metallic gaskets can destabilize the pressure chamber and even cause it to collapse. Therefore, measurements of elastic properties using resistive heating of samples contained in DACs have so far been limited to temperatures of about 900 K. Such experiments require purging of DAC environments with inert or reducing gases, typically mixtures of argon and hydrogen, to prevent oxidation of diamonds and gaskets. Higher temperatures can be achieved with graphite heaters and by surrounding the DAC with a vacuum chamber (Immoor et al., 2020; Liermann et al., 2009). Setups with graphite heaters have been developed for X-ray diffraction experiments and could potentially be combined with measurements of elastic properties. When heating DACs with external heaters, temperatures are typically measured with thermocouples that are placed close to but outside of the pressure chamber. Besides those limitations, resistive heaters create a temperature field that can be assumed to be nearly homogeneous across the pressure chamber and can be held stable for long enough periods of time to perform light scattering and X-ray diffraction experiments on samples inside DACs.

Substantially higher temperatures can be achieved by using infrared (IR) lasers to directly heat a sample inside the pressure chamber of a DAC through the absorption of IR radiation. For a given material, the strength of absorption and hence the heating efficiency depend on the wavelength of the IR laser radiation. The IR radiation emitted by common rare-earth-element (REE) lasers, e.g., lasers based on REE-doped host crystals or optical fibers, is centered at wavelengths between 1 μm and 3 μm and efficiently absorbed by metals and by most opaque or iron-rich minerals. Light scattering experiments, however, are commonly performed on optically transparent materials, such as oxides and silicates with lower iron contents, that may not absorb IR radiation at wavelengths around 1–3 μm efficiently enough for uniform and steady heating. CO_2 gas lasers emit IR radiation with wavelengths of about 10 μm that is absorbed even by many optically transparent materials. As a consequence, CO_2 lasers have been used to heat transparent mineral samples while probing their elastic properties with light scattering (Kurnosov et al., 2019; Murakami et al., 2009a; Sinogeikin et al., 2004; Zhang et al., 2015).

Requirements of uniform heating as well as stabilization and accurate assessment of temperatures impose particular challenges on laser-heating experiments. Typical sample sizes for light scattering experiments on the order of several tens to hundred micrometers may exceed the sizes of hot spots generated by IR lasers. As a result, samples may not be heated uniformly, and the resulting thermal gradients can bias the measurements of both temperature and elastic properties. During laser-heating experiments, temperatures are determined by analyzing the thermal emission spectrum of the hot sample. Modern optical instrumentation allows combining spectral with spatial information of the hot spot to generate temperature maps that reveal thermal gradients and facilitate more accurate temperature measurements (Campbell, 2008; Kavner & Nugent, 2008; Rainey and Kavner, 2014). Analyses of laser-heated hot spots indicate that temperatures may vary by several hundreds of kelvins over a few tens of micrometers across the hot spot. The interaction of the sample with the IR laser often changes in the course of a laser-heating experiment and may lead to temporal temperature fluctuations in addition to thermal gradients. As a consequence, uncertainties of temperature measurements on laser-heated samples tend to be on the order of several hundred kelvins. The combination of sound wave velocity measurements on samples held at high pressures inside DACs with laser heating remains one of the major experimental challenges in mineral physics. The potential to determine elastic properties at pressures and temperatures that resemble those predicted to prevail throughout Earth's mantle has motivated first efforts to combine Brillouin spectroscopy with laser heating (Kurnosov et al., 2019; Murakami

et al., 2009a; Sinogeikin et al., 2004; Zhang et al., 2015) and led to successful measurements of sound wave velocities at combined high pressures and high temperatures (Murakami et al., 2012; Zhang & Bass, 2016).

When large enough crystal specimens are available, sound wave velocities can be derived by measuring the travel time of ultrasonic waves through single crystals. Initially developed for centimeter-sized samples and using frequencies in the megahertz range (e.g., Spetzler, 1970), this technique can be adopted to micrometer-sized samples contained in DACs by raising the frequencies of ultrasonic waves into the gigahertz range (Bassett et al., 2000; Reichmann et al., 1998; Spetzler et al., 1996). While first ultrasonic experiments in DACs were restricted to *P*-wave velocity measurements, Jacobsen et al. (2004, 2002) designed *P*-to-*S* wave converters to generate *S* waves with frequencies up to about 2 GHz and to enable the measurement of *S*-wave velocities on thin single crystals in DACs up to pressures of about 10 GPa (Jacobsen et al., 2004; Reichmann and Jacobsen, 2004). The relatively young techniques of picosecond acoustics and phonon imaging use ultrashort laser pulses to excite sound waves and to measure their travel times on the order of several hundred picoseconds, allowing to further reduce sample thickness. These techniques have been implemented with DACs to study elastic properties at high pressures and bear the potential to derive full elastic stiffness tensors (Decremps et al., 2014, 2010, 2008). At ambient pressure, the ultrasonic resonance frequencies of a specimen with a well-defined shape can be measured as a function of temperature and then be inverted for the elastic properties (Schreuer & Haussühl, 2005). The technique of resonant ultrasound spectroscopy (RUS) has been used, for example, to trace the elastic stiffness tensors of olivine single crystals up to temperatures relevant for the upper mantle (Isaak, 1992; Isaak et al., 1989).

The elastic response of a perfectly isotropic polycrystalline aggregate is, in principle, fully captured by the isotropic bulk and shear moduli. These moduli can be determined from the velocities of sound waves propagating in any direction through an isotropic polycrystal. Consequently, the elastic properties of many minerals have been studied on polycrystalline samples or powders, especially when single crystals of suitable size and quality were not available. Elastic moduli determined on polycrystalline samples, however, do not allow computing absolute bounds on the elastic response nor can they capture the elastic anisotropy of the individual crystals that compose the polycrystal. Polycrystalline samples need to be thoroughly characterized to exclude bias by an undetected CPO or by small amounts of secondary phases that might have segregated along grain boundaries during sample synthesis or sintering. Microcracks or vanishingly small fractions of porosity might also alter the overall elastic

response of a polycrystal (Gwanmesia et al., 1990; Speziale et al., 2014).

Millimeter-sized polycrystalline samples can be compressed and heated in multi-anvil presses while the travel times of ultrasonic waves through the sample are being measured by an interference technique (Li et al., 2004; Li and Liebermann, 2014). When the experiment is conducted at a synchrotron X-ray source, the sample length can be monitored by X-ray radiography, which requires the intense X-rays generated by the synchrotron. Otherwise the sample length can be inferred from an equation of state or solved for iteratively. Sound wave velocities can then be calculated from combinations of travel times and sample length. The stability of modern multi-anvil presses facilitates sound wave velocity measurements on samples held at pressures and temperatures that exceed those of the transition zone in Earth's mantle (Gréaux et al., 2019, 2016). By combining sample synthesis and ultrasonic interferometry in the same experiment, Gréaux et al. (2019) and Thomson et al. (2019) were able to determine the sound wave velocities of the unquenchable cubic polymorph of calcium silicate perovskite, CaSiO_3 . After synthesis at high pressure and high temperature, cubic calcium silicate perovskite cannot be recovered at ambient conditions as its crystal structure instantaneously distorts from cubic to tetragonal symmetry below a threshold temperature (Shim et al., 2002; Stixrude et al., 2007). A similar situation is encountered for stishovite, SiO_2 , which reversibly distorts from tetragonal to orthorhombic symmetry upon compression (Andrault et al., 1998; Karki et al., 1997b). Such displacive phase transitions can substantially change the elastic properties of materials and illustrate the need to determine elastic properties at relevant pressures and temperatures.

The wavelengths of sound waves used to derive the elastic moduli may also affect how the elastic properties of individual grains in a polycrystalline material are averaged by the measurement. At ultrasonic frequencies, sound waves travel with wavelengths between 10 μm and 10 mm that are long enough to probe the collective elastic response of fine-grained polycrystalline samples. Sound waves probed by light scattering techniques, however, typically have wavelengths on the order of 100 nm to 10 μm (Cummins & Schoen, 1972; Fayer, 1982), which is similar to typical grain sizes in polycrystalline samples. When the wavelength is similar to or smaller than the grain size, the measured sound wave velocity may be dominated by the elastic response of individual crystals or of the assembly of only a few crystals. When light is scattered by these single- or oligo-crystal sound waves, the measurement on a polycrystal takes an average over sound wave velocities within single crystals rather than averaging over the elastic properties of a sufficiently large collection of randomly oriented crystals that determine

the aggregate sound wave velocities at longer wavelengths. The intensity of the scattered light also depends on the orientations of the individual crystals via the photoelastic coupling that can enhance light scattering for some orientations and emphasize their sound wave velocities over others (Marquardt et al., 2009a; Speziale et al., 2014). Nevertheless, light scattering experiments on polycrystalline samples have contributed substantially in characterizing the elastic properties of mantle minerals at high pressures (Fu et al., 2018; Murakami et al., 2009b) and at high pressures and high temperatures (Murakami et al., 2012).

Synchrotron X-rays can be used to probe the lattice vibrations of crystalline materials. Inelastic X-ray scattering (IXS) combines the scattering geometry of the X-ray–lattice momentum transfer with measurements of minute energy shifts in scattered X-rays that result from interactions with collective thermal motions of atoms in a crystalline material (Burkel, 2000). At low vibrational frequencies, these collective motions are called acoustic phonons and resemble sound waves. Their velocities can be derived from an IXS experiment by setting the scattering geometry to sample acoustic phonons that propagate along a defined direction and with a defined wavelength and calculating their frequencies from the measured energy shifts of inelastically scattered X-rays. The energy distribution of lattice vibrations, the phonon density of states, can be studied by exciting the atomic nuclei of suitable isotopes and counting the reemitted X-rays (Sturhahn, 2004). Because the atomic nuclei are coupled to lattice vibrations, a small fraction of them absorbs X-rays at energies that are modulated away from the nuclear resonant energy reflecting the energy distribution of phonons that involve motions of the resonant isotope. ^{57}Fe is by far the most important isotope in geophysical applications of nuclear resonant inelastic X-ray scattering (NRIXS). Both IXS and NRIXS can be performed on samples compressed in diamond anvil cells to constrain the elastic properties of single crystals or polycrystalline materials (Fiquet et al., 2004; Sturhahn & Jackson, 2007). Given the low efficiency of inelastic X-ray scattering in general and the selective sensitivity of NRIXS to Mössbauer-active isotopes such as ^{57}Fe , many IXS and NRIXS studies focused on iron-bearing materials, including potential alloys of Earth's core (Antonangeli et al., 2012; Badro et al., 2007; Fiquet et al., 2001) and minerals relevant to Earth's lower mantle (Antonangeli et al., 2011; Finkelstein et al., 2018; Lin et al., 2006; Wicks et al., 2017, 2010).

As mentioned at the beginning of this section, experimentally determined sound wave velocities are ideally combined with measurements of density or volume strain at the same pressure and temperature. Densities are routinely determined by X-ray diffraction, and all methods

outlined above can in principle be combined with X-ray diffraction experiments. X-ray diffraction at high pressures has been treated in numerous review articles (Angel et al., 2000; Boffa Ballaran et al., 2013; Miletich et al., 2005; Norby and Schwarz, 2008) and is used to determine the volume of the crystallographic unit cell of a crystalline material. Particularly instructive examples of combining measurements of elastic properties with measurements of unit cell volumes were given by Zha et al. (1998, 2000), who determined bulk moduli as a function of volume by combining single-crystal Brillouin spectroscopy and X-ray diffraction. Combinations of bulk moduli K and unit cell volumes V at different compression states define the function $K(V)$ that, upon integration, gives a direct measure for pressure:

$$P = P_0 - \int_{V_0}^V \frac{K(V)}{V} dV$$

Sample sizes in diamond anvil cells are very small, and samples are surrounded by heater and thermal insulation materials in multi-anvil presses so that, in most cases, intense and focused X-rays from synchrotron sources are required to generate diffraction patterns of suitable quality. Converting the unit cell volume to density requires information on the atomic content of the unit cell and hence on the chemical composition of the material. Uncertainties on molar masses of chemically complex materials typically subvert the high precision on unit cell volumes achievable with modern X-ray diffraction techniques. Note also that densities based on X-ray diffraction do not capture amorphous materials or porosity that might be present along grain boundaries or cracks in polycrystalline materials. A rather new technique to determine the bulk modulus uses synchrotron X-ray diffraction to capture the elastic response of a polycrystalline sample that is subjected to cyclic loading at seismic frequencies. For this type of experiment, a DAC is attached to a piezoelectric actuator that generates small pressure oscillations. The resulting oscillations in unit cell volume can be measured by recording the time-resolved diffraction of intense X-rays with sufficiently fast and sensitive detectors and be analyzed to constrain the bulk modulus. Marquardt et al. (2018) successfully used this technique to probe the softening of the bulk modulus across the spin transition in ferropericlase at seismic frequencies. When combined with resistive heating, piezo-driven DACs may facilitate cyclic loading experiments at combined high pressures and high temperatures (Méndez et al., 2020).

3.4. COMPUTATIONS

Quantum-mechanical computations and molecular dynamic simulations have evolved to powerful tools in predicting the elastic properties of minerals at high

pressures and high temperatures and complement experiments for conditions that are not readily accessible with current experimental methods (Karki et al., 2001a; Stixrude et al., 1998). First-principle calculations are based on the Schrödinger equation:

$$\hat{H}\Psi(\mathbf{r}) = E\Psi(\mathbf{r})$$

that yields the total energy E of a system of electrons and atomic nuclei as the eigenvalue of the Hamiltonian operator \hat{H} that is applied to the multi-particle wave function $\Psi(\mathbf{r})$. In density functional theory (DFT), the Hamiltonian operator is broken down into contributions of the kinetic energy T of non-interacting electrons, the electrostatic potential energy E_C , and the exchange-correlation energy E_{XC} that describes the electron-electron interaction, all of which are functionals of the electron density $n(\mathbf{r})$ that changes with the location \mathbf{r} (Hohenberg and Kohn, 1964; Kohn and Sham, 1965). The total energy can then be expressed in terms of the electron density:

$$E[n(\mathbf{r})] = T[n(\mathbf{r})] + E_C[n(\mathbf{r})] + E_{XC}[n(\mathbf{r})]$$

While the functionals of kinetic and potential energies can be evaluated exactly, formulations for the exchange-correlation energy rely on approximations (Karki et al., 2001a; Perdew & Ruzsinszky, 2010; Stixrude et al., 1998). These approximations allow computing the total energy E for a given arrangement of atoms, i.e., for a crystal structure. The forces acting between atoms, also called Hellmann-Feynman forces, can be found by evaluating the changes in energy that result from small perturbations of the atomic arrangement (Baroni et al., 2001). When the perturbation of the atomic arrangement is chosen to correspond to a homogeneous strain, the resulting stresses (Nielsen and Martin, 1985) and hence elastic properties can be derived (Baroni et al., 1987a, 2001; Wentzcovitch et al., 1995). Alternatively, an external pressure can be applied to the simulation cell, and the resulting forces and stresses be minimized by relaxing the atomic positions and the shape of the simulation cell (Wentzcovitch et al., 1995, 1993). Note that, apart from being intentionally displaced or being relaxed to their equilibrium configuration, atomic nuclei remain static in these calculations. The results of such static DFT calculations can in principle be compared with those of experiments at ambient temperature as thermal contributions at 298 K are expected to be fairly small for most materials.

In most cases, the exchange-correlation contribution is evaluated based on either the local density approximation (LDA) or on generalized gradient approximations (GGA). The LDA approximates the exchange-correlation potential at each point \mathbf{r} by the exchange-correlation potential of a uniform electron gas with the density $n(\mathbf{r})$ at this point. GGA also take into account gradients in electron density when evaluating the exchange-correlation potential. Both LDA and GGA

have proven successful in reproducing the elastic properties of many mantle minerals where experimental results are available for comparison. However, LDA appears to systematically overestimate bonding forces, i.e., leading to slightly higher elastic moduli and smaller volumes, while GGA tends to underestimate bonding forces with opposite effects on elastic properties and volumes (Karki et al., 2001a). Another aspect becomes important when computing properties of compounds containing transition metal or lanthanide atoms such as iron and its cations that are present in many mantle minerals. Both LDA and GGA take into account mutual repulsion between electrons in an inhomogeneous but diffuse gas of electrons. This approximation breaks down for electrons in the less diffuse d and f orbitals of transition metal and lanthanide atoms as these electrons become effectively localized by the additional repulsion they experience from electrons in similar orbitals on the same and neighboring atoms (e.g., Cox, 1987; Hubbard, 1963). This localization is the reason for the insulating or semi-conducting behavior of some transition metal oxides, such as FeO, despite of their partially filled d orbitals.

By far the most common strategy to account for the repulsion between localized d electrons is to add an energy term E_U that depends on the Hubbard parameter U and on the occupation numbers of d orbitals (Anisimov et al., 1997, 1991; Cococcioni, 2010; Cococcioni and de Gironcoli, 2005). This approach, referred to as LDA+ U or GGA+ U , can reduce discrepancies between predicted and experimentally observed elastic properties (Stackhouse et al., 2010) and led to substantial improvements in treating spin transitions of ferrous and ferric iron with DFT calculations (Hsu et al., 2011, 2010a, 2010b; Persson et al., 2006; Tsuchiya et al., 2006). Despite important progress in modeling the electronic properties of iron cations in oxides and silicates, elastic properties extracted from DFT computations still seem to deviate significantly from experimental observations in particular across spin transitions in major mantle minerals (Fu et al., 2018; Shukla et al., 2016; Wu et al., 2013), highlighting persistent challenges in the treatment of localized d electrons.

While most first-principle calculations assume the atomic nuclei to be static, thermal motions of atoms at finite temperatures can be addressed by coupling DFT to molecular dynamics (MD) (Car & Parrinello, 1985) or by computing vibrational properties using density functional perturbation theory (DFPT) (Baroni et al., 2001, 1987b; Giannozzi et al., 1991). Sometimes referred to as *ab initio* molecular dynamics, DFT-MD allows computing elastic properties at pressures and temperatures that span those in Earth's mantle (Oganov et al., 2001; Stackhouse et al., 2005b). Within the limitations imposed by the finite sizes of systems that can be simulated, DFT-MD includes

anharmonic effects that go beyond the approximation of atomic vibrations as harmonic oscillations and become discernible at high temperatures (Oganov et al., 2001; Oganov and Dorogokupets, 2004, 2003). Alternatively, the frequencies of lattice vibrations can be derived from DFPT for a given volume (Baroni et al., 2001, 1987b) and then used in the quasi-harmonic approximation (QHA) to compute temperature-dependent elastic properties (Karki et al., 1999, 2000; Wentzcovitch et al., 2004, 2006, 2010a). The pressure-temperature space for which the QHA remains valid for a given material can be estimated from the inflexion points $(\partial^2 \alpha / \partial T^2)_P = 0$ in computed curves of the thermal expansivity $\alpha(P, T)$ as the QHA appears to overestimate thermal expansivities at higher temperatures (Carrier et al., 2007; Karki et al., 2001b; Wentzcovitch et al., 2010b). This criterion suggests that the QHA should remain valid throughout most of Earth's mantle for some materials while others are expected to deviate from purely harmonic behavior (Wentzcovitch et al., 2010b; Wu & Wentzcovitch, 2011). The results of QHA-DFT computations can be corrected for anharmonic contributions by adding a semi-empirical correction term to match experimental observations (Wu and Wentzcovitch, 2009). Anharmonic effects can also be addressed in DFPT computations (Baroni et al., 2001; Oganov & Dorogokupets, 2004). For example, a recent study on MgO combined DFPT calculations with infrared spectroscopy and IXS to relate experimentally observed indications of anharmonicity, such as phonon line widths, to multi-phonon interactions (Giura et al., 2019). Such efforts demonstrate the possibility to assess anharmonicity in first-principle calculations. Among other advancements, all these developments facilitate the routine application of DFT computations to study the elastic properties of structurally and chemically complex minerals at high pressures and high temperatures (Kawai and Tsuchiya, 2015; Shukla et al., 2015; Wu et al., 2013; Zhang et al., 2016).

3.5. PARAMETER UNCERTAINTIES

The results of a series of experiments or computations are typically inverted into sets of parameters that describe the variation of elastic properties as a function of finite strain and temperature. Different definitions of finite strain result in different functional forms of expressions for elastic properties. For equations of state, different definitions and assumptions give rise to a remarkable diversity in EOS formulations (Angel, 2000; Angel et al., 2014; Holzapfel, 2009; Stacey & Davis, 2004). The variation of components of the elastic stiffness tensor has been formulated using both the Lagrangian and Eulerian definitions of finite strain (Birch, 1947; Davies, 1974; Thomsen, 1972a). For interpolations between

individual observations, i.e., experiments or computations, differences between formulations should be small since, in a semi-empirical approach, finite-strain parameters are chosen to best reproduce the observations. Extrapolations of elastic properties beyond observational constraints, however, can be extremely sensitive to the chosen formalism. Both different definitions of finite strain and expansions to different orders of finite strain can result in substantial deviations between different finite-strain models when extrapolated beyond observational constraints. Owing to the prevalence of elasticity formalisms based on Eulerian finite strain (Davies & Dziewonski, 1975; Ita & Stixrude, 1992; Jackson, 1998; Sammis et al., 1970; Stixrude & Lithgow-Bertelloni, 2005), this source of uncertainty is not commonly taken into account when computing seismic properties and tends to become less important as experiments and computations are being pushed towards the verges of the relevant pressure–temperature space. Additional uncertainties arise from extrapolating the thermal or vibrational properties of minerals beyond the limitations of underlying assumptions, such as the quasi-harmonic approximation. For example, anharmonic contributions to elastic properties at high temperatures are mostly ignored as they remain difficult to assess in experiments and computations. Cobden et al. (2008) have explored how different combinations of finite-strain equations and thermal corrections, including anelastic contributions, affect the outcomes of mineral-physical models.

Whether derived from experiments or computations, elastic properties are affected by uncertainties that need to be propagated into the uncertainties on finite-strain parameters. Inverting elasticity data on a limited number of pressure–temperature combinations to find the optimal set of finite-strain parameters will inevitably result in correlations between finite-strain parameters. The uncertainties on derived finite-strain parameters are only meaningful when the uncertainties on the primary data have been assessed correctly, a requirement that can be difficult to meet in particular for first-principle computations. Uncertainties on modeled seismic properties of rocks arise from uncertainties on individual finite-strain parameters and from the anisotropy of the rock-forming minerals as captured by the bounds on the elastic moduli. When constructing mineral-physical models, uncertainties have been addressed by varying the parameters that describe the elastic properties of minerals in a randomized way within their individual uncertainties (Cammarano et al., 2003; Cammarano et al., 2005a; Cobden et al., 2008). While capturing the combined variance of the models, randomized sampling of parameters cannot disclose how individual parameters or properties affect the model. Identifying key properties might help to define future experimental and computational strategies to better constrain the related parameters in mineral-physical models.

To illustrate how modeled seismic properties of mantle rocks are affected by different sources of uncertainties, I first concentrate on the properties of monomineralic and isotropic aggregates of major minerals in Earth’s upper mantle, transition zone, and lower mantle, i.e., olivine, wadsleyite and ringwoodite, and bridgmanite. For these minerals, complete elastic stiffness tensors have been determined together with unit cell volumes for relevant compositions and at relevant pressures. Such data sets can be directly inverted for the parameters of the cold parts of finite-strain expressions for the components of the elastic stiffness tensor. For olivine compositions with $\text{Mg}/(\text{Fe}+\text{Mg}) = 0.9$, i.e., San Carlos olivine, high-pressure elastic stiffness tensors at room temperature (Zha et al., 1998) can be combined with recent experiments at simultaneously high pressures and high temperatures (Mao et al., 2015; Zhang & Bass, 2016) to self-consistently constrain most anisotropic finite-strain parameters. For wadsleyite and ringwoodite, recent experimental results on single crystals (Buchen et al., 2018b; Schulze et al., 2018) are combined with tabulated parameters for the isotropic thermal contributions (Stixrude & Lithgow-Bertelloni, 2011). Similarly, high-pressure elastic stiffness tensors of bridgmanite at room temperature (Kurnosov et al., 2017) are complemented with results of DFT computations (Zhang et al., 2013) and high-pressure high-temperature experiments on polycrystals (Murakami et al., 2012) that constrain the isotropic thermal contributions.

For each mineral, P - and S -wave velocities are computed using the Voigt-Reuss-Hill averages for bulk and shear moduli of an isotropic aggregate. The explored pressures and temperatures are spanned by two adiabatic compression paths that start 500 K above and below a typical adiabatic compression path for each mineral. To examine the impact of uncertainties on a given finite-strain parameter, P - and S -wave velocities are then recalculated by first adding (+) and then subtracting (–) the respective uncertainty to a given parameter leaving all other parameters unchanged. The resulting difference in velocities $\Delta v = v^+ - v^-$ is then compared to the original velocity v^{VRH} as:

$$d \ln v = \frac{\Delta v}{v^{\text{VRH}}}$$

The effect of anisotropy is illustrated in the same way by using the Voigt (V) and Reuss (R) bounds on the moduli and setting $\Delta v = v^{\text{V}} - v^{\text{R}}$. The velocity variations $d \ln v$ are mapped over relevant pressures and temperatures for olivine, wadsleyite, ringwoodite, and bridgmanite. Note that, for each of these minerals, the results of experiments and computations need to be substantially inter- and extrapolated across the respective pressure–temperature space.

Figures 3.1 and 3.2 show relative variations $d \ln v$ of P - and S -wave velocities, respectively, that arise from differences between the Voigt and Reuss bounds as well as from uncertainties on the parameters K'_0 , G'_0 , γ_0 , q_0 , and η_0 . Varying the Debye temperature θ_0 within reported uncertainties does not change wave velocities by more than 0.5% for the minerals and conditions considered, and no corresponding plots have been included in Figures 3.1 and 3.2. Parameter values and uncertainties were taken from the respective references or, in the case of San Carlos olivine, derived by fitting finite-strain equations to the combined data set of elastic stiffness tensors and unit cell volumes at high pressures and high temperatures (Mao et al., 2015; Zha et al., 1998; Zhang & Bass, 2016). The uncertainties can therefore be considered to reflect the precision of current experimental and computational methods. The resulting variations in P - and S -wave velocities, however, display the impact of individual parameters rather than absolute uncertainties on wave velocities. This way of propagating uncertainties on individual parameters into uncertainties on wave velocities illustrates how the influence of a given parameter changes with pressure and temperature and allows to identify those parameters that exert the strongest impact on P - and S -wave velocities, respectively.

Aggregate P - and S -wave velocities of olivine, wadsleyite, and bridgmanite all show variations of more than 1% due to elastic anisotropy as reflected in the differences between the Voigt and Reuss bounds. The elastic anisotropy of ringwoodite single crystals is known to be fairly small (Mao et al., 2012; Sinogeikin et al., 1998; Weidner et al., 1984). As a result, aggregate P - and S -wave velocities differ by less than 0.5% for ringwoodite. For minerals with significant elastic anisotropy, including the major mantle minerals olivine, wadsleyite, and bridgmanite, uncertainties on wave velocities that arise from averaging over grains with different orientations may contribute substantially to absolute uncertainties as the actual elastic response of an isotropic polycrystalline aggregate may fall somewhere in between the bounds on elastic moduli. Note that alternative bounding schemes might provide tighter bounds on elastic moduli than the Voigt and Reuss bounds (Watt et al., 1976).

In comparison to the impact of elastic anisotropy on aggregate elastic moduli and wave velocities, the pressure derivatives K'_0 and G'_0 do not appear to strongly affect wave velocities when varied within reported uncertainties. This observation reflects the common approach of experimental and computational methods to address the response of elastic properties to compression and hence to best constrain pressure derivatives. To a certain extent, the comparatively small leverage of pressure derivatives on elastic wave velocities justifies inter- and extrapolations of the finite-strain formalism to pressures and

temperatures not covered by experiments or computations. Along adiabatic compression paths of typical mantle rocks, for example, changes in elastic properties that result from compression or volume reduction surpass changes that result from the corresponding adiabatic increase in temperature.

With the exception of the Debye temperature, the parameters describing the quasi-harmonic or thermal contribution to elastic properties all show significant impact on computed wave velocities. Both P - and S -wave velocities of the minerals included in Figures 3.1 and 3.2 appear to be sensitive to variations in the Grüneisen parameter γ_0 , in particular at low pressures and high temperatures. In general, the isotropic volume strain derivative $q_0 = \eta_{V0}/\gamma_0$ of the Grüneisen parameter has more impact on P -wave velocities while the isotropic shear strain derivative η_{S0} mostly affects S -wave velocities. The S -wave velocities of transition zone minerals seem to be particularly sensitive to η_{S0} . This sensitivity arises from comparatively large uncertainties on η_{S0} for these minerals and from relatively high temperatures in the transition zone at comparatively small finite strains. The exothermic phase transitions from olivine to wadsleyite and from wadsleyite to ringwoodite are expected to raise the temperatures in the transition zone in addition to adiabatic compression (Katsura et al., 2010). For olivine and bridgmanite, adiabatic compression over extended pressure ranges somewhat mitigates the influence of thermoelastic parameters as compressional contributions to elastic moduli increase at the expense of thermal contributions.

A complete analysis of uncertainties on computed P - and S -wave velocities would include correlations between finite-strain parameters that are, however, not regularly reported. The derivation of an internally consistent matrix of covariances between finite-strain parameters requires coherent data sets of elastic properties at high pressures and high temperatures, i.e., data sets that can be simultaneously inverted for all relevant finite-strain parameters. Due to experimental challenges in performing measurements of sound wave velocities at combined high pressures and high temperatures, however, finite-strain parameters for most mantle minerals have been derived from separate but complementary data sets. Elastic moduli and their pressure derivatives are often obtained from sound wave velocity measurements at high pressures but ambient temperatures. Thermoelastic parameters are then independently derived from a thermal EOS, from the results of separate measurements at high temperatures, or from a computational study. This approach does not always generate data sets that can be combined and jointly inverted for complete and consistent sets of finite-strain parameters and their covariances. As a consequence, the results of different studies are combined in terms of finite-strain parameters that have been derived

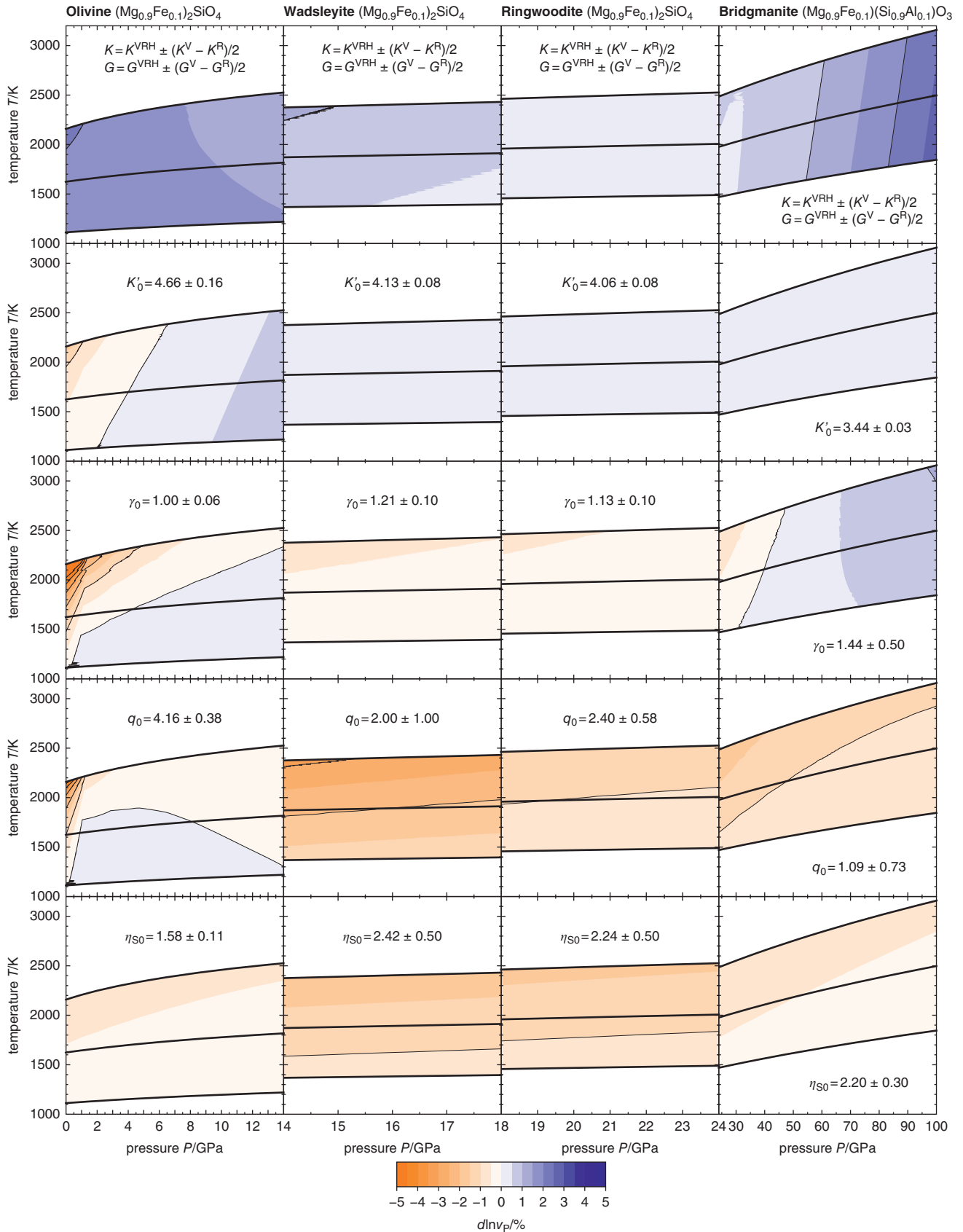


Figure 3.1 Variations in P -wave velocities for isotropic polycrystalline aggregates of olivine (1st column), wadsleyite (2nd column), ringwoodite (3rd column), and bridgmanite (4th column) that result from propagating uncertainties on individual finite-strain parameters. Respective parameters and uncertainties are given in each panel. Bold black curves show adiabatic compression paths separated by temperature intervals of 500 K at the lowest pressure for each mineral. See text for references.

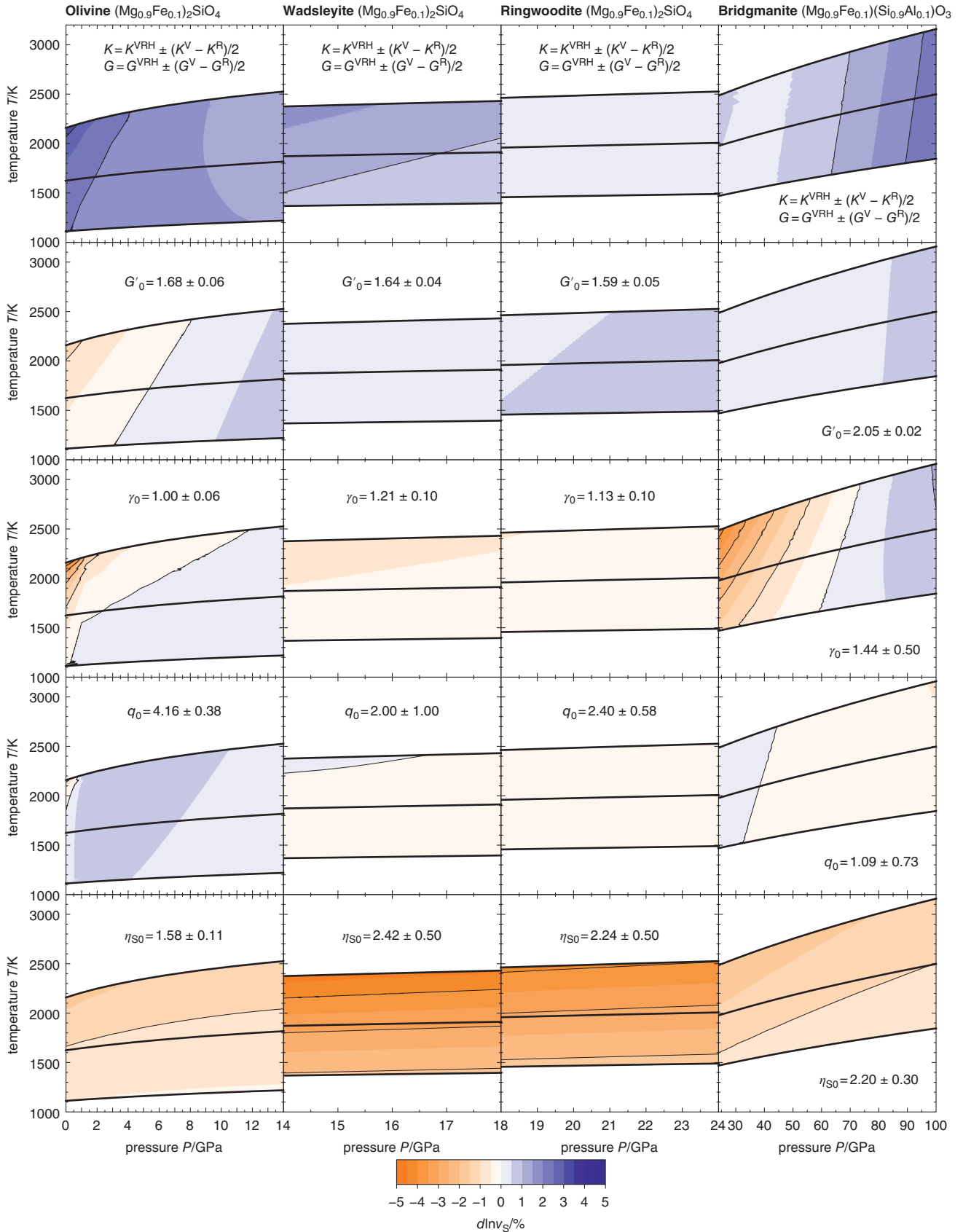


Figure 3.2 Variations in S-wave velocities for isotropic polycrystalline aggregates of olivine (1st column), wadsleyite (2nd column), ringwoodite (3rd column), and bridgmanite (4th column) that result from propagating uncertainties on individual finite-strain parameters. Respective parameters and uncertainties are given in each panel. Bold black curves show adiabatic compression paths separated by temperature intervals of 500 K at the lowest pressure for each mineral. See text for references.

from separate data sets. As an example, the inversion of the combined data set of elastic stiffness tensors and unit cell volumes of San Carlos olivine that have been determined in separate studies at high pressures (Zha et al., 1998) and at combined high pressures and high temperatures (Mao et al., 2015; Zhang and Bass, 2016) required fixing the components of the Grüneisen tensor γ_{ii0} and the Debye temperature θ_0 in order to stabilize the inversion results. Correlations between finite-strain parameters can be reduced by optimizing the sampling of the relevant volume–temperature space. Future studies that provide consistent elasticity data sets at combined high pressures and high temperatures will allow for analyzing parameter correlations and help to reduce uncertainties in computed P - and S -wave velocities by integrating covariances into the propagation of uncertainties.

3.6. ELASTIC PROPERTIES OF SOLID SOLUTIONS

Most minerals form solid solutions spanned by two or more end members. When the molar or unit cell volumes V_i of the end members are known, a complex mineral composition given in terms of molar fractions x_i of the end members is readily converted to volume fractions v_i . Assuming ideal mixing behavior for volumes, the volume of the solid solution is then given by:

$$V = \sum_i x_i V_i$$

Based on the volume fractions $v_i = x_i V_i / V$, the elastic properties of end members can then be combined according to one of the averaging schemes introduced in Section 3.2 to approximate the elastic behavior of the solid solution. Mineral-physical databases compile elastic and thermodynamic properties for many end members of mantle minerals (Holland et al., 2013; Stixrude & Lithgow-Bertelloni, 2011). However, the physical properties of some critical end members remain unknown, either because they have not been determined at relevant pressures and temperatures or because the end members are not stable as pure compounds.

Bridgmanite is believed to be the most abundant mineral in the lower mantle and adopts a perovskite crystal structure. Most bridgmanite compositions can be expressed as solid solutions of the end members MgSiO_3 , FeSiO_3 , Al_2O_3 , and FeAlO_3 . Of these end members, only MgSiO_3 is known to have a stable perovskite-structured polymorph at pressures and temperatures of the lower mantle. FeSiO_3 perovskite is unstable with respect to the post-perovskite form of FeSiO_3 or a mixture of the oxides FeO and SiO_2 (Caracas and Cohen, 2005; Fujino et al., 2009). Al_2O_3 transforms from corundum to a

Rh_2O_3 (II) structured polymorph instead of adopting a perovskite structure (Funamori and Jeanloz, 1997; Kato et al., 2013; Lin et al., 2004). For FeAlO_3 , both perovskite and Rh_2O_3 (II) structures have been proposed (Caracas, 2010; Nagai et al., 2005). Although first-principle calculations can access the elastic properties of compounds in thermodynamically unstable structural configurations, for example for FeSiO_3 and Al_2O_3 in perovskite structures (Caracas & Cohen, 2005; Muir & Brodholt, 2015a; Stackhouse et al., 2005a, 2006), it is unclear to which extent the results are useful for modeling the elastic properties of complex solid solutions that do not extend towards those end member compositions and might be affected by deviations from ideal mixing behavior at intermediate compositions.

When the physical properties of end members are unknown, it might still be possible to approximate the elastic properties of a solid solution as long as the effects of different chemical substitutions on elastic properties are captured by available experiments or computations on intermediate compositions of the solid solution. Let x_{im} be the molar fractions of end member i for a set of intermediate compositions for which volumes and elastic properties are known. For each composition m of this set, the molar fractions x_{im} of all end members form a composition vector \mathbf{x}_m of dimension n equal to the total number of end members. If the set of compositions \mathbf{x}_m forms a vector basis of \mathbb{R}^n , it is possible to construct a matrix $\mathbf{M} = \{\mathbf{x}_{im}\}$ that contains the vectors \mathbf{x}_m as columns. Any composition vector \mathbf{x} of the solid solution can then be transformed into a vector \mathbf{y} by using the inverse matrix: $\mathbf{y} = \mathbf{M}^{-1}\mathbf{x}$. The components of the vector \mathbf{y} express the composition \mathbf{x} in terms of molar fractions y_m of the intermediate compositions \mathbf{x}_m . In this way, the compositions \mathbf{x}_m are combined to match the required composition, and their volumes and elastic properties can be combined according to the mixing laws introduced above. It is important to note that this type of mixing is strictly valid only within the compositional limits defined by the compositions \mathbf{x}_m that may not cover the full compositional space as spanned by the end members. When volumes can be assumed to mix linearly across the entire solid solution, however, it is possible to extrapolate volumes beyond these compositional limits. The extrapolation of elastic properties requires special caution since negative molar fractions $y_m < 0$ can lead to unwanted effects when computing bounds on elastic moduli.

Figure 3.3 illustrates the uncertainties that arise from mixing the elastic properties of bridgmanite compositions. P - and S -wave velocities were calculated for bridgmanite solid solutions in the systems MgSiO_3 - Al_2O_3 - FeAlO_3 and MgSiO_3 - Al_2O_3 - FeSiO_3 at 40 GPa and 2000 K using available high-pressure experimental data on different bridgmanite compositions (Chantel et al., 2012; Fu et al.,

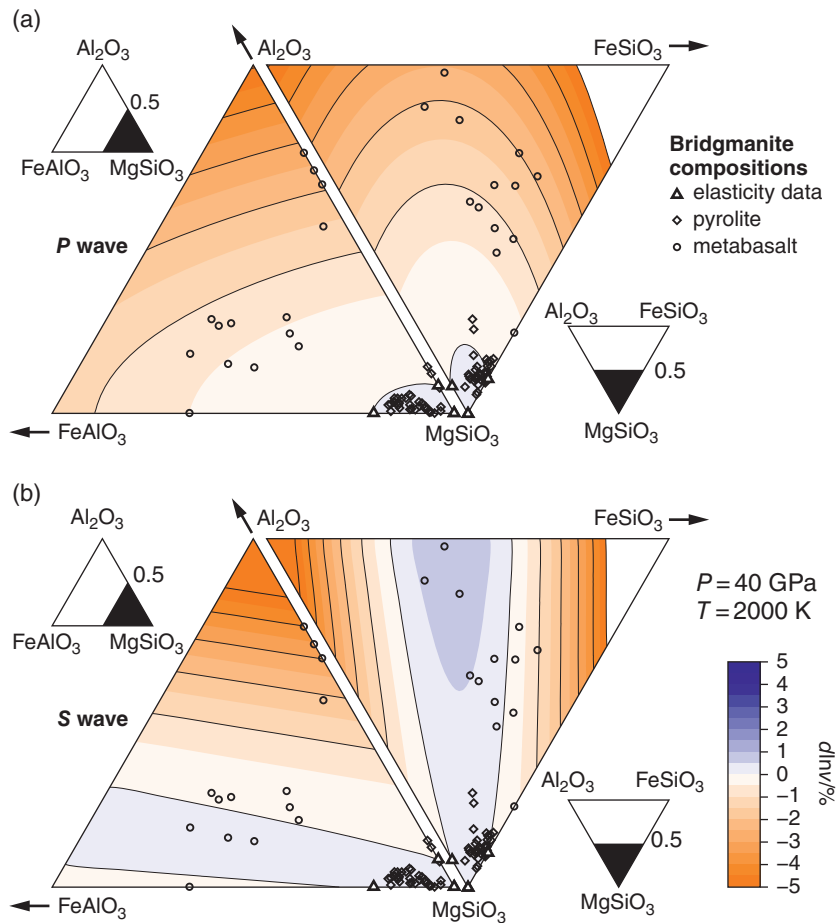


Figure 3.3 Variations in P -wave (a) and S -wave (b) velocities of bridgmanite solid solutions at 40 GPa and 2000 K that reflect the differences between the Voigt and Reuss bounds when combining the elastic properties of bridgmanite compositions (triangles). Each large ternary diagram spans the section marked black in the small full ternary diagram next to each large ternary diagram. See Table 3.1 for references to finite-strain parameters for bridgmanite compositions (triangles) and Figure 3.6 for references to mineral compositions observed in experiments on different bulk rock compositions (circles and diamonds).

2018; Kurnosov et al., 2017; Murakami et al., 2012, 2007) that provided the basis of composition vectors in the approach outlined in the previous paragraph. For all compositions, I adopted the thermoelastic properties given by Zhang et al. (2013). Uncertainties on P - and S -wave velocities due to mixing were estimated as the differences that arise from combining the elastic properties of bridgmanite compositions according to either the Voigt or the Reuss bound relative to velocities of the Voigt-Reuss-Hill average, i.e., $d\ln v = (v^V - v^R)/v^{VRH}$. For bridgmanite compositions that are similar to the compositions studied in experiments and used here to compute P - and S -wave velocities, the uncertainties remain below 0.5%. When extrapolating elastic properties beyond the compositional limits defined by available experimental data, however, uncertainties rise substantially. Note that bridgmanite compositions falling outside the compositional

range as delimited by experiments imply negative molar fractions in terms of the experimental compositions that form the basis of composition vectors. As a result, the Reuss bound may exceed the Voigt bound and $d\ln v < 0$. As mentioned above, such extrapolations may exert strong leverages on sound wave velocities and need to be restricted to compositions that remain close to the compositional limits defined by available data.

In addition to mapping uncertainties on modeled sound wave velocities, Figure 3.3 summarizes bridgmanite compositions observed in experiments on bulk rock compositions of interest for Earth's lower mantle. Many of these compositions, in particular for metabasaltic rocks, fall outside the compositional limits defined by bridgmanite compositions for which elastic properties have been determined in experiments. This highlights the need for further studies on the elastic properties of bridgmanite solid

solutions to expand compositional limits, to establish reliable trends for individual substitution mechanisms, and to resolve inconsistencies between experiments and computations. Although I focused on bridgmanite solid solutions as they are of highest relevance for the lower mantle, there is a similar need to systematically analyze and describe the effect of chemical composition on the elastic properties of other chemically complex mantle minerals such as garnets, pyroxenes, and the calcium ferrite-type aluminous phase. Internally consistent thermodynamic databases on mantle minerals provide highly valuable resources for end member properties (Holland et al., 2013; Komabayashi & Omori, 2006; Stixrude & Lithgow-Bertelloni, 2011, 2005). To date, however, these databases do not include all relevant end members and/or do not include shear properties. Internally consistent thermodynamic properties of hydrous high-pressure phases, for example, have been derived for magnesium end members only (Komabayashi and Omori, 2006). Recent experimental results on the elastic properties of wadsleyite and ringwoodite allowed for modeling the combined effects of iron and hydrogen on sound wave velocities in the mantle transition zone (Buchen et al., 2018b; Schulze et al., 2018). When sufficient data on intermediate compositions of a complex solid solution are available, it might be possible to determine end member properties by making assumptions about how end member elastic properties combine to those of intermediate compositions. Although restricted to the equation of state, Buchen et al. (2017) devised models for wadsleyite solid solutions in the system $\text{Mg}_2\text{SiO}_4\text{-Fe}_2\text{SiO}_4\text{-MgSiO}_2(\text{OH})_2\text{-Fe}_3\text{O}_4$ by assuming solid solutions between end members to follow either the Reuss or the Voigt bound when mixing the properties of end members. In principle, such an approach can be extended to shear properties and other minerals once sufficient data become available.

3.7. ELASTIC ANOMALIES FROM CONTINUOUS PHASE TRANSITIONS

The finite-strain formalism outlined in Section 3.2 describes a smooth variation of elastic properties and pressure with finite strain and temperature. Phase transitions interrupt these smooth trends as, at the phase transition, a new phase with different elastic properties becomes stable. The series of phase transitions in $(\text{Mg,Fe})_2\text{SiO}_4$ compounds from olivine (α) to wadsleyite (β) to ringwoodite (γ), for example, results in abrupt changes of elastic properties and density when going from one polymorph to another. Such abrupt changes in elastic properties typically result from first-order phase transitions that involve a reorganization of the atomic structure of a compound. The elastic properties of the compound

are then best described by constructing a finite-strain model for each polymorph. If the phase transition consists of a gradual distortion of the crystal structure, for example by changing the lengths or angles of chemical bonds, the elastic properties and density of the compound may vary continuously across the phase transition. In this case, it is often possible to describe the effect of the phase transition by adding an excess energy contribution to the energy of the undistorted phase. The changes in elastic properties that result from the phase transition can then be calculated from the excess energy and added to the finite-strain contribution of the undistorted phase.

Ferroelastic phase transitions are a common type of continuous phase transitions that can lead to substantial anomalies in elastic properties (Carpenter & Salje, 1998; Wadhawan, 1982). Upon cooling or compression across the transition point, a high-symmetry phase spontaneously distorts into a phase of lower crystal symmetry. Along with the reduction in symmetry, the crystallographic unit cell changes shape, giving rise to spontaneous strains that describe the distortion of the low-symmetry phase with respect to the high-symmetry phase. Many minerals undergo ferroelastic distortions including the high-pressure phases stishovite (Andrault et al., 1998; Carpenter et al., 2000; Karki et al., 1997b; Lakshmanov et al., 2007) and calcium silicate perovskite (Gréaux et al., 2019; Shim et al., 2002; Stixrude et al., 2007; Thomson et al., 2019). The excess energy associated with ferroelastic phase transitions can be described using a Landau expansion for the excess Gibbs free energy (Carpenter, 2006; Carpenter & Salje, 1998):

$$G_{\text{FE}} = \frac{1}{2}AQ^2 + \frac{1}{4}BQ^4 + \dots \\ + \lambda_{ij,m,n}e_{ij}^m Q^n + \frac{1}{2}c_{ijkl}^0 e_{ij}e_{kl}$$

The first part of this expansion gives the energy contribution that arises from structural rearrangements which drive the phase transition. These rearrangements may be related to changes in the ordering of cations over crystallographic sites, in the vibrational structure, or in other properties of the atomic structure. The progress or extent of these rearrangements is captured by the order parameter Q . The last term gives the elastic energy associated with distorting the high-symmetry phase with the elastic stiffness tensor c_{ijkl}^0 into the low-symmetry phase according to the spontaneous strains e_{ij} . Coupling between the order parameter Q and the spontaneous strains e_{ij} is taken into account by the central term with coupling coefficients $\lambda_{ij,m,n}$. The exact form and order of the coupling terms follow strict symmetry rules (Carpenter et al., 1998; Carpenter & Salje, 1998).

In the high-symmetry phase, $Q = 0$ and $e_{ij} = 0$ so that the excess energy vanishes. At the transition point, the high-symmetry phase spontaneously distorts to the low-symmetry phase, and both the order parameter and the spontaneous strains evolve away from zero. By following a sequence of thermodynamic arguments, expressions for the variation of the order parameter Q , the spontaneous strains e_{ij} , and individual components of the elastic stiffness tensor c_{ijkl} with pressure and temperature can be derived (Carpenter & Salje, 1998). These expressions can be used to analyze experimentally observed or computed spontaneous strains or elastic properties to constrain the parameters A , B , \dots and the coupling coefficients $\lambda_{ij,m,n}$. When all parameters are known, the excess elastic properties can be calculated. For example, elastic anomalies that arise from the ferroelastic phase transitions from stishovite to CaCl_2 -type SiO_2 and from cubic to tetragonal calcium silicate perovskite have been assessed in this way (Buchen et al., 2018a; Carpenter et al., 2000; Stixrude et al., 2007; Zhang et al., 2021).

As the Landau excess energy is typically defined in terms of the Gibbs free energy, the excess elastic properties will be functions of pressure and temperature. In finite-strain theory, however, the variation of elastic properties is formulated in terms of finite strain and temperature. One way to couple Landau theory to finite-strain theory consists in replacing the pressure P in excess terms by an EOS of the form $P(V, T)$ (Buchen et al., 2018a). Alternatively, the excess energy can be defined in terms of the Helmholtz free energy with finite strain and temperature as variables (Tröster et al., 2014, 2002). Both approaches have been used to analyze pressure-induced ferroelastic phase transitions (Buchen et al., 2018a; Tröster et al., 2017).

Compression-induced changes in the electronic configuration of ferrous and ferric iron give rise to another class of continuous phase transitions, often referred to as spin transitions. Spin transitions are associated with substantial elastic softening, mainly of the bulk modulus, and have been the subject of numerous experimental and computational studies (see Lin et al., 2013 and Badro, 2014 for reviews). Most iron-bearing phases that are relevant to Earth's lower mantle have been found to undergo spin transitions, including ferroperricite (Badro et al., 2003; Lin et al., 2005), bridgmanite (Badro et al., 2004; Jackson et al., 2005; Li et al., 2004), and the hexagonal aluminum-rich (NAL) and calcium ferrite-type aluminous (CF) phases (Wu et al., 2017, 2016). In addition to numerous studies on the EOS of these phases, the variation of sound wave velocities across spin transitions has been directly probed by experiments for ferroperricite (Antonangeli et al., 2011; Crowhurst et al., 2008; Lin et al., 2006; Marquardt et al., 2009b, 2009c; Yang et al., 2015) and recently

for bridgmanite (Fu et al., 2018). In parallel to experimental efforts, the effects of spin transitions on elastic properties and potential seismic signatures have been evaluated by DFT computations, e.g., Fe^{2+} in ferroperricite (Lin and Tsuchiya, 2008; Muir and Brodholt, 2015b; Wentzcovitch et al., 2009; Wu et al., 2013, 2009; Wu and Wentzcovitch, 2014) and Fe^{3+} in bridgmanite (Muir and Brodholt, 2015a; Shukla et al., 2016; Zhang et al., 2016). Despite substantial progress in understanding the effect of spin transitions on elastic properties, discrepancies remain between computational and experimental studies at ambient temperature (Fu et al., 2018; Shukla et al., 2016; Wu et al., 2013) and in particular between computational (Holmström & Stixrude, 2015; Shukla et al., 2016; Tsuchiya et al., 2006; Wu et al., 2009) and experimental (Lin et al., 2007; Mao et al., 2011) studies that address the broadening of spin transitions at high temperatures.

Common to most descriptions of elastic properties across spin transitions is the approach to treat phases with iron cations in exclusively high-spin and exclusively low-spin configurations separately and to mix their elastic properties across the pressure–temperature interval where both electronic configurations coexist (Chen et al., 2012; Speziale et al., 2007; Wu et al., 2013, 2009). We will see below that the electronic structure of transition metal cations in crystal structures is more complex than this simple two-level picture and how measurements at room temperature can be exploited to construct more detailed models. Most approaches to spin transitions are based on the Gibbs free energy and hence describe elastic properties as functions of pressure and temperature (Speziale et al., 2007; Tsuchiya et al., 2006; Wu et al., 2013, 2009). Coupling a thermodynamic description of spin transitions to finite-strain theory, however, requires to express the changes in energy that result from the redistribution of electrons in terms of volume strain. Building on the ideas of Sturhahn et al. (2005), a formulation for compression-induced changes in the electronic configurations of transition metal cations can be proposed that accounts for energy changes in terms of an excess contribution to the Helmholtz free energy. Crystal-field theory proves to provide the right balance between complexity and flexibility for a semi-empirical and strain-dependent model for the electronic structure of transition metal cations in crystal structures.

With the aim to interpret the optical absorption spectra of octahedrally coordinated first-row transition metal cations, Tanabe and Sugano (1954a) described the energies of multi-electron states resulting from different $3d$ electron configurations in terms of the crystal-field splitting $\Delta = 10Dq$ and the Racah parameters B and C . The electric field generated by the negative charge of an octahedral coordination environment causes the $3d$ orbitals of

the central transition metal cation to split into the e and t_2 levels, separated by an energy equal to the crystal-field splitting Δ . The Racah parameters B and C account for the interelectronic repulsion between d electrons that results from a given distribution of electrons over the e and t_2 orbitals. In the strong-field limit, as appropriate for the treatment of compression-induced changes in the electronic configuration, the energy of a multi-electron state can be approximated by a sum of the form (Tanabe and Sugano, 1954a):

$$E[{}^M\Gamma] = z_1\Delta + z_2B + z_3C$$

Each multi-electron state is characterized by the symmetry of the electron distribution as expressed by the symbol of the corresponding irreducible representation Γ and by the spin multiplicity $M = 2S + 1$ with the sum S of unpaired electrons. The coefficients z_1 , z_2 , and z_3 depend on the number of d electrons and have been calculated and tabulated for each state (Tanabe & Sugano, 1954a). Figure 3.4 shows how the $3d$ electron configurations d^5 (Fe^{3+}) and d^6 (Fe^{2+}) give rise to multi-electron states and how their energies vary as a function of the ratio Δ/B (Tanabe and Sugano, 1954b). We will see below that the ratio Δ/B increases with compression.

To incorporate the changes in state energies that result from compression, I assume the crystal-field parameters to scale with the volume ratio V_0/V as:

$$\Delta = \Delta_0 \left(\frac{V_0}{V} \right)^{\frac{\delta}{3}}$$

$$B = B_0 \left(\frac{V_0}{V} \right)^{\frac{b}{3}}$$

$$C = C_0 \left(\frac{V_0}{V} \right)^{\frac{c}{3}}$$

An electrostatic point charge model for an octahedrally coordinated transition metal cation suggests that $\delta = 5$ (Burns, 1993). High-pressure spectroscopic measurements, however, have shown that real materials may deviate from this prediction (Burns, 1985; Drickamer & Frank, 1973). Enhanced covalent bonding might also lead to a reduction of the Racah B parameter with increasing compression (Abu-Eid & Burns, 1976; Keppler et al., 2007; Stephens & Drickamer, 1961a, 1961b) and would imply $b < 0$.

Most multi-electron states are degenerate and allow a number $m > 1$ of different electron configurations. The total degeneracy of a given state ${}^M\Gamma$ is then given by the product mM and contributes a configurational entropy equal to $k \ln(mM)$, where k is the Boltzmann constant. The Helmholtz free energy of a given state can then be expressed as (Badro et al., 2005; Sturhahn et al., 2005):

$$F[{}^M\Gamma] = E[{}^M\Gamma] - kT \ln(mM)$$

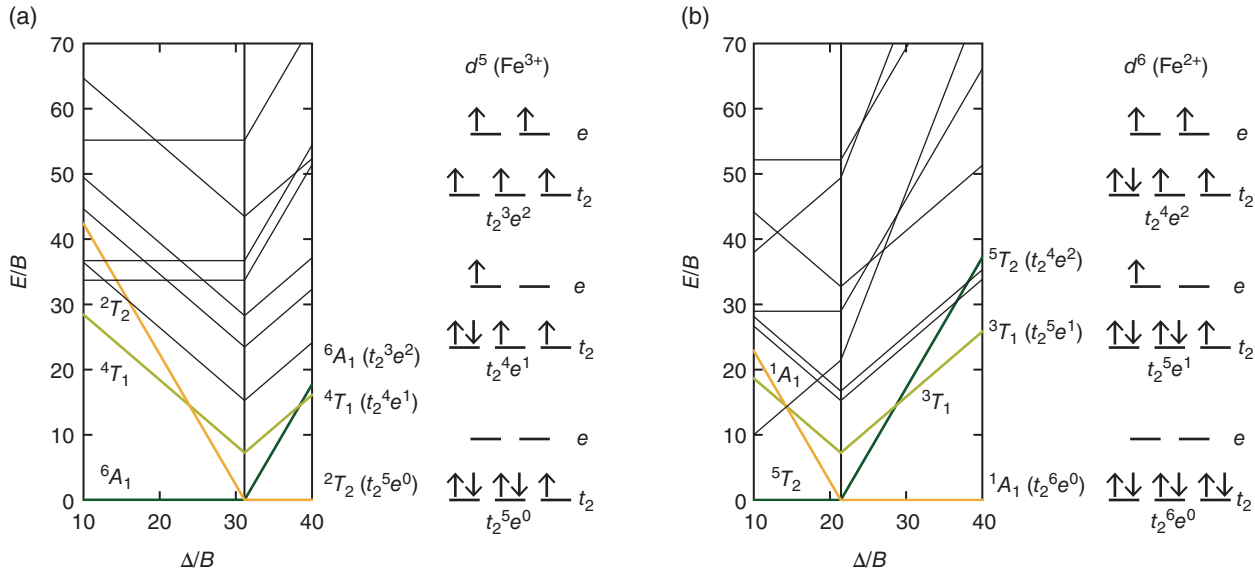


Figure 3.4 Energy diagrams for multi-electron states that arise from the $3d$ electron configurations d^5 (Fe^{3+}) (a) and d^6 (Fe^{2+}) (b) in the limit of strong octahedral crystal fields. Note the change in electronic ground state for each electron configuration when the ratio Δ/B reaches the value marked by a vertical line. The distributions of d electrons over the crystal-field orbitals t_2 and e are illustrated for the three states that have the lowest energies at the change in electronic ground state.

At $T > 0$, and in particular at temperatures of Earth's mantle, the d electron configuration can be thermally excited into states of higher energies. The thermal population of higher energy states becomes most important when the energies of other states approach the energy of the ground state, for example, as a result of compression. A spin transition results from a compression-induced change of the electronic ground state from a high-spin to a low-spin state (Figure 3.4). At finite temperatures, the broadening of the transition reflects the incipient population of the low-spin state before and the decaying population of the high-spin state after their energies cross over as long as the energies of both states remain close enough to allow for thermally induced transitions between both states (Holmström & Stixrude, 2015; Sturhahn et al., 2005; Tsuchiya et al., 2006). However, states other than the high-spin or low-spin state may get close enough in energy to the ground state to become thermally populated by a significant fraction of d electrons. The thermal distribution of electrons over accessible multi-electron states contributes to the overall configurational entropy. The excess contribution to the Helmholtz free energy per transition metal cation that results from compression- and temperature-induced changes in the occupation of electronic states can then be identified as:

$$F_{\text{EL}} = \sum_i \Delta\varphi_i F^{[M\Gamma]}_i + dkT \sum_i (\varphi_i \ln \varphi_i - \varphi_{i0} \ln \varphi_{i0})$$

where $\Delta\varphi = \varphi(V, T) - \varphi_0(V_0, T_0)$ are the changes in the fractions φ of d electrons that occupy each electronic state at a given volume and temperature with respect to the fractions φ_0 at ambient conditions. Note that the configurational entropy term is multiplied by the number d of d electrons per transition metal cation. The fraction of d electrons that occupy a given state can be found by applying the equilibrium condition $(\partial F_{\text{EL}}/\partial n_i)_{V,T,N} = 0$ to a micro-canonical ensemble with the absolute numbers $n_i = \varphi_i N$ of electrons in each state and the total number N of electrons (Sturhahn et al., 2005):

$$\varphi^{[M\Gamma]} = \frac{\exp\left(-\frac{F^{[M\Gamma]}}{dkT}\right)}{\sum_i \exp\left(-\frac{F^{[M\Gamma]}_i}{dkT}\right)}$$

The denominator sums over all multi-electron states being considered.

The excess contributions to pressure and bulk modulus then follow from the definitions:

$$P_{\text{EL}} = -\left(\frac{\partial F_{\text{EL}}}{\partial V}\right)_T$$

and

$$K_{\text{EL}} = -V\left(\frac{\partial P_{\text{EL}}}{\partial V}\right)_T = V\left(\frac{\partial^2 F_{\text{EL}}}{\partial V^2}\right)_T$$

All excess quantities need to be multiplied by the number and fraction of crystallographic sites that are occupied by the transition metal cation.

The parametrization of spin transitions presented above builds on the formulation proposed by Sturhahn et al. (2005) and resembles earlier attempts to predict the effect of spin transitions in Fe^{2+} on thermodynamic properties of mantle minerals (Badro et al., 2005; Gaffney, 1972; Gaffney & Anderson, 1973; Ohnishi, 1978). Unlike these forward modeling approaches, I will use the formulation here in a semi-empirical way with adjustable parameters that will be constrained by experimental observations. In contrast to formulations based on the Gibbs free energy with pressure as variable and elastic compliances as parameters that have proven useful in describing the results of DFT computations (Shukla et al., 2016; Wentzcovitch et al., 2009; Wu et al., 2013), a formulation of excess contributions in terms of volume and temperature is more consistent with finite-strain theory based on the assumption of homogeneous and isotropic finite strain and can, in principle, be generalized to evaluate the effect on individual components of the elastic stiffness tensor and hence on the shear modulus. The impact of spin transitions on the shear modulus, however, appears to be minor (Fu et al., 2018; Marquardt et al., 2009b; Shukla et al., 2016; Wu et al., 2013). Note that by accounting for changes in the electronic configurations in terms of excess properties it is no longer necessary to derive sets of finite-strain parameters for each individual electronic configuration as required by earlier formulations based on high-spin and low-spin states only (Chen et al., 2012; Speziale et al., 2007; Wu et al., 2013, 2009), since the excess contributions are simply added to the (cold) elastic and thermal contributions. Although I assume here that transition metal cations with different electronic configurations mix ideally among each other and with other cations, it is in principle possible to add further terms to account for nonideal mixing behavior and interactions between transition metal cations (Holmström and Stixrude, 2015; Ohnishi and Sugano, 1981; Sturhahn et al., 2005). To some extent and for low concentrations of transition metal cations, deviations from ideal mixing will be captured by the semi-empirical parameters when fit to experimental data.

By taking into account the three electronic states with lowest energies for ratios Δ/B close to the compression-induced change in electronic ground state for ferrous iron, Fe^{2+} (d^6), and ferric iron, Fe^{3+} (d^5), in octahedral coordination, i.e., 5T_2 , 1A_1 , and 3T_1 for Fe^{2+} and 6A_1 , 2T_2 , and 4T_1 for Fe^{3+} (Tanabe & Sugano, 1954a, 1954b), I analyzed recent experimental result on the elastic properties of ferropericlase (Yang et al., 2015), Fe^{3+} -bearing bridgmanite (Chantel et al., 2012; Fu et al., 2018), and Fe^{3+} -bearing CF phase (Wu et al., 2017) across their respective spin transitions. When fitting experimental

data, I assumed a constant ratio $C/B = 4.73$ (Krebs & Maisch, 1971; Lehmann & Harder, 1970; Tanabe & Sugano, 1954b) and consequently set $b = c$. The crystal-field splitting of Fe^{2+} and Fe^{3+} in octahedral coordination in periclase and corundum, respectively, has been derived from optical spectroscopy (Burns, 1993; Krebs and Maisch, 1971; Lehmann and Harder, 1970) and from early quantum-mechanical computations (Sherman, 1991, 1985). Hence, I assumed $\Delta_0 = 10800 \text{ cm}^{-1}$ for Fe^{2+} in ferropericlase (Burns, 1993; Sherman, 1991) and adopted $\Delta_0 = 14750 \text{ cm}^{-1}$ for Fe^{3+} in corundum as approximation for Fe^{3+} in bridgmanite and in the CF phase (Krebs & Maisch, 1971; Lehmann & Harder, 1970; Sherman, 1985). Similarly, the Racah B_0 parameter at ambient conditions has been determined for octahedrally coordinated Fe^{3+} in corundum from optical spectra (Krebs & Maisch, 1971; Lehmann & Harder, 1970) and was set to $B_0 = 655 \text{ cm}^{-1}$ for Fe^{3+} in the CF phase. The volume exponent δ was initially set to $\delta = 5$ as suggested by the point charge model. The exponents $c = b$ and, when required, δ and B_0 were treated as adjustable parameters in addition to the finite-strain parameters that describe the compression-induced changes of elastic moduli without excess contributions.

The fitting results are shown in Figures 3.5a–c and demonstrate that the semi-empirical model captures the softening of the bulk modulus of ferropericlase (Yang et al., 2015), the dip in P -wave velocities of Fe^{3+} -bearing bridgmanite (Fu et al., 2018), and the segment of enhanced volume reduction in the compression curve of the CF phase (Wu et al., 2017) that have been interpreted to result from compression-induced changes in the electronic structures of ferrous and ferric iron. The Racah B_0 parameter found for Fe^{2+} in ferropericlase is compatible with values derived from optical spectroscopy (Burns, 1993; Tanabe & Sugano, 1954b). For all three data sets, $-3 < b = c < -2$ indicating a decrease of the Racah B parameter with compression as suggested by results from high-pressure optical spectroscopy (Abu-Eid & Burns, 1976; Keppler et al., 2007; Stephens & Drickamer, 1961a, 1961b). It is important to note, however, that the exponents $b = c$ are positively correlated with the exponent δ that was fixed at $\delta = 5$ for ferropericlase and the CF phase. A combination of slightly higher values for δ with less negative values of b and c can explain the observations equally well, suggesting that the difference $\delta - b$ might be more meaningful than the individual parameters. The P -wave velocity data for bridgmanite required significantly higher values for the exponent δ and the Racah B_0 parameter than suggested by the point charge model or optical spectroscopy. The very large exponent δ for bridgmanite might reflect the different compression behaviors of A and B sites in the perovskite crystal structure that might not be related in a simple way to the compression mechanism of the

crystal structure as a whole and to the ratio V_0/V of unit cell volumes (Boffa Ballaran et al., 2012; Glazyrin et al., 2014). Distortions of the coordination environment away from an ideal octahedron will also result in crystal-field parameters that deviate from their values for more regular and symmetric arrangements of coordinating anions. However, the general consistency between crystal-field parameters from optical spectroscopy when used in the semi-empirical model for electronic excess properties and high-pressure experimental data on elastic properties, in particular for close-packed oxide structures, may motivate further testing and development of the model.

Figures 3.5d–f show the predicted fractions φ of d electrons that occupy each of the considered multi-electron states for Fe^{2+} in ferropericlase and Fe^{3+} in bridgmanite and in the CF phase along different adiabatic compression paths. The change in electronic ground states from 5T_2 (high spin) to 1A_1 (low spin) for Fe^{2+} and from 6A_1 (high spin) to 2T_2 (low spin) for Fe^{3+} is gradual and broadens with increasing temperatures as suggested earlier (Holmström & Stixrude, 2015; Lin et al., 2007; Sturhahn et al., 2005; Tsuchiya et al., 2006). The crystal-field model outlined above, however, predicts additional broadening that results from thermal population of the higher energy states 3T_1 for Fe^{2+} and 4T_1 for Fe^{3+} . At realistic mantle temperatures, these states are predicted to host up to 25% of d electrons. Population of these states will reduce the effect of spin transitions on mineral densities and elastic properties by diluting the contrasts in properties between pure high-spin and low-spin states. The spin transition of Fe^{2+} in ferropericlase appears to be most susceptible to thermal broadening while spin transitions of Fe^{3+} in bridgmanite and in the CF phase remain somewhat sharper even at high temperatures.

The effect of spin transitions on P -wave velocities is shown in Figures 3.5g–i as relative velocity reductions along typical adiabatic compression paths. In qualitative agreement with results of DFT computations for ferropericlase and Fe^{3+} -bearing bridgmanite (Shukla et al., 2016; Wentzcovitch et al., 2009; Wu et al., 2013), both the pressure interval and the pressure of maximum P -wave velocity reduction increase with temperature. Absolute velocity reductions and their exact pressure intervals at high temperatures as predicted by DFT computations, however, seem to differ from those predicted by the semi-empirical crystal-field model. Figures 3.5g–i also show how ignoring the population of the higher energy states 3T_1 for Fe^{2+} and 4T_1 for Fe^{3+} would overestimate P -wave velocity reductions at realistic mantle temperatures. Although I considered only one additional state for each Fe^{2+} and Fe^{3+} , more high-energy states might become populated at relevant temperatures, further depleting high-spin and low-spin ground states. Experiments at combined

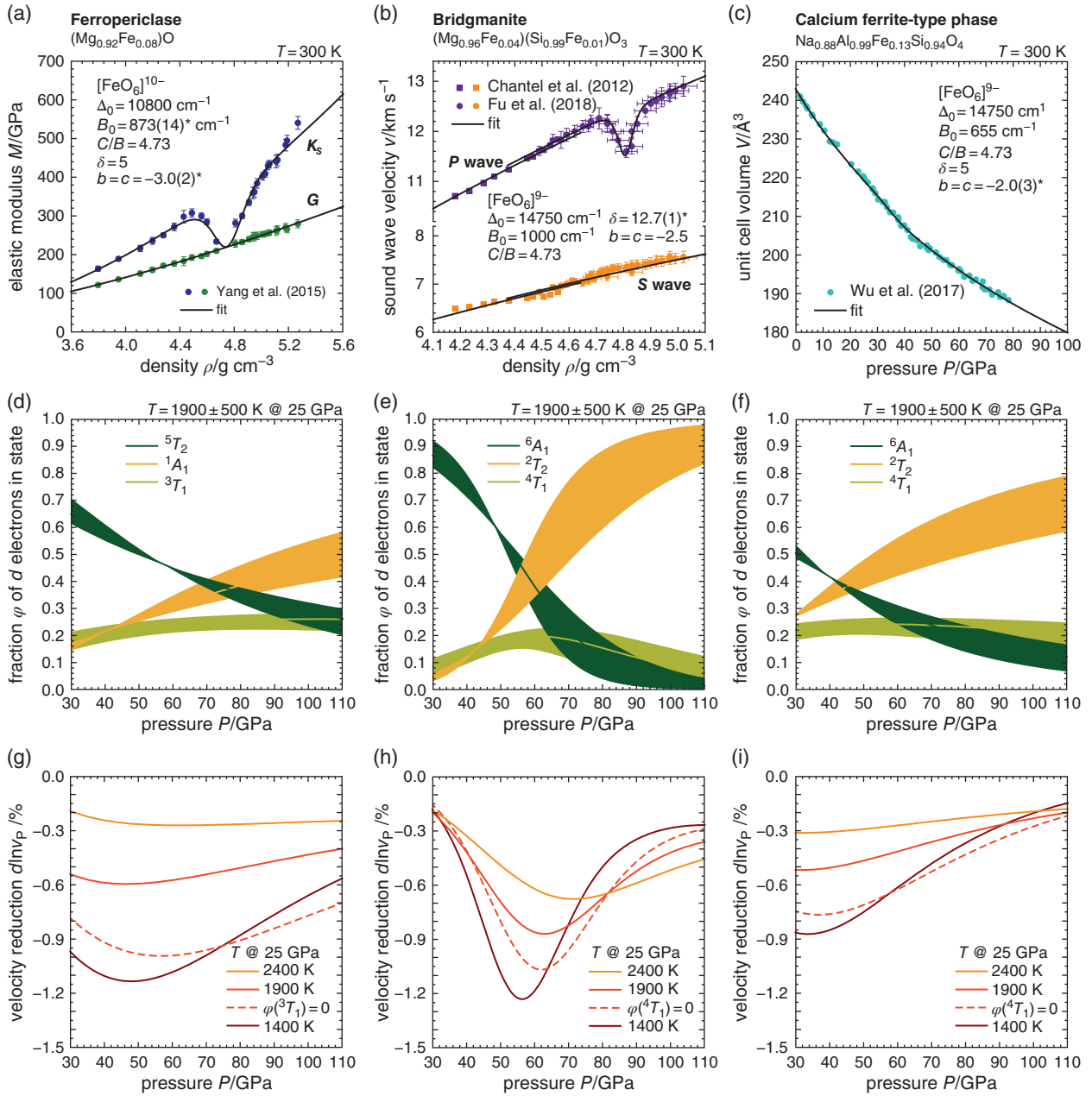


Figure 3.5 (a–c) Reanalysis of elastic moduli of ferroperricase (a), sound wave velocities of bridgmanite (b), and compression data on the CF phase (c) across spin transitions of ferrous (a) and ferric (b,c) iron. Respective data are from Yang et al. (2015) (a), Chantel et al. (2012), and Fu et al. (2018) (b), and Wu et al. (2017) (c). Bold black curves show the results of fitting a semi-empirical crystal-field model to the data as explained in the text with the respective crystal-field parameters given in each panel. The values of crystal-field parameters that were free to vary during fitting are marked with an asterisk (*). For bridgmanite, data of Chantel et al. (2012) and Fu et al. (2018) have been analyzed together to better constrain pressure derivatives of elastic moduli. The offset between both data sets arises from slightly different estimates for densities as reported in both studies. (d–f) Fractions of d electrons in multi-electron states across spin transitions of Fe^{2+} in ferroperricase (d), Fe^{3+} in bridgmanite (on B site) (e), and Fe^{3+} in the CF phase (f) as predicted by the semi-empirical crystal-field model and along typical adiabatic compression paths (see Figure 3.8). Shading indicates differences in fractions that result from starting adiabatic compression at temperatures 500 K above and below 1900 K at 25 GPa. (g–i) P -wave velocity reductions that result from spin transitions of Fe^{2+} in ferroperricase (g), Fe^{3+} in bridgmanite (on B site) (h), and Fe^{3+} in the CF phase (i) as predicted by the semi-empirical crystal-field model and along adiabatic compression paths starting at 1400 K, 1900 K, and 2400 K at 25 GPa (see Figure 3.8). The dashed curves show P -wave velocity reductions along the central compression path (1900 K at 25 GPa) when the population of a third multi-electron state with intermediate spin multiplicity is ignored.

high pressures and high temperatures are needed to directly assess the thermal broadening of spin transitions and their effects on mineral elasticity. Since the volume changes that result from spin transitions can be subtle, in particular at high temperatures and for typical iron contents of mantle minerals (Komabayashi et al., 2010; Mao et al., 2011), experiments that constrain elastic properties in addition to volume might be best suited to resolve the impact of spin transitions on sound wave velocities at high temperatures.

3.8. EARTH'S LOWER MANTLE

Seismic tomography shows lateral variations in P - and S -wave velocities at all depths of the lower mantle and across length scales that are compatible with changes in temperature, chemical composition, and phase assemblage as well as combinations thereof (Durand et al., 2017; Hosseini et al., 2020; Koelemeijer et al., 2016). Scattering of seismic waves in the lower mantle, in contrast, points to changes in the elastic properties of the mantle over length scales that are commonly interpreted to be too short to arise from thermal gradients alone and require compositional heterogeneities or phase changes (Frost et al., 2017; Kaneshima & Helffrich, 2009; Waszek et al., 2018). Lateral and local variations are superimposed on the monotonous increase of seismic velocities that dominates global seismic reference models at depths between 800 km and 2400 km (Dziewonski & Anderson, 1981; Kennett et al., 1995; Kennett & Engdahl, 1991). The seismic structure of the upper mantle and transition zone can be compared with the results of mineral-physical models (Cammarrano et al., 2009; Cobden et al., 2008; Xu et al., 2008) that are based on internally consistent thermodynamic databases (Holland et al., 2013; Stixrude & Lithgow-Bertelloni, 2011). For the lower mantle and depths in excess of 800 km, however, these databases are less reliable since both chemical compositions and elastic properties of relevant mantle minerals are less well constrained as discussed in Section 3.6 for bridgmanite. Moreover, existing thermodynamic databases do not include the effects of continuous phase transitions, such as the ferroelastic phase transition from stishovite to CaCl_2 -type SiO_2 and spin transitions, on elastic properties that are expected to affect seismic velocities in the lower mantle. This section focuses on seismic properties of relevant rock types in the depth interval from about 800 km to 2400 km. Chapter 8 of this volume addresses the lowermost mantle including the D'' layer at depths in excess of 2400 km.

Experiments on peridotitic rock compositions found bridgmanite (bm), ferropericlase (fp), and calcium silicate perovskite (cp) as major phases with approximately

constant volume fractions of $\text{bm:fp:cp} \sim 70:20:10$ at pressures and temperatures of the lower mantle (Irifune et al., 2010; Kesson et al., 1998; Murakami et al., 2005). Depending on composition and temperature, bridgmanite transforms to the post-perovskite phase at pressures in excess of 100 GPa corresponding to an approximate depth of 2400 km (Murakami et al., 2005, 2004; Shim et al., 2004; Sun et al., 2018). Since the composition of calcium silicate perovskite remains close to pure CaSiO_3 and bridgmanite incorporates virtually all available Al_2O_3 , the main compositional variables are the $\text{Mg}/(\text{Fe}+\text{Mg})$ ratios of bridgmanite and ferropericlase that are coupled through Fe-Mg exchange reactions. Fe-Mg exchange between ferropericlase and bridgmanite is sensitive to a large number of thermodynamic parameters including pressure, temperature, composition, oxygen fugacity, and the spin states of Fe^{2+} and Fe^{3+} (Badro, 2014). Despite substantial progress in deciphering the effects of these parameters on the Fe-Mg exchange between bridgmanite and ferropericlase, the variation of the Fe-Mg exchange coefficient $K_{\text{Fe/Mg}}^{\text{bm/fp}} = (\text{Fe}/\text{Mg})_{\text{bm}}/(\text{Fe}/\text{Mg})_{\text{fp}}$ (Badro, 2014) through the lower mantle remains debated. While recent experimental studies found Fe-Mg exchange coefficients of about 0.5 with no clear trend with increasing pressure between 40 GPa and 100 GPa (Piet et al., 2016; Prescher et al., 2014; Sinmyo & Hirose, 2013), DFT computations suggest generally smaller values that decrease with increasing pressure as a result of the progressing spin transition of Fe^{2+} in ferropericlase (Muir & Brodholt, 2016; Xu et al., 2017). The Fe-Mg exchange coefficient for harzburgitic rocks seems to be closer to 0.2 and to decrease with increasing pressure (Auzende et al., 2008; Badro, 2014; Piet et al., 2016; Sakai et al., 2009; Sinmyo et al., 2008; Xu et al., 2017). Figure 3.6a summarizes experimental and computational findings on Fe-Mg exchange between bridgmanite and ferropericlase.

For basaltic compositions that intend to represent recycled oceanic crust, experimental results suggest modal proportions of the major phases bridgmanite (bm), calcium silicate perovskite (cp), CF phase (cf), and stishovite (st) of $\text{bm:cp:cf:st} \sim 45:30:15:10$ throughout most of the lower mantle (Hirose et al., 2005, 1999; Ono et al., 2001; Perrillat et al., 2006; Ricolleau et al., 2010). At pressures between 25 GPa and 40 GPa, the NAL phase has been found to coexist with this assemblage but seems to become destabilized towards higher pressures (Perrillat et al., 2006; Ricolleau et al., 2010). Figure 3.6b shows exchange coefficients for Fe-Mg and Al-Mg exchange between bridgmanite and the CF phase as computed from experimentally observed mineral compositions for the assemblage bm-cp-cf-st in basaltic bulk compositions. Although it appears difficult to assign robust trends of

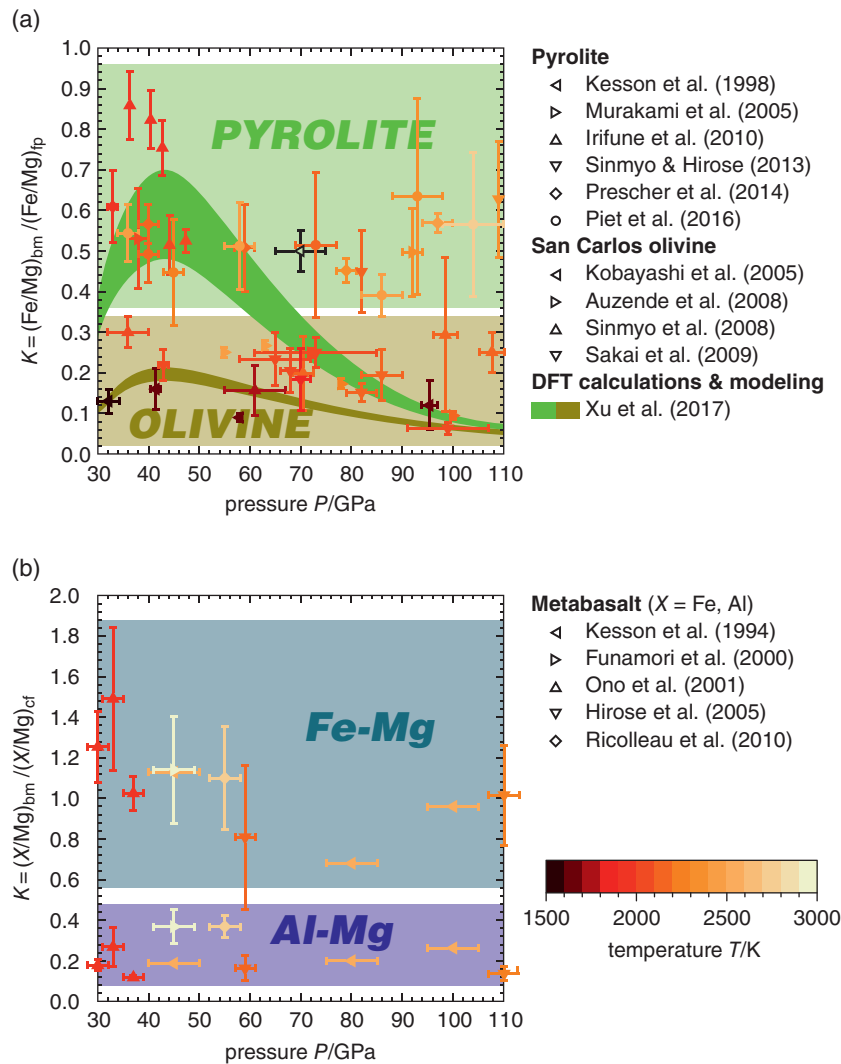


Figure 3.6 Exchange coefficients for Fe-Mg exchange between bridgmanite and ferropericlasite in peridotitic bulk compositions (a) and for Fe-Mg and Al-Mg exchange between bridgmanite and the CF phase in basaltic bulk compositions (b). Color shading indicates the relevant parts of each diagram for different bulk compositions (a) or exchange coefficients (b). Note the reduction in the Fe-Mg exchange coefficient between bridgmanite and ferropericlasite with increasing pressure as predicted by thermodynamic modeling based on DFT computations.

mineral compositions with changes in pressure or temperature, iron tends to be equally distributed between bridgmanite and the CF phase while aluminum seems to preferentially partition into the CF phase. The wide spread in experimentally observed mineral compositions is also reflected in the bridgmanite compositions shown in Figure 3.3. Clearly, more experiments are needed to better understand element partitioning and mineral compositions in peridotitic and metabasaltic rocks at conditions of the lower mantle.

To evaluate the impact of variations in rock composition and thermal state of the lower mantle on seismic properties, I computed P - and S -wave velocities for pyrolite, harzburgite, and metabasalt over relevant pressure

and temperature intervals. Recent experimental and computational results on the high-pressure and high-temperature elasticity of lower-mantle phases are compiled in Table 3.1. This compilation aims at reflecting recent progress on individual mineral phases and does not represent an internally consistent data set in a thermodynamic sense. If not given in the original publication, finite-strain and thermal parameters were determined by fitting experimental data to the finite-strain formalism of Stixrude & Lithgow-Bertelloni (2005). I included the effect of spin transitions of Fe^{2+} in ferropericlasite and of Fe^{3+} in bridgmanite and in the CF phase using the parametrization introduced in Section 3.7 with parameters given in Figures 3.5a–c. The effect of the ferroelastic

Table 3.1 Finite-strain parameters for mineral phases of the lower mantle.

Mineral/Phase	Formula	Volume	Bulk modulus		Shear modulus		Quasi-harmonic parameters				References
		V_0 (\AA^3)	K_0 (GPa)	K_0'	G_0 (GPa)	G_0'	θ_0 (K)	γ_0	q_0	η_{50}	
bridgmanite	MgSiO ₃	162.27(1)	253(9)	3.9(2)	173(2)	1.56(4)	905.9	1.44	1.09	2.2(2)	[1,2,3,4]
	(Mg _{0.95} Fe _{0.05})SiO ₃	163.45(2)	247(2) ^S	3.6(1)	168.3(9)	2.02(3)	905.9	1.44	1.09	2.2	[3,4,5*,6*]
	(Mg _{0.96} Al _{0.04})(Si _{0.96} Al _{0.04})O ₃	163.21(1)	252(5) ^S	3.7(3)	166(1)	1.57(5)	905.9	1.44	1.09	2.2	[3,4,7]
	(Mg _{0.9} Fe _{0.1})(Si _{0.9} Al _{0.1})O ₃	162.96(2)	250.8(4) ^S	3.44(3)	159.7(2)	2.05(2)	905.9	1.44	1.09	2.2	[3,4,8]
ferropericlase	MgO	74.68(2)	163(1) ^S	3.8(1)	131(1)	1.92(2)	770	1.5	2.8	3.0	[9,10,11*]
	(Mg _{0.92} Fe _{0.08})O	74.07(1)	169(2) ^S	4.01(7)	126(2)	2.08(3)	770	1.5	2.8(6)	3.0(3)	[11*,12*]
Ca silicate perovskite	CaSiO ₃	45.57(2)	248(3)	3.6(1)	107(1)	1.66(22)	771(90)	1.67(4)	1.1(2)	3.3	[13]
Ca ferrite-type phase	MgAl ₂ O ₄	236.07	217	3.7	133	1.7	840(20)	1.3(3)	1(1)	2(1)	[14,15]
	FeAl ₂ O ₄	247.49	217	3.7	133	1.7	840	1.3	1	2	[14,15]
	Na _{0.4} Mg _{0.6} Al _{1.6} Si _{0.4} O ₄	239.9(37)	221(2)	4	129.65(6)	2.34(1)	840	1.3	1	2	[15,16,17]
	Na _{0.88} Al _{0.99} Fe _{0.13} Si _{0.94} O ₄	242.79(27)	205(6)	3.6(2)	130	2	840	1.3	1	2	[15,18*]
stishovite	SiO ₂	46.51(2)	320(2)	4	264(2)	1.90(1)	1100	1.7	5.7(3)	2.9(2)	[19,20,21*,22,23]
CaCl ₂ -type SiO ₂	SiO ₂	47.54(18)	238(6)	4.82(2)	264(2)	2.23(1)	1100	1.7	5.7	2.9	[19,20,21*,22,23]

Values in *italics* were estimated or adopted from other compositions/polymorphs of the same phase/compound.

^S Isentropic bulk modulus.

* Original data were refit to the finite-strain formalism of Stixrude & Lithgow-Bertelloni (2005).

References: [1] Fiquet et al. (2000), [2] Murakami et al. (2007), [3] Zhang et al. (2013), [4] Murakami et al. (2012), [5] Chantel et al. (2012), [6] Fu et al. (2018), [7] Jackson et al. (2005), [8] Kurnosov et al. (2017), [9] Sinogeikin & Bass (2000), [10] Murakami et al. (2009), [11] Yang et al. (2016), [12] Yang et al. (2015), [13] Thomson et al. (2019), [14] Mookherjee (2011), [15] Stixrude & Lithgow-Bertelloni (2011), [16] Imada et al. (2012), [17] Dai et al. (2013), [18] Wu et al. (2017), [19] Andrault et al. (2003), [20] Jiang et al. (2009), [21] Gréaux et al. (2016), [22] Fischer et al. (2018), [23] Buchen et al. (2018a).

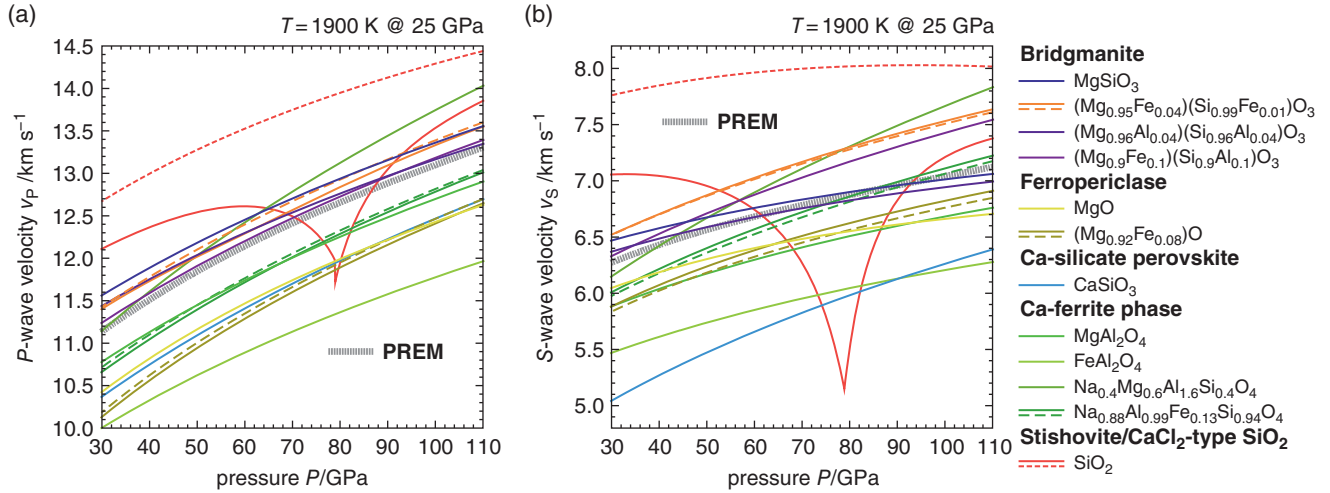


Figure 3.7 *P*-wave (a) and *S*-wave (b) velocities for different mineral phases and compositions along a typical adiabatic compression path starting at 1900 K and 25 GPa (see Figure 3.8). These mineral phases and compositions were mixed to model elastic wave speeds of rocks as shown in Figures 3.8 and 3.9. Dashed curves show *P*- and *S*-wave velocities when the effect of relevant continuous phase transitions on elastic properties is ignored. See Table 3.1 for references.

phase transition from stishovite to CaCl_2 -type SiO_2 was modeled based on the reanalysis of powder diffraction data (Andraut et al., 2003) using Landau theory as given by Buchen et al. (2018a). The experimentally determined phase boundary between stishovite and CaCl_2 -type SiO_2 with a Clapeyron slope of $dP/dT = 15.5 \text{ MPa K}^{-1}$ (Fischer et al., 2018) was used to constrain the temperature dependence of the Landau parameter A . Figure 3.7 shows *P*- and *S*-wave velocities for each mineral composition in Table 3.1 along a typical adiabatic compression path.

Chemical bulk compositions for pyrolite and metabasalt were approximated by the depleted MORB mantle (DMM) and NMORB compositions of Workman and Hart (2005). In analogy to the approach of Xu et al. (2008), a hypothetical harzburgite composition was generated by assuming pyrolite to be an 80:20 mixture of harzburgite:basalt by mass. A basalt fraction of 20% in the mantle corresponds to the upper limit of estimates based on geochemical (Morgan & Morgan, 1999; Sobolev et al., 2007) and geodynamical arguments (Ballmer et al., 2015; Nakagawa et al., 2010). For pyrolite and harzburgite, mineral compositions were computed in the system CFMAS and for metabasalt in the system NCFMAS. Bulk compositions were partitioned into the phase assemblages bm-fp-cp for pyrolite and harzburgite and bm-cp-cf-st for metabasalt resulting in approximate volume fractions of 77:16:7 (bm:fp:cp) in pyrolite, 74:24:2 (bm:fp:cp) in harzburgite, and 45:26:14:15 (bm:cp:cf:st) in metabasalt, respectively. For each phase, the

compositions listed in Table 3.1 were mixed to match the computed mineral compositions as outlined in Section 3.6. For some mineral compositions, this approach required extrapolations beyond the compositional limits defined by the mineral compositions in Table 3.1. In these cases, the extrapolations of elastic moduli were restricted to not transcend compositional limits by more than 10% of the compositional range delimited by the mineral compositions of Table 3.1.

The exact mineral compositions and volume fractions for a given bulk rock composition depend critically on assumptions about element partitioning between minerals and the overall $\text{Fe}^{3+}/\Sigma\text{Fe}$ ratio. To separate the effects of temperature and compositional parameters, I first computed *P*- and *S*-wave velocities for each bulk rock composition setting $\text{Fe}^{3+}/\Sigma\text{Fe} = 0.5$ in bridgmanite for all rock compositions and requiring that $(\text{Fe}/\text{Mg})_{\text{bm}}/(\text{Fe}/\text{Mg})_{\text{fp}} = 0.5$ and 0.2 in pyrolite and harzburgite, respectively (Figure 3.6a), and that $(\text{Fe}/\text{Mg})_{\text{bm}}/(\text{Fe}/\text{Mg})_{\text{cf}} = 1$ and $(\text{Al}/\text{Mg})_{\text{bm}}/(\text{Al}/\text{Mg})_{\text{cf}} = 0.2$ in metabasalt (Figure 3.6b). For these reference scenarios, I computed adiabatic compression paths for each rock composition starting at 1900 K, 1400 K, and 2400 K at 25 GPa and mapped *P*- and *S*-wave velocities between these compression paths based on the Voigt-Reuss-Hill average over all relevant mineral phases.

Figure 3.8 shows the modeling results for the reference scenario of each bulk rock composition in terms of deviations of the computed *P*- and *S*-wave velocities from the seismic velocities of the preliminary reference Earth model (PREM; Dziewonski & Anderson, 1981):

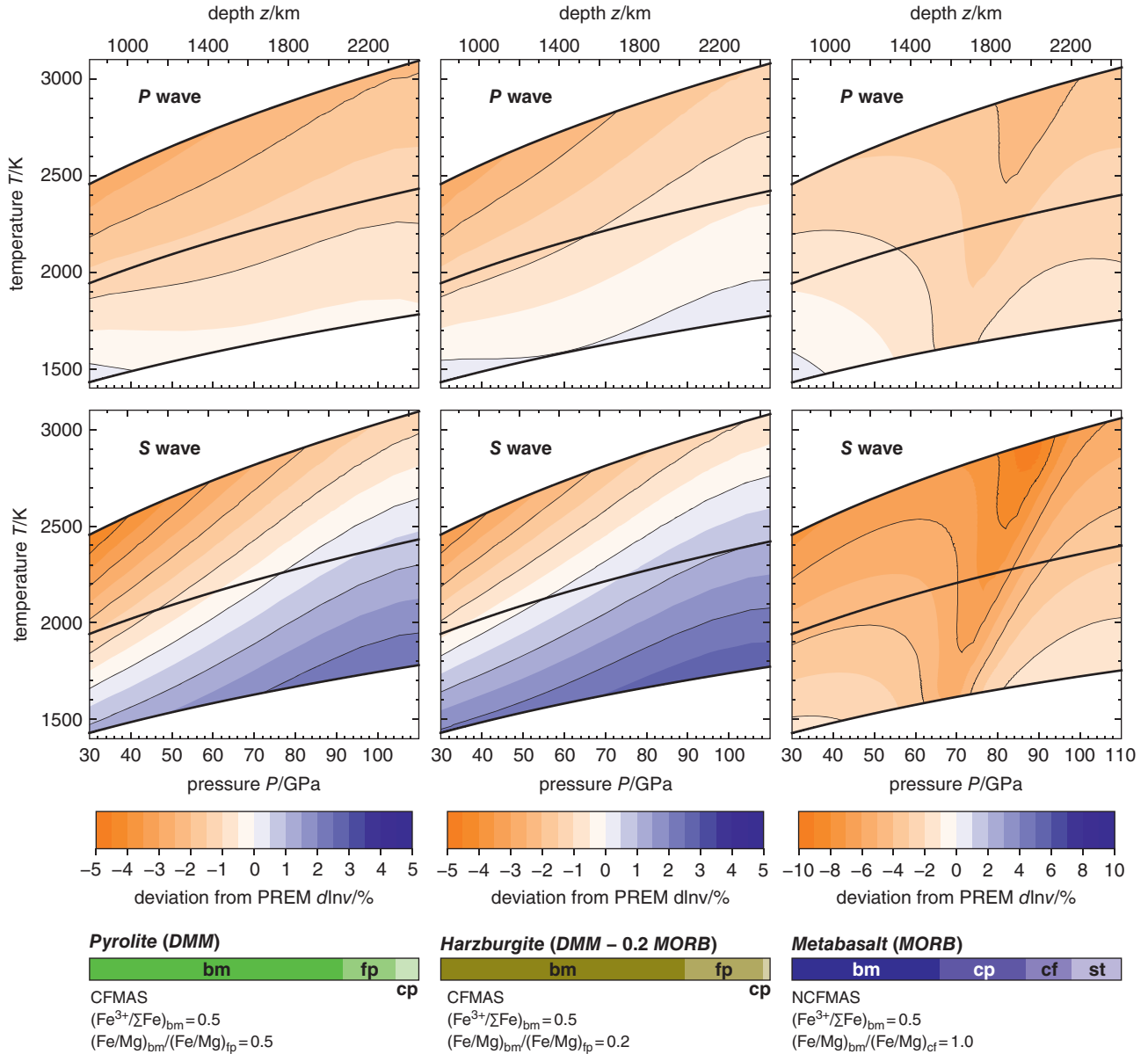


Figure 3.8 Relative contrasts between modeled P -wave (upper row) and S -wave (lower row) velocities for pyrolitic (left column), harzburgitic (central column), and basaltic (right column) bulk rock compositions and PREM. Black curves show adiabatic compression paths for each rock composition and starting at 1400 K, 1900 K, and 2400 K at 25 GPa. For each rock composition, computed volume fractions of minerals and the choice of compositional space and parameters are given below the respective diagrams. See text for details of elastic wave speed modeling.

$$d \ln v = \frac{\Delta v}{v_{\text{PREM}}}$$

where v_{PREM} stands for the P - or S -wave velocity of PREM at the respective pressure and $\Delta v = v - v_{\text{PREM}}$ is the difference in velocity between the model and PREM. P -wave velocities of pyrolite appear to systematically fall below those of PREM except for combinations of lowest pressures and temperatures. With magnitudes of less than 3%, these deviations are similar in magnitude to the

combined uncertainties on computed P -wave velocities that arise from propagating uncertainties on finite-strain parameters, averaging over elastic anisotropy, and mixing mineral compositions with different elastic properties (Figures 3.1 and 3.3a). While affected by the same sources of uncertainties, computed S -wave velocities appear to be more sensitive to temperature than P -wave velocities and match S -wave velocities of PREM, i.e., $d \ln v_S = 0$, within the considered temperature interval. The match with PREM would imply a temperature profile that deviates

substantially from any of the computed adiabatic compression paths. Modeled S -wave velocities match those of PREM for temperatures below the central adiabat down to a depth of around 1800 km where temperatures would need to rise above those of the central adiabat in order to follow PREM. Projecting the pyrolitic temperature profile for $d\ln v_S = 0$ onto the corresponding map for P -wave velocities would lead to deviations of $-1.5\% < d\ln v_P < 0\%$. Maps of deviations $d\ln v$ for harzburgite are similar to those for pyrolite. However, S -wave velocities of harzburgite seem to be systematically higher than those of pyrolite by about 0.5% to 1%, and P -wave velocities show slightly steeper gradients with depths. Computed P -wave and in particular S -wave velocities for metabasalt are significantly lower than those of PREM at most pressure–temperature combinations explored here. Despite the low volume fraction of free SiO_2 phases that go through the phase transition from stishovite to CaCl_2 -type SiO_2 , the related elastic softening of the shear modulus gives rise to a pronounced trough of amplified negative contrasts in P - and S -wave velocities between metabasalt and PREM.

While the maps shown in Figure 3.8 illustrate the temperature dependence of P - and S -wave velocity deviations from PREM, they heavily rely on assumptions about the $\text{Fe}^{3+}/\Sigma\text{Fe}$ ratio in bridgmanite and about Fe–Mg exchange between mineral phases. To explore the impact of these compositional parameters on computed P - and S -wave velocities, I varied the $\text{Fe}^{3+}/\Sigma\text{Fe}$ ratio of bridgmanite and the Fe–Mg exchange coefficients between bridgmanite and ferropericlase in pyrolite and harzburgite and between bridgmanite and the CF phase in metabasalt within the ranges suggested by data plotted in Figures 3.6a and 3.6b. When varying one compositional parameter, all other parameters were fixed to their values in the references scenarios. Figure 3.9 shows the resulting deviations of P - and S -wave velocities from PREM assuming a range of $\text{Fe}^{3+}/\Sigma\text{Fe}$ ratios in bridgmanite or different Fe–Mg exchange coefficients for each bulk rock composition along the central adiabats shown in Figure 3.8. Computed P - and S -wave velocities of both pyrolite and harzburgite are more sensitive to changes in the Fe–Mg exchange coefficient between bridgmanite and ferropericlase than to changes in the $\text{Fe}^{3+}/\Sigma\text{Fe}$ ratio of bridgmanite. The sensitivity to Fe–Mg exchange increases with depth, in particular for S waves. When combined with a reduction of the Fe–Mg exchange coefficient $K_{\text{Fe}/\text{Mg}}^{\text{bm}/\text{fp}}$ with depth as suggested by recent computational studies (Muir & Brodholt, 2016; Xu et al., 2017), the strong sensitivity of P - and S -wave velocities to Fe–Mg exchange between bridgmanite and ferropericlase could result in substantial velocity reductions for peridotitic rocks towards the lowermost mantle, even along typical adiabatic temperature profiles.

The $\text{Fe}^{3+}/\Sigma\text{Fe}$ ratio of bridgmanite dictates the whole-rock $\text{Fe}^{3+}/\Sigma\text{Fe}$ ratio and, for pyrolite and harzburgite, appears to affect velocity gradients dv/dz with higher $\text{Fe}^{3+}/\Sigma\text{Fe}$ ratios leading to steeper gradients dv/dz . Again, the effect seems to be strongest for S waves. Based on a comparison of computed P - and S -wave velocity gradients of pyrolite with PREM, Kurnosov et al. (2017) argued for a reduction of the ferric iron content in bridgmanite with depth. While a steepening of velocity gradients with higher $\text{Fe}^{3+}/\Sigma\text{Fe}$ ratios of bridgmanite is consistent with the modeling results presented here, an actual match of a pyrolitic bulk composition with PREM seems only possible for S -wave velocities and at depths in excess of 1500 km. Assuming a Fe–Mg exchange coefficient of $K_{\text{Fe}/\text{Mg}}^{\text{bm}/\text{fp}} = 0.5$, modeled S -wave velocities match those of PREM at about 1600 km depth for $\text{Fe}^{3+}/\Sigma\text{Fe} = 1$ in bridgmanite. To maintain $d\ln v_S = 0$ at depths greater than 1600 km, the $\text{Fe}^{3+}/\Sigma\text{Fe}$ ratio of bridgmanite would then need to gradually decrease with increasing depth. For harzburgite, the impact of the $\text{Fe}^{3+}/\Sigma\text{Fe}$ ratio of bridgmanite on P - and S -wave velocity profiles is complicated by the stabilization of a Fe_2O_3 component for high Fe^{3+}/Al ratios in bridgmanite due to the lower overall Al_2O_3 content of harzburgite. As long as sufficient aluminum is available, ferric iron is preferentially incorporated into bridgmanite as the component FeAlO_3 (Frost & Langenhorst, 2002; Richmond & Brodholt, 1998; Zhang & Oganov, 2006). While iron cations of the FeSiO_3 and FeAlO_3 components of bridgmanite replace magnesium on the dodecahedral A site and remain in high-spin states at pressures of the lower mantle (Catalli et al., 2010; Jackson et al., 2005a; Lin et al., 2016), one Fe^{3+} cation of the Fe_2O_3 component is located on the octahedral B site and goes through a spin transition at pressures above 40 GPa (Catalli et al., 2010; Liu et al., 2018). For the modeling results shown in Figure 3.9, Fe^{3+}/Al ratios in bridgmanite become high enough to stabilize the Fe_2O_3 component only for harzburgite models with $\text{Fe}^{3+}/\Sigma\text{Fe} > 0.5$ or $K_{\text{Fe}/\text{Mg}}^{\text{bm}/\text{fp}} > 0.2$. The elastic softening of the bulk modulus due to the spin transition of Fe^{3+} on the B site of bridgmanite (Fu et al., 2018) significantly reduces P -wave velocities for the respective harzburgite models at pressures between 40 and 100 GPa. The low overall Al_2O_3 content affects both P - and S -wave velocities.

While dominated by the elastic softening due to the ferroelastic phase transition between stishovite and CaCl_2 -type SiO_2 , modeled P - and S -wave velocity profiles of metabasalt are sensitive to both the $\text{Fe}^{3+}/\Sigma\text{Fe}$ ratio of bridgmanite and Fe–Mg exchange between bridgmanite and the CF phase. In contrast to pyrolite and harzburgite, higher $\text{Fe}^{3+}/\Sigma\text{Fe}$ ratios appear to reduce velocity gradients with depths. Varying the

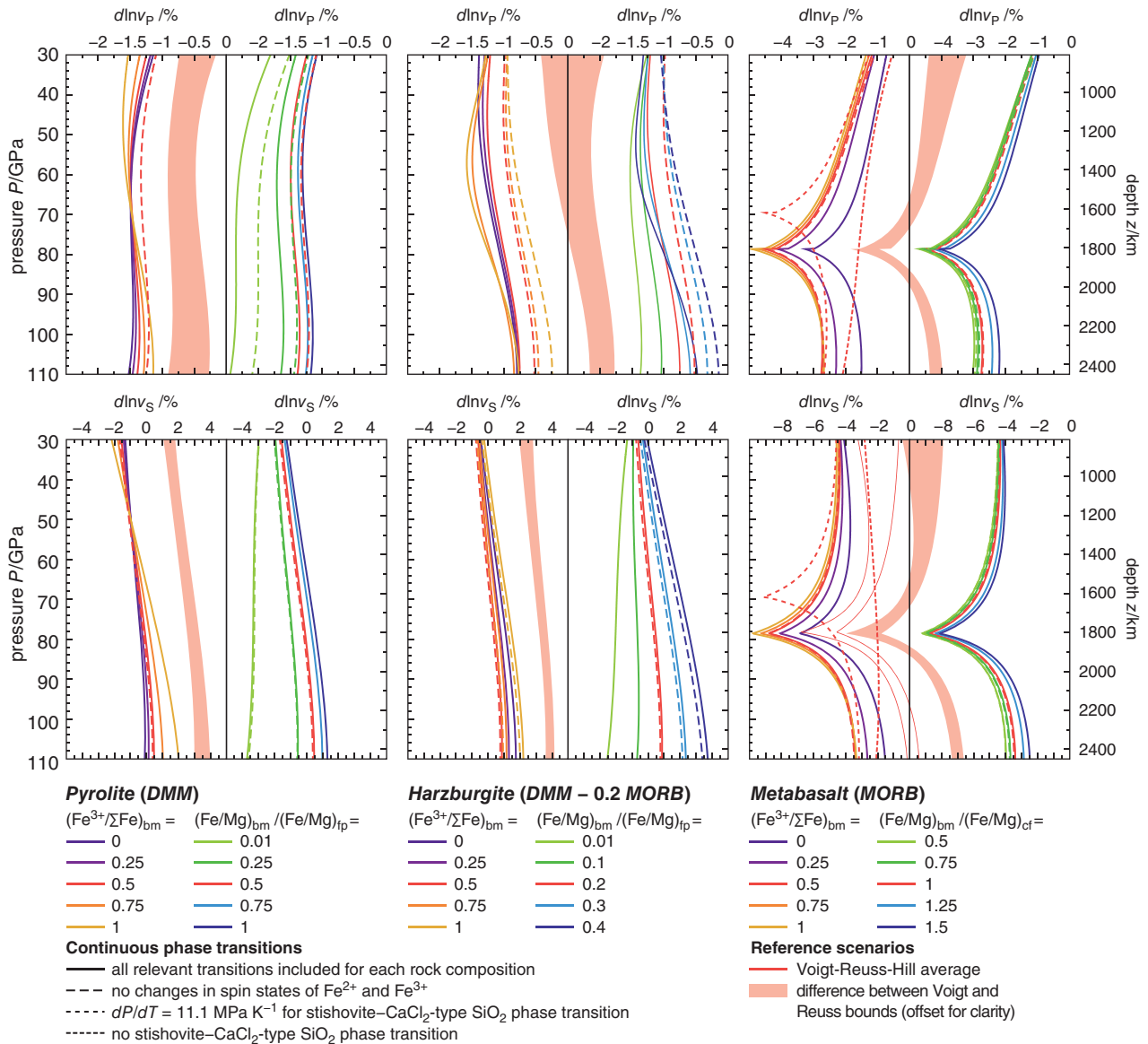


Figure 3.9 Relative contrasts between modeled P -wave (upper row) and S -wave (lower row) velocities for pyrolytic (left column), harzburgitic (central column), and basaltic (right column) bulk rock compositions and PREM along adiabatic compression paths starting at 1900 K and 25 GPa (see Figure 3.8). Variations in the $\text{Fe}^{3+}/\Sigma\text{Fe}$ ratio of bridgmanite and in the Fe-Mg exchange coefficient have been explored for each bulk rock composition as indicated below the respective diagrams. Dashed curves show P - and S -wave velocity contrasts when the effect of different continuous phase transitions on elastic properties is ignored or modified as specified. Red shaded bands indicate the differences in modeled P - and S -wave velocity contrasts that result from combining the elastic properties of mineral phases and compositions according to either the Voigt or the Reuss bound.

Fe-Mg exchange coefficient between bridgmanite and the CF phase has the opposing effect and results in higher P - and S -wave velocities for higher values of the Fe-Mg exchange coefficient. For all three bulk rock compositions addressed here, the sensitivity of P - and S -wave velocities to variations in Fe-Mg exchange coefficients demonstrates the need for better constraining equilibrium mineral compositions at relevant pressures and temperatures. While Fe-Mg exchange coefficients and

$\text{Fe}^{3+}/\Sigma\text{Fe}$ ratios were treated here as independent parameters, they are coupled through the preferred incorporation of ferric iron into bridgmanite (Frost et al., 2004; Irifune et al., 2010). As shown in Figure 3.6, however, available data on element partitioning cannot unambiguously constrain mineral compositions. More experiments and thermodynamic data are required to improve forward models of the petrology and elastic properties of lower-mantle rocks.

To depict the effect of continuous phase transitions on modeled P - and S -wave velocities, I computed additional velocity profiles by ignoring changes in spin states of iron cations and by suppressing the phase transition from stishovite to CaCl_2 -type SiO_2 . The results are included in Figure 3.9 for each reference scenario and for selected combinations of compositional parameters that are expected to be particularly susceptible to the effects of spin transitions. All pyrolite models as well as the reference scenario for harzburgite are only affected by the spin transition of ferrous iron in ferropericlasite as no ferric iron is expected to enter the B site of bridgmanite for the respective combinations of Fe-Mg exchange coefficients and $\text{Fe}^{3+}/\Sigma\text{Fe}$ ratios of bridgmanite. Along an adiabatic compression path, the spin transition of Fe^{2+} in ferropericlasite broadens substantially for reasons discussed in Section 3.7 and mainly reduces P -wave velocities. As mentioned earlier, Fe^{3+} is found to enter the crystallographic B site of bridgmanite only for harzburgite models with $\text{Fe}^{3+}/\Sigma\text{Fe} > 0.5$ or $K_{\text{Fe/Mg}}^{\text{bm}/\text{fp}} > 0.2$. For these scenarios, the spin transition of Fe^{3+} on the B site of bridgmanite gives rise to an additional P -wave velocity reduction over a pressure interval from 40 to 100 GPa. Despite substantial broadening of the Fe^{2+} spin transition in ferropericlasite and the Fe^{3+} spin transition in bridgmanite at high temperatures, both spin transitions can significantly reduce P -wave velocities of pyrolite and harzburgite and need to be taken into account when modeling elastic properties. In addition, the spin transition in ferropericlasite is further expected to affect Fe-Mg exchange between ferropericlasite and bridgmanite (Badro, 2014; Badro et al., 2005, 2003; Lin et al., 2013). Given the strong sensitivity of both P - and S -wave velocities to changes in the Fe-Mg exchange coefficient, the spin transition in ferropericlasite could have a compositional effect on seismic properties that surpasses the elastic effect. Increasing the iron content of ferropericlasite will also shift the spin transition to higher pressures (Fei et al., 2007; Persson et al., 2006; Solomatova et al., 2016; Speziale et al., 2005). Since S -wave velocities are more sensitive to Fe-Mg exchange than P -wave velocities, the compositional contribution would strongly affect S -wave velocities as opposed to the elastic contribution that mostly affects P -wave velocities via elastic softening of the bulk modulus.

The spin transition of ferric iron in the CF phase does not seem to strongly affect P - or S -wave velocities of metabasalt. In contrast, suppressing the effect of the ferroelastic phase transition from stishovite to CaCl_2 -type SiO_2 results in very different velocity profiles for metabasalt. While the softening of the shear modulus was modeled here based on a Landau theory prediction (Buchen et al., 2018a; Carpenter et al., 2000), the full extent of elastic softening remained uncertain until the very recent determination of complete elastic stiffness tensors of SiO_2 single crystals across the

ferroelastic phase transition (Zhang et al., 2021). Zhang et al. (2021) combined Brillouin spectroscopy, ISS, and X-ray diffraction to track the evolution of the elastic stiffness tensor with increasing pressure and across the stishovite– CaCl_2 -type SiO_2 phase transition. In terms of the magnitude of the S -wave velocity reduction, the predictions of Landau theory analyses seem to be consistent with the experimental results by Zhang et al. (2021). The elastic properties of stishovite and CaCl_2 -type SiO_2 had previously been computed for relevant pressures and temperatures using DFT and DFPT (Karki et al., 1997a; Yang and Wu, 2014). While indicating substantial elastic softening in the vicinity of the phase transition, the computations addressed both polymorphs independently and suggested discontinuous changes in the elastic properties at the phase transition, contradicting recent experimental results (Zhang et al., 2021) and earlier predictions based on Landau theory (Buchen et al., 2018a; Carpenter, 2006; Carpenter et al., 2000). First measurements on stishovite single crystals have captured the incipient elastic softening to pressures up to 12 GPa (Jiang et al., 2009) that has further been found to reduce the velocities of sound waves that propagate along selected crystallographic directions in aluminous SiO_2 single crystals at higher pressures (Lakshtanov et al., 2007). For basaltic bulk rock compositions, stishovite was found to incorporate several weight percent Al_2O_3 (Hirose et al., 1999; Kesson et al., 1994; Ricolleau et al., 2010). Aluminum incorporation into stishovite has been shown to reduce the transition pressure to the CaCl_2 -type polymorph (Bolfan-Casanova et al., 2009; Lakshtanov et al., 2007). While the effect of aluminum incorporation into SiO_2 phases has not been addressed in the modeling presented here, I illustrate the effect of changing the Clapeyron slope of the stishovite– CaCl_2 -type SiO_2 phase transition on the velocity profiles for metabasalt by using $dP/dT = 11.1 \text{ MPa K}^{-1}$ as reported by Nomura et al. (2010) instead of 15.5 MPa K^{-1} (Fischer et al., 2018) in an additional scenario shown in Figure 3.9.

While the modeling presented here primarily aims at providing examples for how elastic properties of rocks in Earth's lower mantle can be assessed using mineral-physical information on the elastic properties of mineral phases at high pressures and high temperatures, including the effects of continuous phase transitions, there are several sources of uncertainties that are difficult to evaluate quantitatively. For example, I combined computational with experimental results and used data from studies that used different types of samples, i.e., single crystals or polycrystals, and different methods to determine sound wave velocities, including Brillouin spectroscopy and ultrasonic interferometry. For none of the mineral phases do the available data cover the entire range of relevant pressures and temperatures. To illustrate uncertainties that result from averaging over the elastic properties of different mineral phases and compositions, Figure 3.9 shows the

differences in P - and S -wave velocities for the reference scenario of each bulk rock composition that result from the differences between the Voigt and Reuss bounds on the elastic moduli calculated based on the volume fractions that each mineral composition of Table 3.1 contributes to each of the rocks in Figure 3.9. It is further important to note that some compositions contribute with high volume fractions to all bulk rock compositions, in particular bridgmanite compositions, and revision of their finite-strain parameters could substantially alter the computed velocity profiles.

Despite these uncertainties, some general and potentially more robust features can be observed and related to concepts of material transport in Earth's mantle. P - and S -wave velocities of metabasalt differ substantially from those of PREM throughout the lower mantle and for all compositional scenarios considered here. Deep recycling of oceanic lithosphere can therefore be expected to create strong contrasts in elastic properties between former basaltic crust and surrounding mantle rocks and to affect seismic wave propagation in the lower mantle. Since fragments of subducted oceanic crust can survive several hundred million years of convective stirring while retaining dimensions of several kilometers (Stixrude & Lithgow-Bertelloni, 2012), they would create perturbations in elastic properties of sufficient magnitude and suitable size to efficiently scatter seismic energy. The interpretation of seismic scatterers in Earth's lower mantle in terms of deep recycling of oceanic crust (Frost et al., 2017; Kaneshima and Helffrich, 2009; Rost et al., 2008; Waszek et al., 2018) is therefore compatible with mineral-physical models and further supported by geodynamical simulations (Ballmer et al., 2015; Brandenburg & van Keken, 2007) and geochemical observations (Hofmann, 1997; Stracke, 2012). Modeled P - and S -wave velocities of metabasalt are lower than those of PREM and, with few exceptions, lower than those of most scenarios of pyrolite and harzburgite (Figure 3.9). The low P - and S -wave velocities of metabasalt reflect the low sound wave velocities of calcium silicate perovskite found in recent experimental studies (Gréaux et al., 2019; Thomson et al., 2019) and challenge earlier modeling results that predicted a fast seismic signature for recycled basaltic crust (Davies et al., 2012; Deschamps et al., 2012; Stixrude & Lithgow-Bertelloni, 2012). As a consequence, the hypothesis that recycled oceanic crust might contribute to the velocity reductions of large low-velocity provinces (LLVP) received new attention (Garnero et al., 2016; McNamara, 2019; Thomson et al., 2019). The example of calcium silicate perovskite demonstrates, however, how current mineral-physical models for the lower mantle hinge on the elastic properties of individual mineral phases that, when revised, may exert a strong leverage on computed wave velocities.

For most of the compositional scenarios explored for pyrolite and harzburgite shown in Figure 3.9, S -wave

velocities show steeper gradients with depth than PREM while P -wave velocity gradients are either similar to those of PREM or only slightly steeper than PREM. P - and S -wave velocities are lower than those of PREM at 800 km depth for all scenarios, and only S -wave velocities eventually rise above those of PREM for the majority of scenarios and at depths that depend on the combination of compositional parameters. P -wave velocities remain below those of PREM for all pyrolite and harzburgite scenarios and at all depths considered here. Note that steep S -wave velocity gradients and low P -wave velocities remain characteristic signatures of pyrolite and harzburgite along hotter or colder adiabatic compression paths (Figure 3.8). P - and S -wave velocity gradients that exceed those of seismic reference models have also been found by earlier mineral-physical models for adiabatic compression paths of pyrolite (Cammarano et al., 2005b; Cobden et al., 2009; Matas et al., 2007) with the spin transition of ferropericlase bringing computed P -wave velocity gradients closer to those of seismic reference models (Cammarano et al., 2010). Regions of the lower mantle that exhibit higher-than-average S -wave velocity gradients have been found to coincide with the distribution of geoid lows and locations of former subduction (Richards & Engebretson, 1992; Spasojevic et al., 2010; Steinberger, 2000). In view of the mineral-physical models shown in Figure 3.9, these observations are consistent with the storage of former slabs in the lower mantle that are dominated by peridotitic rocks from the upper mantle.

If we accept steeper-than-PREM S -wave velocity gradients and lower-than-PREM P -wave velocities as signatures of peridotitic rocks in the lower mantle, we find that a complementary lithology with higher-than-PREM P -wave velocities and lower-than-PREM S -wave velocity gradients would be required to match PREM as an average between these two lithologies. Based on the here-used mineral-physical data set (Table 3.1 and Figure 3.7), iron-free bridgmanite compositions, i.e., MgSiO_3 and $(\text{Mg}_{0.96}\text{Al}_{0.04})$ ($\text{Si}_{0.96}\text{Al}_{0.04}$) O_3 , would satisfy these criteria. Rocks that are dominated by iron-poor bridgmanite could therefore compensate for the steep S -wave velocity gradients and low P -wave velocities of former upper-mantle rocks, such as pyrolite and harzburgite, that sink into the lower mantle as cold slabs imaged by seismic tomography (Fukao & Obayashi, 2013; Sigloch et al., 2008; Simmons et al., 2015; van der Hilst et al., 1997). The results of recent geodynamic simulations suggest that domains of bridgmanite-rich rocks may remain isolated by channeling mantle flow around themselves when viscosity contrasts between such highly rigid domains and weaker pyrolitic rocks are high enough (Ballmer et al., 2017a). Mantle domains rich in bridgmanite but at the same time depleted in iron could have formed by fractional crystallization of a magma ocean, from which iron-poor bridgmanite would crystallize first as the liquidus phase (Andrault et al., 2012; Boukaré

et al., 2015; Fiquet et al., 2010). Fe-enriched fractionation products could have been separated from bridgmanite-rich domains by accumulating at the base of the mantle (Ballmer et al., 2017b; Labrosse et al., 2015) and evolving to iron-rich mineral assemblages that have been invoked to explain geodynamic and seismic properties of LLVPs (Deschamps et al., 2012; Garnero et al., 2016) and ultra-low velocity zones (ULVZ) (Bower et al., 2011; Muir and Brodholt, 2015b, 2015a; Wicks et al., 2017, 2010; Yu & Garnero, 2018).

While the idea of a lower mantle composed of complementary peridotitic and bridgmanite-dominated rocks may seem consistent with a number of geophysical observations as discussed above and would also bring the Mg/Si ratio of the mantle as a whole closer to chondritic values (McDonough & Sun, 1995), this interpretation of the modeled P - and S -wave velocity profiles is by no means unique. As mentioned above, S -wave velocities for a pyrolitic bulk composition can in principle be reconciled with those of PREM when accepting deviations from an adiabatic temperature profile (Figure 3.8). The here-modeled S -wave velocity gradients for pyrolite and harzburgite would match PREM along superadiabatic temperature profiles. Superadiabatic thermal gradients have also been inferred from earlier comparisons of mineral-physical models with seismic velocity profiles for the lower mantle and for a range of different compositions (Cammarano et al., 2010, 2005b; Cobden et al., 2009; Deschamps and Trampert, 2004; Khan et al., 2008; Matas et al., 2007). In contrast, an adiabatic pyrolitic lower mantle has been found to be consistent with PREM based on a data set for mineral elasticity derived exclusively from DFT computations (Wang et al., 2015). A recent attempt to reconcile existing data of Fe-Mg exchange between bridgmanite and ferropericlase also found agreement between adiabatic compression of pyrolite and PREM based on S -wave velocities (Hyung et al., 2016).

It is interesting to note that a significant reduction of the Fe-Mg exchange coefficient between bridgmanite and ferropericlase with increasing pressure as indicated by recent thermodynamic models (Nakajima et al., 2012; Xu et al., 2017) could entail substantial reductions of P - and S -wave velocities for peridotitic bulk rock compositions. The resulting low P - and S -wave velocities could help to explain the uppermost protrusions of LLVPs that locally extend more than 1000 km upwards above the core-mantle boundary (Durand et al., 2017; Hosseini et al., 2020; Koelemeijer et al., 2016). Because P -wave velocities of both bridgmanite and ferropericlase seem to be less sensitive to changes in the iron content than S -wave velocities (Figure 3.7), a gradually decreasing Fe-Mg exchange coefficient between these minerals could further contribute to the negative correlation between S -wave and bulk sound velocities that has been detected by seismology and appears to become more

pronounced towards the lowermost mantle (Ishii & Tromp, 1999; Koelemeijer et al., 2016; Masters et al., 2000; Trampert et al., 2004).

If we explore, as an alternative, the effect of thermal anomalies and keep mineral compositions constant throughout the lower mantle, we find from Figure 3.8 that for pyrolite and harzburgite the ratio $d\ln v_S/d\ln v_P$ would increase with temperature at a given depth but would require extremely high temperatures at depths in excess of about 1800 km to attain seismically observed values of $d\ln v_S/d\ln v_P > 1$ (Davies et al., 2012; Koelemeijer et al., 2016). By allowing for temperature variations on the order of 1000 K and taking into account the limited resolution of seismic tomography, a pyrolitic lower mantle may still be reconciled with seismic observations (Davies et al., 2012; Schubert et al., 2009b, 2009a). A reduction of the Fe-Mg exchange coefficient between bridgmanite and ferropericlase with increasing depth, in contrast, would allow for $d\ln v_S/d\ln v_P > 1$ along a typical adiabatic compression path (Figure 3.9). The variety of potential thermochemical structures that comply with seismic constraints on lower-mantle structure highlights the need both for improved forward models of seismic properties for relevant rock compositions and for integrating mineral-physical models with several types of geophysical and geochemical observations.

3.9. CONCLUSIONS

Finite-strain theory provides a compact yet flexible framework for the computation of elastic properties of minerals and rocks at pressures and temperatures of Earth's mantle (Birch, 1947; Davies, 1974; Stixrude & Lithgow-Bertelloni, 2005). This framework is constantly being filled with new elasticity data on mantle minerals as obtained from high-pressure experiments and quantum-mechanical computations. Experimental measurements of elastic properties at simultaneously high pressures and high temperatures, however, remain challenging. Propagation velocities of ultrasonic waves can now be determined for samples being compressed and heated in multi-anvil presses to pressures and temperatures corresponding to conditions of the uppermost lower mantle (Chantel et al., 2012; Gréaux et al., 2019, 2016), and laser-heated diamond anvil cells (DAC) are capable of creating pressures and temperatures as they prevail throughout the entire mantle. Thermal gradients across samples heated in DACs by infrared lasers, however, are not necessarily compatible with requirements imposed by common light or X-ray scattering techniques used to measure sound wave velocities. First successful measurements of sound wave velocities on samples being simultaneously laser-heated and compressed in DACs promise future progress in this direction (Murakami et al., 2012;

Zhang & Bass, 2016). Full elastic stiffness tensors are needed to assess elastic anisotropy and to constrain rigorous bounds on average elastic moduli. For lower-mantle minerals, measurements of full elastic stiffness tensors at relevant pressures are limited to ferropericlase (Antonangeli et al., 2011; Crowhurst et al., 2008; Finkelstein et al., 2018; Marquardt et al., 2009b, 2009c; Yang et al., 2016, 2015), bridgmanite (Fu et al., 2019; Kurnosov et al., 2017), and SiO₂ polymorphs (Zhang et al., 2021).

While density functional theory (DFT) computations are more flexible than experiments in terms of addressing extreme pressure–temperature combinations, they can only be as accurate as their underlying approximations such as the local density approximation (LDA) and generalized gradient approximations (GGA) for the electron density distribution and the quasi-harmonic approximation (QHA) for the vibrational structure. Discrepancies with experimental results have been observed for Fe-bearing compositions and reflect challenges in treating the localized *d* electrons of transition metal cations with LDA and GGA. Important developments in the study of mantle minerals with DFT computations include accounting for *d* electron interactions in terms of the Hubbard parameter *U* (Stackhouse et al., 2010; Tsuchiya et al., 2006) and bypassing the QHA with *ab initio* molecular dynamics (Oganov et al., 2001; Stackhouse et al., 2005b) or density functional perturbation theory (Giura et al., 2019; Oganov & Dorogokupets, 2004). As the full potential of these and other improvements is being explored, future progress in reducing discrepancies between the results of experiments and DFT computations can be expected.

A systematic analysis of the sensitivity of computed elastic wave velocities to individual finite-strain parameters reveals uncertainties on parameters that capture the quasi-harmonic contribution to elastic properties as a main source of uncertainty. Reported uncertainties on Grüneisen parameters and their strain derivatives propagate to relative uncertainties of several percent on elastic wave velocities for realistic pressures and temperatures of Earth’s mantle. While measurements and computations of elastic properties at combined high pressures and high temperatures will certainly help to reduce this source of uncertainty, consequent and systematic analyses of cross-correlations between finite-strain and quasi-harmonic parameters can avoid overestimating uncertainties by accounting for these correlations when propagating uncertainties. The analysis of parameter correlations, however, requires consistent data sets that include data both at high pressures and at high temperatures and ideally at combinations of both, again pointing out the need to perform experiments at combinations of high pressures and high temperatures. *P*- and *S*-wave velocities computed for isotropic polycrystalline aggregates of anisotropic minerals can differ by several percent

when using either the Voigt or the Reuss bound. These bounds provide the extreme values for the elastic response of a polycrystalline aggregate of randomly oriented grains and can only be evaluated when full elastic stiffness tensors are available for the respective minerals and at the pressures and temperatures of interest.

Computing elastic wave velocities for realistic bulk rock compositions requires accurate descriptions of elastic properties across solid solutions of mantle minerals. In contrast to the elastic properties of mantle minerals with compositions spanned by binary solid solutions, *i.e.*, olivine and ferropericlase, the change of elastic properties with chemical composition is not well constrained for mantle minerals that form complex solid solutions between several end member compositions, such as pyroxenes, garnets, bridgmanite, and the calcium ferrite-type aluminous (CF) phase. High-pressure experimental data on bridgmanite, for example, barely span bridgmanite compositions observed in experiments on peridotitic bulk rock compositions. While DFT computations have addressed wider compositional ranges (Shukla et al., 2016, 2015; Zhang et al., 2016), the results are not always consistent with those of direct measurements or are limited to specific combinations of pressure and temperature, making it difficult to derive finite-strain parameters. Inter- and extrapolations of elastic properties between different mineral compositions and beyond compositional limits imposed by available elasticity data are subject to uncertainties that arise from averaging over elastic properties of different mineral compositions and from assumptions about how elastic properties vary across solid solutions. Experiments on peridotitic and basaltic bulk rock compositions at pressures and temperatures of the lower mantle show substantial spread in observed mineral compositions and, as a consequence, in derived element exchange or partition coefficients. Despite progress in deriving trends for element partitioning with pressure, temperature, and compositional parameters for specific bulk compositions (Hyung et al., 2016; Irifune et al., 2010; Nakajima et al., 2012; Piet et al., 2016; Xu et al., 2017), it remains difficult to assess to which extent experimentally observed mineral compositions are representative of chemical equilibrium. While capable of reproducing pressures and temperatures of the lower mantle, laser-heating experiments in diamond anvil cells often give rise to strong thermal gradients across the sample that can drive disparate diffusion of chemical elements and bias mineral compositions (Andrault and Fiquet, 2001; Sinmyo and Hirose, 2010). In comparison to typical sample sizes, thermal gradients tend to be less pronounced for experiments in multi-anvil presses. Recent progress in multi-anvil press technology has extended achievable pressures to those of the lowermost mantle (Ishii et al., 2019; Yamazaki et al., 2019) and promises to facilitate experiments that better

constrain equilibrium mineral compositions at pressures and temperatures of the lower mantle. When modeling seismic properties for a given bulk rock composition, uncertainties on element partitioning and on other compositional variables translate into uncertainties on the chemical compositions of individual mineral phases and hence on computed elastic properties and wave speeds.

Several major mantle minerals go through continuous phase transitions at pressures and temperatures relevant to Earth's lower mantle. Continuous phase transitions include ferroelastic phase transitions between polymorphs of calcium silicate perovskite (Shim et al., 2002; Stixrude et al., 2007) and between stishovite and CaCl₂-type SiO₂ (Andrault et al., 1998; Carpenter et al., 2000; Karki et al., 1997b; Lakshtanov et al., 2007) as well as continuous changes in the electronic configurations of ferrous and ferric iron, i.e., spin transitions (Badro, 2014; Lin et al., 2013). Both ferroelastic phase transitions and spin transitions are associated with substantial softening of elastic moduli that is not commonly accounted for in mineral-physical models. Anomalies in elastic properties that arise from ferroelastic phase transitions can be described in terms of excess properties using Landau theory (Carpenter and Salje, 1998) and integrated into finite-strain formalisms (Buchen et al., 2018a; Tröster et al., 2014, 2002). To model elastic softening due to spin transitions, a similar approach can be adopted by formulating excess properties that arise from compression- and temperature-induced changes in the distribution of *d* electrons of iron cations over multi-electron states. Crystal-field theory provides the basis for a semi-empirical formalism that can be used to describe elastic anomalies associated with spin transitions of Fe²⁺ in ferropervicite and of Fe³⁺ in bridgmanite and in the CF phase at ambient temperature. In the absence of direct measurements of elastic softening at combined high pressures and high temperatures, predictions and extrapolations of elastic properties to realistic mantle temperatures based on Landau theory, crystal-field theory, or DFT computations need to be made with caution.

Integrating elastic anomalies caused by continuous phase transitions into forward models for elastic properties of rocks in Earth's lower mantle leads to discernible perturbations of *P*- and *S*-wave velocities. While the broad spin transition of Fe²⁺ in ferropervicite reduces the computed *P*-wave velocities of peridotitic rocks throughout the entire lower mantle, the spin transition of ferric iron in very Fe³⁺-rich bridgmanite would mostly affect *P*-wave velocities in the upper half of the lower mantle. In addition to their direct impact on *P*-wave velocities, spin transitions are expected to alter the Fe-Mg exchange between ferropervicite and bridgmanite (Badro, 2014; Xu et al., 2017) that appears to exert a strong leverage especially on *S*-wave velocities. The potential compositional effect of spin transitions on

seismic properties could have implications for the interpretations of large low-velocity provinces (LLVP). A comparison of the overall seismic signature of peridotitic rocks with the preliminary reference Earth model (PREM; Dziewonski & Anderson, 1981) reveals trade-offs between feasible interpretations in terms of the chemical and thermal structure of the lower mantle. Despite the low volume fraction of free silica phases found in experiments on basaltic bulk rock compositions, the softening of the shear modulus across the ferroelastic phase transition between stishovite and CaCl₂-type SiO₂ might be strong enough to dominate elastic wave speeds of metabasaltic rocks in the lower mantle. The resulting low elastic wave speeds could give rise to scattering of seismic waves by fragments of recycled oceanic crust and contribute to low elastic wave speeds within LLVPs.

ACKNOWLEDGMENTS

The author would like to thank J. M. Jackson and W. Sturhahn for discussions about spin transitions and G. Steinle-Neumann for providing valuable feedback on parts of the manuscript. The constructive feedback of three anonymous reviewers is highly appreciated and helped to improve the manuscript. National Science Foundation's Collaborative Study of Earth's Deep Interior (EAR-1161046, awarded to J. M. Jackson) supported a portion of this work.

REFERENCES

- Abramson, E.H., Brown, J.M., & Slutsky, L.J. (1999). Applications of impulsive stimulated scattering in the Earth and planetary sciences. *Annu. Rev. Phys. Chem.*, 50, 279–313. <https://doi.org/10.1146/annurev.physchem.50.1.279>
- Abu-Eid, R.M., & Burns, R.G. (1976). The effect of pressure on the degree of covalency of the cation-oxygen bond in minerals. *Am. Mineral.*, 61, 391–397.
- Andrault, D., Angel, R.J., Mosenfelder, J.L., & Bihan, T.L. (2003). Equation of state of stishovite to lower mantle pressures. *Am. Mineral.*, 88, 301–307. <https://doi.org/10.2138/am-2003-2-307>
- Andrault, D., & Fiquet, G. (2001). Synchrotron radiation and laser heating in a diamond anvil cell. *Rev. Sci. Instrum.*, 72, 1283–1288. <https://doi.org/10.1063/1.1343866>
- Andrault, D., Fiquet, G., Guyot, F., & Hanfland, M. (1998). Pressure-induced Landau-type transition in stishovite. *Science*, 282, 720–724. <https://doi.org/10.1126/science.282.5389.720>
- Andrault, D., Petitgirard, S., Lo Nigro, G., Devidal, J.-L., Veronesi, G., Garbarino, G., & Mezouar, M. (2012). Solid-liquid iron partitioning in Earth's deep mantle. *Nature*, 487, 354–357. <https://doi.org/10.1038/nature11294>
- Angel, R.J. (2000). Equations of state. *Rev. Mineral. Geochem.*, 41, 35–59. <https://doi.org/10.2138/rmg.2000.41.2>

- Angel, R.J., Alvaro, M., & Gonzalez-Platas, J. (2014). EosFit7c and a Fortran module (library) for equation of state calculations. *Z. Kristallogr. – Cryst. Mater.*, 229, 405–419. <https://doi.org/10.1515/zkri-2013-1711>
- Angel, R.J., Downs, R.T., & Finger, L.W. (2000). High-temperature–high-pressure diffractometry. *Rev. Mineral. Geochem.*, 41, 559–597. <https://doi.org/10.2138/rmg.2000.41.16>
- Angel, R.J., Jackson, J.M., Reichmann, H.J., & Speziale, S. (2009). Elasticity measurements on minerals: a review. *Eur. J. Mineral.*, 21, 525–550. <https://doi.org/10.1127/0935-1221/2009/0021-1925>
- Anisimov, V.I., Aryasetiawan, F., & Lichtenstein, A.I. (1997). First-principles calculations of the electronic structure and spectra of strongly correlated systems: the LDA + *U* method. *J. Phys.: Condens. Matter*, 9, 767–808. <https://doi.org/10.1088/0953-8984/9/4/002>
- Anisimov, V.I., Zaanen, J., & Andersen, O.K. (1991). Band theory and Mott insulators: Hubbard *U* instead of Stoner *I*. *Phys. Rev. B*, 44, 943–954. <https://doi.org/10.1103/PhysRevB.44.943>
- Antonangeli, D., Komabayashi, T., Occelli, F., Borissenko, E., Walters, A.C., Fiquet, G., & Fei, Y. (2012). Simultaneous sound velocity and density measurements of hcp iron up to 93 GPa and 1100 K: An experimental test of the Birch's law at high temperature. *Earth Planet. Sci. Lett.*, 331–332, 210–214. <https://doi.org/10.1016/j.epsl.2012.03.024>
- Antonangeli, D., Siebert, J., Aracne, C.M., Farber, D.L., Bosak, A., Hoesch, M., et al. (2011). Spin crossover in ferropericlase at high pressure: a seismologically transparent transition? *Science*, 331, 64–67. <https://doi.org/10.1126/science.1198429>
- Auzende, A.-L., Badro, J., Ryerson, F.J., Weber, P.K., Fallon, S.J., Addad, A., et al. (2008). Element partitioning between magnesium silicate perovskite and ferropericlase: New insights into bulk lower-mantle geochemistry. *Earth Planet. Sci. Lett.*, 269, 164–174. <https://doi.org/10.1016/j.epsl.2008.02.001>
- Badro, J. (2014). Spin transitions in mantle minerals. *Annu. Rev. Earth Planet. Sci.*, 42, 231–248. <https://doi.org/10.1146/annurev-earth-042711-105304>
- Badro, J., Fiquet, G., & Guyot, F. (2005). Thermochemical state of the lower mantle: New insights from mineral physics. In van der Hilst, R.D., Bass, J.D., Matas, J., Trampert, J. (Eds.), *Earth's Deep Mantle: Structure, Composition, and Evolution*. American Geophysical Union, Washington, D.C., pp. 241–260. <https://doi.org/10.1029/160GM15>
- Badro, J., Fiquet, G., Guyot, F., Gregoryanz, E., Occelli, F., Antonangeli, D., & d'Astuto, M. (2007). Effect of light elements on the sound velocities in solid iron: Implications for the composition of Earth's core. *Earth Planet. Sci. Lett.*, 254, 233–238. <https://doi.org/10.1016/j.epsl.2006.11.025>
- Badro, J., Fiquet, G., Guyot, F., Rueff, J.-P., Struzhkin, V.V., Vankó, G., & Monaco, G. (2003). Iron partitioning in Earth's mantle: toward a deep lower mantle discontinuity. *Science*, 300, 789–791. <https://doi.org/10.1126/science.1081311>
- Badro, J., Rueff, J.-P., Vankó, G., Monaco, G., Fiquet, G., & Guyot, F. (2004). Electronic transitions in perovskite: possible nonconvecting layers in the lower mantle. *Science*, 305, 383–386. <https://doi.org/10.1126/science.1098840>
- Ballmer, M.D., Houser, C., Hernlund, J.W., Wentzcovitch, R. M., & Hirose, K. (2017a). Persistence of strong silica-enriched domains in the Earth's lower mantle. *Nat. Geosci.*, 10, 236–240. <https://doi.org/10.1038/ngeo2898>
- Ballmer, M.D., Lourenço, D.L., Hirose, K., Caracas, R., & Nomura, R. (2017b). Reconciling magma-ocean crystallization models with the present-day structure of the Earth's mantle. *Geochem. Geophys. Geosystems*, 18, 2785–2806. <https://doi.org/10.1002/2017GC006917>
- Ballmer, M.D., Schmerr, N.C., Nakagawa, T., & Ritsema, J. (2015). Compositional mantle layering revealed by slab stagnation at ~1000-km depth. *Sci. Adv.*, 1, e1500815. <https://doi.org/10.1126/sciadv.1500815>
- Baroni, S., de Gironcoli, S., Dal Corso, A., & Giannozzi, P. (2001). Phonons and related crystal properties from density-functional perturbation theory. *Rev. Mod. Phys.*, 73, 515–562. <https://doi.org/10.1103/RevModPhys.73.515>
- Baroni, S., Giannozzi, P., & Testa, A. (1987a). Elastic constants of crystals from linear-response theory. *Phys. Rev. Lett.*, 59, 2662–2665. <https://doi.org/10.1103/PhysRevLett.59.2662>
- Baroni, S., Giannozzi, P., & Testa, A. (1987b). Green's-function approach to linear response in solids. *Phys. Rev. Lett.*, 58, 1861–1864. <https://doi.org/10.1103/PhysRevLett.58.1861>
- Bass, J.D., & Anderson, D.L. (1984). Composition of the upper mantle: geophysical tests of two petrological models. *Geophys. Res. Lett.*, 11, 229–232. <https://doi.org/10.1029/GL011i003p00229>
- Bassett, W.A., Reichmann, H.-J., Angel, R.J., Spetzler, H., & Smyth, J.R. (2000). New diamond anvil cells for gigahertz ultrasonic interferometry and X-ray diffraction. *Am. Mineral.*, 85, 283–287. <https://doi.org/10.2138/am-2000-2-303>
- Birch, F. (1964). Density and composition of mantle and core. *J. Geophys. Res.*, 69, 4377–4388. <https://doi.org/10.1029/JZ069i020p04377>
- Birch, F. (1952). Elasticity and constitution of the Earth's interior. *J. Geophys. Res.*, 57, 227–286. <https://doi.org/10.1029/JZ057i002p00227>
- Birch, F. (1947). Finite elastic strain of cubic crystals. *Phys. Rev.*, 71, 809–824. <https://doi.org/10.1103/PhysRev.71.809>
- Birch, F. (1939). The variation of seismic velocities within a simplified Earth model, in accordance with the theory of finite strain. *Bull. Seismol. Soc. Am.*, 29, 463–479.
- Birch, F. (1938). The effect of pressure upon the elastic parameters of isotropic solids, according to Murnaghan's theory of finite strain. *J. Appl. Phys.*, 9, 279–288. <https://doi.org/10.1063/1.1710417>
- Boffa Ballaran, T., Kurnosov, A., Glazyrin, K., Frost, D.J., Merlini, M., Hanfland, M., & Caracas, R. (2012). Effect of chemistry on the compressibility of silicate perovskite in the lower mantle. *Earth Planet. Sci. Lett.*, 333–334, 181–190. <https://doi.org/10.1016/j.epsl.2012.03.029>
- Boffa Ballaran, T., Kurnosov, A., & Trots, D. (2013). Single-crystal X-ray diffraction at extreme conditions: a review. *High Press. Res.*, 33, 453–465. <https://doi.org/10.1080/08957959.2013.834052>

- Bolfan-Casanova, N., Andrault, D., Amiguet, E., & Guignot, N. (2009). Equation of state and post-stishovite transformation of Al-bearing silica up to 100 GPa and 3000 K. *Phys. Earth Planet. Inter.*, *174*, 70–77. <https://doi.org/10.1016/j.pepi.2008.06.024>
- Boukaré, C.-E., Ricard, Y., & Fiquet, G. (2015). Thermodynamics of the MgO-FeO-SiO₂ system up to 140 GPa: Application to the crystallization of Earth's magma ocean. *J. Geophys. Res. – Solid Earth*, *120*, 6085–6101. <https://doi.org/10.1002/2015JB011929>
- Bower, D.J., Wicks, J.K., Gurnis, M., & Jackson, J.M. (2011). A geodynamic and mineral physics model of a solid-state ultra-low-velocity zone. *Earth Planet. Sci. Lett.*, *303*, 193–202. <https://doi.org/10.1016/j.epsl.2010.12.035>
- Brandenburg, J.P., v& an Keken, P.E. (2007). Deep storage of oceanic crust in a vigorously convecting mantle. *J. Geophys. Res. – Solid Earth*, *112*, B06403. <https://doi.org/10.1029/2006JB004813>
- Buchen, J., Marquardt, H., Ballaran, T.B., Kawazoe, T., & McCammon, C. (2017). The equation of state of wadsleyite solid solutions: constraining the effects of anisotropy and crystal chemistry. *Am. Mineral.*, *102*, 2494–2504. <https://doi.org/10.2138/am-2017-6162>
- Buchen, J., Marquardt, H., Schulze, K., Speziale, S., Boffa Ballaran, T., Nishiyama, N., & Hanfland, M. (2018a). Equation of state of polycrystalline stishovite across the tetragonal-orthorhombic phase transition. *J. Geophys. Res. – Solid Earth*, *123*, 7347–7360. <https://doi.org/10.1029/2018JB015835>
- Buchen, J., Marquardt, H., Speziale, S., Kawazoe, T., Boffa Ballaran, T., & Kurnosov, A. (2018b). High-pressure single-crystal elasticity of wadsleyite and the seismic signature of water in the shallow transition zone. *Earth Planet. Sci. Lett.*, *498*, 77–87. <https://doi.org/10.1016/j.epsl.2018.06.027>
- Burkel, E. (2000). Phonon spectroscopy by inelastic x-ray scattering. *Rep. Prog. Phys.*, *63*, 171–232. <https://doi.org/10.1088/0034-4885/63/2/203>
- Burns, R.G. (1993). *Mineralogical Applications of Crystal Field Theory*, 2nd ed., Cambridge University Press, Cambridge. <https://doi.org/10.1017/CBO9780511524899>
- Burns, R.G. (1985). Thermodynamic data from crystal field spectra. *Rev. Mineral. Geochem.*, *14*, 277–316.
- Cammarano, F., Deuss, A., Goes, S., & Giardini, D. (2005a). One-dimensional physical reference models for the upper mantle and transition zone: Combining seismic and mineral physics constraints. *J. Geophys. Res. – Solid Earth*, *110*, B01306. <https://doi.org/10.1029/2004JB003272>
- Cammarano, F., Goes, S., Deuss, A., & Giardini, D. (2005b). Is a pyrolytic adiabatic mantle compatible with seismic data? *Earth Planet. Sci. Lett.*, *232*, 227–243. <https://doi.org/10.1016/j.epsl.2005.01.031>
- Cammarano, F., Goes, S., Vacher, P., & Giardini, D. (2003). Inferring upper-mantle temperatures from seismic velocities. *Phys. Earth Planet. Inter.*, *138*, 197–222. [https://doi.org/10.1016/S0031-9201\(03\)00156-0](https://doi.org/10.1016/S0031-9201(03)00156-0)
- Cammarano, F., Marquardt, H., Speziale, S., & Tackley, P.J. (2010). Role of iron-spin transition in ferroperricite on seismic interpretation: A broad thermochemical transition in the mid mantle? *Geophys. Res. Lett.*, *37*, L03308. <https://doi.org/10.1029/2009GL041583>
- Cammarano, F., Romanowicz, B., Stixrude, L., Lithgow-Bertelloni, C., & Xu, W. (2009). Inferring the thermochemical structure of the upper mantle from seismic data. *Geophys. J. Int.*, *179*, 1169–1185. <https://doi.org/10.1111/j.1365-246X.2009.04338.x>
- Campbell, A.J. (2008). Measurement of temperature distributions across laser heated samples by multispectral imaging radiometry. *Rev. Sci. Instrum.*, *79*, 015108. <https://doi.org/10.1063/1.2827513>
- Car, R., Parrinello, M. (1985). Unified approach for molecular dynamics and density-functional theory. *Phys. Rev. Lett.*, *55*, 2471–2474. <https://doi.org/10.1103/PhysRevLett.55.2471>
- Caracas, R. (2010). Spin and structural transitions in AlFeO₃ and FeAlO₃ perovskite and post-perovskite. *Phys. Earth Planet. Inter.*, *182*, 10–17. <https://doi.org/10.1016/j.pepi.2010.06.001>
- Caracas, R., & Cohen, R.E. (2005). Effect of chemistry on the stability and elasticity of the perovskite and post-perovskite phases in the MgSiO₃-FeSiO₃-Al₂O₃ system and implications for the lowermost mantle. *Geophys. Res. Lett.*, *32*, L16310. <https://doi.org/10.1029/2005GL023164>
- Carpenter, M.A. (2006). Elastic properties of minerals and the influence of phase transitions. *Am. Mineral.*, *91*, 229–246. <https://doi.org/10.2138/am.2006.1979>
- Carpenter, M.A., Hemley, R.J., & Mao, H. (2000). High-pressure elasticity of stishovite and the $P4_2/mnm \rightleftharpoons Pnmm$ phase transition. *J. Geophys. Res. – Solid Earth*, *105*, 10807–10816. <https://doi.org/10.1029/1999JB900419>
- Carpenter, M.A., & Salje, E.K.H. (1998). Elastic anomalies in minerals due to structural phase transitions. *Eur. J. Mineral.*, *10*, 693–812. <https://doi.org/10.1127/ejm/10/4/0693>
- Carpenter, M.A., Salje, E.K.H., & Graeme-Barber, A. (1998). Spontaneous strain as a determinant of thermodynamic properties for phase transitions in minerals. *Eur. J. Mineral.*, *10*, 621–691. <https://doi.org/10.1127/ejm/10/4/0621>
- Carrier, P., Wentzcovitch, R., & Tsuchiya, J. (2007). First-principles prediction of crystal structures at high temperatures using the quasiharmonic approximation. *Phys. Rev. B*, *76*, 064116. <https://doi.org/10.1103/PhysRevB.76.064116>
- Catalli, K., Shim, S.-H., Prakapenka, V.B., Zhao, J., Sturhahn, W., Chow, P., et al. (2010). Spin state of ferric iron in MgSiO₃ perovskite and its effect on elastic properties. *Earth Planet. Sci. Lett.*, *289*, 68–75. <https://doi.org/10.1016/j.epsl.2009.10.029>
- Chantel, J., Frost, D.J., McCammon, C.A., Jing, Z., & Wang, Y. (2012). Acoustic velocities of pure and iron-bearing magnesium silicate perovskite measured to 25 GPa and 1200 K. *Geophys. Res. Lett.*, *39*, L19307. <https://doi.org/10.1029/2012GL053075>
- Chen, B., Jackson, J.M., Sturhahn, W., Zhang, D., Zhao, J., Wicks, J.K., & Murphy, C.A. (2012). Spin crossover equation of state and sound velocities of (Mg_{0.65}Fe_{0.35})O ferroperricite to 140 GPa. *J. Geophys. Res. – Solid Earth*, *117*, B08208. <https://doi.org/10.1029/2012JB009162>
- Chung, D.H., & Buessem, W.R. (1967). The Voigt-Reuss-Hill approximation and elastic moduli of polycrystalline MgO,

- CaF₂, β-ZnS, ZnSe, and CdTe. *J. Appl. Phys.*, *38*, 2535–2540. <https://doi.org/10.1063/1.1709944>
- Chust, T.C., Steinle-Neumann, G., Dolejš, D., Schuberth, B.S. A., & Bunge, H.-P. (2017). MMA-EoS: a computational framework for mineralogical thermodynamics. *J. Geophys. Res. – Solid Earth*, *122*, 9881–9920. <https://doi.org/10.1002/2017JB014501>
- Cobden, L., Goes, S., Cammarano, F., & Connolly, J.A.D. (2008). Thermochemical interpretation of one-dimensional seismic reference models for the upper mantle: evidence for bias due to heterogeneity. *Geophys. J. Int.*, *175*, 627–648. <https://doi.org/10.1111/j.1365-246X.2008.03903.x>
- Cobden, L., Goes, S., Ravenna, M., Styles, E., Cammarano, F., Gallagher, K., & Connolly, J.A.D. (2009). Thermochemical interpretation of 1-D seismic data for the lower mantle: The significance of nonadiabatic thermal gradients and compositional heterogeneity. *J. Geophys. Res. – Solid Earth*, *114*, B11309. <https://doi.org/10.1029/2008JB006262>
- Cococcioni, M. (2010). Accurate and efficient calculations on strongly correlated minerals with the LDA+U method: Review and perspectives. *Rev. Mineral. Geochem.*, *71*, 147–167. <https://doi.org/10.2138/rmg.2010.71.8>
- Cococcioni, M., & de Gironcoli, S. (2005). Linear response approach to the calculation of the effective interaction parameters in the LDA+U method. *Phys. Rev. B*, *71*, 035105. <https://doi.org/10.1103/PhysRevB.71.035105>
- Connolly, J.A.D. (2005). Computation of phase equilibria by linear programming: A tool for geodynamic modeling and its application to subduction zone decarbonation. *Earth Planet. Sci. Lett.*, *236*, 524–541. <https://doi.org/10.1016/j.epsl.2005.04.033>
- Cox, P.A. (1987). *The Electronic Structure and Chemistry of Solids*. Oxford University Press, Oxford.
- Crowhurst, J.C., Brown, J.M., Goncharov, A.F., & Jacobsen, S. D. (2008). Elasticity of (Mg,Fe)O through the spin transition of iron in the lower mantle. *Science*, *319*, 451–453. <https://doi.org/10.1126/science.1149606>
- Cummins, H.Z., & Schoen, P.E. (1972). Linear scattering from thermal fluctuations. In Arecchi, F.T., Schulz-DuBois, E.O. (Eds.), *Laser Handbook*. North-Holland Publishing Company, Amsterdam, pp. 1029–1075.
- Dai, L., Kudo, Y., Hirose, K., Murakami, M., Asahara, Y., Ozawa, H., et al. (2013). Sound velocities of Na_{0.4}Mg_{0.6}Al_{1.6}Si_{0.4}O₄ NAL and CF phases to 73 GPa determined by Brillouin scattering method. *Phys. Chem. Miner.*, *40*, 195–201. <https://doi.org/10.1007/s00269-012-0558-0>
- Davies, D.R., Goes, S., Davies, J.H., Schuberth, B.S.A., Bunge, H.-P., & Ritsema, J. (2012). Reconciling dynamic and seismic models of Earth's lower mantle: The dominant role of thermal heterogeneity. *Earth Planet. Sci. Lett.*, *353–354*, 253–269. <https://doi.org/10.1016/j.epsl.2012.08.016>
- Davies, G.F. (1974). Effective elastic moduli under hydrostatic stress—I. Quasi-harmonic theory. *J. Phys. Chem. Solids*, *35*, 1513–1520. [https://doi.org/10.1016/S0022-3697\(74\)80279-9](https://doi.org/10.1016/S0022-3697(74)80279-9)
- Davies, G.F., & Dziewonski, A.M. (1975). Homogeneity and constitution of the earth's lower mantle and outer core. *Phys. Earth Planet. Inter.*, *10*, 336–343. [https://doi.org/10.1016/0031-9201\(75\)90060-6](https://doi.org/10.1016/0031-9201(75)90060-6)
- Decremps, F., Antonangeli, D., Gauthier, M., Ayrinhac, S., Morand, M., Marchand, et al. (2014). Sound velocity of iron up to 152 GPa by picosecond acoustics in diamond anvil cell. *Geophys. Res. Lett.*, *41*, 1459–1464. <https://doi.org/10.1002/2013GL058859>
- Decremps, F., Belliard, L., Gauthier, M., & Perrin, B. (2010). Equation of state, stability, anisotropy and nonlinear elasticity of diamond-cubic (ZB) silicon by phonon imaging at high pressure. *Phys. Rev. B*, *82*, 104119. <https://doi.org/10.1103/PhysRevB.82.104119>
- Decremps, F., Belliard, L., Perrin, B., & Gauthier, M. (2008). Sound velocity and absorption measurements under high pressure using picosecond ultrasonics in a diamond anvil cell: Application to the stability study of AlPdMn. *Phys. Rev. Lett.*, *100*, 035502. <https://doi.org/10.1103/PhysRevLett.100.035502>
- Deschamps, F., Cobden, L., & Tackley, P.J. (2012). The primitive nature of large low shear-wave velocity provinces. *Earth Planet. Sci. Lett.*, *349–350*, 198–208. <https://doi.org/10.1016/j.epsl.2012.07.012>
- Deschamps, F., & Trampert, J. (2004). Towards a lower mantle reference temperature and composition. *Earth Planet. Sci. Lett.*, *222*, 161–175. <https://doi.org/10.1016/j.epsl.2004.02.024>
- Dil, J.G. (1982). Brillouin scattering in condensed matter. *Rep. Prog. Phys.*, *45*, 285–334. <https://doi.org/10.1088/0034-4885/45/3/002>
- Drickamer, H.G., & Frank, C.W. (1973). *Electronic Transitions and the High Pressure Chemistry and Physics of Solids*. Springer, Dordrecht. <https://doi.org/10.1007/978-94-011-6896-0>
- Duffy, T.S., & Anderson, D.L. (1989). Seismic velocities in mantle minerals and the mineralogy of the upper mantle. *J. Geophys. Res. – Solid Earth*, *94*, 1895–1912. <https://doi.org/10.1029/JB094iB02p01895>
- Durand, S., Debayle, E., Ricard, Y., Zanolli, C., & Lambotte, S. (2017). Confirmation of a change in the global shear velocity pattern at around 1000 km depth. *Geophys. J. Int.*, *211*, 1628–1639. <https://doi.org/10.1093/gji/ggx405>
- Dziewonski, A.M., & Anderson, D.L. (1981). Preliminary reference Earth model. *Phys. Earth Planet. Inter.*, *25*, 297–356. [https://doi.org/10.1016/0031-9201\(81\)90046-7](https://doi.org/10.1016/0031-9201(81)90046-7)
- Fayer, M.D. (1982). Dynamics of molecules in condensed phases: picosecond holographic grating experiments. *Annu. Rev. Phys. Chem.*, *33*, 63–87. <https://doi.org/10.1146/annurev.pc.33.100182.000431>
- Fei, Y., Zhang, L., Corgne, A., Watson, H., Ricolleau, A., Meng, Y., & Prakapenka, V. (2007). Spin transition and equations of state of (Mg, Fe)O solid solutions. *Geophys. Res. Lett.*, *34*, L17307. <https://doi.org/10.1029/2007GL030712>
- Finkelstein, G.J., Jackson, J.M., Said, A., Alatas, A., Leu, B.M., Sturhahn, W., & Toellner, T.S. (2018). Strongly anisotropic magnesiowüstite in Earth's lower mantle. *J. Geophys. Res. – Solid Earth*, *123*, 4740–4750. <https://doi.org/10.1029/2017JB015349>
- Fiquet, G., Auzende, A.L., Siebert, J., Corgne, A., Bureau, H., Ozawa, H., & Garbarino, G. (2010). Melting of peridotite to 140 gigapascals. *Science*, *329*, 1516–1518. <https://doi.org/10.1126/science.1192448>

- Fiquet, G., Badro, J., Guyot, F., Bellin, C., Krisch, M., Antonangeli, D., et al. (2004). Application of inelastic X-ray scattering to the measurements of acoustic wave velocities in geophysical materials at very high pressure. *Phys. Earth Planet. Inter.*, 143–144, 5–18. <https://doi.org/10.1016/j.pepi.2003.10.005>
- Fiquet, G., Badro, J., Guyot, F., Requardt, H., & Krisch, M. (2001). Sound velocities in iron to 110 gigapascals. *Science*, 291, 468–471. <https://doi.org/10.1126/science.291.5503.468>
- Fiquet, G., Dewaele, A., Andrault, D., Kunz, M., Bihan, T.L. (2000). Thermoelastic properties and crystal structure of MgSiO₃ perovskite at lower mantle pressure and temperature conditions. *Geophys. Res. Lett.*, 27, 21–24. <https://doi.org/10.1029/1999GL008397>
- Fischer, R.A., Campbell, A.J., Chidester, B.A., Reaman, D.M., Thompson, E.C., Pigott, J.S., et al. (2018). Equations of state and phase boundary for stishovite and CaCl₂-type SiO₂. *Am. Mineral.*, 103, 792–802. <https://doi.org/10.2138/am-2018-6267>
- Frost, D.A., Rost, S., Garnero, E.J., & Li, M. (2017). Seismic evidence for Earth's crusty deep mantle. *Earth Planet. Sci. Lett.*, 470, 54–63. <https://doi.org/10.1016/j.epsl.2017.04.036>
- Frost, D.J., & Langenhorst, F. (2002). The effect of Al₂O₃ on Fe-Mg partitioning between magnesiowüstite and magnesium silicate perovskite. *Earth Planet. Sci. Lett.*, 199, 227–241.
- Frost, D.J., Liebske, C., Langenhorst, F., McCammon, C.A., Trønnes, R.G., & Rubie, D.C. (2004). Experimental evidence for the existence of iron-rich metal in the Earth's lower mantle. *Nature*, 428, 409–412. <https://doi.org/10.1038/nature02413>
- Fu, S., Yang, J., Tsujino, N., Okuchi, T., Purevjav, N., & Lin, J.-F. (2019). Single-crystal elasticity of (Al,Fe)-bearing bridgmanite and seismic shear wave radial anisotropy at the topmost lower mantle. *Earth Planet. Sci. Lett.*, 518, 116–126. <https://doi.org/10.1016/j.epsl.2019.04.023>
- Fu, S., Yang, J., Zhang, Y., Okuchi, T., McCammon, C., Kim, H.-I., et al. (2018). Abnormal elasticity of Fe-bearing bridgmanite in the Earth's lower mantle. *Geophys. Res. Lett.*, 45, 4725–4732. <https://doi.org/10.1029/2018GL077764>
- Fujino, K., Nishio-Hamane, D., Suzuki, K., Izumi, H., Seto, Y., & Nagai, T. (2009). Stability of the perovskite structure and possibility of the transition to the post-perovskite structure in CaSiO₃, FeSiO₃, MnSiO₃ and CoSiO₃. *Phys. Earth Planet. Inter.*, 177, 147–151. <https://doi.org/10.1016/j.pepi.2009.08.009>
- Fukao, Y., & Obayashi, M. (2013). Subducted slabs stagnate above, penetrating through, and trapped below the 660 km discontinuity. *J. Geophys. Res. – Solid Earth*, 118, 5920–5938. <https://doi.org/10.1002/2013JB010466>
- Funamori, N., & Jeanloz, R. (1997). High-pressure transformation of Al₂O₃. *Science*, 278, 1109–1111. <https://doi.org/10.1126/science.278.5340.1109>
- Funamori, N., Jeanloz, R., Miyajima, N., & Fujino, K. (2000). Mineral assemblages of basalt in the lower mantle. *J. Geophys. Res. – Solid Earth*, 105, 26037–26043. <https://doi.org/10.1029/2000JB900252>
- Gaffney, E.S. (1972). Crystal field effects in mantle minerals. *Phys. Earth Planet. Inter.*, 6, 385–390. [https://doi.org/10.1016/0031-9201\(72\)90062-3](https://doi.org/10.1016/0031-9201(72)90062-3)
- Gaffney, E.S., & Anderson, D.L. (1973). Effect of low-spin Fe²⁺ on the composition of the lower mantle. *J. Geophys. Res.*, 78, 7005–7014. <https://doi.org/10.1029/JB078i029p07005>
- Garnero, E.J., McNamara, A.K., & Shim, S.-H. (2016). Continent-sized anomalous zones with low seismic velocity at the base of Earth's mantle. *Nat. Geosci.*, 9, 481–489. <https://doi.org/10.1038/ngeo2733>
- Giannozzi, P., de Gironcoli, S., Pavone, P., & Baroni, S. (1991). Ab initio calculation of phonon dispersions in semiconductors. *Phys. Rev. B*, 43, 7231–7242. <https://doi.org/10.1103/PhysRevB.43.7231>
- Giura, P., Paulatto, L., He, F., Lobo, R.P.S.M., Bosak, A., Calandrini, E., et al. (2019). Multiphonon anharmonicity of MgO. *Phys. Rev. B*, 99, 220304. <https://doi.org/10.1103/PhysRevB.99.220304>
- Glazyrin, K., Boffa Ballaran, T., Frost, D.J., McCammon, C., Kantor, A., Merlini, M., et al. (2014). Magnesium silicate perovskite and effect of iron oxidation state on its bulk sound velocity at the conditions of the lower mantle. *Earth Planet. Sci. Lett.*, 393, 182–186. <https://doi.org/10.1016/j.epsl.2014.01.056>
- Gréaux, S., Irifune, T., Higo, Y., Tange, Y., Arimoto, T., Liu, Z., & Yamada, A. (2019). Sound velocity of CaSiO₃ perovskite suggests the presence of basaltic crust in the Earth's lower mantle. *Nature*, 565, 218–221. <https://doi.org/10.1038/s41586-018-0816-5>
- Gréaux, S., Kono, Y., Wang, Y., Yamada, A., Zhou, C., Jing, Z., et al. (2016). Sound velocities of aluminum-bearing stishovite in the mantle transition zone. *Geophys. Res. Lett.*, 43, 4239–4246. <https://doi.org/10.1002/2016GL068377>
- Gwanmesia, G.D., Liebermann, R.C., & Guyot, F. (1990). Hot-pressing and characterization of polycrystals of β-Mg₂SiO₄ for acoustic velocity measurements. *Geophys. Res. Lett.*, 17, 1331–1334. <https://doi.org/10.1029/GL017i009p01331>
- Haussühl, S. (2007). *Physical Properties of Crystals: An Introduction*. Wiley-VCH, Weinheim. <https://doi.org/10.1002/9783527621156>
- Hill, R. (1952). The elastic behaviour of a crystalline aggregate. *Proc. Phys. Soc.*, A65, 349–354. <https://doi.org/10.1088/0370-1298/65/5/307>
- Hirose, K., Fei, Y., Ma, Y., & Mao, H.-K. (1999). The fate of subducted basaltic crust in the Earth's lower mantle. *Nature*, 397, 53–56. <https://doi.org/10.1038/16225>
- Hirose, K., Takafuji, N., Sata, N., & Ohishi, Y. (2005). Phase transition and density of subducted MORB crust in the lower mantle. *Earth Planet. Sci. Lett.*, 237, 239–251. <https://doi.org/10.1016/j.epsl.2005.06.035>
- Hofmann, A.W. (1997). Mantle geochemistry: the message from oceanic volcanism. *Nature*, 385, 219–229. <https://doi.org/10.1038/385219a0>
- Hohenberg, P., & Kohn, W. (1964). Inhomogeneous electron gas. *Phys. Rev.*, 136, B864–B871. <https://doi.org/10.1103/PhysRev.136.B864>
- Holland, T.J.B., Hudson, N.F.C., Powell, R., & Harte, B. (2013). New thermodynamic models and calculated phase equilibria in NCFMAS for basic and ultrabasic compositions through the transition zone into the uppermost lower mantle.

- J. Petrol.*, 54, 1901–1920. <https://doi.org/10.1093/petrology/egt035>
- Holmström, E., & Stixrude, L. (2015). Spin crossover in ferropericlase from first-principles molecular dynamics. *Phys. Rev. Lett.*, 114, 117202. <https://doi.org/10.1103/PhysRevLett.114.117202>
- Holzappel, W. (2009). Equations of state for solids under strong compression. *Z. Kristallogr. – Cryst. Mater.*, 216, 473–488. <https://doi.org/10.1524/zkri.216.9.473.20346>
- Hosseini, K., Sigloch, K., Tsekhmistrenko, M., Zaheri, A., Nissen-Meyer, T., & Igel, H. (2020). Global mantle structure from multifrequency tomography using *P*, *PP* and *P*-diffracted waves. *Geophys. J. Int.*, 220, 96–141. <https://doi.org/10.1093/gji/ggz394>
- Hsu, H., Blaha, P., Cococcioni, M., & Wentzcovitch, R.M. (2011). Spin-state crossover and hyperfine interactions of ferrous iron in MgSiO₃ perovskite. *Phys. Rev. Lett.*, 106, 118501. <https://doi.org/10.1103/PhysRevLett.106.118501>
- Hsu, H., Umemoto, K., Blaha, P., & Wentzcovitch, R.M. (2010a). Spin states and hyperfine interactions of iron in (Mg,Fe)SiO₃ perovskite under pressure. *Earth Planet. Sci. Lett.*, 294, 19–26. <https://doi.org/10.1016/j.epsl.2010.02.031>
- Hsu, H., Umemoto, K., Wu, Z., & Wentzcovitch, R.M. (2010b). Spin-state crossover of iron in lower-mantle minerals: Results of DFT+U investigations. *Rev. Mineral. Geochem.*, 71, 169–199. <https://doi.org/10.2138/rmg.2010.71.09>
- Hubbard, J. (1963). Electron correlations in narrow energy bands. *Proc. R. Soc. Lond. A*, 276, 238–257. <https://doi.org/10.1098/rspa.1963.0204>
- Hyung, E., Huang, S., Petaev, M.I., Jacobsen, S.B. (2016). Is the mantle chemically stratified? Insights from sound velocity modeling and isotope evolution of an early magma ocean. *Earth Planet. Sci. Lett.*, 440, 158–168. <https://doi.org/10.1016/j.epsl.2016.02.001>
- Imada, S., Hirose, K., Komabayashi, T., Suzuki, T., & Ohishi, Y. (2012). Compression of Na_{0.4}Mg_{0.6}Al_{1.6}Si_{0.4}O₄ NAL and Ca-ferrite-type phases. *Phys. Chem. Miner.*, 39, 525–530. <https://doi.org/10.1007/s00269-012-0508-x>
- Immoor, J., Marquardt, H., Miyagi, L., Speziale, S., Merkel, S., Schwark, I., et al. (2020). An improved setup for radial diffraction experiments at high pressures and high temperatures in a resistive graphite-heated diamond anvil cell. *Rev. Sci. Instrum.*, 91, 045121. <https://doi.org/10.1063/1.5143293>
- Irfune, T., Shinmei, T., McCammon, C.A., Miyajima, N., Rubie, D.C., & Frost, D.J. (2010). Iron partitioning and density changes of pyrolite in Earth's lower mantle. *Science*, 327, 193–195. <https://doi.org/10.1126/science.1181443>
- Isaak, D.G. (1992). High-temperature elasticity of iron-bearing olivines. *J. Geophys. Res. – Solid Earth*, 97, 1871–1885. <https://doi.org/10.1029/91JB02675>
- Isaak, D.G., Anderson, O.L., Goto, T., & Suzuki, I. (1989). Elasticity of single-crystal forsterite measured to 1700 K. *J. Geophys. Res. – Solid Earth*, 94, 5895–5906. <https://doi.org/10.1029/JB094iB05p05895>
- Ishii, M., & Tromp, J. (1999). Normal-mode and free-air gravity constraints on lateral variations in velocity and density of Earth's mantle. *Science*, 285, 1231–1236. <https://doi.org/10.1126/science.285.5431.1231>
- Ishii, T., Liu, Z., & Katsura, T. (2019). A breakthrough in pressure generation by a Kawai-type multi-anvil apparatus with tungsten carbide anvils. *Engineering*, 5, 434–440. <https://doi.org/10.1016/j.eng.2019.01.013>
- Ita, J., & Stixrude, L. (1992). Petrology, elasticity, and composition of the mantle transition zone. *J. Geophys. Res. – Solid Earth*, 97, 6849–6866. <https://doi.org/10.1029/92JB00068>
- Jackson, I. (2015). Properties of rocks and minerals: Physical origins of anelasticity and attenuation in rock. In Schubert, G. (Ed.), *Treatise on Geophysics*, 2nd ed., Elsevier, Amsterdam, pp. 539–571. <https://doi.org/10.1016/B978-0-444-53802-4.00045-2>
- Jackson, I. (1998). Elasticity, composition and temperature of the Earth's lower mantle: a reappraisal. *Geophys. J. Int.*, 134, 291–311. <https://doi.org/10.1046/j.1365-246x.1998.00560.x>
- Jackson, J.M., Sturhahn, W., Shen, G., Zhao, J., Hu, M.Y., Errandonea, D., et al. (2005a). A synchrotron Mössbauer spectroscopy study of (Mg,Fe)SiO₃ perovskite up to 120 GPa. *Am. Mineral.*, 90, 199–205. <https://doi.org/10.2138/am.2005.1633>
- Jackson, J.M., Zhang, J., Shu, J., Sinogeikin, S.V., Bass, J.D. (2005b). High-pressure sound velocities and elasticity of aluminous MgSiO₃ perovskite to 45 GPa: Implications for lateral heterogeneity in Earth's lower mantle. *Geophys. Res. Lett.*, 32, L21305. <https://doi.org/10.1029/2005GL023522>
- Jacobsen, S.D., Reichmann, H.-J., Spetzler, H.A., Mackwell, S. J., Smyth, J.R., et al. (2002). Structure and elasticity of single-crystal (Mg,Fe)O and a new method of generating shear waves for gigahertz ultrasonic interferometry. *J. Geophys. Res. – Solid Earth*, 107, ECV 4-1–ECV 4-14. <https://doi.org/10.1029/2001JB000490>
- Jacobsen, S.D., Spetzler, H., Reichmann, H.J., & Smyth, J.R. (2004). Shear waves in the diamond-anvil cell reveal pressure-induced instability in (Mg,Fe)O. *Proc. Natl. Acad. Sci. U.S.A.*, 101, 5867–5871. <https://doi.org/10.1073/pnas.0401564101>
- Jiang, F., Gwanmesia, G.D., Dyuzheva, T.I., & Duffy, T.S. (2009). Elasticity of stishovite and acoustic mode softening under high pressure by Brillouin scattering. *Phys. Earth Planet. Inter.*, 172, 235–240. <https://doi.org/10.1016/j.pepi.2008.09.017>
- Kaneshima, S., Helffrich, G. (2009). Lower mantle scattering profiles and fabric below Pacific subduction zones. *Earth Planet. Sci. Lett.*, 282, 234–239. <https://doi.org/10.1016/j.epsl.2009.03.024>
- Kantor, I., Prakapenka, V., Kantor, A., Dera, P., Kurnosov, A., Sinogeikin, S., et al. (2012). BX90: A new diamond anvil cell design for X-ray diffraction and optical measurements. *Rev. Sci. Instrum.*, 83, 125102. <https://doi.org/10.1063/1.4768541>
- Karato, S. (2008). *Deformation of Earth Materials: An Introduction to the Rheology of Solid Earth*. Cambridge University Press, Cambridge. <https://doi.org/10.1017/CBO9780511804892>
- Karato, S. (1993). Importance of anelasticity in the interpretation of seismic tomography. *Geophys. Res. Lett.*, 20, 1623–1626. <https://doi.org/10.1029/93GL01767>
- Karki, B.B., Stixrude, L., & Crain, J. (1997a). Ab initio elasticity of three high-pressure polymorphs of silica. *Geophys. Res. Lett.*, 24, 3269–3272. <https://doi.org/10.1029/97GL53196>

- Karki, B.B., Stixrude, L., & Wentzcovitch, R.M. (2001a). High-pressure elastic properties of major materials of Earth's mantle from first principles. *Rev. Geophys.*, *39*, 507–534. <https://doi.org/10.1029/2000RG000088>
- Karki, B.B., Warren, M.C., Stixrude, L., Ackland, G.J., & Crain, J. (1997b). Ab initio studies of high-pressure structural transformations in silica. *Phys. Rev. B*, *55*, 3465–3471. <https://doi.org/10.1103/PhysRevB.55.3465>
- Karki, B.B., Wentzcovitch, R.M., de Gironcoli, S., & Baroni, S. (2000). High-pressure lattice dynamics and thermoelasticity of MgO. *Phys. Rev. B*, *61*, 8793–8800. <https://doi.org/10.1103/PhysRevB.61.8793>
- Karki, B.B., Wentzcovitch, R.M., de Gironcoli, S., & Baroni, S. (2001b). First principles thermoelasticity of MgSiO₃-perovskite: consequences for the inferred properties of the lower mantle. *Geophys. Res. Lett.*, *28*, 2699–2702. <https://doi.org/10.1029/2001GL012910>
- Karki, B.B., Wentzcovitch, R.M., de Gironcoli, S., & Baroni, S. (1999). First-principles determination of elastic anisotropy and wave velocities of MgO at lower mantle conditions. *Science*, *286*, 1705–1707. <https://doi.org/10.1126/science.286.5445.1705>
- Kato, J., Hirose, K., Ozawa, H., & Ohishi, Y. (2013). High-pressure experiments on phase transition boundaries between corundum, Rh₂O₃(II)- and CaIrO₃-type structures in Al₂O₃. *Am. Mineral.*, *98*, 335–339. <https://doi.org/10.2138/am.2013.4133>
- Katsura, T., Yoneda, A., Yamazaki, D., Yoshino, T., & Ito, E. (2010). Adiabatic temperature profile in the mantle. *Phys. Earth Planet. Inter.*, *183*, 212–218. <https://doi.org/10.1016/j.pepi.2010.07.001>
- Kavner, A., & Nugent, C. (2008). Precise measurements of radial temperature gradients in the laser-heated diamond anvil cell. *Rev. Sci. Instrum.*, *79*, 024902. <https://doi.org/10.1063/1.2841173>
- Kawai, K., & Tsuchiya, T. (2015). Small shear modulus of cubic CaSiO₃ perovskite. *Geophys. Res. Lett.*, *42*, 2718–2726. <https://doi.org/10.1002/2015GL063446>
- Kennett, B.L.N., & Engdahl, E.R. (1991). Traveltimes for global earthquake location and phase identification. *Geophys. J. Int.*, *105*, 429–465. <https://doi.org/10.1111/j.1365-246X.1991.tb06724.x>
- Kennett, B.L.N., Engdahl, E.R., & Buland, R. (1995). Constraints on seismic velocities in the Earth from traveltimes. *Geophys. J. Int.*, *122*, 108–124. <https://doi.org/10.1111/j.1365-246X.1995.tb03540.x>
- Keppler, H., Kantor, I., & Dubrovinsky, L.S. (2007). Optical absorption spectra of ferropericlase to 84 GPa. *Am. Mineral.*, *92*, 433–436. <https://doi.org/10.2138/am.2007.2454>
- Kesson, S.E., Gerald, J.D.F., & Shelley, J.M. (1998). Mineralogy and dynamics of a pyrolite lower mantle. *Nature*, *393*, 252–255. <https://doi.org/10.1038/30466>
- Kesson, S.E., Gerald, J.D.F., & Shelley, J.M.G. (1994). Mineral chemistry and density of subducted basaltic crust at lower-mantle pressures. *Nature*, *372*, 767–769. <https://doi.org/10.1038/372767a0>
- Khan, A., Connolly, J.A.D., & Taylor, S.R. (2008). Inversion of seismic and geodetic data for the major element chemistry and temperature of the Earth's mantle. *J. Geophys. Res. – Solid Earth*, *113*, B09308. <https://doi.org/10.1029/2007JB005239>
- Kobayashi, Y., Kondo, T., Ohtani, E., Hirao, N., Miyajima, N., Yagi, T., et al. (2005). Fe-Mg partitioning between (Mg, Fe) SiO₃ post-perovskite, perovskite, and magnesiowüstite in the Earth's lower mantle. *Geophys. Res. Lett.*, *32*, L19301. <https://doi.org/10.1029/2005GL023257>
- Koelemeijer, P., Ritsema, J., Deuss, A., & van Heijst, H.-J. (2016). SP12RTS: a degree-12 model of shear- and compressional-wave velocity for Earth's mantle. *Geophys. J. Int.*, *204*, 1024–1039. <https://doi.org/10.1093/gji/ggv481>
- Kohn, W., & Sham, L.J. (1965). Self-consistent equations including exchange and correlation effects. *Phys. Rev.*, *140*, A1133–A1138. <https://doi.org/10.1103/PhysRev.140.A1133>
- Komabayashi, T., Hirose, K., Nagaya, Y., Sugimura, E., & Ohishi, Y. (2010). High-temperature compression of ferropericlase and the effect of temperature on iron spin transition. *Earth Planet. Sci. Lett.*, *297*, 691–699. <https://doi.org/10.1016/j.epsl.2010.07.025>
- Komabayashi, T., & Omori, S. (2006). Internally consistent thermodynamic data set for dense hydrous magnesium silicates up to 35 GPa, 1600°C: Implications for water circulation in the Earth's deep mantle. *Phys. Earth Planet. Inter.*, *156*, 89–107. <https://doi.org/10.1016/j.pepi.2006.02.002>
- Krebs, J.J., & Maisch, W.G. (1971). Exchange effects in the optical-absorption spectrum of Fe³⁺ in Al₂O₃. *Phys. Rev. B*, *4*, 757–769. <https://doi.org/10.1103/PhysRevB.4.757>
- Kurnosov, A., Marquardt, H., Dubrovinsky, L., & Potapkin, V. (2019). A waveguide-based flexible CO₂-laser heating system for diamond-anvil cell applications. *Comptes Rendus Geosci.*, *351*, 280–285. <https://doi.org/10.1016/j.crte.2018.09.008>
- Kurnosov, A., Marquardt, H., Frost, D.J., Ballaran, T.B., & Ziberna, L. (2017). Evidence for a Fe³⁺-rich pyrolitic lowermantle from (Al,Fe)-bearing bridgmanite elasticity data. *Nature*, *543*, 543–546. <https://doi.org/10.1038/nature21390>
- Labrosse, S., Hernlund, J.W., & Hirose, K. (2015). Fractional melting and freezing in the deep mantle and implications for the formation of a basal magma ocean. In Badro, J., Walter, M. (Eds.), *The Early Earth: Accretion and Differentiation*. American Geophysical Union, Washington, D.C., pp. 123–142. <https://doi.org/10.1002/9781118860359.ch7>
- Lakshmanov, D.L., Sinogeikin, S.V., Litasov, K.D., Praka-penka, V.B., & Hellwig, H., Wang, J., et al. (2007). The post-stishovite phase transition in hydrous alumina-bearing SiO₂ in the lower mantle of the earth. *Proc. Natl. Acad. Sci. U.S.A.*, *104*, 13588–13590. <https://doi.org/10.1073/pnas.0706113104>
- Lehmann, G., Harder, H. (1970). Optical spectra of di- and trivalent iron in corundum. *Am. Mineral.*, *55*, 98–105.
- Li, B., Kung, J., & Liebermann, R.C. (2004). Modern techniques in measuring elasticity of Earth materials at high pressure and high temperature using ultrasonic interferometry in conjunction with synchrotron X-radiation in multi-anvil apparatus. *Phys. Earth Planet. Inter.*, *143–144*, 559–574. <https://doi.org/10.1016/j.pepi.2003.09.020>
- Li, B., Liebermann, R.C. (2014). Study of the Earth's interior using measurements of sound velocities in minerals by

- ultrasonic interferometry. *Phys. Earth Planet. Inter.*, *233*, 135–153. <https://doi.org/10.1016/j.pepi.2014.05.006>
- Li, J., Struzhkin, V.V., Mao, H., Shu, J., Hemley, R.J., Fei, Y., Mysen, B., et al. (2004). Electronic spin state of iron in lower mantle perovskite. *Proc. Natl. Acad. Sci. U.S.A.*, *101*, 14027–14030. <https://doi.org/10.1073/pnas.0405804101>
- Li, X., Mao, Z., Sun, N., Liao, Y., Zhai, S., Wang, Y., et al. (2016). Elasticity of single-crystal superhydrous phase B at simultaneous high pressure-temperature conditions. *Geophys. Res. Lett.*, *43*, 8458–8465. <https://doi.org/10.1002/2016GL070027>
- Liermann, H.-P., Merkel, S., Miyagi, L., Wenk, H.-R., Shen, G., Cynn, H., & Evans, W.J. (2009). Experimental method for *in situ* determination of material textures at simultaneous high pressure and high temperature by means of radial diffraction in the diamond anvil cell. *Rev. Sci. Instrum.*, *80*, 104501. <https://doi.org/10.1063/1.3236365>
- Lin, J.-F., Degtyareva, O., Prewitt, C.T., Dera, P., Sata, N., Gregoryanz, E., et al. (2004). Crystal structure of a high-pressure/high-temperature phase of alumina by *in situ* X-ray diffraction. *Nat. Mater.*, *3*, 389–393. <https://doi.org/10.1038/nmat1121>
- Lin, J.-F., Jacobsen, S.D., Sturhahn, W., Jackson, J.M., Zhao, J., & Yoo, C.-S. (2006). Sound velocities of ferropicliase in the Earth's lower mantle. *Geophys. Res. Lett.*, *33*, L22304. <https://doi.org/10.1029/2006GL028099>
- Lin, J.-F., Mao, Z., Yang, J., Liu, J., Xiao, Y., Chow, P., & Okuchi, T. (2016). High-spin Fe²⁺ and Fe³⁺ in single-crystal aluminous bridgmanite in the lower mantle. *Geophys. Res. Lett.*, *43*, 6952–6959. <https://doi.org/10.1002/2016GL069836>
- Lin, J.-F., Speziale, S., Mao, Z., & Marquardt, H. (2013). Effects of the electronic spin transitions of iron in lower mantle minerals: Implications for deep mantle geophysics and geochemistry. *Rev. Geophys.*, *51*, 244–275. <https://doi.org/10.1002/rog.20010>
- Lin, J.-F., Struzhkin, V.V., Jacobsen, S.D., Hu, M.Y., Chow, P., Kung, J., et al. (2005). Spin transition of iron in magnesiowüstite in the Earth's lower mantle. *Nature*, *436*, 377–380. <https://doi.org/10.1038/nature03825>
- Lin, J.-F., & Tsuchiya, T. (2008). Spin transition of iron in the Earth's lower mantle. *Phys. Earth Planet. Inter.*, *170*, 248–259. <https://doi.org/10.1016/j.pepi.2008.01.005>
- Lin, J.-F., Vanko, G., Jacobsen, S.D., Iota, V., Struzhkin, V.V., Prakapenka, V.B., et al. (2007). Spin transition zone in Earth's lower mantle. *Science*, *317*, 1740–1743. <https://doi.org/10.1126/science.1144997>
- Liu, J., Dorfman, S.M., Zhu, F., Li, J., Wang, Y., Zhang, D., Xiao, Y., et al. (2018). Valence and spin states of iron are invisible in Earth's lower mantle. *Nat. Commun.*, *9*, 1284. <https://doi.org/10.1038/s41467-018-03671-5>
- Mainprice, D. (2015). Seismic anisotropy of the deep Earth from a mineral and rock physics perspective. In Schubert, G. (Ed.), *Treatise on Geophysics*, 2nd ed., Elsevier, Amsterdam, pp. 487–538. <https://doi.org/10.1016/B978-0-444-53802-4.00044-0>
- Mainprice, D., Barruol, G., Ismail, W.B. (2000). The seismic anisotropy of the Earth's mantle: from single crystal to polycrystal. In Karato, S.-I., Forte, A., Liebermann, R., Masters, G., Stixrude, L. (Eds.), *Earth's Deep Interior: Mineral Physics and Tomography From the Atomic to the Global Scale*. American Geophysical Union, Washington, D.C., pp. 237–264. <https://doi.org/10.1029/GM117p0237>
- Mao, Z., Fan, D., Lin, J.-F., Yang, J., Tkachev, S.N., Zhuravlev, K., & Prakapenka, V.B. (2015). Elasticity of single-crystal olivine at high pressures and temperatures. *Earth Planet. Sci. Lett.*, *426*, 204–215. <https://doi.org/10.1016/j.epsl.2015.06.045>
- Mao, Z., Lin, J.-F., Jacobsen, S.D., Duffy, T.S., Chang, Y.-Y., Smyth, J.R., et al. (2012). Sound velocities of hydrous ringwoodite to 16 GPa and 673 K. *Earth Planet. Sci. Lett.*, *331–332*, 112–119. <https://doi.org/10.1016/j.epsl.2012.03.001>
- Mao, Z., Lin, J.-F., Liu, J., & Prakapenka, V.B. (2011). Thermal equation of state of lower-mantle ferropicliase across the spin crossover. *Geophys. Res. Lett.*, *38*, L23308. <https://doi.org/10.1029/2011GL049915>
- Marquardt, H., Buchen, J., Méndez, A.S.J., Kurnosov, A., Wendt, M., Rothkirch, A., et al. (2018). Elastic softening of (Mg_{0.8}Fe_{0.2})O ferropicliase across the iron spin crossover measured at seismic frequencies. *Geophys. Res. Lett.*, *45*, 6862–6868. <https://doi.org/10.1029/2018GL077982>
- Marquardt, H., Speziale, S., Jahn, S., Ganschow, S., & Schilling, F.R. (2009a). Single-crystal elastic properties of (Y,Yb)₃Al₅O₁₂. *J. Appl. Phys.*, *106*, 093519. <https://doi.org/10.1063/1.3245285>
- Marquardt, H., Speziale, S., Reichmann, H.J., Frost, D.J., & Schilling, F.R. (2009b). Single-crystal elasticity of (Mg_{0.9}Fe_{0.1})O to 81 GPa. *Earth Planet. Sci. Lett.*, *287*, 345–352. <https://doi.org/10.1016/j.epsl.2009.08.017>
- Marquardt, H., Speziale, S., Reichmann, H.J., Frost, D.J., Schilling, F.R., & Garnero, E.J. (2009c). Elastic shear anisotropy of ferropicliase in Earth's lower mantle. *Science*, *324*, 224–226. <https://doi.org/10.1126/science.1169365>
- Masters, G., Laske, G., Bolton, H., & Dziewonski, A. (2000). The relative behavior of shear velocity, bulk sound speed, and compressional velocity in the mantle: Implications for chemical and thermal structure. In Karato, S.-I., Forte, A., Liebermann, R., Masters, G., Stixrude, L. (Eds.), *Earth's Deep Interior: Mineral Physics and Tomography From the Atomic to the Global Scale*. American Geophysical Union, Washington, D.C., pp. 63–87. <https://doi.org/10.1029/GM117p0063>
- Matas, J., Bass, J., Ricard, Y., Mattern, E., & Bukowski, M.S. T. (2007). On the bulk composition of the lower mantle: predictions and limitations from generalized inversion of radial seismic profiles. *Geophys. J. Int.*, *170*, 764–780. <https://doi.org/10.1111/j.1365-246X.2007.03454.x>
- Mattern, E., Matas, J., Ricard, Y., & Bass, J. (2005). Lower mantle composition and temperature from mineral physics and thermodynamic modelling. *Geophys. J. Int.*, *160*, 973–990. <https://doi.org/10.1111/j.1365-246X.2004.02549.x>
- McDonough, W.F., & Sun, S.-s. (1995). The composition of the Earth. *Chem. Geol.*, *120*, 223–253. [https://doi.org/10.1016/0009-2541\(94\)00140-4](https://doi.org/10.1016/0009-2541(94)00140-4)
- McNamara, A.K. (2019). A review of large low shear velocity provinces and ultra low velocity zones. *Tectonophysics*, *760*, 199–220. <https://doi.org/10.1016/j.tecto.2018.04.015>
- Méndez, A.S.J., Marquardt, H., Husband, R.J., Schwark, I., Mainberger, J., Glazyrin, K., et al. (2020). A resistively-heated dynamic diamond anvil cell (RHdDAC) for fast

- compression x-ray diffraction experiments at high temperatures. *Rev. Sci. Instrum.*, *91*, 073906. <https://doi.org/10.1063/5.0007557>.
- Miletich, R., Hejny, C., Krauss, G., & Ullrich, A. (2005). Diffraction techniques: Shedding light on structural changes at extreme conditions. In Miletich, R. (Ed.), *Mineral Behaviour at Extreme Conditions*. European Mineralogical Union, pp. 281–338. <https://doi.org/10.1180/EMU-notes.7.13>
- Mookherjee, M. (2011). Mid-mantle anisotropy: Elasticity of aluminous phases in subducted MORB. *Geophys. Res. Lett.*, *38*, L14302. <https://doi.org/10.1029/2011GL047923>
- Morgan, J.P., & Morgan, W.J. (1999). Two-stage melting and the geochemical evolution of the mantle: a recipe for mantle plum-pudding. *Earth Planet. Sci. Lett.*, *170*, 215–239. [https://doi.org/10.1016/S0012-821X\(99\)00114-4](https://doi.org/10.1016/S0012-821X(99)00114-4)
- Muir, J.M.R., & Brodholt, J.P. (2016). Ferrous iron partitioning in the lower mantle. *Phys. Earth Planet. Inter.*, *257*, 12–17. <https://doi.org/10.1016/j.pepi.2016.05.008>
- Muir, J.M.R., & Brodholt, J.P. (2015a). Elastic properties of ferrous bearing MgSiO₃ and their relevance to ULVZs. *Geophys. J. Int.*, *201*, 496–504. <https://doi.org/10.1093/gji/ggv045>
- Muir, J.M.R., & Brodholt, J.P. (2015b). Elastic properties of ferropericlasite at lower mantle conditions and its relevance to ULVZs. *Earth Planet. Sci. Lett.*, *417*, 40–48. <https://doi.org/10.1016/j.epsl.2015.02.023>
- Murakami, M., Asahara, Y., Ohishi, Y., Hirao, N., & Hirose, K. (2009a). Development of in situ Brillouin spectroscopy at high pressure and high temperature with synchrotron radiation and infrared laser heating system: Application to the Earth's deep interior. *Phys. Earth Planet. Inter.*, *174*, 282–291. <https://doi.org/10.1016/j.pepi.2008.07.030>
- Murakami, M., Hirose, K., Kawamura, K., Sata, N., & Ohishi, Y. (2004). Post-perovskite phase transition in MgSiO₃. *Science*, *304*, 855–858. <https://doi.org/10.1126/science.1095932>
- Murakami, M., Hirose, K., Sata, N., & Ohishi, Y. (2005). Post-perovskite phase transition and mineral chemistry in the pyrolytic lowermost mantle. *Geophys. Res. Lett.*, *32*, L03304. <https://doi.org/10.1029/2004GL021956>
- Murakami, M., Ohishi, Y., Hirao, N., & Hirose, K. (2012). A perovskitic lower mantle inferred from high-pressure, high-temperature sound velocity data. *Nature*, *485*, 90–94. <https://doi.org/10.1038/nature11004>
- Murakami, M., Ohishi, Y., Hirao, N., & Hirose, K. (2009b). Elasticity of MgO to 130 GPa: Implications for lower mantle mineralogy. *Earth Planet. Sci. Lett.*, *277*, 123–129. <https://doi.org/10.1016/j.epsl.2008.10.010>
- Murakami, M., Sinogeikin, S.V., Hellwig, H., Bass, J.D., & Li, J. (2007). Sound velocity of MgSiO₃ perovskite to Mbar pressure. *Earth Planet. Sci. Lett.*, *256*, 47–54. <https://doi.org/10.1016/j.epsl.2007.01.011>
- Murnaghan, F.D. (1937). Finite deformations of an elastic solid. *Am. J. Math.*, *59*, 235–260. <https://doi.org/10.2307/2371405>
- Nagai, T., Hamane, D., Devi, P.S., Miyajima, N., Yagi, T., Yamanaka, T., & Fujino, K. (2005). A new polymorph of FeAlO₃ at high pressure. *J. Phys. Chem. B*, *109*, 18226–18229. <https://doi.org/10.1021/jp054409s>
- Nakagawa, T., Tackley, P.J., Deschamps, F., & Connolly, J.A.D. (2010). The influence of MORB and harzburgite composition on thermo-chemical mantle convection in a 3-D spherical shell with self-consistently calculated mineral physics. *Earth Planet. Sci. Lett.*, *296*, 403–412. <https://doi.org/10.1016/j.epsl.2010.05.026>
- Nakajima, Y., Frost, D.J., & Rubie, D.C. (2012). Ferrous iron partitioning between magnesium silicate perovskite and ferropericlasite and the composition of perovskite in the Earth's lower mantle. *J. Geophys. Res. – Solid Earth*, *117*, B08201. <https://doi.org/10.1029/2012JB009151>
- Nielsen, O.H., & Martin, R.M. (1985). Quantum-mechanical theory of stress and force. *Phys. Rev. B*, *32*, 3780–3791. <https://doi.org/10.1103/PhysRevB.32.3780>
- Nomura, R., Hirose, K., Sata, N., & Ohishi, Y. (2010). Precise determination of post-stishovite phase transition boundary and implications for seismic heterogeneities in the mid-lower mantle. *Phys. Earth Planet. Inter.*, *183*, 104–109. <https://doi.org/10.1016/j.pepi.2010.08.004>
- Norby, P., & Schwarz, U. (2008). Powder diffraction under non-ambient conditions. In Dinnebier, R.E., Billinge, S.J.L. (Eds.), *Powder Diffraction: Theory and Practice*. Royal Society of Chemistry, Cambridge, pp. 439–463. <https://doi.org/10.1039/978184758237-00439>
- Nye, J.F. (1985). *Physical Properties of Crystals: Their Representation by Tensors and Matrices*. Oxford University Press, Oxford.
- Oganov, A.R., Brodholt, J.P., & Price, G.D. (2001). The elastic constants of MgSiO₃ perovskite at pressures and temperatures of the Earth's mantle. *Nature*, *411*, 934–937. <https://doi.org/10.1038/35082048>
- Oganov, A.R., & Dorogokupets, P.I. (2004). Intrinsic anharmonicity in equations of state and thermodynamics of solids. *J. Phys.: Condens. Matter*, *16*, 1351–1360. <https://doi.org/10.1088/0953-8984/16/8/018>
- Oganov, A.R., & Dorogokupets, P.I. (2003). All-electron and pseudopotential study of MgO: Equation of state, anharmonicity, and stability. *Phys. Rev. B*, *67*, 224110. <https://doi.org/10.1103/PhysRevB.67.224110>
- Ohnishi, S. (1978). A theory of the pressure-induced high-spin–low-spin transition of transition-metal oxides. *Phys. Earth Planet. Inter.*, *17*, 130–139. [https://doi.org/10.1016/0031-9201\(78\)90054-7](https://doi.org/10.1016/0031-9201(78)90054-7)
- Ohnishi, S., & Sugano, S. (1981). Strain interaction effects on the high-spin–low-spin transition of transition-metal compounds. *J. Phys. C: Solid State Phys.*, *14*, 39–55. <https://doi.org/10.1088/0022-3719/14/1/007>
- Ono, S., Ito, E., & Katsura, T. (2001). Mineralogy of subducted basaltic crust (MORB) from 25 to 37 GPa, and chemical heterogeneity of the lower mantle. *Earth Planet. Sci. Lett.*, *190*, 57–63. [https://doi.org/10.1016/S0012-821X\(01\)00375-2](https://doi.org/10.1016/S0012-821X(01)00375-2)
- Perdew, J.P., & Ruzsinszky, A. (2010). Density functional theory of electronic structure: a short course for mineralogists and geophysicists. *Rev. Mineral. Geochem.*, *71*, 1–18. <https://doi.org/10.2138/rmg.2010.71.1>
- Perrillat, J.-P., Ricolleau, A., Daniel, I., Fiquet, G., Mezouar, M., Guignot, N., & Cardon, H. (2006). Phase transformations of subducted basaltic crust in the uppermost lower mantle. *Phys. Earth Planet. Inter.*, *157*, 139–149. <https://doi.org/10.1016/j.pepi.2006.04.001>

- Persson, K., Bengtson, A., Ceder, G., & Morgan, D. (2006). Ab initio study of the composition dependence of the pressure-induced spin transition in the $(\text{Mg}_{1-x}\text{Fe}_x)\text{O}$ system. *Geophys. Res. Lett.*, *33*, L16306. <https://doi.org/10.1029/2006GL026621>
- Piet, H., Badro, J., Nabiei, F., Dennenwaldt, T., Shim, S.-H., Cantoni, M., Hébert, C., & Gillet, P. (2016). Spin and valence dependence of iron partitioning in Earth's deep mantle. *Proc. Natl. Acad. Sci. U.S.A.*, *113*, 11127–11130. <https://doi.org/10.1073/pnas.1605290113>
- Prescher, C., Langenhorst, F., Dubrovinsky, L.S., Prakapenka, V.B., & Miyajima, N. (2014). The effect of Fe spin crossovers on its partitioning behavior and oxidation state in a pyrolytic Earth's lower mantle system. *Earth Planet. Sci. Lett.*, *399*, 86–91. <https://doi.org/10.1016/j.epsl.2014.05.011>
- Rainey, E.S.G., & Kavner, A. (2014). Peak scaling method to measure temperatures in the laser-heated diamond anvil cell and application to the thermal conductivity of MgO. *J. Geophys. Res. – Solid Earth*, *119*, 8154–8170. <https://doi.org/10.1002/2014JB011267>
- Reichmann, H.J., Angel, R.J., Spetzler, H., & Bassett, W.A. (1998). Ultrasonic interferometry and X-ray measurements on MgO in a new diamond anvil cell. *Am. Mineral.*, *83*, 1357–1360. <https://doi.org/10.2138/am-1998-11-1226>
- Reichmann, H.J., & Jacobsen, S.D. (2004). High-pressure elasticity of a natural magnetite crystal. *Am. Mineral.*, *89*, 1061–1066. <https://doi.org/10.2138/am-2004-0718>
- Reuss, A. (1929.) Berechnung der Fließgrenze von Mischkristallen auf Grund der Plastizitätsbedingung für Einkristalle. *Z. Angew. Math. Mech.*, *9*, 49–58 (in German). <https://doi.org/10.1002/zamm.19290090104>
- Richards, M.A., & Engebretson, D.C. (1992). Large-scale mantle convection and the history of subduction. *Nature*, *355*, 437–440. <https://doi.org/10.1038/355437a0>
- Richmond, N.C., & Brodholt, J.P. (1998). Calculated role of aluminum in the incorporation of ferric iron into magnesium silicate perovskite. *Am. Mineral.*, *83*, 947–951. <https://doi.org/10.2138/am-1998-9-1003>
- Ricolleau, A., Perrillat, J.-P., Fiquet, G., Daniel, I., Matas, J., Addad, A., et al. (2010). Phase relations and equation of state of a natural MORB: Implications for the density profile of subducted oceanic crust in the Earth's lower mantle. *J. Geophys. Res. – Solid Earth*, *115*, B08202. <https://doi.org/10.1029/2009JB006709>
- Rost, S., Garnero, E.J., & Williams, Q. (2008). Seismic array detection of subducted oceanic crust in the lower mantle. *J. Geophys. Res. – Solid Earth*, *113*, B06303. <https://doi.org/10.1029/2007JB005263>
- Sakai, T., Ohtani, E., Terasaki, H., Sawada, N., Kobayashi, Y., Miyahara, M., et al. (2009). Fe-Mg partitioning between perovskite and ferropericlasite in the lower mantle. *Am. Mineral.*, *94*, 921–925. <https://doi.org/10.2138/am.2009.3123>
- Sammis, C., Anderson, D., & Jordan, T. (1970). Application of isotropic finite strain theory to ultrasonic and seismological data. *J. Geophys. Res.*, *75*, 4478–4480. <https://doi.org/10.1029/JB075i023p04478>
- Schreuer, J., & Haussühl, S. (2005). Elastic and piezoelectric properties of minerals I. Principles and experimental approaches. In Miletich, R. (Ed.), *Mineral Behaviour at Extreme Conditions*. European Mineralogical Union, pp. 95–116. <https://doi.org/10.1180/EMU-notes.7.4>
- Schuberth, B.S.A., Bunge, H.-P., & Ritsema, J. (2009a). Tomographic filtering of high-resolution mantle circulation models: Can seismic heterogeneity be explained by temperature alone? *Geochem. Geophys. Geosystems*, *10*, Q05W03. <https://doi.org/10.1029/2009GC002401>
- Schuberth, B.S.A., Bunge, H.-P., Steinle-Neumann, G., Moder, C., Oeser, J. (2009). Thermal versus elastic heterogeneity in high-resolution mantle circulation models with pyrolite composition: High plume excess temperatures in the lowermost mantle. *Geochem. Geophys. Geosystems*, *10*, Q01W01. <https://doi.org/10.1029/2008GC002235>
- Schulze, K., Marquardt, H., Kawazoe, T., Boffa Ballaran, T., McCammon, C., Koch-Müller, M., et al. (2018). Seismically invisible water in Earth's transition zone? *Earth Planet. Sci. Lett.*, *498*, 9–16. <https://doi.org/10.1016/j.epsl.2018.06.021>
- Sherman, D.M. (1991). The high-pressure electronic structure of magnesiowustite (Mg, Fe)O: Applications to the physics and chemistry of the lower mantle. *J. Geophys. Res. – Solid Earth*, *96*, 14299–14312. <https://doi.org/10.1029/91JB01202>
- Sherman, D.M. (1985). The electronic structures of Fe^{3+} coordination sites in iron oxides: Applications to spectra, bonding, and magnetism. *Phys. Chem. Miner.*, *12*, 161–175. <https://doi.org/10.1007/BF00308210>
- Shim, S.-H., Duffy, T.S., Jeanloz, R., & Shen, G. (2004). Stability and crystal structure of MgSiO_3 perovskite to the core-mantle boundary. *Geophys. Res. Lett.*, *31*, L10603. <https://doi.org/10.1029/2004GL019639>
- Shim, S.-H., Jeanloz, R., & Duffy, T.S. (2002). Tetragonal structure of CaSiO_3 perovskite above 20 GPa. *Geophys. Res. Lett.*, *29*, 2166. <https://doi.org/10.1029/2002GL016148>
- Shukla, G., Cococcioni, M., & Wentzcovitch, R.M. (2016). Thermoelasticity of Fe^{3+} - and Al-bearing bridgmanite: Effects of iron spin crossover. *Geophys. Res. Lett.*, *43*, 5661–5670. <https://doi.org/10.1002/2016GL069332>
- Shukla, G., Wu, Z., Hsu, H., Floris, A., Cococcioni, M., & Wentzcovitch, R.M. (2015). Thermoelasticity of Fe^{2+} -bearing bridgmanite. *Geophys. Res. Lett.*, *42*, 1741–1749. <https://doi.org/10.1002/2014GL062888>
- Sigloch, K., McQuarrie, N., & Nolet, G. (2008). Two-stage subduction history under North America inferred from multiple-frequency tomography. *Nat. Geosci.*, *1*, 458–462. <https://doi.org/10.1038/ngeo231>
- Simmons, N.A., Myers, S.C., Johannesson, G., Matzel, E., & Grand, S.P. (2015). Evidence for long-lived subduction of an ancient tectonic plate beneath the southern Indian Ocean. *Geophys. Res. Lett.*, *42*, 9270–9278. <https://doi.org/10.1002/2015GL066237>
- Sinmyo, R., & Hirose, K. (2013). Iron partitioning in pyrolytic lower mantle. *Phys. Chem. Miner.*, *40*, 107–113. <https://doi.org/10.1007/s00269-012-0551-7>
- Sinmyo, R., & Hirose, K. (2010). The Soret diffusion in laser-heated diamond-anvil cell. *Phys. Earth Planet. Inter.*, *180*, 172–178. <https://doi.org/10.1016/j.pepi.2009.10.011>
- Sinmyo, R., Hirose, K., Nishio-Hamane, D., Seto, Y., Fujino, K., Sata, N., & Ohishi, Y. (2008). Partitioning of iron between

- perovskite/postperovskite and ferropericlasite in the lower mantle. *J. Geophys. Res. – Solid Earth*, *113*, B11204. <https://doi.org/10.1029/2008JB005730>
- Sinogeikin, S., Bass, J., Prakapenka, V., Lakshtanov, D., Shen, G., Sanchez-Valle, C., & Rivers, M. (2006). Brillouin spectrometer interfaced with synchrotron radiation for simultaneous x-ray density and acoustic velocity measurements. *Rev. Sci. Instrum.*, *77*, 103905. <https://doi.org/10.1063/1.2360884>
- Sinogeikin, S.V., & Bass, J.D. (2000). Single-crystal elasticity of pyrope and MgO to 20 GPa by Brillouin scattering in the diamond cell. *Phys. Earth Planet. Inter.*, *120*, 43–62. [https://doi.org/10.1016/S0031-9201\(00\)00143-6](https://doi.org/10.1016/S0031-9201(00)00143-6)
- Sinogeikin, S.V., Katsura, T., & Bass, J.D. (1998). Sound velocities and elastic properties of Fe-bearing wadsleyite and ringwoodite. *J. Geophys. Res. – Solid Earth*, *103*, 20819–20825. <https://doi.org/10.1029/98JB01819>
- Sinogeikin, S.V., Lakshtanov, D.L., Nicholas, J.D., & Bass, J.D. (2004). Sound velocity measurements on laser-heated MgO and Al₂O₃. *Phys. Earth Planet. Inter.*, *143–144*, 575–586. <https://doi.org/10.1016/j.pepi.2003.09.017>
- Sobolev, A.V., Hofmann, A.W., Kuzmin, D.V., Yaxley, G.M., Arndt, N.T., Chung, S.-L., et al. (2007). The amount of recycled crust in sources of mantle-derived melts. *Science*, *316*, 412–417. <https://doi.org/10.1126/science.1138113>
- Solomatova, N.V., Jackson, J.M., Sturhahn, W., Wicks, J.K., Zhao, J., Toellner, T.S., et al. (2016). Equation of state and spin crossover of (Mg,Fe)O at high pressure, with implications for explaining topographic relief at the core–mantle boundary. *Am. Mineral.*, *101*, 1084–1093. <https://doi.org/10.2138/am-2016-5510>
- Spasojevic, S., Gurnis, M., & Sutherland, R. (2010). Mantle upwellings above slab graveyards linked to the global geoid lows. *Nat. Geosci.*, *3*, 435–438. <https://doi.org/10.1038/ngeo855>
- Spetzler, H. (1970). Equation of state of polycrystalline and single-crystal MgO to 8 kilobars and 800°K. *J. Geophys. Res.*, *75*, 2073–2087. <https://doi.org/10.1029/JB075i011p02073>
- Spetzler, H., Shen, A., Chen, G., Herrmannsdoerfer, G., Schulze, H., & Weigel, R. (1996). Ultrasonic measurements in a diamond anvil cell. *Phys. Earth Planet. Inter.*, *98*, 93–99. [https://doi.org/10.1016/S0031-9201\(96\)03171-8](https://doi.org/10.1016/S0031-9201(96)03171-8)
- Speziale, S., Lee, V.E., Clark, S.M., Lin, J.F., Pasternak, M.P., & Jeanloz, R. (2007). Effects of Fe spin transition on the elasticity of (Mg, Fe)O magnesiowüstites and implications for the seismological properties of the Earth's lower mantle. *J. Geophys. Res. – Solid Earth*, *112*, B10212. <https://doi.org/10.1029/2006JB004730>
- Speziale, S., Marquardt, H., & Duffy, T.S. (2014). Brillouin scattering and its application in geosciences. *Rev. Mineral. Geochem.*, *78*, 543–603. <https://doi.org/10.2138/rmg.2014.78.14>
- Speziale, S., Milner, A., Lee, V.E., Clark, S.M., Pasternak, M.P., & Jeanloz, R. (2005). Iron spin transition in Earth's mantle. *Proc. Natl. Acad. Sci. U.S.A.*, *102*, 17918–17922. <https://doi.org/10.1073/pnas.0508919102>
- Stacey, F.D., & Davis, P.M. (2004). High pressure equations of state with applications to the lower mantle and core. *Phys. Earth Planet. Inter.*, *142*, 137–184. <https://doi.org/10.1016/j.pepi.2004.02.003>
- Stackhouse, S., Brodholt, J.P., & Price, G.D. (2006). Elastic anisotropy of FeSiO₃ end-members of the perovskite and post-perovskite phases. *Geophys. Res. Lett.*, *33*, L01304. <https://doi.org/10.1029/2005GL023887>
- Stackhouse, S., Brodholt, J.P., & Price, G.D. (2005a). High temperature elastic anisotropy of the perovskite and post-perovskite polymorphs of Al₂O₃. *Geophys. Res. Lett.*, *32*, L13305. <https://doi.org/10.1029/2005GL023163>
- Stackhouse, S., Brodholt, J.P., Wookey, J., Kendall, J.-M., & Price, G.D. (2005b). The effect of temperature on the seismic anisotropy of the perovskite and post-perovskite polymorphs of MgSiO₃. *Earth Planet. Sci. Lett.*, *230*, 1–10. <https://doi.org/10.1016/j.epsl.2004.11.021>
- Stackhouse, S., Stixrude, L., & Karki, B.B. (2010). Determination of the high-pressure properties of fayalite from first-principles calculations. *Earth Planet. Sci. Lett.*, *289*, 449–456. <https://doi.org/10.1016/j.epsl.2009.11.033>
- Steinberger, B. (2000). Slabs in the lower mantle — results of dynamic modelling compared with tomographic images and the geoid. *Phys. Earth Planet. Inter.*, *118*, 241–257. [https://doi.org/10.1016/S0031-9201\(99\)00172-7](https://doi.org/10.1016/S0031-9201(99)00172-7)
- Stephens, D.R., & Drickamer, H.G. (1961a). Effect of pressure on the spectrum of ruby. *J. Chem. Phys.*, *35*, 427–429. <https://doi.org/10.1063/1.1731945>
- Stephens, D.R., & Drickamer, H.G. (1961b). Effect of pressure on the spectra of five nickel complexes. *J. Chem. Phys.*, *34*, 937–940. <https://doi.org/10.1063/1.1731696>
- Stixrude, L., Cohen, R.E., & Hemley, R.J. (1998). Theory of minerals at high pressure. *Rev. Mineral. Geochem.*, *37*, 639–671.
- Stixrude, L., & Lithgow-Bertelloni, C. (2012). Geophysics of chemical heterogeneity in the mantle. *Annu. Rev. Earth Planet. Sci.*, *40*, 569–595. <https://doi.org/10.1146/annurev.earth.36.031207.124244>
- Stixrude, L., & Lithgow-Bertelloni, C. (2011). Thermodynamics of mantle minerals — II. Phase equilibria. *Geophys. J. Int.*, *184*, 1180–1213. <https://doi.org/10.1111/j.1365-246X.2010.04890.x>
- Stixrude, L., & Lithgow-Bertelloni, C. (2005). Thermodynamics of mantle minerals — I. Physical properties. *Geophys. J. Int.*, *162*, 610–632. <https://doi.org/10.1111/j.1365-246X.2005.02642.x>
- Stixrude, L., Lithgow-Bertelloni, C., Kiefer, B., & Fumagalli, P. (2007). Phase stability and shear softening in CaSiO₃ perovskite at high pressure. *Phys. Rev. B*, *75*, 024108. <https://doi.org/10.1103/PhysRevB.75.024108>
- Stracke, A. (2012). Earth's heterogeneous mantle: A product of convection-driven interaction between crust and mantle. *Chem. Geol.*, *330–331*, 274–299. <https://doi.org/10.1016/j.chemgeo.2012.08.007>
- Sturhahn, W. (2004). Nuclear resonant spectroscopy. *J. Phys.: Condens. Matter*, *16*, S497–S530. <https://doi.org/10.1088/0953-8984/16/5/009>
- Sturhahn, W., Jackson, J.M. (2007). Geophysical applications of nuclear resonant spectroscopy. In Ohtani, E. (Ed.), *Advances in High-Pressure Mineralogy*, Geological Society of America, Boulder, CO, pp. 157–174. [https://doi.org/10.1130/2007.2421\(09\)](https://doi.org/10.1130/2007.2421(09))

- Sturhahn, W., Jackson, J.M., Lin, J.-F. (2005). The spin state of iron in minerals of Earth's lower mantle. *Geophys. Res. Lett.*, 32, L12307. <https://doi.org/10.1029/2005GL022802>
- Sun, N., Wei, W., Han, S., Song, J., Li, X., Duan, Y., Praka-penka, V.B., & Mao, Z. (2018). Phase transition and thermal equations of state of (Fe,Al)-bridgmanite and post-perovskite: Implication for the chemical heterogeneity at the lowermost mantle. *Earth Planet. Sci. Lett.*, 490, 161–169. <https://doi.org/10.1016/j.epsl.2018.03.004>
- Tanabe, Y., & Sugano, S. (1954a). On the absorption spectra of complex ions I. *J. Phys. Soc. Jpn.*, 9, 753–766. <https://doi.org/10.1143/JPSJ.9.753>
- Tanabe, Y., & Sugano, S. (1954b). On the absorption spectra of complex ions II. *J. Phys. Soc. Jpn.*, 9, 766–779. <https://doi.org/10.1143/JPSJ.9.766>
- Thomsen, L. (1972a). The fourth-order anharmonic theory: Elasticity and stability. *J. Phys. Chem. Solids*, 33, 363–378. [https://doi.org/10.1016/0022-3697\(72\)90018-2](https://doi.org/10.1016/0022-3697(72)90018-2)
- Thomsen, L. (1972b). Elasticity of polycrystals and rocks. *J. Geophys. Res.*, 77, 315–327. <https://doi.org/10.1029/JB077i002p00315>
- Thomson, A.R., Crichton, W.A., Brodholt, J.P., Wood, I.G., Siersch, N.C., Muir, J.M.R., et al. (2019). Seismic velocities of CaSiO₃ perovskite can explain LLSVPs in Earth's lower mantle. *Nature*, 572, 643–647. <https://doi.org/10.1038/s41586-019-1483-x>
- Trampert, J., Deschamps, F., Resovsky, J., & Yuen, D. (2004). Probabilistic tomography maps chemical heterogeneities throughout the lower mantle. *Science*, 306, 853–856. <https://doi.org/10.1126/science.1101996>
- Tröster, A., Ehsan, S., Belbase, K., Blaha, P., Kreisel, J., & Schranz, W. (2017). Finite-strain Landau theory applied to the high-pressure phase transition of lead titanate. *Phys. Rev. B*, 95, 064111. <https://doi.org/10.1103/PhysRevB.95.064111>
- Tröster, A., Schranz, W., Karsai, F., & Blaha, P. (2014). Fully consistent finite-strain Landau theory for high-pressure phase transitions. *Phys. Rev. X*, 4, 031010. <https://doi.org/10.1103/PhysRevX.4.031010>
- Tröster, A., Schranz, W., & Miletich, R. (2002). How to couple Landau theory to an equation of state. *Phys. Rev. Lett.*, 88, 055503. <https://doi.org/10.1103/PhysRevLett.88.055503>
- Tsuchiya, T., Wentzcovitch, R.M., da Silva, C.R.S., & de Gironcoli, S. (2006). Spin transition in magnesiowüstite in Earth's lower mantle. *Phys. Rev. Lett.*, 96. <https://doi.org/10.1103/PhysRevLett.96.198501>
- van der Hilst, R.D., Widiyantoro, S., & Engdahl, E.R. (1997). Evidence for deep mantle circulation from global tomography. *Nature*, 386, 578–584. <https://doi.org/10.1038/386578a0>
- Voigt, W. (1928). *Lehrbuch der Kristallphysik*. Teubner, Leipzig (in German).
- Wadhawan, V.K. (1982). Ferroelasticity and related properties of crystals. *Phase Transitions*, 3, 3–103. <https://doi.org/10.1080/01411598208241323>
- Wang, X., Tsuchiya, T., & Hase, A. (2015). Computational support for a pyrolitic lower mantle containing ferric iron. *Nat. Geosci.*, 8, 556–559. <https://doi.org/10.1038/ngeo2458>
- Waszek, L., Schmerr, N.C., & Ballmer, M.D. (2018). Global observations of reflectors in the mid-mantle with implications for mantle structure and dynamics. *Nat. Commun.*, 9, 385. <https://doi.org/10.1038/s41467-017-02709-4>
- Watt, J.P., Davies, G.F., & O'Connell, R.J. (1976). The elastic properties of composite materials. *Rev. Geophys.*, 14, 541–563. <https://doi.org/10.1029/RG014i004p00541>
- Weidner, D.J., Sawamoto, H., Sasaki, S., & Kumazawa, M. (1984). Single-crystal elastic properties of the spinel phase of Mg₂SiO₄. *J. Geophys. Res. – Solid Earth*, 89, 7852–7860. <https://doi.org/10.1029/JB089iB09p07852>
- Wentzcovitch, R.M., Justo, J.F., Wu, Z., Silva, C.R.S. da, Yuen, D.A., & Kohlstedt, D. (2009). Anomalous compressibility of ferropericlase throughout the iron spin cross-over. *Proc. Natl. Acad. Sci. U.S.A.*, 106, 8447–8452. <https://doi.org/10.1073/pnas.0812150106>
- Wentzcovitch, R.M., Karki, B.B., Cococcioni, M., & de Gironcoli, S. (2004). Thermoelastic properties of MgSiO₃-perovskite: Insights on the nature of the Earth's lower mantle. *Phys. Rev. Lett.*, 92, 018501. <https://doi.org/10.1103/PhysRevLett.92.018501>
- Wentzcovitch, R.M., Martins, J.L., & Price, G.D. (1993). Ab initio molecular dynamics with variable cell shape: Application to MgSiO₃. *Phys. Rev. Lett.*, 70, 3947–3950. <https://doi.org/10.1103/PhysRevLett.70.3947>
- Wentzcovitch, R.M., Ross, N.L., & Price, G.D. (1995). Ab initio study of MgSiO₃ and CaSiO₃ perovskites at lower-mantle pressures. *Phys. Earth Planet. Inter.*, 90, 101–112. [https://doi.org/10.1016/0031-9201\(94\)03001-Y](https://doi.org/10.1016/0031-9201(94)03001-Y)
- Wentzcovitch, R.M., Tsuchiya, T., & Tsuchiya, J. (2006). MgSiO₃ postperovskite at D'' conditions. *Proc. Natl. Acad. Sci. U.S.A.*, 103, 543–546. <https://doi.org/10.1073/pnas.0506879103>
- Wentzcovitch, R.M., Wu, Z., & Carrier, P. (2010a). First principles quasiharmonic thermoelasticity of mantle minerals. *Rev. Mineral. Geochem.*, 71, 99–128. <https://doi.org/10.2138/rmg.2010.71.5>
- Wentzcovitch, R.M., Yu, Y.G., & Wu, Z. (2010b). Thermodynamic properties and phase relations in mantle minerals investigated by first principles quasiharmonic theory. *Rev. Mineral. Geochem.*, 71, 59–98. <https://doi.org/10.2138/rmg.2010.71.4>
- Wicks, J.K., Jackson, J.M., & Sturhahn, W. (2010). Very low sound velocities in iron-rich (Mg,Fe)O: Implications for the core–mantle boundary region. *Geophys. Res. Lett.*, 37, L15304. <https://doi.org/10.1029/2010GL043689>
- Wicks, J.K., Jackson, J.M., Sturhahn, W., & Zhang, D. (2017). Sound velocity and density of magnesiowüstites: Implications for ultralow-velocity zone topography. *Geophys. Res. Lett.*, 44, 2148–2158. <https://doi.org/10.1002/2016GL071225>
- Workman, R.K., & Hart, S.R. (2005). Major and trace element composition of the depleted MORB mantle (DMM). *Earth Planet. Sci. Lett.*, 231, 53–72. <https://doi.org/10.1016/j.epsl.2004.12.005>
- Wu, Y., Qin, F., Wu, X., Huang, H., McCammon, C.A., Yoshino, T., et al. (2017). Spin transition of ferric iron in the calcium-ferrite type aluminous phase. *J. Geophys. Res. – Solid Earth*, 122, 5935–5944. <https://doi.org/10.1002/2017JB014095>

- Wu, Y., Wu, X., Lin, J.-F., McCammon, C.A., Xiao, Y., Chow, P., et al. (2016). Spin transition of ferric iron in the NAL phase: Implications for the seismic heterogeneities of subducted slabs in the lower mantle. *Earth Planet. Sci. Lett.*, *434*, 91–100. <https://doi.org/10.1016/j.epsl.2015.11.011>
- Wu, Z., Justo, J.F., da Silva, C.R.S., de Gironcoli, S., & Wentzcovitch, R.M. (2009). Anomalous thermodynamic properties in ferropericlase throughout its spin crossover. *Phys. Rev. B*, *80*, 014409. <https://doi.org/10.1103/PhysRevB.80.014409>
- Wu, Z., Justo, J.F., & Wentzcovitch, R.M. (2013). Elastic anomalies in a spin-crossover system: Ferropericlase at lower mantle conditions. *Phys. Rev. Lett.*, *110*, 228501. <https://doi.org/10.1103/PhysRevLett.110.228501>
- Wu, Z., & Wentzcovitch, R.M. (2014). Spin crossover in ferropericlase and velocity heterogeneities in the lower mantle. *Proc. Natl. Acad. Sci. U.S.A.*, *111*, 10468–10472. <https://doi.org/10.1073/pnas.1322427111>
- Wu, Z., & Wentzcovitch, R.M. (2011). Quasiharmonic thermal elasticity of crystals: an analytical approach. *Phys. Rev. B*, *83*, 184115. <https://doi.org/10.1103/PhysRevB.83.184115>
- Wu, Z., & Wentzcovitch, R.M. (2009). Effective semiempirical ansatz for computing anharmonic free energies. *Phys. Rev. B*, *79*, 104304. <https://doi.org/10.1103/PhysRevB.79.104304>
- Xu, S., Lin, J.-F., & Morgan, D. (2017). Iron partitioning between ferropericlase and bridgmanite in the Earth's lower mantle. *J. Geophys. Res. – Solid Earth*, *122*, 1074–1087. <https://doi.org/10.1002/2016JB013543>
- Xu, W., Lithgow-Bertelloni, C., Stixrude, L., & Ritsema, J. (2008). The effect of bulk composition and temperature on mantle seismic structure. *Earth Planet. Sci. Lett.*, *275*, 70–79. <https://doi.org/10.1016/j.epsl.2008.08.012>
- Yamazaki, D., Ito, E., Yoshino, T., Tsujino, N., Yoneda, A., Gomi, H., et al. (2019). High-pressure generation in the Kawai-type multianvil apparatus equipped with tungsten-carbide anvils and sintered-diamond anvils, and X-ray observation on CaSnO_3 and $(\text{Mg,Fe})\text{SiO}_3$. *Comptes Rendus Geosci.*, *351*, 253–259. <https://doi.org/10.1016/j.crte.2018.07.004>
- Yang, J., Lin, J.-F., Jacobsen, S.D., Seymour, N.M., Tkachev, S.N., & Prakapenka, V.B. (2016). Elasticity of ferropericlase and seismic heterogeneity in the Earth's lower mantle. *J. Geophys. Res. – Solid Earth*, *121*, 8488–8500. <https://doi.org/10.1002/2016JB013352>
- Yang, J., Tong, X., Lin, J.-F., Okuchi, T., & Tomioka, N. (2015). Elasticity of ferropericlase across the spin crossover in the Earth's lower mantle. *Sci. Rep.*, *5*, 17188. <https://doi.org/10.1038/srep17188>
- Yang, R., & Wu, Z. (2014). Elastic properties of stishovite and the CaCl_2 -type silica at the mantle temperature and pressure: an ab initio investigation. *Earth Planet. Sci. Lett.*, *404*, 14–21. <https://doi.org/10.1016/j.epsl.2014.07.020>
- Yu, S., & Garner, E.J. (2018). Ultralow velocity zone locations: a global assessment. *Geochem. Geophys. Geosystems*, *19*, 396–414. <https://doi.org/10.1002/2017GC007281>
- Zha, C., Duffy, T.S., Downs, R.T., Mao, H., & Hemley, R.J. (1998). Brillouin scattering and X-ray diffraction of San Carlos olivine: direct pressure determination to 32 GPa. *Earth Planet. Sci. Lett.*, *159*, 25–33. [https://doi.org/10.1016/S0012-821X\(98\)00063-6](https://doi.org/10.1016/S0012-821X(98)00063-6)
- Zha, C.-S., Mao, H.-K., & Hemley, R.J. (2000). Elasticity of MgO and a primary pressure scale to 55 GPa. *Proc. Natl. Acad. Sci. U.S.A.*, *97*, 13494–13499. <https://doi.org/10.1073/pnas.240466697>
- Zhang, F., Oganov, A.R. (2006). Valence state and spin transitions of iron in Earth's mantle silicates. *Earth Planet. Sci. Lett.*, *249*, 436–443. <https://doi.org/10.1016/j.epsl.2006.07.023>
- Zhang, J.S., & Bass, J.D. (2016). Sound velocities of olivine at high pressures and temperatures and the composition of Earth's upper mantle. *Geophys. Res. Lett.*, *43*, 9611–9618. <https://doi.org/10.1002/2016GL069949>
- Zhang, J.S., Bass, J.D., & Zhu, G. (2015). Single-crystal Brillouin spectroscopy with CO_2 laser heating and variable q . *Rev. Sci. Instrum.*, *86*, 063905. <https://doi.org/10.1063/1.4922634>
- Zhang, S., Cottaar, S., Liu, T., Stackhouse, S., & Militzer, B. (2016). High-pressure, temperature elasticity of Fe- and Al-bearing MgSiO_3 : Implications for the Earth's lower mantle. *Earth Planet. Sci. Lett.*, *434*, 264–273. <https://doi.org/10.1016/j.epsl.2015.11.030>
- Zhang, Y., Fu, S., Wang, B., & Lin, J.-F. (2021). Elasticity of a pseudoproper ferroelastic transition from stishovite to post-stishovite at high pressure. *Phys. Rev. Lett.*, *126*, 025701. <https://doi.org/10.1103/PhysRevLett.126.025701>
- Zhang, Z., Stixrude, L., & Brodholt, J. (2013). Elastic properties of MgSiO_3 -perovskite under lower mantle conditions and the composition of the deep Earth. *Earth Planet. Sci. Lett.*, *379*, 1–12. <https://doi.org/10.1016/j.epsl.2013.07.034>

4

From Mantle Convection to Seismic Observations: Quantifying the Uncertainties Related to Anelasticity

Bernhard S. A. Schuberth and Tobias Bigalke

ABSTRACT

One major challenge in studies on mantle convection is to provide a physically consistent link between underlying geophysical hypotheses and predicted surface observables. Here, we first review recent developments targeted toward linking hypothetical temperature fields to seismic recordings in a quantitative way. By combining mantle circulation models with mineralogical thermodynamics and global 3-D seismic wavefield simulations, synthetic traveltimes residuals can be computed that correctly capture the various nonlinearities in the relation to the underlying temperatures. We then highlight the importance of taking uncertainties in the input parameters into account when comparing to real data. Specifically, we investigate the effects of the poorly constrained parameters related to mineral anelasticity on the temperature-velocity conversion and the predicted traveltimes residuals. The anelastic correction increases the temperature sensitivity of seismic velocities, particularly at high temperatures. Assuming maximum values plausible for the frequency dependence of attenuation and the activation enthalpy of the dissipative process, the temperature derivative of shear-wave velocity increases by more than 100% at the top, and up to 70% at the bottom of the lower mantle in regions of elevated temperatures. The standard deviation of the seismic traveltimes residuals, however, is larger only by about 30% compared to the anharmonic case in consequence of the multiple nonlinearity of the physical situation at hand.

4.1. INTRODUCTION

Most of the surface geological activity of Earth arises from processes within the mantle that transport heat from the deep interior of our planet to the surface. Studying the mantle is thus essential to our understanding of how the entire planet works.

Knowledge of the forces within the mantle and in particular at the base of the tectonic plates is a prerequisite for

correctly modeling lithosphere dynamics and tectonic processes (e.g., Day, 1982). Mantle flow also affects the convection in the core and thus the geodynamo through providing thermal and geometrical boundary conditions (i.e., CMB topography). However, many models of mantle dynamics are still largely qualitative in nature to date. To obtain a quantitative understanding of buoyancy forces in the mantle, two different routes have generally been followed:

1. Using seismic observations, tomographic inversions are performed to obtain a best-fit model of seismic velocities in the mantle, which can then be converted to density variations.

*Department of Earth and Environmental Sciences,
Ludwig-Maximilians-Universität München, Munich, Germany*

Mantle Convection and Surface Expressions, Geophysical Monograph 263, First Edition.
Edited by Hauke Marquardt, Maxim Ballmer, Sanne Cottaar, and Jasper Konter.
© 2021 American Geophysical Union. Published 2021 by John Wiley & Sons, Inc.
DOI: 10.1002/9781119528609.ch4

2. Alternatively, mantle flow is simulated using numerical forward-models with (presumably) reasonable assumptions and input parameters.

To judge on the quality of such forward-models, they need to be evaluated either by comparison to seismic tomography or, preferably, by assessment of secondary geophysical predictions against direct observations of the Earth system (seismic data, gravity/geoid and dynamic topography, as well as its time-variability imprinted in the geologic record).

The inverse-approach (1) suffers from a number of inherent difficulties that so far have rendered a conclusive inference of the buoyancy distribution in the mantle impossible. There are three fundamental problems:

1. It is a major challenge in tomography to constrain both length-scales and magnitude of deep Earth seismic heterogeneity with sufficient resolution and accuracy.
2. Seismic observations are not sensitive to density variations directly (except for normal mode eigenfrequencies, which however, only constrain long-wavelength structure).
3. Interpretations of tomographic images are hampered due to trade-offs between thermal and chemical effects.

The general difficulty is the non-uniqueness of tomographic solutions. Owing to the necessity to regularize the inversions, tomographic models are always a blurred and “damped”; that is, low-fidelity version of true Earth structure (e.g., Ritsema et al., 2007; Schuberth et al., 2009a; Simmons et al., 2019). Finite-frequency as well as full-waveform inversions have in the last years been performed to push the models to higher resolution and to provide tomographic images at unprecedented detail (e.g., French and Romanowicz, 2014; Bozdağ et al., 2016; Zaroli et al., 2015; Fichtner et al., 2018). However, it still proves difficult to improve on the resolution limits that are dictated by the inhomogeneous data coverage. Moreover, the magnitude of the seismic heterogeneities is extremely difficult to constrain, and current efforts are directed toward providing unbiased tomographic images as well as estimating uncertainties along with the tomographic solutions (Zaroli, 2016).

Despite this great progress and the success of seismic tomography in the last three decades, it is still not possible on a global scale to image the three-dimensional structure of the mantle at sufficiently high resolution to cover the full range of dynamically inherent length scales (Ritsema et al., 2011; Trampert et al., 2013). Dynamically controlled length scales are, for example, the thickness of subducting oceanic lithosphere (on the order of 90–100 km), which reflects the upper thermal boundary layer, or the size of upwelling plumes. The alternative

to the inverse-approach is therefore to start from hypotheses on the dynamics of the mantle and to generate various predictions based on forward-models of mantle convection. The underlying fluid dynamics equations can be solved on a routine basis on modern high-performance computing (HPC) systems. Important to note, the input parameters such as material properties and the energy input (radioactive heating and heat flux from the core) determine the vigor of convection and thus control the inherent length scales and magnitude of temperature anomalies as well as the associated variations in density and seismic velocities. The problem of improving our understanding of mantle dynamics thus translates into the task of better constraining the input parameters and boundary conditions of the forward model. Once a set of parameters is chosen (i.e., a geodynamic hypothesis), a unique solution to the mantle convection equations can be computed, given that initial and boundary conditions are applied (Serrin, 1959). Through the assimilation of plate motion history models as surface boundary conditions, a geologically informed prediction of the present day flow velocities and temperature field in the mantle is obtained. Such models are then termed *mantle circulation models* (MCMs) by analogy with the circulation in the oceans and the atmosphere. In this forward-modeling approach, temperature variations are thus not a free parameter, but rather, are fully determined by the dynamics of the flow. Most important, both length scales and magnitude of these lateral temperature variations are largely independent of the (unknown) initial condition and are thus an important prediction of mantle circulation models (see Section 4.2.1.1).

Once a solution for the present-day mantle structure in terms of flow velocity and temperature is obtained from the forward modeling procedure, the crucial step is to assess the quality of the models. A classical and widely used criterion are comparisons with tomography in terms of their spectral characteristics (e.g., Becker and Boschi, 2002; Nakagawa and Tackley, 2010; Bull et al., 2009). Care must be taken when dealing with assimilated plate reconstructions, as the spectral characteristics of mantle flow models are then largely controlled by the surface boundary condition. This means that spectral correlations may not so much provide insight into the actual dynamics of the system, but rather are indicative of the accuracy of the plate motion history employed in the simulations. Even more important, comparisons of model spectra are only meaningful, if geodynamic models are converted to seismic velocities using mineralogical models that appropriately capture the complex changes of the mineral phase assemblage. Nowadays, thermodynamic models exist that provide a self-consistent nonlinear relation between temperature and seismic velocities as well as density for mineral phase assemblages representative of

mantle rock (see Section 4.2.1.2). The strong nonlinearity of the temperature sensitivity of seismic velocities in the vicinity of phase transformations (Stixrude and Lithgow-Bertelloni, 2007) results in marked differences between temperature and velocity spectra, in particular in the upper mantle (Schuberth et al., 2009b). This characteristic difference is illustrated in Figure 4.1 (compare Figure 4.1a and 4.1b). More important, by going away from simplified linear scaling relations, the mineralogical models provide the basis for assessing MCMs using quantitative measures, such as the magnitude of the seismic heterogeneity, or the variance of body-wave traveltimes. In the case of comparisons between predicted seismic heterogeneity and tomographic images, it is further crucial to modify the mantle circulation models such that they reflect the effects of limited resolution due to uneven data coverage and damping. For any given tomographic model for which the resolution operator has been computed, it is straightforward to estimate how a given hypothetical mantle structure would be imaged in that same tomographic inversion setup. This so-called *tomographic filtering* of conceptual Earth models has nowadays become a standard tool in geodynamics (Méglin et al., 1997; Bunge and Davies, 2001; Boschi, 2003; Ritsema et al., 2007; Bull et al., 2009; Schuberth et al., 2009a; Davies et al., 2012; Koelemeijer et al., 2018; Simmons et al., 2019). The estimated model provides valuable information on how true Earth structure might actually be seen through tomographic lenses and how heterogeneities are smeared and modified in amplitude. It has been shown that in classical damped least-squares inversions damping can result in a reduction of RMS amplitudes (i.e., the average strength of seismic anomalies) up to a factor of two (Schuberth et al., 2009a).

A good quantitative understanding of the damping effects and related amplitude reductions in a given tomographic model is important, as geodynamic studies are shifting away from classical forward simulations, which start from an unknown initial condition at some time in the geologic past, to so-called adjoint simulations, in which one optimizes for the initial condition based on an (assumed) known “terminal” state of the mantle (e.g., Colli et al., 2018). For such applications, the present-day thermodynamic state of the mantle is estimated from one of the existing tomographic models together with information from mineral physics. This estimate of the terminal state, however, is only meaningful, if the magnitudes of the seismic heterogeneity are correctly mapped into buoyancy variations; that is, if the smearing and the amplitude reduction introduced through the regularization of the tomographic inversion can somehow be accounted and corrected for. Further issues may arise in case of long-period seismic data that render the relation to temperature and buoyancy even more complex.

For this kind of data, wavefront healing can play an important role by obscuring information on short-scale structure (Wielandt, 1987; Marquering et al., 1999; Dahlen et al., 2000; Hung et al., 2000), which, in turn, can also influence the magnitude of heterogeneity in tomographic models. Therefore, to obtain a better understanding on how to best introduce the available seismic information into geodynamic adjoint models on the one hand, and for a rigorous quantitative assessment of forward models of mantle circulations against seismic observations on the other hand, it is desirable to directly compute and investigate full 3-D seismic wave fields in the synthetic Earth models. This chapter gives an overview on the recent developments targeted toward linking the present-day temperature field of mantle circulation models quantitatively to seismic observations. Mantle flow models also provide a number of further predictions, such as the geoid and also time-varying signals such as changes in dynamic topography or true polar wander that can be used for an assessment of the models. Covering those topics, however, is beyond the scope of this chapter.

4.2. FROM GEODYNAMIC HYPOTHESIS TO SEISMIC OBSERVATIONS

4.2.1. Predicting Seismic Mantle Structure

Mantle Evolution and the Present-Day Temperature Field. The time scales of geological processes, typically on the order of millions to hundreds of millions of years, are sufficiently long that the mantle, although capable of transmitting seismic shear waves, can be treated as a fluid. More specifically, the mantle undergoes solid-state thermal convection through creep mechanisms. Thus, mantle convection is governed by the equations of motion of a viscous fluid (i.e., the hydrodynamic field equations) expressing the fundamental principles of mass, momentum, and energy conservation. From a mathematical perspective, this represents an initial- and boundary-value problem. In addition, a set of input parameters need to be specified, such as density, thermal conductivity, viscosity, specific heat capacity, coefficient of thermal expansion, etc. Furthermore, to solve this system, an equation of state relating density to pressure and temperature needs to be specified. Given the very high viscosity of mantle rock, inertial forces are so small (Reynolds number $\mathcal{O}(10^{-21})$) that they can be neglected in the momentum equation. This leads to an instantaneous force balance between viscous resistance and buoyancy, which is referred to as *Stokes flow*. The nonlinear nature of the mantle convection equations; that is, the coupling between velocity and temperature through thermal advection, requires

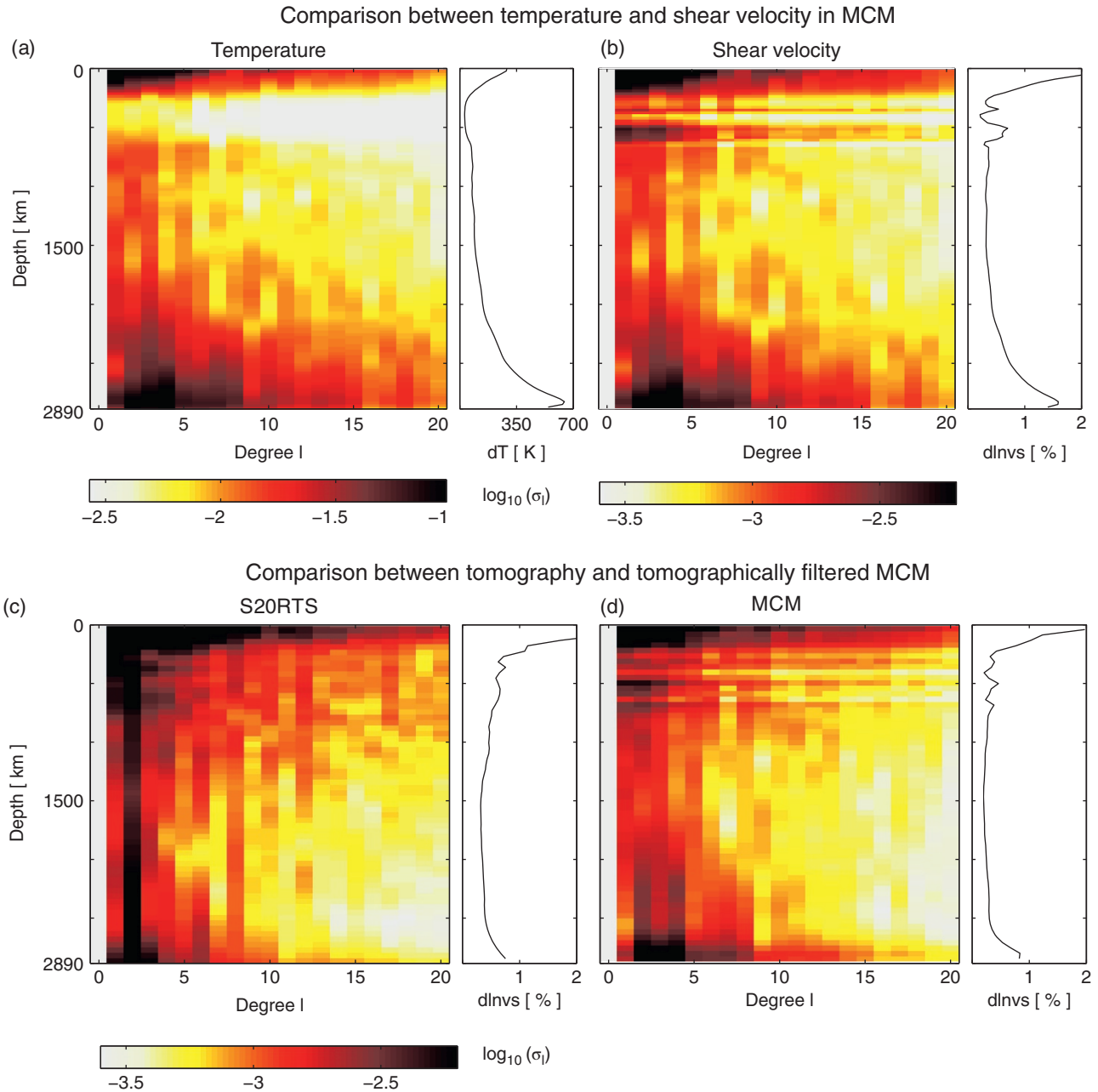


Figure 4.1 Spectral power of heterogeneity in (a) temperature, (b) shear wave velocity for mantle circulation model S09-M2 of Schubert et al. (2009b), (c) tomographic model S20RTS (Ritsema et al., 2004), and (d) the tomographically filtered version of S09-M2 (Schubert et al., 2009a). Spectral power is plotted on a logarithmic scale as a function of spherical harmonic degree l and depth. Only the first 20 spherical harmonics degrees are shown for the MCM in this comparison ($l_{max} \simeq 720$). Subplots on the right show the root-mean-square amplitudes of temperature and v_s perturbations as a function of depth, respectively. Note the marked differences in the spectral characteristics between thermal and seismic heterogeneity in the upper mantle (cf. a and b). The narrow bands of strong power in v_s are a consequence of mineralogical phase changes in the transition zone, even though there is reduced thermal heterogeneity in these depth levels. After taking the effects of tomographic resolution into account, the spectral characteristics of the MCM compare well with those of S20RTS (cf. c and d). Source: Modified from Schubert et al. (2009b) (a,b) and Schubert et al. (2009a) (c,d).

numerical solutions. Geodynamic modeling thus relies on sophisticated computational simulations, and great progress has been made in the past three decades in implementing appropriate numerical techniques. Nowadays, a number of powerful computer codes exist for simulating mantle flow in 3-D spherical shell geometry on a global scale (e.g., Zhong et al., 2000; Tackley, 2008; Bunge et al., 1997; Heister et al., 2017). To obtain accurate estimates of temperatures, it is particularly important to include the effects of compressibility of mantle rocks in the convection simulations (the density increases from top to bottom of the mantle by more than 60%). This, in turn, is crucial if one is interested in relating the magnitude of thermal anomalies to seismic observations.

As noted before, a unique solution to the hydrodynamic equations for the mantle can be computed for a given set of input parameters. This requires an initial condition for temperature and boundary conditions for both temperature and flow velocities (Serrin, 1959). The temperature boundary condition for the top of the model domain (i.e., the surface) typically is fixed to 300 K, and for the CMB can be chosen such as to drive convection with varying amounts of core heat flow. For the velocity boundary conditions, a free-slip boundary is used for the CMB, and for the surface, plate reconstructions can be incorporated through sequential data-assimilation (Bunge et al., 2002). By doing so, the lateral temperature variations for the final (i.e., present-day) stage become, in fact, largely independent of the initial condition and are thus an important prediction of mantle circulation models (the influence of the initial condition reduces with the duration of the assimilated plate motion history; Colli et al., 2015). Recent global plate motion models provide the plate boundary configurations and plate velocities since the late Paleozoic; that is, for the last 400 Ma (e.g., Young et al., 2018), equivalent to around two times the mantle overturn time.

Important to note again, the input parameters to the hydrodynamic field equations, such as material properties and the energy input (radioactive heating and heat flux from the core), determine the vigor of convection and thus control the inherent length scales and magnitudes of temperature anomalies and buoyancy variations. The thickness of subducted oceanic lithosphere, for example, which reflects the upper thermal boundary layer, is governed by the temperature gradient across the lithosphere as well as material parameters such as thermal diffusivity, coefficient of thermal expansion, and viscosity. The spectrum of mantle structures may further be influenced by the potential presence of chemical heterogeneities, such as, for example, the differences between crustal and lithospheric compositions that enter the mantle during subduction (e.g., Allègre and Turcotte, 1986; Agranier et al., 2005). The distribution and length-scales of chemical

heterogeneities and their influence on the dynamics of the mantle, however, are still a matter of debate (e.g., Simmons et al., 2010; Davies et al., 2012; Schubert et al., 2012; Mosca et al., 2012; Li and McNamara, 2013; Li et al., 2014; Tesoniero et al., 2016; Moulik and Ekström, 2016; Lau et al., 2017; Koelemeijer et al., 2018).

Relating Temperatures to Seismic Velocities. As already mentioned, a crucial component for the quantitative assessment of any geodynamic prediction are models of mantle mineralogy relating temperatures to density and seismic velocities. Seismic wave velocities depend on temperature and pressure through anharmonic (elastic) as well as anelastic effects (Karato, 1993; Anderson, 2007). To describe the elastic behavior of rocks, thermodynamically self-consistent models of mantle mineralogy are nowadays available (e.g., Ricard et al., 2005; Connolly, 2009; Stixrude and Lithgow-Bertelloni, 2011; Chust et al., 2017). These models for mineral phases and aggregates provide a natural framework to analyze the dependency of material properties, such as elastic moduli, density, heat capacities, and thermal expansivities, on pressure (p), temperature (T), and composition (X), and to determine their relationships consistently. Starting from a database of thermodynamic parameters for different minerals, a stable phase assemblage at any p , T , X condition can be determined for compositions in the six-component NCFMAS system ($\text{Na}_2\text{O}-\text{CaO}-\text{FeO}-\text{MgO}-\text{Al}_2\text{O}_3-\text{SiO}_2$). Currently, thermodynamic data for 21 compounds and solid solutions are included in those models (Stixrude and Lithgow-Bertelloni, 2005; Xu et al., 2008; Stixrude and Lithgow-Bertelloni, 2011). The stable phase assemblage is computed by minimizing the Gibbs energy of the candidate phases and their solid solutions, and modern open-source tools exist to facilitate such computations through an efficient and extensible software implementation (e.g., EoS-MMA; Chust et al., 2017). In addition to the thermodynamic description, the mineralogical models also adopt a representation of the shear modulus (Stixrude and Lithgow-Bertelloni, 2005).

To be applicable to the deep Earth, the elastic velocities from the mineralogical models have to be corrected for the effects of physical dispersion due to anelasticity. Karato (1993) was among the first to note that the effects of anelasticity might be important, as they can significantly increase the temperature sensitivity of seismic velocities. This could have strong implications, for example, for the interpretation of tomographic images of Earth's mantle in terms of temperature anomalies. Lower temperature anomalies are generally sufficient to explain the observed seismic velocity perturbations compared to the anharmonic case. The necessity to perform the anelastic correction derives from the fact that experiments on

mantle minerals are done at frequencies that are orders of magnitude different from those of seismic waves in the Earth, which are in the range from mHz to Hz. In contrast, laboratory measurements of seismic velocities at high pressure and temperature are typically done in the MHz to GHz frequency range (most notably using ultrasonic interferometry and opto-acoustic techniques such as Brillouin spectroscopy) owing to the small sample sizes (which lie in the μm to mm range). At these very high frequencies, minerals behave quasi-elastically; that is, those measurements represent the unrelaxed velocities. The anelastic correction then serves to relate those measurements to the seismic frequency band by accounting for the physical dispersion (i.e., the modulus deficit between unrelaxed and relaxed moduli). We will introduce the details of the anelastic correction and possible implications of the associated large uncertainties in Section 4.3.

The great benefit of the thermodynamic mineralogical models is that they provide the full nonlinear relation between temperature and elastic moduli as well as density. One study in which this was shown to play an important role was the work of Schubert et al. (2009b), who investigated a particular scenario of mantle flow based on the hypothesis of (1) a high CMB temperature and correspondingly high core heat flux (4200 K and 12 TW, respectively) in combination with (2) isochemical whole mantle flow; (3) a three-layer viscosity profile; and (4) a pyrolite composition. This setup in fact represents a simple, yet sufficiently realistic, model of the mantle general circulation (i.e., complexity is reduced to a minimum). Figure 4.1 shows the spectral characteristics of the temperature field predicted for this scenario as well as its seismic representation in comparison to S20RTS (Figure 4.1c). A number of studies have further shown that such simple models of mantle flow are compatible not only with tomographic images, but also with a broad range of observations (e.g., seismic body-wave traveltime residuals, the geoid as well as true polar wander estimates; Schubert et al., 2009a; Schaber et al., 2009; Davies et al., 2012; Schubert et al., 2012; Koelemeijer et al., 2018). For example, Figure 4.2a shows the comparison of the strength of heterogeneity as a function of depth between the tomographically filtered version of this geodynamic model (Schubert et al., 2009a) and tomographic model S20RTS (Ritsema et al., 2004). This comparison illustrates that the magnitudes of seismic anomalies predicted from the isochemical MCM with strong core heating are compatible with the values seen in S20RTS.

4.2.2. Predicting Seismic Observables – Truly “Synthetic” Data

The studies previously discussed were a first step toward linking the mantle temperature field and the underlying

assumptions to seismic information in a quantitative manner; that is, in terms of the magnitude of 3-D temperature and seismic velocity perturbations. To avoid the problems mentioned in Section 4.1 related to non-uniqueness, limited resolution, amplitude damping and biased estimates affecting the tomographic-geodynamic comparisons, it is desirable to directly predict seismic observables, such as traveltimes of body-wave phases, for the synthetic Earth models. And at best, these observables should be based on entire full waveform synthetic seismograms and measured (i.e., post-processed) in the same way as is done for their real-world counterparts.

A number of studies have followed this philosophy, although one often has to introduce simplifications for the seismic modeling due to the computational burden posed by running full 3-D wave propagation simulations for a sufficiently large number of earthquakes. Bunge and Davies (2001); Davies and Bunge (2001), for example, computed around 780,000 ray-theoretical arrival times for source-receiver configuration from the ISC catalog for a global MCM. The resulting arrival times were, on the one hand, used to compute a synthetic tomographic image of the geodynamic model (Bunge and Davies, 2001), and on the other hand demonstrated that the given data coverage results in a bias toward fast arrivals (Davies and Bunge, 2001). The same methodology and idea were applied by Davies et al. (2015) in a more recent study on the influence of large low shear velocity provinces (LLSVPs) on 1-D average seismic properties of the mantle. In contrast to the aforementioned studies who applied a linear scaling, they used a thermodynamic mineralogical model for the conversion of temperatures to seismic velocities. Several further studies have been performed to systematically investigate the seismic signature of certain parts (or features) of the mantle. Jacobs and van den Berg (2011) computed synthetic seismic transition zone structures and also predicted seismic observables based on 2-D convection simulations in combination with a simplified SiO_2/MgO mineralogy and reflectivity synthetic seismograms for 1-D profiles extracted from their model. A similar approach, based on computing approximate seismic waveforms for 1-D profiles taken from geodynamic modeling results, was used by Bower et al. (2013), who studied the D” region in 2-D compressible mantle convection simulations. The influence of plumes (from regional 2-D axisymmetric geodynamic simulations) on the seismic wavefield was investigated in a series of papers using either axisymmetric (Hwang et al., 2011) or regional 3-D wave propagation simulations (Maguire et al., 2016, 2018; Stockmann et al., 2019).

If a full treatment of the seismic wave equation is employed through numerical solution in 3-D geometry (i.e., without theoretical approximations, such as ray- or finite-frequency theory), it has been shown by Schubert

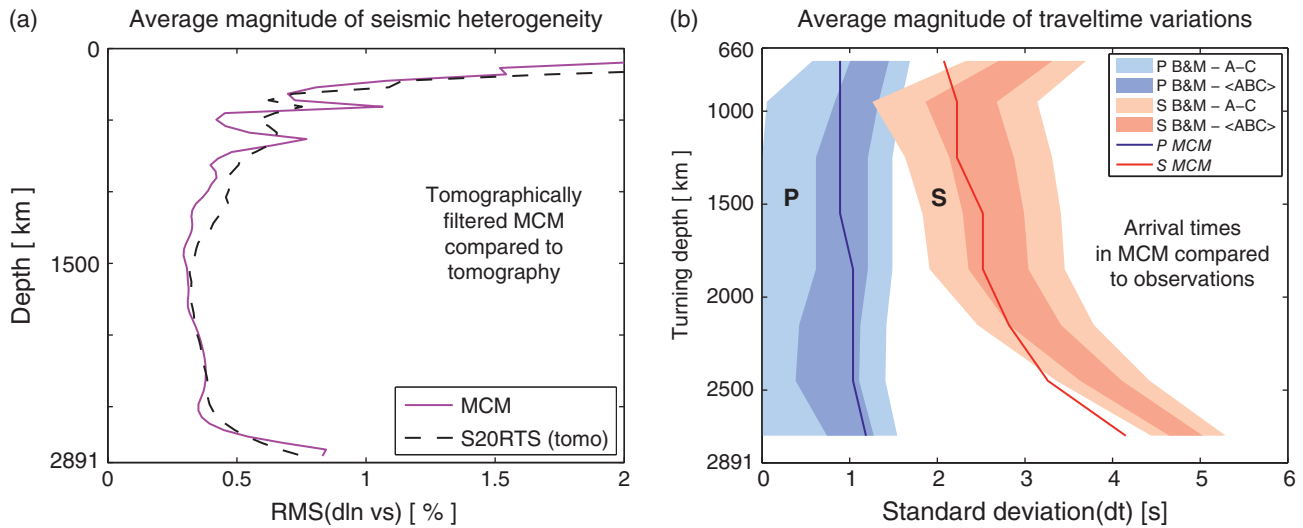


Figure 4.2 (a) Root-mean-square profiles of relative variations in v_s for (magenta) the tomographically filtered mantle circulation model S09-M2 (Schuberth et al., 2009a) and (black dashed) the tomographic model S20RTS (Ritsema et al., 2004). (b) Comparison of the average magnitude (i.e., standard deviation) of traveltime variations between (solid lines) the predictions for model S09-M2 (Schuberth et al., 2012) and (shaded areas) the observations of Bolton and Masters (2001) (blue for P waves, and red for S waves). For the observations, only that part of the standard deviation is taken into account that is associated with 3-D mantle heterogeneity. Intermediate and light shaded areas show the range of values inferred from the observations for measurements of different quality, denoted A, B, and C in Bolton and Masters (2001). Source: Modified from (a) Schuberth et al. (2009a) and (b) Schuberth et al. (2012).

et al. (2012) that one can link the dynamically derived temperature variations – and thus, the underlying input parameters to the hydrodynamic equations – to seismic observations in a quantitative physically consistent manner. They computed long-period body-wave traveltime residuals in mantle circulation models based on spectral-element 3-D global wave propagation simulations and compared them to real data. Figure 4.2b shows the standard deviation of their synthetic traveltime residuals predicted for P and S waves as a function of ray turning depth. This represents the average signal in the travel-times, which is directly related to the average strength of seismic heterogeneity in the underlying model shown in Figure 4.2a, and which, through the mineralogical mapping, can also be linked to the initial (average) temperature variations. Note, however, that they are connected in a strongly nonlinear manner owing to the non-linearity in the mineralogical model as well as the nonlinear wave field effects.

Computing whole waveform synthetic seismograms on a global scale at relevant seismic frequencies became feasible on a routine basis in the last decade thanks to the ever growing computational resources. Using the 3-D velocity structure from geodynamic models in the simulations is, however, somewhat more complex than using tomographic models in two respects: First, the parametrization

with typically orders of magnitude larger numerical grids requires an efficient projection of the geodynamic model onto the grid of the wave propagation simulation (Schuberth et al., 2012). This task has to be performed every time that the underlying geodynamic hypotheses or the mineralogical or compositional model used to compute the seismic velocities change.

The second difference to using tomographic models in the wave propagation simulations is related to the different nature of temperature and seismic velocity perturbations in terms of characteristic length scales (cf. Figure 4.1). The obvious approach would be to first compute seismic velocity and density perturbations from the temperatures of the geodynamic model on the grid of the convection simulation, and then try to do an interpolation of the elastic parameters onto the grid used for simulation of wave propagation. However, as discussed above, the seismic velocities show very strong heterogeneity in the vicinity of phase transitions due to their strong nonlinear dependence on temperature there. To correctly capture this behavior would require complicated high-order interpolation schemes. Temperature, on the other hand, is a much smoother function of space, for which simple linear interpolation is generally sufficient at the typical resolution of both numerical grids. Thus, a more consistent way of implementing geodynamically derived

velocity models is to first project the temperature field onto the wave propagation grid and to do the conversion to seismic velocities there. This way, the nonlinearity of the temperature sensitivity of the seismic velocities and the complicated nature of resulting perturbations in the vicinity of phase transitions is taken into account consistently and represented correctly in the wave propagation simulations.

A further important difference to using tomographic models is that synthetic waveforms are obtained independent of any real Earth seismic observations, as they are computed for synthetic 3-D seismic structures derived from a hypothetical dynamic Earth model. In other words, the full waveform seismograms are in this case “truly” synthetic. This way, one can investigate wave field effects in complex, yet dynamically meaningful media (in contrast to studies based on random media), and without the danger of circular reasoning, as is the case when running wave field simulations for tomographic models. Finally, we note that synthetic seismograms computed for geodynamic models in the way described above in fact represent (predicted) surface expressions of mantle convection.

4.2.3. Linking to Earth Observations – The Importance of Uncertainties

Having the truly synthetic seismic waveforms at hand, one can take the final step and compare the predictions with observations. Figure 4.2b shows the comparison of the predictions of Schuberth et al. (2012) with the data of Bolton and Masters (2001). This comparison reveals that – for both *P* and *S* waves – the standard deviations of long-period traveltimes residuals in purely thermal mantle circulation models agree well with those of the observed seismic data. Most important, the synthetic data reproduced the different magnitudes as well as their different trends with ray turning depth. This indicated that chemical heterogeneity is not required to match the statistics of the seismic data. The finding of a predominance of thermal variations in driving mantle flow seems at odds with the potential presence of chemical heterogeneities expected from the subduction of differentiated oceanic crust and lithosphere. The study of Schuberth et al. (2012), however, does not rule out the possibility of chemical heterogeneity, in particular on short length scales. The HPC resources available at that time allowed for the calculation of accurate seismic wave fields down to a shortest period of 10 s and seismograms were bandpass-filtered at 15 s dominant period before measuring body-wave traveltimes by cross-correlation. Owing to the large width of the Fresnel zone at the ray turning depth, measurements of

arrival times at these periods are effectively influenced by structures with length scales of a few hundred kilometers and larger. Any structure smaller than this could potentially “hide” due to wave field effects (e.g., wavefront healing; Wielandt, 1987). In other words, diffraction effects are important at these periods and need to be taken into account properly. The notion of chemical heterogeneity on small rather than large scales would presumably imply a more passive role of the compositionally distinct material. To answer the question on the dynamic relevance of chemical heterogeneity, it will be crucial to not only rigorously assess various alternative geodynamic hypotheses in future, but also to consider the effects of various sources of uncertainty. While uncertainties in the observed seismic data have been taken into account by Schuberth et al. (2012), it is clear that for linking temperatures to seismic observables in a quantitative manner, a systematic investigation of the effects of uncertainties in the input parameters is also essential. At best, one would aim for a true uncertainty propagation, but this is not straightforward given the complexity of the joint modeling setup and the nonlinearities in each step. A more viable alternative is to consider end-member scenarios; that is, going through the forward-modeling chain using the extreme values of the uncertainty ranges of the input parameters.

4.3. CONSIDERING MINERALOGICAL UNCERTAINTIES

In this study, we concentrate on end-member scenarios and illustrate the impact of uncertainties in some of the mineralogical parameters, specifically those governing the anelastic correction as one important example. Similarly, uncertainties in the parameters controlling the geodynamic model and effects on seismic wave propagation associated with errors in event locations and origin times as well as the impact of the imperfectly known crustal structure play an important role. Investigating these latter effects, however, is beyond the scope of the present study.

As described in Section 4.2, the mineralogical mapping from temperatures to seismic velocities consists of two parts: the anharmonic part and the anelastic correction. Uncertainties on the anharmonic part are composed of the following contributions: phase equilibrium uncertainty (i.e., identity of stable minerals), uncertainties in elastic parameters of single minerals, in the chemical composition of the minerals as well as uncertainties in the equation of state modeling (see for example Connolly and Khan, 2016). A variety of studies tried to quantify these uncertainties and estimated them to each lie in the range of a few percent (with uncertainties on *P*-wave

velocities and density being slightly smaller than those for *S*-wave velocities; Cammarano et al., 2003; Cobden et al., 2009; Deschamps et al., 2012; Connolly and Khan, 2016). More important than the uncertainties in absolute values are the uncertainties in the temperature derivatives of the seismic velocities for relating thermal anomalies to seismic structures. The uncertainty for the anharmonic derivatives have been estimated to lie in the range of about 10–20% (e.g., Trampert et al., 2001; Cammarano et al., 2003). Anelasticity leads to an increase of the temperature sensitivity of the wave velocities, but no consensus was reached yet with respect to its actual magnitude (Karato and Karki, 2001; Trampert et al., 2001; Cammarano et al., 2003; Goes et al., 2004; Brodholt et al., 2007; Matas and Bukowinski, 2007). Karato and Karki (2001) found very strong effects of anelasticity, but Brodholt et al. (2007) argued that they may have overestimated these effects for low values of Q (or high temperatures) by an invalid simplification in their theoretical derivation. This was confirmed by Matas et al. (2007), who revised the respective formulas and examined the rather complex interplay of various parameters that play a role when anelasticity is assessed. The problem lies in determining these material parameters controlling anelastic behavior – namely the activation enthalpy and the frequency dependence of intrinsic anelastic attenuation – at the extreme pressure and temperature conditions of Earth’s mantle. Given the current state of knowledge on both parameters, their effects on the temperature sensitivity of seismic velocities are uncertain by several tens of percent, even in the lowermost mantle, and can exceed 100%, in particular in the upper mantle (e.g., Matas and Bukowinski, 2007, see also Figure 4.5). This means that the uncertainties related to the anelastic correction are much larger than those on the anharmonic elastic temperature sensitivities. Anelasticity, therefore, is considered to be one of the most relevant factors for the investigation of the impact of uncertainties on our quantitative analysis of predicted seismic travel-times. We therefore address it here isolated from any other sources of uncertainty. In the following, we give a brief overview of the theoretical background of anelasticity and the methods for computing the anelastic correction of seismic velocities. Afterward, we investigate the implications for the associated uncertainties in the resulting traveltime residuals for a given temperature field.

4.3.1. Anelasticity – A Crucial Factor for Traveltime Uncertainty

As any real material, rocks do not behave perfectly elastic and the anelasticity causes seismic waves to lose part of their energy by dissipation (i.e. intrinsic attenuation by conversion to heat). More specifically, rocks act as an

absorption band in the teleseismic frequency range (mHz–Hz); that is, attenuation reaches a maximum within the band, while elastic behavior is (theoretically) expected at both very high and very low frequencies. However, laboratory measurements, micromechanical modeling as well as analysis of tidal data suggest that probably, there is a smooth transition from anelastic to viscous behavior with decreasing frequency rather than a return to elastic behavior (Jackson et al., 2014; Lau and Faul, 2019). During the passage of a wave, stresses act on the material, which thereby deforms and subsequently recovers toward its original shape once the stress is released. Anelasticity causes this relaxation mechanism to be time-dependent and has commonly been related to crystal lattice defects on the microscopic scale (e.g., Karato and Weidner, 2008). Loss of energy in the crystal happens due to a variety of microscopic processes, such as migration and vibration of dislocations or, in polycrystalline materials, by diffusively assisted grain boundary sliding. In the latter case, anelastic behavior becomes grain-size dependent (Faul and Jackson, 2005; Jackson and Faul, 2010; Karato and Park, 2018), which potentially can have a significant effect on the seismic signature of flow in the upper mantle as well as the seismic structure of the lithosphere (e.g., McCarthy et al., 2011; Priestley and McKenzie, 2013; Abers et al., 2014; Dalton et al., 2014; Yamauchi and Takei, 2016; Dannberg et al., 2017; Cobden et al., 2018). Most studies on grain-size-dependent anelastic and viscous behavior considered only olivine (or analogues for upper mantle rock) and therefore, any inferred deformation laws can only be applied to the upper mantle. In addition, the complexities of true upper mantle rocks – which include a significant amount of other mineral phases such as pyroxenes – are likely not captured by such treatments. Furthermore, if one were to apply the descriptions of the grain size dependent material behavior, one is faced with the fact that the size of the mineral grains, and its variation with depth, in the mantle is one of the most poorly constrained parameters. As we will see in Section 4.3.1.2, it is possible to get rid of the complexities of grain-size dependence by relating variations in attenuation to a reference value at each depth.

Each of the aforementioned dissipative, microscopic processes causes the attenuation of seismic waves at a specific characteristic frequency, just like a damped oscillator (Anderson, 1989). This behavior commonly is modeled using a standard linear solid (SLS, or Zener model) a Maxwell material consisting of a parallel combination of a spring (with stiffness k_1) and dashpot in series with a spring (with stiffness k_2). The variation of attenuation as a function of frequency can be described by the following expression (e.g., Stein and Wysession, 2002; Anderson, 2007):

$$\begin{aligned}
 Q^{-1}(\omega) &= \frac{k_2}{k_1} \cdot \frac{\omega\tau}{1 + (\omega\tau)^2} \\
 Q^{-1}(\omega) &= 2 \cdot Q_{max}^{-1} \cdot \frac{\omega\tau}{1 + (\omega\tau)^2},
 \end{aligned}
 \tag{4.1}$$

where ω is the angular frequency, k_2 and k_1 are the spring constants mentioned above and τ the relaxation time. The latter is defined as $\tau = \eta/k_2$, with η denoting the viscosity of the dashpot (As a side note: k_1 corresponds to the relaxed modulus M_r of the SLS, while k_2 can be regarded as the modulus deficit $\delta M = M_u - M_r$; that is the difference between unrelaxed modulus M_u and the relaxed modulus; see e.g., Liu et al., 1976; Lay and Wallace, 1995). Q is the dimensionless seismic quality factor; that is, the inverse of the intrinsic anelastic attenuation, which serves as a measure of how much energy is lost during one wave cycle. Depending on the frequency of the applied stress, the system's response will be spontaneous or delayed, and the maximum attenuation is reached for $\omega\tau = 1$. The absorption band then is the superposition of (partly) overlapping absorption peaks associated with the separate microscopic phenomena. Numerous studies confirm that anelasticity can be reasonably simulated by superimposing a finite number of SLSs (often three are sufficient; e.g., Liu et al., 1976; Emmerich and Korn, 1987; Komatitsch et al., 2002; Käser et al., 2007; Savage et al., 2010; Blanc et al., 2016).

On the macroscopic scale, the loss of energy is regarded as internal friction and Q serves to characterize the steady decay of any seismic signal. Attenuation experienced by S and P waves is controlled by their respective quality factors, Q_S and Q_P . Since shear wave velocity depends on the shear modulus μ only, $Q_S = Q_\mu$, with Q_μ being a measure of how much energy is lost in shear motion. P -wave velocity, on the other hand, depends on both elastic moduli μ and κ , which leads to the following expression for Q_P (e.g., Stein and Wysession, 2002):

$$Q_P^{-1} = L \cdot Q_\mu^{-1} + (1 - L) \cdot Q_\kappa^{-1} \quad \text{with} \quad L = \left(\frac{4}{3}\right) \cdot \left(\frac{v_s}{v_p}\right)^2,
 \tag{4.2}$$

where v_s and v_p are S - and P -wave velocity, respectively, and Q_κ^{-1} describes how much energy is lost in compression. Q_κ is generally assumed to be very high and thus the second term of the right hand side of Equation (4.2) is commonly neglected. Despite its importance for seismic wave propagation, Q in the mantle is still rather poorly constrained due to the often indistinguishable effects of elastic (focusing/defocusing effects) and anelastic processes. Figure 4.3 shows a variety of 1-D profiles of Q derived from seismic observations, which differ

considerably, in particular in the lower mantle. All models assume frequency independence of Q and they consider only the anelastic attenuation in shear, Q_μ . 3-D variations in Q are even less well constrained, as tomography of mantle attenuation is more complicated than inversions for the elastic seismic velocities. Amplitudes, which would in principle provide information about anelastic attenuation, can not only be severely contaminated by elastic focusing and defocusing effects, but also by local site effects and instrument mis-calibration (Romanowicz and Mitchell, 2015).

For mapping upper mantle lateral (3-D) variations of Q , a variety of studies have been either using surface waves (e.g., Romanowicz, 1995; Billien et al., 2000; Gung and Romanowicz, 2004; Selby and Woodhouse, 2002; Dalton and Ekstrom, 2006; Dalton et al., 2008; Bao et al., 2016; Karaoğlu and Romanowicz, 2017) or body waves (e.g., Bhattacharyya et al., 1996; Roth and Wiens, 2000; Reid et al., 2001; Warren and Shearer, 2002; Lawrence and Wysession, 2006; Hwang et al., 2011; Deschamps et al., 2019). Owing to even larger measurement uncertainties and comparatively sparse data coverage, reliable global 3-D Q models of the lower mantle are hitherto still practically nonexistent (Romanowicz and Mitchell, 2015; Liu and Grand, 2018). As an attempt to overcome this issue, Ruan and Zhou (2010) exploited the strong relationship of both velocity and Q with temperature. By regarding lateral velocity variations (taken from model S20RTS; Ritsema and Van Heijst, 2000) as a result of temperature variations alone, 3-D perturbations of the frequency-independent Q have then been estimated accordingly, based on the concept of Karato (1993).

Frequency and Temperature Dependence of Q . From seismic observations, it seems that Q is not constant within the absorption band and several studies suggested to introduce a mild frequency dependence of the form: $Q \propto \omega^\alpha$ (e.g., Anderson and Minster, 1979). The value of α is still a matter of debate, but has been estimated to lie roughly between 0 and 1. Lekić et al. (2009) showed that α may even change with frequency, whereas laboratory measurements predict a constant α within the absorption band in the range of 0.2 to 0.4 (Faul and Jackson, 2005). The fundamental problem that results from a frequency-dependent Q is that estimates of attenuation from long-period normal mode data can be significantly different from those using short-period body-wave data. Furthermore, attenuation is not only frequency-, but also temperature-dependent. Most of the relevant microscopic mechanisms that cause intrinsic attenuation of seismic

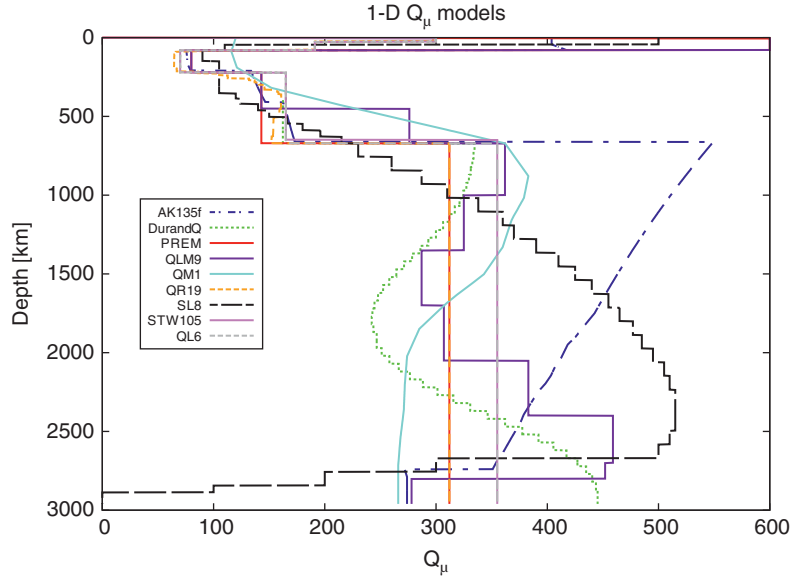


Figure 4.3 A selection of 1-D Q models derived from seismic observations: The profiles show the seismic quality factor in the mantle for shear deformation, Q_{μ} . Sources: **PREM**: Dziewonski and Anderson (1981); **QM1**: Widmer et al. (1991); **QR19**: Romanowicz (1995); **AK135f**: Montagner and Kennett (1996); **QL6**: Durek and Ekström (1996); **STW105**: Kustowski et al. (2008); **SL8**: Anderson and Hart (1978); **QLM9**: Lawrence and Wysession (2006); **DurandQ**: Durand et al. (2013). Apart from the very low- Q asthenosphere in about 80–200 km depth, Q values vary considerably throughout the entire mantle between the models.

waves (e.g., mobility of dislocation or grain boundary sliding) are thermally activated processes (see e.g., Anderson, 1989). For example, the relaxation time is inversely proportional to the mobility of defects and therefore will be temperature dependent (e.g., Takei, 2017). The relaxation time τ may thus be expressed as an exponential function of temperature as follows:

$$\tau = \tau_0 \cdot \exp\left(\frac{E^*}{RT}\right), \quad (4.3)$$

where τ_0 is the characteristic time of the respective microscopic process, E^* an activation energy and R the universal gas constant. By inserting this expression into Equation (4.1), one obtains for the high-frequency portion of the absorption peak (i.e., $\omega\tau \gg 1$):

$$Q^{-1}(\omega) = 2 \cdot \frac{Q_{max}^{-1}}{\omega\tau_0} \cdot \exp\left(-\frac{E^*}{RT}\right). \quad (4.4)$$

For further details on the derivation of Equation (4.4), the reader is referred to Anderson (1989) and Anderson (2007). The variation of Q as a function of temperature can thus be described with an Arrhenius law, which in case of weak frequency-dependence ($0 < \alpha < 1$) has the following form (e.g., Karato, 1993; Jackson, 1993; Romanowicz and Mitchell, 2015):

$$Q(\omega, p, T) = A \cdot \left(\omega \cdot \exp\left[\frac{H^*(p)}{RT}\right]\right)^{\alpha} = A \cdot \omega^{\alpha} \cdot \exp\left(\frac{\alpha H^*(p)}{RT}\right), \quad (4.5)$$

where the pre-exponential term $A = \frac{\tau_0}{2 \cdot Q_{max}}$ is a material constant and H^* the pressure-dependent activation enthalpy for thermally activated processes ($H^* = E^* + pV^*$; that is, the pressure dependence is incorporated via the activation volume, V^*). This description is, however, accompanied by considerable uncertainties as both mineralogical parameters α and H^* are exceedingly challenging to constrain. α has been studied quite extensively already (e.g., Liu et al., 1976; Kanamori and Anderson, 1977; Jackson et al., 2002; Cheng and Kennett, 2002; Shito et al., 2004; Jackson et al., 2004), whereas H^* has been roughly determined only for a few relevant mantle minerals (Webb and Jackson, 2003; Bějina et al., 2003; Holzapfel et al., 2005).

Anelasticity Correction of Seismic Velocities. In addition to the decay of wave amplitudes, anelasticity leads to physical dispersion; that is, the phase velocity of the wave varies with frequency (e.g., Dahlen and Tromp, 1998). Physical dispersion is a necessary consequence of

anelasticity, as otherwise causality would be violated (see, for example, Aki and Richards, 2002). The according frequency dependence of the elastic moduli can be described by (e.g., Dahlen and Tromp, 1998):

$$\mu(\omega) = \mu_0 \left[1 + \frac{2}{\pi} \cdot Q_\mu^{-1} \cdot \ln \left(\frac{\omega}{\omega_0} \right) + iQ_\mu^{-1} \right], \quad (4.6)$$

$$\kappa(\omega) = \kappa_0 \left[1 + \frac{2}{\pi} \cdot Q_\kappa^{-1} \cdot \ln \left(\frac{\omega}{\omega_0} \right) + iQ_\kappa^{-1} \right] \quad (4.7)$$

with μ_0 denoting shear and κ_0 bulk modulus at a certain reference frequency ω_0 . As noted in Section 4.2.1, frequencies used to measure seismic velocities in laboratory experiments lie far above the teleseismic frequency range and thus outside of the absorption band. Therefore, a correction has to be applied to the anharmonic velocities to account for physical dispersion (e.g., Karato, 1993; Karato and Karki, 2001). In case of a mild frequency dependence of Q within the absorption band (i.e., $0 < \alpha < 1$), the anelasticity correction becomes (e.g., Minster and Anderson, 1981; Karato, 1993):

$$v(\omega, p, T) = v_0(p, T) \cdot \left[1 - \left(\frac{1}{2} \right) \cdot \cot \left(\frac{\pi\alpha}{2} \right) \cdot Q^{-1}(\omega, p, T) \right], \quad (4.8)$$

where $v(\omega, p, T)$ is the corrected and $v_0(p, T)$ the (elastic) reference velocity. The pressure-, temperature- and frequency-dependent attenuation $Q^{-1}(\omega, p, T)$ can be taken from Equation 4.5. Strictly speaking, this formulation is only valid for a quality factor $Q \gg 1$. This assumption, however, seems justifiable for the majority of regions within the Earth. Note also that this correction acts on the absolute value of the seismic velocity for a given absolute temperature (i.e., the correction is not applied to the temperature derivatives here).

Owing to the large uncertainty in activation volumes of mantle minerals as well as their change in grain size with depth (i.e., typically the least-known of the relevant parameters), different strategies have been devised to handle the pressure/depth dependence of Q in Equation 4.5: One possibility is to use the homologous temperature (T/T_m) to fold the pressure dependence into the profile of melting temperature $T_m(z)$ via a dimensionless parameter g (Karato, 1993; Cammarano et al., 2003; Goes et al., 2004):

$$Q(z, T) = B \cdot \left(\omega^\alpha \cdot \exp \left[\frac{\alpha g T_m(z)}{T} \right] \right), \text{ with } g = \frac{H^*(z)}{RT_m(z)}. \quad (4.9)$$

Here, z is depth in the mantle, and models of Q are obtained in this method by choosing (i.e., fitting) the parameter g and the pre-exponential factor B such that mean Q values fall within the range of seismically derived 1-D Q profiles. The alternative approach is to fold the

pressure dependence into a reference 1-D Q profile via a reference temperature (e.g., an adiabat; Stixrude and Lithgow-Bertelloni, 2007). In this case, the deviation of Q from the average 1-D profile is approximated by considering the temperature difference between the local and radial reference temperature:

$$Q(z, T) = Q_R(z) \cdot \exp \left[\frac{\alpha E^*}{R} \left(\frac{1}{T(z)} - \frac{1}{T_R(z)} \right) \right]. \quad (4.10)$$

$Q(z, T)$ denotes the depth- and temperature-dependent quality factor, $Q_R(z)$ the depth-dependent Q profile given by the chosen 1-D reference model, and $T_R(z)$ the reference temperature. Note that the pre-exponential factor vanishes, as Equation (4.10) is derived from Equation (4.5) by taking the ratio of $Q(z, T) = Q(T(z))$ and $Q_R(z) = Q(T_R(z))$. This, however, is only legitimate if Q_{max} and τ_0 are not varying laterally. Additional assumptions in the derivation of Equation (4.10), which seem reasonable for the mantle, are: (1) pressure varies only with depth (i.e., lateral pressure variations are negligible) and the pressure dependence of H^* ($=E^* + pV^*$) is therefore reasonably incorporated in the reference temperature- and Q -profiles, such that V^* vanishes; and (2) the activation energy, E^* , and α are constant within the entire mantle. Note that a variation of α with depth could also be modeled without much effort by using $\alpha \rightarrow \alpha(z)$ in Equation (4.10). So far, however, no indication has been found of any substantial depth dependence of α in the lower mantle (Lekić et al., 2009).

The final form of the anelastic correction is then obtained by inserting either Equation (4.9) or Equation (4.10) into Equation (4.8). Both approaches for dealing with the pressure dependence require some choice for the 1-D Q profile and the value for α . Which of the two approaches to prefer depends to some extent on how well the profiles of melting temperature or mean reference temperature are known. A certain disadvantage in case of the homologous temperature approach is that additional assumptions have to be made on the chemical composition of the mantle, and the two tuning parameters B and g are only loosely constrained by the available reference 1-D Q profiles. In the alternative case with a reference mantle temperature, only the activation energy E^* has to be specified in addition to the 1-D Q profile and α . This is a parameter that, in general, can be constrained by laboratory experiments. We therefore opt to use Equation (4.10), and the anelasticity correction then has the following form:

$$v(z, T) = v_0(z, T) \cdot \left[1 - \left(\frac{1}{2} \right) \cot \left(\frac{\pi\alpha}{2} \right) \cdot Q_R^{-1}(z) \cdot \exp \left[\frac{\alpha E^*}{R} \cdot \left(\frac{1}{T_R(z)} - \frac{1}{T} \right) \right] \right]. \quad (4.11)$$

This equation is assumed to hold for S -wave as well as P -wave velocities. By relating the variations in Q due to temperature to a reference Q profile Q_R , the anelasticity correction in this form does not depend directly on frequency ω . The seismic velocity obtained from Equation (4.11) thus corresponds to the frequency at which the reference Q profile is defined. To obtain the anelasticity corrected seismic velocities at other frequencies, one has to apply a correction for the physical dispersion (cf. Equations (4.6), (4.7) and (4.8) considering the change in Q_R with frequency. Note that the software used in this study to compute global 3-D wave propagation, *SPEC-FEM3D_GLOBE* (Komatitsch and Tromp, 2002a,b), is set up such as to account for physical dispersion in case that intrinsic attenuation is considered in the simulations (Savage et al., 2010).

To compute the anelasticity correction with Equation 4.11, Stixrude and Lithgow-Bertelloni (2007) used values of 0.26 for α and 424 kJ/mol for E^* (based on the mineralogical study of Jackson et al., 2002) using an adiabatic reference temperature profile with a potential temperature of 1600 K together with the 1-D Q -model QR19 (Romanowicz, 1995). Figures 4.4a and 4.4b show the changes in P - and S -wave velocities, respectively, due to anelasticity for this parameter combination. As expected from Equation 4.2, the lower Q values for shear waves result in larger velocity reductions in v_s than in v_p . For mean mantle temperatures (cf. Figure 4.4c, showing a typical temperature distribution and mean temperature profile of geodynamic models, here a model from Davies et al., 2012), the changes in v_s are about 1% in the upper mantle and between 0.2% and 0.5% in the lower mantle. Regions with colder than average temperatures are little affected, while for the hottest regions in the geodynamic model, anelasticity can change the shear wave velocity by up to 2%. In other words, the strong nonlinearity of the temperature dependence of Q is also seen in the anelasticity corrected seismic velocities.

4.4. QUANTIFYING THE EFFECTS OF UNCERTAINTIES RELATED TO ANELASTICITY

In the following, we will illustrate the effects of the anelasticity correction, first on the temperature derivatives of seismic velocities, and in a second step, on the traveltimes variations predicted from the temperature field of a mantle circulation model. In contrast to the linearized temperature derivatives, the latter represents a highly complex scenario with a three-fold nonlinearity:

1. The nonlinear relation between temperature and anharmonic velocities in the mineralogical model;
2. The strongly nonlinear effects of the anelasticity correction together with the depth-dependent skewed

temperature distributions in the mantle (cf. Figure 4.4c);

3. Nonlinear wave field effects (see e.g., Schubert et al., 2015).

This strong complexity prohibits any simplified prediction of seismic observables from geodynamic simulations based on, for example, linear scalings from temperature to seismic velocity or the use of approximate physics for computing the seismic data, such as the ray-theoretical prediction of traveltimes. Rather, this complexity calls for a correct treatment of the physics of each individual modeling step (e.g., numerical full 3-D wave field simulations, but also including compressibility in mantle convection simulations) to obtain robust and meaningful results.

In this study, we adopt Equation 4.10 to compute the anelasticity correction; that is, in the form of Equation 4.11, with the difference that the mean temperature profile of the MCM is used as reference rather than an adiabat to ensure internal consistency. In case of “forward” geodynamic models, Equation 4.10 is favored over Equation 4.9, as the reference temperature in this synthetic scenario is perfectly known, in contrast to the solidus profile of the mantle. For the reference profile Q_R , we chose a number of different 1-D seismic Q models (see Figure 4.3) such that they span a large part of the observed variability among them in the lower mantle. Specifically, we use PREM (Dziewonski and Anderson, 1981), AK135f (Montagner and Kennett, 1996), SL8 (Anderson and Hart, 1978) and DurandQ (Durand et al., 2013). PREM features a constant Q value in the lower mantle that allows us to illustrate depth-dependent effects in the other parameters. AK135f, SL8, and DurandQ, in contrast, all have strong variations of Q with depth in the lower mantle, where AK135f with a strong decrease of Q shows exactly the opposite behavior of SL8, which has a smooth transition across the upper mantle–lower mantle boundary and a steady increase of Q down to depths of around 2700 km. Close to the CMB, SL8 features extremely low Q values, where DurandQ, which has a minimum Q -peak in the mid-lower mantle, actually shows the highest values. Since the quality factor in those models is given for shear deformation only ($Q_{R,\mu} = Q_{R,v_s}$), Q_{R,v_p} is approximated with the help of Equation 4.2 and the typical assumption of infinite Q_κ .

In addition to the reference Q -profile, the choice of the values for the factor of frequency dependence α and the activation energy E^* influences the temperature sensitivity of the seismic velocities and thus the strength of seismic heterogeneity predicted for a given temperature (or conversely, the temperature anomaly assigned to a seismic velocity perturbation imaged, for example, in tomographic models). It is important to emphasize once more

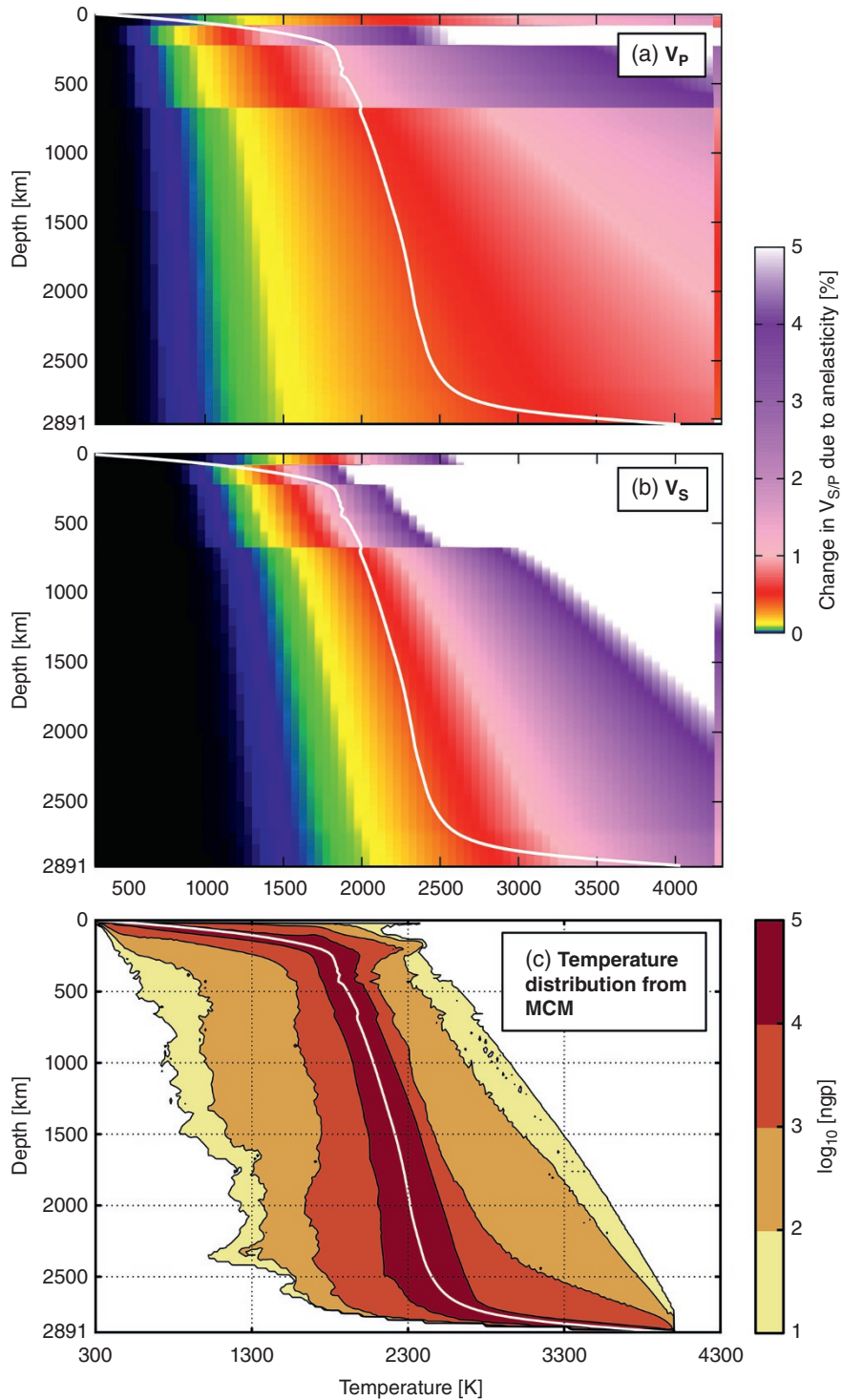


Figure 4.4 (a) Change in P -wave velocity due to the anelastic correction as a function of temperature and depth for the parameter combination $\alpha = 0.26$ and $E^* = 424$ kJ/mol (b) Same for S -wave velocity. Black-to-purple color scale: relative difference between corrected and elastic shear wave velocities (clipped at 5%, as higher differences all occur above typical mantle melting temperatures and are thus unphysical in the solid-state framework of the thermodynamic mineralogical models). (c) A typical distribution of temperatures in MCMs. Yellow-to-brown color scale: total number of model grid points (ngp) at given depth and temperature. White lines in (a–c): profile of average temperature from the histograms of c. Comparison of c with a and b illustrates that only hot anomalies (temperatures above average) in the hypothetical mantle model will be affected significantly by the anelastic correction, which gives rise to an additional nonlinearity in the modeling of traveltime residuals in combination with its skewed temperature distribution. *Source:* (c) Davies et al., 2012.

that these parameters bear large uncertainties. In particular, the activation energy, E^* , which is generally expected to vary strongly throughout the mantle given the broad spectrum of microscopic absorption mechanisms, has only been roughly constrained to lie in the range of 100–1000 kJ/mol (Matas and Bukowinski, 2007). We restrict ourselves to a maximum value of 500 kJ/mol in the following, since otherwise the predicted Q values drop to unreasonably low values (below 15) in the hottest regions of our model that are likely too low for teleseismic waves (see e.g., Romanowicz and Mitchell, 2015; Liu and Grand, 2018). For α , an upper bound of 0.3 is used in the wave propagation simulations (see Figure 4.6), which is consistent with laboratory measurements as well as seismological observations (e.g., Lekić et al., 2009; Romanowicz and Mitchell, 2015). Both the activation energy E^* and α are assumed to be constant within the entire mantle. With this set of parameters, the primary goal of this analysis is to investigate the maximum effects of anelasticity, although in some cases also more moderate values of α and E^* will be tested for illustration purposes.

Figure 4.5 shows the effect of the anelasticity correction on the temperature derivatives of P - and S -wave velocities for the lower mantle using the PREM values for the 1-D Q reference profile. The four panels depict the deviation of the seismic velocities relative to the anharmonic case. As the elastic as well as anelastic temperature derivatives depend on temperature (e.g., Matas and Bukowinski, 2007), this deviation is computed by evaluating both the absolute values of the elastic as well as the anelasticity corrected seismic velocities at a temperature of 3000 K at each depth in the mineralogical table of (Chust et al., 2017). A temperature of 3000 K might seem rather high, but it is used here to illustrate the extreme effects possible in case of anelastic material behavior and it still falls within the range of values found in the lower mantle in mantle convection simulations (cf. Figure 4.4). Furthermore, we want to emphasize that the temperature derivatives of the seismic velocities displayed in Figure 4.5 correspond to one single frequency; that is, the frequency at which the reference Q profile is defined (e.g., 1 Hz in case of PREM). To compute the anelasticity corrected temperature derivatives at other frequencies, one has to correct the absolute values of the anelasticity corrected seismic velocities for physical dispersion prior to computing the temperature derivatives.

To highlight the imprint of the uncertainty in both α and E^* independently, the upper panels show the range of variability induced by α for a constant E^* of 424 kJ/mol, and the lower panels show the variability due to uncertainties in E^* with α being fixed to 0.26. In both cases, the effects on P wave velocities (left panels) is smaller than for S waves (right panels), as expected from the generally lower Q values in the latter case. The comparison between upper

and lower panels shows that the uncertainty in α has a smaller effect compared to the uncertainty in E^* . For the former, the corrected “anelastic” temperature derivatives are at most about 80% larger than the elastic velocities in the uppermost lower mantle in case of S waves (50% in the lowermost mantle), whereas in case of an activation energy of 500 kJ/mol, the deviation from the elastic case reaches up to 150% (uppermost lower mantle; 70% in the lowermost lower mantle). This means that for the extreme cases of α and E^* , anelasticity has a substantial impact on the temperature derivatives for material at high temperatures that amounts to at least half of the contribution from anharmonic behavior even in the lowermost lower mantle. The decrease of the anelastic contribution with depth is largely due to the decrease of the effective temperature anomaly for the fixed temperature of 3000 K relative to the reference temperature.

Our results in Figure 4.5, which show the “deviation from the elastic case,” are compatible with the work of Matas and Bukowinski (2007), who used the “anelastic contribution” to the total derivative instead, which is just a different way of illustrating the effects of anelasticity. Also, our results are in line with the findings of Brodholt et al. (2007), the difference being that they focus on the “most probable” effect of anelasticity (through investigation of probability density functions), while we concentrate on extreme values. For extreme choices of the anelasticity parameters, Brodholt et al. (2007) find that an increase of the temperature derivatives by up to a factor of 2 is possible for $\Delta T = +1000$ K, and factors still larger than 1.6 for $\Delta T = +500$ K (cf. their Figure 4.3).

Finally, we want to illustrate the effects of anelasticity-related uncertainties on predicted seismic traveltime residuals. The following analysis underlines the importance of uncertainty propagation as an important component in our forward modeling approach. Figure 4.6a shows the range of standard deviations of seismic body-wave traveltime residuals resulting from the uncertainty in α and E^* . Here, the anelastic correction is applied to the absolute values of anharmonic seismic velocities obtained from the MCM following Equation 4.11 (i.e., they are not based on the temperature derivatives shown in Figure 4.5). In this example, the underlying 1-D Q -profile is PREM and the standard deviations are given for values of α and E^* of 0.3 and 500 kJ/mol, respectively, as well as for the purely elastic (i.e., anharmonic) case. Simulations, traveltime measurements and the statistical analysis have been done in the same way as in *Schuberth et al.* (2012), only that we performed two sets of wave propagation simulations, one with and one without 3-D attenuation (note that the difference in standard deviations between both cases in fact is very small).

In most of the lower mantle, the differences between the anharmonic and the maximum anelastic case are about

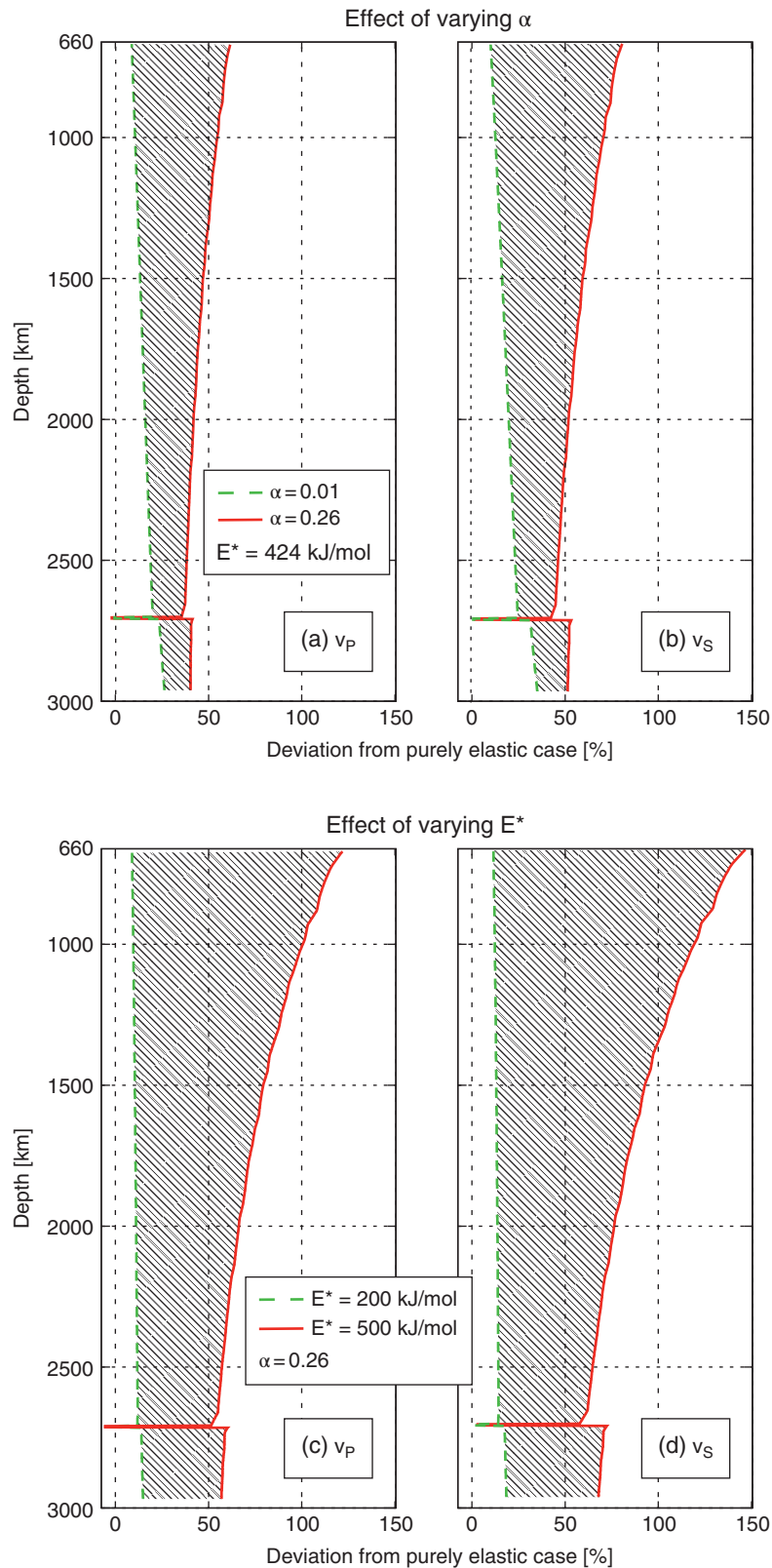


Figure 4.5 Example of the effect of the anelastic correction on the temperature derivatives at a temperature of 3000 K for different values of α and E^* for (a, c) P - and (b, d) S -wave velocities. Note that this high temperature still falls into the plausible range of temperatures in the lower mantle (cf. Figure 4.4) and was chosen to illustrate the potentially dramatic effects of anelasticity for the very hot regions in the mantle. The panels show the relative difference in temperature derivatives between anelastic and elastic case. (a, b) Influence of varying α between (green dashed line) 0.01 and (red line) 0.26. (c, d) Influence of varying the activation energy between (green dashed line) 200 and (red line) 500 kJ/mol. PREM values are used for the reference 1-D Q -profile. The activation energy is kept fix at 424kJ/mol in (a, b) and α is kept fix at 0.26 in (c, d).

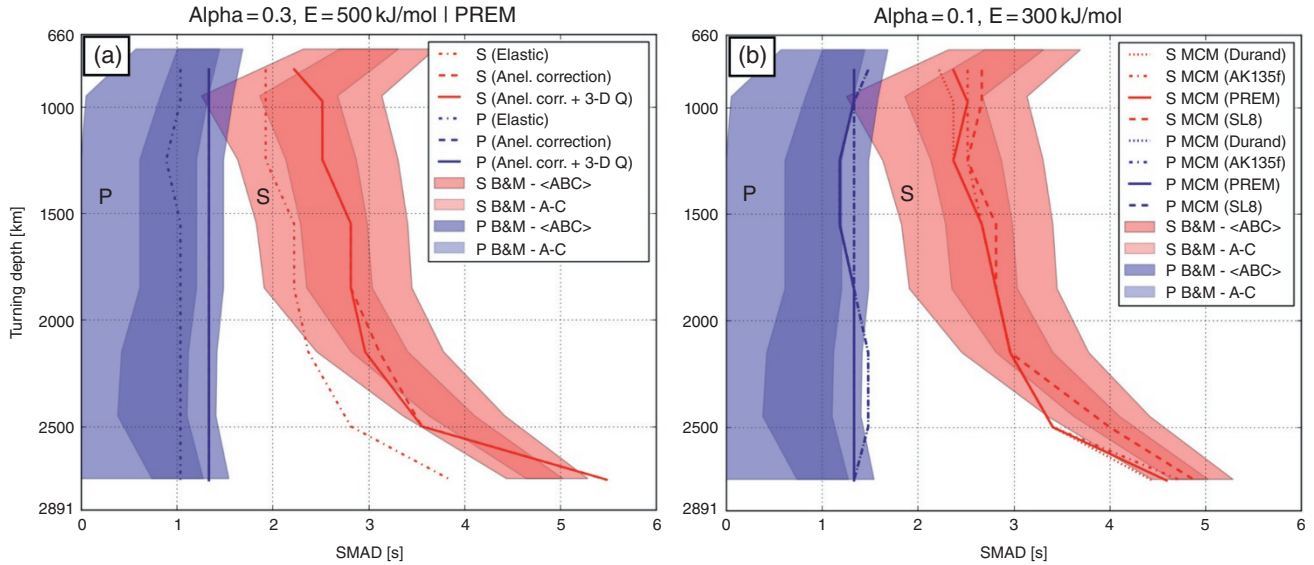


Figure 4.6 Same as Figure 4.2b: (a) for the extreme case with $\alpha = 0.3$ and $E^* = 500$ kJ/mol compared to the elastic case (solid and dash-dotted lines, respectively; PREM values were used for the reference 1-D Q profile); and (b) for different reference 1-D Q profiles with fixed values for α and E^* of 0.1 and 300 kJ/mol, respectively. Note that the standard deviations change only slightly for S waves in case that 3-D attenuation is included in the wave propagation simulations (curves labelled “Anel. corr. + 3-D Q ” in a).

0.6 s for S and 0.3 s for P waves. Only in the lowermost mantle, the differences are much larger in case of S waves reaching around 1.5 s. Given the standard deviations of the P - and S -wave traveltime residuals for the elastic case of 1 and 2–4 s (top to bottom of the lower mantle), respectively, the change due to the anelastic correction amounts to roughly 30% of the initial signal. From the comparison between the elastic and the maximum anelastic case, and bearing the effects of anelasticity on the temperature sensitivities in mind, it is clear that only part of the increased anelastic velocity perturbations “survives” in the wave propagation and shows up in the signal of traveltime residuals. Owing to the nonlinear temperature dependence of attenuation, it is also clear that it is the hot, seismically slow regions that contribute most to the observed increase in the traveltime residuals. Looking at the distribution of temperatures in the geodynamic model in Figure 4.4c, one can also understand why the largest change in the traveltime residuals occurs close to the CMB. There, the histograms are skewed toward high temperatures and also the highest plume excess temperatures are located in this depth range.

In addition to the uncertainty in the mineralogical parameters, Figure 4.6b shows the variability in the traveltime residuals induced by the unknown reference Q structure of the mantle. Standard deviations of P - and S -wave traveltimes are plotted for the 1-D Q models PREM, AK135f, SL8, and DurandQ for a parameter combination of $\alpha = 0.1$ and $E^* = 300$ kJ/mol. Even for these moderate

values, differences on the order of 0.3–0.4 s are observed. As can be seen from the rather small differences in the mid-lower mantle, the variability among the models in Q at that depth does not map linearly into the standard deviations of traveltime residuals. Although we do not show the case for a parameter combination of $\alpha = 0.3$ and $E^* = 500$ kJ/mol, we note that the differences among the various Q models increases in this case, as expected, but does not exceed the difference between the elastic and maximum anelastic case shown in Figure 4.6a. Although it is not the focus of this study, we note that the geophysical hypothesis underlying our current simulations (isochemical convection with pyrolitic bulk composition, a CMB temperature of 4200 K equivalent to 12 TW of core heating, a viscosity increase of a factor of 100 from upper to lower mantle) is compatible with the seismic observations of Bolton and Masters (2001) in case of a moderate to strong contribution of the anelasticity correction.

4.5. SUMMARY AND CONCLUDING REMARKS

The pure forward-modeling approach illustrated in this study bears great potential for providing new insight into deep mantle structure and dynamics. In particular, including systematic investigations of uncertainties in the various input parameters is possible with current modeling

techniques and computational resources and allows for robust conclusions to be drawn from comparisons between predicted and observed data. In complementing tomographic inversions, this approach will help to constrain the buoyancy distribution in the mantle at length-scales so far unresolvable by tomography. The general idea is to predict seismic observables based on some geophysical hypothesis by going through a chain of simulation steps; that is, solving the hydrodynamic equations for the mantle, converting temperatures to seismic velocities via a mineralogical model including the anelastic correction, and running 3-D global wave simulations in the geodynamically derived seismic structures. In the current work, we have provided a first attempt to include input parameter uncertainties in such a comprehensive forward-modeling chain. Specifically, we concentrated on the associated range of possible values of the temperature-seismic velocity conversion related to the poorly constrained parameters controlling anelasticity. Including the anelastic correction in the forward-modeling workflow, used to translate convection related parameters to seismic traveltime residuals results in a complex physical scenario comprising multiple nonlinearities. In addition to the nonlinear relation between temperatures and anharmonic seismic velocities and the nonlinearity of wave field effects, the highly nonlinear anelasticity correction has a strong influence on final predictions. Its effects are largely negligible for cold temperatures and thus for regions with fast seismic velocities, while for very hot regions, the anelastic correction can result in an increase of the relative velocity perturbations in the lower mantle by almost a factor of two compared to the anharmonic case. Our simulations demonstrate that owing to the skewed distributions of temperatures in the mantle and the fact that wavefront healing is particularly important for slow seismic anomalies, it is impossible to predict seismic traveltime residuals correctly by simple linear scaling and ray-theoretical calculations. Rather, it becomes clear from our study that it is vital that all nonlinearities are correctly modeled in each step of the forward-modeling chain in order to obtain consistent seismic predictions and fair comparisons to the real data.

Our results show that the range of values for the activation energy E^* discussed in the literature leads to larger uncertainty in the temperature derivatives of seismic velocities compared to the uncertainties from the factor of frequency dependence of attenuation α . When looking at the most extreme case assuming maximum values plausible for α and E^* of 0.3 and 500 kJ/mol, respectively, the temperature derivative of v_s can change by up to 150% at the top and 70% at the bottom of the lower mantle (120% and 60% in case of v_p , respectively). In the case of little to no frequency dependence of attenuation and more moderate values of E^* of 200 kJ/mol, this change is less than 30%

throughout the lower mantle for both v_p and v_s . We further find that for our high heat-flow thermal MCM, the standard deviation of P - and S -wave traveltime residuals for the extreme values of α and E^* is increased by about 30% compared to the anharmonic case. This result illustrates the strong nonlinearity of the physical situation at hand.

In conclusion, uncertainties on the anelastic behavior of mantle minerals can contribute a large part of the uncertainty in final predictions. Therefore, future efforts in mineral physics should not only be directed toward reducing the uncertainties in the parameters controlling the anharmonic velocities, but also toward better constraining the frequency dependence of attenuation as well as the activation energies and volumes of relevant mantle minerals. Seismological studies, on the other hand, should aim at narrowing the possible range of values for α , taking wave field effects due to 3-D structure into account, in addition to the ongoing efforts of better constraining the 1-D Q profile of Earth.

ACKNOWLEDGMENTS

We want to thank the editors as well as Ian Jackson and two anonymous reviewers for constructive comments that helped to improve the manuscript. We also thank Claudia Gräber for preliminary work on the influence of the anelastic correction. We gratefully acknowledge the Gauss Centre for Supercomputing e.V. (www.gauss-centre.eu) for funding this project by providing computing time on the GCS Supercomputer SuperMUC at Leibniz Supercomputing Centre (LRZ, www.lrz.de).

REFERENCES

- Abers, G. A., K. M. Fischer, G. Hirth, D. A. Wiens, T. Plank, B. K. Holtzman, C. McCarthy, & E. Gazel (2014). Reconciling mantle attenuation-temperature relationships from seismology, petrology, and laboratory measurements. *Geochem. Geophys. Geosyst.*, 15(9), 3521–3542, doi:10.1002/2014gc005444.
- Agranier, A., J. Blicherttoft, D. Graham, V. Debaille, P. Schiano, & F. Albarede (2005). The spectra of isotopic heterogeneities along the mid-Atlantic Ridge. *Earth Planet. Sci. Lett.*, 238(1–2), 96–109, doi:10.1016/j.epsl.2005.07.011.
- Aki, K., & P. G. Richards (2002). *Quantitative seismology*. University Science Books, Sausalito, California.
- Allègre, C. J., & D. L. Turcotte (1986). Implications of a two-component marble-cake mantle. *Nature*, 323(6084), 123–127, doi:10.1038/323123a0.
- Anderson, D. L. (1989). *Theory of the Earth*. Blackwell Scientific Publications, Boston, MA.
- Anderson, D. L. (2007). *New theory of the Earth*. Cambridge University Press, New York.
- Anderson, D. L., & R. S. Hart (1978). Q of the earth. *J. Geophys. Res.*, 83(B12), 5869–5882, doi:10.1029/jb083ib12p05869.

- Anderson, D. L., & J. B. Minster (1979). The frequency dependence of Q in the Earth and implications for mantle rheology and Chandler wobble. *Geophys. J. Int.*, *58*(2), 431–440, doi:10.1111/j.1365-246x.1979.tb01033.x.
- Bao, X., C. A. Dalton, & J. Ritsema (2016). Effects of elastic focusing on global models of Rayleigh wave attenuation. *Geophys. J. Int.*, *207*(2), 1062–1079, doi:10.1093/gji/ggw322.
- Becker, T. W., & L. Boschi (2002). A comparison of tomographic and geodynamic mantle models. *Geochem. Geophys. Geosyst.*, *3*(1), 1003, doi:10.1029/2001GC000168.
- Bhattacharyya, J., G. Masters, & P. Shearer (1996). Global lateral variations of shear wave attenuation in the upper mantle. *J. Geophys. Res.*, *101*(B10), 22,273–22,289.
- Billien, M., J.-J. L ev eque, & J. Trampert (2000). Global maps of Rayleigh wave attenuation for periods between 40 and 150 seconds. *Geophys. Res. Lett.*, doi:10.1029/2000GL011389.
- Blanc, E., D. Komatitsch, E. Chaljub, B. Lombard, & Z. Xie (2016). Highly accurate stability-preserving optimization of the Zener viscoelastic model, with application to wave propagation in the presence of strong attenuation. *Geophys. J. Int.*, *205*(1), 427–439, doi:10.1093/gji/ggw024.
- Bolton, H., & G. Masters (2001). Travel times of P and S from the global digital seismic networks: Implications for the relative variation of P and S velocity in the mantle. *J. Geophys. Res.*, *106*(B7), 13,527–13,540.
- Boschi, L. (2003). Measures of resolution in global body wave tomography. *Geophys. Res. Lett.*, *30*(19), doi:10.1029/2003gl018222.
- Bower, D. J., M. Gurnis, & D. Sun (2013). Dynamic origins of seismic wavespeed variation in D'' . *Phys. Earth Planet. Inter.*, *214*, 74–86, doi:10.1016/j.pepi.2012.10.004.
- Bozdağ, E., D. Peter, M. Lefebvre, D. Komatitsch, J. Tromp, J. Hill, N. Podhorszki, & D. Pugmire (2016). Global adjoint tomography: first-generation model. *Geophys. J. Int.*, *207*(3), 1739–1766, doi:10.1093/gji/ggw356.
- Brodholt, J. P., G. Helffrich, & J. Trampert (2007). Chemical versus thermal heterogeneity in the lower mantle: The most likely role of anelasticity. *Earth Planet. Sci. Lett.*, *262*(3–4), 429–437, doi:10.1016/j.epsl.2007.07.054.
- Bull, A., A. McNamara, & J. Ritsema (2009). Synthetic tomography of plume clusters and thermochemical piles. *Earth Planet. Sci. Lett.*, *278*(3–4), 152–162, doi:10.1016/j.epsl.2008.11.018.
- Bunge, H.-P., & J. H. Davies (2001). Tomographic images of a mantle circulation model. *Geophys. Res. Lett.*, *28*(1), 77–80, doi:10.1029/2000gl011804.
- Bunge, H.-P., M. Richards, & J. Baumgardner (1997). A sensitivity study of 3D-spherical mantle convection at $10\text{exp}8$ Rayleigh number: effects of depth-dependent viscosity, heating mode and an endothermic phase change. *J. Geophys. Res.*, *102*, 11,991–12,007, doi:10.1029/96JB03806.
- Bunge, H.-P., M. Richards, & J. Baumgardner (2002). Mantle circulation models with sequential data-assimilation: Inferring present-day mantle structure from plate motion histories. *Phil. Trans. Roy. Soc. A*, *360*(1800), 2545–2567, doi:10.1098/rsta.2002.1080.
- B ejina, F., O. Jaoul, & R. C. Liebermann (2003). Diffusion in minerals at high pressure: a review. *Phys. Earth Planet. Inter.*, *139*(1–2), 3–20, doi:10.1016/s0031-9201(03)00140-7.
- Cammarano, F., S. Goes, P. Vacher, & D. Giardini (2003). Inferring upper-mantle temperatures from seismic velocities. *Phys. Earth Planet. Inter.*, *138*(3–4), 197–222, doi:10.1016/S0031-9201(03)00156-0.
- Cheng, H.-X., & B. L. N. Kennett (2002). Frequency dependence of seismic wave attenuation in the upper mantle beneath the Australian region. *Geophys. J. Int.*, *150*(1), doi:10.1046/j.1365-246x.2002.01677.x.
- Chust, T. C., G. Steinle-Neumann, D. Dolejř, B. S. A. Schuberth, & H.-P. Bunge (2017). MMA-EoS: A computational framework for mineralogical thermodynamics. *J. Geophys. Res.*, *122*(12), 9881–9920, doi:10.1002/2017JB014501.
- Cobden, L., S. Goes, M. Ravenna, E. Styles, F. Cammarano, K. Gallagher, & J. A. D. Connolly (2009). Thermochemical interpretation of 1-D seismic data for the lower mantle: The significance of nonadiabatic thermal gradients and compositional heterogeneity. *J. Geophys. Res.*, *114*(B11), B11,309, doi:10.1029/2008JB006262.
- Cobden, L., J. Trampert, & A. Fichtner (2018). Insights on upper mantle melting, rheology, and anelastic behavior from seismic shear wave tomography. *Geochem. Geophys. Geosyst.*, *19*(10), 3892–3916, doi:10.1029/2017gc007370.
- Colli, L., H.-P. Bunge, & B. S. A. Schuberth (2015). On retrodictions of global mantle flow with assimilated surface velocities. *Geophys. Res. Lett.*, *42*(20), 8341–8348, doi:10.1002/2015gl066001.
- Colli, L., S. Ghelichkhan, H.-P. Bunge, & J. Oeser (2018). Retrodictions of Mid Paleogene mantle flow and dynamic topography in the Atlantic region from compressible high resolution adjoint mantle convection models: Sensitivity to deep mantle viscosity and tomographic input model. *Gondwana Research*, *53*, 252–272, doi:https://doi.org/10.1016/j.gr.2017.04.027, rifting to Passive Margins.
- Connolly, J. A. D. (2009). The geodynamic equation of state: What and how. *Geochem. Geophys. Geosyst.*, *10*, Q10,014, doi:10.1029/2009GC002540.
- Connolly, J. A. D., & A. Khan (2016). Uncertainty of mantle geophysical properties computed from phase equilibrium models. *Geophys. Res. Lett.*, *43*(10), 5026–5034, doi:10.1002/2016gl068239.
- Dahlen, F. A., & J. Tromp (1998). *Theoretical global seismology*. Princeton, NJ: Princeton University Press.
- Dahlen, F. A., S. H. Hung, & G. Nolet (2000). Fr chet kernels for finite-frequency traveltimes – I. Theory. *Geophys. J. Int.*, *141*(1), 157–174, doi:10.1046/j.1365-246x.2000.00070.x.
- Dalton, C. A., & G. Ekstrom (2006). Constraints on global maps of phase velocity from surface-wave amplitudes. *Geophys. J. Int.*, *167*(2), 820–826.
- Dalton, C. A., G. Ekstr om, & A. M. Dziewoński (2008). The global attenuation structure of the upper mantle. *J. Geophys. Res.*
- Dalton, C. A., C. H. Langmuir, & A. Gale (2014). Geophysical and geochemical evidence for deep temperature variations beneath mid-ocean ridges. *Science*, *344*(6179), 80–83, doi:10.1126/science.1249466.
- Dannberg, J., Z. Eilon, U. Faul, R. Gassm oller, P. Moulik, & R. Myhill (2017). The importance of grain size to mantle dynamics and seismological observations. *Geochem. Geophys. Geosyst.*, *18*(8), 3034–3061, doi:10.1002/2017GC006944.

- Davies, D. R., S. Goes, J. Davies, B. Schuberth, H.-P. Bunge, & J. Ritsema (2012). Reconciling dynamic and seismic models of Earth's lower mantle: The dominant role of thermal heterogeneity. *Earth Planet. Sci. Lett.*, 353–354(0), 253–269, doi:10.1016/j.epsl.2012.08.016.
- Davies, D. R., S. Goes, & H. C. P. Lau (2015). Thermally dominated deep mantle LLSVPs: A review. *The Earth's Heterogeneous Mantle*, pp. 441–477, doi:10.1007/978-3-319-15627-9_14.
- Davies, J. H., & H.-P. Bunge (2001). Seismically “fast” geodynamic mantle models. *Geophys. Res. Lett.*, 28(1), 73–76.
- Day, S. M. (1982). Three-dimensional simulation of spontaneous rupture: the effect of nonuniform prestress. *Bull. Seismol. Soc. Am.*, 72(6A), 1881–1902, doi:10.1016/0148-9062(83)90099-2.
- Deschamps, F., L. Cobden, & P. J. Tackley (2012). The primitive nature of large low shear-wave velocity provinces. *Earth Planet. Sci. Lett.*, 349–350, 198–208, doi:10.1016/j.epsl.2012.07.012.
- Deschamps, F., K. Konishi, N. Fuji, & L. Cobden (2019). Radial thermo-chemical structure beneath western and northern Pacific from seismic waveform inversion. *Earth Planet. Sci. Lett.*, 520, 153–163, doi:10.1016/j.epsl.2019.05.040.
- Durand, S., J. Matas, S. Ford, Y. Ricard, B. Romanowicz, & J.-P. Montagner (2013). Insights from ScS–S measurements on deep mantle attenuation. *Earth Planet. Sci. Lett.*, 374, 101–110, doi:10.1016/j.epsl.2013.05.026.
- Durek, J. J., & G. Ekström (1996). A radial model of anelasticity consistent with long-period surface-wave attenuation. *Bull. Seismol. Soc. Am.*, 86(1A), 144–158.
- Dziewonski, A. M., & D. L. Anderson (1981). Preliminary reference Earth model. *Phys. Earth Planet. Inter.*, 25, 297–356, doi:10.1016/0031-9201(81)90046-7.
- Emmerich, H., & M. Korn (1987). Incorporation of attenuation into time-domain computations of seismic wave fields. *Geophysics*, 52, 1252–1264, doi:10.1190/1.1442386.
- Faul, U. H., & I. Jackson (2005). The seismological signature of temperature and grain size variations in the upper mantle. *Earth Planet. Sci. Lett.*, 234(1–2), 119–134, doi:10.1016/j.epsl.2005.02.008.
- Fichtner, A., A. Zunino, & L. Gebraad (2018). Hamiltonian Monte Carlo solution of tomographic inverse problems. *Geophys. J. Int.*, 216(2), 1344–1363, doi:10.1093/gji/ggy496.
- French, S. W., & B. A. Romanowicz (2014). Whole-mantle radially anisotropic shear velocity structure from spectral-element waveform tomography. *Geophys. J. Int.*, 199(3), 1303–1327, doi:10.1093/gji/ggu334.
- Goes, S., F. Cammarano, & U. Hansen (2004). Synthetic seismic signature of thermal mantle plumes. *Earth Planet. Sci. Lett.*, 218(3–4), 403–419, doi:10.1016/S0012-821X(03)00680-0.
- Gung, Y., & B. Romanowicz (2004). Q tomography of the upper mantle using three-component long-period waveforms. *Geophys. J. Int.*, 157(2), 813–830.
- Heister, T., J. Dannberg, R. Gassmöller, & W. Bangerth (2017). High accuracy mantle convection simulation through modern numerical methods – II: realistic models and problems. *Geophys. J. Int.*, 210(2), 833–851, doi:10.1093/gji/ggx195.
- Holzappel, C., D. C. Rubie, D. J. Frost, & F. Langenhorst (2005). Fe-Mg interdiffusion in (Mg,Fe)SiO₃ perovskite and lower mantle reequilibration. *Science*, 309(5741), 1707–1710, doi:10.1126/science.1111895.
- Hung, S.-H., F. Dahlen, & G. Nolet (2000). Fréchet kernels for finite-frequency traveltimes – II. Examples, *Geophys. J. Int.*, 141(1), 175–203, doi:10.1046/j.1365-246x.2000.00072.x.
- Hwang, Y. K., J. Ritsema, P. E. van Keken, S. Goes, & E. Styles (2011). Wavefront healing renders deep plumes seismically invisible. *Geophys. J. Int.*, 187(1), 273–277, doi:10.1111/j.1365-246X.2011.05173.x.
- Jackson, I. (1993). Progress in the experimental study of seismic wave attenuation, *Ann. Rev. Earth Planet. Sci.*, 21, 375–406, doi:10.1146/annurev.earth.21.1.375.
- Jackson, I., & U. H. Faul (2010). Grain-size-sensitive viscoelastic relaxation in olivine: Toward a robust laboratory-based model for seismological application. *Phys. Earth Planet. Inter.*, 183(1–2), 151–163, doi:10.1016/j.pepi.2010.09.005.
- Jackson, I., J. D. F. Gerald, U. H. Faul, & B. H. Tan (2002). Grain-size-sensitive seismic wave attenuation in polycrystalline olivine. *J. Geophys. Res.*, 107(B12), 2360, doi:10.1029/2001JB001225.
- Jackson, I., U. H. Faul, J. D. F. Gerald, & B. H. Tan (2004). Shear wave attenuation and dispersion in melt-bearing olivine polycrystals: 1. specimen fabrication and mechanical testing. *J. Geophys. Res.*, 109(B6), doi:10.1029/2003JB002407.
- Jackson, I., U. H. Faul, & R. Skelton (2014). Elastically accommodated grain-boundary sliding: New insights from experiment and modeling. *Phys. Earth Planet. Inter.*, 228, 203–210, doi:10.1016/j.pepi.2013.11.014.
- Jacobs, M. H., & A. P. van den Berg (2011). Complex phase distribution and seismic velocity structure of the transition zone: Convection model predictions for a magnesium-endmember olivine-pyroxene mantle. *Phys. Earth Planet. Inter.*, 186(1–2), 36–48, doi:10.1016/j.pepi.2011.02.008.
- Kanamori, H., & D. L. Anderson (1977). Importance of physical dispersion in surface wave and free oscillation problems: Review. *Rev. Geophys.*, 15(1), 105–112, doi:10.1029/rg015i001p00105.
- Karaoğlu, H., & B. Romanowicz (2017). Global seismic attenuation imaging using full-waveform inversion: a comparative assessment of different choices of misfit functionals. *Geophys. J. Int.*, 212(2), 807–826, doi:10.1093/gji/ggx442.
- Karato, S. (1993). Importance of anelasticity in the interpretation of seismic tomography. *Geophys. Res. Lett.*, 20, 1623–1626, doi:10.1029/93gl01767.
- Karato, S., & B. B. Karki (2001). Origin of lateral variation of seismic wave velocities and density in the deep mantle. *J. Geophys. Res.*, 106(B10), 21,771–21,783, doi:10.1029/2001jb000214.
- Karato, S., & J. Park (2018). On the origin of the upper mantle seismic discontinuities. In *Lithospheric discontinuities*, pp. 5–34. Hoboken, NJ: John Wiley & Sons, Inc., doi:10.1002/9781119249740.ch1.
- Karato, S., & D. J. Weidner (2008). Laboratory studies of the rheological properties of minerals under deep-mantle conditions. *Elements*, 4(3), 191–196, doi:10.2113/gselements.4.3.191.
- Käser, M., M. Dumbser, J. D. L. Puente, & H. Igel (2007). An arbitrary high-order discontinuous Galerkin method for elastic waves on unstructured meshes – iii. viscoelastic

- attenuation. *Geophys. J. Int.*, 168(1), 224–242, doi:10.1111/j.1365-246x.2006.03193.x.
- Koelemeijer, P., B. Schubert, D. Davies, A. Deuss, & J. Ritsema (2018). Constraints on the presence of post-perovskite in Earth's lowermost mantle from tomographic-geodynamic model comparisons. *Earth Planet. Sci. Lett.*, 494, 226–238, doi:https://doi.org/10.1016/j.epsl.2018.04.056.
- Komatitsch, D., & J. Tromp (2002a). Spectral-element simulations of global seismic wave propagation - I. Validation. *Geophys. J. Int.*, 149, 390–412.
- Komatitsch, D., & J. Tromp (2002b). Spectral-element simulations of global seismic wave propagation - II. Three-dimensional models, oceans, rotation and self-gravitation. *Geophys. J. Int.*, 150(1), 303–318.
- Komatitsch, D., J. Ritsema, & J. Tromp (2002). The spectral-element method, Beowulf computing, and global seismology. *Science*, 298, 1737–1742, doi:10.1126/science.1076024.
- Kustowski, B., G. Ekström, & A. M. Dziewonski (2008). Anisotropic shear-wave velocity structure of the Earth's mantle: A global model. *J. Geophys. Res.*, 113(B6), B06306, doi:10.1029/2007JB005169.
- Lau, H. C., & U. H. Faul (2019). Anelasticity from seismic to tidal timescales: Theory and observations. *Earth Planet. Sci. Lett.*, 508, 18–29, doi:10.1016/j.epsl.2018.12.009.
- Lau, H. C. P., J. X. Mitrovica, J. L. Davis, J. Tromp, H.-Y. Yang, & D. Al-Attar (2017). Tidal tomography constrains Earth's deep-mantle buoyancy. *Nature*, 551(7680), 321–326, doi:10.1038/nature24452.
- Lawrence, J. F., & M. E. Wysession (2006). QLM9: A new radial quality factor Q_{μ} model for the lower mantle. *Earth Planet. Sci. Lett.*, doi:10.1016/j.epsl.2005.10.030.
- Lay, T., & T. C. Wallace (1995). *Modern Global Seismology*, Academic Press, San Diego, – Sig.: Bc182.
- Lekić, V., J. Matas, M. Panning, & B. Romanowicz (2009). Measurement and implications of frequency dependence of attenuation. *Phys. Earth Planet. Inter.*, 282(1–4), 285–293, doi:10.1016/j.epsl.2009.03.030.
- Li, M., & A. K. McNamara (2013). The difficulty for subducted oceanic crust to accumulate at the Earth's core-mantle boundary. *J. Geophys. Res.*, 118(4), 1807–1816, doi:10.1002/jgrb.50156.
- Li, Y., F. Deschamps, & P. J. Tackley (2014). The stability and structure of primordial reservoirs in the lower mantle: insights from models of thermochemical convection in three-dimensional spherical geometry. *Geophys. J. Int.*, 199(2), 914–930, doi:10.1093/gji/ggu295.
- Liu, C., & S. P. Grand (2018). Seismic attenuation in the african LLSVP estimated from PcS phases. *Earth Planet. Sci. Lett.*, 489, 8–16, doi:10.1016/j.epsl.2018.02.023.
- Liu, H. P., D. L. Anderson, & H. Kanamori (1976). Velocity dispersion due to anelasticity: implications for seismology and mantle composition. *Geophys. J. R. Astron. Soc.*, 47, 41–58, doi:10.1111/j.1365-246x.1976.tb01261.x.
- Maguire, R., J. Ritsema, P. E. van Keken, A. Fichtner, & S. Goes (2016). *P* and *S*-wave delays caused by thermal plumes. *Geophys. J. Int.*, 206(2), 1169–1178, doi:10.1093/gji/ggw187.
- Maguire, R., J. Ritsema, M. Bonnin, P. E. van Keken, & S. Goes (2018). Evaluating the resolution of deep mantle plumes in teleseismic traveltime tomography. *J. Geophys. Res. – Solid Earth*, 123(1), 384–400, doi:10.1002/2017JB014730.
- Marquering, H., F. A. Dahlen, & G. Nolet (1999). Three-dimensional sensitivity kernels for finite-frequency travel-times: the banana-doughnut paradox. *Geophys. J. Int.*, 137, 805–815, doi:10.1046/j.1365-246x.1999.00837.x.
- Matas, J., & M. S. T. Bukowski (2007). On the anelastic contribution to the temperature dependence of lower mantle seismic velocities. *Earth Planet. Sci. Lett.*, 259(1–2), 51–65, doi:10.1016/j.epsl.2007.04.028.
- Matas, J., J. Bass, Y. Ricard, E. Mattern, & M. S. T. Bukowski (2007). On the bulk composition of the lower mantle: predictions and limitations from generalized inversion of radial seismic profiles. *Geophys. J. Int.*, 170, 764–780, doi:10.1111/j.1365-246X.2007.03454.x.
- McCarthy, C., Y. Takei, & T. Hiraga (2011). Experimental study of attenuation and dispersion over a broad frequency range: 2. The universal scaling of polycrystalline materials. *J. Geophys. Res.*, 116(B9), doi:10.1029/2011jb008384.
- Mégnin, C., H.-P. Bunge, B. Romanowicz, & M. Richards (1997). Imaging 3-D spherical convection models: What can seismic tomography tell us about mantle dynamics? *Geophys. Res. Lett.*, 24(11), 1299–1302, doi:10.1029/97GL01256.
- Minster, J. B., & D. L. Anderson (1981). A model of dislocation-controlled rheology for the mantle. *Phil. Trans. Roy. Soc. A*, 299(1449), doi:10.1098/rsta.1981.0025.
- Montagner, J.-P., & B. L. N. Kennett (1996). How to reconcile body-wave and normal-mode reference earth models. *Geophys. J. Int.*, 125(1), 229–248, doi:10.1111/j.1365-246x.1996.tb06548.x.
- Mosca, I., L. Cobden, A. Deuss, J. Ritsema, & J. Trampert (2012). Seismic and mineralogical structures of the lower mantle from probabilistic tomography. *J. Geophys. Res.*, 117(B6), doi:10.1029/2011jb008851.
- Moulik, P., & G. Ekström (2016). The relationships between large-scale variations in shear velocity, density, and compressional velocity in the Earth's mantle. *J. Geophys. Res. – Solid Earth*, 121(4), 2737–2771, doi:10.1002/2015jb012679.
- Nakagawa, T., & P. J. Tackley (2010). Influence of initial CMB temperature and other parameters on the thermal evolution of Earth's core resulting from thermochemical spherical mantle convection. *Geochem. Geophys. Geosyst.*, 11(6), Q06001, doi:10.1029/2010GC003031.
- Priestley, K., & D. McKenzie (2013). The relationship between shear wave velocity, temperature, attenuation and viscosity in the shallow part of the mantle. *Earth Planet. Sci. Lett.*, 381, 78–91, doi:10.1016/j.epsl.2013.08.022.
- Reid, F. J. L., J. H. Woodhouse, & H. J. van Heijst (2001). Upper mantle attenuation and velocity structure from measurements of differential s phases. *Geophys. J. Int.*, 145, 615–630.
- Ricard, Y., E. Mattern, & J. Matas (2005). Synthetic tomographic images of slabs from mineral physics. In *Earth's Deep Mantle: Structure, Composition, and Evolution*, pp. 285–302, American Geophysical Union, Washington, D.C., doi:10.1029/GM160.
- Ritsema, J., & H. J. Van Heijst (2000). Seismic imaging of structural heterogeneity in Earth's mantle: Evidence for large-scale mantle flow. *Science Progress*, 83, 243–259.

- Ritsema, J., H. J. van Heijst, & J. H. Woodhouse (2004). Global transition zone tomography, *J. Geophys. Res.*, *109*(B2), B02,302, doi:10.1029/2003JB002610.
- Ritsema, J., A. K. McNamara, & A. L. Bull (2007). Tomographic filtering of geodynamic models: Implications for model interpretation and large-scale mantle structure. *J. Geophys. Res.*, *112*(B1), B01,303, doi:10.1029/2006JB004566.
- Ritsema, J., A. Deuss, H. J. van Heijst, & J. H. Woodhouse (2011). S40RTS: a degree-40 shear-velocity model for the mantle from new Rayleigh wave dispersion, teleseismic travel-time and normal-mode splitting function measurements. *Geophys. J. Int.*, *184*(3), 1223–1236, doi:10.1111/j.1365-246X.2010.04884.x.
- Romanowicz, B. (1995). A global tomographic model of shear attenuation in the upper-mantle. *J. Geophys. Res.*, *100*(B7), 12,375–12,394, doi:10.1029/95jb00957.
- Romanowicz, B., & B. Mitchell (2015). Deep Earth structure – Q in the Earth from crust to core. In G. Schubert (Ed.), *Treatise of geophysics*, 2 ed., Elsevier: Oxford.
- Roth, E. G., & D. A. Wiens (2000). An empirical relationship between seismic attenuation and velocity anomalies in the upper mantle. *Geophys. Res. Lett.*
- Ruan, Y., & Y. Zhou (2010). The effects of 3-d anelasticity (q) structure on surface wave phase delays. *Geophys. J. Int.*, doi:10.1111/j.1365-246x.2010.04514.x.
- Savage, B., D. Komatitsch, & J. Tromp (2010). Effects of 3D attenuation on seismic wave amplitude and phase measurements. *Bull. Seismol. Soc. Am.*, *100*(3), 1241–1251, doi:10.1785/0120090263.
- Schaber, K., H.-P. Bunge, B. S. A. Schuberth, R. Malservisi, & A. Horbach (2009). Stability of the rotation axis in high-resolution mantle circulation models: Weak polar wander despite strong core heating. *Geochem. Geophys. Geosyst.*, *10*, Q11W04, doi:10.1029/2009GC002541.
- Schuberth, B. S. A., H.-P. Bunge, & J. Ritsema (2009a). Tomographic filtering of high-resolution mantle circulation models: Can seismic heterogeneity be explained by temperature alone? *Geochem. Geophys. Geosyst.*, *10*(5), Q05W03, doi:10.1029/2009GC002401.
- Schuberth, B. S. A., H.-P. Bunge, G. Steinle-Neumann, C. Moder, & J. Oeser (2009b). Thermal versus elastic heterogeneity in high-resolution mantle circulation models with pyrolyte composition: High plume excess temperatures in the lowermost mantle, *Geochem. Geophys. Geosyst.*, *10*(1), Q01W01, doi:10.1029/2008GC002235.
- Schuberth, B. S. A., C. Zaroli, & G. Nolet (2012). Synthetic seismograms for a synthetic Earth: long-period P- and S-wave traveltime variations can be explained by temperature alone, *Geophys. J. Int.*, *188*(3), 1393–1412, doi:10.1111/j.1365-246X.2011.05333.x.
- Schuberth, B. S. A., C. Zaroli, & G. Nolet (2015). Traveltime dispersion in an isotropic elastic mantle: strong lower-mantle signal in differential-frequency residuals. *Geophys. J. Int.*, *203*(3), 2099–2118, doi:10.1093/gji/ggv389.
- Selby, N. D., & J. H. Woodhouse (2002). The Q structure of the upper mantle: Constraints from Rayleigh wave amplitudes. *J. Geophys. Res.*, doi:10.1029/2001JB000257.
- Serrin, J. (1959). Mathematical Principles of Classical Fluid Mechanics. In C. Truesdell (Ed.), *Fluid Dynamics II Strömungsmechanik I, Encyclopedia of Physics / Handbuch der Physik*, vol. 3/8/1, pp. 125–263, Springer Berlin Heidelberg.
- Shito, A., S. Karato, & J. Park (2004). Frequency dependence of Q in Earth's upper mantle inferred from continuous spectra of body waves. *Geophys. Res. Lett.*, *31*(12), L12,603, doi:10.1029/2004gl019582.
- Simmons, N. A., A. M. Forte, L. Boschi, & S. P. Grand (2010). GyPSuM: A joint tomographic model of mantle density and seismic wave speeds. *J. Geophys. Res.*, *115*(B12), B12,310, doi:10.1029/2010JB007631.
- Simmons, N. A., B. S. A. Schuberth, S. C. Myers, & D. R. Knapp (2019). Resolution and covariance of the LLNL-G3D-JPS global seismic tomography model: Applications to travel time uncertainty and tomographic filtering of geodynamic models. *Geophys. J. Int.*, *217*(3), 1543–1557, doi:10.1093/gji/ggz102.
- Stein, S., & M. Wysession (2002). *An Introduction to Seismology, Earthquakes, and Earth Structure*, 2 ed., Wiley-Blackwell.
- Stixrude, L., & C. Lithgow-Bertelloni (2005). Thermodynamics of mantle minerals - I. Physical properties, *Geophys. J. Int.*, *162*(2), 610–632, doi:10.1111/j.1365-246X.2005.02642.x.
- Stixrude, L., & C. Lithgow-Bertelloni (2007). Influence of phase transformations on lateral heterogeneity and dynamics in Earth's mantle. *Earth Planet. Sci. Lett.*, *263*, 45–55, doi:10.1016/j.epsl.2007.08.027.
- Stixrude, L., & C. Lithgow-Bertelloni (2011). Thermodynamics of mantle minerals – II. Phase equilibria. *Geophys. J. Int.*, *184*(3), 1180–1213, doi:10.1111/j.1365-246X.2010.04890.x.
- Stockmann, F., L. Cobden, F. Deschamps, A. Fichtner, & C. Thomas (2019). Investigating the seismic structure and visibility of dynamic plume models with seismic array methods. *Geophysical Journal International*, *219*(Supplement_1), S167–S194, doi:10.1093/gji/ggz334.
- Tackley, P. J. (2008). Modelling compressible mantle convection with large viscosity contrasts in a three-dimensional spherical shell using the yin-yang grid. *Phys. Earth Planet. Inter.*, *171*(1–4), 7–18, doi:10.1016/j.pepi.2008.08.005.
- Takei, Y. (2017). Effects of partial melting on seismic velocity and attenuation: A new insight from experiments. *Annu. Rev. Earth Planet. Sci.*, *45*(1), 447–470, doi:10.1146/annurev-earth-063016-015820.
- Tesoniero, A., F. Cammarano, & L. Boschi (2016). S-to-P heterogeneity ratio in the lower mantle and thermo-chemical implications, *Geochem. Geophys. Geosyst.*, *17*(7), 2522–2538, doi:10.1002/2016gc006293.
- Trampert, J., P. Vacher, & N. Vlaar (2001). Sensitivities of seismic velocities to temperature, pressure and composition in the lower mantle. *Phys. Earth Planet. Inter.*, *124*(3–4), 255–267, doi:10.1016/S0031-9201(01)00201-1.
- Trampert, J., A. Fichtner, & J. Ritsema (2013). Resolution tests revisited: the power of random numbers. *Geophys. J. Int.*, *192*(2), 676–680, doi:10.1093/gji/ggs057.
- Warren, L. M., & P. M. Shearer (2002). Mapping lateral variations in upper mantle attenuation by stacking P and PP spectra. *J. Geophys. Res.*, *107*(B12), doi:10.1029/2001JB001195.
- Webb, S., & I. Jackson (2003). Anelasticity and microcreep in polycrystalline MgO at high temperature: an exploratory

- study. *Physics and Chemistry of Minerals*, 30(3), 157–166, doi:10.1007/s00269-003-0299-1.
- Widmer, R., G. Masters, & F. Gilbert (1991). Spherically symmetric attenuation within the Earth from normal mode data. *Geophys. J. Int.*, 104(3), 541–553, doi:10.1111/j.1365-246x.1991.tb05700.x.
- Wielandt, E. (1987). On the validity of the ray approximation for interpreting delay times. In G. Nolet (Ed.), *Seismic Tomography, Seismology and Exploration Geophysics*, vol. 5, pp. 85–98, Springer Netherlands, doi:10.1007/978-94-009-3899-1_4.
- Xu, W., C. Lithgow-Bertelloni, L. Stixrude, & J. Ritsema (2008). The effect of bulk composition and temperature on mantle seismic structure. *Earth Planet. Sci. Lett.*, 275, 70–79, doi:10.1016/j.epsl.2008.08.012.
- Yamauchi, H., & Y. Takei (2016). Polycrystal anelasticity at near-solidus temperatures. *J. Geophys. Res.: Solid Earth*, 121(11), 7790–7820, doi:10.1002/2016jb013316.
- Young, A., N. Flament, K. Maloney, S. Williams, K. Matthews, S. Zahirovic, & R. D. Müller (2018). Global kinematics of tectonic plates and subduction zones since the late Paleozoic Era. *Geoscience Frontiers*, 10(3), 989–1013, doi:10.1016/j.gsf.2018.05.011.
- Zaroli, C. (2016). Global seismic tomography using Backus–Gilbert inversion. *Geophys. J. Int.*, 207(2), 876–888, doi:10.1093/gji/ggw315.
- Zaroli, C., S. Lambotte, & J.-J. L ev eque (2015). Joint inversion of normal-mode and finite-frequency *S*-wave data using an irregular tomographic grid. *Geophys. J. Int.*, 203(3), 1665–1681, doi:10.1093/gji/ggv388.
- Zhong, S. J., M. T. Zuber, L. Moresi, & M. Gurnis (2000). Role of temperature-dependent viscosity and surface plates in spherical shell models of mantle convection. *J. Geophys. Res.*, 105(B5), 11,063–11,082, doi:10.1029/2000JB900003.

5

Geochemical Diversity in the Mantle

Takeshi Hanyu¹ and Li-Hui Chen²

ABSTRACT

Studies of mid-ocean ridge basalts (MORBs) and ocean island basalts (OIBs) have unraveled the heterogeneous nature of the shallow and deep mantle, respectively. Large variations in radiogenic isotopes and trace element compositions observed in OIBs are thought to originate from ancient recycled subducted materials that once existed near the Earth's surface and that are now stored in the deep mantle. Recent applications of major elements in basalts, minor elements in olivine phenocrysts, and traditional and nontraditional stable isotopes provide opportunities to not only identify subducted materials but also promote an improved understanding of the processes of differentiation and reaction that occur during lithospheric slab subduction and mantle upwelling. Recycled carbonates have recently gained recognition as playing a role in the formation of distinct mantle components. These carbonatitic melts, originating from subducted carbonated materials, metasomatize the surrounding peridotitic mantle and form chemically enriched pyroxenite and fertile peridotite. Recent studies have shown that other volatile elements, such as water and halogens together with carbon, exchange between the Earth's surface and the deep mantle. Moreover, the exchange of materials appears to have influenced mutual changes in chemical compositions and the redox state at the Earth's surface and in the mantle.

5.1. INTRODUCTION

The geochemical diversity in the Earth's mantle is ultimately a consequence of chemical differentiation since the planet's formation. After the segregation of the metallic core, the initially homogeneous silicate Earth experienced both continuous and sporadic differentiation events, which include magma ocean solidification, continental and oceanic crust formation, and the transfer of these crustal

materials to the mantle via slab subduction (Caro et al., 2006; Hofmann, 1997; Labrosse et al., 2007; Stracke, 2012; White, 2010; Zindler & Hart, 1986). Although mantle convection should be able to stir the mantle and promote geochemical homogeneity, the presence of ancient mantle materials, some of which may have formed a few billion years ago documented by radiogenic isotopes, indicates that it does not completely erase geochemical heterogeneity in the mantle (Brandenburg et al., 2008; Christensen & Hofmann, 1994; Hofmann, 1997; Kimura et al., 2017; Li et al., 2014; Tackley, 2000; Van der Hilst & Kárason, 1999). Mantle materials with diverse geochemical compositions may contain evidence of ancient mantle differentiation processes.

¹Research Institute for Marine Geodynamics, Japan Agency for Marine-Earth Science and Technology, Yokosuka, Japan

²Department of Geology, Northwest University, Xi'an, China

Geochemical studies of mantle-derived rocks emplaced at the Earth's surface, such as ophiolites, abyssal peridotites, and mantle xenoliths, offer direct evidence of the nature of the mantle (Dilek & Furnes, 2014; Pearson & Wittig, 2014; Snow et al., 1994; Warren et al., 2009). These rocks should record geochemical heterogeneity at a scale of centimeters to kilometers. However, their origin is generally limited to the uppermost mantle. Mantle-derived magmas, including mid-ocean ridge basalts (MORBs) and ocean island basalts (OIBs), can sample broad mantle domain in the length scale of a few to tens of kilometers and provide clues to the geochemical characteristics of the mantle at various depths. MORBs form via partial melting of upwelling upper mantle rocks at divergent plate margins. On the other hand, OIBs originate from a variety of potential mantle sources ranging from enriched heterogeneities in the upper mantle (Foulger et al., 2001; Meibom & Anderson, 2003) to upwelling plumes from the lower mantle (Courtillot et al., 2003; French & Romanowicz, 2015; Montelli et al., 2006). Consequently, MORBs and OIBs serve as probes to explore the shallow and deep mantle, respectively. By integrating data from a variety of geochemical tracers contained in both MORBs and OIBs, we can unravel the effects of partial melting, mixing, and reaction, which will lead to an improved understanding of geochemical evolution and relevant geodynamic processes that occur in the mantle.

In this contribution, first, we discuss geochemical heterogeneity in the mantle based on MORBs and OIBs and review existing models that account for the geochemical compositions of distinct mantle components that comprise the heterogeneous mantle. The discussion continues with a presentation of the arguments on the lithological nature of the mantle and the role of recycled carbonates during the formation of distinct mantle components parental to OIBs. Finally, we discuss recent progress on the evolutionary connection between the Earth's surface and mantle using nontraditional stable isotopes, volatiles, and redox-sensitive elements. Some stable isotopes can be used as geochemical tracers of crust-mantle recycling because they are susceptible to fractionation processes that occur near the Earth's surface under the low-temperature condition. The role of volatiles in geochemical and geodynamical processes has been widely noticed, and there is an advance in understanding volatile reservoirs and transport mechanism between the mantle, crust, and the Earth's surface layers. The recent studies on redox-sensitive elements provide novel evidence of the condition of ancient surface environments and its impact to the mantle evolution.

5.2. DEFINITIONS AND INTERPRETATIONS OF DISTINCT MANTLE COMPONENTS

Traditionally, radiogenic isotopes and trace element compositions have been used to investigate the causes of geochemical heterogeneity observed in MORBs and OIBs (e.g., Hart et al., 1992; Hofmann, 1997; White, 2010; Zindler & Hart, 1986). The radiogenic isotopic compositions of erupted basalts relate directly to the compositions of primary melts that originate from a single mantle source or mixture of multiple sources, unless weathering or crustal contamination has affected the basalts. The degree of partial melting, residual mineral assemblages, and fractional crystallization control the trace element compositions of basalts. To differentiate the geochemical features of MORB and OIB sources, geochemists often use the ratios of trace element pairs that have similar partition coefficients during partial melting and trace element spider diagrams displaying the relative incompatible element enrichment (e.g., Hofmann, 1997; Stracke & Bourdon, 2009; Willbold & Stracke, 2006). In contrast, major and minor elements are sensitive to residual mineral assemblages (i.e., lithology) rather than the lineage of the basalt source (see Section 3). Stable isotopes are powerful tracers of low-temperature fractionation processes near the Earth's surface. Thanks to recent advances in analytical techniques that allow the detection of small variations in isotopic ratios, their applications have become widespread (see Section 5.1).

MORBs and OIBs exhibit wide variations in isotopic compositions (e.g., Hart et al., 1992; White, 2010; Zindler & Hart, 1986) (Figure 5.1). MORBs occupy the "depleted" corner in isotope diagrams with unradiogenic $^{87}\text{Sr}/^{86}\text{Sr}$, $^{206}\text{Pb}/^{204}\text{Pb}$, $^{207}\text{Pb}/^{204}\text{Pb}$, and $^{208}\text{Pb}/^{204}\text{Pb}$ and radiogenic $^{143}\text{Nd}/^{144}\text{Nd}$ and $^{176}\text{Hf}/^{177}\text{Hf}$ caused by low time-integrated ratios of Rb/Sr, U/Pb, and Th/Pb and high time-integrated ratios of Sm/Nd and Lu/Hf that are characteristic of residues after melt extraction. Despite significant isotopic variations, MORBs represent a group of magmas originated from a distinct group of mantle material, referred to as the *depleted mantle* (DM) component. Ocean island basalts are characterized by wider isotopic variations, which may involve the DM at the depleted corner. Typically, several OIB suites from different localities define an isotopic lineation that trends to a distinct composition, and this implies the presence of a number of mantle components that is each sampled by specific groups of mantle plumes. Accordingly, there is consensus that there are three other distinct mantle components, as main OIB sources, in addition to DM. Moreover, previous studies indicate that a fifth mantle component exists within the isotopic space defined by

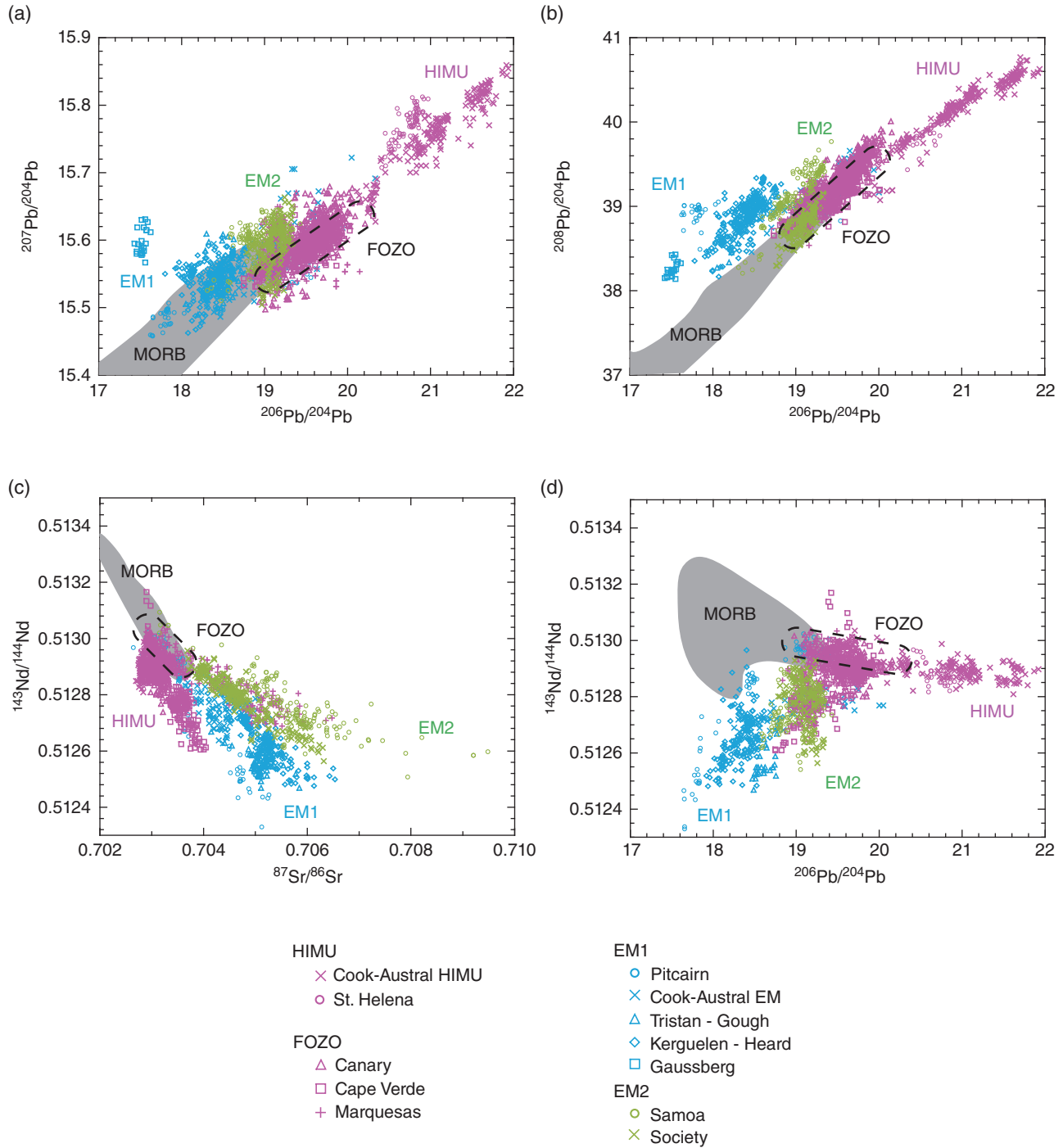


Figure 5.1 Isotopic compositions of OIBs with robust EM1, EM2, HIMU, and FOZO signatures. (a) $^{206}\text{Pb}/^{204}\text{Pb}$ versus $^{207}\text{Pb}/^{204}\text{Pb}$, (b) $^{206}\text{Pb}/^{204}\text{Pb}$ versus $^{208}\text{Pb}/^{204}\text{Pb}$, (c) $^{87}\text{Sr}/^{86}\text{Sr}$ versus $^{143}\text{Nd}/^{144}\text{Nd}$, and (d) $^{206}\text{Pb}/^{204}\text{Pb}$ versus $^{143}\text{Nd}/^{144}\text{Nd}$. The data are compiled from the GEOROC database (<http://georoc.mpch-mainz.gwdg.de/georoc/>). The MORB isotopic range is defined by using the data from the PetDB database (<https://www.earthchem.org/petdb>). *Source:* Data from Stracke et al. (2005).

the four distinct mantle components based on evidence from He isotopes ($^3\text{He}/^4\text{He}$) or the systematic distribution of MORB and OIB data in isotopic space (e.g., Farley et al., 1992; Hanan & Graham, 1996; Hart et al.,

1992; Jackson et al., 2007b; Stracke, 2012). The following discussion focuses on basalts with extreme isotopic compositions that are close to these distinct mantle components.

5.2.1. Depleted Mantle Component

The depleted feature of MORBs is thought to originate from continental crust extraction. In detail, the geochemistry of MORBs is quite variable and ranges from depleted (D-), normal (N-), and enriched (E-) according to their Th/La and La/Sm ratios (Arevalo Jr & McDonough, 2010; Lundstrom et al., 1999; Perfit et al., 1994; Shimizu et al., 2016; Waters et al., 2011). In general, E-MORBs have more enriched radiogenic isotopes when compared with N-MORBs and D-MORBs, which indicates that chemical enrichment/depletion is not a recent process. Chemical variation is observed from the segment scale at spreading ridges to the oceanic scale (Mougel et al., 2014; Paulick et al., 2010; Salters et al., 2011). The extent of heterogeneity is smaller at fast-spreading ridges when compared with slow-spreading ridges, a consequence of increased melt production beneath fast-spreading ridges that results in the formation of a larger magma chamber in which melts are well mixed (Rubin & Sinton, 2007).

Occurrences of highly depleted MORBs are limited (Liu et al., 2008). Their mantle source would have undergone extensive melt extraction in the past, and their refractory nature suppresses melt production from such a mantle source due to an elevated solidus. The presence of a highly depleted mantle component is suggested by the studies of abyssal peridotites, mantle xenoliths, and phenocryst-hosted melt inclusions in MORBs, komatiites, and oceanic plateaus (Bizimis et al., 2007; Jackson et al., 2015a; Laubier et al., 2012; Rampone & Hofmann, 2012; Shimizu et al., 2009; Stracke et al., 2011). In contrast, the occurrences of off-axis alkalic seamounts near spreading ridges and petit-spot basalts adjacent to plate flexure, which show a highly enriched geochemical signature (Graham et al., 1988; Machida et al., 2009), point to the presence of an enriched component in the upper mantle. Small-degree partial melting selectively samples a fertile component that may exist in the form of enriched veins in heterogeneous mantle sources (Rampone & Hofmann, 2012; Sobolev et al., 2007; Stracke & Bourdon, 2009; Warren et al., 2009). The range of MORBs from depleted to enriched types reflects small-scale source heterogeneity produced by long-term depletion and enrichment processes in the upper mantle.

5.2.2. Enriched Mantle Component

The isotopically enriched mantle (EM) components observed in OIBs are separated into EM1 and EM2 (Figure 5.1). Ocean island basalts with a robust EM1 signature occur at Pitcairn–Gambier Islands in the Pacific, Tristan–Gough Islands in the South Atlantic, Kerguelen–Heard Islands in the Indian Ocean, and Gaussberg Volcano in Antarctica (Barling & Goldstein,

1990; Dupuy et al., 1993; Eisele et al., 2002; Frey & Weis, 1995; Gibson et al., 2005; Murphy et al., 2002; Richardson et al., 1982; Woodhead & McCulloch, 1989; Zindler & Hart, 1986). Ocean island basalts from Samoa and Society Islands in the Pacific contain a strong EM2 signature (Farley et al., 1992; Hémond et al., 1994; Palacz & Saunders, 1986; White & Duncan, 1996; Workman et al., 2004; Zindler & Hart, 1986). Both EM signatures have unradiogenic $^{143}\text{Nd}/^{144}\text{Nd}$ and radiogenic $^{87}\text{Sr}/^{86}\text{Sr}$ but EM2 has a more radiogenic $^{87}\text{Sr}/^{86}\text{Sr}$ for a given $^{143}\text{Nd}/^{144}\text{Nd}$ compared with EM1. Lead isotope diagrams also show a striking difference between the EM signatures. Specifically, EM2 has more radiogenic Pb isotopes (in particular, a high $^{208}\text{Pb}/^{204}\text{Pb}$ for a given $^{206}\text{Pb}/^{204}\text{Pb}$) than EM1, which has a notably high $^{207}\text{Pb}/^{204}\text{Pb}$ for a given $^{206}\text{Pb}/^{204}\text{Pb}$.

In isotope diagrams, some OIBs (e.g., Kerguelen and Tristan) plot in between trends defined by the Pitcairn-EM1 and Samoan-EM2 signatures (Figures 5.1c and 5.1d), and the continuity between the EM1 and EM2 signatures has been suggested (Stracke, 2012). However, while most MORBs and OIBs define a plane in a multidimensional isotope diagram, the EM2 OIBs plot exceptionally far from the plane and point to a third compositional direction (Hart et al., 1992; Iwamori & Albarède, 2008). This implies that the EM1 and EM2 components may not actually have the same lineages and that OIBs with apparently intermediate isotopic compositions may not be produced by mixture of the two distinct components. Note that the EM1 and EM2 components (and also other geochemical components) represent conceptual mantle materials that bound isotopic variation defined by MORBs and OIBs. Each OIB grouped in EM1 and EM2 shows an isotopic trend toward a characteristic composition that should reflect individual isotopic evolution of the source material with various parent/daughter ratios and ages. Considering that source materials of OIBs have been formed during differentiation processes in the mantle and crust, as discussed below, there should be ranges of chemical and isotopic variation in their sources even grouped in a specific mantle component.

Several models have been proposed to explain the origin of EM components. Among those, remelting of subducted metasomatized lithospheric mantle is proposed (Halliday et al., 1995; Niu & O'Hara, 2003; Workman et al., 2004) based on evidence that metasomatic enrichment is a dominant process in the lithosphere (Bodinier et al., 2008; Pilet et al., 2005; Reisberg et al., 1991). Melts produced in the asthenospheric mantle migrate and infiltrate the lithospheric mantle, resulting in the formation of metasomatized lithosphere with significant compositional variations, depending on the source composition, source mineralogy, degree of melting, and the presence of

volatiles. Such a metasomatized lithosphere would be the major part of a subducted slab and become the distinct mantle components. Another plausible model is delamination of subcontinental lithosphere (Geldmacher et al., 2008; Gibson et al., 2005; Goldstein et al., 2008; McKenzie & O’Nions, 1983; Tatsumi, 2000). The subcontinental lithospheric mantle has different compositions, and therefore different parent/daughter ratios, compared with the suboceanic mantle (i.e., the MORB source mantle). These different compositions originate from complex depletion mechanisms that occur during continental crust formation and enrichment via the metasomatic addition of slab-derived fluids and melts. Subcontinental material should have low U/Pb and Rb/Sr and high Sm/Nd that are possibly concordant with the EM1 OIB isotopic signature (Geldmacher et al., 2008). The EM components may also originate from the recycling of continental crust and a variety of sediment (plus oceanic crust). The sediment protoliths for EM1 and EM2 are thought to be pelagic sediment with a biogenic component and terrigenous sediment supplied from the upper continental crust via riverine transport, respectively (Delavault et al., 2015; Eisele et al., 2002; Jackson et al., 2007a; Weaver, 1991; Willbold & Stracke, 2006; Woodhead & Devey, 1993).

Since these models account for the characteristic Sr, Nd, and Pb radiogenic isotope and trace element compositions of the EM1 and EM2 components, further geochemical evidence should help to discriminate between the existing models. EM1 OIBs have a more radiogenic $^{187}\text{Os}/^{188}\text{Os}$ than MORBs (Eisele et al., 2002; Reisberg et al., 1993). This fact is not concordant with models that consider subcontinental lithosphere because it has significantly less-radiogenic $^{187}\text{Os}/^{188}\text{Os}$ (Carlson & Irving, 1994; Pearson et al., 2004). In the Os isotopic system, the parent element, Re, is incompatible, whereas the daughter element, Os, is highly compatible. The relatively unradiogenic $^{187}\text{Os}/^{188}\text{Os}$ of the subcontinental lithosphere is the result of long-term Re depletion after continental crust extraction. In contrast, sediment, oceanic crust, and metasomatized lithosphere develop radiogenic $^{187}\text{Os}/^{188}\text{Os}$ after long-term isolation due to their high Re/Os ratios.

Oxygen isotopes are fractionated during low-temperature processes such as sedimentation, weathering, and alteration, and therefore they are an efficient tracer of recycled surface materials. Because the Pitcairn basalts exhibit $^{18}\text{O}/^{16}\text{O}$ that overlap the MORB range (Eiler et al., 1997), oxygen isotopic compositions do not always suggest a contribution from sediment. However, the discovery of mass-independent fractionation (MIF) of S isotopes in sulfide inclusions from Pitcairn basalts demonstrates the involvement of ancient sediment in the EM1 component (Delavault et al., 2016). It is known that

S–MIF only occurs via photochemical reactions in an oxygen-poor atmosphere. The Pitcairn basalt source originates from recycled sediment with S–MIF that was deposited before the Great Oxidation Event (GOE) at 2.45 Ga. Sediment relevant to the EM1 component is predominantly pelagic (biogenic) as suggested by the relatively unradiogenic Pb isotopes (Class & le Roex, 2008; Eisele et al., 2002).

Contrary to the EM1 OIBs, previous studies have reported elevated $^{18}\text{O}/^{16}\text{O}$ in the EM2 OIBs from the Society and Samoan Islands (Eiler et al., 1997; Workman et al., 2008), suggesting the involvement of terrigenous sediment in their source. However, EM2 OIBs are characterized by $^{187}\text{Os}/^{188}\text{Os}$ that are not so radiogenic as might be expected of old sediment (Hauri & Hart, 1993; Jackson & Shirey, 2011; Reisberg et al., 1993; Workman et al., 2004). Moreover, the EM2 OIBs have a smooth pattern in trace element spider diagrams contrary to irregular patterns observed in terrigenous sediment and continental crust (Willbold & Stracke, 2006). These problems may be reconciled by considering mixing or the reaction of recycled sediment with subducted oceanic crust or peridotitic mantle (Jackson & Shirey, 2011; Stracke, 2012).

A sedimentary origin for the EM2 component is consistent with unradiogenic $^3\text{He}/^4\text{He}$ associated with radiogenic $^{87}\text{Sr}/^{86}\text{Sr}$ in the Samoan basalts (Farley et al., 1992; Jackson et al., 2014). Recycled surface materials should have high U and Th but low He concentrations due to He loss during subduction, and therefore develop a more radiogenic ^4He via U and Th decay. The most probable explanation for the correlations between $^3\text{He}/^4\text{He}$ variations and radiogenic isotopic compositions is the mixing of a recycled component (i.e., sediment) and a high- $^3\text{He}/^4\text{He}$ less-degassed mantle component (see below). In contrast, the EM1 OIBs at Pitcairn have an equivocal He isotope signature despite the observation of primordial Ne isotopic signatures (Garapić et al., 2015; Honda & Woodhead, 2005).

5.2.3. HIMU Mantle Component

Radiogenic Pb isotopes, due to elevated time-integrated U/Pb and Th/Pb ratios, define the other distinct mantle component indigenous to OIBs. This component is referred to as HIMU because it should have high μ -values ($\mu = ^{238}\text{U}/^{204}\text{Pb}$). HIMU OIBs, with $^{206}\text{Pb}/^{204}\text{Pb} > 20.5$, occur at limited locations, such as the Cook–Austral Islands in the Pacific and St. Helena in the Atlantic (Chaffey et al., 1989; Chauvel et al., 1992; Hanyu et al., 2014; Hanyu et al., 2011a; Kawabata et al., 2011; Nakamura & Tatsumoto, 1988; Nebel et al., 2013; Palacz & Saunders, 1986; Woodhead, 1996; Zindler & Hart, 1986). The isotopic and trace elemental compositions are very similar between basalts from the

Cook–Austral Islands and St. Helena, despite the distance. Unlike the EM1 and EM2 OIBs, HIMU OIBs have unradiogenic $^{87}\text{Sr}/^{86}\text{Sr}$ similar to MORBs and relatively low $^{176}\text{Hf}/^{177}\text{Hf}$ for a given $^{143}\text{Nd}/^{144}\text{Nd}$ (Chauvel et al., 1992; Salters & White, 1998). Relative depletions in Cs, Rb, Ba, K, and Pb are also features that are exclusive to HIMU OIBs (Kogiso et al., 1997; Weaver, 1991; Willbold & Stracke, 2006). These geochemical features may be explained by the partial melting of pyroxenite and amphibolite veins that exist ubiquitously in the metasomatized lithosphere (Bodinier et al., 2008; Pilet et al., 2008; Pilet et al., 2005; Reisberg et al., 1991). Although this is a viable model, melt infiltration would cause chemical heterogeneity in the metasomatized lithosphere, which appears to be inconsistent with the uniform isotopic and trace elemental characteristics of HIMU OIBs. A prevailing theory for the origin of the HIMU component is the subduction of ancient oceanic crust, although there are numerous derivative models. Fresh oceanic crust does not develop radiogenic Pb isotopic compositions with time. Previous studies have proposed that the alteration of oceanic crust via hydrothermal fluids and subsequent dehydration during subduction is the principal mechanism to selectively remove fluid-mobile elements, such as Pb (elevates U/Pb and Th/Pb), Rb (lowers Rb/Sr), Cs, Ba, and K (Chauvel et al., 1992; Hanyu et al., 2011b; Hofmann & White, 1982; Kawabata et al., 2011; Kogiso et al., 1997; Nebel et al., 2013; Stracke et al., 2005; Weaver, 1991; Woodhead, 1996).

Low $^3\text{He}/^4\text{He}$ and high $^{187}\text{Os}/^{188}\text{Os}$ in HIMU OIBs from the Cook–Austral Islands and St. Helena are consistent with the proposed recycled crust origin (Graham et al., 1992; Hanyu & Kaneoka, 1997; Hanyu et al., 2011a; Hauri & Hart, 1993; Lassiter et al., 2003; Parai et al., 2009; Reisberg et al., 1993; Schiano et al., 2001). Slightly lower $^{18}\text{O}/^{16}\text{O}$ and higher $^7\text{Li}/^6\text{Li}$ in the HIMU OIBs compared with MORBs provide evidence of a contribution from hydrothermally altered oceanic crust (Chan et al., 2009; Eiler et al., 1997; Krienitz et al., 2012; Nishio et al., 2005). However, this model requires further refinement, as discussed in the following sections. Moreover, S affected by MIF, first discovered among OIBs in Mangaia basalts from the Cook Islands, suggests that some sedimentary components are possibly associated with the HIMU precursor (Cabral et al., 2013). Castillo (2015, 2016) proposed an alternative model where subducted marine carbonates plays a key role in the evolution of radiogenic Pb isotopes and other isotopic and trace elemental compositional characteristic of HIMU.

The ubiquitous nature of the HIMU component is a current subject of debate. While oceanic basalts from Walvis Ridge, Manihiki Plateau, and Eastern Chatham Rise generally show EM1 isotopic signature, a small number of basalts have isotopic compositions overlapping with those

of St. Helena HIMU basalts (Homrighausen et al., 2018). Marshall and Wake Seamounts, which are believed to be the extension of the Cook–Austral hotspot chain, show HIMU isotopic signatures, suggesting large volumes of HIMU source regions (Konter et al., 2008). Moreover, OIBs at individual islands and island chains show isotopic variations due to mixing of multiple end-member components. Among these, we often observe an end-member component that points to radiogenic Pb isotope compositions, e.g., Hawaii, Samoa, and Azores (Beier et al., 2008; Hanyu et al., 2010; Jackson et al., 2014). Ocean island basalts with moderately radiogenic $^{206}\text{Pb}/^{204}\text{Pb}$ (>19.5) appear at more localities, which include the Canary and Cape Verde Islands in the Atlantic and the Marquesas Islands in the Pacific (Day et al., 2009; Day et al., 2010; Dupuy et al., 1987; Gurenko et al., 2009; Thirlwall, 1997). This was previously interpreted as the manifestation of Young HIMU component consisting of subducted oceanic crust that is younger than that relevant to the HIMU component (Dupuy et al., 1987; Thirlwall, 1997). Currently, a prevailing theory is the presence of widely distributed mantle domain that involves subducted materials with younger ages in various proportions (Hanan & Graham, 1996; Stracke et al., 2005; see details below). The trace of recently subducted oceanic crust has been discovered in some continental Cenozoic basalts in China. They are characterized by trace element compositions that are similar to HIMU OIB, despite less-radiogenic Pb isotopes. This is a modern example of oceanic crust recycling from the subducted Pacific plate (Sakuyama et al., 2013; Xu, 2014; Xu et al., 2012; Zeng et al., 2010). The influence of the subducted oceanic crust is ubiquitous, though variable in age and proportion, in the source of OIBs and continental basalts (Castillo, 2015, 2016).

5.2.4. FOZO and Primordial Mantle Components

Previous studies have sporadically defined a fifth component. Some OIBs such as those from Hawaii, Iceland, Samoa, and Galapagos have elevated $^3\text{He}/^4\text{He}$, suggesting the presence of an undegassed mantle component that is possibly located in the lower mantle (Farley et al., 1992; Jackson et al., 2007a; Kurz et al., 2009; Kurz et al., 1983; Stuart et al., 2003; Tieloff et al., 2000). There is an ongoing debate as to whether this component was entirely primordial without any chemical modification from the homogeneous early mantle, and hence it has chondritic (bulk silicate Earth) isotopic compositions. Based on a study of Samoan basalts, Farley et al. (1992) suggested that the elevated $^3\text{He}/^4\text{He}$ component (termed PHEM; primitive He mantle) has a moderately depleted Sr and Nd isotope signature distinct from chondritic values. This fact suggests that even lower mantle material is differentiated but not to the same extent as the upper mantle.

The conceptual component, FOZO (Focal Zone), was determined entirely based on Sr, Nd, and Pb isotopes (Hart et al., 1992) (Figure 5.1). Many OIB suites exhibit individual linear trends in multi-isotope diagrams and the convergence of these trends defines FOZO. By its definition, FOZO is a component commonly involved in many OIBs. Since FOZO has intermediate Sr, Nd, and Pb isotopic compositions close to PHEM, FOZO may have originated from a moderately differentiated lower mantle with an elevated $^3\text{He}/^4\text{He}$.

Thereafter, FOZO has been interpreted variously. The point at which the linear Pb isotopic arrays from Atlantic, Pacific, and Indian Ocean MORBs converge represents the C- (Common) component but isotopic trends of individual OIBs also point to the C-component (Hanan & Graham, 1996). The C-component has nearly identical isotopic compositions as FOZO. However, Hanan and Graham (1996) assigned the C-component to the mantle transition zone impregnated with subducted materials, because both MORBs and OIBs share this component. Consequently, OIBs, which include the C-component, may have either high or low $^3\text{He}/^4\text{He}$. More recently, Stracke et al. (2005) redefined the FOZO as a compositional range that overlaps the E-MORB isotopic field. Based on isotopic variations and relatively enriched features, they suggested that FOZO is a ubiquitous mantle component that includes subducted materials with age intervals in various proportions. High $^3\text{He}/^4\text{He}$ in some OIBs with FOZO isotopic signature may be accounted for by the preservation of elevated $^3\text{He}/^4\text{He}$ in variably depleted portion of subducted lithosphere formed from ancient mantle (Jackson et al., 2008; Castillo, 2015). Alternatively, FOZO may entrain primordial mantle component with high $^3\text{He}/^4\text{He}$ that has been potentially reservoirized in the dense lowermost mantle layer (Jackson et al., 2017; Williams et al., 2019).

The nature of the high- $^3\text{He}/^4\text{He}$ component is still an issue, but the recent evidences from nontraditional isotopes may pinpoint its origin. The tungsten isotope ratio ($^{182}\text{W}/^{184}\text{W}$) is only modified by the decay of the short-lived ^{182}Hf within the first ~60 Ma since the birth of the solar system (Touboul et al., 2012; Willbold et al., 2011). The discovery of subchondritic $^{182}\text{W}/^{184}\text{W}$ in the high- $^3\text{He}/^4\text{He}$ OIBs documents the formation and prolonged isolation of a less-differentiated mantle domain, selectively losing siderophile W during the segregation of the metallic core (Mundl et al., 2017). If the superchondritic $^{142}\text{Nd}/^{144}\text{Nd}$, another short-lived decay system of ^{146}Sm , in the Earth's mantle is a consequence of early-stage mantle depletion (Boyet & Carlson, 2005; Caro et al., 2006), then the early-depleted mantle may be characterized by a less-degassed helium signature with moderately depleted radiogenic isotopes (Jackson & Carlson, 2012). Class and Goldstein (2005) pointed out similarly

depleted radiogenic isotopic compositions between MORBs with low $^3\text{He}/^4\text{He}$ and Hawaiian and Icelandic basalts with high $^3\text{He}/^4\text{He}$, suggesting that the whole mantle may be equally differentiated but disproportionately degassed in the upper and lower domains.

5.3. LITHOLOGICAL ASPECTS OF THE MANTLE COMPONENTS

Slab subduction is widely accepted as the main factor responsible for geochemical diversity in the mantle. Despite this, the lithological characteristics of subducted materials remain a subject of debate. A simple scenario is that oceanic crust and sediment are foundered to the deep mantle via subduction and then these materials return to the shallow mantle via mantle upwelling while retaining their lithological form. For example, oceanic crust with a basaltic composition transforms to eclogite at high pressures (>2.5 GPa) with constituent minerals such as clinopyroxene, garnet, \pm quartz/coecite, and minor phases. When this material descends to the lower mantle, the mineral assemblage changes to perovskite, stishovite, and high-pressure aluminous phases (Hirose et al., 1999; Ono et al., 2001). If subducted oceanic crust did not experience chemical interaction or exchange with the surrounding mantle during its storage in the deep mantle (i.e., major element compositions were unmodified), it would have an eclogite lithology when it ascended to the shallow mantle. Partial melting of such eclogites may generate chemically enriched OIBs.

However, based on the following geochemical and petrological evidence, this scenario appears problematic. Pure recycled materials have highly differentiated chemical compositions and fractionated parent/daughter ratios. After storage in the mantle for billions of years, recycled materials should have radiogenic isotopic compositions. A good example is the Os isotopic system, where $^{187}\text{Os}/^{188}\text{Os}$ changes due to the decay of ^{187}Re . Modeled altered oceanic crust has elevated Re/Os with very low concentrations of Os (e.g., Re = 0.33 ppb and Os = 0.006 ppb; Becker, 2000) relative to the DM (e.g., Re = 0.16 ppb and Os = 3.0 ppb; Salters & Stracke, 2004) because Re is highly incompatible, while Os is compatible during partial melting. Beginning with a mantle $^{187}\text{Os}/^{188}\text{Os}$ value of ~0.125, radiogenic $^{187}\text{Os}/^{188}\text{Os}$ ingrowth results in a present-day value of ~3 and ~10 for altered oceanic crust that formed at 0.35 and 2.0 Ga, respectively (Becker, 2000). Indeed, the HIMU and EM1 OIBs are characterized by radiogenic Os isotopes relative to MORBs, which suggests the involvement of recycled materials in their magma sources (Day et al., 2009; Hanyu et al., 2011b; Hauri & Hart, 1993; Reisberg et al., 1993; Schiano et al., 2001). However, $^{187}\text{Os}/^{188}\text{Os}$

thus far reported for these OIBs do not exceed ~ 0.16 , lower than expected for altered oceanic crust. Thus, partial melting of recycled oceanic crust alone does not account for the Os isotopic composition of the OIBs.

Moderately radiogenic Os isotopic composition of OIBs may be explained by mixing of partial melts from oceanic crust and the DM, the latter of which has unradiogenic $^{187}\text{Os}/^{188}\text{Os}$ (~ 0.127). However, for example, the Cook–Austral HIMU OIBs have a small range in their $^{187}\text{Os}/^{188}\text{Os}$ (0.14–0.15) (Hanyu et al., 2011b; Schiano et al., 2001). This indicates that individual basalts from different islands formed from nearly fixed degrees of melting and mixing proportions of the two source components, which seems unlikely. Small variations of the moderately radiogenic Os isotopes may favor an alternative scenario where the subducted materials reacted with ambient depleted mantle to form a hybridized component that inherited its elemental signature from the subducted materials (Day et al., 2009; Hanyu et al., 2011b).

Experimental results indicate that partial melts of oceanic crust and sediment do not resemble alkalic OIBs in terms of their major element compositions. Ocean island basalts that originate from distinct mantle components tend to have low SiO_2 content (< 50 wt%) (Dasgupta et al., 2010; Jackson & Dasgupta, 2008). In contrast, partial melting of oceanic crust and sediment, both of which have initially high SiO_2 content (> 50 wt%), generates dacitic melts with even higher SiO_2 (Pertermann et al., 2004; Spandler et al., 2008; Yaxley & Green, 1998). Consequently, if oceanic crust and sediment are recycled in their original form (i.e., eclogite lithology), they cannot be parental to the alkalic OIBs. Alternatively, the OIB sources would be hybridized materials produced by mixing and/or reaction with other mantle materials.

Currently, two types of materials have been suggested as the source of OIBs: fertile peridotites and pyroxenites. The reaction between depleted peridotites and exotic melts or fluids (in this case, melts or fluids from subducted materials) yields fertile peridotites. These peridotites become rich in specific elements that are transported by melts or fluids without producing large changes in the mineral assemblages. Pyroxenites form via various mechanisms. Substantial melt–peridotite reaction causes olivine consumption and pyroxene crystallization, resulting in a pyroxene-dominated lithology without olivine (Yaxley & Green, 1998). Such reactions occur along veins where siliceous melts from subducted oceanic crust percolate as localized flow in a peridotite matrix (Bodinier et al., 2008; Pilet et al., 2005; Reisberg et al., 1991). Alternatively, the extraction of SiO_2 -rich fluids or melts from subducted oceanic crust modifies the major element composition toward low SiO_2 in the residues, which generates silica-deficient pyroxenites (Kogiso & Hirschmann, 2006; Kogiso et al., 2003).

The lithology of OIB sources have been extensively studied using the minor element compositions of olivine phenocrysts in OIBs, such as Ni, Mn, Ca, and Al. While many minor and trace elements are incompatible with the major minerals that comprise peridotite and pyroxenite, Ni is strongly partitioned to olivine. Therefore, a primary melt from an olivine-poor source (i.e., pyroxenite) is more enriched in Ni than that from an olivine-bearing source (i.e., fertile peridotite). Since erupted basalts are usually chemically fractionated and their Ni signature is obscured accordingly, olivine phenocryst can be used to estimate Ni concentration in the primary melt.

The variation in olivine Ni content has been reported in both MORBs and OIBs (Figure 5.2). Relatively low Ni content in olivine from MORBs is consistent with peridotite melting (Putirka et al., 2011; Sobolev et al., 2007). Ocean island basalts generally have higher Ni content for a given forsterite number in olivine than MORBs, suggesting a greater contribution of pyroxenite melts in their primary magmas. Hawaiian basalts, especially those from the Koolau volcano, have radiogenic isotopic compositions that span toward the EM1 component, as well as having the highest olivine Ni content (Sobolev et al., 2005). Estimates of the melt contribution from pyroxenite sources are 80% in the Koolau primary magmas. These pyroxenites could have a metasomatic origin. Recycled eclogite begins to melt at greater depths due to a lower solidus than coexisting peridotite in the upwelling mantle plume. Eclogite-derived melts segregate from the residue and react with the surrounding depleted peridotite to form chemically enriched pyroxenite.

This method is further applied to identify the lithological nature of other OIB sources. Contributions from HIMU-type (La Gomera) and depleted-type (El Hierro) sources yield the observed radiogenic isotopic variation in basalts from the western Canary Islands (Figure 5.2). Each host basalt, with distinct radiogenic isotopic compositions, also has clearly distinguishable olivine minerals based on their minor element compositions (Gurenko et al., 2009). Olivine in HIMU-type basalts has lower Ni (for a given forsterite number) than that in the depleted-type basalts, which indicates a fertile peridotite source for the HIMU-type basalts and a pyroxenite source for the depleted basalts. The latter appears controversial if a MORB-type mantle with peridotite lithology dominates the depleted-type basalts. Gurenko et al. (2009) suggested that the isotopically depleted source is a relatively young recycled oceanic crust component that experienced incomplete mixing or reaction with the peridotitic mantle. Therefore, this source retains its pyroxenite lithology, while ancient recycled oceanic crust that appears as the HIMU-type source matured and was converted to fertile peridotite.

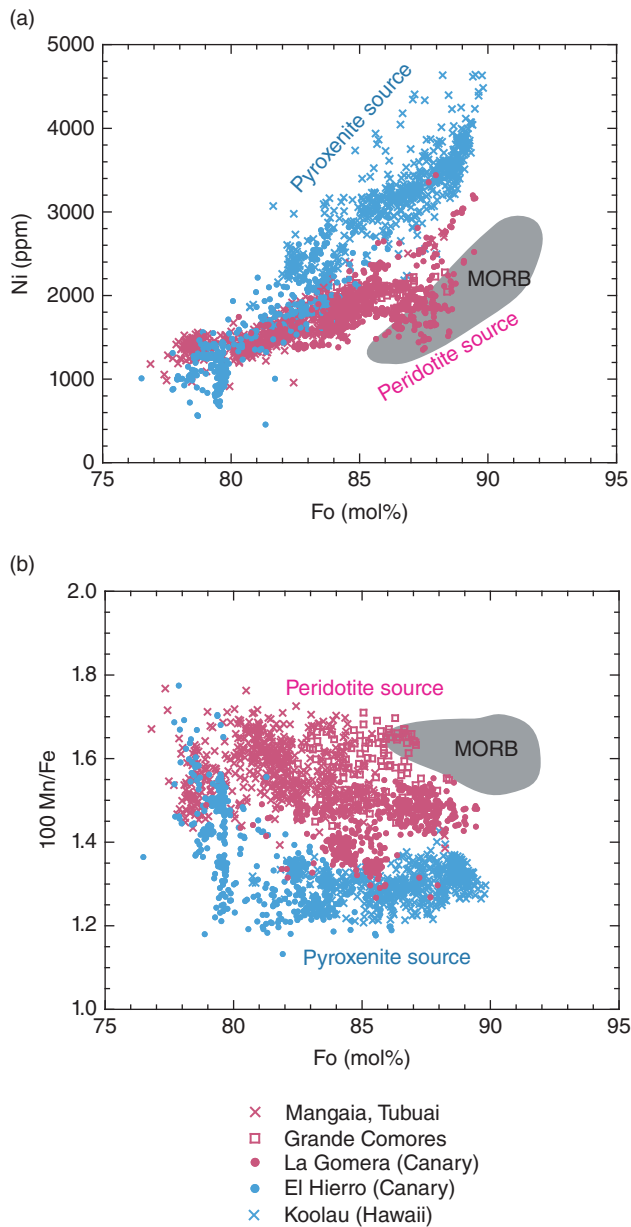


Figure 5.2 Minor element compositions of olivine in OIBs. (a) Fo content versus Ni concentration and (b) Fo content versus $100 \times \text{Mn/Fe}$. Symbols in magenta and cyan denote olivine compositions in HIMU and EM1 OIBs, respectively. Note that La Gomera and El Hierro are representative of HIMU and non-HIMU type rocks from the Canary Islands, respectively. *Source:* (a,b) Data compiled from Gurenko et al. (2009), Sobolev et al. (2007), and Weiss et al. (2016).

The olivine Ni content provides evidence of the source lithology that is hardly explored when using trace elemental or isotopic analyses, but the interpretations must be made with caution. Nickel partitioning between olivine and the melt depends on the temperature and chemical composition of the melt (Li & Ripley, 2010; Matzen

et al., 2017; Wang & Gaetani, 2008). This indicates that these effects may yield some variation in the Ni content of olivine. Combining the Mn/Fe and Ca content with the Ni content in olivine should provide additional information to pinpoint the source lithology. Manganese and Ca preferentially partition into pyroxene and melts from a pyroxene-rich source are depleted in Mn and Ca. Since olivine favors Fe over Mn relative to other major minerals in peridotite and pyroxenite, low Mn/Fe suggests a source that has an olivine-poor lithology (Balta et al., 2011; Humayun et al., 2004). Mn/Fe are less susceptible to temperature, pressure, or melt compositions, and thus provide more reliable evidence.

A number of previous studies present that Mn/Fe correlate with the olivine Ni content. While olivine from the Koolau basalts, which have an EM1 signature, are characterized by relatively high Ni and low Mn/Fe, HIMU-type Canary basalts have low Ni and high Mn/Fe. Similarly, HIMU basalts from the Cook–Austral Islands (Mangaia and Tubuai) also contain olivine with relatively low Ni, high Mn/Fe, and high Ca content (Herzberg et al., 2014; Weiss et al., 2016). Indeed, these olivine phenocrysts from HIMU-type basalts still have slightly higher Ni content than those from MORBs (for a given forsterite content). However, by correcting for the effects of temperature-dependent Ni partition coefficient (Weiss et al., 2016) and of olivine crystallization from mixed magmas (Herzberg et al., 2014), these authors concluded that the HIMU source had a fertile peridotite lithology, which suggests that it formed by the hybridization of subducted materials with the surrounding peridotitic mantle. It is important to note that a recent experimental study demonstrates that even Mn partitioning depends on the melt composition (Matzen et al., 2017).

5.4. THE ROLE OF CARBONATE IN MANTLE GEOCHEMICAL HETEROGENEITY

Evidence from Os isotopes and minor element composition in olivine imply that the original lithology of subducted oceanic crust (and sediment) may be completely modified by hybridization reaction with the surrounding mantle during the formation of primary OIB sources. However, *where* in the mantle such hybridization occurs is poorly understood. Standard models have thus far proposed that hybridization and reactions between recycled oceanic crust and peridotite occur during mantle upwelling (Dasgupta et al., 2007; Sobolev et al., 2007). The solidus of eclogite and pyroxenite is generally lower than peridotites. In an upwelling mantle plume, recycled oceanic crust and sediment (either eclogite or pyroxenite) should melt at depth before the onset of peridotite melting. The presence of volatiles in both eclogite and

pyroxenite further enhances early melting. In particular, carbonated oceanic crust and sediment have significantly lower solidus than carbonate-free equivalents. The first carbonatitic melt appears at ~300 km in depth along the plume adiabat (1600 °C potential temperature) (Dasgupta et al., 2007). The incipient carbonatitic melt has low viscosity and thus easily segregates from the residues and then reacts with the surrounding peridotite, which results in the formation of carbonated (secondary) pyroxenite or fertile peridotite. Similarly, metasomatic addition of slab-derived carbonatitic melts to peridotitic mantle during subduction is a likely process to form carbonated pyroxenite or fertile peridotite, as discussed later.

The significance of carbonated OIB sources is highlighted by the major element compositions. HIMU OIBs with radiogenic Pb isotopes are characterized by low SiO₂, high CaO, and high CaO/Al₂O₃ (Castillo, 2015; Dasgupta et al., 2010; Jackson & Dasgupta, 2008; Kogiso et al., 1997). These characteristics reveal themselves by comparing the major element compositions of basalts with radiogenic and less-radiogenic Pb isotopic compositions that originate from the same island in the Austral Islands (Lassiter et al., 2003; Maury et al., 2013; Miyazaki et al., 2018) (Figure 5.3). Basalts with more radiogenic Pb at Raivavae and Tubuai tend to have lower SiO₂ than those with less-radiogenic Pb. Differences in the SiO₂ content are not due to fractional crystallization because basalt suites define subparallel trends in MgO–SiO₂ space. Broadly, both CaO and CaO/Al₂O₃ negatively correlate with SiO₂. Partial melting of dry peridotite or Si-saturated eclogite/pyroxenite cannot generate melts with low SiO₂ (<45 wt%) coupled with high CaO and CaO/Al₂O₃ (Figure 5.3). Low-SiO₂ melts are potentially produced by partial melting of silica-deficient pyroxenite (Hirschmann et al., 2003). If the extraction of SiO₂-rich fluids or melts chemically modifies subducted mafic materials, the residue would lose free-silica and become biminerale pyroxenite (i.e., comprising pyroxene and garnet; Kogiso & Hirschmann, 2006). Partial melting of silica-deficient pyroxenite reproduces many of the major elemental features in low-SiO₂ HIMU OIBs. However, this reproduction is not complete because of the low MgO, high Al₂O₃, and low CaO/Al₂O₃ at a low SiO₂ content (Gerbode & Dasgupta, 2010) (Figure 5.3d). Moreover, this would negate the general positive correlation of CaO and CaO/Al₂O₃ with radiogenic Pb isotopes (Castillo, 2015; Dasgupta et al., 2010; Jackson & Dasgupta, 2008). An alternative viable model is the partial melting of metasomatized peridotitic mantle by carbonated melts (Dasgupta & Hirschmann, 2006). High-pressure experiments demonstrate that carbonated (fertile) peridotite can generate low-SiO₂ carbonated melts at relatively low-degrees of partial melting (Gerbode & Dasgupta, 2010; Gudfinnsson & Presnall, 2005). These

melts resemble HIMU OIBs in their major element compositions except for TiO₂ (Dasgupta et al., 2007). High TiO₂ in the HIMU OIBs (and other types of OIBs) may require a direct melt contribution from subducted oceanic crust (either carbonated or not) in addition to melts from carbonated metasomatized peridotite (Jackson & Dasgupta, 2008; Prytulak & Elliott, 2007).

Marine carbonates generally have high U/Pb but low Th/U so that after billions of years they would acquire extremely radiogenic Pb isotopic compositions that plot outside the isotopic range defined by OIBs and MORBs. Thus, marine carbonates only cannot be the source of OIBs. The present-day Pb isotopic compositions of the HIMU OIBs can be accounted for by mixing or reaction of Archean carbonates with depleted mantle components (Castillo, 2015; Hanyu et al., 2011). The fact that the HIMU OIBs have characteristically low ⁸⁷Sr/⁸⁶Sr also suggests contribution of Archean carbonates to their source. Despite low Rb/Sr, carbonates precipitated from modern seawater show highly radiogenic Sr isotopes relative to the depleted mantle. However, the deviation in ⁸⁷Sr/⁸⁶Sr between seawater and depleted mantle is much smaller in Archean. Sr isotope ratios would not evolve substantially in the mantle source mixed or reacted with Archean carbonates because of low Rb/Sr and initially low ⁸⁷Sr/⁸⁶Sr (Castillo, 2015). Note that some OIBs with moderately radiogenic Pb isotopes, such as Canary Island basalts, show slightly higher ⁸⁷Sr/⁸⁶Sr than the HIMU OIBs with highly radiogenic Pb isotopes (Thirlwall, 1997). This may be explained by the subduction of carbonated oceanic crust in the post-Archean when the departure of ⁸⁷Sr/⁸⁶Sr in seawater commenced from the depleted mantle value.

The occurrence of carbonatites at the Canary and Cape Verde Islands imply that carbonatitic melts play a role in generating HIMU OIBs (Hoernle et al., 2002). Carbonatites, which are characterized by extremely SiO₂-poor (<25 wt%) and CaO-rich (>45 wt%) compositions, have moderately radiogenic Pb isotopic compositions. Carbonatites have extreme enrichment in the large ion lithophile elements and light rare earth elements and depletion in high field strength elements, but their elemental fractionation trends resemble the HIMU OIBs. Traces of carbonatitic melts have been also found in secondary (metasomatized) pyroxene in mantle xenoliths at Tubuai (Austral Islands) and Savai'i (Samoan Islands), which are known as the HIMU and EM2 OIB localities, respectively (Hauri et al., 1993). The incompatible element abundance pattern of the secondary pyroxene is similar to that of carbonatitic melts, which suggests the occurrence of a reaction between primary pyroxene and carbonatitic melts. The occurrence of carbonate globule inclusions in olivine in the Mangaia basalts (Cook Islands) supports the presence of carbonatitic melts further (Saal et al., 1998;

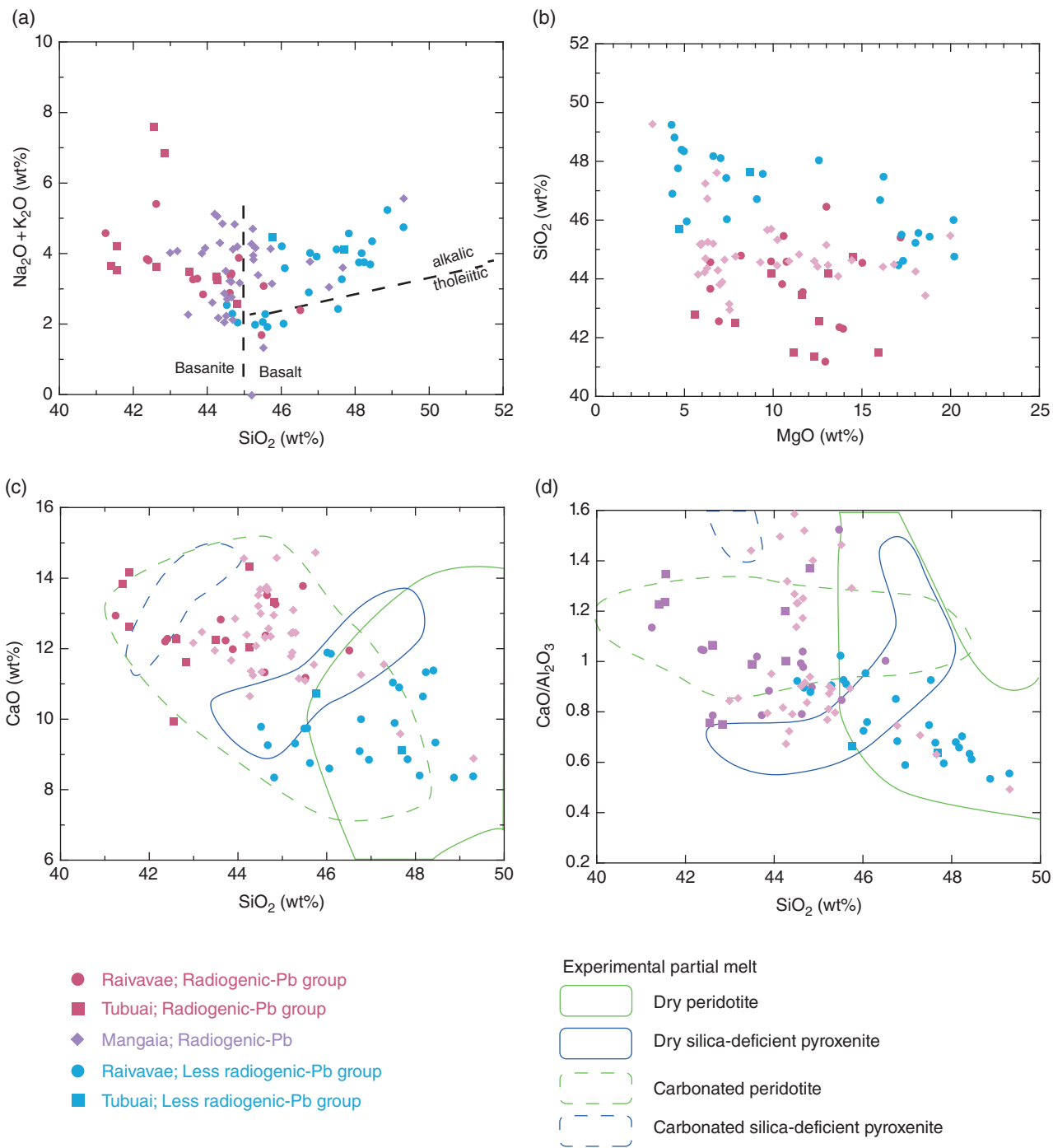


Figure 5.3 Major element compositions of basalts from the Cook–Austral Islands. (a) SiO_2 versus $\text{Na}_2\text{O} + \text{K}_2\text{O}$, (b) MgO versus SiO_2 , (c) SiO_2 versus CaO , and (d) SiO_2 versus $\text{CaO}/\text{Al}_2\text{O}_3$. The major element compositions of OIBs with robust (magenta symbols) and moderate (cyan symbols) HIMU signatures are compared. While all Mangaia basalts have highly radiogenic Pb isotopes, basalts from Raivavae and Tubuai are classified into those with highly and moderately radiogenic Pb isotopes. The fields in (c) and (d) denote experimental partial melts from various source lithologies. *Source:* Data compiled from (Chauvel et al., 1992; Hanyu et al., 2013; Hanyu et al., 2011b; Kogiso et al., 1997; Palacz & Saunders, 1986) and Gerbode and Dasgupta (2010).

Yurimoto et al., 2004). The fact remains that carbonatites are rare in ocean islands (Schmidt & Weidendorfer, 2018); a possible explanation for this is that carbonatitic melts generated in the asthenosphere are converted to alkali basalts by reacting with wall-rock peridotitic materials during transport through the thick lithosphere (Gómez-Ulla et al., 2018; Zhang et al., 2017).

Sediment and mafic/ultramafic protoliths in subducted slabs are possible carbonate carriers to the OIB sources. Hot and cold hydrothermal fluids alter, to various degrees, the basaltic and gabbroic components of the oceanic crust, forming heterogeneously carbonated protoliths, near and far from mid-ocean ridges, respectively. (e.g., Alt & Teagle, 1999; Bach et al., 2003; Staudigel et al., 1996). At slow-spreading ridges, hydrated ultramafic serpentinite rocks are also a major constituent of the oceanic crust (Kerrick & Connolly, 1998). Moreover, carbonation may extend to the slab lithosphere via fluid infiltration along faults near the outer rise of the oceanic plate prior to subduction (Fujie et al., 2013; Korenaga, 2017; Ranero et al., 2003).

An important question is whether carbonated materials survive the process of subduction to deliver a geochemical signature of subducted materials to the OIB source domain. The majority of subducted sediment experiences negligible decarbonation at a sub-arc depth unless hydrous fluids from underlying oceanic crust cause flux melting of sediment (Kerrick & Connolly, 2001a). The fate of subducted sedimentary carbonate beyond the sub-arc depth is twofold: (1) it encounters the solidus, which results in the formation of alkaline carbonatitic melts at 6–9 GPa (Grassi & Schmidt, 2011; Tsuno & Dasgupta, 2015), or (2) it loses CO₂ via decarbonation reactions at <8 GPa before melting (Kakizawa et al., 2015; Martin & Hammouda, 2011). Altered metabasalt can carry a majority of the carbonated component to greater depths along the cold geotherm (Kerrick & Connolly, 2001b; Poli, 2015; Poli et al., 2009). However, the carbonated component melts at between 10 and 20 GPa, depending on whether the slab followed either a hot or cold geotherm (Thomson et al., 2016). In contrast, the carbonated peridotite solidus overlaps the mantle geotherm (Ghosh et al., 2014), which implies that carbonated peridotite in subducted slabs may survive and be transported to the deep mantle without melting.

The argument on the melting conditions suggests that subducted carbonated oceanic crust, which is a possible precursor of geochemically distinct mantle components, is likely to melt due to a lowered solidus with the presence of CO₂ in the lowermost upper mantle and mantle transition zone. Traces of these slab-derived carbonatitic melts have been discovered in diamond inclusions from the subcontinental lithospheric mantle (Walter et al., 2008; Weiss et al., 2011). Carbonatitic melts easily segregate from

subducted materials due to their low viscosity and metasomatize the overlying mantle, thereby transferring the characteristics of enriched incompatible elements in subducted sediment and oceanic crust. Consequently, metasomatism during subduction is a possible alternative process that produces fertile peridotite and pyroxenite that eventually become the distinct mantle components, contrary to the standard model that considers hybridization in upwelling mantle plumes as discussed above.

Studying the minor element compositions of olivine from the Cook–Austral basalts with a HIMU signature and the Grande Comore basalts with a HIMU–EM1 intermediate signature provide evidence of the presence of an oceanic crust-derived carbonated melt in the OIB sources (Weiss et al., 2016). These olivines are characterized by elevated Ca and low Al contents relative to olivines in the other OIBs and MORBs. Such high Ca and low Al contents, together with low SiO₂ in the host basalts, favor a mantle source metasomatized by carbonatitic melts. Moreover, the HIMU basalts show similarity in isotopic compositions and trace element abundance patterns with Group I kimberlites that originate from the subcontinental lithospheric mantle. This fact led Weiss et al. (2016) to propose a model where a slab-derived carbonatitic melt caused metasomatism above the subducted slab. A part of the metasomatized mantle region was incorporated into the subcontinental mantle and the other part foundered to the deep mantle, where it became the HIMU OIB source.

A problem that remains in the hypothesis of carbonate recycling may be whether the trace element characteristic, together with parent/daughter ratios of radiogenic isotopes, of the HIMU OIB source is reproduced by the metasomatic addition of carbonatitic melts to the peridotitic mantle. Except for fluid-mobile elements (Rb, Ba, K, and Pb), the HIMU OIBs exhibit a uniformly smooth pattern in trace element spider diagrams (Kogiso et al., 1997; Weaver, 1991; Willbold & Stracke, 2006). In contrast, marine carbonates and natural carbonatites show large variation in incompatible element abundance with irregular patterns manifested by relative depletion in high field strength elements (Nb, Ta, Zr, and Hf) (Hoernle et al., 2002; Ducea et al., 2005). Although such elemental patterns may be partially moderated by metasomatic processes, quantitative modeling of trace element composition has been hampered by poor understanding of initial composition of carbonated materials, element partitioning during subduction dehydration and partial melting, and element transport during metasomatic addition to the mantle.

Stable Mg isotopes allow us to study the role of sedimentary carbonates in EM1 basalts from Pitcairn Island (Wang et al., 2018). These basalts have distinctly low $\delta^{26}\text{Mg}$ values compared with other OIBs, subcontinental peridotite xenoliths, and abyssal peridotites. It is best

explained if the Pitcairn source contained a subducted sedimentary carbonate that had substantially low $\delta^{26}\text{Mg}$. These characteristically low $\delta^{26}\text{Mg}$ values are also common to continental alkali basalts that have an EM1-like geochemical signature from Northeast China, suggesting that both have a similar origin but different ages and storage sites of source reservoirs (Wang et al., 2017). However, the low Ca/Al ratio characteristic of oceanic and continental EM1 basalts is not concordant with experimental evidence, showing the high Ca/Al ratio in melts originating from carbonate-bearing mantle sources. Wang et al. (2018) proposed an alternative mechanism to form the EM1 source, i.e., a decarbonation process (Kakizawa et al., 2015; Martin & Hammouda, 2011). While carbonate components (e.g., dolomite) in sediments are exhausted by decarbonation reaction with silicate (e.g., SiO_2), low $\delta^{26}\text{Mg}$ values and enriched incompatible element features can be inherited by silicate products (e.g., diopside), which eventually became EM1 mantle source (Wang et al., 2018).

In summary, there is a growing body of evidence that suggests that carbonates play an important role in inducing mantle heterogeneity. However, the behavior of carbonated rocks and elemental differentiation during subduction beneath the sub-arc and beyond is less well constrained in terms of geochemistry and experimental petrology.

5.5. RECENT PROGRESS AND OUTLOOK FOR THE MANTLE EVOLUTION

The recycling of crustal materials into the mantle has long been invoked to explain the mantle heterogeneity. Radiogenic isotopes in combination with lithophile element compositions have provided robust evidence for this recycling processes. However, the precursor of recycled materials and the processes of chemical differentiation have not been well constrained. In the following sections, new approaches to these issues are addressed from the studies using nontraditional stable isotopes, volatile elements, and redox-sensitive elements. Future directions of the studies are presented in the end of each section.

5.5.1. Nontraditional Stable Isotopes as New Proxies to Trace Recycling

Radiogenic isotope evidence for the recycling processes is sometimes equivocal, because a combination of time and parent-daughter fractionation determine the radiogenic isotope ratios, and therefore may yield similar isotopic features in distinct mantle components. Stable isotopes can provide a novel perspective on these issues. Since the equilibrium fractionation of stable isotopes is roughly proportional to $1/T^2$ (e.g., Urey, 1947), isotopic

fractionation is significant under the low-temperature conditions at the Earth's surface but tends to be very limited in most cases at mantle temperatures. This implies that stable isotopes have the potential to be powerful tracers of recycled material that was once at the Earth's surface.

Previous studies have extensively used traditional stable isotopes, such as O, C, N, and S, to trace the "fingerprints" of several possible recycled components in the mantle. Anomalous isotope ratios of these elements (i.e., higher or lower than the normal mantle value) were pervasively found in mantle-derived rocks (e.g., basalt and eclogite) and minerals (e.g., diamond), and provide strong evidence for the recycling of crustal materials into both the upper and deep mantle (see the detailed summary by White (2015a, 2015b)). What is particularly noteworthy is the discovery of mass-independent sulfur isotopic fractionation in lithospheric diamonds (Farquhar et al., 2002) and in olivine sulfide inclusions from Mangaia and Pitcairn basalts (Cabral et al., 2013; Delavault et al., 2016). These examples not only demonstrate the presence of recycled oceanic crust or sediments in the mantle but also constrain the antiquity (~2.45 Ga or older) of the recycled materials.

In the past 15 years, with the development of modern analytical techniques (e.g., multicollector inductively coupled plasma mass spectrometry), high-precision analytical methods for many nontraditional stable isotopes have been established and small fractionation of those isotope can be detected. The stable isotopes of both nonmetallic elements, such as B, Cl and Si, and metallic elements, such as Li, Mg, K, Ca, Ti, Fe, Mo, Ba, Tl, and U, have emerged as powerful or potential tools to trace recycled materials. Similar to traditional stable isotopes, significant variations in these stable isotope ratios within primitive, mantle-derived lavas may unambiguously provide evidence of the contributions from recycled surficial materials. Since White et al. (2015a, 2015b) made an extensive review of the current advances with B, Cl, Li, and U isotopes in the field of mantle geochemistry, here we mainly focus on several recently developed stable isotope tools.

Magnesium, Ca, and Zn isotopes appear to be excellent tracers of recycled carbonates or carbonate-bearing materials, based on considerable differences in isotopic compositions between carbonates and the Bulk Silicate Earth (BSE) (Fantle & Tipper, 2014; Liu et al., 2016; Teng, 2017, and references therein). Some cratonic eclogite xenoliths hosted by kimberlites have light Mg isotopic compositions (i.e., $\delta^{26}\text{Mg}$ value as low as approximately -1% ; $\delta^{26}\text{Mg}$ represents the deviation in parts per thousand of the $^{26}\text{Mg}/^{24}\text{Mg}$ from the ratio of the DSM3 standard) that differ from the peridotitic mantle ($\delta^{26}\text{Mg} = -0.25 \pm 0.04\%$; Teng, 2017), requiring the subduction

of altered, carbonate-bearing oceanic crust into the shallow mantle (Wang et al., 2012, 2015) (Figures 5.4a and 4b). A recent study found that Pitcairn EM1-type OIBs have Mg isotope ratios ($\delta^{26}\text{Mg} = -0.4\text{‰}$) that are lower than the mantle value. Their source is most likely subducted carbonate-bearing sediments that were characterized by the low $\delta^{26}\text{Mg}$ signature (Wang et al., 2018).

Some Hawaiian shield stage tholeiites have lower Ca isotope ratios (i.e., $\delta^{44/40}\text{Ca}$ values as low as 0.75‰; $\delta^{44/40}\text{Ca}$ is the deviation in parts per thousand of the $^{44}\text{Ca}/^{40}\text{Ca}$ from the ratio of the NIST SRM915a standard) than the BSE ($\delta^{44/40}\text{Ca} = 0.94 \pm 0.05\text{‰}$; Kang et al., 2017), and Ca isotopic variations correlate with the Sr/Nb and $^{87}\text{Sr}/^{86}\text{Sr}$ ratios, which can be best explained by addition of up to 4% of ancient carbonates into the mantle source (Huang et al., 2011) (Figure 5.4c). In both locations, the OIBs are produced by deep-seated mantle plumes (down to the core-mantle boundary; French & Romanowicz, 2015); therefore, these results indicate that some surficial materials have even been emplaced near the core-mantle boundary. Furthermore, many continental basalts are also characterized by Mg, Ca, and Zn isotopic compositions that are different from the mantle value. The large-scale Mg and Zn isotope anomalies ($\delta^{26}\text{Mg} = -0.61\text{‰}$ to -0.30‰ ; $\delta^{66}\text{Zn} = 0.30\text{‰}$ to 0.63‰ ; $\delta^{66}\text{Zn}$ is the deviation in parts per thousand of $^{66}\text{Zn}/^{64}\text{Zn}$ from the ratio of the JMC 3-0749L standard) in Cenozoic intra-plate basalts from eastern China suggest that they formed from the mantle sources impregnated with recycled Mg- and Zn-rich carbonates (e.g., Huang et al., 2015; Li et al., 2017; Liu et al., 2016; Yang et al., 2012) (Figure 5.4d). Recycled carbonate-bearing sediments were also invoked to explain the low $\delta^{44/40}\text{Ca}$ feature (0.67‰–0.80‰) observed in Tengchong volcanics in southwestern China (Liu et al., 2017) (Figure 5.4c). However, in several other locations including New Zealand's Antipodes Islands, China's Hainan Island, and central and southern Vietnam, basaltic rocks are thought to have inherited their low $\delta^{26}\text{Mg}$ signatures from recycled carbonated oceanic crust (Hoang et al., 2018; Li et al., 2017; Wang et al., 2016). In any case, the anomalous Mg, Zn and Ca isotope ratios in basalts provide robust evidence for the recycling of carbonates or carbonate-bearing materials.

The Tl isotope system can also provide evidence for the presence of specific recycled material in the mantle. Negative correlations between Tl isotopic compositions and Cs/Tl ratios of Hawaiian picrites point toward an end-member with a heavy Tl isotopic signature and very low Cs/Tl ratio. This is best explained by the addition of recycled ferromanganese sediments to the Hawaii mantle source (Nielsen et al., 2006). Some HIMU OIBs at St. Helena have Tl isotopic compositions that are lighter than the depleted upper mantle, which, together with its

relatively low Ce/Tl ratio, provides strong evidence for a recycled upper altered oceanic crust component in the HIMU source (Blusztajn et al., 2018). Furthermore, Tl isotopes are a promising tool to trace the contributions from subducted sediments (especially pelagic sediments) to arc lavas (e.g., Nielsen et al., 2016, 2017; Shu et al., 2017).

Currently, understanding recycling processes based on iron isotopes is both indirect and tentative. Williams and Bizimis (2014) found that garnet-pyroxenite xenoliths from Oahu, Hawaii, have $\delta^{57}\text{Fe}$ values (0.10 to 0.27‰; $\delta^{57}\text{Fe}$ is the deviation in parts per thousand of the $^{57}\text{Fe}/^{54}\text{Fe}$ from the ratio of the IRMM-014 standard) that are higher than depleted peridotites ($\delta^{57}\text{Fe} = -0.34$ to 0.14‰) and the primitive mantle ($\sim 0.04\text{‰}$). Since melting models, which assume derivation from a $\delta^{57}\text{Fe}$ -homogeneous peridotitic mantle, cannot explain the high $\delta^{57}\text{Fe}$ values, they suggested that the presence of heavy- $\delta^{57}\text{Fe}$ pyroxenite cumulates or pyroxenitic melt components may cause the elevated $\delta^{57}\text{Fe}$ values (Williams & Bizimis, 2014). Furthermore, they suggested that the pyroxenite cumulates or pyroxenitic melt components may possibly originate from recycled oceanic crust and terrigenous sediments in the basalt source. Extremely high $\delta^{57}\text{Fe}$ values (i.e., as high as 0.5‰) were also found in rejuvenated Samoan lavas, which cannot be explained by Fe isotope fractionation that occurred during partial melting of average mantle and subsequent melt differentiation (Konter et al., 2016). The presence of a pyroxenite source component or a metasomatized source with a high $\delta^{57}\text{Fe}$ signature may explain these elevated $\delta^{57}\text{Fe}$ values (Konter et al., 2016). More recently, a secondary pyroxenite source formed by reaction between eclogite-derived melts and ambient peridotite was suggested to be responsible for the high $\delta^{57}\text{Fe}$ values ($\sim 0.3\text{‰}$) observed in some Pitcairn basalts (Nebel et al., 2019).

Previous studies have found large Mo isotopic variations ($\delta^{98}\text{Mo} = -0.88\text{‰}$ to 0.34‰ ; $\delta^{98}\text{Mo}$ is the deviation in parts per thousand of $^{98}\text{Mo}/^{95}\text{Mo}$ from the ratio of the NIST SRM3134 standard) that are higher or lower than the chondritic average in arc lavas (e.g., Freymuth et al., 2015, 2016; Gaschnig et al., 2017; König et al., 2016; Wille et al., 2018). A current topic of debate is whether such Mo isotopic variations represent a recycled input signature or isotope fractionation during Mo removal via fluids during plate subduction (e.g., Freymuth et al., 2015, 2016; Gaschnig et al., 2017; König et al., 2016). Nevertheless, several Lesser Antilles arc lavas have consistently high $\delta^{98}\text{Mo}$, $^{87}\text{Sr}/^{86}\text{Sr}$, and $^{208}\text{Pb}/^{204}\text{Pb}$ values similar to black shales off-board the Lesser Antilles trench, which likely indicates the addition of subducted black shale-derived Mo to the mantle source of these lavas (Freymuth et al., 2016). In addition, Bezard et al. (2016) reported that the $\delta^{98}\text{Mo}$ values of

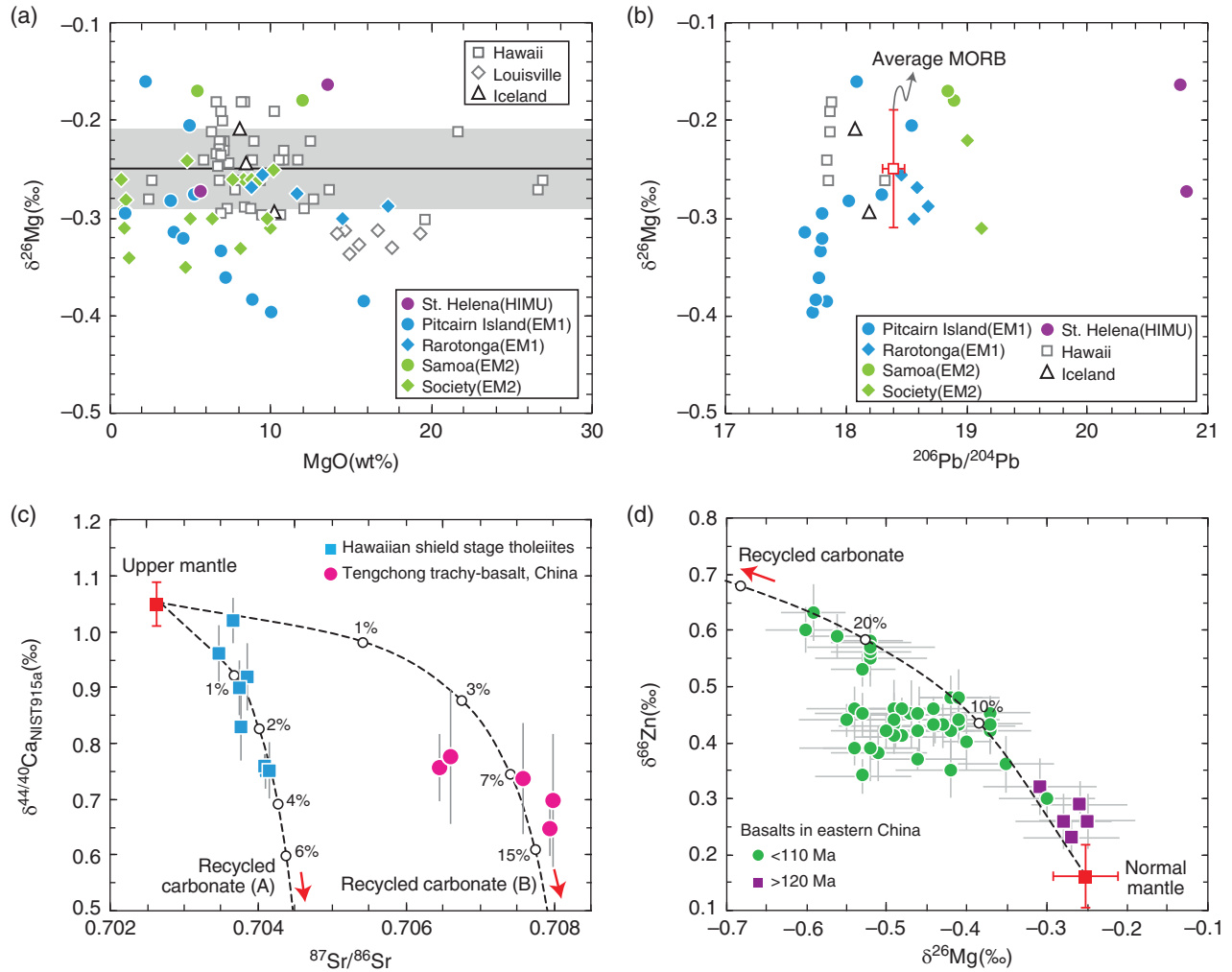


Figure 5.4 Published Mg-Ca-Zn isotopic data for some OIBs and continental basalts. Panels (a) and (b) show the variations in $\delta^{26}\text{Mg}$ versus MgO and $^{206}\text{Pb}/^{204}\text{Pb}$ for some OIBs, respectively. (c) Negative correlations between $\delta^{44/40}\text{Ca}$ and $^{87}\text{Sr}/^{86}\text{Sr}$ for some OIBs and continental basalts. The dashed lines are simple mixing curves between a hypothetical upper mantle source with $\text{CaO} = 3.17$ wt.%, $\text{Sr} = 7.664$ ppm, $\delta^{44/40}\text{Ca} = 1.05$ ‰, $^{87}\text{Sr}/^{86}\text{Sr} = 0.70263$ (Huang et al., 2011; Workman and Hart, 2005) and two different recycled carbonate components (for component A: $\text{CaO} = 56$ wt.%, $\text{Sr} = 800$ ppm, $\delta^{44/40}\text{Ca} = 0.2$ ‰, $^{87}\text{Sr}/^{86}\text{Sr} = 0.7046$, Huang et al., 2011; for component B: $\text{CaO} = 37.8$ wt.%, $\text{Sr} = 800$ ppm, $\delta^{44/40}\text{Ca} = 0.4$ ‰, $^{87}\text{Sr}/^{86}\text{Sr} = 0.708$, after Liu et al. (2017) with minor modification). (d) Negative correlations between $\delta^{66}\text{Zn}$ and $\delta^{26}\text{Mg}$ for some continental basalts from eastern China. The dashed line denotes simple mixing curve between a normal mantle component with $\text{MgO} = 38$ wt.%, $\text{Zn} = 55$ ppm, $\delta^{26}\text{Mg} = -0.25$ ‰, $\delta^{66}\text{Zn} = 0.16$ ‰ (Liu et al., 2019) and a recycled Mg- and Zn-rich carbonate component with $\text{MgO} = 25$ wt.%, $\text{Zn} = 280$ ppm, $\delta^{26}\text{Mg} = -2.2$ ‰, $\delta^{66}\text{Zn} = 0.91$ ‰ (Liu et al., 2019). Source: Data sources for (a) and (b): Bourdon et al. (2010), Teng et al. (2010), Wang et al. (2018), Zhong et al. (2017), and GEOROC database (<http://georoc.mpch-mainz.gwdg.de/georoc/>). In (a) and (b), the uncertainty (2SD) of Mg isotopic compositions for most of the samples is less than 0.07 ‰. The horizontal gray bar in (a) represents the $\delta^{26}\text{Mg}$ value (-0.25 ± 0.04 ‰) of peridotitic mantle (Teng, 2017). Source: Data for average MORB in (b) are from Teng et al. (2010) and Gale et al. (2013). In (c), data for Hawaiian tholeiites and Tengchong trachy-basalts are from Huang et al. (2011) and Liu et al. (2017), respectively. Source: Data for (d) are compiled from Yang et al. (2012) and Liu et al. (2016).

Pacific-Antarctic and Mohns-Knipovich MORBs range from -0.24 to 0.15% , which tend to increase with indices of source enrichment (e.g., $^{87}\text{Sr}/^{86}\text{Sr}$, $^{143}\text{Nd}/^{144}\text{Nd}$, and La/Sm). Furthermore, the superchondritic $\delta^{98}\text{Mo}$ of the enriched endmember that is higher than the depleted mantle was regarded as evidence for the contributions of recycled crustal components.

Other nontraditional stable isotopes with scarce data on high-temperature terrestrial rocks have emerged as potential tracers of recycled materials in the mantle. Nielsen et al. (2018) suggested that the Ba isotope variation in global MORBs, which is coupled with the variation of radiogenic isotopes and trace element ratios, reflects mixing between enriched and depleted MORB melts. Based on the strong similarity between the Ba isotopic compositions in sediments and E-MORBs and a series of geochemical modeling, they argued that subducted sediment components impart the light Ba isotopic signature to enriched MORBs. Regarding Si isotopes, Pringle et al. (2016) found that many HIMU-type (Mangaia, Cape Verde, and the Canary Islands) and Icelandic basalts exhibit light Si isotope enrichments relative to other OIBs, MORBs, and the BSE estimate. Their mass balance calculations suggest that incorporation of a $\sim 25\%$ recycled altered oceanic crust and lithospheric mantle in the mantle source can explain the light Si isotopic compositions.

At this stage, the application of K, Cr, and Cu stable isotopes to trace recycled materials is rather speculative. The discovery of high $\delta^{41/39}\text{K}_{\text{BSE}}$ values in hydrothermally altered oceanic crust relative to BSE suggests the potential of K isotopes to trace recycled altered oceanic crust (Parendo et al., 2017). Serpentinized peridotites, some black shales, and carbonates have $\delta^{53}\text{Cr}$ values (i.e., the deviation in parts per thousand of $^{53}\text{Cr}/^{52}\text{Cr}$ from the ratio of the JMC 3-0749L standard) that are distinct from the BSE (Qin & Wang, 2017, and references therein). Subduction of these components into the mantle may also cause potential geochemical variability in oceanic basalts. Larger Cu isotopic variations in arc and continental basalts relative to MORBs and OIBs likely reflect contributions from recycled crustal materials (Liu et al., 2015).

Currently, considerable challenges remain when applying nontraditional stable isotopes as proxies for recycling:

1. For the stable isotopes of some elements (e.g., Mo and Ba), the isotopic composition of the BSE remains unconstrained.
2. Published isotopic data on terrestrial rocks from high-temperature settings, especially oceanic basalts, are limited for most nontraditional stable isotopes.
3. For most elements, potential isotopic fractionation during magma degassing, fractional crystallization, partial melting, and subduction process lack serious evaluation.

4. Isotopic fractionation mechanisms during different processes (e.g., partial melting and alteration of the oceanic crust) require further exploration.

All of these issues impede the application of nontraditional stable isotopes as proxies to trace recycled materials. Therefore, we must carefully assess potential stable isotopic fractionation that occurs during magmatic process and post-magmatic alteration, before interpreting any isotope anomalies found in mantle-derived rocks. Nevertheless, in the near future, with further improvements to analytical precision, an increasing amount of published isotopic data, and an improved understanding of isotope fractionation during various geological processes, nontraditional stable isotopes will certainly play an irreplaceable role when attempting to trace the material cycle between the shallow layers and the deeper regions of the Earth.

5.5.2. Volatile Recycling

Volatiles play a significant role in the evolution of the solid Earth. The presence of volatiles influences the mode of mantle convection in response to the change of viscoelastic properties of rocks. Volatiles reduces solidus temperature, which enhances chemical differentiation relevant to partial melting and fluid transport in the mantle and crust. Estimating volatile contents and processes of volatile cycling in the mantle is one of fundamental issues, and thus have been a recent focus, in mantle geochemistry.

Conceptually, there exist volatiles with different lineage in the mantle. One is the volatiles that remain in the mantle against early catastrophic and subsequent continual mantle outgassing, the processes of which formed atmosphere and hydrosphere. The other is the volatiles that have been returned from the atmosphere and hydrosphere to the mantle. Portions of volatiles in the atmosphere and hydrosphere can be incorporated into oceanic crust and sediment by fluid percolation and organic and inorganic sedimentation, and then they are delivered to the mantle via slab subduction. Indeed, a large proportion of slab volatiles may be released by melting or breakdown of volatile-bearing minerals beneath the fore-arc and sub-arc regions (Manning, 2004; Peacock, 1990; Schmidt & Poli, 2014; Van Keken et al., 2011). However, studies on subduction-zone metamorphic rocks demonstrate incomplete removal of volatiles beneath the sub-arc (Debret et al., 2016; Kendrick et al., 2011; Pagé et al., 2016). Moreover, high-pressure experiments conducted with model slab materials suggest that some volatiles remain and are potentially transported deeper into the mantle (Kerrick & Connolly, 2001b; Ohtani, 2015; Poli et al., 2009). Based on previous studies for noble gases, which are powerful tracers of volatile elements, it was thought that subduction modification acts as a barrier for noble

gas input to the deep mantle (Staudacher & Allègre, 1988). However, precise analyses of heavy noble gas isotopes (i.e., Xe) demonstrate that atmosphere-derived noble gases are abundant not only in the MORB source upper mantle (Holland & Ballentine, 2006) but also in the plume source lower mantle (Parai & Mukhopadhyay, 2015).

Since lavas that erupt subaerially and in shallow water are degassed, previous studies have generally used submarine glasses quenched at high hydraulic pressure and mineral-hosted melt inclusions to study mantle-derived volatiles. Among the volatiles, the concentration of magmatic CO₂ is the most difficult to determine because it is easily degassed due to low melt solubility. Carbon dioxide-undersaturated melt inclusions in MORBs sampled from the Siqueiros transform fault along the East Pacific Rise provide benchmark estimates of the concentration of CO₂ in the depleted MORB mantle. In the following discussion, we use the ratio of volatile to lithophile elements with similar incompatibility to show relative volatile enrichment in mantle sources. The CO₂/Nb ratios of melt inclusions from the Siqueiros MORBs are, on average, 239 ± 46 (Saal et al., 2002). A compilation of undegassed depleted MORB glasses from the Atlantic, Pacific, and Indian Oceans, at 283 ± 32, recently confirmed this value (Michael & Graham, 2015). For water and chlorine, estimates for the H₂O/Ce and Cl/K in the MORB mantle source are 168 and 0.0075, respectively, based on the CO₂-undersaturated melt inclusions (Saal et al., 2002).

MORBs have radiogenic isotopes and lithophile element compositions that vary on the regional to global scale, which is thought to reflect geochemical heterogeneity associated with crustal recycling in the MORB source mantle. Similarly, volatile compositions (and volatile to lithophile element ratios) vary from a depleted to enriched MORBs (Cartigny et al., 2008; Javoy & Pineau, 1991; Michael & Cornell, 1998; Saal et al., 2002; Schilling et al., 1978; Shimizu et al., 2016). According to a recent study from Shimizu et al. (2016), the ranges of CO₂/Nb, H₂O/Ce, Cl/K, and F/Nd of undegassed quenched glasses are 258–744, 140–384, 0.01–0.10, and 14.3–45.4, respectively, within which the depleted and enriched MORBs define the lower and upper bounds, respectively. Sources that contain recycled volatiles from subducted oceanic lithosphere are a possible explanation for the relative volatile enrichment in the enriched MORBs.

While many OIBs exhibit H₂O/Ce that overlap with the MORB range, OIBs with robust EM1, EM2, and HIMU signatures have significantly lower H₂O/Ce (Figure 5.5). At Pitcairn (EM1) and Society (EM2), as well as isotopically enriched glasses from cores drilled in the Kerguelen Plateau (EM1–EM2 intermediate), H₂O/Ce of submarine quenched glasses range from 50 to 150, and the ratio decreases proportionately with increasing ⁸⁷Sr/⁸⁶Sr

(Kendrick et al., 2014; Wallace, 2002). Indeed, brine assimilation that occurs in the Samoan EM2 basalt glasses may obscure correlations between volatiles and isotopes but the assimilation-corrected H₂O/Ce is 40–170, which is lower than the MORB range (Kendrick et al., 2015). The HIMU basalt volatile compositions were first determined on olivine-hosted melt inclusions from Mangaia basalts (Cook Islands) (Cabral et al., 2014). The majority of melt inclusions have relatively low H₂O/Ce, ranging from 100 to 200 as a group, but show significant overlap with the range defined by MORBs. The low H₂O/Ce in the HIMU mantle source is confirmed using the submarine quenched glasses from Tuvalu (Jackson et al., 2015b). The glasses have variable radiogenic isotopic compositions and the samples that have a HIMU signature (i.e., radiogenic Pb isotopes) have H₂O/Ce as low as ~80 (except for a sample that may have been affected by water degassing).

Depletion in H₂O relative to Ce observed in the HIMU, EM1, and EM2 OIBs are common features of their sources. If their precursor was any type of subducted material, fluid or hydrous melt extraction from the subducted slab reasonably explains the low H₂O/Ce. However, an alternative explanation is a contribution from pyroxenite components in the magma sources (Bizimis & Peslier, 2015; Jackson et al., 2015b). Pyroxenites in Hawaiian mantle xenoliths have low H₂O/Ce (35–115) due to increased partitioning of Ce compared with H for pyroxene, and thus H₂O-rich but low-H₂O/Ce recycled pyroxenite may be parental to OIBs (Bizimis & Peslier, 2015). To assess whether “dry” or “wet” subducted materials play a significant role in the generation of OIB sources, we must consider both the source lithology and volatiles.

Determining the compositions of CO₂ is more challenging. Submarine quenched glasses and even melt inclusions entrapped within crystallizing phenocrysts in magma chambers at crustal levels are generally CO₂-saturated. For example, CO₂/Nb measured in olivine-hosted melt inclusions from Mangaia are only as high as 50, which is much lower than estimates for MORBs (Cabral et al., 2014). Carbon isotopic analyses of submarine glasses found at Pitcairn and Society clearly demonstrate a loss of CO₂ via magma degassing, which indicates the presence of a coupled effect of closed- and open-system degassing (Aubaud et al., 2005, 2006). Future studies of the concentrations and isotopes of C together with other volatile and lithophile elements and their isotopes (e.g., H, S, Cl, Sr, Nd, and Pb) on melt inclusions (Hallis et al., 2015; Koornneef et al., 2015; Reinhard et al., 2018; Saal et al., 1998; Shaw et al., 2008) could provide the means to trace the multiple-step process of degassing and mixing and understand the concentrations and isotopic compositions of carbon in the OIB source.

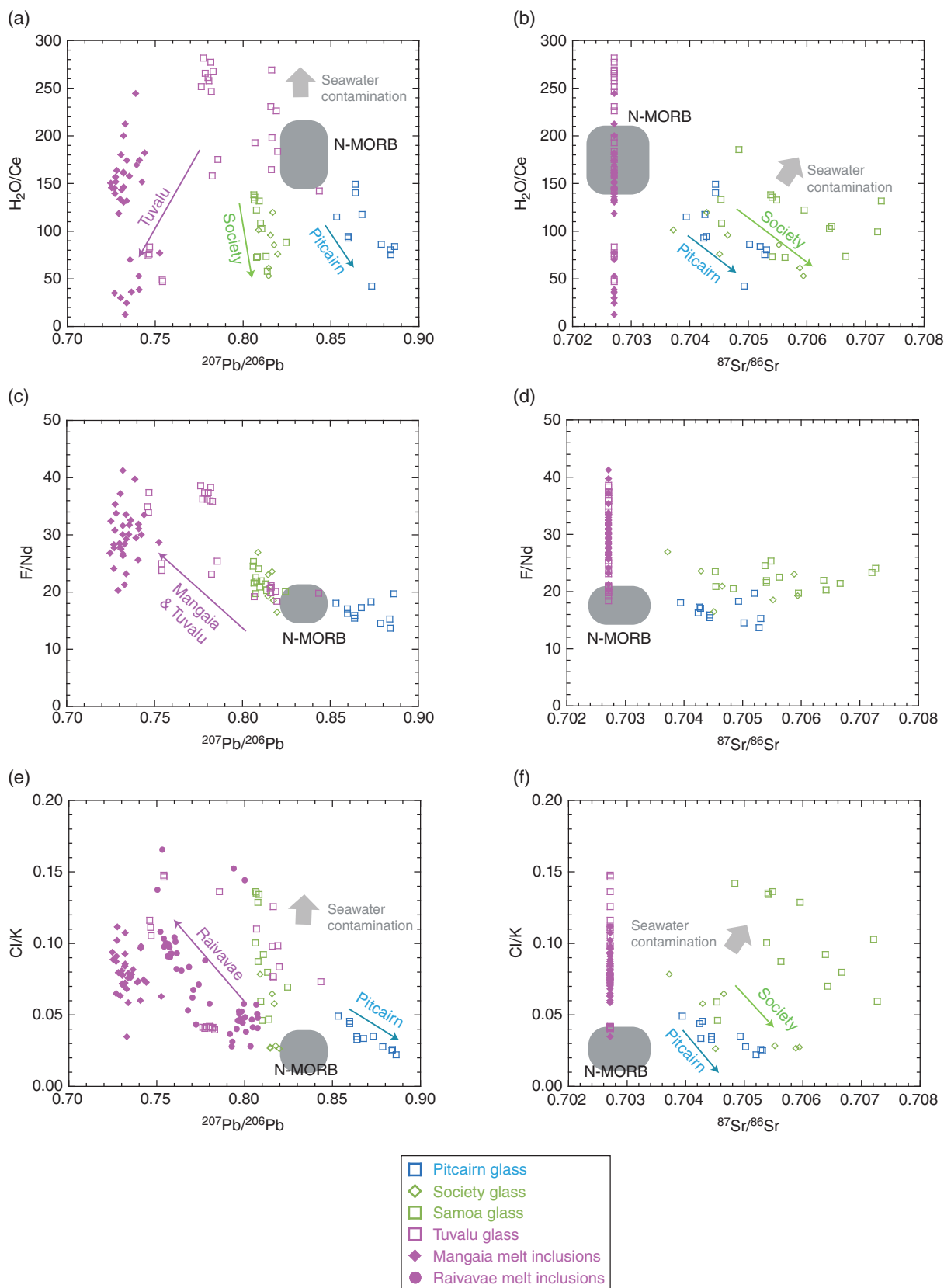


Figure 5.5 Volatile to lithophile element ratios in OIBs with robust EM1, EM2, and HIMU signatures. ²⁰⁷Pb/²⁰⁶Pb versus H₂O/Ce (a), F/Nd (c), and Cl/K (e). ⁸⁷Sr/⁸⁶Sr versus H₂O/Ce (b), F/Nd (d), and Cl/K (f). Data on submarine-quenched glasses and olivine-hosted melt inclusions are denoted by open and closed symbols, respectively. ⁸⁷Sr/⁸⁶Sr of HIMU samples are not available but are assumed to be 0.7027 based on the bulk rock values. Expected trends due to seawater (or brine) contamination are schematically shown by gray arrows. Note that the Pb isotope ratios in (a), (c), and (e) are shown with ²⁰⁷Pb/²⁰⁶Pb because ²⁰⁴Pb is not usually measured during in-situ analysis of melt inclusions. *Source:* Data compiled from Cabral et al. (2014), Jackson et al. (2015b), Kendrick et al. (2014, 2015), and Hanyu et al. (2019). N-MORB compositional ranges are after (Shimizu et al., 2016).

Fluorine and Cl are less affected by degassing owing to their relatively high solubility in basaltic melts. Enrichment in F (i.e., F/Nd) in the EM1 and EM2 OIBs from Pitcairn and Samoa is less clear (Kendrick et al., 2014, 2015) (Figure 5.5). In contrast, melt inclusions from Mangaia HIMU basalts have high F/Nd (~30) as a group relative to the average MORB value (~21) (Cabral et al., 2014; Jackson et al., 2015b). During subduction, amphibole, serpentinite, and mica retain F until ~6 GPa. Fluorine is then transferred to clinohumite, which is stable up to 20 GPa (Grützner et al., 2017). High F/Nd in HIMU OIBs is consistent with the efficient transfer of F to the mantle via subduction. Detecting Cl enrichment in submarine quenched glasses and melt inclusions is not always straightforward because shallow-level magma assimilation of seawater, brines, and altered oceanic crust easily alters the Cl composition (Stroncik & Haase, 2004). Submarine glasses from Pitcairn and Society exhibit decreasing Cl/K with increasing $^{87}\text{Sr}/^{86}\text{Sr}$ (Kendrick et al., 2014) (Figure 5.5). Such covariation precludes assimilation as the principal cause of Cl/K variation, and therefore low Cl/K is the source feature of EM1 and EM2. Chlorine loss from subducted components due to fluid release or hydrous melt extraction explains these low Cl/K. In contrast, HIMU OIBs are Cl-rich relative to K and Nb based on studies of submarine quenched glasses, although potential shallow-level assimilation complicates this argument (John et al., 2010; Stroncik & Haase, 2004). Hanyu et al. (2019) found that Cl/K and Cl/Nb correlate with Pb isotopes, which are a measure of the amount of dehydrated subducted oceanic crust contained in the magma source, in melt inclusions at Raivavae (Austral Islands). Shallow-level assimilation does not explain these correlations, which require a mechanism to return Cl from the hydrosphere to the HIMU mantle source against subduction dehydration. Previous studies have not identified Cl hosting minerals beyond the sub-arc depth and the authors suggest that the lattice defects in major minerals or mineral grain boundaries in subducted oceanic crust can carry small amounts of Cl. However, the transport mechanisms of Cl and other volatiles are a future subject of investigation.

Understanding volatile budgets and volatile transport mechanisms in the mantle are necessary to elucidate not only the influence of volatiles on mantle dynamics but also changes to Earth's surface environment in the past. The volatiles in the atmosphere and hydrosphere originate in the solid Earth. While mass of volatiles in present surface reservoirs is well estimated, the amount of volatiles that exist in the crust and mantle is still unclear. Volatile emissions via volcanism of continental flood basalts and oceanic plateaus (large igneous provinces) may have triggered drastic changes in the surface environment (Bond & Wignall, 2014; Svensen et al., 2007); however, a lack of

knowledge on volatile compositions in mantle sources hampers quantitative arguments. Some volatile elements (e.g., Cl) are harmful to life, and subduction transport may have buffered the amount of these elements in the biosphere (Hanyu et al., 2019).

5.5.3. Ancient Surface Environments and Mantle Evolution

Interaction between the Earth's surface reservoirs and the mantle is an issue of interest. The continuous and sporadic emission of volatiles from the mantle likely had a significant impact on the Earth's surface environment. Another noteworthy argument is that atmospheric oxygen level might have been controlled by geologic processes. Previous studies have questioned why the Great Oxidation Event (GOE), i.e., the change from Archean anoxic to post-Archean oxic conditions in the atmosphere (Holland, 2006), postdated for several hundred Ma after the first appearance of photosynthetic cyanobacteria. Variety of models have been proposed, such as enhanced photosynthesis due to an increase in the nutrient supply from the continents to the oceans during supercontinent formation (Campbell & Allen, 2008), the increased emission of oxidized gases from continental volcanoes rather than submarine volcanoes due to continental growth (Kump & Barley, 2007), the release of oxygen in response to a reduced ocean caused by sulfate supply from large igneous provinces (Ciborowski & Kerr, 2016), and the sequestration of reduced carbon in the mantle via cold slab subduction (Duncan & Dasgupta, 2017).

Inversely, changes in the surface environment may have influenced the mantle through the subduction input of surface materials to the mantle. Galer and O'Nions (1985) originally drew attention to the so-called second Pb paradox, which is the discrepancy between the Th/U ratio (strictly $^{232}\text{Th}/^{238}\text{U}$ or κ) of the average MORB values ($\kappa \sim 2.5$) and that predicted from their Pb isotopic compositions (i.e., time-integrated Th/U; $\kappa \sim 3.8$). Recent high-precision analyses of fresh MORB glasses have revised the average Th/U to higher κ -values of 2.9 and 3.1 (Arevalo Jr & McDonough, 2010; Gale et al., 2013); however, the disagreement is still significant. This paradox is currently believed to reflect temporal changes in Th/U of the mantle. Changes in Th/U recorded in ancient MORBs and komatiites provide evidence that Th/U has remained quite similar to the chondritic ratio ($\kappa = \sim 4.0$) throughout the Archean but decreased in the post-Archean toward the present-day MORB value (Collerson & Kamber, 1999; Nakamura & Kato, 2007; Nielsen, 2010). A model that accounts for such mantle evolution in terms of Th/U requires an increase in the level of oxygen in the hydrosphere during the GOE (Collerson & Kamber, 1999; Elliott et al., 1999; Nielsen,

2010). Uranium is redox-sensitive; it is mobile in the oxic condition, while Th remains quite immobile. In response to the increasing levels of oxygen in the hydrosphere, U moved from the continents to the ocean via weathering where hydrothermal fluids emplaced it possibly in the form of carbonates in the oceanic crust. The transfer of continental U to the mantle may have increased after the GOE.

This theory is confirmed by the measurements of U isotope ratios ($^{238}\text{U}/^{235}\text{U}$) in mantle-derived rocks (Andersen et al., 2015). Superchondritic $\delta^{238}\text{U}$ in MORBs is consistent with recycling of ^{238}U -rich hydrothermally altered oceanic crust in the oxic ocean. In contrast, OIBs have an entirely chondritic $\delta^{238}\text{U}$ signature but decreased Th/U coupled with young ^{207}Pb – ^{206}Pb model ages in the post-Archean. Recycling of surface U to OIB sources can explain these signatures where U isotope ratios did not fractionate during hydrothermal activity under anoxic conditions until the deep ocean was fully oxidized at approximately 0.6 Ga (Holland, 2006; Lyons et al., 2014). Also, the discovery of the mass-independent sulfur isotope ratios in OIBs (Cabral et al., 2013; Delavault et al., 2016) provides independent evidence of ancient surface redox conditions and relevant element recycling between the surface and mantle. Co-evolution of the mantle and surface environment is an important issue for future studies, which may be solved via the analysis of redox-sensitive elements and stable isotopes recorded in OIBs of varying source ages.

ACKNOWLEDGMENTS

We are grateful to P. R. Castillo and an anonymous reviewer for their constructive comments on the manuscript.

REFERENCES

- Alt, J. C., & Teagle, D. A. H. (1999). The uptake of carbon during alteration of ocean crust. *Geochimica et Cosmochimica Acta*, 63(10), 1527–1535. doi:10.1016/S0016-7037(99)00123-4
- Andersen, M. B., Elliott, T., Freymuth, H., Sims, K. W. W., Niu, Y., & Kelley, K. A. (2015). The terrestrial uranium isotope cycle. *Nature*, 517(7534), 356–359. doi:10.1038/nature14062
- Arevalo Jr, R., & McDonough, W. F. (2010). Chemical variations and regional diversity observed in MORB. *Chemical Geology*, 271(1–2), 70–85. doi:10.1016/j.chemgeo.2009.12.013
- Aubaud, C., Pineau, F., Hékinian, R., & Javoy, M. (2005). Degassing of CO₂ and H₂O in submarine lavas from the Society hotspot. *Earth and Planetary Science Letters*, 235(3–4), 511–527. doi.org/10.1016/j.epsl.2005.04.047
- Aubaud, C., Pineau, F., Hékinian, R., & Javoy, M. (2006). Carbon and hydrogen isotope constraints on degassing of CO₂ and H₂O in submarine lavas from the Pitcairn hotspot (South Pacific). *Geophysical Research Letters*, 33(2), L02308. doi:10.1029/2005gl024907
- Bach, W., Peucker-Ehrenbrink, B., Hart, S. R., & Blusztajn, J. S. (2003). Geochemistry of hydrothermally altered oceanic crust: DSDP/ODP Hole 504B – Implications for seawater-crust exchange budgets and Sr- and Pb-isotopic evolution of the mantle. *Geochemistry Geophysics Geosystems*, 4, 8904. doi:10.1029/2002gc000419
- Balta, J. B., Asimow, P. D., & Mosenfelder, J. L. (2011). Manganese partitioning during hydrous melting of peridotite. *Geochimica et Cosmochimica Acta*, 75(20), 5819–5833. doi:10.1016/j.gca.2011.05.026
- Barling, J., & Goldstein, S. L. (1990). Extreme isotopic variations in Heard Island lavas and the nature of mantle reservoirs. *Nature*, 348, 59. doi:10.1038/348059a0
- Becker, H. (2000). Re-Os fractionation in eclogites and blueschists and the implications for recycling of oceanic crust into the mantle. *Earth and Planetary Science Letters*, 177(3–4), 287–300. doi:10.1016/S0012-821X(00)00052-2
- Beier, C., Haase, K. M., Abouchami, W., Krienitz, M.-S., & Hauff, F. (2008). Magma genesis by rifting of oceanic lithosphere above anomalous mantle: Terceira Rift, Azores. *Geochemistry, Geophysics, Geosystems*, 9(12). doi:10.1029/2008GC002112
- Bezard, R., Fischer-Gödde, M., Hamelin, C., Brennecke, G. A., & Kleine, T. (2016). The effects of magmatic processes and crustal recycling on the molybdenum stable isotopic composition of Mid-Ocean Ridge Basalts. *Earth and Planetary Science Letters*, 453, 171–181. doi:10.1016/j.epsl.2016.07.056
- Bizimis, M., Griselin, M., Lassiter, J. C., Salters, V. J. M., & Sen, G. (2007). Ancient recycled mantle lithosphere in the Hawaiian plume: Osmium–Hafnium isotopic evidence from peridotite mantle xenoliths. *Earth and Planetary Science Letters*, 257(1–2), 259–273. doi.org/10.1016/j.epsl.2007.02.036
- Bizimis, M., & Peslier, A. H. (2015). Water in Hawaiian garnet pyroxenites: Implications for water heterogeneity in the mantle. *Chemical Geology*, 397, 61–75. doi:10.1016/j.chemgeo.2015.01.008
- Blusztajn, J., Nielsen, S. G., Marschall, H. R., Shu, Y., Ostrander, C. M., & Hanyu, T. (2018). Thallium isotope systematics in volcanic rocks from St. Helena – Constraints on the origin of the HIMU reservoir. *Chemical Geology*, 476, 292–301. doi:10.1016/j.chemgeo.2017.11.025
- Bodinier, J.-L., Garrido, C. J., Chanefo, I., Bruguier, O., & Ger-villa, F. (2008). Origin of Pyroxenite–Peridotite Veined Mantle by Refertilization Reactions: Evidence from the Ronda Peridotite (Southern Spain). *Journal of Petrology*, 49(5), 999–1025. doi:10.1093/petrology/egn014
- Bond, D. P. G., & Wignall, P. B. (2014). Large igneous provinces and mass extinctions: An update. In G. Keller & A. C. Kerr (Eds.), *Volcanism, Impacts, and Mass Extinctions: Causes and Effects*: Geological Society of America. doi:10.1130/2014.2505(02)
- Bourdon, B., Tipper, E. T., Fitoussi, C., & Stracke, A. (2010). Chondritic Mg isotope composition of the Earth. *Geochimica et Cosmochimica Acta*, 74(17), 5069–5083. doi:10.1016/j.gca.2010.06.008
- Boyet, M., & Carlson, R. W. (2005). ^{142}Nd evidence for early (>4.53 Ga) global differentiation of the silicate Earth. *Science*, 309(5734), 576–581. doi:10.1126/science.1113634

- Brandenburg, J. P., Hauri, E. H., van Keken, P. E., & Ballentine, C. J. (2008). A multiple-system study of the geochemical evolution of the mantle with force-balanced plates and thermochemical effects. *Earth and Planetary Science Letters*, 276(1–2), 1–13. doi:10.1016/j.epsl.2008.08.027
- Cabral, R., Jackson, M. G., Rose-Koga, E. F., Koga, K. T., Whitehouse, M. J., Antonelli, M. A., et al. (2013). Anomalous sulphur isotopes in plume lavas reveal deep mantle storage of Archean crust. *Nature*, 496, 490–493. doi:10.1038/nature12020
- Cabral, R. A., Jackson, M. G., Koga, K. T., Rose-Koga, E. F., Hauri, E. H., Whitehouse, M. J., et al. (2014). Volatile cycling of H₂O, CO₂, F, and Cl in the HIMU mantle: A new window provided by melt inclusions from oceanic hot spot lavas at Mangaia, Cook Islands. *Geochemistry, Geophysics, Geosystems*, 15(11), 4445–4467. doi:10.1002/2014gc005473
- Campbell, I. H., & Allen, C. M. (2008). Formation of supercontinents linked to increases in atmospheric oxygen. *Nature Geoscience*, 1, 554. doi:10.1038/ngeo259
- Carlson, R. W., & Irving, A. J. (1994). Depletion and enrichment history of subcontinental lithospheric mantle: An Os, Sr, Nd and Pb isotopic study of ultramafic xenoliths from the northwestern Wyoming Craton. *Earth and Planetary Science Letters*, 126(4), 457–472. doi:10.1016/0012-821X(94)90124-4
- Caro, G., Bourdon, B., Birck, J.-L., & Moorbath, S. (2006). High-precision ¹⁴²Nd/¹⁴⁴Nd measurements in terrestrial rocks: Constraints on the early differentiation of the Earth's mantle. *Geochimica et Cosmochimica Acta*, 70(1), 164–191. doi:10.1016/j.gca.2005.08.015
- Cartigny, P., Pineau, F., Aubaud, C., & Javoy, M. (2008). Towards a consistent mantle carbon flux estimate: Insights from volatile systematics (H₂O/Ce, δD, CO₂/Nb) in the North Atlantic mantle (14° N and 34° N). *Earth and Planetary Science Letters*, 265(3–4), 672–685. doi:10.1016/j.epsl.2007.11.011
- Castillo, P. R. (2015). The recycling of marine carbonates and sources of HIMU and FOZO ocean island basalts. *Lithos*, 216–217, 254–263. doi:10.1016/j.lithos.2014.12.005
- Castillo, P. R. (2016). A proposed new approach and unified solution to old Pb paradoxes. *Lithos*, 252–253, 32–40. doi:10.1016/j.lithos.2016.02.015
- Chaffey, D. J., Cliff, R. A., & Wilson, B. M. (1989). Characterization of the St Helena magma source. In A. D. Saunders & M. J. Norry (Eds.), *Magmatism in the Ocean Basins, Geological Society Special Publication* (Vol. 42, pp. 257–276). doi:10.1144/GSL.SP.1989.042.01.16
- Chan, L.-H., Lassiter, J. C., Hauri, E. H., Hart, S., & Blusztajn, J. (2009). Lithium isotope systematics of lavas from the Cook-Austral Islands: Constraints on the origin of HIMU mantle. *Earth and Planetary Science Letters*, 277(3–4), 433–442. doi:10.1016/j.epsl.2008.11.009
- Chauvel, C., Hofmann, A. W., & Vidal, P. (1992). HIMU-EM: The French Polynesian connection. *Earth and Planetary Science Letters*, 110(1–4), 99–119. doi:10.1016/0012-821X(92)90042-T
- Christensen, U. R., & Hofmann, A. W. (1994). Segregation of subducted oceanic-crust in the convecting mantle. *Journal of Geophysical Research*, 99(B10), 19867–19884. doi:10.1029/93jb03403
- Ciborowski, T. J. R., & Kerr, A. C. (2016). Did mantle plume magmatism help trigger the Great Oxidation Event? *Lithos*, 246–247, 128–133. doi:10.1016/j.lithos.2015.12.017
- Class, C., & Goldstein, S. L. (2005). Evolution of helium isotopes in the Earth's mantle. *Nature*, 436(7054), 1107–1112. doi:10.1038/nature03930
- Class, C., & le Roex, A. P. (2008). Ce anomalies in Gough Island lavas — Trace element characteristics of a recycled sediment component. *Earth and Planetary Science Letters*, 265(3), 475–486. doi:10.1016/j.epsl.2007.10.030
- Collerson, K. D., & Kamber, B. S. (1999). Evolution of the continents and the atmosphere inferred from Th-U-Nb systematics of the depleted mantle. *Science*, 283(5407), 1519–1522. doi:10.1126/science.283.5407.1519
- Courtillot, V., Davaille, A., Besse, J., & Stock, J. (2003). Three distinct types of hotspots in the Earth's mantle. *Earth and Planetary Science Letters*, 205(3–4), 295–308. doi:10.1016/S0012-821X(02)01048-8
- Dasgupta, R., & Hirschmann, M. M. (2006). Melting in the Earth's deep upper mantle caused by carbon dioxide. *Nature*, 440(7084), 659–662. doi:10.1038/nature04612
- Dasgupta, R., Hirschmann, M. M., & Smith, N. D. (2007). Partial melting experiments of peridotite + CO₂ at 3 GPa and genesis of alkalic ocean island basalts. *Journal of Petrology*, 48(11), 2093–2124. doi:10.1093/petrology/egm053
- Dasgupta, R., Jackson, M. G., & Lee, C.-T. A. (2010). Major element chemistry of ocean island basalts – Conditions of mantle melting and heterogeneity of mantle source. *Earth and Planetary Science Letters*, 289(3), 377–392. doi:10.1016/j.epsl.2009.11.027
- Day, J. M. D., Pearson, D. G., Macpherson, C. G., Lowry, D., & Carracedo, J.-C. (2009). Pyroxenite-rich mantle formed by recycled oceanic lithosphere: Oxygen-osmium isotope evidence from Canary Island lavas. *Geology*, 37(6), 555–558. doi:10.1130/G25613A.1
- Day, J. M. D., Pearson, D. G., Macpherson, C. G., Lowry, D., & Carracedo, J. C. (2010). Evidence for distinct proportions of subducted oceanic crust and lithosphere in HIMU-type mantle beneath El Hierro and La Palma, Canary Islands. *Geochimica et Cosmochimica Acta*, 74(22), 6565–6589. doi:10.1016/j.gca.2010.08.021
- Debret, B., Koga, K. T., Cattani, F., Nicollet, C., Van den Bleeken, G., & Schwartz, S. (2016). Volatile (Li, B, F and Cl) mobility during amphibole breakdown in subduction zones. *Lithos*, 244, 165–181. doi:10.1016/j.lithos.2015.12.004
- Delavault, H., Chauvel, C., Sobolev, A., & Batanova, V. (2015). Combined petrological, geochemical and isotopic modeling of a plume source: Example of Gambier Island, Pitcairn chain. *Earth and Planetary Science Letters*, 426, 23–35. doi:10.1016/j.epsl.2015.06.013
- Delavault, H., Chauvel, C., Thomassot, E., Devey, C. W., & Dazas, B. (2016). Sulfur and lead isotopic evidence of relic Archean sediments in the Pitcairn mantle plume. *Proceedings of the National Academy of Sciences*, 113(46), 12952–12956. doi:10.1073/pnas.1523805113

- Dilek, Y., & Furnes, H. (2014). Ophiolites and Their Origins. *Elements*, 10(2), 93–100. doi:10.2113/gselements.10.2.93
- Ducea, M. N., Saleeby, J., Morrison, J., & Valencia, V. A. (2005). Subducted carbonates, metasomatism of mantle wedges, and possible connections to diamond formation: An example from California. *American Mineralogist*, 90(5–6), 864–870. doi:10.2138/am.2005.1670
- Duncan, M. S., & Dasgupta, R. (2017). Rise of Earth's atmospheric oxygen controlled by efficient subduction of organic carbon. *Nature Geoscience*, 10(5), 387–392. doi:10.1038/ngeo2939
- Dupuy, C., Vidal, P., Barszczus, H. G., & Chauvel, C. (1987). Origin of basalts from the Marquesas Archipelago (south central Pacific Ocean): isotope and trace element constraints. *Earth and Planetary Science Letters*, 82(1–2), 145–152. doi:10.1016/0012-821x(87)90114-2
- Dupuy, C., Vidal, P., Maury, R. C., & Guille, G. (1993). Basalts from Mururoa, Fangataufa and Gambier islands (French Polynesia): Geochemical dependence on the age of the lithosphere. *Earth and Planetary Science Letters*, 117(1–2), 89–100. doi:10.1016/0012-821x(93)90119-t
- Eiler, J. M., Farley, K. A., Valley, J. W., Hauri, E., Craig, H., Hart, S. R., & Stolper, E. M. (1997). Oxygen isotope variations in ocean island basalt phenocrysts. *Geochimica et Cosmochimica Acta*, 61(11), 2281–2293. doi:10.1016/S0016-7037(97)00075-6
- Eisele, J., Sharma, M., Galer, S. J. G., Blichert-Toft, J., Devey, C. W., & Hofmann, A. W. (2002). The role of sediment recycling in EM-1 inferred from Os, Pb, Hf, Nd, Sr isotope and trace element systematics of the Pitcairn hotspot. *Earth and Planetary Science Letters*, 196(3–4), 197–212. doi:10.1016/S0012-821x(01)00601-x
- Elliott, T., Zindler, A., & Bourdon, B. (1999). Exploring the kappa conundrum: the role of recycling in the lead isotope evolution of the mantle. *Earth and Planetary Science Letters*, 169, 129–145
- Fantle, M. S., & Tipper, E. T. (2014). Calcium isotopes in the global biogeochemical Ca cycle: Implications for development of a Ca isotope proxy. *Earth-Science Reviews*, 129, 148–177. doi:10.1016/j.earscirev.2013.10.004
- Farley, K. A., Natland, J. H., & Craig, H. (1992). Binary mixing of enriched and undegassed (primitive?) mantle components (He, Sr, Nd, Pb) in Samoan lavas. *Earth and Planetary Science Letters*, 111(1), 183–199. doi:10.1016/0012-821X(92)90178-X
- Farquhar, J., Wing, B. A., McKeegan, K. D., Harris, J. W., Cartigny, P., & Thiemens, M. H. (2002). Mass-Independent Sulfur of Inclusions in Diamond and Sulfur Recycling on Early Earth. *Science*, 298(5602), 2369–2372. doi:10.1126/science.1078617
- Foulger, G. R., Pritchard, M. J., Julian, B. R., Evans, J. R., Allen, R. M., Nolet, G., et al. (2001). Seismic tomography shows that upwelling beneath Iceland is confined to the upper mantle. *Geophysical Journal International*, 146(2), 504–530. doi:10.1046/j.0956-540x.2001.01470.x
- French, S. W., & Romanowicz, B. (2015). Broad plumes rooted at the base of the Earth's mantle beneath major hotspots. *Nature*, 525(7567), 95–99. doi:10.1038/nature14876
- Frey, F. A., & Weis, D. (1995). Temporal evolution of the kerguelen plume: Geochemical evidence from 38 to 82 ma lavas forming the Ninetyeast ridge. *Contributions to Mineralogy and Petrology*, 121(1), 12–28. doi:10.1007/s004100050087
- Frey, H., Elliott, T., van Soest, M., & Skora, S. (2016). Tracing subducted black shales in the Lesser Antilles arc using molybdenum isotope ratios. *Geology*, 44(12), 987–990. doi:10.1130/G38344.1
- Frey, H., Vils, F., Willbold, M., Taylor, R. N., & Elliott, T. (2015). Molybdenum mobility and isotopic fractionation during subduction at the Mariana arc. *Earth and Planetary Science Letters*, 432, 176–186. doi:10.1016/j.epsl.2015.10.006
- Fujie, G., Kodaira, S., Yamashita, M., Sato, T., Takahashi, T., & Takahashi, N. (2013). Systematic changes in the incoming plate structure at the Kuril trench. *Geophysical Research Letters*, 40(1), 88–93. doi:10.1029/2012GL054340
- Gómez-Ulla, A., Sigmarsson, O., Huertas, M. J., Devidal, J.-L., & Ancochea, E. (2018). The historical basanite–alkali basalt–tholeiite suite at Lanzarote, Canary Islands: Carbonated melts of heterogeneous mantle source? *Chemical Geology*, 494, 56–68. doi:10.1016/j.chemgeo.2018.07.015
- Gale, A., Dalton, C. A., Langmuir, C. H., Su, Y., & Schilling, J.-G. (2013). The mean composition of ocean ridge basalts. *Geochemistry Geophysics Geosystems*, 14(3), 489–518. doi:10.1029/2012GC004334
- Galer, S. J. G., & O'Nions, K. (1985). Residence time of thorium, uranium and lead in the mantle with implications for mantle convection. *Nature*, 316, 778–782
- Garapic, G., Jackson, M. G., Hauri, E. H., Hart, S. R., Farley, K. A., Blusztajn, J. S., & Woodhead, J. D. (2015). A radiogenic isotopic (He-Sr-Nd-Pb-Os) study of lavas from the Pitcairn hotspot: Implications for the origin of EM-1 (enriched mantle 1). *Lithos*, 228–229, 1–11. doi:10.1016/j.lithos.2015.04.010
- Gaschnig, R. M., Reinhard, C. T., Planavsky, N. J., Wang, X., Asael, D., & Chauvel, C. (2017). The Molybdenum Isotope System as a Tracer of Slab Input in Subduction Zones: An Example From Martinique, Lesser Antilles Arc. *Geochemistry, Geophysics, Geosystems*, 18(12), 4674–4689. doi:10.1002/2017GC007085
- Geldmacher, J., Hoernle, K., Klügel, A., van den Bogaard, P., & Bindeman, I. (2008). Geochemistry of a new enriched mantle type locality in the northern hemisphere: Implications for the origin of the EM-I source. *Earth and Planetary Science Letters*, 265(1), 167–182. doi:10.1016/j.epsl.2007.10.001
- Gerbode, C., & Dasgupta, R. (2010). Carbonate-fluxed melting of MORB-like pyroxenite at 2.9 GPa and genesis of HIMU ocean island basalts. *Journal of Petrology*, 51(10), 2067–2088. doi:10.1093/petrology/egq049
- Ghosh, S., Litasov, K., & Ohtani, E. (2014). Phase relations and melting of carbonated peridotite between 10 and 20 GPa: a proxy for alkali- and CO₂-rich silicate melts in the deep mantle. *Contributions to Mineralogy and Petrology*, 167(2), 964. doi:10.1007/s00410-014-0964-z
- Gibson, S. A., Thompson, R. N., Day, J. A., Humphris, S. E., & Dickin, A. P. (2005). Melt-generation processes associated with the Tristan mantle plume: Constraints on the origin of

- EM-1. *Earth and Planetary Science Letters*, 237(3–4), 744–767. doi:10.1016/j.epsl.2005.06.015
- Goldstein, S. L., Soffer, G., Langmuir, C. H., Lehnert, K. A., Graham, D. W., & Michael, P. J. (2008). Origin of a 'Southern Hemisphere' geochemical signature in the Arctic upper mantle. *Nature*, 453, 89. doi:10.1038/nature06919
- Grützner, T., Klemme, S., Rohrbach, A., Gervasoni, F., & Berndt, J. (2017). The role of F-clinohumite in volatile recycling processes in subduction zones. *Geology*, 45(5), 443–446. doi:10.1130/g38788.1
- Graham, D. W., Humphris, S. E., Jenkins, W. J., & Kurz, M. D. (1992). Helium isotope geochemistry of some volcanic rocks from Saint Helena. *Earth and Planetary Science Letters*, 110 (1–4), 121–131. doi:10.1016/0012-821X(92)90043-U
- Graham, D. W., Zindler, A., Kurz, M. D., Jenkins, W. J., Batiza, R., & Staudigel, H. (1988). He, Pb, Sr and Nd isotope constraints on magma genesis and mantle heterogeneity beneath young Pacific seamounts. *Contributions to Mineralogy and Petrology*, 99(4), 446–463. doi:10.1007/bf00371936
- Grassi, D., & Schmidt, M. W. (2011). The Melting of Carbonated Pelites from 70 to 700 km Depth. *Journal of Petrology*, 52(4), 765–789. doi:10.1093/ptrology/egr002
- Gudfinnsson, G. H., & Presnall, D. C. (2005). Continuous Gradations among Primary Carbonatitic, Kimberlitic, Melilititic, Basaltic, Picritic, and Komatiitic Melts in Equilibrium with Garnet Lherzolite at 3–8 GPa. *Journal of Petrology*, 46(8), 1645–1659. doi:10.1093/ptrology/egi029
- Gurenko, A. A., Sobolev, A. V., Hoernle, K. A., Hauff, F., & Schmincke, H.-U. (2009). Enriched, HIMU-type peridotite and depleted recycled pyroxenite in the Canary plume: A mixed-up mantle. *Earth and Planetary Science Letters*, 277(3–4), 514–524. doi:10.1016/j.epsl.2008.11.013
- Hémond, C., Devey, C. W., & Chauvel, C. (1994). Source compositions and melting processes in the Society and Austral plumes (South Pacific Ocean): Element and isotope (Sr, Nd, Pb, Th) geochemistry. *Chemical Geology*, 115(1–2), 7–45. doi:10.1016/0009-2541(94)90143-0
- Halliday, A. N., Lee, D.-C., Tommasini, S., Davies, G. R., Paslick, C. R., Fitton, J. G., & James, D. E. (1995). Incompatible trace elements in OIB and MORB and source enrichment in the sub-oceanic mantle. *Earth and Planetary Science Letters*, 133(3–4), 379–395. doi:10.1016/0012-821X(95)00097-V
- Hallis, L. J., Huss, G. R., Nagashima, K., Taylor, G. J., Halldórsson, S. A., Hilton, D. R., et al. (2015). Evidence for primordial water in Earth's deep mantle. *Science*, 350(6262), 795–797. doi:10.1126/science.aac4834
- Hanan, B. B., & Graham, D. W. (1996). Lead and helium isotope evidence from oceanic basalts for a common deep source of mantle plumes. *Science*, 272(5268), 991–995. doi:10.1126/science.272.5264.991
- Hanyu, T., Dosso, L., Ishizuka, O., Tani, K., Hanan, B. B., Adam, C., et al. (2013). Geochemical diversity in submarine HIMU basalts from Austral Islands, French Polynesia. *Contributions to Mineralogy and Petrology*, 166(5), 1285–1304. doi:10.1007/s00410-013-0926-x
- Hanyu, T., & Kaneoka, I. (1997). The uniform and low $^3\text{He}/^4\text{He}$ ratios of HIMU basalts as evidence for their origin as recycled materials. *Nature*, 390(6657), 273–276. doi:10.1038/36835
- Hanyu, T., Kawabata, H., Tatsumi, Y., Kimura, J.-I., Hyodo, H., Sato, K., et al. (2014). Isotope evolution in the HIMU reservoir beneath St. Helena: Implications for the mantle recycling of U and Th. *Geochimica et Cosmochimica Acta*, 143, 232–252. doi:10.1016/j.gca.2014.03.016
- Hanyu, T., Kimura, J.-I., Katakuse, M., Calvert, A. T., Sisson, T. W., & Nakai, S. (2010). Source materials for inception stage Hawaiian magmas: Pb-He isotope variations for early Kilauea. *Geochemistry Geophysics Geosystems*, 11, Q0AC01. doi: 10.1029/2009GC002760
- Hanyu, T., Shimizu, K., Ushikubo, T., Kimura, J.-I., Chang, Q., Hamada, M., et al. (2019). Tiny droplets of ocean island basalts unveil Earth's deep chlorine cycle. *Nature Communications*, 10(1), 60. doi:10.1038/s41467-018-07955-8
- Hanyu, T., Tatsumi, Y., & Kimura, J.-I. (2011a). Constraints on the origin of the HIMU reservoir from He-Ne-Ar isotope systematics. *Earth and Planetary Science Letters*, 307, 377–386. doi:10.1016/j.epsl.2011.05.012
- Hanyu, T., Tatsumi, Y., Senda, R., Miyazaki, T., Chang, Q., Hirahara, Y., et al. (2011b). Geochemical characteristics and origin of the HIMU reservoir: A possible mantle plume source in the lower mantle. *Geochemistry Geophysics Geosystems*, 12(2), Q0AC09. doi:10.1029/2010GC003252
- Hart, S. R., Hauri, E. H., Oschmann, L. A., & Whitehead, J. A. (1992). Mantle plumes and entrainment—Isotopic evidence. *Science*, 256(5056), 517–520. doi:10.1126/science.256.5056.517
- Hauri, E. H., & Hart, S. R. (1993). Re-Os isotope systematics of HIMU and EMII oceanic island basalts from the south Pacific Ocean. *Earth and Planetary Science Letters*, 114 (2–3), 353–371. doi:10.1016/0012-821X(93)90036-9
- Hauri, E. H., Shimizu, N., Dieu, J. J., & Hart, S. R. (1993). Evidence for hotspot-related carbonatite metasomatism in the oceanic upper mantle. *Nature*, 365(6443), 221–227. doi:10.1038/365221a0
- Herzberg, C., Cabral, R. A., Jackson, M. G., Vidito, C., Day, J. M. D., & Hauri, E. H. (2014). Phantom Archean crust in Mangaia hotspot lavas and the meaning of heterogeneous mantle. *Earth and Planetary Science Letters*, 396, 97–106. doi:10.1016/j.epsl.2014.03.065
- Hirose, K., Fei, Y., Ma, Y., & Mao, H.-K. (1999). The fate of subducted basaltic crust in the Earth's lower mantle. *Nature*, 397(6714), 53–56. doi:10.1038/16225
- Hirschmann, M. M., Kogiso, T., Baker, M. B., & Stolper, E. M. (2003). Alkalic magmas generated by partial melting of garnet pyroxenite. *Geology*, 31(6), 481–484. doi:10.1130/0091-7613(2003)031<0481:AMGBPM>2.0.CO;2
- Hoang, T. H. A., Choi, S. H., Yu, Y., Pham, T. H., Nguyen, K. H., & Ryu, J.-S. (2018). Geochemical constraints on the spatial distribution of recycled oceanic crust in the mantle source of late Cenozoic basalts, Vietnam. *Lithos*, 296–299, 382–395. doi:10.1016/j.lithos.2017.11.020
- Hoernle, K., Tilton, G., Le Bas, M. J., Duggen, S., & Garbeschönberg, D. (2002). Geochemistry of oceanic carbonatites compared with continental carbonatites: mantle recycling of oceanic crustal carbonate. *Contributions to Mineralogy and Petrology*, 142(5), 520–542. doi:10.1007/s004100100308

- Hofmann, A. W. (1997). Mantle geochemistry: the message from oceanic volcanism. *Nature*, 385(6613), 219–229. doi:10.1038/385219a0
- Hofmann, A. W., & White, W. M. (1982). Mantle plumes from ancient oceanic crust. *Earth and Planetary Science Letters*, 57(2), 421–436. doi:10.1016/0012-821X(82)90161-3
- Holland, G., & Ballentine, C. J. (2006). Seawater subduction controls the heavy noble gas composition of the mantle. *Nature*, 441(7090), 186–191. doi:10.1038/nature04761
- Holland, H. D. (2006). The oxygenation of the atmosphere and oceans. *Philosophical Transactions of the Royal Society B*, 361(1470), 903–915. doi:10.1098/rstb.2006.1838
- Homrighausen, S., Hoernle, K., Hauff, F., Geldmacher, J., Wartho, J.-A., Van den Bogaard, P., & Garbe-Schönberg, D. (2018). Global distribution of the HIMU end member: Formation through Archean plume-lid tectonics. *Earth-Science Reviews*, 182, 85–101. doi:10.1016/j.earscirev.2018.04.009
- Honda, M., & Woodhead, J. D. (2005). A primordial solar-neon enriched component in the source of EM-I-type ocean island basalts from the Pitcairn Seamounts, Polynesia. *Earth and Planetary Science Letters*, 236(3–4), 597–612. doi:10.1016/j.epsl.2005.05.038
- Huang, J., Li, S.-G., Xiao, Y., Ke, S., Li, W.-Y., & Tian, Y. (2015). Origin of low $\delta^{26}\text{Mg}$ Cenozoic basalts from South China Block and their geodynamic implications. *Geochimica et Cosmochimica Acta*, 164, 298–317. doi:10.1016/j.gca.2015.04.054
- Huang, S., Farkaš, J., & Jacobsen, S. B. (2011). Stable calcium isotopic compositions of Hawaiian shield lavas: Evidence for recycling of ancient marine carbonates into the mantle. *Geochimica et Cosmochimica Acta*, 75(17), 4987–4997. doi:10.1016/j.gca.2011.06.010
- Humayun, M., Qin, L., & Norman, M. D. (2004). Geochemical Evidence for Excess Iron in the Mantle Beneath Hawaii. *Science*, 306(5693), 91–94. doi:10.1126/science.1101050
- Iwamori, H., & Albarède, F. (2008). Decoupled isotopic record of ridge and subduction zone processes in oceanic basalts by independent component analysis. *Geochemistry, Geophysics, Geosystems*, 9(4), Q04033. doi:10.1029/2007gc001753
- Jackson, M. G., Cabral, R. A., Rose-Koga, E. F., Koga, K. T., Price, A., Hauri, E. H., & Michael, P. (2015a). Ultra-depleted melts in olivine-hosted melt inclusions from the Ontong Java Plateau. *Chemical Geology*, 414, 124–137. doi:10.1016/j.chemgeo.2015.08.014
- Jackson, M. G., & Carlson, R. W. (2012). Homogeneous superchondritic $^{142}\text{Nd}/^{144}\text{Nd}$ in the mid-ocean ridge basalt and ocean island basalt mantle. *Geochemistry Geophysics Geosystems*, 13(6), Q06011. doi:10.1029/2012GC004114
- Jackson, M. G., & Dasgupta, R. (2008). Compositions of HIMU, EM1, and EM2 from global trends between radiogenic isotopes and major elements in ocean island basalts. *Earth and Planetary Science Letters*, 276(1–2), 175–186. doi:10.1016/j.epsl.2008.09.023
- Jackson, M. G., Hart, S. R., Konter, J. G., Kurz, M. D., Blusztajn, J., & Farley, K. A. (2014). Helium and lead isotopes reveal the geochemical geometry of the Samoan plume. *Nature*, 514(7522), 355–358. doi:10.1038/nature13794
- Jackson, M. G., Hart, S. R., Koppers, A. A. P., Staudigel, H., Konter, J., Blusztajn, J., et al. (2007a). The return of subducted continental crust in Samoan lavas. *Nature*, 448, 684–687. doi:10.1038/nature06048
- Jackson, M. G., Hart, S. R., Saal, A. E., Shimizu, N., Kurz, M. D., Blusztajn, J. S., & Skovgaard, A. C. (2008). Globally elevated titanium, tantalum, and niobium (TITAN) in ocean island basalts with high $^3\text{He}/^4\text{He}$. *Geochemistry, Geophysics, Geosystems*, 9(4). doi:10.1029/2007gc001876
- Jackson, M. G., Koga, K. T., Price, A., Konter, J. G., Koppers, A. A. P., Finlayson, V. A., et al. (2015b). Deeply dredged submarine HIMU glasses from the Tuvalu Islands, Polynesia: Implications for volatile budgets of recycled oceanic crust. *Geochemistry, Geophysics, Geosystems*, 16(9), 3210–3234. doi:10.1002/2015gc005966
- Jackson, M. G., Konter, J. G., & Becker, T. W. (2017). Primordial helium entrained by the hottest mantle plumes. *Nature*, 542, 340. doi:10.1038/nature21023
- Jackson, M. G., Kurz, M. D., Hart, S. R., & Workman, R. K. (2007b). New Samoan lavas from Ofu Island reveal a hemispherically heterogeneous high $^3\text{He}/^4\text{He}$ mantle. *Earth and Planetary Science Letters*, 264(3–4), 360–374. doi:10.1016/j.epsl.2007.09.023
- Jackson, M. G., & Shirey, S. B. (2011). Re–Os isotope systematics in Samoan shield lavas and the use of Os-isotopes in olivine phenocrysts to determine primary magmatic compositions. *Earth and Planetary Science Letters*, 312(1), 91–101. doi:10.1016/j.epsl.2011.09.046
- Javoy, M., & Pineau, F. (1991). The volatiles record of a “popping” rock from the Mid-Atlantic Ridge at 14°N: chemical and isotopic composition of gas trapped in the vesicles. *Earth and Planetary Science Letters*, 107(3), 598–611. doi:10.1016/0012-821X(91)90104-P
- John, T., Layne, G. D., Haase, K. M., & Barnes, J. D. (2010). Chlorine isotope evidence for crustal recycling into the Earth’s mantle. *Earth and Planetary Science Letters*, 298(1–2), 175–182. doi:10.1016/j.epsl.2010.07.039
- König, S., Wille, M., Voegelin, A., & Schoenberg, R. (2016). Molybdenum isotope systematics in subduction zones. *Earth and Planetary Science Letters*, 447, 95–102. doi:10.1016/j.epsl.2016.04.033
- Kakizawa, S., Inoue, T., Suenami, H., & Kikegawa, T. (2015). Decarbonation and melting in $\text{MgCO}_3\text{–SiO}_2$ system at high temperature and high pressure. *Journal of Mineralogical and Petrological Sciences*, 110(4), 179–188. doi:10.2465/jmps.150124
- Kang, J.-T., Ionov, D. A., Liu, F., Zhang, C.-L., Golovin, A. V., Qin, L.-P., et al. (2017). Calcium isotopic fractionation in mantle peridotites by melting and metasomatism and Ca isotope composition of the Bulk Silicate Earth. *Earth and Planetary Science Letters*, 474, 128–137. doi:10.1016/j.epsl.2017.05.035
- Kawabata, H., Hanyu, T., Chang, Q., Kimura, J.-I., Nichols, A. R. L., & Tatsumi, Y. (2011). The petrology and geochemistry of St. Helena alkali basalts: evaluation of the oceanic crust-recycling model for HIMU OIB. *Journal of Petrology*, 52(4), 791–838. doi:10.1093/petrology/egr003

- Kendrick, M. A., Jackson, M. G., Hauri, E. H., & Phillips, D. (2015). The halogen (F, Cl, Br, I) and H₂O systematics of Samoan lavas: Assimilated-seawater, EM2 and high-³He/⁴He components. *Earth and Planetary Science Letters*, 410, 197–209. doi:10.1016/j.epsl.2014.11.026
- Kendrick, M. A., Jackson, M. G., Kent, A. J. R., Hauri, E. H., Wallace, P. J., & Woodhead, J. (2014). Contrasting behaviours of CO₂, S, H₂O and halogens (F, Cl, Br, and I) in enriched-mantle melts from Pitcairn and Society seamounts. *Chemical Geology*, 370, 69–81. doi:10.1016/j.chemgeo.2014.01.019
- Kendrick, M. A., Scambelluri, M., Honda, M., & Phillips, D. (2011). High abundances of noble gas and chlorine delivered to the mantle by serpentinite subduction. *Nature Geoscience*, 4(11), 807–812. doi:10.1038/ngeo1270
- Kerrick, D. M., & Connolly, J. A. D. (1998). Subduction of ophicarbonates and recycling of CO₂ and H₂O. *Geology*, 26(4), 375–378. doi:10.1130/0091-7613(1998)026<0375:sooaro>2.3.co;2
- Kerrick, D. M., & Connolly, J. A. D. (2001a). Metamorphic devolatilization of subducted marine sediments and the transport of volatiles into the Earth's mantle. *Nature*, 411(6835), 293–296
- Kerrick, D. M., & Connolly, J. A. D. (2001b). Metamorphic devolatilization of subducted oceanic metabasalts: implications for seismicity, arc magmatism and volatile recycling. *Earth and Planetary Science Letters*, 189(1), 19–29. doi:10.1016/S0012-821X(01)00347-8
- Kimura, J.-I., Gill, J. B., van Keken, P. E., Kawabata, H., & Skora, S. (2017). Origin of geochemical mantle components: Role of spreading ridges and thermal evolution of mantle. *Geochemistry, Geophysics, Geosystems*, 18(2), 697–734. doi:10.1002/2016GC006696
- Kogiso, T., & Hirschmann, M. M. (2006). Partial melting experiments of bimineralec eclogite and the role of recycled mafic oceanic crust in the genesis of ocean island basalts. *Earth and Planetary Science Letters*, 249(3–4), 188–199. doi:10.1016/j.epsl.2006.07.016
- Kogiso, T., Hirschmann, M. M., & Frost, D. J. (2003). High-pressure partial melting of garnet pyroxenite: possible mafic lithologies in the source of ocean island basalts. *Earth and Planetary Science Letters*, 216(4), 603–617. doi:10.1016/S0012-821X(03)00538-7
- Kogiso, T., Tatsumi, Y., Shimoda, G., & Barszczus, H. G. (1997). High μ (HIMU) ocean island basalts in southern Polynesia: New evidence for whole mantle scale recycling of subducted oceanic crust. *Journal of Geophysical Research*, 102(B4), 8085–8103. doi:10.1029/96JB03892
- Konter, J. G., Hanan, B. B., Blichert-Toft, J., Koppers, A. A. P., Plank, T., & Staudigel, H. (2008). One hundred million years of mantle geochemical history suggest the retiring of mantle plumes is premature. *Earth and Planetary Science Letters*, 275(3–4), 285–295. doi:10.1016/j.epsl.2008.08.023
- Konter, J. G., Pietruszka, A. J., Hanan, B. B., Finlayson, V. A., Craddock, P. R., Jackson, M. G., & Dauphas, N. (2016). Unusual $\delta^{56}\text{Fe}$ values in Samoan rejuvenated lavas generated in the mantle. *Earth and Planetary Science Letters*, 450, 221–232. doi:10.1016/j.epsl.2016.06.029
- Koornneef, J. M., Nikogosian, I., van Bergen, M. J., Smeets, R., Bouman, C., & Davies, G. R. (2015). TIMS analysis of Sr and Nd isotopes in melt inclusions from Italian potassium-rich lavas using prototype 10¹³ Ω amplifiers. *Chemical Geology*, 397, 14–23. doi:10.1016/j.chemgeo.2015.01.005
- Korenaga, J. (2017). On the extent of mantle hydration caused by plate bending. *Earth and Planetary Science Letters*, 457, 1–9. doi:10.1016/j.epsl.2016.10.011
- Krienitz, M.-S., Garbe-Schonberg, C. D., Romer, R. L., Meixner, A., Haase, K. M., & Stronck, N. A. (2012). Lithium isotope variations in ocean island basalts—Implications for the development of mantle heterogeneity. *Journal of Petrology*, 53(11), 2333–2347. doi:10.1093/petrology/egs052
- Kump, L. R., & Barley, M. E. (2007). Increased subaerial volcanism and the rise of atmospheric oxygen 2.5 billion years ago. *Nature*, 448, 1033. doi:10.1038/nature06058
- Kurz, M. D., Curtice, J., Fornari, D., Geist, D., & Moreira, M. (2009). Primitive neon from the center of the Galápagos hotspot. *Earth and Planetary Science Letters*, 286(1–2), 23–34. doi:10.1016/j.epsl.2009.06.008
- Kurz, M. D., Jenkins, W. J., Hart, S. R., & Clague, D. (1983). Helium isotopic variations in volcanic rocks from Loihi Seamount and the Island of Hawaii. *Earth and Planetary Science Letters*, 66, 388–406. doi:10.1016/0012-821X(83)90154-1
- Labrosse, S., Hernlund, J. W., & Coltice, N. (2007). A crystallizing dense magma ocean at the base of the Earth's mantle. *Nature*, 450, 866. doi:10.1038/nature06355
- Lassiter, J. C., Blichert-Toft, J., Hauri, E. H., & Barszczus, H. G. (2003). Isotope and trace element variations in lavas from Raitavae and Rapa, Cook-Austral islands: constraints on the nature of HIMU- and EM-mantle and the origin of mid-plate volcanism in French Polynesia. *Chemical Geology*, 202(1–2), 115–138. doi:10.1016/j.chemgeo.2003.08.002
- Laubier, M., Gale, A., & Langmuir, C. H. (2012). Melting and Crustal Processes at the FAMOUS Segment (Mid-Atlantic Ridge): New Insights from Olivine-hosted Melt Inclusions from Multiple Samples. *Journal of Petrology*, 53(4), 665–698. doi:10.1093/petrology/egr075
- Li, C., & Ripley, E. M. (2010). The relative effects of composition and temperature on olivine-liquid Ni partitioning: Statistical deconvolution and implications for petrologic modeling. *Chemical Geology*, 275(1), 99–104. doi:10.1016/j.chemgeo.2010.05.001
- Li, S.-G., Yang, W., Ke, S., Meng, X., Tian, H., Xu, L., et al. (2017). Deep carbon cycles constrained by a large-scale mantle Mg isotope anomaly in eastern China. *National Science Review*, 4(1), 111–120. doi:10.1093/nsr/nww070
- Liu, C.-Z., Snow, J. E., Hellebrand, E., Brüggemann, G., von der Handt, A., Büchl, A., & Hofmann, A. W. (2008). Ancient, highly heterogeneous mantle beneath Gakkel ridge, Arctic Ocean. *Nature*, 452, 311. doi:10.1038/nature06688
- Liu, F., Li, X., Wang, G., Liu, Y., Zhu, H., Kang, J., et al. (2017). Marine Carbonate Component in the Mantle Beneath the Southeastern Tibetan Plateau: Evidence From Magnesium and Calcium Isotopes. *Journal of Geophysical Research: Solid Earth*, 122(12), 9729–9744. doi:10.1002/2017JB014206
- Liu, S.-A., Huang, J., Liu, J., Wörner, G., Yang, W., Tang, Y.-J., et al. (2015). Copper isotopic composition of the silicate

- Earth. *Earth and Planetary Science Letters*, 427, 95–103. doi:10.1016/j.epsl.2015.06.061
- Liu S.-A., Li S.-G. (2019). Tracing the Deep Carbon Cycle Using Metal Stable Isotopes: Opportunities and Challenges. *Engineering*, 5, 448–457. doi: 10.1016/j.eng.2019.03.007
- Liu, S.-A., Wang, Z.-Z., Li, S.-G., Huang, J., & Yang, W. (2016). Zinc isotope evidence for a large-scale carbonated mantle beneath eastern China. *Earth and Planetary Science Letters*, 444, 169–178. doi:10.1016/j.epsl.2016.03.051
- Lundstrom, C. C., Sampson, D. E., Perfit, M. R., Gill, J., & Williams, Q. (1999). Insights into mid-ocean ridge basalt petrogenesis: U-series disequilibria from the Siqueiros Transform, Lamont Seamounts, and East Pacific Rise. *Journal of Geophysical Research: Solid Earth*, 104(B6), 13035–13048. doi:10.1029/1999JB900081
- Lyons, T. W., Reinhard, C. T., & Planavsky, N. J. (2014). The rise of oxygen in Earth's early ocean and atmosphere. *Nature*, 506, 307. doi:10.1038/nature13068
- Machida, S., Hirano, N., & Kimura, J.-I. (2009). Evidence for recycled plate material in Pacific upper mantle unrelated to plumes. *Geochimica et Cosmochimica Acta*, 73(10), 3028–3037. doi:10.1016/j.gca.2009.01.026
- Manning, C. E. (2004). The chemistry of subduction-zone fluids. *Earth and Planetary Science Letters*, 223(1), 1–16. doi:10.1016/j.epsl.2004.04.030
- Martin, A. M., & Hammouda, T. (2011). Role of iron and reducing conditions on the stability of dolomite + coesite between 4.25 and 6 GPa – a potential mechanism for diamond formation during subduction. *European Journal of Mineralogy*, 23(1), 5–16. doi:10.1127/0935-1221/2010/0022-2067
- Matzen, A. K., Wood, B. J., Baker, M. B., & Stolper, E. M. (2017). The roles of pyroxenite and peridotite in the mantle sources of oceanic basalts. *Nature Geoscience*, 10(7), 530–535. doi:10.1038/ngeo2968
- Maury, R. C., Guille, G., Guillou, H., Chauvel, C., Rossi, P., Pallares, C., & Legendre, C. (2013). Temporal evolution of a Polynesian hotspot: New evidence from Raivavae (Austral islands, South Pacific ocean). *Bulletin de la Societe Geologique de France*, 184(6), 557–567. doi:10.2113/gssgfbull.184.6.557
- McKenzie, D., & O'Nions, R. K. (1983). Mantle reservoirs and ocean island basalts. *Nature*, 301, 229–231. doi:10.1038/301229a0
- Meibom, A., Anderson, D. L., Sleep, N. H., Frei, R., Chamberlain, C. P., Hren, M. T., & Wooden, J. L. (2003). Are high $^3\text{He}/^4\text{He}$ ratios in oceanic basalts an indicator of deep-mantle plume components? *Earth and Planetary Science Letters*, 208(3–4), 197–204. doi:10.1016/S0012-821X(03)00038-4
- Michael, P. J., & Cornell, W. C. (1998). Influence of spreading rate and magma supply on crystallization and assimilation beneath mid-ocean ridges: Evidence from chlorine and major element chemistry of mid-ocean ridge basalts. *Journal of Geophysical Research: Solid Earth*, 103(B8), 18325–18356. doi:10.1029/98JB00791
- Michael, P. J., & Graham, D. W. (2015). The behavior and concentration of CO_2 in the suboceanic mantle: Inferences from undegassed ocean ridge and ocean island basalts. *Lithos*, 236–237, 338–351. doi:10.1016/j.lithos.2015.08.020
- Miyazaki, T., Hanyu, T., Kimura, J.-I., Senda, R., Vaglarov, B. S., Chang, Q., et al. (2018). Clinopyroxene and bulk rock Sr–Nd–Hf–Pb isotope compositions of Raivavae ocean island basalts: Does clinopyroxene record early stage magma chamber processes? *Chemical Geology*, 482, 18–31. doi:10.1016/j.chemgeo.2017.12.015
- Montelli, R., Nolet, G., Dahlen, F. A., & Masters, G. (2006). A catalogue of deep mantle plumes: New results from finite-frequency tomography. *Geochemistry Geophysics Geosystems*, 7(11), Q11007. doi: 10.1029/2006GC001248
- Mougel, B., Agranier, A., Hemond, C., & Gente, P. (2014). A highly unradiogenic lead isotopic signature revealed by volcanic rocks from the East Pacific Rise. *Nature Communications*, 5. doi:10.1038/ncomms5474
- Mundl, A., Touboul, M., Jackson, M. G., Day, J. M. D., Kurz, M. D., Lekic, V., et al. (2017). Tungsten-182 heterogeneity in modern ocean island basalts. *Science*, 356(6333), 66–69. doi:10.1126/science.aal4179
- Murphy, D. T., Collerson, K. D., & Kamber, B. S. (2002). Lamproites from Gaussberg, Antarctica: Possible Transition Zone Melts of Archaean Subducted Sediments. *Journal of Petrology*, 43(6), 981–1001. doi:10.1093/petrology/43.6.981
- Nakamura, K., & Kato, Y. (2007). A new geochemical approach for constraining a marine redox condition of Early Archean. *Earth and Planetary Science Letters*, 261(1–2), 296–302. doi:10.1016/j.epsl.2007.07.020
- Nakamura, Y., & Tatsumoto, M. (1988). Pb, Nd, and Sr isotopic evidence for a multicomponent source for rocks of Cook-Austral Islands and heterogeneities of mantle plumes. *Geochimica et Cosmochimica Acta*, 52(12), 2909–2924. doi:10.1016/0016-7037(88)90157-3
- Nebel, O., Arculus, R. J., van Westrenen, W., Woodhead, J. D., Jenner, F. E., Nebel-Jacobsen, Y. J., et al. (2013). Coupled Hf–Nd–Pb isotope co-variations of HIMU oceanic island basalts from Mangaia, Cook-Austral islands, suggest an Archean source component in the mantle transition zone. *Geochimica et Cosmochimica Acta*, 112(0), 87–101. http://dx.doi.org/10.1016/j.gca.2013.03.005
- Nebel O., Sossi P. A., Bénard A., Arculus R. J., Yaxley G. M., Woodhead J. D., Rhodri Davies D., Ruttur S. (2019). Reconciling petrological and isotopic mixing mechanisms in the Pitcairn mantle plume using stable Fe isotopes. *Earth and Planetary Science Letters*, 521, 60–67. doi: 10.1016/j.epsl.2019.05.037
- Nielsen, S. G. (2010). Potassium and uranium in the upper mantle controlled by Archean oceanic crust recycling. *Geology*, 38(8), 683–686. doi:10.1130/g30852.1
- Nielsen, S. G., Horner, T. J., Pryer, H. V., Blusztajn, J., Shu, Y., Kurz, M. D., & Le Roux, V. (2018). Barium isotope evidence for pervasive sediment recycling in the upper mantle. *Science Advances*, 4(7). doi:10.1126/sciadv.aas8675
- Nielsen, S. G., Prytulak, J., Blusztajn, J., Shu, Y., Auro, M., Regelous, M., & Walker, J. (2017). Thallium isotopes as tracers of recycled materials in subduction zones: Review and new data for lavas from Tonga-Kermadec and Central America. *Journal of Volcanology and Geothermal Research*, 339, 23–40. doi:10.1016/j.jvolgeores.2017.04.024

- Nielsen, S. G., Rehkämper, M., Norman, M. D., Halliday, A. N., & Harrison, D. (2006). Thallium isotopic evidence for ferromanganese sediments in the mantle source of Hawaiian basalts. *Nature*, 439, 314. doi:10.1038/nature04450
- Nielsen, S. G., Yogodzinski, G., Prytulak, J., Plank, T., Kay, S. M., Kay, R. W., et al. (2016). Tracking along-arc sediment inputs to the Aleutian arc using thallium isotopes. *Geochimica et Cosmochimica Acta*, 181, 217–237. doi:10.1016/j.gca.2016.03.010
- Nishio, Y., Nakai, S., Kogiso, T., & Barszczus, H. G. (2005). Lithium, strontium, and neodymium isotopic compositions of oceanic island basalts in the Polynesian region: constraints on a Polynesian HIMU origin. *Geochemical Journal*, 39, 91–103. doi:10.2343/geochemj.39.91
- Niu, Y., & O'Hara, M. J. (2003). Origin of ocean island basalts: A new perspective from petrology, geochemistry, and mineral physics considerations. *Journal of Geophysical Research*, 108 (B4), 2209. doi:10.1029/2002JB002048
- Ohtani, E. (2015). Hydrous minerals and the storage of water in the deep mantle. *Chemical Geology*, 418, 6–15. doi:10.1016/j.chemgeo.2015.05.005
- Ono, S., Ito, E., & Katsura, T. (2001). Mineralogy of subducted basaltic crust (MORB) from 25 to 37 GPa, and chemical heterogeneity of the lower mantle. *Earth and Planetary Science Letters*, 190(1–2), 57–63. doi:10.1016/S0012-821X(01)00375-2
- Pagé, L., Hattori, K., de Hoog, J. C. M., & Okay, A. I. (2016). Halogen (F, Cl, Br, I) behaviour in subducting slabs: A study of lawsonite blueschists in western Turkey. *Earth and Planetary Science Letters*, 442, 133–142. doi:10.1016/j.epsl.2016.02.054
- Palacz, Z. A., & Saunders, A. D. (1986). Coupled trace-element and isotope enrichment in the Cook-Austral-Samoa Islands, Southwest Pacific. *Earth and Planetary Science Letters*, 79 (3–4), 270–280. doi:10.1016/0012-821x(86)90185-8
- Parai, R., & Mukhopadhyay, S. (2015). The evolution of MORB and plume mantle volatile budgets: Constraints from fission Xe isotopes in Southwest Indian Ridge basalts. *Geochemistry, Geophysics, Geosystems*, 16(3), 719–735. doi:10.1002/2014GC005566
- Parai, R., Mukhopadhyay, S., & Lassiter, J. C. (2009). New constraints on the HIMU mantle from neon and helium isotopic compositions of basalts from the Cook-Austral Islands. *Earth and Planetary Science Letters*, 277(1–2), 253–261. doi:10.1016/j.epsl.2008.10.014
- Parendo, C. A., Jacobsen, S. B., & Wang, K. (2017). K isotopes as a tracer of seafloor hydrothermal alteration. *Proceedings of the National Academy of Sciences*. doi:10.1073/pnas.1609228114
- Paulick, H., Münker, C., & Schuth, S. (2010). The influence of small-scale mantle heterogeneities on Mid-Ocean Ridge volcanism: Evidence from the southern Mid-Atlantic Ridge (7° 30' S to 11° 30' S) and Ascension Island. *Earth and Planetary Science Letters*, 296(3), 299–310. https://doi.org/10.1016/j.epsl.2010.05.009
- Peacock, S. A. (1990). Fluid Processes in Subduction Zones. *Science*, 248(4953), 329–337. doi:10.1126/science.248.4953.329
- Pearson, D. G., Irvine, G. J., Ionov, D. A., Boyd, F. R., & Dreibus, G. E. (2004). Re–Os isotope systematics and platinum group element fractionation during mantle melt extraction: a study of massif and xenolith peridotite suites. *Chemical Geology*, 208(1), 29–59. doi:10.1016/j.chemgeo.2004.04.005
- Pearson, D. G., & Wittig, N. (2014). The Formation and Evolution of Cratonic Mantle Lithosphere – Evidence from Mantle Xenoliths. In H. D. Holland & K. K. Turekian (Eds.), *Treatise on Geochemistry (Second Edition)* (pp. 255–292). Oxford: Elsevier. doi:10.1016/B978-0-08-095975-7.00205-9
- Perfit, M. R., Fornari, D. J., Smith, M. C., Bender, J. F., Langmuir, C. H., & Haymon, R. M. (1994). Small-scale spatial and temporal variations in mid-ocean ridge crest magmatic processes. *Geology*, 22(4), 375–379. doi:10.1130/0091-7613(1994)022<0375:SSSATV>2.3.CO;2
- Pertermann, M., Hirschmann, M. M., Hametner, K., Günther, D., & Schmidt, M. W. (2004). Experimental determination of trace element partitioning between garnet and silica-rich liquid during anhydrous partial melting of MORB-like eclogite. *Geochemistry Geophysics Geosystems*, 5(5), Q05A01. doi:10.1029/2003GC000638
- Pilet, S., Baker, M. B., & Stolper, E. M. (2008). Metasomatized lithosphere and the origin of alkaline lavas. *Science*, 320 (5878), 916–919. doi:10.1126/science.1156563
- Pilet, S., Hernandez, J., Sylvester, P., & Poujol, M. (2005). The metasomatic alternative for ocean island basalt chemical heterogeneity. *Earth and Planetary Science Letters*, 236(1–2), 148–166. doi:10.1016/j.epsl.2005.05.004
- Poli, S. (2015). Carbon mobilized at shallow depths in subduction zones by carbonatitic liquids. *Nature Geoscience*, 8(8), 633–636. doi:10.1038/ngeo2464
- Poli, S., Franzolin, E., Fumagalli, P., & Crottini, A. (2009). The transport of carbon and hydrogen in subducted oceanic crust: An experimental study to 5 GPa. *Earth and Planetary Science Letters*, 278(3), 350–360. doi:10.1016/j.epsl.2008.12.022
- Pringle, E. A., Moynier, F., Savage, P. S., Jackson, M. G., Moreira, M., & Day, J. M. D. (2016). Silicon isotopes reveal recycled altered oceanic crust in the mantle sources of Ocean Island Basalts. *Geochimica et Cosmochimica Acta*, 189, 282–295. doi:10.1016/j.gca.2016.06.008
- Prytulak, J., & Elliott, T. (2007). TiO₂ enrichment in ocean island basalts. *Earth and Planetary Science Letters*, 263(3), 388–403. doi:10.1016/j.epsl.2007.09.015
- Putirka, K., Ryerson, F. J., Perfit, M., & Ridley, W. I. (2011). Mineralogy and Composition of the Oceanic Mantle. *Journal of Petrology*, 52(2), 279–313. doi:10.1093/petrology/egq080
- Qin, L., & Wang, X. (2017). Chromium Isotope Geochemistry. *Reviews in Mineralogy and Geochemistry*, 82(1), 379–414. doi:10.2138/rmg.2017.82.10
- Rampone, E., & Hofmann, A. W. (2012). A global overview of isotopic heterogeneities in the oceanic mantle. *Lithos*, 148, 247–261. doi:10.1016/j.lithos.2012.06.018
- Ranero, C. R., Phipps Morgan, J., McIntosh, K., & Reichert, C. (2003). Bending-related faulting and mantle serpentinization at the Middle America trench. *Nature*, 425(6956), 367–373. doi:10.1038/nature01961
- Reinhard, A. A., Jackson, M. G., Koornneef, J. M., Rose-Koga, E. F., Blusztajn, J., Konter, J. G., et al. (2018). Sr and Nd

- isotopic compositions of individual olivine-hosted melt inclusions from Hawai'i and Samoa: Implications for the origin of isotopic heterogeneity in melt inclusions from OIB lavas. *Chemical Geology*, 495, 36–49. doi:10.1016/j.chemgeo.2018.07.034
- Reisberg, L., Zindler, A., Marcantonio, F., White, W., Wyman, D., & Weaver, B. (1993). Os isotope systematics in ocean island basalts. *Earth and Planetary Science Letters*, 120 (3–4), 149–167. doi:10.1016/0012-821X(93)90236-3
- Reisberg, L. C., Allègre, C. J., & Luck, J.-M. (1991). The Re-Os systematics of the Ronda Ultramafic Complex of southern Spain. *Earth and Planetary Science Letters*, 105(1), 196–213. doi:10.1016/0012-821X(91)90131-Z
- Richardson, S. H., Erlank, A. J., Duncan, A. R., & Reid, D. L. (1982). Correlated Nd, Sr and Pb isotope variation in Walvis Ridge basalts and implications for the evolution of their mantle source. *Earth and Planetary Science Letters*, 59(2), 327–342. doi:10.1016/0012-821X(82)90135-2
- Rubin, K. H., & Sinton, J. M. (2007). Inferences on mid-ocean ridge thermal and magmatic structure from MORB compositions. *Earth and Planetary Science Letters*, 260(1), 257–276. doi:10.1016/j.epsl.2007.05.035
- Saal, A. E., Hart, S. R., Shimizu, N., Hauri, E. H., & Layne, G. D. (1998). Pb Isotopic variability in melt Inclusions from oceanic island basalts, *Polynesia*. *Science*, 282(5393), 1481–1484. doi:10.1126/science.282.5393.1481
- Saal, A. E., Hauri, E. H., Langmuir, C. H., & Perfit, M. R. (2002). Vapour undersaturation in primitive mid-ocean-ridge basalt and the volatile content of Earth's upper mantle. *Nature*, 419(6906), 451–455. doi:10.1038/nature01073
- Sakuyama, T., Tian, W., Kimura, J.-I., Fukao, Y., Hirahara, Y., Takahashi, T., et al. (2013). Melting of dehydrated oceanic crust from the stagnant slab and of the hydrated mantle transition zone: Constraints from Cenozoic alkaline basalts in eastern China. *Chemical Geology*, 359, 32–48. doi:10.1016/j.chemgeo.2013.09.012
- Salters, V. J. M., Mallick, S., Hart, S. R., Langmuir, C. E., & Stracke, A. (2011). Domains of depleted mantle: New evidence from hafnium and neodymium isotopes. *Geochemistry Geophysics Geosystems*, 12(8), Q08001. doi:10.1029/2011GC003617
- Salters, V. J. M., & Stracke, A. (2004). Composition of the depleted mantle. *Geochemistry Geophysics Geosystems*, 5(5), Q05004. doi:10.1029/2003GC000597
- Salters, V. J. M., & White, W. M. (1998). Hf isotope constraints on mantle evolution. *Chemical Geology*, 145(3–4), 447–460. doi:10.1016/S0009-2541(97)00154-X
- Schiano, P., Burton, K. W., Dupré, B., Birck, J.-L., Guille, G., & Allègre, C. J. (2001). Correlated Os–Pb–Nd–Sr isotopes in the Austral–Cook chain basalts: the nature of mantle components in plume sources. *Earth and Planetary Science Letters*, 186 (3–4), 527–537. doi:10.1016/S0012-821X(01)00265-5
- Schilling, J. G., Unni, C. K., & Bender, M. L. (1978). Origin of chlorine and bromine in the oceans. *Nature*, 273, 631. doi:10.1038/273631a0
- Schmidt, M. W., & Poli, S. (2014). Devolatilization During Subduction. In K. K. Turekian (Ed.), *Treatise on Geochemistry (Second Edition)* (pp. 669–701). Oxford: Elsevier. doi:10.1016/B978-0-08-095975-7.00321-1
- Schmidt, M. W., & Weidendorfer, D. (2018). Carbonatites in oceanic hotspots. *Geology*, 46(5), 435–438. doi:10.1130/G39621.1
- Shaw, A. M., Hauri, E. H., Fischer, T. P., Hilton, D. R., & Kelley, K. A. (2008). Hydrogen isotopes in Mariana arc melt inclusions: Implications for subduction dehydration and the deep-Earth water cycle. *Earth and Planetary Science Letters*, 275(1–2), 138–145. doi:10.1016/j.epsl.2008.08.015
- Shimizu, K., Saal, A. E., Myers, C. E., Nagle, A. N., Hauri, E. H., Forsyth, D. W., et al. (2016). Two-component mantle melting-mixing model for the generation of mid-ocean ridge basalts: Implications for the volatile content of the Pacific upper mantle. *Geochimica et Cosmochimica Acta*, 176, 44–80. doi:10.1016/j.gca.2015.10.033
- Shimizu, K., Shimizu, N., Komiya, T., Suzuki, K., Maruyama, S., & Tatsumi, Y. (2009). CO₂-rich komatiitic melt inclusions in Cr-spinels within beach sand from Gorgona Island, Colombia. *Earth and Planetary Science Letters*, 288(1–2), 33–43. doi:10.1016/j.epsl.2009.09.005
- Shu, Y., Nielsen, S. G., Zeng, Z., Shinjo, R., Blusztajn, J., Wang, X., & Chen, S. (2017). Tracing subducted sediment inputs to the Ryukyu arc-Okinawa Trough system: Evidence from thallium isotopes. *Geochimica et Cosmochimica Acta*, 217, 462–491. doi:10.1016/j.gca.2017.08.035
- Snow, J. E., Hart, S. R., & Dick, H. J. B. (1994). Nd and Sr isotope evidence linking mid-ocean-ridge basalts and abyssal peridotites. *Nature*, 371, 57. doi:10.1038/371057a0
- Sobolev, A. V., Hofmann, A. W., Kuzmin, D., Yaxley, G. M., Arndt, N. T., Chung, S.-L., et al. (2007). The amount of recycled crust in sources of mantle-derived melts. *Science*, 316(5823), 412–417. doi:10.1126/science.1138113
- Sobolev, A. V., Hofmann, A. W., Sobolev, S. V., & Nikogosian, I. K. (2005). An olivine-free mantle source of Hawaiian shield basalts. *Nature*, 434(7033), 590–597. doi:10.1038/nature03411
- Spandler, C., Yaxley, G., Green, D. H., & Rosenthal, A. (2008). Phase Relations and Melting of Anhydrous K-bearing Eclogite from 1200 to 1600°C and 3 to 5 GPa. *Journal of Petrology*, 49(4), 771–795. doi:10.1093/ptrology/egm039
- Staudacher, T., & Allègre, C. J. (1988). Recycling of oceanic crust and sediments: the noble gas subduction barrier. *Earth and Planetary Science Letters*, 89(2), 173–183. doi:10.1016/0012-821X(88)90170-7
- Staudigel, H., Plank, T., White, W. M., & Schmincke, H. U. (1996). Geochemical fluxes during seafloor alteration of the basaltic upper crust: DSDP sites 417 and 418. In G. E. Bebout, D. W. Scholl, S. H. Kirby, & J. P. Platt (Eds.), *Subduction: Top to Bottom, Geophysical Monograph Series* (Vol. 96, pp. 19–38). Washington, D. C.: AGU. doi:10.1029/GM096p0019
- Stracke, A. (2012). Earth's heterogeneous mantle: A product of convection-driven interaction between crust and mantle. *Chemical Geology*, 330–331, 274–299. doi:10.1016/j.chemgeo.2012.08.007
- Stracke, A., & Bourdon, B. (2009). The importance of melt extraction for tracing mantle heterogeneity. *Geochimica et Cosmochimica Acta*, 73(1), 218–238. doi:10.1016/j.gca.2008.10.015

- Stracke, A., Hofmann, A. W., & Hart, S. R. (2005). FOZO, HIMU, and the rest of the mantle zoo. *Geochemistry Geophysics Geosystems*, 6(5), Q05007. doi:10.1029/2004GC000824
- Stracke, A., Snow, J. E., Hellebrand, E., von der Handt, A., Bourdon, B., Birbaum, K., & Günther, D. (2011). Abyssal peridotite Hf isotopes identify extreme mantle depletion. *Earth and Planetary Science Letters*, 308(3), 359–368. doi.org/10.1016/j.epsl.2011.06.012
- Stroncik, N. A., & Haase, K. M. (2004). Chlorine in oceanic intraplate basalts: Constraints on mantle sources and recycling processes. *Geology*, 32(11), 945–948. doi:10.1130/g21027.1
- Stuart, F. M., Lass-Evans, S., Godfrey Fitton, J., & Ellam, R. M. (2003). High $^3\text{He}/^4\text{He}$ ratios in picritic basalts from Baffin Island and the role of a mixed reservoir in mantle plumes. *Nature*, 424, 57. doi:10.1038/nature01711
- Svensen, H., Planke, S., Chevallier, L., Malthe-Sørensen, A., Corfu, F., & Jamtveit, B. (2007). Hydrothermal venting of greenhouse gases triggering Early Jurassic global warming. *Earth and Planetary Science Letters*, 256(3), 554–566. doi:10.1016/j.epsl.2007.02.013
- Tackley, P. J. (2000). Mantle convection and plate tectonics: Toward an integrated physical and chemical theory. *Science*, 288(5473), 2002–2007. doi:10.1126/science.288.5473.2002
- Tatsumi, Y. (2000). Continental crust formation by crustal delamination in subduction zones and complementary accumulation of the enriched mantle I component in the mantle. *Geochemistry, Geophysics, Geosystems*, 1(12). doi:10.1029/2000GC000094
- Teng, F.-Z. (2017). Magnesium Isotope Geochemistry. *Reviews in Mineralogy and Geochemistry*, 82(1), 219–287. doi:10.2138/rmg.2017.82.7
- Teng, F.-Z., Li, W.-Y., Ke, S., Marty, B., Dauphas, N., Huang, S., et al. (2010). Magnesium isotopic composition of the Earth and chondrites. *Geochimica et Cosmochimica Acta*, 74(14), 4150–4166. https://doi.org/10.1016/j.gca.2010.04.019
- Thirlwall, M. F. (1997). Pb isotopic and elemental evidence for OIB derivation from young HIMU mantle. *Chemical Geology*, 139, 51–74. doi:10.1016/S0009-2541(97)00033-8
- Thomson, A. R., Walter, M. J., Kohn, S. C., & Brooker, R. A. (2016). Slab melting as a barrier to deep carbon subduction. *Nature*, 529(7584), 76–79. doi:10.1038/nature16174
- Touboul, M., Puchtel, I. S., & Walker, R. J. (2012). ^{182}W Evidence for Long-Term Preservation of Early Mantle Differentiation Products. *Science*, 335(6072), 1065–1069. doi:10.1126/science.1216351
- Trieloff, M., Kunz, J., Clague, D. A., Harrison, D., & Allègre, C. J. (2000). The nature of pristine noble gases in mantle plumes. *Science*, 288(5468), 1036–1038. doi:10.1126/science.288.5468.1036
- Tsuno, K., & Dasgupta, R. (2015). Fe–Ni–Cu–S phase relations at high pressures and temperatures – The role of sulfur in carbon storage and diamond stability at mid- to deep-upper mantle. *Earth and Planetary Science Letters*, 412, 132–142. doi:10.1016/j.epsl.2014.12.018
- Urey, H. C. (1947). The thermodynamic properties of isotopic substances. *Journal of the Chemical Society (Resumed)*, 562–581. doi:10.1039/JR9470000562
- Van der Hilst, R. D., & Káráson, H. (1999). Compositional heterogeneity in the bottom 1000 kilometers of Earth's mantle: toward a hybrid convection model. *Science*, 283(5409), 1885–1888. doi:10.1126/science.283.5409.1885
- Van Keken, P. E., Hacker, B. R., Syracuse, E. M., & Abers, G. A. (2011). Subduction factory: 4. Depth-dependent flux of H_2O from subducting slabs worldwide *Journal of Geophysical Research*, 116, B01401. doi:10.1029/2010JB007922
- Wallace, P. J. (2002). Volatiles in Submarine Basaltic Glasses from the Northern Kerguelen Plateau (ODP Site 1140): Implications for Source Region Compositions, Magmatic Processes, and Plateau Subsidence. *Journal of Petrology*, 43(7), 1311–1326. doi:10.1093/petrology/43.7.1311
- Walter, M. J., Bulanova, G. P., Armstrong, L. S., Keshav, S., Blundy, J. D., Gudfinnsson, G., et al. (2008). Primary carbonate melt from deeply subducted oceanic crust. *Nature*, 454(7204), 622–625. doi:10.1038/nature07132
- Wang, S.-J., Teng, F.-Z., Rudnick, R. L., & Li, S.-G. (2015). Magnesium isotope evidence for a recycled origin of cratonic eclogites. *Geology*, 43(12), 1071–1074. doi:10.1130/G37259.1
- Wang, S.-J., Teng, F.-Z., & Scott, J. M. (2016). Tracing the origin of continental HIMU-like intraplate volcanism using magnesium isotope systematics. *Geochimica et Cosmochimica Acta*, 185, 78–87. doi:10.1016/j.gca.2016.01.007
- Wang, S.-J., Teng, F.-Z., Williams, H. M., & Li, S.-G. (2012). Magnesium isotopic variations in cratonic eclogites: Origins and implications. *Earth and Planetary Science Letters*, 359–360, 219–226. doi:10.1016/j.epsl.2012.10.016
- Wang, X.-J., Chen, L.-H., Hofmann, A. W., Hanyu, T., Kawabata, H., Zhong, Y., et al. (2018). Recycled ancient ghost carbonate in the Pitcairn mantle plume. *Proceedings of the National Academy of Sciences*, 115(35), 8682–8687. doi:10.1073/pnas.1719570115
- Wang, X.-J., Chen, L.-H., Hofmann, A. W., Mao, F.-G., Liu, J.-Q., Zhong, Y., et al. (2017). Mantle transition zone-derived EM1 component beneath NE China: Geochemical evidence from Cenozoic potassic basalts. *Earth and Planetary Science Letters*, 465, 16–28. doi:10.1016/j.epsl.2017.02.028
- Wang, Z., & Gaetani, G. A. (2008). Partitioning of Ni between olivine and siliceous eclogite partial melt: experimental constraints on the mantle source of Hawaiian basalts. *Contributions to Mineralogy and Petrology*, 156(5), 661–678. doi:10.1007/s00410-008-0308-y
- Warren, J. M., Shimizu, N., Sakaguchi, C., Dick, H. J. B., & Nakamura, E. (2009). An assessment of upper mantle heterogeneity based on abyssal peridotite isotopic compositions. *Journal of Geophysical Research: Solid Earth*, 114(B12). doi:10.1029/2008JB006186
- Waters, C. L., Sims, K. W. W., Perfit, M. R., Blichert-Toft, J., & Blusztajn, J. (2011). Perspective on the Genesis of E-MORB from Chemical and Isotopic Heterogeneity at 9–10°N East Pacific Rise. *Journal of Petrology*, 52(3), 565–602. doi:10.1093/petrology/egq091
- Weaver, B. (1991). The origin of ocean island basalt end-member compositions: trace element and isotopic constraints. *Earth and Planetary Science Letters*, 104(2–4), 381–397. doi:10.1016/0012-821X(91)90217-6

- Weiss, Y., Class, C., Goldstein, S. L., & Hanyu, T. (2016). Key new pieces of the HIMU puzzle from olivines and diamond inclusions. *Nature*, 537(7622), 666–670. doi:10.1038/nature19113
- Weiss, Y., Griffin, W. L., Bell, D. R., & Navon, O. (2011). High-Mg carbonatitic melts in diamonds, kimberlites and the sub-continental lithosphere. *Earth and Planetary Science Letters*, 309(3), 337–347. doi:10.1016/j.epsl.2011.07.012
- White, W. M. (2010). Oceanic island basalts and mantle plumes: The geochemical perspective. *Ann. Rev. Earth Planet. Sci.*, 38(1), 133–160. doi:10.1146/annurev-earth-040809-152450
- White, W. M. (2015a). Isotopes, DUPAL, LLSVPs, and Anekantavada. *Chemical Geology*, 419, 10–28. doi:10.1016/j.chemgeo.2015.09.026
- White, W. M. (2015b). Probing the Earth's Deep Interior through Geochemistry. *Geochemical Perspectives*, 4(2), 95–96. doi:10.7185/geochempersp.4.2
- White, W. M., & Duncan, R. A. (1996). Geochemistry and geochronology of the Society Islands: New evidence for deep mantle recycling. In A. Basu & S. Hart (Eds.), *Earth Processes: Reading the Isotopic Code* (Vol. Geophysical Monograph 95, pp. 183–206). Washington D. C.: American Geophysical Union. doi:10.1029/GM095p0183
- Willbold, M., Elliott, T., & Moorbath, S. (2011). The tungsten isotopic composition of the Earth's mantle before the terminal bombardment. *Nature*, 477(7363), 195–198. doi:10.1038/nature10399
- Willbold, M., & Stracke, A. (2006). Trace element composition of mantle end-members: Implications for recycling of oceanic and upper and lower continental crust. *Geochemistry Geophysics Geosystems*, 7(4), Q04004. doi:10.1029/2005GC001005
- Wille, M., Nebel, O., Pettker, T., Vroon, P. Z., König, S., & Schoenberg, R. (2018). Molybdenum isotope variations in calc-alkaline lavas from the Banda arc, Indonesia: Assessing the effect of crystal fractionation in creating isotopically heavy continental crust. *Chemical Geology*, 485, 1–13. doi:10.1016/j.chemgeo.2018.02.037
- Williams, H. M., & Bizimis, M. (2014). Iron isotope tracing of mantle heterogeneity within the source regions of oceanic basalts. *Earth and Planetary Science Letters*, 404, 396–407. doi:10.1016/j.epsl.2014.07.033
- Williams, C. D., Mukhopadhyay, S., Rudolph, M. L., & Romanowicz, B. (2019). Primitive helium is sourced from seismically slow regions in the lowermost mantle. *Geochemistry, Geophysics, Geosystems*, 20(8), 4130–4145. doi:10.1029/2019gc008437
- Woodhead, J. D. (1996). Extreme HIMU in an oceanic setting: the geochemistry of Mangaia Island (Polynesia), and temporal evolution of the Cook—Austral hotspot. *Journal of Volcanology and Geothermal Research*, 72(1–2), 1–19. doi:10.1016/0377-0273(96)00002-9
- Woodhead, J. D., & Devey, C. W. (1993). Geochemistry of the Pitcairn seamounts, I: source character and temporal trends. *Earth and Planetary Science Letters*, 116(1–4), 81–99. doi:10.1016/0012-821x(93)90046-c
- Woodhead, J. D., & McCulloch, M. T. (1989). Ancient seafloor signals in Pitcairn Island lavas and evidence for large amplitude, small length-scale mantle heterogeneities. *Earth and Planetary Science Letters*, 94(3–4), 257–273. doi:10.1016/0012-821X(89)90145-3
- Workman, R. K., Eiler, J. M., Hart, S. R., & Jackson, M. G. (2008). Oxygen isotopes in Samoan lavas: Confirmation of continent recycling. *Geology*, 36(7), 551–554. doi:10.1130/g24558a.1
- Workman, R. K., Hart, S. R. (2005). Major and trace element composition of the depleted MORB mantle (DMM). *Earth and Planetary Science Letters*, 231, 53–72. doi: 10.1016/j.epsl.2004.12.005
- Workman, R. K., Hart, S. R., Jackson, M., Regelous, M., Farley, K. A., Blusztajn, J., et al. (2004). Recycled metasomatized lithosphere as the origin of the Enriched Mantle II (EM2) end-member: Evidence from the Samoan Volcanic Chain. *Geochemistry, Geophysics, Geosystems*, 5(4), Q04008. doi:10.1029/2003gc000623
- Xu, Y.-G. (2014). Recycled oceanic crust in the source of 90–40Ma basalts in North and Northeast China: Evidence, provenance and significance. *Geochimica et Cosmochimica Acta*, 143, 49–67. doi:10.1016/j.gca.2014.04.045
- Xu, Y.-G., Zhang, H.-H., Qiu, H.-N., Ge, W.-C., & Wu, F.-Y. (2012). Oceanic crust components in continental basalts from Shuangliao, Northeast China: Derived from the mantle transition zone? *Chemical Geology*, 328, 168–184. doi:10.1016/j.chemgeo.2012.01.027
- Yang, W., Teng, F.-Z., Zhang, H.-F., & Li, S.-G. (2012). Magnesium isotopic systematics of continental basalts from the North China craton: Implications for tracing subducted carbonate in the mantle. *Chemical Geology*, 328, 185–194. doi:10.1016/j.chemgeo.2012.05.018
- Yaxley, G. M., & Green, T. H. (1998). Reactions between eclogite and peridotite: Mantle refertilisation by subduction of oceanic crust. *Schweizerische Mineralogische und Petrographische Mitteilungen*, 78, 243–255
- Yurimoto, H., Kogiso, T., Abe, K., Barszczus, H. G., Utsunomiya, A., & Maruyama, S. (2004). Lead isotopic compositions in olivine-hosted melt inclusions from HIMU basalts and possible link to sulfide components. *Physics of the Earth and Planetary Interiors*, 146(1–2), 231–242. doi:10.1016/j.pepi.2003.08.013
- Zeng, G., Chen, L.-H., Xu, X.-S., Jiang, S.-Y., & Hofmann, A. W. (2010). Carbonated mantle sources for Cenozoic intra-plate alkaline basalts in Shandong, North China. *Chemical Geology*, 273(1), 35–45. doi:10.1016/j.chemgeo.2010.02.009
- Zhang, G.-L., Chen, L.-H., Jackson, M. G., & Hofmann, A. W. (2017). Evolution of carbonated melt to alkali basalt in the South China Sea. *Nature Geoscience*, 10(3), 229–235. doi:10.1038/ngeo2877
- Zhong, Y., Chen, L.-H., Wang, X.-J., Zhang, G.-L., Xie, L.-W., & Zeng, G. (2017). Magnesium isotopic variation of oceanic island basalts generated by partial melting and crustal recycling. *Earth and Planetary Science Letters*, 463, 127–135. doi:10.1016/j.epsl.2017.01.040
- Zindler, A., & Hart, S. (1986). Chemical geodynamics. *Annual Review of Earth and Planetary Sciences*, 14, 493–571. doi:10.1146/annurev.ea.14.050186.002425

6

Tracking the Evolution of Magmas from Heterogeneous Mantle Sources to Eruption

Ananya Mallik¹, Sarah Lambart², and Emily J. Chin³

ABSTRACT

This chapter reviews the effects of source heterogeneities, melt-rock reactions, and intracrustal differentiation on magma chemistry across mid-ocean ridges, intraplate settings, and subduction zones using experimental studies and natural data. We compare melting behaviors of pyroxenites and peridotites and their relative contributions to magmas as functions of composition, mantle potential temperature, and lithospheric thickness. We also discuss the fate of chemically distinct melts derived from heterogeneities as they travel through a peridotitic mantle. Using nearly 60,000 natural major element compositions of volcanic rocks, melt inclusions, and crystalline cumulates, we assess broad petrogenetic trends in as large of a global dataset as possible. Consistent with previous studies, major element chemistry of mid-ocean ridge basalts (MORBs), and their cumulates favor a first-order control of intracrustal crystal-liquid segregation, while trace-element studies emphasize the role of melt-rock reactions, highlighting the decoupling between the two. Ocean island basalts (OIB) show a larger compositional variability than MORB, partly attributed to large variations of pyroxenite proportions in the mantle source. However, the estimated proportions vary considerably with heterogeneity composition, melting model and thermal structure of the mantle. For arcs, we highlight current views on the role of the downgoing slab into the source of primary arc magmas, and the role of the overriding lithosphere as a magmatic chemical filter and as the repository of voluminous arc cumulates. Our approach of simultaneously looking at a large database of volcanic + deep crustal rocks across diverse tectonic settings underscores the challenge of deciphering the source signal versus intracrustal/lithospheric processes.

6.1. INTRODUCTION

Magmatism on Earth takes place at three main different tectonic settings: mid-ocean ridges, intraplate settings including ocean islands, and arc magmatism in

subduction zones. The upper mantle, mostly composed of peridotites, is the main source of magma on Earth. However, geophysical, geochemical, and field observations demonstrate that the mantle is heterogeneous. Many studies have proposed that crustal lithologies introduced in the Earth's mantle by subduction, including sediments and oceanic crust, contribute significantly as heterogeneities to the generation of mantle-derived magmas (e.g. Chase, 1981; Helffrich and Wood, 2001; Hirschmann and Stolper, 1996; Hofmann, 1997; Hofmann and White, 1982; Jackson et al., 2007; Lambart, 2017; Lambart et al., 2009, 2016; Mallik and Dasgupta, 2012; Salters and Dick,

¹Department of Geosciences, University of Arizona, Tucson, AZ, USA

²Department of Geology and Geophysics, University of Utah, Salt Lake City, UT, USA

³Scripps Institution of Oceanography, University of California, San Diego, La Jolla, CA, USA

2002; Schiano et al., 1997; Sobolev et al., 2005, 2007). The contribution of a lithology during magma genesis is controlled by four main parameters: (1) the fraction of the lithology in the mantle, (2) its solidus temperature, (3) its melt productivity, and (4) the mantle regime (potential temperature and thickness of the lithosphere). In this chapter, we discuss the current state of understanding how these parameters affect the contribution of heterogeneities in magma generation in the Earth's upper mantle across the three tectonic settings. We also review perspectives on magmatic differentiation, since intracrustal differentiation is the “last mile” of a primary magma's journey from its origin as a partial melt of the mantle to its point of eruption. Disentangling the contributions from differentiation vs. source heterogeneity are therefore non-trivial. To these ends, we review results from experimental studies simulating partial melting under a variety of upper mantle conditions and compositions. Then we compare experimental results with a compilation of nearly 60,000 compositions of natural volcanic rocks, melt inclusions, and plutonic cumulate rocks from ridges, intraplate settings, and volcanic arcs.

6.2. PARTIAL MELTING OF A HETEROGENEOUS MANTLE

6.2.1. Contribution of Mantle Lithologies to Magma Genesis

For the purpose of this section, we use the term *pyroxenite* to refer to mafic and ultramafic-rich plutonic rocks that lack sufficient olivine (40%) to be classified as peridotites (Le Maitre et al., 2005). Based on their abundance in orogenic massifs, it is generally assumed that the Earth's upper mantle contains 2–5% pyroxenites (e.g., Bodinier and Godard, 2003). Magma compositions suggest that the mantle source can be significantly enriched locally (e.g., Sobolev et al., 2005) or even be exclusively composed of pyroxenites (e.g., Zhang et al., 2018). Compositions of the lithologies control their solidus temperatures and melt productivities (Hirschmann, 2000; Lambart et al., 2016; Pickering-Witter and Johnston, 2000), while thermal structure of the mantle and the crust control the melt fluxes and initial and final pressures of melting (Langmuir et al., 1992; Sleep, 1990; Tatsumi et al., 1983). The influence of composition on the solidus temperatures of mantle lithologies has been the subject of several experimental and theoretical studies (Hirschmann, 2000; Kogiso and Hirschmann, 2006; Kogiso et al., 2004; Lambart et al., 2016). These studies demonstrate that, at a given pressure, the solidus temperatures of anhydrous and CO₂-free lithologies are mostly influenced by the bulk alkali content

(Figure 6.1) and Mg-number ($Mg\# = \text{molar MgO} / [\text{molar MgO} + \text{molar FeO}^T]$) of the rock.

Fewer studies, however, discuss the controls on melt productivity. Melt productivities of mantle lithologies tend to increase with the contribution of clinopyroxene (cpx; Lambart et al., 2013; Pertermann and Hirschmann, 2003a; Pickering-Witter and Johnston, 2000; Spandler et al., 2008) and feldspar (Falloon et al., 2008; Lambart et al., 2009; Spandler et al., 2008) in the melting reaction. On the contrary, the presence of other accessory phases like rutile, quartz, spinel, or olivine results in low melt productivities, explained by a low thermodynamic variance of the system (Pertermann and Hirschmann, 2003a). Figure 6.2 compares experimental melt fractions as a function of temperature at 1 and 3 GPa for various pyroxenite and peridotite compositions. The higher solidus temperature difference between pyroxenites and peridotites at 3 GPa than at 1 GPa partly reflects sampling bias (most experiments at 3 GPa were performed on alkali-richer and Mg-poorer lithologies than experiments performed at 1 GPa), but is also consistent with the parameterization of Lambart et al. (2016) showing that the solidus temperature variation in pyroxenites significantly decreases with pressure. Peridotites are marked by a decrease in melt productivity when cpx disappears from the experimental assemblage. However, the productivities of pyroxenites and peridotites are scattered but largely overlap before cpx disappearance. Hence, the cpx disappearance in the mineralogical assemblage is the main parameter influencing the large difference in melt productivity between peridotites and pyroxenites.

Finally, the thermal structure of the mantle and the crust mostly controls the potential temperature (T_P) and the thickness of the lithosphere (considered as the final pressure of melting; e.g., Dasgupta et al., 2010). Decreasing T_P or increasing the thickness of the lithosphere both result in an increase of the low-solidus component contribution (usually, the pyroxenite) in the melt by decreasing the relative height of the melting column where both lithologies are melting (Figure 6.3) (Ellam, 1992; Humphreys and Niu, 2009; Niu et al., 2011; Sobolev et al., 2007).

6.3. PERIDOTITE VS. PYROXENITE: EXPERIMENTAL MELT COMPOSITIONS

6.3.1. Major Elements

Pyroxenites are usually separated into two groups: silica-excess (SE) and silica-deficient (SD) pyroxenites. The garnet–pyroxene thermal divide separating these two groups (defined by the Enstatite–Diopside–Alumina plane in

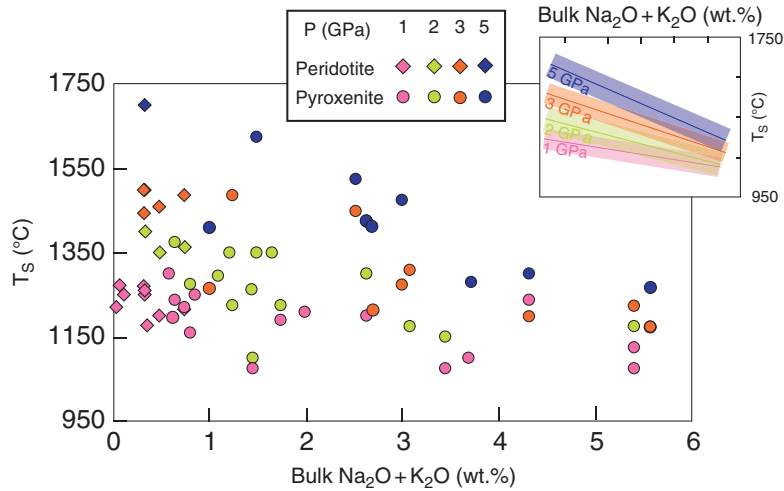


Figure 6.1 Pyroxenite and peridotite solidus temperatures determined experimentally as a function of the bulk alkali content for pressures between 1 and 5 GPa. The inset shows the linear regressions for each pressure and the corresponding error envelopes (1σ). *Sources:* Adam et al., 1992; Baker and Stolper, 1994; Borghini et al., 2017; Hirose and Kushiro, 1993; Hirschmann et al., 2003; Ito and Kennedy, 1974; Kogiso et al., 1998; Kogiso and Hirschmann, 2001, 2006; Kogiso et al., 2003; Kornprobst, 1970; Kushiro, 1996; Lambart et al., 2009, 2012; Pertermann and Hirschmann, 2003a; Pickering-Witter and Johnston, 2000; Rosenthal et al., 2014, 2018; Schwab and Johnston, 2001; Spandler et al., 2008, 2010; Thompson, 1974, 1975; Tsuruta and Takahashi, 1998; Tuff et al., 2005; Walter, 1998; Wasylenki et al., 2003; Yasuda et al., 1994.

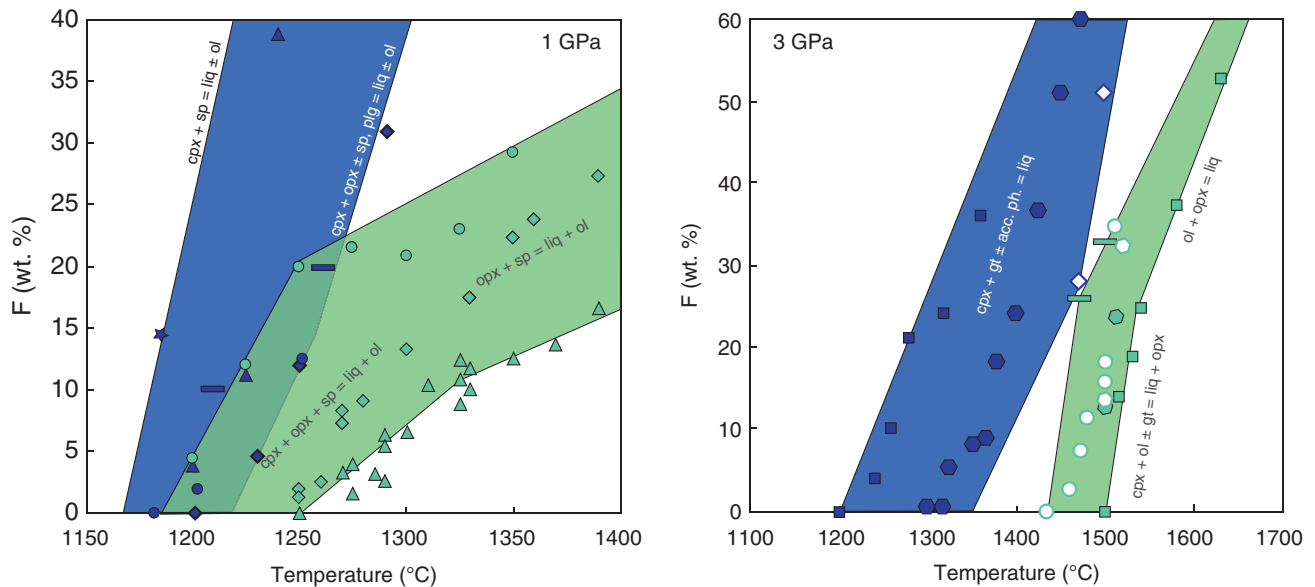


Figure 6.2 Experimental melt fractions as functions of temperature for pyroxenites (blue: M7–16, star; M5–40, triangles; M5–103, diamonds; GV10, rectangles; Ito and Kennedy’s eclogite, circles; GA2, squares; G2, hexagons; B-ECL1, open diamonds) and peridotites (green: PHN-1611, circles; MM3, diamonds; DDMM, triangles; KR4003, square; KLB-1, open circles; HK66, rectangles; KG2, hexagons; KG1, open hexagons) at 1 and 3 GPa. The blue and green fields show the envelopes of melt fractions for pyroxenites and peridotites, respectively. *Sources:* Baker and Stolper, 1994; Baker et al., 1995; Borghini et al., 2017; Hirose and Kushiro, 1993; Hirschmann et al., 1998; Ito and Kennedy, 1974; Kogiso and Hirschmann, 2006; Kogiso et al., 1998; Kushiro 1996; Lambart et al., 2009; Pertermann and Hirschmann, 2003a; Spandler et al., 2008; Walter, 1998; Wasylenki et al., 2003.

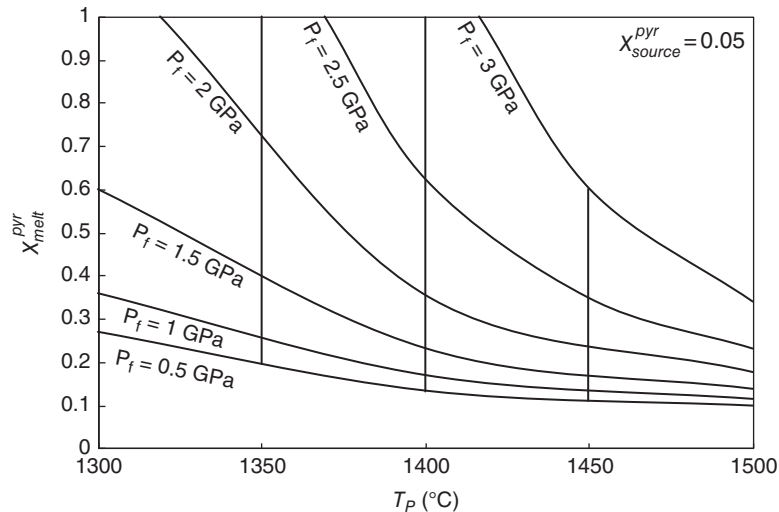


Figure 6.3 Effect of the potential temperature (T_P) and the final pressure of melting (P_f) on the fraction of the pyroxenite G2 in the aggregated magma $X_{melt}^{pyr} = (X_{source}^{pyr} \times F_f^{pyr}) / (X_{source}^{pyr} \times F_f^{pyr} + (1 - X_{source}^{pyr}) \times F_f^{per})$, assuming $X_{source}^{pyr} = 0.05$ and calculated with Melt-PX. Sources: Based on Pertermann and Hirschmann, 2003a and Lambart et al., 2016.

the CaO-MgO-Al₂O₃-SiO₂ tetrahedron; O'Hara, 1976) controls the melting relations of pyroxenites at high pressure (≥ 2 GPa; Kogiso et al., 2004) when clinopyroxene and garnet are dominating the mineralogical assemblage. Lambart et al. (2013) reviewed the melting phase relations of pyroxenites and showed that there is a large overlap of compositions between melt produced by the different mantle lithologies. As a rule, there is a progressive transition from the liquids derived from SE compositions to SD compositions to peridotites rather than a sharp compositional contrast. The extreme variability of the pyroxenite melts and the progressive transition between melts from different lithologies make finding good markers for the presence of pyroxenites in the source challenging.

Yang and Zhou (2013) and Yang et al. (2016) suggested that the FC3MS (FeO/CaO-3*MgO/SiO₂, in wt.%) parameter can help with distinguishing between pyroxenite- and peridotite-derived melts. Their analysis demonstrates that the upper boundary of the FC3MS value for peridotite melts is 0.65, while melts derived from pyroxenites cover a much larger range (-0.9 to 1.7). More recently, Yang et al. (2019) proposed two new parameters (FCMS and FCKANTMS) and showed that using log ratio-based chemical markers help in reducing the temperature and pressure effects on the compositional heterogeneity of melts. However, we note that none of these parameters can help to distinguish between peridotite-derived and pyroxenite-derived melts for compositions producing low parameter values (i.e., peridotites and most SD pyroxenites).

6.3.2. First Row Transition Elements

First Row Transition Element (Sc, Ti, V, Cr, Mn, Fe, Co, Ni, Cu, Zn) concentrations in magmas have been recently suggested as good indicators of the mantle source mineralogy (e.g., Davis et al., 2013; Herzberg, 2011; Humayun et al., 2004; Le Roux et al., 2010, 2011; Prytulak and Elliott, 2007; Qin and Humayun, 2008; Sobolev et al., 2005, 2007). Le Roux et al. (2011) showed that during partial melting of the upper mantle, olivine and orthopyroxene do not significantly fractionate Mn and Fe from each other, and melts from garnet-free peridotite are expected to have similar Mn/Fe ratios as the source. In contrast, clinopyroxene and garnet, the dominant minerals in pyroxenitic assemblages (Kogiso et al., 2004), show strong fractionations, such that melts of pyroxenites or eclogites would be expected to produce melts with low Mn/Fe compared to peridotite partial melts (Humayun et al., 2004). However, experiments by Le Roux and coworkers only explored peridotitic mineral compositions at a limited range of pressure (1.5–2 GPa), while partition coefficients can vary depending on the compositions of the minerals and melts (e.g., Davis et al., 2013; Wang and Gaetani, 2008) as well as with pressure and temperature (P-T) conditions (e.g., Matzen et al., 2013, 2017a). To take into account the potential effects of compositional and P-T variations, we plotted the partition coefficients between melt and mineral compositions using experiments reported in the literature on SE and SD pyroxenites and on peridotites. Partition coefficients for Fe and Mn strongly depend on the

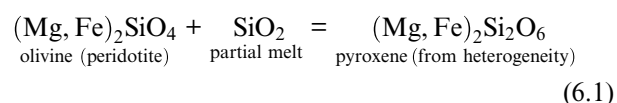
MgO content of the melt (Figure 6.4a,b), but the Mn–Fe K_D are distinct for each mineral, and clinopyroxene–melt and garnet–melt Mn–Fe K_D s are distinctly higher than olivine–melt and opx–melt K_D s (Figure 6.4c). In addition, and in agreement with results from Le Roux et al. (2011), Mn–Fe K_D s are independent of the composition. These results support the conclusions of Le Roux and coworkers: a mineral assemblage dominated by cpx and garnet will produce a melt with lower Mn/Fe ratio than a mineral assemblage dominated by olivine and orthopyroxene and, despite the large variability of bulk compositions that obscures this relationship, Mn/Fe ratio produced by pyroxenite-derived melts are generally lower than that in peridotite-derived melts (Figure 6.4d).

6.4. INTERACTIONS BETWEEN CHEMICAL HETEROGENEITIES AND PERIDOTITE

Solidi of the nominally anhydrous subducted oceanic crust (e.g., Pertermann and Hirschmann, 2003a) and sediments (e.g., Spandler et al., 2010) are at lower temperatures than the solidus of nominally anhydrous peridotite-bearing ambient mantle (Figure 6.5a). This implies that when the ambient peridotitic mantle carrying chemical heterogeneities upwells along an adiabat in the upper mantle (Figure 6.5b), the heterogeneities reach their solidus temperatures deeper than the peridotite. Thus, between the solidi of heterogeneities and the peridotite (indicated by the dashed areas in Figures 6.5a and b), the partial melt from heterogeneities would encounter subsolidus (unmelted) peridotite. The presence of volatiles such as H₂O and/or CO₂ in the heterogeneities further depress the solidi to lower temperatures (e.g., Dasgupta et al., 2004; Hammouda, 2003; Hermann and Spandler, 2008; Poli and Schmidt, 1995; Skora and Blundy, 2010; Yaxley and Brey, 2004) implying that the heterogeneities begin to partially melt even deeper in the upper mantle while the surrounding peridotite is still subsolidus. An exception to this is under highly oxidized regions where CO₂ in peridotites may cause onset of carbonated silicate partial melting deeper than in the case of volatile-free peridotite (Dasgupta et al., 2013).

The partial melts from these heterogeneities are not in equilibrium with subsolidus peridotites and react with them (e.g., Kogiso et al., 1998; Mallik and Dasgupta, 2012; Yaxley and Green, 1998). Such a reactive melt–rock interaction can be illustrated by a simple binary phase diagram between olivine and quartz with double-eutectic at relevant pressures (Figure 6.5c). The readers are reminded that the binary phase diagram, while a useful tool to illustrate the first-order reactive crystallization process, does not capture the complexities imposed on the phase

equilibria by multicomponent systems which are, better analogs to natural systems. The siliceous partial melts from the heterogeneities lie on the liquidus surface of the pyroxene–quartz binary, while the peridotite lies below the solidus of the olivine–pyroxene binary. When the siliceous partial melts react with peridotite, the bulk composition of the melt–peridotite mixture is located between the partial melt and peridotite. Whether the bulk composition lies in the pyroxene–quartz binary or the olivine–pyroxene binary depends on the melt–rock proportion, where a higher proportion would place the bulk composition closer to the pyroxene–quartz binary. Thus, the interaction between the partial melt of the heterogeneities and peridotite would result in reactive crystallization, as observed in the phase diagram. The first-order reaction that takes place in this context is as follows:



A high melt-to-rock proportion would result in the consumption of olivine and melt to crystallize pyroxene, with remaining partial melt that is less siliceous and more Mg-rich than the partial melt derived directly from the heterogeneity. A low melt–rock ratio would result in complete crystallization of the partial melt to form pyroxene, with residual olivine from the peridotite. Similar reasoning can be made with other heterogeneity compositions: silica-deficient pyroxenites will result in olivine production at the expense of orthopyroxene, but for a low melt–rock ratio, the melt will be consumed during the reaction (Lambart et al., 2012). Thus, such a process of reactive crystallization between partial melt from a heterogeneity and peridotite not only produces distinct residual partial melt compositions, but also contributes to further heterogeneity in the upper mantle (Figure 6.5d). Due to the interaction of heterogeneities with peridotite, such melt–rock reactions may occur beneath mid-ocean ridges (Borghini et al., 2017; Lambart et al., 2012), ocean islands (Mallik and Dasgupta, 2012, 2013, 2014; Sobolev et al., 2005), continental lithosphere (Chen et al., 2017; Kiseeva et al., 2013), in subduction zones near depths of arc magma generation (Kelemen, 1995; Mallik et al., 2015, 2016; Prouteau et al., 2001; Tatsumi, 2001; Wang and Foley, 2018), and as deep as the transition zone (Kiseeva et al., 2013; Thomson et al., 2016).

6.5. SAMPLING MELTS OF THE MANTLE: APPROACH AND OVERVIEW

In this section, we present a brief, and by no means comprehensive, survey of the magma-generation processes

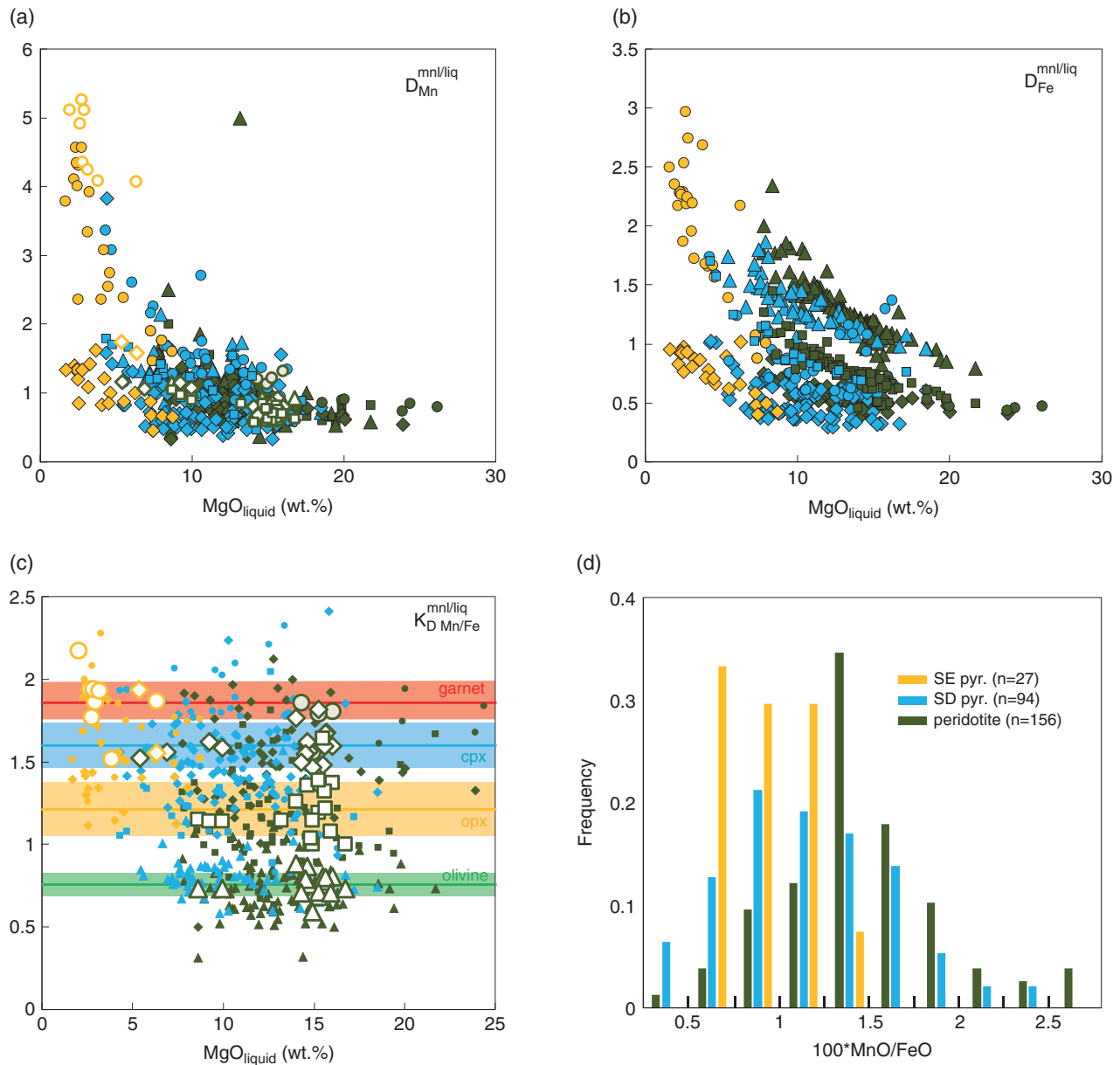


Figure 6.4 (a–b) Partition coefficient of Mn (a) and Fe (b) between minerals (garnet: circles; cpx: diamonds; opx: squares; olivine: triangles) as functions of the MgO content of the liquid for pyroxenites (SE: yellow; SD: blue), and peridotites (green). In (a), open symbols are higher accuracy analyses obtained by LA-ICP-MS or high current microprobe analyses (Davis et al., 2013; Le Roux et al., 2011; Pertermann et al., 2004). (c) Mn-Fe exchange partition coefficients (K_D) between minerals and melts. The colored lines show the average K_D calculated for each mineral using high accuracy measurements and the colored bands show the corresponding standard deviation. (d) Histogram showing the distributions of the $100 * MnO/FeO$ ratios in experimental melts. *Sources:* Baker and Stolper, 1994; Borghini et al., 2017; Davis et al., 2013; Falloon and Danyushevsky, 2000; Keshav et al., 2004; Kogiso and Hirschmann, 2001, 2006; Kogiso et al., 2003; Lambart et al., 2009 (Compositions of the solid phases can be found at <https://doi.org/10.6084/m9.figshare.9926885.v1>), Lambart et al., 2013; Laporte et al., 2004; Le Roux et al., 2011; Pertermann and Hirschmann, 2003b; Pickering-Witter and Johnston, 2000; Pilet et al., 2008; Schwab and Johnston, 2001; Walter, 1998; Wasylenki et al., 2003; Yasuda et al., 1994; Yaxley and Sobolev, 2007.

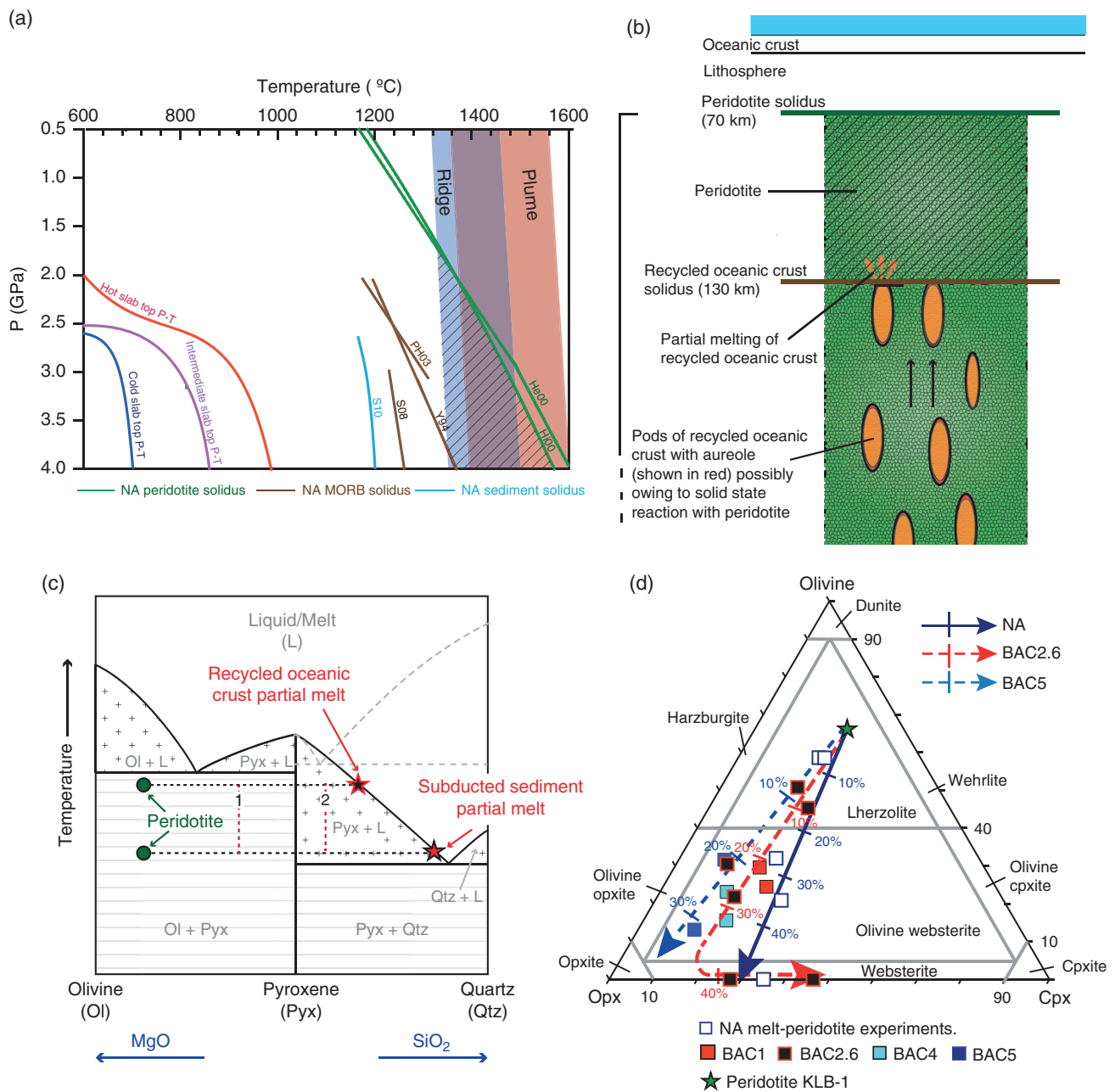


Figure 6.5 (a) Solidus of nominally anhydrous (NA) peridotite, recycled oceanic crust (MORB) and sediment plotted in pressure-temperature space. Also plotted for comparison are the range of adiabats from mid-ocean ridges to plume-settings with the lower end bracketed by mantle potential temperature of 1315 °C and the higher end by 1550 °C, as well as hot, intermediate and cold subducted slab geotherms (Syracuse et al., 2010). The dashed area indicates P-T space where partial melt from recycled oceanic crust and sediments would react with the surrounding subsolidus peridotite. (b) Illustration showing a slice of upwelling peridotitic mantle with pods of lithological heterogeneity (e.g. 5 wt.% recycled oceanic crust). NA recycled oceanic crust encounters its solidus at a depth \approx 130 km, while the NA peridotite is still below the solidus. In the dashed area (the same as in panel a), partial melt derived from recycled oceanic crust undergoes reactive infiltration through the surrounding subsolidus peridotite. (c) Binary phase diagram between olivine and quartz (not to scale) with double eutectic, at 2.5 GPa. Dashed gray lines in the pyroxene-quartz binary represent the solidus and liquidii in a pure MgO-SiO₂ system, solid lines represent solidus and liquidii with alkalis included. "1" indicates a bulk composition with low melt-rock ratio resulting in complete consumption of the melt and producing olivine-pyroxene residue. "2" indicates a bulk composition with high melt-rock ratio which produces a pyroxene residue by consuming olivine, and a residual melt that is less siliceous and more magnesian than the melt directly derived from chemical heterogeneities. (d) Streikeisen diagram for ultramafic rocks. The peridotite KLB-1 (Takahashi, 1986) is representative of a shallow upper mantle peridotite. The other symbols plotted are residues of reactive crystallization between peridotite and melt derived from low to moderate degree of partial melting of recycled oceanic crust with various proportion of CO₂, from 0 wt.% to 5 wt.% (BAC, Mallik and Dasgupta, 2014, 2013) at 2.5–3 GPa. The percentage next to the symbols represent the initial proportion of melt to peridotite. Sources: (a) Herzberg et al., 2007, McKenzie et al., 2005. (c) Chen and Presnall, 1975. (d) NA, Mallik and Dasgupta, 2012.

and compositions of natural samples from the three major tectonic settings on Earth: mid-ocean ridges, ocean islands, and volcanic arcs. For each setting, we review experimental constraints on magma genesis, followed by a discussion of the compilation of natural compositional data. To facilitate as many comparisons between experimental data and natural data across the three settings, we focus exclusively on major element compositions. Obviously, using only major elements rather than emphasizing only primitive samples presents limitations for fingerprinting the nature of the melting source. Our goal here is not to identify the source characteristics, since trace element ratios and isotopes would be better suited for that task, but to make broad comparisons between experimental, modeling, and natural observations in terms of petrogenetic processes across the major tectonic settings of magmatism on Earth.

Supplementary data and literature sources used in this review are summarized in Table 6. S1 and are all reported in Supplementary Tables 6.S6, 6.S7, and 6.S8. Owing to the extremely large number of samples, particularly for arc volcanic rocks (nearly 40,000), we contoured all the volcanic rock data using a smoothed histogram method (Eilers and Goeman, 2004), using 75 histogram bins in the x and y direction and a positive smoothing parameter (λ) of 1.5 (higher values of λ lead to more smoothing; a value near zero would result in a plot of essentially the raw data). Density contours for volcanic rocks in Figure 6.6 were constructed at intervals of 10%. We applied the same parameters in the contouring for the volcanic rock data from each tectonic setting so side-by-side comparisons can be accurately made. Owing to the small number of plutonic cumulate rocks (<500 at any given setting) and melt inclusions (<200, from volcanic arcs only), we did not contour these datasets.

6.5.1. MORBs

Intracrustal Processing. The relatively simple geodynamic setting of mid-ocean ridges serves as a baseline model for mantle melting and magma generation. A primary magma is one formed during adiabatic decompression melting of mantle peridotite that has not been modified during ascent and eruption. It has long been recognized that such a magma is rarely, if ever, sampled at mid-ocean ridges (or any tectonic setting for that matter) – the average Mg# of all MORB is 56, significantly lower than the value of ~70 expected for equilibrium with mantle peridotite. Three main factors are involved in producing the compositional spectrum of mid-ocean ridge basalts (MORBs): (1) mantle source heterogeneity, (2) style of mantle melting, and (3) intracrustal processing. In this section, we focus on the role of intracrustal processing, which marks the boundary

between the melting regime and the onset of crystallization, differentiation, eruption, and eventual sampling.

In order to go from sampled MORBs from the seafloor to how such MORBs looked when they parted ways with the mantle, the contributions from crystallization-differentiation, which occur in the crust, must first be understood. Intracrustal processing of MORB can be broadly considered as variations on the theme of fractional crystallization (FX). The simplest scenario, and still, the paradigm, is that MORBs follow a differentiation path under anhydrous, low-pressure conditions, evolving toward the classic Fe-enrichment (tholeiitic) trend (O'Hara, 1965). Experiments and observations of natural MORBs indicate the generalized low-pressure crystallization sequence of olivine \rightarrow olivine + plagioclase \rightarrow olivine + plagioclase + clinopyroxene \rightarrow plagioclase + clinopyroxene + orthopyroxene + Fe-Ti oxides (Coogan, 2014; Grove et al., 1993). However, detailed study of MORB over the past decades reveals several inconsistencies with the simple FX model: (1) phenocryst assemblages in MORB are not representative of cotectic proportions as predicted by FX (Francis, 1986); (2) FX models require fractionation of clinopyroxene, but it is not commonly observed as a phenocryst; and (3) some incompatible elements, like Th, are overly enriched in global MORB compared to predictions from simple fractional crystallization (Coogan and O'Hara, 2015; Jenner and O'Neill, 2012). Thus, more complex scenarios have been hypothesized to explain the mismatch between trace element data and simple fractional crystallization models. The two major variations on the simple fractional crystallization model are (1) *in situ* crystallization, where crystallization of a magma occurs in a progressive solidification front and involves return of interstitial melt to the magma chamber (Coogan and O'Hara, 2015; Langmuir, 1989; McBirney and Noyes, 1979); and (2) RepTapFrac, wherein a magma chamber is periodically replenished (Rep), melt is extracted (Tap), and then fractionally crystallized (Frac) (Albarede, 1985; O'Hara, 1977; O'Neill and Jenner, 2012). Additionally, recent studies suggest an alternative – reactive porous flow/melt-rock reaction – as another mechanism that could reconcile several of the MORB conundrums, particularly the observed overenrichment in incompatible trace elements (Coumans et al., 2016; Gao et al., 2007; Lissenberg and MacLeod, 2016; Lissenberg et al., 2013). Although trapped melt and melt-rock reaction (Lissenberg and Dick, 2008) in the lower crust and even the oceanic mantle lithosphere are increasingly recognized as additional processes contributing to MORB compositional evolution (especially in the case of incompatible trace elements), the evolved nature of MORB (Mg# ~56) compared to primary mantle melts (Mg# ~70) and the overall fractionation of incompatible elements between lower oceanic crust and upper oceanic crust (Coogan, 2014) still broadly

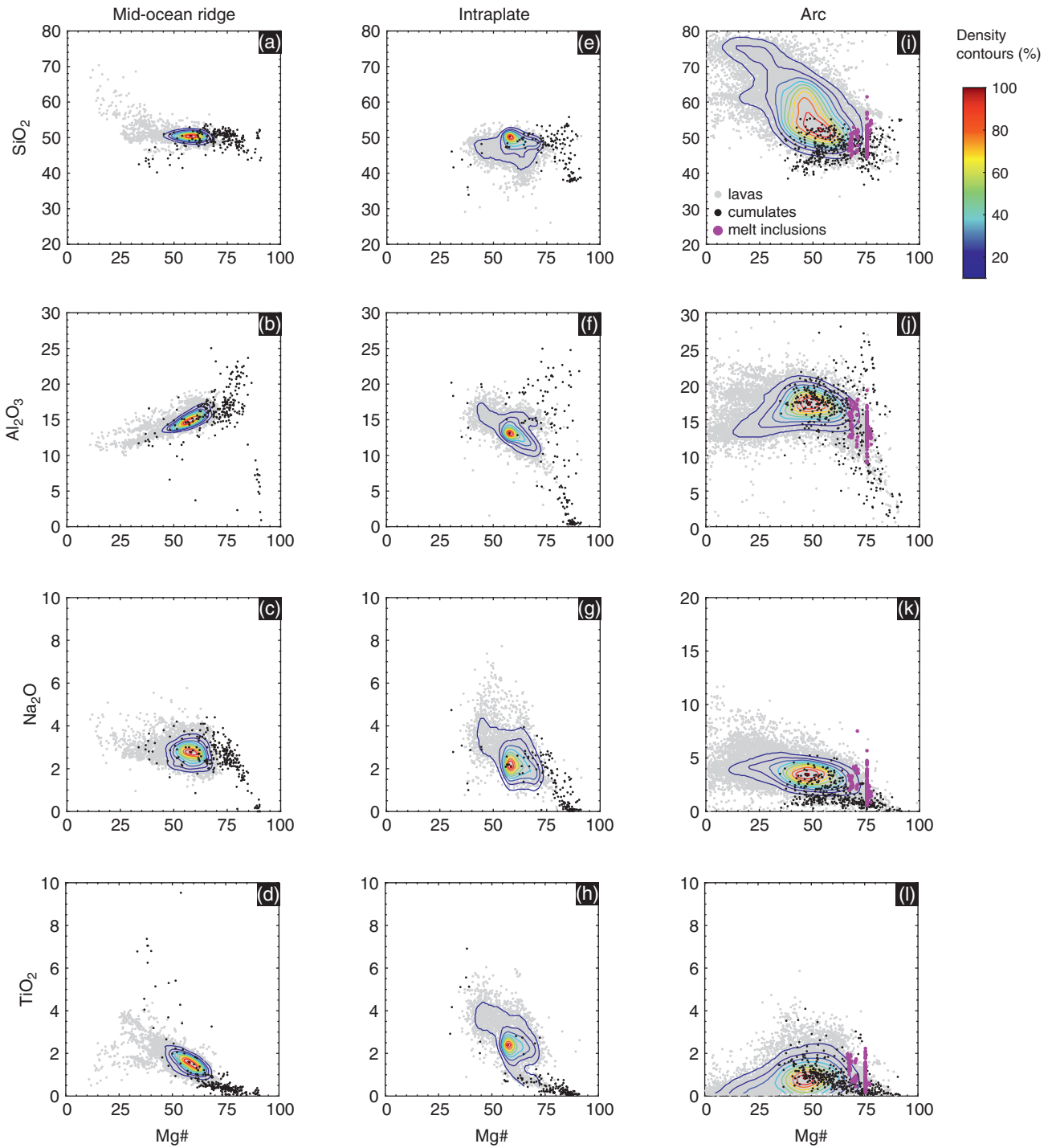


Figure 6.6 Major element oxides (wt.%) vs. Mg# for lavas (gray circles), cumulates (black circles), and melt inclusions (purple circles, from volcanic arcs only). Colored curves show the density contours (at intervals of 10%) for volcanic rocks.

support a fundamental role for crystal-liquid separation in MORB petrogenesis.

Natural MORBs and Their Cumulates. The perspective on MORB and oceanic crust generation has been largely focused on extrusive rocks due to accessibility – there are several thousands of samples of MORB (pillow lavas, glasses) but far fewer samples of complementary subcrustal MORB cumulates (Table 6.S5). A coupled perspective of both MORBs and their cumulates can also be illustrative of the factors involved in MORB evolution. In Figure 6.6 a–d, we plot both global MORBs (lavas and glasses from the database of Gale et al. (2013)) and a recently compiled global MORB cumulate database (Chin et al., 2018). Compared to other tectonic settings (discussed in later sections), the combined global database of MORBs and MORB cumulates collectively falls on tight, minimally scattered compositional trends. Throughout a wide range of Mg# (and thus differentiation index), the SiO₂ content of MORBs remains relatively constant at ~50 wt.% (Figure 6.6a). Crystal fractionation of olivine, followed by olivine + plagioclase, is apparent in plots of Al₂O₃ vs. Mg# (Figure 6.6b) and Na₂O vs. Mg# (Figure 6.6c). The consistently low K₂O vs. Mg# trend of MORB cumulates (Figure 6.S1) also suggests that crystal-liquid segregation is generally efficient (Natland and Dick, 1996). Finally, the classic tholeiitic magma series is revealed in the cumulate counterparts of MORBs – the Fe-enrichment trend of MORB is balanced by the Fe-poor nature of early MORB cumulates, and the late precipitation of Fe–Ti oxides in oxide gabbros is clearly shown in a marked increase in TiO₂ at Mg# ~50 (Figure 6.6d) (Chin et al. 2018). To first order, major element systematics of MORB + MORB cumulates supports crystal-liquid segregation along tholeiitic differentiation trends. Yet, additional observations, such as reaction textures and complex zoning patterns (Lissenberg and MacLeod, 2016), isotopic heterogeneity (Lambart et al., 2019), and phase assemblage disequilibrium (Gillis et al., 2014) in associated cumulates, seem to prevent petrologists from establishing a clear genetic link between them and MORB exclusively through fractional crystallization. Although a summary of trace element systematics of MORB and MORB cumulates is beyond the scope of this study, conflicts persist as to the roles of melt-rock reaction, and secondary melt infiltration – as shown by trace element studies – versus fractional crystallization, which is broadly supported by major element trends.

Primary MORBs. Co-variations observed in MORB suites of isotopic ratios of heavy elements (e.g., Sr, Nd, Pb, Os, Hf), being insensitive to melting and fractionation processes, are usually attributed to mantle heterogeneity (Hofmann, 2003). Additionally, timing constraints from

U-series disequilibria suggest that melt extraction from the mantle is rapid (Elliott & Spiegelman, 2003; Elkins et al., 2019 and references therein). It has been suggested that high-permeability channels from the melt source region toward the surface must exist (Kelemen et al., 1995) to satisfy these constraints. Numerical models (e.g., Weatherley and Katz, 2012, 2016) show that the formation of these channels would be facilitated by the presence of lithological heterogeneities in the mantle owing to thermal interactions between partially molten and subsolidus lithologies.

To decipher source signals, MORBs must be corrected for crystal fractionation. Once corrected for low-pressure fractionation (Klein and Langmuir, 1987), MORBs show evidence for variability in major-element compositions, likely due to compositional (e.g., Niu and O’Hara, 2008) or thermal (e.g., Dalton et al., 2014; Langmuir et al., 1992; Gale et al., 2014) variability in the source. However, Neave et al. (2019) recently showed that the major element composition of a primitive magma also affects the efficiency with which it crystallizes. Additionally, Bennett et al. (2019) demonstrated that the vertical extent of mid-ocean-ridge magmatic systems is not restricted to the first few kilometers as previously thought, but could extend down to the base of the lithospheric mantle. Thus, predominantly shallow-level fractional crystallization of MORB may be more complex than commonly thought. Finally, in comparison to ocean island and arc basalts, the range of primary MORB major-element compositions stays restricted. This restricted variability can be explained by significant low-pressure magma mixing (e.g., Shorttle, 2015; Lambart et al., 2019), and/or by similar melting reactions and melt compositions generated by pyroxenites and peridotites in the melting zone beneath mid-ocean ridges (e.g., Lambart et al., 2009).

It is beyond the scope of this short section to discuss all of these contributing factors to MORB geochemistry in detail. We refer the reader to comprehensive reviews on MORB petrogenesis in the literature (Gale et al., 2014; Langmuir et al., 1992; Lissenberg et al., 2019; Niu and O’Hara, 2008; Rampone and Hofmann, 2012; White and Klein, 2014).

6.5.2. Ocean Island Basalts

Ocean island basalts (OIBs) have received considerable attention in the literature given their potential as a proxy to unravel the composition and thermal state of the mantle. Isotopic and trace element diversity in ocean island basalts are indicative of chemically heterogeneous sources such as the presence of enriched and depleted mantle reservoirs, recycled oceanic crust, continental crust, and sediments. The readers are referred to the seminal reviews by Hofmann (1997, 2003) for details on how geochemical

characteristics of oceanic basalts give us insight into the dynamics of the mantle.

Source Lithologies of Primitive OIBs. Evidence for presence of recycled material in the mantle source of OIB comes from major-, trace-element, and isotopic compositions. In fact, previous studies have argued that the high TiO_2 contents (> 2.5 wt.%) of primary OIBs are indicative of the presence of recycled oceanic crust in the source (Figure 6.6h; Prytulak and Elliott, 2007). In addition, OIB compositions extend toward significantly lower silica contents (Figure 6.6e) than MORB (Figure 6.6a) and primary magma with very low SiO_2 concentrations (≤ 46 wt.%) also display the highest $^{206}\text{Pb}/^{204}\text{Pb}$ ratios, indicative of recycled crust in the source (Jackson and Dasgupta, 2008). Such low SiO_2 contents are observed in experimental partial melts of recycled heterogeneities such as silica-deficient pyroxenites (Hirschmann et al., 2003; Kogiso et al., 2003; Lambart et al., 2009) and carbonated oceanic crust (Mallik and Dasgupta, 2014). However, most partial melts of recycled heterogeneities do not reach Mg# 73 (Kogiso et al., 2004; Pertermann and Hirschmann, 2003b). Such high Mg# can be explained if both pyroxenite- and peridotite-derived melts contribute to OIB genesis or if the pyroxenite-derived melt reacts with the peridotite before directly contributing to magma genesis (Sobolev et al., 2005, 2007; Mallik and Dasgupta, 2012, 2013, 2014; Phipps Morgan, 2001). In fact, the process of reactive crystallization as a consequence of such a reaction between pyroxenite (eclogite)-derived melt and peridotite is described in Section 6.3 and results in MgO enrichment and SiO_2 depletion of the eclogite melt. In summary, it is widely accepted that the mantle source of OIB is heterogeneous, but the lithological nature and chemical composition of this heterogeneity is still debated (e.g., eclogite, pyroxenite, hybrid lithologies, refertilized peridotites). However, the compositions of the various mantle components control their contribution to magma genesis by affecting their melt productivity (Lambart et al., 2016) and reactivity with the surrounding mantle (Lambart et al., 2012; Mallik and Dasgupta, 2012, 2014; Sobolev et al., 2005).

To illustrate the importance of the mode of participation of the heterogeneities in the source of OIBs and their compositions, we performed the following exercise, detailed below. We remind the reader that the primary goal of this exercise is to highlight the effects of the choice of the melting model, and less to quantify the proportion of pyroxenite in the mantle source of OIB. We first consider a simple case where deeper melt derived from recycled crust is channelized through the peridotite matrix (dashed region in Figure 6.5a, b) and mixes with peridotite

partial melt at shallower depths to produce the observed primary magma compositions. We call this the *melt-melt mixing model*. In this model, melt-rock reactions are not taken into account. We consider two pyroxenite compositions: G2, a MORB-type eclogite (Pertermann and Hirschmann, 2003a) and MIX1G, the average natural pyroxenite (Hirschmann et al., 2003), and estimate their proportions in the sources of ocean islands globally as follows: we use the primary melt compositions and LAB (lithosphere–asthenosphere boundary; proxy for the final depth of melting) thicknesses at the time of volcanism for each individual ocean island as reported by Dasgupta et al., (2010) and we use PRIMELT3 MEGA.XLSM software (Herzberg and Asimow, 2015) to estimate the potential temperature (T_P) for each island. As described in Section 6.2, the melts derived from eclogitized crust (or any lithologies dominated by clinopyroxene and garnet) would have a lower Mn/Fe than partial melts of peridotite or high Mg-pyroxenite containing olivine and/or orthopyroxene. Thus, olivines that would crystallize from a melt with contributions from clinopyroxene and garnet-bearing pyroxenites would also mirror the low Mn/Fe signatures. Sobolev et al. (2007) used this observation to derive an empirical relationship between Mn/Fe of olivines in equilibrium with primary basalts and the contribution of pyroxenite in the aggregate basaltic melts (X_{melt}^{pyr}):

$$X_{melt}^{pyr} = 3.48 - 2.071 \times (100 \text{Mn/Fe}) \quad (6.2)$$

We note that Matzen et al. (2017b) demonstrated that the Mn content variation in early crystallizing olivines can be explained by partial melting of peridotite over a range of pressures, and that recycled lithologies may be present in the source but are not required to explain the Mn variations in olivines. However, the goal of the following exercise is to simply demonstrate that the estimated proportion of pyroxenite in the mantle source of OIBs varies with the choice of melting model and composition of pyroxenite.

With the PRIMELT3 MEGA.XLSM software, we calculated the Mn/Fe ratio of the olivine in equilibrium with the primary OIB and used Sobolev's proxy to estimate X_{melt}^{pyr} from the ocean islands. Finally, the proportions of pyroxenites in the source of the ocean islands (X_{source}^{pyr}) are calculated using Melt-PX (Lambart et al., 2016) and assuming the following relation that includes a first-order assumption that the proportion of pyroxenite in the melt is weighted by the abundance of pyroxenite in the source:

$$X_{melt}^{pyr} = \left(X_{source}^{pyr} \times F_f^{pyr} \right) / \left(X_{source}^{pyr} \times F_f^{pyr} + (1 - X_{source}^{pyr}) \times F_f^{per} \right) \quad (6.3)$$

with F_f^{pyr} and F_f^{per} , the final degree of melting of the pyroxenite and the peridotite, respectively, when the parcel of upwelling mantle reaches the LAB.

In a second set of calculations, we use the same constraints on T_P and P_f , but consider that melt derived from G2 first reacts with the peridotite before contributing to magma genesis (e.g., Sobolev et al., 2005). We call this the *reactive crystallization model*. Mallik and Dasgupta (2014) used published experimental results to derive an empirical relation that predicts the major element concentrations in a primary melt that forms by reactive crystallization of partial melts from eclogite-derived crust (similar to G2) as they undergo porous infiltration through a subsolidus peridotite matrix. While the proxy of Sobolev et al. (2007) is based on the trace element compositions in olivine (equation 6.1), Mallik and Dasgupta's model is based on the major element composition of the primary magmas. Using two independent models allows us to test for the consistency of such empirical relationships. In Mallik and Dasgupta's model, melt derived from the recycled crust reacts with the peridotite to form a hybrid lithology and a distinct melt. The distinct melt is in chemical and thermal equilibrium with the hybrid lithology, and this melt, by mixing with peridotite-derived melt results in the observed primary magma composition. The empirical relation of Mallik and Dasgupta provides the fraction of recycled crust-derived melt required to produce the new hybrid lithology (X^{rl}), and the proportion of melt derived from the hybrid lithology (X_{melt}^{hyb}). Using

these, we can estimate the proportion of G2 (before melting) in the source using the following equation (Sobolev et al., 2005)

$$X_{source}^{G2} = \frac{X^{rl}}{F^{G2} \times \left(\frac{1 - X_{melt}^{hyb}}{X_{melt}^{hyb}} \times \frac{F_f^{hyb}}{F_f^{per}} + \frac{1 - F^{G2}}{F^{G2}} \times X^{rl} + 1 \right)} \quad (6.4)$$

where F^{G2} (=8.9 wt.%) is the melting degree undergone by G2 before reacting with the surrounding mantle, and F_f^{hyb} and F_f^{per} , the melting degrees of the hybrid lithology and the peridotite calculated with Melt-PX when the mantle parcel reaches P_f . **Figure 6.7** presents estimated X_{source}^{pyr} for each major group of ocean islands for the two models of melting. Calculations have been performed on individual islands listed in Dasgupta et al. (2010) (see Supplementary Table 6.S9). To facilitate the comparison, we report the results averaged by island groups and the error bars show the variability between islands from the same group. Hence, a group with only a single island, such as Iceland, has no error bars. The proportion of pyroxenites in the mantle source significantly varies between the type of calculations, but also between and within each island group. Using the melt-melt mixing model and the composition G2, the average proportion of pyroxenite in the source contributing to OIB genesis is ~34 % and varies from 8% (Balleny) to 100% (Tristan da Cunha and Gough). Due to its higher solidus temperature than G2

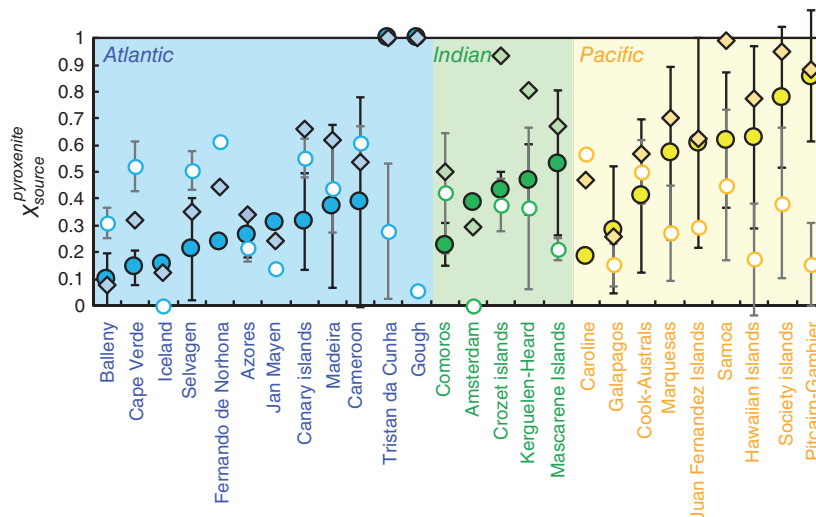


Figure 6.7 Calculated average proportions of pyroxenite in the source of the main island groups using a simple melting model (melt-melt mixing model) with either G2 (filled circles) or MIX1G (diamonds) as pyroxenitic component and using a reactive crystallization model using G2 (open circles) as pyroxenitic component. The error bars on G2 fractions correspond to one standard deviation on each island group calculated from fractions obtained for individual island (Table S9). (Black and gray error bars show variability inside each island group calculated using the melt-melt mixing model with G2 and using the reactive crystallization model, respectively).

(Lambart et al., 2016), using the composition MIX1G results in an overall higher proportion of pyroxenite in the source required to explain the Mn/Fe ratio ($\sim 54\%$ in average). Proportions of G2 estimated with the reactive crystallization model vary from 0% (Iceland and Amsterdam) to 61% (Cameroon and Fernando de Norhona). In summary, despite constraints on the mantle temperature and final pressure of melting, the choice of the model and composition of the enriched component/heterogeneity will significantly affect the estimates of its proportion in the mantle source of magmas. Despite these discrepancies, these models converge to the conclusion that a large fraction [$39 (\pm 28)\%$] of recycled material is present in the mantle source of OIB.

We also note there is no strong correlation between the estimated proportion of pyroxenite in the source and T_P (Figure 6.8a) or LAB thickness (also P_f , Figure 6.8b). This result contrasts with Sobolev et al.'s (2007) conclusions, suggesting that more energetic (i.e., hotter) plumes were more likely to carry a large amount of recycled crust into the upper mantle due to higher buoyancy. However, it is worth noting that the model of Herzberg and Asimow (2015) assumes a peridotite source. Herzberg and Asimow (2008) pointed out that if the mantle source contains pyroxenite and/or volatiles, it might result in overestimation of the calculated potential temperatures by $\sim 100^\circ\text{C}$. This is consistent with Mallik and Dasgupta (2014), who showed that an OIB source with 120–1830 ppm CO_2 (Dasgupta and Hirschmann, 2010) translate to an excess estimation of T_P at $2\text{--}73^\circ\text{C}$ (assuming 5–10% partial melting at the source and incompatible behavior of CO_2 during partial melting). This calls for a recalibration

of mantle thermometers in the future to take into account the effects of a heterogeneous and volatile-bearing mantle. In fact, a higher T_P will result in a lower contribution of the pyroxenite component in the magma (Figure 6.3). In other words, overestimating the potential temperature will also result in an overestimation of the pyroxenite fraction required in the source for a given proportion of pyroxenite in the magma. Nevertheless, consistent estimates for the potential temperatures for Hawaii and MOR by other independent methods, such as calibrating major element compositions of liquids with temperature (Lee et al., 2009; Purtika, 2008), suggest that this temperature overestimation is limited and support the decoupling between the thermal state of the lithosphere and the amount of recycled material in the mantle.

Natural OIB and Their Cumulates. OIB display a wider range of major element compositions compared to MORB, but not nearly as wide and variable as arc lavas (Figure 6.6). Both MORB and OIB show a population density peak around $\text{Mg}\# = 55$, suggesting similar degrees of crystal fractionation. Thus, we could infer that the fractionation process for MORB and OIB are relatively similar and the larger range of compositions displayed by OIB is not due to fractionation processes, but instead reflect a larger variability in primary magma compositions. In detail, major element trends of OIBs differ from MORB trends in the following ways:

1. OIB compositions extend to lower SiO_2 over similar $\text{Mg}\#$ intervals compared to MORB.
2. OIBs have higher TiO_2 (>2.5 wt.%) than MORBs (~ 2 wt.%), and much higher than arc lavas (<2 wt.%).

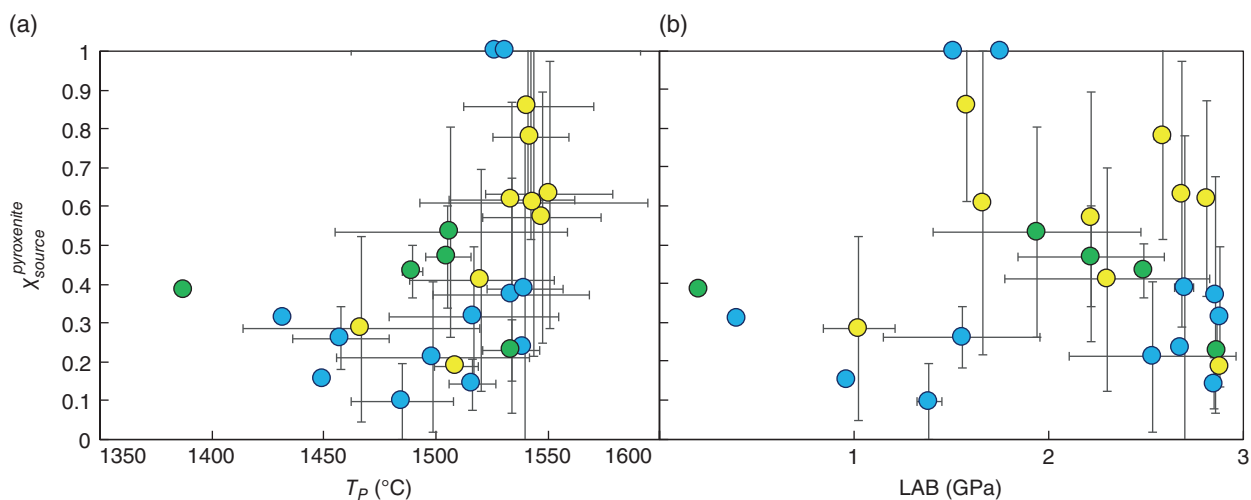


Figure 6.8 Calculated average proportions of G2 using the simple melting model (first set of calculations) as a function of the average T_P (a) and the average pressure of the LAB (b). Same color code as in Figure 6.7. The error bars correspond to the standard deviation on each island group calculated from fractions obtained for individual island.

3. Fe-enrichment is not as extreme in OIBs as it is for MORBs.
4. OIBs follow a trend of Al_2O_3 enrichment with decreasing Mg#, whereas MORBs become depleted in Al_2O_3 .
5. OIBs achieve higher and more variable Na_2O and K_2O contents compared to MORBs (Figure 6.6, Supplementary Figure 6.S1).

The spread in FeO_T , Al_2O_3 , Na_2O , and K_2O in OIBs versus MORBs likely reflects larger variability in primary OIB magma compositions. Part of this contrast of variability between OIBs and MORBs is due to the extensive magma mixing at mid-ocean ridges that significantly restricts the range of primitive compositions displayed by MORBs (Batiza, 1984; Cipriani et al., 2004). In all the binary oxide plots (Figure 6.6, middle panel), the contoured OIB data are skewed toward higher Mg# values compared to MORB, and (near-) primary magmas are commonly sampled, suggesting more limited mixing in oceanic island settings. In addition, and as previously noted, pyroxenites and peridotites produce melt with very similar major element compositions at pressures relevant for mid-ocean ridges (i.e., 1–1.5 GPa, Lambart et al., 2009; Borghini et al., 2017). However, at higher pressures, pyroxenite melting relationships are controlled by the presence of the pyroxene-garnet thermal divide (Kogiso et al., 2004) and can produce highly contrasted melt compositions. Hence, the same amount of lithological heterogeneity in the mantle source results in a higher diversity of magma compositions in OIB settings than in MORB settings. The silica-poor OIB compositions, for instance, are consistent with the partial melting of Si-deficient pyroxenites at high pressure (Hirschmann et al., 2003). As previously mentioned, the high TiO_2 contents are also consistent with the presence of recycled oceanic crust in the OIB source.

Finally, the sources of OIBs are usually assumed to be more heterogeneous than the mantle source of MORBs, mostly because primary OIBs also display larger variability in trace elements and isotopic ratios than MORBs (Hofmann, 1997, 2003). Two causes for OIBs being more heterogeneous in their source than MORBs are proposed as follows. OIBs show a wider range of T_P , spanning to higher T_P than that of MORBs (Figure 6.5a), and a hotter mantle may result in increased thermal buoyancy of dense garnet-bearing heterogeneities, and therefore, easier for such heterogeneities to accumulate within the upper mantle source of the OIBs (Brown and Lesher, 2014; Sobolev et al., 2005). Also, a thicker lithosphere beneath OIBs, and therefore a higher final pressure of melting, may preserve the chemical signature of heterogeneities better due to lesser degree of partial melting of peridotites (Sobolev et al., 2007). However, we do not observe any correlation between the proportion of chemical heterogeneity and T_P

or P_f (Figure 6.8), implying that the thermal state of the mantle and the proportion of mantle heterogeneity are decoupled. This casts doubt on the above two propositions about why MORBs may have less heterogeneous sources than OIBs. Ultimately, the answer might lie in the process of melt generation such that MORBs undergo greater magma mixing than OIBs (e.g. Zindler et al., 1984), resulting in a tighter range in the concentrations of trace elements and isotopic ratios, and the presence of variability in geochemical signatures in OIBs (or their lack in MORBs) may not be an indicator of how heterogeneous their sources are.

6.5.3. Arc Magmas

Arc Magma Genesis – A Complexity of Factors. Compared to the relatively simple geometry of spreading centers at mid-ocean ridges and the nontectonic origin of OIBs, the geodynamic setting of volcanic arcs is far more complex, involving multiple moving parts: a hydrated downgoing plate, a convective mantle wedge continuously fluxed by volatiles from the downgoing plate, and overriding plate lithosphere, which itself may be old and heterogeneous (e.g., at continental arcs). As a result, arc magmas worldwide show incredible compositional diversity compared to MORBs and OIBs, reflecting the interplay of the different tectonic components involved. Arc magmas range from basalts (40 – 52 wt.% SiO_2) to rhyolites (>70 wt.% SiO_2) (Figure 6.6i). Mg#'s of arc volcanic rocks range from <10 to ~80 (Figure 6.6, right panel). Such compositional variation is attributed to both primary processes – e.g., those involving melting and melt-rock interaction of peridotitic source rocks in the mantle wedge (and generation of primary melts *sensu stricto*), and secondary processes – such as fractional crystallization and assimilation of preexisting crust. In addition, there is increasing recognition that partial melting and involvement of nonperidotitic source rocks, such as the downgoing, metamorphosed oceanic slab and sediments, may also contribute to arc magma genesis (as discussed in section 4.3.3). Below, we review experimental constraints on primary melt generation in arcs, discuss recent advances in nonperidotitic contributions to arc magmatism, and summarize key major element compositional trends in natural arc magmas and their cumulates.

Experimental Perspectives on Primary Arc Magma Generation: Melting of the Peridotitic Mantle Wedge. We will first investigate the formation of primary arc magmas derived from the peridotitic mantle wedge. The geodynamic scenario for such melting, which constitutes the majority of arc magmatism, is devolatilization of the downgoing slab, which induces hydrous flux melting of the dominantly peridotitic mantle wedge (Grove et al., 2006; Till et al., 2012). The chemistry of primary arc

magmas depends on the pressure–temperature conditions of partial melting in the mantle, composition of sub-arc peridotite and slab fluxes, and the H₂O content, and oxygen fugacity at the source of melting. Previous experimental studies have investigated the effect of H₂O on partial melting of peridotite (e.g., Gaetani and Grove, 1998; Grove et al., 2006; Hirose, 1997; Hirose and Kawamoto, 1995; Tenner et al., 2012; Till et al., 2012), and mixtures of hydrous siliceous crustal melt and peridotite (Mallik et al., 2015, 2016; Pirard and Hermann, 2014, 2015; Prouteau et al., 2001; Rapp et al., 1999). The partial melts span a wide range in total alkali-silica space covering the entire spectrum of primary arc magmas from basaltic to andesitic and basaltic trachy-andesitic (Figure 6.9a).

Given the importance of H₂O in subduction zone magmatism, it is important to constrain the effect that H₂O has on the chemistry of magmas produced in the sub-arc mantle and experiments investigating partial melting behavior of the sub-arc mantle can give us insight into this. Experimental melt compositions that coexist with both olivine and orthopyroxene (the two most abundant minerals in the upper mantle) are compiled and their H₂O contents are plotted against their silica contents (Figure 6.9b). Two trends emerge. Melt compositions produced at pressures lower than 2 GPa show increasing silica contents with H₂O, whereas, for melt compositions produced at pressures greater than 2 GPa, silica contents are anticorrelated with H₂O (Figure 6.9b). This observation indicates that pressure and H₂O contents affect the chemistry of partial melts, and approach toward the development of a model of subduction zone melting requires that we understand the reason behind such trend. Mallik et al. (2016) explained that the increasing SiO₂ trend at lower pressures is caused by the expansion of olivine stability over orthopyroxene with H₂O. The reverse trend at higher pressures is caused by an expanded orthopyroxene stability field over olivine. Thus, future development of a holistic model of partial melting of the mantle in subduction zones requires in-depth understanding of how phase equilibria are affected by such factors. While the effect of pressure, temperature, and bulk composition (including H₂O content) have been investigated in previous studies, the effect of oxygen fugacity on differentiation in arcs is still debated. It has long been known that arc lavas are more oxidized than MORBs (Carmichael, 1991), but the origin of the oxidized signature remains debated. Analyses of Fe³⁺/total Fe in primitive melt inclusions from subduction zones also indicate that arc lavas are more oxidized than mid-ocean ridge basalts and back-arcs, suggesting an origin from a mantle wedge that has been oxidized by slab-derived materials (Brounce et al., 2014, 2015; Grocke et al., 2016; Kelley and Cottrell, 2009; Tollan and Hermann, 2019). Other studies using redox-sensitive trace elements (Lee et al., 2005; Lee

et al., 2010) and isotopic constraints (Dauphas et al., 2009) challenge this hypothesis, and suggest instead that arc lavas acquired their oxidized state via fractional crystallization (Chin et al., 2018; DeBari and Greene, 2011; Jagoutz, 2010; Lee et al., 2006; Tang et al., 2018, 2019), mixing and crustal assimilation (Grove et al., 1982; Patiño Douce, 1999), or upper crustal differentiation and open system processes (Blatter et al., 2013; Humphreys et al., 2015).

Melting of Nonperidotitic Sources in Arc Magma Generation.

Downgoing plate contributions to fluid flux and sediment melt diapirs. Based on the similarity of geochemical signatures between subducting sediment and volcanic arc lavas (Plank, 2005), and reproduction of the geochemistry of arc basalts by dehydration of subducted slab (sediments and hydrothermally altered oceanic crust) along with subsequent metasomatism of the sub-arc mantle (Tatsumi and Kogiso, 2003), the involvement of the subducted slab in arc magma production is well-established. Aqueous fluids released from the dehydration of subducted sediments and altered oceanic crust lower the solidus temperatures of sub-arc mantle peridotite due to cryoscopic depression of melting temperatures by H₂O flux. Also, these aqueous fluids metasomatize or alter the mineralogy of the sub-arc mantle to produce hydrous minerals such as mica (phlogopite), amphibole, and chlorite. The solidus of such metasomatized peridotites are also lower than that of nominally anhydrous peridotite (Figure 6.9c). The latest global thermal models of subduction (Syracuse et al., 2010) show that the solidi of fluid-fluxed peridotite and metasomatized peridotite lie in the thermal regime of the mantle wedge, hence, the sub-arc mantle undergoes fluid-fluxed partial melting. However, it is interesting that fluxing fluids from the dehydration of the slab also lower the solidus of the sediments and altered oceanic crust (Figure 6.9c). The latest global thermal models of subduction show that for intermediate subduction zones (such as Guatemala/El Salvador) and hot subduction zones (such as Central Cascadia), the aqueous fluid-fluxed solidi of sediments and altered oceanic crust intersect the pressure-temperature paths of the slabs (Figure 6.9c). This implies that sediments and altered oceanic crust partially melt in intermediate to hot subduction zones, and the partial melts are expected to participate in primary arc magma formation. Based on geochemical proxies such as elevated Th/Yb and low Lu/Hf, contribution of slab partial melts to the source of arc magma have been inferred for Central Mexican Volcanic Belt (Cai et al., 2014), Sunda and Lesser Antilles

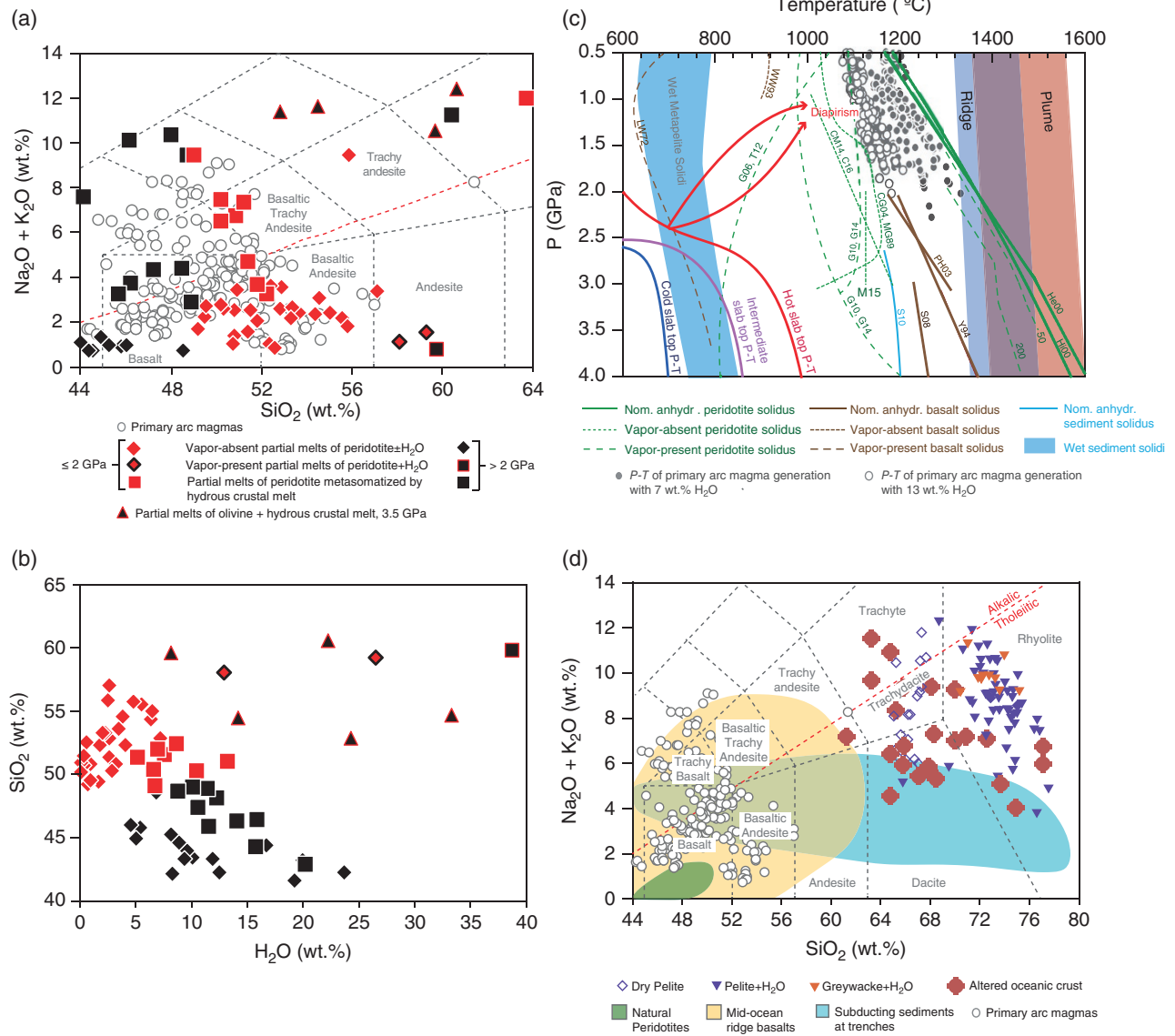


Figure 6.9 (a) Experimentally produced peridotite partial melts without H_2O , with H_2O but no co-existing aqueous vapor, and coexisting with aqueous vapor plotted in SiO_2 versus total alkali space. Partial melts of peridotite metasomatized by hydrous crustal partial melts are also plotted. (b) H_2O versus SiO_2 concentrations of experimentally derived partial melts in equilibrium with olivine and orthopyroxene. This subplot is a modification of Figure 6.7. All compositions plotted in the subplots have been normalized to a volatile-free basis. (c) P-T space showing the solidi of nominally anhydrous peridotite, peridotite with 50 and 200 ppm H_2O , wet but vapor absent peridotite solidi, nominally anhydrous oceanic crust or basalt, vapor present basalt, wet but vapor absent basalt, nominally anhydrous sediments and wet sediments. The ridge and plume adiabats as well as the hot, intermediate and cold subduction geotherms are the same as in Figure 6.5. Primary arc magma compositions with 7 and 13 wt.% H_2O , corrected to be in equilibrium with olivine of Mg# 91 are also plotted. (d) SiO_2 versus total alkali ($\text{Na}_2\text{O} + \text{K}_2\text{O}$) space with partial melts of sediments and altered oceanic crust produced in experiments, primary arc magmas (same as plotted in panel a), and naturally occurring peridotites, mid-ocean ridge basalts and subducting sediments (are plotted. The classifications of rock types in the figure are based on Le Bas et al., 1986. For details about primary arc magma calculation and the references for the sources of data, see Supplementary Text S1. Source: (a, b) Mallik et al. (2016). (d) Le Bas et al., 1986.

(Woodhead et al., 2001), and the Marianas (Tamura et al., 2014)

The following two observations can be made about partial melt of subducted crust and the dynamics of subduction zones. First, the partial melts of subducted sediments and altered oceanic crust are much more siliceous ($\text{SiO}_2 > 60$ wt.%) than primary arc basalts (Figure 6.9d); hence, by themselves cannot explain the chemistry of primary magmas produced in subduction zones. Also, the partial melts are more siliceous than partial melts derived from peridotites (Figure 6.9d). Second, according to the thermal models of subduction zones, the isotherms are very closely spaced along the slab top, thus, the slabtop can be as much as 400 °C colder than the overlying sub-arc mantle within a narrow distance of less than around 25 km (Syracuse et al., 2010). These observations imply that slab-derived partial melts are colder (i.e., in thermal disequilibrium) and also chemically distinct (i.e. in chemical disequilibrium) from the adjacent sub-arc mantle. Therefore, as described before, slab partial melts undergo reactive crystallization as they react with the overlying sub-arc mantle (Johnston and Wyllie, 1989; Mallik et al., 2015, 2016; Prouteau et al., 2001; Rapp et al., 1999; Sekine and Wylle, 1982). Previous studies have shown that such melt-rock reaction produces geochemical signatures of certain primitive arc magma types such as high Mg-andesites and dacites (Prouteau et al., 2001; Tatsumi, 2001; Kepezhinskis et al., 1996), adakites (Rapp et al., 1999) and potassic to ultra-potassic arc magmas (Mallik et al., 2015, 2016).

Geodynamics of subduction zones are further complicated by the potential for buoyant diapirs rising from the subducted slab. As shown by previous studies from geodynamic simulations and geochemistry (Behn et al., 2011; Castro and Gerya, 2008; Marschall and Schumacher, 2012; Nielsen and Marschall, 2017), a *mélange* comprised of physical mixtures of sediment, altered oceanic crust and metasomatized slab lithosphere can advectively ascend into the overlying hotter mantle wedge from the subducted slab, where it can partially melt and contribute to primary arc magma formation (Figure 6.9c). Partial melting of physical mixtures of *mélange*-like compositions and metasomatized lithosphere have been shown to produce alkaline arc magmas (Cruz-Urbe et al., 2018) and ultrapotassic to potassic magmas in arcs and cratons (Förster et al., 2017, 2018; Wang et al., 2017). Finally, the hybridization of the mantle wedge by melts derived from *mélange* can also produce a range of primary arc magmas, from tholeiitic to calc-alkaline compositions (Codillo et al., 2018).

Upper plate processes. In addition to contributions from the downgoing slab, arc magmas may also be influenced by processes in the upper (overriding) plate

lithosphere. Since the seminal work of Hildreth and Moorbath (1988) in the Chilean Andes, the concept of a MASH (mixing, assimilation, storage, homogenization) zone in the overriding plate has become widely accepted and refined by experimental petrology and geodynamic modeling. The most recent iteration of the MASH hypothesis, Annen et al.'s (2006) Deep Crustal Hot Zone model, involves both fractional crystallization of primary arc magmas in the uppermost mantle and deep crust, as well as partial melting of preexisting crustal rocks in the upper plate. Although by no means an exhaustive list, detailed field studies of arc plutonic rocks from Kohistan (Jagoutz, 2010), Famatinian arc, Argentina (Otamendi et al., 2012; Walker Jr et al., 2015), as well as studies of deep crustal cumulate xenoliths from the Sierra Nevada, California (Ducea, 2002; Lee et al., 2006), Arizona (Erdman et al., 2016) support a primary role for crystallization-differentiation as the mechanism of growing new arc crust, and support the petrological requirement that mafic to ultramafic cumulates be the necessary complements to silicic, calc-alkaline batholiths that are the hallmark of convergent margins. Crystal fractionation of so-called “primary” arc magmas may occur even deeper than the lower crust, as evidenced by residual arc mantle lithosphere that experienced refertilization by basaltic arc melts, resulting in the precipitation of clinopyroxene and garnet (arclogites) as the melts evolved at depth (Chin et al., 2014; Chin et al., 2016). However, similar pyroxenite enrichment can also occur via melt-rock reaction in the convecting mantle wedge (Berly et al., 2006; Green et al., 2004; Kelemen et al., 1998), and recent studies of global arc volcano trace element systematics suggest that the mantle wedge itself may be periodically metasomatized by enriched continental lithosphere that is eroded during arc magmatism (Turner and Langmuir, 2015). It is thus difficult to separate the contributions from a “contaminated” wedge vs. lithospheric components by using arc volcanic rocks and shallow plutons alone, since both experienced protracted evolution throughout the arc crust, and therefore likely record a combination of both processes (Farmer et al., 2013). Nevertheless, mass balance constraints for the bulk continental crust require at least a 2:1 (but likely to be 10:1 or more) ratio of mafic-ultramafic cumulates and restites as counterparts to the silica-rich arc/continental crust; provided those cumulates are not always convectively removed due to negative buoyancy, they make up the greatest contribution to the overriding arc crust. This, combined with the long-lived (but episodic) nature of continental arcs (Cao et al., 2017; Ducea et al., 2015), indicates that magmatic differentiation and the fractionation of massive amounts of mafic cumulates must be a primary driver of the compositional evolution of arc magmas. Thus, in addition to assimilation and partial melting of preexisting (and

usually older) crustal rocks of the upper plate lithosphere, partial melting of upper plate cumulates may also contribute to the wide variation in arc magma compositions. Foundering, eclogitized lower crust may heat up and partially melt as it descends into the mantle (Gao et al., 2004; Lustrino, 2005), providing yet another way to generate buoyant, silica-rich melts that rise up and become incorporated into the continental crust. As discussed in an earlier section, the solidus of pyroxenitic assemblages is lower than that of peridotitic ones, and so pyroxenites are more easily melted. Experimental partial melts of clinopyroxene-rich cumulates similar to those found in arcs (Médard et al., 2005) show that their partial melts are Ca-rich and Si-undersaturated and similar to some primitive arc melt inclusions (Schiano et al., 2000).

Natural Arc Magmas and Their Cumulates. Erupted primary lavas in volcanic arcs are rare, as they are usually modified by secondary processes as the melt migrates from the mantle source to eruption at the surface. Direct samples of putative primary arc melts occur as melt inclusions hosted in high Mg# olivine phenocrysts. Such high Mg# (89–92) olivines are in equilibrium with mantle peridotite, and thus it is assumed that any liquid trapped in such olivines are also mantle-derived and therefore primary. However, olivine-hosted melt inclusions are not sampled in every arc, are not as abundant as erupted primitive lavas, and also may experience diffusive re-equilibration, potentially compromising any primary chemical signatures (Gaetani et al., 2012). In the righthand panels of Figure 6.6, we plot nearly 40,000 compositions of arc volcanic rocks downloaded from the GEOROC online database, nearly 400 cumulates of arc magmas previously compiled by Chin et al. (2018), and 205 primary arc melt inclusion compositions (see Supplementary Table 6.S5 for references). One of the clearest features of the data to emerge from a simple visual inspection of the major element plots is that, unlike the tightly coherent trends described by MORBs and their cumulates, arc volcanic rocks show considerable scatter and a much wider range in nearly every major element. By contrast, melt inclusions plot in a restricted Mg# window but interestingly span a wide range of compositions in certain elements, notably CaO, K₂O, and Na₂O (Figure 6.6k, S1). Such large variations at high Mg# suggest primary melts sample heterogeneous sources in the mantle wedge and over-riding plate (Sadofsky et al. 2008). Recent studies on arc lavas using trace element systematics also point to an important role of mantle wedge heterogeneity in generating the diversity of arc magma compositions (Turner and Langmuir, 2015; Turner et al., 2016). The utility of major elements in fingerprinting subduction fluxes is limited compared to the sensitivities of trace element compositions, trace element ratios, and isotopic data, but a

comprehensive survey of all the available data is beyond the scope of this contribution.

As seen in the righthand panels of Figure 6.6, arc cumulates also generally span a larger compositional variation than MORB and OIB cumulates. This observation implies that arc magmas and their cumulates reflect more complex petrogenesis compared to MORBs and OIBs, as discussed earlier. For example, despite the highest concentration of arc lavas falling within a similar range of SiO₂ content as MORB and OIB (darkest red contours in Figure 6.6i), the contoured arc lava data skew toward higher SiO₂, in contrast to MORB and OIB, the former having a more-or-less symmetrical distribution in SiO₂ and the latter skewing towards lower SiO₂. One explanation for the overall higher SiO₂ in arc lavas is that they experience a greater degree of fractional crystallization and/or assimilation of crustal rocks, starting at fairly primitive compositions and therefore deep and early in their evolution (Lackey et al., 2005; Nelson et al., 2013).

When arc volcanic rocks and arc cumulates are viewed together, several complementary trends consistent with an important role for fractional crystallization emerge. In the contoured data of CaO vs. Mg#, most arc volcanic rocks have CaO <10 wt.%, but MORBs have CaO >10 wt.% (Supplementary Figure 6.S1a.g). This can be explained by the early precipitation of anorthite and/or clinopyroxene as a major cumulate mineral in arcs, whereas in mid-ocean ridges plagioclase saturates early and tends to be albitic (Beard, 1986; Chin et al., 2018; Grove et al., 1993). This is also borne out in the systematics of Al₂O₃ and Na₂O (Figure 6.6j,k). MORB cumulates define a tight trend in Al₂O₃ vs. Mg# space and show a peak in Al₂O₃ at high Mg# (Figure 6.6b), whereas arc cumulates define a looser trend with a weaker peak at high Mg# (Figure 6.6j). Indeed, the median Al₂O₃ of the most primitive MORB cumulates (Mg# 80–90) is substantially higher than arc cumulates in the same Mg# range (Chin et al. 2018 and Figure 6.3 therein). These cumulate systematics subsequently control the Al₂O₃ content of differentiating arc magmas. In MORBs, Al₂O₃ defines a tight, decreasing trend as Mg# decreases, reflecting the simple mineralogy of MORB cumulates (gabbroic). By contrast, Al₂O₃ in arc volcanic rocks span a wide range of Al₂O₃ (10–20 wt.%) with decreasing Mg#, indicating multiple mineral contributions (pyroxene, amphibole, etc.) to the fractionating cumulate assemblage in contrast to the simple gabbroic mineralogy of MORB cumulates, including an important role for garnet (Tang et al. 2018), especially in continental arcs. Most arc lavas have Al₂O₃ of 16–18 wt.% (e.g., the classic “high alumina arc basalts,” Crawford et al., (1987)) compared to MORBs, which peak below 16 wt.% Al₂O₃, and, importantly, skew toward lower Al₂O₃ compared to arc lavas (Figure 6.6j). The plot of Na₂O vs. Mg# also reflects

the plagioclase-dominated gabbroic cumulates of MORB compared to arcs and complementary trends in the lavas. Lastly, as discussed in the MORB section, the classic tholeiitic vs. calc-alkaline trends clearly emerge in comparing MORBs vs. arcs. The diagnostic feature of calc-alkaline lavas is Fe-depletion with increasing differentiation (Supplementary Figure 6.S1i), attributed to crystal fractionation of Fe- and Ti-bearing phases such as garnet and magnetite (Figure 6.6l).

6.6. FUTURE DIRECTIONS

The summary of experimental data presented in Section 6.2 and in previous review articles (Kogiso et al., 2004; Lambart et al., 2013) emphasize the large range of compositions covered by the potential lithologies present in the mantle source of magmas. This makes it challenging to determine a unique proxy as a tracer of heterogeneities in the mantle source of magmas. In addition, calculations presented in Section 6.4.2 highlight that different proxies can result in different estimates of the nature and proportion of the heterogeneity in the mantle. Similarly, compositional observations of natural MORB and their cumulates point out a decoupling between the major element compositions that support fractional crystallisation as the main process of magma differentiation, and trace element compositions that indicate the strong influence of porous flow and melt-rock interactions. Hence, it is crucial for the geochemical community to concentrate their future efforts into the construction of a comprehensive dataset, with studies combining major-element, trace element, and isotopic analyses. In order to correctly interpret the geochemical dataset, we need parameterizations and geochemical models that take into account such a large range of compositions. Hence, we need better constraints on the role of the lithological composition on partial melting behavior and element partitioning, especially in the presence of volatiles. As far as volatiles are concerned, the focus has largely been on H₂O and/or CO₂, but a growing consensus has emerged that other species, notably S and N are important contributors to the solid Earth volatile recycling budget (Evans, 2012; Cartigny and Marty, 2013; Mallik et al., 2018), and so also influence the partial melting behavior and consequent differentiation of the upper mantle. Future studies should not only investigate the effect of S and N, but should also constrain the effect of the presence of mixed volatile species of H-C-N-S on partial melting of the upper mantle.

As mentioned earlier in this chapter, the thermal state of the mantle, expressed in terms of potential temperature (T_P) is an extremely important aspect in the chemical differentiation of the Earth. T_P is currently estimated based

on the magnesian content of erupted primary lavas, assuming that a hotter mantle produces magmas with higher magnesia contents (e.g. Herzberg et al., 2007; Herzberg and Gazel, 2009). It has been shown that melt-rock reactions involving heterogeneities in the upper mantle and the presence of volatiles produce magnesia-rich magmas at colder mantles than that predicted earlier (Mallik and Dasgupta, 2014). This begs for further studies that would calibrate a mantle thermometer to estimate T_P taking into account factors such as melt-rock reactions and influence of volatiles, else we may overpredict the thermal state of the Earth's mantle beneath tectonic settings.

As far as subduction zones are concerned, there is broad agreement on the behavior of aqueous fluids and partial melts from the subducting slab and their effects on generation of arc magmas, and transfer of elements from the subducted crust to the mantle. However, one of the least understood phases in subduction zones are supercritical fluids, which are the products of complete miscibility between aqueous fluids and partial melts. The reason why supercritical fluids remain so poorly understood is due primarily to experimental difficulty in studying them. Most experimental techniques employ ex-situ analyses of samples, where the sample, after being "cooked" at the P-T of interest, are quenched to room P-T and investigated, assuming that modifications during the quenching process are not significant. Kessel et al. (2004) went a step further and cryogenically preserved the fluid in their quenched capsules during laser ablation mass spectroscopy, in order to preserve the fluid phase in their capsules. However, supercritical fluids may separate into two phases during the quenching, rendering ex-situ analyses of this phase nearly impossible. A few studies have experimentally demonstrated the closing of the miscibility gap between aqueous fluids and silicate melts under P-T conditions applicable to subduction zones (Bureau and Keppler, 1999; Kawamoto et al., 2012; Mibe et al., 2007, 2011; Ni et al., 2017; Shen and Keppler, 1997) using a Bassett-type hydrothermal diamond anvil cell or X-ray radiography using a multianvil apparatus. However, the current state-of-the-art in such in-situ experimental techniques have limitations in terms of chemical analyses that can be performed to constrain how these fluids may affect element transport in subduction zones. A future challenge for experimental geoscientists would be to improve the techniques of in-situ analysis such that supercritical fluids can be investigated better.

Finally, melt-rock interactions are increasingly recognized as important petrogenetic processes, both in the mantle and in the crust, across all geological settings. One of the major challenges faced by the experimental community is to develop tools and provide experimental constraints to predict the system behavior during these

interactions including complex feedback between compositions and melting and crystallization behaviors and kinetics of interaction during melt transport. Some of the questions we need to address are: (1) the required conditions for the preservation of the source signal in primary magmas, (2) the effect of chromatographic melting on the range of isotopic compositions and major and trace elements concentrations in MORB and OIB (Navon and Stolper, 1987), (3) the mechanisms of transition between the various types of magma flow in the upper mantle (porous versus focused flow; e.g., Kelemen et al., 1997), and (4) the implications of crustal melt-rock interaction on the composition of the cumulate minerals and lavas (e.g., Lissenberg et al., 2013).

ACKNOWLEDGMENTS

All three authors have contributed equally to the manuscript. AM thanks the editors for their invitation to contribute to this special volume and Katie Kelley for discussions about sources of primary arc melt inclusion data. EJC thanks GM Bybee, K Shimizu, and CTA Lee for informal discussions regarding deep crustal arc cumulates. SL was supported by the NSF grant EAR-1834367. We also thank the reviewers for their constructive comments, especially the thorough review from Fred Davis, which really helped improve the manuscript. The data supporting the findings of this study are available in the Figshare data repository: Text 6.S1, Figure 6.S1 and Table 6.S5: <https://doi.org/10.6084/m9.figshare.9926867.v1>;

Tables 6.S1–S4 and 6.S6–S9: <https://doi.org/10.6084/m9.figshare.9926885.v1>

REFERENCES

- Adam, J., Green, T.H., & Day, R.A. (1992). An experimental study of two garnet pyroxenite xenoliths from the Bullenmerri and Gnotuk Maars of western Victoria, Australia. *Contributions to Mineralogy and Petrology* 111, 505–514.
- Albarede, F. (1985). Regime and trace-element evolution of open magma chambers. *Nature* 318, 356.
- Annen, C., Blundy, J.D., & Sparks, R.S.J. (2006). The Genesis of Intermediate and Silicic Magmas in Deep Crustal Hot Zones. *Journal of Petrology* 47, 505–539.
- Baker, M., Hirschmann, M., Ghiorso, M., & Stolper, E. (1995). Compositions of near-solidus peridotite melts from experiments and thermodynamic calculations. *Nature* 375, 308.
- Baker, M.B., & Stolper, E.M. (1994). Determining the composition of high-pressure mantle melts using diamond aggregates. *Geochimica et Cosmochimica Acta* 58, 2811–2827.
- Batiza, R. (1984). Inverse relationship between Sr isotope diversity and rate of oceanic volcanism has implications for mantle heterogeneity. *Nature* 309, 440.
- Beard, J.S. (1986). Characteristic mineralogy of arc-related cumulate gabbros: implications for the tectonic setting of gabbroic plutons and for andesite genesis. *Geology* 14, 848–851.
- Behn, M.D., Kelemen, P.B., Hirth, G., Hacker, B.R., & Massonne, H.-J. (2011). Diapirs as the source of the sediment signature in arc lavas. *Nature Geoscience* 4, 641–646.
- Bennett, E. N., Jenner, F. E., Millet, M. A., Cashman, K. V., Lissenberg, C. J. (2019). Deep roots for mid-ocean-ridge volcanoes revealed by plagioclase-hosted melt inclusions. *Nature* 572(7768), 235–239.
- Berly, T.J., Hermann, J., Arculus, R.J., & Lapiere, H. (2006). Supra-subduction zone pyroxenites from San Jorge and Santa Isabel (Solomon Islands). *Journal of Petrology* 47, 1531–1555.
- Blatter, D., Sisson, T., & Hankins, W.B. (2013). Crystallization of oxidized, moderately hydrous arc basalt at mid- to lower-crustal pressures: implications for andesite genesis. *Contributions to Mineralogy and Petrology* 166, 861–886.
- Bodinier, J.-L., & Godard, M. (2003). Orogenic, ophiolitic, and abyssal peridotites. *Treatise on Geochemistry* 2, 568. doi:10.1016/B0-08-043751-6/02004-1
- Borghini, G., Fumagalli, P., & Rampone, E. (2017). Partial melting of secondary pyroxenite at 1 and 1.5 GPa, and its role in upwelling heterogeneous mantle. *Contributions to Mineralogy and Petrology* 172, 70–70.
- Brounce, M., Kelley, K.A., Cottrell, E., & Reagan, M.K. (2015). Temporal evolution of mantle wedge oxygen fugacity during subduction initiation. *Geology* 43, 775–778.
- Brounce, M.N., Kelley, K.A., Cottrell, E. (2014). Variations in $Fe^{3+}/\sum Fe$ of Mariana Arc Basalts and Mantle Wedge fO_2 . *Journal of Petrology* 55, 2513–2536.
- Brown, E. L., & Leshner, C. E. (2014). North Atlantic magmatism controlled by temperature, mantle composition and buoyancy. *Nature Geoscience* 7, 820–824.
- Bureau, H., & Keppler, H. (1999). Complete miscibility between silicate melts and hydrous fluids in the upper mantle: experimental evidence and geochemical implications. *Earth and Planetary Science Letters* 165, 187–196.
- Cai, Y., LaGatta, A., Goldstein, S.L., Langmuir, C.H., Gómez-Tuena, A., Martín-del Pozzo, A.L., & Carrasco-Núñez, G. (2014). Hafnium isotope evidence for slab melt contributions in the Central Mexican Volcanic Belt and implications for slab melting in hot and cold slab arcs. *Chemical Geology* 377, 45–55.
- Cao, W., Lee, C.-T.A., & Lackey, J.S. (2017). Episodic nature of continental arc activity since 750 Ma: A global compilation. *Earth and Planetary Science Letters* 461, 85–95.
- Carmichael, I.S.E. (1991). The redox states of basic and silicic magmas: a reflection of their source regions? *Contributions to Mineralogy and Petrology* 106, 129–141.
- Cartigny, P., & Marty, B. (2013). Nitrogen Isotopes and Mantle Geodynamics: The Emergence of Life and the Atmosphere–Crust–Mantle Connection. *Elements* 9(5), 359–366.
- Castro, A., Gerya, T.V. (2008). Magmatic implications of mantle wedge plumes: Experimental study. *Lithos* 103, 138–148.
- Chase, C.G. (1981). Oceanic island Pb: Two-stage histories and mantle evolution. *Earth and Planetary Science Letters* 52, 277–284.

- Chen, C., Liu, Y., Foley, S.F., Ducea, M.N., Geng, X., Zhang, W., Xu, R., Hu, Z., Zhou, L., & Wang, Z. (2017). Carbonated sediment recycling and its contribution to lithospheric refertilization under the northern North China Craton. *Chemical Geology* 466, 641–653.
- Chen C.-H. & Presnall D. C. (1975). System magnesium ortho-silicate-silicon dioxide at pressures up to 25 kilobars. *American Mineralogist* 60, 398–406.
- Chin, E.J., Lee, C.-T.A., & Barnes, J.D. (2014). Thickening, refertilization, and the deep Lithosphere filter in continental arcs: Constraints from major and trace elements and oxygen isotopes. *Earth and Planetary Science Letters* 397, 184–200.
- Chin, E.J., Shimizu, K., Bybee, G.M., & Erdman, M.E. (2018). On the development of the calc-alkaline and tholeiitic magma series: A deep crustal cumulate perspective. *Earth and Planetary Science Letters* 482, 277–287.
- Chin, E.J., Soustelle, V., Hirth, G., Saal, A., Kruckenberg, S.C., & Eiler, J. (2016). Microstructural and geochemical constraints on the evolution of deep arc Lithosphere. *Geochemistry, Geophysics, Geosystems* 17, 2497–2521, doi:10.1002/2015GC006156.
- Cipriani, A., Brueckner, H.K., Bonatti, E., & Brunelli, D. (2004). Oceanic crust generated by elusive parents: Sr and Nd isotopes in basalt-peridotite pairs from the Mid-Atlantic Ridge. *Geology* 32, 657–660.
- Codillo, E. A., Le Roux, V., & Marschall, H. R. (2018). Arc-like magmas generated by mélange-peridotite interaction in the mantle wedge. *Nature Communications* 9(1), 2864.
- Coogan, L.A. (2014). 4.14 – The Lower Oceanic Crust A2 – Holland, Heinrich D, in: Turekian, K.K. (Ed.), *Treatise on Geochemistry* (Second Edition). Elsevier, Oxford, pp. 497–541.
- Coogan, L., O’Hara, M. (2015). MORB differentiation: In situ crystallization in replenished-tapped magma chambers. *Geochimica et Cosmochimica Acta* 158, 147–161.
- Coumans, J.P., Stix, J., Clague, D.A., Minarik, W.G., & Layne, G.D. (2016). Melt-rock interaction near the Moho: Evidence from crystal cargo in lavas from near-ridge seamounts. *Geochimica et Cosmochimica Acta* 191, 139–164.
- Crawford, A., Falloon, T., & Eggins, S. (1987). The origin of island arc high-alumina basalts. *Contributions to Mineralogy and Petrology* 97, 417–430.
- Cruz-Urbe, A.M., Marschall, H.R., Gaetani, G.A., & Le Roux, V. (2018). Generation of alkaline magmas in subduction zones by partial melting of mélange diapirs—An experimental study. *Geology* 46 (4): 343–346.
- Dalton, C.A., Langmuir, C.H., & Gale, A. (2014). Geophysical and Geochemical Evidence for Deep Temperature Variations Beneath Mid-Ocean Ridges. *Science* 344, 80–83.
- Dasgupta R. & Hirschmann M. M. (2010). The deep carbon cycle and melting in Earth’s interior. *Earth Planet. Sci. Lett.* 298, 1–13.
- Dasgupta, R., Hirschmann, M.M., & Withers, A.C. (2004). Deep global cycling of carbon constrained by the solidus of anhydrous, carbonated eclogite under upper mantle conditions. *Earth and Planetary Science Letters* 227, 73–85.
- Dasgupta, R., Jackson, M.G., & Lee, C.-T.A. (2010). Major element chemistry of ocean island basalts -- Conditions of mantle melting and heterogeneity of mantle source. *Earth and Planetary Science Letters* 289, 377–392.
- Dasgupta R., Mallik A., Tsuno K., Withers A. C., Hirth G. and Hirschmann M. M. (2013). Carbon-dioxide-rich silicate melt in the Earth’s upper mantle. *Nature* 493, 211–215.
- Dauphas, N., Craddock, P.R., Asimow, P.D., Bennett, V.C., Nutman, A.P., & Ohnenstetter, D. (2009). Iron isotopes may reveal the redox conditions of mantle melting from Archean to Present. *Earth and Planetary Science Letters* 288, 255–267.
- Davis, F.A., Humayun, M., Hirschmann, M.M., & Cooper, R.S. (2013). Experimentally determined mineral/melt partitioning of first-row transition elements (FRTE) during partial melting of peridotite at 3GPa. *104*, 232–260.
- DeBari, S.M., & Greene, A.R. (2011). Vertical Stratification of Composition, Density, and Inferred Magmatic Processes in Exposed Arc Crustal Sections, Arc-Continent Collision. Springer Berlin Heidelberg, pp. 121–144.
- Ducea, M.N. (2002). Constraints on the bulk composition and root foundering rates of continental arcs: A California arc perspective. *J. Geophys. Res.* 107, 2304.
- Ducea, M.N., Saleeby, J.B., & Bergantz, G. (2015). The architecture, chemistry, and evolution of continental magmatic arcs. *Annual Review of Earth and Planetary Sciences* 43, 299–331.
- Eilers, P.H., & Goeman, J.J. (2004). Enhancing scatterplots with smoothed densities. *Bioinformatics* 20, 623–628.
- Elkins, L. J., Bourdon, B., & Lambart, S. (2019). Testing pyroxenite versus peridotite sources for marine basalts using U-series isotopes. *Lithos*, 332–333, 226–244.
- Ellam R. M. (1992). Lithospheric thickness as a control on basalt geochemistry. *Geology* 20, 153–156.
- Elliott, T., & Spiegelman, M. (2003). Melt migration in oceanic crustal production: a U-series perspective. *Treatise on Geochemistry*, 3, 659.
- Erdman, M.E., Lee, C.-T.A., Levander, A., & Jiang, H. (2016). Role of arc magmatism and lower crustal foundering in controlling elevation history of the Nevadaplano and Colorado Plateau: A case study of pyroxenitic lower crust from central Arizona, USA. *Earth and Planetary Science Letters* 439, 48–57.
- Evans, K. A. (2012). The redox budget of subduction zones. *Earth-Science Reviews* 113(1–2), 11–32.
- Falloon, T.J., Danyushevsky, L.V. (2000). Melting of refractory mantle at 1.5, 2 and 2.5 GPa under anhydrous and H₂O-undersaturated conditions: Implications for the petrogenesis of high-Ca boninites and the influence of subduction components on mantle melting. *Journal of Petrology* 41, 257–283.
- Falloon, T.J., Green, D.H., Danyushevsky, L.V., & McNeill, A.W. (2008). The composition of near-solidus partial melts of fertile peridotite at 1 and 1.5 GPa: implications for the petrogenesis of MORB. *Journal of Petrology* 49, 591–613.
- Farmer, G.L., Glazner, A.F., Kortemeier, W.T., Cosca, M.A., Jones, C.H., Moore, J.E., & Schweickert, R.A. (2013). Mantle Lithosphere as a source of post subduction magmatism, northern Sierra Nevada, California. *Geosphere* 9, 1102–1124.
- Förster, M.W., Prelević, D., Schmück, H.R., Buhre, S., Marschall, H.R., Mertz-Kraus, R., & Jacob, D.E. (2018).

- Melting phlogopite-rich MARID: Lamproites and the role of alkalis in olivine-liquid Ni-partitioning. *Chemical Geology* 476, 429–440.
- Förster, M.W., Prelević, D., Schmück, H.R., Buhre, S., Veter, M., Mertz-Kraus, R., Foley, S.F., & Jacob, D.E. (2017). Melting and dynamic metasomatism of mixed harzburgite+glimmerite mantle source: Implications for the genesis of orogenic potassic magmas. *Chemical Geology* 455, 182–191.
- Francis, D. (1986). The pyroxene paradox in MORB glasses—A signature of picritic parental magmas? *Nature* 319, 586–589.
- Gaetani, G.A., & Grove, T.L. (1998). The influence of water on melting of mantle peridotite. *Contributions to Mineralogy and Petrology* 131, 323–346.
- Gaetani, G.A., O’Leary, J.A., Shimizu, N., Bucholz, C.E., & Newville, M. (2012). Rapid reequilibration of H₂O and oxygen fugacity in olivine-hosted melt inclusions. *Geology* 40, 915–918.
- Gale, A., Langmuir, C. H., Dalton, C. A. (2014). The global systematics of ocean ridge basalts and their origin. *Journal of Petrology* 55(6), 1051–1082.
- Gale, A., Dalton, C.A., Langmuir, C.H., Su, Y., & Schilling, J.G. (2013). The mean composition of ocean ridge basalts. *Geochemistry, Geophysics, Geosystems* 14, 489–518.
- Gao, S., Rudnick, R.L., Yuan, H.-L., Liu, X.-M., Liu, Y.-S., Xu, W.-L., Ling, W.-L., Ayers, J., Wang, X.-C., & Wang, Q.-H. (2004). Recycling lower continental crust in the North China craton. *Nature* 432, 892.
- Gao, Y., Hoefs, J., Hellebrand, E., von der Handt, A., & Snow, J. E. (2007). Trace element zoning in pyroxenes from ODP Hole 735B gabbros: diffusive exchange or synkinematic crystal fractionation?. *Contributions to Mineralogy and Petrology* 153(4), 429–442.
- Gillis, K.M., Snow, J.E., Klaus, A., Abe, N., Adrião, Á.B., Akizawa, N., Ceuleneer, G., Cheadle, M.J., Faak, K., & Falloon, T.J. (2014). Primitive layered gabbros from fast-spreading lower oceanic crust. *Nature* 505 (204–207).
- Green, D., Schmidt, M., Hibberson, W. (2004). Island-arc ankaramites: primitive melts from fluxed refractory lherzolitic mantle. *Journal of Petrology* 45, 391–403.
- Grocke S. B., Cottrell E., de Silva S., & Kelley K. A. (2016). The role of crustal and eruptive processes versus source variations in controlling the oxidation state of iron in Central Andean magmas. *Earth Planet. Sci. Lett.* 440, 92–104.
- Grove, T.L., Chatterjee, N., Parman, S.W., & Médard, E. (2006). The influence of H₂O on mantle wedge melting. *Earth and Planetary Science Letters* 249, 74–89.
- Grove, T. L., D. C. Gerlach, and Sando, T. W. (1982). Origin of calc-alkaline series lavas at Medicine Lake volcano by fractionation, assimilation and mixing. *Contributions to Mineralogy and Petrology* 80(2), 160–182.
- Grove, T.L., Kinzler, R.J., & Bryan, W.B. (1993). Fractionation of mid-ocean ridge basalt (MORB). *Mantle Flow and Melt Generation at Mid-Ocean Ridges*, 281–310.
- Hammouda, T. (2003). High-pressure melting of carbonated eclogite and experimental constraints on carbon recycling and storage in the mantle. *Earth and Planetary Science Letters* 214, 357–368.
- Helfrich, G.R., & Wood, B.J. (2001). The Earth’s mantle. *Nature* 412, 501–507.
- Hermann, J., & Spandler, C.J. (2008). Sediment Melts at Sub-arc Depths: an Experimental Study. *Journal of Petrology* 49, 717–740.
- Herzberg, C. (2011). Identification of Source Lithology in the Hawaiian and Canary Islands: Implications for Origins. *Journal of Petrology* 52, 113–146.
- Herzberg, C., & Asimow, P.D. (2015). PRIMELT3 MEGA. XLSM software for primary magma calculation: Peridotite primary magma MgO contents from the liquidus to the solidus. *Geochemistry, Geophysics, Geosystems*. doi: 10.1002/2014GC005631
- Herzberg, C., Asimow, P.D., Arndt, N., Niu, Y., Leshner, C.M., Fitton, J.G., Cheadle, M.J., & Saunders, A.D. (2007). Temperatures in ambient mantle and plumes: Constraints from basalts, picrites, and komatiites. *Geochem. Geophys. Geosyst.* 8, Q02006–Q02006.
- Herzberg C. and Asimow P. D. (2008). Petrology of some oceanic island basalts: PRIMELT2.XLS software for primary magma calculation. *Geochemistry, Geophysics, Geosystems* 9.
- Herzberg, C., & Gazel, E. (2009). Petrological evidence for secular cooling in mantle plumes. *Nature* 458, 619–622.
- Hildreth, W., & Moorbath, S. (1988). Crustal contributions to arc magmatism in the Andes of Central Chile. *Contributions to Mineralogy and Petrology* 98, 455–489.
- Hirose, K. (1997). Melting experiments on lherzolite KLB-1 under hydrous conditions and generation of high-magnesian andesitic melts. *Geology* 25, 42–44.
- Hirose, K., & Kawamoto, T. (1995). Hydrous partial melting of lherzolite at 1 Gpa: The effect of H₂O on the genesis of basaltic magmas. *Earth and Planetary Science Letters* 133, 463–473.
- Hirose, K., & Kushiro, I. (1993). Partial melting of dry peridotites at high pressures: determination of compositions of melts segregated from peridotite using aggregates of diamond. *Earth and Planetary Science Letters* 114, 477–489.
- Hirschmann, M.M. (2000). Mantle solidus: Experimental constraints and the effects of peridotite composition. *Geochemistry, Geophysics, Geosystems* 1, 2000GC000070.
- Hirschmann M. M., Baker M. B., & Stolper E. M. (1998). The Effect of Alkalis on the Silica Content of Mantle-Derived Melts. *Geochim. Cosmochim. Acta* 62, 883–902.
- Hirschmann, M.M., Kogiso, T., Baker, M.B., & Stolper, E.M. (2003). Alkalic magmas generated by partial melting of garnet pyroxenite. *Geology* 31, 481–484.
- Hirschmann, M.M., & Stolper, E.M. (1996). A possible role for garnet pyroxenite in the origin of the “garnet signature” in MORB. *Contributions to Mineralogy and Petrology* 124, 185–208.
- Hofmann, A.W. (1997). Mantle geochemistry: the message from oceanic volcanism. *Nature* 385, 219–229.
- Hofmann A. W. (2003). Sampling Mantle Heterogeneity through Oceanic Basalts: Isotopes and Trace Elements. *Treatise Geochemistry Second Ed.* 3, 67–101.
- Hofmann, A.W., & White, W.W. (1982). Mantle plumes from ancient oceanic-crust. *Earth Planet. Sci. Lett.* 57, 421–421.

- Humayun, M., Qin, L.P., & Norman, M.D. (2004). Geochemical evidence for excess iron in the mantle beneath Hawaii. *Science* 306, 91–94.
- Humphreys, M.C.S., Brooker, R.A., Fraser, D.G., Burgisser, A., Mangan, M.T., & McCammon, C. (2015). Coupled Interactions between Volatile Activity and Fe Oxidation State during Arc Crustal Processes. *Journal of Petrology* 56, 795–814.
- Humphreys E. R. & Niu Y. (2009). On the composition of ocean island basalts (OIB): The effects of Lithospheric thickness variation and mantle metasomatism. *Lithos* 112, 118–136.
- Ito, K., & Kennedy, G.C. (1974). The composition of liquids formed by partial melting of eclogites at high temperatures and pressures. *The Journal of Geology* 82, 383–392.
- Jackson, M.G., & Dasgupta, R. (2008). Compositions of HIMU, EM1, and EM2 from global trends between radiogenic isotopes and major elements in ocean island basalts. *Earth and Planetary Science Letters* 276, 175–186.
- Jackson M. G., Hart S. R., Koppers A. A. P., Staudigel H., Konter J., Blusztajn J., Kurz M. & Russell J. A. (2007). The return of subducted continental crust in Samoan lavas. *Nature* 448, 684–687.
- Jagoutz, O.E. (2010). Construction of the granitoid crust of an island arc. *Part II: a quantitative petrogenetic model. Contributions to Mineralogy and Petrology* 160, 359–381.
- Jenner, F.E., & O'Neill, H.S.C. (2012). Analysis of 60 elements in 616 ocean floor basaltic glasses. *Geochemistry, Geophysics, Geosystems* 13, Q02005, DOI:10.1029/2011GC004009.
- Johnston, A.D., & Wyllie, P.J. (1989). The system tonalite-peridotite-H₂O at 30 kbar, with applications to hybridization in subduction zone magmatism. *Contributions to Mineralogy and Petrology* 102, 257–264.
- Kawamoto, T., Kanzaki, M., Mibe, K., Matsukage, K.N., & Ono, S. (2012). Separation of supercritical slab-fluids to form aqueous fluid and melt components in subduction zone magmatism. *Proceedings of the National Academy of Sciences* 109, 18695–18700.
- Kelemen, P.B. (1995). Genesis of high Mg# andesites and the continental crust. *Contributions to Mineralogy and Petrology* 120, 1–19.
- Kelemen, P.B., Hart, S.R., & Bernstein, S. (1998). Silica enrichment in the continental upper mantle via melt/rock reaction. *Earth and Planetary Science Letters* 164, 387–406.
- Kelemen P. B., Hirth G., Shimizu N., Spiegelman M. & Dick H. J. (1997). A review of melt migration processes in the adiabatically upwelling mantle beneath oceanic spreading ridges. *Philos. Trans. R. Soc. London. Ser. A Math. Phys. Eng. Sci.* 355, 283–318.
- Kelemen, P.B., Whitehead, J.A., Aharonov, E., & Jordahl, K.A. (1995). Experiments on flow focusing in soluble porous media, with applications to melt extraction from the mantle. *Journal of Geophysical Research: Solid Earth* 100, 475–496.
- Kelley, K.A., & Cottrell, E. (2009). Water and the Oxidation State of Subduction Zone Magmas. *Science* 325, 605–607.
- Kepezhinskas, P., M. J. Defant, & M. S. Drummond. (1996). Progressive enrichment of island arc mantle by melt-peridotite interaction inferred from Kamchatka xenoliths, *Geochimica et Cosmochimica Acta* 60(7), 1217–1229, doi:10.1016/0016-7037(96)00001-4.
- Keshav, S., Gudfinnsson, G.H., Sen, G., & Fei, Y. (2004). High-pressure melting experiments on garnet clinopyroxenite and the alkalic to tholeiitic transition in ocean-island basalts. *Earth and Planetary Science Letters* 223, 365–379.
- Kessel R., Ulmer P., Pettko T., Schmidt M. W. & Thompson A. B. (2004). A novel approach to determine high-pressure high-temperature fluid and melt compositions using diamond-trap experiments. *Am. Mineral.* 89, 1078–1086.
- Kiseeva, E.S., Litasov, K.D., Yaxley, G.M., Ohtani, E., & Kamenetsky, V.S. (2013). Melting and Phase Relations of Carbonated Eclogite at 9–21 GPa and the Petrogenesis of Alkali-Rich Melts in the Deep Mantle. *Journal of Petrology* 54(8), 1555–1583.
- Klein, E.M., & Langmuir, C.H. (1987). Global correlations of ocean ridge basalt chemistry with axial depth and crustal thickness. *J. Geophys. Res.* 92, 8089–8089.
- Kogiso, T., Hirose, K., & Takahashi, E. (1998). Melting experiments on homogeneous mixtures of peridotite and basalt: application to the genesis of ocean island basalts. *Earth and Planetary Science Letters* 162, 45–61.
- Kogiso, T., & Hirschmann, M.M. (2001). Experimental study of clinopyroxenite partial melting and the origin of ultra-calcic melt inclusions. *Contributions to Mineralogy and Petrology* 142, 347–360.
- Kogiso, T., & Hirschmann, M.M. (2006). Partial melting experiments of bimineraleclogite and the role of recycled mafic oceanic crust in the genesis of ocean island basalts. *Earth and Planetary Science Letters* 249, 188–199.
- Kogiso, T., Hirschmann, M.M., & Frost, D.J. (2003). High-pressure partial melting of garnet pyroxenite: possible mafic lithologies in the source of ocean island basalts. *Earth and Planetary Science Letters* 216, 603–617.
- Kogiso, T., Hirschmann, M.M., & Pertermann, M. (2004). High-pressure Partial Melting of Mafic Lithologies in the Mantle. *Journal of Petrology* 45, 2407–2422.
- Kornprobst, J. (1970). Les péridotites et les pyroxénolites du massif ultrabasique de Beni Bouchera: une étude expérimentale entre 1100 et 1550°C, sous 15 à 30 kilobars de pression sèche. *Contributions to Mineralogy and Petrology* 29, 290–309.
- Kushiro, I. (1996). Partial melting of fertile mantle peridotite at high pressures: an experimental study using aggregates of diamond. *Geophysical Monograph, American Geophysical Union* 95, 109–122.
- Lackey, J.S., Valley, J.W., & Saleeby, J.B. (2005). Supracrustal input to magmas in the deep crust of Sierra Nevada batholith: Evidence from high- $\delta^{18}\text{O}$ zircon. *Earth and Planetary Science Letters* 235, 315–330.
- Lambart, S. (2017). No direct contribution of recycled crust in Icelandic basalts. *Geochemical Perspectives Letters*, 4. doi: 10.7185/geochemlet.1728
- Lambart, S., Koornneef, J. M., Millet, M. A., Davies, G. R., Cook, M., & Lissenberg, C. J. (2019). Highly heterogeneous depleted mantle recorded in the lower oceanic crust. *Nature Geoscience* 12(6), 482. doi: 10.1038/s41561-019-0368-9
- Lambart, S., Baker, M.B., & Stolper, E.M. (2016). The role of pyroxenite in basalt genesis: Melt-PX, a melting parameterization for mantle pyroxenites between 0.9 and 5 GPa. *Journal of Geophysical Research: Solid Earth* 121(8), 5708–5735.

- Lambart, S., Laporte, D., Provost, A., & Schiano, P. (2012). Fate of Pyroxenite-derived Melts in the Peridotitic Mantle: Thermodynamic and Experimental Constraints. *Journal of Petrology* 53, 451–476.
- Lambart, S., Laporte, D., & Schiano, P. (2009). An experimental study of pyroxenite partial melts at 1 and 1.5 GPa: Implications for the major-element composition of Mid-Ocean Ridge Basalts. *Earth and Planetary Science Letters* 288, 335–347.
- Lambart, S., Laporte, D., & Schiano, P. (2013). Markers of the pyroxenite contribution in the major-element compositions of oceanic basalts: Review of the experimental constraints. *Lithos* 160–161, 14–36.
- Langmuir, C.H. (1989). Geochemical consequences of in situ crystallization. *Nature* 340, 199.
- Langmuir, C.H., Klein, E.M., & Plank, T. (1992). Petrological Systematics of Mid-Ocean Ridge Basalts: Constraints on Melt Generation Beneath Ocean Ridges. *Geophysical Monograph - American Geophysical Union* 71, 183–280.
- Laporte D., Toplis M. J., Seyler M., & Devidal J. L. (2004). A new experimental technique for extracting liquids from peridotite at very low degrees of melting: Application to partial melting of depleted peridotite. *Contributions to Mineralogy and Petrology* 146, 463–484.
- Le Bas M. J., Maitre R. W. L., Streckeisen A., & Zanettin B. (1986). A chemical classification of volcanic rocks based on the total alkali-silica diagram. *Journal of Petrology* 27, 745–750.
- Le Maitre, R.W., Streckeisen, A., Zanettin, B., Le Bas, M., Bonin, B., & Bateman, P. (2005). *Igneous rocks: a classification and glossary of terms: recommendations of the International Union of Geological Sciences Subcommission on the Systematics of Igneous Rocks*. Cambridge University Press.
- Le Roux, V., Dasgupta, R., & Lee, C.T.A. (2011). Mineralogical heterogeneities in the Earth's mantle: Constraints from Mn, Co, Ni and Zn partitioning during partial melting. *Earth and Planetary Science Letters* 307, 395–408.
- Le Roux, V., Lee, C.-T., & Turner, S. (2010). Zn/Fe systematics in mafic and ultramafic systems: Implications for detecting major element heterogeneities in the Earth's mantle. *Geochimica et Cosmochimica Acta* 74, 2779–2796.
- Lee, C.-T.A., Cheng, X., & Horodyskyj, U. (2006). The development and refinement of continental arcs by primary basaltic magmatism, garnet pyroxenite accumulation, basaltic recharge and delamination: insights from the Sierra Nevada. *Contributions to Mineralogy and Petrology* 151, 222–242.
- Lee, C.-T.A., Leeman, W.P., & Canil, D., A, L.Z.-X. (2005). Similar V/Sc Systematics in MORB and Arc Basalts: Implications for the Oxygen Fugacities of their Mantle Source Regions. *Journal of Petrology* 46, 2313–2336.
- Lee, C.-T.A., Luffi, P., Le Roux, V., Dasgupta, R., Albarède, F., & Leeman, W.P. (2010). The redox state of arc mantle using Zn/Fe systematics. *Nature* 468, 681–685.
- Lee C. T. A., Luffi P., Plank T., Dalton H., & Leeman W. P. (2009). Constraints on the depths and temperatures of basaltic magma generation on Earth and other terrestrial planets using new thermobarometers for mafic magmas. *Earth Planet. Sci. Lett.* 279, 20–33.
- Lissenberg, C.J., & Dick, H.J. (2008). Melt–rock reaction in the lower oceanic crust and its implications for the genesis of mid-ocean ridge basalt. *Earth and Planetary Science Letters* 271, 311–325.
- Lissenberg, C.J., & MacLeod, C.J. (2016). A Reactive Porous Flow Control on Mid-ocean Ridge Magmatic Evolution. *Journal of Petrology* 57, 2195–2220.
- Lissenberg, C. J., MacLeod, C. J., & Bennett, E. N. (2019). Consequences of a crystal mush-dominated magma plumbing system: a mid-ocean ridge perspective. *Philosophical Transactions of the Royal Society A*, 377(2139), 20180014.
- Lissenberg, C.J., MacLeod, C.J., Howard, K.A., & Godard, M. (2013). Pervasive reactive melt migration through fast-spreading lower oceanic crust (Hess Deep, equatorial Pacific Ocean). *Earth and Planetary Science Letters* 361, 436–447.
- Lustrino, M. (2005). How the delamination and detachment of lower crust can influence basaltic magmatism. *Earth-Science Reviews* 72, 21–38.
- Mallik, A., & Dasgupta, R. (2012). Reaction between MORB-eclogite derived melts and fertile peridotite and generation of ocean island basalts. *Earth and Planetary Science Letters* 329, 97–108.
- Mallik, A., & Dasgupta, R. (2013). Reactive Infiltration of MORB-Eclogite-Derived Carbonated Silicate Melt into Fertile Peridotite at 3 GPa and Genesis of Alkalic Magmas. *Journal of Petrology* 54, 2267–2300.
- Mallik, A., & Dasgupta, R. (2014). Effect of variable CO₂ on eclogite-derived andesite and lherzolite reaction at 3 GPa: Implications for mantle source characteristics of alkalic ocean island basalts. *Geochemistry, Geophysics, Geosystems* 15, 1533–1557.
- Mallik, A., Dasgupta, R., Tsuno, K., & Nelson, J. (2016). Effects of water, depth and temperature on partial melting of mantle-wedge fluxed by hydrous sediment-melt in subduction zones. *Geochimica et Cosmochimica Acta* 195, 226–243.
- Mallik, A., Nelson, J., & Dasgupta, R. (2015). Partial melting of fertile peridotite fluxed by hydrous rhyolitic melt at 2–3 GPa: implications for mantle wedge hybridization by sediment melt and generation of ultrapotassic magmas in convergent margins. *Contributions to Mineralogy and Petrology* 169, 1–24.
- Mallik, A., Li, Y., & Wiedenbeck, M. (2018). Nitrogen evolution within the Earth's atmosphere–mantle system assessed by recycling in subduction zones. *Earth and Planetary Science Letters* 482, 556–566.
- Marschall, H.R., & Schumacher, J.C. (2012). Arc magmas sourced from melange diapirs in subduction zones. *Nature Geoscience* 5, 862–867.
- Matzen, A.K., Baker, M.B., Beckett, J.R., & Stolper, E.M. (2013). The Temperature and Pressure Dependence of Nickel Partitioning between Olivine and Silicate Melt. *Journal of Petrology* 54(12), 2521–2545.
- Matzen, A.K., Baker, M.B., Beckett, J.R., Wood, B.J., & Stolper, E.M. (2017a). The effect of liquid composition on the partitioning of Ni between olivine and silicate melt. *Contributions to Mineralogy and Petrology* 172, 3–3, doi: 10.1007/s00410-016-1319-8.

- Matzen, A. K., Wood, B. J., Baker, M. B., & Stolper, E. M. (2017b). The roles of pyroxenite and peridotite in the mantle sources of oceanic basalts. *Nature Geoscience* 10(7), 530.
- McBirney, A.R., & Noyes, R.M. (1979). Crystallization and layering of the Skaergaard intrusion. *Journal of Petrology* 20, 487–554.
- McKenzie D., Jackson J., & Priestley K. (2005). Thermal structure of oceanic and continental *Lithosphere*. *Earth and Planetary Science Letters* 233, 337–349.
- Médard, E., Schmidt, M.W., Schiano, P., & Ottolini, L. (2005). Melting of amphibole-bearing wehrlites: an experimental study on the origin of ultra-calcic nepheline-normative melts. *Journal of Petrology* 47, 481–504.
- Mibe, K., Kanzaki, M., Kawamoto, T., Matsukage, K.N., Fei, Y., & Ono, S. (2007). Second critical endpoint in the peridotite-H₂O system. *Journal of Geophysical Research: Solid Earth* 112.
- Mibe, K., Kawamoto, T., Matsukage, K.N., Fei, Y., & Ono, S. (2011). Slab melting versus slab dehydration in subduction-zone magmatism. *Proceedings of the National Academy of Sciences of the United States of America* 108, 8177–8182.
- Natland, J.H., & Dick, H.J. (1996). Melt migration through high-level gabbroic cumulates of the East Pacific Rise at Hess Deep: the origin of magma lenses and the deep crustal structure of fast-spreading ridges, Proceedings-Ocean Drilling Program Scientific Results. National Science Foundation, pp. 21–58.
- Navon, O., & Stolper, E. (1987). Geochemical consequences of melt percolation: the upper mantle as a chromatographic column. *The Journal of Geology* 285–307.
- Neave, D. A., Namur, O., Shorttle, O., & Holtz, F. (2019). Magmatic evolution biases basaltic records of mantle chemistry towards melts from recycled sources. *Earth and Planetary Science Letters* 520, 199–211. doi:10.1016/j.epsl.2019.06.003
- Nelson, W.R., Dorais, M.J., Christiansen, E.H., & Hart, G.L. (2013). Petrogenesis of Sierra Nevada plutons inferred from the Sr, Nd, and O isotopic signatures of mafic igneous complexes in Yosemite Valley, California. *Contributions to Mineralogy and Petrology* 165, 397–417.
- Ni, H., Zhang, L., Xiong, X., Mao, Z., & Wang, J. (2017). Supercritical fluids at subduction zones: Evidence, formation condition, and physicochemical properties. *Earth-Science Reviews* 167, 62–71.
- Nielsen, S.G., & Marschall, H.R. (2017). Geochemical evidence for mélange melting in global arcs. *Science Advances* 3.
- Niu Y., Wilson M., Humphreys E. R. & O'Hara M. J. (2011). The origin of intra-plate ocean island basalts (OIB): The lid effect and its geodynamic implications. *Journal of Petrology* 52, 1443–1468.
- Niu, Y., & O'Hara, M. J. (2008). Global correlations of ocean ridge basalt chemistry with axial depth: a new perspective. *Journal of Petrology* 49(4), 633–664.
- O'Hara, M. (1965). Primary magmas and the origin of basalts. *Scottish Journal of Geology* 1, 19–40.
- O'Hara, M. (1977). Geochemical evolution during fractional crystallisation of a periodically refilled magma chamber. *Nature* 266, 503.
- O'Hara, M. (1976). Data reduction and projection schemes for complex compositions. Third progress report of research supported by NERC in Edinburgh and Manchester Universities (1972–75) 6, 103–126.
- O'Neill, H.S.C., & Jenner, F.E. (2012). The global pattern of trace-element distributions in ocean floor basalts. *Nature* 491, 698.
- Otamendi, J.E., Ducea, M.N., & Bergantz, G.W. (2012). Geological, petrological and geochemical evidence for progressive construction of an arc crustal section, Sierra de Valle Fertil, Famatinian Arc, Argentina. *Journal of Petrology* 53, 761–800.
- Patiño Douce, A. E. (1999). What do experiments tell us about the relative contributions of crust and mantle to the origin of granitic magmas? *Geological Society, London, Special Publications* 168(1), 55–75, doi:10.1144/gsl.sp.1999.168.01.05.
- Pertermann, M., & Hirschmann, M.M. (2003a). Partial melting experiments on a MORB-like pyroxenite between 2 and 3GPa: Constraints on the presence of pyroxenite in basalt source regions from solidus location and melting rate. *J. Geophys. Res. Solid Earth* 108, 2125–2125.
- Pertermann, M., & Hirschmann, M.M. (2003b). Anhydrous partial melting experiments on a MORB-like eclogite: phase relations, phase compositions and mineral-melt partitioning of major elements at 2–3 GPa. *Journal of Petrology* 44, 2173–2201.
- Pertermann, M., Hirschmann, M. M., Hametner, K., Günther, D., & Schmidt, M. W. (2004). Experimental determination of trace element partitioning between garnet and silica-rich liquid during anhydrous partial melting of MORB-like eclogite. *Geochemistry, Geophys. Geosystems* 5, 5.
- Phipps Morgan J. (2001). Thermodynamics of pressure release melting of a veined plum pudding mantle. *Geochemistry, Geophys. Geosystems* 2 (2000GC000049).
- Pickering-Witter, J., & Johnston, A.D. (2000). The effects of variable bulk composition on the melting systematics of fertile peridotitic assemblages. *Contributions to Mineralogy and Petrology* 140, 190–211.
- Pilet, S., Baker, M.B., & Stolper, E.M. (2008). Metasomatized *Lithosphere* and the Origin of Alkaline Lavas. *Science* 320, 916–919.
- Pirard, C., & Hermann, J. (2014). Experimentally determined stability of alkali amphibole in metasomatised dunite at sub-arc pressures. *Contributions to Mineralogy and Petrology* 169, 1–26.
- Pirard, C., Hermann, J. (2015). Focused fluid transfer through the mantle above subduction zones. *Geology* 43, 915–918.
- Plank, T. (2005). Constraints from Thorium/Lanthanum on Sediment Recycling at Subduction Zones and the Evolution of the Continents. *Journal of Petrology* 46, 921–944.
- Poli, S., & Schmidt, M.W. (1995). H₂O transport and release in subduction zones: Experimental constraints on basaltic and andesitic systems. *Journal of Geophysical Research: Solid Earth* 100, 22299–22314.
- Prouteau, G., Scaillet, B., Pichavant, M., & Maury, R. (2001). Evidence for mantle metasomatism by hydrous silicic melts derived from subducted oceanic crust. *Nature* 410, 197–200.

- Prytulak, J., & Elliott, T. (2007). TiO₂ enrichment in ocean island basalts. *Earth and Planetary Science Letters* 263, 388–403.
- Putirka K. D. (2008). Thermometers and barometers for volcanic systems. *Rev. Mineral. Geochemistry* 69, 61–120.
- Qin, L., & Humayun, M. (2008). The Fe/Mn ratio in MORB and OIB determined by ICP-MS. *Geochimica et Cosmochimica Acta* 72, 1660–1677.
- Rampone, E., & Hofmann, A.W. (2012). A global overview of isotopic heterogeneities in the oceanic mantle. *Lithos* 148, 247–261.
- Rapp, R., Shimizu, N., Norman, M., & Applegate, G. (1999). Reaction between slab-derived melts and peridotite in the mantle wedge: experimental constraints at 3.8 GPa. *Chemical Geology* 160, 335–356.
- Rosenthal, A., Yaxley, G.M., Crichton, W.A., Kovacs, I., Spandler, C., Hermann, J., Sándorné, J.K., Rose-Koga, E., & Pelletier, A.-A. (2018). Phase relations and melting of nominally ‘dry’ residual eclogites with variable CaO/Na₂O from 3 to 5 GPa and 1250 to 1500° C; implications for refertilisation of upwelling heterogeneous mantle. *Lithos* 314, 506–519.
- Rosenthal, A., Yaxley, G.M., Green, D.H., Hermann, J., Kovacs, I., & Spandler, C. (2014). Continuous eclogite melting and variable refertilisation in upwelling heterogeneous mantle. *Sci. Rep.* 4, 6099.
- Sadofsky, S.J., Portnyagin, M., Hoernle, K., & van den Bogaard, P. (2008). Subduction cycling of volatiles and trace elements through the Central American volcanic arc: evidence from melt inclusions. *Contributions to Mineralogy and Petrology* 155, 433–456.
- Salter, V.J.M., & Dick, H.J.B. (2002). Mineralogy of the mid-ocean-ridge basalt source from neodymium isotopic composition of abyssal peridotites. *Nature* 418, 68–72.
- Schiano, P., Birck, J.-L., & Allègre, C.J. (1997). Osmium-strontium-neodymium-lead isotopic covariations in mid-ocean ridge basalt glasses and the heterogeneity of the upper mantle. *Earth and Planetary Science Letters* 150, 363–379.
- Schiano, P., Eiler, J.M., Hutcheon, I.D., & Stolper, E.M. (2000). Primitive CaO-rich, silica-undersaturated melts in island arcs: Evidence for the involvement of clinopyroxene-rich lithologies in the petrogenesis of arc magmas. *Geochemistry, Geophysics, Geosystems* 1, 1018, doi:10.1029/1999GC000032.
- Schwab, B.E., & Johnston, A.D. (2001). Melting Systematics of Modally Variable, Compositionally Intermediate Peridotites and the Effects of Mineral Fertility. *Journal of Petrology* 42, 1789–1811.
- Sekine, T., & Wyllie, P.J. (1982). Phase relationships in the system KAlSiO₄–Mg₂SiO₄–SiO₂–H₂O as a model for hybridization between hydrous siliceous melts and peridotite. *Contributions to Mineralogy and Petrology* 79, 368–374.
- Shen, A.H., & Keppler, H. (1997). Direct observation of complete miscibility in the albite–H₂O system. *Nature* 385, 710–710.
- Shorttle, O. (2015). Geochemical variability in MORB controlled by concurrent mixing and crystallisation. *Earth and Planetary Science Letters*, 424, 1–14.
- Skora, S., & Blundy, J. (2010). High-pressure Hydrous Phase Relations of Radiolarian Clay and Implications for the Involvement of Subducted Sediment in Arc Magmatism. *Journal of Petrology* 51, 2211–2243.
- Sleep, N.H. (1990). Hotspots and mantle plumes: Some phenomenology. *Journal of Geophysical Research: Solid Earth* 95, 6715–6736.
- Sobolev, A.V., Hofmann, A.W., Kuzmin, D.V., Yaxley, G., Arndt, N., Chung, S.L., Danyushevsky, L.V., Elliott, T., Frey, F.A., Garcia, M.O. & Gurenko, A.A. (2007). The amount of recycled crust in sources of mantle-derived melts. *Science* 316, 412–412.
- Sobolev, A.V., Hofmann, A.W., Sobolev, S.V., & Nikogosian, I. K. (2005). An olivine-free mantle source of Hawaiian shield basalts. *Nature* 434, 590–597.
- Spandler, C., Yaxley, G., Green, D., & Scott, D. (2010). Experimental phase and melting relations of metapelite in the upper mantle: implications for the petrogenesis of intraplate magmas. *Contributions to Mineralogy and Petrology* 160, 569–589.
- Spandler, C., Yaxley, G., Green, D.H., & Rosenthal, A. (2008). Phase Relations and Melting of Anhydrous K-bearing Eclogite from 1200 to 1600°C and 3 to 5 GPa. *Journal of Petrology* 49, 771–795.
- Syracuse, E.M., van Keken, P.E., & Abers, G.A. (2010). The global range of subduction zone thermal models. *Physics of the Earth and Planetary Interiors* 183, 73–90.
- Takahashi E. (1986). Melting of a dry peridotite KLB-1 up to 14 GPa: Implications on the Origin of peridotitic upper mantle. *J. Geophys. Res.* 91, 9367.
- Tamura, Y., Ishizuka, O., Stern, R.J., Nichols, A.R.L., Kawabata, H., Hirahara, Y., Chang, Q., Miyazaki, T., Kimura, J.-I., Embley, R.W., & Tatsumi, Y. (2014). Mission Immiscible: Distinct Subduction Components Generate Two Primary Magmas at Pagan Volcano, Mariana Arc. *Journal of Petrology* 55, 63–101.
- Tang, M., Erdman, M., Eldridge, G., & Lee, C.-T.A. (2018). The redox “filter” beneath magmatic orogens and the formation of continental crust. *Science Advances* 4.
- Tang, M., Lee, C.-T.A., Chen, K., Erdman, M., Costin, G., & Jiang, H. (2019). Nb/Ta systematics in arc magma differentiation and the role of arclogites in continent formation. *Nature Communications* 10, 235.
- Tatsumi, Y. (2001). Geochemical modeling of partial melting of subducting sediments and subsequent melt-mantle interaction: Generation of high-Mg andesites in the Setouchi volcanic belt, southwest Japan. *Geology* 29, 323–326.
- Tatsumi, Y., & Kogiso, T. (2003). The subduction factory: its role in the evolution of the Earth’s crust and mantle. *Geological Society, London, Special Publications* 219, 55 LP-80.
- Tatsumi, Y., Sakuyama, M., Fukuyama, H., & Kushiro, I. (1983). Generation of Arc Basalt Magmas and Thermal Structure of the Mantle Wedge in Subduction Zones. *J. Geophys. Res.* 88, 5815–5825.
- Tenner, T.J., Hirschmann, M.M., & Humayun, M. (2012). The effect of H₂O on partial melting of garnet peridotite at 3.5 GPa. *Geochem. Geophys. Geosyst.* 13, Q03016–Q03016.

- Thompson, R.N. (1974). Primary Basalts and Magma Genesis I. Skye, North-West Scotland. *Contributions to Mineralogy and Petrology* 45, 317–341.
- Thompson, R. N. (1975). Primary basalts and magma genesis. *Contributions to Mineralogy and Petrology* 52(3), 213–232.
- Thomson, A.R., Walter, M.J., Kohn, S.C., & Brooker, R.A. (2016). Slab melting as a barrier to deep carbon subduction. *Nature* 529, 76–79.
- Till, C.B., Grove, T.L., & Withers, A.C. (2012). The beginnings of hydrous mantle wedge melting. *Contributions to Mineralogy and Petrology* 163, 669–688.
- Tollan P. & Hermann J. (2019). Arc magmas oxidized by water dissociation and hydrogen incorporation in orthopyroxene. *Nature Geoscience* 12, 667–671.
- Tsuruta, K., & Takahashi, E. (1998). Melting study of an alkali basalt JB-1 up to 12.5 GPa: behavior of potassium in the deep mantle. *Physics of the Earth and Planetary Interiors* 107, 119–130.
- Tuff, J., Takahashi, E., & Gibson, S. (2005). Experimental constraints on the role of garnet pyroxenite in the genesis of high-Fe mantle plume derived melts. *Journal of Petrology* 46, 2023–2058.
- Turner, S.J., & Langmuir, C.H. (2015). The global chemical systematics of arc front stratovolcanoes: Evaluating the role of crustal processes. *Earth and Planetary Science Letters* 422, 182–193.
- Turner, S.J., Langmuir, C.H., Katz, R.F., Dungan, M.A., & Escrig, S. (2016). Parental arc magma compositions dominantly controlled by mantle-wedge thermal structure. *Nature Geosci* 9, 772–776.
- Walker Jr, B.A., Bergantz, G.W., Otamendi, J.E., Ducea, M. N., & Cristofolini, E.A. (2015). A MASH zone revealed: the mafic complex of the Sierra Valle Fértil. *Journal of Petrology* 56, 1863–1896.
- Walter, M.J. (1998). Melting of Garnet Peridotite and the Origin of Komatiite and Depleted Lithosphere. *Journal of Petrology* 39, 29–60.
- Wang, Y., & Foley, S.F. (2018). Hybridization Melting Between Continent-Derived Sediment and Depleted Peridotite in Subduction Zones. *Journal of Geophysical Research: Solid Earth* 123, 3414–3429.
- Wang, Y., Prelević, D., Buhre, S., & Foley, S.F. (2017). Constraints on the sources of post-collisional K-rich magmatism: The roles of continental clastic sediments and terrigenous blueschists. *Chemical Geology* 455, 192–207.
- Wang, Z., & Gaetani, G.A. (2008). Partitioning of Ni between olivine and siliceous eclogite partial melt: experimental constraints on the mantle source of Hawaiian basalts. *Contributions to Mineralogy and Petrology* 156, 661–678.
- Wasylenki, L.E., Baker, M.B., Kent, A.J.R., & Stolper, E.M. (2003). Near-solidus Melting of the Shallow Upper Mantle: Partial Melting Experiments on Depleted Peridotite. *Journal of Petrology* 44, 1163–1191.
- Weatherley, S.M., & Katz, R.F. (2012). Melting and channelized magmatic flow in chemically heterogeneous, upwelling mantle. *Geochemistry, Geophysics, Geosystems* 13.
- Weatherley, S.M., & Katz, R.F. (2016). Melt transport rates in heterogeneous mantle beneath mid-ocean ridges. *Geochimica et Cosmochimica Acta* 172, 39–54.
- White, W., & Klein, E. (2014). Composition of the Oceanic Crust. *Treatise on Geochemistry (Second Edition)*, 4, 457–496. doi: 10.1016/B978-0-08-095975-7.00315-6.
- Woodhead, J.D., Hergt, J.M., Davidson, J.P., & Eggins, S.M. (2001). Hafnium isotope evidence for ‘conservative’ element mobility during subduction zone processes. *Earth and Planetary Science Letters* 192, 331–346.
- Yang, Z. F., Li, J., Jiang, Q. B., Xu, F., Guo, S. Y., Li, Y., & Zhang, J. (2019). Using major element logratios to recognize compositional patterns of basalt: implications for source lithological and compositional heterogeneities. *Journal of Geophysical Research: Solid Earth*. doi: 10.1029/2018JB016145
- Yang, Z. F., Li, J., Liang, W. F., & Luo, Z. H. (2016). On the chemical markers of pyroxenite contributions in continental basalts in Eastern China: implications for source lithology and the origin of basalts. *Earth-Science Reviews*, 157, 18–31.
- Yang, Z. F., & Zhou, J. H. (2013). Can we identify source lithology of basalt? *Scientific Reports* 3, 1856.
- Yasuda, A., Fujii, T., & Kurita, K. (1994). Melting phase relations of an anhydrous mid-ocean ridge basalt from 3 to 20 GPa: Implications for the behavior of subducted oceanic crust in the mantle. *J. Geophys. Res.* 99, 9401–9414.
- Yaxley, G., & Brey, G. (2004). Phase relations of carbonate-bearing eclogite assemblages from 2.5 to 5.5 GPa: implications for petrogenesis of carbonatites. *Contributions to Mineralogy and Petrology* 146, 606–619.
- Yaxley, G., Sobolev, A.V. (2007). High-pressure partial melting of gabbro and its role in the Hawaiian magma source. *Contributions to Mineralogy and Petrology* 154, 371–383.
- Yaxley, G.M., & Green, D.H. (1998). Reactions between eclogite and peridotite: mantle refertilisation by subduction of oceanic crust. *Schweiz. Mineral. Petrogr. Mitt* 78, 243–255.
- Zhang, G.L., Sun, W.D., & Seward, G. (2018). Mantle source and magmatic evolution of the dying spreading ridge in the South China Sea. *Geochemistry, Geophysics, Geosystems* 19, 4385–4399.
- Zindler A., Staudigel H. & Batiza R. (1984). Isotope and trace element geochemistry of young Pacific seamounts: implications for the scale of upper mantle heterogeneity. *Earth Planet. Sci. Lett.* 70, 175–195.

7

Super-Deep Diamonds: Emerging Deep Mantle Insights from the Past Decade

Evan M. Smith¹ and Fabrizio Nestola²

ABSTRACT

Some rare diamonds originate below the lithosphere, from depths of 300–800 km and perhaps deeper. Ongoing sublithospheric or super-deep diamond research is providing new insight into the mantle and the hidden consequences of plate tectonics. Here we highlight several advances in the past decade, stemming from the discovery of inclusions from oceanic crust at lower mantle depths; inclusions having geochemical imprints of low-degree carbonatitic melt, possibly from subducted slabs; hydrous ringwoodite and other signs of deep water; major mantle minerals preserved in their original crystal structure, including ringwoodite and CaSiO₃-perovskite; additional diamond varieties with a super-deep origin (CLIPPIR and type IIb diamonds), greatly increasing the known prevalence and diversity of super-deep diamonds; and consistent, recurring Fe-Ni-C-S metallic melt inclusions from depths of 360–750 km. Redox freezing of oxidized, slab-derived fluid/melt upon interaction with ambient metal-saturated mantle appears to be a phenomenon broadly recorded by many super-deep diamonds. Melting of carbonate, as well as dehydration reactions, from subducted slabs are relevant mechanisms that may generate fluid/melt contributing to diamond growth. Fe-Ni metal, with dissolved carbon, sulfur, and other elements is also indicated as a possible diamond-forming melt. These mobile and dynamic phases are agents of chemical mass-transfer in the deep mantle.

7.1. INTRODUCTION

Diamonds and their trapped inclusion cargo can retain their original geological features over billion-year timescales and survive volcanic transport from mantle to surface. For these reasons, diamonds provide an invaluable means to access physical samples of the deep earth. Such deep samples serve as a basis of comparison for high-pressure experiments and geophysical studies.

While the majority of diamonds originate from the base or “keel” of old, thick continental lithosphere at depths of about 150–200 km, some have been established to originate from the sublithospheric mantle based on inclusion mineralogy (see reviews by Harte, 2010; Harte & Hudson, 2013; Kaminsky, 2012, 2017; Nestola, 2017; Shirey et al., 2013; Stachel et al., 2005). Sublithospheric diamonds are often called super-deep diamonds, or sometimes ultra-deep diamonds (not to be confused with metamorphic ultra-high-pressure diamonds). In general, super-deep diamonds undergo more plastic strain and resorption compared to lithospheric diamonds. They also have generally lower nitrogen concentrations, <50 ppm on average, compared

¹Gemological Institute of America, New York, NY, USA

²Department of Geosciences, University of Padova, Padova, Italy

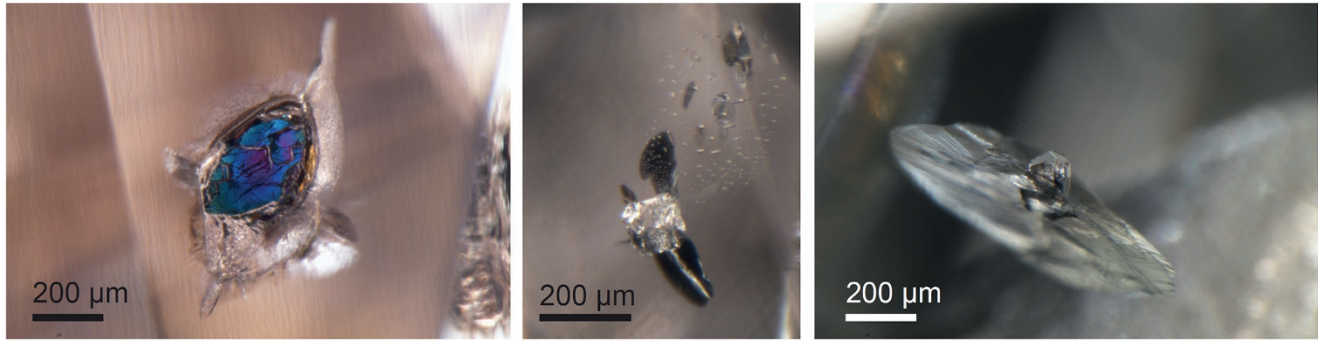


Figure 7.1 Examples of inclusions in super-deep diamonds. Left: Iridescent ferropericlase inclusion, with the right edge showing the brown color of light transmitted through the inclusion interior. Center: Breyite inclusion with a group of tiny Ca-silicate inclusions in a healed lobate crack extending toward top-right, plus a later stage black graphitic decompression crack. Right: Majoritic garnet inclusion surrounded by a roughly circular decompression crack, trapped along with metallic Fe-Ni-C-S melt in a CLIPPIR diamond (Smith et al., 2016).

to an average of 235 ppm for lithospheric diamonds (Smith and Kopylova, 2014 and references therein).

In lithospheric diamonds, the included minerals are derived primarily from peridotitic, eclogitic, and to a much lesser extent websteritic, host rocks. Super-deep diamonds also contain mineral inclusions that broadly reflect diamond growth in host rocks of peridotitic and basaltic/eclogitic bulk compositions (Figure 7.1). The mineralogy, however, changes with increasing pressure-temperature conditions and shows distinct assemblages through the asthenosphere, transition zone, and lower mantle. Inclusions in super-deep diamonds mimic experimentally determined high-pressure mineral assemblages.

The principal high-pressure minerals expected for meta-peridotitic compositions are olivine, wadsleyite, ringwoodite, majoritic garnet, CaSiO_3 -perovskite, ferropericlase, and bridgmanite, while those of meta-basaltic compositions are majoritic garnet, stishovite, CaSiO_3 -perovskite, bridgmanite, and the aluminous CF- and NAL-phases (see diagrams in Harte, 2010; Harte & Hudson, 2013; Stachel et al., 2005).

Identifying key minerals and mineral assemblages can reveal information about the host rocks and bracket the depth of diamond growth. Some mineral inclusions, however, such as ferropericlase, are not necessarily diagnostic of sublithospheric origin if found as single inclusions, as they could potentially be part of stable assemblages in the lithospheric mantle. When mineralogy alone does not constrain the depth of origin, methods such as plasto-elasto-geobarometry can still yield firm sublithospheric depth constraints (Anzolini et al., 2019).

During exhumation from the mantle, some high-pressure minerals trapped in super-deep diamonds, such as CaSiO_3 -perovskite and bridgmanite, become unstable and break down into lower-pressure minerals. In simple cases, when a high-pressure mineral breaks down to a

single lower-pressure mineral of the same composition, it is called *inversion*. When a high-pressure mineral breaks down into multiple phases (e.g., majoritic garnet breaking down to jeffbenite plus NaAl-pyroxene), it is called *retrogression* (Harte & Hudson, 2013). Thus, super-deep diamonds often contain multiphase inclusions, and the observed inclusion mineralogy requires interpretation to deduce the original high-pressure mineralogy. For example, inclusions of CaSiO_3 -perovskite typically invert to breyite (formerly called CaSiO_3 -walstromite), inclusions of bridgmanite retrogress to orthopyroxene, sometimes with jeffbenite (formerly called TAPP) and spinel, and inclusions of stishovite invert to coesite (Harte, 2010; Harte & Hudson, 2013; Kaminsky, 2012). Minerals like jeffbenite, breyite, and CaSi_2O_5 -titanite have only been found in nature within inclusions in super-deep diamonds, where they are thought to be formed by inversion or retrogression. Retrogressed phases can have a distinct compositional signature inherited from the original mineralogy, such as low nickel content in orthopyroxene from former bridgmanite (Stachel et al., 2005).

In detail, many inclusions do not appear to be pristine grains of ambient mantle rocks, but instead bear evidence of variable chemical modification by, or crystallization from, low-degree melts or fluids prior to their entrapment in diamond, possibly related to diamond formation (Stachel et al., 2000; Thomson et al., 2016a; Walter et al., 2008). Strong support that at least some super-deep diamonds are tied to subducted protoliths has been built from observations of Eu anomalies in majoritic garnet and former CaSiO_3 -perovskite inclusions, as well as carbon and nitrogen stable isotopic signatures (Cartigny et al., 2014; Palot et al., 2014; Stachel et al., 2005; Tappert et al., 2005). Unexpectedly, ferropericlase inclusions (Mg-rich (Mg,Fe)O) can exhibit a range of more Fe-rich compositions (to magnesiowüstite) and are sometimes

found in apparent disequilibrium association with stishovite (Stachel et al., 2005). The behavior is likely the result of reactions involving low-degree melts during diamond formation (Nimis et al., 2018; Seitz et al., 2018; Thomson et al., 2016b), though an alternative explanation involving the D" layer has been proposed (Haggerty, 1994; Harte et al., 1999; Hayman et al., 2005).

Super-deep diamonds show a surprisingly complex and information-rich inclusion cargo. Over the past decade, numerous publications have emerged from super-deep diamond research. This chapter gives a synopsis of some of the major themes that have been advanced as a result of these studies, including: (1) the finding of inclusions from oceanic crust at lower mantle depths (Walter et al., 2011); (2) the recognition that many inclusions bear a geochemical imprint of low-degree carbonatitic melt, possibly derived from subducted slabs (Thomson et al., 2016b; Walter et al., 2008); (3) the discovery of signs of deep water, including hydrous ringwoodite and ice-VII (Pearson et al., 2014; Tschauner et al., 2018); (4) the finding of major deep mantle phases preserved in their original high-pressure crystal structure, including ringwoodite and CaSiO₃-perovskite (Nestola et al., 2018; Pearson et al., 2014); (5) the discovery of additional diamond varieties with a super-deep origin (CLIPPIR and type IIb diamonds), which greatly increase the known prevalence, size, and diversity of super-deep diamonds (Smith et al., 2016, 2018); (6) the finding of consistent, recurring Fe-Ni-C-S metallic melt inclusions derived from depths of 360–750 km (Smith et al., 2016). Several reviews exist that give useful background context for the discussion herein (e.g., Harte, 2010; Harte & Hudson, 2013; Kaminsky, 2012, 2017; Nestola, 2017; Shirey et al., 2013; Stachel et al., 2005).

7.2. OCEAN CRUST AND CARBON RECYCLED TO THE LOWER MANTLE

Seismological observations unequivocally show subduction of lithospheric slabs deep into the mantle (van der Hilst et al., 1997), and variable geochemical signatures of these subducted materials are borne by ocean island basalts. An inclusion of phase Egg (AlSiO₃OH) was seen as a mineralogical indication that diamonds might sample deeply subducted ocean crust (Wirth et al., 2007). In 2011, Walter et al. (2011) found mineral inclusions in super-deep diamonds from the Juina-5 kimberlite, Brazil, that provided firm petrological evidence of ocean crust subducted down to lower mantle depths. The inclusions encompass the calcium-ferrite-structured (CF) phase, the new aluminum silicate (NAL) phase, Al-Ti-Fe-rich bridgmanite, and Ti-rich CaSiO₃-perovskite. Although the original single-phase inclusions have retrogressed to multiple coexisting phases,

the reconstructed bulk composition estimates for the inclusions compare very favorably with the major element composition of experimental phases for basaltic rocks at lower mantle conditions. Thus, the inclusion suite spans the mineralogy expected to comprise basaltic oceanic crust at lower mantle conditions.

When combined with the light to heavy range of carbon isotopic signatures of their diamond hosts, this inclusion suite is convincing evidence that the host rocks represent carbon-bearing oceanic crust subducted to lower mantle depths (Walter et al., 2011). Prior to this study, all recognized lower mantle diamonds had inclusions indicating a peridotitic host rock paragenesis and carbon isotope values centered on mantle-like carbon, –6‰ to –4‰ (Harte, 2010). Therefore, a key implication of this new finding was that the surface carbon cycle extends down into the lower mantle. Not only does subducting ocean crust convey surface-derived carbon past the 660 km discontinuity to lower mantle depths, but also mechanisms exist that are capable of returning some of that carbon to surface in the form of diamond. This is reinforced by later findings, including boron-bearing (type IIb) diamonds, which also carry a similar inclusion suite and related features from subducted oceanic lithosphere reaching lower mantle depths (Smith et al., 2018).

Such a geodynamic pathway raises questions about the timing of subduction relative to diamond formation and exhumation. If a plume or normal mantle convection is responsible for bringing these diamonds up from the lower mantle (e.g., Stachel et al., 2005), then diamond growth and exhumation could be independent and therefore separated by a substantial time gap. Alternatively, the activity related to diamond-formation itself may induce localized buoyancy that triggers upwelling/ascent. Ringwood (1991) proposed the existence “megaliths” of accumulated slab material at the top of the lower mantle, which may be sites of growth and perhaps storage for super-deep diamonds (Stachel et al., 2005). At least one preliminary super-deep diamond date has been measured. The inclusion age of $101 \pm 7 \text{ Ma}^{206}\text{Pb}/^{238}\text{U}$ for a Ca(Ti,Si)O₃-perovskite is close to the host kimberlite (Collier 4, Juina, Brazil) age, $93.1 \pm 1.5 \text{ Ma}$ (Bulanova et al., 2010). Other age indications from Nd and Sr isotopic data from majoritic garnets in related Juina diamonds have been argued to link diamond formation with a subducting slab between about 190 and 90 Ma (Harte & Richardson, 2012). These results suggest relatively short mantle residence compared to the billion-year mantle residence times of many lithospheric diamonds. However, the timeline of growth, residence, and exhumation for super-deep diamonds, especially for those tied to subduction into the lower mantle, has yet to be explored in detail.

7.3. RECOGNIZING CARBONATITIC MELT SIGNATURES IN THE DEEP MANTLE

The super-deep origin of some diamonds is underpinned by the recognition that their inclusions coincide with the expected sublithospheric mineralogy of peridotitic and eclogitic bulk compositions from experiments. But in detail, the composition of these mineral inclusions differ in some important ways (Harte et al., 1999; Stachel et al., 2000). Walter et al. (2008) examined Juina diamonds containing inclusions of former $\text{Ca}(\text{Ti},\text{Si})\text{O}_3$ -perovskite, which, on the basis of experiments, are too Mg-poor and Ti-rich to represent trapped subsolidus minerals from peridotitic or eclogitic bulk compositions at transition zone or lower mantle depths. Trace elements in both the $\text{Ca}(\text{Ti},\text{Si})\text{O}_3$ -perovskite inclusions as well as co-existing majoritic garnets support this observation, with extreme enrichment in incompatible trace elements such as thorium, niobium, and REEs, making it highly improbable that the inclusions sample pristine host rocks (Walter et al., 2008). Rather, the major and trace element characteristics point to the involvement of carbonatitic melts, argued to be derived from partial melting of carbonated oceanic crust. Walter et al. (2008) proposed silicate inclusions in super-deep diamonds record diamond growth from carbonatitic melts derived from deeply subducted slabs. Subsequent findings have supported this model that low-degree carbonatitic melts are a key ingredient for the growth of many sublithospheric diamonds (Bulanova et al., 2010; Burnham et al., 2015; Thomson et al., 2016a; Thomson et al., 2016b; Walter et al., 2011). It is clear that super-deep inclusions are best not to be assumed to reflect pristine ambient mantle mineralogy, but rather interpreted as being crystallized from, or at least modified by, low-degree melts or fluids (e.g., Nimis et al., 2018).

Rare primary inclusions of calcite and dolomite in super-deep diamonds from Juina (Brenker et al., 2007; Bulanova et al., 2010) lend further support for the association with carbonate species. Inclusions with coexisting CaCO_3 with CaSiO_3 (Zedgenizov et al., 2016) may be evidence for carbonates contributing to Ca-rich assemblages (Brenker et al., 2005). Kaminsky et al. (2009; 2013) have documented mixtures of more carbonate minerals, including nyerereite and nahcolite, in multiphase micro- and nanoscale inclusions, with oxides, silicates, halides, and a surprising variety of other species. Exotic mixtures like these are evidence of interaction with carbonatitic melt. While diamond-forming melt can certainly be trapped in a growing crystal, it is also possible for a diamond to trap small droplets of melt post-growth, along healed cracks (Smith et al., 2014, 2018). Any melt/fluid inclusions should therefore be examined carefully for their morphology and distribution to consider whether they are

primary, secondary, or even pseudo-secondary with respect to the diamond host.

Carbonatitic melts may be produced under various mantle conditions and do not necessarily require input from subduction (e.g., Kaminsky et al., 2009, 2013). However, mounting isotopic evidence continues to support the interpretation of subducted crustal signatures in some diamonds. Super-deep diamonds with light $\delta^{13}\text{C}$, containing inclusions with heavy $\delta^{18}\text{O}$ values, have been recorded from Jagersfontein (Ickert et al., 2015), Juina-5, Collier-4, and Machado River (Burnham et al., 2015) and are compelling evidence of recycled crustal material.

It is probable that subducting slabs carry surface-derived carbon, and that the slabs not only serve as host rocks but also contribute carbonatitic melt for at least some diamond growth (e.g., Brenker et al., 2007; Bulanova et al., 2010; Burnham et al., 2015; Thomson et al., 2016a, 2016b; Walter et al., 2011). In 2016, Thomson et al. (b) presented experimental results showing a larger-than-expected depression in the solidus of carbonated oceanic crust during subduction, such that most slab geotherms intersect the melting curve at about 300–700 km depths. The low-degree partial melts produced as a result of intersecting the solidus are alkaline carbonatites (Thomson et al., 2016b), which should react with ambient reduced mantle to undergo redox-freezing and produce diamond (Rohrbach & Schmidt, 2011). Reactions between carbonatitic melts and mantle peridotite are experimentally demonstrated to yield compositions similar to majoritic garnet and ferropericlasite compositions measured in inclusions in super-deep diamonds (Thomson et al., 2016b). The melting behavior of carbonated oceanic crust could contribute to mantle heterogeneity by focusing the geochemical contribution of subducted carbonate to the upper mantle and transition zone, while the remaining slab entering the lower mantle is largely stripped of its carbonate.

7.4. SIGNS OF DEEP WATER

Small amounts of “water” in the form of hydrogen or hydroxide can reside in mineral structures at high pressure, even in minerals that are nominally anhydrous (Bell & Rossman, 1992). Water is also suspected to be subducted with slabs, though the amount and its eventual fate are poorly constrained. Even modest amounts of hydrogen in its major mineral phases could mean there is at least another ocean’s worth of water stored in the mantle (e.g., Pearson et al., 2014), playing an important role in its properties and behavior.

Ringwoodite, a high-pressure olivine polymorph in the lower transition zone, may store significant amounts of

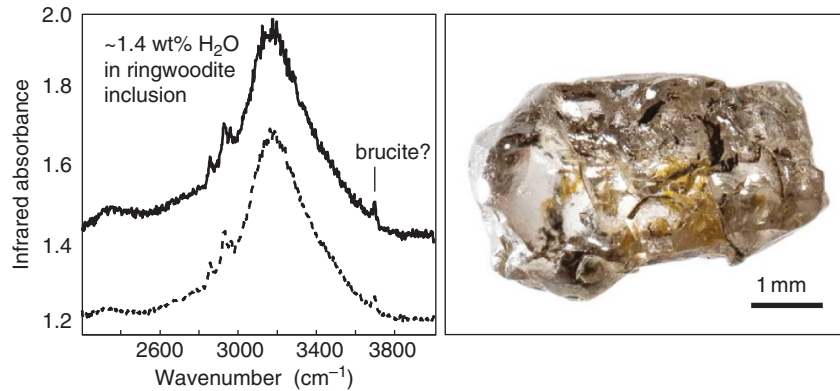


Figure 7.2 Hydrous ringwoodite inclusion infrared absorption spectrum, with possible minor brucite (noted by Palot et al., 2016). The inclusion was discovered in a rough diamond (right) from the Juina district, Brazil. *Source:* (Right) Photo credit R. Siemens/U. of Alberta. (Left) Pearson et al., 2014.

water. Initial speculation of a transition zone water reservoir by Smyth in 1987 was later met with experimental evidence that ringwoodite (and wadsleyite) could host up to 2.7–3.1 wt% H₂O (Inoue, 1994; Kohlstedt et al., 1996). Several studies have focused on the synthesis and investigation of hydrous ringwoodite to monitor the effect of water on its physical properties and extract larger-scale geophysical implications (e.g., Fei et al., 2017; Jacobsen & Smyth, 2006; Mao et al., 2012; Schulze et al., 2018; Ye et al., 2012).

In 2014, Pearson et al. discovered a hydrous ringwoodite inclusion in a diamond from the Juina district, Brazil. The discovery was exciting not only because it was preserved in the ringwoodite structure but also because it contained water. Water was recognized using infrared absorption spectroscopy (Figure 7.2), which clearly showed strong bands between 3200 and 3600 cm⁻¹, typical bands of OH stretching vibrations in synthetic ringwoodites with variable compositions between Mg₂SiO₄ and Mg_{1.2}Fe_{0.8}SiO₄ (Bolfan-Casanova et al., 2000; Jacobsen et al., 2004; Keppler & Bolfan-Casanova, 2006; Smyth et al., 2003). A later study (Thomas et al., 2015) confirmed that the hydrous ringwoodite found by Pearson et al. (2014) hosted 1.43 wt% H₂O, which is about half its maximum water solubility.

Realistically, the water measured in this ringwoodite inclusion might reflect a local enrichment in the mantle, possibly related to diamond forming melts or fluids. However, if the hydrous ringwoodite were to be taken as representative of the whole transition zone, it would imply a massive water reservoir. For example, Nestola and Smyth (2016) projected a hypothetical value of $1.0\text{--}1.2 \times 10^{25}$ g for Earth's total water, which would be three or four times more than generally accepted values near 3×10^{24} g (Bodnar et al., 2013).

A recent report of ice-VII within diamonds has generated great interest for the possibility of representing liquid

water, argued to be trapped as deep as the mantle transition zone (Tschauner et al., 2018). It suggests liquid water can accompany diamond formation in the transition zone and asthenosphere. However, the extreme physical pressure preserved in these ice-VII micro-inclusions, as high as 24 GPa, might require further consideration of thermal parameters, volume change upon solidification, and other factors for interpreting the depth of origin. The true depth of origin for these inclusions remains slightly unclear, as the ice-VII bearing diamonds are consistent with the characteristics of lithospheric fibrous diamonds, even in having typical lithospheric mineral inclusions (Tschauner et al., 2018). Regardless, the tentative finding of water sourced from the mantle transition zone is an exciting discovery that will no doubt spark further study to clarify their implications.

Beyond 660 km, in the lower mantle, the water content is thought to be lower than in the transition zone. Lower mantle minerals exhibit a more meagre water carrying capacity in experiments. However, lower mantle diamonds do still have signs of water, perhaps carried down in dense hydrous magnesium silicate (DHMS) phases in subducted oceanic lithosphere (Harte, 2010). A lower mantle diamond from the Juina region, Brazil, was found with an inclusion containing brucite in association with ferropericlase (Palot et al., 2016). The inclusion is interpreted as an original ferropericlase inclusion trapped along with a hydrous fluid film, which could react to form brucite upon exhumation.

Additional support for water reaching the lower mantle might be recorded in type IIb diamonds (nitrogen-free, boron-bearing). Their lower mantle inclusion assemblages recreate the mineralogy of subducted oceanic lithosphere (Smith et al., 2018). Some inclusions have a fluid film of methane (CH₄) and hydrogen (H₂). The original high-pressure phases likely contained considerable dissolved hydrogen that is no longer soluble in the

lower-pressure inclusion structures. The hydrogen exsolves as fluid and reacts with the host diamond to form methane. This hydrous signature is hypothesized to be part of a boron-enriched diamond-forming fluid released from DHMS phases carried by subducted oceanic lithosphere (Smith et al., 2018). Similar to the inclusions in type IIb diamonds, formerly dissolved hydrogen has also been found in association with Fe-Ni-C-S metallic melt inclusions (Smith et al., 2016, 2017), raising the possibility that ambient metal in the mantle below ~250 km (up to about 1 wt% metal) could be a reservoir of deep mantle hydrogen.

7.5. PRESERVED DEEP MANTLE MINERALS WITH ORIGINAL CRYSTAL STRUCTURE

High-pressure experiments permit recreation of deep mantle settings in a lab and allow prediction of the mineralogy of the mantle (e.g., Shen & Mao, 2016). For example, experiments show that olivine transforms at high pressures, first to wadsleyite and then ringwoodite, which are thought to demarcate the seismically recognized mantle transition zone, spanning a depth of 410 to 660 km (Ringwood, 1991). Ringwoodite $[(\text{Mg,Fe})_2\text{SiO}_4]$ is stable between 525 and 660 km, at temperatures between 1300 and 1800 °C. It is cubic with cell edge $a = 8.07 \text{ \AA}$, which increases up to $a = 8.23 \text{ \AA}$ for complete substitution of Mg by Fe^{2+} (Nestola, 2015).

Pioneering studies done on hydrous ringwoodite made it one of the more studied of Earth's mantle phases, but one that had never actually been found in the Earth. The first natural ringwoodite was found within meteorites in 1969 by Binns and coauthors. However, meteoritic ringwoodite in general does not represent a deep mantle mineral from different planetary bodies. Rather, it is an impact product from olivine, which is quite common in meteorites.

Wadsleyite and ringwoodite, when included in diamond, have a strong tendency to invert to olivine during exhumation. But in 2014, Pearson et al. discovered a hydrous ringwoodite inclusion in a diamond from Juina that was preserved in its original crystal structure (Figure 7.2). The inclusion was about 30–40 μm in size and was first detected by Raman spectroscopy and then confirmed by single-crystal x-ray diffraction. This discovery was important for providing firm evidence of the host diamond's transition zone origin, this time in the form of a major mantle phase preserved in its high-pressure state.

Another preserved high-pressure mantle phase found more recently in a super-deep diamond is CaSiO_3 perovskite. More commonly, its inferred inversion product, breyite (CaSiO_3 -walsstromite), is found in super-deep diamonds. Breyite can be found both as large single

inclusions (up to 200 μm , see Anzolini et al., 2016) and as small and composite inclusions (even 5–20 μm) often coexisting with larnite ($\beta\text{-Ca}_2\text{SiO}_4$) and CaSi_2O_5 -titanite (Brenker et al., 2005, 2007; Joswig et al., 1999). Until 2018, all works reporting breyite inclusions in diamonds referred to it as the back-transformation product from CaSiO_3 -perovskite, which, based on experiments and deep mantle geodynamic models, is stable in the lowermost part of the transition zone and in the lower mantle (e.g., Facenda and Dal Zilio, 2017; Stixrude and Lithgow-Bertelloni, 2012).

The pressure and temperature stability field of breyite within the pure CaSiO_3 system is reported by Gasparik et al. (1994). It shows that this phase is stable at maximum pressures between 9 and 11 GPa (about 270 and 330 km depth) at temperatures between 780 and 2200 °C. Although the effect of Ti substitution is not fully explored, the CaSiO_3 -perovskite to breyite transformation should occur well within the upper mantle.

In 2018, Nestola and coauthors found an example of noninverted CaSiO_3 -perovskite within a diamond from the Cullinan mine, South Africa. The 25 μm inclusion, investigated by Nestola et al. (2018), contained ~6% CaTiO_3 , indicating a bulk composition consistent with derivation from deeply subducted basaltic ocean crust. Experiments by Hirose and Fei (2002) show the bulk composition of this CaSiO_3 -perovskite inclusion can be obtained in an oceanic basalt bulk composition at 26 GPa and 2200 °C, taken to suggest diamond crystallization within the lower mantle (Nestola et al., 2018).

Some doubts have been expressed about the identification of the inclusion as CaSiO_3 -perovskite, mainly due to the fact that experimental attempts to quench synthetic CaSiO_3 -perovskite to room temperature and pressure have been unsuccessful. However, it should be noted that it is almost impossible to experimentally reproduce the exact temperature-pressure-time path followed by a CaSiO_3 -perovskite inclusion (enclosed in diamond) from the lower mantle to the Earth's surface.

It is possible that other preserved CaSiO_3 -perovskite inclusions may have been encountered in previous studies, but were simply assumed to be breyite based on composition, without checking its crystal structure. In studies relying on Raman spectroscopy, CaSiO_3 -perovskite could easily be misidentified as CaTiO_3 perovskite (e.g., Smith et al., 2017; 2018), because the spectra are very similar (Nestola et al. 2018) and CaTiO_3 would be a more conservative interpretation, in line with previously documented inclusions having grains of CaTiO_3 within breyite (e.g., Walter et al., 2008).

CaTiO_3 and CaSiO_3 -perovskite are almost indistinguishable based on their Raman signal, without additional information. Interestingly, the inclusion reported by Nestola et al. (2018) was exposed by polishing and it

appeared colorless. Since colorless CaTiO_3 is not known to exist in nature, it may be a distinguishing feature, such that colorless inclusions having a “ CaTiO_3 perovskite” Raman spectrum are actually CaSiO_3 -perovskite. Another option to help identify CaSiO_3 -perovskite inclusions in situ, while still protected in the diamond host, would be to use synchrotron 3D micro x-ray fluorescence imaging (Garrevoet et al., 2014). Even a qualitative 3D micro x-ray fluorescence measurement could allow discrimination between CaTiO_3 and CaSiO_3 -perovskite based on TiO_2 content.

The finding of ringwoodite and CaSiO_3 -perovskite inclusions provides an additional line of evidence to support the super-deep origin of the host diamonds. It also reinforces our understanding of deep mantle mineralogy based on experiments and geophysics. Future studies are expected to encounter further examples of ringwoodite, CaSiO_3 -perovskite, and other preserved high-pressure phases in super-deep diamonds.

7.6. NEW KINDS OF SUPER-DEEP DIAMONDS: CLIPPIR AND TYPE IIB DIAMONDS

Recent work examining samples screened from millions of diamonds in the gem marketplace has established that two additional varieties of diamond of previously unknown geological parageneses are actually sublithospheric in origin. The addition comes from examining inclusions in diamonds whose nitrogen content falls below the ~ 5 ppm detection limit of infrared spectroscopy,

classified as type IIa, or type IIb if boron is detected. In 2016, Smith et al. established that the conspicuous variety of diamonds that includes large, top gem quality type IIa diamonds like the historic 3106 carat Cullinan diamond constitute a genetically distinct diamond variety. These Cullinan-like diamonds encompass many, but not all type IIa diamonds, as well as rare examples that are technically type IaB, with low, but measurable nitrogen concentrations in the form of B centers (four nitrogen atoms surrounding a vacancy). The overall distinguishing characteristics of this diamond variety were combined into an acronym, CLIPPIR: *Cullinan-like*, having characteristics like the 3106 carat Cullinan diamond; *Large*, with frequent occurrence of diamonds exceeding a few centimeters in diameter; *Inclusion Poor*, with many diamonds being free of inclusions; *Pure*, being almost always type IIa; *Irregular*, with most rough diamonds being anhedral; *Resorbed*, with strongly resorbed surfaces. CLIPPIR diamonds are more abundant at some mines than others. The Letseng mine in Lesotho is an especially prolific producer of such diamonds (e.g., Bowen et al., 2009).

Although relatively inclusion-poor as a population, those CLIPPIR diamonds that do have inclusions contain majoritic garnet, breyite, and most prominently, metallic Fe-Ni-C-S inclusions that were trapped as melt (Figure 7.3) (Smith et al., 2016; Smith et al., 2017). These inclusions show CLIPPIR diamonds originate from a depth between 360 and 750 km, and that they form in the presence of iron-rich metallic liquid.

In addition to CLIPPIR diamonds, type IIb diamonds have also been found to have a super-deep origin (Smith

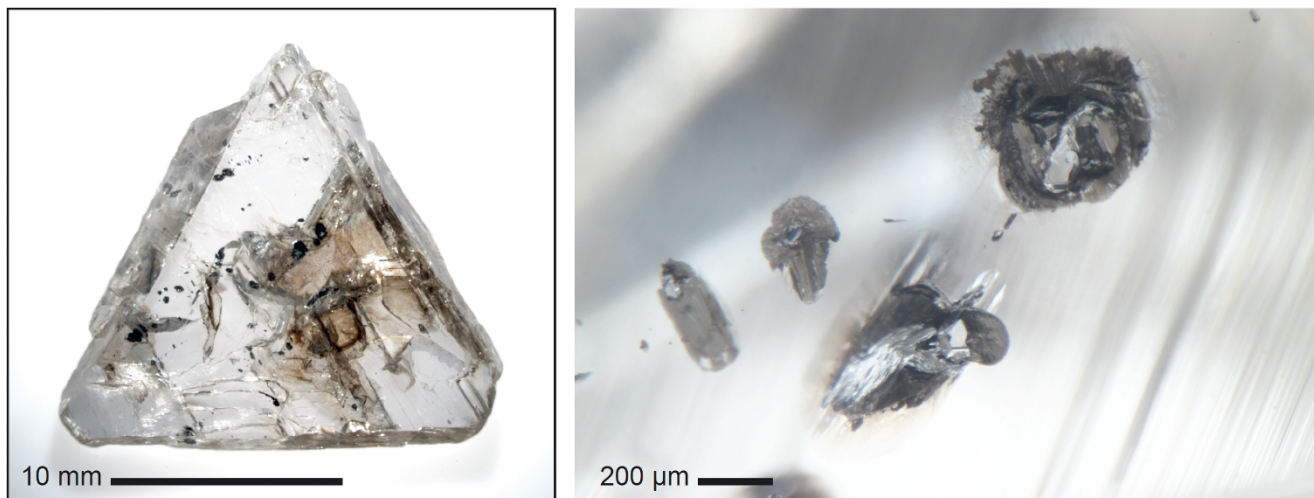


Figure 7.3 Example of a CLIPPIR diamond with metallic inclusions. This inclusion-bearing type IIa sample (left) is a cleavage fragment trimmed off a larger diamond in the 1970s, during the manufacturing of a premium-quality, faceted diamond by Harry Winston Inc. in New York. The brown region is an open fracture coated with Fe-oxides, while the black specks are inclusions. The inclusions (right) are metallic Fe-Ni-C-S mixtures, surrounded by irregular black, graphitic decompression cracks. Sample courtesy of J.E. Butler.

et al., 2018). These diamonds are unusual for their lack of nitrogen and for their boron content, which is typically within 0.01–10 ppm (Gaillou et al., 2012) and can impart an attractive blue color. Boron is strongly depleted in the mantle, instead being partitioned into the earth's upper crust. Despite scientific interest, the geological origin of these diamonds long remained unknown (Gaillou et al., 2012; King et al., 1998). In a study that screened more than 1000 type IIb diamonds to find examples with inclusions, Smith et al. (2018) documented 46 samples, from undisclosed geographic origins, except for one known to be from the Cullinan mine, South Africa. Examination of these 46 inclusion-bearing diamonds revealed consistent examples of super-deep phases recreating basaltic to peridotitic bulk compositions at transition zone to lower mantle depths, and attributed to deeply subducted oceanic lithosphere.

Extreme remnant inclusion pressures give an additional, physical constraint that the examined type IIb samples are sublithospheric. For example, ferropericlase in one sample had an internal pressure of 1.8 GPa, which, using a new combined elastic and elasto-plastic model (Anzolini et al., 2019), constrains the *minimum* entrapment pressure to 15.5 GPa, well within the transition zone and consistent with lower mantle entrapment (i.e., an origin beyond 15.5 GPa). Carbon isotope analysis of three diamonds, in combination with three historical type IIb diamond measurements (Milledge et al., 1983), establish a $\delta^{13}\text{C}$ range from -20.8‰ to -1.8‰ that is consistent with subducted carbon signatures (Smith et al., 2018).

Given the subducted nature of the host rocks, the boron in type IIb diamonds is argued to have been transported down from the surface in serpentinized peridotite in the mantle portion of the slab. Other potential boron hosts, such as metasediments, organic matter, or white micas in the oceanic crust are destabilized at relatively shallow depths during subduction, but boron in the mantle portion of the slab can survive down to greater depths. Serpentinized lithospheric mantle peridotite is expected to be the greatest boron cache within deeply subducted slabs (Deschamps et al., 2013; Konrad-Schmolke et al., 2016; Leeman et al., 2017; Pagé et al., 2018). Serpentine breakdown during subduction should strip much of this boron, releasing fluid into the overlying mantle wedge and arc, although experiments and fluid inclusion analyses suggest a maximum fluid/residue boron partition coefficient of about 5 (Scambelluri et al., 2004; Tenthorey & Hermann, 2004). So residual nominally anhydrous minerals should retain modest amounts of boron for deeper transport. However, a much greater boron budget might be retained with serpentine being metamorphosed to dense hydrous magnesium silicates (DHMS). In this scenario, the eventual breakdown of DHMS phases is proposed to release hydrous fluid conducive to diamond growth (e.g., Harte,

2010). If DHMS phases retain some of the boron originally sourced from seafloor hydrothermal alteration, then the breakdown of DHMS should yield a boron-enriched hydrous fluid. Evidence of this fluid may be preserved not only in the elevated boron content of type IIb diamonds, but also in the hydrogen-saturated nature of their mineral inclusions. Many inclusions in type IIb diamonds have a fluid layer of $\text{CH}_4 \pm \text{H}_2$ around them, interpreted as hydrogen atoms that have diffused out of the solid mineral phases at lower pressures and accumulated around the inclusion walls, where the hydrogen can react with diamond to make methane. Type IIb diamonds and their inclusions might therefore reveal a major pathway for the recycling of crustal elements, such as boron, and possibly hydrogen down to lower mantle depths (Smith et al., 2018).

Although it cannot be ruled out that some type IIb diamonds might grow at shallower depths, in the lithosphere, the present observations do not provide evidence of multiple type IIb diamond varieties. Rather, the examined type IIb diamonds have self-consistent features and inclusions that suggest they all share a super-deep genetic framework. However, the notion that type IIb diamonds form a coherent genetic group does not strictly mean that boron only occurs in super-deep diamonds. There may be yet-undetected elevated boron concentrations residing in some type I (nitrogen bearing) diamonds, such as in lithospheric fibrous diamonds or in their fluid inclusions.

Together, the finding that CLIPPIR and type IIb diamonds are sublithospheric in origin represents a marked increase in the known prevalence of super-deep diamonds. In a sample of 3.5 million gem diamonds, approximately 1.3% were deemed to be type IIa and proposed to belong to the CLIPPIR variety (Smith et al., 2017). Given that they can often be several centimeters in diameter, even after significant resorption, CLIPPIR diamonds that remain in the deep mantle may represent a style of deep carbon sequestration that helps explain the H/C ratios of Earth's reservoirs (Hirschmann & Dasgupta, 2009). Type IIb diamonds are apparently less common, estimated to account for $<0.02\%$ of mined diamonds (Smith et al., 2018). Previously, it was widely held that super-deep diamonds are always small and never of gem quality. The revised picture means super-deep diamonds are more common and varied in their properties, conveying a wider array of information from the deep mantle.

7.7. A REDUCED IRON-SATURATED SUBLITHOSPHERIC MANTLE

In 2016, Smith et al. described a new variety of super-deep diamond, called CLIPPIR diamonds (see above), originating from depths of 360–750 km. A distinguishing

feature of CLIPPPIR diamonds is that their most common type of inclusion is the relict of Fe-Ni-C-S metallic melt. This metal was interpreted in terms of previous experimental and theoretical predictions that the mantle below ~250 km is metal-saturated due to the effect of iron disproportionation (Ballhaus, 1995; Frost et al., 2004; Rohrbach et al., 2007, 2011, 2014). In essence, the increased stability of Fe^{3+} in some mineral structures as a function of increasing pressure leads to Fe^{2+} disproportionation ($3\text{Fe}^{2+} \rightarrow 2\text{Fe}^{3+} + \text{Fe}^0$), with Fe^0 being exsolved as metal.

However, subsequent investigation into the iron isotopic signature of metal in CLIPPPIR diamonds suggests the iron is subducted and originates from serpentinization rather than from Fe^{2+} disproportionation (Smith et al., 2021). Iron-nickel alloys precipitated during serpentinization and later subducted into the mantle could therefore present a second mechanism to deliver metal-saturated conditions in the sublithospheric mantle, in addition to disproportionation. Of 83 inclusion-bearing CLIPPPIR diamonds, ~80% contained metallic Fe-Ni-C-S melt inclusions, with a mineralogy dominated by cohenite $[(\text{Fe},\text{Ni})_3\text{C}]$, Fe-Ni alloy, and pyrrhotite. Most of these inclusions have a thin fluid layer of $\text{CH}_4 \pm \text{H}_2$ around them, indicating the original melt contained dissolved hydrogen (Smith et al., 2016). Minor accessory Fe-oxide, Cr-Fe-oxide, and Fe-phosphate indicate the melt also contained P, Cr, and O. Carbon and sulfur in this Fe-Ni-C-S mix are responsible for depressing its solidus, accounting for its molten state upon trapping, whereas a more pure Fe-Ni alloy should be solid in the mantle (e.g., Rohrbach et al., 2014).

Iron disproportionation, as mentioned above, is driven by the increasing stability of Fe^{3+} in some minerals as a function of increasing pressure. In the upper mantle and transition zone, garnet is the dominant Fe^{3+} -bearing mineral at play, whereas in the lower mantle it is bridgmanite. In the lithospheric mantle, a general trend of decreasing $f\text{O}_2$ with depth is observed for garnet peridotite xenoliths, due to the increasing stability of Fe^{3+} -bearing garnet with depth (Frost & McCammon, 2008). Experiments demonstrate continued increasing stabilization of Fe^{3+} in garnet as a function of increasing pressure to 14 GPa, even in the presence of metallic Fe^0 (Rohrbach et al., 2007). This pronounced relationship between Fe^{3+} in garnet and pressure has now been observed in natural majoritic garnet inclusions in super-deep diamonds (Kiseeva et al., 2018). The inclusions exhibit $\text{Fe}^{3+}/\Sigma\text{Fe}$ values with a marked pressure dependence that overlaps those of metal-saturated experimental garnets at similar pressures (Figure 7.4). Both “reduced” experimental garnets (in equilibrium with metal) and the “oxidized” inclusions (above iron-wüstite buffer based on calculated $f\text{O}_2$) show $\text{Fe}^{3+}/\Sigma\text{Fe}$ reaching 0.3 at transition zone depths. The fact that natural inclusions uphold the trend in Figure 7.4 reinforces the

underpinning premise established by mineral physics calculations and experiments, that pressure stabilizes Fe^{3+} in garnet to such an extent that Fe^{2+} disproportionation is required for ambient mantle rocks, leading to metal saturation below ~250 km (Rohrbach et al., 2007; Rohrbach et al., 2011).

The metallic iron budget of the deep mantle is relevant for several super-deep diamond varieties, because it is expected to have a closely coupled redox relationship with carbon (Rohrbach & Schmidt, 2011). Models of super-deep diamond formation from carbonate-bearing melts or fluids often invoke metallic Fe as a redox buffer with a substantial ability to reduce carbonate species and drive diamond forming reactions (Burnham et al., 2015; Palyanov et al., 2013; Rohrbach & Schmidt, 2011; Thomson et al., 2014).

Metallic Fe in the mantle has been proposed to take up nitrogen, as a possible contributing factor to the low nitrogen content both of CLIPPPIR diamonds, as well as other super-deep diamonds that may form from carbonate-bearing media reacting with metallic Fe (Smith & Kopylova, 2014). Ultimately, metallic phases in the mantle will affect the storage and cycling of the many elements that dissolve into it, such as oxygen, carbon, nitrogen, and hydrogen, making it a critical factor for the behavior and evolution of the mantle.

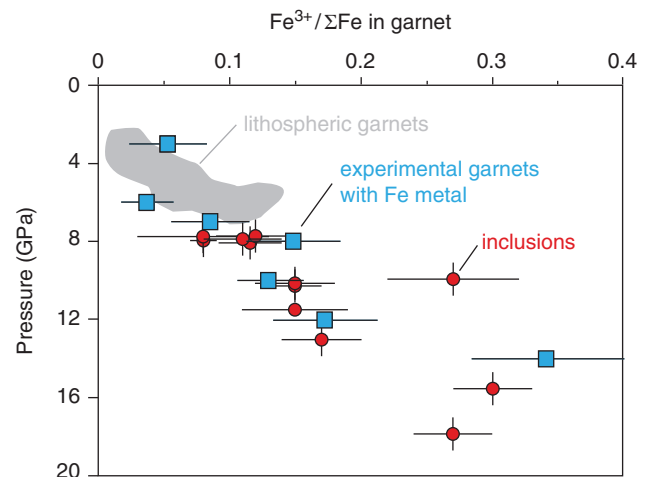


Figure 7.4 Relationship of increasing ferric iron proportion ($\text{Fe}^{3+}/\Sigma\text{Fe}$) in garnets with increasing pressure. Majoritic garnet inclusions from Jagersfontein super-deep diamonds (Kiseeva et al., 2018) exhibit comparable $\text{Fe}^{3+}/\Sigma\text{Fe}$ to experimental garnets in a model mantle rock enclosed in Fe-metal capsules (Rohrbach et al., 2007). The slope of this trend may be different for different garnet compositions. Lithospheric garnet field is from combined references in Kiseeva et al. (2018). *Source:* Kiseeva et al. (2018).

7.8. DISCUSSION

Super-deep diamonds are gaining momentum as a tool for examining the inaccessible interior of the Earth. Following from the compositionally based recognition of super-deep inclusions, additional evidence to reaffirm their sublithospheric origin has emerged. The residual pressure within some inclusions is very high and can be quantified to show that inclusion entrapment must have occurred at sublithospheric depths (Anzolini et al., 2018, 2019; Smith et al., 2018). Similar information is reflected by deformation of the host diamond surrounding the inclusions (Zedgenizov et al., 2015). Even more convincing is the finding of ringwoodite (Pearson et al., 2014) and CaSiO₃-perovskite (Nestola et al., 2018) with preserved crystal structures, which confirm that they are derived from the sublithospheric mantle based on intact primary mineralogy. It is possible that preserved inclusions of bridgmanite, likely Earth's most abundant mineral, may eventually be found in super-deep diamonds.

Multiple lines of evidence connect many super-deep diamonds to subducted oceanic lithosphere (Bulanova et al., 2010; Burnham et al., 2015; Ickert et al., 2015; Seitz et al., 2018; Smith et al., 2018; Thomson et al., 2016a; Walter et al., 2008; Walter et al., 2011). The emerging picture of recycling of oceanic material is consistent with a global-scale study of mid-ocean ridge and ocean island basalts that argues for extensive deep recycling of seawater components in subducted partially serpentinized lithosphere (Kendrick et al., 2017). Diamonds are a unique sample that testify to the influx of volatiles (including hydrogen and carbon) into the Earth. Recycled volatiles must, of course, be distinguished from and compared against signatures of primordial volatile reservoirs (Cartigny et al., 2014). The mantle contains considerable nonrecycled carbon reserves and the interplay between different branches of deep carbon cycling will undoubtedly remain a focus of future research.

Super-deep diamond studies clearly show carbonatitic melts are important reactive and mobile media in the deep earth, but with the additional recent discoveries of new super-deep diamond varieties, CLIPPIR diamonds and type IIb diamonds introduce metallic melt and hydrous fluid as additional players in the deep mantle. Subducted slabs flux deep activity, beyond arc volcanism, by virtue of melting carbonate, as well as the possible breakdown of hydrous phases in the serpentinized mantle portion of slabs.

There are limits placed on the potential depth of carbon recycling via carbonates (transition zone), and deeper transport may be scant, relying on refractory graphitic carbon or diamond, or perhaps dissolution into liquid Fe-rich metal or Fe-carbide. There also appear to be limits

on the depth and extent of water recycling, especially if water is primarily carried by dense hydrous magnesium silicates in subducting slabs, which likely become unstable as slabs warm to ambient mantle temperatures (e.g., Harte, 2010). Inclusions in super-deep diamonds have shown the potential for water storage, in nominally anhydrous minerals, such as ringwoodite, and in the form of hydrogen in Fe-rich metallic phases. The pronounced depth horizons for super-deep diamond growth may be related to the style of carbonate melting and dehydration of subducting slabs.

Based on observed mineral and melt inclusions, as well as experiments, there are at least three important mechanisms responsible for generating carbon-bearing fluids/melts for super-deep diamond crystallization (Figure 7.5):

1. The first is melting of carbonated oceanic crust, to produce an alkaline carbonatitic melt, which is thought to undergo a redox reaction to produce diamond upon interacting with reduced ambient mantle materials (Rohrbach & Schmidt, 2011; Thomson et al., 2016b; Walter et al., 2008). Most super-deep diamonds studied to date appear to be linked to formation from low-degree carbonatitic melts, based on both major and trace element characteristics of their mineral inclusions (Kaminsky et al., 2009; Thomson et al., 2016a, 2016b; Walter et al., 2008; Zedgenizov et al., 2016).
2. A second variety of carbon-bearing diamond-forming fluid is that which may be triggered by dehydration reactions (Harte, 2010). The release of water, for example from the breakdown of dense hydrous magnesium silicates in a subducting slab, will trigger partial melting. Although the melt could quickly evolve to be carbonatitic in nature, it is distinguished as a second source of diamond-forming fluid here because the trigger is distinct (i.e., the melting of carbonate minerals versus breakdown of hydrous minerals). This second origin of super-deep diamond forming fluid was incorporated into the model for the growth of blue boron-bearing (type IIb) diamonds (Smith et al., 2018).
3. A third apparent medium for diamond formation is represented by metallic melt inclusion of Fe-Ni-C-S composition that are prevalent in CLIPPIR diamonds, a super-deep diamond variety encompassing large and highly pure gem diamonds such as the 3106 carat Cullinan diamond (Smith et al., 2016; Smith et al., 2017). The origin of the metal in these inclusions was initially attributed to iron disproportionation reactions, although it was later shown their iron isotopic characteristics suggest the iron is sourced from subducted serpentinites (Smith et al., 2021). Both metallic iron derived from

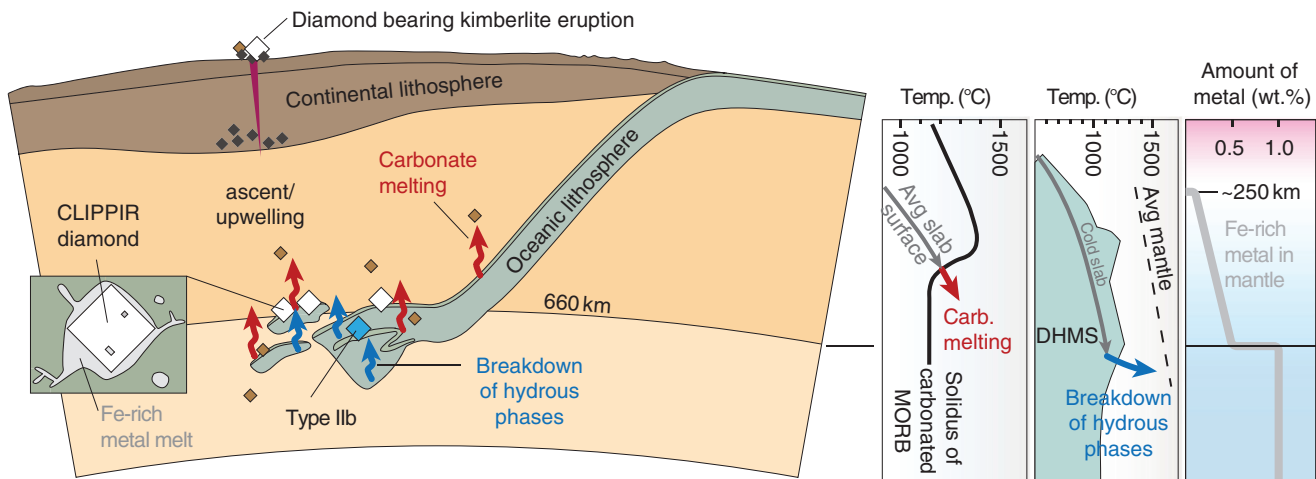


Figure 7.5 Three mechanisms of melt/fluid development related to super-deep diamonds. The three panels at right show: (1) carbonatitic melt triggered by the deep depression of the solidus for carbonated oceanic crust; (2) the release of hydrous fluid from the breakdown of DHMS (dense hydrous magnesium silicates) in the mantle portion of a cold slab as it warms/subducts, which may evolve to a carbonatitic melt; (3) Fe-Ni metal saturation in the mantle, due to Fe disproportionation, generating a metallic phase capable of acting as a reducing agent (for redox freezing) and a diamond-forming medium (Fe-Ni-C-S melt). Source: (1) Redrawn from Thomson et al., 2016b. (2) Redrawn from Harte, 2010. (3) Redrawn from Rohrbach & Schmidt, 2011.

serpentinization as well as that from disproportionation could be reflected in the super-deep diamond record. Metallic iron is implicated both as a key ingredient for some diamond-forming media and as a redox-buffering agent. CLIPPIR diamonds grown from metallic melt might be the most common variety of super-deep diamond, considering that most of the ~1% of gem diamonds that qualify as type IIa (e.g., in a gemological laboratory) are proposed to belong to the CLIPPIR variety (Smith et al., 2017).

All three are important, not only for describing diamond growth but also for facilitating chemical mass-transfer in the mantle and for actuating zones of local weakness that accommodate strain, especially for subducting slabs. The three mechanisms are outlined above as end members to differentiate their provenance, but in reality mantle fluids/melts likely evolve in composition, mix, and react in complex ways. Super-deep diamonds have emerged as a powerful way to study the fate of subducted slabs and the dynamic interior of our planet.

ACKNOWLEDGMENTS

F.V. Kaminsky and an anonymous reviewer are thanked for their helpful insights and suggestions that greatly improved the manuscript. The editors are thanked for arranging this special AGU feature. F.N. is supported

by the European Research Council through the ERC Starting Grant n. 307322.

REFERENCES

- Anzolini, C., Angel, R., Merlini, M., Derzsi, M., Tokár, K., Milani, S., et al. (2016). Depth of formation of CaSiO_3 -walsstromite included in super-deep diamonds. *Lithos*, 265, 138–147.
- Anzolini, C., Nestola, F., Mazzucchelli, M. L., Alvaro, M., Nimis, P., Gianese, A., et al. (2019). Depth of diamond formation obtained from single periclase inclusions. *Geology*, 47(3), 219–222. 10.1130/g45605.1
- Anzolini, C., Prencipe, M., Alvaro, M., Romano, C., Vona, A., Lorenzon, S., et al. (2018). Depth of formation of super-deep diamonds: Raman barometry of CaSiO_3 -walsstromite inclusions. *American Mineralogist*, 103(1), 69–74. 10.2138/am-2018-6184
- Ballhaus, C. (1995). Is the upper mantle metal-saturated? *Earth and Planetary Science Letters*, 132(1–4), 75–86. 10.1016/0012-821X(95)00047-G
- Bell, D. R., & G. R. Rossman (1992). Water in Earth's Mantle: The Role of Nominally Anhydrous Minerals, *Science*, 255 (5050), 1391–1397.
- Binns, R., Davis, R., & Reed, S. (1969). Ringwoodite, natural (Mg, Fe) 2SiO_4 spinel in the Tenham meteorite. *Nature*, 221(5184), 943.
- Bodnar, R.J., Azbej, T., Becker, S.P., Cannatelli, C., Fall, A., & Severs, M.J. (2013). Whole Earth geohydrologic cycle, from the clouds to the core: the distribution of water in the dynamic Earth system. In M.E. Bickford (Ed.), *The web of geological sciences: Advances, impacts, and interactions*, Geological

- Society of America Special Paper* (Vol. 500, pp. 431–461). Boulder, CO, The Geological Society of America.
- Bolfan-Casanova, N., Keppler, H., & Rubie, D.C. (2000). Water partitioning between nominally anhydrous minerals in the MgO–SiO₂–H₂O system up to 24 GPa: implications for the distribution of water in the Earth's mantle. *Earth and Planetary Science Letters*, 182(3–4), 209–221. 10.1016/S0012-821X(00)00244-2.
- Bowen, D. C., R. D. Ferraris, C. E. Palmer, & J. D. Ward (2009). On the unusual characteristics of the diamonds from Letšeng-la-Terae kimberlites, *Lesotho, Lithos*, 112S(0), 767–774.
- Brenker, F. E., Vincze, L., Vekemans, B., Nasdala, L., Stachel, T., Vollmer, C., et al. (2005). Detection of a Ca-rich lithology in the Earth's deep (> 300 km) convecting mantle. *Earth and Planetary Science Letters*, 236(3), 579–587. 10.1016/j.epsl.2005.05.021
- Brenker, F.E., Vollmer, C., Vincze, L., Vekemans, B., Szymanski, A., Janssens, K., et al. (2007). Carbonates from the lower part of transition zone or even the lower mantle. *Earth and Planetary Science Letters*, 260(1), 1–9. <https://doi.org/10.1016/j.epsl.2007.02.038>
- Bulanova, G.P., Walter, M.J., Smith, C.B., Kohn, S.C., Armstrong, L.S., Blundy, J., et al. (2010). Mineral inclusions in sublithospheric diamonds from Collier 4 kimberlite pipe, Juina, Brazil: Subducted protoliths, carbonated melts and primary kimberlite magmatism. *Contributions to Mineralogy and Petrology*, 160(4), 489–510. 10.1007/s00410-010-0490-6
- Burnham, A.D., Thomson, A.R., Bulanova, G.P., Kohn, S.C., Smith, C.B., & Walter, M.J. (2015). Stable isotope evidence for crustal recycling as recorded by superdeep diamonds. *Earth and Planetary Science Letters*, 432, 374–380. 10.1016/j.epsl.2015.10.023
- Cartigny, P., M. Palot, E. Thomassot, & J. W. Harris (2014). Diamond formation: a stable isotope perspective, *Annual Review of Earth and Planetary Sciences*, 42(1).
- Deschamps, F., Godard, M., Guillot, S., & Hattori, K. (2013). Geochemistry of subduction zone serpentinites: a review. *Lithos*, 178, 96–127.
- Faccenda, M., & Dal Zilio, L. (2017). The role of solid–solid phase transitions in mantle convection. *Lithos*, 268–271, 198–224. 10.1016/j.lithos.2016.11.007
- Fei, H.Z., Yamazaki, D., Sakurai, M., Miyajima, N., Ohfuji, H., Katsura, T. et al. (2017). A nearly water-saturated mantle transition zone inferred from mineral viscosity. *Science Advances*, 3(6), Article Number e1603024. 10.1126/sciadv.1603024.
- Frost, D.J., Liebske, C., Langenhorst, F., McCammon, C.A., Trønnes, R.G., & Rubie, D.C. (2004). Experimental evidence for the existence of iron-rich metal in the Earth's lower mantle. *Nature*, 428(6981), 409–412. 10.1038/nature02413
- Frost, D.J., & McCammon, C.A. (2008). The redox state of Earth's mantle. *Annual Review of Earth and Planetary Sciences*, 36, 389–420. 10.1146/annurev.earth.36.031207.124322.
- Gaillou, E., Post, J.E., Rost, D., & Butler, J.E. (2012). Boron in natural type IIb blue diamonds: Chemical and spectroscopic measurements, *Am. Mineral.*, 97(1), 1–18.
- Garrevoet, J., Vekemans, B., Tack, P., De Samber, B. R., Schmitz, S., Brenker, F. E., et al. (2014). Methodology toward 3D micro X-ray fluorescence imaging using an energy dispersive charge-coupled device detector. *Analytical Chemistry*, 86(23), 11826–11832.
- Gasparik, T., Wolf, K., & Smith, C. M. (1994). Experimental determination of phase relations in the CaSiO₃ system from 8 to 15 GPa. *American Mineralogist*, 79(11–12), 1219–1222.
- Haggerty, S. E. (1994). Superkimberlites: A geodynamic diamond window to the Earth's core. *Earth and Planetary Science Letters*, 122(1–2), 57–69.
- Harte, B. (2010). Diamond formation in the deep mantle: the record of mineral inclusions and their distribution in relation to mantle dehydration zones. *Mineralogical Magazine*, 74(2), 189–215. 10.1180/minmag.2010.074.2.189
- Harte, B., Harris, J. W., Hutchison, M. T., Watt, G. R., & Wilding, M. C. (1999). Lower mantle mineral associations in diamonds from Sao Luiz, Brazil. In Y. Fei, C. M. Bertka, & B. O. Mysen (Eds.), *Mantle Petrology: Field Observations and High Pressure Experimentation: A tribute to Francis R. (Joe) Boyd* (pp. 125–153). Houston: The Geochemical Society.
- Harte, B., & Hudson, N.C.F. (2013). Mineral associations in diamonds from the lowermost upper mantle and uppermost lower mantle. *Proceedings of 10th International Kimberlite Conference*, 1, 235–253. 10.1007/978-81-322-1170-9_15
- Harte, B., & Richardson, S. (2012). Mineral inclusions in diamonds track the evolution of a Mesozoic subducted slab beneath West Gondwanaland, *Gondwana Research*, 21(1), 236–245.
- Hayman, P., Kopylova, M., & Kaminsky, F. (2005). Lower mantle diamonds from Rio Soriso (Juina area, Mato Grosso, Brazil). *Contributions to Mineralogy and Petrology*, 149(4), 430–445. 10.1007/s00410-005-0657-8
- Hirose, K., & Fei, Y. (2002). Subsolvus and melting phase relations of basaltic composition in the uppermost lower mantle. *Geochimica et Cosmochimica Acta*, 66(12), 2099–2108. 10.1016/S0016-7037(02)00847-5
- Ickert, R.B., Stachel, T., Stern, R.A., & Harris, J.W. (2015). Extreme 18O-enrichment in majorite constrains a crustal origin of transition zone diamonds. *Geochemical Perspectives Letters*, 1(0), 65–74. 10.7185/geochemlet.1507
- Inoue, T. (1994). Effect of water on melting phase relations and melt composition in the system Mg₂SiO₄–MgSiO₃–H₂O up to 15 GPa. *Physics of the Earth and Planetary Interiors*, 85 (3–4), 237–263. 10.1016/0031-9201(94)90116-3
- Jacobsen, S. D. & J. R. Smyth (2006). Effect of water on the sound velocities of ringwoodite in the transition zone. *Earth's deep water cycle, AGU Geoph. Monograph, AGU. 168.* 131–145.
- Jacobsen, S.D., Smyth, J.R., Spetzler, H., Holl, C.M., & Frost, D.J. (2004). Sound velocities and elastic constants of iron-bearing hydrous ringwoodite. *Physics of the Earth and Planetary Interiors*, 143, 47–56. 10.1016/j.pepi.2003.07.019.
- Joswig, W., Stachel, T., Harris, J. W., Baur, W. H., & Brey, G. P. (1999). New Ca-silicate inclusions in diamonds — tracers from the lower mantle. *Earth and Planetary Science Letters*, 173(1–2), 1–6. 10.1016/S0012-821X(99)00210-1
- Kaminsky, F. (2012). Mineralogy of the lower mantle: A review of 'super-deep' mineral inclusions in diamond. *Earth-Science Reviews*, 110(1–4), 127–147. 10.1016/j.earscirev.2011.10.005
- Kaminsky, F. (2017). *The Earth's Lower Mantle*, Springer, 10.1007/978-3-319-55684-0

- Kaminsky, F., Wirth, R., Matsyuk, S., Schreiber, A., & Thomas, R. (2009). Nyerereite and nahcolite inclusions in diamond: evidence for lower-mantle carbonatitic magmas. *Mineralogical Magazine*, 73(5), 797–816. 10.1180/minmag.2009.073.5.797
- Kaminsky, F. V., Wirth, R., & Schreiber, A. (2013). Carbonatitic inclusions in Deep Mantle diamond from Juina, Brazil: New minerals in the carbonate-halide association. *The Canadian Mineralogist*, 51(5), 669–688. 10.3749/canmin.51.5.669
- Kendrick, M.A., Hemond, C., Kamenetsky, V.S., Danyush-evsky, L., Devey, C.W., Rodemann, T., et al. (2017). Seawater cycled throughout Earth's mantle in partially serpentinized lithosphere. *Nature Geoscience*, 10(3), 222–228. Article. 10.1038/ngeo2902
- Keppeler, H., & Bolfan-Casanova, N. (2006). Thermodynamics of water solubility and partitioning. In H. Keppeler, J.R. Smyth (Eds.), *Water in nominally anhydrous minerals, Reviews in Mineralogy and Geochemistry* (Vol. 62, pp. 193–230). Chantilly, VA, Mineralogical Society of America.
- King, J. M., T. M. Moses, J. E. Shigley, C. M. Welbourn, S. C. Lawson, and M. Cooper (1998). Characterizing natural-color type IIb blue diamonds. *Gems & Gemology*, 34(4), 246–268.
- Kiseeva, E.S., Vasiukov, D.M., Wood, B.J., McCammon, C., Stachel, T., Bykov, M., et al. (2018). Oxidized iron in garnets from the mantle transition zone. *Nature Geoscience*, 11(2), 144–147. 10.1038/s41561-017-0055-7
- Kohlstedt, D., Keppeler, H., & Rubie, D. (1996). Solubility of water in the α , β and γ phases of $(\text{Mg, Fe})_2\text{SiO}_4$. *Contributions to Mineralogy and Petrology*, 123(4), 345–357.
- Konrad-Schmolke, M., Halama, R., & Manea, V.C. (2016). Slab mantle dehydrates beneath Kamchatka—Yet recycles water into the deep mantle. *Geochemistry, Geophysics, Geosystems*, 17(8), 2987–3007. 10.1002/2016GC006335
- Leeman, W.P., Tonarini, S., & Turner, S. (2017). Boron isotope variations in Tonga-Kermadec-New Zealand arc lavas: Implications for the origin of subduction components and mantle influences. *Geochemistry, Geophysics, Geosystems*, 18(3), 1126–1162. 10.1002/2016GC006523
- Mao, Z., Lin, J.-F., Jacobsen, S. D., Duffy, T. S., Chang, Y.-Y., Smyth, J. R., Frost, D. J., Hauri, E. H., & Prakapenka, V. B. (2012). Sound velocities of hydrous ringwoodite to 16 GPa and 673 K. *Earth and Planetary Science Letters*, 331–332 (0), 112–119.
- Milledge, H.J., Mendelssohn, M.J., Seal, M., Rouse, J.E., Swart, P.K., & Pillinger, C.T. (1983). Carbon isotopic variation in spectral type II diamonds. *Nature*, 303(5920), 791–792. 10.1038/303791a0.
- Nestola, F. (2015). Ringwoodite: its importance in Earth Sciences. In T. Armbruster, R.M. Danisi (Eds.), *Highlights in Mineralogical Crystallography* (pp. 127–147). De Gruyter, Berlin.
- Nestola, F. (2017). Inclusions in super-deep diamonds: windows on the very deep Earth. *Rendiconti Lincei*, 28(4), 595–604. 10.1007/s12210-017-0607-1
- Nestola, F., & Smyth, J.R. (2016) Diamonds and water in the deep Earth: a new scenario. *International Geology Review*, 58(3), 263–276. 10.1080/00206814.2015.1056758
- Nestola, F., Korolev, N., Kopylova, M., Rotiroti, N., Pearson, D. G., Pamato, M. G., et al. (2018). CaSiO_3 perovskite in diamond indicates the recycling of oceanic crust into the lower mantle. *Nature*, 555(7695), 237–241. 10.1038/nature25972
- Nimis, P., Nestola, F., Schiazza, M., Reali, R., Agrosi, G., Mele, D., et al. (2018). Fe-rich ferropericlae and magnesio-wüstite inclusions reflecting diamond formation rather than ambient mantle. *Geology*, 47(1), 27–30. 10.1130/g45235.1
- Pagé, L., Hattori, K., & Guillot, S. (2018). Mantle wedge serpentinites: a transient reservoir of halogens, boron, and nitrogen for the deeper mantle. *Geology*. 10.1130/G45204.1
- Palot, M., Jacobsen, S. D., Townsend, J., Nestola, F., Marquardt, K., Miyajima, N., et al. (2016). Evidence for H_2O -bearing fluids in the lower mantle from diamond inclusion. *Lithos*, 265, 237–243.
- Palot, M., Pearson, D. G., Stern, R. A., Stachel, T., & Harris, J. W. (2014). Isotopic constraints on the nature and circulation of deep mantle C–H–O–N fluids: Carbon and nitrogen systematics within ultra-deep diamonds from Kankan (Guinea). *Geochimica et Cosmochimica Acta*, 139, 26–46. 10.1016/j.gca.2014.04.027
- Palyanov, Y. N., Bataleva, Y. V., Sokol, A. G., Borzdov, Y. M., Kupriyanov, I. N., Reutsky, V. N., & Sobolev, N. V. (2013). Mantle-slab interaction and redox mechanism of diamond formation. *Proceedings of the National Academy of Sciences*, 110(51), 20408–20413. 10.1073/pnas.1313340110
- Pearson, D.G., Brenker, F.E., Nestola, F., McNeill, J., Nasdala, L., Hutchison, M.T., et al. (2014). Hydrous mantle transition zone indicated by ringwoodite included within diamond. *Nature*, 507(7491), 221–224.
- Ringwood, A. E. (1991). Phase transformations and their bearing on the constitution and dynamics of the mantle, *Geochim. Cosmochim.*, 55(8), 2083–2110.
- Rohrbach, A., Ballhaus, C., Golla-Schindler, U., Ulmer, P., Kamenetsky, V.S., & Kuzmin, D.V. (2007). Metal saturation in the upper mantle. *Nature*, 449(7161), 456–458. 10.1038/nature06183
- Rohrbach, A., Ballhaus, C., Ulmer, P., Golla-Schindler, U., & Schönbohm, D. (2011). Experimental evidence for a reduced metal-saturated upper mantle. *Journal of Petrology*, 52(4), 717–731. 10.1093/petrology/egq101
- Rohrbach, A., Ghosh, S., Schmidt, M. W., Wijbrans, C. H., & Klemme, S. (2014). The stability of Fe-Ni carbides in the Earth's mantle: Evidence for a low Fe-Ni-C melt fraction in the deep mantle. *Earth and Planetary Science Letters*, 388 (0), 211–221. 10.1016/j.epsl.2013.12.007
- Rohrbach, A., & Schmidt, M. W. (2011). Redox freezing and melting in the Earth's deep mantle resulting from carbon-iron redox coupling. *Nature*, 472(7342), 209–212. 10.1038/nature09899
- Scambelluri, M., Müntener, O., Ottolini, L., Pettke, T. T., & Vannucci, R. (2004). The fate of B, Cl and Li in the subducted oceanic mantle and in the antigorite breakdown fluids. *Earth and Planetary Science Letters*, 222(1), 217–234. 10.1016/j.epsl.2004.02.012
- Schulze, K., Marquardt, H., Kawazoe, T., Boffa Ballaran, T., McCammon, C., Koch-Müller, M., Kurnosov, A. & Marquardt, K. (2018). Seismically Invisible Water in Earth's Transition Zone? *Earth and Planetary Science Letters*, 498, 9–16.
- Seitz, H.-M., Brey, G.P., Harris, J.W., Durali-Müller, S., Ludwig, T., & Höfer, H.E. (2018). Ferropericlae inclusions

- in ultradeep diamonds from Sao Luiz (Brazil): high Li abundances and diverse Li-isotope and trace element compositions suggest an origin from a subduction mélange. *Mineralogy and Petrology*. 10.1007/s00710-018-0572-0
- Shen, G., & Mao, H. K. (2016). High-pressure studies with x-rays using diamond anvil cells. *Reports on Progress in Physics*. 80(1), 016101.
- Shirey, S. B., Cartigny, P., Frost, D. J., Keshav, S., Nestola, F., Nimis, P., et al. (2013). Diamonds and the geology of mantle carbon. *Reviews in Mineralogy and Geochemistry*, 75, 355–421.
- Smith, E.M., & Kopylova, M.G. (2014). Implications of metallic iron for diamonds and nitrogen in the sublithospheric mantle. *Canadian Journal of Earth Sciences*, 51(5), 510–516. 10.1139/cjes-2013-0218
- Smith, E. M., Kopylova, M. G., Frezzotti, M. L., & Afanasiev, V. P. (2014). N-rich fluid inclusions in octahedrally-grown diamond. *Earth and Planetary Science Letters*, 393(0), 39–48. 10.1016/j.epsl.2014.02.033
- Smith, E. M., Ni, P., Shirey, S. B., Richardson, S. H., Wang, W., & Shahar, A. (2021). Heavy iron in large gem diamonds traces deep subduction of serpentinized ocean floor. *Science Advances*, 7(14), eabe9773. 10.1126/sciadv.abe9773
- Smith, E.M., Shirey, S.B., Nestola, F., Bullock, E.S., Wang, J., Richardson, S.H., & Wang, W. (2016). Large gem diamonds from metallic liquid in Earth's deep mantle. *Science*, 354(6318), 1403–1405. 10.1126/science.aal1303
- Smith, E.M., Shirey, S.B., Richardson, S.H., Nestola, F., Bullock, E.S., Wang, J., & Wang, W. (2018). Blue boron-bearing diamonds from Earth's lower mantle. *Nature*, 560(7716), 84–87. 10.1038/s41586-018-0334-5
- Smith, E.M., Shirey, S.B., & Wang, W. (2017). The very deep origin of the world's biggest diamonds. *Gems & Gemology*, 53(4), 388–403. 10.5741/GEMS.53.4.388
- Smyth, J. R. (1987). β -Mg₂SiO₄: a potential host for water in the mantle? *American Mineralogist*, 72(11–12), 1051–1055.
- Smyth, J., Holl, C.M., Frost, D.J., Jacobsen, S.D., Langenhorst, F., & McCammon, C. (2003) Structural systematics of hydrous ringwoodite and water in Earth's interior. *American Mineralogist*, 88(10), 1402–1407.
- Stachel, T., Brey, G., & Harris, J. W. (2005). Inclusions in sublithospheric diamonds: glimpses of deep earth. *Elements*, 1, 73–78.
- Stachel, T., Harris, J. W., Brey, G. P., & Joswig, W. (2000). Kankan diamonds (Guinea) II: lower mantle inclusion parageneses. *Contributions to Mineralogy and Petrology*, 140(1), 16–27. journal article. 10.1007/s004100000174
- Stixrude, L., & Lithgow-Bertelloni, C. (2012). Geophysics of Chemical Heterogeneity in the Mantle. *Annual Review of Earth and Planetary Sciences*, 40(1), 569–595. 10.1146/annurev.earth.36.031207.124244
- Tappert, R., Stachel, T., Harris, J., Muehlenbachs, K., Ludwig, T., & Brey, G. (2005). Diamonds from Jagersfontein (South Africa): messengers from the sublithospheric mantle. *Contributions to Mineralogy and Petrology*, 150(5), 505–522. 10.1007/s00410-005-0035-6
- Tenthorey, E., & Hermann, J. (2004). Composition of fluids during serpentinite breakdown in subduction zones: evidence for limited boron mobility. *Geology*, 32(10), 865–868. 10.1130/G20610.1
- Thomas, S.M., Jacobsen, S.D., Bina, C.R., Reichart, P., Moser, M., Hauri, E.H. (2015) Quantification of water in hydrous ringwoodite. *Frontiers in Earth Sciences*, 2, article number UNSP 38. 10.3389/feart.2014.00038.
- Thomson, A., Kohn, S., Bulanova, G., Smith, C., Araujo, D., & Walter, M. (2014). Origin of sub-lithospheric diamonds from the Juina-5 kimberlite (Brazil): constraints from carbon isotopes and inclusion compositions. *Contributions to Mineralogy and Petrology*, 168(6), 1081. 10.1007/s00410-014-1081-8
- Thomson, A.R., Kohn, S.C., Bulanova, G.P., Smith, C.B., Araujo, D., & Walter, M.J. (2016a). Trace element composition of silicate inclusions in sub-lithospheric diamonds from the Juina-5 kimberlite: Evidence for diamond growth from slab melts. *Lithos*, 265, 108–124. 10.1016/j.lithos.2016.08.035
- Thomson, A.R., Walter, M.J., Kohn, S.C., & Brooker, R.A. (2016b). Slab melting as a barrier to deep carbon subduction. *Nature*, 529(7584), 76–79.
- Tschauner, O., Huang, S., Greenberg, E., Prakapenka, V.B., Ma, C., Rossman, G. R., et al. (2018). Ice-VII inclusions in diamonds: Evidence for aqueous fluid in Earth's deep mantle. *Science*, 359(6380), 1136–1139. 10.1126/science.aao3030
- van der Hilst, R.D., Widiyantoro, S., & Engdahl, E.R. (1997). Evidence for deep mantle circulation from global tomography. *Nature*, 386, 578. 10.1038/386578a0
- Walter, M.J., Bulanova, G.P., Armstrong, L.S., Keshav, S., Blundy, J.D., Gudfinnsson, G., et al. (2008). Primary carbonatite melt from deeply subducted oceanic crust. *Nature*, 454(7204), 622–625. 10.1038/nature07132.
- Walter, M.J., Kohn, S.C., Araujo, D., Bulanova, G.P., Smith, C.B., Gaillou, E., et al. (2011). Deep mantle cycling of oceanic crust: Evidence from diamonds and their mineral inclusions. *Science*, 334(6052), 54–57. 10.1126/science.1209300
- Wirth, R., Vollmer, C., Brenker, F., Matsyuk, S., & Kaminsky, F. (2007). Inclusions of nanocrystalline hydrous aluminium silicate “Phase Egg” in superdeep diamonds from Juina (Mato Grosso State, Brazil). *Earth and Planetary Science Letters*, 259(3), 384–399.
- Zedgenizov, D.A., Ragozin, A.L., Kalinina, V.V., & Kagi, H. (2016). The mineralogy of Ca-rich inclusions in sublithospheric diamonds. *Geochemistry International*, 54(10), 890–900. 10.1134/S0016702916100116
- Zedgenizov, D.A., Zedgenizova, D.A., Shatskya, V.S., Paninc, A.V., & Evtushenkoc, O.V. (2015). Evidence for phase transitions in mineral inclusions in superdeep diamonds of the Sao Luiz deposit (Brazil). *Russian Geology and Geophysics*, 56(1–2), 296–305. 10.1016/j.rgg.2015.01.021
- Ye, Y., Brown, D.A., Smyth, J.R., Panero, W.R., Jacobsen, S.D., Chang, Y.Y., et al. (2012). Compressibility and thermal expansion of hydrous ringwoodite with 2.5(3) wt% H₂O. *American Mineralogist*, 97(4), 573–582. 10.2138/am.2012.4010

Seismic and Mineral Physics Constraints on the D'' Layer

Jennifer M. Jackson¹ and Christine Thomas²

ABSTRACT

We present a synthesis of results from seismic and mineral physics studies of the D'' layer to improve constraints on Earth's lowermost mantle. We focus on structures of two length scales, the seismic reflector at the top of this region and the structures of smaller scale known as ultralow velocity zones (ULVZs). A review of seismic observations for the D'' layer and their interpretation is followed by a case study, where we combine new data with published results for the D'' region beneath the Bering Sea and Alaska. Our evaluation of plausible interpretations includes features related to subducted slab debris that trade-off with petrology (mineral phase assemblage) and post-perovskite crystal chemistry. For the smaller-scale structures that exhibit lower than average seismic wave-speeds, the ULVZs, we consider hypotheses involving either iron-rich (Mg,Fe)O magnesiowüstite or iron-rich (Mg,Fe)SiO₃ post-perovskite. We use mineral physics data and previously published seismic reduction ratios of S- and P-wave speeds with their respective uncertainties for a best-fit optimization approach with parameter correlations. Seismic wave reduction ratios ranging from 2 to 3 are well explained by phase assemblages containing elastically anisotropic iron-rich (Mg,Fe)O. Observations outside this range require different explanations than those considered here, thus suggesting diverse origins for ULVZs.

8.1. INTRODUCTION

The boundary between the core and mantle is a primary interface within the deep interior of Earth and has a fundamental influence on the cooling of the planet. Thus, this region may provide essential clues in revealing the planet's thermo-chemical evolution. The lowermost mantle is characterized by anomalous seismic gradients that were first noted by Gutenberg (1914). This particular region of the mantle, referred to as the D'' layer (Bullen, 1950) hosts a myriad of seismic features. These features range from abrupt velocity increases to regions characterized by a

decrease in the velocity gradients, and have been the focus of several reviews (e.g., Cobden et al., 2015; Garnero, 2000; Garnero et al., 2016; Kendall and Silver, 1998; Lay, 2015; Nowacki et al., 2011; Romanowicz and Wenk, 2017; Weber et al., 1996; Wyssession et al., 1998; Yu and Garnero, 2018). The various anomalous features have been associated with structures of different length scales, ranging from large-scale seismic velocity anomalies and seismic anisotropy to small-scale scatterers and ultralow velocity zones. Thermal and chemical heterogeneity, solid-solid phase transitions, lattice or shape preferred orientation, complex rheology, and melting are probably all necessary to explain the observed structures. Understanding the origin of these multi-scale structures requires, in part, advances in mineral physics, tightly coupled with seismological observations, geodynamic modeling, and geochemical analysis (e.g.,

¹*Seismological Laboratory, California Institute of Technology, Pasadena, CA, USA*

²*Institut für Geophysik, Westfälische Wilhelms-Universität, Münster, Germany*

Bower et al., 2013a, 2011; Cobden et al., 2015; Deschamps and Tackley, 2008; Deschamps and Trampert, 2003; McNamara et al., 2010; Nowacki et al., 2011; Pisconti et al., 2019; Sun et al., 2019, 2016), while taking into account mutual uncertainties (e.g., Dobrosavljevic et al., 2019).

The D" layer is situated just above the largest radial density jump within the planet. Despite the relatively small volume of D", it may be the site of long-term differentiation and is often made a significant component of global mass balance problems; for example, the observed small-scale heterogeneity within D" may reveal long-term storage sites of heat-producing elements and/or volatiles (e.g., Albarède, 2005; Becker et al., 1999; Corgne and Wood, 2005; Helffrich and Wood, 2001; Hirose et al., 2004; Trønnes et al., 2019; Turcotte et al., 2001). The nature of this layer in multicomponent chemical systems, how this layer's character and location change with mantle composition, the influence of texture on observed seismic anisotropy, and the implications for mantle processes are important for understanding the dynamic evolution of the mantle and represent ongoing pursuits (e.g., Auzende et al., 2008; Bower et al., 2013b; Grocholski et al., 2012; Hernlund et al., 2005; Hirose, 2006; Hirose et al., 2008, 2005; Lay et al., 2008; Lay and Garnero, 2007; Lay and Helmberger, 1983a; Merkel et al., 2002; Miyagi et al., 2010; Murakami et al., 2005; Ono and Oganov, 2005; Pisconti et al., 2019; Ricolleau et al., 2008; Sakai et al., 2010; Shim, 2008; Sun and Helmberger, 2008; van der Hilst et al., 2007; Vinnik et al., 1989; Williams and Garnero, 1996).

The D" region is often marked by a reflector at its top that can provide information on the layer. The size of the velocity contrast across the layer and the depth of the reflector have been used to constrain the mineralogy. Other observables such as topography, velocity, and density contrasts across the reflector also help to infer the nature of the material within D" (see reviews by Cobden et al., 2015; Lay, 2015). The first part of this chapter will focus on the D" seismic reflector, including the range of seismic observations and plausible mineral physics interpretations with their associated trade-offs.

Small-scale structures within the D" layer that exhibit slower-than-average seismic wave speeds are typically termed *ultralow velocity zones* (ULVZs). In a recent review, Yu and Garnero (2018) present several key findings of ULVZs. In particular, modeling of seismic arrivals indicates the following with respect to the Preliminary Reference Earth Model, PREM (Dziewonski and Anderson, 1981) at the core-mantle boundary: a 3–25% decrease in V_P , and 6–50% decrease in V_S , thus indicating $\delta V_S/\delta V_P$ could range from 1:1 to 6:1, and that ULVZ density contrast ranges from 0 to 22% higher than PREM. Nevertheless, it remains unclear whether these structures could harbor primordial material, are correlated with hotspot locations on Earth's surface, or share a common origin

with larger structures in the lower mantle, such as large low seismic velocity provinces. Many of these interpretations rely on understanding the composition of ULVZs. The second part of this chapter will discuss the range of ULVZ seismic observations, the distribution of these features, and present new results from best-fit minimizations of mineral phase assemblages.

8.2. THE D" REFLECTOR(S)

8.2.1. Visibility of the Reflection

Lateral variations of seismic velocities in the lower mantle have been described in the past. For example, in the early 1970s, Wright and Cleary (1972) and Wright (1973), analyzing P waves, concluded that lateral velocity variations in the lowermost mantle exist. They suggest that these structures display features that vary depending on the region, from a reduced (or increased) velocity gradient, to abrupt changes in seismic velocity, and may be due to phase-changes in the mantle.

About a decade later, small seismic arrivals that appear between the S and ScS wave and the P and PcP wave, respectively, were observed and reveal a move-out (slowness) different from the main phases S and ScS (or P and PcP). These small additional arrivals have been interpreted as reflections off (triplifications due to) a high-velocity layer near the core-mantle boundary (e.g., Lay and Helmberger, 1983b; Weber and Davis, 1990; Young and Lay, 1990). In the following we will call these arrivals SdS and PdP and include the reflected and refracted waves in this name (i.e., SdS and SDS , or Sbc and Scd , same for P waves) (Figure 8.1).

There have been many different studies on the D" reflection, and this review cannot cover all of the previous studies for every region. Therefore, the reader is also referred to several previous reviews on this topic (e.g., Cobden et al., 2015; Lay, 2015, 2007; Wyssession et al., 1998). A summary of regions imaged with D" reflected waves is shown in Figure 8.2, which is based on the maps shown in Wyssession et al. (1998) and Cobden et al. (2015) with the addition of a few more studies (Durand et al., 2019; Pisconti et al., 2019; Thomas and Laske, 2015; Whittaker et al., 2016; Yao et al., 2015).

The first observations of SdS arrivals (Lay and Helmberger, 1983b) were from regions where we expect paleo-subduction (Lithgow-Bertelloni and Richards, 1998), and tomographic inversions display fast seismic velocities (e.g., French and Romanowicz, 2014; Grand, 2002; Li et al., 2008; Ritsema et al., 2011). Due to the different move-out of these SdS phases compared with the S and ScS wave, the arrival could not be due to depth phases or other structures near the surface. Modeling confirmed

that a distinct layer with thickness of approximately 300 km at the CMB and an increase in impedance (i.e., the product of velocity and density) could produce arrivals that can explain the observations (Houard and Nataf, 1993; Lay and Helmberger, 1983b; Weber, 1993; Young and Lay, 1990). Using array measurements, Weber and Davis (1990) used the travel time and the slowness of the new arrival compared with P and PcP values (Figure 8.1) and confirmed that the phase PdP had to be reflected off an approximately 300 km thick layer at the CMB (model PWDK: Weber and Davis, 1990; Weber et al., 1996).

The reflections off the D'' discontinuity are generally small and often not easily distinguishable in single records and in noisy data (e.g., Figure 8.3). Therefore, either distance dependent record sections aligned on either the direct wave (P or S) or the core reflected wave (PcP or ScS) or stacks of record sections help to distinguish between noise, Moho multiples, or D'' reflected arrivals, since the move-out (slowness) of the D'' reflection differs from that of the main phases. Vespagrams (i.e., velocity spectral analysis) (e.g., Davies et al., 1971; Rost and Thomas, 2002; Schweitzer et al., 2009) are constructed using recordings of a seismic array and, after shifting for different slowness values (related to the angle of incidence of the wave at the surface), the traces are stacked, either linearly

or after some weighting with, for example the instantaneous phase (Schimmel and Paulssen, 1997), or after taking the N th root (e.g., Muirhead and Datt, 1976) before stacking. The vespagram process amplifies coherent waves, reduces the amplitude of the (incoherent) noise, and allows to identify the different seismic arrivals by their slowness (Figure 8.3). Often, the frequency-wavenumber (fk -analysis) (e.g., Capon, 1973; Rost and Thomas, 2009) or slowness backazimuth analysis are used to confirm that the wave, interpreted as a D'' reflection, travels with the slowness and backazimuth of such a reflected D'' wave. For a review on seismic array techniques, the reader is referred to Schweitzer et al. (2009) and Rost and Thomas (2002, 2009).

Since the early observations of SdS and PdP that were detected mostly from high-velocity regions in the lowermost mantle as seen in tomographic inversions, the interpretation as a reflection off the top of subducted lithosphere was a preferred explanation (e.g., Lay and Garnero, 2004; Scherbaum et al., 1997; Thomas et al., 2004b; Weber, 1993), while other possible scenarios are solid-solid phase transitions (Sidorin et al., 1999, 1998) and accumulation of mid-ocean ridge basalt (MORB) or other chemically different layers, possibly including partial melting (e.g., Garnero, 2000; Lay et al., 2004b; Lay and Garnero, 2004). In 2004, experimental and theoretical mineral physics observed that the major lower mantle phase $MgSiO_3$ bridgmanite undergoes a structural phase transition to post-perovskite at D'' conditions (Murakami et al., 2004; Oganov and Ono, 2004; Tsuchiya et al., 2004). More detailed discussion on the range of interpretations for the reflected D'' wave can be found in section 8.2.4.

In the years following these early observations, many studies found evidence for D'' reflections in other high-velocity regions (see reviews by Cobden et al., 2015; Lay 2007, 2015; Wyssession et al., 1998; see also Figure 8.2), and further details arose during those studies: the reflector, which was initially modeled as a one-dimensional structure, showed evidence for topography in that the differential travel time of the reflected phase with respect to the main phases (P , S or PcP , ScS) varied between different events or locations (e.g., Hutko et al., 2006; Kendall and Nangini, 1996; Kendall and Shearer, 1994; Thomas et al., 2004a, 2004b). For example, the reflector beneath the Caribbean showed a strong variation in depth, estimated from the arrival time of the reflection, dropping from around 400 km above the CMB to around 200 km above the CMB (e.g., Hutko et al., 2006; Kendall and Nangini, 1996; Kito et al., 2007; Lay et al., 2004a; Thomas et al., 2004a; Thorne et al., 2007; van der Hilst et al., 2007). Other places also seemed to exhibit strong topography, for example beneath Siberia (e.g., Gaherty and Lay, 1992; Houard and Nataf, 1993; Thomas et al.,

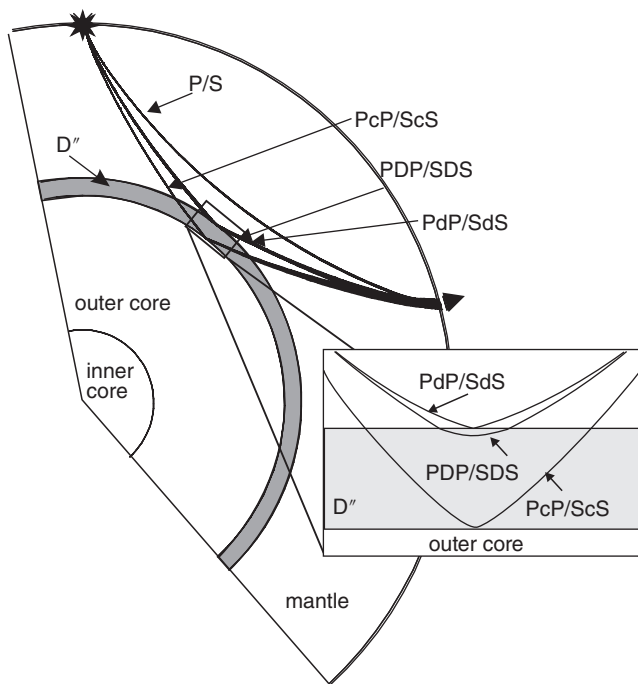


Figure 8.1 Ray paths of seismic phases, PdP and SdS , sampling D'' that are discussed in this Chapter. The inset shows the reflected and diving wave PdP (or SdS) and PDP (or SDS). SdS is also called Sbc , SDS is also called Scd , same for P waves.

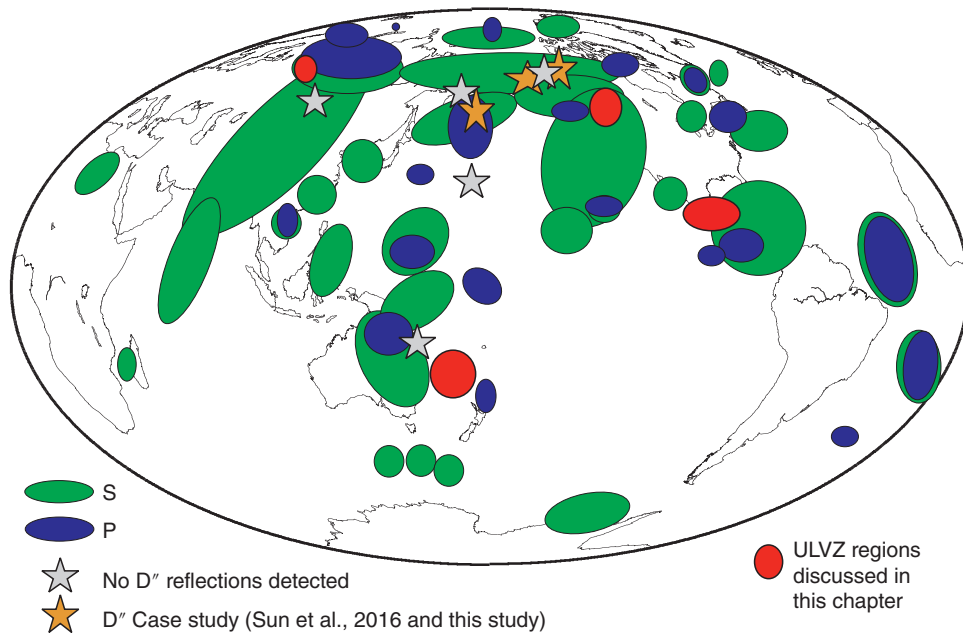


Figure 8.2 Places with D'' detections in different studies following the maps in Wysession et al. (1998) and Cobden et al. (2015). Green areas indicate S wave studies, blue areas are P wave studies. Grey stars show places where no D'' reflection was detected (e.g. Neuberg and Wahr, 1991; Thomas and Laske, 2015; Chambers and Woodhouse, 2006) and yellow stars indicate the place of the D'' case study from both Sun et al. (2016) and this work. The ULVZ regions discussed in the text are shown as red areas. Sources: From D'' studies summarized in this figure are given in Wysession et al. (1998) and Cobden et al. (2015). In addition, locations from Thomas and Laske (2015), Yao et al. (2015), Whittaker et al. (2016), Durand et al. (2019), Pisconti et al. (2019), and Pisconti (pers. comm.) are shown. For more information, see text.

2004b; Thomas and Weber, 1997), Southeast Asia (Chaloner et al., 2009; Kendall and Shearer, 1995), the mid-Pacific (Lay et al., 2006) and recently, the northern Atlantic (Durand et al., 2019; Yao et al., 2015).

In addition to reflections found in fast-velocity regions, regions that exhibit low seismic velocities in tomographic inversions have been investigated and D'' reflections from these areas are visible (e.g., Yamada and Nakanishi 1996, 1998; Kito and Krüger 2001; Lay et al. 2006; Ohta et al. 2008; Kawai and Geller 2010; Takeuchi and Obara 2010; Cobden and Thomas 2013). Areas that transition between fast and slow seismic velocities in tomographic models also seem to generate arrivals that arrive between P and PcP or S and ScS . These areas include but are not limited to the Atlantic and the western Pacific (e.g., Durand et al., 2019; Pisconti et al., 2019; Thomas and Laske, 2015; Whittaker et al., 2016; Yao et al., 2015). In many cases, array methods were used for these reflections to confirm that they have the appropriate travel time, slowness, and the back azimuth that classify them as D'' reflections. The amplitude of reflections at a discontinuity with a velocity decrease would be smaller than for a reflector with a positive velocity contrast, and the influence of the diving wave (SdS or PdP) would be decreased for a low-velocity

layer compared with high-velocity layer. This could be a reason for fewer detections in low-velocity regions.

It should be noted that sampling of the D'' region with reflected waves is limited due to source-receiver combinations that can be used to test the CMB region. The best epicentral distance to search for the reflector is 60–85 degrees distance (e.g., Cobden et al., 2015; Weber, 1993; Wysession et al., 1998), but smaller epicentral distances have been used as well (e.g., Rost and Thomas, 2010; Schimmel and Paulssen, 1996). Those smaller epicentral distances corresponding to a small angle of incidence at the reflector suffer from a small reflection coefficient and hence generally produce weaker reflections (Figure 8.4).

There seem to be very few places where no reflected wave from D'' is unequivocally visible when using stacking of seismic data, i.e., array methods (gray stars in Figure 8.2). Neuberg and Wahr (1991) reported an absence of the D'' arrival east of Australia, however, the epicentral distance for this study was 35 degrees where the reflection coefficient for PdP and SdS is very small (see Figure 8.4). Another region where no arrival is detected between P and PdP is the area beneath the Pacific Ocean (Thomas and Laske, 2015); however, this

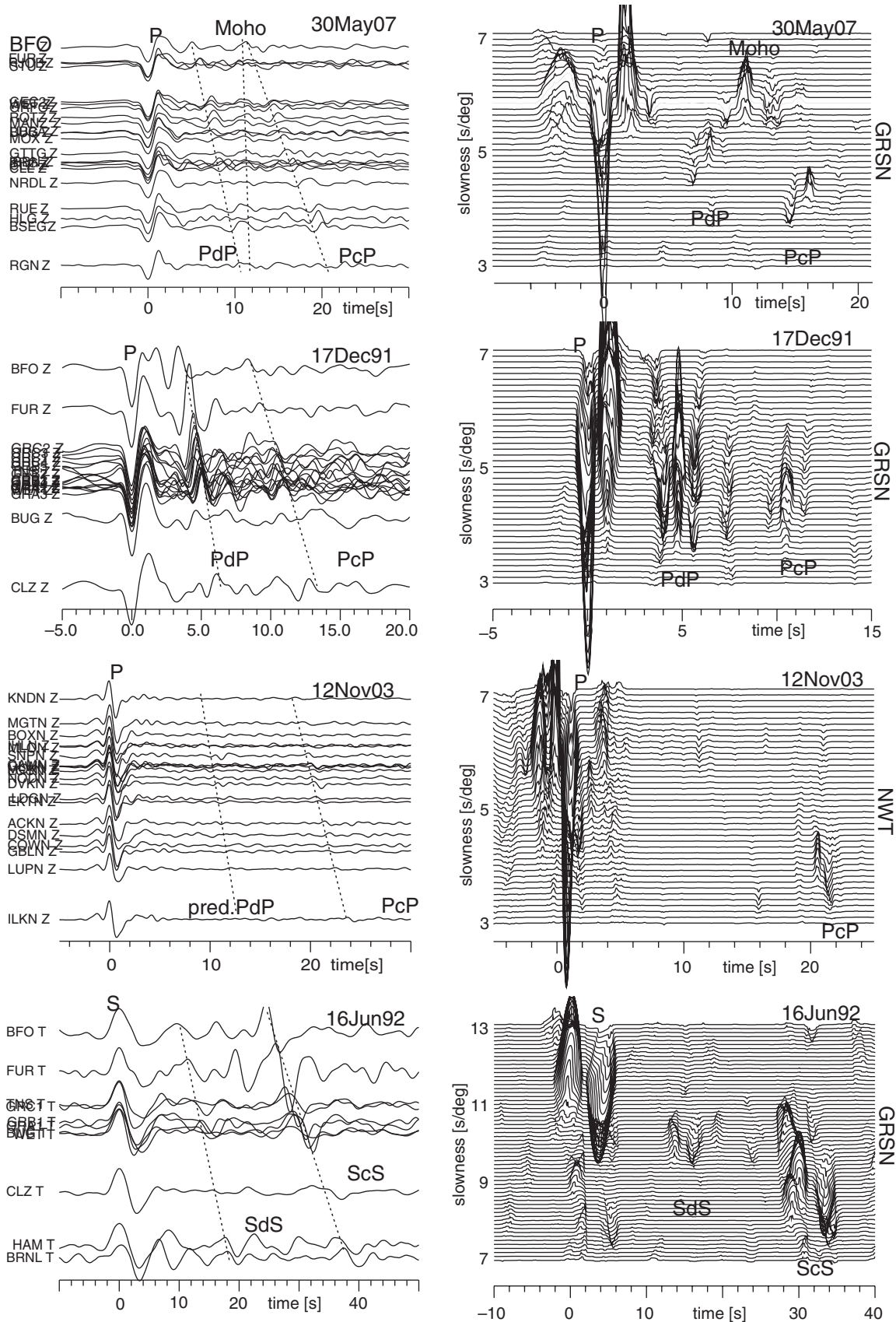


Figure 8.3 Examples of *PdP* observations in different regions showing amplitude differences and polarity variations. Event dates and arrays are given for each event, see also Appendix Table 8.A2. GRSN - German Regional Seismic Network; NWT- Polaris array, Northwest Territories, Canada. On the left are the seismic traces, aligned on *P* and *S*, respectively, and on the right the corresponding vespagrams. For the 12 November 2003 event, the predicted arrival time of *PdP* for a 300 km thick *D''* layer is indicated. In the other cases, the dashed lines indicate the arrivals of *PdP/SdS* and *PcP/ScS*. In the seismogram of 30 May 2007 the Moho arrival is also marked. The amplification is 100 for all *P* wave vespagrams after normalizing the traces and stacking them with a nonlinear stacking technique (4th root).

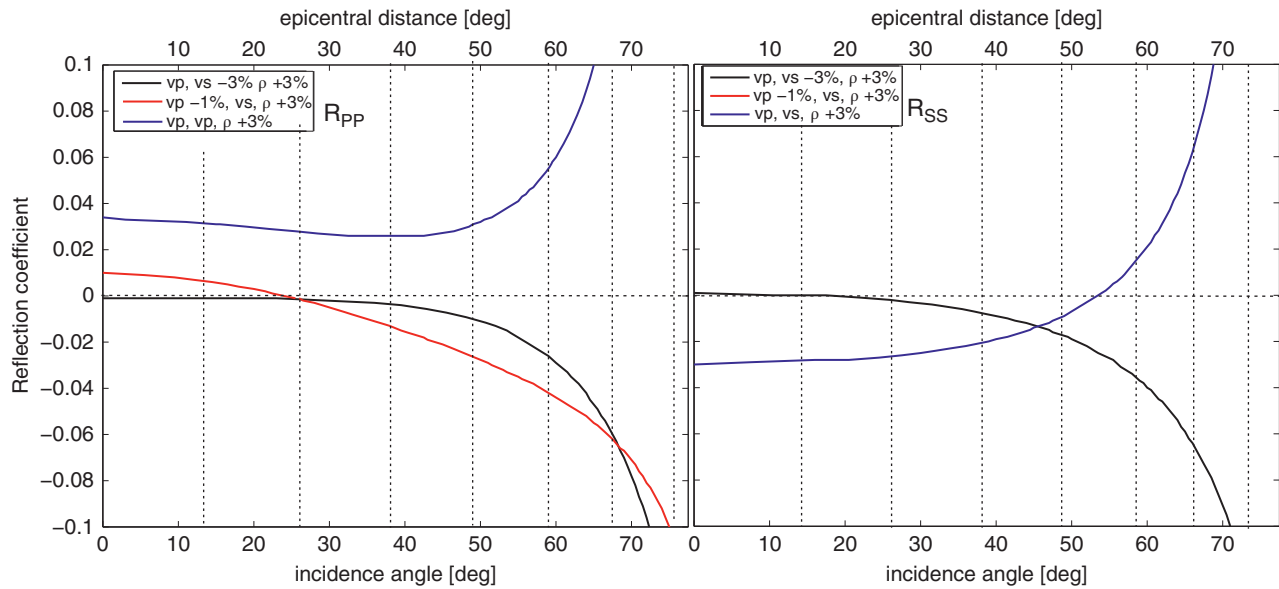


Figure 8.4 Examples of the reflection coefficients for P waves (R_{PP}) and S waves (R_{SS}) for select D'' scenarios. Blue line: for velocity contrast of V_P and V_S of +3%, based on model PWDK, black line for V_P and V_S of -3% and red line for V_P of -1% and V_S of +3%. The density contrast is always set to a 3% increase but it does not affect the reflection coefficient in distance ranges between 60 degrees and above. The red curve for R_{SS} is underneath the blue curve. The critical incidence angle for the blue curve (i.e., from which total reflection happens) is 76.09 deg for P waves and 76.12 deg for S waves, which corresponds to a distance of 70 and 71 degrees, respectively. The epicentral distance that corresponds to the incidence angle is given above the graph for P and S waves and is calculated for a reflector 300 km above the CMB and a P and S velocity for the D'' region consistent with PWDK.

is also an example where the epicentral distances are short and the amplitude of PdP is predicted to be very small. Beneath the Aleutians it seems that areas without a D'' reflector exist in two different regions (Figure 8.3 and 8.5; Sun et al., 2006, 2016), but they are close to regions where a reflector is found. Scherbaum et al. (1997) suggested that localized inhomogeneity (scatterers) could be a reason for intermittent observation of D'' reflections. It has also been suggested that strong topography can create record sections without a D'' reflection or with two arrivals, due to focusing and defocusing effects (e.g., Thomas and Weber, 1997; Whittaker et al., 2016), while Sun et al. (2016, 2006) indicate an interrupted reflector due to an upwelling plume, i.e., a more dynamically inspired cause. A similar scenario as the one observed by Sun et al. (2016) has been reported by Chambers and Woodhouse (2006) beneath North-central Asia. Taking all reports of the presence or absence of D'' reflections together suggests that in almost all tested regions, where data quality is good and the epicentral distances ensure a large reflection coefficient, arrivals have been detected in the datasets with a move-out (slowness) and timing that agree with a D'' reflected PdP or SdS (e.g., Cobden et al., 2015; Lay, 2015; Wysession et al., 1998). The cases where data quality is good but no D'' reflection has been consistently observed in one region seem to be the exception rather than the rule. In this latter case, it is still possible

that a reflector is present but cannot be imaged with currently available source-receiver combinations, that there is topography, and hot upwelling (e.g., Sun et al., 2016), or that the impedance contrast is too small to allow detections (Thomas and Weber, 1997; Whittaker et al., 2016).

In many cases a clear distinction of the D'' reflection from other interfering phases is difficult: Moho multiples and depth phases make observations of the weaker D'' reflections difficult, and even though the move-out, i.e., the slowness, would help to distinguish these waves, the often-high amplitude depth phases or Moho multiples may interfere with the D'' reflection and may render it invisible (Lessing et al., 2015).

In several regions, a second arrival between P and PcP or S and ScS , in addition to PdP/SdS , has been reported: beneath the Caribbean (Hutko et al., 2009; Kawai et al., 2007; Kito et al., 2007; Thomas et al., 2004a), Southeast Asia (Chaloner et al., 2009), Siberia (Thomas et al., 2004b), and the Pacific (Kawai and Geller, 2010). Lay et al. (2006) and Ohta et al. (2008) report up to three arrivals between S and ScS in the Pacific. These additional arrivals point to a second and possibly third reflector beneath the top of the D'' layer that is visible beneath at least parts of the examined regions. Beneath the Caribbean, for example, the second reflector seems to be absent where the upper D'' reflector is found closer to the CMB (e.g., Hutko et al., 2006; Kito

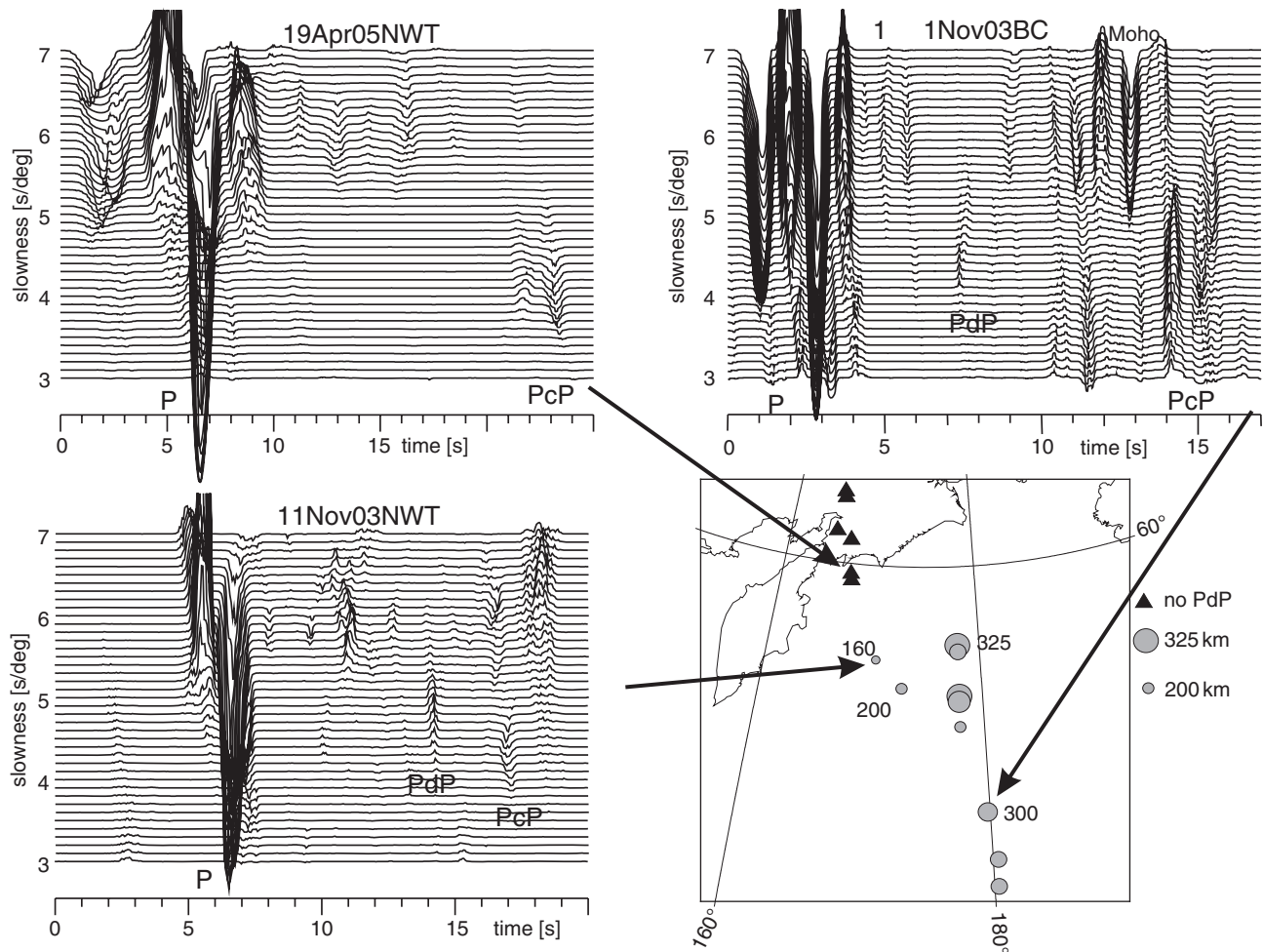


Figure 8.5 Vesagrams (slowness vs. time) for selected events sampling the D'' region beneath the Bering Sea (see Appendix Table 8.A2 for event details). *P*, *PcP* and, if visible, *PdP* are indicated on the vesagrams. Arrows point to the reflection points (gray circles) for the events. The arrays used are given in the event name: Polaris arrays: NWT – Northwest Territories, BC – British Columbia. Reflector height from the CMB estimated from travel times between *PdP* and *PcP* is given as the size of circle (shallower depths are displayed as larger circles) and the reflector height above the CMB is indicated next to some circles in the figure. The amplification is 100 for all *P* wave vesagrams after normalizing the traces and stacking them with a nonlinear stacking technique (4th root).

et al., 2007; Thomas et al., 2004a). Using an extensive dataset, van der Hilst et al. (2007) show an anti-correlation in depth of the lower reflector with the top reflector.

8.2.2. Travel Times of the Reflection(s)

The travel time between the main phase (*P*, *S*, and *PcP*, *ScS*) and the D'' reflection (*PdP*, *SdS*) is an important observable to establish whether the arrival is indeed a D'' reflection, and it also helps to measure the depth of the reflector assuming a horizontal (i.e., 1D) reflector. For a reflector 300 km above the CMB and an epicentral distance of around 65–75 degrees, the D'' reflection is

expected with a travel time between *P* and *PcP* (or *S* and *ScS*), as can be seen in Figure 8.3 (see also Weber, 1993). For deeper reflectors, the D'' reflection arrival appears closer to the core-mantle boundary reflection, whereas for shallower reflectors one expects the reflected wave closer to the direct wave (Weber et al., 1996). For large distances, the diving wave PDP or SDS may arrive before the *P* or *S* wave (e.g., Wyssession et al., 1998; Young and Lay, 1990).

The differential travel time to either the *P* (*S*) wave or the *PcP* (*ScS*) wave can be used to constrain the depth of the reflector (e.g., Chaloner, et al., 2009). Often, the differential travel time between *PcP* and *PdP* (same for *S* waves) is used because the two waves travel along a

similar path through the mantle and it is assumed that the influence from mantle structure on the travel time is negligible. The calculation of the depth of the reflector for this case, however, then depends on the velocity inside D" since a seismically fast layer would speed up the *PcP* reflection and lower the differential travel time between *PcP* and *PdP* and therefore place the D" reflector at deeper depths. This trade-off between thickness of the D" layer and the velocity contrast within the D" layer should be kept in mind when interpreting reflector depths. On the other hand, using the differential travel time between *P* and *PdP* would allow constraints on the depth of the reflector, and *PcP* could then be used to constrain the velocity in D". However, the *P* and *PdP* waves travel through different parts of the mantle and could be influenced by different velocity structures in the mantle. Hence, the travel time difference could in part be due to different structures encountered by either *P* or *PdP* on the path and may therefore lead to an estimated reflector depth either too shallow or too deep. Travel time corrections for mantle structure are often applied, based on tomographic models (e.g., Hutko et al., 2006; Kito et al., 2007; Thomas et al., 2004b) and for large-scale velocity variations this helps to reduce the influence from mantle structure, but these corrections depend strongly on the tomographic model used. A good knowledge of seismic velocities along the path is important for the depth estimation of the reflector. Since the *PdP* or *SdS* wave can arrive before the *P* or *S* wave for large distances (e.g., Lay and Young, 1991), this wave could potentially be used to constrain the velocity within D", thus reducing or eliminating some of the uncertainty.

Many studies find the D" reflection at travel times that correspond to a structure near 2650–2600 km depth, i.e. 250–300 km above the CMB (e.g., Lay and Helmberger, 1983b; Weber, 1993); see also reviews by Wysession et al. (1998), Cobden et al. (2015), and Lay (2015). In some regions strong topography has been detected, for example beneath the Caribbean (e.g., Hutko et al., 2006; Kendall and Nangini, 1996; Kendall and Shearer, 1994; Kito et al., 2007; Lay et al., 2004a; Thomas et al., 2004a, 2004b), Siberia (Houard and Nataf, 1993; Scherbaum et al., 1997; Thomas and Weber, 1997; Weber, 1993), and the Eastern Pacific (Takeuchi and Obara, 2010; Yamada and Nakanishi, 1998, 1996). The variation in depth is usually around ± 100 –150 km from a reflector with an average height of 250 km above the CMB. The Central and Western Pacific region shows strong topography of the reflector toward the western edge of the large low seismic velocity anomaly (Lay et al., 2006; Ohta et al., 2008), and the region beneath the Bering Sea indicates topography up to 300 km (see Figure 8.5 and Kendall and Shearer 1994; Sun et al., 2016).

It should be noted that the topography of the reflector is usually estimated using arrival times for single events and bins of stations and is calculated using 1D models. This might lead to wrong estimates of reflector depths: topography will change the wave path, and a reflection at an inclined surface will likely be in a different position and depth compared with the one calculated for a 1D model. Migration of *PdP* and *SdS* waves could reduce errors (e.g., Hutko et al., 2006; Thomas et al., 2004b, 2004a), but a large amount of source-receiver combinations is needed to gain a complete picture of the reflector topography (e.g., van der Hilst et al., 2007). Thorne et al. (2007) and Whittaker et al. (2016) analyze the effects of topography on D" reflected waves and find that topography may generate double reflections that might lead to misinterpretation. A thorough investigation of the influence of 2D or 3D structures on the travel times, and hence on the estimated reflector depth, would be beneficial for future studies.

8.2.3. Amplitude and Polarity of the Reflection(s)

The early reported *SdS* arrivals as well as some *PdP* arrivals show large amplitudes (Figure 8.3) and are clearly visible in single seismograms (e.g., Kendall and Shearer, 1995, 1994; Lay and Helmberger, 1983b; Thomas and Weber, 1997), which led to seismic velocity models that exhibit a large velocity jump of 2–3% for *P* and *S* waves at the top of the D" reflector: e.g., SYL0 (Young and Lay, 1990) and PWDK (Weber and Davis, 1990). Wysession et al. (1998) provide a compilation of velocity jumps across D". Many observed *SdS* and especially *PdP* arrivals, however, have smaller amplitude and point to a smaller velocity jump in *S*- and particularly in *P*-wave velocity (see also the examples in Figure 8.3). Calculations of synthetic data using full waveform modeling showed an agreement for *PdP* amplitudes with a 1% velocity jump at a first-order discontinuity (e.g., Chaloner et al., 2009). In most cases the arrivals, especially for *P* waves, are not visible for single seismograms or distance-dependent seismogram sections, but can be detected using array seismic methods (e.g., Rost and Thomas, 2002; Schweitzer et al., 2009).

One way to explain the large amplitude of *PdP* and *SdS* waves seen in some cases (e.g., Figure 8.3, 17 Dec 1991) compared with *P* and *S* amplitudes could be topography of the reflector. Focusing and defocusing effects will change the amplitude of the wave considerably, and in some cases render the reflection invisible (e.g., Thomas and Weber, 1997). Such strong topography is detected in several regions as detailed above (for example, beneath the Caribbean and Siberia), as well as in those regions where events with large amplitude reflections and events without a discernible D" reflection have been reported

side by side (e.g., Chambers and Woodhouse, 2006; Hutko et al., 2006; Kito et al., 2007; Sun et al., 2016, 2006; Thomas and Weber, 1997).

On the other hand, it is also possible that large lateral velocity variations exist in D" and those could cause regions with stronger reflections due to larger velocity contrasts across the boundary (e.g., Kendall and Nangini, 1996; Lay et al., 2004a). It is, however, difficult to explain such strong velocity variations over such short distances (e.g., Thomas and Weber, 1997) unless scattering is invoked as a cause (e.g., Scherbaum et al., 1997). The reflection points of events with and without D"-reflected waves are essentially within the 1D Fresnel zone (e.g., Thomas and Weber, 1997; Weber, 1993) for the region beneath Siberia; however, beneath the Aleutians and Bering Sea (Figure 8.5), the region where no reflections are found is distinct from the region exhibiting D" reflections and separated by approximately 8–10 degrees (which is larger than one Fresnel zone for the dominant periods of the waves of 1 to 3 s used here).

A third possibility for the variation in amplitude could be changes in the velocity gradient across the D" reflector, i.e., the sharpness of the reflector. A gradient would likely reduce the amplitude of the reflected wave (Lay, 2008; Weber, 1993), but the detailed shape of the gradient zone will also influence the amplitude of the reflection (Hernlund, 2008) and possibly lead to different depth-estimates of the reflector. A region where the gradient changes from steep to shallow within the gradient zone may be interpreted as a lower reflector, and vice versa. This, however, would overlook the fact that if the gradient is due to a mineral phase transition, then this transition may occur at shallower depths than seismically imaged, and this could lead to discrepancies between seismic observations and mineral physics results.

The amplitudes of waves reflected at additional structures beneath the top of D" as seen by several investigations (e.g., Hutko et al., 2006; Lay et al., 2006; Thomas et al., 2004a, 2004b; van der Hilst et al., 2007) are much smaller compared with the top reflections. This makes them difficult to observe and in some cases, their existence has been cast into doubt, as discussed by Flores and Lay (2005). The modeling attempt of Whittaker et al. (2016) also shows that topography could create a secondary reflector, and it would be important to test the lateral variation of this phenomenon (i.e., anti-correlation, lateral extent of second reflector) to distinguish between this scenario and a true deeper reflector. The additional arrival's appearance in vespagrams and slowness-back azimuth analyses, however, indicates that they are coherent arrivals that agree with a reflection from a deeper structure rather than a processing artifact, and modeling confirms that the negative velocity contrasts needed for these reflections can indeed generate small reflected arrivals (e.g.,

Hernlund et al., 2005). It should be noted that the size of the velocity contrast for the lower reflector is not well constrained yet.

While amplitude measurements can be influenced by many different factors such as attenuation (e.g., Durand et al., 2013), energy partitioning, as well as anisotropy in D" (Pisconti et al., 2019; Thomas et al., 2011), the polarity of the seismic wave (i.e. the waveform) is another observable that can be used to analyze the D" reflectors. If the radiation pattern of an event is such that *PcP* and *P* (or *ScS* and *S*) have the same polarity, the reflection off of D" should have the same polarity as the main phases for a positive velocity jump across the D" reflector, because the D"-reflected wave has a take-off angle between *P* and *PcP* (or *S* and *ScS*) for distances between 60 and 80 degrees. This means that if the *P* wavelet has an up-swing first, the *PdP* wave will also have an upswing first (e.g. Figure 8.3, *S* wave example). Conversely, a negative velocity jump should create a polarity opposite to *P* and *PcP* (or *S* and *SdS*), as shown in Figure 8.4.

Opposite polarity observations have been found in several studies for *PdP* waves (Chaloner et al., 2009; Cobden and Thomas, 2013; Hutko et al., 2008; Pisconti et al., 2019; Thomas et al., 2004a, 2004b). This would point to a negative velocity jump for *P* waves. One explanation for these opposite polarity *PdP* waves could be the negative *P* velocity jump associated with the phase transition from bridgmanite ("Br") to post-perovskite ("PPv"), a result of the large drop in bulk modulus for PPv compared with Br (Wookey et al., 2005), although a recent theoretical study predicts an increase in both *P* and *S* waves across the Br-PPv transition (Zhang et al., 2016). Interestingly, to our knowledge, no opposite *SdS*-wave polarities compared with *S* and *ScS* have been reported in regions with either lower or higher than average velocity in tomographic models. This leads to velocity models including a D" layer with a positive *S* wave jump and either a negative gradient or positive gradient below the top of D" (e.g. SYLO: Lay and Young (1991), SWDK: Weber and Davis, 1990)). Regions where *PdP* waves exhibit opposite polarities compared with *P* and *PcP*, *SdS* waves have the same polarity as *S* and *ScS* (e.g., Cobden and Thomas, 2013), ruling out a simple thermal origin, thus pointing to the Br to PPv transition or a chemically different D" region. For these scenarios it is important to verify that the polarities are the same in all travel directions to rule out anisotropy in D" (e.g., Pisconti et al., 2019; Thomas et al., 2011).

It should be noted that the reflection coefficient of *P* and *S* waves depends on the impedance contrast (velocity times density) across the D" reflector and the incidence angle of the reflected wave. An example using model PWDK is shown in Figure 8.4. Here, if the wave arrives with an incidence angle of 60 degrees, the reflection

polarity of *SdS* would change compared with that for an incidence angle of 50 degrees (epicentral distance of 53 compared with 42 degrees). Therefore, caution is needed to explain the reflection amplitudes and modeling is necessary for both *P*- and *S*-wave reflection coefficients for a variety of impedance contrasts.

8.2.4. Plausible Explanations

Early interpretations of the reflector at the top of the *D''* region include debris from subducted oceanic slabs associated with a possible change of flow (e.g., Hutko et al., 2006; Kendall and Silver, 1998; Ohta et al., 2008; Weber, 1993) or as disconnected scattering bodies (e.g., Scherbaum et al., 1997), and thermo-chemical layering (e.g., Lay et al., 2004b). Models with solid-solid phase-changes, when merged with global *S*-velocity tomography or detailed seismic waveforms (Sidorin et al., 1999, 1998) led to the prediction of the *D''* boundary with a positive Clapeyron slope, which was later confirmed by experimental and theoretical mineral physics studies observing the MgSiO_3 bridgmanite to post-perovskite structural phase-transition (Murakami et al., 2004; Oganov and Ono, 2004; Tsuchiya et al., 2004).

The phase transition from Br to PPv, discovered in 2004 (Murakami et al., 2004; Tsuchiya et al., 2004; Oganov and Ono, 2004), has been used to explain the reflections and many other structures in the *D''* region due to its density and velocity contrasts (e.g., Murakami et al., 2004; Wentzcovitch et al., 2007), although uncertainties remain. The phase transition in pure MgSiO_3 occurs at pressures and temperatures associated with the *D''* reflector depth in cold and average-temperature regions. Topography of the reflector could thus be explained by temperature variations (Hernlund et al., 2005) and predicted temperature estimates for the Br to PPv transition using a Clapeyron slope (γ) of 9 MPa/K produce a distribution of heights of the *D''* reflector, ranging from zero to a few 100 km above the CMB (Sun et al., 2009), in agreement with many observations. However, strong changes in topography, e.g., beneath the Bering Sea (Figure 8.5 and Sun et al., 2016) would need a large temperature contrast over fairly small distances, which is difficult to explain with most geodynamic scenarios, unless a hot upwelling intersects the *D''* region (Sun et al., 2016).

Short-period seismic waves with dominant periods of 1 s detect the reflector (e.g., Weber 1993), thus the velocity gradient needs to be sharp, on the order of a few 10 s of km (e.g., Cobden and Thomas, 2013; Lay, 2008; Thomas and Weber, 1997). However, the Br-PPv phase transition poses some problems to explain the sharpness: when using a more likely situation in the deep mantle, that is bridgmanite in solid solution with Fe and Al (i.e., other than pure MgSiO_3), a relatively wide Br-PPv coexistence phase-loop

is observed (Akber-Knutson et al., 2005; Caracas and Cohen, 2007; Catalli et al., 2009; Grocholski et al., 2012; Sun et al., 2018), as opposed to a sharp transition for the MgSiO_3 end-member. Depending on the Al and Fe concentration of PPv, the onset depth of the phase transition also changes (e.g., Grocholski et al., 2012; Mao et al., 2004; Sun et al., 2018). To detect this larger gradient with seismic data, long-period seismic waves, likely with dominant periods larger than 5s, are needed, and this may be the reason that the *SdS* wave is more readily observed due to its longer periods compared with *PdP*. As mentioned above, the shape of the gradient is also important (Hernlund, 2008); thus far, it seems difficult to simultaneously constrain the size and shape of the gradient across *D''* with reflected waves.

Another challenge that the PPv phase transition presents is that experiments at room-temperature on the magnesium end-member suggest a shear wave velocity increase (e.g. Murakami et al., 2007) that is much smaller than the shear wave contrast found in the *D''* models (e.g., SYLO, PWDK). There is likely an even smaller contrast in *P*-wave velocity (Wookey et al., 2005) as discussed above, both of which contradict the large *PdP* and *SdS* observations as seen in some studies (e.g., Lay and Helmberger, 1983b; Weber, 1993; Young and Lay, 1990) (see also Figure 8.3). Where *PdP* and *SdS* have strong amplitudes would therefore likely represent regions where there is either very little Fe and Al in PPv (a narrow Br-PPv phase-loop) (e.g., Murakami et al., 2004; Sun et al., 2018), focusing or defocusing effects, or a chemistry distinct enough, such as an isolated pile of primordial mantle (Hansen and Yuen, 1988). Variations in amplitude could also be due to changes in velocity inside a thermochemical boundary layer, possibly with internal convection (e.g., Lay and Garnero, 2004). On the other hand, a recent study by Langrand et al. (2019) shows that it is possible that kinetics of the phase transition from Br to PPv could influence the reflection amplitude and generate large reflections for large gradient zones, although more work on this subject is needed.

D'' anisotropy (e.g., Kendall, 2000; Kendall and Silver, 1998; Lay et al., 1998; Nowacki et al., 2011; Wookey and Kendall, 2007) has been explained by aligned minerals inside slabs or sheared melt pockets (e.g., Kendall and Silver, 1998, 2000, Lay et al., 1998). Provided that PPv is weak (Amman et al., 2010), partial alignment of PPv could sharpen the reflector (Amman et al., 2010; Thomas et al., 2011) and cause seismic anisotropy. The link between seismic anisotropy and the PPv phase in the *D''* region has been evaluated in many previous studies (e.g., Ford et al., 2015; Merkel et al., 2007, 2006; Nowacki et al., 2011; Thomas et al., 2011; Wookey and Kendall, 2007; Wu et al., 2017) and we refer the reader to several of these reviews. Here, we simply point out that seismic

anisotropy caused by alignment of PPv could also generate variations in reflection polarities (Thomas et al., 2011; Pisconti et al., 2019) due to variations of the velocity contrast with azimuth across the discontinuity. Therefore, the observation of variable polarities of *PdP* waves with distance or travel direction together with polarity observations of *SdS* waves (and splitting measurements, if possible) can be a powerful approach to constrain the style of deformation in D" (e.g., Creasy et al., 2019; Pisconti et al., 2019; Thomas et al., 2011).

The deeper reflector that has been observed in several studies beneath the top of D" has been explained with a range of causes. Hernlund et al. (2005) show that it can be due to the back-transformation from PPv to Br closer to the CMB due to high temperatures in the thermal boundary layer near the core. Other studies explain additional reflectors as being due to phase-changes in metabasalt (e.g., Ohta et al., 2008), folding of lithosphere (e.g., Hutko et al., 2006), ultralow velocity zones (Ohta et al., 2008, Lay et al., 2006), heating up and partially melting of material beneath a subducted slab (Tan et al., 2002), or a combination of these (e.g., Lay et al., 2006).

In order to explain the wide range of observables, variations in mineralogy, temperature, topography and deformation are likely required, each connected to a range of processes. However, it is important to emphasize that the various mechanisms described here affect not just one observable but other observables as well (i.e., there are trade-offs). For example, variations in Fe- and Al-concentrations in bridgmanite undergoing the transition to PPv affects the sharpness, depth, and the velocity contrast of the reflected wave. Topography of a reflector would affect the depth estimation of the reflector, since slanted sides of a reflector would change the wavepath and hence the travel time would no longer reflect the 1D interpretation of reflector depth. Lastly, to explain reflectors in areas identified as low-velocity regions in tomography studies, strong compositional boundaries may be needed. In the next section, we consider the above interpretations and trade-offs in a case study underneath the northern Pacific region.

8.2.5. Case Study: Observations and Interpretations of D" Underneath the Northern Pacific Region

The lowermost mantle underneath the northern Pacific region, spanning the Bering Sea to Alaska, has been sampled by several investigators (Castle and van der Hilst, 2000; Kendall and Shearer, 1994; Nowacki et al., 2011; Persh et al., 2001; Revenaugh and Meyer, 1997; Rost and Thomas, 2010; Sun et al., 2016; Vidale and Benz, 1992), many of which sampled the eastern part of the Aleutians and Alaska. The region lies to the north of the large low-velocity anomaly beneath the Pacific and

is likely characterized by past subduction (Lithgow-Bertelloni and Richards, 1998). The seismic observations of the D" region have been strongly variable, with reflector depths ranging from an absence of a reflector to deep reflections of around 100 km above the CMB (e.g., Kendall and Shearer, 1994; Rost and Thomas, 2010), to observations of up to 400 km above the CMB (e.g., Kendall and Shearer, 1994; Sun et al., 2016; Young and Lay, 1990). In this study, we include new observations underneath the Bering Sea using *P* waves (Figure 8.5) and combine them with previous *S* wave observations underneath the Alaska region (Sun et al., 2016) to gain a better understanding of the dynamics and mineralogy in this area.

Our *P*-wave data cover a region that had previously been explored by Young and Lay (1990) with *S*-wave data, and it lies next to the region imaged by Kendall and Shearer (1994). We use events from the Western Pacific (Appendix Table 8.A2) and stations in Canada, specifically the POLARIS array Northwest Territories (NWT) and British Columbia (BC) deployments (Eaton et al., 2005). We use array methods to detect arrivals between *P* and *PcP*, that have a slowness and travel time indicative for a D" reflection. We confirm these reflections with slowness-back azimuth analyses, to ensure that they also have the correct back azimuth and are coherent arrivals. The amplitudes of the detected *PdP* arrivals are small and agree better with a 1% *P*-wave contrast than a 3% *P*-wave contrast, in agreement with other *P*-wave studies (e.g., Chaloner et al., 2009; Kito et al., 2007). We find several events that show no additional reflection between *P* and *PcP* with the appropriate slowness and travel time, and these nonobservations all cluster in one area (see Figures 8.3, 8.5, and 8.6). We also find differential travel times between the reflected waves and the *P*-wave that suggest strong topography of the reflector, in that in some cases the D" reflection arrives close to *PcP* and can be interpreted as a deeper reflector (Figure 8.5). Combining our new observations with previous work, we find a range of complex features in the D" layer, which are summarized in Figure 8.6 from west to east (regions A to F) and described below. Again, it should be kept in mind that the depth of the reflector is estimated using a 1D model.

The western area underneath the Bering Sea (region B) shows evidence for a D" reflector at depths around 300–400 km above the CMB, in agreement with Kendall and Shearer (1994) and the observations of Young and Lay (1990). Both studies used *S*-wave reflections, in contrast to the *P*-wave observations used here (Figure 8.5 and 8.6). The superposition of the D" reflection points and their respective depth are superimposed on the *S*-wave tomography model S40RTS (Ritsema et al., 2011), taken at 2700 km depth (Figure 8.6). Figure 8.6 indicates that we image a structure with low velocity that is surrounded by

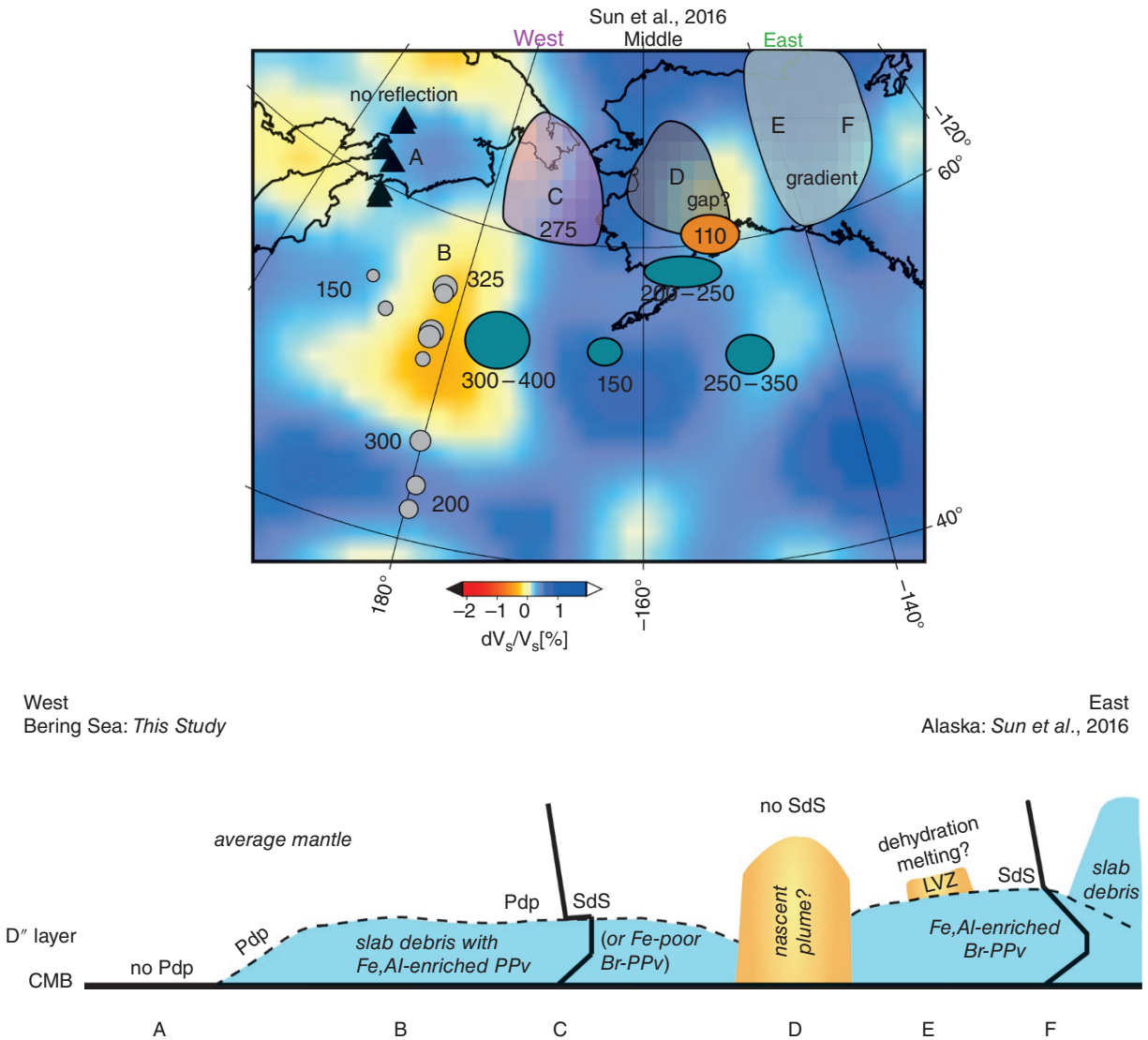


Figure 8.6 top) Observations from this study (gray circles for observations, black triangles for no D'' reflection in the data). Indicated are also regions where Sun et al. (2016) find D'' reflections (pink and turquoise areas) and where D'' reflections are not clearly observed (gray area). Green areas show previous D'' detections from Kendall and Shearer (1994) and the orange area the detection of Rost and Thomas (2010). Young and Lay (1990) find reflections throughout the northern area that agree with model SYLO. Estimated positions of the D'' reflector above the CMB are given as numbers. The observations are superimposed on model S40RTS (Ritsema et al., 2011, bottom). **bottom)** Possible interpretations of seismic features in the D'' region spanning the Bering Sea to Alaska (after Sun et al., 2016). Observed lateral variation of D'' beneath Alaska, where the black dashed line denotes the D'' discontinuity, and the two thick black lines display the local seismic velocity profiles (this study and Sun et al., 2016). Regions producing strong PdP and SdS reflections (region B and C) are compatible with either a chemical boundary between an average mantle bridgmanite assemblage above and slab debris with Fe-enriched PPv below or Br-PPv in an Fe-depleted system, based on experimental data. Our analysis indicates that the structure appears to have steep sides and falls off northwestward to CMB level (region A). See text for eastward interpretations and more details.

an area of relatively high velocities. Our analysis using *P*-waves indicates that the structure appears to have steep sides and falls off north-westward to CMB level (region A), over a distance of approximately 300 km. Although several tomography models, including the one shown in

Figure 8.6, display a slow velocity region at 2700 km depth, other models such as the PRI-S05 and PRI-P05 models (Montelli et al., 2006) indicate fast velocities at this depth. At shallower depths (2500–2600 km depth), many tomography models display relatively fast velocities

and others show changes between slow and fast velocities (for a range of models see Hosseini et al., (2018)). The westernmost region (region A) displays no obvious *PdP* (Figure 8.5), which could point to the wide and incomplete Br-PPv phase transition loop (~450 km) recently reported for average (or pyrolitic) mantle material (Sun et al., 2018). Toward the East, the reported D" reflector from Kendall and Shearer (1994) is imaged at heights between 150 and 350 km above the CMB.

In region C of our investigation region, north of the observations made by Kendall and Shearer (1994), a relatively sharp D" reflector is observed based on clear and strong D" reflections: Sun et al. (2016) reported strong *SdS* waves, requiring a sharp $\delta V_S = 2.5\%$ increase at 270 km above the CMB, also in agreement with models SYLO (Young and Lay, 1990); this region resides directly adjacent to region B, where we find *PdP* reflections from a structure around 300 km above the CMB. Collectively, these observations suggest a continuous structure in regions B and C of Figure 8.6. The regions where *PdP* and *SdS* are strong could represent a mantle with relatively depleted Fe and Al in PPv (e.g., Murakami et al., 2004; Sun et al., 2018), in order to explain the sharp increase in reflected *S* and *P* velocities. One could explain this depletion in Fe by the nearby nascent plume (region D, discussed below); that is, Fe could be partitioned into the (partially molten?) plume root. However, an Fe-depleted Br-PPv transition would not explain the low velocities proximal to the CMB in the tomography studies in region B; thus, we consider another possibility.

One scenario that could produce reflections in regions of slow velocities inferred from tomography (regions B and C) is if subducted mid-ocean ridge basalt (MORB) could reach the bottom of the mantle (e.g., Komabayashi et al., 2009; Nakagawa and Tackley, 2008; Tan et al., 2002). MORB is denser than the surrounding mantle material at lower mantle conditions (Hirose et al., 2005) and therefore could be present at the base of the mantle, representing a chemical boundary (e.g., Lay and Garnero, 2004). At these depths, the PPv phase is stabilized in subducted MORB, as the Br-PPv transition occurs about 550 km above the CMB (Sun et al., 2018). Based on recent experiments, the bulk sound velocity contrast between Br in pyrolitic mantle and PPv in MORB (Fe- and Al-rich PPv) would likely be positive with respect to PREM (Sun et al., 2018), and capable of producing *PdP* and *SdS* reflections. Although our data are not clear enough to confirm this, the velocity contrast for *PdP* appears to be positive. Waveform modeling of *S*-waves in region C is consistent with a relatively sharp velocity increase that creates strong *SdS* waves, followed by a small positive velocity contrast down to about 2800 km depth, and a further significant drop in velocity down the CMB, similar to model SYLO.

To the east of the region with strong *PdP* (region B) and *SdS* phases (region C) lies a region where no clear *SdS* phases are found (region D) (Lay and Garnero, 1997; Sun et al., 2016). Kendall and Shearer (1994) find deep *SdS* reflections (200–250 km above the CMB), whereas Rost and Thomas (2010) find low-amplitude *PdP* reflections deeper than that (~110 km above the CMB). Sun et al. (2016) used detailed modeling to show that the distinct pattern of *S*-wave travel time delays, waveform distortions, and amplitude patterns in region D reveals a circular anomaly about 100 km wide and about 400 km high (based on measurements of *S*-wave turning points) with a reduction in shear velocity of 5%. By considering dynamic modeling of relic slabs at the CMB that reveal plumes preferentially develop at the edge of slabs (e.g., Bower et al., 2013b; Heron et al., 2015; Nakagawa and Tackley, 2008; Tan et al., 2002), Sun et al. (2016) interpret their observations as a plume-like structure. A hot plume would produce a gap in the continuity of a D" reflector due to the temperature-dependent Br-PPv boundary (Bower et al., 2013b; Sun et al., 2009). This high, but relatively narrow, plume-like structure could be a feature that tomography models average over, thus explaining why several tomography models display low velocities near the CMB in this region.

The easternmost region (regions E and F) displays more complexity, such that the strong *SdS* phase from a structure 270 km above the CMB requires a gradient increase in V_S down to a depth of 2800 km, followed by a decrease in V_S down to the CMB (Sun et al., 2016). This region F is also likely influenced by relic subducted slab debris that has reached the lowermost mantle (e.g., Bower et al., 2013a; Davies and Gurnis, 1986; Tackley, 2002). In their recent experimental investigations of the Br-PPv phase transition, Sun et al. (2018) showed that a pyrolite-like composition, $(\text{Mg}_{0.9}\text{Fe}_{0.1}\text{Al}_{0.1}\text{Si}_{0.9}\text{O}_3)$ (Catalli et al., 2009), and a more Fe-rich composition $(\text{Mg}_{0.735}\text{Fe}_{0.21}\text{Al}_{0.07}\text{Si}_{0.965}\text{O}_3)$ are characterized by Br-PPv phase transition widths of about 25 GPa and 450 km, respectively, with the more Fe- and Al-rich composition transitioning about 8 GPa lower (150 km shallower) than the pyrolite-like Br, a result that is in qualitative agreement with earlier experiments (Mao et al., 2004) and theoretical studies (e.g., Caracas and Cohen, 2008, 2007, 2005; Stackhouse et al., 2006). Both transitions are essentially incomplete at the CMB, thus unlikely to produce a sharp seismic reflector. As discussed above, anisotropy and/or focusing effects associated with the presence of relic slab debris could act to sharpen such an otherwise diffuse reflector. Nevertheless, the results presented in Sun et al. (2018) show that the bulk sound velocity gradient associated with a $(\text{Mg}_{0.735}\text{Fe}_{0.21}\text{Al}_{0.07}\text{Si}_{0.965}\text{O}_3)$ -Br to PPv transition is positive, which is consistent with the seismic observation of a gradient increase in V_S (region F, lower panel) (Sun et al., 2016). Some of the variability in seismic observations can also be explained by successive

phase-changes in MORB-like components (e.g., CaCl_2 -type to $\alpha\text{-PbO}_2$ type SiO_2) (Andrault et al., 2014; Grocholski et al., 2013; Hirose, 2006; Ohta et al., 2008).

This easternmost region was also modeled with a low velocity zone (Cobden and Thomas, 2013) with $\delta V_s = -2.5\%$ just above the strong *SdS* reflector (region E), indicated by a yellow region labeled “LVZ” in the lower panel of Figure 8.6. The presence of phases such as $\delta\text{-(Al,Fe)OOH}$ (Ohira et al., 2019) and/or the NAL phase (Wu et al., 2016) could contribute to the observed seismic anomalies. For example, if a hydrated phase similar to that of $\delta\text{-(Al,Fe)OOH}$ is present (Ohira et al., 2019) and dehydrates as it heats up in the thermal boundary layer, then dehydration of this phase could partially melt the surrounding material, explaining the LVZ above the speculated slab-like feature. More petrology-inspired experiments under CMB conditions are certainly required to test these hypotheses.

The region beneath Alaska and the Bering Sea has also been shown to exhibit seismic anisotropy, such that observations of $V_{SH} > V_{SV}$ are interpreted as horizontally emplaced relic slabs (e.g., Cottaar et al., 2014; Fouch et al., 2001; Garnero and Lay, 1997; Lay and Young, 1991; Long, 2013; Matzel et al., 1996; Wyssession et al., 1999); see also Nowacki et al. (2011) for a review. Similar observations of seismic complexity in D" have been reported in other regions thought to be influenced by paleo slab subduction processes, such as underneath eastern Eurasia (e.g., He and Wen, 2011), northeast Pacific (e.g., Sun et al., 2019), and northern Atlantic (e.g., Durand et al., 2019).

In summary, the structure beneath the Aleutians, from the Bering Sea to Alaska, is complex. Considering that many tomographic models show an area of low velocities near the CMB beneath the Aleutians and fast velocities at ~ 2400 km depth, together with the regional waveform studies presented here, a consistent interpretation involves relatively large variations in temperature and composition, associated with the dynamics of relic slab debris. Recent experimental results on the complex characteristics of the bridgmanite to post-perovskite phase transition in a multicomponent system underscore these interpretations.

8.3. ULTRALOW VELOCITY ZONES

8.3.1. Seismic Observations

Within the D" layer, near the base of the mantle, lies a distribution of low and ultralow velocity zones (ULVZs) that are generally characterized by dimensions ranging from a few to tens of km thick, with lateral dimensions ranging from tens of km to ~ 800 km (e.g., Garnero and Helmberger, 1995; Hutko et al., 2009; Mori and

Helmberger, 1995; Revenaugh and Meyer, 1997; Rost et al., 2006; Thorne et al., 2013). Several studies provide locations of ULVZs at the base of the mantle, which were summarized in McNamara et al. (2010) and more recently in Yu and Garnero (2018). The locations of select ULVZs near the borders of the large low seismic velocity (LLSVP) anomalies beneath the Pacific and Africa led to the hypothesis that ULVZs may be connected to mantle upwellings and hotspots near the surface of the Earth (e.g., Burke et al., 2008; Torsvik et al., 2006; Williams et al., 1998; Yuan and Romanowicz, 2017).

ULVZs have been observed with a variety of seismic waves (see Figure 8.7). Figure 8.8 provides examples of detections of ULVZ in seismic data together with model ak135 (Kennett et al., 1995). Most often, the observations of SPdKS and SKPdS waves are used (e.g., Garnero and Helmberger, 1998, 1996; Thorne et al., 2020, 2013; Thorne and Garnero, 2004) and the modeling of travel times, amplitudes, and waveform of these waves yields velocity differences with respect to the average velocity at the CMB (e.g., Figure 8.8). SPdKS and SKPdS are waves that diffract for a short distance around the core (Pd) and travel as an SKS wave for the rest of the path with their amplitudes and travel times influenced by strong low-velocity regions near the CMB (e.g., Garnero and Helmberger, 1998; Thorne et al., 2020). Enhanced PKPbdiff waves, i.e., waves that are diffracted around the core for a short distance, but traveling as PKP waves otherwise, can also be explained by trapping the diffracted energy near the CMB due to an ULVZ (Thomas et al., 2009; Wen and Helmberger, 1998a).

Another approach to image ULVZs is detailed modeling of pre- and postcursor amplitudes of *PcP* and *ScP* waves (Figures 8.7 and 8.8); the travel times and polarities of these waves surrounding *PcP* or *ScP* can be used to extract the velocity contrast, while also allowing the determination of the density contrast (e.g., Gassner et al., 2015; Hansen et al., 2020; Rost et al., 2010, 2006). Trade-offs in density and velocity were discussed in Zhang et al. (2018) for the small amplitude *PcP* waves at near podal distances (0–12 degrees) and also by Braña and Helffrich (2004) for larger epicentral distances. In addition, as discussed in the section on the D" reflector, there is often a trade-off between velocity contrast and the modeled thickness of the patch. The 3D character of an ULVZ may also influence the results. Modeling studies by Wen and Helmberger (1998b), Thorne et al. (2013) and Vanacore et al. (2016) showed that some amplitude and timing differences of the waves used to detect ULVZs can result from the modeling method used (1D versus 2D, 2.5D modeling), a subject for more detailed studies in the future.

Coherent scattered waves (Figures 8.7 and 8.8) that arrive as precursors to PKPdf have been explained by Ma et al. (2019) and Ma and Thomas (2020) as a result

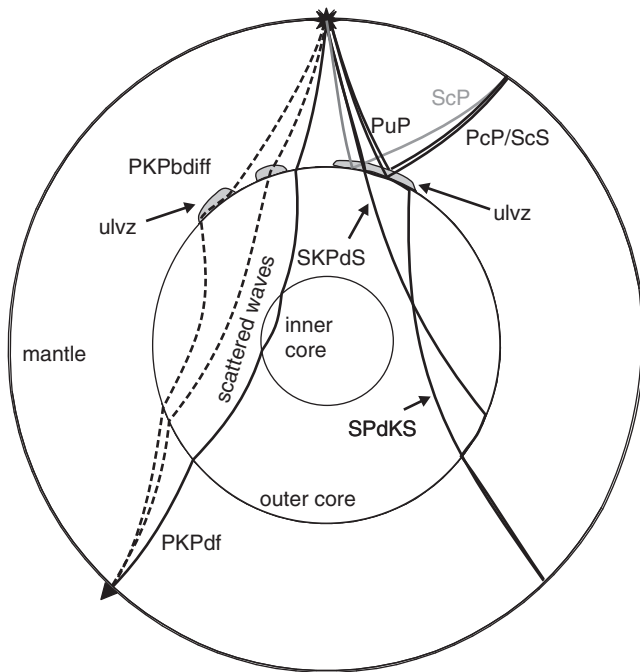


Figure 8.7 Ray paths of seismic phases for detection of ULVZs referred to in this chapter: SPdKS and SKPdS, PKPdif, and (coherent) PKP precursors, enhanced amplitudes of PKPbdiff, as well as PuP (reflection off the top of a ULVZ) together with PcP, ScS, and ScP. SPdKS and SKPdS differ by having the *P*-diffracted wave either on the source or on the receiver side. PKPbdiff and SPdKS/SKPdS are also standard phases and their changes in amplitude and travel time with respect to a standard Earth model are used for ULVZ detection.

of PKP waves with an ULVZ at the core-mantle boundary. Scattering observations as precursors to the PKP wave were reported in the 1930s (Gutenberg and Richter, 1934) and explored in more detail in the 1970s (e.g., Doornbos and Vlaar, 1973; Haddon and Cleary, 1974; King et al., 1974). Since these scattered waves travel a different path compared with PKP (e.g., Cleary and Haddon, 1972; Thomas et al., 1999; Vidale and Hedlin, 1998), they have shorter travel times and arrive up to 30 s before the PKP wave (Figure 8.7) and appear to display variations in amplitudes (e.g., Hedlin and Shearer, 2000; Mancinelli et al., 2016; Waszek et al., 2015). While globally observed PKP precursors are explained by a 0.1% rms velocity variation and a scale length of 10 km (e.g., Mancinelli and Shearer, 2013), velocity variations for individual scattering regions are much stronger: 6% (Niu and Wen, 2001), 0.5 to 3% for *P* and *S* waves (Ma et al., 2016), and 3–10% (Vanacore et al., 2010; Wen and Helmberger, 1998a). Many precursors are incoherent waves but if coherent scattered waves are present, as shown in Figure 8.8c (e.g., Ma and Thomas, 2020; Niu and Wen, 2001), they can be modeled with strong small-scale

velocity anomalies at the CMB, providing an additional possibility to map new regions of ULVZs. Detailed analyses of density variations related to PKP precursors are, to our knowledge, not provided in the literature.

In a comprehensive global assessment of ULVZ studies, Yu and Garnero (2018) present several key findings: (i) modeling of seismic arrivals indicates a 3–25% drop in V_P , 6–50% drop in V_S , and that $\delta V_S:\delta V_P$ range from 1:1 to 6:1 (noting that many studies fix this ratio *a priori* at integer levels), (ii) ULVZ density contrast ranges from 0 to 22% higher than PREM following seismic waveform modeling, (iii) there is no statistically significant correlation of ULVZs detected using core-reflected phases and the location of hotspots on Earth's surface, and (iv) there is no simple mapping of ULVZ locations and lowermost mantle reduced tomographic velocities, showing that a significant fraction of ULVZs are located outside these provinces. At the time of the Yu and Garnero (2018) global assessment, only 17.1% of the CMB had been sampled by ULVZ studies, with 10.3% of the total CMB amounting to positive ULVZ detection. In a new collection of 58,155 broadband recordings of the seismic phase SPdKS, roughly half of the CMB has now been sampled in a search for anomalous SPdKS waveforms (Thorne et al., 2020). Using a Bayesian approach, Thorne et al. (2020) determine the regions that have the highest probability of containing ULVZs. In their work they find several regions with ULVZ presence that were not previously detected. They also confirm other regions that were known to have ULVZs, but they find no obvious correlation with hotspots or LLSVP edges, as inferred from *S*-wave tomography. The source-receiver ambiguity (e.g., Thorne et al., 2020) creates some uncertainty, in that it is difficult to determine whether the wave was altered by structures at the entry into or exit from the core. A recent study using core-reflected ScP waves recorded by the Transantarctic Mountains Northern Network in Antarctica concluded that ULVZs may be ubiquitous along the CMB, thus not particularly associated with hotspot locations on Earth's surface (Hansen et al., 2020).

Other characteristics of ULVZs include structures with a diffusive top or a vertical velocity gradient within, whereas others have been interpreted as multilayered structures (e.g., Yu and Garnero, 2018). However, it is likely premature to draw firm conclusions in this respect due to the effects of finite frequency on the sensitivity of different probes to the range of structures (e.g., Yu and Garnero, 2018). It is important to add to this summary that there have been few studies investigating the presence of seismic anisotropy within ULVZ structures. In a recent study using differential SKS-SKKS shear-wave splitting underneath Central Africa, Reiss et al. (2019) identify strongly discrepant splitting for those two waves in an area previously mapped as an ULVZ. Reiss et al.

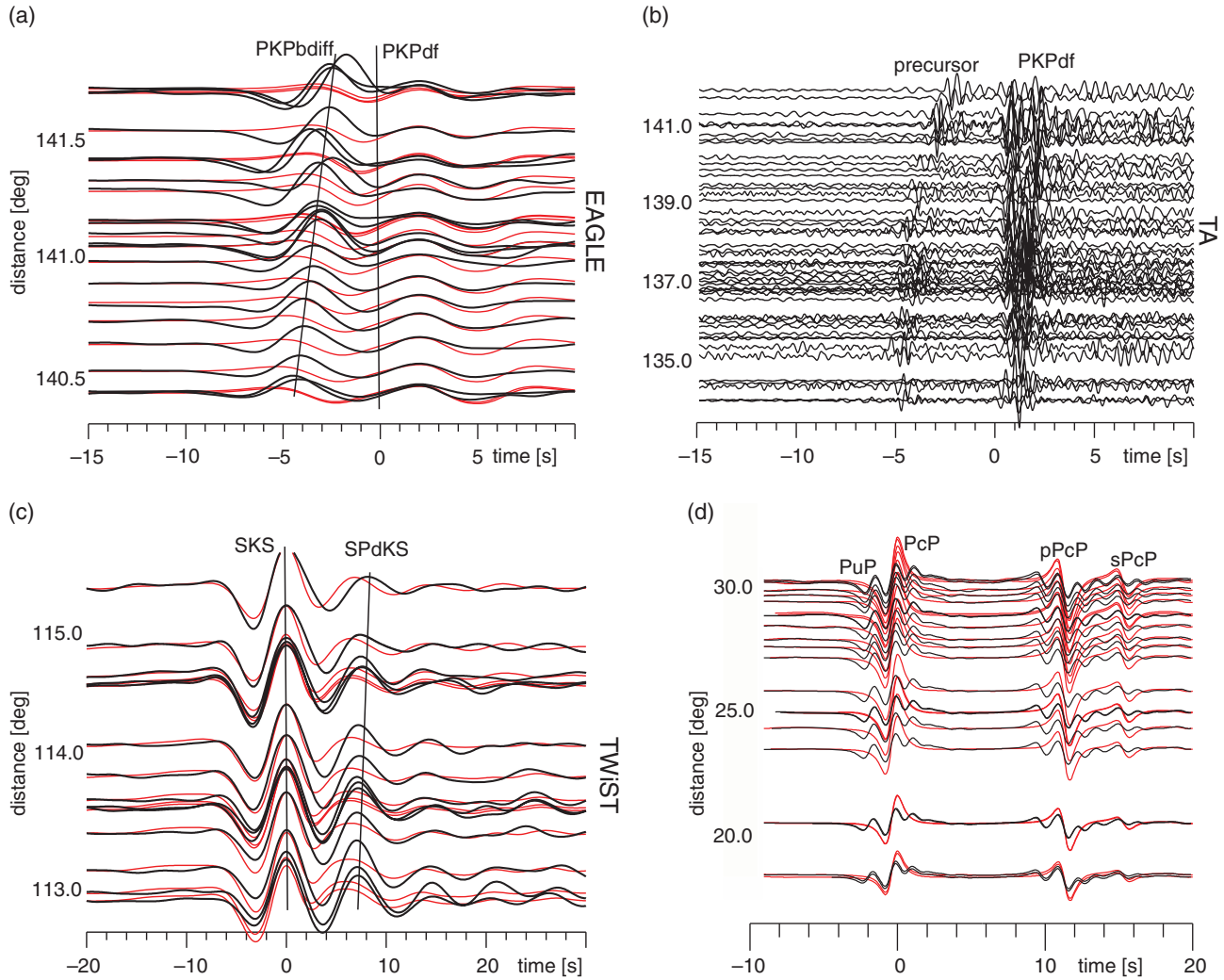


Figure 8.8 (a–c) Examples of waves used for the detection of a ULVZ (black lines) with model ak135 (red lines). (a) Stronger amplitudes of PKP diffracted waves than predicted by standard Earth models. Event 4. Oct 2002 recorded at EAGLE stations. (b) SPdKS waves with higher amplitudes and shifted travel times compared with ak135. Event 25. May 1997 recorded at TWIST array (Kendall et al., 2002). (c) Coherent precursors to the wave PKPdf (event 9). April 2009 recorded at TA stations. Model ak135 is not shown here. (d) *PuP* waves as precursors and postcursors to the wave *PcP*. Note that this example shows synthetic data for ak135 (red) and a model with a 7 km thick ULVZ (black).

(2019) suggest that this anomalous structure could be a ULVZ that contains certain alignments of partial melt or iron-rich (Mg,Fe)O (Finkelstein et al., 2018).

8.3.2. Plausible Explanations

Considering the wide range of anomalous wave speed reductions, two scenarios have been the primary focus for explaining the origin of ULVZs, namely partial melting and/or extreme chemical and phase heterogeneity. A third scenario, anisotropy of a low-velocity and low-viscosity solid phase, like iron-rich (Mg,Fe)O magnesio-wüstite (Finkelstein et al., 2018; Reali et al., 2019a), will

be explored here as well. We briefly summarize these three scenarios below.

Partial Melt. A partial melt origin for ULVZs presents a model suggesting that the *S* to *P* wavespeed reduction would be about 3:1 (e.g., Berryman, 2000; Hier-Majumder, 2014; Williams and Garnero, 1996), in which the velocities of the average assemblage are decreased by melt formed due to partial melting of the mantle and/or by fluid reaction products of the Fe-rich liquid outer core with silicate-rich mantle (e.g., Andrault et al., 2014; Jackson et al., 1987; Liu et al., 2016; Nomura et al., 2014; Ohtani and Maeda, 2001; Pradhan et al., 2015). The

hypothesis of melt origin has been drawn based in part on suggestions of a correlation between ULVZs and plume generation zones or hotspots (Torsvik et al., 2014; Williams et al., 1998). However, the assessment provided in Yu and Garnero (2018) showed that there is no statistically significant correlation of ULVZs and the location of hotspots on Earth's surface. The recent studies of Thorne et al. (2020) and Hansen et al. (2020) also cast this correlation into doubt.

Although early dynamical calculations questioned the possibility to produce a dense and nonpercolating melt phase in the deep Earth (Hernlund and Tackley, 2007), a later study showed that the stirring of ULVZs by the larger-scale convective motions of the mantle can potentially maintain a partially molten region (Hernlund and Jellinek, 2010; McNamara et al., 2010). However, not only does the range of S to P wave speed reductions of partial melt assemblages depend on the melt distribution, but the actual reductions are not constrained experimentally or theoretically at CMB conditions. Shock wave measurements that constrained the densities of Fe-bearing silicate liquids suggest that for a range of plausible mantle compositions, candidate partial melts such as those similar to mid-ocean ridge basalt, would not be dense enough to remain at the CMB over reasonable timescales to be seismically observable at the base of the mantle today (Thomas and Asimow, 2013). The explanation of partial melt also requires a relatively special circumstance, that is the mantle geotherm needs to intersect the mantle solidus (neither of which are tightly constrained) just a few kilometers above the core-mantle boundary.

Extreme Chemical or Phase Heterogeneity. Iron enrichment of solid phases, specifically the increase in Fe/(Fe+Mg) ratio, can simultaneously increase density and reduce compressional and shear velocity (e.g., Karato and Karki, 2001; Muir and Brodholt, 2015). This hypothesis partly inspired the notion of solid, iron-rich ULVZs, such as a metal-bearing layer (Knittle and Jeanloz, 1991), subducted banded iron formations (Dobson and Brodholt, 2005), hydrous iron peroxide (Liu et al., 2017), iron-rich post-perovskite (e.g., Mao et al., 2004; Stackhouse et al., 2006), and iron-rich (Mg,Fe)O (Chen et al., 2012; Dobrosavljevic et al., 2019; Labrosse et al., 2007; Solomatova et al., 2016; Wicks et al., 2017, 2010). The enhanced density of iron-rich systems compared to the surrounding mantle is also helpful in explaining the locations of ULVZs at the base of the mantle (e.g., Li et al., 2017).

Anisotropy. As discussed above, recent studies have shown evidence for significant seismic anisotropy in the D" region near the edges of LLSVPs (e.g., Cottaar and Romanowicz, 2013; Ford et al., 2015; Lynner and Long, 2014; Pisconti et al., 2019), which may be generated by solid-state mantle convection (e.g., McNamara et al.,

2002, 2001). The preferential alignment of post-perovskite crystals has been implicated as the primary source for explaining such anisotropy near the base of the mantle (e.g., Ford et al., 2015; Oganov et al., 2005; Pisconti et al., 2019; Tommasi et al., 2018; Wu et al., 2017). However, these are relatively large regions compared with most ULVZs, and in regions characterized by high temperatures, such as at the base of upwellings or edges of slabs, the post-perovskite phase is not stable (e.g., Hernlund et al., 2005; Hirose, 2006; Shim, 2008) and other mechanisms are then required to explain the anisotropy, in particular, for regions of very low velocities.

Finkelstein et al. (2018) conducted high-resolution inelastic scattering measurements up to 41 GPa on a single crystal of (Mg,Fe)O magnesiowüstite with 76 mol% FeO and constrained the pressure dependence of the elastic tensor. They show that the cubic form of magnesiowüstite develops extreme elastic anisotropy at high pressures. Using the following definition of anisotropy:

$$\text{anisotropy (\%)} = 100 * \left(\frac{V_{max} - V_{min}}{(V_{max} + V_{min})/2} \right),$$

the compressional and shear wave anisotropies of iron-rich (Mg,Fe)O rise up to $18 \pm 3\%$ and $58 \pm 2\%$, respectively, at 31 GPa. Note that the shear anisotropy of PPv and iron-poor (Mg,Fe)O ferropereclase only reach values of about 30% and 40%, respectively, at lower mantle conditions, as summarized in Finkelstein et al. (2018). We compute the velocity ratios for magnesiowüstite along specific crystallographic directions from the elastic tensor measured at 31 GPa (see Table S3a in Finkelstein et al. 2018) and they are: [100] $V_P:V_S = 3.15 \pm 0.16$ and for [110] $V_P:V_S$ ranges from 1.52 ± 0.08 (V_{S2}) to 2.76 ± 0.08 (V_{S1}). Provided the temperatures are below magnesiowüstite's solidus, a 3:1 reduction ratio of S to P wave speeds could be explained with a preferred alignment of iron-rich magnesiowüstite, thus not requiring partial melt. We will quantitatively explore this hypothesis in the next section.

Provided the range and geographic diversity of ULVZ seismic observations to date (e.g., Thorne et al., 2020; Yu and Garnero, 2018), it is reasonable to consider that the chemical and physical characterizations of these structures vary from one ULVZ to another.

8.3.3. Inversion of Iron-Rich Phase Assemblages with Seismic Observations

Studies have indicated preferential iron partitioning into (Mg,Fe)O coexisting with bridgmanite or post-perovskite under the pressure-temperature conditions of Earth's lower and lowermost mantle (e.g., Sinmyo et al., 2008; Tange et al., 2009). Further interest in the role of iron-rich (Mg,Fe)O at Earth's core-mantle boundary has been drawn based on the very low sound speeds of this

material at pressures up to 120 GPa (Wicks et al., 2017, 2010) and the ability of silicate mixtures containing this material to reproduce the topography of some ULVZs (Bower et al., 2011). To broaden the scope of this hypothesis, we have developed a forward modeling approach through misfit minimization to solve for the concentration of a range of iron-rich (Mg,Fe)O compositions coexisting with bridgmanite (Dobrosavljevic et al., 2019; Sturhahn, 2020) that could match two different ULVZ seismic observations, underneath the S. Atlantic (Simmons and Grand, 2002) and Coral Sea (Rost et al., 2006).

In this chapter, we expand this approach by looking at several ULVZ case studies, while considering two iron-rich systems, (Mg,Fe)O and (Mg,Fe)SiO₃ PPv, as well as preferred alignments of iron-rich (Mg,Fe)O magnesiowüstite. Our approach consists of several phases with various material properties to match a set of target seismically observable ULVZ properties (V_P , V_S , and density) given in the literature. The seismically observable properties and estimated uncertainties are then converted to bulk and shear moduli in the mixing model. Specifically, the forward model is the set of minerals with elastic properties mixed together using the Voigt and Reuss mixing bounds (Watt et al., 1976), and the approach optimizes the concentrations of each mineral phase to minimize the misfit with the seismic observables. The variances (or uncertainties) of mineral properties and seismic targets (observations) are included in the inversion strategy, and best-fit properties of the inversion are evaluated with parameter correlations.

For the iron-rich (Mg,Fe)O assemblage, the description and selection of elastic properties are given in Dobrosavljevic et al. (2019) and briefly summarized here. The composition of bridgmanite coexisting with (Mg_{0.16}Fe_{0.84})O was calculated using $K_D^{Br/Mw} = 0.03$ (Tange et al., 2009). The mineral phases are thus (Mg_{0.86}Fe_{0.14})SiO₃-bridgmanite “Br14,” (Mg_{0.16}Fe_{0.84})O magnesiowüstite “Mw84,” and CaSiO₃ perovskite “CaPv”; their respective elastic properties at 135.8 GPa and 3800 K are given in Dobrosavljevic et al. (2019).

For the Fe-rich post-perovskite (PPv) assemblage, we test properties reported in two different studies. One set of elastic properties was reported by Mao et al. (2006) for (Mg_{0.60}Fe_{0.40})SiO₃ PPv and they calculate properties at 130 GPa and 3000 K. The other set of values comes from a theoretical study on the effect of iron on the elasticity of MgSiO₃ post-perovskite (Caracas and Cohen, 2008) at 0 K and lowermost mantle pressures; we thus combine the results from Caracas & Cohen (2008) with a temperature dependence reported by Wentzcovitch et al. (2010) to compute the relevant properties at 130 GPa and 3000 K for (Mg_{0.60}Fe_{0.40})SiO₃ PPv. We assume the composition of (Mg,Fe)O coexisting with Fe-rich PPv is relatively iron-poor and thus in the low-spin state at 130

GPa and 3000 K. The elastic properties for low-spin ferroperricline are taken from a theoretical study of the thermoelastic properties of (Mg_{0.80}Fe_{0.20})O through the spin crossover up to 130 GPa and 4000 K (Wu and Wentzcovitch, 2014). The elastic properties of these three phases used in the Fe-rich PPv inversions are listed in Appendix Table 8.A1.

In the case where we explore the anisotropy of magnesiowüstite (Case 5), we use recent high-energy resolution inelastic x-ray scattering results on single-crystal B1-structured (Mg,Fe)O containing 76 mol% FeO, measured at 31 GPa (Finkelstein et al., 2018). This particular compression point displays the largest measured elastic anisotropy in the measured dataset. As an estimate of the properties of an assemblage containing preferred alignments of anisotropic magnesiowüstite, we start from the isotropic velocities and density of (Mg_{0.16}Fe_{0.84})O at 135.8 GPa and 3800 K, as given in Dobrosavljevic et al. (2019) and used in our assemblages of randomly oriented crystals. We then apply the V_P/V_S ratios computed at 31 GPa from the elastic tensor (see section on *Anisotropy* above) and obtain the following values for preferred alignments along [110]: $V_P = 9.07 \pm 0.14$ km/s, $V_S = 3.29 \pm 0.09$ km/s and along [100]: $V_P = 9.07 \pm 0.14$ km/s, $V_S = 2.88 \pm 0.08$ km/s. From these values, we then calculate the bulk and shear moduli for the mixing model.

With these inversions, we aim to quantify the phase proportions within the proposed assemblages that can generate ULVZ seismic signatures within their respective uncertainties. We constrain the concentrations of two of the phases, such as Br14 and Mw84, which allows the determination of the CaPv concentration. We analyze five different ULVZ case studies, which are described below and summarized in Table 8.1. The locations of these case studies are shown as red areas in Figure 8.2. Select results are plotted in Figures 8.9 and 8.10. In this study, we focus on the Reuss bound results. For ULVZ case studies that include Voigt bound results, see Dobrosavljevic et al. (2019).

ULVZ Case 1: Europe and Western Asia. Gassner et al. (2015) studied the CMB under the Volga River region of Europe and western Asia. Their study searched for and analyzed precursors to *PcP* to assess characteristics of the CMB in this region. Modeling of the amplitudes and travel times of the precursors showed that a range of V_P and V_S reductions were needed to explain the *PcP* precursors (δV_P : -5% to -10%, δV_S : -15% to -30%), as well as a gradient in density ($\delta\rho$: +5% to $\delta\rho$: +15%, including up to +30%) for a ~13 km thick ULVZ. The ULVZ properties are estimated with respect to PREM velocities and density at 135.8 GPa. We use the following seismic observables in our inversion: -5% δV_P , -15% δV_S , and +15% $\delta\rho$, with respect to PREM,

Table 8.1 Seismic observations and best fitting Reuss-bound results for the five ULVZ case studies. (a) Mineral phase properties for Cases 1–4 are $(\text{Mg}_{0.86}\text{Fe}_{0.14})\text{SiO}_3$ -bridgmanite, $(\text{Mg}_{0.16}\text{Fe}_{0.84})\text{O}$, and CaSiO_3 perovskite (Dobrosavljevic et al. 2019). For Case 5, we use the elastic properties of Mw84 computed for the two crystallographic directions in magnesiowüstite representing the highest levels of elastic anisotropy. Given are vol% of Br14, Mw84 and CaPv. (b) Mineral phases are $(\text{Mg}_{0.60}\text{Fe}_{0.40})\text{SiO}_3$ post-perovskite, low-spin $(\text{Mg}_{0.80}\text{Fe}_{0.20})\text{O}$ ferropericlase and CaSiO_3 perovskite (Appendix Table 8.A1). Given are vol% of PPv40, Fp20 and CaPv. Results for all cases of percent reductions (δV_P and δV_S) and elevations ($\delta\rho$) are with respect to PREM at the CMB. For Central America and the Coral Sea, a few different seismic studies are used. See text for details on the individual case studies and Dobrosavljevic et al. (2019) for a description of the inversion approach.

Table 8.1a									
Input seismic values for inversion [Values or range from seismic studies]			Best fit mineral proportions			Best fit seismic properties [Deviation from PREM at the CMB]			
$\delta V_P, \delta V_S, \delta\rho$ (%)	$\delta V_S:\delta V_P$	Br14* (vol%)	Mw84 (vol%)	CaPv (vol%)	V_P (km/s)	V_S (km/s)	$\delta V_S:\delta V_P$	ρ (g/cm ³)	
Case 1. Europe and W Asia									
(Volga River Region)									
-5(3), -15(3), 15(10)	[2 to 3]	71(5)	17(7)	12	12.9(4)	6.3(2)	2.1(1)	5.95(20)	
[-5 to -10, -15 to -30, 5 to 30]									
Case 2. NW America									
-5(3), -8(2), 0(3)	[2 to 3]	69(7)	12(5)	20	13.3(4)	6.7(2)	2.3(1)	5.8(1)	
[-2 to -8, -6 to -10, no $\delta\rho$ constraints]									
Case 3. Central America									
case (a) -10(2), -20(2), 14(5)	[2]	70(2)	26(2)	4	12.3(3)	5.8(1)	1.94(9)	6.20(7)	
[-10, -20, 14]									
case (b) -10(2), -30(2), 1(1)	[3]	62(34)	15(15)	23	12.9(5)	6.4(6)	2.0(3)	5.9(4)	
[-10, -30, 1]									
-10, -30, 1	[3]	No solution within 1 σ : target $\delta V_S:\delta V$ too high, density too low, with no uncertainties on targets							
(no uncertainties)									
Case 4. Coral Sea									
case (a) -10(2), -10(2), 6(3)	[1]	70(6)	15(4)	15	13.1(3)	6.5(2)	2.2(1)	5.9(1)	
[-10, -10, 6]									
case (b) -10(2), -30(2), 10(5)	[3]	No solution within 1 σ : target density and $\delta V_S:\delta V$ too high							
[-10, -30, 10]									
case (c) -10(2), -35(2), 20(5)	[3.5]	No solution within 1 σ : target density and $\delta V_S:\delta V$ too high							
[10, -35, 20]									
case (d) -10(2), -50(2), 15(5)	[5]	No solution within 1 σ : target density and $\delta V_S:\delta V$ too high							
[-10, -50, 15]									
case (e) -8(3), -35(15), 5(5)	[2.5 to 5]	70(6)	17(10)	13	12.9(5)	6.4(5)	2.0(2)	5.9(4)	
[-5 to -10, -25 to -50, no $\delta\rho$ constraints]									
Case 5. Anisotropic magnesiowüstite									
[100] alignment		Br14	Aligned Mw84	CaPv					
case (a)	NW America	[2 to 3]	69(5)	8(2)	23	13.37(35)	6.66(20)	3.3(1)	5.70(7)
-5(3), -8(2), 0(3)									
case (b)	Europe and W Asia	3	70.0(8)	13.0(5)	17	12.94(30)	6.18(10)	2.64(8)	5.84(4)
-5(2), -15(2), 5(5)									
case (c)	Central America	3	65(26)	16(10)	19	12.6(4)	5.8(5)	2.5(3)	5.94(30)
-10(2), -30(2), 1(1)									

(continued overleaf)

Table 8.1 (continued)

Input seismic values for inversion [Values or range from seismic studies]		Best fit mineral proportions			Best fit seismic properties [Deviation from PREM at the CMB]			
$\delta V_P, \delta V_S, \delta \rho$ (%)	$\delta V_S: \delta V_P$	Br14* (vol%)	Mw84 (vol%)	CaPv (vol%)	V_P (km/s)	V_S (km/s)	$\delta V_S: \delta V_P$	ρ (g/cm ³)
case (d)	-10(2), -30(2), 10(5)	3	70(4)	29(3)	1	11.9(3) [-13.2%]	5.1(1) [-30.3%]	2.3(1) 6.28(9) [12.8%]
[110] alignment								
case (a)	NW America -5(3), -8(2), 0(3)	[2 to 3]	69(6)	11(4)	20	13.3(4) [-3%]	6.7(2) [-7.9%]	2.6(1) 5.77(10) [3.6%]
case (b)	Central America -10(2), -30(2), 1(1)	3	63(32)	16(14)	21	12.8(5) [-7%]	6.2(6) [-14%]	2.0(3) 5.92(38) [6.3%]

Target seismic input values and their estimated uncertainties (in parentheses) are provided. The 1σ (68%) uncertainties for the results are given in parentheses for the last reported significant digit(s) of the best fitting phase assemblage (mineral proportions and phase assemblage seismic wave speeds and density). *For Br14, a starting value of 0.70 with a prior window of 0.05 was used, because of the strong trade-off between Br and CaPv due to their similar elastic properties at the CMB.

Input seismic values for inversion [Values or range from seismic studies]		Best fit mineral proportions			Best fit seismic properties [Deviation from PREM at the CMB]			
$\delta V_P, \delta V_S, \delta \rho$ (%)	$\delta V_S: \delta V_P$	PPv40 ^{a,b} (vol%)	Fp20 (vol%)	CaPv (vol%)	V_P (km/s)	V_S (km/s)	$\delta V_S: \delta V_P$	$\delta \rho$ (g/cm ³)
Case 1. Europe & west Asia (Volga River Region)								
-5(3), -15(3), +15(10)	[2-3]	8 ^a	72(17)	20(14)*	13.3(3)	6.6(5)	3.2(3)	5.5(1)
[-5 to -10, -15 to -30, +5 to +30]		69(16) ^{b**}	0	31(16)	13.2(3) [-3%]	7.0(2) [-9%]	1.0(3)	5.8(1) [-1.4%]
Case 2. NW America								
-5(3), -8(2), 0(3)	[2-3]	6 ^a	74(7)	20(6)*	13.4(3)	6.7(2)	3.3(2)	5.48(4)
[-2 to -8, -6 to -10, no $\delta \rho$ constraints]		62(16) ^{b**}	16	24(24)	13.2(3) [-2.2%]	7.0(3) [-7.3%]	1.0(3)	5.7(2) [-1.6%]
Case 3. Central America								
-10(2), -30(2), +1(1)	[~3]	47 ^a	34(7)	19(6)	12.4(3)	5.1(1)	3.1(2)	5.67(4)
[-10, -30, 1]		no solution ^b			13.2(3) [-3.6%]	7.0(3) [-3.4%]		5.7(2) [3%]

Target seismic input values and their estimated uncertainties (in parentheses) are provided. The 1σ uncertainties for the results are given in parentheses for the last reported significant digit of the best fitting phase assemblage (mineral proportions and phase assemblage seismic wave speeds and density). ^a Mao et al. (2006); ^b Caracas and Cohen (2008); Dorfman and Duffy (2014); Wentzcovitch et al. (2010). *For CaPv, a starting value of 0.20 for CaPv with a prior window of 0.10 was used, because of the strong trade-off with Fp20 due to their similar elastic properties at the CMB (Appendix Table 8.A1). **These inversions use a starting value of 0.70 for PPv40^b with a prior window of 0.10, because of the strong trade-offs with Fp20 and CaPv.

and assigned uncertainties of 3% for V_P and V_S and 10% for ρ , to account for the range of seismic models presented in Gassner et al. (2015), and determine the best-fit mineral proportions. Our best-fitting model results in 71(5) vol% Br14, 17(7) vol% Mw84 and 12 vol% CaPv, where the number in parentheses represents the 1σ error of the last significant digit from the inversion. This implies that within the uncertainties of both the mineral elastic properties and the estimated uncertainties in the seismic observations, $\delta V_S = -13\%$, $\delta V_P = -6\%$ and a density contrast of $\delta\rho: +7\%$, with $\delta V_S:\delta V_P$ of 2.1(1) provides a good fit for this region (see Figure 8.9a and Table 8.1a).

When testing whether the presence of iron-rich post-perovskite can fit these seismic observations, the results are not well-constrained, in part due to the wide range of elastic properties reported for iron-rich PPv (Caracas and Cohen, 2008; Mao et al., 2006) (Appendix Table 8. A1). Using these different sets of elastic properties, the results of the inversions show very large uncertainties and point to a mantle phase assemblage that requires either a very large fraction of (Mg,Fe)O ferropericlasite and a negative density anomaly or no ferropericlasite and a positive density anomaly: 8% PPv40 (Mao et al., 2006), 72(17)% Fp20, and 20(14)% CaPv (with $\delta\rho: -1.4\%$), for an assemblage with 69(16)% PPv40 (Caracas and Cohen, 2008), 31(16)% CaPv, and no ferropericlasite, with $\delta\rho: +4\%$ (Table 8.1b).

ULVZ Case 2: NW America. Sun et al. (2013) used SKPdS and SKKS to study the CMB region underneath Nevada and British Columbia in a region where high velocities were reported in most tomographic models and previously thought devoid of ULVZs (Rost et al., 2010). Their analysis of differential travel times for SKPdS and SKKS show regions with and without small-scale structures near the CMB, with heights ranging from 0 to 100 km and velocity variations for δV_P and δV_S centered on -5 ± 3 and $-8 \pm 2\%$, respectively, indicating large-topography lowvelocity regions that are not detected with tomographic inversions (Sun et al. 2013). Although their modeling of travel times does not provide constraints on density, their interpretation of the proportion of iron-rich oxides in this region suggested a density elevation of 1.5–2%. However, this density elevation was calculated using older equations of state and did not consider the presence of CaPv. We model concentrations of Br14, Mw84, and CaPv with the consideration that no constraints on density were reported (a value of $0\% \pm 3\%$ for $\delta\rho$ was used as an input). We find 69(7) vol% of Br14, 12(5) vol% of Mw84, and 20 vol% CaPv, which leads to a best-fit density of $5.8(1) \text{ g/cm}^3$ ($\delta V_P, \delta V_S, \delta\rho: -3.2\%, -7.6\%, +4\%$ compared with PREM) (see Table 8.1a and Figure 8.9a). When testing whether an Fe-rich PPv assemblage can explain these observations,

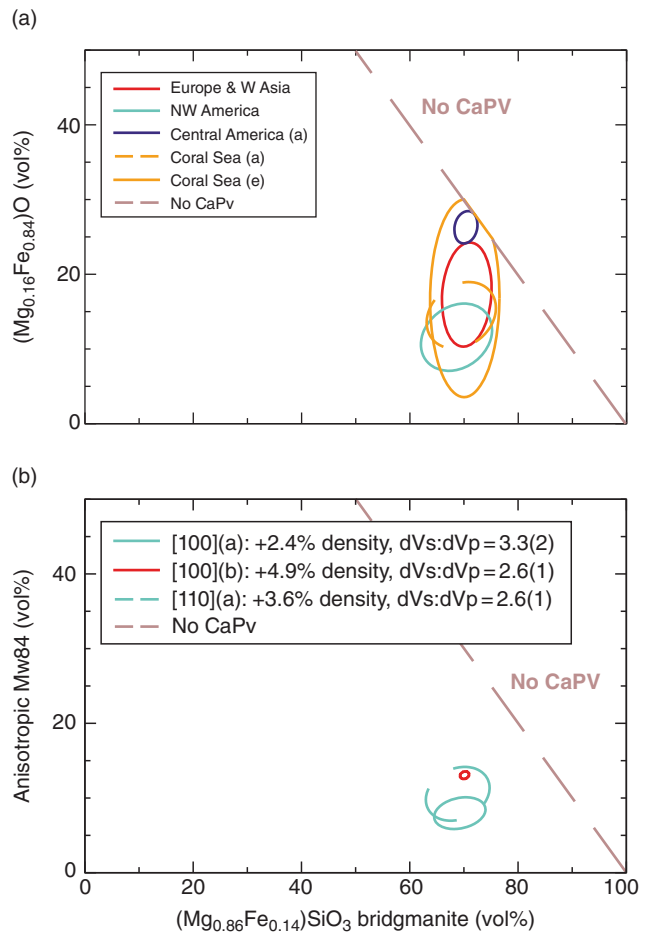


Figure 8.9 Best-fitting mineral assemblages results for the ULVZ case studies. (a) Cases 1–4: The target ULVZ seismic properties were varied with respect to PREM at the CMB for a number of regional studies (see Table 8.1a). Mineral concentrations are $(\text{Mg}_{0.86}\text{Fe}_{0.14})\text{SiO}_3$ -bridgmanite “Br14,” $(\text{Mg}_{0.16}\text{Fe}_{0.84})\text{O}$ magnesiowüstite “Mw84,” and CaSiO_3 perovskite “CaPv.” (b) Case 5: A subset of the ULVZ seismic studies in (a) were tested with the same mineral assemblage as in Cases 1–4, except that isotropic Mw84 elastic properties were replaced with elastic properties along the [110] and [100] crystallographic directions in Fe-rich (Mg,Fe)O (Finkelstein et al., 2018). Color scheme in (b) matches the same regions in (a). The diagonal line represents cases of only Br14 and Mw84, without CaPv. The area inside the colored ellipses represents 1σ uncertainties resulting from the χ^2 analysis. Select cases are plotted. The best-fit results and marginalized 1σ errors for all inversions are reported in Table 8.1a.

we find similar extreme ranges of phase assemblages as we found for Case 1 (Table 8.1b).

ULVZ Case 3: Central America. In their review of ULVZs, Yu and Garnero (2018) also assessed ULVZ location with respect to high-velocity regions in a range of tomographic models, finding 11% of the ULVZs are

located within seismically fast regions of tomography models, regions often associated with down-wellings (e.g., Frost and Rost, 2014; Koelemeijer et al., 2016; Ritsema et al., 2011; Simmons et al., 2010). One of these regions lies beneath Central America and has been extensively sampled by core-reflected phases (*PcP* and *ScS*, e.g., Kito et al., 2007). This is a region where strong lateral seismic velocity gradients exist (Thorne et al., 2004) and a transition from relatively slow wave speeds in the northeast Pacific LLSVP to relatively fast wave speeds eastward (Frost and Rost, 2014; Simmons et al., 2010).

Near this region, Havens and Revenaugh (2001) use *PcP*-waves and detect a 10–20 km thick ULVZ beneath Mexico. They find $\delta V_S:\delta V_P = 2$ with $\delta\rho = 14\%$ relative to PREM for three of their four models/locations studied, which leads to a well-constrained presence of 26(2) % iron-rich (Mg,Fe)O as Mw84, coexisting with 70(2)% Br14 and 4% CaPv, resulting in $\delta V_S:\delta V_P$ of 1.94(9) with $\delta\rho = 11.3\%$ (see Table 8.1a and Figure 8.9a).

In their fourth location underneath Central America, they report -10% in V_P and -30% in V_S ($\delta V_S:\delta V_P = 3$ with $\delta\rho = 1\%$). Using these values as inputs with a rough estimate of the uncertainties, the inversion results in a smaller δV_S (-12%). If no uncertainties are placed on the seismic observation for the inversion, no solution is reached for the case of iron-rich (Mg,Fe)O. Thus, with such a negligible elevation in density and a large decrease in S -wave speed, iron-rich (Mg,Fe)O is an unlikely explanation (Table 8.1a). When testing whether the presence of Fe-rich PPv can fit these seismic observations, the results require a significant fraction of ferropericlase: 47% PPv40 (Mao et al., 2006), 34(6)% Fp20, and 19(6)% CaPv (Table 8.1b). There is no solution within 1σ if the elastic properties of PPv40 from Caracas and Cohen (2008) are used. In this scenario, where the velocities are significantly reduced (-10% in V_P and -30% in V_S) and the density contrast is close to zero, partial melt may provide an explanation. Indeed, as discussed in our case study in the D" section, dynamic simulations predict patches of very low seismic velocity beneath and at the edges of large-scale high-velocity structures (slabs) at the CMB (Tan et al., 2002), due to higher-than-average temperatures. This scenario could lead to partial melting. However, there remains a challenge of stabilizing partial melts such that they are seismically observable, and the range of S to P wave speed reductions of a partial melt assemblage, melt-pocket geometries and the relative thermal profiles of the solidus and geotherm are not well constrained at CMB conditions.

ULVZ Case 4: Coral Sea. The CMB region underneath the Coral Sea, located just off of the east coast of Australia, has been extensively studied using core-reflected phases (e.g., Brown et al., 2015; Koper and Pyle, 2004; Rost et al., 2010, 2006, 2005; Rost and Revenaugh,

2003), PKP (Koper and Pyle, 2004; Thomas et al., 2009) and SKS (Jensen et al., 2013). This region is within the southwest corner of the Pacific LLSVP (Frost and Rost, 2014; Simmons et al., 2010).

In many of these studies, both δV_S and δV_P have been reported (typically δV_P around -10%), but vary significantly in their relative δV_S decrements. In most of these studies, density elevations have also been reported. We consider the following observations that have been made: (Case 4a) $\delta V_S:\delta V_P = 1$ and $\delta\rho = 6\%$ (Brown et al., 2015), (Case 4b) $\delta V_S:\delta V_P = 3$ (Jensen et al., 2013; Rost et al., 2010, 2006; Rost and Revenaugh, 2003) and $\delta V_S:\delta V_P = 3.125$ (Rost et al., 2005) with $\delta\rho = 10\%$, (Case 4c) $\delta V_S:\delta V_P = 3.5$ and $\delta\rho = 20\%$ (Koper and Pyle, 2004), (Case 4d) $\delta V_S:\delta V_P = 5$ and $\delta\rho = 15\%$ (Rost and Revenaugh, 2003), and (Case 4e) $\delta V_S:\delta V_P = 2.5-5$ with no constraints on density elevation, using PKP diffracted waves (Thomas et al., 2009) (Table 8.1a).

We primarily focus on iron-rich (Mg,Fe)O assemblages, due to the challenges discussed above involving Fe-rich PPv assemblages. The best-fit concentrations of the minerals for the Coral Sea observations are provided in Table 8.1a. We find for Cases 4a and 4e that although the resulting best fit concentrations of Br14, Mw84, and CaPv are similar, the uncertainties for case 4e are significantly larger, mostly due to the loose seismic constraints provided in Case 4e (Figure 8.9a). The best fit value that considers the mutual uncertainties in mineral physics properties and seismic observations is for density elevations around $6-7\%$, with a $\delta V_S:\delta V_P \approx 2.2$ for concentrations of around 70% Br14, 15% Mw84, and 15% CaPv. Therefore, in the Coral Sea region, seismic observations that tightly constrain $\delta V_S:\delta V_P \approx 2$ can be explained by the presence of iron-rich (Mg,Fe)O. Whereas higher ratios of seismic reductions associated with large negative velocity contrasts and large positive density contrasts yield no solution for Fe-rich (Mg,Fe)O or Fe-rich PPv, within 1σ , and likely require different explanations.

ULVZ Case 5: Anisotropy. The cases we have explored thus far have assumed isotropic wave velocities of the individual phases and randomly orientated aggregates. As discussed in the section on D", mantle dynamics could induce large-scale flow (McNamara et al., 2002, 2001), which could be seismically detected (e.g., Kendall and Silver, 1998, 2000, Nowacki et al., 2010). Crystals in this flow field could align to produce observable seismic anisotropy and this has been tested for the D" region using mineral physics results of iron-poor PPv and iron-poor (Mg,Fe)O (e.g., Antonangeli et al., 2011; Crowhurst et al., 2008; Immoor et al., 2018; Jackson et al., 2006; Marquardt et al., 2009; Tommaseo et al., 2006; Tommasi et al., 2018). The role of anisotropy for the detection and seismic properties of ULVZs, in particular the role of

iron-rich (Mg,Fe)O magnesiowüstite, has only recently been explored (Finkelstein et al. 2018; Reiss et al. 2019).

The northeast Pacific region is characterized by complex seismic anisotropy signatures (see Nowacki et al., 2011 for a review), where some studies suggest $V_{SH} > V_{SV}$ (Fouch et al., 2001; Vinnik et al., 1998, 1995, 1989), $V_{SH} < V_{SV}$ (Kawai and Geller, 2010; Ritsema et al., 1998) as well as both (Pulliam and Sen, 1998; Russell et al., 1999, 1998) and, further south, isotropy (Kendall and Silver, 1998). As described above, (Mg,Fe)O magnesiowüstite displays compressional and shear wave anisotropies approaching 20% and 60%, respectively. We now replace randomly oriented Mw84 with preferred alignments of magnesiowüstite in the [110] and [100] crystallographic directions ($V_S:V_P$ of 2.76 and 3.15, respectively) and explore a few of the ULVZ regions discussed above. We find that $\delta V_S:\delta V_P = 3.3(1)$ and $2.64(8)$ can be achieved by aligning 8(2)% and 13.0(5)% of the magnesiowüstite crystals in the [100] crystallographic direction. For the ULVZ cases explored, $\delta V_S:\delta V_P \approx 2$ to 3.3 can be achieved with preferred alignments of iron-rich (Mg,Fe)O (Table 8.1a). Thus, $\delta V_S:\delta V_P \approx 3$ is achieved without the need for partial melt to be present. In general, the cases of preferred alignment of magnesiowüstite lead to reduced 1σ uncertainties and less parameter correlations, compared with the assemblages involving randomly orientated crystallites. These conclusions are best illustrated in Figures 8.9 and 8.10.

Evidence from studies on iron-poor (Mg,Fe)O suggest that the magnitude of seismic anisotropy originating from (Mg,Fe)O would be determined by the active slip systems and deformation partitioning between all coexisting phases (e.g., Merkel et al., 2007; Miyagi et al., 2010; Girard et al., 2012; Yamazaki et al., 2014; Marquardt and Miyagi, 2015; Wu et al., 2017; Immoor et al., 2018; Thielmann, et al., 2020). Currently, the active slip systems in iron-rich (Mg,Fe)O and the effect of deformation partitioning between silicates (e.g., Reali et al., 2019b) and relatively low-viscosity magnesiowüstite (Reali et al., 2019a) are not well-understood at lower-mantle conditions, thus we refrain from speculating further on this topic. Future work is needed in order to precisely map alignment of magnesiowüstite from strain fields induced by mantle convection.

8.3.4. ULVZ Topography

The density of a magnesiowüstite-bearing ULVZ has been shown to affect ULVZ topography (Bower et al., 2011). Many of the ULVZ case studies examined here show that for seismic observations of $\delta V_S:\delta V_P \approx 2$ to 3, an assemblage containing iron-rich (Mg,Fe)O provides a good explanation, corresponding to $\delta\rho$ ranging from

about +2 to +13%. The lower-density elevations would correspond to a buoyancy number of about 1, which would maintain topographic relief (~20–70 km) (Bower et al., 2011; Sun et al., 2013). Density elevations of around 7% would lead to buoyancy values between 4 and 5, sustaining structures up to about 35 km thick. For density elevations greater than 7%, the buoyancy values would be > 5 , normally leading to topographically “flat” structures at the CMB. However, there may be a possibility to produce a garden of assorted ULVZ structures (variable heights and topography) at the CMB (Wen and Helmberger, 1998b) with magnesiowüstite-bearing assemblages, considering the possibility of dynamic stirring of a low-viscosity phase such as iron-rich (Mg,Fe)O (Reali et al., 2019a). Similar mechanisms were explored with partially molten ULVZs, that is stirring or deformation of ULVZs by the larger-scale convective motions of the mantle (Hernlund and Jellinek, 2010; McNamara et al., 2010), suggesting the possibility of maintaining such a low-viscosity solid phase like iron-rich magnesiowüstite with relatively high topographic relief.

8.3.5. Summary of ULVZ Case Studies

We explored four distinct geographic regions containing ULVZs and performed a best-fitting analysis with assemblages containing Fe-rich (Mg,Fe)O and PPv, and preferred alignments of Fe-rich (Mg,Fe)O. We see that the large discrepancy in elastic properties of Fe-rich PPv reported from ab initio calculations (Caracas and Cohen, 2008) compared with those from experiments (Mao et al., 2006) (Appendix Table 8.A1) lead to very different conclusions about the amount of PPv present and density contrasts (some are negative), while yielding relatively unconstrained proportions of phases (Table 8.1b).

The case studies explored here show that seismic observations providing $\delta V_S:\delta V_P \approx 2$ to 3, with $\delta\rho$ ranging from about +2 to +13%, can be explained by the presence of an aggregate containing randomly oriented or preferred alignments of iron-rich (Mg,Fe)O magnesiowüstite (Table 8.1a and Figure 8.9). In many cases, preferred alignments of magnesiowüstite significantly improve the fits to the seismic observations (Figure 8.10). For example, preferred alignment of 8% magnesiowüstite grains with [100] orientations provides a very good match to $\delta V_S:\delta V_P = 3.3(1)$. These results are consistent with the recent seismic study of Reiss et al. (2019) that performed forward modeling of single-crystal elasticity data presented in Finkelstein et al. (2018) to suggest that the alignment of 12% magnesiowüstite crystals is a viable interpretation of SKS-SKKS splitting discrepancy beneath Central Africa. A full quantitative evaluation of the hypothesis that aligned iron-rich (Mg,Fe)O can explain ULVZ properties would require the inclusion of

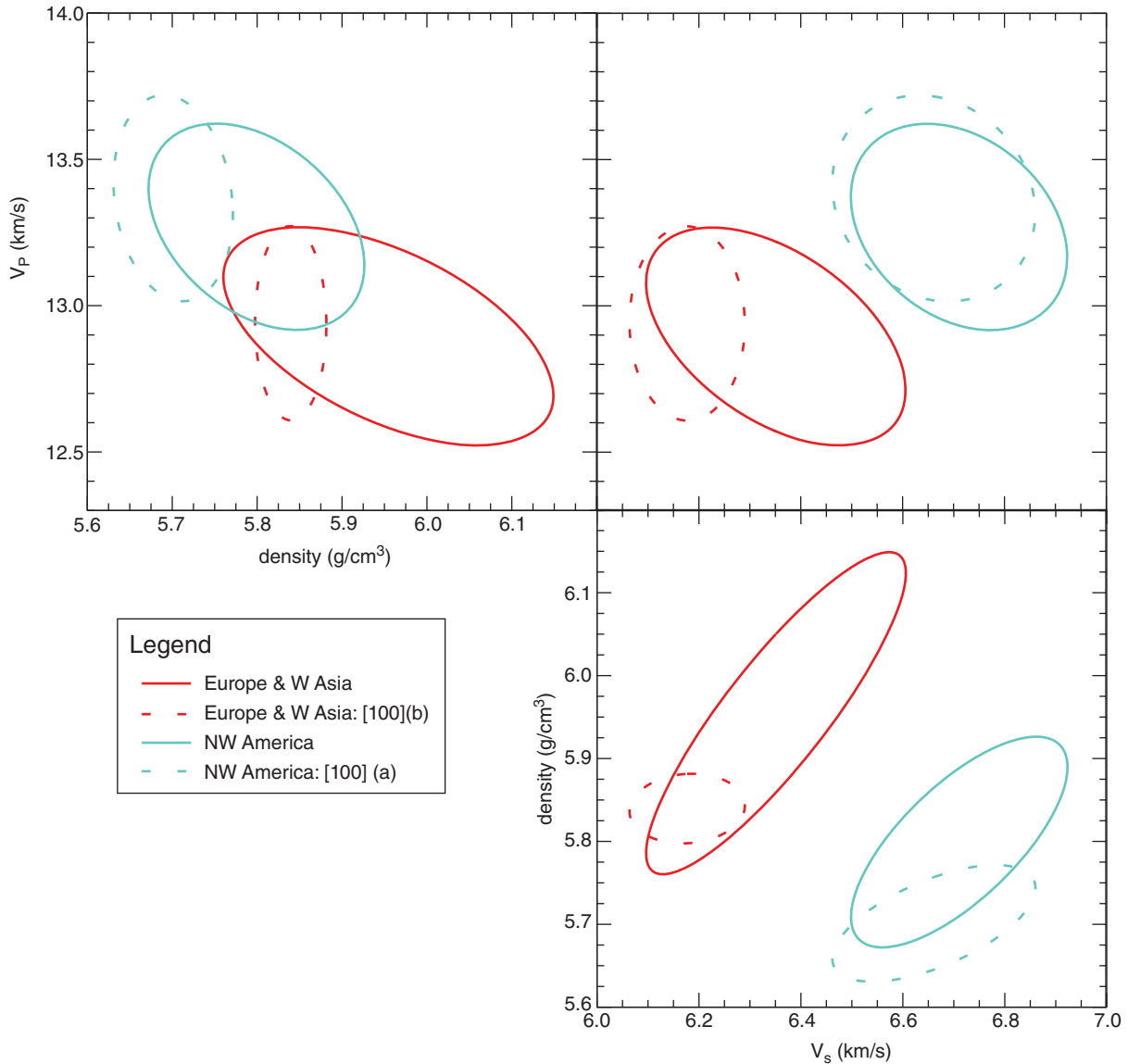


Figure 8.10 Corner plot showing error correlation ellipses (1σ) from the best-fitting results of select ULVZ case studies (Table 8.1a and Figure 8.9). Solid ellipses correspond to the results with randomly oriented Br14, Mw84, and CaPv. Dotted ellipses are for the same regional ULVZ seismic observations, but for cases involving anisotropy; preferred orientations of Mw84 are indicated in the legend. For reference, $V_P = 13.72$ km/s, $V_S = 7.26$ km/s, and density = 5.57 g/cm^3 at the CMB (PREM).

a geodynamic model that predicts total strain development, as well as knowledge of the active slip systems of iron-rich (Mg,Fe)O and how strain partitions between lower mantle phases that are characterized by relatively large viscosity contrasts.

For cases of well-constrained velocity ratios (that is seismic uncertainties of less than 1%), the observations of $\delta V_S:\delta V_P \geq 3$ associated with larger velocity reductions (-10% in V_P and $\geq -30\%$ in V_S) and $\delta\rho \approx 1\%$ (some regions under Central America, for example) yield no solution for

Fe-rich (Mg,Fe)O or Fe-rich PPv, within 1σ . Small density contrasts could be achieved by partial melts of the lowermost mantle (Thomas and Asimow, 2013), although the velocity reductions of these assemblages require more study. Observations reporting $\delta V_S:\delta V_P \geq 3$ associated with large velocity reductions and high density contrasts ($\delta\rho \approx 6$ to 13%) remain challenging to explain. Explaining these latter cases not only require having better experimental and theoretical constraints on the range of expected petrologies and their elastic properties at CMB

conditions, but a better understanding of how melt would be distributed, and the trade-offs between shape, thickness, and velocity reduction of these structures.

8.4. SUMMARY AND CONCLUSIONS

We have shown a range of observations for the D'' region, while exploring some of the complexity and causes for select seismically observed structures, such as reflectors and ultralow velocity zones (Figure 8.11).

While several observables such as travel time, amplitudes, polarities and waveforms constrain certain properties of the structures, there are trade-offs within these observables and with other factors. For example, travel times, which constrain the depth of a reflector are influenced not only by the reflection depth but by path deviations, attenuation, and anisotropy. Amplitudes are affected by attenuation, velocity, and density jumps and their gradients, as well as anisotropy. It is therefore not straightforward to interpret observables without taking all factors into consideration.

We present a case study of the D'' reflector in a region beneath the Aleutians where our observations range from nondetection to complex waveforms, with most of the imaged region characterized by a positive velocity jump across D''. Tomographic models of this region also show strong variations in their resolved velocities, both laterally and with depth, with some tomographic models indicating a low velocity region. Our interpretation of the complex seismicity in this region indicates that there is a need for changes in mineral phase assemblages, their compositions, and their temperature across relatively small distances, all of which requires changes in the dynamics over similarly small distances. A consistent interpretation involves the dynamics of subducted slab debris, corroborated with the complex mineral physics characteristics of the bridgmanite to post-perovskite phase transition in multicomponent systems.

On the shorter-scale end of observations, we concentrate on ultralow velocity zones: the travel times and amplitudes of waves imaging ultralow velocity zones lead to a large number of published velocity variations in V_P and V_S , while a subset of these studies also provide constraints on density. The observables of these structures can be influenced by other factors as discussed above, thus requiring the need to consider their trade-offs and exercise caution when interpreting one observable alone. We use the published V_P to V_S decrements and density for a range of case studies to invert for compositionally distinct ULVZ phase assemblages. In this chapter, we also explore the effect of preferred alignments of elastically anisotropic magnesiowüstite for causing ultralow velocity regions.

While considering assemblages that contain either iron-rich (Mg,Fe)O or iron-rich post-perovskite, we discussed

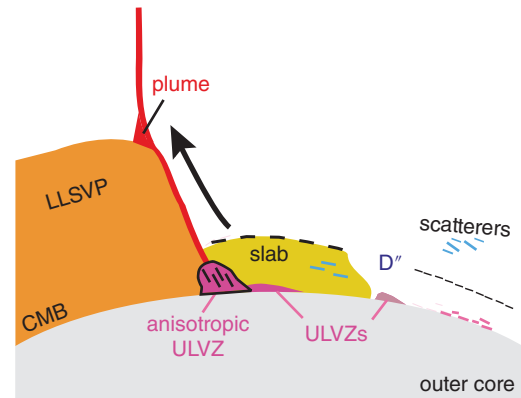


Figure 8.11 Schematic showing possible interactions between slabs, plumes, ultralow velocity zones (ULVZs) and large low seismic velocity provinces (LLSVP). Scatterers could be parcels of relic slab debris (faster wave velocities: blue dashes) or iron-rich parcels related to ULVZs (slower wave velocities: red dashes). Slabs can induce large-scale flow to push LLSVPs aside, while crystals such as iron-rich (Mg,Fe)O magnesiowüstite could align (black lines) within ULVZs, producing observable seismic anisotropy. Dynamics involving slabs and/or the presence of iron-rich (Mg,Fe)O may also feed or cause upwellings in the form of deep-seated plumes. Note that the D'' reflector (black dashed thick and thin lines) could be located in regions that are imaged as faster or slower than average seismic wave speeds in tomography studies. Source: Modified from Sun et al. (2019).

several challenges to explain ULVZs with iron-rich post-perovskite. Phase assemblages that include iron-rich (Mg,Fe)O magnesiowüstite provide the best matches to many of the ULVZ case studies examined here: (i) if the seismic observations have the uncertainties and trade-offs that we apply in our analysis, then a velocity reduction ratio of $\delta V_S/\delta V_P \approx 2$ for a wide-range of velocity decrements and density elevations can be explained by a mixture of randomly oriented magnesiowüstite, bridgmanite, and calcium silicate perovskite, and (ii) for cases with $\delta V_S/\delta V_P$ ranging from 2 to 3, preferred alignment of a small amount of iron-rich (Mg,Fe)O crystals could explain the observations. Reduction ratios below 2 or above 3, particularly with large density enhancements for the latter, require different explanations than those considered here. Our analysis therefore suggests a large diversity of ULVZs, rather than a single origin.

The mounting collection of seismic studies observing the D'' region, in particular the increase in spatial coverage, will provide unprecedented constraints on the three-dimensional characteristics and distribution of these structures. In combination with geochemical analysis, mineral physics results, and geodynamical modeling, future studies will enhance our understanding of the causal links between the diversity and origin of structures at Earth's core-mantle boundary and the changes in surface processes over geologic time.

ACKNOWLEDGMENTS

We are sincerely thankful to our dear friend and colleague, Don Helmberger (Caltech), for all the thoughtful discussions about D" and Earth's interior. We would also like to thank Wolfgang Sturhahn (Caltech) for his help with developing the mineral mixing model and Vasilije Dobrosavljevic (Caltech) for related discussions, and

Angelo Pisconti (U. Münster) for comments on the chapter. We thank Jeroen Ritsema (U. MI), two anonymous reviewers, and the editor Hauke Marquardt for their careful reviews. J.M.J. thanks the National Science Foundation's Collaborative Study of Earth's Deep Interior (EAR-1161046 and 2009935), the Internationalization Office of WWU, Münster, and Caltech for support.

APPENDIX

Appendix Table 8.A1 Seismic properties and their uncertainties for $(\text{Mg}_{0.60}\text{Fe}_{0.40})\text{SiO}_3$ post-perovskite, $(\text{Mg}_{0.80}\text{Fe}_{0.20})\text{O}$ ferropericlasite, CaSiO_3 perovskite, calculated at 130 GPa and 3000 K from their bulk and shear elastic moduli.

	$(\text{Mg}_{0.60}\text{Fe}_{0.40})\text{SiO}_3$	$(\text{Mg}_{0.60}\text{Fe}_{0.40})\text{SiO}_3$	$(\text{Mg}_{0.80}\text{Fe}_{0.20})\text{O}$	CaSiO_3
	PPv40 ^a	PPv40 ^b	Fp20 ^c	CaPv ^d
V_P (km/s)	11.91 ± 0.12	13.03 ± 0.33	13.74 ± 0.34	13.45 ± 0.34
V_S (km/s)	4.05 ± 0.03	7.02 ± 0.18	7.16 ± 0.18	6.94 ± 0.35
ρ (g/cm ³)	5.900 ± 0.059^b	5.900 ± 0.059	5.430 ± 0.054	5.526 ± 0.055

^aMao et al., (2006)

^bCaracas and Cohen (2008); Dorfman and Duffy (2014); Wentzcovitch et al. (2010)

^cWu and Wentzcovitch (2014)

^dGréaux et al. (2019)

Appendix Table 8.A2 Events used for examples in Figures 3, 5, and 8 (1–10) and events for the Bering Sea study (11–28). Earthquake parameters are from NEIC (National Earthquake Information Centre, United States Geological Survey). For events 11–28, reflector depths are calculated with the P wave as reference phase. A star (*) means no PdP reflection despite good signal to noise ratio. '--' indicates events for which not enough traces were recorded for the event or where the epicentral distance was too large.

#	Date dd/mm/yy	lat [deg N]	lon [deg W]	Depth [km]	Wave used	Array used	
Events shown in Figures 3, 5, 8							
1	30/05/07	52.14	157.29	116	PdP	GRSN	
2	17/12/91	47.39	151.50	157	PdP	GRSN	
3	12/11/03	33.17	137.07	384	PdP	POLARIS NWT	
4	16/06/92	45.70	142.26	317	PdP	GRSN	
5	19/04/05	29.64	138.89	425	PdP	POLARIS NWT	
6	11/11/03	22.32	143.25	101	PdP	POLARIS BC and NWT	
7	04/10/02	-20.99	-179.02	621	PKPbdiff	EAGLE	
8	25/05/97	-32.115	179.79	333	SPdKS	TWiST	
9	09/04/09	6.26	94.44	83	PKPdf precursors	TA	
10	synthetics	based on the events in Rost and Thomas (2010)		35	PuP waves	YKA	
Bering Sea Study					Refl. depth (BC) [km]	Refl. depth (NWT) [km]	
11	09/07/03	29.74	129.97	57	2695	noise	POLARIS BC and NWT
12	11/11/03	22.32	143.25	101	2605	2745	POLARIS BC and NWT
13	12/11/03	33.17	137.07	384	2645	*	POLARIS BC and NWT
14	22/02/04	18.50	145.39	197	2635	--	POLARIS BC and NWT
15	05/02/05	16.01	145.87	142	noise	--	POLARIS BC and NWT

Appendix Table 8.A2 (continued)

#	Date dd/mm/yy	lat [deg N]	lon [deg W]	Depth [km]	Wave used		Array used
16	22/02/05	33.18	137.15	369	2560 and 2740	noise	POLARIS BC and NWT
17	19/04/05	29.64	138.89	425	2705	*	POLARIS BC and NWT
18	01/07/05	31.92	139.06	206	--	2625	POLARIS BC and NWT
19	23/10/05	37.38	134.56	380	2555 and 2735	*	POLARIS BC and NWT
20	28/03/06	31.71	137.75	401	2575 and 2690	2780	POLARIS BC and NWT
21	16/04/06	30.24	138.57	431	--	*	POLARIS BC and NWT
22	11/06/06	33.13	131.15	140	noise	noise	POLARIS BC and NWT
23	21/08/06	33.63	135.82	411	--	*	POLARIS BC and NWT
24	01/04/07	32.35	137.61	378	noise	--	POLARIS BC and NWT
25	16/07/07	36.81	134.85	350	2620	*	POLARIS BC and NWT
26	01/08/07	33.90	136.61	370	noise	--	POLARIS BC and NWT
27	28/09/07	22.01	142.67	260	noise	noise	POLARIS BC and NWT
28	31/10/07	18.90	145.36	223	2630	--	POLARIS BC and NWT

REFERENCES

- Akber-Knutson, S., Steidle-Neumann, G., & Asimow, P.D. (2005). Effect of Al on the sharpness of the MgSiO₃ perovskite to post-perovskite phase transition. *Geophysical Research Letters* 32, <https://doi.org/10.1029/2005GL023192>.
- Albarède, F. (2005). The survival of mantle geochemical heterogeneities, in: Van der Hilst, R.D., Bass, J.D., Matas, J., Trampert, J. (Eds.), *Earth's deep mantle structure, composition and evolution*. American Geophysical Union Monograph, pp. 27–46.
- Ammann, M.W., Brodholt, J.P., Wookey, J., & Dobson, D.P. (2010). First-principles constraints on diffusion in lower-mantle minerals and a weak D" layer. *Nature* 465, 462–465.
- Andrault, D., Pesce, G., Bouhifd, M.A., Bolfan-Casanova, N., Henot, J.M., & Mezouar, M. (2014). Melting of subducted basalt at the core-mantle boundary. *Science* 344, 892–895.
- Antonangeli, D., Siebert, J., Aracne, C.M., Farber, D.L., Bosak, A., Hoesch, M., Krisch, M., Ryerson, F.J., Fiquet, G., & Badro, J. (2011). Spin crossover in ferropervicase at high pressure: A seismologically transparent transition? *Science* 331, 64–67. <https://doi.org/10.1126/science.1198429>
- Auzende, A.-L., Badro, J., Ryerson, F.J., Weber, P.K., Fallon, S.J., Addad, A., Siebert, J., & Fiquet, G. (2008). Element partitioning between magnesium silicate perovskite and ferropervicase: New insights into bulk lower-mantle geochemistry. *Earth and Planetary Science Letters* 269, 164–174.
- Becker, T.W., Kellogg, J.B., & O'Connell, R.J. (1999). Thermal constraints on the survival of primitive blobs in the lower mantle. *Earth and Planetary Science Letters* 171, 351–365.
- Berryman, J.G. (2000). Seismic velocity decrement ratios for regions of partial melt in the lower mantle. *Geophysical Research Letters* 27, 421–424.
- Bower, D.J., Gurnis, M., & Seton, M. (2013a). Lower Mantle structure from paleogeography constrained dynamic Earth models. *Geochemistry, Geophysics, Geosystems* 14, 44–63. <https://doi.org/10.1029/2012GC004267>
- Bower, D.J., Gurnis, M., & Sun, D. (2013b). Dynamic origins of seismic wavespeed variation in D". *Physics of Earth and Planetary Interiors* 214, 74–86. <https://doi.org/10.1016/j.pepi.2012.10.004>
- Bower, D.J., Wicks, J.K., Gurnis, M., & Jackson, J.M. (2011). A geodynamic and mineral physics model of a solid-state ultralow velocity zone. *Earth and Planetary Science Letters*. <https://doi.org/10.1016/j.epsl.2010.12.035>
- Braña, L., Helffrich, G. (2004). A scattering region the core-mantle boundary under the North Atlantic. *Geophysical Journal International* 158, 625–636.
- Brown, S.P., Thorne, M.S., Miyagi, L., & Rost, S. (2015). A compositional origin to ultralow-velocity zones. *Geophysical Research Letters* 42, 1039–1045.
- Bullen, K.E. (1950). An earth model based on a compressibility-pressure hypothesis. *Geophys. J. Int.* 6, 50–59.
- Burke, K., Steinberger, B., Torsvik, T., & Smethurst, M. (2008). Plume Generation Zones at the margins of Large Low Shear Velocity Provinces on the core–mantle boundary. *Earth and Planetary Science Letters* 265, 49–60.
- Capon, J. (1973). Signal processing and frequency-wavenumber spectrum analysis for a large aperture seismic array. *Methods in Computational Physics* 13, 1–59.
- Caracas, R., Cohen, R.E. (2008). Ferrous iron in post-perovskite from first-principles calculations. *Phys Earth Planet In* 168, 147–152.
- Caracas, R., & Cohen, R.E. (2007). Effect of chemistry on the physical properties of perovskite and post-perovskite, in: Hirose, K., Brodholt, J.P., Lay, T., Yuen, D. (Eds.), *Post-Perovskite. The Last Mantle Phase Transition*. AGU Monograph Series, pp. 115–128.
- Caracas, R., & Cohen, R.E. (2005). Effect of chemistry on the stability and elasticity of the perovskite and post-perovskite phases in the MgSiO₃-FeSiO₃-Al₂O₃ system and implications for the lowermost mantle. *Geophysical Research Letters* 32, <https://doi.org/10.29/2005GL023164>.
- Castle, J.C., & van der Hilst, R.D. (2000). The core-mantle boundary under the Gulf of Alaska: No ULVZ for shear waves. *Earth and Planetary Science Letters* 176, 311–321.

- Catalli, K., Shim, S.-H., & Prakapenka, V.B. (2009). Thickness and Clapeyron slope of the post-perovskite boundary. *Nature* 462, 782–785.
- Chaloner, J.W., Thomas, C., & Rietbrock, A. (2009). P- and S-wave reflectors in D" beneath southeast Asia. *Geophys J. Int* 179, 1080–1092.
- Chambers, K., & Woodhouse, J.H. (2006). Transient D" discontinuity revealed by seismic migration. *Geophysical Research Letters* 33.
- Chen, B., Jackson, J.M., Sturhahn, W., Zhang, D., Zhao, J., Murphy, C.A., & Wicks, J.K. (2012). Spin crossover equation of state and sound velocities for $(\text{Mg}_{0.65}\text{Fe}_{0.35})\text{O}$ ferropericlasite to 140 GPa. *Journal of Geophysical Research: Solid Earth* <https://doi.org/10.1029/2012JB009162>.
- Cleary, J.R., & Haddon, R.A.W. (1972). Seismic wave scattering near the core-mantle boundary: a new interpretation of precursors to PKP. *Nature* 240, 549–551.
- Cobden, L., & Thomas, C. (2013). The origin of D" reflections: a systematic study of seismic array datasets. *Geophys J. Int* 194. <https://doi.org/doi:10.1093/gji/ggt152>
- Cobden, L., Thomas, C., & Trampert, J. (2015). Seismic detection of post-perovskite inside the Earth, in: Khan, A., Deschamps, F. (Eds.), *The Earth's Heterogeneous Mantle*. Springer.
- Corgne, A., & Wood, B.J. (2005). Trace element partitioning and substitution mechanisms in calcium perovskites. *Contrib. Mineral. Petrol.* 149, 85–97. *Contributions to Mineralogy and Petrology* 149, 85–97.
- Cottaar, S., & Romanowicz, B. (2013). Observations of changing anisotropy across the southern margin of the African LLSVP. *Geophysical Journal International* 10.1093/gji/ggt285.
- Cottaar, S., Romanowicz, B., & Wenk, H.-R. (2014). Synthetic seismic anisotropy models within a slab impinging on the core-mantle boundary. *Geophys. J. Int.* 199, 164–177. <https://doi.org/doi:10.1093/gji/ggu244>
- Creasy, N., Piscinti, A., Long, M.D., Thomas, C., & Woakey, J. (2019). Constraining lowermost mantle anisotropy with body waves: A synthetic modeling study. *Geophys J. Int.* <https://doi.org/10.1093/gji/ggz049>
- Crowhurst, J.C., Brown, J.M., Goncharov, A.F., & Jacobsen, S. D. (2008). Elasticity of $(\text{Mg,Fe})\text{O}$ through the spin transition of iron in the lower mantle. *Science* 319, 451–453.
- Davies, D., Kelly, E.J., & Filson, J.R. (1971). Vespa process for analysis of seismic signals. *Nature Physical Science* 232, 8–13.
- Davies, G.F., & Gurnis, M. (1986). Interaction of mantle dregs with convection: Lateral heterogeneity at the core-mantle boundary. *Geophysical Research Letters* 13, 1517–1520. <https://doi.org/10.1029/GL013i013p01517>
- Deschamps, F., & Tackley, P.J. (2008). Searching for models of thermo-chemical convection that explain probabilistic tomography: I. Principles and influence of rheological parameters. *Phys. Earth Planet. Inter.* 171, 357–373. <https://doi.org/10.1016/j.pepi.2008.04.016>
- Deschamps, F., & Trampert, J. (2003). Mantle tomography and its relation to temperature and composition. *Physics Of The Earth And Planetary Interiors* 277–291.
- Dobrosavljevic, V.V., Sturhahn, W., & Jackson, J.M. (2019). Evaluating the role of iron-rich $(\text{Mg,Fe})\text{O}$ in ultralow velocity zones. *Minerals* 9. <https://doi.org/10.3390/min9120762>
- Dobson, D.P., & Brodholt, J.P. (2005). Subducted banded iron formations as a source of ultralow-velocity zones at the core-mantle boundary. *Nature* 434, 371–374.
- Doornbos, D.J., & Vlaar, N.J. (1973). Regions of seismic wave scattering in the Earth's mantle and precursors to PKP. *Nature Phys Sci* 243, 58–61.
- Durand, S., Matas, J., Ford, S., Ricard, Y., Romanowicz, B., & Montagner, J.-P. (2013). Insights from ScS-S measurements on deep mantle attenuation. *Earth Planet Sci. Lett* 374, 101–110.
- Durand, S., Thomas, C., & Jackson, J.M. (2019). Constraints on D" beneath the North Atlantic region from P and S travel times and amplitudes. *Geophysical Journal International* 216, 1132–1144.
- Dziewonski, A.M., & Anderson, D.L. (1981). Preliminary reference Earth model. *Physics of the Earth and Planetary Interiors* 25, 297–356.
- Eaton, D.W., Adams, J., Asudeh, I., Atkinson, G.M., Bostock, M.G., Cassidy, J.F., Ferguse, J., Samson, C., Snyder, D.B., Tiampo, K., & Unsworth, M.J. (2005). Investigating Canada's lithosphere and earthquake hazards with portable arrays, *EOS, Trans. Am. geophys. Un.*, 86, 169–173.
- Finkelstein, G.J., Jackson, J.M., Said, A., Alatas, A., Leu, B.M., Sturhahn, W., & Toellner, T.S. (2018). Strongly anisotropic magnesiowüstite in Earth's lower mantle. *Journal of Geophysical Research: Solid Earth* 123. <https://doi.org/10.1029/2017JB015349>
- Flores, C., & Lay, T. (2005). The trouble with seeing double. *Geophys Res Lett* 32.
- Ford, H.A., Long, M.D., He, X., & Lynner, C. (2015). Lowermost mantle flow at the eastern edge of the African Large Low Shear Velocity Province. *Earth and Planetary Science Letters* 420, 12–22.
- Fouch, M.J., Fischer, K.M., & Wyssession, M. (2001). Lowermost mantle anisotropy beneath the Pacific: Imaging the source of the Hawaiian plume. *Earth Planet Sci Lett* 190, 167–180.
- French, S.W., & Romanowicz, B.A. (2014). Whole-mantle radially anisotropic shear velocity structure from spectral-element waveform tomography. *Geophysical Journal International* 199, 1303–1327.
- Frost, D.A., & Rost, S. (2014). The P-wave boundary of the Large-Low Shear Velocity Province beneath the Pacific. *Earth and Planetary Science Letters* 403, 380–392.
- Gaherty, J.B., & Lay, T. (1992). Investigation of laterally heterogeneous shear velocity structure in D" beneath Eurasia. *Journal of Geophysical Research: Solid Earth* 97, 417–435.
- Garnero, E.J. (2000). Heterogeneity of the lowermost mantle. *Annu. Rev. Earth Planet Sci* 28, 509–537.
- Garnero, E.J., & Helmberger, D.V. (1998). Further structural constraints and uncertainties of a thin laterally varying ultralow-velocity layer at the base of the mantle. *Journal of Geophysical Research* 103, 12495–12509.
- Garnero, E.J., & Helmberger, D.V. (1996). Seismic detection of a thin laterally varying boundary layer at the base of the mantle beneath the central-Pacific. *Geophys. Res. Lett.* 23, 977–980.
- Garnero, E.J., & Helmberger, D.V. (1995). A very slow basal layer underlying large-scale low-velocity anomalies in the

- lower mantle beneath the Pacific - evidence from core phases. *Phys. Earth Planet. Inter.* 91, 161–176.
- Garnero, E.J., & Lay, T. (1997). Lateral variations in lowermost mantle shear wave anisotropy beneath the north Pacific and Alaska. *Journal of Geophysical Research: Solid Earth* 102, 8121–8135.
- Garnero, E.J., McNamara, A.K., & Shim, S.-H. (2016). Continent-sized anomalous zones with low seismic velocity at the base of Earth's mantle. *Nature Geoscience* 9, 481–489.
- Gassner, A., Thomas, C., Krüger, F., & Weber, M. (2015). Probing the core-mantle boundary beneath Europe and Western Eurasia: A detailed study using *PcP*. *Physics of the Earth and Planetary Interiors* 246, 9–24.
- Girard, J., Chen, J., & Raterron, P. (2012). Deformation of periclase single crystals at high pressure and temperature: Quantification of the effect of pressure on slip-system activities. *Journal of Applied Physics* 111, 112607. <https://doi.org/10.1063/1.4726200>
- Grand, S.P. (2002). Mantle shear-wave tomography and the fate of subducted slabs. *Phil. Trans. R. Soc. London, Ser. A* 360, 2475–2491.
- Gréaux, S., Irifune, T., Higo, Y., Tange, Y., Arimoto, T., Liu, Z., & Yamada, A. (2019). Sound velocity of CaSiO₃ perovskite suggests the presence of basaltic crust in the Earth's lower mantle. *Nature* 565, 218–221. <https://doi.org/10.1038/s41586-018-0816-5>
- Grocholski, B., Catalli, K., Shim, S.-H., & Prakapenka, V. (2012). Mineralogical effects on the detectability of the post-perovskite boundary. *Proc. Natl. Acad. Sci.* 109, 2275–2270.
- Grocholski, B., Shim, S.-H., & Prakapenka, V.B. (2013). Stability, metastability, and elastic properties of a dense silica polymorph, seifertite. *Journal of Geophysical Research: Solid Earth* 118, 4745–4757. <https://doi.org/10.1002/jgrb.50360>
- Gutenberg, B. (1914). Über Erdbebenwellen. VII A Beobachtungen an Registrierungen von Fernbeben in Göttingen und Folgerungen über die Konstitution des Erdkörpers, in: *Nachrichten von Der Gesellschaft Der Wissenschaften Zu Göttinge - Mathematisch-Physikalische Klasse*. pp. 125–177.
- Gutenberg, B., & Richter, C.F. (1934). On seismic waves, I. *Gerlands Beitr Geophys* 43, 56–133.
- Haddon, R.A.W., Cleary, J.R. (1974). Evidence for scattering of seismic PKP waves near the core mantle boundary. *Physics Earth Planet. Inter* 8, 211–234.
- Hansen, S.E., Carson, S.E., Garnero, E.J., Rost, S., & Yu, S. (2020). Investigating ultra-low velocity zones in the southern hemisphere using an Antarctic dataset. *Earth And Planetary Science Letters* 536. <https://doi.org/10.1016/j.epsl.2020.116142>
- Hansen, U., & Yuen, D. (1988). Numerical Simulations of thermal-chemical instabilities at the core-mantle boundary. *Nature* 334, 237–240.
- Havens, E., & Revenaugh, J. (2001). A broadband seismic study of the lowermost mantle beneath Mexico: Constraints on ultralow velocity zone elasticity and density. *Journal of Geophysical Research: Solid Earth* 106, 30809–30820.
- He, Y.M., & Wen, L.X. (2011). Seismic velocity structures and detailed features of the D" discontinuity near the core-mantle boundary beneath eastern Eurasia. *Physics of the Earth and Planetary Interiors* 189(3–4), 176–184. <https://doi.org/10.1016/j.pepi.2011.09.002>
- Hedlin, M., & Shearer, P. (2000). An analysis of large-scale variations in small-scale mantle heterogeneity using Global Seismographic Network recordings of precursors to PKP. *J. Geophys. Res* 105, 13655–13673.
- Helffrich, G.R., & Wood, B.J. (2001). The Earth's Mantle. *Nature* 412, 501–507.
- Hernlund, J.W. (2008). On the interaction of the geotherm with a post-perovskite phase transition in the deep mantle. *Phys Earth Planet Inter* 180, 222–234.
- Hernlund, J.W., & Jellinek, A.M. (2010). Dynamics and structure of a stirred partially molten ultralow-velocity zone. *Earth and Planetary Science Letters* 296, 1–8. <https://doi.org/10.1016/j.epsl.2010.04.027>
- Hernlund, J.W., & Tackley, P.J. (2007). Some dynamical consequences of partial melting in Earth's deep mantle. *Physics of the Earth and Planetary Interiors* 162, 149–163.
- Hernlund, J.W., Thomas, C., Tackley, P.J. (2005). A doubling of the post-perovskite phase boundary and structure of the Earth's lowermost mantle. *Nature* 434, 882–886.
- Heron, P.J., Lowman, J.P., & Stein, C. (2015). Influences on the positioning of mantle plumes following supercontinent formation. *Journal of Geophysical Research – Solid Earth* 120, 3628–3648.
- Hier-Majumder, S. (2014). Melt redistribution by pulsed compaction within ultralow velocity zones. *Physics Of The Earth And Planetary Interiors* 229, 134–143.
- Hirose, K. (2006). Postperovskite phase transition and its geophysical implications. *Reviews of Geophysics* 44, RG3001. <https://doi.org/10.1029/2005RG000186>
- Hirose, K., Nobumichi, S., Van Westrenen, W., & Fei, Y. (2004). Trace element partitioning in Earth's lowermantle and implications for geochemical consequences of partial melting at the core-mantle boundary. *Physics of the Earth and Planetary Interiors* 146, 249–260.
- Hirose, K., Takafuji, N., Fujino, K., Shieh, S., & Duffy, T. (2008). Iron partitioning between perovskite and post-perovskite: A transmission electron microscope study. *The American Mineralogist* 93, 1678–1681.
- Hirose, K., Takafuji, N., Sata, N., & Ohishi, Y. (2005). Phase transition and density of subducted MORB crust in the lower mantle. *Earth and Planetary Science Letters* 237, 239–251.
- Hosseini, K., Matthews, K.J., Sigloch, K., Shephard, G.E., Domeier, M., & Tsekhmistrenko, M. (2018). SubMachine: Web-Based tools for exploring seismic tomography and other models of Earth's deep interior. *Geochemistry, Geophysics, Geosystems* 19. <https://doi.org/10.1029/2018GC007431>
- Houard, S., & Nataf, H.-C. (1993). Laterally varying reflector at the top of beneath Northern Siberia. *Geophys J. Int* 115, 183–210.
- Hutko, A.R., Lay, T., Garnero, E.J., & Revenaugh, J. (2006). Seismic detection of folded, subducted lithosphere at the core-mantle boundary. *Nature* 441, 333–336.
- Hutko, A.R., Lay, T., & Revenaugh, J. (2009). Localized double-array stacking analysis of *PcP*: D" and ULVZ structure beneath the Cocos plate, Mexico, central Pacific, and north

- Pacific. *Physics of the Earth and Planetary Interiors* 173, 60–74.
- Hutko, A.R., Lay, T., Revenaugh, J., & Garnero, E.J. (2008). Anticorrelated seismic velocity anomalies from post-perovskite in the lowermost mantle. *Science* 320, 1070–1074.
- Immoor, J., Marquardt, H., Miyagi, L., Lin, F., Speziale, S., Merkel, S., Buchen, J., Kurnosov, A., & Liermann, H.-P. (2018). Evidence for {100}<011>slip in ferropericlase in Earth's lower mantle from high-pressure/high-temperature experiments. *Earth and Plan. Sci. Lett.* 489. <https://doi.org/10.1016/j.epsl.2018.02.045>
- Jackson, J.M., Sinogeikin, S.V., Jacobsen, S.D., Reichmann, H.-J., Mackwell, S.J., & Bass, J.D. (2006). Single-crystal elasticity and sound velocities of (Mg_{0.94}Fe_{0.06})O ferropericlase to 20 GPa. *Journal of Geophysical Research* 111, <https://doi.org/10.1029/2005JB004052>.
- Jackson, W.E., Knittle, E., Brown Jr., G.E., & Jeanloz, R. (1987). Partitioning of Fe within high-pressure silicate perovskite: Evidence for unusual geochemistry in the lower mantle. *Geophysical Research Letters* 14, 224–226.
- Jensen, K.J., Thorne, M.S., & Rost, S. (2013). SPdKS analysis of ultralow-velocity zones beneath the western Pacific. *Geophysical Research Letters* 40.
- Karato, S., & Karki, B.B. (2001). Origin of lateral variation of seismic wave velocities and density in the deep mantle. *Journal of Geophysical Research* 106, B10.
- Kawai, K., & Geller, R.J. (2010). Waveform inversion for localized seismic structure and an application to D'' structure beneath the Pacific. *J. Geophys. Res* 115. <https://doi.org/10.1029/2009JB006503>
- Kawai, K., Takeuchi, N., Geller, R.J., & Fuji, N. (2007). Possible evidence for a double crossing phase transition in D'' beneath Central America from inversion of seismic waveforms. *Geophysical Research Letters* 34.
- Kendall, J.-M. (2000). Seismic anisotropy in the boundary layers of the mantle, in: S. Karato, A.M.F. (Ed.), *Earth's Deep Interior: Mineral Physics and Tomography From the Atomic to the Global Scale*, Geophysical Monograph Series. American Geophysical Union, Washington D.C., p. 289.
- Kendall, J.-M., & Nangini, C. (1996). Lateral variations in D'' below the Caribbean. *Geophysical Research Letters* 23, 399–402.
- Kendall, J.-M., & Shearer, P.M. (1995). On the structure of the lowermost mantle beneath the southwest Pacific, southeast Asia and Australasia. *Physics Of The Earth And Planetary Interiors* 92, 85–98.
- Kendall, J.-M., & Shearer, P.M. (1994). Lateral variations in D'' thickness from long period shear wave data. *Journal of Geophysical Research: Solid Earth* 99, 11–575.
- Kendall, J.-M., & Silver, P. (1998). Investigating causes of D'' anisotropy, in: Gurnis, M., Wyssession, M., Knittle, E., Buffett, B.A. (Eds.), *The Core Mantle Boundary Region*, Geodynamic Series. American Geophysical Union, pp. 97–118.
- Kennett, B.L.N., Engdahl, E.R., & Buland, R. (1995). Constraints on seismic velocities in the earth from travel times. *Geophysical Journal International* 122, 108–124.
- King, D.W., Haddon, R.A.W., & Cleary, J.R. (1974). Array analysis of precursors to PKIKP in the distance range 128deg to 142deg. *Geophys. J. R., Astron. Soc* 37, 157–173.
- Kito, T., & Krüger, F. (2001). Heterogeneities in D'' beneath the southwestern Pacific inferred from scattered and reflected P-waves. *Geophysical Research Letters* 28, 2245–2548.
- Kito, T., Rost, S., Thomas, C., & Garnero, E. (2007). New insights into the P- and S-wave velocity structure of the D'' discontinuity beneath the Cocos plate. *Geophys. J. Int* 169, 631–645.
- Knittle, E., & Jeanloz, R. (1991). Earth's core-mantle boundary - Results of experiments at high-pressures and temperatures. *Science* 251, 1438–1443.
- Koelemeijer, P., Ritsema, J., Deuss, A., & Van Heijst, H.J. (2016). SP12RTS: A degree-12 model of shear- and compressional-wave velocity for Earth's mantle. *Geophysical Journal International* 204, 1024–1039.
- Komabayashi, T., Maruyama, S., & Rino, S. (2009). A speculation on the structure of the D'' layer: The growth of anti-crust at the core-mantle boundary through the subduction history of the Earth. *Gondwana Research* 15, 342–353.
- Koper, K.D., & Pyle, M.L. (2004). Observations of PKiKP/PcP amplitude ratios and implications for Earth structure at the boundaries of the liquid core. *Journal of Geophysical Research: Solid Earth* 109, 03301.
- Labrosse, S., Hernlund, J.W., & Coltice, N. (2007). A crystallizing dense magma ocean at the base of the Earth's mantle. *Nature* 450, 866–869. <https://doi.org/10.1038/nature06355>
- Langrand, C., Andrault, D., Durand, S., Konopkova, Z., Hilairat, N., Thomas, C., & Merkel, S. (2019). Kinetics and detectability of the bridgmanite to post-perovskite transformation in the Earth's D'' layer. *Nature Communications*. <https://doi.org/10.1038/s41467-019-13482-x>
- Lay, T. (2015). Deep Earth Structure: Lower Mantle and D'', in: *Treatise on Geophysics*. pp. 683–723.
- Lay, T. (2008). Sharpness of the D'' discontinuity beneath the Cocos plate: implications for the perovskite to post-perovskite phase transition. *Geophys Res Lett* 35.
- Lay, T. (2007). Deep earth structure — lower mantle and D'', in: Romanowicz, B., Dziewonski, A. (Eds.), *Treatise on geophysics. Seismology and structure of the Earth*, Vol. 1. Elsevier. Amsterdam, pp. 619–654.
- Lay, T., & Garnero, E.J. (2007). Reconciling the post-perovskite phase with seismological observations of lowermost mantle structure, in: Hirose, K., Brodholt, J.P., Lay, T., Yuen, D. A. (Eds.), *Post-Perovskite: The last mantle phase transition*. American Geophysical Union Monograph, pp. 129–153.
- Lay, T., & Garnero, E.J. (2004). Core-mantle boundary structures and processes, in: Sparkes, R.S.J., Hawkesworth, C.J. (Eds.), *State of the planet: Frontiers and challenges in geophysics*. American Geophysical Union, Washington D.C, pp. 25–41.
- Lay, T., & Garnero, E.J. (1997). Scale lengths of shear velocity heterogeneity at the base of the mantle from S wave differential travel times. *Journal of Geophysical Research* 102, 9887–9909.
- Lay, T., Garnero, E.J., & Russell, S.A. (2004a). Lateral variation of the D'' discontinuity beneath the Cocos plate. *Geophysical Research Letters* 15612. <https://doi.org/doi:10.1029/2004GL020300>
- Lay, T., Garnero, E.J., & Williams, Q. (2004b). Partial melting in a thermochemical boundary layer at the base of the mantle. *Physics of the Earth and Planetary Interiors* 146, 441–467.

- Lay, T., & Helmberger, D.V. (1983a). The shear-wave velocity gradient at the base of the mantle. *Journal of Geophysical Research* 88, 8161–8170. <https://doi.org/10.1029/JB088iB10p08160>
- Lay, T., & Helmberger, D.V. (1983b). A lower mantle S-wave triplication and the shear velocity structure of D". *Geophys J Roy Astron Soc* 75, 799–837.
- Lay, T., Hernlund, J., & Buffett, B.A. (2008). Core-mantle boundary heat flow. *Nature Geoscience* 1, 25–32. <https://doi.org/10.1038/ngeo.2007.44>
- Lay, T., Hernlund, J., Garnero, E.J., & Thorne, M.S. (2006). A post-perovskite lens and D" heat flux beneath the central Pacific. *Science* 314, 1272–1276. <https://doi.org/10.1126/science.1133280>
- Lay, T., Williams, Q., Garnero, E.J., Kellogg, L., & Wysession, M.E. (1998). Seismic wave anisotropy in the D" region and its implications, in: Gurnis, M., Wysession, M.E., Knittle, E., Buffett, B.A. (Eds.), *The core-mantle boundary region*. American Geophysical Union, Washington D.C., pp. 299–318.
- Lay, T., & Young, C. (1991). Analysis of seismic SV waves in the core's penumbra. *Geophysical Research Letters* 18, 1371–1376.
- Lessing, S., Thomas, C., Saki, M., Schmerr, N., & Vanacore, L. (2015). On the difficulty of detecting PP precursors. *Geophys J. Int* 201, 1666–1681. <https://doi.org/doi:10.1093/gji/ggv105>
- Li, C., van der Hilst, R.D., Engdahl, E.R., & Burdick, S. (2008). A new global model for P wave speed variations in Earth's mantle. *Geochemistry, Geophysics, Geosystems* 9, Q05018.
- Li, M., McNamara, A.K., Garnero, E.J., & Yu, S. (2017). Compositionally-distinct ultra-low velocity zones on Earth's core-mantle boundary. *Nature Communications* 8, 177.
- Lithgow-Bertelloni, C., & Richards, M.A. (1998). The dynamics of Cenozoic and Mesozoic plate motions. *Reviews of Geophysics* 36, 27–78.
- Liu, J., Hu, Q., Kim, D.Y., Wu, Z., Wang, W., Xiao, Y., Chow, P., Meng, Y., Prakapenka, V.B., Mao, H.-K., & Mao, W.L. (2017). Hydrogen-bearing iron peroxide and the origin of ultralow-velocity zones. *Nature* 551. <https://doi.org/10.1038/nature24461>
- Liu, J., Li, J., Hrubiak, R., & Smith, J.S. (2016). Origins of ultralow velocity zones through slab-derived metallic melt. *Proceedings of the National Academy of Sciences* 113, 5547–5551.
- Long, M.D. (2013). Constraints on Subduction Geodynamics from Seismic Anisotropy. *Reviews of Geophysics* 51, 76–112. <https://doi.org/doi:10.1002/rog.20008>
- Lynner, C., & Long, M.D. (2014). Lowermost mantle anisotropy and deformation along the boundary of the African LLSVP. *Geophysical Research Letters* 41, 10.1002/2014GL059875.
- Ma, X., Sun, X., & Thomas, C. (2019). Localized ultra-low velocity zones at the eastern boundary of Pacific LLSVP. *Earth And Planetary Science Letters* 507, 40–49.
- Ma, X., Sun, X., Wiens, D.A., Wen, L., Nyblade, A., Anandakrishnan, S., Aster, R., Huerta, A., & Wilson, T. (2016). Strong seismic scatterers near the core–mantle boundary north of the Pacific Anomaly. *Physics of the Earth and Planetary Interiors* 253, 21–30.
- Ma, X., & Thomas, C. (2020). Small-scale scattering heterogeneities in the lowermost mantle from a global analysis of PKP precursors. *Journal of Geophysical Research-Solid Earth*. <https://doi.org/10.1029/2019JB018736>
- Mancinelli, N.J., & Shearer, P.M. (2013). Reconciling discrepancies among estimates of small-scale mantle heterogeneity from PKP precursors. *Geophys J. Int* 195, 1721–1729. <https://doi.org/10.1093/gji/ggt319>
- Mancinelli, N.J., Shearer, P.M., & Thomas, C. (2016). On the frequency dependence and spatial coherence of PKP precursor amplitudes. *J. Geophys. Res.* <https://doi.org/10.1002/2015JB012768>
- Mao, W.L., Mao, H.-K., Sturhahn, W., Zhao, J., Prakapenka, V.B., & Meng, Y. (2006). Iron-rich post-perovskite and the origin of ultralow-velocity zones. *Science* 312, 564–565.
- Mao, W.L., Shen, G., Prakapenka, V., Meng, Y., Campbell, A. J., Heinz, D.L., Shu, J., Hemley, R.J., & Mao, H.-K. (2004). Ferromagnesian postperovskite silicates in the D" layer of the Earth. *Proceedings of the National Academy of Science* 101, 15867–15869. <https://doi.org/10.1073/pnas.0407135101>
- Marquardt, H., & Miyagi, L. (2015). Slab stagnation in the shallow lower mantle linked to an increase in mantle viscosity. *Nature Geosci* 8, 311–314. <https://doi.org/doi:10.1038/ngeo2393>
- Marquardt, H., Speziale, S., Reichmann, H.J., Frost, D.J., Schilling, F.R., & Garnero, E.J. (2009). Elastic shear anisotropy of ferropericlase in Earth's lower mantle. *Science* 324, 224–225. <https://doi.org/10.1126/science.1169365>
- Matzel, E., Sen, M., & Grand, S.P. (1996). Evidence for anisotropy in the deep mantle beneath Alaska. *Geophysical Research Letters* 23, 2417–2420.
- McNamara, A.K., Garnero, E.J., & Rost, S. (2010). Tracking deep mantle reservoirs with ultra-low velocity zones. *Earth and Planetary Science Letters* 299, 1–9.
- McNamara, A.K., Karato, S.-I., & van Keken, P.E. (2001). Localization of dislocation creep in the lower mantle: implications for the origin of seismic anisotropy. *Earth Planet. Sci. Lett.* 191, 85–99.
- McNamara, A.K., van Keken, P.E., & Karato, S.-I. (2002). Development of anisotropic structure in the Earth's lower mantle by solid-state convection. *Nature* 416, 310–314.
- Merkel, S., Kubo, A., Miyagi, L., Speziale, S., Duffy, T., & Wenk, H.-R. (2006). Plastic Deformation of MgGeO₃ Post-Perovskite at Lower Mantle Pressures. *Science*, 644–646.
- Merkel, S., McNamara, A., Kubo, S., Speziale, S., Miyagi, L., Meng, Y., Duffy, T., & Wenk, H.R. (2007). Deformation of (Mg,Fe)SiO₃ post-perovskite and D" anisotropy. *Science* 316, 1729–1732. <https://doi.org/10.1126/science.1140609>
- Merkel, S., Wenk, H.R., Shu, J.F., Shen, G.Y., Gillet, P., Mao, H.K., & Hemley, R.J. (2002). Deformation of polycrystalline MgO at pressures of the lower mantle. *Journal of Geophysical Research-Solid Earth* 107.
- Miyagi, L., Kanitpanyacharoen, W., Kaercher, P., Lee, K.K. M., & Wenk, H.-R. (2010). Slip systems in MgSiO₃ post-perovskite: Implications for D" anisotropy. *Science* 329, 1639.
- Montelli, R., Nolet, G., Dahlen, F.A., & Masters, G. (2006). A catalogue of deep mantle plumes: New results from finite-frequency tomography. *Geochemistry, Geophysics, Geosystems* 7. <https://doi.org/10.1029/2006GC001248>

- Mori, J., & Helmberger, D.V. (1995). Localized boundary layer below the mid-Pacific velocity anomaly identified from a *PcP* precursor. *Journal of Geophysical Research* 100, 20359–20365.
- Muir, J.M.R., & Brodholt, J.P. (2015). Elastic properties of ferropericlase at lower mantle conditions and its relevance to ULVZs. *Earth and Planetary Science Letters* 417, 40–48.
- Muirhead, K.J., & Datt, R. (1976). The *N*-th root process applied to seismic array data. *Geophysical Journal of the Royal Astronomical Society* 47, 197–210.
- Murakami, M., Hirose, K., Kawamura, K., Sata, N., & Ohishi, Y. (2004). Post-perovskite phase transition in MgSiO₃. *Science* 304, 855–858. <https://doi.org/10.1126/science.1095932>
- Murakami, M., Hirose, K., Sata, N., & Ohishi, Y. (2005). Post-perovskite phase transition and mineral chemistry in the pyrolytic lowermost mantle. *Geophysical Research Letters* 32. <https://doi.org/10.1029/2004GL021956>
- Nakagawa, T., & Tackley, P.J. (2008). Lateral variations in CMB heat flux and deep mantle seismic velocity caused by a thermal-chemical-phase boundary layer in 3D spherical convection. *Earth Planet. Sci. Lett.* 271, 348–358. <https://doi.org/10.1016/j.epsl.2008.04.013>
- Neuberg, J., & Wahr, J. (1991). Detailed investigation of a spot on the core mantle boundary using digital *PcP* data. *Phys Earth Planet Inter* 68, 132–143.
- Niu, F., & Wen, L. (2001). Strong seismic scatterers near the core-mantle boundary west of Mexico. *Geophysical Research Letters* 28, 3557–3560. <https://doi.org/10.1029/2001gl013270>
- Nomura, R., Hirose, K., Uesugi, K., Ohishi, Y., Tsuchiyama, A., & Miyake, A. (2014). Low core-mantle boundary temperature inferred from the solidus of pyrolite. *Science* 343, 522–525.
- Nowacki, A., Wookey, J., & Kendall, J. (2011). New advances in using seismic anisotropy, mineral physics and geodynamics to understand deformation in the lowermost mantle. *Journal of Geodynamics* 52, 205–228.
- Oganov, A.R., Martonak, R., Laio, A., Raiteri, P., & Parinello, M. (2005). Anisotropy of Earth's D'' layer and stacking faults in the MgSiO₃ post-perovskite phase. *Nature* 438, 1142–1144.
- Oganov, A.R., & Ono, S. (2004). Theoretical and experimental evidence for a post-perovskite phase of MgSiO₃ in Earth's D'' layer. *Nature* 430, 445–448. <https://doi.org/10.1038/nature02701>
- Ohira, I., Jackson, J.M., Solomatova, N.V., Sturhahn, W., Finkelstein, G.J., Kamada, S., Kawazoe, T., Maeda, F., Hirao, N., Nakano, S., Suzuki, A., & Ohtani, E. (2019). Compressional behavior and spin state of δ -(Al,Fe)OOH at high pressures. *American Mineralogist* 104, 1273–1284. <https://doi.org/10.2138/am-2019-6913>
- Ohta, K., Hirose, K., Lay, T., Sata, N., & Ohishi, Y. (2008). Phase transitions in pyrolite and MORB at lowermost mantle conditions: Implications for a MORB-rich pile above the core-mantle boundary. *Earth Planet. Sci. Lett.* 267, 107–117.
- Ohtani, E., & Maeda, M. (2001). Density of basaltic melt at high Pressure and stability of the melt at the base of the lower mantle. *Earth And Planetary Science Letters* 344, 892–895.
- Ono, S., & Oganov, A. (2005). In situ observations of a phase transition between perovskite and CaIrO₃-type phase in MgSiO₃ and pyrolytic mantle composition. *Earth and Planetary Science Letters* 236, 914–932.
- Persh, S.E., Vidale, J.E., & Earle, P.S. (2001). Absence of short-period ULVZ precursors to *PcP* and *ScP* from two regions of the CMB. *Geophysical Research Letters* 28, 387–390.
- Pisconti, A., Thomas, C., & Wookey, J. (2019). Discriminating between causes of D'' anisotropy using reflections and splitting measurements for a single path. *Journal of Geophysical Research: Solid Earth* 124. <https://doi.org/10.1029/2018JB016993>
- Pradhan, G.K., Fiquet, G., Siebert, J., Auzende, A.-A., Morard, G., Antonangeli, D., & Garbarino, G. (2015). Melting of MORB at core-mantle boundary. *Earth and Planetary Science Letters* 431, 247–255. <http://dx.doi.org/10.1016/j.epsl.2015.09.034>
- Pulliam, J., Sen, M. (1998). Seismic anisotropy in the core-mantle transition zone. *Geophysical Journal International* 135, 113–128. <https://doi.org/10.1046/j.1365-246X.1998.00612.x>
- Reali, R., Jackson, J.M., Van Orman, J., Bower, D.J., Carrez, P., & Cordier, P. (2019a). Modeling viscosity of (Mg,Fe)O at lowermost mantle conditions. *Physics Of The Earth And Planetary Interiors* 287, 65–75. <https://doi.org/10.1016/j.pepi.2018.12.005>
- Reali, R., Van Orman, J., Pigott, J.S., Jackson, J.M., Boioli, F., Carrez, P., & Cordier, P. (2019b). The role of diffusion-driven pure climb creep on the rheology of bridgmanite under lower mantle conditions. *Scientific Reports*. <https://doi.org/10.1038/s41598-018-38449-8>
- Reiss, M.C., Long, M.D., & Creasy, N. (2019). Lowermost Mantle Anisotropy Beneath Africa From Differential SKS-SKKS Shear-Wave Splitting. *Journal of Geophysical Research: Solid Earth* 124. <https://doi.org/10.1029/2018JB017160>
- Revenaugh, J., & Meyer, R. (1997). Seismic evidence of partial melt within a possibly ubiquitous low-velocity layer at the base of the mantle. *Science* 277, 670–673.
- Ricolleau, A., Fiquet, G., Addad, A., Menguy, N., Vanni, C., Perrillat, J.-P., Daniel, I., Cardon, H., & Guignot, N. (2008). Analytical transmission microscopy study of natural MORB sample assemblage transformed at high pressure and high temperature. *American Mineralogist* 93, 144–153.
- Ritsema, J., Deuss, A., van Heijst, H.J., & Woodhouse, J.H. (2011). S40RTS: a degree-40 shear-velocity model for the mantle from new Rayleigh wave dispersion, teleseismic travel-time and normal-mode splitting function measurements. *Geophysical Journal International* 183, 1223–1236. <https://doi.org/10.1111/j.1365-246X.2010.04884.x>
- Ritsema, J., Ni, S., Helmberger, D.V., & Crotwell, H.P. (1998). Evidence for strong shear velocity reductions and velocity gradients in the lower mantle beneath Africa. *Geophys. Res. Lett.* 25, 4245–4248.
- Romanowicz, B.A., & Wenk, H.-R. (2017). Anisotropy in the deep Earth. *Physics of the Earth and Planetary Interiors* 269, 58–90. <https://doi.org/10.1016/j.pepi.2017.05.005>
- Rost, S., Garnero, E.J., & Stefan, W. (2010). Thin and intermittent ultralow-velocity zones. *Journal of Geophysical Research: Solid Earth* 115, 06312.
- Rost, S., Garnero, E.J., & Williams, Q. (2006). Fine-scale ultralow-velocity zone structure from high-frequency seismic array

- data. *J. Geophys. Res.* **111**. <https://doi.org/10.1029/2005JB004088>
- Rost, S., Garnero, E.J., Williams, Q., & Manga, M. (2005). Seismological constraints on a possible plume root at the core-mantle boundary. *Nature* **435**, 666–669. <https://doi.org/10.1038/nature03620>
- Rost, S., & Revenaugh, J. (2003). Small-scale ultralow-velocity zone structure imaged by ScP. *J. Geophys. Res.* **108**. <https://doi.org/10.1029/2001JB001627>
- Rost, S., & Thomas, C. (2010). High resolution CMB imaging from migration of short period core reflected phases. *Physics Of The Earth And Planetary Interiors* **183**. <https://doi.org/10.1016/j.pepi.2010.04.005>
- Rost, S., & Thomas, C. (2009). Improving seismic resolution through seismic arrays. *Surveys of Geophysics*. <https://doi.org/10.1007/s10712-009-9070-6>
- Rost, S., & Thomas, C. (2002). Array Seismology: Methods and Applications. *Rev. of Geophys.* <https://doi.org/10.1029/2000RG000100>
- Russell, S.A., Lay, T., & Garnero, E.J. (1999). Small-scale lateral shear velocity and anisotropy heterogeneity near the core-mantle boundary beneath the central Pacific imaged using broadband ScS waves. *Journal of Geophysical Research* **104**, 13183–13199. <http://dx.doi.org/10.1029/1999JB900114>
- Russell, S.A., Lay, T., & Garnero, E.J. (1998). Seismic evidence for small-scale dynamics in the lowermost mantle at the root of the Hawaiian hotspot. *Nature* **396**, 255–258. <http://dx.doi.org/10.1038/24364>
- Sakai, T., Ohtani, E., Terasaki, H., Miyahara, M., Nishijima, M., Hirao, N., Ohishi, Y., & Sata, N. (2010). Fe-Mg partitioning between post-perovskite and ferropericlase in the lowermost mantle. *Physics and Chemistry of Minerals* **37**, 487–496. <https://doi.org/10.1007/S00269-009-0349-4>
- Scherbaum, F., Krüger, F., & Weber, M. (1997). Double beam imaging: mapping lowermantle heterogeneities using combinations of source and receiver arrays. *J. Geophys. Res.* **102**, 507–522.
- Schimmel, M., & Paulssen, H. (1996). Steeply reflected ScSH precursors from the D" region. *J. Geophys. Res.* **101**, 16077–16087.
- Schweitzer, J., Fyen, J., Mykkeltveit, S., & Kvaerna, T. (2009). Seismic arrays, in: *New Manual of Seismological Observatory Practice (NMSOP-1)*, IASPEI. GFZ German Research Centre for Geosciences, Potsdam, Germany, p. 1–52. https://doi.org/10.2312/GFZ.NMSOP_r1_ch9
- Shim, S.-H. (2008). The postperovskite transition. *Annual Review of Earth and Planetary Sciences* **36**, 569–599. <https://doi.org/10.1146/annurev.earth.36.031207.124309>
- Sidorin, I., Gurnis, M., & Helmberger, D.V. (1999). Evidence for a ubiquitous seismic discontinuity at the base of the mantle. *Science* **286**, 1326–1331.
- Sidorin, I., Gurnis, M., Helmberger, D.V., & Ding, X.M. (1998). Interpreting D" seismic structure using synthetic waveforms computed from dynamic models. *Earth Planet. Sci. Lett.* **163**, 31–41.
- Simmons, N.A., Forte, A.M., Boschi, L., & Grand, S.P. (2010). GyPSuM: A joint tomographic model of mantle density and seismic wave speeds. *Journal of Geophysical Research: Solid Earth* **115**, 12310.
- Simmons, N.A., & Grand, S.P. (2002). Partial melting in the deepest mantle. *Geophysical Research Letters* **29**, 1552.
- Sinmyo, R., Hirose, K., Nishio-Hamane, D., Seto, Y., Fujino, K., Sata, N., & Ohishi, Y. (2008). Partitioning of iron between perovskite/postperovskite and ferropericlase in the lower mantle. *Journal of Geophysical Research* **113**. <https://doi.org/10.1029/2008JB005730>
- Solomatova, N.V., Jackson, J.M., Sturhahn, W., Wicks, J.K., Zhao, J., Toellner, T.S., Kalkan, B., & Steinhardt, W.M. (2016). Equation of state and spin crossover of (Mg,Fe)O at high pressures, with implications for explaining topographic relief at the core-mantle boundary. *American Mineralogist* **101**, 1084–1093. <http://dx.doi.org/10.2138/am-2016-5510>
- Stackhouse, S., Brodholt, J.P., & Price, G.D. (2006). Elastic anisotropy of FeSiO₃ end-members of the perovskite and post-perovskite phases. *Geophysical Research Letters*. <https://doi.org/10.1029/2005GL023887>
- Sturhahn, W. (2020). MINUTI (MINeral physics UTILities): Open source software [WWW Document]. URL <http://www.nrixs.com>
- Sun, D., Helmberger, D. (2008). Lower mantle tomography and phase change mapping. *Journal of Geophysical Research* **113**.
- Sun, D., Helmberger, D., Lai, V.H., Gurnis, M., Jackson, J. M., & Yang, H.-Y. (2019). Slab Control on the Northeastern Edge of the Mid-Pacific LLSVP Near Hawaii. *Geophysical Research Letters* **46**. <https://doi.org/10.1029/2018GL081130>
- Sun, D., Helmberger, D., Ni, S., & Bower, D. (2009). Direct measures of lateral velocity variation in the deep Earth. *Journal of Geophysical Research: Solid Earth* **114**, 05303.
- Sun, D., Helmberger, D.V., Jackson, J.M., Clayton, R.W., & Bower, D.J. (2013). Rolling hills on the core-mantle boundary. *Earth and Planetary Science Letters* **361**, 333–342.
- Sun, D., Helmberger, D.V., Miller, M.S., & Jackson, J.M. (2016). Major disruption of D" beneath Alaska. *Journal of Geophysical Research: Solid Earth* **121**. <https://doi.org/10.1002/2015JB012534>
- Sun, D., Song, T.R., & Helmberger, D.V. (2006). Complexity of D" in the presence of slab-debris and phase changes. *Geophysical Research Letters* **33**. <https://doi.org/10.1029/2005GL025384>
- Sun, N., Wei, W., Han, S., Song, J., Li, S., Duan, Y., Prakapenka, V.B., & Mao, Z. (2018). Phase transition and thermal equations of state of (Fe,Al)-bridgmanite and post-perovskite: Implication for the chemical heterogeneity at the lowermost mantle. *Earth And Planetary Science Letters* **490**, 161–169. <https://doi.org/10.1016/j.epsl.2018.03.004>
- Tackley, P.J. (2002). Strong heterogeneity caused by deep mantle layering. *Geochemistry, Geophysics, Geosystems* **3**(4). <https://doi.org/10.1029/2001gc000167>
- Takeuchi, N., & Obara, K. (2010). Fine-scale topography of the D" discontinuity and its correlation to volumetric velocity fluctuations. *Phys. Earth Planet. Int.* **183**, 126–135.
- Tan, E., Gurnis, M., & Han, L. (2002). Slabs in the lower mantle and their modulation of plume formation. *Geochemistry, Geophysics, Geosystems* **3**. <https://doi.org/10.1029/2001GC000238>
- Tange, Y., Takahashi, E., Nishihara, Y., Funakoshi, K., & Sata, N. (2009). Phase relations in the system MgO-FeO-SiO₂ to 50 GPa and 2000 degrees C: An application of experimental

- techniques using multianvil apparatus with sintered diamond anvils. *Journal of Geophysical Research* 114.
- Thielmann, M., Golabek, G.J., & Marquardt, H. (2020). Ferropericline Control of Lower Mantle Rheology: Impact of Phase Morphology. *Geochem. Geophys. Geosys.* 21. <https://doi.org/10.1029/2019GC008688>
- Thomas, C., Garnero, E.J., & Lay, T. (2004a). High-resolution imaging of lowermost mantle structure under the Cocos plate. *Journal of Geophysical Research* 109, B0830.
- Thomas, C., Kendall, J.-M., & Helffrich, G. (2009). Probing two low-velocity regions with PKPb-caustic amplitudes and scattering. *Geophysical Journal International* 178, 503–512.
- Thomas, C., Kendall, J.-M., & Lowmann, J. (2004b). Lower mantle seismic discontinuities and the thermal morphology of subducted slabs. *Earth and Plan. Sci. Lett.* 225 (1–2), 105–113.
- Thomas, C., & Laske, G. (2015). D" observations in the Pacific from PLUME Ocean Bottom Seismometer recordings. *Geophys J. Int* 200, 851–862. <https://doi.org/doi:10.1093/gji/ggu441>
- Thomas, C., & Weber, M. (1997). P-velocity heterogeneities in the lower mantle determined with the German Regional Seismic Network: Improvement of previous models and results of 2D modelling. *Phys. Earth Planet. Inter.* 101, 105–117.
- Thomas, C., Weber, M., Wicks, C.W., & Scherbaum, F. (1999). Small scatterers in the lower mantle observed at German broadband arrays. *J. Geophys. Res* 104, 15073–15088.
- Thomas, C., Wookey, J., Brodholt, J.P., & Fieseler, T. (2011). Anisotropy as cause for polarity reversals of D" reflections. *Earth And Planetary Science Letters* 307, 369–376.
- Thomas, C.W., & Asimow, P.D. (2013). Direct shock compression experiments on premolten forsterite and progress toward a consistent high-pressure equation of state for CaO-MgO-Al₂O₃-SiO₂-FeO liquids. *Journal of Geophysical Research: Solid Earth* 118, 5738–5752. <https://doi.org/10.1002/jgrb.50374>
- Thorne, M.S., & Garnero, E.J. (2004). Inferences on ultralow-velocity zone structure from a global analysis of SPdKS waves. *J. Geophys. Res.* 109, 22. <https://doi.org/10.1029/2004jb003010>
- Thorne, M.S., Garnero, E.J., & Grand, S.P. (2004). Geographic correlation between hot spots and deep mantle lateral shear-wave velocity gradients. *Physics of the Earth and Planetary Interiors* 146, 47–63.
- Thorne, M.S., Garnero, E.J., Jahnke, G., Igel, H., & McNamara, A.K. (2013). Mega ultra-low velocity zone and mantle flow. *Earth and Planetary Science Letters* 364, 59–67.
- Thorne, M.S., Lay, T., Garnero, E.J., Jahnke, G., & Igel, H. (2007). Seismic imaging of the laterally varying D" region beneath the Cocos Plate. *Geophysical Journal International* 170, 635–648. <https://doi.org/10.1111/j.1365-246X.2006.03279.x>
- Thorne, M.S., Pachhai, S., Leng, K., Wicks, J.K., & Nissen-Meyer, T. (2020). New Candidate Ultralow-Velocity Zone Locations from Highly Anomalous SPdKS Waveforms. *Minerals* 10. <https://doi.org/10.3390/min10030211>
- Tommaseo, C., Devine, J., Merkel, S., Speziale, S., & Wenk, H.-R. (2006). Texture development and elastic stresses in magnesio-wüstite at high pressure. *Phys. Chem. Miner.* 33, 84–97.
- Tommasi, A., Goryaeva, A., Carrez, P., Cordier, P., & Mainprice, D. (2018). Deformation, crystal preferred orientations, and seismic anisotropy in the Earth's D" layer. *Earth And Planetary Science Letters* 492, 35–46. <https://doi.org/10.1016/j.epsl.2018.03.032>
- Torsvik, T.H., Smethurst, M.A., Burke, K., & Steinberger, B. (2006). Large igneous provinces generated from the margins of the large low-velocity provinces in the deep mantle. *Geophysics Journal International*. <https://doi.org/10.1111/j.1365-1246X.2006.03158>
- Torsvik, T.H., van der Voo, R., Doubrovine, P.V., Burke, K., Steinberger, B., & Ashwal, L.D. (2014). Deep mantle structure as a reference frame for movements. In *And on the Earth. Proceedings of the National Academy of Sciences of United States of America*. pp. 8735–8740.
- Trønnes, R.G., Baron, M.A., Eigenmann, K.R., Guren, M.G., Heyn, B.H., Løken, A., & Mohn, C.E. (2019). Core formation, mantle differentiation and core-mantle interaction within Earth and the terrestrial planets. *Tectonophysics* 760, 165–198. <https://doi.org/10.1016/j.tecto.2018.10.021>
- Tsuchiya, T., Tsuchiya, J., Umamoto, K., & Wentzcovitch, R.A. (2004). Phase transition in MgSiO₃ perovskite in the earth's lower mantle. *Earth and Planetary Science Letters* 224, 241–248.
- Turcotte, D.L., Paul, D., White, W.M. (2001). Thorium-uranium systematics require layered mantle convection. *Journal of Geophysical Research* 106, 4265–4276.
- van der Hilst, R.D., de Hoop, M.V., Wang, P., Shim, S.H., & Tenorio, L. (2007). Seismostratigraphy and thermal structure of Earth's core-mantle boundary region. *Science* 315, 1813–1817.
- Vanacore, E.A., Niu, F., & Ma, Y. (2010). Large angle reflection from a dipping structure recorded as a PKIKP precursor: Evidence for a low velocity zone at the core-mantle boundary beneath the Gulf of Mexico. *Earth Planet. Sci. Lett* 293, 54–62.
- Vanacore, E.A., Rost, S., & Thorne, M.S. (2016). Ultralow-velocity zone geometries resolved by multidimensional waveform modelling. *Geophysical Journal International* 206, 659–674.
- Vidale, J.E., & Benz, H.M. (1992). A sharp and flat section of the core-mantle boundary. *Nature* 359, 627–629.
- Vidale, J.E., & Hedlin, M.A.H. (1998). Evidence for partial melt at the core-mantle boundary north of Tonga from the strong scattering of seismic waves. *Nature* 391, 682–685.
- Vinnik, L.P., Breger, L., & Romanowicz, B. (1998). Anisotropic structures at the base of the Earth's mantle. *Nature* 393, 564–567.
- Vinnik, L.P., Farra, V., & Romanowicz, B. (1989). Observational evidence for diffracted SV in the shadow of the Earth's core. *Geophysical Research Letters* 16, 519–522.
- Vinnik, L.P., Romanowicz, B., Stunff, Y.L., Makeyeva, L. (1995). Seismic anisotropy in the D". *Geophysical Research Letters* 22, 1657–1660.
- Waszek, L., Thomas, C., Deuss, A. (2015). PKP precursors: implications for global scattering. *Geophys. Res. Lett.* 42 (10), <https://doi.org/10.1002/2015GL063869>
- Watt, P.J., Davies, G.F., O'Connell, R.J. (1976). The elastic properties of composite materials. *Reviews of Geophysics and Space Physics* 14, 541–563.

- Weber, M. (1993). P- and S-wave reflections from anomalies in the lowermost mantle. *Geophysical Journal International* 115, 183–210.
- Weber, M., Davis, J.P. (1990). Evidence of a laterally variable lower mantle structure from P- and S waves. *Geophys. J. Int* 102, 231–255.
- Weber, M., Davis, J.P., Thomas, C., Krüger, F., Scherbaum, F., Schlittenhardt, J., & Körnig, M. (1996). The structure of the lowermost mantle as determined from using seismic arrays. In Boschi, E., Ekström, G., Morelli, A. (Eds.), *Seismic modelling of the Earth's structure*. Instituto Nazionale di Geofisica, Rome, Italy, pp. 399–442.
- Wen, L., Helmberger, D.V. (1998a). Ultra-low velocity zones near the core-mantle boundary from broadband PKP precursors. *Science* 279, 1701–1703. <https://doi.org/10.1126/science.279.5357.1701>
- Wen, L., Helmberger, D.V. (1998b). A two-dimensional P-SV hybrid method and its application to modeling localized structures near the core-mantle boundary. *Journal of Geophysical Research: Solid Earth* 103, 17901–17918.
- Wentzcovitch, R.M., Wu, Z., & Carrier, P. (2010). First principles quasiharmonic thermoelasticity of mantle minerals. *Reviews in Mineralogy and Geochemistry* 71.
- Whittaker, S., Thorne, M.S., Schmerr, N.C., and Miyagi, L. (2016). Seismic array constraints on the D" discontinuity beneath Central America. *Journal of Geophysical Research: Solid Earth* 120, 1–18. <https://doi.org/10.1002/2015JB012392>
- Wicks, J.K., Jackson, J.M., & Sturhahn, W. (2010). Very low sound velocities in iron-rich (Mg,Fe)O: Implications for the core-mantle boundary region. *Geophysical Research Letters* 37. <https://doi.org/10.1029/2010GL043689>
- Wicks, J.K., Jackson, J.M., Sturhahn, W., & Zhang, D. (2017). Sound velocity and density of magnesiowüstites: Implications for ultralow-velocity zone topography. *Geophysical Research Letters* 44. <https://doi.org/10.1002/2016GL071225>
- Williams, Q., & Garnero, E.J. (1996). Seismic evidence for partial melt at the base of Earth's mantle. *Science* 273, 1528–1530. <https://doi.org/doi:10.1126/science.273.5281.1528>
- Williams, Q., Revenaugh, J., & Garnero, E.J. (1998). A correlation between ultra-low basal velocities in the mantle and hot spots. *Science* 281, 546–549.
- Wookey, J., & Kendall, J.M. (2007). Seismic anisotropy of post-perovskite and the lowermost mantle. In *Post-perovskite, the last mantle phase transition*, *Geophysical Monograph Series*. American Geophysical Union, Washington D.C, pp. 171–189.
- Wookey, J., Stackhouse, S., Kendall, J.M., Brodholt, J.P., & Price, G.D. (2005). Efficacy of the post-perovskite phase as an explanation of lowermost mantle seismic properties. *Nature* 438, 1004–1008.
- Wright, C. (1973). Array studies of P phases and the structure of the D" region of the mantle. *J. Geophys. Res* 78, 4965–4982.
- Wright, C., & Cleary, J.R. (1972). wave travel-time gradient measurements for the Warramunga seismic array and lower mantle structure. *Physics of the Earth and Planetary Interiors* 5, 213–230.
- Wu, X., Lin, J.-F., Kaercher, P., Mao, Z., Liu, J., Wenk, H.-R., & Prakapenka, V.B. (2017). Seismic anisotropy of the D" layer induced by (001) deformation of post-perovskite. *Nature Communications* 8, 14,669. <https://doi.org/10.1038/ncomms14669>
- Wu, Z., & Wentzcovitch, R.M. (2014). Spin crossover in ferro-periclase and velocity heterogeneities in the lower mantle. *Proceedings of the National Academy of Science* 111, 10468–10472
- Wu, Y., Wu, X., Lin, J.-F., McCammon, C.A., Xiao, Y., Prakapenka, V.B., Yoshino, T., Zhai, S., & Qin, S. (2016). Spin transition of ferric iron in the NAL phase: Implications for the seismic heterogeneities of subducted slabs in the lower mantle. *Earth and Planetary Science Letters* 434, 91–100.
- Wysession, M.E., Langenhorst, A., Fouch, M.J., Fischer, K.M., Al-Eqabi, G., Shore, P., & Clarke, T. (1999). Lateral variations in compressional/shear velocities at the base of the mantle. *Science* 284, 120–125.
- Wysession, M.E., Lay, T., Revenaugh, J., Williams, Q., Garnero, E.J., & Kellogg, L. (1998). The D" discontinuity and its implications, in: Gurnis, M., Wysession, M.E., Knittle, E., Buffett, B.A. (Eds.), *The Core-Mantle Boundary Region*. American Geophysical Union, Washing D.C.
- Yamada, A., & Nakanishi, I. (1998). Short-wavelength lateral variation of a D" P-wave reflector beneath the southwestern Pacific. *Geophysical Research Letters* 25, 4545–4548.
- Yamada, A., & Nakanishi, I. (1996). Detection of P-wave reflector in D" beneath the south-western Pacific using double-array stacking. *Geophysical Research Letters* 23, 1553–1556.
- Yamazaki, D., Yoshino, T., & Nakakuki, T. (2014). Interconnection of ferro-periclase controls subducted slab morphology at the top of the lower mantle. *Earth And Planetary Science Letters* 403, 352–357. <https://doi.org/10.1016/j.epsl.2014.07.017>
- Yao, Y., Whittaker, S., & Thorne, M.S. (2015). D" discontinuity structure beneath the North Atlantic from Scd observations. *Geophysical Research Letters* 42. <https://doi.org/10.1002/2015GL063989>
- Young, C.J., & Lay, T. (1990). Multiple phase-analysis of the shear velocity structure in the D" region beneath Alaska. *J Geophys Res Solid Earth Planets* 95.
- Yu, S., & Garnero, E.J. (2018). Ultralow velocity zone locations: A global assessment. *Geochemistry, Geophysics, Geosystems*. <https://doi.org/10.1002/2017GC007281>
- Yuan, K., & Romanowicz, B. (2017). Seismic evidence for partial melting at the root of major hot spot plumes. *Science* 357, 393–397.
- Zhang, B., Ni, S., Sun, D., Shen, Z., Jackson, J.M., & Wu, W. (2018). Constraints on small scale heterogeneity in the lowermost mantle from observations of near podal PcP precursors. *Earth And Planetary Science Letters* 489, 267–276. <https://doi.org/10.1016/j.epsl.2018.01.033>
- Zhang, S., Cottaar, S., Liu, T., Stackhouse, S., & Militzer, B. (2016). High-pressure, temperature elasticity of Fe- and Al-bearing MgSiO₃: Implications for the Earth's lower mantle. *Earth and Planetary Science Letters* 434, 264–273.

Toward Consistent Seismological Models of the Core–Mantle Boundary Landscape

Paula Koelemeijer

ABSTRACT

The dynamic topography of the core-mantle boundary (CMB) provides important constraints on dynamic processes in the mantle and core. However, inferences on CMB topography are complicated by uneven data coverage and strong lower mantle heterogeneity. Particularly, a trade-off exists with density variations, which ultimately drive mantle flow and are vital for determining the origin of mantle structures. Here, I review existing models of CMB topography and lower mantle density, focusing on seismological constraints. While most density models image two areas of dense anomalies beneath Africa and the Pacific, their exact location and relationship to seismic velocity structure differs. CMB topography strongly influences the retrieved density structure, helping to resolve differences between existing studies. Current CMB topography models vary both in pattern and amplitude, with a discrepancy between body-wave and normal-mode models. As existing models feature elevated topography below the Large-Low-Velocity Provinces (LLVPs), geodynamic predictions indicate that very dense compositional anomalies may currently be ruled out as possibility. To achieve a similar consistency as observed in S-wave and P-wave tomography models, future studies should develop models of CMB topography consistent with body-wave, normal-mode and geodetic data. This will help to break existing trade-offs with lower mantle density, thus aiding in narrowing down possible explanations for the LLVPs and providing additional insights into mantle dynamics.

9.1. INTRODUCTION

The Earth's surface exhibits a range of features that reflect the fact that we live on a dynamic planet. Dynamic surface topography informs us about mantle flow and upwellings (Austermann & Hoggard, this volume). Similarly, the landscape of the core–mantle

boundary (CMB), the largest physical and chemical boundary within the Earth located ~ 3000 km below our feet, holds important clues for understanding the nature and evolution of mantle flow.

Lateral variations in CMB topography break the symmetry of the dynamic regime in the outer core and are linked to lateral heat flow variations, thereby influencing core flow and possibly the geodynamo (e.g., Gubbins & Richards, 1986; Calkins et al., 2012; Davies et al., 2014; Tarduno et al., 2015). The pressure torque induced by topography has been thought to give rise to length-of-day variations (e.g., Jault & Le Mouél, 1990;

Department of Earth Sciences, Royal Holloway University of London, Egham, UK; and Department of Earth Sciences, University College London, London, UK

Hide et al., 1993; Kuang & Bloxham, 1993; Asari et al., 2006; Dehant et al., 2017) by transferring angular momentum between the mantle and core (see Buffett, 2015, for a review of possible core–mantle interactions). In addition, estimates of CMB topography aid in constraining mantle viscosity (e.g., Yoshida, 2008; Steinberger & Holme, 2008). Furthermore, Deschamps et al. (2018) suggested that accurate constraints on CMB topography could provide complimentary insights into the density structure of the lower mantle.

Studies of CMB topography have been performed since the 1970s, constraining topographic variations on 10–1000 km length scales, as discussed more in Section 9.2. Important constraints are provided by the traveltimes of seismic body waves that reflect or refract along the boundary (e.g., Menke, 1986; Garcia & Souriau, 2000; Koper et al., 2003; Rost & Revenaugh, 2004; Tanaka, 2010; Colombi et al., 2014; Soldati et al., 2012), while observations of seismic energy scattered by small-scale variations provide additional insights on the roughness of the boundary (e.g., Haddon & Cleary, 1974; Doornbos, 1978; Bataille et al., 1990; Earle & Shearer, 1998; Shearer et al., 1998; Mancinelli & Shearer, 2016). Constraints on longer wavelengths come from observations of normal modes (Earth’s free oscillations) as well as from geodetic data (e.g., Hide & Horai, 1968; Hager et al., 1985; Gwinn et al., 1986; Li et al., 1991; Jault & Le Mouél, 1990; Forte et al., 1995; Ishii & Tromp, 1999; Mathews et al., 2002; Koelemeijer et al., 2017). Numerical modelling of mantle flow and the induced dynamic topography aids in the interpretation of these observational constraints (e.g., Forte, 2007; Yoshida, 2008; Steinberger & Holme, 2008; Simmons et al., 2009; Lassak et al., 2010; Liu & Zhong, 2015; Deschamps et al., 2018).

Despite a range of sensitive data and a plethora of models, existing models of CMB topography continue to differ in both pattern and amplitude (see also Section 9.2). This is primarily because the data employed in studies of CMB topography are also sensitive to lower mantle structures, requiring joint inversions or corrections. However, the lower mantle is highly heterogeneous, mimicking the complexities found in the upper boundary layer of the mantle, as discussed in various other chapters in this volume. Many excellent reviews cover the range of seismological structures that have been imaged on different spatial scales in the lower mantle, including observations of seismic reflectors, anisotropy, scattering and ultra-low-velocity zones (e.g. Forte, 2007; Garnero and McNamara, 2008; Hernlund and McNamara, 2015), which are therefore not repeated here. However, it is worth briefly noting the most pronounced features on the longest wavelengths and the debate that surrounds them.

Two antipodal regions of lower-than-average seismic velocity are imaged underneath the Pacific and Africa

(Figure 9.1), covering about 25% of the core surface and rising up to ~ 1000 km above the core (Garnero & McNamara, 2008; Cottaar & Lekic, 2016; Garnero et al., 2016). Initially dubbed LLSVPs for large-low-*shear-velocity-provinces* (LLSVPs) due to their low S-wave velocities (V_S), these structures should now be referred to as LLVPs (large-low-velocity-provinces, adopted here as well), as they are also observed to have low P-wave velocities (V_P) (e.g., Koelemeijer et al., 2016; Garnero et al., 2016). The LLVPs are imaged consistently in different tomographic models (Figure 9.1), as demonstrated using cross-model correlation (Becker & Boschi, 2002), clustering analysis (Lekić et al., 2012; Cottaar & Lekic, 2016), and vote maps (Shephard et al., 2017). However, several questions regarding their origin, longevity, and influence on mantle dynamics are still debated: Can their seismic properties be solely explained by thermal variations, or are large-scale chemical variations required? If they are chemically distinct, what is their intrinsic density, and how do density variations vary within these structures? Have they been present since the formation of the Earth, or have they formed from the accumulation of subducted oceanic crust or reaction products between the core and mantle? Are they large-scale coherent structures, or are they made up of several smaller structures? The answers to these questions are important, as the LLVPs have a large influence on global mantle dynamics (e.g., Dziewonski et al., 2010; Davies et al., 2012; Bower et al., 2013; Nakagawa & Tackley, 2014), changing the cooling efficiency of the mantle (Nakagawa & Tackley, 2014), altering the heat flow distribution at the CMB and thus potentially inducing magnetic field reversals (e.g., Zhang & Zhong, 2011; Olson et al., 2015).

To unravel the nature of the LLVPs, knowledge of more than one elastic parameter is needed, i.e., constraints on V_P , bulk-sound velocity V_C or density ρ are required in addition to V_S . Observations of a high ratio of V_S over V_P variations and its distribution at a given depth, as well as a negative correlation between V_S and V_C variations in the lower mantle have often been interpreted as evidence for chemically distinct LLVPs (e.g., Karato & Karki, 2001; Su & Dziewonski, 1997; Ishii & Tromp, 1999; Masters et al., 2000a; Deschamps & Trampert, 2003; McNamara & Zhong, 2005; Houser et al., 2008). However, more recent studies have indicated that the V_S/V_P ratio or its distribution do not provide constraints on mantle composition and that a lower mantle phase transition can also explain the negative correlation between V_S and V_C variations (Tesoniero et al., 2016; Koelemeijer et al., 2018). Many arguments exist for either side of the debate, with evidence from geochemical data for the presence of an unmixed primordial reservoir in the mantle (e.g., Zindler & Hart, 1986; Hofmann, 1997; Mukhopadhyay, 2012; Rizo et al., 2019), geodynamical simulations supporting either possibility (e.g., Forte &

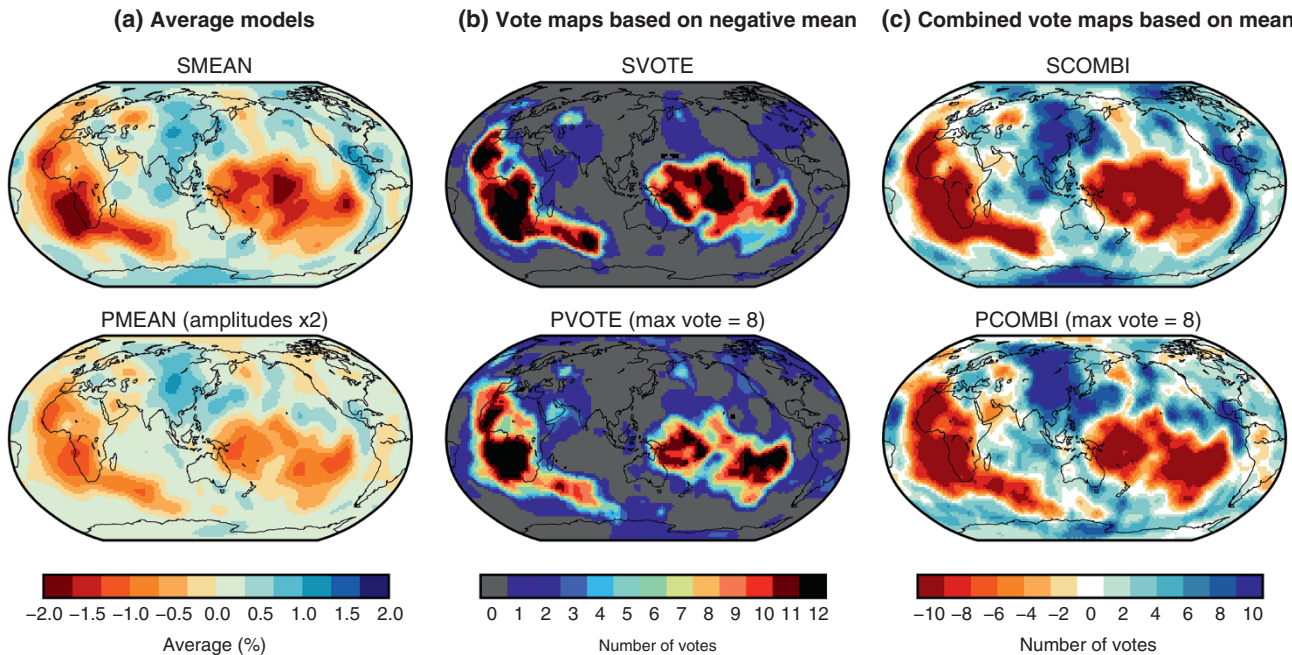


Figure 9.1 Typical long-wavelength (up to spherical harmonic degree 12) velocity structure at 2800 km depth showing (top) V_S and (bottom) V_P showing (a) average models (“MEAN”) similarly to Becker & Boschi (2002), (b) vote maps (“VOTE”) based on negative velocity anomalies and (c) combined vote maps based on both positive and negative velocity anomalies (“COMBI”), computed following Shephard et al. (2017). Only models developed since 2010 have been included, resulting in 12 models for V_S : GYPSUM-S (Simmons et al., 2010), SAW642ANb (Panning et al., 2010), S40RTS (Ritsema et al., 2011), METAL12-S (Mosca et al., 2012), S362ANI+M (Moulik and Ekström, 2014), SAVANI (Auer et al., 2014), SEMUCB-WM1 (French & Romanowicz, 2014), SGLOBE-rani (Chang et al., 2015), SPani-S (Tesoniero et al., 2015), SP12RTS-S (Koelemeijer et al., 2016), TX2015 (Lu and Grand, 2016) and SEISGLOBE2 (Durand et al., 2017). 8 V_P models are included: GYPSUM-P (Simmons et al., 2010), LLNL_G3Dv3 (Simmons et al., 2012), METAL12-P (Mosca et al., 2012), GAP-P4 (Obayashi et al., 2013), SPani-P (Tesoniero et al., 2015), SP12RTS-P (Koelemeijer et al., 2016), MIT2016 (Burdick et al., 2017) and H2016 (Hosseini, 2016). It is evident that the LLVPs are imaged consistently across both S - and P -wave models.

Mitrović, 2001; Schubert et al., 2004; Schuberth et al., 2009; Davies et al., 2012; McNamara & Zhong, 2004, 2005; McNamara et al., 2010; Deschamps et al., 2011; Nakagawa et al., 2012; Li et al., 2014; Nakagawa & Tackley, 2014; Davies et al., 2015b), and the geographical correlation between LLVPs and surface features related to mantle upwellings being interpreted in different ways (e.g., Burke et al., 2008; Torsvik et al., 2010; Auermann et al., 2014; Davies et al., 2015a). This ongoing debate has been perfectly well summarised by many recent reviews (e.g., Davies et al., 2015b; Hernlund & McNamara, 2015; Garnero et al., 2016), and will therefore not be repeated in detail here.

Robust constraints on LLVP density structure have been at the center of the debate regarding the origin of the LLVPs (e.g., Davies et al., 2015b; Garnero et al., 2016; Lau et al., 2017; Koelemeijer et al., 2017), as an increased density in combination with low seismic

velocities would unequivocally point to a thermochemical nature (Karato & Karki, 2001). Knowledge of lower mantle density is also important to understand the driving forces of mantle flow and for studies of CMB topography, which are inherently linked to each other through isostasy and dynamic flow, often giving rise to a strong trade-off in observational data sets.

While density variations are vital for understanding lower mantle dynamics, they are not easy to determine from seismological data. Body wave data are only indirectly sensitive to density, while surface waves only provide constraints on upper mantle structure. Density models are therefore primarily constructed from normal-mode or geodetic observations, with several lower mantle models existing in the literature (e.g., Ishii & Tromp, 1999; Trampert et al., 2004; Mosca et al., 2012; Moulik & Ekström, 2016; Koelemeijer et al., 2017; Lau et al., 2017). However, there remains controversy

regarding the density of the LLVPs, whether they are lighter or denser than the ambient mantle, and what the depth-extent of a dense layer is, as discussed further in Section 9.3.

The aim of this contribution is to review the large-scale seismological landscape of the core–mantle boundary. Lower mantle V_S and V_P variations are now consistently imaged on large-scales (Lekić et al., 2012; Cottaar & Lekic, 2016), as demonstrated in Figure 9.1 for tomographic models developed since 2010. This chapter focuses on some remaining questions: how much progress have been made on CMB topography and density? How consistent are our images after 35 years of CMB topography studies and 20 years since the first model of lateral density variations in the mantle? First of all, I will review studies of CMB topography and density, focusing on seismological results, as recent reviews (Hernlund & McNamara, 2015; Deschamps et al., 2018) and other chapters in this volume already focus on dynamical aspects of lowermost mantle structure. Subsequently, I will analyze existing topography and density models in a quantitative way, identify consistent features, and discuss the insights these provide about deep mantle structure and dynamics. Finally, I will discuss future directions for reconciling differences and developing consistent models of the core–mantle boundary landscape.

9.2. EXISTING MODELS OF CMB TOPOGRAPHY

This overview primarily follows historical developments (see also Table 9.1), e.g., starting with early studies of CMB topography based on scattered waves, core-reflected (PcP, ScS), core-refracted (PKP, PKKP, PKmP) and inner core (PKIKP, PKiKP) phases. This is followed by a discussion of global CMB topography models developed using body-wave and normal-mode data. As I focus on seismological insights, I only briefly discuss geodynamic predictions and other insights toward the end of this section.

9.2.1. Regional CMB Topography Studies

The first studies of CMB topography arose in the 1970s from the detailed analysis of precursors of core-refracted phases recorded (see Bataille et al., 1990; Loper & Lay, 1995, for a review of these early studies). The classic studies of Haddon (1972) and Cleary & Haddon (1972) first recognized that the onset of PKP precursors required scattering from small-scale heterogeneities near the CMB, confirmed by the analysis of PKP and PKKP precursors in subsequent studies (Doornbos & Vlaar, 1973; Doornbos, 1974). Haddon & Cleary (1974) first raised the possibility that ~ 200 m bumps on the core with 10–20 km length scales could explain the data. Follow-up studies

investigating PKP and PKKP precursors found similar topography values (e.g., Doornbos, 1976, 1978; Van den Berg et al., 1978; Doornbos, 1980; Bataille & Flatté, 1988), although results based on PmKP (Aleshin & Vinnik, 1975) and PKKP backscattered precursors (Chang & Cleary, 1978, 1981) hinted at larger topography values of a few km. Since the 1990s, there has been a constant interest in PKP and PKKP precursors, with studies moving toward more global analysis and shorter wavelengths (e.g., Bataille et al., 1990; Earle & Shearer, 1998; Shearer et al., 1998; Mancinelli & Shearer, 2016).

Scattering studies provide excellent constraints on small-scale roughness of the CMB (wavelengths of 7–30 km), but the analysis of other seismic phases is required to determine topographic variations on longer wavelengths. Menke (1986) was the first to utilize core-reflected phases (PcP amplitude dependence) in the study of CMB topography, finding undulations of a few 100 m on short length scales (10 km). Core-reflected phases were studied further, often by considering PcP/P amplitude ratios or their simple pulse shapes, to find topographic variations of up to 3 km on wavelengths of 50–400 km (Neuberg & Wahr, 1991; Vidale & Benz, 1992; Emmerich, 1993; Rost & Revenaugh, 2004). Recent regional studies on PcP and ScP arrivals have suggested a range of amplitudes; Wu et al. (2014) found a best fit for a depression of 6 km over 300–400 km under Alaska, while Shen et al. (2016) concluded that topography of 1.2 km on length scales of 140 km was required to fit their seismic observations under Japan. These studies indicate that topography values found in individual studies vary significantly and depend strongly on length scale and location.

With an increase in the number of body-wave observations, issues with their interpretations in terms of CMB topography were identified. Particularly, it proved difficult to separate out the topography effect from lower mantle structure (Kampfmann & Müller, 1989; Murphy et al., 1997). Furthermore, a bias in traveltimes due to focusing and unfocusing was identified (Rekdal & Doornbos, 1992; Emmerich, 1993). To overcome some of these issues, joint studies of PcP observations and core-refracted phases were performed (e.g., Gudmundsson, 1989; Rekdal & Doornbos, 1992). Specifically, the study of Garcia and Souriau (2000) combined PcP, PKP, and PKKP observations to deduce that 95% of the core surface was between -4.0 and 4.0 km on wavelengths of 300–1500 km. Differential traveltimes measurements relative to direct arrivals (e.g., PcP–P) or inner core phases (e.g., PKP–PKIKP, PKiKP–PcP) were also utilized to minimize the influence of mantle structure (e.g., Neuberg and Wahr, 1991; Poupinet et al., 1993; Koper et al., 2003). Furthermore, with the development of independent tomographic models of lower mantle structure, these were adopted to test the influence of velocity heterogeneity in synthetic examples (Emmerich, 1993; Murphy

Table 9.1 Overview of past observational studies of CMB topography and density. Note that for global CMB topography models, the peak-to-peak (PTP) amplitude is indicated, while for other constraints the amplitude is given instead (unless otherwise specified). The length scale generally relates to the period of the waves used in the study, and indicates either the wavelength or the correlation length. c_{st} stands for splitting function measurements, while Y_{lm} indicates spherical harmonics up to maximum degree l . Models in bold italic are used in the current study in the computation of average models and vote maps.

Constraints on CMB topography amplitude Reference	Data / methodology	Region	Length scale	Amplitude
Haddon & Cleary (1974)	PKP precursors	Regional	30 km	Few 100 m
Aleshin & Vinnik (1975)	PKP precursors, PmKP reflections	Regional	10 km	10 km
Doornbos (1978)	PKP precursors	Regional	10–20 km	200 m
Chang & Cleary (1978)	PKKP precursors	Regional	–	Few km
Doornbos (1980)	PKKP precursors	Regional	10–20 km	100–200 m
Chang & Cleary (1981)	PKKP precursors	Regional	–	Few km
Menke (1986)	PcP amplitudes	Regional	10 km	Few 100 m
Bataille & Flatté (1988)	PKP precursors	Regional	–	300 m
Gudmundsson (1989)	PcP, PKP _{ab, bc, cd, df}	Regional	–	4 km PTP
Bataille et al. (1990)	PKP, PKKP, PKiKP precursors	Global patches	–	300 m
Neuberg & Wahr (1991)	PcP - P, PcP / P amplitude ratio	Regional	50–400 km	2–3 km
Vidale & Benz (1992)	PcP, ScP	Regional	50–200 km	<500 m
Poupinet et al. (1993)	PKP _{ab} -PKiKP	Regional	–	<4 km
Earle & Shearer (1998)	PKKP precursors	Regional	7–10 km	0.35 km
Shearer et al. (1998)	PKKP precursors	Regional	8 (20) km	300 (600) m
Garcia & Souriau (2000)	PcP, PKP _{bc} , PKKP _{bc}	Global patches	300–1500 km	95 % below 4 km
Koper et al. (2003)	PKiKP - PcP	Regional	–	3.5 km PTP
Colombi et al. (2014)	PcP, ScS, P _{diff} , PKP _{dir} , SKS _{ac}	Global	$Y_{lm}, l \leq 10$	7 km PTP
Wu et al. (2014)	PcP	Regional	300–400 km	6 km
Ventosa & Romanowicz (2015)	PcP - P	Regional	–	2.7 km
Schlaphorst et al. (2015)	P4KP - PKP	Regional	150 km	60 km over 3 points
Mancinelli & Shearer (2016)	PKKP precursors	Regional	7 km	390 m
Shen et al. (2016)	PcP, ScP	Regional	140 km	1.2 km
Hide & Horai (1968)	Geoid modelling	Global	$Y_{lm}, l \leq 4$	8.7 km PTP
Hager et al. (1985)	Geoid modelling	Global	$Y_{lm}, l = 2, 3$	<3 km
Gwinn et al. (1986)	Nutation measurements (VLBI)	Global	Y_{20} only	490 m
Wahr & De Vries (1989)	Nutation measurements (VLBI)	Global	Y_{20} only	0.5–0.87 km
Jault & Le Mouél (1990)	Dynamic flow modelling	Global	Odd $Y_{lm}, l \leq 5$	11.9 km PTP
Forte & Peltier (1991)	Seismic-geodynamic modelling	Global	$Y_{lm}, l \leq 4$	<8 km
Forte et al. (1995)	Seismic-geodynamic modelling	Global	$Y_{lm}, l \leq 8$	<6 km
Mathews et al. (2002)	Nutation measurements (VLBI)	Global	Y_{20} only	390 m
Forte (2007)	Seismic-geodynamic modelling	Global	$Y_{lm}, l \leq 20$	2.6 km PTP
Steinberger & Holme (2008)	Seismic-geodynamic modelling	Global	$Y_{lm}, l \leq 15$	6 km PTP
Simmons et al. (2009)	Joint seismic-geodynamic-mineralogical inversion	Global	275 km blocks	3.5 km PTP
Koelemeijer et al. (2012)	Lower mantle sensitive modes c_{st}	Global	$Y_{lm}, l = 2$ only	5 km PTP

(continued overleaf)

Table 9.1 (continued)

Global CMB topography Reference	Model name	Data	Velocity model	Parameterisation	PTP amplitude
Creager & Jordan (1986)	CJ1986	PKP _{ab, df}	M84C + thin layers	All $Y_{lm}, l \leq 5$	20.1 km
Morelli & Dziewonski (1987)	MD1987	PcP, PKP _{bc}	HELM46	All $Y_{lm}, l \leq 4$	12.3 km
Doombos & Hilton (1989)	DH1989-M6	PcP, PKP _{ab, bc}, PKKP_{bc}, PnKP_{ab}}}	M84C + thin layer	All $Y_{lm}, l \leq 4$	7.7 km
Doombos & Hilton (1989)	DH1989-M7	PcP, PKP _{ab, bc}, PKKP_{bc}, PnKP_{ab}}}	M84C	All $Y_{lm}, l \leq 4$	8.3 km
Obayashi & Fukao (1997)	OF1997	P, PcP	Own V_P	All $Y_{lm}, l \leq 5$	14 km / 4 km
Vasco et al. (1999)	Vetal1999	P, S, PP, PcP, SS, ScS, PKP _{ab, bc, df}, SKS_{acr}, SS-S410S, SS-S660S}}	Own V_S, V_P	2° equal area	12 km
Boschi & Dziewonski (2000)	BD2000	P, PcP, PKP _{bc, df}}	Own V_P	5° equal area	<20 km
Soldati et al. (2003)	Setal2003	P, PcP, PKP _{bc, df}}	Own V_P	1656 equal area blocks	<20 km
Sze & van der Hilst (2003)	SV2003	PcP, PKP _{ab, bc, df}, PKKP_{ab, bc}}}	KH2001	All $Y_{lm}, l \leq 4$	2.4 km
Tanaka (2010)	T2010	P4KP - PcP	PMEAN + layer	Even $Y_{lm}, l \leq 4$	4.5 km
Soldati et al. (2012)	SBF2012-T	P, PcP, PKP _{bc, df}}	Own V_P	5° equal area	12.4 km
Soldati et al. (2012)	Setal2012-TG	P, PcP, PKP _{bc, df} with geodynamic coupling}	Own V_P	5° equal area	8.7 km
Soldati et al. (2012)	SBF2012-TGppv	P, PcP, PKP _{bc, df} with geodynamic coupling}	Own V_P	5° equal area	2.1 km
Li et al. (1991)	LGW1991-SAT	Normal modes spectra	Own V_S	Even $Y_{lm}, l \leq 4$	3.7 km
Li et al. (1991)	LGW1991-SAF	Normal modes c_{st}	Own V_S	Even $Y_{lm}, l \leq 4$	5.2 km
Ishii & Tromp (1999)	IT1999	Normal modes c_{st} gravity	Own V_S, V_P	Even $Y_{lm}, l \leq 6$	14.4 km
Koelemeijer et al. (2017)	KDR2017-neg	Stoneley modes c_{st}	SP12RTS	Even $Y_{lm}, l \leq 6$	4.7 km
Koelemeijer et al. (2017)	KDR2017-pos	Stoneley modes c_{st}	SP12RTS	Even $Y_{lm}, l \leq 6$	5.7 km
Koelemeijer et al. (2017)	KDR2017	Stoneley modes c_{st}	SP12RTS	Even $Y_{lm}, l \leq 6$	5.7 km
Global density models Reference	Model name	Data	Velocity model	Lateral param.	Vertical param.
Ishii & Tromp (1999)	IT1999	Normal modes c_{st} gravity	Own V_S, V_P	Even $Y_{lm}, l \leq 6$	Chebyshev polynomials to order 13
Trampert et al. (2004)	Tetal2004	Surface waves, normal modes c_{st} gravity	Own V_S, V_P	Even $Y_{lm}, l \leq 6$	5 constant layers
Mosca et al. (2012)	Metal2012	Surface waves, body waves, normal modes c_{st}	Own V_S, V_P	Even $Y_{lm}, l \leq 6$	10 cubic splines
Moulik and Ekström (2016)	ME2016	Surface waves, body waves, normal modes c_{st} waveforms	Own V_S, V_P	362 spherical splines	16 cubic splines
Lau et al. (2017)	Letal2017	Tidal GPS measurements	S40RTS	2 scaling factors	3 constant layers
Koelemeijer et al. (2017)	KDR2017-neg	Stoneley modes c_{st}	SP12RTS	2 scaling factors	1–2 constant layers
Koelemeijer et al. (2017)	KDR2017-pos	Stoneley modes c_{st}	SP12RTS	2 scaling factors	1–2 constant layers
Koelemeijer et al. (2017)	KDR2017-all	Stoneley modes c_{st}	SP12RTS	2 scaling factors	1–2 constant layers

et al., 1997) or to correct traveltimes residuals for mantle structure (Garcia & Souriau, 2000; Koper et al., 2003).

In the last decade, increases in computational power have led to a renewed interest in body-wave studies of CMB topography, accompanied by several advances in theory and methodologies. Using waveform synthetics rather than ray theory, Colombi et al. (2012) and Colombi et al. (2014) studied the sensitivity of different phases to CMB topography and performed waveform inversions, while Ventosa and Romanowicz (2015) illustrated the importance of improved stacking techniques for measuring core-reflected phases. At the same time, improved instrumentation enables observations of phases such as P4KP and P7KP, which, when used in differential traveltime measurements, are less affected by mantle heterogeneity (Tanaka, 2010; Schlaphorst et al., 2015). Although difficult to interpret due to their multiple bounce points, such exotic phases lead to new ideas and methodologies that can be employed in future work.

9.2.2. Global Body-Wave Models of CMB Topography

Body-wave studies of CMB topography based on core-reflected and core-refracted phases, as discussed in the previous section, are naturally done on a regional scale. However, the resulting traveltime measurements that provide information on the depth to the CMB are often incorporated into global models, which I will now discuss (see also Table 9.1 and Figure 9.2a).

The first global models of CMB topography were developed by Creager and Jordan (1986) and Morelli and Dziewonski (1987), both making use of arrival times reported by the Bulletins of the International Seismological Centre (ISC). Morelli and Dziewonski (1987), combining PKP_{bc} data with PcP observations, found topography amplitudes of 6 km (Figure 9.2a). In contrast, Creager & Jordan (1986) only used core-refracted data (PKP_{ab} and PKP_{df}) and obtained significantly larger amplitudes (peak-to-peak amplitude of 20 km), which they concluded were too large to be due to dynamic topography. These studies typically performed a least-squares inversion after correcting traveltime residuals for mantle heterogeneity using a long-wavelength velocity model. Recognizing the influence of lowermost mantle structure, Doornbos and Hilton (1989) additionally inverted for velocity variations in the lowermost mantle, finding that this reduced topography amplitudes.

These early global models were followed by critical studies that argued that no reliable topography model could be obtained from ISC data (Rodgers & Wahr, 1993; Gudmundsson & Clayton, 1991). This was likely due to discrepancies between different seismic phases (particularly PcP and PKP/PKPP) as a consequence of heterogeneous mantle structure. In addition, Pulliam and Stark (1993) showed that spurious topographic

variations arose from fitting long-wavelength spherical harmonics to patchy body-wave observations, as commonly done in these studies. Furthermore, Stark & Hengartner (1993) concluded that uncertainties due to earthquake relocation, ellipticity, and mantle corrections introduced larger errors in CMB topography than the inferred amplitudes, and that smoothing of data into spherical harmonics also increased the apparent correlation between models without having any physical meaning.

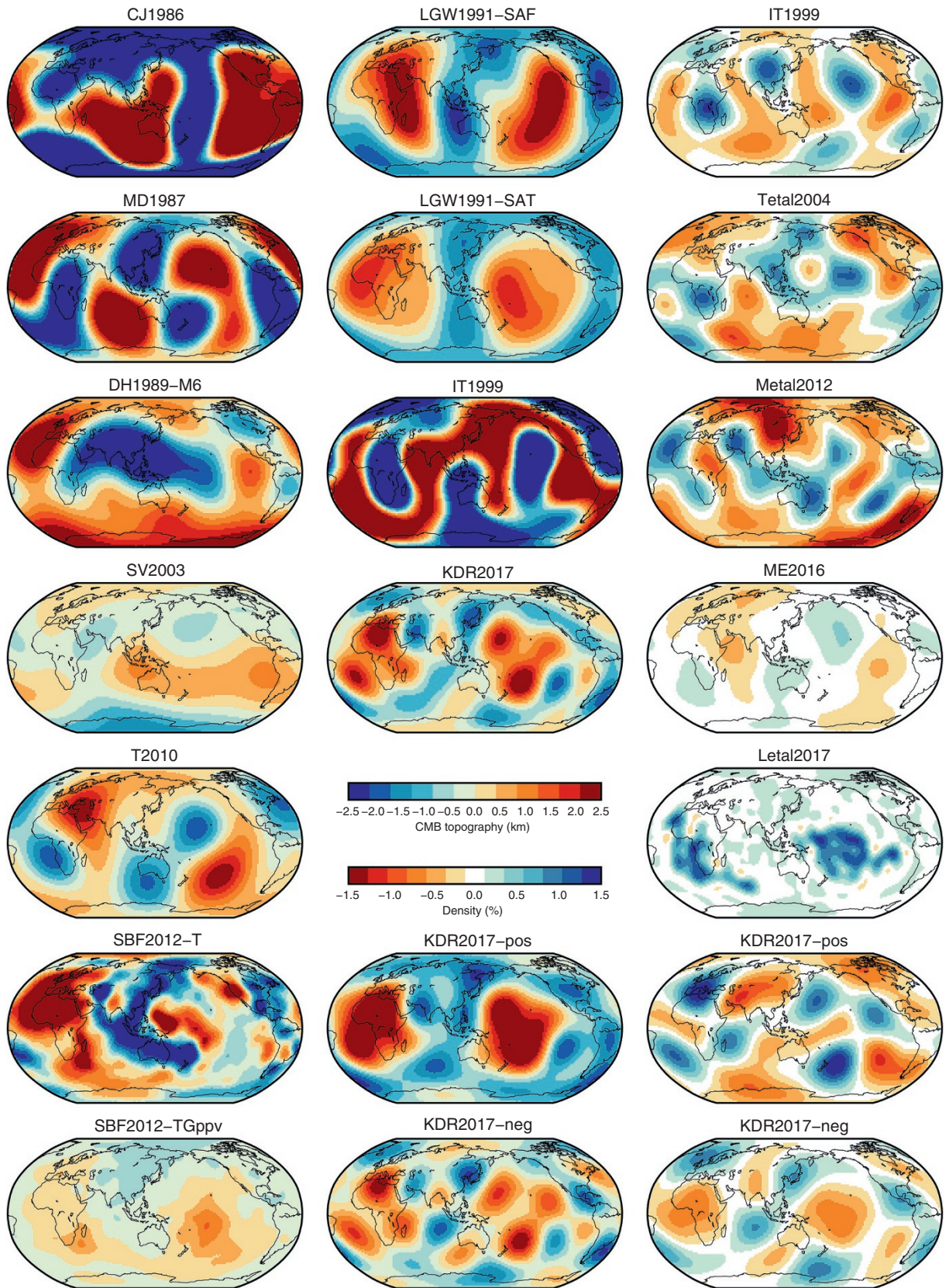
Addressing some of this criticism, a number of studies performed separate inversions for topography alone and for joint volumetric-topographic inversions (Obayashi & Fukao, 1997; Vasco et al., 1999; Boschi & Dziewonski, 2000; Sze & van der Hilst, 2003; Soldati et al., 2003; Soldati & Boschi, 2005). While a discrepancy between models based on PcP or PKP/PKPP data remains present, the consensus is that lowermost mantle heterogeneity should be included in any study of CMB topography, which also tends to decrease amplitudes in the resulting models (Figures 9.2a and 9.3a). More recently, Tanaka (2010) utilized differential P4KP–PcP traveltime measurements to minimize the influence of mantle structure and improve data coverage, resulting in topography amplitudes of only 2–2.5 km. Furthermore, instead of treating velocity and topography heterogeneity separately, Soldati et al. (2012) accounted for their coupling by mantle flow in their inversions. This gives rise to a reduction in topography amplitude (Figure 9.2a), solving also the discrepancy between PcP and PKP data according to the authors. At the same time, topography models developed through a joint tomographic-geodynamic approach improve the fit to normal-mode data, particularly when a decrease in viscosity associated with the post-perovskite phase is included (Soldati et al., 2013). These recent contributions illustrate that novel observations, improved estimates of mantle structure, and considerations of dynamic flow effects are important factors in future studies.

9.2.3. CMB Topography Constrained by Normal Modes

Due to the heterogeneous distribution of seismic stations and events, body-wave studies of global CMB topography will always suffer from a sampling bias, especially when a global parameterization is employed (Stark & Hengartner, 1993). Due to the large density contrast between the core and mantle, normal modes display a large sensitivity to CMB topography. Observations of their resonance frequencies are made after large-magnitude earthquakes, which provide complementary insights into CMB topography, albeit only on the longest wavelengths, while small-scale variations are averaged out.

Li et al. (1991) were the first to consider CMB topography in their analyses of normal modes. They performed both direct inversions of normal-mode frequency spectra,

(a) CMB topography from body waves (b) CMB topography from normal modes (c) Lowermost mantle density



as well as a two-step approach using so-called splitting function measurements, that describe the lateral frequency variations attributed to a particular normal mode. The resulting models are relatively similar (Figure 9.2b), showing elevated topography at the LLVPs. Although the degree-2 amplitude differs slightly (Figure 9.3b), both models have peak-to-peak amplitudes of 4–5 km, which are lower than most body-wave models of that time. Similar peak-to-peak topography amplitudes were found by Koelemeijer et al. (2012) in a forward-modeling analysis of lower mantle sensitive normal modes.

Few other normal-mode models of CMB topography exist, primarily including it in studies of lowermost density structure (Section 9.3). Noticeably is the CMB topography model by Ishii & Tromp (1999), famously known for being the first normal-mode density study. This model features much larger amplitudes than Li et al. (1991), particularly in spherical harmonic degree 4 (Figure 9.3b) and includes topography of an opposite amplitude at LLVP locations (Figure 9.2b). This results in a positive degree-2 correlation with V_S structure (Figure 9.3d), whereas other CMB topography models show mostly a negative correlation.

Recently, Koelemeijer et al. (2017) performed a forward modeling parameter search for both lower mantle density and CMB topography, finding consistently elevated topographies for the LLVPs, irrespective of whether they were denser or lighter (Figure 9.2b). Noticeably, the largest amplitudes are found around the edges of the LLVPs, with the center showing only moderate elevation. However, the topography amplitudes depend on the density anomalies (see bottom two rows of Figure 9.2b). Larger amplitudes are required in the case of dense LLVPs (model KDR2017-pos), whereas lower CMB topography amplitudes are present in the case of light LLVPs (model KDR2017-neg), as also evident in Figure 9.3b. While the topography models KDR2017-pos and KDR2017-neg

are only included to demonstrate this dependence, the corresponding density models will be discussed and analyzed further in following sections.

9.2.4. Other Constraints on CMB Topography

Additional constraints on CMB topography are obtained from geoid, gravity and nutation observations. To explain gravitational field measurements, Hide & Horai (1968) invoked peak-to-peak amplitudes of 8.7 km for CMB topography up to degree 4. In addition, Hager et al. (1985) estimated that a geoid anomaly of 2–3 km corresponds to relief on the CMB of less than 3 km, which has been used as constraint in many subsequent studies of CMB topography. The main drawback of using geodetic data to constrain CMB topography (and density) is that knowledge of the radial (and lateral) viscosity variations in the mantle are required (e.g., Hager & Richards, 1989), which remain debated (see Rudolph et al., this volume). In addition, Liu and Zhong (2015) showed that structures in the lowermost mantle compensate each other, leading to a zero net effect on the geoid. Whether the geoid provides constraints on deep mantle structures remains thus to be determined.

To explain the period of the free core nutation, determined in length-of-day variations by very-long-baseline-interferometry, Gwinn et al. (1986) deduced that the CMB ellipticity was 5% larger than for an Earth in hydrostatic equilibrium. This implies a value of 490 ± 110 m for the degree-2 zonal coefficient of CMB topography, a value that was revised by Mathews et al. (2002) to be ~ 390 m. Although this provides a strong constraint, and several subsequent studies have considered it, it remains difficult to fully reconcile this value with seismological observations. By calculating the pressure torque due to topography and analysing its effect on length-of-day variations, Jault and Le Mouél

Figure 9.2 Overview of global (a–b) CMB topography models and (c) lowermost mantle density structure at 2800 km depth. CMB topography models are derived from (a) body-wave data (CJ1986 (Creager & Jordan (1986), MD1987 (Morelli & Dziewonski (1987), DH1989-M6 (Doornbos & Hilton (1989), SV2003 (Sze & van der Hilst (2003), T2010 (Tanaka (2010), SBF2012-T and SBF2012-TGppv Soldati et al. (2012)) or (b) normal-mode data (LGW1991-SAF and LGW1991-SAT Li et al. (1991), IT1999 (Ishii & Tromp (1999) and KDR2017, KDR2017-pos and KDR2017-neg (Koelemeijer et al. (2017) – with the latter two only included for comparison to the density models). Density models are primarily constrained by normal-mode data combined with other seismic data (IT1999 (Ishii & Tromp (1999), Tetal2004 (the mean model of Trampert et al. (2004), Metal2012 (the mean model of Mosca et al. (2012), ME2016 (Moulik and Ekström (2016), KDR2017-pos and KDR2017-neg (the best-fitting models of Koelemeijer et al. (2017)) or derived from Earth’s tides (Letal2017, the mean model of Lau et al. (2017)). CMB topography models based on body-wave data (a) show a large variety in both pattern and amplitude, while those derived from normal modes (b) generally show elevated topography for the LLVP locations (with IT1999 the odd one out). Density models (c) differ in detail, but most models have dense LLVPs (with the exception of KDR2017-neg). Note that the maximum degree of the spherical harmonic expansion differs between models, as detailed in Table 9.1.

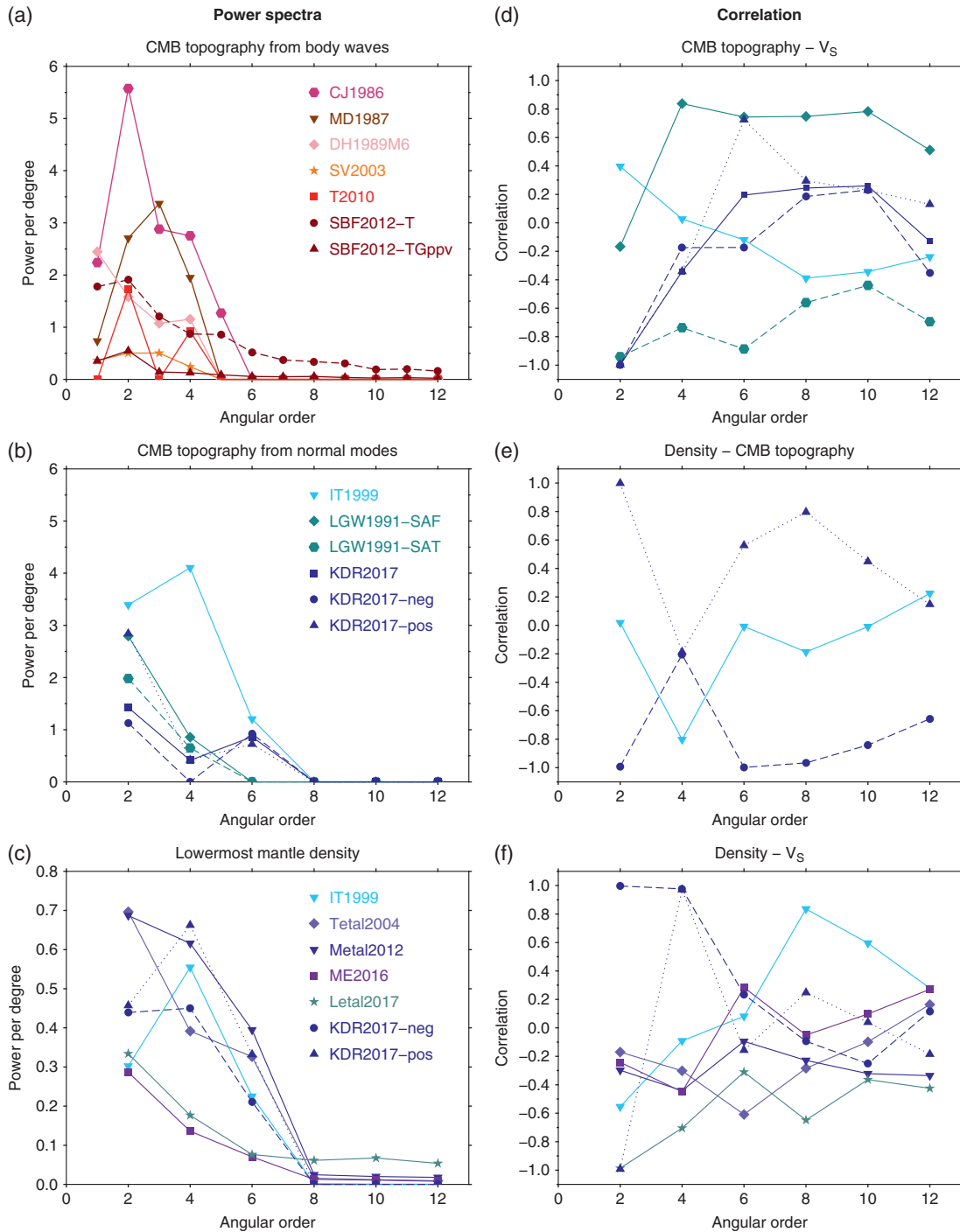


Figure 9.3 Properties of global CMB topography and density models shown in Figure 9.2 and listed in Table 9.1, showing (a–c) the power spectra of individual models and (d–f) the correlation between different model properties: (d) V_S structure and CMB topography, (e) density and CMB topography and (f) density and V_S structure. The correlation is only computed when both properties are provided in a consistent manner. Topography models KDR2017-neg and KDR2017-pos are best-fitting models, only shown to demonstrate their relationship to the corresponding density models, while mean models are used for Tetal2004, Metal2012, and Letal2017. For CMB topography models based on body waves (a), models with large amplitudes are typically older (developed prior to 2000), while newer models show smaller amplitudes. The IT2001 model shows a larger power in degree 4 (Moulik & Ekström (2016; Lau et al. (2017) or larger degree-4 power (all other models). The correlation between CMB topography models and V_S structure (d) in the lowermost mantle tends to be negative for degree 2 except for the IT1999 model. Only few models exist that provide both CMB topography and density structure (e) in a consistent way, with the models by Koelemeijer et al. (2017) showing a clear opposite relationship for degree 2. Most density models have the same relationship with V_S (f), except the KDR2017-neg model. Note that KDR2017-pos and Letal2017 have a similar degree-2 correlation between density and V_S .

(1990) also obtained estimates of odd-degree CMB topography coefficients, finding amplitudes of a few km. The importance of topographic variations for explaining length-of-day variations has been questioned in more recent studies (Kuang & Bloxham, 1997; Kuang & Chao, 2001; Mound & Buffett, 2005), with a gravitational coupling mechanism currently favored (see Buffett, 2015, for an discussion). Nevertheless, gravitational coupling remains dependent on flow-induced deformation of the CMB (Mound & Buffett, 2006), while small-scale roughness is still thought to influence frictional dissipation at the CMB (Le Mouél et al., 2006). Due to their complementary nature to seismological data, gravity, geoid, and nutation observations will be able to contribute important constraints on CMB topography in future studies, particularly with more precise observations available (Cesare & Sechi, 2013; Bacchetta et al., 2017; Ros et al., 2018; Gurvits, 2019).

9.2.5. Dynamic Predictions of CMB Topography

Before reviewing the density structure of the lowermost mantle, first a few remarks on geodynamic predictions of CMB topography. The correlation of the non-hydrostatic geoid (Hager et al., 1985; Hager & Richards, 1989) and large-scale plate motions (Forte & Peltier, 1987) with lower mantle structure was recognized early on. As a result, geodynamic predictions of density structure and CMB topography have been compared to seismological models with the aim to unravel the contribution of thermal and compositional variations and to further our understanding of lower mantle dynamics. Excellent reviews on these topics are given by Forte (2007) and Deschamps et al. (2018), and thus are only summarized briefly here.

Dynamic predictions of CMB topography generally take one of two possible approaches. Often, seismic velocity variations are converted to density variations (generally using a scaling factor), which drive mantle flow and lead to dynamically induced CMB topography (e.g., Forte et al., 1995; Forte, 2007; Steinberger and Holme, 2008). Although the resulting models show a strong correlation with seismic tomography, several assumptions regarding the velocity-density scaling factors and viscosity structure of the mantle affect the results. An alternative approach is the modeling of mantle flow over time and analyzing the present-day dynamic topography (e.g., Yoshida, 2008; Lassak et al., 2010; Liu & Zhong, 2015; Deschamps et al., 2018). Interestingly, Liu and Zhong (2015) found that the largest topography amplitudes may occur outside the LLVPs on relatively short wavelengths, while the CMB underneath the LLVPs is relatively smooth and only slightly depressed or elevated. By investigating both purely thermal and thermochemical models, Lassak et al. (2010)

found that it is difficult to distinguish between the two based on long-wavelength patterns of topography up to spherical harmonic degree 4, precisely what most seismological studies have been able to constrain. However, more recent work by Deschamps et al. (2018) suggests that the relationship between S -wave velocity and CMB topography may also hold clues to the density structure of the lower mantle, even if the lowermost mantle post-perovskite phase is included (Deschamps and Li, 2019). These studies serve thus as useful guide in the interpretation of seismological results, but, as they are not derived from observations, are not of focus here.

9.3. TWENTY YEARS OF DENSITY MODELS

Most studies of lowermost density have focused on the nature of the LLVPs by considering the relationship between density and V_S variations. Although geodetic observations provide some constraints on density variations, on long wavelengths it is difficult to pinpoint anomalies in depth, while knowledge of the mantle's viscosity structure is generally required. Studies that utilize seismic tomography depend on conversion factors from velocity to density (e.g., Forte et al., 1995; Simmons et al., 2009), which tend to have large uncertainties. Here, the focus is instead on constraints from normal modes, which are thought to provide the most direct estimates of density. Nevertheless, the sensitivity of normal modes to density structure is smaller than the sensitivity to velocity or topography (due to the oscillatory nature of the kernels around zero) and building a density model from normal-mode observations remains tricky, as this overview will show. I again take a historical view, discussing the first model that was developed 20 years ago and the criticism it received, as well as recent attempts in constraining the density structure of the lower mantle based on normal modes and tidal tomography. Note that these models generally provide a depth-averaged picture, as studies parameterize density in thick constant depth layers due to the broad depth sensitivity of the data. In reality, however, the density structure is likely to have strong three-dimensional variations, even within the LLVPs (e.g., Mulyukova et al., 2015; Li et al., 2018).

9.3.1. Early Normal-Mode Studies

The first normal-mode based density model was developed by Ishii & Tromp (1999), based on splitting function measurements up to 3 mHz (Tromp & Zanzerkia, 1995; He and Tromp, 1996; Resovsky & Ritzwoller, 1998). The dense LLVPs and their negative correlation with V_S structure (Figures 9.2c and 9.3f) that characterized this model had a large impact on the deep Earth community, given they could not be explained by purely thermal

variations. The implication that the LLVPs were chemically distinct and long-term stable due to their higher density provided geochemists with a possible primordial reservoir in the mantle, prompting a range of geodynamic studies modeling thermochemical LLVPs (e.g., Tackley, 2002; McNamara & Zhong, 2004, 2005; Tan & Gurnis, 2005).

This model also immediately prompted a number of critical studies: Resovsky and Ritzwoller (1999) argued that the results were dependent on regularization, while both Masters et al. (2000b) and Romanowicz (2001) illustrated that the available data could not distinguish between different density scenarios. In addition, no clear correlation (positive or negative) is observed between CMB topography and density, which are expected to be dynamically related. However, subsequent studies of the same authors (Ishii & Tromp, 2001, 2004) again found dense LLVPs using different methodologies and parameterizations. The notion of dense LLVPs was confirmed by powerful probabilistic inversions of normal-mode data up to 3 mHz by Trampert et al. (2004) and Mosca et al. (2012), who also utilized mineral physics data to separately estimate the thermal and chemical contributions to density. Although these density models differ in pattern (Figure 9.2c) and show a larger degree-2 component (Figure 9.3c), all show a similar negative correlation with V_S structure (Figure 9.3f). Consequently, the debate regarding the LLVP density structure seemed settled.

9.3.2. Recent Studies Utilizing Improved Data Sets

In the last decade, splitting function data sets have improved with measurements up to higher frequencies (Deuss et al., 2013; Koelemeijer et al., 2013). Moulik & Ekström (2016) stressed the importance of utilizing multiple data sets, combining normal-mode measurements with body-wave and surface-wave data in their least-squares inversions, finding that dense anomalies in the lowermost mantle were necessary to fit their data (Figure 9.2c). Taking a different approach, Koelemeijer et al. (2017) instead focused on particular modes with unique sensitivity to lowermost mantle structure, so-called CMB Stoneley modes (Koelemeijer et al., 2013). Rather than performing a least-squares inversion, they performed a model space search of scaling factors with S -wave velocity. Their results showed two model classes, which have a similar degree-2 amplitude (Figures 9.2c and 9.3c), but are characterized by either dense (KDR2017-pos) or light (KDR2017-neg) LLVPs with an opposite relationship to CMB topography (Figure 9.3e, see also Section 9.2.3). The authors favored the models with light LLVPs and elevated topography based on geodynamic considerations (e.g., isostasy

dominating on these long wavelengths). However, depending on the density contrast and viscosity structure, topography may have a more complex relationship with velocity and density structure (Deschamps et al., 2018), casting doubt on these earlier interpretations. Irrespectively, the study by Koelemeijer et al. (2017) demonstrates the strong influence of CMB topography on density models, which cannot be ignored.

All density models discussed above have been based on splitting function measurements, which are generally obtained using a self-coupling or group-coupling approximation in which a mode or group of modes is treated as isolated (Dahlen & Tromp, 1998; Deuss & Woodhouse, 2001; Al-Attar et al., 2012). Al-Attar et al. (2012) showed that these approximations are not appropriate for studies of density, as the theoretical error due to using the approximation is of similar magnitude to the density signal itself. Akbarashrafi et al. (2017) demonstrated the limitations of self-coupled splitting functions in more practical applications, but their investigations were restricted to a selection of normal modes with primary sensitivity to V_S structure. Therefore, it remains to be investigated how appropriate the self-coupling approximation is in practical analysis of density studies that use higher-frequency and Stoneley modes. Fact remains nevertheless, that only even spherical harmonic degrees can be constrained while the self-coupling approximation is utilized.

9.3.3. New Developments in Density Studies

A new approach to constrain the density structure of the lower mantle was introduced by Lau et al. (2015), which makes use of satellite observations of the Earth's tides. These data are very sensitive to the degree-2 structure of the deep mantle, but contain little information on higher degree structure. Although the tidal signal is modeled using normal modes, it uses full-coupling instead of the self-coupling approximation. With this tidal tomography approach, Lau et al. (2017) performed a probabilistic study, finding dense LLVPs in the deepest mantle with a range of possible scaling factors (mean model shown in Figure 9.2c). As the model was developed using scaling factors to S -wave tomography models, it features a strong negative correlation between density and V_S (Figure 9.3f). It is worth noting that the dense-LLVP model by Koelemeijer et al. (2017, KDR2017-pos), which was also built using scaling factors, has a similar negative correlation, while other studies that did not use scaling factors have smaller values. This indicates that the model parameterization still has an important influence on current model results. Ding and Chao (2018) also deduced the presence of excess density in LLVP regions based on GPS observations and their correlation to periodic variations in the length-of-day. While these are very

promising developments, certain assumptions that may influence the results (atmospheric corrections, ocean tidal loading, influence of CMB topography) still require further investigation. The density structure of the deep mantle has been and will continue to be debated. Most studies report observations of dense LLVPs (Figure 9.2c), but it is unclear how much studies agree on the location of dense anomalies. In the following, I will investigate how consistent current density models are, indicate where some of the differences arise from, and finally discuss ways to reconcile these in future.

9.4. QUANTITATIVE ASSESSMENT OF EXISTING SEISMOLOGICAL MODELS

To identify similarities and differences in models of CMB topography and density, a more quantitative analysis is required than a visual inspection of Figures 9.2 and 9.3. I take a similar approach as previous studies for finding consistent features, following the work on the SMEAN model by Becker & Boschi (2002) and the vote map approach of Shephard et al. (2017) to develop average models and vote maps of CMB topography and density. These provide complementary information on model consistency as amplitudes are included in the computation of average models (i.e., a particular model may dominate), while vote maps are only based on patterns and relative amplitudes within models themselves.

Most models considered here are long-wavelength, global models, often derived from normal-mode data and/or defined by a set of spherical harmonic coefficients. Therefore, spherical harmonics are adopted here, which also facilitates to explore just the degree-2 signal of the LLVPs. Global models are thus expanded into spherical harmonics up to degree $l = 20$ and truncated at lower degree to reduce spectral aliasing. In the following, I will use $l_{cut} = 6$, as most models only describe heterogeneity up to $l = 4$ or $l = 6$ with not much power in higher degrees (Figure 9.3a–c).

Velocity and density are three-dimensional fields that vary with depth, while CMB topography only varies laterally. Given the primary interest in the relationship between CMB topography and density structure, a representative depth of 2800 km is considered only, thus treating velocity and density also as two-dimensional fields. Currently this is a justifiable choice, as most studies parameterise the density structure in thick layers of constant structure (e.g., Trampert et al., 2004; Koelemeijer et al., 2017; Lau et al., 2017), but depth variations will have to be considered when more complex seismological models become available. Furthermore, I only use lateral variations and consequently set the degree 0 coefficients to zero, with the importance of a nonzero radial average discussed in

Section 9.5. Note that for probabilistic studies (Trampert et al., 2004; Mosca et al., 2012; Koelemeijer et al., 2017; Lau et al., 2017) only the mean models are used here even though these studies provide model uncertainties.

I consider all available global models of density and CMB topography listed in Table 9.1. The topography model of Creager and Jordan (1986) is excluded due to its high amplitude and the interpretation by the authors that this cannot all be due to CMB topography. In addition, multiple models from a particular study are only included if they differ significantly in their methodology; i.e., both LGW1991-SAT and LGW1991-SAF (derived from normal-mode spectra or splitting functions) and both SBF2012-T and SBF2012-TGppv (developed using a seismic or coupled seismic-geodynamic approach). However, DH1989-M7 and SBF2012-TG are not included due to their strong similarity to DH1989-M6 and SBF2012-TGppv, respectively. Both model classes of Koelemeijer et al. (2017) are considered for density structure, as these models have a contrasting degree-2 component. For CMB topography, I only include KDR2017 though, as Stoneley mode data prefer this model and it has intermediate amplitudes compared to KDR2017-pos and KDR2017-neg (see Figure 9.2b). The final selection of models includes 10 CMB topography and 7 density models, which are indicated in bold in Table 9.1.

9.4.1. Cross-Model Correlation

The similarity of any two models is calculated using the correlation between their spherical harmonic expansions. The cross-model correlation for density is mostly positive for degree 2 (Figure 9.4a), with the exception of model KDR2017-neg as expected. However, the correlation of Metal2012 or ME2016 with IT1999 is also visibly lower. This is likely because the extrema in density are not collocated with the LLVPs for these models, as evident from the lower correlation between V_S and density structure (Figure 9.3f). The correlation between Letal2017 and KDR2017-pos is very high (0.96) for degree 2, as the studies use a similar approach in which they search for optimal scaling factors with velocity. The cross-model correlation is weaker when structure up to degree 6 is considered (Figure 9.4b), but it remains mostly positive.

CMB topography models do not display as much consistency as density models for degree-2 structure only or all structure up to degree 6 (Figure 9.4c–d), particularly when body-wave models are considered (top left quadrant of the plots). In contrary, normal-mode models are generally consistent (except for IT1999) and also correlate positively with SBF2012T and SBF2012TGppv (correlation values above 0.60). Therefore, when analyzing average models or vote maps, it will be important to consider

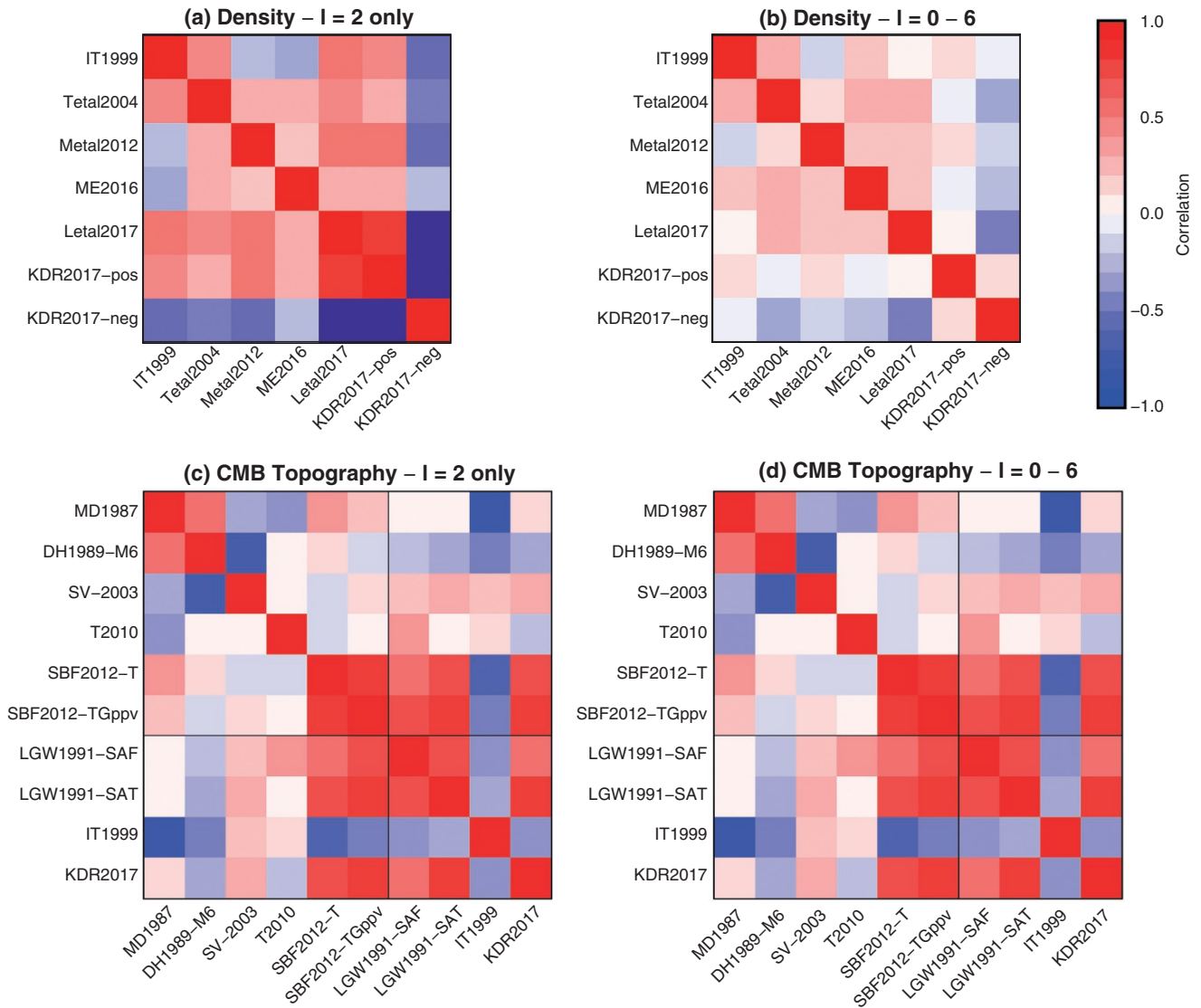


Figure 9.4 Cross-model correlation for global models included in Table 9.1 of (a–b) lowermost mantle density structure and (c–d) CMB topography, showing (a,c) the correlation for degree-2 structure only and (b,d) the correlation for structure up to degree 6. The thin black lines in (c–d) separate out body-wave models (top left) and normal-mode models (bottom right). Density models show a high cross-model correlation (particularly between Letal2017 and KDR2017-pos), with the exception of KDR2017-neg. Body-wave models of CMB topography do not show much consistency, but normal-mode models (except IT1999) have a high correlation. For structure up to degree 6, results are similar for CMB topography, whereas the correlation values are lower (albeit still positive) for density.

body-wave and normal-mode models separately, and to bear in mind that IT1999 stands out based on the cross-model correlation.

9.4.2. Average Models

Using insights from the previous section, I calculate average models for density and CMB topography for different selections of models. These average models should

not be interpreted as tomographic models themselves. Instead, they act merely as useful means to condense information from a suite of models.

Including either KDR2017-neg or KDR2017-pos to calculate the average density ($RMEAN_{neg}$ and $RMEAN_{pos}$ in Figure 9.5a) makes little difference, as only one out of six models is changed. Positive densities are observed under the North Pacific and Southern Africa (the rough locations of the LLVPs), as well as under

Indonesia and South America (where subducted material may be present), while negative anomalies are mainly found under the Indian Ocean and the poles. Due to inconsistencies between KDR2017-neg and the other models included, RMEAN_{neg} shows more small-scale variations compared to RMEAN_{pos} . Overall, observed amplitudes are reasonable (0.2–0.3 times V_S amplitudes), with maximum amplitudes of 0.6% relative to the radial average.

For CMB topography, average models based on normal-mode, body-wave data, or both, show similar amplitudes up to ~ 2.5 km, which is within the range suggested by Koelemeijer et al. (2012). There is a disparity between models based on normal modes (that show a ring of elevated topography around the North Pacific and Southern Africa) and those based on body waves (where the peaks in elevated topography are shifted – i.e., located more south in the Pacific and more north under Europe). TMEAN_{modes} features an interesting gap of depressed topography under southern Africa and the North Pacific. Before this feature is interpreted, it should be noted that IT1999 model differs from other models in having a large negative amplitude at these locations (see Figure 9.2b). TMEAN_{body} also shows hints of depressed topography under southern Africa and contains a pronounced area of elevated topography under northwestern Africa, which is observed in a few individual models as well.

9.4.3. Vote Maps of Density and CMB Topography

Following Shephard et al. (2017), I calculate vote maps of density and CMB topography using the same model selections. In constructing vote maps, only model amplitudes above a particular threshold are considered, which are assigned a unit vote. These are subsequently summed together for a particular selection of models (Shephard et al., 2017). Vote maps based on a positive mean (Figure 9.5b) allow the identification of higher-density anomalies and elevated topography. I also visualize “combined” vote maps in which vote maps based on a positive and negative mean are combined (Figure 9.5c), so that they can be more readily compared to average models (Figure 9.5a). Note that these vote maps do not serve to replace tomographic models, but merely serve to identify consistent model features.

For density, high vote locations are consistent with the average models, e.g., positive densities under the North Pacific and southern Africa and negative anomalies under the Indian Ocean and the Poles, with the addition of the East Pacific. The vote count increases when KDR2017-pos is included instead of KDR2017-neg, although this is more evident for degree-2 structure only. The strong similarity between RMEAN and RCOMBI implies that no particular model is dominating the results and that

there is large consistency between models. This allows locating the most robust dense anomalies, identified below southern Africa (around Angola and Namibia) and in the North Pacific (close to Hawaii).

For CMB topography, normal-mode models (TVOTE_{modes}) show strong agreement on the location of elevated topography in the central Pacific and central Africa, while they also agree on the location of depressions under Australia and Central America. On the contrary, body-wave models (TVOTE_{body}) show less agreement, evidenced by a lower vote number, but several of these models indicate elevated topography under the Pacific as well. The vote maps further strengthen the notion of a disparity between normal-mode and body-wave models, with a shift in the location of elevated topography. The low vote count in TVOTE_{all} and TCOMBI_{all} reflects this disagreement, which needs to be resolved in future studies.

Finally, the disagreement between TMEAN and TCOMBI models raises the suspicion that average models are dominated by particular models, likely MD1987 and IT1999, which have large amplitudes and are poorly correlated to other topography models (Figure 9.4). The distinct ring of elevated topography in TMEAN_{modes} , which coincides with the location of high density anomalies, is not present in TVOTE_{modes} and TCOMBI_{modes} . This implies that this is due solely to poor agreement between IT1999 and other models. This serves as a reminder of why average models should be treated with care and why vote maps may be more reliable for finding consistent features, even though they do not provide amplitude information.

9.4.4. Comparison to Geodynamic Predictions

As mentioned in Section 9.2.5, Deschamps et al. (2018) suggested that the correlation between V_S and CMB topography provides constraints on the density structure of the lowermost mantle. This study thus provides seismologists a simple metric to compare results to without necessarily having constraints on the density structure. Of course, this is only one way of comparing geodynamic predictions with seismology, and the results will inevitably be dependent on the parameters and assumptions of the geodynamic simulations (e.g., Rayleigh number, viscosity structure, mineral physics conversions), which may particularly impact the resulting topography amplitudes and implied chemical density difference. Nevertheless, if we are to make progress in constraining deep mantle structures, such simple metrics and comparisons will be crucial.

For purely thermal (TH) models, mantle flow enhances isostatic topography so that plumes cause positive topography, while increased temperatures lead to slower seismic velocity variations. Consequently, a negative V_S -topography correlation is expected. For thermochemical models (TC), an increased intrinsic density depresses the

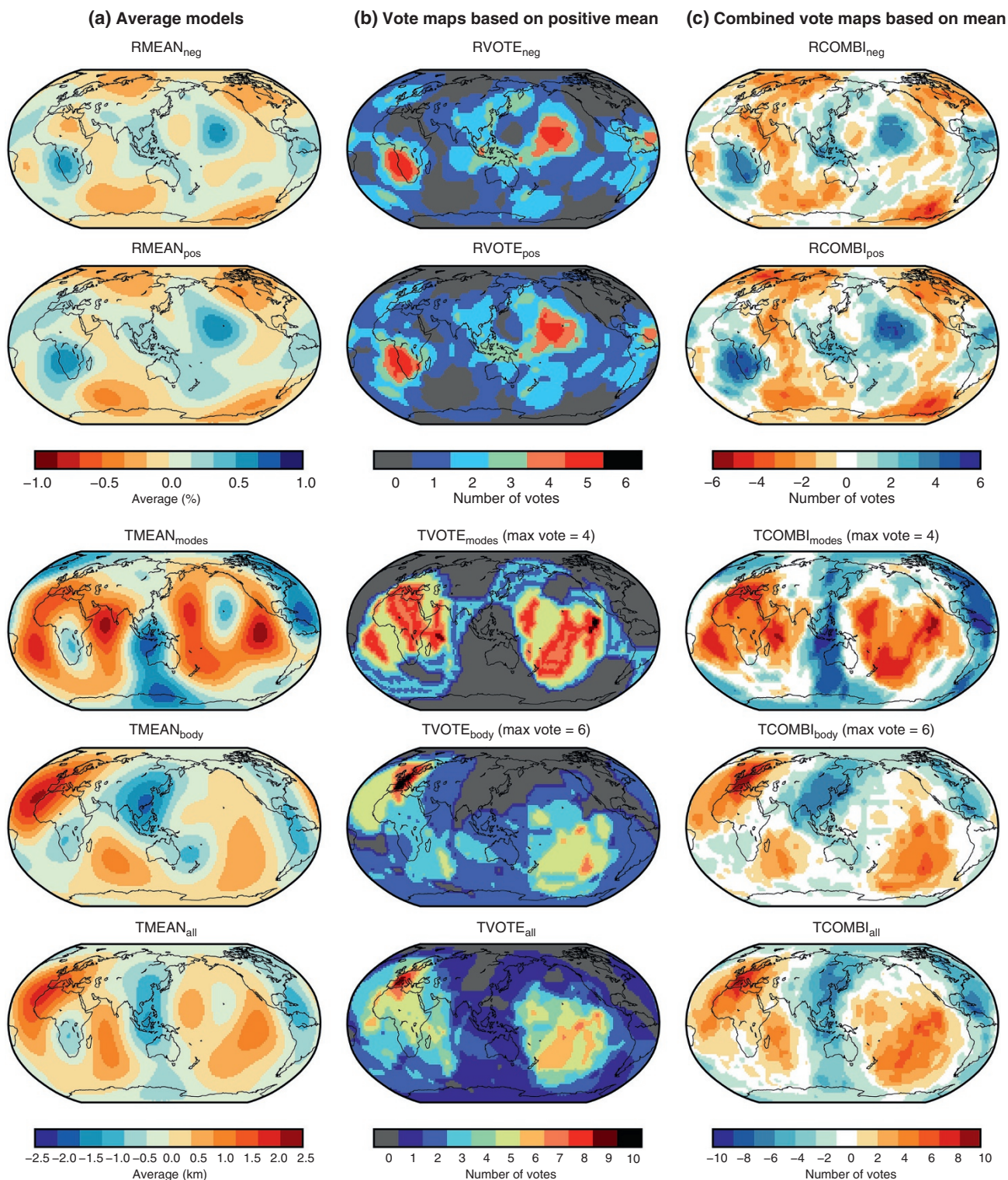


Figure 9.5 Summary models of lowermost mantle density structure (top two rows) and CMB topography (bottom three rows) based on global models indicated in bold in Table 9.1, showing (a) average models (“MEAN”) computed similarly to Becker and Boschi (2002), (b) vote maps based on positive anomalies (“VOTE”) and (c) combined vote maps based on both positive and negative anomalies (“COMBI”), computed following Shephard et al. (2017). For density, the only difference between the top and bottom row is the inclusion of KDR2017-neg instead of KDR2017-pos besides 5 other models. For CMB topography, summary models are shown for models based on normal-mode data (including the KDR2017 model), based on body-wave data or using all models. In the computation of average models, amplitudes are included and it is possible for one model to dominate the results, while vote maps are only based on patterns and amplitude distribution within the models. Note the difference in maximum vote for vote maps based on body-wave (6) and normal-mode (4) data.

boundary through isostatic compensation, which is balanced by flow-induced dynamic topography (as hotter piles tend to rise, stretching the CMB upward and strongly reducing the depression due to their weight). The net effect depends on the density difference between thermochemical piles and the surrounding mantle and the wavelengths we are considering. On long wavelengths, due to a smoothing effect, small-scale variations will be averaged out, even when the largest topography amplitudes may be outside the piles. Deschamps et al. (2018) found that for a density difference $\delta\rho_C < 100 \text{ kg/m}^3$ (weakly thermochemical), the long-wavelength topography component is positive beneath piles leading to an anti-correlation with V_S anomalies. On the contrary, for a large density contrast $\delta\rho_C > 100 \text{ kg/m}^3$ (strongly thermochemical models), hot iron-enriched piles depress the CMB and have slow seismic velocities, so that V_S anomalies and CMB topography are strongly correlated. While uncertainties in thermal viscosity contrast and the presence of post-perovskite influence the topography-velocity relationships, Deschamps et al. (2018) and Deschamps and Li (2019) mapped out the ranges of resulting possibilities, which are shown in Figure 9.6. These predictions are compared to the seismological models presented here, considering both the V_S -topography correlation and peak-to-peak amplitudes of CMB topography. Note that this correlation is only computed for one particular depth, while the structures in the Earth are expected to vary with depth as well.

Most seismological models feature a peak-to-peak CMB topography below 4.7 km for degree 2 (Figure 9.6a), with the exception of IT1999, a model that shows poor consistency to others (Figure 9.2 and 9.4). These amplitudes can be reproduced by a range of geodynamic scenarios, including TH, weakly TC and strongly TC models. A larger range is found for structures up to degree 4 (Figure 9.6b), with amplitudes up to ~ 12 km (excluding IT1999). However, if only models since 2000 are considered, which have utilized more recent mantle models for velocity corrections, only amplitudes up to ~ 7 km are found. Irrespective of which models are considered, several geodynamic scenarios produce similar values, leading to the same conclusion as previous studies (Lassak et al., 2010; Deschamps et al., 2018); that peak-to-peak topography amplitudes cannot discriminate between thermal and thermochemical structures. Note, however, that for structures up to degree 4, seismological models tend to show smaller amplitudes than those predicted, particularly for normal-mode based models, although the predicted amplitudes may be overestimates depending on the Rayleigh number of the simulations (Liu & Zhong, 2015).

The correlation between velocity and CMB topography is mostly negative or close to zero, although it spans a wide range (Figure 9.6c). Considering only models that

demonstrated consistency in the cross-model correlation (Figure 9.4), the V_S -topography correlation is lower than -0.4 , which would rule out strongly TC models with $\delta\rho_C > 100 \text{ kg/m}^3$ (though the exact value will depend on the Rayleigh number of the simulations). While this inference is based mostly on models derived from normal-mode data, these have the advantage that they provide global coverage, have a clear sensitivity to CMB topography, and make fewer approximations in the theoretical treatment. In addition, several body-wave models show similar relationships; for example, Soldati et al. (2003) found a strong negative correlation in their joint inversions of CMB topography and velocity. The V_S -topography correlation for the average (MEAN) and vote map (COMBI) models of Figure 9.5 support this notion, with values of -0.52 and -0.75 , respectively. These values only fall within the range of geodynamic predictions for TH or weakly TC models with a large thermal viscosity contrast, with or without post-perovskite, suggesting that strongly thermochemical models are inconsistent with seismological constraints on CMB topography. However, current models still span a wide range in peak-to-peak amplitudes and correlation values, preventing us from drawing more decisive conclusions regarding the state of the lower mantle. Naturally, these inferences will require reconsideration when improved seismological models of CMB topography become available.

9.4.5. Summary of Current Model Features

A number of inferences can be drawn from the average models and vote maps of lower mantle density structure and CMB topography introduced here:

- For density, average models and vote maps consistently identify two areas of dense anomalies; one located below southern Africa (around Angola), roughly in the core of the LLVP imaged in seismic velocity. The other one is found under the North Pacific (close to Hawaii), located more on the edge of the LLVP as imaged in seismic velocity.
- Considering both model classes of Koelemeijer et al. (2017) allows to resolve recent results based on Stoneley modes and tidal measurements (Lau et al., 2017). The cross-model correlation between Letal2017 and KDR2017-pos is particularly high (0.96 for degree 2) as the two studies employ a similar scaling to velocity.
- Topography models mostly show elevated topographies under the Pacific and Africa, but details differ between average models and vote maps. All models have a peak-to-peak amplitude below 4.7 km for degree 2, with the exception of the IT1999 model, that also appears inconsistent with other normal-mode models.

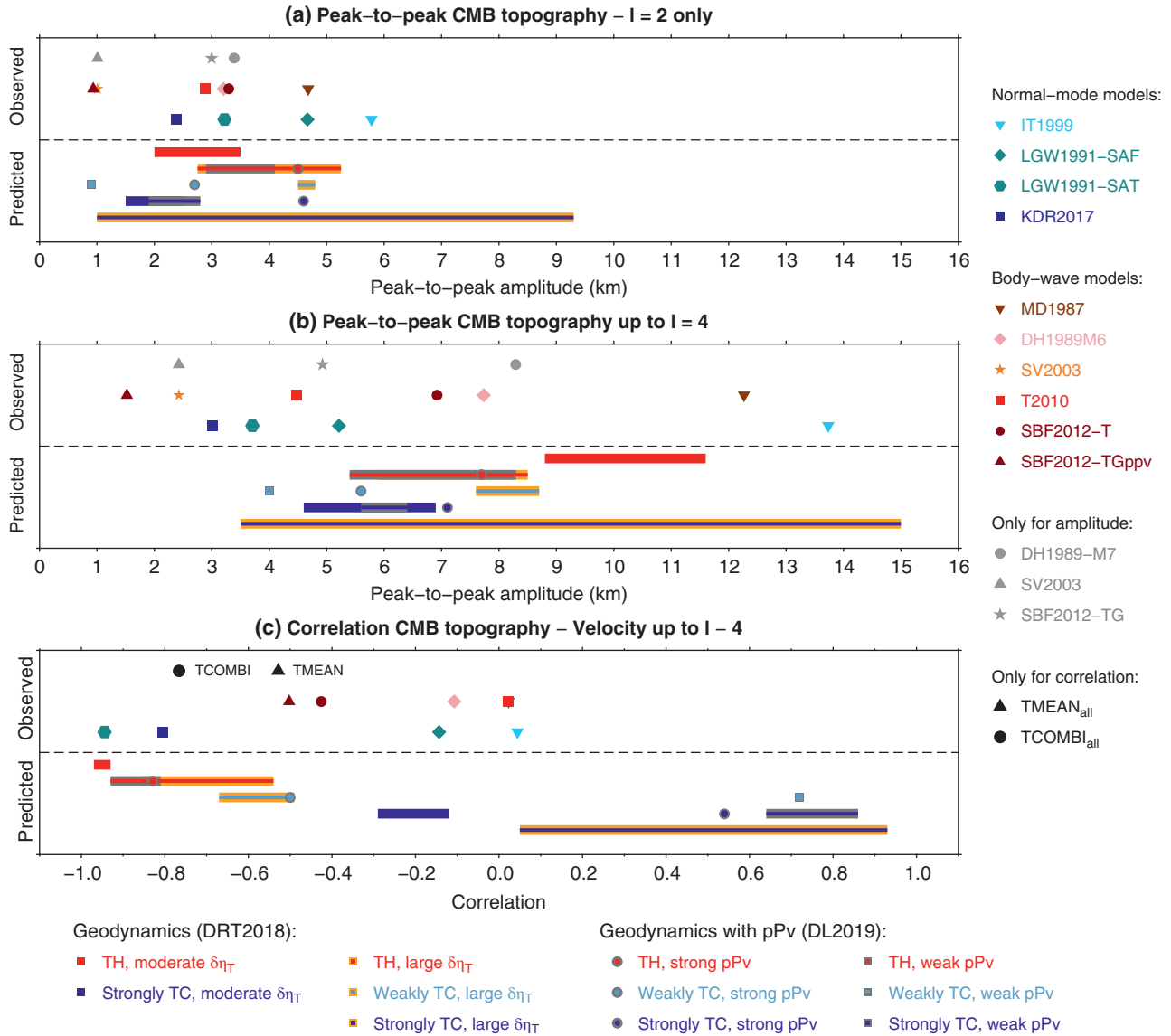


Figure 9.6 Comparison between seismic constraints and geodynamic predictions calculated on the same length scales, showing (a) degree 2 and (b) degree 4 peak-to-peak CMB topography amplitudes and (c) the correlation of topography with velocity structure at 2800 km depth. Geodynamic predictions are taken from Deschamps et al. (2018, DRT2018) and Deschamps and Li (2019, DL2019). DRT2018 computed properties for purely thermal (TH) models and strongly thermochemical (TC) models ($\delta\rho_C \geq 100 \text{ kg/m}^3$) with a moderate ($\delta\eta_T = 10^6$) or large ($\delta\eta_T \geq 10^9$) thermal viscosity contrast, as well as for a weak TC model ($\delta\rho_C \leq 100 \text{ kg/m}^3$) with a strong thermal viscosity contrast ($\delta\eta_T \geq 10^9$). DL2019 followed up on these results by including post-perovskite (pPv) with a viscosity difference of 1 (strong pPv) or ranging between 10^{-1} and 10^{-3} (weak pPv) at the same time as a large thermal viscosity contrast ($\delta\eta_T \geq 10^9$). The correlation between velocity and CMB topographic variations is only computed for models that provide both or use a known velocity model. I compute the correlation with V_S variations for normal-mode models, whereas for body-wave models I show the correlation with V_P variations, as these are constructed from P-wave sensitive data. Given the large positive correlation between lower mantle P- and S-wave models, this does not make a large difference. Corresponding values for the average models and vote maps developed in this study (TMEAN-SMEAN and TCOMBI-SCOMBI) are shown as well. These are only given for topography-velocity correlation (c), as amplitudes are only constrained in average models, which are biased by particular large-amplitude models.

- A discrepancy is observed between body-wave and normal-mode models of CMB topography, with normal-mode models showing a stronger relationship with velocity structure.
- The correlation between current models of CMB topography and V_S shows a range of values, but tends to be mostly negative.
- Although unique interpretations are difficult, a comparison with recent work by Deschamps et al. (2018) suggests that strongly thermochemical models are inconsistent with current seismological models.

The fact that the studies of Koelemeijer et al. (2017) and Lau et al. (2017) can be reconciled when a different relationship to CMB topography is adopted is a step forward to building consistent models of the deep mantle. It will thus be crucial to develop robust models of CMB topography that are compatible with a range of data: reflected and refracted body waves, normal modes, and geodetic data, in addition to developing improved density models.

9.5. EFFORTS TOWARD MORE CONSISTENT MODELS

Here, I first discuss several factors that I believe are important to consider when interpreting density models, followed by suggestions for the future development of consistent density and CMB topography models.

9.5.1. Factors Influencing the Interpretation of Density Models

In visualizations of seismic models, we tend to plot lateral variations with respect to a radial average, which may be significantly different from zero. Particularly, several normal-mode studies have found a positive density in the lowest 150–500 km of the mantle compared to the PREM model (Dziewonski & Anderson, 1981), ranging in amplitude between 0.1% and 0.6% (Montagner & Kennett, 1996; Masters & Gubbins, 2003; De Wit et al., 2014). When thinking about the buoyancy of the LLVPs, these constraints on the radial density structure should be integrated in interpretations. It also remains important to consider the dynamic implications of density variations in regions surrounding the LLVPs (e.g., if these constitute of colder, subducted slabs), we may expect them to be denser. Furthermore, the LLVPs are likely very three-dimensional structures, with possibly near neutral buoyancy and density variations within (Mulyukova et al., 2015; Li et al., 2018). Current density models that often have thick constant layers should thus be interpreted with caution, as they represent depth averages of complex structures.

Unraveling the relative importance of thermal and chemical contributions to density as imaged in tomography is not straightforward. Advances in mineral physics

will have to be made to reduce uncertainties in partial derivatives that are needed to relate variations in temperature and chemical composition to seismic velocity and density. Another difficulty in interpreting density results arises when models provide a range of possibilities (Koelemeijer et al., 2017; Lau et al., 2017) or a mean model with uncertainties (Trampert et al., 2004; Mosca et al., 2012). These approaches are very powerful and clearly the way forward, especially when combining multiple data sets with different sensitivities. In such probabilistic studies, care should be taken in communicating the results to ensure that both the model and the uncertainties are fully exploited in subsequent work.

We should also consider the effect that the transition from bridgmanite to post-perovskite (~ 0.5 – 1.5% increase in density, Murakami et al., 2004; Oganov and Ono, 2004; Tsuchiya et al., 2004; Cobden et al., 2015) may have on our interpretations. Even if post-perovskite is only present in colder (fast-velocity) regions, this will affect the radial average at those depths, which leads to a bias in interpretations of lateral variations (Styles et al., 2011). In addition, the presence of weak pPv will influence lower mantle dynamics and alter the relationships between velocity, density, and CMB topography (Deschamps and Li, 2019).

Finally, we tend to think of the African and Pacific LLVP as two of the same kind. This is partly because many older V_S models (and most density models) utilized normal-mode data that only provided even-degree constraints, thus resulting in an inherent symmetry. However, such an even-degree expansion may no longer be warranted, given that density anomalies change from positive to negative within the Pacific LLVP, while they are collocated for the African LLVP (Figure 9.5). In addition, V_S and V_P anomalies show a consistent pattern for the African LLVP, but the extrema seem shifted with respect to each other for the Pacific LLVP (Figure 9.1). This suggests that the Pacific anomaly locations are not as well constrained as under Africa, with possible artefacts due to the even-degree expansion of the data and models. In interpreting these anomalies, it is thus important to always verify that the relationships between velocity, density, and topography are consistent with our understanding of mineral physics and mantle dynamic processes. To improve our understanding of lower mantle dynamics, we may have to move away from even-degree expansions and consider different explanations for the African and Pacific LLVP.

9.5.2. Future Development of Density Models

Several avenues can be followed to improve density models and reconcile present model differences, both in terms of theory and methodology.

Most importantly, to reduce theoretical errors (Al-Attar et al., 2012), it is crucial to perform direct spectral inversions using full-coupling instead of using self-coupled splitting function measurements. Ideally, in order to reconcile differences with current models, the results of such spectral inversions will be compared to models developed using self-coupled splitting functions based on the same spectra, similar to Li et al. (1991). At the same time, the robustness of current self- and group-coupled splitting function measurements (particularly Stoneley modes) should be assessed, similar to what has been done for a selection of V_S - and V_P -sensitive modes (Akbarashrafi et al., 2017). An increased availability of geodetic data will enable more detailed tidal tomography studies, which provide independent constraints on density. By combining insights and constraints from such different data sets (including gravity), future studies should be able to resolve the trade-off between density and CMB topography and narrow down the available parameter space.

Past studies have taken different approaches to solving the inverse problem, mostly adopting a least-squares inversion (e.g., Ishii and Tromp, 1999; Moulik and Ekström, 2016) or performing probabilistic model space searches (e.g., Trampert et al., 2004; Mosca et al., 2012; Koelemeijer et al., 2017; Lau et al., 2017). The data sets utilized in these studies differ in quantity, quality, and type; older studies only had normal-mode data up to 3 mHz available (Ishii and Tromp, 1999; Trampert et al., 2004), while recent studies have focused on different normal modes that vary in their sensitivity to density. Moulik and Ekström (2016) emphasized the importance of mode ${}_0S_2$, Koelemeijer et al. (2017) focused their analysis on CMB Stoneley modes, while Lau et al. (2017) include 16 modes in their modeling. Understanding the implications of these subjective choices and testing their effect in future inversions, ideally through comprehensive studies in which different mode selections, data uncertainties, and inverse techniques are compared, will be important to reconcile current differences.

Choices regarding the vertical and lateral parameterization should also be carefully considered. A finer depth parameterization than in previous studies has to be incorporated to find out the depth extent of any dense material within the LLVPs, such as whether it is confined to a thin layer at the bottom or several hundreds kilometers thick (Romanowicz, 2017). As the density structure is likely to have strong three-dimensional variations, it will be important to determine which parts of the LLVPs (if any) are neutrally buoyant (Mulyukova et al., 2015; Li et al., 2018). The choice of lateral parameterization also influences inversion results (discussed in Section 9.4), while it should be remembered that global correlation

values are not just affected by the LLVPs. Particularly, the scaling of density to velocity may result in unrealistic scenarios; if the lowest velocities in the center of the LLVPs represent the highest temperatures, we would expect an overall zero density anomaly instead of finding the strongest density anomalies in the center as well. In such a scenario, even though the strongest anomalies are found near the edges of the LLVPs, the degree-2 component may still show a higher density, which is compensated by higher degree structure (as is the case for the KDR2017-pos density model).

Finally, unmodeled complexities (e.g., anisotropy, discontinuity topography, source complexity, scattering, and focusing effects) should also be considered in future inversions, as these trade off with density (Moulik and Ekström, 2016). Particularly, the work by Koelemeijer et al. (2017) and earlier results from Koelemeijer et al. (2012) demonstrate the strong trade-offs between CMB topography and density structure. Including CMB topography in future inversion for density will not only help to reconcile current models but also aid in distinguishing different dynamic scenarios by analysing the relationship of CMB topography and velocity.

9.5.3. Developing Consistent CMB Topography Models

Seismological inferences of CMB topography will always be complicated by trade-offs with lower mantle and outermost core structure. Particularly for PmKP waves and Stoneley modes, it will be important to consider the possibility of both radial and lateral structures at the top of the outer core. Ideally, studies should consider the two boundary regions of CMB together instead of treating them separately. Such efforts will also aid in reconciling inferences from body-wave and normal-mode data.

Instead of ray theory, body-wave studies should make use of finite-frequency theory, including joint volumetric and topographic kernels (Colombi et al., 2014). The choice of phases in these endeavors will be important, as reflected phases will provide good constraints on short-scale structure and amplitudes, while diffracted phases will aid in constraining long-wavelength structures and patterns (Colombi et al., 2012). Differential measurements of exotic phases (e.g., PK4P-P or PK7P-PK4P) form useful complementary data, but complicate interpretation due to their multiple bounce points. Similar to studies of dynamic surface topography (see Austermann & Hoggard, this volume), care should be taken when laterally expanding body-wave data to prevent spurious amplitudes (Pulliam & Stark, 1993) and an apparent consistency between models (Stark and Hengartner, 1993).

Normal modes have an important role to play in constraining long-wavelength topographic variations. Current available data sets of splitting function measurements have not yet been fully exploited and can be used to develop improved normal-mode based models. Although the treatment of lower mantle density structure should be an important consideration in such studies, Koelemeijer et al. (2017) demonstrate that relatively consistent CMB topography models are obtained independently of density. In addition, improved normal-mode models of CMB topography may provide additional constraints on lower mantle density (Deschamps et al., 2018), warranting intensified efforts.

Ideally, body-wave and normal-mode data are exploited together to build a consistent model of CMB topography, either through joint inversions or combined model space searches. In these studies, it will be crucial to address differences in length scales and to perform joint inversions of CMB topography and structure in the lower mantle and outermost core. If the largest topography amplitudes are on the side of or outside the LLVPs (Liu & Zhong, 2015), normal modes would provide a smooth representation of this topography, which should be combined with spot measurements using body waves to find these extreme topography amplitudes (similar to Wu et al., 2014). Such a focus on specific regions with good data coverage will also enable the use of appropriate theory for the treatment of body-wave data. With advances in computing power and data coverage, it may be possible in the future to expand such an approach to the entire surface of the CMB.

9.5.4. Integrating Seismology With Other Constraints

In this contribution, I have quantitatively compared seismological models with insights from geodynamics, utilizing the correlation between velocity and CMB topography as suggested by Deschamps et al. (2018). While the results of these comparisons (e.g., the maximum chemical density contrast $\delta\rho_C$) will depend on the parameters of the geodynamic simulations and approximations, such a simple metric provides seismologists a powerful tool to compare observations to. Naturally, when new seismological models are available, other inferences may be drawn.

In future studies, it will be crucial to integrate geodetic data and insights from geodynamics with seismological observations. In order to achieve this, improved estimates of mantle viscosity as well as smaller uncertainties in mineral physics will be required. Especially, obtaining a sufficient fit to the geoid as well as satisfying constraints on excess ellipticity from nutation data at the same time as seismological data will be a challenge. Therefore, it would be best to take a probabilistic approach so that the different data uncertainties can be included. This will

likely be the only way to make substantial progress in studies of lower mantle density and CMB topography.

9.6. CONCLUSIONS

Robust models of lower mantle density and CMB topography provide vital information on mantle upwellings and dynamics. Despite studies spanning several decades, models still lack consistency in both pattern and amplitude. Most density models find two areas of dense anomalies roughly co-located with the LLVPs imaged in *S*- and *P*-wave velocity models, but details vary and the effect of CMB topography on the retrieved density structure requires more investigation. Current models of CMB topography differ in their patterns but generally feature elevated topography at LLVP locations, and most have a degree-2 peak-to-peak amplitude below 4.7 km.

Lower mantle models of *S*-wave and *P*-wave velocity have converged more and more in the last 10 years, so how do we achieve the same for models of lower mantle density and CMB topography? Future studies of density should not only utilize improved normal mode theory and the advances in computation power, but also investigate the effects of subjective choices (e.g., data, parameterization) and combine several seismological and geodetic data types to break trade-offs with CMB topography. Simultaneously, efforts to obtain independent constraints on CMB topography should be intensified, particularly with the aim to develop models that are consistent with both body-wave and normal-mode data across a range of wavelengths. Such consistent models of the seismological landscape of the CMB will not only provide insights into lowermost mantle dynamics but also be important for studies of outer core flow, inner core structure, and evolution.

ACKNOWLEDGMENTS

The author thanks the associate editor (Sanne Cottaar), Satoru Tanaka, and two anonymous reviewers for their constructive comments, which have improved this manuscript. The author is funded by a Royal Society University Research Fellowship (URF\R1\180377) and gratefully acknowledges their support. This work has also received support from a Junior Research Fellowship awarded by University College, Oxford. The author is grateful to Ed Garnero, Frédéric Deschamps, Jeff Winterbourne, Jeroen Ritsema, Arwen Deuss, Harriet Lau, and Raj Moulik for stimulating discussions. Thanks also to all authors of CMB topography, velocity, and density models for sharing their models and insights. Figures have been produced using the Generic Mapping Tools (GMT) version 5 software (Wessel et al., 2013).

REFERENCES

- Akbarashrafi, F., Al-Attar, D., Deuss, A., Trampert, J., & Valentine, A. (2017). Exact free oscillation spectra, splitting functions and the resolvability of Earth's density structure. *Geophysical Journal International* 213 (1), 58–76.
- Al-Attar, D., Woodhouse, J., & Deuss, A. (2012). Calculation of normal mode spectra in laterally heterogeneous Earth models using an iterative direct solution method. *Geophysical Journal International* 189 (2), 1038–1046.
- Aleshin, H., & Vinnik, L. (1975). The topography of the core–mantle interface. *Bull. Acad. Sci. USSR, Phys. Solid Earth* 11 (7).
- Asari, S., Shimizu, H., & Utada, H. (2006). Variability of the topographic core–mantle torque calculated from core surface flow models. *Phys. Earth Planet. Inter.* 154 (1), 85–111.
- Auer, L., Boschi, L., Becker, T., Nissen-Meyer, T., & Giardini, D. (2014). Savani: A variable resolution whole-mantle model of anisotropic shear velocity variations based on multiple data sets. *J. Geophys. Res.* 119 (4), 3006–3034.
- Austermann, J., Kaye, B. T., Mitrovica, J. X., & Huybers, P. (2014). A statistical analysis of the correlation between large igneous provinces and lower mantle seismic structure. *Geophysical Journal International* 197 (1), 1–9.
- Bacchetta, A., Colangelo, L., Canuto, E., Dionisio, S., Massotti, L., Novara, C., et al. (2017). From GOCE to NGGM: Automatic Control Breakthroughs for European future Gravity Missions. *IFAC-PapersOnLine* 50 (1), 6428–6433.
- Bataille, K., & Flatté, S. M. (1988). Inhomogeneities near the core–mantle boundary inferred from short-period scattered PKP waves recorded at the global digital seismograph network. *J. Geophys. Res.* 93 (B12), 15057–15064.
- Bataille, K., Wu, R., & Flatte, S. (1990). Inhomogeneities near the core–mantle boundary evidenced from scattered waves: A review. *Pure Appl. Geophys.* 132 (1–2), 151–173.
- Becker, T., & Boschi, L. (2002). A comparison of tomographic and geodynamic mantle models. *Geophys. Geochem. Geosys.* 3 (1), 1003.
- Boschi, L., & Dziewonski, A. M. (2000). Whole Earth tomography from delay times of P, PcP, and PKP phases: Lateral heterogeneities in the outer core or radial anisotropy in the mantle? *J. Geophys. Res.* 105 (B6), 13675–13696.
- Bower, D. J., Gurnis, M., & Seton, M. (2013). Lower mantle structure from paleogeographically constrained dynamic Earth models. *Geophys. Geochem. Geosys.* 14 (1), 44–63.
- Buffett, B. (2015). Core–mantle interactions. In: Schubert, G. (Ed.), *Treatise on Geophysics*. Vol. 8. Elsevier, pp. 213–224.
- Burdick, S., Vernon, F. L., Martynov, V., Eakins, J., Cox, T., Tytell, J., et al. (2017). Model update May 2016: Upper-mantle heterogeneity beneath North America from travel-time tomography with global and USArray data. *Seism. Res. Lett.* 88 (2A), 319–325.
- Burke, K., Steinberger, B., Torsvik, T. H., & Smethurst, M. A. (2008). Plume generation zones at the margins of large low shear velocity provinces on the core–mantle boundary. *Earth and Planetary Science Letters* 265 (1), 49–60.
- Calkins, M. A., Noir, J., Eldredge, J. D., & Aurnou, J. M. (2012). The effects of boundary topography on convection in Earth's core. *Geophysical Journal International* 189 (2), 799–814.
- Cesare, S., & Sechi, G. (2013). Next generation gravity mission. In: *Distributed Space Missions for Earth System Monitoring*. Springer, pp. 575–598.
- Chang, A. C., & Cleary, J. R. (1978). Precursors to PKKP. *Bull. Seismol. Soc. Am.* 68 (4), 1059–1079.
- Chang, A. C., & Cleary, J. R. (1981). Scattered PKKP: Further evidence for scattering at a rough core–mantle boundary. *Phys. Earth Planet. Inter.* 24 (1), 15–29.
- Chang, S.-J., Ferreira, A. M., Ritsema, J., Heijst, H. J., & Woodhouse, J. H. (2015). Joint inversion for global isotropic and radially anisotropic mantle structure including crustal thickness perturbations. *Journal of Geophysical Research: Solid Earth*.
- Cleary, J., & Haddon, R. (1972). Seismic wave scattering near the core–mantle boundary: a new interpretation of precursors to PKP. *Nature* 240 (5383), 549.
- Cobden, L., Thomas, C., & Trampert, J. (2015). Seismic detection of post-perovskite inside the Earth. In: Khan, A., Deschamps, F. (Eds.), *The Earth's heterogeneous mantle*. Springer, pp. 391–440.
- Colombi, A., Nissen-Meyer, T., Boschi, L., & Giardini, D. (2012). Seismic waveform sensitivity to global boundary topography. *Geophysical Journal International* 191 (2), 832–848.
- Colombi, A., Nissen-Meyer, T., Boschi, L., & Giardini, D. (2014). Seismic waveform inversion for core–mantle boundary topography. *Geophysical Journal International* 198 (1), 55–71.
- Cottaar, S., & Lekic, V. (2016). Morphology of seismically slow lower-mantle structures. *Geophysical Journal International* 207 (2), 1122–1136.
- Creager, K., Jordan, T. (1986). Aspherical structure of the core–mantle boundary from PKP travel times. *Geophys. Res. Lett.* 13 (13), 1497–1500.
- Dahlen, F., Tromp, J. (1998). *Theoretical global seismology*. Princeton University Press.
- Davies, C. J., Stegman, D. R., Dumberry, M. (2014). The strength of gravitational core–mantle coupling. *Geophys. Res. Lett.* 41 (11), 3786–3792.
- Davies, D., Goes, S., Sambridge, M. (2015a). On the relationship between volcanic hotspot locations, the reconstructed eruption sites of large igneous provinces and deep mantle seismic structure. *Earth Planet. Sci. Lett.* 411, 121–130.
- Davies, D. R., Goes, S., Davies, J. H., Schubert, B. S. A., Bunge, H., & Ritsema, J. (2012). Reconciling dynamic and seismic models of Earth's lower mantle: The dominant role of thermal heterogeneity. *Earth Planet. Sci. Lett.* 353, 253–269.
- Davies, D. R., Goes, S., & Lau, H. C. P. (2015b). Thermally Dominated Deep Mantle LLSVPs: A Review. In: Khan, A., Deschamps, F. (Eds.), *The Earth's Heterogeneous Mantle*. Springer International Publishing, pp. 441–477.
- De Wit, R., Käufel, P., Valentine, A., & Trampert, J. (2014). Bayesian inversion of free oscillations for Earth's radial (an)-elastic structure. *Phys. Earth Planet. Inter.* 237, 1–17.
- Dehant, V., Laguerre, R., Requier, J., Rivoldini, A., Triana, S. A., Trinh, A., et al. (2017). Understanding the effects of the

- core on the nutation of the Earth. *Geodesy and Geodynamics* 8 (6), 389–395.
- Deschamps, F., Kaminski, E., & Tackley, P. J. (2011). A deep mantle origin for the primitive signature of ocean island basalt. *Nature Geosci.* 4 (12), 879.
- Deschamps, F., & Li, Y. (2019). Core–mantle boundary dynamic topography: influence of post-perovskite viscosity. *J. Geophys. Res.*, 9247–9264.
- Deschamps, F., Rogister, Y., & Tackley, P. J. (2018). Constraints on core–mantle boundary topography from models of thermal and thermochemical convection. *Geophysical Journal International* 212 (1), 164–188.
- Deschamps, F., & Trampert, J. (2003). Mantle tomography and its relation to temperature and composition. *Phys. Earth Planet. Inter.* 140 (4), 277–291.
- Deuss, A., Ritsema, J., & van Heijst, H.-J. (2013). A new catalogue of normal-mode splitting function measurements up to 10 mHz. *Geophysical Journal International* 192 (3), 920–937.
- Deuss, A., & Woodhouse, J. (2001). Theoretical free-oscillation spectra: the importance of wide band coupling. *Geophysical Journal International* 146 (3), 833–842.
- Ding, H., & Chao, B. F. (2018). A 6-year westward rotary motion in the Earth: Detection and possible MICG coupling mechanism. *Earth Planet. Sci. Lett.* 495, 50–55.
- Doornbos, D. (1974). Seismic wave scattering near caustics: Observations of PKKP precursors. *Nature* 247 (5440), 352.
- Doornbos, D. (1976). Characteristics of lower mantle inhomogeneities from scattered waves. *Geophysical Journal International* 44 (2), 447–470.
- Doornbos, D. (1978). On seismic-wave scattering by a rough core–mantle boundary. *Geophysical Journal International* 53 (3), 643–662.
- Doornbos, D. (1980). The effect of a rough core–mantle boundary on PKKP. *Phys. Earth Planet. Inter.* 21 (4), 351–358.
- Doornbos, D., & Hilton, T. (1989). Models of the core–mantle boundary and the travel times of internally reflected core phases. *J. Geophys. Res.* 94 (B11), 15741–15751.
- Doornbos, D., & Vlaar, N. (1973). Regions of seismic wave scattering in the Earth’s mantle and precursors to PKP. *Nature Phys. Sci.* 243 (126), 58.
- Durand, S., Debayle, E., Ricard, Y., Zanolli, C., & Lambotte, S. (2017). Confirmation of a change in the global shear velocity pattern at around 1000 km depth. *Geophysical Journal International* 211 (3), 1628–1639.
- Dziewonski, A., & Anderson, D. (1981). Preliminary reference Earth model. *Phys. Earth Planet. Inter.* 25 (4), 297–356.
- Dziewonski, A. M., Lekić, V., & Romanowicz, B. A. (2010). Mantle anchor structure: An argument for bottom up tectonics. *Earth Planet. Sci. Lett.* 299 (1), 69–79.
- Earle, P. S., & Shearer, P. M. (1998). Observations of high-frequency scattered energy associated with the core phase PKKP. *Geophys. Res. Lett.* 25 (3), 405–408.
- Emmerich, H. (1993). Theoretical study on the influence of CMB topography on the core reflection ScS. *Phys. Earth Planet. Inter.* 80 (3–4), 125–134.
- Forte, A. (2007). Constraints on seismic models from other disciplines – Implications for mantle dynamics and composition. In: Dziewonski, A., Romanowicz, B. (Eds.), *Treatise on Geophysics*. Vol. 1. Elsevier, pp. 805–858.
- Forte, A., & Mitrovica, J. (2001). Deep-mantle high-viscosity flow and thermochemical structure inferred from seismic and geodynamic data. *Nature* 410 (6832), 1049–1056.
- Forte, A., Mitrovica, J., & Woodward, R. (1995). Seismic-geodynamic determination of the origin of excess ellipticity of the core–mantle boundary. *Geophys. Res. Lett.* 22 (9), 1013–1016.
- Forte, A., & Peltier, W. (1987). Surface plate kinematics and mantle convection. In Fuchs, K., Froidevaux, C. (Eds.), *Composition, structure and dynamics of the lithosphere–asthenosphere system*. Vol. 16. Wiley Online Library, pp. 125–136.
- Forte, A. M., & Peltier, W. R. (1991). Mantle convection and core mantle boundary topography: explanations and implications. *Tectonophysics* 187 (1–3), 91–116.
- French, S., & Romanowicz, B. (2014). Whole-mantle radially anisotropic shear velocity structure from spectral-element waveform tomography. *Geophysical Journal International* 199 (3), 1303–1327.
- Garcia, R., & Souriau, A. (2000). Amplitude of the core–mantle boundary topography estimated by stochastic analysis of core phases. *Phys. Earth Planet. Inter.* 117, 345–359.
- Garnero, E., & McNamara, A. (2008). Structure and dynamics of Earth’s lower mantle. *Science* 320 (5876), 626.
- Garnero, E., McNamara, A., & Shim, S.-H. (2016). Continent-sized anomalous zones with low seismic velocity at the base of Earth’s mantle. *Nature Geosci.* 9 (7), 481–489.
- Gubbins, D., & Richards, M. (1986). Coupling of the core dynamo and mantle: thermal or topographic. *Geophys. Res. Lett.* 13 (13), 1521–1524.
- Gudmundsson, O. (1989). Some problems in global tomography: Modeling the core–mantle boundary and statistical analysis of travel-time data. PhD thesis, Calif. Inst. of Techn.
- Gudmundsson, O., & Clayton, R. W. (1991). A 2-D synthetic study of global traveltimes tomography. *Geophysical Journal International* 106 (1), 53–65.
- Gurvits, L. I. (2019). Space VLBI: from first ideas to operational missions. *Advances in Space Research*.
- Gwinn, C. R., Herring, T. A., & Shapiro, I. I. (1986). Geodesy by radio interferometry: Studies of the forced nutations of the Earth: 2. Interpretation. *J. Geophys. Res.* 91 (B5), 4755–4765.
- Haddon, R. (1972). Corrugations on the mantle-core boundary or transition layers between inner and outer cores? *Eos Trans. AGU* 53, 600.
- Haddon, R., Cleary, J. (1974). Evidence for scattering of seismic PKP waves near the mantle-core boundary. *Phys. Earth Planet. Inter.* 8 (3), 211–234.
- Hager, B., Clayton, R., Richards, M., Comer, R., & Dziewonski, A. (1985). Lower mantle heterogeneity, dynamic topography and the geoid. *Nature* 313 (6003), 541–545.
- Hager, B., & Richards, M. (1989). Long-wavelength variations in Earth’s geoid: physical models and dynamical implications. *Phil. Trans. R. Soc. Lond.* 328 (1599), 309–327.
- He, X., & Tromp, J. (1996). Normal-mode constraints on the structure of the Earth. *J. Geophys. Res.* 101 (B9) (20–053).

- Hernlund, J., & McNamara, A. (2015). The core–mantle boundary region. In: Schubert, G. (Ed.), *Treatise on geophysics*. Vol. 7. Elsevier, pp. 461–519.
- Hide, R., Clayton, R., Hager, B., Spieth, M., & Voorhies, C. (1993). Topographic core–mantle coupling and fluctuations in the Earth’s rotation. In: *Geophys. Monograph AGU: Relating geophysical structures and processes*. Vol. 76. AGU American Geophysical Union, pp. 107–107.
- Hide, R., & Horai, K. (1968). On the topography of the core–mantle interface. *Phys. Earth Planet. Inter.* 1 (5), 305–308.
- Hofmann, A. (1997). Mantle geochemistry: the message from oceanic volcanism. *Nature* 385 (6613), 219–229.
- Hosseini, K. (2016). Global multiple-frequency seismic tomography using teleseismic and core-diffracted body waves. PhD thesis, LMU Munich.
- Houser, C., Masters, G., Shearer, P., & Laske, G. (2008). Shear and compressional velocity models of the mantle from cluster analysis of long-period waveforms. *Geophysical Journal International* 174 (1) (195–212).
- Ishii, M., & Tromp, J. (1999). Normal-mode and free-air gravity constraints on lateral variations in velocity and density of Earth’s mantle. *Science* 285 (5431), 1231.
- Ishii, M., & Tromp, J. (2001). Even-degree lateral variations in the Earth’s mantle constrained by free oscillations and the free-air gravity anomaly. *Geophysical Journal International* 145 (1), 77–96.
- Ishii, M., & Tromp, J. (2004). Constraining large-scale mantle heterogeneity using mantle and inner-core sensitive normal modes. *Phys. Earth Planet. Inter.* 146 (1–2), 113–124.
- Jault, D., & Le Mouél, J. (1990). Core–mantle boundary shape: constraints inferred from the pressure torque acting between the core and the mantle. *Geophysical Journal International* 101 (1), 233–241.
- Kampfmann, W., & Müller, G. (1989). PcP amplitude calculations for a core–mantle boundary with topography. *Geophys. Res. Lett.* 16 (7), 653–656.
- Karato, S.-i., & Karki, B. B. (2001). Origin of lateral variation of seismic wave velocities and density in the deep mantle. *J. Geophys. Res.* 106 (R10), 21771–21783.
- Koelemeijer, P., Deuss, A., & Ritsema, J. (2013). Observations of core–mantle boundary Stoneley modes. *Geophys. Res. Lett.* 40 (11), 2557–2561.
- Koelemeijer, P., Deuss, A., & Ritsema, J. (2017). Density structure of Earth’s lowermost mantle from Stoneley mode splitting observations. *Nature Comm.* 8, 15241.
- Koelemeijer, P., Deuss, A., & Trampert, J. (2012). Normal mode sensitivity to Earth’s D” layer and topography on the core–mantle boundary: what we can and cannot see. *Geophysical Journal International* 190, 553–568.
- Koelemeijer, P., Ritsema, J., Deuss, A., & Van Heijst, H.-J. (2016). SP12RTS: a degree-12 model of shear- and compressional-wave velocity for Earth’s mantle. *Geophysical Journal International* 204 (2), 1024–1039.
- Koelemeijer, P., Schuberth, B. S., Davies, D. R., Deuss, A., & Ritsema, J. (2018). Constraints on the presence of post-perovskite in Earth’s lowermost mantle from tomographic-geodynamic model comparisons. *Earth Planet. Sci. Lett.* 494, 226–238.
- Koper, K. D., Pyle, M. L., & Franks, J. M. (2003). Constraints on aspherical core structure from PKiKP-PcP differential travel times. *J. Geophys. Res.* 108 (B3).
- Kuang, W., & Bloxham, J. (1993). On the effect of boundary topography on flow in the Earth’s core. *Geophysical & Astrophysical Fluid Dynamics* 72 (1–4), 161–195.
- Kuang, W., & Bloxham, J. (1997). On the dynamics of topographical core–mantle coupling. *Phys. Earth Planet. Inter.* 99 (3–4), 289–294.
- Kuang, W., & Chao, B. F. (2001). Topographic core–mantle coupling in geodynamo modeling. *Geophys. Res. Lett.* 28 (9), 1871–1874.
- Lassak, T., McNamara, A., Garnero, E., & Zhong, S. (2010). Core–mantle boundary topography as a possible constraint on lower mantle chemistry and dynamics. *Earth Planet. Sci. Lett.* 289, 232–241.
- Lau, H. C., Mitrovica, J. X., Davis, J. L., Tromp, J., Yang, H.-Y., & Al-Attar, D. (2017). Tidal tomography constrains Earth’s deep-mantle buoyancy. *Nature* 551 (7680), 321.
- Lau, H. C., Yang, H.-Y., Tromp, J., Mitrovica, J. X., Latychev, K., & Al-Attar, D. (2015). A normal mode treatment of semi-diurnal body tides on an aspherical, rotating and anelastic Earth. *Geophysical Journal International* 202 (2), 1392–1406.
- Le Mouél, J.-L., Narteau, C., Greff-Lefftz, M., & Holschneider, M. (2006). Dissipation at the core–mantle boundary on a small-scale topography. *J. Geophys. Res.* 111 (B4).
- Lekić, V., Cottaar, S., Dziewonski, A., & Romanowicz, B. (2012). Cluster analysis of global lower mantle tomography: A new class of structure and implications for chemical heterogeneity. *Earth Planet. Sci. Lett.* 357, 68–77.
- Li, M., McNamara, A. K., & Garnero, E. J. (2014). Chemical complexity of hotspots caused by cycling oceanic crust through mantle reservoirs. *Nature Geosci.* 7 (5), 366.
- Li, M., Zhong, S., & Olson, P. (2018). Linking lowermost mantle structure, core–mantle boundary heat flux and mantle plume formation. *Phys. Earth Planet. Inter.* 277, 10–29.
- Li, X., Giardini, D., & Woodhouses, J. (1991). Large-scale three-dimensional even-degree structure of the Earth from splitting of long-period normal modes. *J. Geophys. Res.* 96 (B1), 551–577.
- Liu, X., & Zhong, S. (2015). Constraining mantle viscosity structure for a thermochemical mantle using the geoid observation. *Geophys. Geochem. Geosys.* 17 (3), 895–913.
- Loper, D. E., & Lay, T. (1995). The core–mantle boundary region. *J. Geophys. Res.* 100 (B4), 6397–6420.
- Lu, C., & Grand, S. P. (2016). The effect of subducting slabs in global shear wave tomography. *Geophysical Journal International* 205 (2), 1074–1085.
- Mancinelli, N., & Shearer, P. (2016). Scattered energy from a rough core–mantle boundary modeled by a Monte Carlo seismic particle method: Application to PKKP precursors. *Geophys. Res. Lett.* 43 (15), 7963–7972.
- Masters, G., & Gubbins, D. (2003). On the resolution of density within the Earth. *Phys. Earth Planet. Inter.* 140 (1–3), 159–167.
- Masters, G., Laske, G., Bolton, H., & Dziewonski, A. (2000a). The relative behavior of shear velocity, bulk sound speed, and compressional velocity in the mantle: Implications for

- chemical and thermal structure. In Karato, S., Forte, A., Liebermann, R., Masters, G., & Stixrude, L. (Eds.), *Geophys. Monograph AGU: Earth's Deep Interior: Mineral Physics and Tomography From the Atomic to the Global Scale*. Vol. 117. Wiley Online Library, pp. 63–87.
- Masters, G., Laske, G., & Gilbert, F. (2000b). Matrix autoregressive analysis of free-oscillation coupling and splitting. *Geophysical Journal International* 143 (2), 478–489.
- Mathews, P. M., Herring, T. A., & Buffett, B. A. (2002). Modeling of nutation and precession: New nutation series for non-rigid Earth and insights into the Earth's interior. *J. Geophys. Res.* 107 (B4), ETG–3.
- McNamara, A., Garnero, E., & Rost, S. (2010). Tracking deep-mantle reservoirs with ultra-low-velocity zones. *Earth Planet. Sci. Lett.* 299 (1), 1–9.
- McNamara, A. K., & Zhong, S. (2004). Thermochemical structures within a spherical mantle: Superplumes or piles? *J. Geophys. Res.* 109 (B7).
- McNamara, A. K., & Zhong, S. (2005). Thermochemical structures beneath Africa and the Pacific Ocean. *Nature* 437 (7062), 1136–1139.
- Menke, W. (1986). Few 2–50 km corrugations on the core–mantle boundary. *Geophys. Res. Lett.* 13 (13), 1501–1504.
- Montagner, J., & Kennett, B. (1996). How to reconcile body-wave and normal-mode reference Earth models. *Geophysical Journal International* 125 (1), 229–248.
- Morelli, A., & Dziewonski, A. (1987). Topography of the core–mantle boundary and lateral homogeneity of the liquid core. *Nature* 325, 678–683.
- Mosca, I., Cobden, L., Deuss, A., Ritsema, J., & Trampert, J. (2012). Seismic and mineralogical structures of the lower mantle from probabilistic tomography. *J. Geophys. Res.* 117 (B6), B06304.
- Moulik, P., & Ekström, G. (2014). An anisotropic shear velocity model of the Earth's mantle using normal modes, body waves, surface waves and long-period waveforms. *Geophysical Journal International* 199 (3), 1713–1738.
- Moulik, P., & Ekström, G. (2016). The relationships between large-scale variations in shear velocity, density, and compressional velocity in the Earth's mantle. *J. Geophys. Res.* 121 (4), 2737–2771.
- Mound, J., & Buffett, B. (2005). Mechanisms of core–mantle angular momentum exchange and the observed spectral properties of torsional oscillations. *J. Geophys. Res.* 110 (B8).
- Mound, J. E., & Buffett, B. A. (2006). Detection of a gravitational oscillation in length-of-day. *Earth Planet. Sci. Lett.* 243 (3–4), 383–389.
- Mukhopadhyay, S. (2012). Early differentiation and volatile accretion recorded in deep-mantle neon and xenon. *Nature* 486 (7401), 101–104.
- Mulyukova, E., Steinberger, B., Dabrowski, M., & Sobolev, S. V. (2015). Survival of LLSVPs for billions of years in a vigorously convecting mantle: replenishment and destruction of chemical anomaly. *J. Geophys. Res.* 120 (5), 3824–3847.
- Murakami, M., Hirose, K., Kawamura, K., Sata, N., & Ohishi, Y. (2004). Post-perovskite phase transition in MgSiO₃. *Science* 304 (5672), 855.
- Murphy, F., Neuberg, J., & Jacob, A. (1997). Alternatives to core–mantle boundary topography. *Phys. Earth Planet. Inter.* 103 (3–4), 349–364.
- Nakagawa, T., & Tackley, P. J. (2014). Influence of combined primordial layering and recycled MORB on the coupled thermal evolution of Earth's mantle and core. *Geophys. Geochem. Geosys.* 15 (3), 619–633.
- Nakagawa, T., Tackley, P. J., Deschamps, F., & Connolly, J. A. (2012). Radial 1-D seismic structures in the deep mantle in mantle convection simulations with self-consistently calculated mineralogy. *Geophys. Geochem. Geosys.* 13 (11).
- Neuberg, J., & Wahr, J. (1991). Detailed investigation of a spot on the core mantle boundary using digital PcP data. *Phys. Earth Planet. Inter.* 68 (1–2), 132–143.
- Obayashi, M., & Fukao, Y. (1997). P and PcP travel time tomography for the core–mantle boundary. *J. Geophys. Res.* 102 (B8), 17825.
- Obayashi, M., Yoshimitsu, J., Nolet, G., Fukao, Y., Shiobara, H., Sugioka, H., et al. (2013). Finite frequency whole mantle P wave tomography: Improvement of subducted slab images. *Geophys. Res. Lett.* 40 (21), 5652–5657.
- Oganov, A., & Ono, S. (2004). Theoretical and experimental evidence for a post-perovskite phase of MgSiO₃ in Earth's D'' layer. *Nature* 430 (6998), 445–448.
- Olson, P., Deguen, R., Rudolph, M. L., & Zhong, S. (2015). Core evolution driven by mantle global circulation. *Phys. Earth Planet. Inter.* 243, 44–55.
- Panning, M., Lekić, V., & Romanowicz, B. (2010). Importance of crustal corrections in the development of a new global model of radial anisotropy. *J. Geophys. Res.* 115 (B12).
- Poupinet, G., Souriau, A., & Jenatton, L. (1993). A test on the Earth's core–mantle boundary structure with antipodal data: example of Fiji-Tonga earthquakes recorded in Tamanrasset, Algeria. *Geophysical Journal International* 113 (3), 684–692.
- Pulliam, R. J., & Stark, P. B. (1993). Bumps on the core–mantle boundary: Are they facts or artifacts? *J. Geophys. Res.* 98 (B2) (1943–1955).
- Rekdal, T., & Doornbos, D. (1992). The times and amplitudes of core phases for a variable core–mantle boundary layer. *Geophysical Journal International* 108 (2), 546–556.
- Resovsky, J., & Ritzwoller, M. (1999). Regularization uncertainty in density models estimated from normal mode data. *Geophys. Res. Lett.* 26 (15), 2319–2322.
- Resovsky, J. S., & Ritzwoller, M. H. (1998). New and refined constraints on three-dimensional Earth structure from normal modes below 3 mHz. *J. Geophys. Res.* 103 (B1), 783–810.
- Ritsema, J., Deuss, A., van Heijst, H.-J., & Woodhouse, J. H. (2011). S40RTS: a degree-40 shear-velocity model for the mantle from new Rayleigh wave dispersion, teleseismic travel-time and normal-mode splitting function measurements. *Geophysical Journal International* 184 (3), 1223–1236.
- Rizo, H., Andraut, D., Bennett, N., Humayun, M., Brandon, A., Vlastélic, I., et al. (2019). 182W evidence for core–mantle interaction in the source of mantle plumes. *Geochemical Perspectives Letters* 11, 6–11.
- Rodgers, A., & Wahr, J. (1993). Inference of core–mantle boundary topography from ISC PcP and PKP traveltimes. *Geophysical Journal International* 115 (3), 991–1011.

- Romanowicz, B. (2001). Can we resolve 3D density heterogeneity in the lower mantle? *Geophys. Res. Lett.* 28 (6), 1107–1110.
- Romanowicz, B. (2017). Geophysics: The buoyancy of Earth's deep mantle. *Nature* 551 (7680), 308.
- Ros, E., Schwarz, D. J., & Vocks, C. (2018). Community paper on radio astronomy infrastructures. arXiv preprint arXiv:1802.08467.
- Rost, S., & Revenaugh, J. (2004). Small-scale changes of core–mantle boundary reflectivity studied using core reflected PcP. *Phys. Earth Planet. Inter.* 145 (1–4) (19–36).
- Schlaphorst, D., Thomas, C., Holme, R., & Abreu, R. (2015). Investigation of core–mantle boundary topography and lowermost mantle with P4KP waves. *Geophysical Journal International* 204 (2), 1060–1071.
- Schubert, G., Masters, G., Olson, P., & Tackley, P. (2004). Superplumes or plume clusters? *Phys. Earth Planet. Inter.* 146 (1–2), 147–162.
- Schuberth, B., Bunge, H.-P., Steinle-Neumann, G., Moder, C., & Oeser, J. (2009). Thermal versus elastic heterogeneity in high-resolution mantle circulation models with pyrolite composition: High plume excess temperatures in the lowermost mantle. *Geophys. Geochem. Geosys.* 10 (1).
- Shearer, P. M., Hedlin, M. A., & Earle, P. S. (1998). PKP and PKKP precursor observations: Implications for the small-scale structure of the deep mantle and core. In *Geophys. Monograph AGU: The Core–mantle Boundary Region, Geodyn. Ser. Vol. 28*. Wiley Online Library, pp. 37–55.
- Shen, Z., Ni, S., Wu, W., & Sun, D. (2016). Short period ScP phase amplitude calculations for core–mantle boundary with intermediate scale topography. *Phys. Earth Planet. Inter.* 253, 64–73.
- Shephard, G. E., Matthews, K. J., Hosseini, K., & Domeier, M. (2017). On the consistency of seismically imaged lower mantle slabs. *Scientific Reports* 7 (1), 10976.
- Simmons, N., Forte, A., & Grand, S. (2009). Joint seismic, geodynamic and mineral physical constraints on three-dimensional mantle heterogeneity: Implications for the relative importance of thermal versus compositional heterogeneity. *Geophysical Journal International* 177 (5), 1284–1304.
- Simmons, N. A., Forte, A. M., Boschi, L., & Grand, S. P. (2010). GyPSuM: A joint tomographic model of mantle density and seismic wave speeds. *J. Geophys. Res.* 115 (B12).
- Simmons, N. A., Myers, S. C., Johannesson, G., & Matzel, E. (2012). LLNL-G3Dv3: Global P wave tomography model for improved regional and teleseismic travel time prediction. *J. Geophys. Res.* 117 (B10).
- Soldati, G., & Boschi, L. (2005). The resolution of whole earth seismic tomographic models. *Geophysical Journal International* 161 (1), 143–153.
- Soldati, G., Boschi, L., & Forte, A. (2012). Tomography of core–mantle boundary and lowermost mantle coupled by geodynamics. *Geophysical Journal International* 189 (2), 730–746.
- Soldati, G., Boschi, L., & Piersanti, A. (2003). Outer core density heterogeneity and the discrepancy between PKP and PcP travel time observations. *Geophys. Res. Lett.* 30 (4), 1190.
- Soldati, G., Koelemeijer, P., Boschi, L., & Deuss, A. (2013). Constraints on core–mantle boundary topography from normal mode splitting. *Geophys. Geochem. Geosys.* 14 (5), 1333–1342.
- Stark, P. B., & Hengartner, N. W. (1993). Reproducing Earth's kernel: Uncertainty of the shape of the core–mantle boundary from PKP and PcP travel times. *J. Geophys. Res.* 98 (B2) (1957–1971).
- Steinberger, B., & Holme, R. (2008). Mantle flow models with core–mantle boundary constraints and chemical heterogeneities in the lowermost mantle. *J. Geophys. Res.* 113 (B5).
- Styles, E., Davies, D. R., & Goes, S. (2011). Mapping spherical seismic into physical structure: biases from 3D phase-transition and thermal boundary-layer heterogeneity. *Geophysical Journal International* 184 (3), 1371–1378.
- Su, W., & Dziewonski, A. (1997). Simultaneous inversion for 3-D variations in shear and bulk velocity in the mantle. *Phys. Earth Planet. Inter.* 100 (1–4), 135–156.
- Sze, E., & van der Hilst, R. (2003). Core mantle boundary topography from short period PcP, PKP, and PKKP data. *Phys. Earth Planet. Inter.* 135 (1), 27–46.
- Tackley, P. J. (2002). Strong heterogeneity caused by deep mantle layering. *Geophys. Geochem. Geosys.* 3 (4), 1–22.
- Tan, E., & Gurnis, M. (2005). Metastable superplumes and mantle compressibility. *Geophys. Res. Lett.* 32 (20).
- Tanaka, S. (2010). Constraints on the core–mantle boundary topography from P4KP-PcP differential travel times. *J. Geophys. Res.* 115 (B4), B04310.
- Tarduno, J. A., Watkeys, M. K., Huffman, T. N., Cottrell, R. D., Blackman, E. G., Wendt, A., et al. (2015). Antiquity of the South Atlantic Anomaly and evidence for top-down control on the geodynamo. *Nature Comm.* 6, 7865.
- Tesoniero, A., Auer, L., Boschi, L., & Cammarano, F. (2015). Hydration of marginal basins and compositional variations within the continental lithospheric mantle inferred from a new global model of shear and compressional velocity. *J. Geophys. Res.* 120 (11), 7789–7813.
- Tesoniero, A., Cammarano, F., & Boschi, L. (2016). S- to P heterogeneity ratio in the lower mantle and thermochemical implications. *Geophys. Geochem. Geosys.* 17 (7), 2522–2538.
- Torsvik, T. H., Burke, K., Steinberger, B., Webb, S. J., & Ashwal, L. D. (2010). Diamonds sampled by plumes from the core–mantle boundary. *Nature* 466 (7304), 352–355.
- Trampert, J., Deschamps, F., Resovsky, J., & Yuen, D. (2004). Probabilistic tomography maps chemical heterogeneities throughout the lower mantle. *Science* 306 (5697), 853.
- Tromp, J., & Zanker, E. (1995). Toroidal splitting observations from the great 1994 Bolivia and Kuril Islands earthquakes. *Geophys. Res. Lett.* 22 (16), 2297–2300.
- Tsuchiya, T., Tsuchiya, J., Umemoto, K., & Wentzcovitch, R. (2004). Phase transition in MgSiO₃ perovskite in the Earth's lower mantle. *Earth Planet. Sci. Lett.* 224 (3–4), 241–248.
- Van den Berg, A., Cloetingh, S., & Doornbos, D. (1978). A comparison of PKP precursor data from several seismic arrays. *J. Geophys. Res.* 44, 499–510.

- Vasco, D., Johnson, L. R., & Marques, O. (1999). Global Earth structure: inference and assessment. *Geophysical Journal International* 137 (2), 381–407.
- Ventosa, S., & Romanowicz, B. (2015). Extraction of weak PcP phases using the slant-stacklet transform–II: constraints on lateral variations of structure near the core–mantle boundary. *Geophysical Journal International* 203 (2), 1227–1245.
- Vidale, J. E., & Benz, H. M. (1992). A sharp and flat section of the core–mantle boundary. *Nature* 359 (6396), 627.
- Wahr, J., & De Vries, D. (1989). The possibility of lateral structure inside the core and its implications for nutation and Earth tide observations. *Geophysical Journal International* 99 (3), 511–519.
- Wessel, P., Smith, W. H. F., Scharroo, R., Luis, J., & Wobbe, F. (2013). Generic mapping tools: Improved version released. *Eos, Transactions American Geophysical Union* 94 (45), 409–410.
- Wu, W., Ni, S., & Shen, Z. (2014). Constraining the short scale core–mantle boundary topography beneath Kenai Peninsula (Alaska) with amplitudes of core-reflected PcP wave. *Phys. Earth Planet. Inter.* 236, 60–68.
- Yoshida, M. (2008). Core–mantle boundary topography estimated from numerical simulations of instantaneous mantle flow. *Geophys. Geochem. Geosys.* 9 (7).
- Zhang, N., & Zhong, S. (2011). Heat fluxes at the Earth’s surface and core–mantle boundary since Pangea formation and their implications for the geomagnetic superchrons. *Earth Planet. Sci. Lett.* 306 (3–4) (205–216).
- Zindler, A., & Hart, S. (1986). Chemical geodynamics. *Ann. Rev. Earth Planet Sci.* 14, 493–571.

Part II

Material Transport Across the Mantle: Geophysical Observations and Geodynamic Predictions

Dynamics of the Upper Mantle in Light of Seismic Anisotropy

Thorsten W. Becker^{1,2} and Sergei Lebedev³

ABSTRACT

Seismic anisotropy records continental dynamics in the crust and convective deformation in the mantle. Deciphering this archive holds huge promise for our understanding of the thermo-chemical evolution of our planet, but doing so is complicated by incomplete imaging and non-unique interpretations. Here, we focus on the upper mantle and review seismological and laboratory constraints as well as geodynamic models of anisotropy within a dynamic framework. Mantle circulation models are able to explain the character and pattern of azimuthal anisotropy within and below oceanic plates at the largest scales. Using inferences based on such models provides key constraints on convection, including plate-mantle force transmission, the viscosity of the asthenosphere, and the net rotation of the lithosphere. Regionally, anisotropy can help further resolve smaller-scale convection, e.g., due to slabs and plumes in active tectonic settings. However, the story is more complex, particularly for continental lithosphere, and many systematic relationships remain to be established more firmly. More integrated approaches based on new laboratory experiments, consideration of a wide range of geological and geophysical constraints, as well as hypothesis-driven seismological inversions are required to advance to the next level.

10.1. INTRODUCTION

Anisotropy of upper mantle rocks records the history of mantle convection and can be inferred remotely from seismology. Seismic anisotropy refers to the orientational dependence of propagation velocities for waves traveling at different azimuths, or a difference in velocities for waves that are polarized in the horizontal or vertical plane such as Love and Rayleigh waves, respectively. “Anisotropy” without any qualifier shall here refer to the seismic kind caused by an anisotropic elastic stiffness tensor

unless noted otherwise. Anisotropy is a common property of mineral assemblages and appears throughout the Earth, including in its upper mantle. There, anisotropy can arise due to the shear of rocks in mantle flow. As such, it provides a unique link between seismological observations and the evolution of our planet. However, given the need to resolve more parameters for an anisotropic than for an isotropic solid, seismological models for anisotropy are more uncertain, and the interpretation and link to flow necessarily non-unique.

Our personal views of seismic anisotropy have oscillated from a near-useless can of worms to the most useful constraint on convection ever, and we strive to present a more balanced view here. Anisotropy matters for all layers of the Earth, and there exist a number of excellent reviews covering the rock record, seismological observations, and laboratory constraints (e.g., Nicolas and

¹*Institute for Geophysics, Jackson School of Geosciences, The University of Texas at Austin, Austin, TX, USA*

²*Department of Geological Sciences, Jackson School of Geosciences, The University of Texas at Austin, Austin, TX, USA*

³*Dublin Institute for Advanced Studies, Dublin, Ireland*

Christensen, 1987; Silver, 1996; Savage, 1999; Mainprice, 2007; Skemer and Hansen, 2016; Romanowicz and Wenk, 2017), as well as comprehensive treatments in textbooks (e.g., Anderson, 1989). Also, most of what was said in the overview of Long and Becker (2010) remains relevant. However, here we shall focus our discussion on the upper mantle within and underneath oceanic plates, the seemingly best understood part of mantle convection. We will highlight some of the insights afforded by seismic anisotropy within a convective context, and discuss selected open questions and how to possibly answer them.

10.2. OBSERVATIONS OF SEISMIC ANISOTROPY

A range of seismic observations show the presence of anisotropy in the Earth. In tomographic imaging of its three-dimensional distribution, anisotropy must normally be resolved simultaneously with the isotropic seismic velocity heterogeneity, typically greater in amplitude. Substantial non-uniqueness of the solutions for anisotropy can arise (e.g., Laske and Masters, 1998), and other sources of uncertainties include the treatment of the crust (e.g., Ferreira et al., 2010) and earthquake locations (Ma and Masters, 2015). In fact, the very existence of intrinsic anisotropy (e.g., due to lattice preferred orientation (LPO) of anisotropic mantle peridotite minerals) as opposed to apparent anisotropy (e.g., caused by layering of isotropic material of different wave speeds; e.g., Backus, 1962) has been debated (Fichtner et al., 2013; Wang et al., 2013).

At least regionally, the occurrence of anisotropy is, of course, not really in doubt since different lines of seismic evidence for it are corroborated by observations from mantle rocks (e.g., Ben Ismail and Mainprice, 1998; Mainprice, 2007). However, accurate determination of anisotropy is clearly not straightforward. Models based on data of different types, or even of the same type, are often difficult to reconcile and only agree on large spatial scales. Improvements in data sampling and anisotropy analysis methods are therefore subjects of active research, aimed at yielding more accurate and detailed information on the dynamics of the lithosphere and underlying mantle.

In order to ground the dynamics discussion, we first address the scales of resolution and distribution of seismic anisotropy coverage that are currently available to guide global mantle circulation assessment.

10.2.1. *P_n* Anisotropy

Historically, the detection of *P* wave anisotropy just below the Moho from refraction experiments in the Pacific Ocean was important in terms of establishing the existence of seismic anisotropy in the upper mantle and linking it to plate tectonics (e.g., Hess, 1964; Morris

et al., 1969). It can be shown that the azimuth, φ , dependence of *P* wave speed anomalies, δv , for small seismic anisotropy at location \mathbf{x} can be approximated by

$$\begin{aligned} \delta v(\varphi, \mathbf{x}) \approx & A_0(\mathbf{x}) + A_1(\mathbf{x}) \cos(2\varphi) \\ & + A_2(\mathbf{x}) \sin(2\varphi) + A_3(\mathbf{x}) \cos(4\varphi) + A_4(\mathbf{x}) \sin(4\varphi) \end{aligned} \quad (10.1)$$

(Backus, 1965). The simplest form of azimuthal anisotropy is due to the 2φ terms alone, and the corresponding 180° periodic pattern seen in Morris et al.'s (1969) results, for example (Figure 10.1). Based on such patterns, Hess (1964) concluded that the oceanic lithosphere and uppermost mantle must have undergone convective flow and made the connection to seafloor spreading (Vine and Matthews, 1963).

Anisotropy beneath continents was also detected, using both refraction and quarry-blast data (e.g., Bamford, 1977). More recently, *P_n* and *S_n* waves propagating from earthquakes have been used for mapping azimuthal anisotropy in the uppermost mantle, just beneath the Moho (e.g., Smith and Ekström, 1999; Buehler and Shearer, 2010), where they form a connection between shallow, crustal anisotropy and the deeper mantle observations such as from *SKS* splitting which we discuss next.

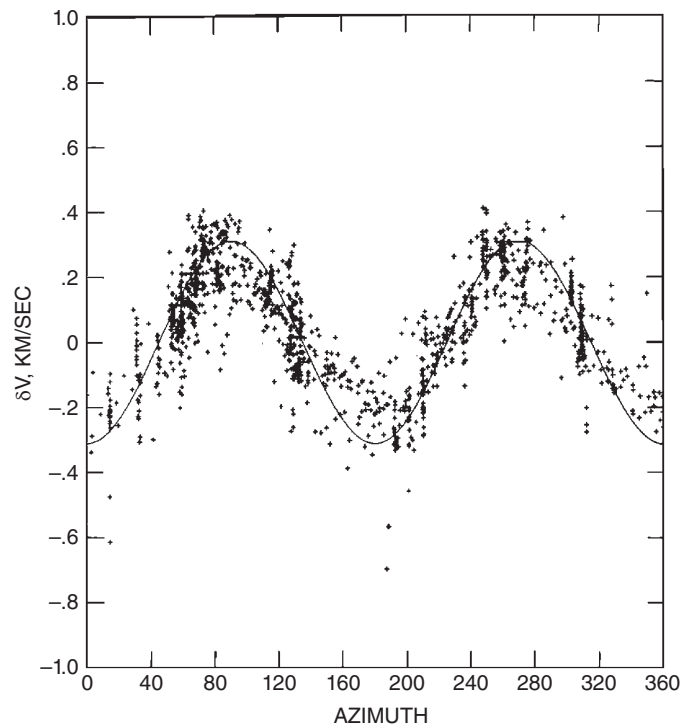


Figure 10.1 Velocity deviation for *P_n* from the mean ($v_P = 8.159$ km/s) in the central Pacific N and NW of Hawaii as a function of propagation azimuth along with a 2φ fit (eq. 1). Source: Modified from Morris et al. (1969).

10.2.2. Shear Wave Splitting

In the presence of azimuthal anisotropy, a shear wave pulse traveling into an anisotropic layer will be separated into two orthogonal pulses, one propagating within the medium's fast polarization plane (containing its "fast axis," or fast-propagation azimuth), and the other within the orthogonally oriented, slow propagation plane. At a seismic station, those split pulses will arrive separated by a delay time, δt , that is proportional to the integral of anisotropy strength and path length, assuming a uniform anisotropy orientation within the anisotropic layer (e.g., Silver and Chan, 1988; Vinnik et al., 1989). Such "splitting" is akin to optical birefringence and observed for local shear wave arrivals in the shallow crust ($\delta t \lesssim 0.2$ s) where it mainly reflects anisotropy due to aligned cracks, whose opening is controlled by tectonic stresses (Crampin and Chastin, 2003). For teleseismic shear waves, $\delta t \sim 1.2$ s, on average, and the splitting measurements can be related to whole-crustal and mantle anisotropy (Vinnik et al., 1992; Silver, 1996). *SKS* splitting due to anisotropic fabric within the crust is typically $\lesssim 0.3$ s, much smaller than that accumulated in the mantle. Areas with anomalously thick crust, for example Tibet, are the exception where crustal delay times have been estimated to be up to ~ 0.8 s (e.g., Agius and Lebedev, 2017).

The popular shear-wave splitting method yields a direct indication of anisotropy in the Earth (e.g., Savage, 1999). Outer-core-traversing waves such as *SKS* and *SKKS* are often used for the splitting measurements because they can yield information on receiver side anisotropy; source effects are excluded because of the *P* to *S* conversion upon exiting the core. The advantages of the method are its ease of use and its high lateral resolution. Figure 10.2 shows the current distribution of teleseismic shear wave splitting measurements with fairly dense sampling in most of the actively deforming continental regions.

The main disadvantage of *SKS* splitting is its poor vertical resolution; anisotropy may arise anywhere along the path. In the presence of one dominant anisotropic layer (say, the asthenosphere) with azimuthal anisotropy, the splitting parameters (delay times and fast azimuth) will characterize this layer directly. However, if multiple layers with different fast axes or more complex types of anisotropy are present, the net splitting will depend nonlinearly on backazimuth and the depth-variable anisotropy (e.g., Silver and Savage, 1994; Rumpker and Silver, 1998; Saltzer et al., 2000). Resolving some of the depth-dependence is possible with dense spatial coverage but requires long station deployment times and good back-azimuthal sampling (e.g., Chevrot et al., 2004; Long et al., 2008; Abt and Fischer, 2008; Monteiller and Chevrot, 2011).

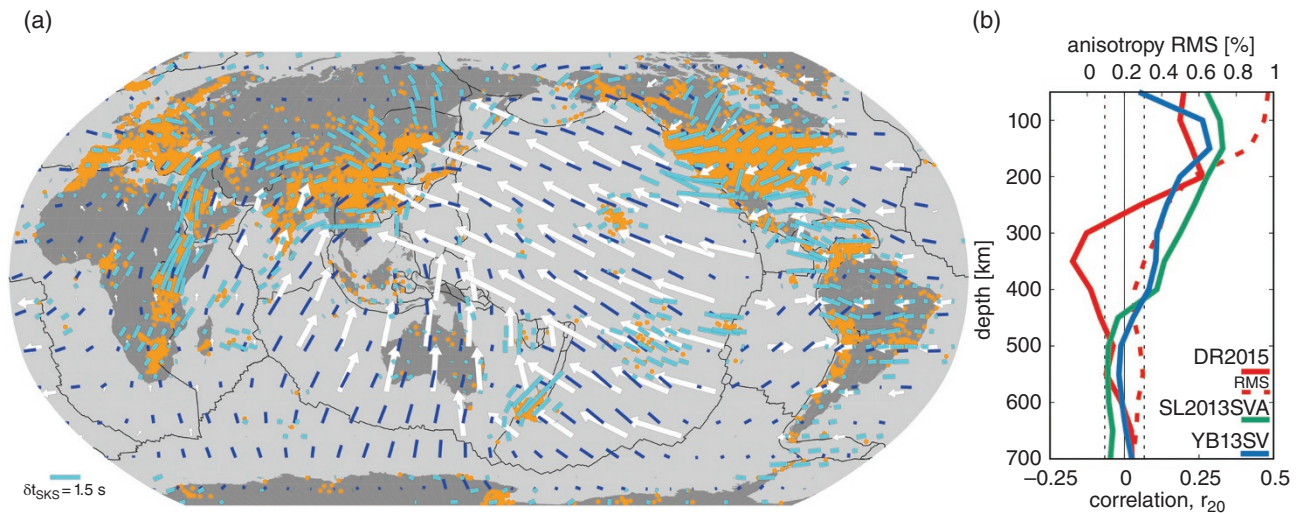


Figure 10.2 Azimuthal anisotropy of the upper mantle. (a) Non-zero *SKS* splitting observations (orange dots) fit using spherical harmonics up to degree, $\ell = 20$ (cyan sticks, processed as in Becker et al. 2012, and updated as of 01/2019), and compared to the global azimuthal anisotropy model SL2013SVA at 200 km depth (blue sticks; Schaeffer et al. 2016), and MORVEL (DeMets et al., 2010) plate motions in a spreading-aligned reference frame (white vectors; Becker et al. 2015). (b) Correlation up to $\ell = 20$, r_{20} (solid lines), between *SKS* splitting (a) and three seismological models: DR2015 (Debayle and Ricard, 2013, RMS anisotropy also shown with dashed line), SL2013SVA (Schaeffer et al. 2016), and YB13SV (Yuan and Beghein, 2013). Dashed vertical lines are 95% significance levels for r_{20} (cf. Becker et al., 2007a, 2012; Yuan and Beghein, 2013). Source: (a) Becker et al. (2012), Schaeffer et al. (2016), Becker et al. (2016), DeMets et al. (2010), Becker et al. (2015). (b) Debayle and Ricard (2013), Schaeffer et al. (2016), Yuan and Beghein (2013), Becker et al. (2007a).

When considering the uncertainty in the mantle depths where teleseismic splitting arises, we can focus on high stress/low temperature boundary layers where dislocation creep might dominate (Karato, 1992; Gaherty and Jordan, 1995; McNamara et al., 2001). For *SKS* splitting, this means uncertainty on whether the delay times are caused by anisotropy in the lithosphere, asthenosphere, the transition zone between the upper and lower mantle (e.g., Fouch and Fischer, 1996; Wookey and Kendall, 2004), and/or the core-mantle boundary/D" region (reviewed elsewhere in this volume).

The integrated anisotropy of the lithosphere alone is typically not enough to fully explain *SKS* splitting delay times (e.g., Vinnik et al., 1992; Silver, 1996). Comparisons between local and teleseismic splitting from subduction zones are usually consistent with an origin of most *SKS* splitting observations within the top ~ 400 km of the mantle (e.g., Fischer and Wiens, 1996; Long and van der Hilst, 2006). Together with surface wave models of anisotropy (Figure 10.2b) as well as mineral physics and dynamics considerations discussed below, this suggests a dominant asthenospheric cause of *SKS* splitting.

10.2.3. Surface Waves

There are a range of other approaches used for mapping anisotropy, including study of *P*-wave polarization (Schulte-Pelkum et al., 2001), body-wave imaging (e.g., Plomerová et al., 1996; Ishise and Oda, 2005; Wang and Zhao, 2008), receiver-function anisotropy analysis (e.g., Kosarev et al., 1984; Farra and Vinnik, 2002; Schulte-Pelkum and Mahan, 2014), and normal-mode measurements (e.g., Anderson and Dziewoński, 1982; Beghein et al., 2008). However, for global-scale imaging of the upper mantle, surface wave analysis holds the most promise for making the link to depth-dependent convection scenarios.

Just as the response of the Earth to a seismic event can be expressed as a superposition of normal modes (standing waves), it can be decomposed into a sum of surface waves (traveling waves; Dahlen and Tromp, 1998). The depth sensitivity of surface waves depends on their period; the longer the period, the deeper the sample. Global maps of surface-wave phase velocities at periods from ~ 35 – 150 s, sampling the mantle lithosphere and asthenosphere have been available for over two decades (e.g., Ekström et al., 1997; Trampert and Woodhouse, 2003). More recently, global models have been constructed with surface waves in broadening period ranges, up to ~ 25 – 250 s (Ekström, 2011) and even up to 10 – 400 s (Schaeffer and Lebedev, 2013), although at the shortest of the periods the event-station measurements can no longer cover the entire globe.

Using the ambient noise wave field, speeds of the surface waves excited by ocean waves are routinely measured in a 1 – 35 s period range, i.e., sensing from the uppermost crust to the uppermost mantle (Shapiro et al., 2005; Bensen et al., 2007; Ekström et al., 2009). Anthropogenic noise yields measurements at frequencies of a few Hz to a few tens of Hz, sampling within the shallowest, sedimentary layers (Mordret et al., 2013). Cross-correlations of seismograms from teleseismic earthquakes yield phase-velocity measurements down to periods as short as 5 – 10 s, sampling the upper and middle crust (Meier et al., 2004; Adam and Lebedev, 2012) (Figure 10.3) and up to periods over 300 s (e.g., Lebedev et al., 2006), sampling the deep upper mantle and transition zone.

Rayleigh waves are mainly sensitive to vertically polarized shear wave speed, v_{SV} , with smaller, although non-negligible, sensitivity to horizontally polarized shear wave velocity, v_{SH} , and v_P (e.g., Montagner and Nataf, 1986; Romanowicz and Snieder, 1988; Dahlen and Tromp, 1998). The azimuthal expansion of eq. 1 holds for surface waves as well (Smith and Dahlen, 1973), and in the olivine dominated upper mantle, the 2φ terms of eq. 1 are expected to be the main signature of azimuthal anisotropy for Rayleigh waves (Montagner and Nataf, 1986; Montagner and Anderson, 1989, cf. Figure 10.3). At the same periods, Love waves are mainly sensitive to v_{SH} at shallower depths, and the 4φ terms of azimuthal anisotropy, depending on assumptions about petrology (Montagner and Nataf, 1986).

Radial anisotropy (the difference between v_{SV} and v_{SH}) was documented based on the finding that Love and Rayleigh waves could not be fit simultaneously by the same Earth model (Anderson, 1961; Aki and Kaminuma, 1963; McEvelly, 1964). Azimuthal anisotropy of surface waves was also established early (Forsyth, 1975), and Montagner and Tanimoto (1991) presented an integrated model of upper mantle anisotropy capturing both radial and azimuthal contributions.

A full description of seismic anisotropy is achieved by an elastic stiffness tensor with 21 independent components instead of the isotropic two (e.g., Anderson, 1989), but often hexagonal symmetry (or “transverse isotropy”) is assumed. In this case, five parameters fully specify the tensor, for example the vertically and horizontally polarized *S* and *P* wave speeds, v_{SV} , v_{SH} , v_{PV} , and v_{PH} , respectively, and a parameter η , which determines how waves polarized between the horizontal and vertical plane transition from v_{SH} to v_{SV} (e.g., Dziewoński and Anderson, 1981; Kawakatsu, 2016). In the case of radial anisotropy imaging, the hexagonal symmetry axis is assumed vertical, and $\xi = (v_{SH}/v_{SV})^2$ is commonly used as a measure of anisotropy strength. For the case of azimuthal anisotropy, the hexagonal symmetry axis is in the horizontal plane and its azimuth determines the 2φ terms of eq. (1), e.g., for

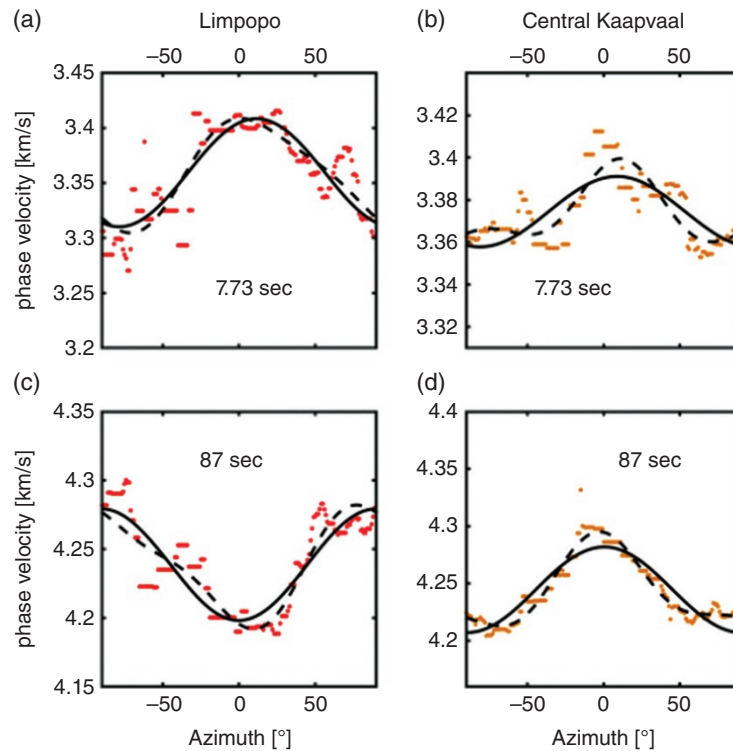


Figure 10.3 Azimuth, φ , dependent anisotropy of Rayleigh-wave phase velocities in different regions (a and c vs. b and d) in southern Africa. Rayleigh waves at the 7.73 s period (a and b) sample primarily the upper and middle crust, and at 87 s (c and d), the lower part of the cratonic lithosphere, respectively. Dots show the phase-velocity measurements, binned and smoothed with a 30° sliding window. Solid black lines: best-fitting models with isotropic and 2φ terms (see eq. 1). Dashed black lines: best-fitting models with isotropic, 2φ , and 4φ terms. Source: Modified from Ravenna (2018), using measurements from Adam and Lebedev (2012).

the Rayleigh wave, v_{SV} , anisotropy or the fast axes of *SKS* splitting.

The construction of large waveform datasets over the last two decades has enabled increasingly detailed surface-wave tomography of upper-mantle anisotropy on global scales. A number of 3-D radial (e.g., Nataf et al., 1984; Ekström and Dziewoński, 1998; Panning and Romanowicz, 2006; Kustowski et al., 2008; French and Romanowicz, 2014; Auer et al., 2014; Moulik and Ekström, 2014; Chang et al., 2015) and azimuthal (e.g., Tanimoto and Anderson, 1984; Montagner, 2002; Debayle and Ricard, 2013; Yuan and Beghein, 2013; Schaeffer et al., 2016) (Figure 10.2) anisotropy models have been presented.

Many features of anisotropic structure are now consistently mapped for the upper mantle on continent scales. The mutual agreement of different anisotropy models, however, remains well below that of models of isotropic heterogeneity (Becker et al., 2007a; Auer et al., 2014; Chang et al., 2015; Schaeffer et al., 2016). Given the typical period range for fundamental mode surface wave measurements, both radial and azimuthal anisotropy

are best constrained in the uppermost ~ 350 km of the mantle, even though comprehensive waveform analysis (e.g., Lebedev et al., 2005; Priestley et al., 2006; Panning and Romanowicz, 2006) or the explicit use of overtones (e.g., Trampert and van Heijst, 2002; Beghein and Trampert, 2004) extends the depth range to the bottom of the transition zone (~ 700 km) and beyond, at least theoretically.

Dense arrays of seismic stations enable higher lateral resolution surface wave anisotropy imaging regionally (e.g., Shapiro et al., 2004; Deschamps et al., 2008a; Lin et al., 2011; Takeo et al., 2018; Lin et al., 2016). On those scales, it is also easier to explore uncertainties, and probabilistic 1-D profiles obtained with Monte Carlo inversion schemes can be used, for example, to explore the trade-off between the radial and azimuthal anisotropy layer imaging (e.g., Beghein and Trampert, 2004; Agius and Lebedev, 2014; Bodin et al., 2016; Ravenna et al., 2018).

Uncertainties aside, array measurements can present unambiguous evidence of anisotropy in the crust and upper mantle beneath the array footprint. Figure 10.3 shows an example for a continental plate site. The

measurements of phase velocities for different period Rayleigh waves clearly indicate seismic azimuthal anisotropy of the 2φ kind (cf. Figure 10.1), and a change in the fast propagation azimuth from the shallow to the deeper layers.

10.3. INTERPRETATION OF SEISMIC ANISOTROPY

10.3.1. Origin of Upper Mantle Anisotropy

Shear due to convective flow is expected to lead to the formation of lattice (or, more appropriately, “crystallographic”) preferred orientation anisotropy in the olivine-dominated upper mantle, meaning that anisotropy should be a record of mantle flow (e.g., McKenzie, 1979; Tanimoto and Anderson, 1984; Ribe, 1989). The foundations for this common assumption include the observation that natural xenolith and exhumed mantle massif samples show such alignment (e.g., Nicolas and Christensen, 1987; Ben Ismail and Mainprice, 1998), and that laboratory experiments indicate a link between the orientation and amount of shear induced deformation and the resulting LPO (e.g., Karato et al., 2008; Skemer and Hansen, 2016). For olivine single crystals $\sim 75\%$ of the total elastic anisotropy is hexagonal, while most of the remainder is of orthorhombic symmetry (e.g., Browaes and Chevrot, 2004). For assemblages, the hexagonal contribution ranges from $\sim 80\%$ for peridotites from spreading centers to $\sim 55\%$ in xenoliths from kimberlites in the compilation of Ben Ismail and Mainprice (1998). This apparent predominance of hexagonal anisotropy for mantle assemblages motivates the approximations usually made in seismology.

LPO development is usually assumed to require not just solid state convection but deformation within the dislocation creep regime. For typical olivine grain sizes of order mm, this implies that LPO formation and hence seismic anisotropy will be enhanced in the mantle’s boundary layers (e.g., Karato, 1998; Podolefsky et al., 2004; Becker, 2006). Thus, shear within the asthenosphere underneath the lithospheric plates, say within the top ~ 400 km of the mantle, is expected to dominate the upper mantle signal of geologically recent anisotropy formation. The more slowly deforming lithosphere may record past episodes of deformation or creation in the case of continental and oceanic lithosphere, respectively (e.g., Vinnik et al., 1992; Silver, 1996).

There are possible other contribution to anisotropy besides LPO due to past and present mantle flow, such as preserved shape preferred fabrics or LPO within the crust (e.g., Godfrey et al., 2000; Brownlee et al., 2017), or the effects of partial melt (e.g., Blackman et al.,

1996; Holtzman and Kendall, 2010; Hansen et al., 2016a). An effectively anisotropic partial-melt layer at the base of the lithosphere can explain observed impedance contrasts, for example (e.g., Kawakatsu et al., 2009). However, it is commonly held that regions of large partial melt fraction are of limited spatial extent away from spreading centers and continental rifts. This will be revisited below.

When deforming olivine aggregates in the laboratory, anisotropy strength due to LPO saturates at linear strains, γ , of $\lesssim 5 \dots 10$ (e.g., Zhang and Karato, 1995; Bystricky et al., 2000; Hansen et al., 2014). Preexisting textures likely require larger strain values for reorientation, in broad accordance with observations from the field (e.g., Skemer and Hansen, 2016). For strain-rates that might be typical for the asthenosphere, say $\sim 5 \times 10^{-15} \text{ s}^{-1}$ (e.g., a plate moving at 5 cm/yr inducing shear over a ~ 300 km thick layer), $\gamma = 5$ is achieved in ~ 30 Myr. Using circulation computations and finite strain tracking, one arrives at similar numbers; times of advection in mantle flow are commonly between 10 and 30 Myr over path lengths between 500 km to 1500 km, respectively (Becker et al., 2006a). In the highly deforming asthenosphere, these relatively short saturation or reworking times of order of 10s of Myr then determine the “memory” of seismic anisotropy, i.e., how much convective history and changes in plate motions are recorded. Within the cold and hence slowly deforming lithosphere, older episodes of deformation may be partially frozen-in for very long times, say $\gtrsim 300$ Myr in continents. This is longer than the characteristic lifetime of an oceanic plate, though it is most likely not a continuous record that is being preserved (e.g., Silver, 1996; Boneh et al., 2017).

In strongly and coherently deforming regions of the upper mantle, we therefore expect that the amplitude of anisotropy is mainly governed by the orientation of olivine LPO near saturation. Exceptions include spreading centers and subduction zones where a transition from simple to pure shear during vertical mass transport will lead to strong reworking of fabrics (e.g., Blackman and Kendall, 2002; Kaminski and Ribe, 2002; Becker et al., 2006a). Such reworking is where different mineral physics approaches regrettably diverge in their predictions (e.g., Castelnaud et al., 2009), and constraints from the lab and field indicate a mismatch with widely used LPO modeling approaches (Skemer et al., 2012; Boneh et al., 2015).

Irrespective of the details of the LPO formation mechanism, we note that anisotropy strength is not expected to scale with absolute plate or slab velocity, rather it is spatial variations in velocities (i.e. strain-rates) that control the rate of anisotropy saturation. Any relationship between plate speed and the signature of anisotropy is thus likely indirect, for example such that LPO formation under plate-motion induced shear is more efficient

compared to other processes like small-scale convection for faster plates with higher strain-rates (van Hunen and Čadež, 2009; Husson et al., 2015).

10.3.2. Anisotropy and Plate Motions

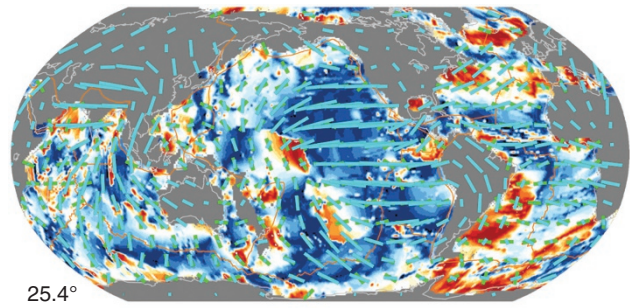
Given the link between LPO induced anisotropy and mantle flow, a first-order constraint on convection can thus be provided by the existence of significant radial anisotropy in the upper mantle (e.g., Dziewoński and Anderson, 1981; Nataf et al., 1986; Beghein et al., 2006; Wang et al., 2013). Due to the alignment of the fast symmetry axis of an LPO aggregate in the vertical or horizontal direction, a simple mantle convection cell with an oceanic plate forming at its top limb should display $v_{SH} > v_{SV}$ within and below the plate's interiors (dominating the global average), and $v_{SV} > v_{SH}$ within the up- and downwelling limbs underneath spreading centers and subduction zones, respectively (e.g., Montagner and Guillot, 2000).

Relatively few studies have addressed the distribution of average radial anisotropy in light of mantle dynamics (e.g., Regan and Anderson, 1984; Montagner and Tani moto, 1991; Chastel et al., 1993; Montagner, 1994; Babuška et al., 1998; Plomerová et al., 2002; Gung et al., 2003). Both average and broad-scale patterns of radial anisotropy can be shown to be consistent with the predictions from mantle convection computations with dislocation/diffusion creep olivine rheologies at grain sizes of order mm (Becker et al., 2008; Behn et al., 2009). Amplitudes of radial anisotropy appear underpredicted within the lithosphere by convective LPO models, particularly within continental regions (Becker et al., 2008). This hints at an additional contribution, e.g., due to frozen in anisotropy similar to what has been suggested for oceanic plates (e.g., Beghein et al., 2014; Auer et al., 2015).

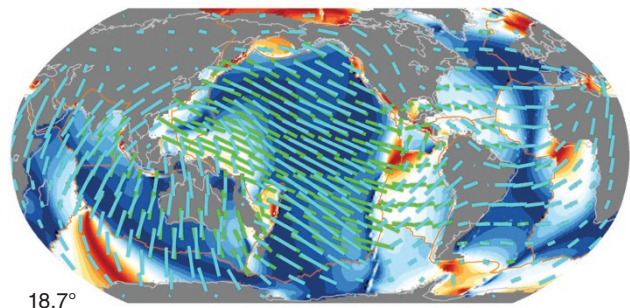
We now proceed to discuss the large-scale origin of azimuthal seismic anisotropy (Figure 10.2) in light of oceanic plate boundary dynamics (cf. Montagner and Guillot, 2000). Within the low-strain-rate lithosphere, we expect azimuthal anisotropy to record past deformation during creation of the plate. This deformation may be inferred from the spreading directions and rates that are recorded in the gradients of seafloor age (e.g., Conrad and Lithgow-Bertelloni, 2007). We can then compare the fast axes with paleo-spreading orientations (e.g., Hess, 1964; Forsyth, 1975; Nishimura and Forsyth, 1989).

Figure 10.4a shows a typical result for such a comparison. Spreading orientations overall represent a good first-order model of azimuthal anisotropy in the lithosphere. They appear recorded more clearly in anisotropy in younger rather than in older seafloor, particularly in the Pacific plate (e.g., Smith et al., 2004; Debayle and Ricard,

(a) spreading - lithosphere



(b) APM - asthenosphere



(c) LPO from flow - asthenosphere

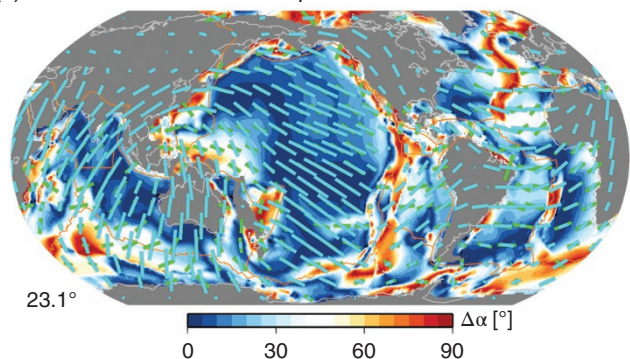


Figure 10.4 Angular orientational misfit, $\Delta\alpha$, in the oceanic plate regions, computed between azimuthal anisotropy from SL2013SA (cyan sticks; Schaeffer et al., 2016) and geodynamic models (green). (a) Seismology at 50 km depth vs. paleo-spreading orientations inferred from seafloor age gradients. (b) SL2013SA at 200 km depth vs. absolute plate motions in the spreading-aligned reference frame (Becker et al., 2015). (c) SL2013SA at 200 km depth vs. synthetic anisotropy based on LPO formed in mantle flow (model of Becker et al., 2008). Numbers in lower left indicate average angular misfit in the oceanic regions. See Becker et al. (2014) for more detail on the analysis. Source: (a) Schaeffer et al. 2016. (b) Becker et al. 2015. (c) Becker et al. (2008). Becker et al. (2014).

2013; Becker et al., 2014), perhaps due to small-scale reheating at ages older than ~ 80 Ma (cf. Nagihara et al., 1996; Ritzwoller et al., 2004). Seafloor that was generated during higher spreading rate activity shows smaller orientational misfits with lithospheric azimuthal

anisotropy than regions that were generated by slower spreading (Becker et al., 2014), possibly indicating variations in the degree of ductile to brittle deformation (Gaherty et al., 2004), asymmetry or non-ridge-perpendicular orientation of slow spreading, or the relative importance of small-scale convection (e.g., van Hunen and Čadek, 2009).

Besides controlling factors such as spreading rate and seafloor age which may have general relevance for the creation of oceanic lithosphere, there are also geographic differences (Figure 10.4a); the Atlantic displays larger misfits than the Pacific, for example. This might be an overall reflection of tectonics (Atlantic spreading rates are slower than Pacific ones). However, the resolution of surface wave anisotropy imaging is also spatially variable (e.g., Laske and Masters, 1998; Becker et al., 2003) and in particular earthquake source location errors are mapped into larger variations in fast azimuths in the Atlantic than the Pacific domain (Ma and Masters, 2015).

If we seek an explanation for deeper, asthenospheric, layers, we can consider the orientation of azimuthal anisotropy compared to plate motions. The underlying assumption for such comparisons is that the direction of surface velocities in some absolute reference frame, e.g., as based on hotspots (e.g., Minster and Jordan, 1978) are indicative of the orientation of shear due to motion of the lithosphere with respect to a relatively stationary deep mantle. This is called an absolute plate motion (APM) model.

Even in the absence of convective contributions due to density anomalies, plate-induced mantle flow can lead to regionally significant deviations from the shear deformation that is indicated by the APM model. This is true in terms of the velocity magnitude, i.e. if the plate is leading the mantle or vice versa in simple shear (Couette) type flow (with possible effects on anisotropy dip angle), and it is also important in that the orientation of mantle flow may be very different from that of plate motion (Hager and O'Connell, 1981). The sense of asthenospheric shear may thus be at large angles to APM orientations. Moreover, the degree to which asthenospheric flow is of the plug (Poiseuille) type matters because the depth distribution of strain-rates will be different for each case (Natarov and Conrad, 2012; Becker, 2017; Semple and Lenardic, 2018). These effects are likely most relevant for slowly moving plates.

Setting aside these complexities, the comparison between APM and azimuthal anisotropy in the asthenosphere can provide some guidance as to how much of the pattern of anisotropy might be related to convection and, importantly, it does not require any further modeling assumptions. Comparisons with APM have thus been used extensively to explore how anisotropy might be related to mantle flow (e.g., Montagner and Tanimoto, 1991; Debayle and Ricard, 2013).

Figure 10.4b shows such a comparison of azimuthal anisotropy with APM orientations at nominally 200 km depth. Much of the patterns of azimuthal anisotropy in the oceanic regions can be matched by APM alignment, indicating a relationship between flow-induced LPO and seismological constraints. The global oceanic misfit is smaller than for the lithospheric match to paleo-spreading, at average angular misfit $\lesssim 20^\circ$. This is of the order of orientational uncertainties for surface wave studies for azimuthal anisotropy (e.g., Laske and Masters, 1998; Becker et al., 2003; Ma and Masters, 2015; Schaeffer et al., 2016). In this sense, the APM model, its inherently non-physical nature notwithstanding, provides a plausible explanation for asthenospheric anisotropy and confirms that plates are an integral part of mantle convection.

However, there appear to be systematic geographic variations in misfit in the APM asthenospheric match of Figure 10.4b whose origin is unclear. Moreover, any use of crustal kinematics in an absolute sense, of course, requires a choice of reference frame. Figure 10.4b uses the spreading-aligned reference frame, which was argued by Becker et al. (2015) to provide a parsimonious explanation to a range of constraints for geologically recent plate dynamics. This reference frame is similar to hotspot reference frames with relatively small net rotation of the lithosphere with respect to the deep mantle (e.g., Ricard et al., 1991; Becker, 2006; Conrad and Behn, 2010).

10.3.3. Mantle Circulation Modeling

If we seek to make use of our understanding of the physics of mantle circulation instead of comparing anisotropy to APM, we need to approximate the details of mantle flow and LPO formation. In particular, we need to make choices as to how to infer density anomalies and viscosity variations within the mantle. In fact, comparisons of azimuthal anisotropy with the seminal mantle circulation model of Hager and O'Connell (1981) followed soon after (Tanimoto and Anderson, 1984).

To arrive at estimates of mantle flow, typically slab structure from seismicity (Hager, 1984) or isotropic seismic tomography is scaled to temperature using simplified approximations to what would be inferred from mineral physics and assumptions as to mantle composition (e.g., Hager et al., 1985). Such circulation model predictions can, for example, explain geoid anomalies as long as there is an increase in viscosity toward the lower mantle (e.g., Richards and Hager, 1984; King and Masters, 1992), and the associated mantle tractions also provide a powerful explanation for the patterns and rates of plate motions (e.g., Ricard and Vigny, 1989; Forte et al., 1991; Lithgow-Bertelloni and Richards, 1998; Becker and O'Connell, 2001). However, mantle velocities are strongly dependent on the variable force transmission that results from lateral

viscosity variations (e.g., Conrad and Lithgow-Bertelloni, 2002; Becker, 2006; van Summeren et al., 2012; Alisc et al., 2012), and those will affect strain rates and hence anisotropy development. In the case of seismic anisotropy, we can thus ask if geodynamic models of mantle flow that are constructed based on other constraints (e.g., geoid or plate motions) also fit seismic anisotropy, and we can use anisotropy to further refine such models.

Assuming that velocities of mantle flow are estimated, we need to make the link to seismic anisotropy. This can be done by simply examining shear in a certain layer of the mantle (i.e. velocity differences; e.g., Tanimoto and Anderson, 1984), computing the finite strain ellipsoid (FSE) accumulated along a particle path (e.g., McKenzie, 1979; Ribe, 1989), or estimating LPO using more complex micro-physical models (e.g., Ribe and Yu, 1991; Wenk and Tomé, 1999; Tommasi, 1998; Kaminski and Ribe, 2001; Blackman et al., 2002). Such approaches have the capability to incorporate laboratory results that indicate the importance of recrystallization during LPO anisotropy formation under sustained shear (e.g., Zhang and Karato, 1995; Bystricky et al., 2000). Experiments also suggest that olivine slip system strength and hence the type of LPO being formed depends on deformation conditions and volatile content (e.g., Jung and Karato, 2001; Katayama et al., 2004).

The most common, A-type LPO regime (Karato et al., 2008; Mainprice, 2007) appears most prevalent among xenolith and mantle massif samples (Ben Ismail and Mainprice, 1998; Bernard et al., 2019). The corresponding modeled LPO predictions of best-fit hexagonal symmetry axis alignment in flow are broadly consistent with the orientation of the longest FSE axis. Exceptions are regions of strong fabric reworking such as underneath spreading centers or other complex flow scenarios (Ribe and Yu, 1991; Blackman et al., 2002; Kaminski and Ribe, 2002; Becker et al., 2006a; Conrad et al., 2007). Other approximations of the LPO such as the infinite strain axis (Kaminski and Ribe, 2002) appear to perform less well in comparisons with surface wave based anisotropy than LPO estimates (Becker et al., 2014). These tests indicate that anisotropy from mantle flow may perhaps be best modeled either by using the FSE (equivalent to whisker orientation in analog experiments; Buttles and Olson, 1998) or by computing bulk-approximate (Goulding et al., 2015; Hansen et al., 2016b) or grain-oriented (e.g., Kaminski et al., 2004; Castelnau et al., 2009) descriptions of actual LPO formation, on which we will focus here.

Once LPO is estimated for olivine or olivine-orthopyroxene assemblages by some scheme (e.g., Kaminski et al., 2004), we then need to assign elastic tensors to each virtual grain to compute effective anisotropy. Choices as to the pressure and temperature dependence of

elasticity tensor components as well as the averaging scheme have noticeable effects (Becker et al., 2006a; Mainprice, 2007), but are likely smaller than uncertainties in seismological imaging on global scales.

Given dramatic improvements in seismological constraints during the 20 years after the fundamental comparison of Tanimoto and Anderson (1984), a number of groups revisited mantle circulation modeling in light of azimuthal anisotropy ~ 15 years ago. Gaboret et al. (2003) and Becker et al. (2003) focused on Pacific and global-scale surface wave models, respectively, while Behn et al. (2004) and Conrad et al. (2007) explored matching *SKS* splitting in oceanic plate regions and globally. These models usually find that moving from APM models to mantle flow computations that respect the return flow effects caused by plate motions alone does not improve, or sometimes rather significantly degrades, the fit to seismologically inferred anisotropy. The added physical realism of estimating flow and LPO does come into play once density anomalies are considered for the flow computations, and such models typically outperform APM approaches (Gaboret et al., 2003; Becker et al., 2003; Behn et al., 2004; Conrad et al., 2007; Conrad and Behn, 2010; Becker et al., 2014).

Figure 10.4c shows an example of how LPO formed under dislocation creep in a global circulation model that includes density anomalies (as used in Becker et al., 2008, to study radial anisotropy) matches azimuthal anisotropy (Schaeffer et al., 2016) at asthenospheric depths. While the average misfit for the LPO model is larger than for the comparison with APM (Figure 10.4b), the regions of large misfit appear now more easily associated with tectonic processes. In particular, large misfits are found underneath spreading centers, where LPO is expected to be reworked (e.g., Blackman and Kendall, 2002; Kaminski and Ribe, 2002), a process that is as of yet fairly poorly constrained experimentally (Skemer et al., 2012; Hansen et al., 2014, 2016b). In the models, a consequence of this reworking is that elastic anisotropy locally displays slow axis hexagonal symmetry as well as significant non-hexagonal contributions in regions with pure shear type of flow (Becker et al., 2006a). Besides, non-LPO contributions due to partial melting is expected to matter close to the spreading centers (Blackman et al., 1996; Blackman and Kendall, 1997; Holtzman and Kendall, 2010; Hansen et al., 2016a). However, given that regions of large misfit appear confined to “special” places and that all oceanic basins otherwise fit quite well (Figure 10.4c), we consider the match of LPO predictions from mantle flow and anisotropy a first-order achievement of “applied geodynamics” (Gaboret et al., 2003; Becker et al., 2003; Behn et al., 2004; Conrad et al., 2007).

The LPO model of Figure 10.4c relies on the approach of Becker et al. (2006a) who computed fabrics using the

method of Kaminski et al. (2004) along particle paths. Tracers are first followed back in time until, upon iteration, their advective forward paths accumulate a critical finite strain, γ_c , at each observational point. The idea is that any existing textures will be overprinted, and in the case of the example in Figure 10.4c, $\gamma_c \approx 6$. This choice leads to a good match to radial anisotropy averages and patterns (Becker et al., 2008) as well as regional SKS splitting delay times (e.g., Becker et al., 2006b; Miller and Becker, 2012), and is consistent with overprinting strains from field and laboratory deformation (Skemer and Hansen, 2016).

Assuming that the LPO that is predicted from mantle flow modeling provides at least a statistically appropriate estimate of anisotropy in the upper mantle, we can then use geodynamic models to revisit the hexagonal approximation of seismological imaging. Globally, $\sim 80\%$ of LPO anisotropy is found to be of hexagonal character on average; within regional anomalies, the orthorhombic contribution can reach $\lesssim 40\%$ (Becker et al., 2006a). This is close to the orthorhombic fraction ($\sim 45\%$) invoked by the subducted asthenosphere model of Song and Kawakatsu (2012). However, on global scales, geodynamic models confirm that the simplifying assumption of hexagonal anisotropy made by seismology appear justified if olivine LPO is the major source of anisotropy in the upper mantle.

The flow computation used in Figure 10.4c assumes that mantle circulation is stationary over the timescales needed to achieve γ_c . This is a potentially questionable approximation, and time-evolving scenarios expectedly produce larger complexity of LPO predictions, e.g., compared to steady-state subduction scenarios (Buttles and Olson, 1998; Faccenda and Capitanio, 2013; Zhou et al., 2018). However, reconstructing the time-evolution of convective flow introduces additional uncertainties due to having to use plate reconstructions and the nonreversibility of the energy equation (e.g., Steinberger and O'Connell, 1997; Conrad and Gurnis, 2003). More to the point, Becker et al. (2003) found that the improvements in terms of the match of anisotropy predictions when allowing for time-dependent mantle circulation were ambiguous. Preliminary tests with newer models confirm that asthenospheric anisotropy predictions are not affected much compared to steady-state approximations as in Figure 10.5c, as expected given the relatively short advective times. However, the shallower regions within the lithosphere appear somewhat sensitive to which plate reconstruction is used. This provides an avenue for further research.

Boundary Layer Anisotropy. One of the major achievements of geodynamics is to have linked the bathymetry and heatflow of oceanic seafloor to the half-space cooling

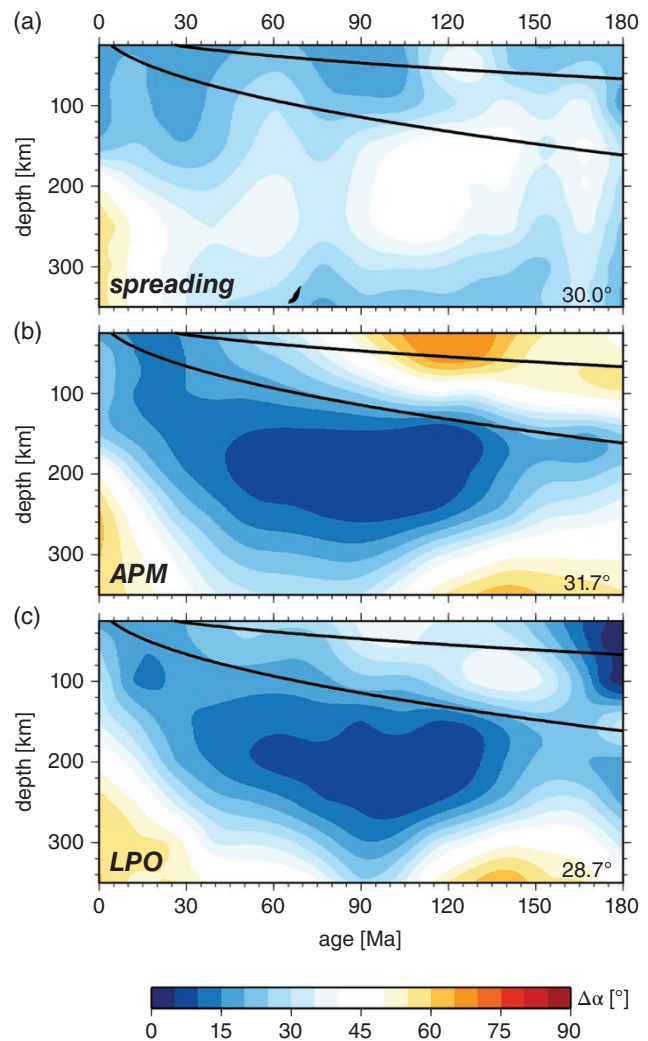


Figure 10.5 (a) Angular orientational misfit, $\Delta\alpha$, underneath the Pacific plate, computed between fast propagation orientations from SL2013SA (Schaeffer et al., 2016) and paleo-spreading orientations, as a function of depth and seafloor age bins (cf. Figure 10.4a). Black lines are 600°C and 1200°C isotherms from half-space cooling, respectively. (b) Angular misfit between azimuthal anisotropy and absolute plate motions in the spreading-aligned reference frame (Becker et al. 2015). (c) Angular misfit between azimuthal anisotropy and synthetics based on computing LPO formation in global mantle flow (model of Becker et al. 2008). Numbers in lower right indicate average angular misfit for each panel. See Becker et al. (2014) for more detail. Source: (a) Schaeffer et al. (2016). (b) Becker et al. (2015). (c) Becker et al. (2014).

of a convective thermal boundary layer (Turcotte and Oxburgh, 1967; Parsons and Sclater, 1977). Shear in the region below the mechanical boundary layer that is contained within the thermal lithosphere should determine LPO formation (Podolefsky et al., 2004). This is indeed seen when considering the amplitude of azimuthal

anisotropy as a function of seafloor age (e.g., Burgos et al., 2014; Beghein et al., 2014) though alignment with APM is perhaps a better measure as anisotropy orientations should be better constrained than amplitudes (Debayle and Ricard, 2013).

Figure 10.5 shows a typical result where the misfit of the three geodynamic models of Figure 10.4 is shown for the Pacific plate as a function of age. As noted, paleospreading is only a good model for the shallowest oceanic lithosphere and relatively young ages. However, alignment with APM or LPO provides a good explanation of azimuthal anisotropy within a 150–200 km thick layer below the $\sim 1200^\circ\text{C}$ isotherm (cf. Burgos et al., 2014; Beghein et al., 2014), as expected given the depth distribution of deformation within the dislocation creep regime (Becker et al., 2008; Behn et al., 2009). Alignment with both LPO and APM underneath the cold isotherm breaks down at ages older than ~ 150 Ma (cf. Figures 8.4b and 8.4c), perhaps a reflection of small-scale convection (van Hunen and Čadek, 2009).

Comparison of geodynamic predictions with different seismological models leads to similar conclusions (Becker et al., 2014). However, radial anisotropy does not appear to follow half-space cooling (Burgos et al., 2014), and those discrepancies will be revisited below. The approach of computing mantle circulation and then inferring LPO anisotropy from it to constrain convection, of course, translates to the bottom boundary layer of the mantle as well (Romanowicz and Wenk, 2017), and a separate chapter in this volume is dedicated to this problem.

10.3.4. Examples of Inferences That Extend Beyond the Reference Model

As the previous section illustrates, we can indeed use azimuthal seismic anisotropy as a constraint for mantle rheology and upper mantle convection, and in particular arrive at a consistent and quantitative, first-order description of lithosphere-asthenosphere dynamics underneath oceanic plates. The formation of olivine LPO within the “typical” A type slip system under convective flow and plates forming according to half-space cooling appears to provide a globally appropriate geodynamic reference model, and seismic anisotropy is another constraint for plate formation. We should keep in mind the relative success of this “reference” model (e.g., Figures 8.4 and 8.5) as we move on to briefly discuss some of the more indirect inferences based on seismic anisotropy, and in particular when we conclude by discussing regional or process level complications.

Mantle flow is driven by density anomalies and modulated by viscosity, and in theory both of these can be inverted for using seismic anisotropy assuming it is formed by the shear due to spatial variations in velocity.

In practice, additional constraints are needed for all but the simplest tests. One important question in mantle dynamics is that of the appropriate reference frame for surface motions with respect to the lower mantle. Different reference frames yield a range of estimates for trench advance or rollback, for example (e.g., Chase, 1978; Funiello et al., 2008) with implications for regional tectonics and orogeny.

Given that seismic anisotropy due to LPO is formed under the shear that corresponds to the motion of the surface relative to the stagnant lower mantle, one may thus postulate that the best APM is that which minimizes the misfit to anisotropy. This was addressed by Kreemer (2009) based on *SKS* splitting and explored by Montagner and Anderson (2015) for surface waves and individual plate motions with focus on the Pacific. The spreading-aligned reference of Figure 10.4b naturally minimizes the misfit with a number of surface-wave based estimates of azimuthal anisotropy, and their individual best-fit poles are very similar. This implies that the anisotropy-constrained reference frame may have general relevance, with implications for the relative strength of transform faults, for example (Becker et al., 2015).

One can also use mantle circulation modeling to explore the depth-distribution of the shear that corresponds to different degrees of net rotation of the lithosphere (Zhong, 2001; Becker, 2006), and then test how such a shear component would affect the match of global circulations models to seismic anisotropy. This exploits the fact that the match to anisotropy is sensitive to where in the mantle shear is localized (Becker et al., 2003; Conrad and Behn, 2010). Becker (2008) used the match to surface wave based azimuthal anisotropy to argue that net rotation should be less than $\lesssim 0.2^\circ/\text{Myr}$. Conrad and Behn (2010) considered both *SKS* splitting and surface wave anisotropy and further explored this “speed limit” on net rotation. They find a permissible net rotation of $\sim 0.25^\circ/\text{Myr}$ for an asthenospheric viscosity that is one order of magnitude smaller than that of the upper mantle.

Using models that self-consistently generate plate motions, Becker (2017) showed that anisotropy constraints on asthenospheric viscosity are consistent across different modern azimuthal anisotropy models, and that even slab-driven flow alone leads to perturbations of the large-scale match of LPO anisotropy from flow that is seen in Figure 10.4c. A moderate sub-oceanic viscosity reduction to $\sim 0.01 \dots 0.1$ times the upper mantle viscosity is strongly preferred by both the model match to azimuthal anisotropy and the fit to plate motions (Figure 10.6), even though there exists a typical trade-off with layer thickness (Richards and Lenardic, 2018). In particular, suggested high partial melt, lubricating zones underneath oceanic plates (e.g., Kawakatsu et al., 2009; Schmerr, 2012) appear to not be widespread enough

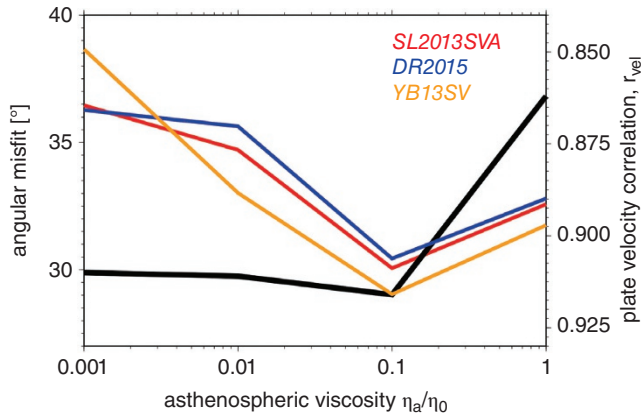


Figure 10.6 Angular misfit (minimum with depth) between flow model predictions and azimuthal seismic anisotropy for oceanic domain for three different seismological models: SL2013SVA (Schaeffer et al., 2016, as in Figure 10.4), DR2015 (Debayle and Ricard, 2013), and YB13SV (Yuan and Beghein, 2013) (colored lines), and misfit of predicted plate velocities (black line), as a function of asthenospheric viscosity reduction for a 300 km thick layer. Source: Modified from Becker (2017), see there for detail.

to affect largescale mantle shear, or else it should be seen in the match to seismic anisotropy (Becker, 2017).

On a regional scale, *SKS* splitting provides better lateral resolution than traditional surface wave analyses and is thus widely used to infer the role of mantle flow for tectonics, particularly within continental plates (Figure 10.2). When combined with flow models, we can exploit the sensitivity of mantle circulation to density anomalies and viscosity variations (e.g., Fouch et al., 2000; Hall et al., 2000; Behn et al., 2004; Becker et al., 2006b). This was done by Miller and Becker (2012) in a quasi-inverse sense, exploring a large number of global mantle flow computations with a range of density and viscosity models to test which (in particular with respect to continental keel geometry and strength) are consistent with *SKS* splitting in NE South America. A similar approach was used on a larger-scale for South America by Hu et al. (2017), and Faccenna et al. (2013) to infer a low viscosity channel underneath the Red Sea, for example.

Another possible approach to explore the effects of mantle convection, helpful in the absence of good isotropic tomography for example, is to test different forward models of the effect of density anomalies, e.g., compared to plate-scale flow for plumes (e.g., Walker et al., 2005; Ito et al., 2014) or details of subduction and delamination scenarios (e.g., Zandt and Humphreys, 2008; Alpert et al., 2013). In such regional contexts, mantle flow models provide the capability to explore the impact of depth variations in seismic anisotropy, as those are ideally recorded in the back-azimuthal dependence of

SKS splitting (e.g., Blackman and Kendall, 2002; Hall et al., 2000; Becker et al., 2006b). Subduction zone *SKS* splitting anisotropy is, however, complex to the extent that the correct background model becomes questionable (e.g., Long, 2013), as discussed in a different chapter of this volume.

A question to ask whenever seismic anisotropy observations are used to infer mantle dynamics is how consistent any model is with a range of observations besides the anisotropy data, e.g., in terms of the geoid, dynamic topography, or plate motions. Some studies invoke different effects that may impact mantle flow (e.g., a small-scale plume, inherited structure in the lithosphere, volatile variations in the asthenosphere) for nearly every single different *SKS* split, often without any consistent flow modeling, and so trivially explain all data perfectly in the extreme case. Other studies, such as the approach illustrated in Figure 10.4c, strive for a broad-scale match to the observations, within an actual geodynamic framework that respects continuum mechanics conservation laws. This can then invite further study as to which effects (e.g., intra-plate deformation, volatile variations of frozen in structure) may be required regionally on top of the reference model. Clearly, there is a continuum between those quasi end-members.

10.4. OPEN QUESTIONS

10.4.1. Regional Complexities and Scale-Dependent Resolution

Navigating between the extremes of a possibly very complicated model or simulation that matches all data, and a simple model which may or may not be a good reference given large regional misfits is, of course, not an uncommon challenge in the Earth sciences. However, the complexities of anisotropy, both in terms of spatially variable resolution and in terms of possible mechanisms for anisotropy generation, seem to make these trade-offs more acute for efforts of linking anisotropy to mantle flow.

Oceanic Plates Revisited. The previous discussion of convection dynamics as seen by seismic anisotropy focused on large spatial scales and seismic models that are derived from global surface wave datasets. *SKS* splitting for oceanic island stations (Figure 10.2) are also usually well fit by the density-driven mantle circulation models (e.g., Behn et al., 2004; Conrad et al., 2007). Increasingly, we can interpret results from ocean bottom seismometer deployments, which slowly infill the oceanic plates in terms of high-resolution and high-quality regional constraints (e.g., Isse et al., 2019). In particular,

deployments that are designed to image “normal” or at least “melt free” oceanic plates are very valuable to further develop the thermo-mechanical reference model of plate generation that was alluded to previously (e.g., Lin et al., 2016; Takeo et al., 2018; Kawakatsu and Utada, 2017; Russell et al., 2019).

Alas, the regional results are often at odds with inferences from global models, particularly when it comes to the variation in strength of radial and azimuthal anisotropy with depth. This has long been debated and results are sensitive to the dataset selection and applied corrections (e.g., Ferreira et al., 2010; Ekström, 2011; Rychert and Harmon, 2017). For presumably typical oceanic lithosphere, there is evidence for radial anisotropy with $v_{SH} > v_{SV}$ in the lithosphere (e.g., Gaherty et al., 1996; Russell et al., 2019), but regional (Takeo et al., 2013) and many global models show a deeper peak in radial anisotropy (~80...150 km, e.g., Nettles and Dziewoński, 2008; French and Romanowicz, 2014; Auer et al., 2014; Moulik and Ekström, 2014). The latter would be more consistent with a geologically recent, convective LPO origin of radial anisotropy.

Moreover, while azimuthal anisotropy strength appears to follow half-space cooling similar to the region of low angular misfit in Figure 10.5, radial anisotropy appears to have limited seafloor age dependence (Burgos et al., 2014; Beghein et al., 2014; Auer et al., 2015; Isse et al., 2019). This might indicate that LPOs due to spreading and/or petrological heterogeneities (e.g., Kawakatsu et al., 2009; Schmerr, 2012; Sakamaki et al., 2013; Ohira et al., 2017) are frozen in during the generation of plates (e.g., Beghein et al., 2014; Auer et al., 2015; Russell et al., 2019), or that the effects of melt-induced LPO mask the age dependence that would be expected (Hansen et al., 2016a).

At least some mid-lithospheric structure appears required for oceanic plates that is unrelated to simple LPO anisotropy (Rychert and Harmon, 2017), perhaps indicating a mid-lithospheric discontinuity similar to what has been discussed for continental plates (e.g., Yuan and Romanowicz, 2010; Selway et al., 2015). However, the mechanical effects of the lithospheric component of convection in terms of asthenospheric shear appear to be captured by half-space cooling and azimuthal anisotropy as reflected in Figure 10.5 (Becker et al., 2014).

Anisotropy in Continents. Referring to his analysis of P wave seismic anisotropy in oceanic plates, Hess (1964) noted that “the structure and history of the whole ocean floor can probably be worked out much more rapidly than the more complicated land surface of the Earth,” and this has been very much true. Thermal mantle convection explains the motions of the nearly rigid oceanic plates well, but the distributed and protracted deformation

record of the continental lithosphere is strongly affected by rheological and compositional effects, and still presents many questions.

One way to explore the consistency between different ways of imaging anisotropy is to consider the match between SKS splitting estimates and surface wave based azimuthal anisotropy in continents where SKS splits are preferentially measured, because of station logistics (Figure 10.2). Montagner et al. (2000) conducted such a comparison using an approximate method and found that agreement in terms of the fast azimuth pattern was limited. A more positive assessment with a more complete SKS dataset was provided by Wüstefeld et al. (2009) who found a match at the longest wavelengths. Becker et al. (2012) revisited this comparison and showed that full waveform modeling of SKS splitting leads to only moderate differences in the apparent splitting compared to averaging for the current generation of global surface models. Indeed, the agreement in terms of fast azimuths is limited when SKS splits are smoothed over less than ~2000 km length scales. This does at least partly reflect the inherent resolution limits of global models (e.g., Debayle and Ricard, 2013; Schaeffer et al., 2016). Most surface wave models also underpredict SKS delay times, likely because of the required regularization (cf. Schaeffer et al., 2016).

Figure 10.2b shows that the long-wavelength correlation between SKS fast axis patterns and different surface wave models is best in the upper ~400 km of the mantle, where azimuthal anisotropy models show the largest power and are most in agreement with each other (Becker et al., 2012; Yuan and Beghein, 2013). This finding is consistent with a common origin, the suggested dominance of an uppermost mantle, asthenospheric anisotropy to typical SKS splitting results (e.g., Fischer and Wiens, 1996; Silver, 1996), and an LPO induced by mantle flow origin (Figure 10.5; e.g., Becker et al., 2008, 2014). Figure 10.2b also indicates a hint of a drop in correlation in the lithosphere, and regionally, it is clear that there is both depth-dependence in the surface-wave imaged anisotropy and the match with SKS splitting (e.g., Deschamps et al., 2008b; Yuan et al., 2011; Lin et al., 2016; Takeo et al., 2018).

Such discrepancies motivate an alternative approach that exploits the difference in depth sensitivity between SKS and Rayleigh waves (Marone and Romanowicz, 2007; Yuan and Romanowicz, 2010). One can use surface waves to constrain the shallow part of a model, say above ~250 km, and then use the complementary resolution of the path component of teleseismic waves beneath that region to exploit SKS constraints on anisotropy. Along with constraints from radial anisotropy (e.g., Gung et al., 2003) and alignment of 2ϕ anisotropy with APM motions, such models have been used to infer a thermochemically layered structure of the North American

craton (Yuan and Romanowicz, 2010; Yuan et al., 2011), for example.

Given the now more complete coverage of the continental US with *SKS* splitting thanks to USArray (Figure 10.2a), we recently revisited the question of agreement between surface wave models and *SKS*, and found that *SKS* remain poorly matched even by newer surface wave models. An exception is the model of Yuan et al. (2011) for most of North America, but that model attempts to fit *SKS* splits by design. This implies that the depth resolution of large-scale surface wave models is, on a continent-scale, not at the level where details in possible anisotropic layering could be consistently determined, particularly below ~ 200 km (Yuan et al., 2011).

10.4.2. Uncertainties About Microphysics

Formation of Olivine LPO. There is now a range of experimental work that documents how olivine develops LPO under shear. Among the modern studies, Zhang and Karato (1995) and the large-strain experiments of Bystricky et al. (2000) showed how olivine *a*-axes cluster within the shear plane for the common, A type fabric, or the high-stress D type. A-type LPO is found most commonly in natural samples (Ben Ismail and Mainprice, 1998; Bernard et al., 2019), and provides the most straightforward link between anisotropy and flow as was explored in section 3.3.

However, Jung and Karato (2001) and Katayama et al. (2004) found that additional LPO types can develop depending on deviatoric stress, temperature, and water content conditions, and mineral physics modeling approaches can reproduce those fabrics by assigning different relative strength to the major olivine slip systems (Kaminski, 2002; Becker et al., 2008). The predictions for anisotropy can be markedly different from A: The B (high-water, high-stress/low-temperature type) would lead us to expect azimuthal anisotropy to be oriented perpendicular to shear, and this might explain some of the subduction zone complexities, though likely not all trench-parallel splitting (Kneller et al., 2005; Lassak et al., 2006). Effective B types are also seen in high partial-melt experiments (Holtzman et al., 2003). The C (high-water, low-stress/high-temperature) type is expressed such that $v_{SV} > v_{SH}$ under horizontal shear, implying a complete reorientation of the relationship between flow and radial anisotropy (Karato et al., 2008; Becker et al., 2008).

At present, it is not entirely clear how olivine LPO formation depends on deformation conditions, in particular in conjunction with ambient pressure (Karato et al., 2008). For example, Ohuchi et al. (2012) substantiated a transition from A \rightarrow B LPO as a function of water content at low confining pressures. However, Ohuchi and Irifune

(2013) showed that the dependence on volatile content appears reversed at higher pressures (below ~ 200 km depth), such that A would be the high-volatile content LPO, and changes in LPO, perhaps mainly depth-dependent (cf. Mainprice et al., 2005; Jung et al., 2009).

If we consider the range of natural xenolith and ophiolite samples, all of the LPO types documented in the lab are indeed found in global compilations (Mainprice, 2007; Bernard et al., 2019). However, samples from individual sites show a range of different LPOs, at presumably similar deformation conditions in terms of volatile content and deviatoric stress. Moreover, when such conditions are estimated from the samples, no clear systematics akin to the laboratory-derived phase diagrams arise (Bernard et al., 2019). This implies that the style and history of deformation may be more important in controlling natural sample LPO, and perhaps, by inference, seismic anisotropy, particularly in the lithosphere where deformation is commonly more localized and where preservation potential is high.

Besides these uncertainties regarding the formation of different LPO types under dislocation creep by changes in slip system activity due to ambient conditions, it is not straightforward to predict where dislocation creep should dominate (Hirth and Kohlstedt, 2004). The estimate of predominant dislocation creep between ~ 100 – 300 km for grain sizes of order mm (Podolefsky et al., 2004) is compatible with the depth distribution of radial anisotropy, for example (Becker et al., 2008; Behn et al., 2009). However, using different assumptions about grain growth and evolution, Dannberg et al. (2017) constructed mantle convection models, which are consistent with seismic attenuation, but would predict the dominance of diffusion creep within the asthenosphere. The assumption that LPOs only form under dislocation creep and are preserved or destroyed under diffusion creep has been challenged (e.g., Sundberg and Cooper, 2008; Miyazaki et al., 2013; Maruyama and Hiraga, 2017), but it remains to be seen where most of the discrepancies arise.

While geodynamic modeling can easily incorporate stress, temperature, and pressure-dependent changes in slip systems for LPO predictions, for example, it is thus not clear if such a modeling approach is warranted. If volatile content is used as a free parameter, for example, we can construct upper mantle models with a range of seismic anisotropy predictions for the exact same convective model. This is not the most satisfying situation, unless other constraints such as from magneto-tellurics or phase boundary deflections provide further constraints on volatile variations. Moreover, the good match of the geodynamic reference model to azimuthal and radial anisotropy discussed in Section 10.3.3 implies that A type LPO, formed under dislocation creep, may well be dominant in the upper mantle.

Mechanical Anisotropy. Besides seismic, we also expect mechanical anisotropy as a result of the formation of LPO, i.e., the deformation behavior of olivine will depend on the sense and type of shear. Such viscous anisotropy is one potential mechanism for lithospheric strain-localization and deformation memory in plate boundaries (e.g., Tommasi et al., 2009; Montési, 2013). Mechanical anisotropy has been documented in the laboratory for olivine LPO (Hansen et al., 2012), and was implemented in microstructural modeling approaches (Castelnau et al., 2009; Hansen et al., 2016c).

We expect viscous anisotropy to increase the wavelength of convection (Honda, 1986; Busse et al., 2006) and localize flow in the asthenosphere if the weak plane is aligned with plate shear, possibly stabilizing time-dependent plate motions (Christensen, 1987; Becker and Kawakatsu, 2011). The response of a mechanically anisotropic layer will also lead to a modification of the growth rates of folding or density driven instabilities (Mühlhaus et al., 2002; Lev and Hager, 2008). However, trade-offs between isotropically weakened layers and anisotropic viscosity may make any effects on post-glacial response, the geoid, or the planform of convection hard to detect (Han and Wahr, 1997; Becker and Kawakatsu, 2011), in analogy to the bulk seismic anisotropy of a layered medium with isotropic velocity variations (Backus, 1962).

On regional scales, the effect of viscous anisotropy may be more easily seen in tectonic or dynamic observables, and any treatment of the development of texture should in principle account for the mechanical effects of LPO formation on flow for self-consistency and to account for possible feedback mechanisms (Knoll et al., 2009). The joint development of mechanical and seismic anisotropy may be of relevance in subduction zones, where seismic anisotropy is widespread, and time-dependent fluctuations in the mantle wedge temperature may result (Lev and Hager, 2011).

Self-consistent modeling of both seismic and viscous anisotropy was implemented by Chastel et al. (1993) for an idealized convective cell, and more recently by Blackman et al. (2017) for a more complete convection model of a spreading center. Models that include the LPO feedback show generally similar flow patterns than simpler models, but there can be up to a factor ~ 2 enhancement of predicted surface wave azimuthal anisotropy close to the ridge because of increased strain-rates, and the transverse isotropy symmetry axes are more horizontally aligned (Blackman et al., 2017) than those of earlier one-way LPO predictions (Blackman and Kendall, 2002). It remains to be seen if such effects of viscous anisotropy feedback are relevant for the interpretation of regional or global convection, or if other uncertainties such as the effects of temperature, composition, and volatile anomalies on isotropic olivine rheology swamp the signal.

10.5. WAYS FORWARD

Our general understanding of upper mantle convection thus appears to be reflected in seismic anisotropy, and anisotropy allows broad inferences on asthenospheric viscosity and regional tectonics, for example. Yet, many uncertainties remain and become most acute if the strength of anisotropy is to be exploited quantitatively. What can we do to raise the water levels of this glass-half-full scenario?

For one, more data, and in particular more seafloor, or oceanic realm, observations, as well as dense continental seismometer deployments, certainly help. Higher-density imaging should resolve many of the uncertainties, including the depth distribution of seismic anisotropy in oceanic plates over the next decade. Seismometer arrays such as USArray have transformed our view of mantle structure under continental plates, even though much work is still to be done to integrate the newly imaged complexity into dynamic models of mantle evolution. Availability of high-density passive seismic data means better resolution for surface wave studies. Moreover, many deployments are now also sampling the upper mantle with strongly overlapping Fresnel zones (3-D sensitivity kernels) for SKS splitting (Chevrot et al., 2004; Long et al., 2008). Using methods that make use of the array station density (Ryberg et al., 2005; Abt and Fischer, 2008; Monteiller and Chevrot, 2011; Lin et al., 2014; Mondal and Long, 2019) rather than presenting individual splits without concern as to the likely implications of back-azimuthal dependencies and overlapping sensitivity is still the exception, however. It should become the rule, even if the methodological burden is higher.

Yet, even for well-constrained regions, at least some trade-offs between structural model parameters will likely persist, which is when inversion choices as to parameterization and regularization become even more important. Any mixed- or underdetermined inverse problem requires regularization, and often choices are made based on the intuition, or preconceptions, of seismologists as to the degree of isotropic and anisotropic heterogeneity. Different structural representations can result, depending on the treatment of the preferred spectral character of isotropic and anisotropic heterogeneity. One way to approach the problem is to quantify the statistical character of heterogeneity of anisotropy and isotropic velocity anomalies (e.g., due to temperature and compositional variations) from field observations or convection modeling (e.g., Holliger and Levander, 1992; Becker et al., 2007b; Kennett et al., 2013; Alder et al., 2017), and then have those properties guide regularization.

Another, more narrow, but perhaps in our context more productive, way to introduce a priori information is to use assumptions about the symmetry types of anisotropy and

conditions for the formation of certain LPO types for imaging or joint seismological and geodynamic inversion. This spells out a project to integrate as much information about the link between seismic anisotropy and convection from laboratory and field work, to seismology, to geodynamic modeling for a better understanding of the evolution of plate tectonics. Once firm links are established, such an approach should, in principle, allow extending the use of seismic anisotropy much further back in time than the last few 10s of Myr, if we are able to capture the lithospheric memory of “frozen in” structure alongside the asthenospheric convection contribution.

The simplifications of hexagonal symmetry axes being oriented vertically (radial anisotropy) or horizontally (azimuthal anisotropy) is one example of imposing a priori assumptions to simplify imaging. More generally, we can solve for the overall orientation of the symmetry axes of a medium with hexagonal anisotropy, for example. This approach is called *vectorial tomography* (Montagner and Nataf, 1988; Chevrot, 2006) and has been in use for a long time (Montagner and Jobert, 1988), though not widely so. Vectorial tomography exploits the fact that individual minerals such as olivine show certain characteristics which link different elastic parameters, allowing reduction in the parameter space that has to be explored by a seismological inversion (Montagner and Anderson, 1989; Plomerová et al., 1996; Xie et al., 2015). Similar relationships between parameters such as P - and S -wave anisotropy, for example, can be established for upper-mantle LPO assemblages (Becker et al., 2006a, 2008) or crustal rocks (Brownlee et al., 2017), and the resulting scaling relationships can improve inversion robustness (Panning and Nolet, 2008; Chevrot and Monteiller, 2009; Xie et al., 2015; Mondal and Long, 2019).

Use of such petrological scalings limits the interpretation to, say, determining the orientation and saturation of a certain type of olivine LPO in the mantle, rather than being general and allowing for other causes of anisotropy. However, the images of lateral variations should be more robust than the general inversion which will itself be subject to other assumptions, even if it is just regularization. Moreover, different assumptions as to which types of LPOs might be present can also be tested in a vectorial tomography framework. In this context, surface wave anomalies in 2φ and 4φ patterns (e.g., Montagner and Tanimoto, 1990; Trampert and Woodhouse, 2003; Visser et al., 2008) also appear underutilized. Based on a simple petrological model for peridotite, *Montagner and Nataf* (1986) showed that mantle-depth Rayleigh and Love waves should be mainly sensitive to the 2φ and 4φ signal, respectively. However, there is evidence for additional Rayleigh and Love wave structure in 4φ and 2φ , respectively, for the mantle (e.g., Trampert and Woodhouse, 2003), and such signals are often seen for the crust

(cf. Figure 10.3; e.g., Adam and Lebedev, 2012; Xie et al., 2015). For many petrological models, there exist strong relationships between the 2φ and 4φ signature in each wave type, meaning that Rayleigh and Love waves can be inverted jointly for azimuthal anisotropy for certain a priori assumptions, yet this is not often done (e.g., Xie et al., 2015; Russell et al., 2019) as horizontal records are usually noisier than vertical seismograms. Moreover, the sensitivity of each surface wave type depends on the dip angle and olivine LPO type which might be diagnostic. This could be further utilized in vectorial tomography imaging, particularly for joint surface and body wave inversions (Romanowicz and Yuan, 2012).

In order to proceed with such joint inversions, we need to better understand the predictions of laboratory experiments as to LPO formation under different deformation conditions. This requires more experimental work, particularly under low deviatoric stress (Skemer and Hansen, 2016; Bernard et al., 2019). Moreover, a better handle on the degree to which dislocation creep dominates LPO formation needs to be established. Using improved microstructural relationships, we can also revisit the treatment of grain-size evolution to better explore which parts of the mantle should form anisotropy under what conditions. Among other improvements of time-dependent mantle flow models, such a consistent picture of the across-scale deformation of the upper mantle will not only provide better constraints on convection but also clarify the role of grain-size evolution and inherited fabrics for the formation and preservation of plate boundaries (e.g., Tommasi et al., 2009; Montési, 2013; Bercovici et al., 2015).

10.6. CONCLUSIONS

So, which is it, a can of worms or the most useful constraint? We think that the pitfalls of non-uniqueness and uncertainties in the relationship between convection and seismic observations can be overcome. Using a combination of targeted laboratory experiments, further comparison with field analogs and samples, improved seismological imaging, and geodynamic modeling we can achieve a powerful, integrated interpretation of seismic and other data and models, including those from geodesy, the geological record, mineralogy, and geodynamics. In particular, we look forward to seeing more work using vectorial tomography in multidisciplinary constrained, densely sampled key study areas. The promise of being able to potentially resolve the depth distribution of shear in convection, and hence mantle rheology, and the potential to unlock the deformation memory of both continental and oceanic plates for a new set of constraints on the mechanisms governing their evolution make the headaches worth while.

ACKNOWLEDGMENTS

We thank Whitney Behr, Donna Blackman, and Clint Conrad as well as Barbara Romanowicz and an anonymous reviewer who provided very helpful comments on an earlier version of this manuscript. Most plots were made with the Generic Mapping Tools (Wessel and Smith, 1998). TWB was partly supported by the National Science Foundation (NSF) under grant EAR-1460479. This publication has emanated from research supported in part by research grants from Science Foundation Ireland (SFI) under grant numbers 16/IA/4598 and 13/RC/2092, co-funded under the European Regional Development Fund and by iCRAG industry partners.

REFERENCES

- Abt, D. L., & K. M. Fischer (2008). Resolving three-dimensional anisotropic structure with shear-wave splitting tomography, *Geophys. J. Int.*, *173*, 859–886.
- Adam, J. M.-C., & S. Lebedev (2012). Azimuthal anisotropy beneath southern Africa from very broad-band surface-wave dispersion measurements, *Geophys. J. Int.*, *191*, 155–174.
- Agius, M. R., & S. Lebedev (2014). Shear-velocity structure, radial anisotropy and dynamics of the Tibetan crust, *Geophys. J. Int.*, *199*, 1395–1415.
- Agius, M. R., & S. Lebedev (2017). Complex, multilayered azimuthal anisotropy beneath Tibet: evidence for co-existing channel flow and pure-shear crustal thickening, *Geophys. J. Int.*, *210*, 1823–1844.
- Aki, K., & K. Kaminuma (1963). Phase velocity in Japan. Part I. Love waves from the Aleutian shock of March 9, 1957, *Bull. Earthq. Res. Inst. Tokyo Univ.*, *41*, 243–259.
- Alder, C., T. Bodin, Y. Ricard, Y. Capdeville, E. Debayle, & J. P. Montagner (2017). Quantifying seismic anisotropy induced by small-scale chemical heterogeneities, *Geophys. J. Int.*, *211*, 1585–1600.
- Alisic, L., M. Gurnis, G. Stadler, C. Burstedde, & O. Ghattas (2012). Multi-scale dynamics and rheology of mantle flow with plates, *J. Geophys. Res.*, *117*(B10402), doi:10.1029/2012JB009234.
- Alpert, L. A., M. S. Miller, T. W. Becker, & A. A. Allam (2013). Structure beneath the Alboran from geodynamic flow models and seismic anisotropy, *J. Geophys. Res.*, *118*, 1–13, doi:10.1002/jgrb.50309.
- Anderson, D. L. (1961). Elastic wave propagation in layered anisotropic media, *J. Geophys. Res.*, *66*, 2953–2963.
- Anderson, D. L. (1989). *Theory of the Earth*, Blackwell Scientific Publications, Boston, available online at <http://resolver.caltech.edu/CaltechBOOK:1989.001>, accessed 01/2019.
- Anderson, D. L., & A. M. Dziewoński (1982). Upper mantle anisotropy: evidence from free oscillations, *Geophys. J. R. Astr. Soc.*, *69*, 383–404.
- Auer, L., L. Boschi, T. W. Becker, T. Nissen-Meyer, & D. Giardini (2014). Savani: A variable-resolution whole-mantle model of anisotropic shear-velocity variations based on multiple datasets, *J. Geophys. Res.*, *119*, 3006–3034, doi: 10.1002/2013JB010773.
- Auer, L., T. W. Becker, L. Boschi, & N. Schmerr (2015). Thermal structure, radial anisotropy, and dynamics of oceanic boundary layers, *Geophys. Res. Lett.*, *42*, 9740–9742, doi:10.1002/2015GL066246.
- Babuška, V., J.-P. Montagner, J. Plomerová, & N. Girardin (1998). Age-dependent large-scale fabric of the mantle lithosphere as derived from surface-wave velocity anisotropy, *Pure Appl. Geophys.*, *151*, 257–280.
- Backus, G. E. (1962). Long-wave elastic anisotropy produced by horizontal layering, *J. Geophys. Res.*, *67*, 4427–4440.
- Backus, G. E. (1965). Possible forms of seismic anisotropy of the uppermost mantle under oceans, *J. Geophys. Res.*, *70*, 3429–3439.
- Bamford, D. (1977). Pn velocity anisotropy in a continental upper mantle, *Geophys. J. R. Astr. Soc.*, *49*, 29–48.
- Becker, T. W. (2006). On the effect of temperature and strain-rate dependent viscosity on global mantle flow, net rotation, and plate-driving forces, *Geophys. J. Int.*, *167*, 943–957.
- Becker, T. W. (2008). Azimuthal seismic anisotropy constrains net rotation of the lithosphere, *Geophys. Res. Lett.*, *35* (L05303). doi:10.1029/2007GL032928, correction: doi:10.1029/2008GL033946.
- Becker, T. W. (2017). Superweak asthenosphere in light of upper-mantle seismic anisotropy, *Geochem., Geophys., Geosys.*, *18*, 1986–2003, doi:10.1002/2017GC006886.
- Becker, T. W., & H. Kawakatsu (2011). On the role of anisotropic viscosity for plate-scale flow, *Geophys. Res. Lett.*, *38* (L17307). doi:10.1029/2011GL048584.
- Becker, T. W., & R. J. O’Connell (2001). Predicting plate velocities with geodynamic models, *Geochem., Geophys., Geosys.*, *2*(12). doi:10.1029/2001GC000171.
- Becker, T. W., J. B. Kellogg, G. Ekström, & R. J. O’Connell (2003). Comparison of azimuthal seismic anisotropy from surface waves and finite-strain from global mantle-circulation models, *Geophys. J. Int.*, *155*, 696–714.
- Becker, T. W., S. Chevrot, V. Schulte-Pelkum, & D. K. Blackman (2006a). Statistical properties of seismic anisotropy predicted by upper mantle geodynamic models, *J. Geophys. Res.*, *111*(B08309). doi:10.1029/2005JB004095.
- Becker, T. W., V. Schulte-Pelkum, D. K. Blackman, J. B. Kellogg, & R. J. O’Connell (2006b). Mantle flow under the western United States from shear wave splitting, *Earth Planet. Sci. Lett.*, *247*, 235–251.
- Becker, T. W., G. Ekström, L. Boschi, & J. W. Woodhouse (2007a). Length-scales, patterns, and origin of azimuthal seismic anisotropy in the upper mantle as mapped by Rayleigh waves, *Geophys. J. Int.*, *171*, 451–462.
- Becker, T. W., J. T. Browaeys, & T. H. Jordan (2007b). Stochastic analysis of shear wave splitting length scales, *Earth Planet. Sci. Lett.*, *259*, 29–36.
- Becker, T. W., B. Kustowski, & G. Ekström (2008). Radial seismic anisotropy as a constraint for upper mantle rheology, *Earth Planet. Sci. Lett.*, *267*, 213–237.
- Becker, T. W., S. Lebedev, & M. D. Long (2012). On the relationship between azimuthal anisotropy from shear wave splitting and surface wave tomography, *J. Geophys. Res.*, *117* (B01306). doi:10.1029/2011JB008705, original and updated splitting data base available online from <http://www-udc.ig.utexas.edu/external/becker/sksdata.html>, accessed 01/2019.

- Becker, T. W., C. P. Conrad, A. J. Schaeffer, & S. Lebedev (2014). Origin of azimuthal seismic anisotropy in oceanic plates and mantle, *Earth Planet. Sci. Lett.*, *401*, 236–250.
- Becker, T. W., A. J. Schaeffer, S. Lebedev, & S. P. Conrad (2015). Toward a generalized plate motion reference frame, *Geophys. Res. Lett.*, *42*, 3188–3196, doi: 10.1002/2015GL063695.
- Beghein, C., & J. Trampert (2004). Probability density functions for radial anisotropy: implications for the upper 1200 km of the mantle, *Earth Planet. Sci. Lett.*, *217*, 151–162.
- Beghein, C., J. Trampert, & H. J. van Heijst (2006). Radial anisotropy in seismic reference models of the mantle, *J. Geophys. Res.*, *111*, doi:10.1029/2005JB00372.
- Beghein, C., J. Resovsky, & R. D. van der Hilst (2008). The signal of mantle anisotropy in the coupling of normal modes, *Geophys. J. Int.*, *175*, 1209–1234.
- Beghein, C., K. Yuan, N. Schmerr, & Z. Xing (2014). Changes in seismic anisotropy shed light on the nature of the Gutenberg discontinuity, *Science*, *343*, 1237–1240.
- Behn, M. D., C. P. Conrad, & P. G. Silver (2004). Detection of upper mantle flow associated with the African Superplume, *Earth Planet. Sci. Lett.*, *224*, 259–274.
- Behn, M. D., G. Hirth, & J. R. Elsenbeck II (2009). Implications of grain size evolution on the seismic structure of the oceanic upper mantle, *Earth Planet. Sci. Lett.*, *282*, 178–189.
- Ben Ismail, W., & D. Mainprice (1998). An olivine fabric database; an overview of upper mantle fabrics and seismic anisotropy, *Tectonophysics*, *296*, 145–157.
- Bensen, G. D., M. H. Ritzwoller, M. P. Barmin, A. L. Levshin, F. Lin, M. P. Moschetti, N. M. Shapiro, & Y. Yang (2007). Processing seismic ambient noise data to obtain reliable broad-band surface wave dispersion measurements, *Geophys. J. Int.*, *169*, 1239–1260.
- Bercovici, D., P. T. Tackley, & Y. Ricard (2015). The generation of plate tectonics from mantle convection, in *Treatise on Geophysics*, 2 ed., pp. 271–318, Elsevier.
- Bernard, R., W. M. Behr, T. W. Becker, & D. Young (2019). Relationships between olivine CPO and deformation parameters in naturally deformed rocks and implications for mantle seismic anisotropy, *Geochem., Geophys., Geosys.*, doi: 10.1002/2019GC008289.
- Blackman, D., D. Boyce, O. Castelnau, P. R. Dawson, & G. Laske (2017). Effects of crystal preferred orientation on upper-mantle flow near plate boundaries: rheologic feedbacks and seismic anisotropy, *Geophys. J. Int.*, *210*, 1481–1493.
- Blackman, D. K., & J.-M. Kendall (1997). Sensitivity of teleseismic body waves to mineral texture and melt in the mantle beneath a mid-ocean ridge, *Phil. Trans. Roy. Soc. Lond. A*, *235*, 217–231.
- Blackman, D. K., & J.-M. Kendall (2002). Seismic anisotropy of the upper mantle: 2. Predictions for current plate boundary flow models, *Geochem., Geophys., Geosys.*, *3*(2001GC000247).
- Blackman, D. K., J.-M. Kendall, P. R. Dawson, & H.-R. Wenk (1996). Teleseismic imaging of subaxial flow at mid-ocean ridges: traveltimes effects of anisotropic mineral texture in the mantle, *Geophys. J. Int.*, *127*, 415–426.
- Blackman, D. K., H.-R. Wenk, & J.-M. Kendall (2002). Seismic anisotropy of the upper mantle: 1. Factors that affect mineral texture and effective elastic properties, *Geochem., Geophys., Geosys.*, *3*(2001GC000248).
- Bodin, T., J. Leiva, B. A. Romanowicz, V. Maupin, & H. Yuan (2016). Imaging anisotropic layering with Bayesian inversion of multiple data types, *Geophys. J. Int.*, *206*, 605–629.
- Boneh, Y., L. F. Morales, É. Kaminski, & P. Skemer (2015). Modeling olivine CPO evolution with complex deformation histories: Implications for the interpretation of seismic anisotropy in the mantle, *Geochem., Geophys., Geosys.*, *16*(10), 3436–3455, doi:10.1002/2015GC005964.
- Boneh, Y., D. Wallis, L. N. Hansen, M. Krawczynski, & P. Skemer (2017). Oriented grain growth and modification of “frozen anisotropy” in the lithospheric mantle, *Earth Planet. Sci. Lett.*, *474*, 368–374.
- Browaews, J., & S. Chevrot (2004). Decomposition of the elastic tensor and geophysical applications, *Geophys. J. Int.*, *159*, 667–678.
- Brownlee, S. J., V. Schulte-Pelkum, A. Raju, K. Mahan, C. Condit, & O. F. Orlando (2017). Characteristics of deep crustal seismic anisotropy from a compilation of rock elasticity tensors and their expression in receiver functions, *Tectonics*, *36*, 1835–1857, doi:10.1002/2017TC004625.
- Buehler, J. S., & P. M. Shearer (2010). *Pn* tomography of the western United States using US Array, *J. Geophys. Res.*, *115*(B09315), doi:10.1029/2009JB006874.
- Burgos, G., J.-P. Montagner, E. Beucler, Y. Capdeville, A. Mocquet, & M. Drilleau (2014). Oceanic lithosphere/asthenosphere boundary from surface wave dispersion data, *J. Geophys. Res.*, *119*, 1079–1093, doi:10.1002/2013JB010528.
- Busse, F. H., M. A. Richards, & A. Lenardic (2006). A simple model of high Prandtl and high Rayleigh number convection bounded by thin low-viscosity layers, *Geophys. J. Int.*, *164*, 160–167.
- Buttles, J., & P. Olson (1998). A laboratory model of subduction zone anisotropy, *Earth Planet. Sci. Lett.*, *164*, 245–262.
- Bystricky, M., K. Kunze, L. Burlini, & J.-P. Burg (2000). High shear strain of olivine aggregates: rheological and seismic consequences, *Science*, *290*, 1564–1567.
- Castelnau, O., D. K. Blackman, & T. W. Becker (2009). Numerical simulations of texture development and associated rheological anisotropy in regions of complex mantle flow, *Geophys. Res. Lett.*, *36*(L12304), doi:10.1029/2009GL038027.
- Chang, S.-J., A. M. G. Ferreira, J. Ritsema, H. J. van Heijst, & J. H. Woodhouse (2015). Joint inversion for global isotropic and radially anisotropic mantle structure including crustal thickness perturbations, *J. Geophys. Res.*, *120*, 4278–4300, doi:10.1002/2014JB011824.
- Chase, C. G. (1978). Extension behind island arcs and motion relative to hot spots, *J. Geophys. Res.*, *83*, 5385–5387.
- Chastel, Y. B., P. R. Dawson, H.-R. Wenk, & K. Bennett (1993). Anisotropic convection with implications for the upper mantle, *J. Geophys. Res.*, *98*, 17,757–17,771.
- Chevrot, S. (2006). Finite-frequency vectorial tomography: a new method for high-resolution imaging of upper mantle anisotropy, *Geophys. J. Int.*, *165*, 641–657.
- Chevrot, S., & V. Monteiller (2009). Principles of vectorial tomography – the effects of model parametrization and regularization in tomographic imaging of seismic anisotropy, *Geophys. J. Int.*, *179*, 1726–1736.
- Chevrot, S., N. Favier, & D. Komatitsch (2004). Shear wave splitting in three-dimensional anisotropic media, *Geophys. J. Int.*, *159*, 711–720.

- Christensen, U. R. (1987). Some geodynamical effects of anisotropic viscosity, *Geophys. J. R. Astr. Soc.*, *91*, 711–736.
- Conrad, C. P., & M. D. Behn (2010). Constraints on lithosphere net rotation and asthenospheric viscosity from global mantle flow models and seismic anisotropy, *Geochem., Geophys., Geosys.*, *11*(Q05W05). doi:10.1029/2009GC002970.
- Conrad, C. P., & M. Gurnis (2003). Seismic tomography, surface uplift, and the breakup of Gondwanaland: Integrating mantle convection backwards in time, *Geochem., Geophys., Geosys.*, *4*(2001GC000299).
- Conrad, C. P., & C. Lithgow-Bertelloni (2002). How mantle slabs drive plate tectonics, *Science*, *298*, 207–209.
- Conrad, C. P., & C. Lithgow-Bertelloni (2007). Faster seafloor spreading and lithosphere production during the mid-Cenozoic, *Geology*, *35*, 29–32.
- Conrad, C. P., M. D. Behn, & P. G. Silver (2007). Global mantle flow and the development of seismic anisotropy: Differences between the oceanic and continental upper mantle, *J. Geophys. Res.*, *112*(B07317). doi:10.1029/2006JB004608.
- Crampin, S., & S. Chastin (2003). A review of shear wave splitting in the crack-critical crust, *Geophys. J. Int.*, *155*, 221–240.
- Dahlen, F. A., & J. Tromp (1998). *Theoretical Global Seismology*, Princeton University Press, Princeton, New Jersey.
- Dannberg, J., Z. Eilon, U. Faul, R. Gassmüller, P. Moulik, & R. Myhill (2017). The importance of grain size to mantle dynamics and seismological observations, *Geochem., Geophys., Geosys.*, *18*, 3034–3061, doi:10.1002/2017GC006944.
- Debayle, E., & Y. Ricard (2013). Seismic observations of large-scale deformation at the bottom of fast-moving plates, *Earth Planet. Sci. Lett.*, *376*, 165–177.
- DeMets, C., R. G. Gordon, & D. F. Argus (2010). Geologically current plate motions, *Geophys. J. Int.*, *181*, 1–80.
- Deschamps, F., S. Lebedev, T. Meier, & J. Trampert (2008a). Azimuthal anisotropy of Rayleigh-wave phase velocities in the east-central United States, *Geophys. J. Int.*, *173*, 827–843.
- Deschamps, F., S. Lebedev, T. Meier, & J. Trampert (2008b). Stratified seismic anisotropy reveals past and present deformation beneath the East-central United States, *Earth Planet. Sci. Lett.*, *274*, 489–498.
- Dziewoński, A. M., & D. L. Anderson (1981). Preliminary reference Earth model, *Phys. Earth Planet. Inter.*, *25*, 297–356.
- Ekström, G. (2011). A global model of Love and Rayleigh surface wave dispersion and anisotropy, 25–250 s, *Geophys. J. Int.*, *187*, 1668–1686.
- Ekström, G., & A. M. Dziewoński (1998). The unique anisotropy of the Pacific upper mantle, *Nature*, *394*, 168–172.
- Ekström, G., J. Tromp, & E. Larson (1997). Measurements and global models of surface wave propagation, *J. Geophys. Res.*, *102*, 8137–8157.
- Ekström, G., G. A. Abers, & S. C. Webb (2009). Determination of surface-wave phase velocities across USArray from noise and Aki's spectral formulation, *Geophys. Res. Lett.*, *36* (L18301). doi:10.1029/2009GL039131.
- Faccenda, M., & F. A. Capitanio (2013). Seismic anisotropy around subduction zones: Insights from three-dimensional modeling of upper mantle deformation and SKS splitting calculations, *Geochem., Geophys., Geosys.*, *14*, doi: 10.1029/2012GC004451.
- Faccenna, C., T. W. Becker, L. Jolivet, & M. Keskin (2013). Mantle convection in the Middle East: Reconciling Afar upwelling, Arabia indentation and Aegean trench rollback, *Earth Planet. Sci. Lett.*, *375*, 254–269.
- Farra, V., & L. Vinnik (2002). Upper mantle stratification by P and S receiver functions, *Geophys. J. Int.*, *141*, 699–712.
- Ferreira, A. M. G., J. H. Woodhouse, K. Visser, & J. Trampert (2010). On the robustness of global radially anisotropic surface wave tomography, *J. Geophys. Res.*, *115*(B04313). doi:10.1029/2009JB006716.
- Fichtner, A., B. L. N. Kennett, & J. Trampert (2013). Separating intrinsic and apparent anisotropy, *Phys. Earth Planet. Inter.*, *219*, 11–20.
- Fischer, K. M., & D. A. Wiens (1996). The depth distribution of mantle anisotropy beneath the Tonga subduction zone, *Earth Planet. Sci. Lett.*, *142*, 253–260.
- Forsyth, D. W. (1975). The early structural evolution and anisotropy of the oceanic upper mantle, *Geophys. J. R. Astr. Soc.*, *43*, 103–162.
- Forte, A. M., W. R. Peltier, & A. M. Dziewoński (1991). Inferences of mantle viscosity from tectonic plate velocities, *Geophys. Res. Lett.*, *18*, 1747–1750.
- Fouch, M. J., & K. M. Fischer (1996). Mantle anisotropy beneath Northwest Pacific subduction zones, *J. Geophys. Res.*, *101*, 15,987–16,002.
- Fouch, M. J., K. M. Fischer, E. M. Parmentier, M. E. Wysession, & T. J. Clarke (2000). Shear wave splitting, continental keels, and patterns of mantle flow, *J. Geophys. Res.*, *105*, 6255–6275.
- French, S. W., & B. A. Romanowicz (2014). Whole-mantle radially anisotropic shear velocity structure from spectral-element waveform tomography, *Geophys. J. Int.*, *199*, 1303–1327.
- Funicello, F., C. Faccenna, A. Heuret, E. Di Giuseppe, S. Lallemand, & T. W. Becker (2008). Trench migration, net rotation and slab-mantle coupling, *Earth Planet. Sci. Lett.*, *271*, 233–240.
- Gaboret, C., A. M. Forte, & J.-P. Montagner (2003). The unique dynamics of the Pacific Hemisphere mantle and its signature on seismic anisotropy, *Earth Planet. Sci. Lett.*, *208*, 219–233.
- Gaherty, J. B., & T. H. Jordan (1995). Lehmann discontinuity as the base of an anisotropic layer beneath continents, *Science*, *268*, 1468–1471.
- Gaherty, J. B., T. H. Jordan, & L. S. Gee (1996). Seismic structure of the upper mantle in a central Pacific corridor, *J. Geophys. Res.*, *101*, 22,291–22,310.
- Gaherty, J. B., D. Lizarralde, J. A. Collins, G. Hirth, & S. Kim (2004). Mantle deformation during slow seafloor spreading constrained by observations of seismic anisotropy in the western Atlantic, *Earth Planet. Sci. Lett.*, *228*, 225–265.
- Godfrey, N. J., N. I. Christensen, & D. A. Okaya (2000). Anisotropy of schists: Contribution of crustal anisotropy to active source seismic experiments and shear wave splitting observations, *J. Geophys. Res.*, *105*, 27,991–28,007.
- Goulding, N. J., N. M. Ribe, O. Castelnau, A. M. Walker, & J. Wookey (2015). Analytical parametrization of self-consistent polycrystal mechanics: Fast calculation of upper mantle anisotropy, *Geophys. J. Int.*, *203*, 334–350.
- Gung, Y., M. Panning, & B. A. Romanowicz (2003). Global anisotropy and the thickness of continents, *Nature*, *422*, 707–711.

- Hager, B. H. (1984). Subducted slabs and the geoid: constraints on mantle rheology and flow, *J. Geophys. Res.*, *89*, 6003–6015.
- Hager, B. H., & R. J. O’Connell (1981). A simple global model of plate dynamics and mantle convection, *J. Geophys. Res.*, *86*, 4843–4867.
- Hager, B. H., R. W. Clayton, M. A. Richards, R. P. Comer, & A. M. Dziewoński (1985). Lower mantle heterogeneity, dynamic topography and the geoid, *Nature*, *313*, 541–545.
- Hall, C. E., K. M. Fischer, E. M. Parmentier, & D. K. Blackman (2000). The influence of plate motions on three-dimensional back arc mantle flow and shear wave splitting, *J. Geophys. Res.*, *105*, 28,009–28,033.
- Han, D., & J. Wahr (1997). An analysis of anisotropic mantle viscosity, and its possible effects on post-glacial rebound, *Phys. Earth Planet. Inter.*, *102*, 33–50.
- Hansen, L. N., M. E. Zimmerman, & D. L. Kohlstedt (2012). Laboratory measurements of the viscous anisotropy of olivine aggregates, *Nature*, *492*, 415–418.
- Hansen, L. N., Y.-H. Zhao, M. E. Zimmerman, & D. L. Kohlstedt (2014). Protracted fabric evolution in olivine: Implications for the relationship among strain, crystallographic fabric, and seismic anisotropy, *Earth Planet. Sci. Lett.*, *387*, 157–158.
- Hansen, L. N., C. Qib, & J. M. Warren (2016a). Olivine anisotropy suggests Gutenberg discontinuity is not the base of the lithosphere, *Proc. Natl. Acad. Sci. USA*, *113*, 10,503–10,506.
- Hansen, L. N., C. P. Conrad, Y. Boneh, P. Skemer, J. M. Warren, & D. L. Kohlstedt (2016b). Viscous anisotropy of textured olivine aggregates: 2. Micromechanical model, *J. Geophys. Res.*, *121*, 7137–7160, doi:10.1002/2016JB013240.
- Hansen, L. N., J. M. Warren, M. E. Zimmerman, & D. L. Kohlstedt (2016c). Viscous anisotropy of textured olivine aggregates, Part 1: Measurement of the magnitude and evolution of anisotropy, *Earth Planet. Sci. Lett.*, *445*, 92–103.
- Hess, H. H. (1964). Seismic anisotropy of the uppermost mantle under oceans, *Nature*, *203*, 629–631.
- Hirth, G., & D. L. Kohlstedt (2004). Rheology of the upper mantle and the mantle wedge: A view from the experimentalists, in *Inside the Subduction Factory*, *Geophys. Monograph*, vol. 138, edited by J. Eiler, pp. 83–105, American Geophysical Union, Washington DC.
- Holliger, K., & A. R. Levander (1992). A stochastic view of lower crustal fabric based on evidence from the Ivrea Zone, *Geophys. Res. Lett.*, *19*, 1153–1156.
- Holtzman, B. K., & J. Kendall (2010). Organized melt, seismic anisotropy, and plate boundary lubrication, *Geochem., Geophys., Geosys.*, *11*(Q0AB06). doi:10.1029/2010GC003296.
- Holtzman, B. K., D. L. Kohlstedt, M. E. Zimmerman, F. Heidelbach, T. Hiraga, & J. Hustoft (2003). Melt segregation and strain partitioning: Implications for seismic anisotropy and mantle flow, *Science*, *301*, 1227–1230.
- Honda, S. (1986). Strong anisotropic flow in a finely layered asthenosphere, *Geophys. Res. Lett.*, *13*, 1454–1457.
- Hu, J., M. Faccenda, & L. Liu (2017). Subduction-controlled mantle flow and seismic anisotropy in South America, *Earth Planet. Sci. Lett.*, *470*, 13–24.
- Husson, L., P. Yamato, & A. Bézous (2015). Ultraslow, slow, or fast spreading ridges: Arm wrestling between mantle convection and far-field tectonics, *Earth Planet. Sci. Lett.*, *429*, 205–215.
- Ishise, M., & H. Oda (2005). Three-dimensional structure of P-wave anisotropy beneath the Tohoku district, northeast Japan, *J. Geophys. Res.*, *110*(B07304). doi: 10.1029/2004JB003599.
- Isse, T., H. Kawakatsu, K. Yoshizawa, A. Takeo, H. Shiobara, H. Sugioka, A. Ito, D. Suetsugu, & D. Reymond (2019). Surface wave tomography for the Pacific Ocean incorporating seafloor seismic observations and plate thermal evolution, *Earth Planet. Sci. Lett.*, *510*, 116–130.
- Ito, G., R. Dunn, A. Li, C. J. Wolfe, A. Gallego, & Y. Fu (2014). Seismic anisotropy and shear wave splitting associated with mantle plume-plate interaction, *J. Geophys. Res.*, *119*, 4923–4937, doi:10.1002/2013JB010735.
- Jung, H., & S.-i. Karato (2001). Water-induced fabric transitions in olivine, *Science*, *293*, 1460–1463.
- Jung, H., W. Mo, & H. W. Green (2009). Upper mantle seismic anisotropy resulting from pressure-induced slip transitions in olivine, *Nature Geosci.*, *2*, 73–77.
- Kaminski, É. (2002). The influence of water on the development of lattice preferred orientation in olivine aggregates, *Geophys. Res. Lett.*, *29*, 10.1029/2002GL014,710.
- Kaminski, É., & N. M. Ribe (2001). A kinematic model for recrystallization and texture development in olivine polycrystals, *Earth Planet. Sci. Lett.*, *189*, 253–267.
- Kaminski, É., & N. M. Ribe (2002). Time scales for the evolution of seismic anisotropy in mantle flow, *Geochem., Geophys., Geosys.*, *3*(2001GC000222).
- Kaminski, É., N. M. Ribe, & J. T. Browaeys (2004). D-Rex, a program for calculation of seismic anisotropy due to crystal lattice preferred orientation in the convective upper mantle, *Geophys. J. Int.*, *157*, 1–9.
- Karato, S.-i. (1992). On the Lehmann discontinuity, *Geophys. Res. Lett.*, *51*, 2255–2258.
- Karato, S.-i. (1998). Seismic anisotropy in the deep mantle, boundary layers and the geometry of convection, *Pure Appl. Geophys.*, *151*, 565–587.
- Karato, S.-i., H. Jung, I. Katayama, & P. Skemer (2008). Geodynamic significance of seismic anisotropy of the upper mantle: new insights from laboratory studies, *Ann. Rev. Earth Planet. Sci.*, *36*, 59–95.
- Katayama, I., H. Jung, & S.-i. Karato (2004). New type of olivine fabric from deformation experiments at modest water content and low stress, *Geology*, *32*, 1045–1048.
- Kawakatsu, H. (2016). A new fifth parameter for transverse isotropy, *Geophys. J. Int.*, *204*, 682–685.
- Kawakatsu, H., & H. Utada (2017). Seismic and electrical signatures of the litho-sphere-asthenosphere system of the normal oceanic mantle, *Ann. Rev. Earth Planet. Sci.*, *45*, 139–167.
- Kawakatsu, H., P. Kumar, Y. Takei, M. Shinohara, T. Kanazawa, E. Araki, & K. Suyehiro (2009). Seismic evidence for sharp lithosphere-asthenosphere boundaries of oceanic plates, *Science*, *324*, 499–502.

- Kennett, B. L., & T. Furumura (2013). High-frequency Po/So guided waves in the oceanic lithosphere: long-distance propagation, *Geophys. J. Int.*, *195*, 1862–1877.
- King, S. D., & G. Masters (1992). An inversion for radial viscosity structure using seismic tomography, *Geophys. Res. Lett.*, *19*, 1551–1554.
- Kneller, E. A., P. E. van Keken, S.-i. Karato, & J. Park (2005). B-type olivine fabric in the mantle wedge: insights from high-resolution non-newtonian subduction zone models, *Earth Planet. Sci. Lett.*, *237*, 781–797.
- Knoll, M., A. Tommasi, R. Logé, & J. Signorelli (2009). A multiscale approach to model the anisotropic deformation of lithospheric plates, *Geochem., Geophys., Geosys.*, *10*(Q08009). doi:10.1029/2009GC002423.
- Kosarev, G. L., L. I. Makeyeva, & L. P. Vinnik (1984). Anisotropy of the mantle inferred from observations of P to S converted waves, *Geophys. J. R. Astr. Soc.*, *76*, 209–220.
- Kreemer, C. (2009). Absolute plate motions constrained by shear wave splitting orientations with implications for hot spot motions and mantle flow, *J. Geophys. Res.*, *114* (B10405). doi:10.1029/2009JB006416.
- Kustowski, B., G. Ekström, & A. M. Dziewoński (2008). Anisotropic shear-wave velocity structure of the Earth's mantle: A global model, *J. Geophys. Res.*, *113*, doi:10.1029/2007JB005169.
- Laske, G., & G. Masters (1998). Surface-wave polarization data and global anisotropic structure, *Geophys. J. Int.*, *132*, 508–520.
- Lassak, T. M., M. J. Fouch, C. E. Hall, & É. Kaminski (2006). Seismic characterization of mantle flow in subduction systems: Can we resolve a hydrated mantle wedge?, *Earth Planet. Sci. Lett.*, *243*, 632–649.
- Lebedev, S., G. Nolet, T. Meier, & R. D. van der Hilst (2005). Automated multimode inversion of surface and S waveforms, *Geophys. J. Int.*, *162*, 951–964.
- Lebedev, S., T. Meier, & R. D. van der Hilst (2006). Asthenospheric flow and origin of volcanism in the Baikal Rift area, *Earth Planet. Sci. Lett.*, *249*, 415–424.
- Lev, E., & B. H. Hager (2008). Rayleigh-Taylor instabilities with anisotropic lithospheric viscosity, *Geophys. J. Int.*, *173*, 806–814.
- Lev, E., & B. H. Hager (2011). Anisotropic viscosity changes subduction zone thermal structure, *Geochem., Geophys., Geosys.*, *12*(Q04009). doi:10.1029/2010GC003382.
- Lin, F. C., M. H. Ritzwoller, Y. Yang, M. P. Moschetti, & M. J. Fouch (2011). Complex and variable crustal and uppermost mantle seismic anisotropy in the western United States, *Nature Geosci.*, *4*, 55–61.
- Lin, P.-Y. P., J. B. Gaherty, J. G., J. A. Collins, D. Lizarralde, R. L. Evans, & G. Hirth (2016). High-resolution seismic constraints on flow dynamics in the oceanic asthenosphere, *Nature*, *535*, 538–541.
- Lin, Y.-P., L. Zhao, & S.-H. Hung (2014). Full-wave multiscale anisotropy tomography in Southern California, *Geophys. Res. Lett.*, *41*, 8809–8817, doi:10.1002/2014GL061855.
- Lithgow-Bertelloni, C., & M. A. Richards (1998). The dynamics of Cenozoic and Mesozoic plate motions, *Rev. Geophys.*, *36*, 27–78.
- Long, M. D. (2013). Constraints on subduction geodynamics from seismic anisotropy, *Rev. Geophys.*, *51*, 76–112.
- Long, M. D., & T. W. Becker (2010). Mantle dynamics and seismic anisotropy, *Earth Planet. Sci. Lett.*, *297*, 341–354.
- Long, M. D., & R. D. van der Hilst (2006). Shear wave splitting from local events beneath the Ryukyu arc: Trench-parallel anisotropy in the mantle wedge, *Phys. Earth Planet. Inter.*, *155*, 300–312.
- Long, M. D., M. V. de Hoop, & R. D. van der Hilst (2008). Wave equation shear wave splitting tomography, *Geophys. J. Int.*, *172*, 311–330.
- Ma, Z. T., & G. Masters (2015). Effect of earthquake locations on Rayleigh wave azimuthal anisotropy models, *Geophys. J. Int.*, *203*, 1319–1333.
- Mainprice, D. (2007). Seismic anisotropy of the deep Earth from a mineral and rock physics perspective, in *Treatise on Geophysics*, vol. 2, edited by G. Schubert and D. Bercovici, pp. 437–492, Elsevier.
- Mainprice, D., A. Tommasi, H. Couvy, P. Cordier, & N. J. J. Frost (2005). Pressure sensitivity of olivine slip systems and seismic anisotropy of Earth's upper mantle, *Nature*, *433*, 731–733.
- Marone, F., & B. A. Romanowicz (2007). The depth distribution of azimuthal anisotropy in the continental upper mantle, *Nature*, *447*, 198–201.
- Maruyama, G., & T. Hiraga (2017). Grain- to multiple-grain-scale deformation processes during diffusion creep of forsterite + diopside aggregate: 2. Grain boundary sliding-induced grain rotation and its role in crystallographic preferred orientation in rocks, *J. Geophys. Res.*, *122*, 5916–5934, doi:10.1002/2017JB014255.
- McEvelly, T. V. (1964). Central U.S. crust—Upper mantle structure from Love and Rayleigh wave phase velocity inversion, *Bull. Seismol. Soc. Am.*, *54*, 1997–2015.
- McKenzie, D. P. (1979). Finite deformation during fluid flow, *Geophys. J. R. Astr. Soc.*, *58*, 689–715.
- McNamara, A., S.-i. Karato, & P. E. van Keken (2001). Localization of dislocation creep in the lower mantle: implications for the origin of seismic anisotropy, *Earth Planet. Sci. Lett.*, *191*, 85–99.
- Meier, T., K. Dietrich, B. Stöckhert, & H.-P. Harjes (2004). One-dimensional models of shear wave velocity for the eastern Mediterranean obtained from the inversion of Rayleigh wave phase velocities and tectonic implications, *Geophys. J. Int.*, *156*, 45–58.
- Miller, M. S., & T. W. Becker (2012). Mantle flow deflected by interactions between subducted slabs and cratonic keels, *Nat. Geosci.*, *5*, 726–730.
- Minster, J. B., & T. H. Jordan (1978). Present-day plate motions, *J. Geophys. Res.*, *83*, 5331–5354.
- Miyazaki, T., K. Sueyoshi, & T. Hiraga (2013). Olivine crystals align during diffusion creep of Earth's upper mantle, *Nature*, *502*, 321–327.
- Mondal, P., & M. D. Long (2019). A model space search approach to finite-frequency SKS splitting intensity tomography in a reduced parameter space, *Geophys. J. Int.*, *217*, 238–256.

- Montagner, J.-P. (1994). What can seismology tell us about mantle convection?, *Rev. Geophys.*, *32*, 115–137.
- Montagner, J.-P. (2002). Upper mantle low anisotropy channels below the Pacific plate, *Earth Planet. Sci. Lett.*, *202*, 263–274.
- Montagner, J.-P., & D. L. Anderson (1989). Petrological constraints on seismic anisotropy, *Phys. Earth Planet. Inter.*, *54*, 82–105.
- Montagner, J.-P., & D. L. Anderson (2015). The Pacific Megagash: A future plate boundary?, in *D. L. Anderson Honor Volume, GSA Spec. Papers*, vol. 514, edited by G. R. Foulger, *Geol. Soc. Amer.*, doi:10.1130/2015.2514(10).
- Montagner, J.-P., & L. Guillot (2000). Seismic anisotropy in the Earth's mantle, in *Problems in Geophysics for the New Millennium*, edited by E. Boschi, G. Ekström, & A. Morelli, pp. 217–253, Istituto Nazionale di Geofisica e Vulcanologia, Editrice Compositori, Bologna, Italy.
- Montagner, J.-P., & N. Jobert (1988). Vectorial tomography; II. application to the Indian Ocean, *Geophys. J. Int.*, *94*, 309–344.
- Montagner, J.-P., & H.-C. Nataf (1986). A simple method for inverting the azimuthal anisotropy of surface waves, *J. Geophys. Res.*, *91*, 511–520.
- Montagner, J.-P., & H. C. Nataf (1988). Vectorial tomography-I. Theory, *Geophys. J.*, *94*, 295–307.
- Montagner, J.-P., & T. Tanimoto (1990). Global anisotropy in the upper mantle inferred from the regionalization of phase velocities, *J. Geophys. Res.*, *95*, 4797–4819.
- Montagner, J.-P., & T. Tanimoto (1991). Global upper mantle tomography of seismic velocities and anisotropies, *J. Geophys. Res.*, *96*, 20,337–20,351.
- Montagner, J.-P., D.-A. Griot-Pommerer, & J. Lavé (2000). How to relate body wave and surface wave anisotropy?, *J. Geophys. Res.*, *105*, 19,015–19,027.
- Monteiller, V., & S. Chevrot (2011). High-resolution imaging of the deep anisotropic structure of the San Andreas Fault system beneath southern California, *Geophys. J. Int.*, *182*, 418–446.
- Montési, L. G. J. (2013). Fabric development as the key for forming ductile shear zones and enabling plate tectonics, *J. Struct. Geol.*, *50*, 254–266.
- Mordret, A., M. Landès, N. Shapiro, S. Singh, P. Roux, & O. Barkved (2013). Near-surface study at the Valhall oil field from ambient noise surface wave tomography, *Geophys. J. Int.*, *193*, 1627–1643.
- Morris, G. B., R. W. Raitt, & G. G. Shor Jr (1969). Velocity anisotropy and delaytime maps of the mantle near Hawaii, *J. Geophys. Res.*, *74*, 4300–4316.
- Moulik, P., & G. Ekström (2014). An anisotropic shear velocity model of the Earth's mantle using normal modes, body waves, surface waves and long-period waveforms, *Geophys. J. Int.*, *199*, 1713–1738.
- Mühlhaus, H.-B., L. N. Moresi, B. Hobbs, & F. Dufour (2002). Large amplitude folding in finely layered viscoelastic rock structures, *Pure Appl. Geophys.*, *159*, 2311–2333.
- Nagihara, S., C. R. B. Lister, & J. G. Sclater (1996). Reheating of old oceanic lithosphere: Deductions from observations, *Earth Planet. Sci. Lett.*, *139*, 91–104.
- Nataf, H.-C., I. Nakanishi, & D. L. Anderson (1984). Anisotropy and shear velocity heterogeneity in the upper mantle, *Geophys. Res. Lett.*, *11*, 109–112.
- Nataf, H.-C., I. Nakanishi, & D. L. Anderson (1986). Measurements of mantle wave velocities and inversion for lateral heterogeneities and anisotropy. Part III. Inversion, *J. Geophys. Res.*, *91*, 7261–7307.
- Natarov, S. I., & C. P. Conrad (2012). The role of Poiseuille flow in creating depth-variation of asthenospheric shear, *Geophys. J. Int.*, *190*, 1297–1310.
- Nettles, M., & A. M. Dziewoński (2008). Radially anisotropic shear-velocity structure of the upper mantle globally and beneath North America, *J. Geophys. Res.*, *113*(B02303). doi:10.1029/2006JB004819.
- Nicolas, A., & N. I. Christensen (1987). Formation of anisotropy in upper mantle peridotites; a review, in *Composition, structure and dynamics of the lithosphere-asthenosphere system, Geodynamics*, vol. 16, edited by K. Fuchs and C. Froidevaux, pp. 111–123, American Geophysical Union, Washington DC.
- Nishimura, C. E., & D. W. Forsyth (1989). The anisotropic structure of the upper mantle in the Pacific, *Geophys. J. Int.*, *96*, 203–229.
- Ohira, A., S. Kodaira, Y. Nakamura, G. Fujie, R. Arai, & S. Miura (2017). Evidence for frozen melts in the mid-lithosphere detected from active-source seismic data, *Sci. Rep.*, *7*(15770). doi:10.1038/s41598-017-16047-4.
- Ohuchi, T., & T. Irifune (2013). Development of A-type olivine fabric in water-rich deep upper mantle, *Earth Planet. Sci. Lett.*, *361*, 20–30.
- Ohuchi, T., T. Kawazoe, Y. Nishihara, & T. Irifune (2012). Change of olivine a-axis alignment induced by water: Origin of seismic anisotropy in subduction zones, *Earth Planet. Sci. Lett.*, *317*, 111–119.
- Panning, M., & B. A. Romanowicz (2006). A three-dimensional radially anisotropic model of shear velocity in the whole mantle, *Geophys. J. Int.*, *167*, 361–379.
- Panning, M. P., & G. Nolet (2008). Surface wave tomography for azimuthal anisotropy in a strongly reduced parameter space, *Geophys. J. Int.*, *174*, 629–648.
- Parsons, B., & J. G. Sclater (1977). An analysis of the variation of ocean floor bathymetry and heat flow with age, *J. Geophys. Res.*, *82*, 803–827.
- Plomerová, J., J. Šílený, & V. Babuška (1996). Joint interpretation of upper-mantle anisotropy based on teleseismic P-travel time delays and inversion of shear-wave splitting parameters, *Phys. Earth Planet. Inter.*, *95*, 293–309.
- Plomerová, J., D. Kouba, & V. Babuška (2002). Mapping the lithosphere-asthenosphere boundary through changes in surface-wave anisotropy, *Tectonophysics*, *58*, 175–185.
- Podolefsky, N. S., S. Zhong, & A. K. McNamara (2004). The anisotropic and rheological structure of the oceanic upper mantle from a simple model of plate shear, *Geophys. J. Int.*, *158*, 287–296.
- Priestley, K., E. Debayle, D. McKenzie, & S. Pilidou (2006). Upper mantle structure of eastern Asia from multimode surface waveform tomography, *J. Geophys. Res.*, *111*(B10304). doi:10.1029/2005JB004082.
- Ravenna, M. (2018). Bayesian inversion of surface-wave data for radial and azimuthal shear-wave anisotropy and the structure and evolution of southern Africa's lithosphere, Ph.D. thesis, University College Dublin, Dublin.

- Ravenna, M., S. Lebedev, J. Fullea, & J. M.-C. Adam (2018). Shear-wave velocity structure of Southern Africa's lithosphere: Variations in the thickness and composition of cratons and their effect on topography, *Geochem., Geophys., Geosys.*, *19*, 1499–1518, doi:10.1029/2017GC007399.
- Regan, J., & D. L. Anderson (1984). Anisotropic models of the upper mantle, *Phys. Earth Planet. Inter.*, *35*, 227–263.
- Ribe, N. M. (1989). Seismic anisotropy and mantle flow, *J. Geophys. Res.*, *94*, 4213–4223.
- Ribe, N. M., & Y. Yu (1991). A theory for plastic deformation and textural evolution of olivine polycrystals, *J. Geophys. Res.*, *96*, 8325–8335.
- Ricard, Y., & C. Vigny (1989). Mantle dynamics with induced plate tectonics, *J. Geophys. Res.*, *94*, 17,543–17,559.
- Ricard, Y., C. Doglioni, & R. Sabadini (1991). Differential rotation between lithosphere and mantle: A consequence of lateral mantle viscosity variations, *J. Geophys. Res.*, *96*, 8407–8415.
- Richards, M., & B. H. Hager (1984). Geoid anomalies in a dynamic Earth, *J. Geophys. Res.*, *89*, 5987–6002.
- Richards, M. A., & A. Lenardic (2018). The Cathles parameter (Ct): A geodynamic definition of the asthenosphere and implications for the nature of plate tectonics, *Geochem., Geophys., Geosys.*, *19*, 4858–4875, doi:10.1029/2018GC007664.
- Ritzwoller, M. H., N. M. Shapiro, & S. Zhong (2004). Cooling history of the Pacific lithosphere, *Earth Planet. Sci. Lett.*, *226*, 69–84.
- Romanowicz, B. A., & R. Snieder (1988). A new formalism for the effect of lateral heterogeneity on normal modes and surface waves. II. General anisotropic perturbation, *Geophys. J.*, *93*, 91–99.
- Romanowicz, B. A., & H.-R. Wenk (2017). Anisotropy in the deep Earth, *Phys. Earth Planet. Inter.*, *269*, 58–90.
- Romanowicz, B. A., & H. Yuan (2012). On the interpretation of SKS splitting measurements in the presence of several layers of anisotropy, *Geophys. J. Int.*, *188*, 1129–1140.
- Rümpker, G., & P. G. Silver (1998). Apparent shear-wave splitting parameters in the presence of vertically varying anisotropy, *Geophys. J. Int.*, *135*, 790–800.
- Russell, J. B., J. B. Gaherty, P.-Y. P. Lin, D. Lizarralde, J. A. Collins, G. Hirth, & R. L. Evans (2019). High-resolution constraints on Pacific upper mantle petrofabric inferred from surface-wave anisotropy, *J. Geophys. Res.*, *124*, doi: 10.1029/2018JB016598.
- Ryberg, T., G. Rümpker, C. Haberland, D. Stromeier, & M. Weber (2005). Simultaneous inversion of shear wave splitting observations from seismic arrays, *J. Geophys. Res.*, *110* (B03301). doi:10.1029/2004JB003303.
- Rychert, C. A., & N. Harmon (2017). Constraints on the anisotropic contributions to velocity discontinuities at ~60 km depth beneath the Pacific, *Geochem., Geophys., Geosys.*, *18*, 2855–2871.
- Sakamaki, T., A. Suzuki, E. O. an H. Terasaki, S. Urakawa, Y. Katayama, K.-I. Funakoshi, Y. Wang, J. W. Hernlund, & M. D. Ballmer (2013). Ponded melt at the boundary between the lithosphere and asthenosphere, *Nature Geosc.*, *6*, 1041–1044.
- Saltzer, R. L., J. B. Gaherty, & T. H. Jordan (2000). How are vertical shear wave splitting measurements affected by variations in the orientation of azimuthal anisotropy with depth?, *Geophys. J. Int.*, *141*, 374–390.
- Savage, M. K. (1999). Seismic anisotropy and mantle deformation: What have we learned from shear wave splitting?, *Rev. Geophys.*, *37*, 65–106.
- Schaeffer, A., & S. Lebedev (2013). Global shear speed structure of the upper mantle and transition zone, *Geophys. J. Int.*, *194*, 417–449.
- Schaeffer, A., S. Lebedev, & T. W. Becker (2016). Azimuthal seismic anisotropy in the Earth's upper mantle and the thickness of tectonic plates, *Geophys. J. Int.*, *207*, 901–933.
- Schmerr, N. (2012). The Gutenberg discontinuity: Melt at the lithosphere-asthenosphere boundary, *Science*, *335*, 1480–1483.
- Schulte-Pelkum, V., & K. H. Mahan (2014). A method for mapping crustal deformation and anisotropy with receiver functions and first results from USArray, *Earth Planet. Sci. Lett.*, *402*, 221–233.
- Schulte-Pelkum, V., G. Masters, & P. M. Shearer (2001). Upper mantle anisotropy from long-period *P* polarization, *J. Geophys. Res.*, *106*, 21,917–21,934.
- Selwig, K., H. Ford, & P. Kelemen (2015). The seismic mid-lithosphere discontinuity, *Earth Planet. Sci. Lett.*, *414*, 45–57.
- Semple, A. G., & A. Lenardic (2018). Plug flow in the Earth's asthenosphere, *Earth Planet. Sci. Lett.*, *496*, 29–36.
- Shapiro, N. M., M. H. Ritzwoller, P. Molnar, & V. Levin (2004). Thinning and flow of Tibetan crust constrained by seismic anisotropy, *Science*, *305*, 233–236.
- Shapiro, N. M., M. Campillo, L. Stehly, & M. H. Ritzwoller (2005). High-resolution surface-wave tomography from ambient seismic noise, *Science*, *307*, 1615–1618.
- Silver, P. G. (1996). Seismic anisotropy beneath the continents: Probing the depths of geology, *Ann. Rev. Earth Planet. Sci.*, *24*, 385–432.
- Silver, P. G., & H. H. Chan (1988). Implications for continental structure and evolution from seismic anisotropy, *Nature*, *335*, 34–39.
- Silver, P. G., & M. K. Savage (1994). The interpretation of shear wave splitting parameters in the presence of two anisotropic layers, *Geophys. J. Int.*, *119*, 949–963.
- Skemer, P., & L. N. Hansen (2016). Inferring upper-mantle flow from seismic anisotropy: An experimental perspective, *Tectonophys.*, *668*, 1–14.
- Skemer, P., J. M. Warren, & G. Hirth (2012). The influence of deformation history on the interpretation of seismic anisotropy, *Geochem., Geophys., Geosys.*, doi: 10.1029/2011GC003988.
- Smith, D. B., M. H. Ritzwoller, & N. M. Shapiro (2004). Stratification of anisotropy in the Pacific upper mantle, *J. Geophys. Res.*, *109*, doi:10.1029/2004JB003200.
- Smith, G. P., & G. Ekström (1999). A global study of P_n anisotropy beneath continents, *J. Geophys. Res.*, *104*, 963–980.
- Smith, M. L., & F. A. Dahlen (1973). The azimuthal dependence of Love and Rayleigh wave propagation in a slightly anisotropic medium, *J. Geophys. Res.*, *78*, 3321–3333, correction in doi: 10.1029/JB080i014p01923.
- Song, T.-R. A., & H. Kawakatsu (2012). Subduction of oceanic asthenosphere: evidence from sub-slab seismic anisotropy, *Geophys. Res. Lett.*, *39*(L17301). doi: 10.1029/2012 GL052639.
- Steinberger, B., & R. J. O'Connell (1997). Changes of the Earth's rotation axis owing to advection of mantle density heterogeneities, *Nature*, *387*, 169–173.

- Sundberg, M., & R. F. Cooper (2008). Crystallographic preferred orientation produced by diffusional creep of harzburgite: Effects of chemical interactions among phases during plastic flow, *J. Geophys. Res.*, *113*(B12208). doi:10.1029/2008JB005618.
- Takeo, A., K. Nishida, T. Isse, H. Kawakatsu, H. Shiobara, H. Sugioka, & T. Kanazawa (2013). Radially anisotropic structure beneath the Shikoku Basin from broadband surface wave analysis of ocean bottom seismometer records, *J. Geophys. Res.*, *118*, 2878–2892, doi:10.1002/jgrb.50219.
- Takeo, A., H. Kawakatsu, T. Isse, K. Nishida, H. Shiobara, H. Sugioka, A. Ito, & H. Utada (2018). In situ characterization of the lithosphere-asthenosphere system beneath NW Pacific ocean via broadband dispersion survey with two OBS arrays, *Geochem., Geophys., Geosys.*, *19*, 3529–3539, doi:10.1029/2018GC007588.
- Tanimoto, T., & D. L. Anderson (1984). Mapping convection in the mantle, *Geophys. Res. Lett.*, *11*, 287–290.
- Tommasi, A. (1998). Forward modeling of the development of seismic anisotropy in the upper mantle, *Earth Planet. Sci. Lett.*, *160*, 1–13.
- Tommasi, A., M. Knoll, A. Vauchez, J. W. Signorelli, C. Thoraval, & R. Logé (2009). Structural reactivation in plate tectonics controlled by olivine crystals anisotropy, *Nature Geosci.*, *2*, 423–427.
- Trampert, J., & H. J. van Heijst (2002). Global azimuthal anisotropy in the transition zone, *Science*, *296*, 1297–1299.
- Trampert, J., & J. H. Woodhouse (2003). Global anisotropic phase velocity maps for fundamental mode surface waves between 40 and 150 s, *Geophys. J. Int.*, *154*, 154–165.
- Turcotte, D. L., & E. R. Oxburgh (1967). Finite amplitude convective cells and continental drift, *J. Fluid Mech.*, *28*, 29–42.
- van Hunen, J., & O. Čadež (2009). Reduced oceanic seismic anisotropy by small-scale convection, *Earth Planet. Sci. Lett.*, *284*, 622–629.
- van Summeren, J., C. P. Conrad, & C. Lithgow-Bertelloni (2012). The importance of slab pull and a global asthenosphere to plate motions, *Geochem., Geophys., Geosys.*, *13* (Q0AK03). doi:10.1029/2011GC003873.
- Vine, F. J., & D. H. Matthews (1963). Magnetic anomalies over ocean ridges, *Nature*, *199*, 947–949.
- Vinnik, L. P., V. Farra, & B. A. Romanowicz (1989). Azimuthal anisotropy in the Earth from observations of SKS at Geoscope and Nars broadband stations, *Bull. Seismol. Soc. Am.*, *79*, 1542–1558.
- Vinnik, L. P., L. I. Makeyeva, A. Milev, & Y. Usenko (1992). Global patterns of azimuthal anisotropy and deformation in the continental mantle, *Geophys. J. Int.*, *111*, 433–447.
- Visser, K., J. Trampert, & B. L. N. Kennett (2008). Global anisotropic phase velocity maps for higher mode Love and Rayleigh waves, *Geophys. J. Int.*, *172*, 1016–1032.
- Walker, K. T., G. H. R. Bokelmann, S. L. Klempner, & A. Nyblade (2005). Shear-wave splitting around hotspots: Evidence for upwelling-related mantle flow?, in *Plates, Plumes, and Paradigms, Geolog. Soc. Amer. Spec. Pap.*, vol. 388, edited by G. Foulger, J. H. Natland, D. C. Prentiss, & D. L. Anderson, pp. 171–192, Geological Society of America.
- Wang, J., & D. Zhao (2008). P-wave anisotropic tomography beneath Northeast Japan, *Phys. Earth Planet. Inter.*, *170*, 115–133.
- Wang, N., J.-P. Montagner, A. Fichtner, & Y. Capdeville (2013). Intrinsic versus extrinsic seismic anisotropy: The radial anisotropy in reference Earth models, *Geophys. Res. Lett.*, *40*, 4284–4288.
- Wenk, H.-R., & C. N. Tomé (1999). Modeling dynamic recrystallization of olivine aggregates deformed in simple shear, *J. Geophys. Res.*, *104*, 25,513–25,527.
- Wessel, P., & W. H. F. Smith (1998). New, improved version of the Generic Mapping Tools released, *Eos Trans. AGU*, *79*, 579.
- Wookey, J., & J.-M. Kendall (2004). Evidence of midmantle anisotropy from shear wave splitting and the influence of shear-coupled P waves, *J. Geophys. Res.*, *109*, doi:10.1029/2003JB002871.
- Wüstefeld, A., G. H. R. Bokelmann, G. Barruol, & J.-P. Montagner (2009). Identifying global seismic anisotropy patterns by correlating shear-wave splitting and surface-wave data, *Phys. Earth Planet. Inter.*, *176*, 198–212, available online at www.gm.univ-montp2.fr/splitting/DB/, accessed 01/2019.
- Xie, J., M. H. Ritzwoller, S. Brownlee, & B. Hacker (2015). Inferring the oriented elastic tensor from surface wave observations: preliminary application across the western United States, *Geophys. J. Int.*, *201*, 996–1021.
- Yuan, H., & B. A. Romanowicz (2010). Lithospheric layering in the North American continent, *Nature*, *466*, 1063–1069.
- Yuan, H., B. A. Romanowicz, K. M. Fischer, & D. Abt (2011). 3-D shear wave radially and azimuthally anisotropic velocity model of the North American upper mantle, *Geophys. J. Int.*, *184*, 1237–1260.
- Yuan, K., & C. Beghein (2013). Seismic anisotropy changes across upper mantle phase transitions, *Earth Planet. Sci. Lett.*, *374*, 132–144.
- Zandt, G., & E. Humphreys (2008). Toroidal mantle flow through the western U.S. slab window, *Geology*, *36*, 295–298.
- Zhang, S., & S.-i. Karato (1995). Lattice preferred orientation of olivine aggregates deformed in simple shear, *Nature*, *375*, 774–777.
- Zhong, S. (2001). Role of ocean-continent contrast and continental keels on plate motion, net rotation of lithosphere, & the geoid, *J. Geophys. Res.*, *106*, 703–712.
- Zhou, Q., J. S. Hu, L. J. Liu, T. Chaparro, D. Stegman, & M. Faccenda (2018). Western US seismic anisotropy revealing complex mantle dynamics, *Earth Planet. Sci. Lett.*, *500*, 156–167.

Mantle Convection in Subduction Zones: Insights from Seismic Anisotropy Tomography

Zhouchuan Huang¹ and Dapeng Zhao²

ABSTRACT

Lithospheric plates descend into the mantle and drive mantle upwelling in subduction zones, causing large earthquakes and vigorous magmatism along island arcs and continental margins. These processes induce different stress and strain regimes at different depths and generate varying seismic anisotropies. Hence, measurements of seismic anisotropy provide straightforward constraints on the subduction processes, in particular, mantle convection in subduction zones. High-resolution images of seismic anisotropy tomography obtained in the past decade have provided essential and direct information on the anisotropy in subduction zones. These new findings well constrain deformations in the overriding plates, subducting slabs, and mantle flows adjacent to the slabs. The anisotropy in the slabs, either trench-normal or trench-parallel, changes at different depths, reflecting either frozen-in fossil anisotropy or current slab deformations accompanying subduction. In the mantle wedge, dominant trench-normal anisotropy arises from extensive corner flow caused by the subduction, with notable 3D flow and trench-parallel anisotropy due to along-arc variations. In the subduction channel, trench-parallel and subduction-parallel anisotropies are revealed in strong and weak coupling areas, respectively. In the sub-slab mantle, there is still debate on entrained flow caused by subduction (inducing trench-normal anisotropy) and 3D flow caused by trench retreat (inducing trench-parallel anisotropy).

11.1. INTRODUCTION

Subduction zones are located at convergent boundaries between different lithospheric plates on the Earth (Figure 11.1) (e.g., Stern, 2002; Zhao, 2012). They are characterized by deep ocean trenches and island arcs or continental margins, as well as frequent earthquakes, in particular, intermediate-depth and deep earthquakes that

form a dipping Wadati-Benioff seismic zone. On the surface, plate subduction causes extensive crustal faulting and mountain building, as well as trench-parallel linear belt of active volcanoes, i.e., the volcanic front. The plate subduction and accompanying arc magmatism are a fundamental and unique process in terrestrial tectonics and geodynamics, and play a key role in the evolution of the Earth. Therefore, the study of subduction zones is one of the most important subjects in geoscience.

Seismic tomography, which images three-dimensional (3D) structures of the Earth's interior, was first developed in the mid-1970s (Aki et al., 1977). It was soon applied to study the 3D seismic velocity structure of subduction

¹School of Earth Sciences and Engineering, Nanjing University, Nanjing, China

²Department of Geophysics, Tohoku University, Sendai, Japan

zones (see Zhao, 2012 for a detailed review). Subduction zones are ideal regions for the application of seismic tomography, because strong contrasts in seismic velocity exist, and abundant shallow and deep earthquakes provide crisscrossing seismic rays in a 3D volume in the crust and upper mantle (Zhao, 2015). Clear images of cold subducting slabs (higher seismic velocity) and hot partial-melting materials in the mantle wedge (lower velocity) have demonstrated that seismic tomography is a powerful tool for imaging subduction zones (e.g., Hirahara, 1977; Hasemi et al., 1984; Zhao et al., 1992; Zhou, 1996). During the past four decades, many important tomographic results have greatly improved our understanding of subduction dynamics. On the other hand, the special tectonic setting and distribution of seismic rays in a subduction zone have also led to important technical advances in seismic tomography (see a recent review by Zhao, 2015).

Seismic anisotropy is a phenomenon that some features of seismic waves (e.g., velocity, attenuation) depend on the propagating direction. Anisotropic media exist widely in the Earth, from the crust and mantle to the inner core, which have been revealed by both seismological observations and laboratory studies (see Silver, 1996; Fouch & Rondenay, 2006; Long, 2013 for detailed reviews). Seismic anisotropy provides a unique constraint on past and present deformations in the lithosphere and sublithospheric mantle. Both body-wave and surface-wave capture information of anisotropy and thus can be used to study seismic anisotropy. Fouch & Rondenay (2006) made a detailed review of the methods for investigating seismic anisotropy and their advantages and limitations.

Seismic anisotropy is mainly caused by lattice-preferred orientation (LPO) and shape-preferred orientation (SPO) of materials in the Earth (see Chapter 10 by Becker & Lebedev in this book for a comprehensive review of the origin of anisotropy in different layers within the Earth). In subduction zones, anisotropies in different domains have different causes. In the upper crust, aligned cracks (i.e., SPO) due to tectonic stresses are thought to be the most important cause of anisotropy, with fast-propagation direction parallel to the cracks (e.g., Crampin, 1984). In the lower crust and mantle wedge above the subducting slab, the LPOs of mica and olivine dominate the patterns of anisotropy as a result of the plate interactions and mantle-wedge convection. However, in the middle of the mantle wedge, the SPOs of melts may be the most important factor, because high temperature there leads to mineral diffusion creep that does not produce notable anisotropy (Katayama, 2009). In the upper part of the subducting slab, the LPO of highly anisotropic hydrous minerals (serpentine and talc) formed along steeply dipping hydrated faults may be another origin of anisotropy beside commonly referred olivine (Faccenda et al., 2008).

P-wave anisotropy tomography is a relatively new method that has been developed and applied in the past

decade (see a review by Zhao et al., 2016), though *Pn*-anisotropy tomography has a longer history (e.g., Hearn 1996). *Pn*-wave tomography can only estimate two-dimensional *P*-wave velocity (V_p) variations and azimuthal anisotropy in the uppermost mantle directly beneath the Moho discontinuity, whereas *P*-wave anisotropy tomography can determine 3D distribution of V_p anisotropy in the crust and upper mantle beneath a seismic network (e.g., Eberhart-Phillips & Henderson, 2004; Ishise & Oda, 2005; Wang & Zhao, 2008, 2013; Liu & Zhao, 2016a). In this chapter, we review major results of *P*-wave tomography for azimuthal and radial anisotropies in subduction zones obtained in the past decade (Figure 11.1), and discuss their implications for subduction geodynamics.

11.2. METHOD

Twenty-one independent elastic moduli are necessary to fully express a general anisotropic medium, which are very hard to handle. In practice, an approximation to the Earth material with hexagonal symmetry may reduce the number of physical parameters describing seismic anisotropy (e.g., Christensen, 1984; Park & Yu, 1993; Maupin & Park, 2007). Furthermore, we may assume horizontal hexagonal symmetry when azimuthal anisotropy is concerned in shear-wave splitting analysis (e.g., Crampin, 1984; Silver, 1996; Savage, 1999; Long, 2013) and *P*-wave velocity studies (e.g., Hess, 1964; Backus, 1965; Raitt et al., 1969; Hearn, 1996; Eberhart-Phillips & Henderson, 2004; Wang & Zhao, 2008, 2013). On the other hand, we assume vertical hexagonal symmetry for radial anisotropy, which is in the form of V_{sh}/V_{sv} variation (horizontal/vertical polarized S wave) in surface-wave studies (e.g., Nettles & Dziewonski, 2008; Fichtner et al., 2010; Yuan et al., 2011) and in the form of V_{ph}/V_{pv} variation (horizontal/vertical propagating *P* wave) in *P*-wave velocity studies (e.g., Wang & Zhao, 2013; Ishise et al., 2018).

The assumption of hexagonal anisotropy with a horizontal or vertical symmetry axis is computationally necessary, because the resolving power of the seismic data is hard to constrain more complicated anisotropy. However, the assumption of hexagonal symmetry is justified. The dominant minerals in the upper mantle are olivine and enstatite. Browaeys & Chevrot (2004) found that hexagonal symmetry accounts for ~75% and >50% of the total anisotropy for olivine and enstatite, respectively. Furthermore, the alignment of olivine in the mantle is not perfect along all three axes, and the inherent anisotropy of several minerals combines in such a way as to make the typical mantle and crustal petrofabric even closer to hexagonal. For example, Becker et al. (2006)

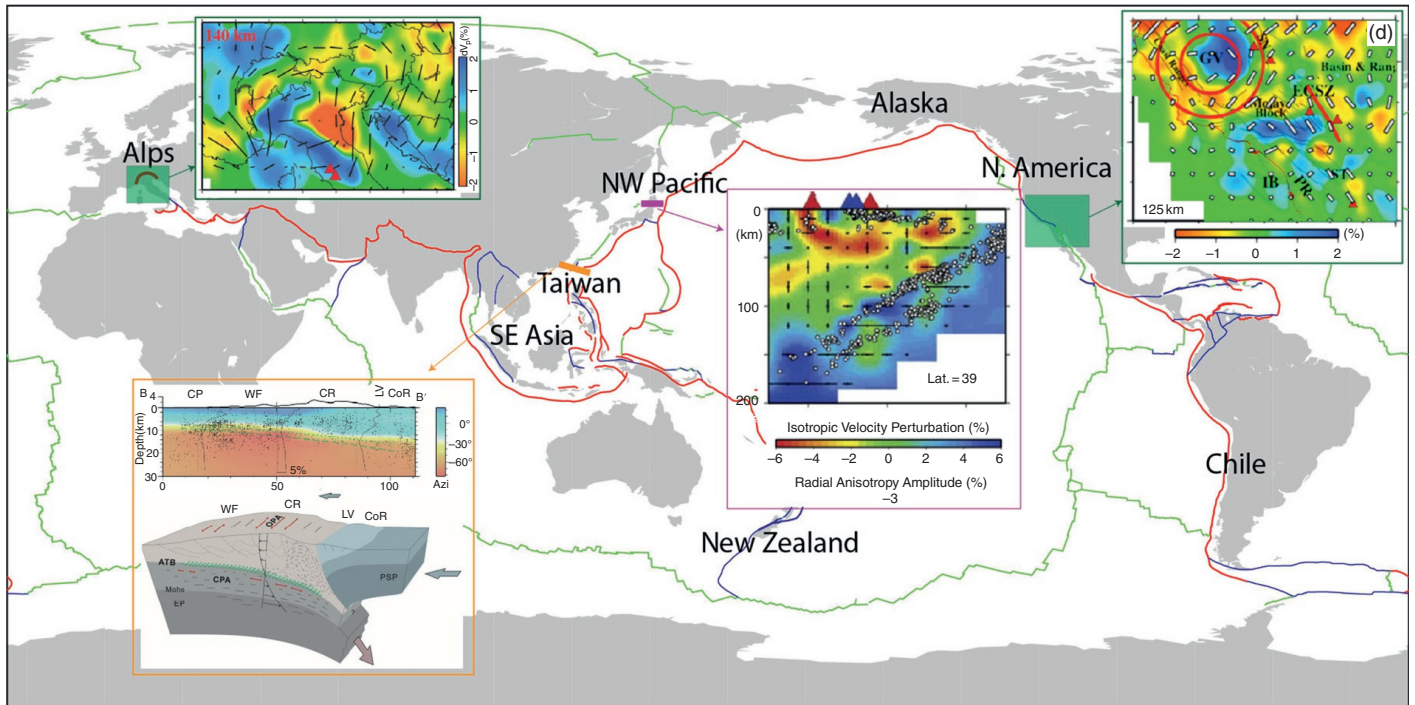


Figure 11.1 World map showing the distribution of major plate boundaries. Red, green, and blue lines denote convergent, divergent, and strike-slip plate boundaries, respectively (Coffin et al., 1998). Insets show seismic anisotropy tomography of four regions.

- (top-left) P -wave azimuthal-anisotropy tomography at 140 km depth in Alps. Red and blue colors denote low and high velocity anomalies, respectively. The orientation and length of the short black bars represent the horizontal FVD and its amplitude, respectively. Red triangles are Cenozoic volcanoes. *Source:* Hua et al., 2017.
- (top-right) P -wave azimuthal-anisotropy tomography at 125 km depth in Southern California. The red circles and the red thick line depict a circular pattern of azimuthal anisotropy and deflected mantle flow, respectively. GV: Great Valley; PR: Peninsular Ranges; SN: Sierra Nevada. *Source:* Yu & Zhao, 2018.
- (center) East-west vertical cross-section of P -wave radial-anisotropy tomography beneath Northeast Japan. The horizontal bars denote faster horizontal V_p than vertical V_p at each grid node, whereas the vertical bars denote faster vertical V_p . The red and blue triangles denote the active and quaternary arc volcanoes, respectively. The white dots denote background seismicity that occurred within a 10-km width of the profile. *Source:* Wang & Zhao, 2013.
- (bottom-left) Vertical cross-section showing rotation of anisotropic fabrics with depth beneath Taiwan (T. Huang et al., 2015). The resolved fast directions of azimuthal anisotropy are color coded to highlight the rotation from 30° to 0° , to -60° , and to -90° over a narrow depth range. Green dotted lines represent the transitional boundary of different anisotropy (ATB). The bottom cartoon illustrates the layered deformation zones in the Taiwan orogen. The compressional tectonics and the subduction-dominated shear deformation are characterized by the orogen-parallel anisotropy (OPA) and the convergence-parallel anisotropy (CPA), respectively. The green dots separate the two deformation regimes and couples of the upper crust of the orogen with the subduction. *Source:* Modified from T. Huang et al. (2015).

confirmed that the hexagonal approximation for seismic anisotropy may capture ~80% of the total anisotropy in the upper mantle. However, inclined hexagonal symmetry is not unusual, particularly in subduction zones due to the existence of dipping slabs and 3D mantle flows (e.g., Wang and Zhao, 2013; Huang et al., 2015b).

11.2.1. Azimuthal Anisotropy Tomography

Traveltime seismic tomography for 3D isotropic velocity structure relates observed traveltime residuals (r) to perturbations of hypocentral parameters (i.e., latitude $\Delta\varphi_e$, longitude $\Delta\lambda_e$, focal depth Δh_e , and origin time ΔT_e) and 3D velocity perturbations (ΔV) relative to a 1D reference velocity model. In isotropic tomography, P -wave is assumed to travel with the same velocity (V_p) in all directions (the corresponding slowness is defined as $S_0 = 1/V_p$). For weak azimuthal anisotropy with hexagonal symmetry, variations of V_p with the azimuth of wave propagation (ϕ) can be written as a linear combination of terms proportional to $\sin 2\phi$ and $\cos 2\phi$ (Backus, 1965; Raitt et al., 1969). A simple expression for Pn -wave velocity (or slowness) is (Hearn, 1996):

$$S(\phi) = S_0 + M \cos 2(\psi - \phi) = S_0 + A \cos 2\phi + B \sin 2\phi \quad (11.1)$$

where $M = \sqrt{A^2 + B^2}$ is related to the strength of anisotropy, and ϕ is the fast velocity direction (FVD). The parameters A and B describe the azimuthal anisotropy (see Wang & Zhao, 2008 for details), specifically, the anisotropic amplitude (α , i.e., the strength of anisotropy) and FVD (ψ) are given by:

$$\alpha = \frac{V_f - V_s}{2V_0} = \frac{M}{S_0 - M^2/S_0} \quad (11.2)$$

$$\psi(A, B) = \begin{cases} \frac{1}{2} \tan^{-1}\left(\frac{B}{A}\right) + \begin{cases} \frac{\pi}{2}, A > 0 \\ 0, A < 0 \end{cases} \\ -\frac{\pi}{4}, B > 0 \\ \frac{\pi}{4}, B < 0 \end{cases}, A = 0 \quad (11.3)$$

where V_f and V_s denote P -wave velocities in the fast and slow velocity directions, respectively.

More generally, for a P -wave ray with incidence angle i , Equation (11.1) was further extended to (e.g., Eberhart-Phillips & Henderson, 2004):

$$S(\phi) = S_0 - \cos^2 i \sqrt{A^2 + B^2} + \sin^2 i (A \cos 2\phi + B \sin 2\phi) \quad (11.4)$$

for media with a hexagonal symmetry and a horizontally oriented, slow symmetry axis.

Thus, the observation equations for weak P -wave azimuthal anisotropy are:

$$r = \frac{\partial T}{\partial \varphi_e} \cdot \Delta \varphi_e + \frac{\partial T}{\partial \lambda_e} \cdot \Delta \lambda_e + \frac{\partial T}{\partial h_e} \cdot \Delta h_e + \Delta T_e + \sum_{n=1}^N \left(\frac{\partial T}{\partial S_n} \cdot \Delta S_n \right) + \sum_{m=1}^M \left(\frac{\partial T}{\partial A_m} \cdot \Delta A_m + \frac{\partial T}{\partial B_m} \cdot \Delta B_m \right) \quad (11.5)$$

where $\partial T/\partial \varphi_e$, $\partial T/\partial \lambda_e$ and $\partial T/\partial h_e$ are partial derivatives of traveltime with respect to the hypocentral parameters of a local earthquake (Engdahl & Lee, 1976), and $\partial T/\partial S_n$ are partial derivative of traveltime with respect to velocity at each node ($1 \dots N$) of a 3D grid for isotropic V_p structure (Thurber, 1983), $\partial T/\partial A_m$ and $\partial T/\partial B_m$ are partial derivatives of traveltime with respect to the anisotropic parameters (A and B) at each node ($1 \dots M$) of another 3D grid for V_p anisotropy (Eberhart-Phillips & Henderson, 2004; Wang & Zhao, 2008; Eberhart-Phillips & Reyners, 2009). Note that the grid intervals for the isotropic and anisotropic V_p structures may be chosen differently, because the anisotropic V_p structure is usually resolved with a lower resolution than the isotropic V_p structure.

11.2.2. Radial Anisotropy Tomography

When the hexagonal symmetry axis is vertical, Equation (11.1) can be rewritten as a function of ray incidence angle i (see Wang & Zhao, 2013; Ishise et al., 2018 for details):

$$S(\phi) = S_0 + M \cos 2i \quad (11.6)$$

The anisotropic amplitude β is then defined as:

$$\beta = \frac{V_{ph} - V_{pv}}{2V_0} = \frac{M}{S_0 - M^2/S_0} \quad (11.7)$$

Hence, $\beta > 0$ indicates a faster velocity for a horizontally-propagating P wave than the vertical one, i.e., $V_{ph} > V_{pv}$.

Similarly, the observation equations for weak P -wave radial anisotropy are:

$$r = \frac{\partial T}{\partial \varphi_e} \cdot \Delta \varphi_e + \frac{\partial T}{\partial \lambda_e} \cdot \Delta \lambda_e + \frac{\partial T}{\partial h_e} \cdot \Delta h_e + \Delta T_e + \sum_{n=1}^N \left(\frac{\partial T}{\partial S_n} \cdot \Delta S_n \right) + \sum_{k=1}^K \left(\frac{\partial T}{\partial M_k} \cdot \Delta M_k \right) \quad (11.8)$$

The right-hand side includes terms for the hypocentral parameters, isotropic V_p perturbations, and anisotropic V_p parameters at 3D grid nodes arranged in a study volume.

11.3. APPLICATIONS

In comparison with isotropic tomography, V_p anisotropic tomography requires better coverage of ray paths in different directions (for azimuthal anisotropy) or incidence angles (for radial anisotropy) in the study volume. It is a challenge to most applications of seismic anisotropic tomography. In subduction zones, seismicity is much more intense than that in other tectonic regions. Hence, a better result of anisotropic tomography can be obtained in a subduction zone region, if a good seismic network is installed there.

11.3.1. Northwest Pacific

Northwest Pacific is composed of mature subduction zones that are characterized by subduction of the old Pacific Plate. A dense seismic network has been deployed on the Japan Islands for over a century for monitoring seismicity and reducing the heavy earthquake hazard, leading to high-quality data and high-resolution seismic models of the Japan subduction zone. Isotropic tomography models obtained in the past four decades clearly revealed the high-velocity (high-V) subducting Pacific slab under northeast Japan and the Philippine Sea (PHS) slab under southwest Japan and Ryukyu (e.g., Hirahara, 1977; Hasemi et al., 1984; Umino & Hasegawa 1984; Zhao et al., 1992, 1994; Tsumura et al., 2000; Huang et al., 2011; Liu and Zhao, 2016b). Above the slabs are extensive low-velocity (low-V) zones that are subparallel to the subducting slab and sometimes reach the Moho discontinuity right beneath active volcanoes along the volcanic front. The low-V zones are also characterized as high-attenuation (low-Q) anomalies (e.g., Liu et al., 2014). The low-V and low-Q zones are interpreted to represent hot and wet upwelling flow of active convection in the mantle wedge driven by the active subduction and related dehydration reactions of the Pacific and PHS slabs.

Seismic anisotropy tomography has provided direct evidence for the mantle convection in the subduction zones. Ishise & Oda (2005) and Wang & Zhao (2008) first conducted P -wave anisotropy tomography beneath Tohoku (NE Japan). Following the approach of Zhao et al. (1992), Wang & Zhao (2008) considered the geometries of the Conrad and Moho discontinuities and the upper boundary of the subducting Pacific slab to compute theoretical traveltimes and ray paths accurately, and so obtained a better result of V_p azimuthal anisotropy. Their results were updated later using more and better data sets (Huang et al., 2011c; Liu and Zhao, 2016a, 2017a,b). These studies have revealed dominant E-W FVDs in the lower crust and mantle wedge, and N-S FVDs in the subducting Pacific slab to the first order (Figure 11.2). In the mantle wedge, the FVDs are

generally trench-parallel in the forearc area while trench-normal in the backarc area. The mantle wedge anisotropy may be caused by preferred orientations of mantle minerals arising from the current mantle processes such as mantle-wedge convection and plate motion. The FVDs in the Pacific slab are N-S, roughly perpendicular to the magnetic lineation of the oceanic plate under the Northwest Pacific, hence the slab may preserve the original anisotropic property that the Pacific plate gained at the mid-ocean ridge.

Wang & Zhao (2009) determined the first tomography for V_p azimuthal anisotropy beneath Hokkaido of the southern Kuril arc. The mantle-wedge anisotropy is similar to that in Tohoku, i.e., the FVD is generally trench-normal under the backarc, but it becomes trench-parallel under the Pacific coast (forearc) area (Figure 11.2). Beneath the volcanic front, the FVD is trench-parallel, suggesting a complex 3D mantle flow in the mantle wedge. The N-S FVD in the Pacific slab may reflect either the original fossil anisotropy or is affected by the olivine fabric transition due to the changes in water content, stress and temperature (Wang & Zhao, 2009). A similar V_p anisotropic model was presented by Koulakov et al. (2015b). The crustal anisotropy was closely related to the major faults and suture zones. A fan-shaped anisotropy was found in the mantle, reflecting possible mantle flows starting in southern Hokkaido and splitting into three directions. The western and eastern flows proceed toward the two volcanic groups on Hokkaido, which may carry fluids to trigger the eruptions (Koulakov et al., 2015b).

The sP depth phases identified in the forearc area of NE Japan make it possible to relocate the suboceanic earthquake precisely (Umino et al., 1995), which further motivated high-resolution tomographic imaging of the Tohoku forearc region where large megathrust earthquakes occurred frequently (Zhao et al., 2002; Mishra et al., 2003; Zhao et al., 2011; Huang & Zhao, 2013a; Liu & Zhao, 2018). P -wave anisotropic tomography has been extended to the entire Tohoku and Hokkaido arcs from the Kuril-Japan Trench to the Japan Sea by adding data from many well-relocated suboceanic events (Wang & Zhao, 2010; Huang et al., 2011c; Liu et al., 2013; Liu & Zhao, 2017a). Significant V_p anisotropy was also found in the forearc area under the Pacific Ocean and the backarc area beneath the Japan Sea.

A novel approach is developed to invert S -wave travel-times for 3D V_s azimuthal anisotropy in the Japan subduction zone (Liu & Zhao, 2016a). The obtained V_s anisotropic tomography has a resolution comparable to that of V_p anisotropic tomography. A joint inversion of P - and S -wave arrival times has significantly improved the azimuthal anisotropy tomography of the Japan subduction zone (Liu & Zhao, 2016a). They confirmed the first-order pattern of V_p anisotropy revealed by the previous studies.

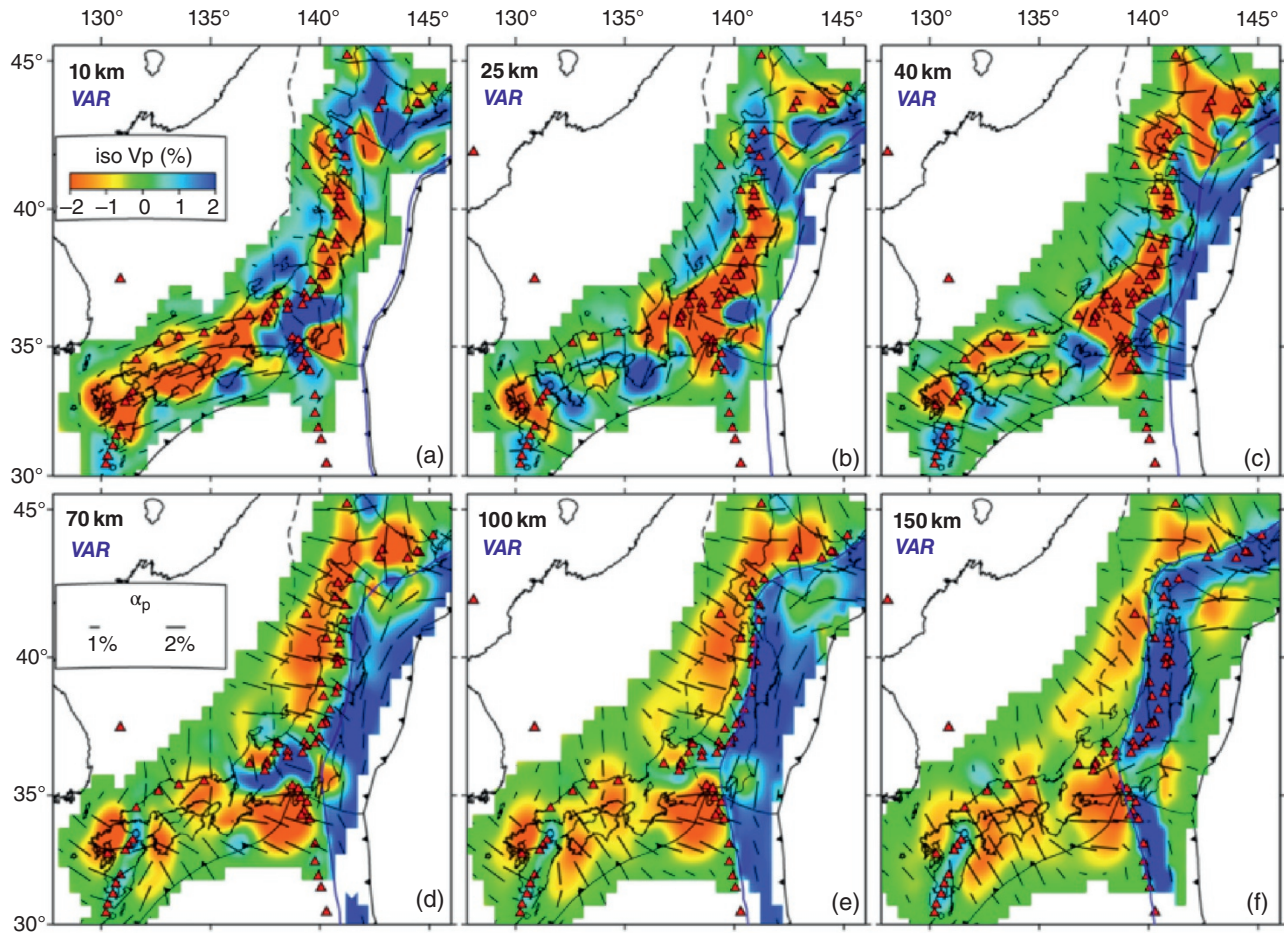


Figure 11.2 Map views of isotropic V_p and its azimuthal anisotropy of the Japan subduction zone (a–f). The layer depth is shown at the upper-left corner of each map. The blue line denotes the location of the upper boundary of the subducting Pacific slab at each depth. The red and blue colors denote low and high isotropic velocities, respectively. The isotropic V_p perturbation (in percent) scale is shown in (a). The orientation and length of the short black bars represent the horizontal FVD and its amplitude, respectively. The saw-tooth black lines denote the trenches. Red triangles denote active volcanoes. *Source:* Liu & Zhao, 2017b.

V_p radial anisotropy tomography is also determined for the Tohoku and Hokkaido areas (Wang & Zhao, 2013; Niu et al., 2016). The results show faster vertical velocity than horizontal velocity (i.e., $V_{pv} > V_{ph}$) in the mantle-wedge low-V zones under the arc volcanoes (Figure 11.1, inset), which may reflect hot upwelling flows and transitions of olivine fabrics with the presence of water in the mantle wedge, due to the dehydration reactions of the Pacific slab. In contrast, $V_{pv} < V_{ph}$ in the subducting Pacific slab, which, together with the azimuthal anisotropy results, suggest that the Pacific slab keeps its frozen-in anisotropy, or the slab anisotropy is induced by LPO of the B-type olivine (e.g., Karato et al., 2008). Huang et al. (2015b) and Ishise et al. (2018) checked the radial-anisotropy tomography beneath Tohoku and confirmed the main features. In addition, Huang et al. (2015b) found significant along-arc variations of V_p radial anisotropy in the mantle wedge, and stronger radial

anisotropy under the active volcanoes. Given the general interpretations that the vertical-fast anisotropy results from mantle upwelling in the mantle wedge, the along-arc variations of V_p radial anisotropy indicate along-arc variations of subduction dynamics. The stronger radial anisotropy suggests stronger mantle-wedge convection, leading to stronger volcanic activity and more volcanic rocks at the surface (Huang et al., 2015b).

V_p anisotropic tomography beneath SW Japan has been also investigated (Ishise & Oda, 2008; Wang & Zhao, 2012, 2013). In Kyushu, the V_p FVD is generally trench-normal in the mantle wedge under the backarc (Figure 11.2), which is consistent with the existence of corner flow driven by the PHS slab subduction. The FVD is trench-parallel in the subducting PHS slab under Kyushu. V_p radial anisotropy (Wang & Zhao, 2013) shows $V_{ph} < V_{pv}$ in the mantle-wedge low-V zones under the arc volcanoes and in the low-V zones below the PHS slab, which

may reflect hot upwelling flows and transitions of olivine fabrics with the presence of water due to the slab dehydration there. Trench-parallel FVDs and positive radial anisotropy (i.e., $V_{ph} > V_{pv}$) in the PHS slab may indicate that the PHS slab keeps its frozen-in anisotropy formed at the mid-ocean ridge, or that the slab anisotropy is induced by LPO of the B-type olivine (Wang & Zhao, 2013).

To clarify the mechanism of the great 2011 Tohoku-oki earthquake (Mw 9.0), Liu & Zhao (2017a, 2018) investigated detailed 3D structure and anisotropy of the Tohoku subduction channel using P - and S -wave arrivals of sub-oceanic events relocated precisely with sP depth phases and OBS data. The shallow portion of the Tohoku megathrust zone (<30 km depth) generally shows trench-normal FVDs, except for the mainshock (Mw 9.0) area where the FVD is nearly trench-parallel (Figure 11.3). In contrast, the deeper portion of the megathrust zone (at depths of \sim 30–50 km) mainly exhibits trench-parallel FVDs. Trench-normal FVDs are revealed in the mantle wedge beneath the volcanic front and the backarc area. The Pacific plate mainly shows trench-parallel FVDs, except for the top portion of the subducting Pacific slab where visible trench-normal FVDs are revealed (Figure 11.3). These results indicate first-order transposition of earlier fabrics in the oceanic lithosphere into subduction-induced new structures in the subduction channel (Liu & Zhao, 2017a).

It is also found that high- V anomalies exist both above and below the mainshock hypocenter of the 2011 Tohoku-oki earthquake, suggesting that the generation of the Mw 9.0 earthquake was controlled by structural heterogeneities in both the overriding Okhotsk plate and the subducting Pacific plate (Liu & Zhao, 2018). Huang et al. (2019) also found high correlation between V_p azimuthal anisotropy and the degree of interplate locking along the megathrust zone in the northern Chile subduction zone.

P - and S -wave tomography as well as V_p azimuthal anisotropy in a broad region of Western Pacific and East Asia (Figure 11.4) are determined by inverting a great number of local and regional P - and S -wave arrivals (Wei et al., 2015, 2016). The NE-SW FVD in the subducting PHS slab beneath the Ryukyu arc is consistent with the spreading direction of the West Philippine Basin during its initial opening stage, suggesting that it may reflect the fossil anisotropy. A striking variation of the FVD with depths is revealed in the subducting Pacific slab beneath the Tohoku arc, which may result from slab dehydration that changed elastic properties of the slab with depth. The FVD in the mantle wedge beneath the Tohoku and Ryukyu arcs is trench-normal, which reflects subduction-induced convection (e.g., Wang & Zhao, 2008, 2013; Huang et al., 2011c; Liu and Zhao, 2016a). Beneath the Kuril and Izu-Bonin arcs where oblique subduction occurs, the FVD in the mantle wedge is nearly normal to the moving direction of the down-going Pacific

plate, suggesting that the oblique subduction has disturbed the mantle flow (Wei et al., 2015).

11.3.2. Southeast Asia

Southeast Asia is located in the southeastern part of the Eurasian Plate (Figure 11.1). It is surrounded by active subduction zones where several lithospheric plates are subducting beneath the Eurasian Plate (Bird, 2003). An important tectonic feature of SE Asia is the extrusion of the rigid Indochina Block driven by the Indo-Asian collision since 34 Ma (e.g., Aitchison et al., 2007), which may further induce spreading of the South China Sea (e.g., Tapponnier et al., 1982, 2001).

Huang et al. (2015c) used arrival-time data of local and regional earthquakes to determine 3D V_p tomography and azimuthal anisotropy in the mantle beneath entire Southeast Asia (Figure 11.5). High- V anomalies representing the subducting slabs are clearly visible in the upper mantle and the mantle transition zone. Low- V zones with trench-normal anisotropy are revealed in the uppermost mantle, which indicate backarc spreading or secondary mantle-wedge flow induced by the slab subduction. In contrast, trench-parallel anisotropy dominates in the deep upper mantle and reflects structures either in the subducting slab or in the upper mantle surrounding the slab. A low- V body extending down to the lower mantle is visible under Hainan volcano that is located far away from plate boundaries, suggesting that Hainan is a hotspot fed by a lower-mantle plume, being consistent with a result of teleseismic tomography (Xia et al., 2016). The low- V body under Hainan is connected with low- V zones in the upper mantle under SE Tibet and Vietnam. The V_p anisotropy results reflect that significant mantle flow exists in the asthenosphere from SE Tibet to Hainan and further southwestward to Vietnam (Liu et al., 2004).

11.3.3. New Zealand

New Zealand is also a well-studied subduction zone where the Pacific plate is subducting beneath the Australian plate in North Island. Various seismological methods have been applied to study the 3D crust and upper mantle structure of the region (for recent reviews, see Reyners, 2013; Eberhart-Phillips et al., 2013). V_p azimuthal-anisotropy tomography beneath central New Zealand is determined using local-earthquake arrival-time data (Eberhart-Phillips & Henderson, 2004; Eberhart-Phillips & Reyners, 2009). The strongest anisotropy is revealed in the subducting Pacific slab rather than within the mantle wedge or below the subducted slab. The slab FVD is trench-parallel and the strength of V_p anisotropy is 5–9% at depths of 32–185 km, which may reflect bending-induced yielding in the slab offshore as it passes through the trench. Beneath the Taupo

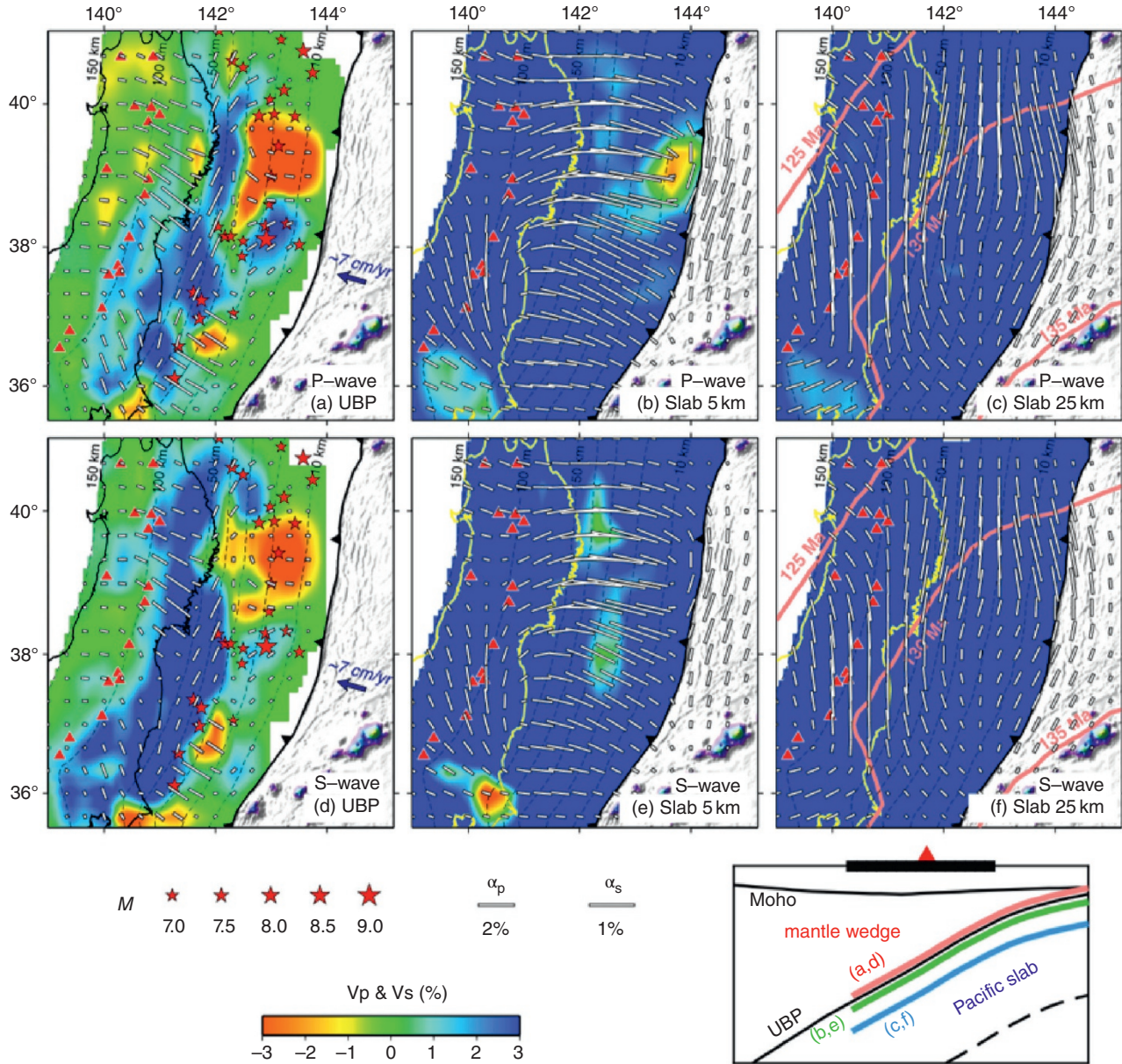


Figure 11.3 V_P and V_S azimuthal-anisotropy tomography along three planes in Northeast Japan that are located (a, d) directly (1 km) above the upper boundary of the subducting Pacific slab (UBP), (b, e) 5 km below the UBP (Slab 5 km), and (c, f) 25 km below the UBP (Slab 25 km), as shown in the sketch at the bottom. Labeling for anisotropy is the same as in Figure 11.1. The red triangles denote active arc volcanoes. The red stars in (a, d) denote large earthquakes (M 7.0–9.0) during January 1900 to December 2016, which occurred in the Tohoku megathrust zone beneath the Pacific Ocean. The saw-tooth black line denotes the Japan Trench. The black dashed lines denote the UBP depth contours. The purple lines in (c, f) denote the lithospheric ages of the Pacific slab. *Source:* (a–f) Liu & Zhao, 2017a.

volcanic zone (TVZ), there is 1–4% trench-normal anisotropy within 30 km of the slab upper boundary, within a region entrained with motion of the slab. In contrast, only very weak (0–2%) anisotropy is imaged in the region of high-temperature partial melt arising from active corner flow in the mantle wedge. Significant anisotropy aligned with the margins of the TVZ was revealed, which

may reflect extensive fracturing on the margins as the TVZ actively extends. Within the heavily intruded and underplated TVZ lower crust, the FVD switches to align with the extensional direction, which is consistent with other geophysical data, suggesting the presence of connected melt in this region (Eberhart-Phillips & Reyners, 2009).

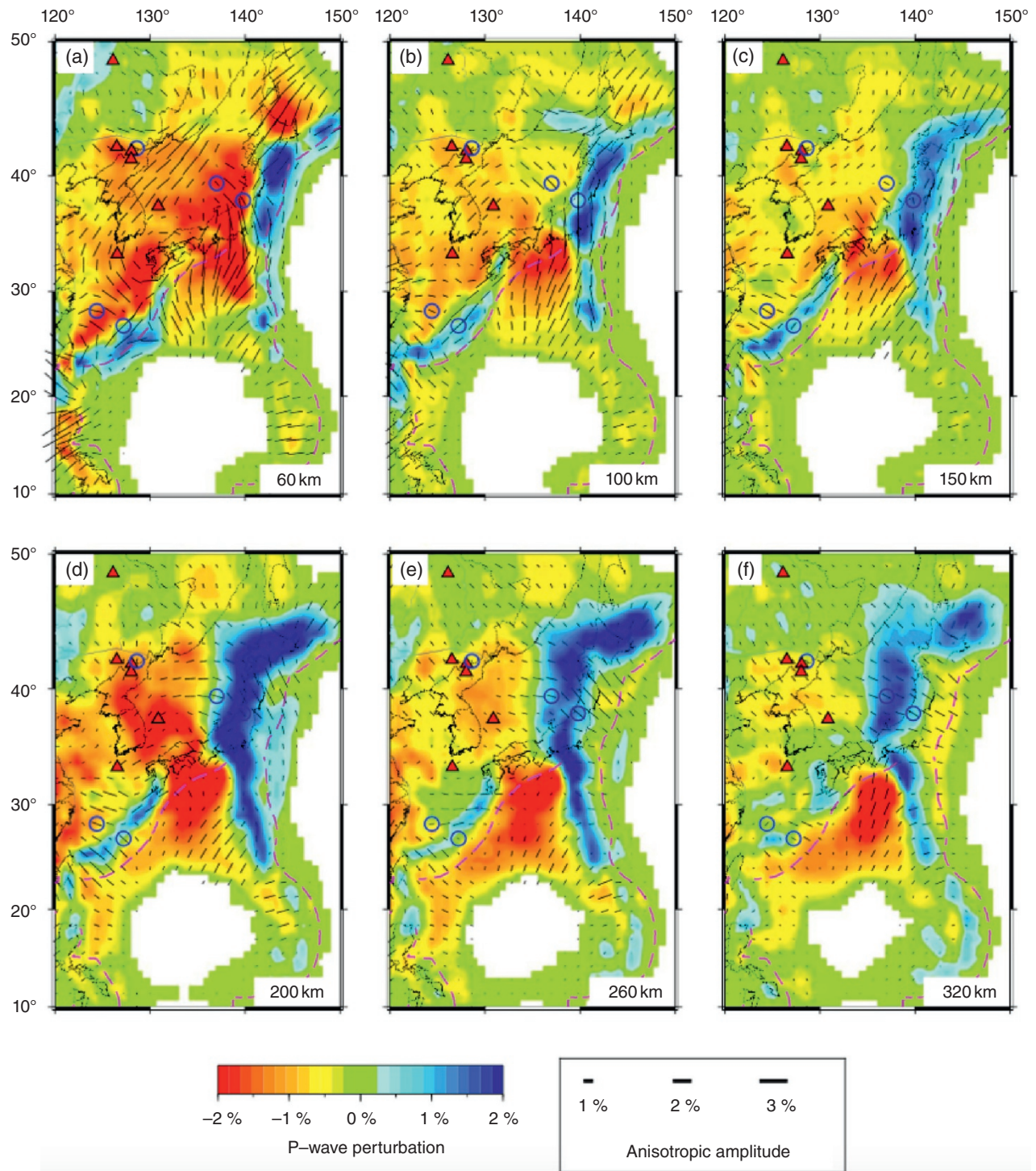


Figure 11.4 Map views of *P*-wave azimuthal-anisotropy tomography beneath Western Pacific and East Asia. The red and blue colors denote low and high isotropic velocities, respectively. The red triangles denote active intraplate volcanoes in NE Asia. For the other labeling, see Figure 11.2. *Source:* (a–f) Wei et al., 2015.

11.3.4. Alaska

In south-central Alaska, the Pacific plate is subducting beneath the North American plate, causing active seismicity and arc volcanism along the Alaska-Aleutian

subduction zone. In the past two decades many researchers have investigated the 3D crustal and upper mantle structure of the Alaska subduction zone using various seismological methods, revealing the high-*V* subducting Pacific slab and low-*V* anomalies in the crust and

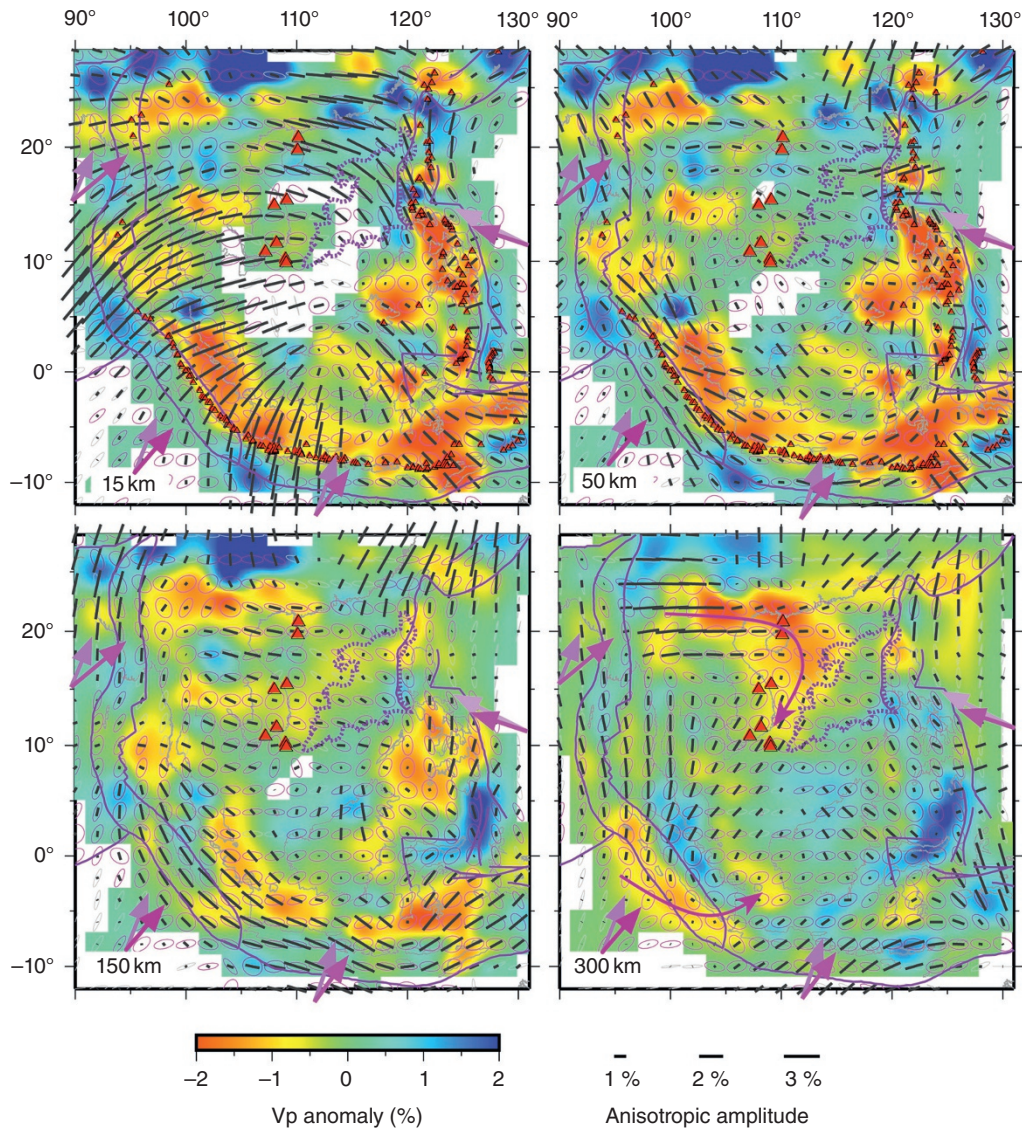


Figure 11.5 Map views of P -wave azimuthal-anisotropy tomography at six depths in Southeast Asia. Labeling for anisotropy is the same as in Figure 11.2. The ellipses at the grid nodes represent azimuthal coverage of rays. The magenta and gray ellipses indicate that the ratio between the short and the long axes is ≥ 0.3 and < 0.3 , respectively. The purple curves denote the plate boundaries, whereas the dashed curves outline the ocean basin under the South China Sea. The dark and light purple arrows denote the absolute plate-motion directions of the surrounding plates in the HS3-Nuvel-1A model and the NNR-MORVEL56 model, respectively. The red triangles denote active volcanoes. Sources: Huang et al., (2015c), Bird (2003), Gripp & Gordon (2002), Argus et al., (2011).

upper-mantle wedge associated with the arc magmatism (e.g., Zhao et al., 1995; Qi et al., 2007; Tian & Zhao, 2012b; Wang & Tape, 2014; Gou et al., 2019).

Tian & Zhao (2012b) determined detailed V_p and V_s tomography and 3D V_p azimuthal anisotropy beneath South-Central Alaska using local-earthquake arrival times in South-Central Alaska, which has been updated by Gou et al. (2019) recently. The results clearly revealed the high- V Pacific slab and low- V anomalies in the mantle wedge with significant along-arc variations beneath the

volcanic front. Significant V_p anisotropy is revealed, and the predominant FVD is trench-parallel in the shallow part of the mantle wedge (< 90 km depth) and in the subslab mantle, whereas the FVD is trench-normal within the subducting Pacific slab. The trench-parallel FVDs in the mantle wedge and subslab mantle reflect the 3D mantle flow induced by the complex geometry and strong curvature of the Pacific slab, as well as its flat and oblique subduction under Alaska. The trench-normal FVD within the Pacific slab may reflect the original fossil

anisotropy produced at the mid-ocean ridge (Tian & Zhao, 2012b; Gou et al., 2019).

11.3.5. North America

The deployment of the EarthScope/USArray since 2004 has greatly improved our understanding of the mantle structure and dynamics beneath the United States (US). Many high-resolution seismic models have been obtained beneath the western US (e.g., Becker, 2012; Tian & Zhao, 2012a). The tectonic involution of western US, including the active subduction of the Juan der Fuca plate, extensive subduction-related volcanism and intraplate volcanism (e.g., the Yellowstone hotspot), as well as mountain building, was thoroughly discussed and many models have been proposed on the basis of slab–mantle interactions revealed by the seismic images (e.g., Becker, 2012; Tian & Zhao, 2012a; Chen et al., 2014, 2015; Wang et al., 2016).

A 3D model of V_p azimuthal-anisotropy tomography of the crust and upper mantle beneath the US was determined by inverting traveltimes recorded by the USArray (Huang & Zhao, 2013b). FVDs in the lithosphere under the tectonically active areas correlate well with the surface tectonic features, suggesting that the V_p anisotropy mainly reflects the present deformation. In contrast, beneath the stable cratonic region, the FVDs revealed are consistent with the features of gravity and magnetic anomalies, indicating that the P -wave FVDs mainly reflect the fossil anisotropy in the lithosphere. Yu & Zhao (2018) determined a 3D model of V_p azimuthal and radial anisotropies of the crust and upper mantle beneath southern California (Figure 11.1, inset). They revealed significant depth-dependent anisotropy. In the asthenosphere the FVDs are characterized as a predominantly circular pattern centered in the robust high-V Isabella anomaly beneath the Great Valley (Figure 11.1, inset). The Isabella anomaly is possibly a remnant of the fossil Farallon slab and is currently a descending lithospheric remnant, contributing to the development of a circular asthenospheric flow. High-V anomalies are revealed below 300 km depth beneath areas surrounding the Great Valley, which may reflect the delaminated lithospheric segments.

11.3.6. Europe

The Alps is an arc-shaped mountain produced by continental convergence between the European and Adriatic plates since the Mesozoic (Qorbani et al., 2015; Handy et al., 2010, and references therein). The subduction of the European plate beneath the African plate initiated at ~80 Ma ago, followed by the collision between the European and Adriatic plates since ~35 Ma ago and the uplift of the Alpine orogenic belt after 23 Ma

(Castellarin & Cantelli, 2000; Handy et al., 2010, and references therein). Complex deformations in and around the Alps are controlled by interactions between several microplates or blocks. Lithospheric and deep mantle processes also affect the tectonic activity and strong surface deformation in the Alps (Koulakov et al., 2009).

Hua et al. (2017) determined the first tomographic images of V_p azimuthal and radial anisotropies in the crust and upper mantle beneath the Alps by joint inversions of local and teleseismic traveltimes data (Figure 11.1, inset). V_p azimuthal anisotropy in the western central Alps is characterized by mountain chain-parallel FVDs, which may result from the crustal deformation at a shallow depth and mantle flow in the deeper part induced by the southeastward subduction of the European plate. The FVDs beneath the Eastern Alps and the northern Dinarides are mainly NE-SW, consistent with the mantle flow induced by the northeastward subduction of the Adriatic plate. Negative radial anisotropy ($V_{ph} < V_{pv}$) within the high-V subducting European and Adriatic slabs may be caused by the nearly vertical subduction of the two slabs. In contrast, positive radial anisotropy ($V_{ph} > V_{pv}$) in the low-V mantle wedge may reflect mantle flow induced by the slab subduction.

11.4. DISCUSSION

11.4.1. Surface-Wave Anisotropic Tomography

Surface waves can also capture anisotropy in the crust and upper mantle. Surface-wave data have long been used to invert for anisotropy in the upper mantle (e.g., Tanimoto & Anderson, 1984; Montagner & Tanimoto, 1991; Yuan et al., 2011), mostly in global and regional scales (see Montagner, 2011 for a detailed review). Because of fewer stations and earthquakes in the middle of oceans, structures of the upper mantle there can hardly be constrained by body waves. In this case, surface-wave observations and inversions provide important information on the upper mantle structures (i.e., velocity and anisotropy) under oceans. Surface waves usually have a very low frequency (Montagner, 2011), which makes it difficult to reveal detailed structures in local scales comparable to body-wave inversions. However, dense seismic networks deployed in a few regions in the past decade have resulted in high-resolution models of surface-wave tomography (e.g., Lin et al., 2011; T. Huang et al., 2015; Liu & Zhao, 2016c; Chen et al., 2018).

Rayleigh-wave phase-velocity data are used to determine a 3D V_s azimuthal-anisotropy tomography down to a depth of ~300 km beneath the Japan Islands and the Japan Sea (Liu & Zhao, 2016c). The subducting

Pacific slab is imaged clearly as a dipping high- V_s zone with trench-parallel FVDs, which may indicate anisotropy arising from normal faults produced at the outer-rise area near the Japan trench axis, overprinting the slab fossil fabric. The mantle wedge generally exhibits lower V_s with trench-normal FVDs that reflect subduction-driven corner flow and anisotropy. Depth variations of azimuthal anisotropy are revealed in the big mantle wedge beneath the Japan Sea, which may reflect past deformations in the Eurasian lithosphere related to backarc spreading during 21–15 Ma and complex current convection in the asthenosphere induced by active subductions of both the Pacific and PHS plates.

Taiwan is located in a collision zone between the PHS plate and the Eurasian plate (e.g., Lallemand et al., 2001; Sibuet & Hsu, 2004). Global and local tomographic studies have revealed structural heterogeneities in the crust and upper mantle and provided clear evidence for the subduction of the Eurasian and PHS plates (e.g., Lallemand et al., 2001; Wang et al., 2006; Huang et al., 2010). Koulakov et al. (2015a) presented a 3D anisotropic V_p model of the crust and uppermost mantle based on traveltimes inversion. T. Huang et al. (2015) obtained a 3D V_s model and its azimuthal variation in the crust of the Taiwan orogen (Figure 11.1, inset) from ambient seismic noises, which are comparable to the 3D V_p model (Koulakov et al., 2015a). These studies found that anisotropic fabrics rotated nearly 90° across a 10–20 km depth, consistent with the presence of two layers of deformation. The upper crust is dominated by collision-related compressional deformation, whereas the lower crust of Taiwan, mostly the crust of the subducted Eurasian plate, is dominated by convergence-parallel shear deformation. They interpreted this lower crustal shearing as driven by continuous sinking of the Eurasian mantle lithosphere when the surface of the subducted plate is coupled with the orogen. The two-layer deformation clearly defines the role of subduction in the formation of the Taiwan orogen (T. Huang et al., 2015).

11.4.2. Shear-Wave Splitting Tomography

Shear-wave splitting is a popular method to study anisotropy in the Earth (e.g., Silver, 1996; Savage, 1999; Long, 2013). From three-component waveforms of a single event recorded at a single station, we may obtain shear-wave splitting parameters (i.e., fast polarization direction and delay time) that reflect anisotropy over the corresponding ray path (Silver & Chan, 1991). Shear-wave splitting measurements made on waveforms of local S waves in NE Japan revealed anisotropic patterns that are comparable to seismic anisotropy tomography (e.g., Nakajima & Hasegawa, 2004; Huang et al., 2011a,b; Watanabe & Oda, 2014). The interpretation of shear-wave splitting is not unique because its vertical resolution is poor. One method

to overcome this drawback is to compare shear-wave splitting measurements of earthquakes at different depths (e.g., Huang et al., 2011a), so that anisotropy of the media between earthquake pairs may be estimated. However, such estimation is not straightforward in general because neither the fast direction nor the delay time is accumulated linearly. Only when the fast direction along a ray path is always parallel or perpendicular to each other, the delay time can accumulate over the ray path similar to traveltimes. With this assumption, Zhang et al. (2007) proposed a shear-wave splitting tomography method, which was then applied to estimate spatial distribution of crustal anisotropy in the San Andreas Fault near California and the North Anatolian Fault in western Turkey (Li et al., 2014).

Splitting intensity proposed for low-frequency shear-wave splitting (i.e., the period of a shear wave is much larger than the delay time) was adopted to conduct a general 3D tomographic inversion based on splitting parameters (Chevrot, 2000). The splitting intensity is a parameter that accumulates linearly over the whole ray path, like traveltimes (e.g., Silver & Long, 2011). It is therefore possible to invert for depth-dependent anisotropy, similar to traveltimes tomography (Chevrot, 2006). In addition, in order to increase the ray coverage, finite-frequency effect in the shear-wave splitting is usually considered. Southern California is so far the sole region where shear-wave splitting tomography has been conducted to reveal upper-mantle anisotropy, thanks to the dense broadband stations deployed there over past decades. Monteiller and Chevrot (2011) built a data set of ~3400 SKS splitting measurements at all the broadband stations. Resolution tests demonstrate that they could resolve anisotropic structures smaller than the size of the first Fresnel zone of SKS waves (~100 km). Lin et al. (2014) conducted an improved tomography by applying a full-wave approach to image the upper-mantle anisotropy in southern California using 5954 SKS splitting data (Figure 11.6). They adopted 3D sensitivity kernels combined with a wavelet-based model parameterization in a multiscale inversion. Spatial resolution lengths were estimated based on a statistical resolution matrix approach, showing a finest resolution length of ~25 km in regions with densely distributed stations. Their anisotropic model displays structural fabric in relation to surface geologic features such as the Salton Trough, the Transverse Ranges, and the San Andreas Fault. At long wavelengths, the fast directions of anisotropy are aligned with the absolute plate motion inside the Pacific and North American plates (Lin et al., 2014).

Alternatively, Eilon et al. (2016) proposed a method to invert differential traveltimes data and splitting data from teleseismic S arrivals for 3D velocity and anisotropy simultaneously. They found analytic solutions to the Christoffel equations in terms of fast and slow horizontal velocities by constructing a simple parametrization to describe an elastic tensor with hexagonal symmetry.

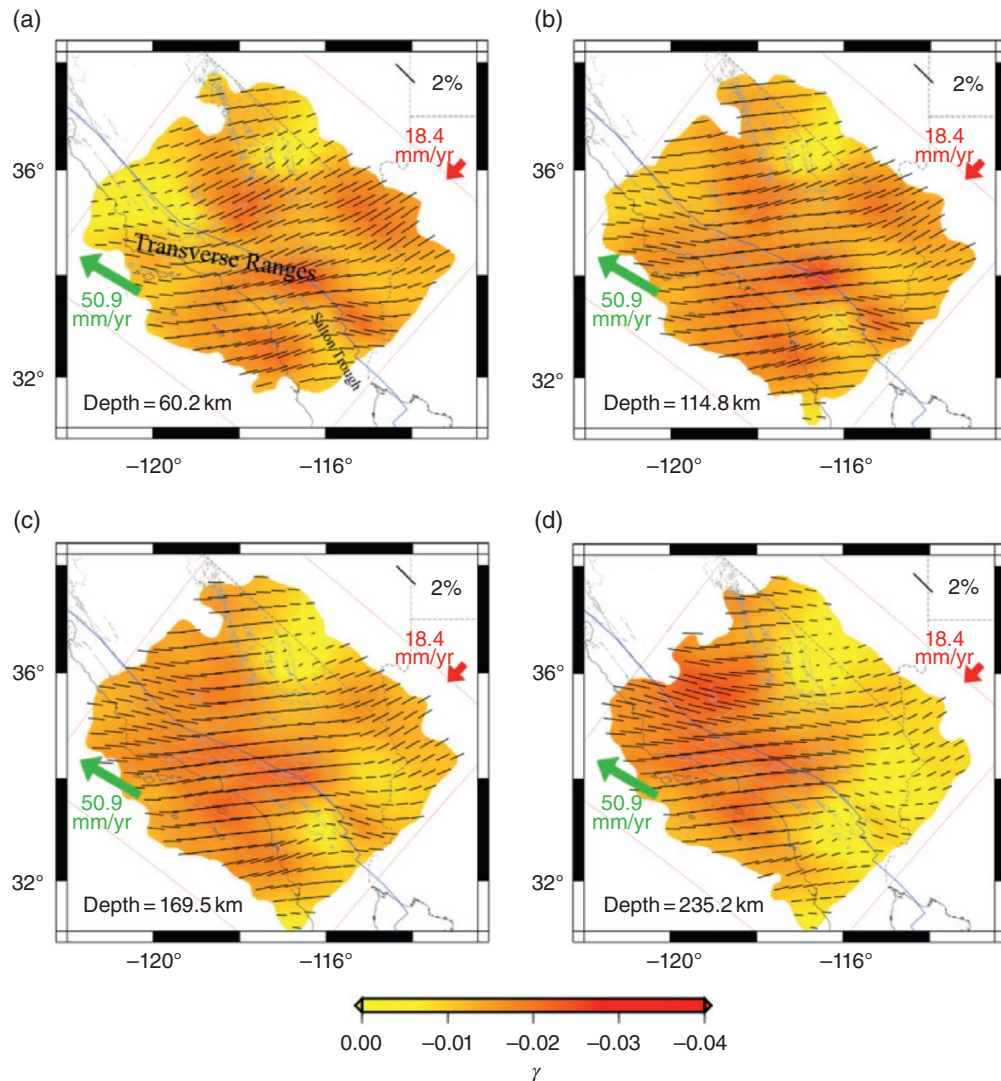


Figure 11.6 Three-dimensional anisotropy model for Southern California at depths of (a) 60.2 km, (b) 114.8 km, (c) 169.5 km, and (d) 235.2 km. The background colors indicate the strength of the shear wave anisotropy γ , whereas the black bars depict the directions of the fast axes at every two nodes, and their lengths are proportional to the anisotropy strength. The green and red arrows denote absolute plate motions of the Pacific and North America plates, respectively, with their lengths proportional to the rates of motion, which are calculated using the model NNR-MORVEL56 (Argus et al., 2011). The plate boundary and fault branches of the San Andreas Fault system are shown in the blue and gray lines, respectively. *Source:* (a–d) Lin et al., 2014.

Applying the method to young Woodlark Rift between the Australian and Pacific plates revealed a low- V rift axis with $<4\%$ spreading-parallel anisotropy at 50–100 km depths, suggesting that the technique could provide a constraint on the depth-extent of shallow anisotropy.

11.4.3. Anisotropic Tomography: What Can We Learn and Expect?

The advantage of seismic anisotropy tomography is its power to detect 3D anisotropies at different depths, which provide direct evidence for deformations in the crust and

upper mantle. In subduction zones, we are concerned about anisotropies in the crust of the overlying plate, the mantle wedge, and the subducting slab. Seismic anisotropy tomography provides unique constraints on the 3D P -wave anisotropies and deformations in these layers, rather than just qualitative estimates as shear-wave splitting analysis does. The S -wave anisotropy in the upper crust can be well determined from shear-wave splitting measurements of local crustal earthquakes (e.g., Huang et al., 2011a).

In the mantle wedge, seismic anisotropy tomography provides direct information on the mantle flow. Trench-normal anisotropy in the wedge is generally revealed in

most subduction zones (e.g., Wang & Zhao, 2008; Huang et al., 2011; Wei et al., 2015; Zhao et al., 2016; Liu & Zhao, 2017b). Furthermore, radial anisotropy tomography detected faster vertical velocity (than horizontal velocity) in the mantle wedge, which is direct evidence for mantle flow and upwelling (Wang & Zhao, 2013). An important observation of shear-wave splitting in subduction zones is the trench-parallel FPD in the forearc region (e.g., Long & Silver, 2008). Its popular explanation is that B-type olivine develops in the environment of low temperature, high stress, and high fluid content in the forearc (e.g., Zhang & Karato, 1995). This feature has been also revealed by anisotropic tomography, at least in part of the forearc mantle wedge beneath NE Japan (e.g., Huang et al., 2011; Liu & Zhao, 2016a, 2017a), suggesting that B-type olivine may exist in the forearc mantle wedge.

Another important information provided by seismic anisotropy tomography is the anisotropy and deformation along the subduction channel or megathrust zone (Liu & Zhao, 2017a; Huang et al., 2019). They are closely related to the interplate coupling at the slab interface that is generally represented as a thin layer. The studies of northeast Japan and northern Chile show different patterns of seismic anisotropy in areas of strong and weak interplate coupling. The FVDs are generally trench-parallel in areas where the subducting and overriding plates are strongly coupled, suggesting dominant horizontal compression along the slab interface when the two plates are locked. In contrast, the FVDs are parallel to the subduction direction when the two plates are decoupled, resulting from stable shear deformation along the slab interface. These results suggest that seismic anisotropy could provide essential constraints on the seismotectonics in the megathrust zone. In Taiwan, surface wave inversion revealed a thin layer of stable shear in the lower crust that could account for the deformation induced by the subduction of the Eurasian plate (T. Huang et al., 2015), which is similar to the feature in the subduction thrust zone.

Seismic anisotropy tomography also provides direct information on deformations within the subducting slabs. In northeast Japan, previous studies of focal mechanisms of intra-slab earthquakes have characterized the first-order deformations in the subducting Pacific slab (e.g., Hasegawa et al., 1978; Gamage et al., 2009). Under the outer-rise region to the east of the Japan Trench, the upper and middle parts of the Pacific plate are in E-W extension and compression, respectively. After the plate subduction, the stress regime has changed (i.e., the upper and middle parts of the slab are in E-W compression and extension, respectively). The FVDs of P -wave azimuthal anisotropy in the slab under northeast Japan could be explained by the mineral fabrics produced by the above-mentioned

stress regime (Liu & Zhao, 2017a). Similar results are also obtained in northern Chile (Huang et al., 2019).

However, P -wave anisotropic tomography requires crisscrossing subhorizontal ray paths to well constrain the azimuthal anisotropy, which may be achieved in the crust and uppermost mantle by a data set of local earthquakes in the crust and the subducting slab. In the depth range of 100–300 km, however, most ray paths have steep incidence angles, which may bring unexpected anomalies from radial anisotropy. In contrast, shear-wave splitting tomography could hardly reveal 3D anisotropy at depths of 0–100 km. Hence, a joint inversion of P - and S -wave traveltimes and shear-wave splitting measurements may result in a much-improved anisotropy model of the crust and upper mantle. Thus, a quantitative relationship between P - and S -wave anisotropies may be obtained, which is actually an unresolved issue at present. Such effort may provide important new insight into anisotropy in the lower part of the subducting slab and the mantle below the slab.

The studies of anisotropic tomography have generally assumed a horizontal or vertical symmetry axis, which accounts for azimuthal and radial anisotropies, respectively. However, the actual symmetry axis may be inclined, especially in some parts of subduction zones where dipping slabs exist. Munzarova et al. (2018a) developed a new code of anisotropic teleseismic V_p tomography. While the same weak hexagonal anisotropy is assumed as in V_p azimuthal and radial anisotropies as mentioned above, the symmetry axis is oriented in 3D in their approach, which could account for dipping anisotropy symmetry. They applied the method to teleseismic data recorded by a passive seismic experiment in northern Fennoscandia (Munzarova et al., 2018b), because the ray coverage seems good in 3D for a fully anisotropic inversion. But the study for inclined anisotropy using local earthquake data is still a difficult task, because the method requires more parameters to describe anisotropy. Therefore, much better ray coverage in a 3D volume is necessary, which may be achieved by joint use of the first and later phases (i.e., reflected and converted waves) of local shallow and deep earthquakes as well as teleseismic events recorded by a dense seismic network. Thus, a fully anisotropic inversion for inclined symmetry axis may be realized in a subduction zone in the near future.

11.5. CONCLUSIONS

Seismic anisotropy tomography has been successfully applied to several subduction zones to resolve 3D isotropic and anisotropic velocity structures simultaneously. The obtained results provide direct evidence for deformations in different domains of subduction zones, including

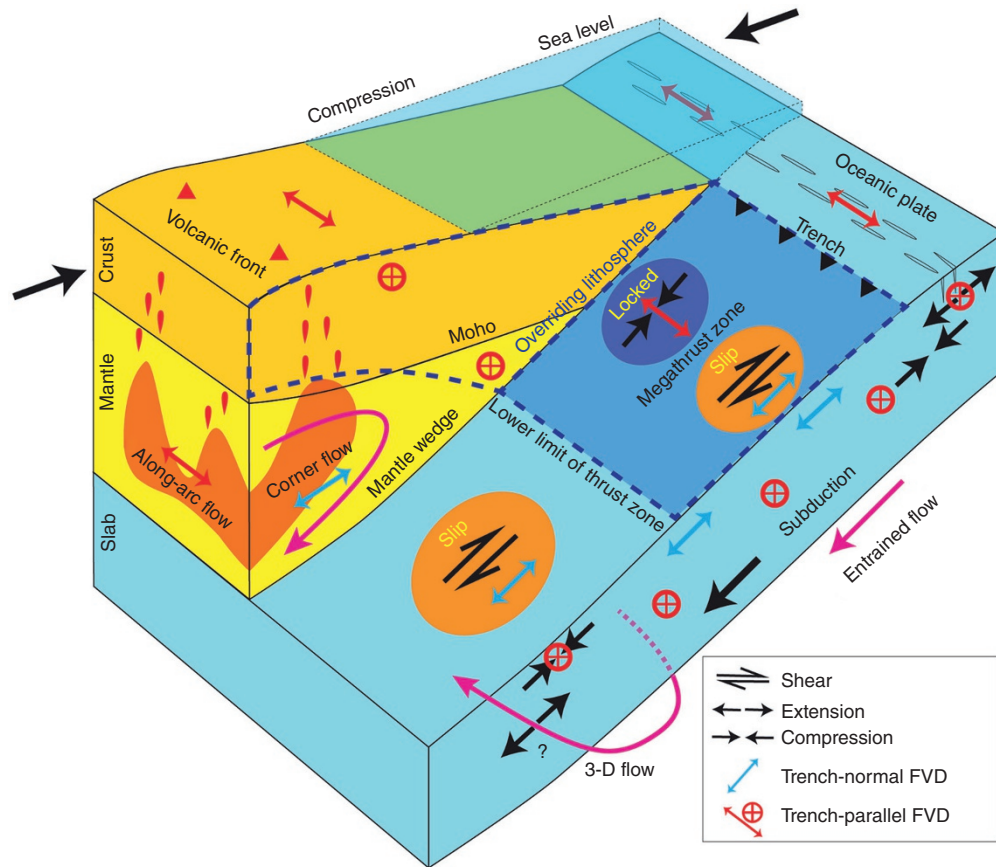


Figure 11.7 A sketch showing the deformation and anisotropy in subduction zones. Orange, yellow, and blue blocks denote the crust, mantle wedge, and a subducting slab, respectively. Dashed blue lines show the overriding lithosphere that includes the crust and part of the rigid upper mantle. Red colors in the mantle wedge indicate partial-melting materials. Magenta lines with arrow denote different types of mantle flow around the subducting slab.

the overriding lithosphere, the mantle wedge, the subducting slab, and the mantle below the slab (Figure 11.7). The crustal anisotropy may be attributed to the alignment or preferred orientations of micro-cracks (in the upper crust) and crustal minerals (in the lower crust), which may be strongly affected by local geological structures such as active faults, folds, and volcanoes.

Mantle wedge is an important part of subduction zones. To the first order, mantle-wedge convection is driven by the active subduction, generating trench-normal azimuthal anisotropy as well as faster vertical velocities in general. At the same time, strong along-arc variations of the slab geometry and other features may induce significant along-arc mantle flow, resulting in trench-parallel anisotropy.

The anisotropy in the subducting slab may arise from either fossil anisotropy or present deformations. In the top portion of the slab, the FVDs show systematic transition from trench-parallel in the out-rise to trench-normal

under the forearc, and back to trench-parallel under the volcanic front. In contrast, within the slab, the FVD is generally trench-parallel. These results suggest that the V_p anisotropy reflects present deformations rather than the frozen-in “fossil” anisotropy.

Under the forearc area, the anisotropy indicates complex deformations along the megathrust zone. In and around asperities for large earthquakes or areas where interplate coupling is very strong, the FVD is generally trench-parallel, which may reflect trench-parallel preferred fabrics under trench-normal compression during the interseismic period. However, in patches dominated by aseismic slip or weak interplate coupling, the FVDs are trench-normal, which may be produced by strong shear along the plate interface.

Anisotropy in the sub-slab mantle estimated from shear-wave splitting measurements is still ambiguous, because neither local nor teleseismic data set could provide proper constraints on the azimuthal anisotropy

beneath the slab. SKS splitting can sample the sub-slab region, but the interpretations are not unique. The V_p anisotropic results obtained to date revealed both trench-normal and trench-parallel anisotropies, which may reflect subduction-driven entrained flow and 3D mantle flow, respectively.

ACKNOWLEDGMENTS

We thank Prof. Maxim D. Ballmer for inviting us to contribute this chapter to the AGU monograph. Profs. H. Marquardt, S. Cottaar, and two anonymous reviewers provided constructive comments that have improved the manuscript. We are grateful to many coworkers for their effective collaborations with us on seismic anisotropy tomography, in particular, Drs. Jian Wang, You Tian, Wei Wei, Xin Liu, Xiongwei Niu, Youqiang Yu, Jianke Fan, Yuanyuan Hua, and Tao Gou. This work was partially supported by research grants from the National Natural Science Foundation of China (41674044) to Z. Huang and those from Japan Society for the Promotion of Science (19H01996) and Ministry of Education, Culture, Sports, Science and Technology (26106005) to D. Zhao.

REFERENCES

- Aitchison, J. C., Ali, J. R., & Davis, A. M. (2007). When and where did India and Asia collide? *Journal of Geophysical Research*, *112*, B05423.
- Aki, K., Christofferson, A., & Husebye, E. (1977). Determination of the three-dimensional seismic structure of the lithosphere. *Journal of Geophysical Research*, *82*, 277–296
- Argus, D. F., Gordon, R. G., & DeMets, C. (2011). Geologically current motion of 56 plates relative to the no-net-rotation reference frame. *Geochemistry, Geophysics, Geosystems*, *12*, Q11001.
- Backus, G.E. (1965). Possible forms of seismic anisotropy of the uppermost mantle under oceans. *Journal of Geophysical Research*, *70*, 3429–3439.
- Becker, T. (2012). On recent seismic tomography for the western United States. *Geochemistry, Geophysics, Geosystems*, *13*, Q01W10.
- Becker, T.W., Chevrot, S., Schulte-Pelkum, V., & Blackman, D. K. (2006). Statistical properties of seismic anisotropy predicted by upper mantle geodynamic models. *Journal of Geophysical Research*, *111*, 12253.
- Becker, T.W., & Lebedev, S. (2019). Dynamics of the lithosphere and upper mantle in light of seismic anisotropy. Chapter 10 of this book.
- Bird, P. (2003). An updated digital model of plate boundaries. *Geochemistry, Geophysics, Geosystems*, *4* (3), 1027.
- Browaeys, J.T., & Chevrot, S. (2004). Decomposition of the elastic tensor and geophysical applications. *Geophysical Journal International*, *159*, 667–678.
- Castellarin, A., & Cantelli, L. (2000). Neo-Alpine evolution of the Southern Eastern Alps. *Journal of Geodynamics*, *30* (1–2), 251–274.
- Chen, C., Zhao, D., & Wu, S. (2014). Crust and upper mantle structure of New Madrid Seismic Zone: Insight into intraplate earthquakes. *Physics of the Earth and Planetary Interiors*, *230*, 1–14.
- Chen, C., Zhao, D., & Wu, S. (2015). Tomographic imaging of the Cascadia subduction zone: Constraints on the Juan de Fuca slab. *Tectonophysics*, *647*, 73–88.
- Chen, K.-X., Gung, Y., Kuo, B.-Y., & Huang, T.-Y. (2018). Crustal magmatism and deformation fabrics in northeast Japan revealed by ambient noise tomography. *Journal of Geophysical Research: Solid Earth*, *123*. <https://doi.org/10.1029/2017JB015209>
- Chevrot, S. (2000). Multichannel analysis of shear wave splitting. *Journal of Geophysical Research*, *105*, 21579–21590.
- Chevrot, S. (2006). Finite-frequency vectorial tomography: a new method for high-resolution imaging of upper mantle anisotropy. *Geophysical Journal International*, *165*, 641–657.
- Christensen, N.I. (1984). The magnitude, symmetry and origin of upper mantle anisotropy based on fabric analyses of ultramafic tectonites. *Geophysical Journal of the Royal Astronomical Society*, *76*, 89–111.
- Coffin, M.F., Gahagan, L.M., & Lawver, L.A. (1998). *Present-day Plate Boundary Digital Data Compilation*. University of Texas Institute for Geophysics Technical Report, No. 174, pp. 5.
- Crampin, S. (1984). Effective anisotropic constants for wave-propagation through cracked solids. *Geophysical Journal of the Royal Astronomical Society*, *76*, 135–145.
- Eberhart-Phillips, D., & Henderson, C. M. (2004). Including anisotropy in 3D velocity inversion and application to Marlborough, New Zealand. *Geophysical Journal International*, *156* (2), 237–254.
- Eberhart-Phillips, D., & Reyners, M. (2009). Three-dimensional distribution of seismic anisotropy in the Hikurangi subduction zone beneath the central North Island, New Zealand. *Journal of Geophysical Research*, *114*, B06301.
- Eberhart-Phillips, D., Reyners, M., Faccenda, M., & Naliboff, J. (2013). Along-strike variation in subducting plate seismicity and mantle wedge attenuation related to fluid release beneath the North Island, New Zealand. *Physics of the Earth and Planetary Interiors*, *225*, 12–27.
- Eilon, Z., Abers, G. A., & Gaherty, J. B. (2016). A joint inversion for shear velocity and anisotropy: the Woodlark Rift, Papua New Guinea. *Geophysical Journal International*, *206*, 807–824.
- Engdahl, E.R., & Lee, W.H.K. (1976). Relocation of local earthquakes by seismic ray tracing. *Journal of Geophysical Research*, *81*, 4400–4406.
- Faccenda, M., L. Burlini, T. Gerya, and D. Mainprince (2008). Fault-induced seismic anisotropy by hydration in subducting oceanic plates. *Nature*, *455*, 1097–1101.
- Fichtner, A., Kennett, B., Igel, H., & Bunge, H. (2010). Full waveform tomography for radially anisotropic structure: new insights into present and past states of the Australasian upper mantle. *Earth and Planetary Science Letters*, *290*, 270–280.

- Fouch, M., & Rondenay, S. (2006). Seismic anisotropy beneath stable continental interiors. *Physics of the Earth and Planetary Interiors*, 158, 292–320.
- Garage, S., Umino, N., Hasegawa, A., Kirby, S. (2009). Off-shore double-planed shallow seismic zone in the NE Japan forearc region revealed by sP depth phases recorded by regional networks. *Geophysical Journal International*, 178, 195–214.
- Gou, T., Zhao, D., Huang, Z., & Wang, L. (2019). Aseismic deep slab and mantle flow beneath Alaska: Insight from anisotropic tomography. *Journal of Geophysical Research*, 124, 1700–1724.
- Gripp, A., & Gordon, R. (2002). Young tracks of hotspots and current plate velocities. *Geophysical Journal International*, 150, 321–361.
- Handy, M. R., Schmid, S. M., Bousquet, R., Kissling, E., & Bernoulli, D. (2010). Reconciling plate-tectonic reconstructions of Alpine Tethys with the geological–geophysical record of spreading and subduction in the Alps. *Earth-Science Reviews*, 102 (3–4), 121–158.
- Hasegawa, A., Umino, N. & Takagi, A. (1978). Double-planed deep seismic zone and upper-mantle structure in the north-eastern Japan arc, *Geophysical Journal of the Royal Astronomical Society*, 54, 281–296.
- Hasemi, A., Ishii, H., & Takagi, A. (1984). Fine structure beneath the Tohoku District, northeastern Japan arc, as derived by an inversion of *P*-wave arrival times from local earth- quakes. *Tectonophysics*, 101, 245–265.
- Hearn, T. (1996). Anisotropic Pn tomography in the western United States. *Journal of Geophysical Research*, 101, 8403–8414.
- Hess, H. (1964). Seismic anisotropy of uppermost mantle under oceans. *Nature*, 203, 629–631.
- Hirahara, K. (1977). A large-scale three-dimensional seismic structure under the Japan Islands and the Sea of Japan. *Journal of Physics of the Earth*, 25, 393–417.
- Hua, Y., Zhao, D., & Xu, Y. (2017). P wave anisotropic tomography of the Alps. *Journal of Geophysical Research*, 122, 4509–4528.
- Huang, T.Y., Gung, Y., Kuo, B.Y., Chiao, L.Y., & Chen, Y.N. (2015). Layered deformation in the Taiwan orogen. *Science*, 349, 720–723.
- Huang, Z., & Zhao, D. (2013a). Mechanism of the 2011 Tohoku-oki earthquake (Mw 9.0) and tsunami: Insight from seismic tomography. *Journal of Asian Earth Sciences* 70, 160–168.
- Huang, Z., & Zhao, D. (2013b). Mapping *P*-wave azimuthal anisotropy in the crust and upper mantle beneath the United States. *Physics of the Earth and Planetary Interiors*, 225, 28–40.
- Huang, Z., Zhao, D., & Wang, L. (2011a). Shear-wave anisotropy in the crust, mantle wedge and the subducting Pacific slab under Northeast Japan. *Geochemistry, Geophysics, Geosystems*, 12, Q01002.
- Huang, Z., Zhao, D., & Wang, L. (2011b). Frequency-dependent shear-wave splitting and multilayer anisotropy in Northeast Japan. *Geophysical Research Letters*, 38, L08302.
- Huang, Z., Zhao, D., & Wang, L. (2011c). Seismic heterogeneity and anisotropy of the Honshu arc from the Japan Trench to the Japan Sea. *Geophysical Journal International*, 184, 1428–1444.
- Huang, Z., Wang, P., Xu, M., Wang, L., Ding, Z., Wu, Y., et al. (2015a). Mantle structure and dynamics beneath SE Tibet revealed by new seismic images. *Earth and Planetary Science Letters*, 411, 100–111.
- Huang, Z., Zhao, D., & Liu, X. (2015b). On the trade-off between seismic anisotropy and heterogeneity: Numerical simulations and application to Northeast Japan. *Journal of Geophysical Research*, 120, 3255–3277.
- Huang, Z., Zhao, D., & Wang, L. (2015c). P wave tomography and anisotropy beneath Southeast Asia: Insight into mantle dynamics. *Journal of Geophysical Research*, 120, 5154–5174.
- Huang, Z., Tilmann, F., Comte, D., & Zhao, D. (2019). P wave azimuthal anisotropic tomography in northern Chile: Insight into deformation in the subduction zone. *Journal of Geophysical Research*, 124, 742–765.
- Ishise, M., & Oda, H. (2005). Three-dimensional structure of *P*-wave anisotropy beneath the Tohoku district, northeast Japan. *Journal of Geophysical Research*, 110, B07304.
- Ishise, M., & Oda, H. (2008). Subduction of the Philippine Sea slab in view of *P*-wave anisotropy. *Physics of the Earth and Planetary Interiors*, 166, 83–96.
- Ishise, M., Kawakatsu, H., Morishige, M., & Shiomi, K. (2018). Radial and azimuthal anisotropy tomography of the NE Japan subduction zone: Implications for the Pacific slab and mantle wedge dynamics. *Geophysical Research Letters*, 45, 3923–3931.
- Karato, S., Jung, H., Katayama, I., & Skemer, P. (2008). Geodynamic significance of seismic anisotropy of the upper mantle: new insights from laboratory studies. *Annual Review of Earth and Planetary Sciences*, 36, 59–95.
- Katayama, I. (2009). Thin anisotropic layer in the mantle wedge beneath northeast Japan. *Geology*, 27, 211–214.
- Koulakov, I., Jakovlev, A., Wu, Y.-M., Dobretsov, N.L., Khrepy, El, S., & Al-Arifi, N. (2015a). Three-dimensional seismic anisotropy in the crust and uppermost mantle beneath the Taiwan area revealed by passive source tomography. *Journal of Geophysical Research*, 120, 7814–7829.
- Koulakov, I., Kukarina, E., Fathi, I., Khrepy, S., & Al-Arifi, N. (2015b). Anisotropic tomography of Hokkaido reveals delamination-induced flow above a subducting slab. *Journal of Geophysical Research*, 120, 3219–3239.
- Koulakov, I., Kaban, M. K., Tesauero, M., & Cloetingh, S. (2009). *P*- and *S*-velocity anomalies in the upper mantle beneath Europe from tomographic inversion of ISC data. *Geophysical Journal International*, 179 (1), 345–366.
- Lallemand, S., Font, Y., Bijwaard, H., & Kao, H. (2001). New insights on 3D plates interaction near Taiwan from tomography and tectonic implications. *Tectonophysics*, 335, 229–253.
- Li, S., Moreno, M., Bedford, J., Rosenau, M., & Oncken, O. (2015). Revisiting viscoelastic effects on interseismic deformation and locking degree: A case study of the Peru-North Chile subduction zone. *Journal of Geophysical Research*, 120 (6), 4522–4538.

- Li, Z., Zhang, H., & Peng, Z. (2014). Structure-controlled seismic anisotropy along the Karadere–Düzce branch of the North Anatolian Fault revealed by shear-wave splitting tomography. *Earth and Planetary Science Letters*, *391*, 319–326.
- Lin, F., Ritzwoller, M., Yang, Y., Moschetti, M., & Fouch, M. (2011). Complex and variable crustal and uppermost mantle seismic anisotropy in the western United States. *Nature Geosciences*, *4*, 55–61.
- Lin, Y.-P., Zhao, L., & Hung, S.-H. (2014). Full-wave multiscale anisotropy tomography in Southern California. *Geophysical Research Letters*, *41*, 8809–8817.
- Liu, M., Cui, X., & Liu, F. (2004). Cenozoic rifting and volcanism in eastern China: A mantle dynamic link to the Indo-Asian collision? *Tectonophysics*, *393*, 29–42.
- Liu, X., & Zhao, D. (2016a). Seismic velocity azimuthal anisotropy of the Japan subduction zone: Constraints from P and S wave traveltimes. *Journal of Geophysical Research*, *121*, 5086–5115.
- Liu, X., & Zhao, D. (2016b). P and S wave tomography of Japan subduction zone from joint inversions of local and teleseismic travel times and surface-wave data. *Physics of the Earth and Planetary Interiors*, *252*, 1–22.
- Liu, X., & Zhao, D. (2016c). Backarc spreading and mantle wedge flow beneath the Japan Sea: Insight from Rayleigh-wave anisotropic tomography. *Geophysical Journal International*, *207*, 357–373.
- Liu, X., & Zhao, D. (2017a). Depth-varying azimuthal anisotropy in the Tohoku subduction channel. *Earth and Planetary Science Letters*, *473*, 33–43.
- Liu, X., & Zhao, D. (2017b). P-wave anisotropy, mantle-wedge flow and olivine fabrics beneath Japan. *Geophysical Journal International*, *210*, 1410–1431.
- Liu, X., & Zhao, D. (2018). Upper and lower plate controls on the great 2011 Tohoku-oki earthquake. *Science Advances*, *4*, eaat4396.
- Liu, X., Zhao, D., & Li, S. (2013). Seismic heterogeneity and anisotropy of the southern Kuril arc: Insight into megathrust earthquakes. *Geophysical Journal International*, *194*, 1069–1090.
- Liu, X., Zhao, D., & Li, S. (2014). Seismic attenuation tomography of the Northeast Japan arc: Insight into the 2011 Tohoku earthquake (Mw 9.0) and subduction dynamics. *Journal of Geophysical Research*, *119*, 1094–1118.
- Long, M.D., & Silver, P.G. (2008). The subduction zone flow field from seismic anisotropy: A global view. *Science*, *319*, 315–318.
- Long, M. (2013). Constraints on subduction geodynamics from seismic anisotropy. *Reviews of Geophysics*, *51*, 76–112.
- Maupin, V., & Park, J. (2007). Theory and observations – wave propagation in anisotropic media. In: Schubert, G. (Ed.), *Treatise on Geophysics*. Elsevier, Netherlands, pp. 289–321.
- Mishra, O.P., Zhao, D., Umino, N., & Hasegawa, A. (2003). Tomography of northeast Japan forearc and its implications for interplate seismic coupling. *Geophysical Research Letters*, *30*, GL017736.
- Montagner, J. (2011). Earth's structure: Global. In: Gupta, H. (Ed.), *Encyclopedia of Solid Earth Geophysics*. Springer, Netherlands, pp. 144–154.
- Montagner, J., & Tanimoto, T. (1991). Global upper mantle tomography of seismic velocities and anisotropies. *Journal of Geophysical Research*, *96*, 20337–20351.
- Munzarova, H., Plomerova, J., & Kissling, E. (2018a). Novel anisotropic teleseismic body-wave tomography code Ani-Tomo to illuminate heterogeneous anisotropic upper mantle: Part I – Theory and inversion tuning with realistic synthetic data. *Geophysical Journal International*, *215*, 524–545.
- Munzarová, H., Plomerová, J., Kissling, E., Vecsey, L., & Babuška, V. (2018b). Novel anisotropic teleseismic body-wave tomography code AniTomo to illuminate heterogeneous anisotropic upper mantle: Part II – Application to data of passive seismic experiment LAPNET in northern Fennoscandia. *Geophysical Journal International*, *215* (2), 1388–1409.
- Nakajima, J., & Hasegawa, A. (2004). Shear-wave polarization anisotropy and subduction-induced flow in the mantle wedge of northeastern Japan. *Earth and Planetary Science Letters*, *225*, 365–377.
- Nettles, M., & Dziewonski, A. (2008). Radially anisotropic shear velocity structure of the upper mantle globally and beneath North America. *Journal of Geophysical Research*, *113*, B02303.
- Niu, X., Zhao, D., Li, J., & Ruan, A. (2016). P wave azimuthal and radial anisotropy of the Hokkaido subduction zone. *Journal of Geophysical Research*, *121*, 2636–2660.
- Park, J., & Yu, Y. (1993). Seismic determination of elastic anisotropy and mantle flow. *Science*, *261*, 1159–1162.
- Qi, C., Zhao, D., & Chen, Y. (2007). Search for deep slab segments under Alaska. *Physics of the Earth and Planetary Interiors*, *165*, 68–82.
- Qorbani, E., Bianchi, I., & Bokelmann, G. (2015). Slab detachment under the Eastern Alps seen by seismic anisotropy. *Earth and Planetary Science Letters*, *409*, 96–108.
- Raitt, R., Shor, G., Francis, T., & Morris, G. (1969). Anisotropy of Pacific upper mantle. *Journal of Geophysical Research*, *74*, 3095–3109.
- Reyners, M. (2013). The central role of the Hikurangi Plateau in the Cenozoic tectonics of New Zealand and the Southwest Pacific. *Earth and Planetary Science Letters*, *361*, 460–468.
- Savage, M.K. (1999). Seismic anisotropy and mantle deformation: what have we learned from shear wave splitting? *Reviews of Geophysics*, *37*, 65–106.
- Sibuet, J., & Hsu, S. (2004). How was Taiwan created? *Tectonophysics*, *379*, 159–181.
- Silver, P.G. (1996). Seismic anisotropy beneath the continents: Probing the depths of geology. *Annual Review of Earth and Planetary Sciences*, *24*, 385–432.
- Silver, P.G., & Chan, W.W. (1991). Shear wave splitting and subcontinental mantle deformation. *Journal of Geophysical Research*, *96*, 16429–16454.
- Silver, P.G., & Long, M.D. (2011). The non-commutivity of shear wave splitting operators at low frequencies and implications for anisotropy tomography. *Geophysical Journal International*, *184*, 1415–1427.
- Stern, R. (2002). Subduction zones. *Reviews of Geophysics*, *40*, RG000108.

- Tanimoto, T., & Anderson, D. (1984). Mapping convection in the mantle. *Geophysical Research Letters*, *11*, 327–336.
- Tapponnier, P., Peltzer, G., Le Dain, A. Y., Armijo, R., Jussieu, P., & Cobbold, P. (1982). Propagating extrusion tectonics in Asia: New insights from simple experiments with plasticine. *Geology*, *10*, 611–616.
- Tapponnier, P., Xu, Z., Roger, F., Meyer, B., Arnaud, N., Wittlinger, G., et al. (2001). Oblique stepwise rise and growth of the Tibet plateau. *Science*, *294*, 1671–1677.
- Teng, L., Lee, C., Tsai, Y., & Hsiao, L. (2000). Slab break-off as a mechanism for flipping of subduction polarity in Taiwan. *Geology*, *28*, 155–158.
- Thurber, C. (1983). Earthquake locations and three-dimensional crustal structure in the Coyote Lake area, central California. *Journal of Geophysical Research*, *88*, 8226–8236.
- Tian, Y., & Zhao, D. (2012a). *P*-wave tomography of the Western United States: Insight into the Yellowstone hotspot and the Juan de Fuca slab. *Physics of the Earth and Planetary Interiors*, *200*, 72–84.
- Tian, Y., & Zhao, D. (2012b). Seismic anisotropy and heterogeneity in the Alaska subduction zone. *Geophysical Journal International*, *190*, 629–649.
- Tsumura, N., Matsumoto, S., Horiuchi, S., & Hasegawa, A. (2000). Three-dimensional attenuation structure beneath the northeastern Japan arc estimated from spectra of small earthquakes. *Tectonophysics*, *319*, 241–260.
- Umino, N., & Hasegawa, A. (1984). Three-dimensional *Q_s* structure in the northeastern Japan arc. *Journal of Seismological Society of Japan*, *37*, 217–228.
- Umino, N., Hasegawa, A., & Matsuzawa, T. (1995). *sP* depth phase at small epicentral distances and estimated subducting plate boundary. *Geophysical Journal International*, *120*, 356–366.
- Wang, J., & Zhao, D. (2008). *P*-wave anisotropic tomography beneath Northeast Japan. *Physics of the Earth and Planetary Interiors*, *170*, 115–133.
- Wang, J., & Zhao, D. (2009). *P*-wave anisotropic tomography of the crust and upper mantle under Hokkaido, Japan. *Tectonophysics*, *469*, 137–149.
- Wang, J., & Zhao, D. (2010). Mapping *P*-wave anisotropy of the Honshu arc from Japan Trench to the backarc. *Journal of Asian Earth Sciences*, *39*, 396–407.
- Wang, J., & Zhao, D. (2012). *P* wave anisotropic tomography of the Nankai subduction zone in Southwest Japan. *Geochemistry, Geophysics, Geosystems*, *13*, Q05017.
- Wang, J., & Zhao, D. (2013). *P*-wave tomography for 3D radial and azimuthal anisotropy of Tohoku and Kyushu subduction zones. *Geophysical Journal International*, *193*, 1166–1181.
- Wang, X., Zhao, D., & Li, J. (2006). The 2013 Wyoming upper-mantle earthquakes: tomography and tectonic implications. *Journal of Geophysical Research*, *121*, 6797–6808.
- Wang, Y., & Tape, C. (2014). Seismic velocity structure and anisotropy of the Alaska subduction zone based on surface wave tomography. *Journal of Geophysical Research*, *119*, 8845–8865.
- Wang, Z., Zhao, D., Wang, J., & Kao, H. (2006). Tomographic evidence for the Eurasian lithosphere subducting beneath south Taiwan. *Geophysical Research Letters*, *33*, L18306.
- Watanabe, M., & Oda, H. (2014). Regional variations of the shear-wave polarization anisotropy in the crust and mantle wedge beneath the Tohoku district. *Physics of the Earth and Planetary Interiors*, *235*, 49–65.
- Wei, W., Zhao, D., Xu, J., Wei, F., & Liu, G. (2015). *P* and *S* wave tomography and anisotropy in Northwest Pacific and East Asia: Constraints on stagnant slab and intraplate volcanism. *Journal of Geophysical Research*, *120*, 1642–1666.
- Wei, W., Zhao, D., Xu, J., Zhou, B., & Shi, Y. (2016). Depth variations of *P*-wave azimuthal anisotropy beneath Mainland China. *Scientific Reports*, *6*, 29614, doi:10.1038/srep29614.
- Xia, S., Zhao, D., Sun, J., & Huang, H. (2016). Teleseismic imaging of the mantle beneath southernmost China: New insights into the Hainan plume. *Gondwana Research*, *36*, 33–43.
- Yu, Y., & Zhao, D. (2018). Lithospheric deformation and asthenospheric flow associated with the Isabella anomaly in Southern California. *Journal of Geophysical Research*, *123*, 8842–8857.
- Yuan, H., Romanowicz, B., Fischer, K., & Abt, D. (2011). 3D shear wave radially and azimuthally anisotropic velocity model of the North American upper mantle. *Geophysical Journal International*, *184*, 1237–1260.
- Zhang, H.J., Liu, Y., Thurber, C., & Roecker, S. (2007). Three-dimensional shear-wave splitting tomography in the Parkfield, California, region. *Geophysical Research Letters*, *34*, L24308.
- Zhang, S., & S. Karato (1995). Lattice preferred orientation of olivine aggregates deformed in simple shear, *Nature*, *375*, 774–777.
- Zhao, D. (2012). Tomography and dynamics of Western-Pacific subduction zones. *Monographs on Environment, Earth and Planets*, *1*, 1–70.
- Zhao, D. (2015). *Multiscale Seismic Tomography*. Springer, Tokyo, pp. 304.
- Zhao, D., Hasegawa, A., & Horiuchi, S. (1992). Tomographic imaging of *P* and *S* wave velocity structure beneath northeastern Japan. *Journal of Geophysical Research*, *97*, 19909–19928.
- Zhao, D., Hasegawa, A., & Kanamori, H. (1994). Deep structure of Japan subduction zone as derived from local, regional, and teleseismic events. *Journal of Geophysical Research*, *99*, 22313–22329.
- Zhao, D., Christensen, D., & Pulpan, H. (1995). Tomographic imaging of the Alaska subduction zone. *Journal of Geophysical Research*, *100*, 6487–6504.
- Zhao, D., Mishra, O.P., & Sanda, R. (2002). Influence of fluids and magma on earthquakes: seismological evidence. *Physics of the Earth and Planetary Interiors*, *132*, 249–267.
- Zhao, D., Huang, Z., Umino, N., Hasegawa, A., & Kanamori, H. (2011). Structural heterogeneity in the megathrust zone and mechanism of the 2011 Tohoku-oki earthquake (Mw 9.0). *Geophysical Research Letters*, *38*, L17308.
- Zhao, D., Yu, S., & Liu, X. (2016). Seismic anisotropy tomography: New insight into subduction dynamics. *Gondwana Research*, *33*, 24–43.
- Zhou, H. (1996). A high-resolution *P*-wave model for the top 1200 km of the mantle. *Journal of Geophysical Research*, *101*, 27791–27810.

12

The Cycling of Subducted Oceanic Crust in the Earth's Deep Mantle

Mingming Li

ABSTRACT

The oceanic crust is created at mid-ocean ridges and returned to the Earth's deep mantle at subduction zones. A clear picture on the dynamics and distribution of the subducted oceanic crust in the deep mantle is crucial for understanding the nature of compositional heterogeneities and the chemical evolution of the deep Earth. This chapter reviews observational constraints, mineral physics experiments, and geodynamic studies on the distribution, physical properties, and dynamics of the subducted oceanic crust in the deep mantle. It has been found that the subducted oceanic crust may exhibit a variety of behaviors when interacting with the surrounding mantle, depending on the volume, density, and viscosity of the subducted crustal materials and the surrounding mantle dynamics. The subducted oceanic crust may sink directly to the lowermost mantle, or pond at the base of the mantle transition zone with some part episodically sinking to the bottom of the mantle. The subducted oceanic crust in the lowermost mantle may either be directly carried up to shallower depths by entrainment, or accumulate on the core–mantle boundary with some part entrained into, and carried upward by, mantle plumes. The entrained oceanic crust may be directly carried to the base of the lithosphere, pond at a variety of mantle depths, or sink downward due to its negative buoyancy, and it is eventually mixed into the background mantle. The cycling of subducted oceanic crust throughout the deep mantle provides an understanding on the geochemical complexities in volcanic rocks and the seismic anomalies in the deep mantle.

12.1. INTRODUCTION

The Earth's deep mantle contains compositional heterogeneities ranging from mineral to lithological (or even larger) scale (Stixrude & Lithgow-Bertelloni, 2012). One of the major sources of the compositional heterogeneities is from subducted oceanic crust (e.g., Tackley, 2007). The oceanic crust is produced at mid-ocean ridges through decompression partial melting, and is primarily made of mafic rocks. Over time, the oceanic crust is covered by

a thin (~500 meters on average) layer of sediments which, in this chapter, is not considered as part of the oceanic crust. The oceanic crust is later subducted to the deep mantle at subduction zones, and some amount of the previously subducted oceanic crust can be recycled back to the uppermost mantle by mantle convection.

The cycling of subducted oceanic crust through the deep mantle significantly affects the structure, dynamics and evolution of the deep Earth. Seismic heterogeneities of the deep mantle and geochemical complexities found in volcanic lavas are often interpreted as caused by the presence of subducted oceanic crust in the deep mantle (e.g., Hofmann & White, 1982; Christensen & Hofmann,

School of Earth and Space Exploration, Arizona State University, Tempe, AZ, USA

Mantle Convection and Surface Expressions, Geophysical Monograph 263, First Edition.
Edited by Hauke Marquardt, Maxim Ballmer, Sanne Cottaar, and Jasper Konter.
© 2021 American Geophysical Union. Published 2021 by John Wiley & Sons, Inc.
DOI: 10.1002/9781119528609.ch12

1994; Tolstikhin & Hofmann, 2005). The oceanic crust is more oxidized than mantle rocks (e.g., McCammon, 2005; Frost & McCammon, 2008), and as a result, the subducted oceanic crust may significantly affect the oxidation state of the deep mantle (e.g., Lécuyer & Ricard, 1999) which is crucial for the near-surface partial melting and degassing processes that regulate the atmosphere composition (Ballhaus et al., 1990; Kasting et al., 1993; Kump et al., 2001). The subducted oceanic crust has also been suggested to be an important water carrier in the lower mantle due to its high concentration of hydrous Aluminum-rich phase D (Pamato et al., 2014).

Depending on its intrinsic density and viscosity anomaly compared to the surrounding mantle (e.g., Ringwood & Irifune, 1988; Irifune & Ringwood, 1993; Karato et al., 1995; Hirose et al., 1999), the subducted oceanic crust may either accelerate or hinder the sinking of cold slabs to the deep mantle (e.g., Christensen, 1997; van Hunen & van den Berg, 2008). The entrainment of oceanic crust into mantle plumes has been found to strongly affect plume dynamics (e.g., Farnetani & Samuel, 2005; Kumagai et al., 2008; Dannberg & Sobolev, 2015), which in turn, significantly influences the surface topography and melt production caused by mantle plumes (e.g., Sobolev et al., 2011b). The accumulation of subducted oceanic crust on the core–mantle boundary (CMB) may insulate the core and reduce the CMB heat flux, therefore significantly influence the thermal evolution of the Earth (e.g., Nakagawa & Tackley, 2004; Li & McNamara, 2018).

This chapter aims to give a historical review of studies concerning the dynamics and the evolving distribution of subducted oceanic crust in the deep mantle, with focuses on understanding (1) the ability of subducted oceanic crust to sink to the lower mantle, and to accumulate on the CMB, (2) the process of entraining subducted oceanic crust to shallow depths and how it affects plume dynamics, and (3) how the cycling of subducted oceanic crust is related to the complexities of geochemical and seismic observations.

12.2. OBSERVATIONAL CONSTRAINTS ON THE DISTRIBUTION OF OCEANIC CRUST IN THE DEEP MANTLE

12.2.1. Geochemical Observations

While mid-ocean ridge basalts (MORBs) are caused by decompression partial melting at spreading centers, the ocean island basalts (OIBs) are generally accepted to be caused by hot, upwelling mantle plumes that are often away from plate boundaries. Compared to the geochemistry of MORBs, the OIBs are often more enriched and exhibit larger variation in isotope ratios (e.g., Hofmann & White, 1982; Hofmann, 1997; White, 2015a). Studies have

revealed that the OIB sources consist of a mixture of multiple compositional components, including the recycled oceanic crust (e.g., Hofmann & White, 1982; Zindler & Hart, 1986; Hofmann, 1988; Hauri & Hart, 1993; Reisberg et al., 1993; Hofmann, 1997; Schersten et al., 2004; Tackley, 2007; Li et al., 2014a; Shorttle et al., 2015; White, 2015b; Pringle et al., 2016). The fraction of the recycled oceanic crust in the OIB sources has been estimated, through isotopic analysis and petrological modeling, to be in a wide range, varying from 0% to ~30% (Sobolev et al., 2007; Sobolev et al., 2011b; Pietruszka et al., 2013; Brown & Lesher, 2014; Delavault et al., 2015).

It has also been found that the OIB sources contain subducted oceanic crust with vastly different ages. While subducted oceanic crust as young as 200–650 Myr has been reported in the melting sources of the Hawaiian lavas (Sobolev et al., 2011a) and the Hainan plume basalts (Wang et al., 2013), Delavault et al. (2015) suggested that there is ~1.5 Ga old subducted oceanic crust in the Gambier plume source beneath Polynesia, and Cabral et al. (2013) estimated that the subducted oceanic crust in the source of the Mangaia lavas is older than 2.45 Ga.

12.2.2. Seismic Observations

Seismic heterogeneities have been detected throughout the Earth's deep mantle. Analyses of *P*-to-*S* receiver functions have shown widespread negative seismic discontinuities within and at the base of the mantle transition zone, which are often interpreted as subducted oceanic crust (Shen & Blum, 2003; Shen et al., 2008; Eagar et al., 2010; Tauzin et al., 2013; Shen et al., 2014; Gréaux et al., 2019; Wang et al., 2019). Through the incorporation of mineral physics models, (Khan et al., 2009) performed seismic inversion on surface wave data at 12 selected locations distributed across the globe to predict the concentration of subducted oceanic crust at depth ranges of 0–1200 km, and (Cammarano et al., 2009) conducted seismic inversion on a 1D average of tomography model for the concentration of subducted oceanic crust at 250–800 km depth. Both studies showed that the crustal concentration changes with depth. Specifically, Khan et al. (2009) suggested that the upper mantle is generally more depleted in subducted oceanic crust than the upper part of the lower mantle.

Seismic tomography results have revealed two large low shear velocity provinces (LLSVPs) in the lowermost mantle beneath Africa and the Pacific oceans (e.g., Li & Romanowicz, 1996; Grand, 2002; Ritsema et al., 2004; Garnero et al., 2016), which occupy ~30% of the CMB area and perhaps between ~1.6% (Burke et al., 2008) and ~8% (Cottaar & Lekic, 2016) of whole mantle volume. One hypothesis is that the LLSVPs are caused by

accumulations of subducted oceanic crust in the lowermost mantle (e.g., Hofmann & White, 1982; Christensen & Hofmann, 1994; Tolstikhin & Hofmann, 2005). Compared to the size of LLSVPs, much smaller-scale ultra-low velocity zones (ULVZs) have been reported on the CMB, with a height of 5–40 km and a lateral extent ranging from less than hundreds to thousands of kilometers long (e.g., McNamara et al., 2010; McNamara, 2019; Yu & Garnero, 2018). Most of the ULVZs are found within or near the edges of the LLSVPs, but some occur outside the LLSVPs (McNamara et al., 2010; Li et al., 2017; Yu & Garnero, 2018), which, in addition to several other hypotheses (e.g., McNamara, 2019), have been proposed to be caused by the partial melting of subducted oceanic crust (Andraut et al., 2014).

Widespread seismic scatterers with a thickness of ~10 km and a lateral extent ranging from ~50 km to >500 km (Kaneshima & Helffrich, 1999, 2003; Niu et al., 2003; Li & Yuen, 2014; Niu, 2014) have been reported in subducting regions of the mid-lower mantle (~700–2,000 km) through analyzing *P*-to-*P* and *S*-to-*P* converted waveforms (see a recent review by Kaneshima (2016) and reference within). Hedlin & Shearer (2002) showed that PKP coda waves can be explained by 8 km scale seismic anomalies uniformly distributed throughout the mantle. More recently, Waszek et al. (2018) analyzed the SS precursor signals, and they showed a global distribution of seismic reflectors throughout the mid-lower mantle in the range of 800–1,300 km, with a lateral extent varying from <500 km to ~2,000 km. Widespread seismic scatterers are also found in the lowermost mantle and on the CMB (Bataille & Lund, 1996; Earle & Shearer, 1997; Shearer et al., 1998; Cormier, 1999; Niu & Wen, 2001; Miller & Niu, 2008; Rost & Earle, 2010; Waszek et al., 2015; Ma et al., 2016; Frost et al., 2017). Seismic scatterers and reflectors in the deep mantle are often interpreted as caused by subducted oceanic crust, although SiO₂-enriched materials such as the subducted oceanic sediments and the products of core–mantle interaction (e.g., Helffrich et al., 2018) may also cause seismic scattering in the deep mantle. Furthermore, it has been reported that the subducted oceanic crust that once reached ~700–1,400 km depth is found in diamond inclusions (Walter et al., 2011; Nestola et al., 2018; Smith et al., 2018).

12.3. THE CYCLING OF SUBDUCTED OCEANIC CRUST IN THE DEEP MANTLE

The questions are what controls the present-day distribution of subducted oceanic crust in the deep mantle, and how does the oceanic crust distribution evolve with time? The present-day oceanic crust is ~6–7 km thick, and

occupies the topmost part of an oceanic plate. Beneath the oceanic crust is a layer of depleted lithosphere that includes sequential layers of depleted harzburgite (~24 km), depleted lherzolite (~10 km) and depleted pyrolite (~40 km) (e.g., Ringwood, 1982; Ringwood & Irifune, 1988). The oceanic crust and the depleted lithosphere may be much thicker in the early hotter Earth due to deeper depths of melting and larger volumes of melt production (e.g., McKenzie, 1984; Herzberg et al., 2010). Being an essential part of the oceanic plates, the advection of the oceanic crust in the deep mantle is expected to be strongly controlled by the dynamics of oceanic plates.

The lifespan of oceanic plates from their formation to subduction has been recently summarized by Cramer et al. (2019). After subduction, the oceanic plates in the deep mantle are called subducting slabs. Seismic tomography studies have shown that while some subducting slabs directly penetrate to the deep lower mantle (e.g., Grand et al., 1997; van der Hilst et al., 1997), other slabs are deflected horizontally at the base of the transition zone or in the uppermost lower mantle (Zhou & Anderson, 1989; Zhou & Clayton, 1990; Van der hilst et al., 1991; Fukao et al., 1992; van der Hilst, 1995; Bijwaard et al., 1998; Fukao et al., 2001; Grand, 2002; Zhao, 2004; Li et al., 2008; Fukao et al., 2009; Fukao & Obayashi, 2013). Numerical modeling experiments have shown that the horizontal deflections of subducted oceanic crust are significantly controlled by the endothermic phase transition at 660 km (e.g., Christensen & Yuen, 1985), the viscosity structure from the transition zone to the mid-lower mantle (e.g., Yoshioka & Naganoda, 2010; Rudolph et al., 2015; Mao & Zhong, 2018), the surface trench migration (e.g., Goes et al., 2008), and the strength, dipping angle and buoyancy of the subducting slabs (e.g., Tackley et al., 1994; Zhong & Gurnis, 1994; Christensen, 1996; Torii & Yoshioka, 2007; Billen, 2008; King et al., 2015). The horizontal deflection of slabs in the deep mantle has been summarized in several review papers by Tackley (1995), Billen (2008) and Goes et al. (2017). Nevertheless, it is generally accepted that, unless the negativity of the Clapeyron slope for the 660 km phase transition is unrealistically high (e.g., at least about –4MPa/K), the ponding slabs at 660 km would eventually sink to the deep lower mantle (Christensen & Yuen, 1984, 1985; Machel & Weber, 1991; Peltier & Solheim, 1992; Tackley et al., 1993; Weinstein, 1993; Solheim & Peltier, 1994; Tackley et al., 1994; Christensen, 1996; Jarvis & Lowman, 2007; Davies, 2008; Nakakuki et al., 2010). It is likely that different slab morphologies in tomography models represent different stages of slab subduction toward the lowermost mantle (Agrusta et al., 2017; Goes et al., 2017).

One may expect the subducted oceanic crust to be coupled and sink with the subducting slabs to the

lowermost mantle. However, the subducted oceanic crust may also act independently from the rest of the subducting slabs, because the oceanic crust may have different intrinsic density and viscosity than the surrounding mantle (e.g., Ringwood & Irifune, 1988; Irifune & Ringwood, 1993; Karato et al., 1995; Hirose et al., 1999). This section first examines the ability of the subducted oceanic crust to separate from the rest of the slab and accumulate at the base of the mantle transition zone (Section 3.1) and the CMB (Section 3.2), and then focuses on the process of entraining subducted oceanic crust from deep to shallow depths (Section 3.3 and Section 3.4).

12.3.1. The Separation of Slab Components at the Base of Transition Zone

One question is whether the subducted oceanic crust can separate from the rest of the subducting slabs and be trapped at the base of the mantle transition zone. The dynamics of the subducted oceanic crust in the deep mantle are strongly controlled by the density anomaly of the crust compared to its surroundings. The subducted oceanic crust transforms to eclogite at depths larger than ~50 km and becomes intrinsically denser than the surrounding mantle (Green & Ringwood, 1967; Peacock, 1993; Hacker, 1996), although it has been suggested that subducted oceanic crust may remain metastable at deeper depths, particularly when the oceanic crust is dry (Hacker, 1996). After eclogite transformation, the subducted oceanic crust remains ~1–5% (sometimes larger than 5% around 400 km depth) intrinsically denser than pyrolytic rocks in most part of the mantle (Ringwood & Irifune, 1988; Kesson et al., 1994; Aoki & Takahashi, 2004; Hirose et al., 2005; Ganguly et al., 2008; Kawai et al., 2009; Ricolleau et al., 2010; Tsuchiya, 2011), except from 660 km to ~720–800 km depth where the crust may be up to ~2.5% intrinsically less dense (Ringwood & Irifune, 1988; Ringwood, 1990; Irifune & Ringwood, 1993; Hirose et al., 1999; Ono et al., 2001; Kubo et al., 2002). However, Litasov et al. (2006) suggested that there would not be density deficits of subducted oceanic crust in the uppermost lower mantle under wet conditions with ~2–5 wt% water. The depleted harzburgite is intrinsically less dense than pyrolytic mantle at most mantle depths, except the uppermost lower mantle where the harzburgite is slightly denser (e.g. Ringwood & Irifune, 1988; Irifune & Ringwood, 1993). A slab consisting of oceanic crust and a relatively thicker harzburgite is essentially neutrally buoyant.

As an example, Figure 12.1a compares the density anomaly of MORB, Harzburgite and Pyrolite from 150 km to 800 km as estimated by (Ringwood & Irifune, 1988). They showed that MORB is always ~100–200 kg/m³ denser than Pyrolite except at ~660–720 km, where it is

~100 kg/m³ less dense than the pyrolite. Interestingly, the density anomaly of MORB compared to pyrolite reaches a maximum value of ~250 kg/m³ at ~400 km depth, or ~7% denser than the density of ~3,540 kg/m³ in the PREM model (Dziewonski & Anderson, 1981) at this depth. In contrast, the harzburgite is always ~80–110 kg/m³ less dense than the pyrolite, except at ~670–700 km, where it is slightly denser than the pyrolite. Figure 12.1b compares the density of MORB from mineral physics experiments by (Hirose et al., 2005) with the density in PREM model from 800 km to the CMB, showing that the MORB is ~100–200 kg/m³ denser than PREM model after 800 km throughout the lower mantle.

It has been proposed that the density deficits of subducted oceanic crust in the uppermost lower mantle may lead to separation of crustal materials from the rest of the slabs and storage of subducted oceanic crust in the mantle transition zone, causing compositional layering between the upper mantle and the lower mantle (Anderson, 1979; Ringwood & Irifune, 1988). This hypothesis was later examined through numerical modeling experiments. Isoviscous numerical models (Richards & Davies, 1989) show that it is impossible to separate components of a slab that consists of a layer with negative buoyancy and a layer with positive buoyancy, unless the positive buoyancy and the negative buoyancy (density contrast × component volume) are equal, meaning that the whole slab needs to be neutrally buoyant (Figure 12.2a). Even in this case, separation only happens on a timescale much longer than it takes for the subducted slabs to sink through the upper mantle and transition zone. Gaherty & Hager (1994) performed calculations with temperature-dependence of viscosity and a 30–100 times viscosity jump across the 660 km discontinuity. Similar to (Richards & Davies, 1989), they did not find separation of slab components near the base of the transition zone (Figure 12.2b). Christensen (1997) also included the effects of phase transition and density deficits of subducted oceanic crust in the uppermost lower mantle. Temporal slab stagnation at 660 km depth is observed in their models, but there is still no separation of oceanic crust from the rest of the slab (Figure 12.2c).

The difficulty for the subducted oceanic crust to separate from the rest of the slabs may be due to the high viscosity of the subducting slabs and the overall negative buoyancy of the cold slabs. If so, one way to facilitate the crustal separation may be through lowering the slab viscosity. Indeed, van Keken et al. (1996) and Karato (1997) showed that crustal separation happens when there is a weak layer between the oceanic crust and the cold core of a slab, and if the weak layer has lower viscosity than the mantle surrounding the slab (Figure 12.2d). The presence of the weak layer may be caused by the relatively strong, garnet-enriched crust and the cold, high-viscosity core of

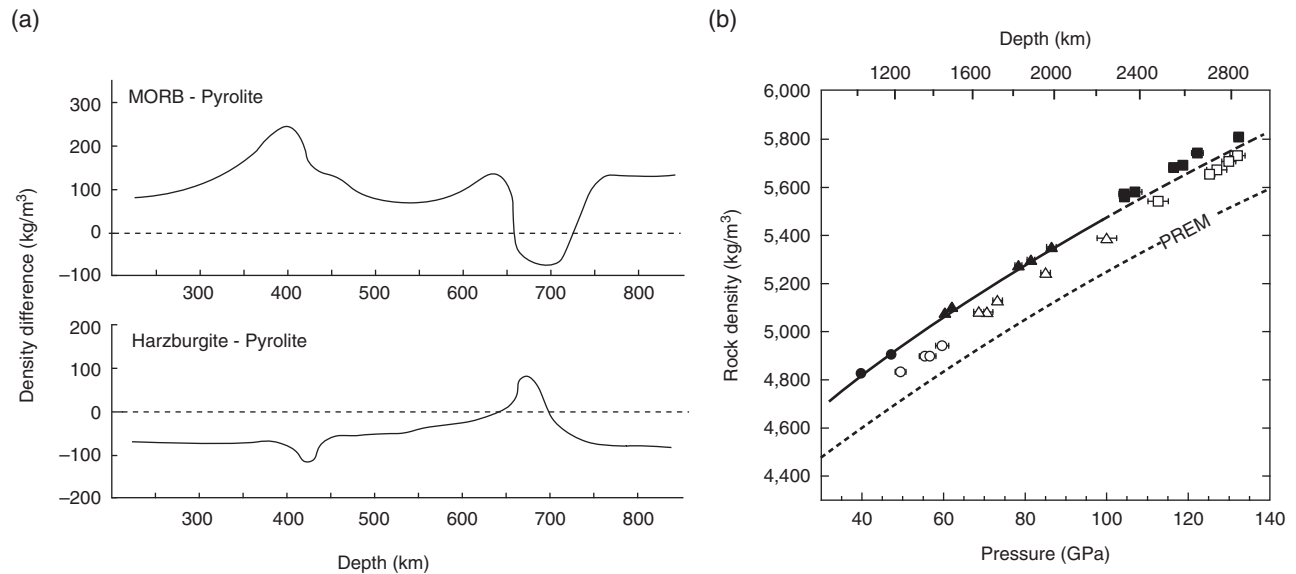


Figure 12.1 (a) Density difference between MORB, Harzburgite and pyrolite from 150 km to 800 km. The density of each compositional component is calculated from experimentally determined phase assemblages and is corrected for compressibility and thermal expansion along a mantle geotherm by Brown and Shankland (1981). Upper: density of MORB minus pyrolite; Lower: Harzburgite minus pyrolite. (b) Density profile of MORB compared to PREM model (dashed curve) from 800 km to the CMB. Closed and open symbols show MORB density at 300 K and 2750–2290 K, respectively. The shape of symbols represents different phase assemblages of MORB at different depth. The solid line shows a density profile at 300 K for Bridgmanite-dominant assembly fitted to the Birch-Murnaghan equation of state. Reproduced and modified from Hirose et al. (2005). *Source:* (a) Modified from Ringwood and Irifune (1988), (b) Hirose et al. (2005).

the slab (van Keken et al., 1996; Karato, 1997). However, Christensen (1997) argued that the viscosity of the weak layer may not be lower than the mantle surrounding the slab, because this layer still has a lower temperature than the background mantle. In addition, as he pointed out, the garnet is not a major phase in the oceanic crust and so its effect on viscosity is limited.

Later, wet garnet was suggested to be less viscous than the background mantle (Katayama & Karato, 2008), and based on this result, Yoshida et al. (2012) and Yoshida & Tajima (2013) showed that it is possible for a dense, wet and therefore, low-viscosity subducted oceanic crust to separate from the main body of the slabs. As shown in Figure 12.2e, they found that when slabs are deflected horizontally above the 660 km discontinuity, the weak oceanic crust moves faster than the rest of the slabs, resulting in crustal separation. The subducted oceanic crust temporarily accumulates on the 660 km discontinuity, but most of it eventually sinks to the deep lower mantle together with the subducting slabs, and only small amounts of crustal materials are left over at the base of the mantle transition zone.

It has also been proposed that a reduction in grain size in cold slabs due to metastable olivine-spinel phase transition and the enrichment of water may reduce the slab

viscosity (Riedel & Karato, 1997; Richard & Bercovici, 2009). Motoki & Ballmer (2015) showed that thermal instabilities develop in weak stagnant slabs above the 660 km discontinuity, with the denser subducted oceanic crust sinking to the bottom of the models at 660 km, and the less dense depleted lithospheric materials rising up and mixed into the background upper mantle.

The separation of subducted oceanic crust from other parts of subducting slabs may be more likely to happen in the early hotter mantle. First, the oceanic crust in Archean may be much thicker than present-day (McKenzie, 1984; Herzberg et al., 2010). The density deficits of a larger volume of subducted oceanic crust in the uppermost lower mantle may lead to larger positive buoyancy to help the crustal materials separate from the subducting slabs and accumulate near the base of the mantle transition zone. Second, the subducting slabs in a hotter Archean mantle may be warmer and less viscous than present-day slabs (van Hunen & Moyen, 2012). A weaker subducting slab may facilitate the separation of oceanic crust from other slab components.

Figure 12.3 show a time series of snapshots of temperature (left panels) and compositional fields (right panels) from the numerical modeling experiments of (Davies, 2008). The thickness of oceanic crust increases with upper

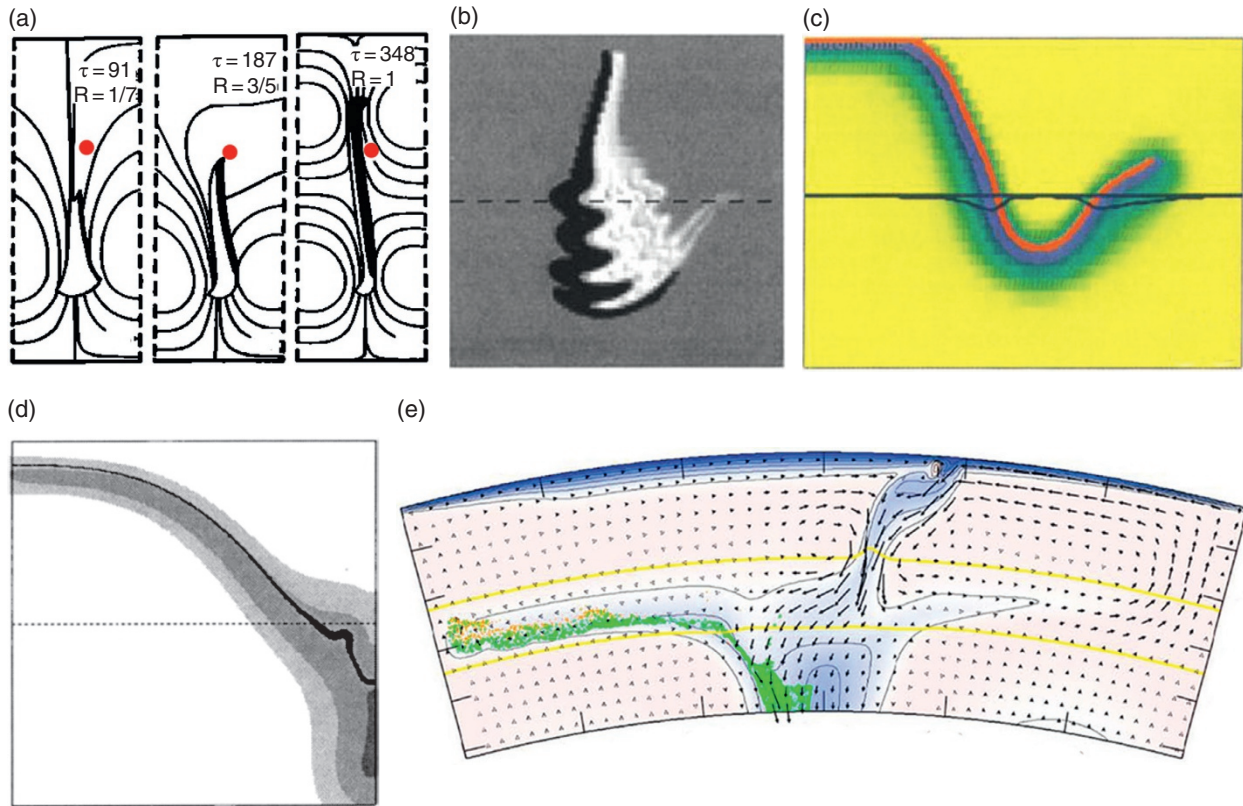


Figure 12.2 Numerical modeling experiments showing the dynamics of a sinking slab in the deep mantle and its interaction with the 660 km seismic discontinuity. (a) The slab consists of a positively buoyant layer (black) and a negatively buoyant layer (white). Both layers have the same magnitude of intrinsic density anomaly and R represents the ratio of initial thickness between the negatively buoyant layer and the positive buoyant layer. The red dot in each panel shows the original upper-right corner of the slab. Partial separation of slab components only occurs for $R = 1$ after a nondimensional time of $\tau = 348$. The solid curves show streamlines of mantle flow velocity. (b) The slab consists of negatively buoyant subducted oceanic crust (black) and positively buoyant harzburgite (white). The gray color shows the background mantle that is neutrally buoyant. The dashed line marks the depth of 660 km with a 100x viscosity increase from upper to lower mantle. No separation of slab components occurs as they sink from the upper mantle to the lower mantle. (c) The slab consists of subducted oceanic crust (red) and harzburgite (purple). The color scale indicates temperature ranging from 1300°C (yellow) to <500°C (dark blue). Black lines show the reference and the deflected 660 km phase boundary. The sinking of the slab is impeded near the 660 km phase boundary, but the subducted oceanic crust is not detached from the slab. (d) The black color shows the subducted oceanic crust and temperature increases from dark grey to light grey and to white regions. The dashed line marks the 660 km depth. Note that the oceanic crust is decoupled from the relatively colder parts of the slab. (e) The subducted oceanic crust (green) separates from the slab (blue) and accumulates on the 660 km discontinuity after the slab is horizontally deflected at the base of transition zone, caused by the lower viscosity and faster movement of the subducted oceanic crust relative to the rest of the slab. A large amount of oceanic crust that previously accumulate at 660 km discontinuity later sinks into the lower mantle with the slab. *Source:* (a) Modified from Richards and Davies (1989), (b) Gaherty and Hager (1994), (c) Christensen (1997), (d) van Keken et al. (1996), (e) Modified from Yoshida et al. (2012).

mantle temperature in these experiments. When including the effects of density deficits of oceanic crust in the uppermost lower mantle, Davies (2008) showed that the subducted oceanic crust accumulates into large pools at the bottom of mantle transition zone in the early hotter Earth (Figures 12.3b, 3d, 3f, the crustal materials are shown by blue to purple colors), which later episodically sink

to the deep lower mantle due to mantle avalanche (Figures 12.3c–d). However, Davies (2008) found that there are no more crustal accumulation and episodic overturn after the mantle cools down (Figures 12.3g–h). He suggested that, because of the preferential sinking of oceanic crust to the bottom of the mantle, the upper mantle may be depleted in oceanic crustal materials (Davies,

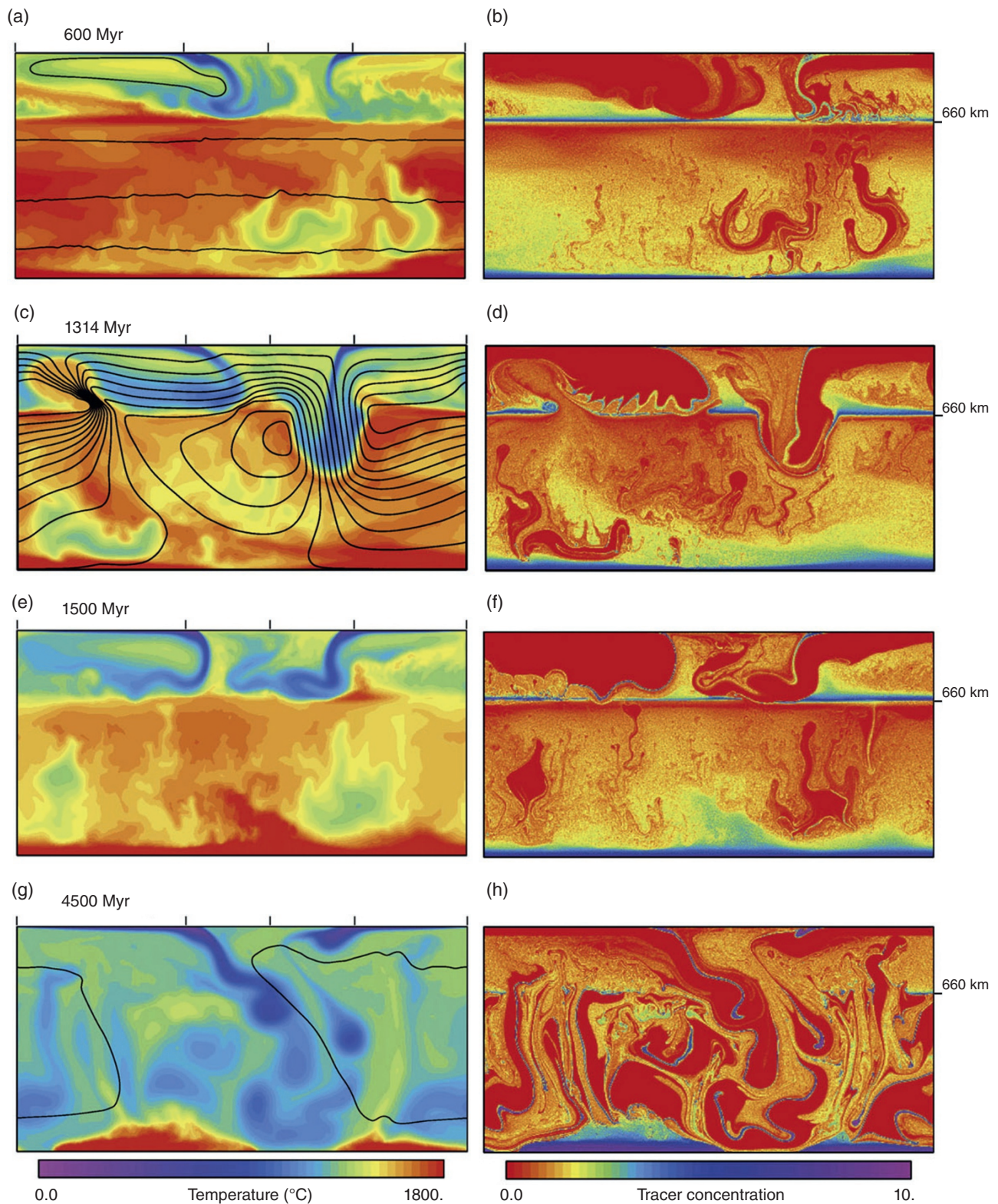


Figure 12.3 Snapshots of temperature fields (left column) and the corresponding compositional fields (right column) from the numerical models of Davies (2008). The black curves in the temperature fields show the streamlines. The subducted oceanic crust in the compositional fields is shown by purple to green colors. (a–b) At 600 Myr, the subducted oceanic crust accumulates at the base of transition zone. (c–d) At 1314 Myr, the accumulations of crustal materials sink to the lower mantle. (e–f) At 1500 Myr, the subducted oceanic crust accumulates at the base of transition zone again. (g–h) At 4500 Myr, the subducted oceanic crust stops to accumulate at the base of transition zone when mantle becomes cooler. Note that the subducted oceanic crust accumulates on the CMB for all time snapshots. *Source:* Modified from Davies (2008).

2006; Davies, 2007, 2008). The temporal accumulation of large volume of thick subducted oceanic crust at the base of mantle transition zone has also been reported by (Ogawa, 2000, 2003). van Thienen et al. (2004) also tested the effects of the crustal density deficits; however, they did not find crustal separation and accumulation at the base of the mantle transition zone.

One debate is that, there may not be modern-like plate tectonics and subduction process in the early Earth (e.g., Davies, 1992). Therefore, the oceanic crust may not sink to the deep mantle (e.g., Davies, 1992; van Hunen et al., 2008), or it may enter the deep mantle through small-scale dripping (e.g., Johnson et al., 2014; Fischer & Gerya, 2016). In the latter case, the oceanic crust may not be associated with a cold and strong slab, and may be more likely to accumulate at the base of the transition zone due to the crustal density deficits in the uppermost lower mantle.

12.3.2. The Accumulation of Subducted Oceanic Crust on the CMB

For a subducted oceanic crust that penetrates through the physical barriers at the base of the mantle transition zone and in the uppermost lower mantle, it may sink all the way down to the bottom of the mantle. One question is whether the subducted oceanic crust can accumulate on the CMB.

The accumulation of subducted oceanic crust on the CMB and its later entrainment to the uppermost mantle by mantle plumes were first proposed by Hofmann & White (1982) to explain isotope geochemistry of OIBs. Subsequently, the ability of subducted oceanic crust to accumulate on the CMB has been extensively studied through numerical modeling and laboratory experiments. One of the earliest studies was conducted by Gurnis (1986), who performed 2D Cartesian models with constant mantle viscosity, and showed that if a subducted oceanic crust is able to separate from the rest of the slab in the lowermost mantle, it is marginally possible for the crustal materials to accumulate at the bottom of the mantle. Later, Christensen et al. (1989) performed 2D modeling with strong temperature-dependence of viscosity and showed that ~5–20% of subducted oceanic crust segregates and accumulates on the CMB. They also found that a pre-existing pool of crustal materials on the CMB helps crustal segregation, which is also found by Tackley (2011) through implementing 2D and 3D models. Olson & Kincaid (1991) conducted laboratory experiments in which a fixed length of slab segment, consisting of a layer of intrinsically denser materials on top of a layer of less dense materials, was introduced into a convecting fluid (Figure 12.4a). The slab segment sank and settled down at the bottom of the tank (Figure 12.4b), where it was heated, and thermal instabilities developed within the slab

(Figure 12.4c). Later, the denser materials accumulate into piles at the bottom and the less dense materials were entrained up by plumes (Figure 12.4d). The laboratory experiment results were later reproduced by Tackley (2011) through numerical modeling (Figures 12.4e–h).

In the studies of Christensen et al. (1989), Olson & Kincaid (1991), and Tackley (2011), a fixed length of slab segment was once introduced in the models. Christensen & Hofmann (1994) updated the 2D models of Christensen et al. (1989) to allow slabs, that consist of a thin layer of denser oceanic crust and a thick layer of less dense harzburgite, to be continuously subducted to the lowermost mantle. They found that ~1/6 of the subducted oceanic crust accumulates on the CMB (Figure 12.5a), for reasonable parameter values. They also showed that the fraction of subducted oceanic crust accumulating on the CMB increases strongly with the intrinsic density anomaly of the oceanic crust and the degree of temperature dependence of viscosity, but decreases moderately with the Rayleigh number, which is defined as:

$$Ra = \frac{\rho g \alpha \Delta T D^3}{\kappa \eta}, \quad (12.1)$$

where ρ is the density, g is the gravitational acceleration, α is the thermal expansivity, ΔT is the reference temperature, D is the mantle thickness, κ is the thermal diffusivity, and η is the viscosity. Limited by computational power, only three relatively low Rayleigh numbers were investigated by Christensen & Hoffmann (1994) with $Ra = 2.5 \times 10^5$, 5×10^5 and 1×10^6 . For comparison, the Rayleigh number for the true Earth's mantle is calculated to be approximately 10^7 using the typical average physical properties of $\rho = 4000 \text{ kg/m}^3$, $g = 10 \text{ m/s}^2$, $\alpha = 3 \times 10^{-5} \text{ K}^{-1}$, $\Delta T = 3000 \text{ K}$, $D = 2900 \text{ km}$, $\kappa = 1 \times 10^{-6} \text{ m}^2/\text{s}$, and $\eta = 10^{22} \text{ Pa s}$.

An analysis of Stokes flow helps understand the sinking of subducted oceanic crust in the deep mantle. The steady descending velocity of a sphere in an isoviscous fluid is given by (e.g., Turcotte & Schubert, 2014):

$$V_{\text{sphere}} = \frac{2\Delta\rho g a^2}{9\eta_f}, \quad (12.2)$$

where $\Delta\rho$ is the density anomaly of the sphere compared to the surrounding fluid, g is the gravitational acceleration, a is the sphere radius, and η_f is the fluid viscosity. If the sphere is introduced to a fluid that is already convecting with a velocity of V_f , the advection of the sphere is controlled by both V_{sphere} and V_f . If $V_f \gg V_{\text{sphere}}$, the sphere would be generally dragged by the background flow. Instead, if $V_{\text{sphere}} \gg V_f$, the sphere would sink downward more freely due to its own negative buoyancy. In terms of the advection of subducted oceanic crust in the lowermost mantle, the faster (slower) the lowermost

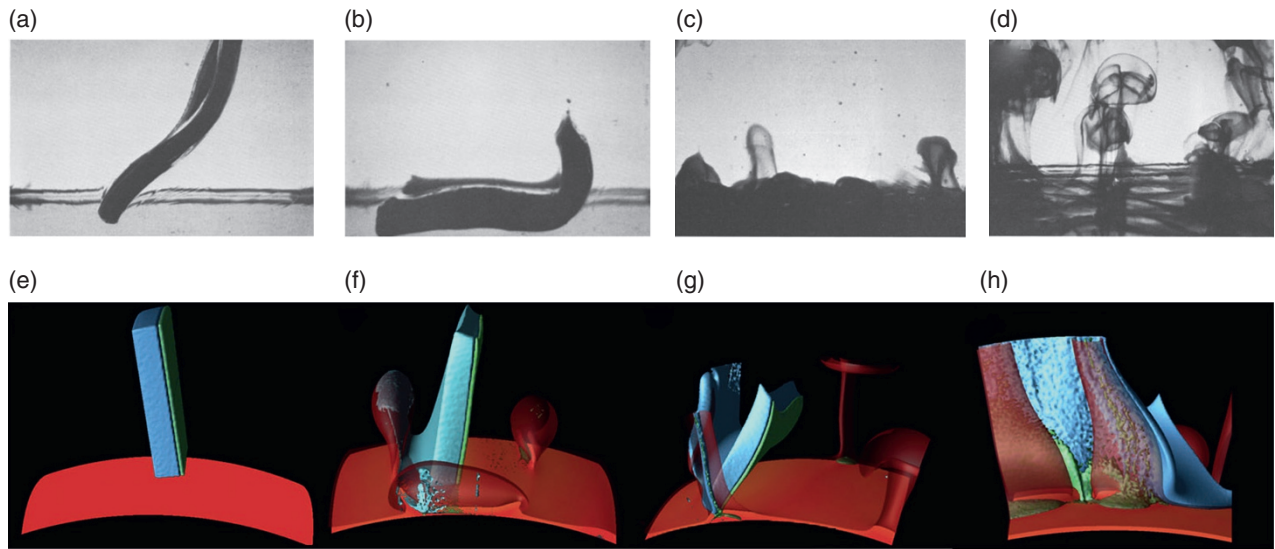


Figure 12.4 Snapshots from geodynamic experiments showing the segregation of subducted oceanic crust from the rest of a slab in the lowermost mantle. (a–d) Laboratory experiment results. (a) At 150 s, a cold, high-viscosity slab reaching the thermal boundary layer. (b) At 250 s, the slab lays down on the thermal boundary layer where it is heated. (c) At 2200 s, the slab materials spread and form uneven layers, with some light slab components rising up. (d) At 2400 s, dense slab components reside at the bottom and light slab components entrained into thermal plumes. (e–h) Numerical modeling results. Green shows the subducted oceanic crust, blue shows the harzburgite, and mantle plumes are shown by red colors. (e) Initially, a slab consists of a thin layer of subducted oceanic crust and a much thicker layer of harzburgite is imposed vertically to the bottom of the model. (f) At 36 Myr, the slab is rotated with the denser oceanic crust facing the CMB. Mantle plumes form above the thermal boundary layer (red horizontal plane at the bottom). (g) At 72 Myr, part of the less dense harzburgite is entrained upward by plumes. (h) At 108 Myr, a majority of the harzburgite is entrained upward by plumes and the subducted oceanic crust accumulates at the bottom of the model. *Source:* (a–d) Olson and Kincaid (1991), (e–h) Modified from Tackley (2011).

mantle flow velocity V_f compared to the steady sinking speed of the subducted oceanic crust V_{sphere} , the more (less) likely that the crust would be passively advected with the surrounding mantle flow, and the less (more) likely that the crust would segregate and accumulate on the CMB.

The increase of crustal accumulation rate with the crustal density anomaly as found by Christensen and Hofmann (1994) is predicted by the Stokes equation (12.2), because the steady sinking speed V_{sphere} of the crust increases with the density anomaly according to Equation (12.2). The increase of temperature dependence of viscosity reduces the viscosity of the hot basal thermal boundary layer (TBL), which results in increase of the sinking speed of V_{sphere} in the basal TBL. A reduction of the basal TBL viscosity may also increase the mantle flow velocity V_f , but because the V_f in the lowermost mantle is controlled by the large-scale mantle convection as well, it is not clear how much V_f would increase as the basal TBL viscosity decreases. In the models of Christensen & Hofmann (1994), the V_{sphere} likely increases more than the V_f as the degree of temperature-dependence of

viscosity increases and the basal TBL viscosity decreases, which results in an increase of the crustal accumulation rate.

The decrease of crustal accumulation rate with increasing Rayleigh number was explained by Christensen and Hofmann (1994) as follows. First, the thickness of the oceanic crust in their models decreases with Rayleigh number, and less volume of oceanic crust is produced per transit time (defined as the time it takes for materials to sink from the surface to the CMB) at larger Rayleigh number. Second, they argued that the segregation of subducted oceanic crust occurs in the basal TBL where the slabs are warmed and become less viscous. As the Rayleigh number increases, the basal TBL becomes thinner, and as a result, less amount of subducted oceanic crust enters the basal TBL to segregate. However, it was later found that the change of crustal accumulation rate with Rayleigh number is more complex. Brandenburg and van Keken (2007a) showed that the fraction of accumulated oceanic crust decreases with Ra when $5 \times 10^6 < Ra < 2 \times 10^7$, but this is not always the case for $1 \times 10^6 < Ra < 5 \times 10^6$. Later, Nakagawa and

Tackley (2014) found much more crustal accumulations in cases with high Ra (e.g., 1×10^8) than cases with lower Ra (e.g., 1×10^7).

The influence of Rayleigh number on crustal accumulation rate can be examined with Stokes equation. The Rayleigh number, Ra , is a measure of vigor of mantle convection. As Ra increases, the lowermost mantle flow velocity V_f increases. However, Ra is controlled by mantle viscosity, η , and several other parameters in Equation 12.1. If η is fixed and the increase of Ra is caused by the change of other parameters, the V_{sphere} would not change. As a result, an increase of Ra leads to a faster advection of the subducted oceanic crust with the lateral movement of the background mantle flow, which may result in less crustal accumulation. However, if the increase of Ra is partly due to reducing mantle viscosity η , the V_{sphere} would also increase according to Stokes' equation (2). In such case, whether an increase of Ra leads to increases of crustal accumulation rate depends on whether V_{sphere} or V_f increases more. An end member scenario is that the increase of Ra is solely caused by the

decreasing of mantle viscosity η . It has been found that the V_f scales with Rayleigh number by $V_f \sim Ra^{2/3}$ (e.g., Turcotte & Oxburgh, 1967). Because the Ra is inversely proportional to η , V_f scales with η by $V_f \sim \eta^{-2/3}$. According to Equation 12.2, the V_{sphere} scales with η by $V_{\text{sphere}} \sim \eta^{-1}$. Therefore, an increase of Ra caused solely by a decrease of η leads to larger increase of V_{sphere} than V_f , which, in turn, may result in more crustal accumulation.

Following Christensen and Hofmann (1994), many numerical modeling studies have shown accumulations of subducted oceanic crust on the CMB, but with (1) higher Rayleigh number (Davies, 2002, 2006; Brandenburg & van Keken, 2007a; Davies, 2007, 2008; Nakagawa & Tackley, 2014), (2) a decreasing vigor of convection with time (Xie & Tackley, 2004b; a), (3) a crustal thickness that depends on mantle temperature (Ogawa, 2003; Davies, 2006; Davies, 2007; Ogawa, 2007; Davies, 2008; Fujita & Ogawa, 2009; Nakagawa et al., 2009; 2010; Ogawa, 2010; Nakagawa & Tackley, 2011; Ogawa, 2014), (4) 2D spherical models (Figure 12.5b) (Xie & Tackley, 2004b; Nakagawa &

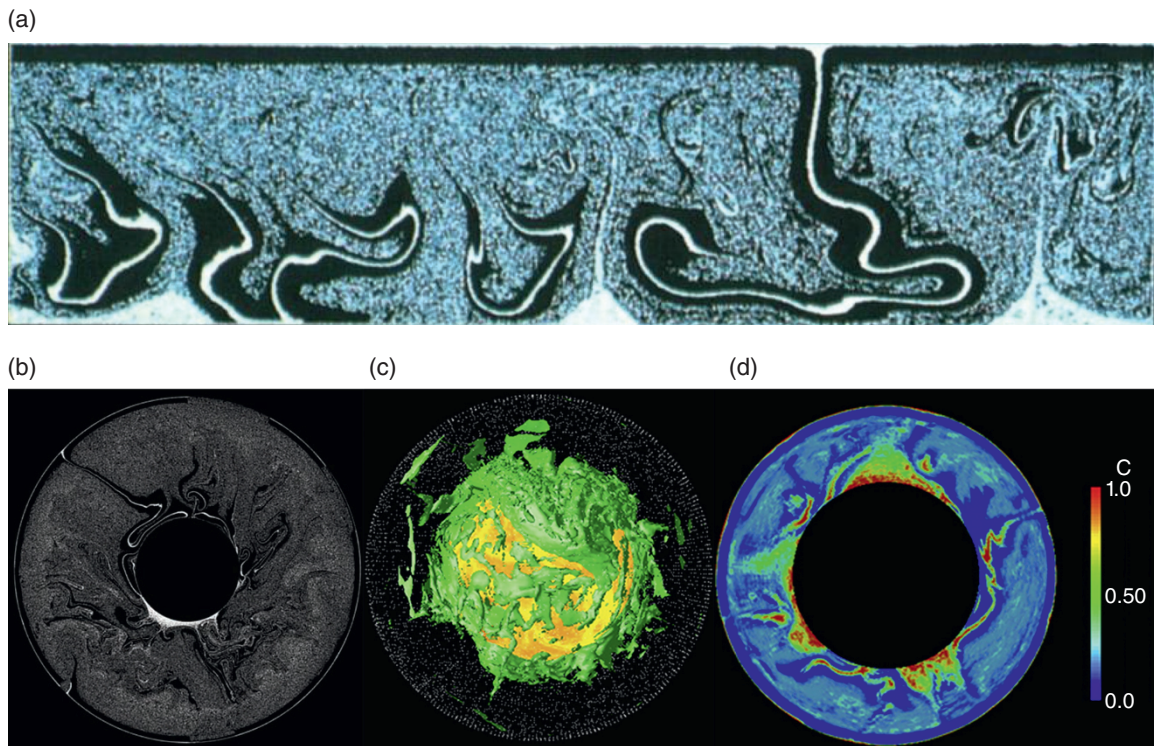


Figure 12.5 Snapshots of compositional field showing the accumulation of subducted oceanic crust on the CMB. (a) 2D Cartesian model. White is subducted oceanic crust, black is harzburgite. (b) 2D cylindrical model. White is subducted oceanic crust, black is harzburgite. Note that size of the core is rescaled to provide the same ratio between core area and surface area in 2D cylindrical models as the true Earth. (c) 3D global spherical model. Green color shows an isosurface of compositional field $C = 0.5$ with high concentration of subducted oceanic crust. (d) A vertical cross-section of panel (c). *Source:* (a) Reproduced from Christensen and Hofmann (1994), (b) Reproduced and modified from Brandenburg and van Keken (2007), (c,d) Reproduced from Nakagawa et al. (2010).

Buffett, 2005; Brandenburg & van Keken, 2007b; Nakagawa et al., 2009; 2010), (5) 3D regional models (Figure 12.4b) (Tackley, 2011) and (6) 3D global spherical models (Figures 12.5c–d) (Huang & Davies, 2007; Nakagawa et al., 2009; 2010; Nakagawa & Tackley, 2011). One note is that, the thickness of the oceanic crust at the surface in most previous studies often reaches tens of km, which may be justified if a hotter early Earth produced deeper and more partial melting than the present-day (McKenzie, 1984; Herzberg et al., 2010).

In addition to the crustal density, the temperature-dependence of viscosity and the Rayleigh number, several other factors may affect the crustal accumulation rate. It was found that the crustal segregation in the lowermost mantle was more significant in internally heated models than in basally heated models (Gurnis, 1986), but was not very sensitive to the partitioning between internal and basal heating in models with mixed heating mode (Christensen & Hofmann, 1994). Davies (Davies, 2002, 2006; Davies, 2007, 2008) used purely internally heated models to inhibit the formation of mantle plumes in 2D models as he argued that the effects of plume entrainment of subducted oceanic crust may be overestimated in 2D models compared to 3D models. This idea was supported by the numerical modeling results of Tackley (2011), who found that the fraction of accumulated oceanic crust increases from 15–25% in 2D models to 25–45% in 3D models. However, the entrainment rate may be underestimated in Davies' models that did not have upwelling plumes, meaning that the crustal accumulation rate may be overestimated. Another factor that affects the crustal segregation is the Bridgmanite to post-Perovskite (pPv)

phase transition, which has been proposed to cause viscosity reduction in cold slabs in the lowermost mantle (Hunt et al., 2009; Ammann et al., 2010). Nakagawa & Tackley (2011) found that the weak pPv helps subducted oceanic crust to segregate within the D''.

It is also found that a thin subducted oceanic crust is difficult to segregate in the lowermost mantle and accumulate on the CMB into large sizes comparable to the LLSVPs. Brandenburg and van Keken (2007a) employed a 10 km thick oceanic crust in their models, and showed that significant accumulation of oceanic crust is possible for an Earth-like Rayleigh number of 2×10^7 , but only if the excess density of the oceanic crust is larger than that suggested from laboratory experiments. Similarly, Li & McNamara (2013) found that a ~6 km thick oceanic crust is difficult to accumulate on the CMB (Figure 12.6a). However, the opposite conclusion was reached by Mulyukova et al. (2015), who showed that the subduction of a 6 km thick oceanic crust is able to accumulate on the CMB and form piles with similar size as the LLSVPs (Figure 12.6b). In (Li & McNamara, 2013), the convection pattern in a 2D Cartesian box evolves naturally with free-slip boundary conditions, and the majority of the subducted oceanic crust in the lowermost mantle is often dragged horizontally by mantle flow to upwelling regions without contacting the CMB (Figure 12.6a). However, in the 2D spherical models of Mulyukova et al. (2015), the subducted oceanic crust sinks directly from the surface to the CMB, which is likely caused by the imposed surface velocity boundary condition that is fixed with time. After reaching the CMB, the subducted oceanic crust in the models of Mulyukova et al. (2015) migrates laterally

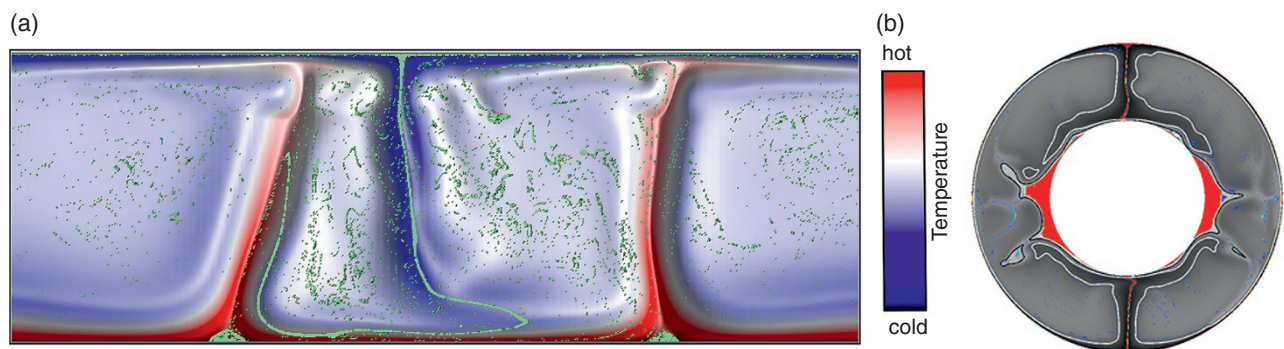


Figure 12.6 (a) A snapshot of temperature field with subducted oceanic crust (green) super imposed. After entering the lowermost mantle, the subducted oceanic crust is dragged horizontally and directly entrained up by mantle flows that are viscously coupled with the upwelling mantle plumes (red), without reaching the CMB. Only small piles of subducted oceanic crust accumulate at the base of plumes, which are consistently entrained up by the plumes. Also shown are subducted oceanic crustal materials that have been stirred into the background mantle. (b) A snapshot of the compositional field showing the accumulation of subducted oceanic crust (red) into large thermochemical piles on the CMB. The oceanic crust sinks directly to the CMB. The white contours outline the subducting slabs. *Source:* (a) Reproduced and modified from Li and McNamara (2013), (b) Reproduced from Mulyukova et al. (2015).

along the CMB without being entrained up (Figure 12.6b).

Conceptually, after a slab reaches the lowermost mantle, it is dragged horizontally by mantle flow toward upwelling regions. The slab becomes warmer due to thermal diffusion, and perhaps less viscous as well, which facilitates the separation of subducted oceanic crust from the rest of the slab. If the oceanic crust separates from the slab and reaches the CMB before being advected to upwelling regions, the oceanic crust is likely to accumulate on the CMB (e.g., Mulyukova et al., 2015), because the vertical mantle flow velocity on the CMB is zero and the subducted oceanic crust on the CMB can only be advected laterally. The oceanic crust that migrates along the CMB may accumulate into large blobs and become difficult to entrain up as a whole. However, if a thin subducted oceanic crust is directly advected to upwelling regions without reaching the CMB, the crust may be much easier to be entrained up to shallow depths (e.g., Li & McNamara, 2013).

It has also been proposed that the subducted oceanic crust may temporarily accumulate at the base of the mantle transition zone and then episodically sink to the bottom of the mantle (Davies, 2008; Yoshida et al., 2012). In such case, the subducted oceanic crust may have already accumulated into large sizes at the base of transition zone, making it easier to accumulate on the CMB than a relatively thin subducted oceanic crust.

The accumulation of subducted oceanic crust on the CMB may form thermochemical piles in the lowermost mantle, with mantle plumes forming on top of the piles (either above the middle or at the edges of the piles) (Burke et al., 2008; Tan et al., 2011; Steinberger & Torsvik, 2012; Li & Zhong, 2017). Figure 12.7 shows a time series of snapshots of compositional fields from the model of (Li et al., 2014a), with the thermochemical pile shown by cyan color and the subducted oceanic crust shown by yellow color. It is found that part of the subducted oceanic crust that does not directly reach the CMB is entrained by mantle flow to the top of the pile

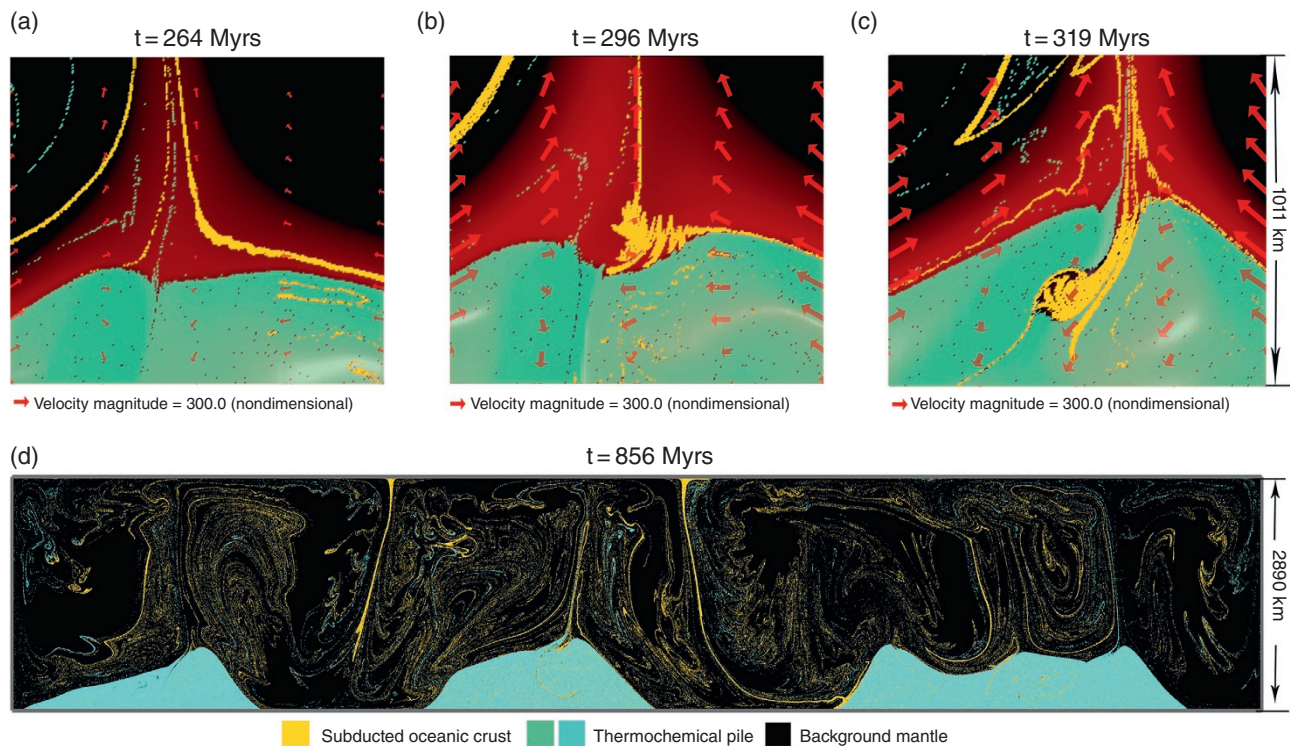


Figure 12.7 (a–c) Zoomed-in view near the cusp of a thermochemical pile showing the interaction between subducted oceanic crust (yellow), thermochemical pile (cyan) and a mantle plume (partially transparent red). The red arrows show mantle flow velocity. (a) Some oceanic crust near the upper-left corner is entrained up by background mantle flow outside of a plume, and some oceanic crust is entrained into the plume. (b) Some subducted oceanic crust accumulates at the base of the plume or at the top of the thermochemical pile, with a small amount directly entrained up by the mantle plume. (c) The accumulation of oceanic crust at the base of the plume is stirred into the pile, with some entrained up by the plume. (d) Zoomed-out panel showing the interaction of subducted oceanic crust with the entire thermochemical pile. *Source:* (a–c) Modified from Li et al. (2014a).

(e.g., Figure 12.7a), where the crust accumulates (e.g., Figure 12.7b), and the majority of it is eventually flushed into the pile (e.g., Figure 12.7c) (Li et al., 2014a). This mechanism may increase the crustal accumulation rate and explain why preexisting dense materials on the CMB helps later crustal accumulation (Christensen et al., 1989; Tackley, 2011).

12.3.3. Stability and Entrainment of the Crustal Accumulations on the CMB

After the subducted oceanic crust accumulates on the CMB, materials from the crustal accumulations are consistently entrained by mantle convection to shallower depths. Although this chapter focuses on the cycling of subducted oceanic crust, the entrainment process also applies to other forms of compositional heterogeneities that are intrinsically or compositionally denser than the background mantle, such as the more-primitive materials, which are remnants of Earth's early differentiation (e.g., Labrosse et al., 2007; Lee et al., 2010) and the products of core–mantle interaction (e.g., Kellogg & King, 1993; Buffett et al., 2000; O'Rourke & Stevenson, 2016; Hirose et al., 2017). For simplification, all these types of compositional heterogeneities are denoted as “compositionally denser materials,” or CDMs.

The entrainment rate is significantly controlled by the density anomaly of the CDMs. In numerical modeling and laboratory experiments, the intrinsic density anomaly is often represented by a nondimensional buoyancy number B , which is the ratio between the intrinsic density anomaly and the density anomaly due to thermal expansion, or $B = \Delta\rho/(\rho\alpha\Delta T)$, where $\Delta\rho$ is the intrinsic density anomaly of the CDMs compared to the background mantle whose density is ρ , α is the reference thermal expansivity, and ΔT is the reference temperature. Care must be exerted when relating buoyancy number to intrinsic density anomaly, because for the same $\Delta\rho/\rho$, different choices of α and/or ΔT lead to different buoyancy number.

While the CDMs are consistently being entrained up and mixed into the background mantle, a significant part of background mantle materials can be stirred into the CDMs as well, which reduces the overall intrinsic density anomaly of the CDMs (e.g., Davaille, 1999a; Le Bars, 2004; Li et al., 2014a). If the buoyancy number of the CDMs is too low, often lower than ~ 0.5 , mantle plumes typically entrain large blobs of CDMs to shallow depths, which are quickly mixed into the background mantle. Interestingly, laboratory experiments by Davaille (1999a) showed that when the buoyancy number is larger than ~ 0.15 and smaller than ~ 0.35 – 0.55 and the CDMs are more viscous than the background mantle, the CDMs form a dome-like structure that oscillates: they are heated

at the bottom and rise to the top, where they are cooled down and sink back to the bottom (Figure 12.8a). A fraction of the CDMs is mixed into the background mantle after each cycle, and up to five oscillation cycles are observed until the CDMs are completely mixed into the surroundings.

The higher the buoyancy number, the more stable the CDMs become. For a buoyancy number larger than ~ 0.5 but smaller than ~ 1.0 , large topography typically develops on the interface between a lower layer of CDMs and an upper layer of intrinsically less-dense materials (e.g., Montague et al., 1998; Tackley, 1998; Montague & Kellogg, 2000; Samuel & Farnetani, 2003; Le Bars, 2004; Le Bars & Davaille, 2004; McNamara & Zhong, 2004). If the thickness of the lower layer is less than several hundred kilometers, the CDMs would be pushed into isolated thermochemical piles (e.g., Figure 12.7d). The topography decreases as the buoyancy number further increases and the isolated thermochemical piles of CDMs spread out and form a global layer (e.g., Tackley, 1998; Davaille, 1999a, b; Le Bars & Davaille, 2004). Figure 12.8b is a shadowgraph from the laboratory experiments of Davaille (1999a), showing that a much denser and viscous lower layer with a buoyancy number of 2.4 convects separately from the layer above, and the interface between the two layers remains flat and sharp.

The entrainment of a stable layer or isolated piles of CDMs in the lowermost mantle by a mantle plume is characterized by the plume dragging the top of the dense layer and piles to form a cusp at the plume root, and some materials are brought up from the cusp (e.g., Figures 12.7a–c, 12.8c) (Sleep, 1988). It is found through theoretical analysis (Sleep, 1988), laboratory experiments (e.g., Davaille, 1999a; Davaille et al., 2002; Gonnermann et al., 2002; Jellinek & Manga, 2002; Namiki, 2003), and numerical modeling experiments (e.g., Tackley, 1998; Zhong & Hager, 2003) that the entrainment rate increases strongly with the decrease of buoyancy number. Laboratory experiments also showed that the entrainment rate increases moderately with the Rayleigh number by $Ra^{1/3}$ (Davaille, 1999b; Jellinek & Manga, 2002). Tackley (1998) argued that entrainment rate in 100% internally heated models is much lower than in 100% basally heated models, because there is no actively upwelling in the former case to entrain the CDMs. Zhong and Hager (2003) performed 2D isoviscous models in which they treated both the plume conduit radius (r_{plume}) and the buoyancy number of the CDMs (B) as model inputs and varied these parameters systematically. They showed that the entrainment rate of the CDMs scales as $B^{-2.48} r_T^{3.80}$, when other parameters including the Rayleigh number and heating mode are fixed. Furthermore, the entrainment rate strongly depends on the viscosity

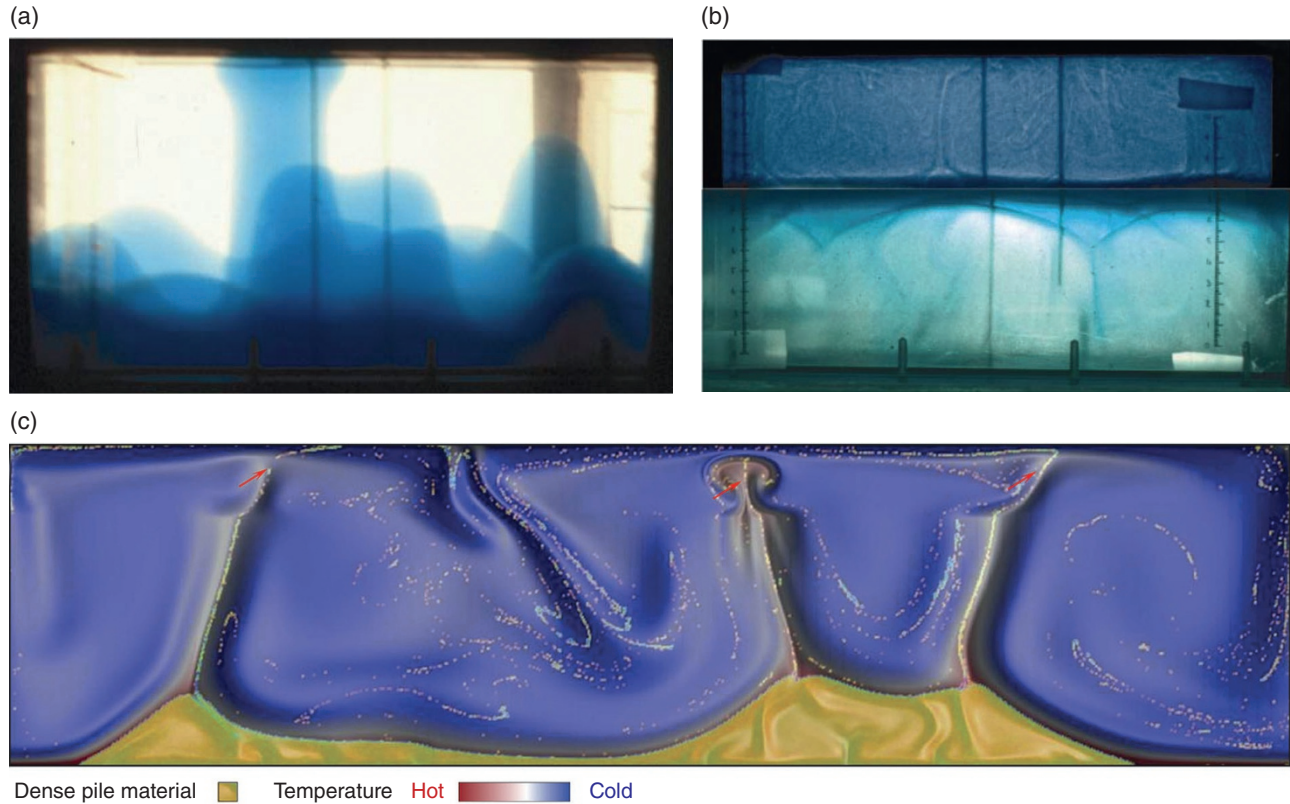


Figure 12.8 Snapshot of laboratory (a–b) and numerical modeling experiments (c) showing the stability and entrainment of CDMs in the deep mantle. (a) With a buoyancy number of 0.2, domes of CDMs (blue) form with one reaching the top of the model. (b) With a buoyancy number of 2.4, a stable layer of CDMs form beneath an upper layer of less dense materials. (c) Entrainment of CDMs with a buoyancy number of 0.8 by mantle plumes (red) from the top of thermochemical piles (yellow). The entrained filaments of materials in plumes rise to the base of the lithosphere (pointed by red arrows). *Source:* (a, b) Reproduced from Davaille (1999a), (c) Reproduced from Williams et al. (2015).

contrast between the background mantle and the CDMs: it reaches maximum when the two have similar viscosity and decreases rapidly as the viscosity of the CDMs becomes much lower or higher than the background mantle. This may be because, as pointed out by Sleep (1988), “a high viscosity would cause the entrained material to behave nearly rigidly and not flow toward the cusp. Conversely, the denser material resists entrainment by draining back into the cusp if it has a very low viscosity.”

Later, Deschamps and Tackley (2008, 2009) performed systematic experiments utilizing 3D Cartesian models and showed that the stability of the CDMs increases with buoyancy number and viscosity of the lower mantle but decreases with Rayleigh number. They also found that the CDMs become more stable by increasing the degree of temperature-dependence of viscosity, the negativity of the Clapeyron slope for the 660 km phase transition, and the intrinsic viscosity of the CDMs. Similar conclusions have been reached by Li et al. (2014c) with 3D global spherical models. Li et al. (2014b) also showed that the

weak post-Perovskite in the lowermost mantle slightly reduces the stability of the CDMs. More recently, Heyn et al. (2018) also found that the stability of the CDMs increases with their intrinsic density and viscosity anomalies compared to the background mantle.

Deschamps et al. (2011) quantified the average mass fraction of CDMs in mantle plumes in the upper mantle. For each element of plume regions whose temperature is higher than a threshold, they multiplied the density of the CDMs with the concentration of CDM particles in the element to get the mass fraction of CDMs. They found that the fraction of entrained CDMs within mantle plumes strongly depends on the intrinsic density of the CDMs. However, in case of stable piles, this fraction does not exceed 9%. The entrainment rate has been found to be strongly time-dependent (Williams et al., 2015), perhaps due to the episodic formation of mantle plumes and changes in plume dynamics (Lin & van Keken, 2005; Williams et al., 2015; Li et al., 2018). A big plume head may entrain more CDMs than a thin plume tail (Jones et al., 2019).

12.3.4. The Fate of the Entrained Oceanic Crust

Collectively, the results described demonstrate that, depending on the density and viscosity of the subducted oceanic crust, the strength (e.g., size, temperature, and viscosity) of mantle plumes, and the vigor of mantle convection, a variable fraction of the recycled oceanic crust from the crustal accumulations on the CMB can be entrained into mantle plumes. Recently, numerical modeling experiments by Jones et al. (2016) predicted that materials carried up from a dense pool of crustal accumulation on the CMB are preferentially entrained into the hottest center of the plume conduits. Through both numerical modeling and laboratory experiments, Cagney et al. (2016) showed that most of the composition within a plume that reaches the lithosphere originates from the lowermost 260–750 km in the mantle. The questions are, how does the entrainment of intrinsically dense recycled oceanic crust affect the plume dynamics, and where does the recycled oceanic crust go once being entrained upward?

The plume dynamics is strongly controlled by the difference between the magnitude of the positive thermal buoyancy of plumes and the negative buoyancy of recycled oceanic crust. However, the net buoyancy of mantle plumes may change with depth because of the following reasons. First, the temperature of a mantle plume decreases as it rises (e.g., Farnetani, 1997; Zhong, 2006; Leng & Zhong, 2008). Second, the plume radius decreases significantly from the lower mantle to the upper mantle due to the decrease in mantle viscosity. Third, the intrinsic density anomaly of the recycled oceanic crust compared to the pyrolytic mantle changes with depth (Figure 12.1). Fourth, plume buoyancy may change due to the 410 km and 660 km phase transitions. Because of the changes of net plume buoyancy with depth, a fraction of recycled oceanic crust that was entrained into the root of a plume in the lowermost mantle may not be carried by the plume all the way to the base of the lithosphere.

For a small amount (a few percent) of oceanic crust that is entrained in plumes, its effect on plume dynamics is limited, and it is likely that the crust would be entrained by upwelling plumes to the base of the lithosphere (e.g., Figure 12.8c). However, for a thermochemical plume that entrains a large amount of recycled oceanic crust (typically more than ~10%), its morphology and dynamics may differ significantly from purely thermal plumes.

Using numerical modeling, Farnetani and Samuel (2005) showed that a thermochemical plume, which is 1% intrinsically denser than the surrounding mantle, becomes stagnant beneath the transition zone, with only narrow filaments of plume materials rising to the base of the lithosphere (Figure 12.9a). They attributed the plume stagnation to the endothermic 660 km phase transition. However, the negative buoyancy of the entrained

materials and the reduction of mantle viscosity in the upper mantle may also play a significant role. Ballmer et al. (2013) performed regional models to study the plume dynamics in the upper mantle, and they showed that thermochemical plumes pond at ~300–400 depth, and secondary plumes form on top of the ponding primary plumes and rise to the base of the lithosphere. Dannberg & Sobolev (2015) also showed that, depending on the plume size and temperature, a thermochemical plume that contains ~15% recycled oceanic crust may directly rise to the uppermost mantle, or pond at ~300–400 km with or without the secondary plumes rising to the base of the lithosphere (Figures 12.9b–d). The ponding of thermochemical plumes at ~300–400 km in (Ballmer et al., 2013) and (Dannberg & Sobolev, 2015) was attributed to the peaks of intrinsic density anomaly of recycled oceanic crust at this depth range (e.g., Figure 12.1a) (Ringwood & Irifune, 1988; Aoki & Takahashi, 2004). In addition, both numerical modeling studies (e.g., Samuel & Bercovici, 2006) and laboratory experiments (e.g., Davaille, 1999a; Kumagai et al., 2008) have predicted that, depending on the intrinsic density of the entrained materials, a thermochemical plume may rise directly to the uppermost mantle, or pond, and even start sinking, at a variety of mantle depths (e.g., Figure 12.9e). It has been found that the entrained oceanic crust in the background mantle may be trapped near the base of the mantle transition zone, which may be caused by the density deficits of recycled oceanic crust in the uppermost mantle and the decrease of viscosity from the lower mantle to the upper mantle (e.g., Davies, 2002; Nakagawa & Buffett, 2005; Brandenburg & van Keken, 2007a; Ballmer et al., 2015; Nakagawa et al., 2010).

Although some subducted oceanic crust in the lowermost mantle can accumulate on the CMB and later be entrained into plumes, a significant fraction of the subducted oceanic crust may be directly entrained to shallower depths by mantle flow without accumulating on the CMB (Li & McNamara, 2013; Li et al., 2014a). The latter is entrained either by mantle plumes (e.g., Figures 7a–c) or by the upwelling background flows that are viscously coupled with mantle plumes (e.g., Figures 6a, 7a). The oceanic crust directly entrained to the uppermost mantle by mantle plumes is generally much younger than that which first accumulates on the CMB and is later sampled by mantle plumes, although only materials entrained into the hottest centers of plumes may contribute to partial melting (e.g., Farnetani & Richards, 1995). Some oceanic crust accumulated at the base of the mantle transition zone may also be entrained up by strong upwellings to the base of the lithosphere (Yasuda & Fujii, 1998; Korenaga, 2004). Regardless of the mechanism by which the subducted oceanic crust is entrained upward, the entrained oceanic crustal materials

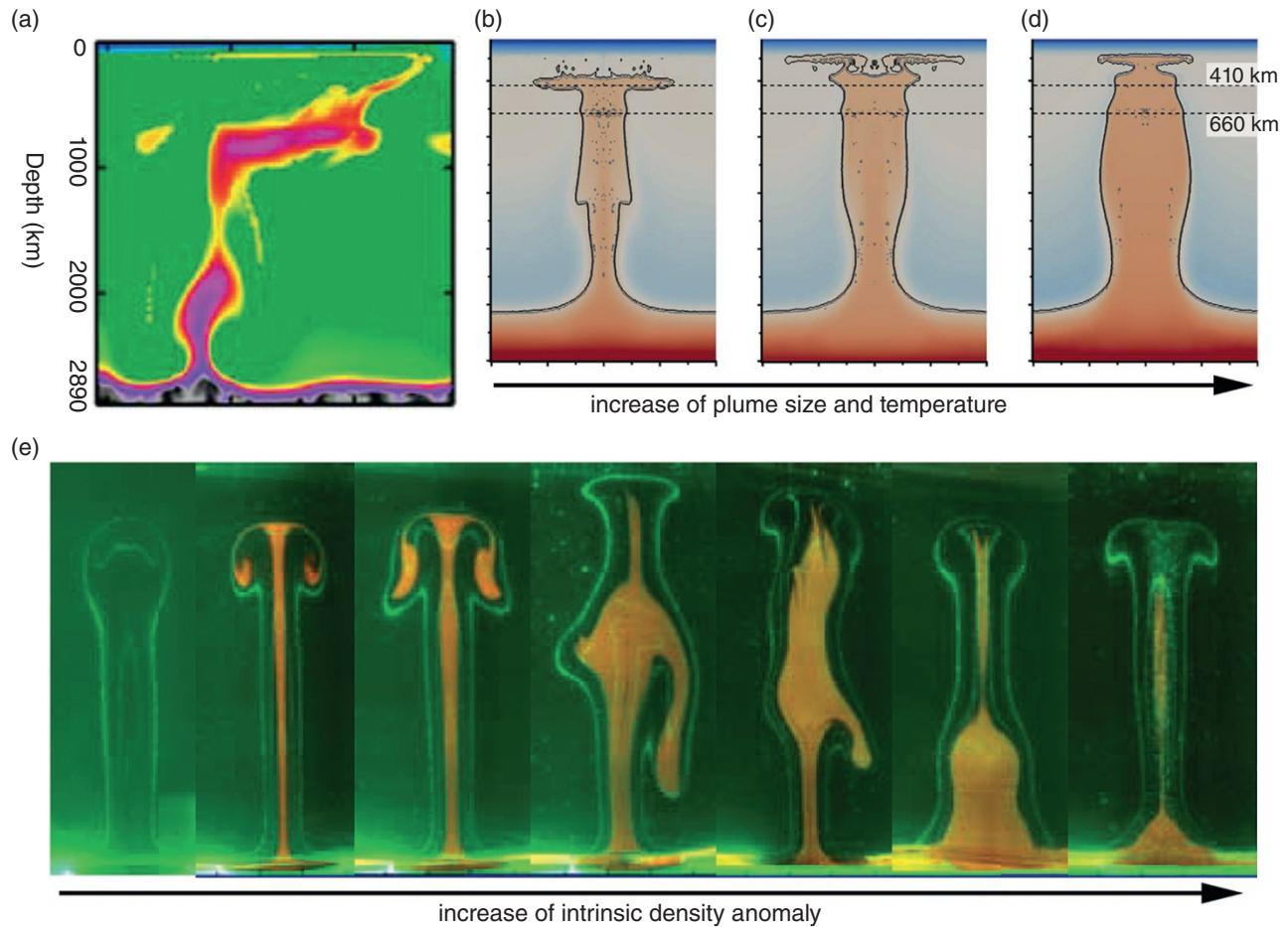


Figure 12.9 A variety of behaviors of thermochemical plumes that entrain CDMs. (a) Results from numerical modeling experiments showing a thermochemical plume ponding at the base of mantle transition zone with a small filament rising to the upper mantle. (b) A small thermochemical plume ponding at ~300–400 km depth. (c) An intermediate, primary, thermochemical plume ponding at ~300–400 km. Secondary plumes form on the top the primary plume and reach the base of the lithosphere. (d) A large thermochemical plume rising directly to the base of the lithosphere. (e) Changing morphology of thermochemical plumes (orange) as the intrinsic density of the entrained CDMs increases. *Source:* (a) Farnetani and Samuel (2005), (b–d) Modified from Dannberg and Sobolev (2015), (e) Kumagai et al. (2008).

are gradually mixed into the background mantle. The size of the entrained oceanic crust also decreases with time due to stretching (e.g., McKenzie, 1979; Manga, 1996). Similar to the recycled oceanic crust, the entrainment of other types of CDMs (e.g., the more-primitive materials and the products of core–mantle interaction) into mantle plumes may also cause ponding of plumes at a variety of depths, and these materials may be gradually mixed into the background mantle.

This chapter focuses on the fate of subducted oceanic crust in the deep mantle. However, there is possibility that some subducted oceanic crust may not sink to the deep mantle at all. Through numerical modeling, Castro & Gerya (2008) showed that the subducted upper oceanic crust may be partially molten at subduction channels and rise through the hot asthenospheric wedge to the base of the lithosphere. It has

also been suggested that the subducted oceanic crust may remain buoyant at depths up to 140 km, due to mixing with buoyant sediments, partial melting and a greater depth for the eclogite transform for dry crust (Hacker, 1996). In that case, the subducted oceanic crust may rise from ~80–120 km to the base of the lithosphere without entering the deeper mantle (Mauder et al., 2016).

12.4. SUMMARY AND FUTURE WORK

The variable behaviors of subducted oceanic crust in the deep mantle is summarized in Figure 12.10. Although slabs may be laterally deflected at 660 km depth or in the lowermost upper mantle, they may eventually sink to the lowermost mantle (Figures 12.10a–c). The subducted

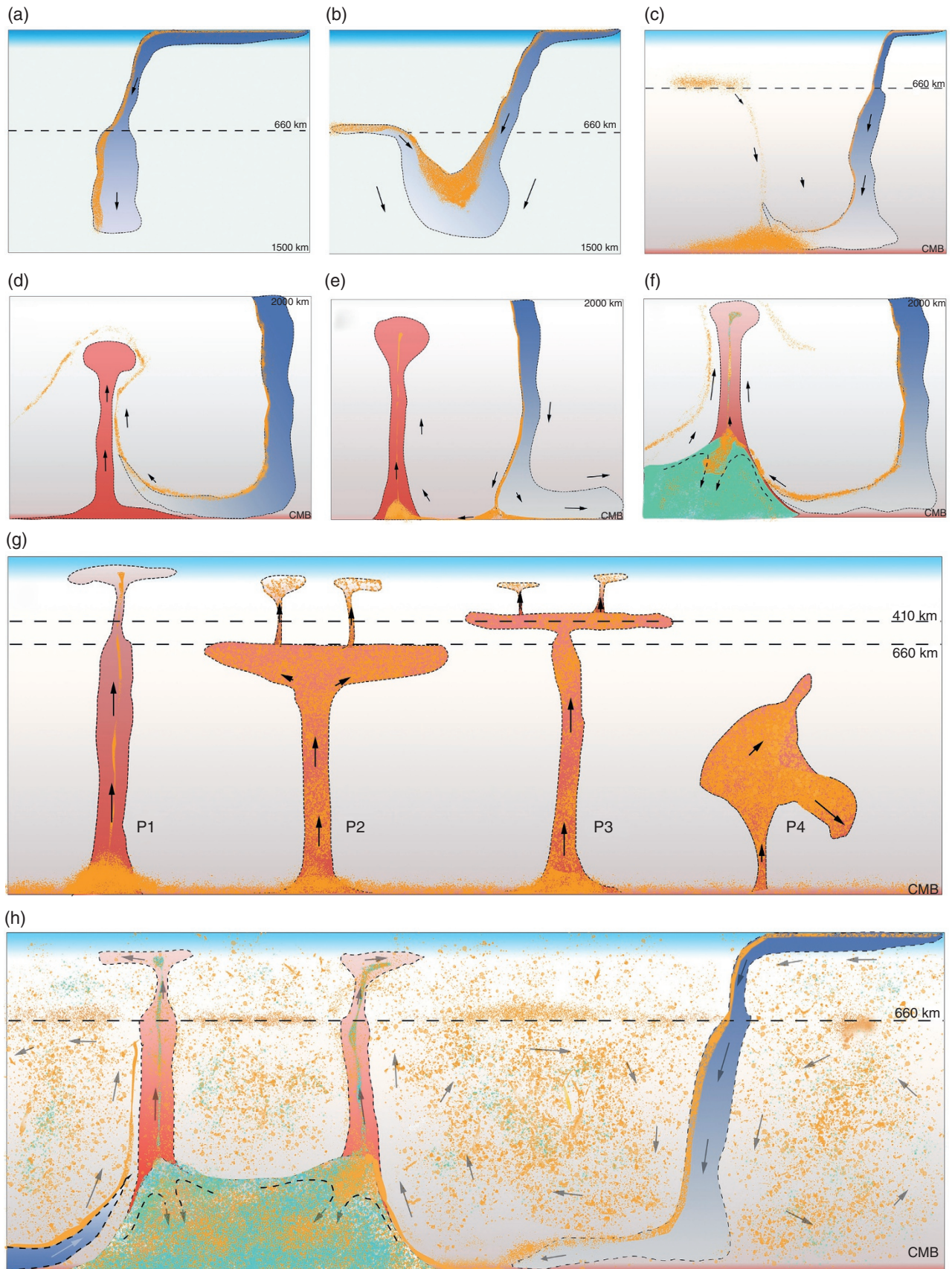


Figure 12.10 Cartoons showing the cycling of subducted oceanic crust in the deep mantle. Yellow: subducted oceanic crust; blue = subducting slabs; red: mantle plume; cyan: thermochemical piles; arrows: mantle flow velocity. (a) Subducted oceanic crust directly sinks to the lower mantle with a slab. (b) Previous accumulation

oceanic crust may be carried with the cold slabs to the lowermost mantle (Figure 12.10a) or may be separated from the rest of the slabs near the base of the transition zone (Figure 12.10b). The separated crustal materials may accumulate in the transition zone, and episodically sink to the bottom of the mantle (Figures 12.10b–c).

The ability of the subducted oceanic crust to accumulate on the CMB is strongly controlled by the thickness and the intrinsic density of the crust, and the lowermost mantle viscosity and mantle flow velocity. As predicted by the Stokes equation, a thick and dense subducted oceanic crust in a low viscosity lowermost mantle is more likely to segregate and accumulate on the CMB than a thin and light crust in a high viscosity lowermost mantle. A subducted oceanic crust being directly dragged to upwelling regions without contacting the CMB is less likely to accumulate on the CMB (Figure 12.10d) than a crust that reaches the CMB before being advected to upwelling regions in the lowermost mantle (Figure 12.10e). Accumulated oceanic crust on the CMB can be shaped into thermochemical piles by mantle flows, and newly subducted oceanic crust could be stirred into the existing thermochemical piles from their top (Figure 12.10f).

Some of the compositional heterogeneities in the lowermost mantle that are intrinsically denser than the background mantle (e.g., the accumulations of subducted oceanic crust), which are referred to CDMs in this study, are gradually entrained upward by mantle plumes. The entrainment rate strongly increases with a decrease in the intrinsic density anomaly of the CDMs and is affected by the vigor of mantle convection. The entrainment process is also controlled by the viscosity contrast between the CDMs and the background mantle and may reach maximum entrainment rate when they have similar viscosity. The entrainment of negatively buoyant materials reduces the buoyancy of mantle plumes. While a mantle plume

that entrains relatively small amount of CDMs may carry the entrained materials to the base of the lithosphere (Figure 12.10g, P1), a thermochemical plume that entrains a great amount of CDMs may pond at the base of mantle transition zone (Figure 12.10g, P2), at ~300–400 km (Figure 12.10g, P3) or the deep lower mantle (Figure 12.10g, P4), where it may sink downward (Figure 12.10g, P4).

Subducted oceanic crust that does not accumulate on the CMB may be directly entrained upward by plumes or by upwelling mantle flows that are viscously coupled with plumes (Figures 12.10d, 10f). Recycled oceanic crust may be gradually mixed into the background mantle, and a variety of crustal concentrations in the background mantle is expected due to variations of degree of mixing (Figure 12.10h). The oceanic crust directly entrained up by mantle plumes from the lowermost mantle to melting regions may be much younger than that which first accumulates on the CMB and is later sampled by mantle plumes.

Given the possibilities above, the geochemical, petrological, and seismic constraints on the distribution of subducted oceanic crust in the deep mantle may be a consequence of the long-term cycling of subducted oceanic crust throughout the mantle. The greater enrichment of recycled oceanic crust in OIB sources relative to MORB sources may be because large amount of recycled oceanic crust can be entrained upward by plumes to the uppermost mantle, whereas the concentration of recycled oceanic crust in MORB sources is diluted through efficient mixing with background mantle materials. The relative depletion of subducted oceanic crust in the upper mantle may be caused by the preferential sinking of the subducted oceanic crust to the lower mantle (e.g., Davies, 2006). The vastly different ages of recycled oceanic crust in OIB sources may be due to mantle plumes entraining both young subducted oceanic crust from the newly

Figure 12.10 (Continued) of subducted oceanic crust at the base of mantle transition zone sinks to the lower mantle. Some oceanic crust remains at the base of the transition zone. (c) When large blobs of accumulated oceanic crust at the base of the transition zone sinks to the lowermost mantle, they easily accumulate on the CMB due to its large negative buoyancy. (d) As the subducted oceanic crust reaches the lowermost mantle, it is directly carried up by a mantle plume without contacting the CMB. The crust does not enter plume regions. (e) The subducted oceanic crust directly sinks to the CMB and accumulates at the base of a mantle plume. A small amount of the crustal accumulation is entrained into the plume and carried to shallower depths. (f) The subducted oceanic crust flushes into the intrinsically dense thermochemical piles from the top of the piles. The mantle plume entrains both subducted oceanic crust and pile materials that may be previously accumulated subducted oceanic crust or other types of CDMs. (g) Variable behaviors of thermochemical plumes. P1: a plume entrains a small amount of recycled oceanic crust and rises to the base of the lithosphere. P2: a thermochemical plume ponding beneath the 660 km discontinuity with secondary plumes forming on top of it and rising to the base of the lithosphere. P3: a thermochemical plume ponding at 400 km depth with secondary plumes forming on top of it and rising to the base of the lithosphere. P4: a thermochemical plume becomes stagnant at deep lower mantle with part of it sinking down. (h) A global distribution of subducted oceanic crust in the deep mantle. The subducted oceanic crust is eventually mixed into the background mantle.

subducted slabs and old oceanic crustal materials from the relatively old crustal accumulations on the CMB. The seismic anomalies near the base of the mantle transition zone may be caused by the separation of subducted oceanic crust from the rest of the subducting slabs, the ponding of thermochemical plumes in the uppermost lower mantle, and the trapped recycled oceanic crustal materials that are passively advected in the background mantle flow. The widespread seismic scatterers with different sizes distributed throughout the mantle may be caused by subducting oceanic crust and/or entrained oceanic crust that is sinking, rising, or in the process of mixing with the background mantle. Large accumulations of subducted oceanic crust on the CMB are not physically impossible and may cause the LLSVPs. Partial melting of subducted oceanic crust that reaches the CMB before being advected to upwelling regions may explain the ULVZs outside of the LLSVPs.

However, as discussed in this chapter, the dynamics and distribution of the subducted oceanic crust in the deep mantle are controlled by many factors, including the viscosity, density, and thickness of the subducted oceanic crust, the nature of the phase transition at 660 km, the dynamics of subducting slabs, the lowermost mantle viscosity, the vigor and pattern of mantle convection, and the strength of mantle plumes. Our current limited understanding on these factors obscures a more complete story regarding the evolving distribution of subducted oceanic crust in the deep mantle. Looking forward, we need more seismic and geochemical constraints of the distribution of subducted oceanic crust in the deep mantle and improved understanding on the seismic velocities of subducted oceanic crust. Improved understanding of how composition of lavas provides information about the composition of melting sources is also required. We need to further examine the density and viscosity of subducted oceanic crust and how these properties are affected by changes of crustal composition and water content, through high-pressure-temperature experiments. Some future work on the numerical modeling and laboratory experiments include: (1) better quantifying the time-evolution of the entrainment rate of recycled oceanic crust, (2) systematically examining the dynamics of thermochemical plumes and how this evolves with time, (3) better understanding the mechanism for the generation of asymmetric subduction and how it affects the dynamics of subducted oceanic crust in the deep mantle, (4) better understanding the role of continental lithosphere on the subduction of oceanic crust, and (5) performing high-resolution 3D global calculations with realistic mantle convection patterns emulating the past several hundred millions of years to help understand the present-day distribution of subducted oceanic crust in the deep mantle.

ACKNOWLEDGMENTS

I thank Julian Lowman and an anonymous reviewer for their reviews, and Editor Maxim Ballmer for his comments. This work is supported by NSF grant EAR-1849949 and EAR-1855624.

REFERENCES

- Agrusta, R., S. Goes, & J. van Hunen (2017). Subducting-slab transition-zone interaction: Stagnation, penetration and mode switches, *Earth Planet. Sci. Lett.*, *464*, 10–23, doi:10.1016/j.epsl.2017.02.005.
- Ammann, M. W., J. P. Brodholt, J. Wookey, & D. P. Dobson (2010). First-principles constraints on diffusion in lower-mantle minerals and a weak D" layer, *Nature*, *465*(7297), 462–465, doi:10.1038/nature09052.
- Anderson, D. L. (1979). Chemical Stratification of the Mantle, *J. Geophys. Res.*, *84*(Nb11), 6297–6298, doi:10.1029/JB084iB11p06297.
- Andraut, D., G. Pesce, M. A. Bouhifd, N. Bolfan-Casanova, J.-M. Hénot, & M. Mezouar (2014). Melting of subducted basalt at the core–mantle boundary, *Science*, *344*(6186), 892–895, doi:10.1126/science.1250466.
- Aoki, I., & E. Takahashi (2004). Density of MORB eclogite in the upper mantle, *Phys. Earth Planet. Int.*, *143–44*, 129–143, doi:10.1016/j.pepi.2003.10.007.
- Ballhaus, C., R. F. Berry, & D. H. Green (1990). Oxygen fugacity controls in the Earth's upper mantle, *Nature*, *348*(6300), 437–440.
- Ballmer, M. D., G. Ito, C. J. Wolfe, & S. C. Solomon (2013). Double layering of a thermochemical plume in the upper mantle beneath Hawaii, *Earth Planet. Sci. Lett.*(0), doi:10.1016/j.epsl.2013.06.022.
- Ballmer, M. D., N. C. Schmerr, T. Nakagawa, & J. Ritsema (2015). Compositional mantle layering revealed by slab stagnation at ~1000-km depth, *Sci Adv*, *1*(11), e1500815, doi:10.1126/sciadv.1500815.
- Bataille, K., & F. Lund (1996). Strong scattering of short-period seismic waves by the core–mantle boundary and the P-diffracted wave, *Geophys. Res. Lett.*, *23*(18), 2413–2416, doi:10.1029/96gl02225.
- Bijwaard, H., W. Spakman, & E. R. Engdahl (1998). Closing the gap between regional and global travel time tomography, *J. Geophys. Res.*, *103*(B12), 30055–30078, doi:10.1029/98jb02467.
- Billen, M. I. (2008). Modeling the Dynamics of Subducting Slabs, *Annual Review of Earth and Planetary Sciences*, *36*(1), 325–356, doi:10.1146/annurev.earth.36.031207.124129.
- Brandenburg, J. P., & P. E. van Keken (2007a). Deep storage of oceanic crust in a vigorously convecting mantle, *J. Geophys. Res.*, *112*(B6), B06403, doi:10.1029/2006jb004813.
- Brandenburg, J. P., & P. E. van Keken (2007b). Methods for thermochemical convection in Earth's mantle with force-balanced plates, *Geochem. Geophys. Geosyst.*, *8*(11), Q11004, doi:10.1029/2007gc001692.

- Brown, E. L., & C. E. Lesher (2014). North Atlantic magmatism controlled by temperature, mantle composition and buoyancy, *Nat. Geosci.*, doi:10.1038/ngeo2264.
- Brown, J. M., & T. J. Shankland (1981). Thermodynamic Parameters in the Earth as Determined from Seismic Profiles, *Geophysical Journal of the Royal Astronomical Society*, 66(3), 579–596, doi:10.1111/j.1365-246X.1981.tb04891.x.
- Buffett, B. A., E. J. Garnero, & R. Jeanloz (2000). Sediments at the Top of Earth's Core, *Science*, 290(5495), 1338–1342, doi:10.1126/science.290.5495.1338.
- Burke, K., B. Steinberger, T. H. Torsvik, & M. A. Smethurst (2008). Plume generation zones at the margins of large low shear velocity provinces on the core–mantle boundary, *Earth Planet. Sci. Lett.*, 265(1–2), 49–60, doi:10.1016/j.epsl.2007.09.042.
- Cabral, R. A., M. G. Jackson, E. F. Rose-Koga, K. T. Koga, M. J. Whitehouse, M. A. Antonelli, J. Farquhar, J. M. Day, & E. H. Hauri (2013). Anomalous sulphur isotopes in plume lavas reveal deep mantle storage of Archaean crust, *Nature*, 496(7446), 490–493, doi:10.1038/nature12020.
- Cagney, N., F. Cramer, W. H. Newsome, C. Lithgow-Bertelloni, A. Cotel, S. R. Hart, & J. A. Whitehead (2016). Constraining the source of mantle plumes, *Earth Planet. Sci. Lett.*, 435, 55–63, doi:10.1016/j.epsl.2015.12.008.
- Cammarano, F., B. Romanowicz, L. Stixrude, C. Lithgow-Bertelloni, & W. Xu (2009). Inferring the thermochemical structure of the upper mantle from seismic data, *Geophys. J. Int.*, 179(2), 1169–1185, doi:10.1111/j.1365-246X.2009.04338.x.
- Castro, A., & T. V. Gerya (2008). Magmatic implications of mantle wedge plumes: Experimental study, *Lithos*, 103(1), 138–148, doi:10.1016/j.lithos.2007.09.012.
- Christensen, U. R. (1996). The influence of trench migration on slab penetration into the lower mantle, *Earth Planet. Sci. Lett.*, 140(1–4), 27–39, doi:10.1016/0012-821x(96)00023-4.
- Christensen, U. R. (1997). Influence of chemical buoyancy on the dynamics of slabs in the transition zone, *J. Geophys. Res.*, 102(B10), 22435–22443, doi:10.1029/97jb01342.
- Christensen, U. R., & A. W. Hofmann (1994). Segregation of subducted oceanic crust in the convecting mantle, *J. Geophys. Res.*, 99(B10), 19867–19884, doi:10.1029/93JB03403.
- Christensen, U. R., R. K. O. Apos, Nions, R. Clayton, & B. Parsons (1989). Models of mantle convection: one or several layers, *Philosophical Transactions of the Royal Society of London. Series A, Mathematical and Physical Sciences*, 328(1599), 417–424, doi:10.1098/rsta.1989.0045.
- Christensen, U. R., & D. A. Yuen (1984). The Interaction of a Subducting Lithospheric Slab with a Chemical or Phase-Boundary, *J. Geophys. Res.*, 89(Nb6), 4389–4402, doi:10.1029/Jb089ib06p04389.
- Christensen, U. R., & D. A. Yuen (1985). Layered Convection Induced by Phase-Transitions, *J. Geophys. Res.*, 90(B12), 10, 291–210, 300, doi:10.1029/Jb090ib12p10291.
- Cormier, V. F. (1999). Anisotropy of heterogeneity scale lengths in the lower mantle from PKIKP precursors, *Geophys. J. Int.*, 136(2), 373–384, doi:10.1046/j.1365-246X.1999.00736.x.
- Cottaar, S., & V. Lekic (2016). Morphology of seismically slow lower-mantle structures, *Geophys. J. Int.*, 207(2), 1122–1136, doi:10.1093/gji/ggw324.
- Cramer, F., Conrad, C. P., Montési, L., & Lithgow-Bertelloni, C. R. (2019). The dynamic life of an oceanic plate. *Tectonophysics*, 760, 107–135, doi: 10.1016/j.tecto.2018.03.016.
- Dannberg, J., & S. V. Sobolev (2015). Low-buoyancy thermochemical plumes resolve controversy of classical mantle plume concept, *Nat Commun*, 6, doi:10.1038/ncomms7960.
- Davaille, A. (1999a). Simultaneous generation of hotspots and superswells by convection in a heterogeneous planetary mantle, *Nature*, 402(6763), 756–760, doi:10.1038/45461.
- Davaille, A. (1999b). Two-layer thermal convection in miscible viscous fluids, *J. Fluid Mech.*, 379, 223–253, doi:10.1017/S0022112098003322.
- Davaille, A., F. Girard, & M. Le Bars (2002). How to anchor hotspots in a convecting mantle?, *Earth Planet. Sci. Lett.*, 203(2), 621–634, doi:10.1016/S0012-821X(02)00897-X.
- Davies, G. F. (1992). On the Emergence of Plate-Tectonics, *Geology*, 20(11), 963–966, doi:10.1130/0091-7613(1992)020<0963:Oteopt>2.3.Co;2.
- Davies, G. F. (2002). Stirring geochemistry in mantle convection models with stiff plates and slabs, *Geochim. Cosmochim. Acta*, 66(17), 3125–3142, doi:10.1016/S0016-7037(02)00915-8.
- Davies, G. F. (2006). Gravitational depletion of the early Earth's upper mantle and the viability of early plate tectonics, *Earth Planet. Sci. Lett.*, 243(3–4), 376–382, doi:10.1016/j.epsl.2006.01.053.
- Davies, G. F. (2007). Controls on density stratification in the early mantle, *Geochem. Geophys. Geosyst.*, 8(4), Q04006, doi:10.1029/2006gc001414.
- Davies, G. F. (2008). Episodic layering of the early mantle by the 'basalt barrier' mechanism, *Earth Planet. Sci. Lett.*, 275(3–4), 382–392, doi:10.1016/j.epsl.2008.08.036.
- Delavault, H., C. Chauvel, A. Sobolev, & V. Batanova (2015). Combined petrological, geochemical and isotopic modeling of a plume source: Example of Gambier Island, Pitcairn chain, *Earth Planet. Sci. Lett.*, 426(0), 23–35, doi:10.1016/j.epsl.2015.06.013.
- Deschamps, F., E. Kaminski, & P. J. Tackley (2011). A deep mantle origin for the primitive signature of ocean island basalt, *Nat. Geosci.*, 4(12), 879–882, doi:10.1038/Ngeo1295.
- Deschamps, F., & P. J. Tackley (2008). Searching for models of thermo-chemical convection that explain probabilistic tomography, *Phys. Earth Planet. Int.*, 171(1–4), 357–373, doi:10.1016/j.pepi.2008.04.016.
- Deschamps, F., & P. J. Tackley (2009). Searching for models of thermo-chemical convection that explain probabilistic tomography. II—Influence of physical and compositional parameters, *Phys. Earth Planet. Int.*, 176(1–2), 1–18, doi:10.1016/j.pepi.2009.03.012.
- Dziewonski, A. M., & D. L. Anderson (1981). Preliminary Reference Earth Model, *Phys. Earth Planet. Int.*, 25(4), 297–356, doi:10.1016/0031-9201(81)90046-7.
- Eagar, K. C., M. J. Fouch, & D. E. James (2010). Receiver function imaging of upper mantle complexity beneath the Pacific Northwest, United States, *Earth Planet. Sci. Lett.*, 297(1–2), 141–153, doi:10.1016/j.epsl.2010.06.015.
- Earle, P. S., & P. M. Shearer (1997). Observations of PKKP precursors used to estimate small-scale topography on the core–mantle boundary, *Science*, 277(5326), 667–670, doi:10.1126/science.277.5326.667.

- Farnetani, D. G., & M. A. Richards (1995). Thermal entrainment and melting in mantle plumes, *Earth Planet. Sci. Lett.*, *136*(3–4), 251–267, doi:10.1016/0012-821x(95)00158-9.
- Farnetani, C. G. (1997). Excess temperature of mantle plumes: The role of chemical stratification across D", *Geophys. Res. Lett.*, *24*(13), 1583–1586, doi:10.1029/97gl01548.
- Farnetani, C. G., & H. Samuel (2005). Beyond the thermal plume paradigm, *Geophys. Res. Lett.*, *32*(7), doi:10.1029/2005gl022360.
- Fischer, R., & T. Gerya (2016). Early Earth plume-lid tectonics: A high-resolution 3D numerical modelling approach, *Journal of Geodynamics*, *100*, 198–214, doi:10.1016/j.jog.2016.03.004.
- Frost, D. A., S. Rost, E. J. Garnero, & M. Li (2017). Seismic evidence for Earth's crusty deep mantle, *Earth Planet. Sci. Lett.*, *470*, 54–63, doi:10.1016/j.epsl.2017.04.036.
- Frost, D. J., & C. A. McCammon (2008). The redox state of Earth's mantle, *Annual Review of Earth and Planetary Sciences*, *36*, 389–420, doi:10.1146/annurev.earth.36.031207.124322.
- Fujita, K., & M. Ogawa (2009). Basaltic accumulation instability and chaotic plate motion in the earliest mantle inferred from numerical experiments, *J. Geophys. Res.*, *114*, B10402, doi:10.1029/2008jb006222.
- Fukao, Y., & M. Obayashi (2013). Subducted slabs stagnant above, penetrating through, and trapped below the 660 km discontinuity, *J. Geophys. Res.*, *118*(11), 5920–5938, doi:10.1002/2013jb010466.
- Fukao, Y., M. Obayashi, H. Inoue, & M. Nenbai (1992). Subducting Slabs Stagnant in the Mantle Transition Zone, *J. Geophys. Res.*, *97*(B4), 4809–4822, doi:10.1029/91jb02749.
- Fukao, Y., M. Obayashi, & T. Nakakuki (2009). Stagnant Slab: A Review, *Annual Review of Earth and Planetary Sciences*, *37*(1), 19–46, doi:10.1146/annurev.earth.36.031207.124224.
- Fukao, Y., S. Widiyantoro, & M. Obayashi (2001). Stagnant slabs in the upper and lower mantle transition region, *Rev. Geophys.*, *39*(3), 291–323, doi:10.1029/1999rg000068.
- Gaherty, J. B., & B. H. Hager (1994). Compositional vs. thermal buoyancy and the evolution of subducted lithosphere, *Geophys. Res. Lett.*, *21*(2), 141–144, doi:10.1029/93gl03466.
- Ganguly, J., A. M. Freed, & S. K. Saxena (2008). Density profiles of oceanic slabs and surrounding mantle: Integrated thermodynamic and thermal modeling, and implications for the fate of slabs at the 660km discontinuity, *Phys. Earth Planet. Int.*, *172*(3–4), 257–267, doi:10.1016/j.pepi.2008.10.005.
- Garnero, E. J., A. K. McNamara, & S.-H. Shim (2016). Continent-sized anomalous zones with low seismic velocity at the base of Earth's mantle, *Nat. Geosci.*, *9*(7), 481–489, doi:10.1038/ngeo2733.
- Goes, S., R. Agrusta, J. Van Hunen, & F. Garel (2017). Subduction-transition zone interaction: A review, *Geosphere*, *13*(3), 644–664.
- Goes, S., F. Capitanio, & G. Morra (2008). Evidence of lower-mantle slab penetration phases in plate motions, *Nature*, *451* (7181), 981–985, doi:10.1038/nature06691.
- Gonnermann, H. M., M. Manga, & A. M. Jellinek (2002). Dynamics and longevity of an initially stratified mantle, *Geophys. Res. Lett.*, *29*(10), doi:10.1029/2002gl014851.
- Grand, S. P. (2002). Mantle shear-wave tomography and the fate of subducted slabs, *Philosophical Transactions of the Royal Society of London Series a-Mathematical Physical and Engineering Sciences*, *360*(1800), 2475–2491, doi:10.1098/rsta.2002.1077.
- Grand, S. P., R. D. van der Hilst, & S. Widiyantoro (1997). Global seismic tomography: a snapshot of convection in the Earth, *GSA Today*, *7*, 1–7.
- Gréaux, S., T. Irifune, Y. Higo, Y. Tange, T. Arimoto, Z. Liu, & A. Yamada (2019). Sound velocity of CaSiO₃ perovskite suggests the presence of basaltic crust in the Earth's lower mantle, *Nature*, *565*(7738), 218–221, doi:10.1038/s41586-018-0816-5.
- Green, D. H., & A. E. Ringwood (1967). An experimental investigation of the gabbro to eclogite transformation and its petrological applications, *Geochim. Cosmochim. Acta*, *31*(5), 767–833, doi:10.1016/s0016-7037(67)80031-0.
- Gurnis, M. (1986). The Effects of Chemical Density Differences on Convective Mixing in the Earth's Mantle, *J. Geophys. Res.*, *91*(B11), 1407–1419, doi:10.1029/Jb091ib11p11407.
- Hacker, B. R. (1996). Eclogite formation and the Rheology, Buoyancy, Seismicity, and H₂O Content of Oceanic Crust, in *Subduction Top to Bottom*, edited, pp. 337–346, doi:10.1029/GM096p0337.
- Hauri, E. H., & S. R. Hart (1993). Re-Os Isotope Systematics of Himu and Emii Oceanic Island Basalts from the South-Pacific Ocean, *Earth Planet. Sci. Lett.*, *114*(2–3), 353–371, doi:10.1016/0012-821x(93)90036-9.
- Hedlin, M. A. H., & P. M. Shearer (2002). Probing mid-mantle heterogeneity using PKP coda waves, *Phys. Earth Planet. Int.*, *130*(3–4), 195–208.
- Helfrich, G., M. D. Ballmer, & K. Hirose (2018). Core-Exsolved SiO₂ Dispersal in the Earth's Mantle, *J. Geophys. Res.*, *123*(1), 176–188, doi:10.1002/2017jb014865.
- Herzberg, C., K. Condie, & J. Korenaga (2010). Thermal history of the Earth and its petrological expression, *Earth Planet. Sci. Lett.*, *292*(1–2), 79–88, doi:10.1016/j.epsl.2010.01.022.
- Heyn, B. H., C. P. Conrad, & R. G. Trønnes (2018). Stabilizing Effect of Compositional Viscosity Contrasts on Thermochemical Piles, *Geophys. Res. Lett.*, *0*(ja), doi:10.1029/2018gl078799.
- Hirose, K., Y. W. Fei, Y. Z. Ma, & H. K. Mao (1999). The fate of subducted basaltic crust in the Earth's lower mantle, *Nature*, *397*(6714), 53–56, doi:10.1038/16225.
- Hirose, K., G. Morard, R. Sinmyo, K. Umemoto, J. Hernlund, G. Helfrich, & S. Labrosse (2017). Crystallization of silicon dioxide and compositional evolution of the Earth's core, *Nature*, *543*(7643), 99–102, doi:10.1038/nature21367.
- Hirose, K., N. Takafuji, N. Sata, & Y. Ohishi (2005). Phase transition and density of subducted MORB crust in the lower mantle, *Earth Planet. Sci. Lett.*, *237* (1–2), 239–251, doi:10.1016/j.epsl.2005.06.035.
- Hofmann, A. W. (1988). Chemical differentiation of the Earth: the relationship between mantle, continental crust, and oceanic crust, *Earth Planet. Sci. Lett.*, *90*(3), 297–314, doi:10.1016/0012-821x(88)90132-X.
- Hofmann, A. W. (1997). Mantle geochemistry: The message from oceanic volcanism, *Nature*, *385*(6613), 219–229, doi:10.1038/385219a0.
- Hofmann, A. W., & W. M. White (1982). Mantle Plumes from Ancient Oceanic-Crust, *Earth Planet. Sci. Lett.*, *57*(2), 421–436, doi:10.1016/0012-821x(82)90161-3.
- Huang, J., & G. F. Davies (2007). Stirring in three-dimensional mantle convection models and implications for geochemistry:

2. Heavy tracers, *Geochemistry, Geophysics, Geosystems*, 8(7), doi:10.1029/2007gc001621.
- Hunt, S. A., D. J. Weidner, L. Li, L. P. Wang, N. P. Walte, J. P. Brodholt, & D. P. Dobson (2009). Weakening of calcium iridate during its transformation from perovskite to post-perovskite, *Nat. Geosci.*, 2(11), 794–797, doi:10.1038/Ngeo663.
- Irifune, T., & A. E. Ringwood (1993). Phase-Transformations in Subducted Oceanic-Crust and Buoyancy Relationships at Depths of 600–800 Km in the Mantle, *Earth Planet. Sci. Lett.*, 117(1–2), 101–110, doi:10.1016/0012-821x(93)90120-X.
- Jarvis, G. T., & J. P. Lowman (2007). Survival times of subducted slab remnants in numerical models of mantle flow, *Earth Planet. Sci. Lett.*, 260(1–2), 23–36, doi:10.1016/j.epsl.2007.05.009.
- Jellinek, A. M., & M. Manga (2002). The influence of a chemical boundary layer on the fixity, spacing and lifetime of mantle plumes, *Nature*, 418(6899), 760–763, doi:10.1038/Nature00979.
- Johnson, T. E., M. Brown, B. J. P. Kaus, & J. A. VanTongeren (2014). Delamination and recycling of Archaean crust caused by gravitational instabilities, *Nat. Geosci.*, 7(1), 47–52, doi:10.1038/Ngeo2019.
- Jones, T. D., D. R. Davies, I. H. Campbell, C. R. Wilson, & S. C. Kramer (2016). Do mantle plumes preserve the heterogeneous structure of their deep-mantle source?, *Earth Planet. Sci. Lett.*, 434, 10–17, doi:10.1016/j.epsl.2015.11.016.
- Jones, T. D., D. R. Davies, & P. A. Sossi (2019). Tungsten isotopes in mantle plumes: Heads it's positive, tails it's negative, *Earth Planet. Sci. Lett.*, 506, 255–267, doi:10.1016/j.epsl.2018.11.008.
- Kaneshima, S. (2016). Seismic scatterers in the mid-lower mantle, *Phys. Earth Planet. Int.*, 257, 105–114, doi:10.1016/j.pepi.2016.05.004.
- Kaneshima, S., & G. Helffrich (1999). Dipping low-velocity layer in the mid-lower mantle: evidence for geochemical heterogeneity, *Science*, 283(5409), 1888–1891, doi:10.1126/science.283.5409.1888.
- Kaneshima, S., & G. Helffrich (2003). Subparallel dipping heterogeneities in the mid-lower mantle, *J. Geophys. Res.*, 108(B5), doi:10.1029/2001jb001596.
- Karato, S. (1997). On the separation of crustal component from subducted oceanic lithosphere near the 660 km discontinuity, *Phys. Earth Planet. Int.*, 99(1–2), 103–111, doi:10.1016/S0031-9201(96)03198-6.
- Karato, S., Z. C. Wang, B. Liu, & K. Fujino (1995). Plastic-Deformation of Garnets - Systematics and Implications for the Rheology of the Mantle Transition Zone, *Earth Planet. Sci. Lett.*, 130(1–4), 13–30, doi:10.1016/0012-821x(94)00255-W.
- Kasting, J. F., D. H. Egger, & S. P. Raeburn (1993). Mantle Redox Evolution and the Oxidation State of the Archaean Atmosphere, *The Journal of Geology*, 101(2), 245–257, doi:10.2307/30081150.
- Katayama, I., & S. I. Karato (2008). Effects of water and iron content on the rheological contrast between garnet and olivine, *Phys. Earth Planet. Int.*, 166(1–2), 57–66, doi:10.1016/j.pepi.2007.10.004.
- Kawai, K., T. Tsuchiya, J. Tsuchiya, & S. Maruyama (2009). Lost primordial continents, *Gondwana Research*, 16(3–4), 581–586, doi:10.1016/J.Gr.2009.05.012.
- Kellogg, L. H., & S. D. King (1993). Effect of mantle plumes on the growth of D” by reaction between the core and mantle, *Geophys. Res. Lett.*, 20(5), 379–382, doi:10.1029/93gl00045.
- Kesson, S. E., J. D. Fitz Gerald, & J. M. G. Shelley (1994). Mineral Chemistry and Density Subducted Basaltic Crust at Lower-Mantle Pressures, *Nature*, 372(6508), 767–769, doi:10.1038/372767a0.
- Khan, A., L. Boschi, & J. A. D. Connolly (2009). On mantle chemical and thermal heterogeneities and anisotropy as mapped by inversion of global surface wave data, *J. Geophys. Res.*, 114(B9), doi:10.1029/2009jb006399.
- King, S. D., D. J. Frost, & D. C. Rubie (2015). Why cold slabs stagnate in the transition zone, *Geology*, 43(3), 231–234, doi:10.1130/g36320.1.
- Korenaga, J. (2004). Mantle mixing and continental breakup magmatism, *Earth Planet. Sci. Lett.*, 218(3–4), 463–473, doi:10.1016/S0012-821X(03)00674-5.
- Kubo, T., E. Ohtani, T. Kondo, T. Kato, M. Toma, T. Hosoya, A. Sano, T. Kikegawa, & T. Nagase (2002). Metastable garnet in oceanic crust at the top of the lower mantle, *Nature*, 420(6917), 803–806, doi:10.1038/nature01281.
- Kumagai, I., A. Davaille, K. Kurita, & E. Stutzmann (2008). Mantle plumes: Thin, fat, successful, or failing? Constraints to explain hot spot volcanism through time and space, *Geophys. Res. Lett.*, 35(16), L16301, doi:10.1029/2008GL035079.
- Kump, L. R., J. F. Kasting, & M. E. Barley (2001). Rise of atmospheric oxygen and the “upside-down” Archaean mantle, *Geochemistry, Geophysics, Geosystems*, 2(1), 2000GC000114, doi:10.1029/2000GC000114.
- Labrosse, S., J. W. Hernlund, & N. Coltice (2007). A crystallizing dense magma ocean at the base of the Earth’s mantle, *Nature*, 450(7171), 866–869, doi:10.1038/Nature06355.
- Le Bars, M. (2004). Whole layer convection in a heterogeneous planetary mantle, *J. Geophys. Res.*, 109(B3), doi:10.1029/2003jb002617.
- Le Bars, M., & A. Davaille (2004). Large interface deformation in two-layer thermal convection of miscible viscous fluids, *J. Fluid Mech.*, 499, 75–110, doi:10.1017/S0022112003006931.
- Lécuyer, C., & Y. Ricard (1999). Long-term fluxes and budget of ferric iron: implication for the redox states of the Earth’s mantle and atmosphere, *Earth Planet. Sci. Lett.*, 165(2), 197–211, doi:10.1016/S0012-821X(98)00267-2.
- Lee, C. T. A., P. Luffi, T. Hoink, J. Li, R. Dasgupta, & J. Hernlund (2010). Upside-down differentiation and generation of a ‘primordial’ lower mantle, *Nature*, 463(7283), 930–U102, doi:10.1038/Nature08824.
- Leng, W., & S. J. Zhong (2008). Controls on plume heat flux and plume excess temperature, *J. Geophys. Res.*, 113(B4), B04408, doi:10.1029/2007jb005155.
- Li, C., R. D. van der Hilst, E. R. Engdahl, & S. Burdick (2008). A new global model for P wave speed variations in Earth’s mantle, *Geochem. Geophys. Geosyst.*, 9(5), Q05018, doi:10.1029/2007gc001806.
- Li, J., & D. A. Yuen (2014). Mid-mantle heterogeneities associated with Izanagi plate: Implications for regional mantle viscosity, *Earth Planet. Sci. Lett.*, 385, 137–144, doi:10.1016/j.epsl.2013.10.042.
- Li, M., & A. K. McNamara (2013). The difficulty for subducted oceanic crust to accumulate at the Earth’s core–mantle boundary, *J. Geophys. Res.*, 118(4), 1807–1816, doi:10.1002/Jgrb.50156.

- Li, M., & A. K. McNamara (2018). The influence of deep mantle compositional heterogeneity on Earth's thermal evolution, *Earth Planet. Sci. Lett.*, 500, 86–96, doi:10.1016/j.epsl.2018.08.009.
- Li, M., A. K. McNamara, & E. J. Garnero (2014a). Chemical complexity of hotspots caused by cycling oceanic crust through mantle reservoirs, *Nat. Geosci.*, 7(5), 366–370, doi:10.1038/Ngeo2120.
- Li, M., A. K. McNamara, E. J. Garnero, & S. Yu (2017). Compositionally-distinct ultra-low velocity zones on Earth's core–mantle boundary, *Nature Communications*, 8, 177, doi:10.1038/s41467-017-00219-x.
- Li, M., & S. J. Zhong (2017). The source location of mantle plumes from 3D spherical models of mantle convection, *Earth Planet. Sci. Lett.*, 478, 47–57, doi:10.1016/j.epsl.2017.08.033.
- Li, M., S. J. Zhong, & P. Olson (2018). Linking lowermost mantle structure, core–mantle boundary heat flux and mantle plume formation, *Phys. Earth Planet. Int.*, 277, 10–29, doi:10.1016/j.pepi.2018.01.010.
- Li, X. D., & B. Romanowicz (1996). Global mantle shear velocity model developed using nonlinear asymptotic coupling theory, *J. Geophys. Res.*, 101(B10), 22245–22272, doi:10.1029/96JB01306.
- Li, Y., F. Deschamps, & P. J. Tackley (2014b). Effects of low-viscosity post-perovskite on the stability and structure of primordial reservoirs in the lower mantle, *Geophys. Res. Lett.*, 41(20), 7089–7097, doi:10.1002/2014GL061362.
- Li, Y., F. Deschamps, & P. J. Tackley (2014c). The stability and structure of primordial reservoirs in the lower mantle: insights from models of thermochemical convection in three-dimensional spherical geometry, *Geophys. J. Int.*, 199(2), 914–930, doi:10.1093/gji/ggu295.
- Lin, S. C., & P. E. van Keken (2005). Multiple volcanic episodes of flood basalts caused by thermochemical mantle plumes, *Nature*, 436(7048), 250–252, doi:10.1038/Nature03697.
- Litasov, K. D., E. Ohtani, & A. Sano (2006). Influence of Water on Major Phase Transitions in the Earth's Mantle, in *Earth's Deep Water Cycle*, edited, pp. 95–111, doi:10.1029/168gm08.
- Ma, X., X. Sun, D. A. Wiens, L. Wen, A. Nyblade, S. Anandkrishnan, et al. (2016). Strong seismic scatterers near the core–mantle boundary north of the Pacific Anomaly, *Phys. Earth Planet. Int.*, 253, 21–30, doi:10.1016/j.pepi.2016.01.007.
- Machetel, P., & P. Weber (1991). Intermittent Layered Convection in a Model Mantle with an Endothermic Phase-Change at 670 Km, *Nature*, 350(6313), 55–57, doi:10.1038/350055a0.
- Manga, M. (1996). Mixing of heterogeneities in the mantle: Effect of viscosity differences, *Geophys. Res. Lett.*, 23(4), 403–406, doi:10.1029/96gl00242.
- Mao, W., & S. Zhong (2018). Slab stagnation due to a reduced viscosity layer beneath the mantle transition zone, *Nat. Geosci.*, doi:10.1038/s41561-018-0225-2.
- Maunder, B., J. van Hunen, V. Magni, & P. Bouilhol (2016). Relamination of mafic subducting crust throughout Earth's history, *Earth Planet. Sci. Lett.*, 449, 206–216, doi:10.1016/j.epsl.2016.05.042.
- McCammon, C. (2005). The Paradox of Mantle Redox, *Science*, 308(5723), 807–808, doi:10.1126/science.1110532.
- McKenzie, D. (1979). Finite Deformation during Fluid-Flow, *Geophysical Journal of the Royal Astronomical Society*, 58(3), 689–715, doi: 10.1111/j.1365–246X.1979.tb04803.x.
- McKenzie, D. (1984). The Generation and Compaction of Partially Molten Rock, *J. Petrol.*, 25(3), 713–765, doi:10.1093/ptrology/25.3.713.
- McNamara, A. K. (2019). A review of large low shear velocity provinces and ultra low velocity zones, *Tectonophysics*, doi:10.1016/j.tecto.2018.04.015.
- McNamara, A. K., E. J. Garnero, & S. Rost (2010). Tracking deep mantle reservoirs with ultra-low velocity zones, *Earth Planet. Sci. Lett.*, 299(1–2), 1–9, doi:10.1016/j.epsl.2010.07.042.
- McNamara, A. K., & S. J. Zhong (2004). Thermochemical structures within a spherical mantle: Superplumes or piles?, *J. Geophys. Res.*, 109(B7), B07402, doi:10.1029/2003jb002847.
- Miller, M. S., & F. Niu (2008). Bulldozing the core–mantle boundary: Localized seismic scatterers beneath the Caribbean Sea, *Phys. Earth Planet. Int.*, 170(1–2), 89–94, doi:10.1016/j.pepi.2008.07.044.
- Montague, N. L., & L. H. Kellogg (2000). Numerical models of a dense layer at the base of the mantle and implications for the geodynamics of D", *J. Geophys. Res.*, 105(B5), 11101–11114, doi:10.1029/1999jb900450.
- Montague, N. L., L. H. Kellogg, & M. Manga (1998). High Rayleigh number thermo-chemical models of a dense boundary layer in D", *Geophys. Res. Lett.*, 25(13), 2345–2348, doi:10.1029/98GL51872.
- Motoki, M. H., & M. D. Ballmer (2015). Intraplate volcanism due to convective instability of stagnant slabs in the mantle transition zone, *Geochemistry, Geophysics, Geosystems*, 16(2), 538–551, doi:10.1002/2014GC005608.
- Mulyukova, E., B. Steinberger, M. Dabrowski, & S. V. Sobolev (2015). Survival of LLSVPs for billions of years in a vigorously convecting mantle: Replenishment and destruction of chemical anomaly, *J. Geophys. Res.*, 120(5), 3824–3847, doi:10.1002/2014jb011688.
- Nakagawa, T., & B. A. Buffett (2005). Mass transport mechanism between the upper and lower mantle in numerical simulations of thermochemical mantle convection with multicomponent phase changes, *Earth Planet. Sci. Lett.*, 230(1), 11–27, doi:10.1016/j.epsl.2004.11.005.
- Nakagawa, T., & P. J. Tackley (2004). Effects of thermochemical mantle convection on the thermal evolution of the Earth's core, *Earth Planet. Sci. Lett.*, 220(1–2), 107–119, doi:10.1016/S0012-821x(04)00055-X.
- Nakagawa, T., & P. J. Tackley (2011). Effects of low-viscosity post-perovskite on thermo-chemical mantle convection in a 3-D spherical shell, *Geophys. Res. Lett.*, 38(4), L04309, doi:10.1029/2010gl046494.
- Nakagawa, T., & P. J. Tackley (2014). Influence of combined primordial layering and recycled MORB on the coupled thermal evolution of Earth's mantle and core, *Geochemistry, Geophysics, Geosystems*, 15(3), 619–633, doi:10.1002/2013GC005128.
- Nakagawa, T., P. J. Tackley, F. Deschamps, & J. A. D. Connolly (2009). Incorporating self-consistently calculated mineral physics into thermochemical mantle convection simulations in a 3-D spherical shell and its influence on seismic anomalies in Earth's mantle, *Geochem. Geophys. Geosyst.*, 10(3), Q03004, doi:10.1029/2008gc002280.

- Nakagawa, T., P. J. Tackley, F. Deschamps, & J. A. D. Connolly (2010). The influence of MORB and harzburgite composition on thermo-chemical mantle convection in a 3-D spherical shell with self-consistently calculated mineral physics, *Earth Planet. Sci. Lett.*, 296(3–4), 403–412, doi:10.1016/j.epsl.2010.05.026.
- Nakakuki, T., M. Tagawa, & Y. Iwase (2010). Dynamical mechanisms controlling formation and avalanche of a stagnant slab, *Phys. Earth Planet. Int.*, 183(1–2), 309–320, doi:10.1016/j.pepi.2010.02.003.
- Namiki, A. (2003). Can the mantle entrain D “?, *J. Geophys. Res.*, 108(B10), doi:10.1029/2002jb002315.
- Nestola, F., et al. (2018). CaSiO₃ perovskite in diamond indicates the recycling of oceanic crust into the lower mantle, *Nature*, 555(7695), 237–241, doi:10.1038/nature25972.
- Niu, F. (2014). Distinct compositional thin layers at mid-mantle depths beneath northeast China revealed by the USArray, *Earth Planet. Sci. Lett.*, 402(0), 305–312, doi:10.1016/j.epsl.2013.02.015.
- Niu, F., H. Kawakatsu, & Y. Fukao (2003). Seismic evidence for a chemical heterogeneity in the midmantle: A strong and slightly dipping seismic reflector beneath the Mariana subduction zone, *J. Geophys. Res.*, 108(B9), doi:10.1029/2002jb002384.
- Niu, F., & L. Wen (2001). Strong seismic scatterers near the core–mantle boundary west of Mexico, *Geophys. Res. Lett.*, 28(18), 3557–3560, doi:10.1029/2001gl013270.
- O’Rourke, J. G., & D. J. Stevenson (2016). Powering Earth’s dynamo with magnesium precipitation from the core, *Nature*, 529(7586), 387–389, doi:10.1038/nature16495.
- Ogawa, M. (2000). Numerical models of magmatism in convecting mantle with temperature-dependent viscosity and their implications for Venus and Earth, *J. Geophys. Res.*, 105(E3), 6997–7012, doi:10.1029/1999JE001162.
- Ogawa, M. (2003). Chemical stratification in a two-dimensional convecting mantle with magmatism and moving plates, *J. Geophys. Res.*, 108(B12), doi:10.1029/2002jb002205.
- Ogawa, M. (2007). Superplumes, plates, & mantle magmatism in two-dimensional numerical models, *J. Geophys. Res.*, 112(B6), B06404, doi:10.1029/2006JB004533.
- Ogawa, M. (2010). Variety of plumes and the fate of subducted basaltic crusts, *Phys. Earth Planet. Int.*, 183(1–2), 366–375, doi:10.1016/j.pepi.2010.05.001.
- Ogawa, M. (2014). Two-stage evolution of the Earth’s mantle inferred from numerical simulation of coupled magmatism–mantle convection system with tectonic plates, *J. Geophys. Res.*, 119(3), 2013JB010315, doi:10.1002/2013JB010315.
- Olson, P., & C. Kincaid (1991). Experiments on the Interaction of Thermal-Convection and Compositional Layering at the Base of the Mantle, *J. Geophys. Res.*, 96(B3), 4347–4354, doi:10.1029/90jb02530.
- Ono, S., E. Ito, & T. Katsura (2001). Mineralogy of subducted basaltic crust (MORB) from 25 to 37 GPa, and chemical heterogeneity of the lower mantle, *Earth Planet. Sci. Lett.*, 190(1–2), 57–63, doi:10.1016/S0012-821x(01)00375-2.
- Pamato, M. G., R. Myhill, T. Boffa Ballaran, D. J. Frost, F. Heidelbach, & N. Miyajima (2014). Lower-mantle water reservoir implied by the extreme stability of a hydrous aluminosilicate, *Nat. Geosci.*, 8(1), 75–79, doi:10.1038/ngeo2306.
- Peacock, S. M. (1993). The Importance of Blueschist -) Eclogite Dehydration Reactions in Subducting Oceanic-Crust, *Geol. Soc. Am. Bull.*, 105(5), 684–694, doi:10.1130/0016-7606(1993)105<0684:Tiobed>2.3.Co;2.
- Peltier, W. R., & L. P. Solheim (1992). Mantle phase transitions and layered chaotic convection, *Geophys. Res. Lett.*, 19(3), 321–324, doi:10.1029/91GL02951.
- Pietruszka, A. J., M. D. Norman, M. O. Garcia, J. P. Marske, & D. H. Burns (2013). Chemical heterogeneity in the Hawaiian mantle plume from the alteration and dehydration of recycled oceanic crust, *Earth Planet. Sci. Lett.*, 361(0), 298–309, doi:10.1016/j.epsl.2012.10.030.
- Pringle, E. A., F. Moynier, P. S. Savage, M. G. Jackson, M. Moreira, & J. M. D. Day (2016). Silicon isotopes reveal recycled altered oceanic crust in the mantle sources of Ocean Island Basalts, *Geochim. Cosmochim. Acta*, 189, 282–295, doi:10.1016/j.gca.2016.06.008.
- Reisberg, L., A. Zindler, F. Marcantonio, W. White, D. Wyman, & B. Weaver (1993). Os Isotope Systematics in Ocean Island Basalts, *Earth Planet. Sci. Lett.*, 120(3–4), 149–167, doi:10.1016/0012-821x(93)90236-3.
- Richard, G. C., & D. Bercovici (2009). Water-induced convection in the Earth’s mantle transition zone, *J. Geophys. Res.*, 114(B1), doi:10.1029/2008jb005734.
- Richards, M. A., & G. F. Davies (1989). On the separation of relatively buoyant components from subducted lithosphere, *Geophys. Res. Lett.*, 16(8), 831–834, doi:10.1029/GL016i008p00831.
- Ricolleau, A., J.-P. Perrillat, G. Fiquet, I. Daniel, J. Matas, A. Addad, N. Menguy, H. Cardon, M. Mezouar, & N. Guignot (2010). Phase relations and equation of state of a natural MORB: Implications for the density profile of subducted oceanic crust in the Earth’s lower mantle, *J. Geophys. Res.*, 115(B8), B08202, doi:10.1029/2009jb006709.
- Riedel, M. R., & S. Karato (1997). Grain-size evolution in subducted oceanic lithosphere associated with the olivine-spinel transformation and its effects on rheology, *Earth Planet. Sci. Lett.*, 148(1–2), 27–43, doi:10.1016/S0012-821x(97)00016-2.
- Ringwood, A. E. (1982). Phase-Transformations and Differentiation in Subducted Lithosphere - Implications for Mantle Dynamics, Basalt Petrogenesis, and Crustal Evolution, *Journal of Geology*, 90(6), 611–643, doi:10.1086/628721.
- Ringwood, A. E. (1990). Slab-Mantle Interactions. 3. Petrogenesis of Intraplate Magmas and Structure of the Upper Mantle, *Chem. Geol.*, 82(3–4), 187–207, doi:10.1016/0009-2541(90)90081-H.
- Ringwood, A. E., & T. Irifune (1988). Nature of the 650-km seismic discontinuity: implications for mantle dynamics and differentiation, *Nature*, 331(6152), 131–136, doi:10.1038/331131a0.
- Ritsema, J., H. J. van Heijst, & J. H. Woodhouse (2004). Global transition zone tomography, *J. Geophys. Res.*, 109(B2), B02302, doi:10.1029/2003jb002610.
- Rost, S., & P. S. Earle (2010). Identifying regions of strong scattering at the core–mantle boundary from analysis of PKKP precursor energy, *Earth Planet. Sci. Lett.*, 297(3–4), 616–626, doi:10.1016/j.epsl.2010.07.014.
- Rudolph, M. L., V. Lekić, & C. Lithgow-Bertelloni (2015). Viscosity jump in Earth’s mid-mantle, *Science*, 350(6266), 1349–1352, doi:10.1126/science.aad1929.

- Samuel, H., & D. Bercovici (2006). Oscillating and stagnating plumes in the Earth's lower mantle, *Earth Planet. Sci. Lett.*, 248(1–2), 90–105, doi:10.1016/j.epsl.2006.04.037.
- Samuel, H., & C. G. Farnetani (2003). Thermochemical convection and helium concentrations in mantle plumes, *Earth Planet. Sci. Lett.*, 207(1–4), 39–56, doi:10.1016/S0012-821x(02)01125-1.
- Schersten, A., T. Elliott, C. Hawkesworth, & M. Norman (2004). Tungsten isotope evidence that mantle plumes contain no contribution from the Earth's core, *Nature*, 427(6971), 234–237, doi:10.1038/Nature02221.
- Shearer, P. M., M. A. H. Hedlin, & P. S. Earle (1998). PKP and PKKP precursor observations: Implications for the small-scale structure of the deep mantle and core, in *The Core-Mantle Boundary Region*, edited, pp. 37–55, doi:10.1029/GD028p0037.
- Shen, X., H. Zhou, & H. Kawakatsu (2008). Mapping the upper mantle discontinuities beneath China with teleseismic receiver functions, *Earth, Planets and Space*, 60(7), 713–719, doi:10.1186/bf03352819.
- Shen, X. Z., X. H. Yuan, & X. Q. Li (2014). A ubiquitous low-velocity layer at the base of the mantle transition zone, *Geophys. Res. Lett.*, 41(3), 836–842, doi:10.1002/2013gl058918.
- Shen, Y., & J. Blum (2003). Seismic evidence for accumulated oceanic crust above the 660-km discontinuity beneath southern Africa, *Geophys. Res. Lett.*, 30(18), doi:10.1029/2003gl017991.
- Shorttle, O., Y. Moussallam, M. E. Hartley, J. Maclennan, M. Edmonds, & B. J. Murton (2015). Fe-XANES analyses of Reykjanes Ridge basalts: Implications for oceanic crust's role in the solid Earth oxygen cycle, *Earth Planet. Sci. Lett.*, 427, 272–285, doi:10.1016/j.epsl.2015.07.017.
- Sleep, N. H. (1988). Gradual Entrainment of a Chemical Layer at the Base of the Mantle by Overlying Convection, *Geophys. J. Int.*, 95(3), 437–447, doi:10.1111/j.1365-246X.1988.tb06695.x.
- Smith, E. M., S. B. Shirey, S. H. Richardson, F. Nestola, E. S. Bullock, et al. (2018). Blue boron-bearing diamonds from Earth's lower mantle, *Nature*, 560(7716), 84–87, doi:10.1038/s41586-018-0334-5.
- Sobolev, A. V., A. W. Hofmann, K. P. Jochum, D. V. Kuzmin, & B. Stoll (2011a). A young source for the Hawaiian plume, *Nature*, 476(7361), 434–437, doi:10.1038/nature10321.
- Sobolev, A. V., et al. (2007). The amount of recycled crust in sources of mantle-derived melts, *Science*, 316(5823), 412–417, doi:10.1126/science.1138113.
- Sobolev, S. V., A. V. Sobolev, D. V. Kuzmin, N. A. Krivoluts-kaya, A. G. Petrunin, N. T. Arndt, et al. (2011b). Linking mantle plumes, large igneous provinces and environmental catastrophes, *Nature*, 477(7364), 312–316, doi:10.1038/nature10385.
- Solheim, L. P., & W. R. Peltier (1994). Avalanche effects in phase transition modulated thermal convection: A model of Earth's mantle, *J. Geophys. Res.*, 99(B4), 6997–7018, doi:10.1029/93jb02168.
- Steinberger, B., & T. H. Torsvik (2012). A geodynamic model of plumes from the margins of Large Low Shear Velocity Provinces, *Geochem. Geophys. Geosyst.*, 13, Q01W09, doi:10.1029/2011gc003808.
- Stixrude, L., & C. Lithgow-Bertelloni (2012). Geophysics of Chemical Heterogeneity in the Mantle, *Annual Review of Earth and Planetary Sciences*, 40(1), 569–595, doi:10.1146/annurev.earth.36.031207.124244.
- Tackley, P. (1995). Mantle dynamics: Influence of the transition zone, *Rev. Geophys.*, doi:10.1029/95RG00291.
- Tackley, P. (1998). Three-Dimensional Simulations of Mantle Convection with a Thermo-Chemical Basal Boundary Layer: D⁹⁹, *AGU Geophysical Monograph on the CMB ed. M. Gurnis*.
- Tackley, P. J. (2007). Mantle Geochemical Geodynamics, in *Treatise on Geophysics*, edited by D. Bercovici, pp. 437–505, Elsevier.
- Tackley, P. J. (2011). Living dead slabs in 3–D: The dynamics of compositionally-stratified slabs entering a “slab graveyard” above the core–mantle boundary, *Phys. Earth Planet. Int.*, 188(3–4), 150–162, doi:10.1016/j.pepi.2011.04.013.
- Tackley, P. J., D. J. Stevenson, G. A. Glatzmaier, & G. Schubert (1993). Effects of an Endothermic Phase-Transition at 670 Km Depth in a Spherical Model of Convection in the Earth's Mantle, *Nature*, 361(6414), 699–704, doi:10.1038/361699a0.
- Tackley, P. J., D. J. Stevenson, G. A. Glatzmaier, & G. Schubert (1994). Effects of multiple phase transitions in a three-dimensional spherical model of convection in Earth's mantle, *J. Geophys. Res.*, 99(B8), 15877–15901, doi:10.1029/94JB00853.
- Tan, E., W. Leng, S. J. Zhong, & M. Gurnis (2011). On the location of plumes and lateral movement of thermochemical structures with high bulk modulus in the 3–D compressible mantle, *Geochem. Geophys. Geosyst.*, 12(7), Q07005, doi:10.1029/2011gc003665.
- Tauzin, B., R. D. van der Hilst, G. Wittlinger, & Y. Ricard (2013). Multiple transition zone seismic discontinuities and low velocity layers below western United States, *J. Geophys. Res.*, 118(5), 2307–2322, doi:10.1002/jgrb.50182.
- Tolstikhin, I., & A. W. Hofmann (2005). Early crust on top of the Earth's core, *Phys. Earth Planet. Int.*, 148(2–4), 109–130, doi:10.1016/j.pepi.2004.05.011.
- Torii, Y., & S. Yoshioka (2007). Physical conditions producing slab stagnation: Constraints of the Clapeyron slope, mantle viscosity, trench retreat, and dip angles, *Tectonophysics*, 445(3–4), 200–209, doi:10.1016/j.tecto.2007.08.003.
- Tsuchiya, T. (2011). Elasticity of subducted basaltic crust at the lower mantle pressures: Insights on the nature of deep mantle heterogeneity, *Phys. Earth Planet. Int.*, 188(3–4), 142–149, doi:10.1016/j.pepi.2011.06.018.
- Turcotte, D., & G. Schubert (2014). *Geodynamics*, 3rd edition ed., Cambridge University Press.
- Turcotte, D. L., & E. R. Oxburgh (1967). Finite Amplitude Convective Cells and Continental Drift, *J. Fluid Mech.*, 28(1), 29–&, doi:10.1017/S0022112067001880.
- van der Hilst, R. (1995). Complex morphology of subducted lithosphere in the mantle beneath the Tonga trench, *Nature*, 374(6518), 154–157, doi:10.1038/374154a0.
- van der hilst, R., R. Engdahl, W. Spakman, & G. Nolet (1991). Tomographic Imaging of Subducted Lithosphere Below Northwest Pacific Island Arcs, *Nature*, 353(6339), 37–43, doi:10.1038/353037a0.
- van der Hilst, R. D., S. Widiyantoro, & E. R. Engdahl (1997). Evidence for deep mantle circulation from global tomography, *Nature*, 386(6625), 578–584, doi:10.1038/386578a0.

- van Hunen, J., & J.-F. o. Moyn (2012). Archean Subduction: Fact or Fiction?, *Annual Review of Earth and Planetary Sciences*, 40 (1), 195–219, doi:10.1146/annurev-earth-042711-105255.
- van Hunen, J., & A. P. van den Berg (2008). Plate tectonics on the early Earth: Limitations imposed by strength and buoyancy of subducted lithosphere, *Lithos*, 103(1), 217–235, doi:10.1016/j.lithos.2007.09.016.
- van Hunen, J., P. E. van Keken, A. Hynes, G. F. Davies, K. Condie, & V. Pease (2008). Tectonics of early Earth: Some geodynamic considerations, *When did plate tectonics begin on planet Earth*, 157–171.
- van Keken, P. E., S. Karato, & D. A. Yuen (1996). Rheological control of oceanic crust separation in the transition zone, *Geophys. Res. Lett.*, 23(14), 1821–1824, doi:10.1029/96gl01594.
- van Thienen, P., A. P. van den Berg, & N. J. Vlaar (2004). Production and recycling of oceanic crust in the early Earth, *Tectonophysics*, 386(1–2), 41–65, doi:10.1016/j.tecto.2004.04.027.
- Walter, M. J., S. C. Kohn, D. Araujo, G. P. Bulanova, C. B. Smith, E. Gaillou, et al. (2011). Deep Mantle Cycling of Oceanic Crust: Evidence from Diamonds and Their Mineral Inclusions, *Science*, 334(6052), 54–57, doi:10.1126/science.1209300.
- Wang, X.-C., Z.-X. Li, X.-H. Li, J. Li, Y.-G. Xu, & X.-H. Li (2013). Identification of an ancient mantle reservoir and young recycled materials in the source region of a young mantle plume: Implications for potential linkages between plume and plate tectonics, *Earth Planet. Sci. Lett.*(0), doi:10.1016/j.epsl.2013.07.003.
- Wang, Y., G. L. Pavlis, & M. Li (2019). Heterogeneous distribution of water in the mantle transition zone inferred from wavefield imaging, *Earth Planet. Sci. Lett.*, 505, 42–50, doi:10.1016/j.epsl.2018.10.010.
- Waszek, L., N. C. Schmerr, & M. D. Ballmer (2018). Global observations of reflectors in the mid-mantle with implications for mantle structure and dynamics, *Nature Communications*, 9 (1), 385, doi:10.1038/s41467-017-02709-4.
- Waszek, L., C. Thomas, & A. Deuss (2015). PKP precursors: Implications for global scatterers, *Geophys. Res. Lett.*, 2015GL063869, doi:10.1002/2015GL063869.
- Weinstein, S. A. (1993). Catastrophic overturn of the Earth's mantle driven by multiple phase changes and internal heat generation, *Geophys. Res. Lett.*, 20(2), 101–104, doi:10.1029/93GL00044.
- White, W. (2015a). Probing the Earth's Deep Interior Through Geochemistry, *Geochemical Perspectives*, 95–251, doi:10.7185/geochempersp.4.2.
- White, W. M. (2015b). Isotopes, DUPAL, LLSVPs, & Anekan-tavada, *Chem. Geol.*, 419, 10–28, doi:10.1016/j.chemgeo.2015.09.026.
- Williams, C. D., M. Li, A. K. McNamara, E. J. Garnero, & M. C. van Soest (2015). Episodic entrainment of deep primordial mantle material into ocean island basalts, *Nat. Commun.*, 6, 8937, doi:10.1038/ncomms9937.
- Xie, S., & P. J. Tackley (2004a). Evolution of helium and argon isotopes in a convecting mantle, *Phys. Earth Planet. Int.*, 146 (3–4), 417–439, doi:10.1016/j.pepi.2004.04.003.
- Xie, S., & P. J. Tackley (2004b). Evolution of U-Pb and Sm-Nd systems in numerical models of mantle convection and plate tectonics, *J. Geophys. Res.*, 109(B11), B11204, doi:10.1029/2004jb003176.
- Yasuda, A., & T. Fujii (1998). Ascending subducted oceanic crust entrained within mantle plumes, *Geophys. Res. Lett.*, 25(10), 1561–1564, doi:10.1029/98gl01230.
- Yoshida, M., & F. Tajima (2013). On the possibility of a folded crustal layer stored in the hydrous mantle transition zone, *Phys. Earth Planet. Int.*(0), doi:10.1016/j.pepi.2013.03.004.
- Yoshida, M., F. Tajima, S. Honda, & M. Morishige (2012). The 3D numerical modeling of subduction dynamics: Plate stagnation and segmentation, & crustal advection in the wet mantle transition zone, *J. Geophys. Res.*, 117(B4), B04104, doi:10.1029/2011jb008989.
- Yoshioka, S., & A. Naganoda (2010). Effects of trench migration on fall of stagnant slabs into the lower mantle, *Phys. Earth Planet. Int.*, 183(1–2), 321–329, doi:10.1016/j.pepi.2010.09.002.
- Yu, S. L., & E. J. Garnero (2018). Ultralow Velocity Zone Locations: A Global Assessment, *Geochem. Geophys. Geosyst.*, 19 (2), 396–414, doi:10.1002/2017gc007281.
- Zhao, D. P. (2004). Global tomographic images of mantle plumes and subducting slabs: insight into deep Earth dynamics, *Phys. Earth Planet. Int.*, 146(1–2), 3–34, doi:10.1016/j.pepi.2003.07.032.
- Zhong, S. (2006). Constraints on thermochemical convection of the mantle from plume heat flux, plume excess temperature, and upper mantle temperature, *J. Geophys. Res.*, 111(B4), B04409 doi:10.1029/2005jb003972.
- Zhong, S. J., & M. Gurnis (1994). Role of Plates and Temperature-Dependent Viscosity in Phase-Change Dynamics, *J. Geophys. Res.*, 99(B8), 15903–15917, doi:10.1029/94jb00545.
- Zhong, S. J., & B. H. Hager (2003). Entrainment of a dense layer by thermal plumes, *Geophys. J. Int.*, 154(3), 666–676, doi:10.1046/j.1365-246X.2003.01988.x.
- Zhou, H. W., & D. L. Anderson (1989). Search for deep slabs in the Northwest Pacific mantle, *Proc. Natl. Acad. Sci. U.S.A.*, 86(22), 8602–8606, doi:10.1073/pnas.86.22.8602.
- Zhou, H. W., & R. W. Clayton (1990). P and S-Wave Travel Time Inversions for Subducting Slab under the Island Arcs of the Northwest Pacific, *J. Geophys. Res.*, 95(B5), 6829–6851, doi:10.1029/JB095iB05p06829.
- Zindler, A., & S. Hart (1986). Chemical Geodynamics, *Annual Review of Earth and Planetary Sciences*, 14(1), 493–571, doi:10.1146/annurev.ea.14.050186.002425.

Toward Imaging Flow at the Base of the Mantle with Seismic, Mineral Physics, and Geodynamic Constraints

Andy Nowacki¹ and Sanne Cottaar²

ABSTRACT

Perhaps the least ambiguous signal that the mantle is convecting comes from observations of seismic anisotropy – the variation of wave speed with direction – which must arise due to the ordering of material as deformation occurs. Therefore, significant effort has been made over many years to infer the direction and nature of mantle flow from these data. Observations have focused on the boundary layers of the mantle, where deformation is expected to be strongest and where anisotropy is usually present. While prospects for mapping flow seem good, the lack of knowledge of several key issues currently holds back progress. These include the cause of anisotropy in the lowermost mantle, the causative material's response to shear, and the single-crystal or -phase seismic properties of the causative materials. In this chapter we review recent observations of lowermost mantle anisotropy, constraints on mineral elasticity and deformation mechanisms, and challenges in linking geodynamic modeling with seismic observations.

13.1. INTRODUCTION

Seismic anisotropy, i.e., the variation of seismic velocity with propagation direction and polarization, is observed in a number of regions within the Earth. The strength of anisotropy is particularly strong in the crust, at the top and the bottom of the mantle, and in the inner core (Mainprice, 2007). In the upper mantle, observed seismic anisotropy has been used to map asthenospheric flows (Becker & Lebedev, 2021) and understand slab dynamics (Huang and Zhao, 2021). In the lowermost mantle, understanding anisotropy in terms of flow is more elusive, as seismic observations are sparse, and mineral physical constraints more uncertain. The dynamics of the lowermost mantle

are of particular interest, as they reflect the lower thermal and mechanical boundary layer of the convecting mantle. Mapping flow directions in this region would significantly help our understanding of the role of this boundary in mantle dynamics, and more specifically the role of the large low-shear velocity provinces (LLSVPs) (Rudolph, 2021).

Albeit challenging, significant efforts have been made to use seismic anisotropy to understand the underlying crystal preferred orientations (CPO) and flow directions (e.g., Karato, 1998). This is based on the assumption that flow, and the internal crystallographic deformation mechanisms that accommodate the flow, cause alignment of intrinsically anisotropic crystals. This chapter offers a condensed review of seismic observations and mineral physical and geodynamical constraints on seismic anisotropy, and for a more in-depth review we refer to Nowacki et al. (2011) and Romanowicz & Wenk (2017). Here, we focus on the endeavors, mainly over the last decade, to tie these disciplines together and map flow directions in the

¹*School of Earth and Environment, University of Leeds, Leeds, UK*

²*Department of Earth Sciences, University of Cambridge, Cambridge, UK*

lowermost mantle, and the specific challenges posed when comparing these results to seismic observations.

13.2. OBSERVATIONAL CONSTRAINTS ON LOWERMOST MANTLE FLOW

13.2.1. Global Tomographic Models

A number of tomographic modelers invert for seismic anisotropy in the lowermost mantle. Inverting the full anisotropic elastic tensor (i.e., all 21 parameters) is unfeasible. The only component of anisotropy generally inverted for in the lowermost mantle is the velocity difference between horizontally polarized shear velocity, V_{SH} , and vertically polarized shear velocity, V_{SV} . This component of anisotropy is named radial anisotropy (or vertically transverse isotropy), and the degree of anisotropy can be expressed by the value $\xi = V_{SH}^2/V_{SV}^2 = C_{66}/C_{44}$, where C is the Voigt matrix representation of elasticity and the 3-axis is vertical.

For the upper mantle, radial anisotropy is well constrained due to the unique sensitivities of the two types of surface waves (Becker & Lebedev, 2021). For the lower mantle, one or both of normal modes and body waves must be used. Normal mode inversions for 1D radial models show no significant component of ξ (Beghein et al., 2006; de Wit & Trampert, 2015). 3D tomographic models show a mainly isotropic lower mantle with lateral variations in ξ on the order of 0.97–1.03 in the lowermost mantle (e.g., Moulik & Ekstrom, 2014; Auer et al., 2014; Chang et al., 2015; French & Romanowicz, 2015). There are strong differences between these models, some of which can be attributed to their treatment of the crust in the inversion, which is shown to affect the radial anisotropic signature of the lowermost mantle (Ferreira et al., 2010; Panning et al., 2010). In general, a geographical trend emerges where $\xi > 1$ (equivalently, $V_{SH} > V_{SV}$) in regions with fast shear-wave velocity interpreted to be slab graveyards, and the opposite signature of $\xi < 1$ is seen in regions of slow shear-wave velocity, i.e., the LLSVPs. In Figure 13.1 this relationship is illustrated with histograms of ξ values for the fast and slow regions as interpreted by Cottaar & Lekić (2016), as well as a vote map of ξ values, which at each point at 2800 km depth shows the count of all tomography models which have a value of ξ above or below 1. While all models show a significant shift in their histograms for the fast and slow region, the shifts between their mean values is small, with the largest shift of 1.1% in SEMUCBwm1, and the smallest shift of 0.38% in SAVANI. The vote map also suggests a relationship between dV_S and ξ . Interpreting this general trend should be done with caution as any relationship between dV_S and ξ could be an artefact of the inversion,

specifically the negative ξ values appear prone to be leakage of the slow isotropic velocities (Chang et al., 2015). One thing that is interesting to note from the vote map is the smaller slow shear region beneath the Ural mountains, dubbed the Perm anomaly (Lekić et al., 2012), does not correlate directly with a signal of $\xi < 1$, but a small anomaly showing $\xi < 1$ appears offset to the south.

Studies are even more limited in constraining P -wave radial anisotropy ($\phi = V_{PV}^2/V_{PH}^2 = C_{33}/C_{11}$). Global studies constraining 1D radial P -wave anisotropy show no agreement in the likely signature (Beghein et al., 2006; de Wit & Trampert, 2015). Global 3D studies have often applied an assumed scaling between the S - and P -wave anisotropy as a starting model. When they do include P -wave radial anisotropy independently (Soldati et al., 2003; Tesoniero et al., 2016), they judge their results not to be robust. Inversions using body waves are heavily underconstrained (Boschi & Dziewoński, 2000). The synthetic study of Koelmeijer et al. (2012) shows general sensitivity of normal modes to P -wave anisotropy, although it also predicts it is sensitive to trade-offs.

A potential way forward for global studies lies in the understanding of a third anisotropic parameter, $\eta = C_{13}/(C_{11} - 2C_{44})$, which is related to the S and P velocities at intermediate incidence angles. Wit & Trampert (2015) show that this parameter has a robust 1D signature of $\eta < 1$ across the lower 1000 km of the mantle. Kawakatsu (2015) suggests a rewrite of η for a more physical relationship with wave incidence angle, and shows that constraining this parameter, η_c , can help resolve whether horizontally isotropic layers could cause the observed anisotropy.

13.2.2. Regional Body-Wave Observations

Locally, deep mantle seismic anisotropy can be observed through shear-wave splitting of body waves. One of the main challenges is to determine the relative contribution to splitting from the uppermost and lowermost mantle, and whilst often assuming the rest of the lower mantle is isotropic. A general approach is to use two seismic phases with comparable ray paths across the upper mantle, while one reference phase has a different or no ray path across the lowermost mantle. Ideally the reference phase shows no or minimal splitting and all splitting in the other phase can be attributed to the lowermost mantle. Otherwise corrections for splitting from the upper mantle need to be applied to attribute splitting to the lower mantle (e.g., Wookey et al., 2005).

One potential set consists of the ScS and S phases (Figure 13.2). For the distance range of 60–85°, the S phase turns above the lowermost mantle, while the ScS phase samples the lowermost mantle (e.g., Lay & Young, 1991; Wookey & Kendall, 2008). A second set is the SKS

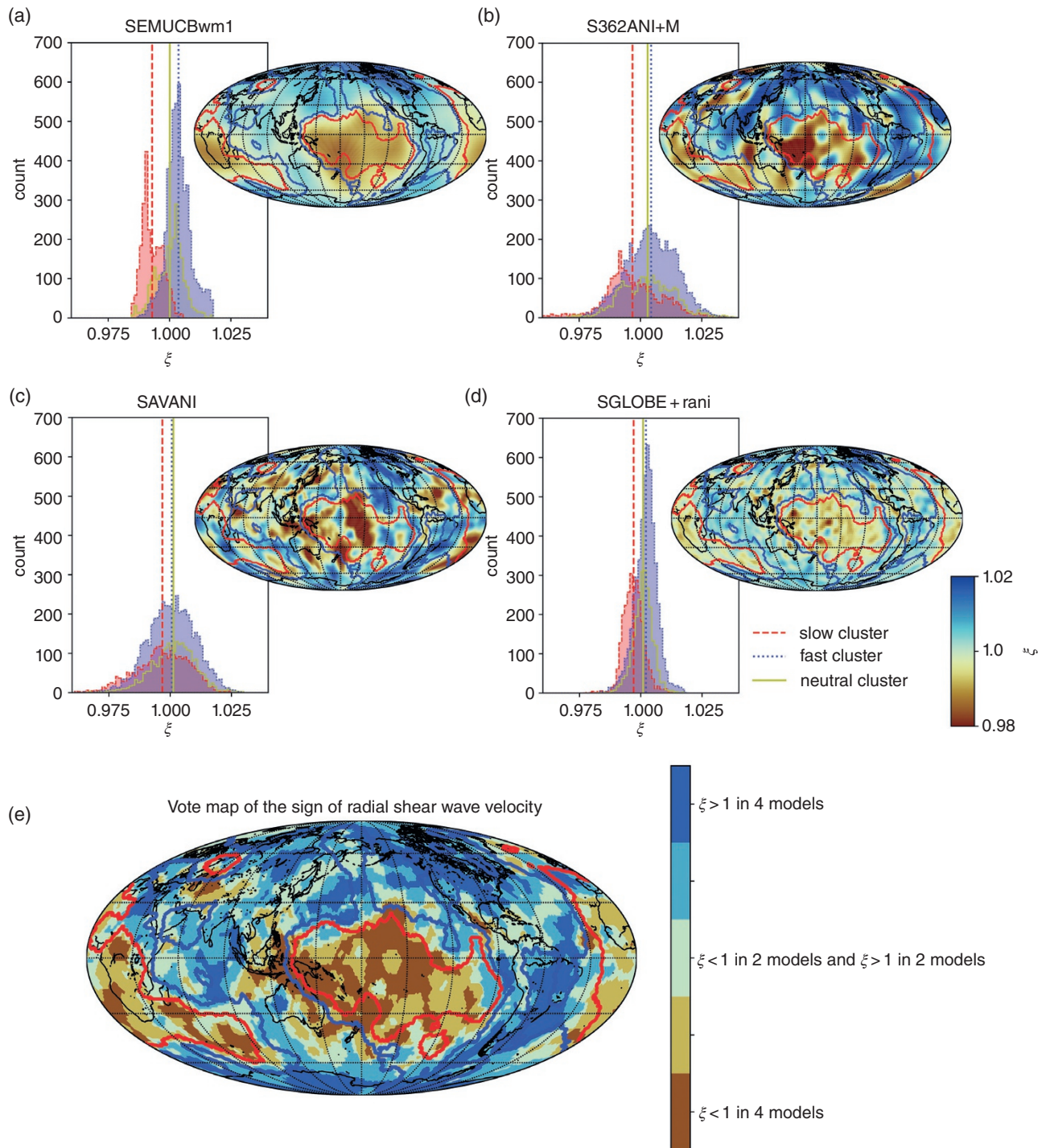


Figure 13.1 (a–d) Maps show shear-wave radial anisotropic parameter ξ at 2800 km depth for SEMUCBwm1, S362ANI+M, SAVANI, SGLOBE-rani. Red and blue contours show bounds at three votes for the isotropic slow and fast cluster based on votes across five isotropic models. Histograms show distribution and mean values of ξ in the different cluster vote areas, red = slow, blue = fast, yellow = neutral (boundaries for “neutral” cluster are not shown on the maps). (e) Vote map showing where models agree on $\xi > 1$ or $\xi < 1$ (V_{SH} or V_{SV} being faster, respectively). All models agree that $\xi > 1$ for 18% of the map, while for $\xi < 1$ the area is 13%. Source: (a–d) French and Romanowicz (2014), Moulik and Ekstrom (2014), Auer et al., (2014), Chang et al., (2015), Cottaar & Lekić (2016).

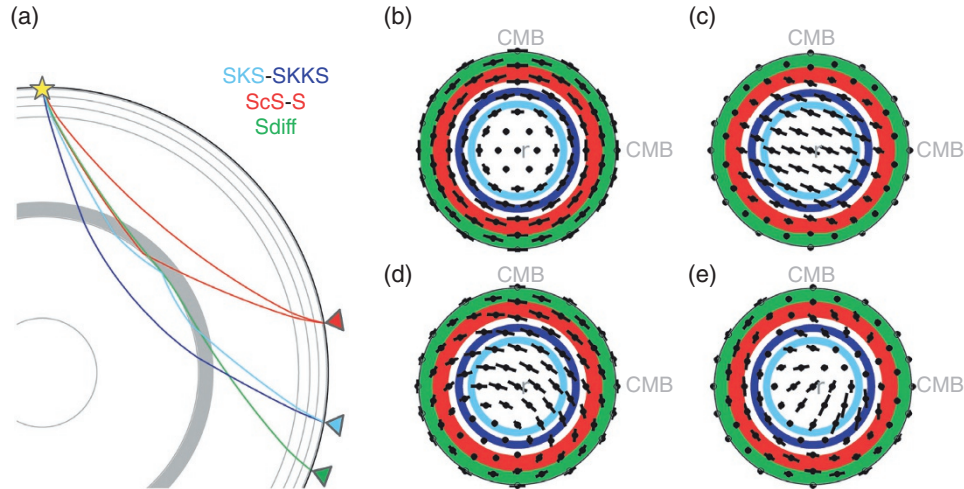


Figure 13.2 (a) Ray paths for general body wave (pairs) used to constrain lowermost mantle anisotropy: *SKS-SKKS* (blue), *ScS-S* (red), *S_{diff}* (green) (made with Obspy; Krischer et al., 2015). (b–e) Hemisphere projections of various assumed anisotropic symmetries viewed from above (made with MSAT; Walker & Wookey, 2012). Bars show splitting direction and bar lengths show splitting strength as a function of shear-wave propagation direction. Colored shading shows general sensitivity of body waves (see a), although there is some overlap. (b) Radial anisotropy with $\xi = 1.03$ (c) 3% azimuthal anisotropy with a fast axis direction of 112° . (d) Tilted anisotropy, i.e., anisotropy in c tilted by 40° . (e) Full anisotropic tensor for 75% post-perovskite and 25% periclase in a downgoing slab (see Section 13.4.2). Source: (a) Krischer et al., (2015), (b,e) Walker & Wookey (2012).

and *SKKS* phases (at epicentral distances $108\text{--}122^\circ$), for which the ray paths exit the core at different locations and converge across the mantle (e.g., Niu & Perez, 2004; Wang & Wen, 2007; M. Long, 2009). *SKS-SKKS* pairs have the additional advantages over *S-ScS* that in an isotropic or radially-anisotropic mantle they exit the core purely polarized along the *SV* component, and any anisotropy along the down-going leg of the path can be ignored. Their disadvantage is that both phases can accrue splitting in the lowermost mantle and in the upper mantle. At times it is difficult to retrieve splitting parameters, and these phases are usually only used to highlight discrepant phase pairs (e.g., Deng et al., 2017).

Lastly, *S_{diff}* phases (at $100\text{--}130^\circ$ distance) are compared either to *S/ScS* at shorter distances, or to *SKKS* (or *SKS*) at longer distances (e.g., Kendall & Silver, 1996; Vinnik et al., 1998). The *SV* component of the diffracted wave attenuates much faster than the *SH* along the core–mantle boundary, which means *S_{diff}* at large distances ($>120^\circ$) becomes a purely *SH* polarized wave, and any splitting can be attributed to the upgoing leg of the ray path (Cottaar & Romanowicz, 2013).

In all cases, caution is required in interpreting body-wave observations if modeled using approximate methods such as ray theory, since shear waves at the base of the mantle have a large region of finite-frequency sensitivity. For *S_{diff}*, travel time differences between *S_{diff}* and *SV_{diff}* can arise for purely isotropic models, especially with

strong isotropic velocity gradients as one might expect due to the thermal boundary layer, due to different finite-frequency sensitivity of the two components along the boundary (Maupin, 1994; Komatitsch et al., 2010; Borgeaud et al., 2016; Parisi et al., 2018). *ScS* suffers to a lesser extent from finite-frequency effects in 1D models, but ray theoretical interpretations can badly misrepresent the strength and orientation of anisotropy when lateral variations in anisotropy may exist (Nowacki & Wookey, 2016).

The different phases have different sensitivity to the anisotropic tensor due to their propagation angle and the length of their propagating path across the lowermost mantle (Figure 13.2). *S_{diff}* has long horizontal propagation paths in the mantle, and therefore good sensitivity to radial anisotropy. *SKS* propagates at sub-vertical angles ($18\text{--}33^\circ$) across the lowermost mantle, so splitting is caused by the component of azimuthal anisotropy, i.e., variation of wave speed in the horizontal plane. *SKKS* ($40\text{--}50^\circ$) and *ScS* ($62\text{--}78^\circ$) propagate at intermediate angles, and are sensitive to tilted anisotropy. While early studies focused mainly on constraining the radial anisotropic component (e.g., Young & Lay, 1990; Matzel et al., 1996; Garnero & Lay, 1997), recent studies interpret their observations as tilted anisotropy, the main component constrained when accounting for the incidence angles in the lowermost mantle (e.g., Thomas et al., 2007; Wookey & Kendall, 2008; Nowacki et al., 2010).

One additional, unique type of observation worth mentioning are polarity observations of phases bouncing off of the so-called D'' discontinuities in the lowermost mantle (Thomas et al., 2011; Cobden & Thomas, 2013; Creasy et al., 2019; Pisconti et al., 2019). Azimuthal variations in the polarity measurements suggest these are sensitive to underlying anisotropy. As observations can be applied to S and P reflections (SdS and PdP), they are to our knowledge the only body-wave studies that have resolved a component of both S - and P -wave anisotropy for a single location.

Most observational studies focus on a single observational method, as well as a single azimuthal direction. To sufficiently constrain anisotropy in a single location to uniquely interpret flow direction, multiple techniques need to be combined (Creasy et al., 2019). Efforts have been made to target a single region from multiple angles using ScS (Nowacki et al., 2010; Wookey & Kendall, 2008) and polarization measurements (Thomas et al., 2011), as well as combining multiple angles with multiple body-wave phases (Ford & Long, 2015; Creasy et al., 2019; Wolf et al., 2019).

13.2.3. Observed Regional Anisotropy

This is not an exhaustive overview of body wave studies. For a full table of studies, we refer to Romanowicz and Wenk (2017). Here we highlight consistencies across these studies, mainly focusing on more recent studies which benefit from increased coverage by seismic arrays. Regional body wave studies largely agree with tomographic models on geographical trends in radial anisotropy, i.e. $\xi > 1$ where isotropic velocities are fast, and $\xi < 1$ where isotropic velocities are slow (e.g., Wookey & Kendall, 2007; Kawai & Geller, 2010). Models interpreting tilted anisotropy have overwhelmingly sampled isotropically fast areas and many find a sub-horizontal fast axis and thus a component of $\xi > 1$ (e.g., Thomas et al., 2007; Garnero et al., 2004; Wookey & Dobson, 2008; Nowacki et al., 2010), while several studies find a fast axis that is tilted from the horizontal by around 45° (Wookey et al., 2005; Cottaar & Romanowicz, 2013), which is not compatible with radial anisotropy. Particularly, regions just outside of LLSVPs appear to have strong and variable anisotropy, as is observed along the boundaries of the African LLSVP (Wang & Wen, 2007; Cottaar & Romanowicz, 2013; Lynner & Long, 2014; Grund & Ritter, 2019; Romanowicz & Wenk, 2017; Reiss et al., 2019), the Pacific LLSVP (Deng et al., 2017), and the Perm Anomaly (M. D. Long & Lynner, 2015). These observations show stronger anisotropy outside of the LLSVP and little to no anisotropy within the LLSVP, both in terms of tilted anisotropy (Cottaar & Romanowicz, 2013) and in terms of azimuthal anisotropy (e.g., Lynner & Long,

2014; Grund & Ritter, 2019). A change in sign from $\xi > 1$ to $\xi < 1$ is also observed toward the base of the Icelandic plume (Wolf et al., 2019).

While some consistency emerges on the types of anisotropy, and correlations with isotropic velocities, uncertainty lies in the strength of anisotropy observed. Tomographic models contain radial anisotropy on the order of several percent, and amplitudes vary between models (see Figure 13.1). Local observations interpret tilted anisotropy of 0.8–1.5% across a layer of 250 km beneath North America (Nowacki et al., 2010) and up to 8% across 150 km beneath the Antarctic Ocean (Cottaar & Romanowicz, 2013). Such variations could represent true geographical observations, but biases could also occur as propagation angles used might not be optimal to observe the strongest splitting or assumed layer thicknesses. In these two example studies, interpreted amplitudes might also differ as one is interpreted ray-theoretically (Nowacki et al., 2010) and one by forward modeling (Cottaar & Romanowicz, 2013). Potentially, consistently constrained relative amplitudes in splitting might help map lateral variations in flow strength or direction.

13.3. FORWARD MODELING

To provide synthetic tests for the hypothesis that anisotropy is caused by crystal preferred orientation (CPO), multidisciplinary models are built that span many spatial scales (see flow chart in Figure 13.3). Geodynamic models provide maps of strain across tens to thousands of kilometers. The strain observed is accommodated on the micro scale by deformation mechanisms in a set of crystals, assuming a degree is accommodated by dislocation glide to create preferential orientation. The individual elastic constants of each of the deformed set of crystals are averaged using their orientations, giving the fully anisotropic tensor for a single location. This process needs to be repeated for many locations, to provide an anisotropic model with signatures that can be observed over tens to thousands of kilometers by seismic waves. Here we explain the main choices and assumptions made in these models.

While we focus on the hypothesis that CPO is the cause of seismic anisotropy in the lowermost mantle, studies have forward modeled the potential of shape preferred orientation (SPO) as well. SPO anisotropy is caused by layering or inclusions of strongly heterogeneous (but potentially intrinsically isotropic) material (Kendall & Silver, 1998; Hall et al., 2004; Creasy et al., 2019; Reiss et al., 2019). In the case of inclusions, anisotropy can be observed in the effective medium to which the waves are sensitive if a degree of alignment or preferred

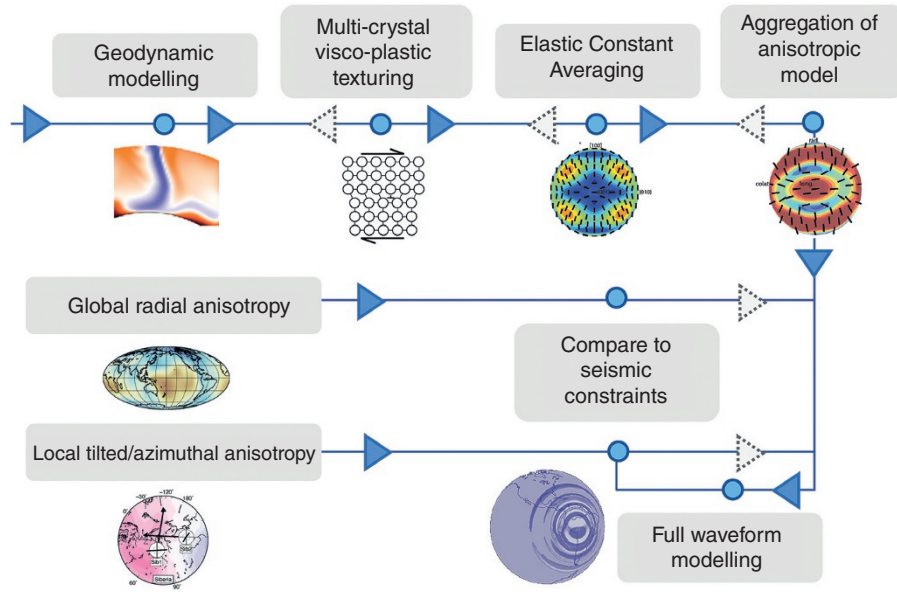


Figure 13.3 Showing the general steps in forward modeling from a flow model to interpreting seismic observations following the filled blue arrows as discussed in Section 13.3. Dashed arrows indicate the inverse steps to go from seismic observations to flow directions, for which challenges and limitations are discussed in Section 13.5.

orientation persists over a broad area. This alignment of inclusions would result from local deformation, and thus also contain information about mantle flow. However, studies observing high frequency scatterers in the lowermost mantle observe very weak velocity contrasts (<0.1%: Mancinelli & Shearer, 2013). Extremely strong isotropic velocity anomalies (10–30%) are only observed in thin patches of several tens of km on top of the core–mantle boundary, the so-called ultra-low-velocity zones (e.g., Garnero et al., 1998; Yu & Garnero, 2018).

13.3.1. Geodynamic Models

Assumptions on the flow occurring in the lowermost mantle have varying degrees of complexities. In the simplest of models, horizontal flow is assumed causing simple horizontal shear as one might expect in an iso-chemical thermal boundary layer (as used in Wookey & Kendall, 2007). Anisotropy observed, however, does not have to represent local deformation, but could represent fossilized anisotropy. Anisotropic material can be formed elsewhere and be transported and rotated without overriding the preferred orientation. Therefore, it is important to track the history of deformation for material in a given location. To represent change in flow direction in downwellings and upwellings in the lowermost mantle, corner flow streamlines can be used (Tommasi et al., 2018).

A range of studies use fully numerical models, where a number of assumptions on parameters for the lower mantle need to be made. The history of deformation is tracked

by passive tracers that are advected through the model and record the velocity gradient at each step. The deformation history is generally used from the top of the lower mantle (e.g., Cottaar et al., 2014), or from the bridgmanite to post-perovskite transition (e.g., Walker et al., 2011).

In one approach (Cottaar et al., 2014; Chandler et al., 2018), the CitcomS program (Zhong et al., 2000) is used to solve for the conservation of mass, momentum, and energy in a system that is heated from below, and where a slab is forced down from the top. Tracers are introduced at the top of the slab, and a large number of them eventually end up in the lowermost mantle, although the final distribution is irregular and shows clumping of tracers.

In a different approach (Walker et al., 2011; Nowacki et al., 2013), the flow field is the instantaneous flow predicted by isotropic wave velocities, the gravity field, a 1D viscosity model, and other geophysical constraints (Simmons et al., 2009). Because the inversion assumes that flow does not change with time, regularly spaced tracers can be back-propagated to the top of D'' across the flow field, after which they are forward-propagated to track the deformation along the path. The advantage of this method is that one retrieves a regularly sampled global anisotropic model that holds some potential relationship to the isotropic velocities, and that can thus be compared to global or regional seismic observations. Additionally, this method tests a prior assumed relationship between isotropic velocities and the flow field, testing models of thermal and/or thermo-chemical heterogeneity in the lower mantle.

While these geodynamical models represent test cases to explain lowermost seismic anisotropy, they are simplified in many ways. The geodynamical models have not explicitly included the bridgmanite to post-perovskite transitions, which only has a small density jump (Murakami et al., 2004; Oganov & Ono, 2004), but would cause significant viscosity weakening (Hunt et al., 2009) and allow slab material to spread more easily (Nakagawa & Tackley, 2011). The viscosity model would be even more complex if the formation of CPO could be fed back into the geodynamical model, creating anisotropic viscosity. So far, models have not tested the hypothesis of LLSVPs representing a different composition (e.g., Garnero et al., 2016), which appears important to understand the laterally varying anisotropy around LLSVP boundaries.

13.3.2. Mineralogical Constraints

In the upper mantle, the mineral olivine is abundant, and, with a highly anisotropic crystal, represents a straightforward candidate to explain CPO anisotropy (Becker & Lebedev, 2021). For the lowermost mantle, the debate is still open as to which mineral or polymineralic assemblage can explain the observed anisotropy. For a candidate mineral or assemblage, we need to know its single crystal elasticity, which – depending on crystal symmetry – can be described by 3–21 independent parameters. We mostly rely on first-principle or *ab initio* calculations, which solve the electronic Schrödinger equation to obtain the crystal structure and the elasticity at high pressures and temperatures (Buchen, 2021). Merely obtaining isotropic average elasticity information from experiments under these extreme conditions is very challenging, let alone measuring the independent anisotropic parameters (e.g., Marquardt et al., 2009; Finkelstein et al., 2018).

Additionally, we need to know how the candidate mineral or assemblage deforms (Miyagi, 2021). To create seismic anisotropy, a mineral must significantly deform by dislocation glide. In dislocation glide, dislocations within the crystal move along crystallographic planes. Preferred orientation results when crystals rotate to accommodate glide along its weakest glide planes. Other mechanisms like diffusion creep or dislocation climb are not usually thought to cause preferred orientation, though this is not always the case (Wheeler, 2009, 2010; Dobson et al., 2019). If dislocation glide is the preferred mechanism, the next question that arises is what are the relative strengths of the different slip systems (i.e., glide plane and slip directions). Calculations explore the relative strengths of different deformation mechanisms and glide systems by calculating lattice friction and forces required to slip a dislocation (Peierls stress) in atomistic models (Walker et al., 2010; Cordier

et al., 2012). Experimentally, slip system activities cannot usually be measured for single crystals of the phases of interest here. Instead, materials are deformed under compressive or shear stress in a large-volume apparatus (usually on analogue materials), or in a diamond-anvil cell (For further details see Miyagi, 2021; Romanowicz & Wenk, 2017). The resulting deformation may be imaged by x-ray diffraction. Dominant slip systems may be estimated by inspection of the orientation distribution functions (ODFs) of the crystallographic planes of interest, or inverted for by comparing forward calculations of the experimental deformation with the results obtained.

To determine macroscopic anisotropy from these mineralogical constraints, the set of slip systems is combined with a deformation tensor to model a set of deformed crystals. Most often this is done using a homogenization method such as the viscoplastic self-consistent method (VPSC; Lebensohn & Tomé, 1993).

Forming the majority of the lowermost mantle, and thus the likeliest candidates to be the anisotropy-causing phases, are bridgmanite, post-perovskite, and ferropericlase.

Bridgmanite. Bridgmanite, (Mg,Fe)SiO₃-perovskite, is the most abundant mineral in the lower mantle (and in the Earth). Its pure Mg-endmember shows ~11% *P*-wave and up to 15% *S*-wave anisotropy (Oganov et al., 2001; Wentzcovitch et al., 2006; Stackhouse, Brodholt, Wooley, et al., 2005), and shows little (Li et al., 2005; Zhang et al., 2016) or variable (Fu et al., 2019) variation with the inclusion of iron.

There are mixed results on bridgmanite being a suitable candidate to explain anisotropy. Both experiments and calculations proposed a dominant glide plane of (001) (Wenk et al., 2004; Merkel et al., 2007; Ferré et al., 2007), which results in the opposite radial anisotropy to that observed (e.g., Wenk et al., 2011), while other experiments and calculations argue for a dominant (100) glide plane (Mainprice et al., 2008; Tsujino et al., 2016), which can create the observed $V_{SH} > V_{SV}$ in simple shear. Miyagi and Wenk (2016) report a change from (001)-dominated glide to (100) around 55 GPa.

Bridgmanite is also known to be a very strong mineral. Experiments deforming a multiphase mixture of bridgmanite and a smaller fraction of the weaker phase ferropericlase (or analogs), show in some cases that the ferropericlase takes up the majority of the deformation (Girard et al., 2016; Kaercher et al., 2016; Miyagi & Wenk, 2016), while in others the strong bridgmanite phase still dominates deformation (Wang et al., 2013) in line with simulations in a finite element model (Madi et al., 2005). Recently atomistic calculations have shown that the resistance to dislocation glide is very high, and

dislocation climb should dominate (Boioli et al., 2017). Dislocation climb dominance could explain the general lack of anisotropy across most of the lower mantle, as well as the high viscosity of the lower mantle (Reali et al., 2019). However, attempts to explain weak anisotropy around ponded subducted slabs in the uppermost lower mantle in terms of bridgmanite CPO (Tsujino et al., 2016; Walpole et al., 2017; Ferreira et al., 2019; Fu et al., 2019) would be therefore puzzling.

Post-perovskite. Post-perovskite is a high-pressure polymorph of bridgmanite, which could become stable in the lowermost mantle (Murakami et al., 2004; Oganov & Ono, 2004). Compared to bridgmanite, post-perovskite is (1) more anisotropic (Iitaka et al., 2004; Stackhouse et al., 2005; Wentzcovitch et al., 2006; Zhang et al., 2016), and (2) much weaker to deform (Hunt et al., 2009; Ammann et al., 2010; Goryaeva et al., 2016). Therefore, it is an attractive candidate to explain anisotropy observed in the lowermost mantle.

If, and to what degree, post-perovskite is actually stable at the pressures in the lowermost mantle is still up for debate (see overviews in Cobden et al. (2015) and Hirose et al. (2015)), but invoking the presence of post-perovskite helps explain *S*-to-*P* velocity ratios in the lowermost mantle (Koelemeijer et al., 2018). If present, the strongly positive Clapeyron slope of its phase transition from bridgmanite implies post-perovskite is stable in a thicker layer in cold regions than in hot regions (Oganov & Ono, 2004; Tsuchiya et al., 2004). Potentially, post-perovskite becomes unstable again in the thermal boundary layer close to the core–mantle boundary, creating a lens of post-perovskite (Hernlund et al., 2005).

Testing post-perovskite as a candidate to explain anisotropy is difficult as the preferred slip system of post-perovskite is uncertain and diamond-anvil cell experimental results have varied widely over the past 15 years. (For further details, see Miyagi, 2021, in this volume.) The most recent results can be split in two categories. Experiments using MgSiO_3 post-perovskite, and MnGeO_3 or MgGeO_3 analogs show a preferred slip plane of (001) (e.g., Miyagi et al., 2010; Hirose et al., 2010; Nisr et al., 2012; X. Wu et al., 2017). Experiments using CaIrO_3 post-perovskite as an analog show a dominant slip system of [100](010) (where $[hkl]$ gives the Burgers vector; e.g., Yamazaki et al., 2006; Niwa et al., 2012; Hunt et al., 2016). Atomistic models confirm the results of the latter category, showing both slip systems [100](010) and [001](010) (Cordier et al., 2012; Goryaeva et al., 2015, 2017) as well as the occurrence of twinning $1/2\{110\}\{1\bar{1}0\}$ (Carrez et al., 2017). Additionally, it is suggested that post-perovskite could inherit preferred orientation or texture through the phase transition from bridgmanite (Dobson et al., 2013). Interpretation of

the texture inheritance in deformation experiments has been specifically argued to explain part of the variation in interpreted preferred glide plane (e.g., Walte et al., 2009; Miyagi et al., 2011). This could only be the case if bridgmanite forms CPO texture due to dislocation glide, which is debatable (Boioli et al., 2017). A more feasible scenario is bridgmanite inheriting texture from post-perovskite in a reverse transition, which could occur in the hotter regions (Dobson et al., 2013; Walker et al., 2018).

The importance of the incorporation of aluminum and iron into post-perovskite for our purposes depends on its effect on the stability field, deformation mechanisms, rheology, and single-crystal anisotropy of the non-endmember phase. Iron- and aluminum-bearing post-perovskite is likely to be as anisotropic as the magnesian end-member at lowermost mantle conditions (Mao et al., 2010; Caracas et al., 2010; Zhang et al., 2016), but there is little evidence for its effect on plasticity. Recent work suggests that iron will strongly partition into ferropericlase in the lowermost mantle in any event (Gialampouki et al., 2018); thus, its importance may be limited.

Ferropericlase. Ferropericlase (Mg, Fe)O is present in the lower mantle with a molar abundance of 10–30% (e.g., McDonough & Sun, 1995). Before post-perovskite was discovered in 2004, ferropericlase was already considered a potential explanation of lowermost mantle anisotropy (Yamazaki & Karato, 2002). It is cubic, and its elasticity can thus be described by three independent parameters. These are constrained both through *ab initio* calculations (Karki et al., 2000; Z. Wu et al., 2013) and through experiments (e.g., Jackson et al., 2006). The results of these studies show significant single crystal anisotropy, as well as an increase of anisotropy with Fe content, related to changes in C_{12} and C_{44} with cell volume via pressure (Marquardt et al., 2009; Antonangeli et al., 2011; Finkelstein et al., 2018).

Ferropericlase is much weaker than bridgmanite (Cordier et al., 2012). Atomistic calculations of pure MgO endmember have shown dominating slip systems of $\langle 110 \rangle \{1\bar{1}0\}$ and $\langle 110 \rangle \{100\}$ (Carrez et al., 2009; Amodio et al., 2011, 2016). Experiments on pure MgO (Merkel et al., 2002; Girard et al., 2012) and (Mg, Fe)O (Lin et al., 2009) show dominant slip on $\langle 110 \rangle \{1\bar{1}0\}$, while higher-temperature experiments on (Mg, Fe)O also activate $\langle 110 \rangle \{100\}$, consistent with the calculations. Whether ferropericlase can explain the observed anisotropy depends on the degree of single crystal anisotropy (related to the Fe content), its abundance in the lowermost mantle (i.e., whether ferropericlase grains become interconnected), and the general strength contrast between ferropericlase and bridgmanite or post-perovskite. However,

it should be noted that even in the two-phase experiments discussed earlier, where ferropericlase takes up the bulk of the deformation, coherent CPO does not develop in the ferropericlase, potentially due to the polyphase geometry causing strain heterogeneity in the ferropericlase crystals (Kaercher et al., 2016; Miyagi & Wenk, 2016).

Other Phases. Although post-perovskite, bridgmanite and ferropericlase are expected to dominate the lowermost mantle, it is possible that other phases play a role in causing anisotropy.

Though peridotite comprises $\sim 5\%$ of Ca-perovskite (CaMgSiO_3) in the lower mantle, basaltic compositions may hold up to 30% (McDonough & Sun, 1995), and hence Ca-pv may be important if subducted material can accumulate at the base of the mantle. Sample recovery issues mean that high-pressure and -temperature experiments are difficult and the phase boundary between cubic and tetragonal Ca-pv is still being determined (Thomson et al., 2019), but molecular dynamics simulations (Li et al., 2006) show maximum single-crystal shear-wave anisotropy of 25%, similar to other phases mentioned here. Room-temperature diamond-anvil cell experiments (Miyagi et al., 2009) and Peierls–Nabarro modeling (Ferré et al., 2009) suggest Ca-pv might form a CPO in deformation by glide on the cubic slip system $\langle 1\bar{1}0 \rangle \{110\}$, and experiments on the analog CaGeO_3 suggest Ca-perovskite may be weaker than MgO (Wang et al., 2013), but relatively few studies have yet examined this further.

Silica phases may also make up $\sim 20\%$ of a basaltic lower mantle. While it seems likely that stishovite is stable until about 1500 km depth, uncertainty remains as to when in the lower mantle silica transitions from the CaCl_2 structure to seifertite (e.g., Sun et al., 2019). This may be important since, while seifertite appears to be only moderately anisotropic (Karki et al., 1997) and hence is likely not be a large contributor to lowermost mantle anisotropy, CaCl_2 -type silica may have much stronger shear-wave anisotropy of about 30% (Yang & Wu, 2014). Unfortunately, we do not currently have constraints on how silica phases may accommodate strain.

If hydrogen can be carried to the deep mantle, then hydrous phases such as aluminous phase D or phase H might occur in D'' (e.g., Pamato et al., 2015; Panero & Caracas, 2017), while aluminous phase δ -AlOOH is likely present in basaltic compositions (e.g., Duan et al., 2018), and iron-rich regions could contain Fe-rich phases such as FeO_2 or FeOOH (e.g., Hu et al., 2016). Some of these phases may be strongly anisotropic, however compared to the nominally anhydrous silicates like bridgmanite and post-perovskite, little work has been done to understand their deformation mechanisms.

13.4. JOINT GEODYNAMIC-SEISMIC MODELING

13.4.1. Recent Developments

Several endeavors – mainly over the last decade – have tried to tie together all the fields and constraints discussed so far, in order to interpret anisotropy in the lowermost mantle. The long-term, sometimes enigmatic, goal of these studies is to map flow directions in the lowermost mantle to understand its role in the overall mantle convection (as the title of this chapter suggests). Most studies to this date, however, attempt to constrain the underlying cause of anisotropy taking their best guess at the flow regime.

In terms of the cause of anisotropy, recent studies rely heavily on post-perovskite being stable in the lowermost mantle to explain the observed anisotropy, arguing that bridgmanite produces the wrong radial anisotropic signature, and ferropericlase is not abundant enough to dominate anisotropic signatures. Bridgmanite not playing a major role can also be argued in light of the recent results that bridgmanite is too strong to cause dislocation glide and develop preferred orientation (Boioli et al., 2017).

The dominant glide plane in post-perovskite that is argued to explain anisotropy varies with studies arguing for dominant glide on (010) (Walker et al., 2011; Nowacki et al., 2013; Creasy et al., 2017; Tommasi et al., 2018; Ford et al., 2015) and (001) (Nowacki et al., 2010; Cottaar et al., 2014; Walker et al., 2018; X. Wu et al., 2017; Chandler et al., 2018). These studies range from finding a best-fitting model from a qualitative comparison to previously published observations (i.e., Cottaar et al., 2014; Tommasi et al., 2018) to a quantitative misfit with local observations (Nowacki et al., 2010; Ford et al., 2015; Creasy et al., 2017) or with global anisotropic models (Walker et al., 2011, 2018). Of course, all of these studies have made different assumptions and choices, which may affect the final conclusion. One example is the choice of elastic constants—for instance, a dominant glide system on the (010) plane results in $V_{SH} > V_{SV}$ when using elastic constants of Stackhouse et al. (2005), and in $V_{SV} > V_{SH}$ when using those of Wentzcovitch et al. (2006) (Yamazaki & Karato, 2007; Wenk et al., 2011). Similarly, studies may choose to use constants derived at a single pressure and temperature – not necessarily those of the part of the mantle of interest – or attempt to include the variable anisotropic effects, as P and T vary (Walker et al., 2011).

A number of recent studies are worth highlighting. Tommasi et al. (2018) explore the anisotropy resulting from deformation constraints from atomistic modeling instead of experimental results, arguing for a dominant glide plane of (010). Atomistic calculations, which will hopefully converge with experimental results in the future,

offer a great step forward into constraining the deformation in the lowermost mantle. Their modeling finds weak radial anisotropy of $V_{SH} > V_{SV}$ and sub-horizontal fast polarization directions in simple corner flow.

Their modeled elastic tensors with post-perovskite and periclase in an upwelling tracer can also fit the recent observations of changing anisotropy beneath Iceland by Wolf et al. (2019). However, their study also presents models of pure bridgmanite and periclase that can fit the observations for the assumed change in flow.

Walker et al. (2018) explore texture inheritance from (001) slip in post-perovskite to bridgmanite (Dobson et al., 2013) on a global scale. Such a model can explain the observed sharp changes in the signature of anisotropy from regions dominated by cold downwellings, to regions dominated by hot upwellings or LLSVPs. Comparable results for texture inheritance were shown by Chandler et al. (2018) using the tracking of single tracers from downwelling to upwelling.

Most of the studies mentioned have preassumed the flow pattern either locally or globally, and the models of different compositions are tested against seismic observations. Only the studies of Ford et al. (2015) and Creasy et al. (2017) both fit the compositional model as well as the flow direction. For both cases, this is applied to one locality where anisotropy is constrained from different azimuthal directions. Ford et al. (2015) suggest mainly vertical flows occur just to the east of the African LLSVP, while Creasy et al. (2017) suggest horizontal flows in a region of fast isotropic velocities beneath New Zealand and Australia.

13.4.2. Example Case: Comparing a Model to Seismic Observations

Many of the multidisciplinary modeling studies discussed above compare their synthetic elasticity models to ray-theoretically derived local body-wave observations. A number of studies explore the limitations of interpreting body-wave observations in terms of anisotropy by analyzing synthetic observations; for example for 1D isotropic or radially anisotropic models for S_{diff} waves (Maupin, 1994; Komatitsch et al., 2010; Borgeaud et al., 2016; Parisi et al., 2018) and for ScS waves (Kawai & Geller, 2010). Nowacki and Wookey (2016) extend the analysis for ScS waves to full synthetic anisotropic models with small-scale variations from the model of Walker et al. (2011) (cf. Figure 13.3). They conclude that ray-theoretical interpretations hold up for the simplest anisotropic models, but break down for those with variable anisotropy. Additionally, the finite-frequency wave senses less splitting than a ray-theoretical interpretation of an anisotropic model would suggest, as the finite-frequency sensitivity will average over

the strongly varying anisotropic medium, sensing an effective medium.

Here we explore these limitations further by combining the forward modeling in a subducting slab of Cottaar et al. (2014) with the full-wave modeling of Nowacki and Wookey (2016) and analyse S_{diff} , ScS , SKS , and $SKKS$ phases in a finite-frequency framework.

Geodynamic and Texture Modeling. We use the results of Cottaar et al. (2014). We refer the reader to the original work for a full description of parameters used, but note that in this type of modeling, uncertainty can be introduced via a number of parameters, including the chosen relative critical resolved shear stresses on each slip system; the lack of a non-glide mechanism to accommodate strain and reset texture (such as diffusion creep); the phase boundary between phases; the single-crystal elastic constants; and the stress-strain homogenization scheme. In the following, we give a short summary of the modeling details.

Deformation is tracked along tracer particles (Figure 13.4a) across the lowermost mantle using CitcomS (Zhong et al., 2000), where 500 grains are modeled with the viscoplastic self-consistent method (VPSC; Lebensohn & Tomé, 1993) to accommodate the deformation; 75% of these grains are post-perovskite (ppv) or bridgmanite (pv), and 25% are periclase. For post-perovskite, a dominant glide plane of (100) (ppv 100 model), (010) (ppv 010), or (001) (ppv 001) is assumed. The assumed glide planes for periclase are weaker, and this phase ends up accommodating 35–40% of the deformation. For the elastic constants, the values of Stackhouse et al. (2005) are used for post-perovskite and bridgmanite, and those of Karki et al. (2000) for periclase. Cottaar et al. (2014) note that model ppv 001 is in general agreement with the radial anisotropy observed at the bottom of slabs and fast directions of azimuthal anisotropy is parallel to flow directions. The radial anisotropy in model ppv 010 also has the right sign, but is very weak in nature.

Seismic Modeling. We seek to compare the predicted seismic characteristics of our geodynamic slab model to regional observations of anisotropy, including splitting in S_{diff} , SKS – $SKKS$, and S – ScS differential splitting, as well as observations of changes in splitting intensity (Chevrot, 2000). In order to do this, we simulate the propagation of waves through the model in two directions—along the slab and across it—for a range of geometries. We use synthetics in the epicentral distance range $55^\circ \leq \Delta \leq 80^\circ$ for ScS , $100^\circ \leq \Delta \leq 130^\circ$ for SKS , $110^\circ \leq \Delta \leq 130^\circ$ for $SKKS$ and $95^\circ \leq \Delta \leq 120^\circ$ for S_{diff} . Table 13.1 outlines the geometries used in this study and which phases are investigated for each, whilst

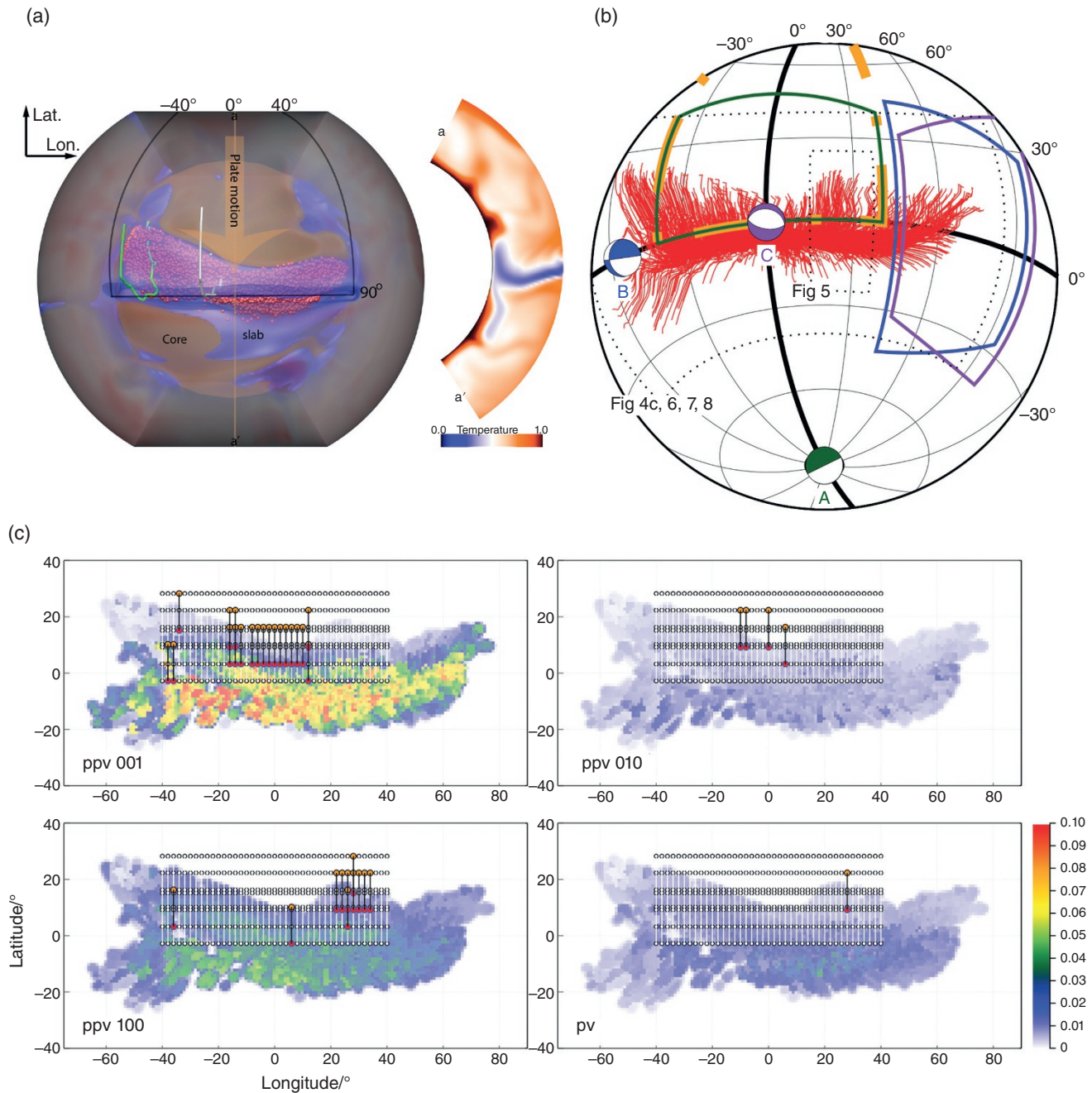


Figure 13.4 (a) Geodynamical setup of forward calculation, taken from Figure 1 of Cottaar et al. (2014). A slab is imposed, moving from north to south, which subducts along the equator. Tracer particles are shown by orange dots, with the path for two highlighted as green and white lines. Section a–a' along longitude 0° to the right shows nondimensional temperature. (b) Geometry of synthetic seismic sources and receivers in relation to the slab model. Sources are shown by color-coded lower-hemisphere focal mechanisms (annotated with the code in Table 13.1), matching the receiver locations, shown by open areas with solid boundaries. Red lines show the paths of tracer particles, and orange dash-dotted lines show the slab edges in panel (a). Areas shown by other figures are indicated by dotted black lines and labeled. (c) Discrepant *SKS-SKKS* splitting for path A (Table 13.1) for each plasticity model. Red and orange circles, respectively, show the core piercing points for *SKKS* and *SKS* waves for pairs that are discrepant, whilst white circles denote the piercing points of pairs that are not. Underlying color shows the strength of anisotropy at the bottom of the slab texture model, using the universal elastic anisotropy index, A^U (Ranganathan & Ostoja-Starzewski, 2008) according to the color scale on the bottom right. (For approximate path lengths of *SKS* and *SKKS* in the lowermost mantle, see Figure 13.6.). Source: (a) Cottaar et al., (2014).

Table 13.1 Summary of synthetic paths used to investigate anisotropy in the geodynamic slab model.

Code	Description, phases ^a	Source longitude (°)	Source latitude (°)	Focal mechanism ^b
A	Across slab: <i>SKS</i> – <i>SKKS</i>	0	–90	090/0/–90
B	Along slab: <i>SKS</i> – <i>SKKS</i> , <i>S_{diff}</i>	–55	0	180/30/0
C	Along slab: <i>ScS</i> , <i>S_{diff}</i>	0	0	280/30/–90

^a Phases analyzed from full-wavefield synthetics.

^b Given as strike/dip/rake of the fault plane in °.

All events at 650 km depth.

Figure 13.4b shows the location of the events and receivers.

We calculate the seismic response of the slab using the spectral element method as implemented in the SPEC-FEM3D_GLOBE code (Komatitsch & Tromp, 2002). In order to remove time in writing intermediate files, we use a version of the code where creating the spectral element mesh and solving the equations of motion are performed in the same program (Komatitsch et al., 2003; Nowacki & Wookey, 2016). We use two chunks of the cubed sphere with 800 spectral elements along each side, giving seismograms accurate at frequencies below 0.2 Hz, similar to the dominant period of the waves at these distances.

The elasticity model is mapped to the seismic computational mesh by finding the nearest neighboring tracer particle within a defined “slab” region, which is below 400 km above the CMB and within 150 km from any given particle. Beyond this distance, the nearest particle’s elasticity grades smoothly to the background 1D velocity, given by AK135 (Kennett et al., 1995), over a 100 km distance using Voigt averaging between the isotropic and full elastic tensor. This smoothing distance was chosen to avoid artificially extending the region of the mantle influenced by the slab, while avoiding seismic artifacts from a spatially abrupt transition between isotropic and anisotropic mantle.

Synthetic Analysis. We can process synthetics from our forward model in the same way as data and compare the two. For the purposes of this example, we show a selection of results for the three paths, for different combinations of seismic phases, analysing the shear-wave splitting in *ScS*, *S_{diff}*, and differential splitting between *SKS* and *SKKS*. In all cases, we analyse the shear-wave splitting in a window around the arrival of interest using the minimum-eigenvalue method of Silver & Chan (1991), with errors as updated by Walsh et al. (2013). The fast axis here is defined as the angle ϕ' from the radial component (or the vertical at the bottoming point of the seismic ray, Figure 13.1c in Nowacki et al. (2010)). We also consider the splitting intensity (*SI*; Chevrot, 2000) for *SKS* and *SKKS* waves, where the polarization is known to be radial, and *S_{diff}* waves, where almost all *SV* energy is lost along the diffracted path, rendering them horizontally

polarized. For this reason, *S_{diff}* *SI* is calculated in the opposite sense to usual for *SK* (*K*)*S* waves, interchanging the radial and transverse components in the calculation. Discrepant *SKS*–*SKKS* splitting pairs are identified where either one of the phases shows null splitting, whilst the other does within error, or the two phases’ 95% confidence region of the small-eigenvalue surface do not overlap. Additionally, for all splitting measurements we use the automatic classification method of Wuestefeld et al. (2010) to calculate *Q*, a measure of quality between –1 and 1, where –1 indicates a null, 1 a good measurement, and 0 a likely poor measurement.

We consider first the splitting in *ScS* for path C (Figure 13.5). This path is similar to observations of splitting along palaeosubduction zones such as beneath the Caribbean (Garnero et al., 2004; Maupin et al., 2005; Nowacki et al., 2010, e.g.). In general, it seems that $\phi' \approx 90^\circ$ ($\xi > 1$) in many slab regions (Nowacki et al., 2011; Romanowicz & Wenk, 2017); in the Caribbean in particular, Garnero et al. (2004) infer a systematic rotation in the fast angle across the palaeoslab region, giving a change in ϕ' from $\sim 105^\circ$ to $\sim 75^\circ$.

Returning to Figure 13.5, it is clear that plasticity models ppv 010 and ppv 100 are better candidates than the remaining models at reproducing the $V_{SH} > V_{SV}$ and variable ϕ' signals seen in data. Note that this is a different conclusion from Cottaar et al. (2014), which could be due to the added complexity in this study of investigating the non-horizontal orientation of the waves, which can cause rotations in ϕ' (see Figure 13.2). The models produce values of δt which are mostly comparable to those seen in nature, though larger at up to 6 s in the synthetics versus ~ 2 –3 s as observed. The strength of anisotropy present in the models is up to $A^U = 0.1$, which is about one-third of the predicted single crystal anisotropy of ppv in the lowermost mantle (Stackhouse et al., 2005).

We next show results for path B, which samples the slab similarly, but using *S_{diff}* and *SKS*–*SKKS* phases in Figures 13.6 and 13.7. *SI* for *S_{diff}* should be large only when a significant nonradial anisotropy is present, which is generally the case within and at the edges of the slab.

It is notable in all cases that the pattern of ϕ' and δt is complex and variable across the slab, with large regions of null splitting even where strong anisotropy is present.

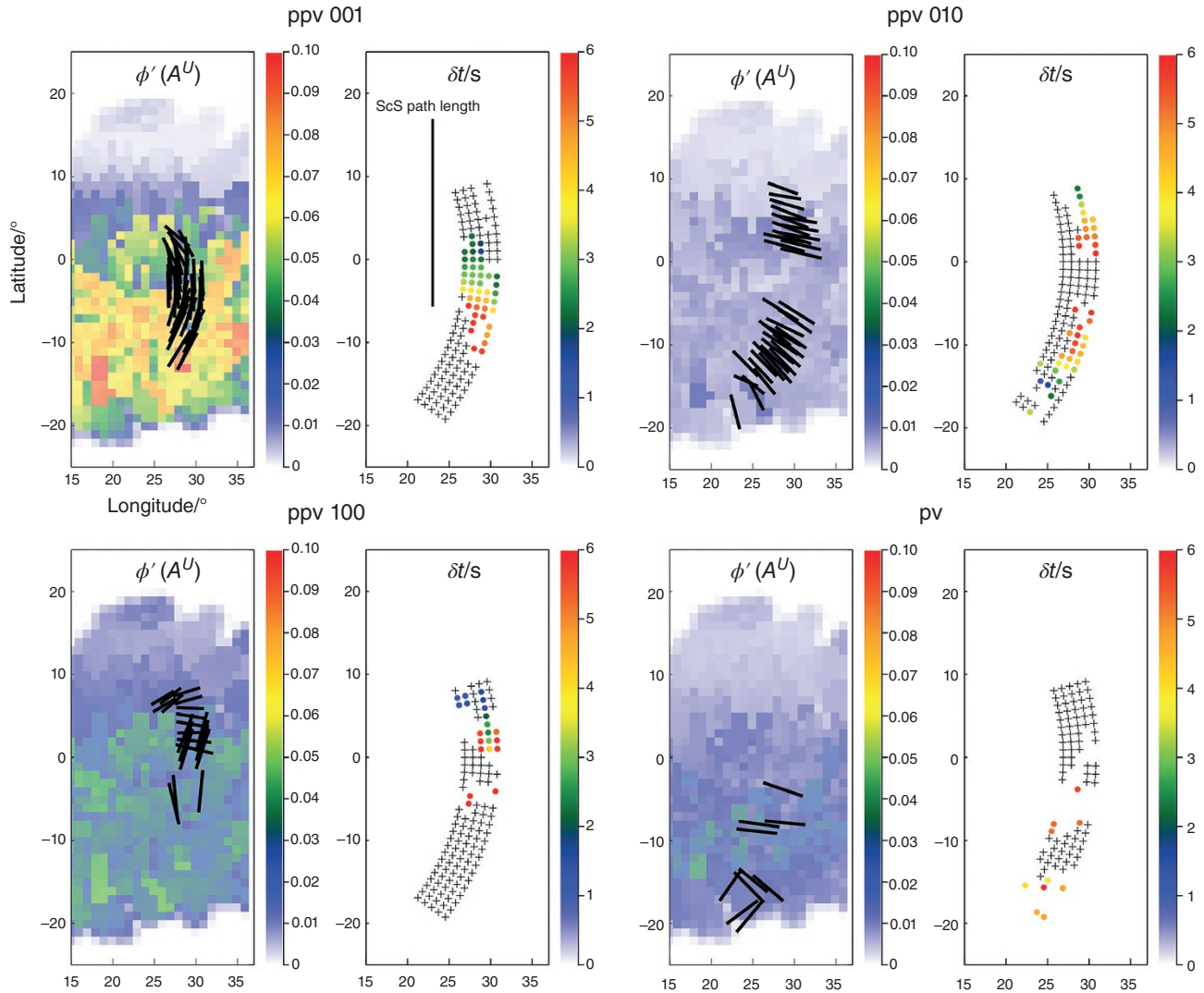


Figure 13.5 Shear-wave splitting results for the ScS phase for path C (Table 13.1), for each slab texture. Each panel shows on the left the fast shear-wave orientation in the ray frame (see Nowacki et al., 2010, Figure 1c), ϕ' , as a black bar located at the ScS core bounce point. Bars oriented left–right ($\phi' = 90^\circ$) correspond to radial anisotropy with $\xi > 1$, and vertical bars mean $\xi < 1$ ($\phi' = 0^\circ$), with nonradial anisotropy otherwise (when $0^\circ \neq \phi' \neq 90^\circ$). Color beneath the bars is as in Figure 13.4c. On the right we show the amount of splitting, δt at each bounce point, colored by the second scale bar. Crosses signify null measurements. The length of the ray path of ScS in the lowermost 250 km of the mantle is shown in the right-hand panel for the ppv 001 case.

Null splitting may occur when the polarization of a shear wave traveling through an anisotropic medium is close to the fast or slow shear-wave orientations (which are perpendicular) in that direction, and this may be the cause here. Variability in ϕ' is expected because of the pattern of flow in the model, and we observe fairly smooth rotations of ϕ' from north to south in the ppv models, similarly to data. However, the pv case shows δt variations do not correlate strongly to simple features in the elasticity model. This illustrates the sometimes-nonintuitive manner in which the seismic wave averages structure, and cautions against

the use of approximate methods like ray theory when calculating synthetics in such models for data comparison.

SKS–SKKS pairs, in contrast, show relatively straightforward behavior, with discrepant pairs concentrating near the edges of the high-anisotropy areas, as expected. The “core” of the deformed material does not show discrepant splitting, as both phases show similar behavior. Notably, for ppv 001 there is a region in the northeast that does not show the expected behavior. We see a similar nonintuitive behavior in path A (Figure 13.4b). Here, although some discrepant pairs straddle the edge of the

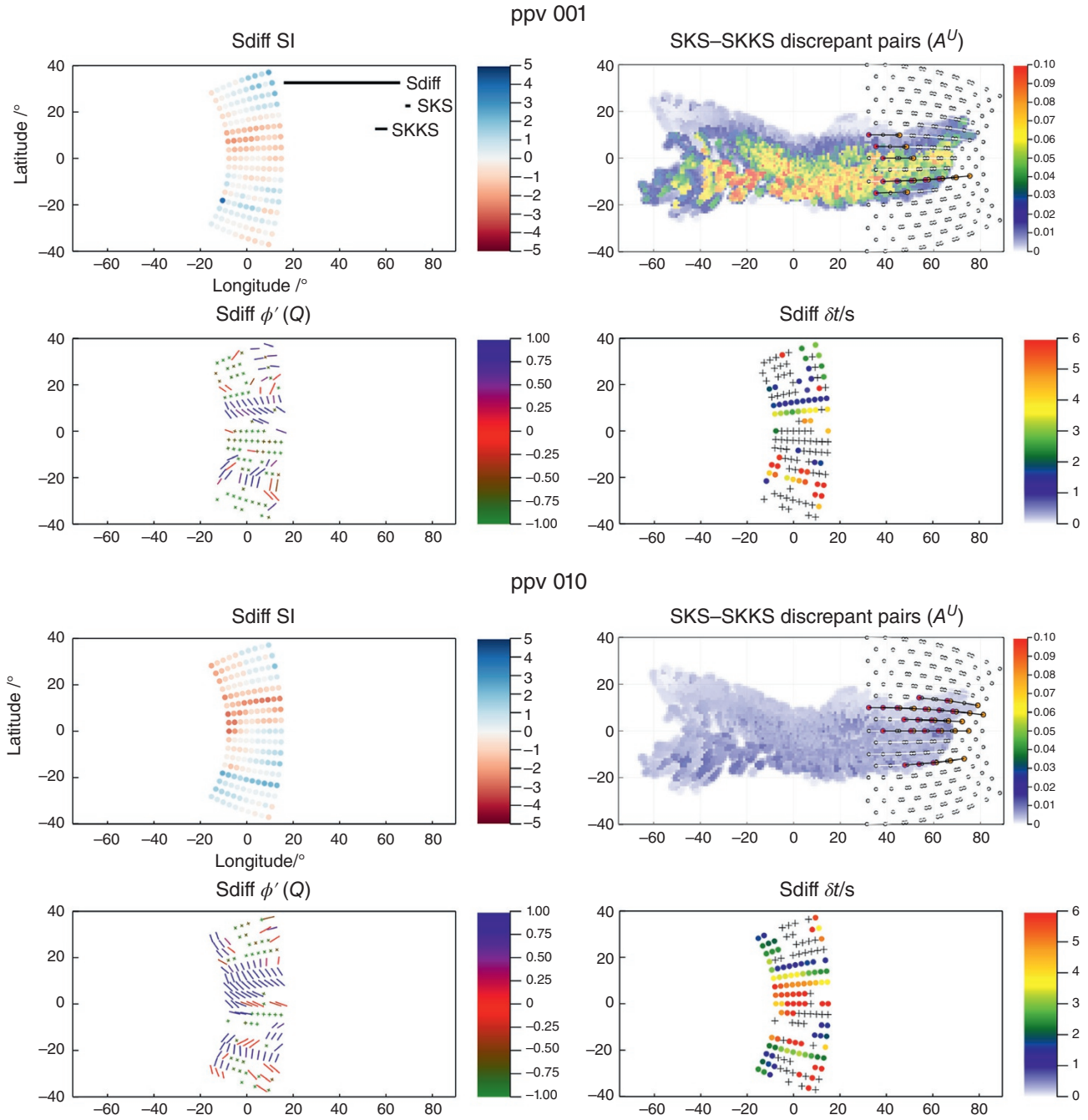


Figure 13.6 Shear-wave splitting results for the path B (Table 13.1) and models ppv001 and ppv010. For each plasticity model, four panels show: (top left) the splitting intensity of S_{diff} as color (Chevrot, 2000); (bottom left) the ray-frame fast shear-wave orientation of S_{diff} , colored by the splitting quality measure Q (Wuestefeld et al., 2010); (bottom right) slow shear-wave delay time δt , colored as per the scale bar; and (top right) pairs of discrepant SKS – $SKKS$ splitting, where the red and orange circles show the core piercing point of $SKKS$ and SKS , respectively, and white circles indicate no discrepant splitting; background color shows strength of anisotropy as in Figure 13.4c. S_{diff} points are plotted at the end of the core-diffracted part of the path. The lengths of the ray paths of S_{diff} , SKS and $SKKS$ in the lowermost 250 km of the mantle, are shown in the SI panel for the ppv001 case.

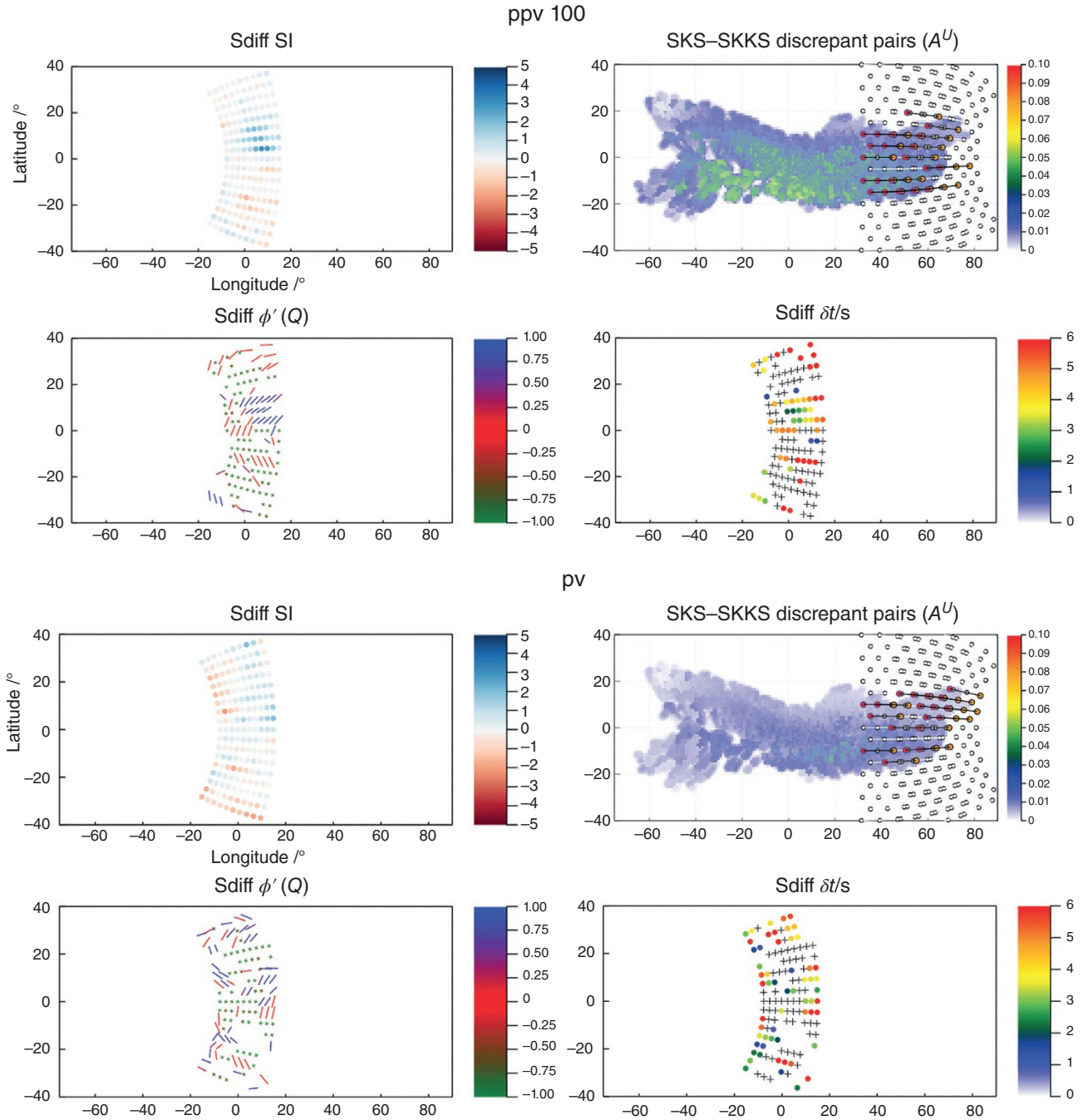


Figure 13.7 Shear-wave splitting results for the path B (Table 13.1) and models ppv100 and pv. Features as for Figure 13.6.

slab for ppv 001, very few paths show this for any of the other models. Inferring the edges of anisotropic regions, therefore, must again be done with caution.

We also examine the raw difference in splitting intensity between *SKS* and *SKKS* at the same seismograms, $\Delta SI = SI_{SKS} - SI_{SKKS}$ (Figure 13.8). Measuring ΔSI is computationally simple, and hence holds the promise for

automatic global mapping of D'' anisotropy. Comparing with the differential splitting predictions (Figures 4c, 6 and 7), it appears that the along-slab path B (Figure 13.8b) shows straightforward behavior, where ΔSI deviates significantly from 0 where the slab is significantly anisotropic, either positively or negatively depending on the exact elastic structure in the model. This agrees well with

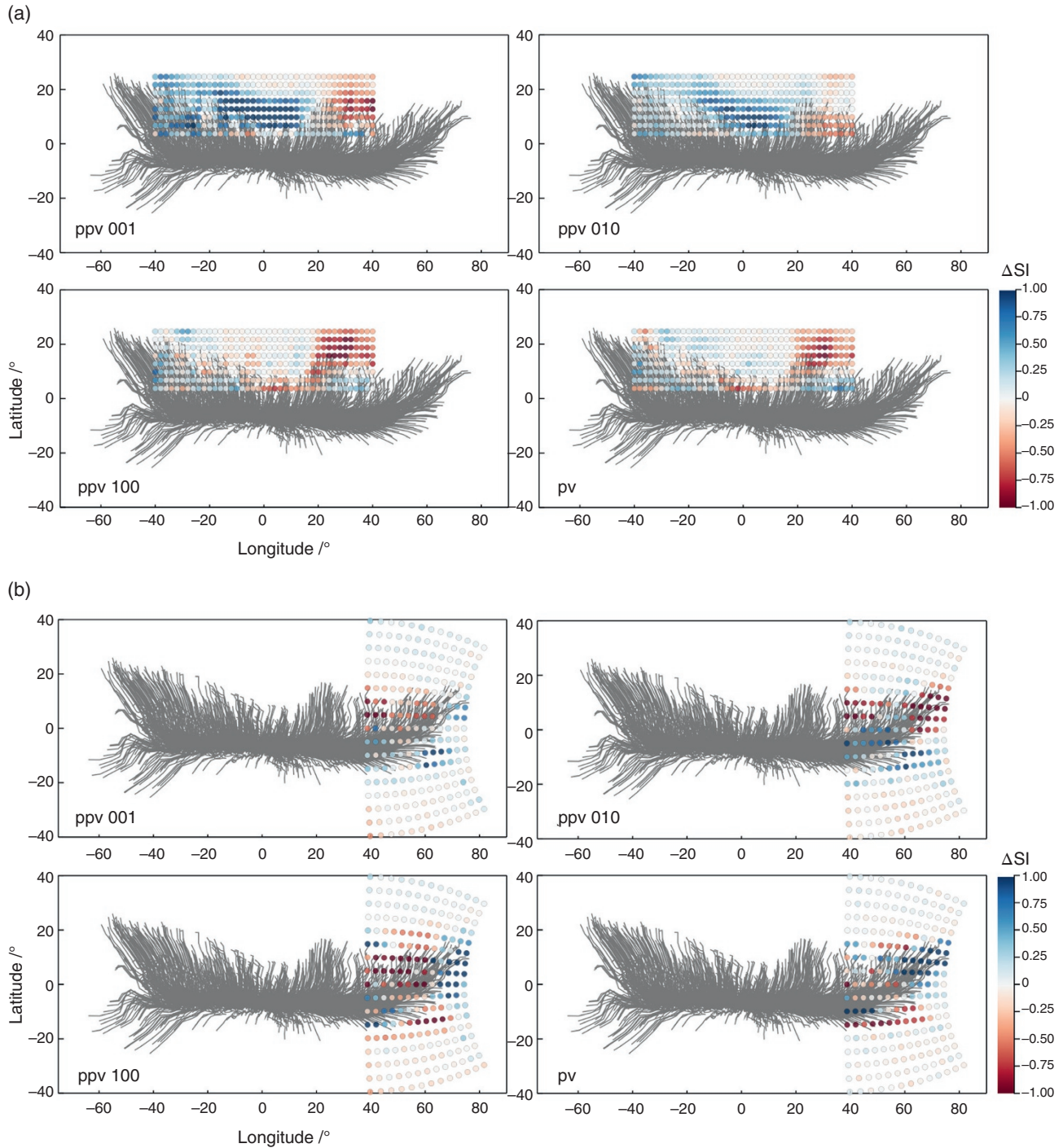


Figure 13.8 Difference in splitting intensity between *SKS* and *SKKS*, ΔSI for (a) path A and (b) path B (Table 13.1). ΔSI is shown by color according to the scale, lower right, at the midpoint between *SKS* and *SKKS* core–mantle boundary piercing points. Gray lines in the background show the path of tracers particles in the geodynamic model.

the differential splitting interpretation. For path A, however (Figure 13.8a), a large negative ΔSI signal is present at the eastern end of most models, though this is not correlated to significant differential splitting (Figure 13.4c). Most models also show large ΔSI in the central northern

part, but again this is not reflected in differential splitting. This suggests that although there is significant difference between the elastic structure experienced by the *SKS* and *SKKS* waves in these regions as they cross the edge of the anisotropic part of the slab, the shear-wave splitting is not

sufficiently coherent and clear to provide a strong signal. Nevertheless, these calculations suggest that a more global *SKS*–*SKKS* comparison holds promise for detecting regions where anisotropy changes rapidly.

13.5. LIMITATIONS, ADVANCES, AND THE WAY FORWARD

13.5.1. The Inverse Problem

The final goal of observing anisotropy in the lowermost mantle is, as the title of this chapter suggests, to map flow directions. We have discussed the forward model and the large number of assumptions required to create an anisotropic model and compare it to seismic observations. For most studies discussed in Section 13.4.1 the flow model was one of the prior assumptions and different potential compositions are explored; only the recent studies of Ford et al. (2015) and Creasy et al. (2017) locally interpret flow direction.

Results for a suite of candidate deformation mechanisms, like those in Figure 13.5, immediately make tempting a potentially circular line of reasoning: given an assumed flow model and the data, can we infer the deformation mechanism responsible for anisotropy? And with that improved estimate of deformation mechanism, can we then infer the flow field? As discussed, uncertainty as to the very cause of anisotropy in the lowermost mantle makes such reasoning perilous. It is also worth noting that if the rheology in geodynamic models is set in part based on observations of seismic anisotropy, and the assumption made of a particular deformation mechanism, then there is an added danger in the use of such dynamic models to then infer the mechanism of anisotropy.

Despite these problems, we can proceed with caution if we hold in mind that it is the *combination* of the flow model, deformation mechanism, and mineral elasticity that is being tested against the data in each instance, not any one of these in isolation. Intuitively, varying any one of these might lead to an equally well-fitting set of synthetic observations when varying another.

Is finding the dominant mineral (or multiphase system) and deformation systems creating lowermost mantle anisotropy the biggest hurdle in the way to mapping flow? If we constrain the main source of anisotropy, could we create a map of flow across the mantle? To do that, we would be interested in making a number of inverse steps (shown in Figure 13.3 by the white dashed arrows), each of which is nonlinear and underdetermined:

1. *Using the seismic observations to find the constrained parts of the seismic anisotropic tensor.* Constraints on the anisotropic tensor will always be limited by the propagation direction of the seismic phases used

(Figure 13.2) and the azimuthal coverage, generally leaving large parts of the anisotropic tensor unconstrained, and resorting studies to assume symmetries (i.e., radial or azimuthal anisotropy). Additionally, the resulting anisotropic tensor would always reflect the effective elastic tensor that the seismic waves observed at long wavelengths, and could result from an entire suite of small-scaled heterogeneously (an) isotropic media (e.g., Backus, 1962; Capdeville & Cance, 2014; Fichtner et al., 2013). In this chapter we have frequently made the major assumption that the anisotropy of the effective tensor is due to underlying intrinsic anisotropy (CPO), and not caused by small-scale isotropic heterogeneity (SPO).

2. *Mapping from the effective anisotropic tensor to a set of textured minerals or a specific mineral with preferred orientation.* Accounting for the null-space in the elastic tensor, there would be no unique fit here, and many assumptions on the mineral physics need to be made. One could not account for the entire suite of potential deformation mechanisms occurring, presence of other minerals and the related multiphase deformation effects. With the assumption of a single dominant mineral and glide mechanism, the main imaged fast polarization direction in the elastic tensor would be preferentially fit. There is no value in mapping the strength of the anisotropy into a degree of preferentially aligned minerals, as the amplitudes of the effective elastic tensor will be underestimated (as shown by the synthetic results in Section 13.4.2).
3. *Mapping from textured minerals to potential deformation history and flow directions.* A single textured mineral can result from various deformation histories as it can both reflect the deformation it is undergoing, or fossilized deformation, which could be displaced and rotated. To uniquely constrain the flow model, many observations in different locations will have to be combined, as well as including other constraints, i.e., isotropic velocities, the gravity field, and past plate tectonic models.

While we choose to highlight the true inverse steps of this problem, this poses multiple layers of non-uniqueness, which makes a flow map for the lowermost mantle based on anisotropy appear unobtainable. For the foreseeable future, mapping mantle flow will have to rely on simplified relationships between fast polarization directions and flow with understanding of the conditions under which these are valid. For the upper mantle, a simple relationship is posed as the fast axis of deformed olivine generally aligns with the flow direction, which has allowed interpretation of asthenospheric flow from anisotropy, although the validity of this under volatile-rich conditions, e.g., in the mantle wedge above subduction

zones, where observations also become more complex (see Becker & Lebedev, 2021). For the lowermost mantle, Cottaar et al. (2014) pose a similar relationship between horizontal fast direction and horizontal flow direction specifically for post-perovskite with dominant (001)-glide for a simple case of a slab spreading out on the CMB. Such a relationship should be tested statistically under many flow conditions, rotations, and deformations, and using full-waveform modeling. Tommasi et al. (2018) present a relationship of sub-parallel fast polarization directions to the flow direction for post-perovskite with dominant (010)-glide and twinning for simple horizontal flow. Their study tests, not statistically but very systematically, the limitations of this relationship in corner flows and the ability of different seismic phases to detect these polarization directions.

Creasy et al. (2019) pose a different question: with our current level of non-uniqueness in the interpretation, how many independent seismic observations do we need in a single location to interpret composition and flow? They show statistically that roughly 10 or more measurements of fast direction or reflection polarizations with various azimuths and incidence angles are needed to uniquely constrain the anisotropic tensor to make an interpretation with some confidence. It is challenging to find locations to which this can be applied due to available earthquake-station geometries.

While it is unlikely that the mineralogical parameters we have discussed will be tightly constrained for some time, and similarly seismic data coverage will probably not improve vastly, it is conceivable that probabilistic approaches to inferring flow from anisotropy may enable progress by incorporating uncertainties in all the input parameters as in Figure 13.3 and retrieving an ensemble of acceptable flow histories. Such a model suite would, however, likely be a vast undertaking, requiring many millions of forward iterations, including geodynamic and full waveform modeling. This is unfeasible with the current combination of forward numerical methods and computational resources, but the future may bring this within our grasp.

13.5.2. Outlook

While mapping flow clearly remains an ambitious goal, current studies of anisotropy do provide new insights into the deepest mantle. Specifically, the goal to find the source of anisotropy reveals the potential importance of post-perovskite to be stable in the mantle, as bridgmanite might be too strong to cause texturing (Boioli et al., 2017) and ferropericlase, as the minor phase, might not deform coherently (Miyagi & Wenk, 2016). Observations of lateral changes in anisotropy could highlight where post-perovskite is present, which relates to the

temperature field and thus the convective patterns. A major step forward in understanding the role of post-perovskite would be to resolve its dominant deformation mechanisms. It remains to be seen if the latest theoretical calculations (e.g., Goryaeva et al., 2017) will converge with future experimental results.

Studies of anisotropy are also illuminating the nature of the LLSVP boundaries. From a seismological point of view, the claim that the radial anisotropy switches sign inside and outside the LLSVPs needs to be further tested for its robustness. Any relationship between the isotropic and anisotropic velocities in tomographic models could be an artefact (e.g., Chang et al., 2015). Local observations of splitting, however, have confirmed strong changes in anisotropy around the edges of the LLSVPs (e.g., Cottaar & Romanowicz, 2013; Wang & Wen, 2007; Lynner & Long, 2014). The nature of the LLSVPs poses major unanswered questions, and understanding the changing signatures of anisotropy can help resolve to what degree their boundaries represent a purely thermal or a thermo-chemical gradient. In the thermal case, change in anisotropy could be explained by a phase transition from post-perovskite to perovskite (Dobson et al., 2013) or by a change in flow direction, likely from horizontal outside to vertical within the LLSVPs or plumes (e.g. Wolf et al., 2019). In the case where LLSVPs represent thermo-chemical piles, the boundary could also be mechanical with separate convection inside and outside the piles (e.g., Garnero & McNamara, 2008). Currently, capturing all the variation in parameters that contribute to the development of anisotropy while correctly relating these to observations is computationally constrained. However, while we are far from producing a global flow map based on anisotropic variations, anisotropic studies play a role in answering these fundamental questions on the nature of the lowermost mantle. With the answers to these questions, flow can be more easily interpreted on the basis of mapped isotropic velocity variations.

ACKNOWLEDGMENTS

The authors thank Andrew Walker for discussion and improvement of the manuscript, and acknowledge two anonymous reviewers and editor Hauke Marquardt for helpful and constructive comments. AN is supported by the Natural Environment Research Council (NERC grant reference number NE/R001154/1). SC is supported by the European Research Council (ERC) under the European Union's Horizon 2020 research and innovation program (grant agreement No. 804071 – ZoomDeep) and the Natural Environment Research Council (NERC grant reference number NE/R010862/1). Computations were performed on ARCHER.

REFERENCES

- Ammann, M. W., Brodholt, J. P., Wookey, J., & Dobson, D. P. (2010). First-principles constraints on diffusion in lower-mantle minerals and a weak D'' layer. *Nature*, *465* (7297), 462–465. doi: 10.1038/nature09052
- Amodeo, J., Carrez, P., Devincre, B., & Cordier, P. (2011). Multiscale modeling of MgO plasticity. *Acta Materialia*, *59* (6), 2291–2301.
- Amodeo, J., Dancette, S., & Delannay, L. (2016). Atomistically informed crystal plasticity in MgO polycrystals under pressure. *International Journal of Plasticity*, *82*, 177–191.
- Antonangeli, D., Siebert, J., Aracne, C. M., Farber, D. L., Bosak, A., Hoesch, M., ... Badro, J. (2011). Spin crossover in ferropericlase at high pressure: A seismo-logically transparent transition? *Science*, *331* (6013), 64–67.
- Auer, L., Boschi, L., Becker, T. W., Nissen-Meyer, T., & Giardini, D. (2014). Savani: A variable resolution whole-mantle model of anisotropic shear velocity variations based on multiple data sets. *Journal Of Geophysical Research-Solid Earth*, *119* (4), 3006–3034. doi: 10.1002/2013JB010773
- Backus, G. (1962). Long-wave elastic anisotropy produced by horizontal layering. *Journal Of Geophysical Research*, *67* (11), 4427–4440. doi: 10.1029/JZ067i011p04427
- Becker, T., & Lebedev, S. (2021). Dynamics of the lithosphere and upper mantle in light of seismic anisotropy. In H. Marquardt, M. Ballmer, S. Cottaar, & J. Konter (Eds.), *Mantle convection and surface expressions*. American Geophysical Union.
- Beghein, C., Trampert, J., & van Heijst, H. J. (2006). Radial anisotropy in seismic reference models of the mantle. *Journal Of Geophysical Research-Solid Earth*, *111* (B2), B02303. doi: 10.1029/2005JB003728
- Boioli, F., Carrez, P., Cordier, P., Devincre, B., Gouriet, K., Hirel, P., ... Ritterbex, S. (2017). Pure climb creep mechanism drives flow in Earth's lower mantle. *Science Advances*, *3* (3), e1601958.
- Borgeaud, A. F., Konishi, K., Kawai, K., & Geller, R. J. (2016). Finite frequency effects on apparent S-wave splitting in the D'' layer: Comparison between ray theory and full-wave synthetics. *Geophysical Journal International*, *207* (1), 12–28.
- Boschi, L., & Dziewoński, A. (2000). Whole Earth tomography from delay times of P, PcP, and PKP phases: Lateral heterogeneities in the outer core or radial anisotropy in the mantle? *Journal of Geophysical Research-Solid Earth*, *105* (B6), 13675–13696.
- Buchen. (2021). Seismic wave velocities in earth's mantle from mineral elasticity. In H. Marquardt, M. Ballmer, S. Cottaar, & J. Konter (Eds.), *Mantle Convection and Surface Expressions*. American Geophysical Union.
- Capdeville, Y., & Cance, P. (2014). Residual homogenization for elastic wave propagation in complex media. *Geophysical Journal International*, *200* (2), 986–999.
- Caracas, R., Mainprice, D., & Thomas, C. (2010). Is the spin transition in Fe²⁺-bearing perovskite visible in seismology? *Geophysical Research Letters*, *37*, L13309. doi: 10.1029/2010GL043320
- Carrez, P., Ferr e, D., & Cordier, P. (2009). Peierls-Nabarro modeling of dislocations in MgO from ambient pressure to 100 GPa. *Modeling And Simulation In Materials Science And Engineering*, *17* (3), 035010. doi: 10.1088/0965-0393/17/3/035010
- Carrez, P., Goryaeva, A. M., & Cordier, P. (2017). Prediction of mechanical twinning in magnesium silicate post-perovskite. *Scientific reports*, *7* (1), 17640.
- Chandler, B., Yuan, K., Li, M., Cottaar, S., Romanowicz, B., Tomé, C., & Wenk, H. (2018). A refined approach to model anisotropy in the lowermost mantle. In *Iop conference series: Materials Science and Engineering* (Vol. 375, p. 012002).
- Chang, S.-J., Ferreira, A. M. G., Ritsema, J., van Heijst, H. J., & Woodhouse, J. H. (2015). Joint inversion for global isotropic and radially anisotropic mantle structure including crustal thickness perturbations. *Journal of Geophysical Research: Solid Earth*, *120* (6), 4278–4300. doi: 10.1002/2014JB011824
- Chevrot, S. (2000). Multichannel analysis of shear wave splitting. *Journal Of Geophysical Research-Solid Earth*, *105* (B9), 21579–21590.
- Cobden, L., & Thomas, C. (2013). The origin of D'' reflections: A systematic study of seismic array data sets. *Geophysical Journal International*, *194* (2), 1091–1118.
- Cobden, L., Thomas, C., & Trampert, J. (2015). Seismic detection of post-perovskite inside the Earth. In *The earth's heterogeneous mantle* (pp. 391–440). Springer.
- Cordier, P., Amodeo, J., & Carrez, P. (2012). Modeling the rheology of MgO under Earth's mantle pressure, temperature and strain rates. *Nature*, *481* (7380), 177–180. doi: 10.1038/nature10687
- Cottaar, S., & Lekic, V. (2016). Morphology of seismically slow lower-mantle structures. *Geophys. J. Int.*, *207* (2), 1122–1136. doi: 10.1093/gji/ggw324
- Cottaar, S., Li, M., McNamara, A. K., Romanowicz, B., & Wenk, H.-R. (2014). Synthetic seismic anisotropy models within a slab impinging on the core-mantle boundary. *Geophysical Journal International*, *199* (1), 164–177. doi: 10.1093/gji/ggu244
- Cottaar, S., & Romanowicz, B. (2013). Observations of changing anisotropy across the southern margin of the African LLSVP. *Geophysical Journal International*, *195* (2), 1184–1195. doi: 10.1093/gji/ggt285
- Creasy, N., Long, M. D., & Ford, H. A. (2017). Deformation in the lowermost mantle beneath Australia from observations and models of seismic anisotropy. *Journal of Geophysical Research: Solid Earth*, *122* (7), 5243–5267. doi: 10.1002/2016JB013901
- Creasy, N., Pisconti, A., Long, M. D., Thomas, C., & Wookey, J. (2019). Constraining lowermost mantle anisotropy with body waves: a synthetic modeling study. *Geophysical Journal International*, *217* (2), 766–783.
- de Wit, R., & Trampert, J. (2015). Robust constraints on average radial lower mantle anisotropy and consequences for composition and texture. *Earth and Planetary Science Letters*, *429*, 101–109. doi: 10.1016/j.epsl.2015.07.057
- Deng, J., Long, M. D., Creasy, N., Wagner, L., Beck, S., Zandt, G., ... Minaya, E. (2017). Lowermost mantle anisotropy near the eastern edge of the Pacific LLSVP: constraints from SKS-SKKS splitting intensity measurements. *Geophysical Journal International*, *210* (2), 774–786.

- Dobson, D. P., Lindsay-Scott, A., Hunt, S., Bailey, E., Wood, I., Brodholt, J. P., et al. (2019). Anisotropic diffusion creep in postperovskite provides a new model for deformation at the core–mantle boundary. *Proceedings of the National Academic of Sciences*, 116 (52), 26389–26393.
- Dobson, D. P., Miyajima, N., Nestola, F., Alvaro, M., Casati, N., Liebske, C., et al. (2013). Strong inheritance of texture between perovskite and post-perovskite in the D'' layer. *Nature Geoscience*, 6 (7), 575–578. doi: 10.1038/ngeo1844
- Duan, Y., Sun, N., Wang, S., Li, X., Guo, X., Ni, H., et al. (2018). Phase stability and thermal equation of state of δ -AAIOOH: Implication for water transportation to the Deep Lower Mantle. *Earth and Planetary Science Letters*, 494, 92–98. doi: 10.1016/j.epsl.2018.05.003
- Ferré, D., Carrez, P., & Cordier, P. (2007). First principles determination of dislocations properties of MgSiO_3 perovskite at 30 GPa based on the Peierls–Nabarro model. *Physics of the Earth and Planetary Interiors*, 163 (1–4), 283–291.
- Ferré, D., Cordier, P., & Carrez, P. (2009). Dislocation modeling in calcium silicate perovskite based on the Peierls–Nabarro model. *American Mineralogist*, 94 (1), 135–142. doi: 10.2138/am.2009.3003
- Ferreira, A. M. G., Faccenda, M., Sturgeon, W., Chang, S.-J., & Schardong, L. (2019). Ubiquitous lower-mantle anisotropy beneath subduction zones. *Nature Geoscience*, 12 (4), 301. doi: 10.1038/s41561-019-0325-7
- Ferreira, A. M. G., Woodhouse, J. H., Visser, K., & Trampert, J. (2010). On the robustness of global radially anisotropic surface wave tomography. *Journal Of Geophysical Research-Solid Earth*, 115, B04313. doi: 10.1029/2009JB006716
- Fichtner, A., Kennett, B. L., & Trampert, J. (2013). Separating intrinsic and apparent anisotropy. *Physics of the Earth and Planetary Interiors*, 219, 11–20.
- Finkelstein, G. J., Jackson, J. M., Said, A., Alatas, A., Leu, B. M., Sturhahn, W., & Toellner, T. S. (2018). Strongly anisotropic magnesiowüstite in Earth's lower mantle. *Journal of Geophysical Research: Solid Earth*, 123 (6), 4740–4750.
- Ford, H. A., & Long, M. D. (2015). A regional test of global models for flow, rheology, and seismic anisotropy at the base of the mantle. *Physics of the Earth and Planetary Interiors*, 245, 71–75. doi: 10.1016/j.pepi.2015.05.004
- Ford, H. A., Long, M. D., He, X., & Lynner, C. (2015). Lowermost mantle flow at the eastern edge of the African Large Low Shear Velocity Province. *Earth and Planetary Science Letters*, 420, 12–22. doi: 10.1016/j.epsl.2015.03.029
- French, S. W., & Romanowicz, B. (2015). Broad plumes rooted at the base of the Earth's mantle beneath major hotspots. *Nature*, 525 (7567), 95–99. doi: 10.1038/nature14876
- Fu, S., Yang, J., Tsujino, N., Okuchi, T., Purevjav, N., & Lin, J.-F. (2019). Singlecrystal elasticity of (Al, Fe)-bearing bridgmanite and seismic shear wave radial anisotropy at the topmost lower mantle. *Earth and Planetary Science Letters*, 518, 116–126.
- Garnero, E. J., & Lay, T. (1997). Lateral variations in lowermost mantle shear wave anisotropy beneath the north Pacific and Alaska. *Journal of Geophysical Research – Solid Earth*, 102 (B4), 8121–8135. doi: 10.1029/96JB03830
- Garnero, E. J., Maupin, V., Lay, T., & Fouch, M. J. (2004). Variable azimuthal anisotropy in Earth's lowermost mantle. *Science*, 306 (5694), 259–261. doi: 10.1126/science.1103411
- Garnero, E. J., & McNamara, A. K. (2008). Structure and dynamics of Earth's lower mantle. *Science*, 320 (5876), 626–628. doi: 10.1126/science.1148028
- Garnero, E. J., McNamara, A. K., & Shim, S.-H. (2016). Continent-sized anomalous zones with low seismic velocity at the base of Earth's mantle. *Nature Geoscience*, 9 (7), 481–489. doi: 10.1038/ngeo2733
- Garnero, E. J., Revenaugh, J., Williams, Q., Lay, T., & Kellogg, L. (1998). Ultralow velocity zone at the core–mantle boundary. In M. Gurnis, M. E. Wysession, E. Knittle, & B. A. Buffett (Eds.), *The Core–Mantle Boundary Region* (pp. 319–334). Washington, D.C., USA: American Geophysical Union.
- Gialampouki, M. A., Xu, S., & Morgan, D. (2018). Iron valence and partitioning between post-perovskite and ferropericlase in the Earth's lowermost mantle. *Physics of the Earth and Planetary Interiors*, 282, 110–116. doi: 10.1016/j.pepi.2018.06.005
- Girard, J., Amulele, G., Farla, R., Mohiuddin, A., & Karato, S.-i. (2016). Shear deformation of bridgmanite and magnesio-wüstite aggregates at lower mantle conditions. *Science*, 351 (6269), 144–147. doi: 10.1126/science.aad3113
- Girard, J., Chen, J., & Raterron, P. (2012). Deformation of periclase single crystals at high pressure and temperature: Quantification of the effect of pressure on slip-system activities. *Journal of Applied Physics*, 111 (11), 112607.
- Goryaeva, A. M., Carrez, P., & Cordier, P. (2015). Modeling defects and plasticity in MgSiO_3 post-perovskite: Part 2—Screw and edge [100] dislocations. *Physics and chemistry of minerals*, 42 (10), 793–803.
- Goryaeva, A. M., Carrez, P., & Cordier, P. (2016). Low viscosity and high attenuation in MgSiO_3 post-perovskite inferred from atomic-scale calculations. *Scientific reports*, 6, 34771.
- Goryaeva, A. M., Carrez, P., & Cordier, P. (2017). Modeling defects and plasticity in MgSiO_3 post-perovskite: Part 3 – Screw and edge [001] dislocations. *Physics and Chemistry of Minerals*, 44 (7), 521–533.
- Grund, M., & Ritter, J. R. (2019). Widespread seismic anisotropy in Earth's lowermost mantle beneath the Atlantic and Siberia. *Geology*, 47 (2), 123–126.
- Hall, S. A., Kendall, J.-M., & Van der Baan, M. (2004). Some comments on the effects of lower-mantle anisotropy on SKS and SKKS phases. *Physics of The Earth and Planetary Interiors*, 146 (3–4), 469–481. doi: 10.1016/j.pepi.2004.05.002
- Hernlund, J., Thomas, C., & Tackley, P. J. (2005). A doubling of the post-perovskite phase boundary and structure of the Earth's lowermost mantle. *Nature*, 434 (7035), 882–886. doi: 10.1038/nature03472
- Hirose, K., Nagaya, Y., Merkel, S., & Ohishi, Y. (2010). Deformation of MnGeO_3 post-perovskite at lower mantle pressure and temperature. *Geophysical Research Letters*, 37 (L20302), 1–5. doi: 10.1029/2010GL044977
- Hirose, K., Wentzcovitch, R., Yuen, D., & Lay, T. (2015). Mineralogy of the deep mantle – The post-perovskite phase and its geophysical significance. *Treatise on Geophysics*, 85–115.
- Hu, Q., Kim, D. Y., Yang, W., Yang, L., Meng, Y., Zhang, L., & Mao, H.-K. (2016). FeO_2 and FeOOH under deep lower-mantle conditions and Earth's oxygen–hydrogen cycles. *Nature*, 534 (7606), 241–244. doi: 10.1038/nature18018

- Hunt, S. A., Walker, A. M., & Mariani, E. (2016). In-situ measurement of texture development rate in CaIrO₃ post-perovskite. *Physics of the Earth and Planetary Interiors*. doi: 10.1016/j.pepi.2016.05.007
- Hunt, S. A., Weidner, D. J., Li, L., Wang, L., Walte, N. P., Brodholt, J. P., & Dobson, D. P. (2009). Weakening of calcium iridate during its transformation from perovskite to post-perovskite. *Nature Geoscience*, 2 (11), 794–797. doi: 10.1038/NGEO663
- Iitaka, T., Hirose, K., Kawamura, K., & Murakami, M. (2004). The elasticity of the MgSiO₃ post-perovskite phase in the Earth's lowermost mantle. *Nature*, 430 (6998), 442–445. doi: 10.1038/nature02702
- Jackson, J. M., Sinogeikin, S. V., Jacobsen, S. D., Reichmann, H. J., Mackwell, S. J., & Bass, J. D. (2006). Single-crystal elasticity and sound velocities of (Mg_{0.94}Fe_{0.06})O ferropericlasite to 20 GPa. *Journal of Geophysical Research: Solid Earth*, 111 (B9).
- Kaercher, P., Miyagi, L., Kanitpanyacharoen, W., Zepeda-Alarcon, E., Wang, Y., Parkinson, D., ... Wenk, H. (2016). Two-phase deformation of lower mantle mineral analogs. *Earth and Planetary Science Letters*, 456, 134–145. doi: 10.1016/j.epsl.2016.09.030
- Karato, S.-i. (1998). Some remarks on the origin of seismic anisotropy in the D'' layer. *Earth Planets Space*, 50, 1019–1028.
- Karki, B., Stixrude, L., & Crain, J. (1997). Ab initio elasticity of three high-pressure polymorphs of silica. *Geophysical Research Letters*, 24 (24), 3269–3272. doi: 10.1029/97GL53196
- Karki, B., Wentzcovitch, R., de Gironcoli, S., & Baroni, S. (2000). High-pressure lattice dynamics and thermoelasticity of MgO. *Physical Review B*, 61 (13), 8793.
- Kawai, K., & Geller, R. J. (2010). The vertical flow in the lowermost mantle beneath the Pacific from inversion of seismic waveforms for anisotropic structure. *Earth and Planetary Science Letters*, 297 (1–2), 190–198. doi:10.1016/j.epsl.2010.05.037
- Kawakatsu, H. (2015). A new fifth parameter for transverse isotropy. *Geophysical Journal International*, 204 (1), 682–685.
- Kendall, J.-M., & Silver, P. G. (1996). Constraints from seismic anisotropy on the nature of the lowermost mantle. *Nature*, 381 (6581), 409–412. doi: 10.1038/381409a0
- Kendall, J.-M., & Silver, P. G. (1998). Investigating causes of D'' anisotropy. In *The core-mantle boundary region* (p. 97–118). American Geophysical Union.
- Kennett, B. L. N., Engdahl, E., & Buland, R. (1995). Constraints on seismic velocities in the Earth from travel-times. *Geophysical Journal International*, 122 (1), 108–124. doi: 10.1111/j.1365-246X.1995.tb03540.x
- Koelemeijer, P., Schuberth, B., Davies, D., Deuss, A., & Ritsema, J. (2018). Constraints on the presence of post-perovskite in Earth's lowermost mantle from tomographic-geodynamic model comparisons. *Earth and Planetary Science Letters*, 494, 226–238. doi: 10.1016/j.epsl.2018.04.056
- Koelemeijer, P. J., Deuss, A., & Trampert, J. (2012). Normal mode sensitivity to earth's D'' layer and topography on the core-mantle boundary: what we can and cannot see. *Geophysical Journal International*, 190 (1), 553–568. doi: 10.1111/j.1365-246X.2012.05499.x
- Komatitsch, D., & Tromp, J. (2002). Spectral-element simulations of global seismic wave propagation - I. *Validation. Geophysical Journal International*, 149 (2), 390–412.
- Komatitsch, D., Tsuboi, S., Ji, C., & Tromp, J. (2003). A 14.6 billion degrees of freedom, 5 teraflops, 2.5 terabyte earthquake simulation on the Earth Simulator. *Proceedings of the ACM/IEEE SC2003 Conference (SC'03)*, 1–8. doi: 10.1145/1048935.1050155
- Komatitsch, D., Vinnik, L. P., & Chevrot, S. (2010). SHdiff-SVdiff splitting in an isotropic Earth. *Journal Of Geophysical Research-Solid Earth*, 115, B07312. doi: 10.1029/2009JB006795
- Krischer, L., Megies, T., Barsch, R., Beyreuther, M., Lecocq, T., Caudron, C., & Wassermann, J. (2015). Obspy: A bridge for seismology into the scientific Python ecosystem. *Computational Science & Discovery*, 8 (1), 014003.
- Lay, T., & Young, C. (1991). Analysis of seismic SV waves in the core's penumbra. *Geophysical Research Letters*, 18 (8), 1373–1376. doi: 10.1029/91GL01691
- Lebensohn, R., & Tomé, C. (1993). A self-consistent anisotropic approach for the simulation of plastic-deformation and texture development of polycrystals – application to zirconium alloys. *Acta Metallurgica Et Materialia*, 41 (9), 2611–2624. doi: 10.1016/0956-7151(93)90130-K
- Lekić, V., Cottaar, S., Dziewoński, A., & Romanowicz, B. (2012). Cluster analysis of global lower mantle tomography: A new class of structure and implications for chemical heterogeneity. *Earth and Planetary Science Letters*, 357–358, 68–77. doi: 10.1016/j.epsl.2012.09.014
- Li, L., Brodholt, J. P., Stackhouse, S., Weidner, D. J., Alfredsson, M., & Price, G. D. (2005). Elasticity of (Mg, Fe) (Si, Al) O₃-perovskite at high pressure. *Earth and Planetary Science Letters*, 240 (2), 529–536.
- Li, L., Weidner, D. J., Brodholt, J. P., Alfé, D., Price, G. D., Caracas, R., & Wentzcovitch, R. M. (2006). Elasticity of CaSiO₃ perovskite at high pressure and high temperature. *Physics of the Earth and Planetary Interiors*, 155 (3–4), 249–259. doi: 10.1016/j.pepi.2005.12.006
- Lin, J.-F., Wenk, H.-R., Voltolini, M., Speziale, S., Shu, J., & Duffy, T. S. (2009). Deformation of lower-mantle ferropericlasite (Mg, Fe)O across the electronic spin transition. *Physics and Chemistry of Minerals*, 36 (10), 585.
- Long, M. (2009). Complex anisotropy in D'' beneath the eastern Pacific from SKS-SKKS splitting discrepancies. *Earth and Planetary Science Letters*, 283 (1–4), 181–189. doi: 10.1016/j.epsl.2009.04.019
- Long, M. D., & Lynnner, C. (2015). Seismic anisotropy in the lowermost mantle near the Perm Anomaly. *Geophysical Research Letters*, 42 (17), 7073–7080. doi: 10.1002/2015GL065506
- Lynnner, C., & Long, M. D. (2014). Lowermost mantle anisotropy and deformation along the boundary of the African LLSVP. *Geophysical Research Letters*, 41 (10), 3447–3454. doi: 10.1002/2014GL059875
- Madi, K., Forest, S., Cordier, P., & Boussuge, M. (2005). Numerical study of creep in two-phase aggregates with a large rheology contrast: Implications for the lower mantle. *Earth and Planetary Science Letters*, 237 (1–2), 223–238.

- Mainprice, D. (2007). Seismic anisotropy of the deep Earth from a mineral and rock physics perspective. In *Treatise on Geophysics* (p. 437–491). Elsevier. doi:10.1016/B978-044452748-6.00045-6
- Mainprice, D., Tommasi, A., Ferré, D., Carrez, P., & Cordier, P. (2008). Predicted glide systems and crystal preferred orientations of polycrystalline silicate Mg-Perovskite at high pressure: Implications for the seismic anisotropy in the lower mantle. *Earth and Planetary Science Letters*, 271 (1-4), 135-144. doi: 10.1016/j.epsl.2008.03.058
- Mancinelli, N. J., & Shearer, P. M. (2013). Reconciling discrepancies among estimates of small-scale mantle heterogeneity from PKP precursors. *Geophysical Journal International*, 195 (3), 1721–1729.
- Mao, W. L., Meng, Y., & Mao, H. (2010). Elastic anisotropy of ferromagnesian post-perovskite in Earth's D'' layer. *Physics of The Earth and Planetary Interiors*, 180 (3–4), 203–208. doi: 10.1016/j.pepi.2009.10.013
- Marquardt, H., Speziale, S., Reichmann, H. J., Frost, D. J., & Schilling, F. R. (2009). Single-crystal elasticity of (Mg_{0.9}Fe_{0.1})O to 81 GPa. *Earth and Planetary Science Letters*, 287 (3–4), 345–352. doi: 10.1016/j.epsl.2009.08.017
- Matzel, E., Sen, M., & Grand, S. (1996). Evidence for anisotropy in the deep mantle beneath Alaska. *Geophysical Research Letters*, 23 (18), 2417–2420. doi: 10.1029/96GL02186
- Maupin, V. (1994). On the possibility of anisotropy in the D'' layer as inferred from the polarization of diffracted S waves. *Physics of The Earth and Planetary Interiors*, 87 (1–2), 1–32. doi: 10.1016/0031-9201(94)90019-1
- Maupin, V., Garnero, E. J., Lay, T., & Fouch, M. J. (2005). Azimuthal anisotropy in the D'' layer beneath the Caribbean. *Journal of Geophysical Research – Solid Earth*, 110 (B8), B08301. doi: 10.1029/2004JB003506
- McDonough, W., & Sun, S. (1995). The composition of the Earth. *Chemical Geology*, 120 (3–4), 223-253.
- Merkel, S., McNamara, A. K., Kubo, A., Speziale, S., Miyagi, L., Meng, Y., ... Wenk, H.-R. (2007). Deformation of (Mg,Fe)SiO₃ post-perovskite and “D” anisotropy. *Science*, 316 (5832), 1729-1732. doi: 10.1126/science.1140609
- Merkel, S., Wenk, H.-R., Shu, J., Shen, G., Gillet, P., Mao, H., & Hemley, R. (2002). Deformation of polycrystalline MgO at pressures of the lower mantle. *Journal Of Geophysical Research-Solid Earth*, 107 (B11), 2271. doi: 10.1029/2001JB000920
- Miyagi, L. (2021). Experimental deformation of lower mantle rocks and minerals. In H. Marquardt, M. Ballmer, S. Cottaar, & J. Konter (Eds.), *Mantle Convection and Surface Expressions*. American Geophysical Union.
- Miyagi, L., Kanitpanyacharoen, W., Kaercher, P., Lee, K. K. M., & Wenk, H.-R. (2010). Slip systems in MgSiO₃ post-perovskite: Implications for “D” anisotropy. *Science*, 329 (5999), 1639–1641. doi: 10.1126/science.1192465
- Miyagi, L., Kanitpanyacharoen, W., Stackhouse, S., Militzer, B., & Wenk, H.-R. (2011). The enigma of post-perovskite anisotropy: Deformation versus transformation textures. *Physics and Chemistry of Minerals*, 38 (9), 665–678. doi: 10.1007/s00269-011-0439-y
- Miyagi, L., Merkel, S., Yagi, T., Sata, N., Ohishi, Y., & Wenk, H.-R. (2009). Diamond anvil cell deformation of CaSiO₃ perovskite up to 49 GPa. *Physics of the Earth and Planetary Interiors*, 174 (1–4), 159–164. doi: 10.1016/j.pepi.2008.05.018
- Miyagi, L., & Wenk, H.-R. (2016). Texture development and slip systems in bridgmanite and bridgmanite + ferropericlasite aggregates. *Physics and Chemistry of Minerals*, 43 (8), 597–613.
- Moulik, P., & Ekstrom, G. (2014). An anisotropic shear velocity model of the Earth's mantle using normal modes, body waves, surface waves and long-period waveforms. *Geophys. J. Int.*, 199 (3), 1713–1738. doi: 10.1093/gji/ggu356
- Murakami, M., Hirose, K., Kawamura, K., Sata, N., & Ohishi, Y. (2004). Post-perovskite phase transition in MgSiO₃. *Science*, 304 (5672), 855–858. doi: 10.1126/science.1095932
- Nakagawa, T., & Tackley, P. J. (2011). Effects of low-viscosity post-perovskite on thermo-chemical mantle convection in a 3-D spherical shell. *Geophysical research letters*, 38 (4).
- Nisr, C., Ribárik, G., Ungar, T., Vaughan, G. B. M., Cordier, P., & Merkel, S. (2012). High resolution three-dimensional X-ray diffraction study of dislocations in grains of MgGeO₃ post-perovskite at 90 GPa. *Journal of Geophysical Research*, 117 (B3), B03201. doi: 10.1029/2011JB008401
- Niu, F., & Perez, A. (2004). Seismic anisotropy in the lower mantle: A comparison of waveform splitting of SKS and SKKS. *Geophysical Research Letters*, 31 (24), L24612. doi: 10.1029/2004GL021196
- Niwa, K., Miyajima, N., Seto, Y., Ohgushi, K., Gotou, H., & Yagi, T. (2012). In situ observation of shear stress-induced perovskite to post-perovskite phase transition in CaIrO₃ and the development of its deformation texture in a diamond-anvil cell up to 30 GPa. *Physics of The Earth and Planetary Interiors*, 194–195 (C), 10–17. doi: 10.1016/j.pepi.2012.01.007
- Nowacki, A., Walker, A. M., Wookey, J., & Kendall, J.-M. (2013). Evaluating post-perovskite as a cause of D'' anisotropy in regions of palaeosubduction. *Geophysical Journal International*, 192 (3), 1085–1090. doi: 10.1093/gji/ggs068
- Nowacki, A., & Wookey, J. (2016). The limits of ray theory when measuring shear wave splitting in the lowermost mantle with ScS waves. *Geophysical Journal International*, 207, 1573–1583. doi: 10.1093/gji/ggw358
- Nowacki, A., Wookey, J., & Kendall, J.-M. (2010). Deformation of the lowermost mantle from seismic anisotropy. *Nature*, 467 (7319), 1091–1095. http://eprints.whiterose.ac.uk/91922/1/2010_Nowackietal_Nature.pdf.
- Nowacki, A., Wookey, J., & Kendall, J.-M. (2011). New advances in using seismic anisotropy, mineral physics and geodynamics to understand deformation in the lowermost mantle. *Journal of Geodynamics*, 52 (3–4), 205–228. doi:10.1016/j.jog.2011.04.003
- Oganov, A., Brodholt, J. P., & Price, G. D. (2001). The elastic constants of MgSiO₃ perovskite at pressures and temperatures of the Earth's mantle. *Nature*, 411 (6840), 934–937. doi: 10.1038/35082048
- Oganov, A., & Ono, S. (2004). Theoretical and experimental evidence for a post-perovskite phase of MgSiO₃ in Earth's D'' layer. *Nature*, 430 (6998), 445–448. doi: 10.1038/nature02701

- Pamato, M. G., Myhill, R., Boffa Ballaran, T., Frost, D. J., Heidelbach, F., & Miyajima, N. (2015). Lower-mantle water reservoir implied by the extreme stability of a hydrous aluminosilicate. *Nature Geoscience*, 8 (1), 75–79. doi: 10.1038/ngeo2306
- Panero, W. R., & Caracas, R. (2017). Stability of phase H in the $\text{MgSiO}_4\text{H}_2\text{-AlOOH-SiO}_2$ system. *Earth and Planetary Science Letters*, 463, 171–177. doi:10.1016/j.epsl.2017.01.033
- Panning, M., Lekić, V., & Romanowicz, B. (2010). Importance of crustal corrections in the development of a new global model of radial anisotropy. *Journal of Geophysical Research-Solid Earth*, 115, B12325. doi: 10.1029/2010JB007520
- Parisi, L., Ferreira, A. M. G., & Ritsema, J. (2018). Apparent splitting of S waves propagating through an isotropic lowermost mantle. *Journal of Geophysical Research: Solid Earth*, 123 (5), 3909–3922. doi: 10.1002/2017JB014394
- Pisconti, A., Thomas, C., & Wookey, J. (2019). Discriminating between causes of D'' anisotropy using reflections and splitting measurements for a single path. *Journal of Geophysical Research: Solid Earth*. doi: 10.1029/2018JB016993
- Ranganathan, S. I., & Ostoja-Starzewski, M. (2008). Universal elastic anisotropy index. *Physical Review Letters*, 101 (5), 055504. doi: 10.1103/PhysRevLett.101.055504
- Reali, R., Van Orman, J. A., Pigott, J. S., Jackson, J. M., Boioli, F., Carrez, P., & Cordier, P. (2019). The role of diffusion-driven pure climb creep on the rheology of bridgmanite under lower mantle conditions. *Scientific Reports*, 9 (1), 2053.
- Reiss, M., Long, M., & Creasy, N. (2019). Lowermost mantle anisotropy beneath Africa from differential SKS–SKKS shear-wave splitting. *Journal of Geophysical Research – Solid Earth*. doi: 10.1029/2018JB017160
- Romanowicz, B., & Wenk, H.-R. (2017). Anisotropy in the deep Earth. *Physics of the Earth and Planetary Interiors*, 269, 58–90. doi: 10.1016/j.pepi.2017.05.005
- Rudolph, M. (2021). Long-wavelength mantle structure: geophysical constraints and dynamical models. In H. Marquardt, M. Ballmer, S. Cottaar, & J. Konter (Eds.), *Mantle Convection and Surface Expressions*. American Geophysical Union.
- Silver, P. G., & Chan, W. W. (1991). Shear-wave splitting and subcontinental mantle deformation. *Journal of Geophysical Research – Solid Earth*, 96 (B10), 16429–16454. doi: 10.1029/91JB00899
- Simmons, N. A., Forte, A. M., & Grand, S. (2009). Joint seismic, geodynamic and mineral physical constraints on three-dimensional mantle heterogeneity: Implications for the relative importance of thermal versus compositional heterogeneity. *Geophysical Journal International*, 177 (3), 1284–1304. doi: 10.1111/j.1365-246X.2009.04133.x
- Soldati, G., Boschi, L., & Piersanti, A. (2003). Outer core density heterogeneity and the discrepancy between PKP and PcP travel time observations. *Geophysical Research Letters*, 30 (4), 1190. doi: 10.1029/2002GL016647
- Stackhouse, S., Brodholt, J. P., & Price, G. D. (2005). High temperature elastic anisotropy of the perovskite and post-perovskite Al_2O_3 . *Geophysical Research Letters*, 32 (13), L13305. doi: 10.1029/2005GL023163
- Stackhouse, S., Brodholt, J. P., Wookey, J., Kendall, J.-M., & Price, G. D. (2005). The effect of temperature on the seismic anisotropy of the perovskite and post-perovskite polymorphs of MgSiO_3 . *Earth and Planetary Science Letters*, 230 (1–2), 1–10. doi: 10.1016/j.epsl.2004.11.021
- Sun, N., Shi, W., Mao, Z., Zhou, C., & Prakapenka, V. B. (2019). High pressure-temperature study on the thermal equations of state of seifertite and CaCl_2 -type SiO_2 . *Journal of Geophysical Research: Solid Earth*, 124 (12), 12620–12630. doi: 10.1029/2019JB017853
- Tesoniero, A., Cammarano, F., & Boschi, L. (2016). S-to-P heterogeneity ratio in the lower mantle and thermo-chemical implications. *Geochemistry, Geophysics, Geosystems*, 17 (7), 2522–2538. doi: 10.1002/2016GC006293
- Thomas, C., Wookey, J., Brodholt, J. P., & Fieseler, T. (2011). Anisotropy as cause for polarity reversals of D'' reflections. *Earth and Planetary Science Letters*, 307 (3–4), 369–376. doi: 10.1016/j.epsl.2011.05.011
- Thomas, C., Wookey, J., & Simpson, M. (2007). D'' anisotropy beneath Southeast Asia. *Geophysical Research Letters*, 34 (4), L04301. doi: 10.1029/2006GL028965
- Thomson, A. R., Crichton, W. A., Brodholt, J. P., Wood, I. G., Siersch, N. C., Muir, J. M., et al. (2019). Seismic velocities of CaSiO_3 perovskite can explain LLSVPs in Earth's lower mantle. *Nature*, 572 (7771), 643–647. doi: 10.1038/s41586-019-1483-x
- Tommasi, A., Goryaeva, A., Carrez, P., Cordier, P., & Mainprice, D. (2018). Deformation, crystal preferred orientations, and seismic anisotropy in the Earth's D'' layer. *Earth and Planetary Science Letters*, 492, 35–46. doi:10.1016/j.epsl.2018.03.032
- Tsuchiya, T., Tsuchiya, J., Umamoto, K., & Wentzcovitch, R. M. (2004). Phase transition in MgSiO_3 perovskite in the earth's lower mantle. *Earth and Planetary Science Letters*, 224 (3–4), 241–248. doi: 10.1016/j.epsl.2004.05.017
- Tsujino, N., Nishihara, Y., Yamazaki, D., Seto, Y., Higo, Y., & Takahashi, E. (2016). Mantle dynamics inferred from the crystallographic preferred orientation of bridgmanite. *Nature*, 539 (7627), 81–84. doi: 10.1038/nature19777
- Vinnik, L. P., Breger, L., & Romanowicz, B. (1998). Anisotropic structures at the base of the Earth's mantle. *Nature*, 393 (6685), 564–567. doi: 10.1038/31208
- Walker, A. M., Carrez, P., & Cordier, P. (2010). Atomic-scale models of dislocation cores in minerals: Progress and prospects. *Mineralogical Magazine*, 74 (3), 381–413. doi: 10.1180/minmag.2010.074.3.381
- Walker, A. M., Dobson, D. P., Wookey, J., Nowacki, A., & Forte, A. M. (2018). The anisotropic signal of topotaxy during phase transitions in D'' . *Physics of the Earth and Planetary Interiors*, 276, 159–171. doi: 10.1016/j.pepi.2017.05.013
- Walker, A. M., Forte, A. M., Wookey, J., Nowacki, A., & Kendall, J.-M. (2011). Elastic anisotropy of D'' predicted from global models of mantle flow. *Geochemistry Geophysics Geosystems*, 12 (10), Q10006. doi: 10.1029/2011GC003732
- Walker, A. M., & Wookey, J. (2012). MSAT – A new toolkit for the analysis of elastic and seismic anisotropy. *Computers & Geosciences*, 49, 81–90. doi: 10.1016/j.cageo.2012.05.031
- Walpole, J., Wookey, J., Kendall, J.-M., & Masters, T.-G. (2017). Seismic anisotropy and mantle flow below subducting slabs. *Earth and Planetary Science Letters*, 465, 155–167.

- Walsh, E., Arnold, R., & Savage, M. K. (2013). Silver and Chan revisited. *Journal of Geophysical Research: Solid Earth*, *118* (10), 5500–5515. doi: 10.1002/jgrb.50386
- Walte, N. P., Heidelbach, F., Miyajima, N., Frost, D. J., Rubie, D. C., & Dobson, D. P. (2009). Transformation textures in post-perovskite: Understanding mantle flow in the D'' layer of the Earth. *Geophysical Research Letters*, *36*, L04302. doi: 10.1029/2008GL036840
- Wang, Y., Hilaret, N., Nishiyama, N., Yahata, N., Tsuchiya, T., Morard, G., & Fiquet, G. (2013). High-pressure, high-temperature deformation of CaGeO₃ (perovskite)±MgO aggregates: Implications for multiphase rheology of the lower mantle. *Geochemistry, Geophysics, Geosystems*, *14* (9), 3389–3408.
- Wang, Y., & Wen, L. (2007). Complex seismic anisotropy at the border of a very low velocity province at the base of the Earth's mantle. *Journal of Geophysical Research-Solid Earth*, *112* (B9), B09305. doi: 10.1029/2006JB004719
- Wenk, H.-R., Cottaar, S., Tomé, C. N., McNamara, A. K., & Romanowicz, B. (2011). Deformation in the lowermost mantle: From polycrystal plasticity to seismic anisotropy. *Earth and Planetary Science Letters*, *306* (1–2), 33–45. doi: 10.1016/j.epsl.2011.03.021
- Wenk, H.-R., Lonardeli, I., Pehl, J., Devine, J., Prakapenka, V., Shen, G., & Mao, H.-K. (2004). In situ observation of texture development in olivine, ringwoodite, magnesiowüstite and silicate perovskite at high pressure. *Earth and Planetary Science Letters*, *226* (3), 507–519. doi: 10.1016/j.epsl.2004.07.033
- Wentzcovitch, R. M., Tsuchiya, T., & Tsuchiya, J. (2006). MgSiO₃ postperovskite at D'' conditions. *Proceedings of the National Academy of Sciences of the United States of America*, *103* (3), 543–546. doi: 10.1073/pnas.0506879103
- Wheeler, J. (2009). The preservation of seismic anisotropy in the Earth's mantle during diffusion creep. *Geophysical Journal International*, *178* (3), 1723–1732. doi: 10.1111/j.1365-246X.2009.04241.x
- Wheeler, J. (2010). Anisotropic rheology during grain boundary diffusion creep and its relation to grain rotation, grain boundary sliding and superplasticity. *Philosophical Magazine*, *90* (21), 2841–2864. doi: 10.1080/14786431003636097
- Wolf, J., Creasy, N., Pisconti, A., Long, M. D., & Thomas, C. (2019). An investigation of seismic anisotropy in the lowermost mantle beneath iceland. *Geophysical Journal International*. doi: 10.1093/gji/ggz312
- Wookey, J., & Dobson, D. P. (2008). Between a rock and a hot place: The coremantle boundary. *Philosophical Transactions of the Royal Society of London Series A-Mathematical Physical and Engineering Sciences*, *366* (1885), 4543–4557. doi: 10.1098/rsta.2008.0184
- Wookey, J., & Kendall, J.-M. (2007). Seismic anisotropy of post-perovskite and the lowermost mantle. In K. Hirose, J. Brodholt, T. Lay, & D. A. Yuen (Eds.), *Post-perovskite: The last mantle phase transition* (pp. 171–189). Washington, DC: American Geophysical Union Geophysical Monograph 174.
- Wookey, J., & Kendall, J.-M. (2008). Constraints on lowermost mantle mineralogy and fabric beneath Siberia from seismic anisotropy. *Earth and Planetary Science Letters*, *275* (1–2), 32–42. doi: 10.1016/j.epsl.2008.07.049
- Wookey, J., Kendall, J.-M., & Rumpker, G. (2005). Lowermost mantle anisotropy beneath the north Pacific from differential S–ScS splitting. *Geophysical Journal International*, *161* (3), 829–838. doi: 10.1111/j.1365-246X.2005.02623.x
- Wu, X., Lin, J.-F., Kaercher, P., Mao, Z., Liu, J., Wenk, H.-R., & Prakapenka, V. B. (2017). Seismic anisotropy of the D'' layer induced by (001) deformation of postperovskite. *Nature Communications*, *8*, 14669.
- Wu, Z., Justo, J. F., & Wentzcovitch, R. M. (2013). Elastic anomalies in a spin-crossover system: Ferropericlase at lower mantle conditions. *Physical review letters*, *110* (22), 228501.
- Wuestefeld, A., Al-Harrasi, O., Verdon, J. P., Wookey, J., & Kendall, J.-M. (2010). A strategy for automated analysis of passive microseismic data to image seismic anisotropy and fracture characteristics. *Geophysical Prospecting*, *58* (5), 753–771. doi: 10.1111/j.1365-2478.2010.00891.x
- Yamazaki, D., & Karato, S. (2007). Lattice-preferred orientation of lower mantle materials and seismic anisotropy in the D'' layer. In *Post-perovskite: The last mantle phase transition* (pp. 69–78). Washington, D.C., USA: American Geophysical Union.
- Yamazaki, D., & Karato, S.-i. (2002). Fabric development in (Mg,Fe)O during large strain, shear deformation: implications for seismic anisotropy in Earth's lower mantle. *Physics of The Earth and Planetary Interiors*, *131* (3–4), 251–267. doi: 10.1016/S0031-9201(02)00037-7
- Yamazaki, D., Yoshino, T., Ohfuji, H., Ando, J.-i., & Yoneda, A. (2006). Origin of seismic anisotropy in the D'' layer inferred from shear deformation experiments on post-perovskite phase. *Earth and Planetary Science Letters*, *252* (3–4), 372–378. doi: 10.1016/j.epsl.2006.10.004
- Yang, R., & Wu, Z. (2014). Elastic properties of stishovite and the CaCl₂-type silica at the mantle temperature and pressure: An ab initio investigation. *Earth and Planetary Science Letters*, *404*, 14–21. doi: 10.1016/j.epsl.2014.07.020
- Young, C. J., & Lay, T. (1990). Multiple phase analysis of the shear velocity structure in the D'' region beneath Alaska. *Journal of Geophysical Research: Solid Earth*, *95* (B11), 17385–17402.
- Yu, S., & Garnero, E. J. (2018). Ultra-low velocity zone locations: A global assessment. *Geochemistry, Geophysics, Geosystems*, *19* (2), 396–414.
- Zhang, S., Cottaar, S., Liu, T., Stackhouse, S., & Militzer, B. (2016). High-pressure, temperature elasticity of Fe-and Al-bearing MgSiO₃: Implications for the Earth's lower mantle. *Earth and Planetary Science Letters*, *434*, 264–273.
- Zhong, S., Zuber, M. T., Moresi, L., & Gurnis, M. (2000). Role of temperature-dependent viscosity and surface plates in spherical shell models of mantle convection. *Journal of Geophysical Research: Solid Earth*, *105* (B5), 11063–11082.

Seismic Imaging of Deep Mantle Plumes

Jeroen Ritsema¹, Ross Maguire², Laura Cobden³, and Saskia Goes⁴

ABSTRACT

The plume model has been the leading hypothesis for hotspot volcanism for five decades. Whereas experiments have clarified how plumes form and rise, the onus has been put on seismologists to find plumes in Earth. Seismic evidence has almost always been contentious because plumes perturb waves slightly and interpretations are inherently nonunique. Using simulations of convection and experimental constraints, we show that traveltime delays of teleseismic shear waves are less than a second and that it is difficult to resolve the plume conduit in the lower mantle using teleseismic traveltime tomography. We discuss the effects of plumes on the transition zone and review analyses of wave diffraction around plumes in the deep mantle, which indicate that plume stems may leave a detectable imprint on the seismic wavefield. We anticipate significant progress in the imaging of deep mantle plumes if seismologists continue their commitment to the deployment of seismic instrumentation in the oceans. Seismic studies will continue to benefit from three-dimensional waveform modeling techniques and advances in adjoint tomography. It is essential to compare seismic modeling results with the seismic signatures predicted by dynamic models and to test them against other geophysical and geological observations.

14.1. INTRODUCTION

Hotspots provide an invaluable window into the deep Earth and the nature of mantle convection. A hotspot is a center of prolonged volcanism far from plate boundaries or excess volcanism at plate boundaries. Many hotspots are at the end of age-progressive lines of volcanoes. In some cases, they are linked to large igneous provinces

(Morgan, 1972; Richards et al., 1989), continental break-up (e.g., Hill, 1991; Hawkesworth et al., 1999), and mass extinctions (e.g., Courtillot & Renne, 2003). Hotspot volcanism is predominantly basaltic but the distinct radiogenic isotope characteristics and major-element compositions are usually interpreted as due to a deeper and higher temperature source of melting compared to the source of mid-ocean ridge (MORB) basalts (e.g., Hart et al., 1973; Farley & Neroda, 1998; Jackson & Dasgupta, 2008). For reviews, see Jackson (1998), Davies (1999), Nataf (2000), Condie (2001), Ribe et al. (2007), Ballmer et al. (2015), and Zhao (2015).

Since the seminal papers by Wilson (1963) and Morgan (1971), many geophysicists and geochemists have attributed hotspot volcanism to mantle plumes – buoyant upwellings of anomalously hot mantle rock. A plume begins as a thermal instability in the thermal boundary layer between

¹Department of Earth and Environmental Sciences, University of Michigan, Ann Arbor, MI, USA

²Department of Geology, University of Maryland, College Park, MD, USA

³Department of Earth Sciences, Utrecht University, Utrecht, The Netherlands

⁴Department of Science and Engineering, Imperial College London, London, UK

the mantle and the 1000–1500 K hotter core and rises as a voluminous head followed by a narrow tail. Partial melting of the plume head on arrival at the base of the lithosphere is thought to produce flood basalts, whereas the tail provides a long-lived source of volcanism with a relatively fixed mantle position. Plume volume, morphology, and rise time depend on the heat flux through the core-mantle boundary (CMB), the composition of entrained mantle material, and the thermal expansion and viscosity of mantle rock. A large number of analog and numerical experiments have described the structure of the plume head and tail (e.g., Whitehead & Luther, 1975; Campbell & Griffiths, 1990; Olson et al., 1993; Kellogg & King, 1997), the tilting of a plume conduit (e.g., Skilbeck & Whitehead, 1978, Richards & Griffiths, 1989, Steinberger & O’Connell, 1998), the entrainment of ambient mantle material (e.g., Griffiths, 1986; Campbell & Griffiths, 1990; Farnetani et al., 2002; Farnetani & Hofmann, 2010; Jones et al., 2016), plume interaction with the lithosphere (e.g., Olson et al., 1988; Ribe & Christensen, 1994; Phipps Morgan et al., 1995; Sleep, 1997; Moore et al., 1998; Burov & Gerya, 2014) and with mid-ocean ridges (e.g., Ito et al., 1996; Ribe et al., 1999; Albers & Christensen, 2001; Hall & Kincaid, 2003; Georgan, 2014), effects of compositional heterogeneities (e.g., Davaille, 1999; Lin & van Keken, 2006; Samuel & Bercovici, 2006; Adam et al., 2017; Jones et al., 2017), and the effects of variable mantle properties (e.g., Matyska et al., 1994; Larsen & Yuen, 1997; Goes et al., 2004; Koronaga, 2005; King & Redmond, 2007; Matyska et al., 2011; Leng & Gurnis, 2012; Davaille et al., 2018).

Roughly eight plumes explain broad swells on the seafloor, geoid highs, low-velocity anomalies in the mantle transition zone, and the geochemical characteristics of hotspot basalts (e.g., Courtillot et al., 2003; Ritsema & Allen, 2003; Montelli et al., 2006). Nevertheless, the concept of mantle plumes in Earth has been questioned because the interpretation of geological, geochemical, or geophysical data is non-unique (e.g., Anderson, 2000; Foulger & Natland, 2003; Fouch, 2012; Foulger et al., 2015). The difficulty to seismologically image the deep mantle with high resolution is at the core of the contention, for two reasons. First, the seismic imaging artifacts are profound, especially near hotspots in the oceans where seismic station coverage is limited. Second, narrow plume conduits do not affect seismic waves strongly. Due to what seismologists call *wavefront healing* (e.g., Nolet & Dahlen, 2000), the recorded delay of a seismic wave that has traversed a plume in the lower mantle may be smaller than the uncertainty of the traveltime measurement (e.g., Hwang et al., 2011; Rickers et al., 2012; Xue et al., 2015; Maguire et al., 2016). Moreover, reflections and scattered waves in the heterogeneous crust and upper mantle may overwhelm the low-amplitude signals from

wave diffraction around a plume conduit. The inconsistent seismic imaging of structure in the lower mantle, as illustrated in Figure 14.1 for 11 global tomographic models, underscores the difficulty of resolving weak and small-scale structure in the deep mantle. Without rigorous and quantitative analyses of model resolution and image artifacts, it is impossible to reconcile model differences and to ascertain the physical origins of seismic anomalies.

In this chapter, we conduct sensitivity tests aimed at understanding the expected seismic structure of plumes and whether plumes are identifiable by seismic methods. Using numerical simulations of convection and parameters constrained by mineral physics, we estimate the shear-velocity perturbations in the mantle due to plumes, how plumes decelerate seismic waves, and how traveltimes tomography would resolve plumes in the lower mantle. We also explore how plumes may perturb the phase boundaries of the mantle transition zone. Finally, we discuss future directions in seismic imaging of plumes with preliminary studies of scattered or diffracted waves.

14.2. PHYSICAL MODELS OF DEEP MANTLE PLUMES

To interpret seismic images and recordings of waves that have propagated through the mantle beneath hotspots, it is essential to understand the physical and seismic structure of physically viable plumes. The purely thermal plume R1c from the study of Maguire et al. (2016) is an example that we will explore in this chapter. R1c is determined by solving the equations governing conservation of mass, momentum, and energy in an axisymmetric spherical shell following Bossmann & van Keken (2013). It began as a harmonic perturbation to the thermal boundary layer above the core-mantle boundary (CMB) and has a steady-state structure after 175 Myr, which is the stage shown in Figure 14.2. Above D”, the excess temperature is higher than 150 K within a cylindrical conduit with a diameter of about 400 km. R1c reflects the main characteristics expected for a whole-mantle plume. It has a relatively narrow tail of only a few 100 km diameter. The tail further narrows in the lower-viscosity upper mantle and flattens and spreads to form a hot layer below the lithosphere.

The shape of plumes depends on the thermodynamics of the mantle. R1c is calculated for a compressible mantle with a thermal Rayleigh number of 2×10^6 , a temperature contrast across the CMB of 750 K, and a Clapeyron slope of the ringwoodite-bridgmanite transition (the “660” from here on) of -2.5 MPa K^{-1} (e.g., Bina & Helffrich, 1994). The viscosity η depends on depth and temperature by $(T, z) = \eta_0(z) \exp(-b(T - T_{\text{REF}}))$ with $b = \ln(10)$. In the lower mantle $\eta_0 = 10^{22} \text{ Pa s}$. Above the 660, we reduce the viscosity by a factor of 30 and $\eta_0 = 10^{24} \text{ Pa s}$ in the

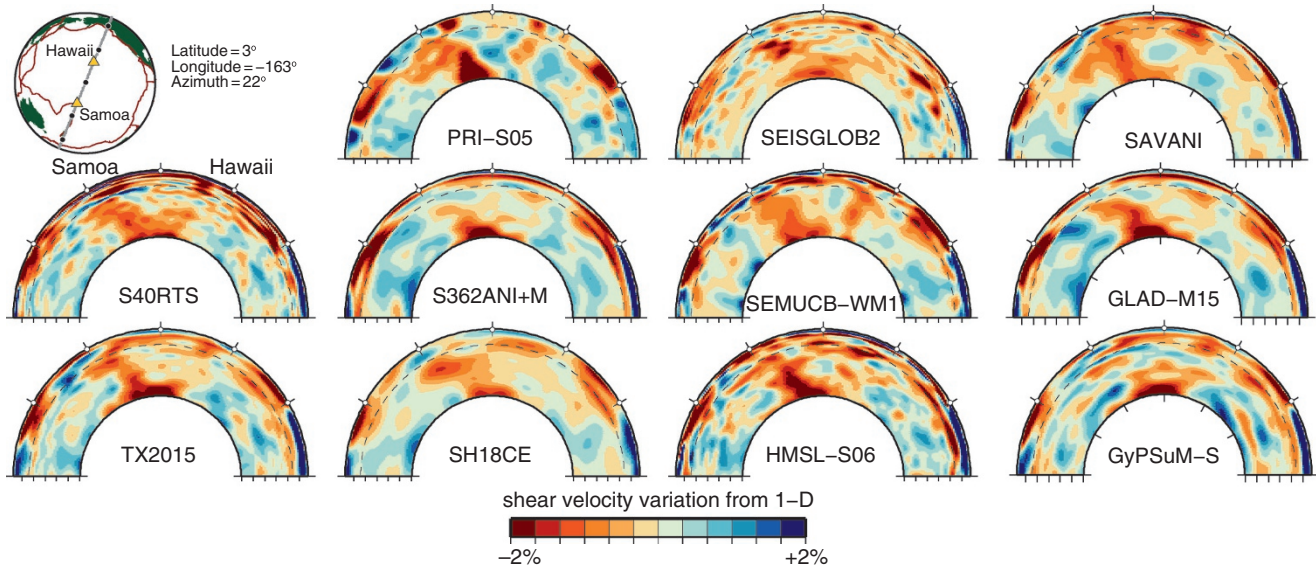


Figure 14.1 Vertical cross-sections of shear velocity variations (shown up to spherical harmonic degree 40) according to models S40RTS (Ritsema et al., 2011), TX2015 (Lu & Grand, 2016), PRI-S05 (Montelli et al., 2006), S362ANI+M (Moulik & Ekström, 2014), SH18CE (Takeuchi, 2007), SEISGLOB2 (Durand et al., 2017), SEMUCB-WM1 (French & Romanowicz, 2014), HMSL-S06 (Houser et al., 2008a), SAVANI (Auer et al., 2014), GLAD-M15 (Bozdağ et al., 2016), and GyPSuM-S (Simmons et al., 2010). The SSW-NNE oriented cross-sections are centered on the location 3°N; 163°W in the Pacific and include the Samoa and Hawaii hotspots. Note the difference in the resolved seismic structure. Sources: Ritsema et al., (2011), Lu & Grand (2016), Montelli et al., (2006), Moulik & Ekström (2014), Takeuchi (2007), Durand et al., (2017), French & Romanowicz (2014), Houser et al., (2008a), Auer et al., (2014), Bozdağ et al., (2016), Simmons et al., (2010).

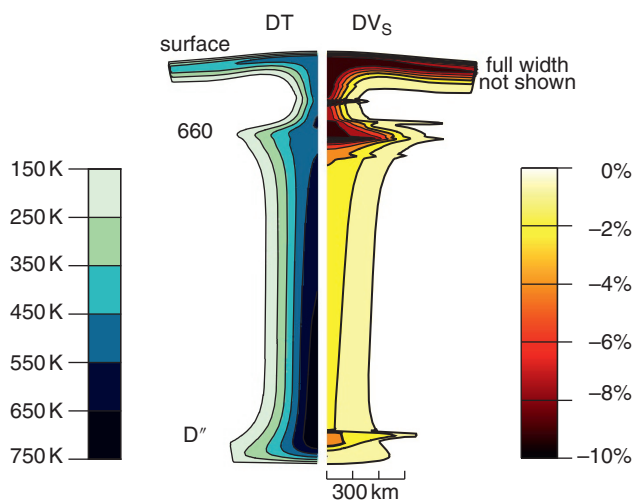


Figure 14.2 Perturbations of temperature in Kelvin (left) and percent shear velocity (right) of thermal plume R1c. We artificially truncate the width of the plume head so it does not overwhelm the travelt ime delay signal from the tail in the deep mantle.

lithosphere. Plumes are narrower if the dependence of viscosity on temperature is stronger, if viscosity depends also on stress, or if thermal expansivity decreases less with depth (e.g., Goes et al., 2004; King & Redmond, 2007).

Chemical entrainment of dense material in the lowermost mantle may reduce buoyancy and broaden plumes and modify their internal temperature structure (e.g., Farnetani, 1997; Lin & van Keken, 2006; Dannberg & Sobolev, 2015; Adam et al., 2017). The entrainment may contribute as much as 10–20% to the plume volume (e.g., Deschamps et al., 2011; Dannberg & Sobolev, 2015; Sobolev et al., 2007). The travelt ime delays in the plume tails are approximately linear with respect to velocity perturbation (e.g., Mercerat & Nolet, 2013; Maguire et al., 2016). Therefore, seismic analyses of purely thermal plumes can provide insight into the resolvability of stronger or weaker thermochemical plume tails with similar widths.

To determine the wave speed structure of a plume, we must assume a mantle composition and relationships between composition, temperature and wave speeds. In the case of R1c, the mantle has a homogeneous pyrolytic composition (Workman & Hart, 2005), defined in terms of the oxides Na_2O , CaO , FeO , MgO , Al_2O_3 , and SiO_2 . The thermal and velocity perturbations of R1c are relative to the background profile of the thermal models. We use the program *Perple_X* (Connolly, 2005) and the thermodynamic database of Stixrude & Lithgow-Bertelloni (2011) to compute the equilibrium mineral assemblage and the corresponding elastic parameters and density as a function of pressure and temperature. We determine

seismic velocity of the bulk mineral assemblage as the Voigt-Reuss-Hill average of the velocities and add a correction for pressure, temperature, and frequency-dependent attenuation using semi-empirical Arrhenius-style formulations (e.g., Matas et al., 2007; Styles et al., 2011). We construct the 3D velocity structure for a mantle with plume R1c by superposing the velocity perturbations on the Preliminary Reference Earth Model (PREM) (Dziewonski & Anderson, 1981). The significant uncertainties in the relationships between temperature and wave speed perturbations have been documented elsewhere (e.g., Cammarano et al., 2003, Deschamps & Trampert, 2004, Cobden et al., 2008, 2009; Matas et al., 2007, Deschamps et al., 2012).

14.3. TRAVELTIME ANALYSIS

14.3.1. Expected Traveltime Delays

To illustrate how plume R1c slows down shear waves, we determine traveltime delays of *S* and *SKS* for the idealized source-receiver geometry shown in Figure 14.3. The *S* and *SKS* waves are generated by events A and B at distances of 50° and 100° from the plume axis, respectively, and recorded by seismic stations on the opposite side of R1c. This geometry is typical for a regional seismic experiment aimed at interrogating mantle structure using teleseismic seismograms. We compute waveforms (Figure 14.3b) for PREM and R1c using the SPEC-FEM3d_Globe software (Komatitsch et al., 2015) to ensure that the full 3D propagation effects are included in the waveforms. Since the R1c velocity structure represents shear-velocity perturbations from PREM, the differences in the waveforms are entirely due to the presence of the plume. Figure 14.3c shows the delays of *S* and *SKS* determined by cross-correlating the PREM and R1c waveforms.

At seismic stations directly behind the plume (for $X < 10^\circ$ in Figure 14.3), *S* and *SKS* propagate through the plume beneath the lithosphere. The plume head amplifies the *S* wave and retards the *S* and *SKS* arrivals between 8 to 10 s at $X < 5^\circ$. At stations more than 10° from the plume axis, the *S* wave crosses R1c's tail in the deep mantle. Since *SKS* propagates steeply through the mantle, the effects of R1c on its propagation are apparent only at stations within 20° from the plume axis.

At stations furthest from R1c (i.e., $X > 20^\circ$) the *S*-wave delay decreases steadily with distance because *S* crosses the plume tail in the lower mantle more perpendicularly, the shear-velocity anomaly weakens slightly with depth (see Figure 14.2), and wave delays diminish with propagation distance due to wave diffraction (i.e., wavefront healing). The *S*-wave traveltime delay is about 0.6 s at $X = 30^\circ$. The small increase at $X = 40^\circ$ when the *S* wave turns near

2650 km depth is due to the post-perovskite phase transition.

Maguire et al. (2016) examined the frequency dependence for the same source-receiver geometry. They show that *S*-wave delays are smallest when the waveforms are analyzed using the longest period pass bands and that they are at least two times smaller than ray-theoretical traveltime delays for periods longer than 10 s. Further they show that the *P*-wave delays are smaller than the *S* delays because *P* waves have broader Fresnel zones than *S* waves at the same period.

By visual inspection of waveform fits and experimentation with cross-correlation windows we estimate that we can measure the *S*-wave delay with an uncertainty of about 0.1 seconds at periods of $T = 10$ s. When analyzing recorded waveforms, however, we expect that an uncertainty of 0.5 s may be more realistic given the typical dissimilarity between recorded and synthetic waveforms.

The expected *P* or *S* traveltime delay of 1 s or less imparted by a plume tail is smaller than the delays produced by large-low shear velocity provinces at the base of the mantle (e.g., Wen et al., 2001) and comparable to the traveltime variations due to the crust (e.g., Ritsema et al., 2009). It is therefore not straightforward to uniquely attribute relatively small traveltime delays to plumes in the mantle, but it may be possible to recognize a systematic traveltime perturbation due to plumes in recordings from dense regional seismic networks. The study by Nataf & VanDecar (1993) is, to our knowledge, the only published study of traveltime variations due to plumes. These authors documented systematic *P*-wave delays of up to 0.15 s in recordings of 12 earthquakes in Alaska at the Washington Regional Seismic Network. They associated these delays to *P*-wave interaction with a low-velocity structure beneath the Bowie hotspot at a depth of ~ 700 km.

14.3.2. Synthetic Tomography of Deep Mantle Plumes

To determine how recorded teleseismic *S*-wave traveltime delays could constrain the shear-velocity structure in the mantle modeled below hotspot-centered seismic networks, we consider tomographic images of plume R1c using the finite-frequency traveltime inversion approach of Bonnín et al. (2014) and Maguire et al. (2018) and the traveltime delays of *S* and *SKS*. Teleseismic traveltime inversion is a common procedure for studying the structure of the mantle beneath hotspots such as Iceland (Allen et al., 2002), Hawaii (Wolfe et al., 2009), the Afar region (Hammond et al., 2013), and Yellowstone (Nelson & Grand, 2018). As in section 14.3.1, we estimate the traveltime delays by cross-correlating spectral-element method synthetics for PREM and R1c. We assume that the delay times have an uncertainty of

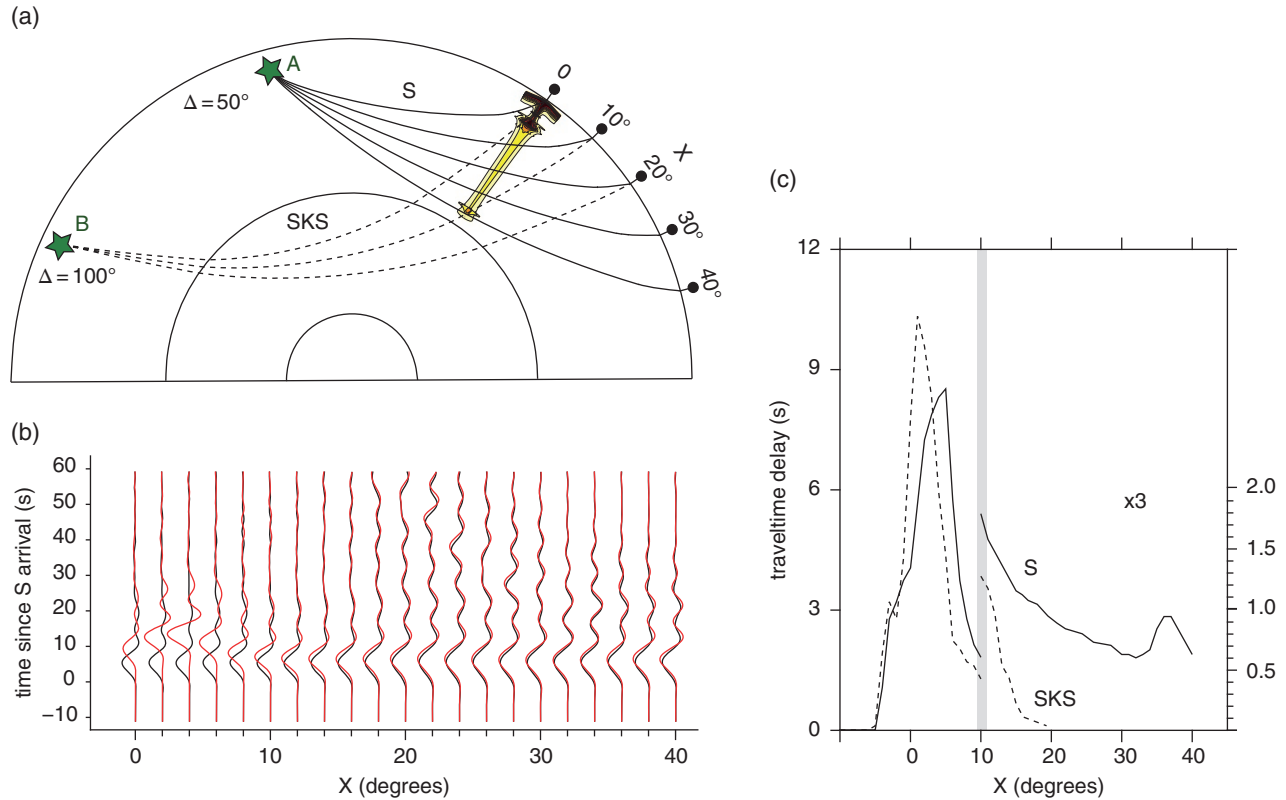


Figure 14.3 (a) Ray paths of S waves (solid lines) and SKS waves (dashed lines) originating from two 400-km deep earthquakes (stars) at 50° (event A) and 100° (event B) distance from the axis of plume R1c. X is the angular distance (in degrees) from the plume axis. For the rays shown, the S waves and SKS waves are recorded at X up to 20° and 40° , respectively. (b) Waveforms for PREM (black) and R1c (red) aligned on the PREM S wave arrival time (time = 0) and X from 0 to 40° . The waveforms are scaled so the PREM waveforms have amplitudes of 1 for any distance. (c) The delay times of S (solid line) and SKS (dashed line) measured by waveform analysis of the SEM synthetics for the ray geometry shown in (a). The delays for $X > 10^\circ$ are shown with the scale indicated to the right.

0.5 seconds and we select the preferred model from an L-curve analysis of data fit and model complexity. Since the R1c plume is placed in a mantle with the PREM velocity structure, large-scale crust and mantle structure do not affect the inversions.

We use the source-receiver geometry for two case studies from the literature. In Figure 14.4a, plume R1c is placed under Hawaii and its synthetic image is based on the recording of teleseismic S and SKS waves by stations from the PLUME experiment (Laske et al., 2009; Wolfe et al., 2009). This network includes seismic stations on the islands of Hawaii and 73 ocean-bottom seismometers distributed more than a thousand kilometers. In Figure 14.4b, plume R1c is placed under Yellowstone and is imaged using traveltimes of S and SKS waves recorded by hundreds of Transportable Array stations throughout the western US following the analysis of Nelson & Grand (2018). Figure 14.4c shows the actual and resolved shear-velocity anomalies along the vertical plume axis of R1c. Maguire et al. (2018) show inversion

results for different station distributions and modeling parameters (i.e., data errors, regularization).

Along the axis of R1c, the shear-velocity reduction with respect to the ambient mantle, abbreviated as dV_S , is 3–5% below about 1500 km depth. The resolved dV_S is at least two times weaker due to the effects of parameterization, regularization, and damping. The dV_S in the tail of R1c is smaller than 0.5% beneath Hawaii and invisible with the chosen colour diagram.

The differences between the resolved structure of R1c in Figures 14.4a and 14.4b are entirely due to the different source-receiver geometries. In particular, the network dimensions (1000 km for Hawaii and 2000 km for Yellowstone) explain the differences in the resolution at depth but using the recording by TA stations of the relatively steep SKS phases helps to improve the illumination of the deep mantle. Maguire et al. (2018) have demonstrated with similar experiments that image resolution in the lower mantle is primarily determined by network extent. They argue in particular that improvement of plume imaging

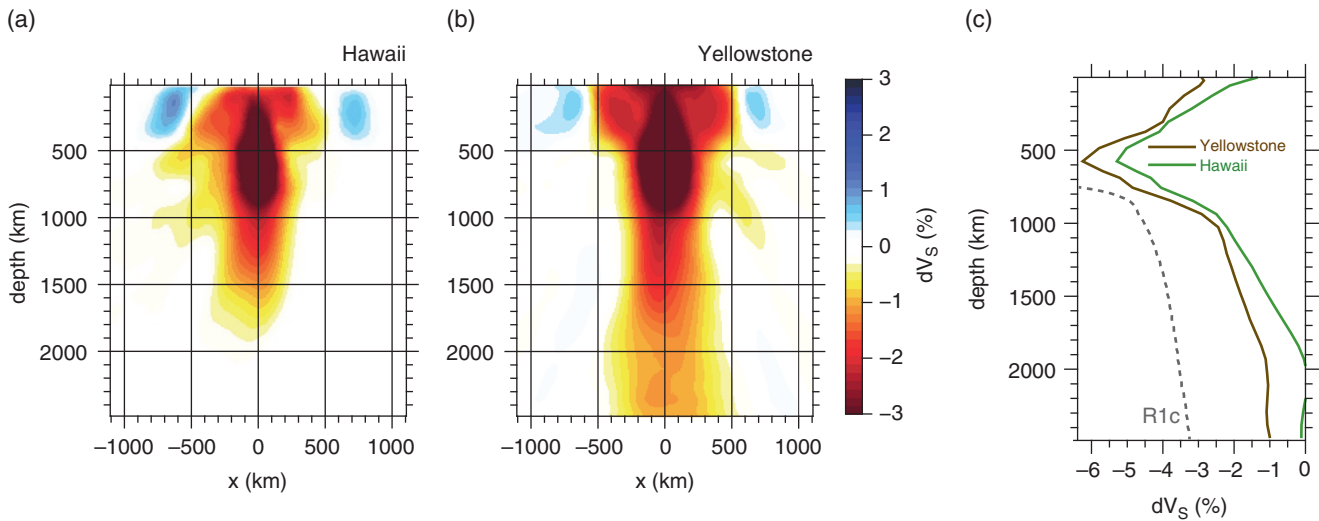


Figure 14.4 Tomographic images of plume R1c by finite-frequency inversion of S -wave and SKS -wave delay times using the earthquake-station geometry for (a) Hawaii (Wolfe et al., 2009), and (b) Yellowstone (Nelson & Grand, 2018). Panel (c) shows the shear velocity perturbations along the plume axis (at $x = 0$) of R1c (dashed line) and the synthetic images of R1c at Yellowstone (brown line) and Hawaii (green line). Source: (a) Wolfe et al., (2009), (b) Nelson & Grand, (2018).

in oceanic basins (i.e., Hawaii) is possible with wide-aperture (> 5000 km) arrays of ocean-bottom seismometers. We emphasize that the costs of such an array are much higher than the relatively modest budget available to the scientists who designed and installed the PLUME network.

14.4. UNDULATIONS OF THE 410-KM AND 660-KM PHASE TRANSITIONS

The morphology of a plume across the mantle transition zone (MTZ) is complex. For example, plume R1c in Figure 14.2 is relatively broad below the 660 and thin above the 660 because we assume for R1c that the viscosity above the 660 is lower by a factor of 30 and that the Clapeyron slope of the phase transition is negative. A plume also modifies the MTZ because the increase in temperature changes the pressures at which phase transitions occur and compositional heterogeneity in the plume may affect seismic velocity contrasts and gradients.

Typically, seismological investigations of the MTZ focus on wave speed gradients, the depths of the 410 (i.e., the olivine to wadsleyite transition) and the 660, and layering within the MTZ. Almost all studies provide estimates of the thickness of the MTZ, defined as the distance between the 410 and 660, which can be estimated more robustly than the depths of the 410 and 660 individually because it does not depend strongly on corrections for the effects of the wave speed structure above the discontinuities.

Figure 14.5 illustrates the dominant effects of temperature and composition on the radial velocity structure of transition zone for a mantle with a pyrolite composition (in Figure 14.5a) and a mantle in which the composition is described by a mixture of basalt and harzburgite (in Figures 14.5b and 14.5c) following simulations of mantle mixing (e.g., Nakagawa & Tackley, 2004; Xu et al., 2008). In a warm mantle, the 410 is deeper and the 660 is shallower than in cooler mantle but, due to the higher Clapeyron slope, temperature affects the 410 the most. The 660 is relatively sharp (< 1 km). However, the concurrent transformation of garnet to postspinel phases extends to about 750 km depth. It enhances the velocity gradients and may produce a second discontinuity below 700 km, depending on the degree of silica saturation (note that MORB is SiO_2 -enriched) and the manner of mixture. The depths and sharpnesses of the 410 and 660 are insensitive to chemical composition in a mechanical mixture of basalt and harzburgite but not in a mantle with different equilibrium assemblages. In addition, ringwoodite dissociates into majorite garnet and magnesiowüstite at high temperatures, reducing the sharpness of the 660.

The effects of water on seismic characteristics of the MTZ are poorly constrained (Thio et al., 2016). Initial studies (at relatively low temperatures) suggested that the presence of water reduces wave speeds and increases the thickness of the MTZ (e.g. Jacobsen & Smyth, 2006), although experimental work by Bercovici & Karato (2003) indicates that this effect may be small at plume temperatures. Recent experiments by Buchen et al. (2018) and Schulze et al. (2018) suggest that hydration does not

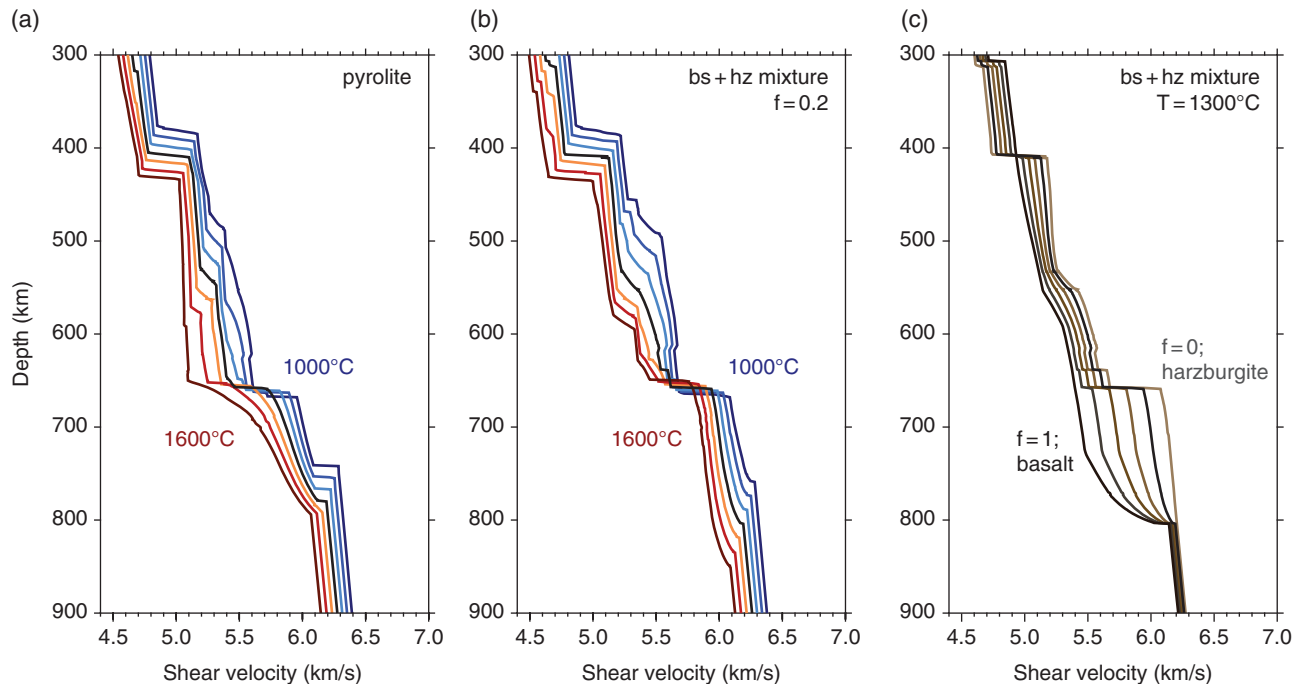


Figure 14.5 Theoretical profiles of shear velocity as a function of depth for (a) pyrolite and for (b and c) mixtures of harzburgite and basalt. In (a) and (b), the profiles are shown for adiabats with potential temperatures T between 1000°C and 1600°C. In (c), $T = 1300^\circ\text{C}$ and the basalt fraction f ranges from 0 (pure harzburgite) to 1 (pure basalt) with steps of 0.2. Profiles are calculated using the equation-of-state and elastic parameters from Stixrude & Lithgow-Bertelloni (2011) as implemented in the thermo-dynamic modelling code PerPle_X (Connolly, 2005), with an anelastic correction using model Q7 (Yu et al., 2018, Styles et al., 2011). Sources: (a–c) Connolly (2005), Stixrude & Lithgow-Bertelloni (2011), Styles et al., 2011, Matas et al., 2007.

reduce wave speeds in wadsleyite and ringwoodite as much as previously estimated, although their experiments were done with relatively low water contents. Moreover, new experiments on olivine at upper mantle conditions indicate that wave speed reductions previously attributed to the effect of the presence of water on attenuation may in fact have been controlled by redox reactions (Cline et al., 2018). The experiments by Mrosko et al. (2015) on the wadsleyite to ringwoodite transition at around 520 km depth indicate that the combination of water and redox conditions control transition width.

The seismological characteristics of the MTZ have been analyzed using the waveforms of waves turning in the MTZ (e.g., Song et al., 2004; Stähler et al., 2012) and, more frequently, using underside P -wave and S -wave reflections (i.e., often referred to as SS and PP precursors) (e.g., Shearer, 1991) and P -wave to S -wave conversions (i.e., transition zone receiver functions) (e.g., Vinnik, 1977) at seismic boundaries in the MTZ. SS and PP precursors have been examined primarily to constrain seismic layering in the MTZ on a global scale (e.g., Flanagan & Shearer, 1998; Gu & Dziewonski, 2002; Chambers et al., 2005; Houser et al., 2008b). Focused studies of

hotspot regions include Niu et al. (2002), Deuss (2007), Gu et al. (2009), Schmerr et al. (2010), Lessing et al. (2014), Saki et al. (2015), Zheng et al. (2015), and Wei & Shearer (2017). The receiver function technique provides constraints on the MTZ directly beneath seismic stations and with higher spatial resolution than SS precursor studies. Chevrot et al. (1999) and Tauzin et al. (2008) compared receiver functions for hotspot regions on a global scale. Recent analyses of data from regional seismic networks near hotspots include the studies of eastern Africa by Mulibo & Nyblade (2013) and Reed et al. (2016), of Hawaii by Agius et al. (2017), of Yellowstone by Schmandt et al. (2012) and Zhou (2018), and of Iceland by Jenkins et al. (2016).

Most seismic studies indicate that the 410 is slightly deeper (~10–30 km) beneath hotspot regions and that the structure of the 660 is more complex, as may be expected from Figure 14.5. The garnet to postspinel rather than ringwoodite to postspinel transition may determine the behavior of the 660 when MTZ temperatures are relatively high and when plumes tend to broaden beneath the 660 (e.g., Deuss et al., 2006). In upwelling regions, the low viscosity of the mantle may facilitate chemical

unmixing and enrich harzburgite below and MORB above the 660 (e.g., Nagakawa & Tackley, 2004; Ballmer et al., 2013; Maguire et al., 2017; Yu et al., 2018).

Studies of *PP* and *SS* precursors and receiver function studies of the MTZ have produced variable results that suggests that plume structures across the MTZ cannot be interpreted easily in a 1D framework. For example, Yu et al. (2017) resolve a thick MTZ to the southwest of the Hawaiian hotspot and a thinner MTZ to the north and east of the Hawaiian hotspot. Using receiver functions from the PLUME network, Agius et al. (2017) estimate that the MTZ thickness varies laterally by ± 13 km. It is thin beneath north-central Hawaii and thick farther away in a horseshoe-shaped structure around Hawaii. Reed et al. (2016) found a strong depression of the 410 and 660 by 40–60 km but a normal MTZ thickness beneath the Afar Depression and the northern Main Ethiopian Rift, while Thompson et al. (2015) found little variation in discontinuity depth across the same region. Further to the south along the East African Rift, Mulibo & Nyblade (2013) find that the MTZ is ~ 30 –40 km thinner than the global average in a 200–400 km region from central Zambia into Kenya. The authors suggest that the lower mantle African superplume structure connects to thermally perturbed upper mantle beneath eastern Africa.

The interpretation of seismic studies of the MTZ is also complicated by the choices in data processing and theoretical simplifications in the migration of waveforms. It is difficult to compare the results of *SS* precursor and receiver function analyses because *SS* waves have wider Fresnel zones (e.g., Chaljub & Tarantolla, 1997; Neele et al., 1997; Zhao & Chevrot, 2003). Moreover, imaging errors can be significant if the *SS*-precursor or receiver function images are interpreted using ray theory (e.g., Lawrence & Shearer, 2008; Bai et al., 2012). It is essential to consider 3D sensitivity kernels in the analysis of *SS* precursors (e.g., Koroni & Trampert, 2015) and receiver functions to account for effect of velocity structure throughout the mantle and the effects of wave diffraction due to topography on the 410 and 660 (e.g., Deng & Zhou, 2015).

14.5. DIFFRACTION AND SCATTERING EFFECTS

Traditionally, tomographic imaging of mantle plumes has primarily been based upon the traveltimes of body waves. The traveltimes of *P* waves and *S* waves may not be influenced by a narrow plume in the deep mantle when their Fresnel zones are comparable to or wider than this heterogeneity (e.g., Nolet & Dahlen, 2000). Waves propagating through and diffracting around small-scale

heterogeneities, such as deep mantle plumes, may interfere destructively (i.e., wavefront healing) to modify the recorded signal (Malcolm & Trampert, 2011). Wavefront healing is especially problematic for seismic inversions based on fitting the traveltimes of the *P* and *S* wavelets at teleseismic distances. The controversy surrounding the resolution of deep mantle plumes (e.g., Montelli et al., 2004; Van der Hilst & de Hoop, 2005; Trampert & Spetzler, 2006; Hwang et al., 2011) relates in large part to whether we can image the deep mantle with only *P*-wave and *S*-wave wavelets when wave coverage is incomplete and the traveltime shifts may be immeasurably small. Whereas wavefront healing may reduce the amplitudes of the first-arriving wave phases, signals of constructive interference may be present later in the seismogram and indicate the presence of plumes.

The first numerical models of wave diffraction by plumes appeared about 20 years ago. The plumes were conceptualized as narrow vertical cylinders on top of the CMB (e.g., Ji & Nataf, 1998a; Tilmann et al., 1998; Dalkolmo & Friederich, 2000; Capdeville et al., 2002). Although each study used different numerical methods and approximations of wave behavior to simulate scattering, they consistently showed that the amplitudes of scattered phases are typically a few percent of the amplitude of direct phases. They may be difficult to identify in recorded waveforms (Figure 14.6) and to uniquely associate with the origin of the scattering. For example, Ji & Nataf (1998b) located a strong scatterer hundreds of kilometers northwest of the presumed location of the Hawaiian plume. Because of the lateral offset and the strength of the anomaly – much stronger than would be expected for a purely thermal origin – it was difficult to determine how or to what extent this scattering structure could be related to the Hawaiian hotspot.

Currently, the access to cheap random-access memory and computer clusters has made it possible to study 3D wave propagation through plume-like structures in the deep mantle in spherical 3D geometry for wave periods around 5 s, similar to the periods of teleseismic *S*-wave signals (e.g., Cobden et al., 2015). The spectral-element method (SEM) (e.g., Komatitsch & Villote, 1998; Komatitsch & Tromp, 2002) is frequently used to compute waveforms on regional and global scales. Rickers et al. (2012) investigated the seismic signals at periods longer than 25 s in the coda of a *P* wave that propagated through a 300-km wide, low-velocity ($dV_P = -5\%$) cylinder, broadly analogous to R1c in the deep mantle. They used a metric known as the instantaneous phase misfit (Bozdağ et al., 2011), which is an amplitude-independent measurement of the signal phase within an extended time window, to emphasize low-amplitude wave arrivals. They demonstrated the systematic decay of the traveltime delay with increasing distance from the plume and decreasing plume

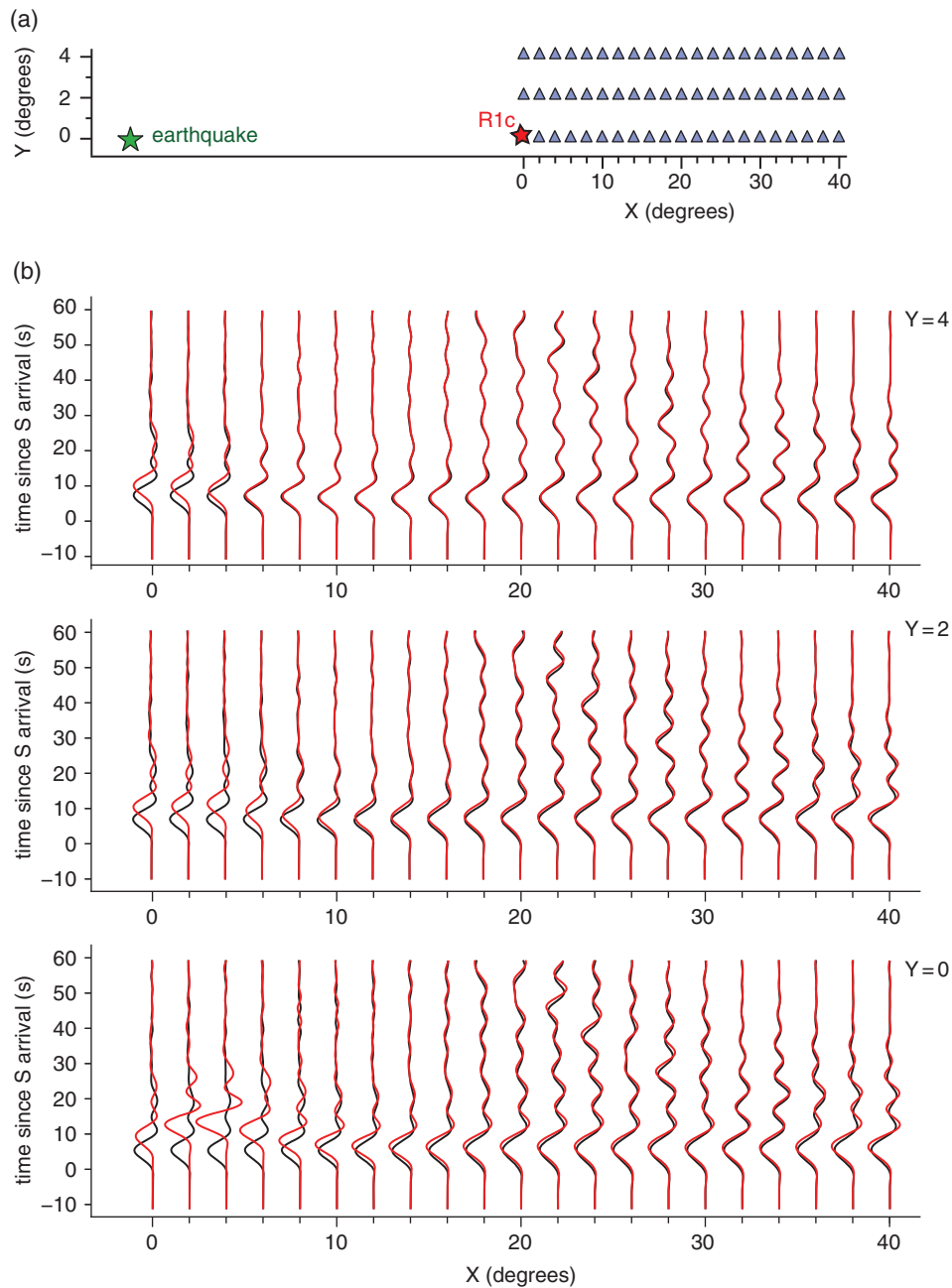


Figure 14.6 SEM waveforms for PREM (black) and R1c (red) for plume model R1c for the source-receiver geometry shown in (a). See the caption of Figure 14.3 for further details. There is no clear evidence for wave diffraction in the synthetics at periods longer than 10 s, most likely because the horizontal gradients in shear velocity across the tail of R1c are too small.

diameter due to wavefront healing and time shifts (and sometimes early arrivals) indicative of wave diffraction. Rickers et al. (2013) used instantaneous phase measurements to resolve a low shear wave speed anomaly beneath Iceland extending to at least 1300 km depth, the maximum depth of the model domain.

Stockmann et al. (2019) investigated the possibility of identifying scattering from plumes by mapping seismic array synthetics as a function of slowness and back azimuth over sliding time windows. Following a similar procedure to Maguire et al. (2016, 2018) they converted thermochemical plume models into seismic structures

and simulated synthetic seismograms using the SEM. Stockmann et al. (2019) could not detect any direct scattering or back-scattering from the plumes, for their chosen array configuration and at seismic periods longer than 15 s. However, they did observe out-of-plane energy from phases due to bending of wavefronts around the plume conduit. Interestingly, this effect was stronger and more visible at lower frequencies, presumably as lower frequencies “see” the average structure over a wider spatial window. This proof-of-concept study suggests that the origin of apparently scattered energy off a plume is optimally constrained by studying waveforms at a range of azimuths and at both low and high frequencies.

Several observational studies of 3D wave propagation have been conducted to study the crust and mantle beneath hotspot regions. Using waveforms from USArray stations near Yellowstone, Chu et al. (2010) reported opposite polarities of P waves on vertical and radial component seismograms near Yellowstone which they interpreted as due to the bending of waves around a plume-derived magma body in the crust. Cottaar & Romanowicz (2012), To et al. (2016), and Yuan & Romanowicz (2017) analyzed direct and diffracted S waves with strong amplitude reductions and azimuth-dependent secondary arrivals. The seismic observations indicate that the S waves interacted with roughly 900-km wide and 20-km thick ultra-low velocity zones (ULVZ) at the base of the mantle beneath the Pacific Ocean and northern Atlantic. These ULVZ have similar dimensions as the ULVZ resolved by Thorne et al. (2013) using SKS waveforms and may be related to the source of plume upwelling beneath Samoa, Hawaii, and Iceland.

Bozdağ et al. (2016) developed the first global-scale tomography model in which both the forward and inverse modelling are based on SEM simulations of wave propagation for the entire globe. Although the method accounts for wave behavior with exact theories, the simulations require substantial computational resources so the analysis was limited to waveforms for 253 earthquakes and multitaper traveltimes measurements with a minimum period of 17 s. After 15 iterations the tomographic image enhances plume-like structures in the lower mantle beneath Tahiti, Samoa, and the Caroline islands that appear to be tilted from about 1000 km depth upward. Hybrid procedures that combine SEM (Capdeville et al., 2003) for computing the forward wavefield, and asymptotic coupling theory (Li & Romanowicz, 1996) for the inverse wavefield have lower computational cost. Tomography model SEMUCB-WM1 (French & Romanowicz, 2015) based on this approach features ~500–800 km wide (broader than R1c), low-velocity anomalies beneath several hotspots. If confirmed, such widths provide constraints on plume dynamics (e.g., Dannberg & Sobolev, 2015; Davaille et al., 2018). It would also raise

questions about the subdued swells above many hotspots (King & Adam, 2014), although plume induced vertical surface motions may be complicated by crustal layering (e.g. Burov & Gerya, 2014).

14.6. CONCLUDING REMARKS

Progress in understanding plume formation and ascent will continue to rely on interdisciplinary investigations. New mantle circulation simulations, including in 3D and spherical geometries, advance our understanding of plume morphologies for plausible mantle rheology, thermal properties, and entrainment of chemically dense material. Comparing computed seismic signals predicted from such dynamic models with actual observations is in our view an essential step for making physical interpretations of seismic structures.

From the comparison of models and observations, it is clear that plume ascent and evolution is moderated and complicated by entrained dense material that is possibly derived from recycled oceanic crust (e.g., Farnetani, 1997; Lin & van Keken, 2006; Dannberg & Sobolev, 2015; Adam et al., 2017). Ample geochemical and petrological evidence documents that the mantle source material of hotspot volcanism contains chemically distinct components (e.g., Hofmann, 1997; Sobolev et al., 2007), plausibly in concentrations large enough to affect plume buoyancy and temperature. Several studies have proposed that such thermo-chemical plumes can be deflected near 1000 km depth or at the 660 or above the 410, or pond and form secondary instabilities (e.g., Ballmer et al., 2013; Civiero et al., 2015; Dannberg & Sobolev, 2015; Saki et al., 2015; Jenkins et al. 2017). In addition, plume shapes (from seismic imaging) and ascent velocities (from evolution of topography) can provide constraints on mantle rheology (e.g., van Hunen & Zhong, 2003; Davaille et al. 2018). A range of other surface observations, including the geoid, the evolution of surface topography, spatio-temporal distributions of volcanism and compositions of magmas complement the testing of model-predicted plume dynamics (e.g., Ito et al., 1999; Lin et al., 2005; Armitage et al., 2015; Koptev et al., 2015; Jones et al., 2017). Interdisciplinary efforts such as those listed above will ultimately help to determine how much plumes contribute to heat and mass fluxes through the mantle (e.g. Nolet et al., 2006; Zhong, 2006; Deschamps et al., 2011).

Ongoing method developments and further (targeted) expansion of seismic data sets are promising avenues for delivering new constraints on the fine-scale seismic structure of the mantle, particularly beneath hotspots. Full 3D simulations of seismic waveforms are now routine at 0.1 Hz and will be possible at higher frequencies as computational resources improve. Forward modeling

may elucidate the expected waveform perturbations either as wavelet traveltime delays or by changes in the P -wave or S -wave amplitude and additional arrivals in the P -wave or S -wave coda. The off-path wave propagation can be explored by array techniques such as slowness–back-azimuth analysis (Rost & Thomas, 2009) that has been successful in the mapping of wave scattering in the deep mantle (e.g., Kaneshima & Helffrich, 1998; Schumacher & Thomas, 2016). Hybrid forward-modeling techniques that have lower computational cost (e.g., Leng et al., 2016) are likely to be important to deep Earth imaging in the coming years, especially for high-frequency (~ 1 Hz) waveform modeling.

Tomographic imaging will advance with the implementation of accurate wave propagation theories and inversions based on substantially larger data sets. For example, the most recent published global images based on adjoint tomography are based on about 1480 earthquakes (Lei et al., 2020). Additional model iterations using a larger number of earthquakes and increasingly shorter periods will improve the images obtained.

In addition to the development of new seismic imaging techniques, seismic imaging will rely on new data sets. Global tomography is based on surface-wave and body-wave signals as well as waveform segments in between the major seismic phases. Incorporating nontraditional seismic datasets, such as ambient noise correlations (e.g., Poli et al., 2012, Spica et al., 2017, Pham et al., 2018) will help to improve seismic images in regions of the mantle outside earthquake-receiver corridors. Finally, it is important that seismologists continue their commitment to the development of seismic deployments, especially in oceanic regions. Previous deployments (e.g., Suetsugu et al., 2009; Laske et al., 2009; Barruol & Sigloch, 2013) have demonstrated that offshore instrumentation around oceanic hotspots are essential for seismic studies of plumes. Progress in the imaging of the mantle, and the mantle beneath hotspots in particular, may experience the most significant boost if we can achieve widespread coverage of the oceans with ocean-bottom seismometers (e.g., Suetsugu & Shiobara., 2014) or floating hydrophones (e.g., Sukhovich et al., 2015; Nolet et al., 2019).

ACKNOWLEDGMENTS

JR was supported by NSF grant EAR-1565511. RM acknowledges computational support from XSEDE via grant TG-EAR15001. LC was supported by a Vidi grant from The Netherlands Organisation for Scientific Research (NWO), on grant number 016.Vidi.171.022. SG acknowledges support from NERC (NE/J008028/1). We thank Scott King and an anonymous reviewer for

helpful comments. We thank Sanne Cottaar for inviting us to write this chapter.

REFERENCES

- Adam, C., Caddick, M. J., & King, S. D. (2017). Pyroxenite causes fat plumes and stagnant slabs. *Geophysical Research Letters*, *40* (10), 4,730–4,737. <https://doi.org/10.1002/2017GL072943>.
- Albers, M., & Christensen, U. R. (2001). Channeling of plume flow beneath mid-ocean ridges. *Earth and Planetary Science Letters*, *187* (1–2), 207–220.
- Agius, M. R., Rychert, C. A., Harmon, N., & Laske, G. (2017). Mapping the mantle transition zone beneath Hawaii from Ps receiver functions: Evidence for a hot plume and cold mantle downwellings. *Earth and Planetary Science Letters*, *474*, 226–236. <https://doi.org/10.1016/j.epsl.2017.06.033>.
- Allen, R. M., Nolet, G., Morgan, W. J., Vogtjard, K., Bergsson, B. H., Erlandsson, P., Foulger, G. R., Jakobsdottir, S., Julian, B. R., Pritchard, M., Ragnarsson, S., & Stefansson, R. (2002). Imaging the mantle beneath Iceland using integrated seismological techniques. *Journal of Geophysical Research*, *107*. <https://doi.org/10.1029/2001JB000595>.
- Anderson, D. L. (2000). The thermal state of the upper mantle; No role for mantle plumes. *Geophysical Research Letters*, *27*, 3623–3626. <https://doi.org/10.1029/2000GL011533>.
- Armitage, J. J., Ferguson, D. J., Goes, S., Hammond, J. O. S., Calais, E., Rychert, C. A., & Harmon, N. (2015). Upper mantle temperature and the onset of extension and break-up in Afar, Africa. *Earth and Planetary Science Letters*, *418*, 78–90.
- Auer, L., Boschi, L., Becker, T. W., Nissen-Meyer, T., & Giardini, D. (2014). Savani: A variable resolution whole-mantle model of anisotropic shear velocity variations based on multiple data sets. *Journal of Geophysical Research, Solid Earth*, *119*, 3006–3034. doi:10.1002/2013JB010773.
- Bai, L., Zhang, Y., & Ritsema, J. (2012). An analysis of SS precursors using spectral–element method seismograms. *Geophysical Journal International*, *188*, 293–300. doi: 10.1111/j.1365-246X.2011.06256x.
- Ballmer, M. D., Ito, G., Wolfe, C. J., & Solomon, S. C. (2013). Double layering of a thermochemical plume in the upper mantle beneath Hawaii. *Earth and Planetary Science Letters*, *376*, 155–164. doi: 10.1016/j.epsl.2013.06.022.
- Ballmer, M. D., van Keken, P. E., & Ito, G. (2015). Hotspots, large igneous provinces and melting anomalies, in: *Treatise of Geophysics, 2nd ed.*, edited by G. Schubert, Vol. 7, 393–459, Elsevier, Oxford.
- Barruol, G., & Sigloch, K. Investigating La Réunion hot spot from crust to core. (2013). *EOS, Trans. American Geophysical Union*, *94* (23), 205–207. <https://doi.org/10.1002/2013EO230002>.
- Bercovici, D., & Karato, S. I. (2003). Whole-mantle convection and the transition-zone water filter. *Nature*, *425* (6953), 39.
- Bina, C. R., & Helffrich, G. (1994). Phase–transition, Clapeyron slopes and transition zone seismic discontinuity. *Journal of Geophysical Research*, *99*, 15,853–15,860.
- Bonnin, M., Nolet, G., Villaseñor, A., Gallart, J., & Thomas, C. (2014). Multiple-frequency tomography of the upper mantle

- beneath the African/Iberian collision zone. *Geophysical Journal International*, 198, 1458–1473. <https://doi.org/10.1093/gji/ggu214>.
- Bossmann, A. B., & van Keken, P. E. (2013). Dynamics of plumes in a compressible mantle with phase changes: implications for phase boundary topography. *Physics Earth Planetary Interiors*, 224, 21–31. <https://doi.org/10.1016/j.pepi.2013.09.002>.
- Bozdağ, E., Trampert, J., & Tromp, J. (2011). Misfit functions for full waveform inversion based on instantaneous phase and envelope measurements. *Geophysical Journal International*, 185, 845–870. <https://doi.org/10.1111/j.1365-246X.2011.04970.x>
- Bozdağ, E., Peter, D., Lefebvre, M., Komatitsch, D., Tromp, J., Hill, J., Podhorszki, N., & Pugmire, D. (2016). Global adjoint tomography: first-generation model. *Geophysical Journal International*, 207, 1739–1766. <https://doi.org/10.1093/gji/ggw356>
- Buchen, J., Marquardt, H., Speziale, S., Kawazoe, T., Boffa Ballaran, T., & Kurnosov, A. (2018). High-pressure single-crystal elasticity of wadsleyite and the seismic signature of water in the shallow transition zone. *Earth and Planetary Science Letters*, 498, 77–87. <https://doi.org/10.1016/j.epsl.2018.06.027>.
- Burov, E., & Gerya, T. (2014). Asymmetric three-dimensional topography over mantle plumes. *Nature*, 513, 85–89. <https://doi.org/10.1038/nature13703>.
- Campbell, I. H., & Griffiths, R. W. (1990). Implications of mantle plume structure for the evolution of flood basalts. *Earth and Planetary Science Letters*, 99, 79–93.
- Cammarano, F., Goes, S., Vacher, P., & Giardini, D. (2003). Inferring upper-mantle temperatures from seismic velocities. *Physics Earth Planetary Interiors*, 138, 197–222. [https://doi.org/10.1016/S0031-9201\(03\)00156-0](https://doi.org/10.1016/S0031-9201(03)00156-0).
- Capdeville, Y., Larmat, C., Vilotte, J.-P., & Montagner, J.-P. (2002). A new coupled spectral element and modal solution method for global seismology: A first application to the scattering induced by a plume-like anomaly. *Geophysical Research Letters*, 29, 1318. <https://doi.org/10.1029/2001GL013747>
- Capdeville Y., Chaljub, E., Vilotte, J. P., & Montagner, J. P. (2003). Coupling the spectral element method with a modal solution for elastic wave propagation in global earth models. *Geophysical Journal International*, 152, 34–67. [doi:10.1046/j.1365-246X.2003.01808.x](https://doi.org/10.1046/j.1365-246X.2003.01808.x)
- Chaljub, E., & Tarantola, A. (1997). Sensitivity of SS precursors to topography on the upper-mantle 660-km discontinuity. *Geophysical Research Letters*, 24, 2613–2616.
- Chambers, K., Woodhouse, J. H., & Deuss, A. (2005). Topography of the 410-km discontinuity from PP and SS precursors. *Earth and Planetary Science Letters*, 235 (3–4), 610–622. <https://doi.org/10.1016/j.epsl.2005.05.014>.
- Chevrot, S., Vinnik, L., & Montagner, J. P. (1999). Global-scale analysis of the mantle Pds phases. *Journal of Geophysical Research*, 104 (20), 203–20, 219. <https://doi.org/10.1029/1999JB900087>.
- Chu, R., Helmberger, D. V., Sun D., Jackson, J. M., & Zhu, L. (2010). Mushy magma beneath Yellowstone. *Geophysical Research Letters*, 37, L01306. <https://doi.org/10.1029/2009GL041656>.
- Civiero, C., Hammond, J. O. S., Goes, S., Fishwick, S., Ahmed, A., Ayele, A., et al. (2015). Multiple mantle upwellings in the transition zone beneath the northern East African Rift system from relative P wave travel-time tomography. *Geochemistry, Geophysics, Geosystems*, 16, 2949–2968. [doi:10.1002/2015GC005948](https://doi.org/10.1002/2015GC005948).
- Cline, C. J., Faul, U. H., David, E. C., Berry, A. J., & Jackson, I. (2018). Redox-influenced seismic properties of upper-mantle olivine. *Nature*, 555, 355–358. <https://doi.org/10.1038/nature25764>.
- Cobden, L. J., Goes, S., Cammarano, F., & Connolly, J. A. D. (2008). Thermo-chemical interpretation of one-dimensional seismic reference models for the upper mantle: evidence for bias due to heterogeneity. *Geophysical Journal International*, 175, 627–648. <https://doi.org/10.1111/j.1365-246X.2008.03903.x>.
- Cobden, L., Goes, S., Ravenna, M., Styles, E., Cammarano, F., Gallagher, K., & Connolly, J. A. D. (2009). Thermochemical interpretation of 1-D seismic data for the lower mantle: The significance of nonadiabatic thermal gradients and compositional heterogeneity. *Journal of Geophysical Research*, 114, B11309. <https://doi.org/10.1029/2008JB006262>.
- Cobden, L., Fichtner, A., & Tong, V. C. H. (2015). Waveform tomography in geophysics and helioseismology. In: *Extraterrestrial Seismology*, editors V. Tong & R. Garcia, Cambridge University Press, 365–377.
- Condie, K. C. (2001). *Mantle Plumes and Their Record in the Earth History*, Cambridge University Press.
- Connolly, J. A. D. (2005). Computation of phase equilibria by linear programming: A tool for geodynamic modeling and an application to subduction zone decarbonation. *Earth and Planetary Science Letters*, 236, 524–541. <https://doi.org/10.1016/j.epsl.2005.04.033>.
- Cottaar, S., & Romanowicz, B. (2012). An unusually large ULVZ at the base of the mantle near Hawaii. *Earth and Planetary Science Letters*, 355–356, 213–222. <https://doi.org/10.1016/j.epsl.2012.09.005>.
- Courtilot, V., & Renne, P. R. (2003). On the ages of flood basalt events. *Comptes Rendus Geoscience*, 335, 113–140.
- Courtilot, V., Davaille, A., Besse, J., & Stock, J. (2003). Three distinct types of hotspots in the Earth's mantle. *Earth and Planetary Science Letters*, 205, 295–308.
- Dalkolmo, J., & Friederich, W. (2000). Born scattering of long-period body waves. *Geophysical Journal International*, 142, 876–888. <https://doi.org/10.1046/j.1365-246x.2000.00212.x>
- Dannberg, J., & Sobolev, S. V. (2015). Low-buoyancy thermochemical plumes resolve controversy of classical mantle plume concept. *Nature Communications*, 6. <http://dx.doi.org/10.1038/ncomms7960>
- Davaille, A. (1999). Simultaneous generation of hotspots and superswells by convection in a heterogeneous planetary mantle. *Nature*, 402 (6763), 756.
- Davaille, A., Carrez, Ph., & Cordier, P. (2018). Fat plumes may reflect complex rheology of the lower mantle. *Geophysical Research Letters*, 45, 1349–1354. <https://doi.org/10.1002/2017GL076575>.
- Davies G. F. (1999). *Dynamic Earth: Plates, Plumes, and Mantle Convection*. Cambridge Univ. Press, Cambridge, UK 458 pp.

- Deng, K., & Zhou, Y. (2015). Wave diffraction and resolution of mantle transition zone discontinuities in receiver function imaging. *Geophysical Journal International*, 201, 2008–2025. <https://doi.org/10.1093/gji/ggv124>.
- Deschamps, F., & Trampert J. (2004). Towards a lower mantle reference temperature and composition. *Earth and Planetary Science Letters*, 222, 161–175. doi:10.1016/j.epsl.2004.02.024.
- Deschamps, F., Kaminski, E., & Tackley, P. J. (2011). A deep mantle origin for the primitive signature of ocean island basalt. *Nature Geoscience*, 4, 879–882. <https://doi.org/10.1038/ngeo1295>.
- Deschamps, F., Cobden, L., & Tackley, P. J. (2012). The primitive nature of large low shear-wave velocity provinces. *Earth and Planetary Science Letters*, 349–350, 198–208. <https://doi.org/10.1016/j.epsl.2012.07.012>.
- Deuss, A., Redfern, S. A. T., Chambers, K., & Woodhouse, J. H. (2006). The nature of the 660-kilometer discontinuity in Earth's mantle from global seismic observations of PP precursors. *Science*, 311 (5758), 198–201. doi:10.1126/science.1120020.
- Deuss, A. (2007). Seismic observations of transition-zone discontinuities beneath hotspot locations. Special Paper Geological Society of America, *Plates Plumes and Planetary Processes*, 430, 121–136. doi: 10.1130/2007.2430(07).
- Durand, S., Debayle, E., Ricard, Y., Zaroли, C., & Lambotte, S. (2017). Confirmation of a change in the global shear velocity pattern at around 1000 km depth. *Geophysical Journal International*, 211(3), 1628–1639. <https://doi.org/10.1093/gji/ggx405>.
- Dziewonski A. M., & Anderson D. L. (1981). Preliminary reference Earth model. *Physics of the Earth Planetary Interiors*, 25, 297–356.
- Farley, K. A., & Neroda, E. (1998). Noble gases in the Earth's mantle. *Annual Reviews Earth Planetary Science*, 26, 189–218.
- Farnetani, C. G. (1997). Excess temperature of mantle plumes: the role of chemical stratification of D". *Geophysical Research Letters*, 24, 1583–1586.
- Farnetani, C. G., & Hofmann, A. W. (2010). Dynamics and internal structure of the Hawaiian plume. *Earth and Planetary Science Letters*, 295, 231–240.
- Farnetani, C. G., Legras, B., & Tackley, P. J. (2002). Mixing and deformations in mantle plumes. *Earth and Planetary Science Letters*, 196, 1–15.
- Flanagan, M. P., & Shearer, P. M. (1998). Global mapping of topography on transition zone velocity discontinuities by stacking of SS precursors. *Journal of Geophysical Research*, 103, 2673–2692.
- Fouch, M. J. (2012). The Yellowstone hotspot: plume or not? *Geology*, 40, 479–480.
- Foulger, G. R., & Natland, J. H. (2003). Is hotspot volcanism a consequence of plate tectonics? *Science*, 300, 921–922.
- Foulger, G. R., Panza, G. F., Artemieva, I. M., Bastow, I. D., Cammarano, F., Doglioni, C., et al. (2015). What lies deep in the mantle below? *Eos Transactions American Geophysical Union*, 96. <https://doi.org/10.1029/2015EO034319>.
- French, S. W., & Romanowicz, B.A. (2014). Whole-mantle radially anisotropic shear velocity structure from spectral-element waveform tomography. *Geophysical Journal International*, 199 (3), 1303–1327.
- French, S. W., & Romanowicz, B. (2015). Broad plumes rooted at the base of the Earth's mantle beneath major hotspots. *Nature*, 525, 95–99. doi:10.1038/nature14876.
- Georgen, J. E. (2014). Interaction of a mantle plume and a segmented mid-ocean ridge: Results from numerical modeling. *Earth and Planetary Science Letters*, 392, 113–120.
- Goes, S., Cammarano, F., & Hansen, U. (2004). Synthetic seismic signature of thermal mantle plumes. *Earth and Planetary Science Letters*, 218, 403–419.
- Gu, Y. J., & Dziewonski, A. M. (2002). Global variability of transition zone thickness. *Journal of Geophysical Research*, 107 (B7), 2135. doi:10.1029/2001JB000489.
- Gu, Y. J., An, Y., Sacchi, M., Schultz, R., & Ritsema, J. (2009). Mantle reflectivity structure beneath oceanic hotspots. *Geophysical Journal International*, 178, 1456–1472. doi: 10.1111/j.1365-246X.2009.04242.x
- Griffiths, R. W. (1986). The differing effects of compositional and thermal buoyancies on the evolution of mantle diapirs. *Physics of the Earth and Planetary Interiors*, 43 (4), 261–273.
- Hammond, J. O. S, Kendall, J.-M., Stuart, G. W., Ebinger, C. J., Bastow, I. D., Keir, D., et al. (2013). Mantle upwelling and initiation of rift segmentation beneath the Afar Depression. *Geology*, 41 (6), 635–638. <https://doi.org/10.1130/G33925.1>
- Hart, S. R., Schilling, J. G., & Powell, J. L. (1973). Basalts from Iceland and along the Reykjanes Ridge: Sr isotope geochemistry. *Nature Physical Science*, 246, 104–107.
- Hawkesworth, C., Kelley, S., Turner, S., Le Roex, A. P., & Storey, B. C. (1999). Mantle processes during Gondwana break-up and dispersal. *Journal of African Earth Science*, 28, 239–261.
- Hall, P. S., & Kincaid, C. (2003). Melting, dehydration, and the dynamics of off-axis plume-ridge interaction. *Geochemistry, Geophysics, Geosystems*, 4 (9), 8510, doi:10.1029/2002GC000567.
- Hill, R. I. (1991). Starting plumes and continental break-up. *Earth and Planetary Science Letters*, 104, 398–416.
- Hofmann, A. W. (1997). Mantle geochemistry: The message from oceanic volcanism. *Nature*, 385, 219–229.
- Houser, C., Masters, G., Shearer, P. M., & Laske, G. (2008a). Shear and compressional velocity models of the mantle from cluster analysis of long period waveforms. *Geophysical Journal International*, 174, 195–212.
- Houser, C., Masters G., Flanagan, M., & Shearer, P. (2008b). Determination and analysis of long-wavelength transition zone structure using SS precursors. *Geophysical Journal International*, 174, 178–194. doi:10.1111/j.1365-246X.2008.03719.x.
- Hwang, Y. K., Ritsema, J., van Keken, P. E., Goes, S., & Styles, E. (2011). Wavefront healing renders deep plumes seismically invisible. *Geophysical Journal International*, 187, 273–277. doi: 10.1111/j.1365-246X.2011.05173.x.
- Ito, G., Lin, J., & Gable, C. W. (1996). Dynamics of mantle flow and melting at a ridge-centered hotspot: Iceland and the Mid-Atlantic Ridge. *Earth and Planetary Science Letters*, 144, 53–74.
- Ito, G., Shen, Y., Hirth, G., Wolfe, C. J. (1999). Mantle flow, melting, and dehydration of the Iceland mantle plume. *Earth and Planetary Science Letters*, 165 (1), 81–96.

- Jackson, I., (1998) Elasticity, composition, and temperature of the Earth's lower mantle: a reappraisal. *Geophysical Journal International*, 134, 291–311
- Jackson, M. G., & Dasgupta, R. (2008). Compositions of HIMU, EM1, and EM2 from global trends between radiogenic isotopes and major elements in ocean island basalts. *Earth and Planetary Science Letters*, 276, 175–186. <https://doi.org/10.1016/j.epsl.2008.09.023>.
- Jacobsen, S. D., & Smyth, J. R. (2006). Effect of water on the sound velocities of ringwoodite in the transition zone. *Earth's Deep Water Cycle Geophysical Monograph Series 168*, 131–144. [doi:10.1029/168GM09](https://doi.org/10.1029/168GM09).
- Jenkins, J., Cottaar, S., White, R. S., & Deuss, A. (2016). Depressed mantle discontinuities beneath Iceland: Evidence of a garnet controlled 660 km discontinuity? *Earth and Planetary Science Letters*, 433, 159–168. [doi:10.1016/j.epsl.2015.10.053](https://doi.org/10.1016/j.epsl.2015.10.053).
- Jenkins, J., Deuss, A., & Cottaar, S. (2017). Converted phases from sharp 1000 km depth mid-mantle heterogeneity beneath Western Europe. *Earth and Planetary Science Letters*, 459, 196–207.
- Ji, Y., & Nataf, H. C. (1998a). Detection of mantle plumes in the lower mantle by diffraction tomography: theory. *Earth and Planetary Science Letters*, 159, 87–98.
- Ji, Y., & Nataf, H. C. (1998b). Detection of mantle plumes in the lower mantle by diffraction tomography: Hawaii. *Earth and Planetary Science Letters*, 159, 99–115.
- Jones, T. D., Davies, D. R., Campbell, I. H., Wilson, C. R., & Kramer. (2016). Do mantle plumes preserve the heterogeneous structure of their deep-mantle source? *Earth and Planetary Science Letters*, 434, 10–17. [doi:10.1016/j.epsl.2015.11.016](https://doi.org/10.1016/j.epsl.2015.11.016).
- Jones, T. D., Davies, D. R., Campbell, I. H., Iaffaldano, G., Yaxley, G., Kramer, S. C., & Wilson, C. R. (2017). The concurrent emergence and causes of double volcanic hotspot tracks on the Pacific plate, *Nature*, 545, 472–476. [doi: 10.1038/nature22054](https://doi.org/10.1038/nature22054)
- Kaneshima, S., & Helffrich, G. (1998). Detection of lower mantle scatterers northeast of the Mariana subduction zone using short-period array data. *Journal of Geophysical Research*, 103, (B3), 4825–4838. <https://doi.org/10.1029/97JB02565>
- Kellogg, L. H., & King, S. D. (1997). The effect of temperature dependent viscosity on the structure of new plumes in the mantle; results of a finite element model in a spherical axisymmetric shell. *Earth and Planetary Science Letters*, 148, 13–26.
- King, S. D., & Adam, C. (2014). Hotspot swells revisited. *Physics Earth Planetary Interiors*, 235, 66–83. [doi:10.1016/j.pepi.2014.07.006](https://doi.org/10.1016/j.pepi.2014.07.006).
- King, S. D., & Redmond, H. L. (2007). The structure of thermal plumes and geophysical observations, in *Plates, Plumes, and Planetary Processes*, edited by G. R. Foulger and D. M. Jurdy, *Geological Society of America, Special Papers*, 430, pp. 103–120.
- Komatitsch, D., & Vilotte, J.-P. (1998). The Spectral Element Method: An efficient tool to simulate the seismic response of 2-D and 3-D geological structures. *Bulletin Seismological Society America*, 88, 368–392.
- Komatitsch, D., & Tromp, J. (2002). Spectral-element simulations of global seismic wave propagation, Part I: Validation. *Geophysical Journal International*, 149, 390–412.
- Komatitsch, D., Vilotte, J.-P., Tromp, J., Afanasiev, M., Bozdag, E., Charles, J., et al. (2015). SPECfEM3D GLOBE v7.0.0. *Computational Infrastructure for Geodynamics*. https://geodynamic.org/cig/software/specfem3d_globe/
- Koptev, A., Calais, E., Burov, E., Leroy, S., & Gerya, T. (2015). Dual continental rift systems generated by plume–lithosphere interaction. *Nature Geoscience*, 8, 388–392.
- Korenaga, J. (2005). Firm mantle plumes and the nature of the core-mantle boundary region. *Earth and Planetary Science Letters*, 232, 29–37. <https://doi.org/10.1016/j.epsl.2005.01.016>.
- Koroni, M., & Trampert, J. (2015). The effect of topography of upper-mantle discontinuities on SS precursors. *Geophysical Journal International*, 204, 667–681. <https://doi.org/10.1093/gji/ggv471>.
- Larsen, T. B., & Yuen, D. A. (1997). Ultrafast upwelling bursting through the upper mantle. *Earth and Planetary Science Letters*, 146 (3-4), 393–399.
- Laske, G., Collins, J. A., Wolfe, C. J., Solomon, S. C., Detrick, R. S., Orcutt, J. A., Bercovici, D., & Hauri, E. H. (2009). Probing the Hawaiian hot spot with new ocean bottom instruments. *Eos Transactions AGU*, 90, 362–363. <https://doi.org/10.1029/2009EO410002>
- Lawrence, J. F., & Shearer, P. M. (2008). Imaging mantle transition zone thickness with SdS-SS finite-frequency sensitivity kernels. *Geophysical Journal International*, 174, 143–158. <https://doi.org/10.1111/j.1365-246X.2007.03673.x>
- Lei, W., Ruan, Y., Bozdag, E., Peter, D., Lefebvre, M., Komatitsch, D., Tromp, J., Hill, J., Podhorszki, N., & Pugmire, D. (2020). Global adjoint tomography–model GLAD-M25. *Geophysical Journal International*, 223, 1–21. [10.1093/gji/ggaa253](https://doi.org/10.1093/gji/ggaa253)
- Leng, K., Nissen-Meyer, T., & van Driel, M. (2016). Efficient global wave propagation adapted to 3-D structural complexity: A pseudospectral/spectral-element approach. *Geophysical Journal International*, 207, 1700–1721. <https://doi.org/10.1093/gji/ggw363>
- Leng, W., & Gurnis, M. (2012). Shape of thermal plumes in a compressible mantle with depth-dependent viscosity. *Geophysical Research Letters*, 39, L05310. <https://doi.org/10.1029/2012GL050959>.
- Lessing, S., Thomas, C., Rost, S., Cobden, L., & Dobson, D. P. (2014). Mantle transition zone structure beneath India and Western China from migration of PP and SS precursors. *Geophysical Journal International*, 197, 396–413. <https://doi.org/10.1093/gji/ggt511>
- Li, X.-D., & Romanowicz, B. (1996). Global mantle shear velocity model developed using nonlinear asymptotic coupling theory. *Journal of Geophysical Research*, 101 (22), 245–22,272. <https://doi.org/10.1029/96JB01306>.
- Lin, S.-C., Kuo, B.-Y., Chiao, L.-Y., & van Keken, P. E. (2005). Thermal plume models and melt generation in East Africa: A dynamic modelling approach. *Earth and Planetary Science Letters*, 237, 175–192. [doi: 10.1016/j.epsl.2005.04.049](https://doi.org/10.1016/j.epsl.2005.04.049)
- Lin, S. C., & van Keken, P. E. (2006). Dynamics of thermochemical plumes: 1. Plume formation and entrainment of a dense layer. *Geochemistry, Geophysics, and Geosystems*, 7. [doi:10.1029/2005GC001071](https://doi.org/10.1029/2005GC001071).

- Lu, C., & Grand, S. P. (2016). The effect of subducting slabs in global shear wave tomography. *Geophysical Journal International*, 205 (2), 1074–1085. <https://doi.org/10.1093/gji/ggw072>
- Maguire, R., Ritsema, J., van Keken, P. E., Goes, S., & Fichtner, A. (2016). P and S wave delays caused by thermal plumes. *Geophysical Journal International*, 206, 1169–1178. <https://doi.org/10.1093/gji/ggw187>.
- Maguire, R., Ritsema, J., & Goes, S. (2017). Signals of 660 km topography and harzburgite enrichment in seismic images of whole-mantle upwellings. *Geophysical Research Letters*, 44 (8), 3600–3607.
- Maguire, R., Ritsema, J., Bonnin, M., van Keken, P. E., & Goes, S. (2018). Evaluating the resolution of deep mantle plumes in teleseismic traveltimes tomography. *Journal of Geophysical Research*, 123, 384–400. <https://doi.org/10.1002/2017JB014730>.
- Malcolm, A. E., & Trampert, J. (2011). Tomographic errors from wavefront healing: more than just a fast bias. *Geophysical Journal International*, 185, 385–402. <https://doi.org/10.1111/j.1365-246X.2011.04945.x>
- Matas, J., Bass, J., Ricard, Y., Mattern, E., & Bukowinski, M. (2007). On the bulk composition of the lower mantle: predictions and limitations from generalized inversion of radial seismic profiles. *Geophys. J. Int.*, 170 (2), 764–780. <https://doi.org/10.1111/j.1365-246X.2007.03454.x>
- Matyska, C., Moser, J., & Yuen, D. A. (1994). The potential influence of radiative heat transfer on the formation of megaplumes in the lower mantle. *Earth and Planetary Science Letters*, 125, 255–266. doi: 10.1016/0012-821X(94)90219-4.
- Matyska, C., Yuen, D. A., Wentzcovitch, R. M., & Cizkova H. (2011). The impact of variability in the rheological activation parameters on lower-mantle viscosity stratification and its dynamics. *Physics of the Earth Planetary Interiors*, 188, 1–8. doi:10.1016/j.pepi.2011.05.012.
- Mercerat, D., & Nolet, G. (2013). On the linearity of cross-correlation delay times in finite-frequency tomography. *Geophysical Journal International*, 192, 681–687. <https://doi.org/10.1093/gji/ggs017>.
- Montelli, R., Nolet, G., Dahlen, F. A., Masters, G., Engdahl, E. R., & Hung, S. H. (2004). Finite-frequency tomography reveals a variety of plumes in the mantle. *Science*, 303, 338–343. doi:10.1126/science.1092485.
- Montelli, R., Nolet, G., Dahlen, F. A., & Masters, G. (2006). A catalogue of deep mantle plumes: New results from finite frequency tomography. *Geochemistry, Geophysics, Geosystems*, 7. doi: 10.1029/2006GC001248.
- Moore, W. B., Schubert, G., & Tackley, P. J. (1998). Three-dimensional simulations of plume–lithosphere interaction at the Hawaiian swell. *Science*, 279, 1008–1011.
- Morgan, W. J. (1971). Convection plumes in the lower mantle. *Nature*, 230, 42–43.
- Morgan, W. J. (1972). Plate motions and deep mantle convection. *The Geological Society of America Memoir* 132, 7–22.
- Moulik, P., & Ekström, G. (2014). An anisotropic shear velocity model of the Earth’s mantle using normal modes, body waves, surface waves and long-period waveforms. *Geophys. Journal International*, 199 (3), 1713–1738.
- Mrosko, M., Koch-Müller, M., McCammon, C., Rhede, D., Smyth, J. R., & Wirth, R. (2015). Water, iron, redox environment: Effects on the wadsleyite–ringwoodite phase transition. *Contributions to Mineralogy and Petrology*, 170 (1), 1–12. <https://doi.org/10.1007/s00410-015-1163-2>.
- Mulibo, G. D., & Nyblade, A. A. (2013). Mantle transition zone thinning beneath eastern Africa: Evidence for a whole-mantle superplume structure. *Geophysical Research Letters*, 40, 3562–3566. doi:10.1002/grl.50694.
- Nakagawa, T., & Tackley, P. J. (2004). Thermo-chemical structure in the mantle arising from a three-component convective system and implications for geochemistry. *Physics of the Earth Planetary Interiors*, 146, 125–138. <https://doi.org/10.1016/j.pepi.2003.05.006>.
- Nataf, H. C. (2000). Seismic imaging of mantle plumes. *Annual Reviews of Earth Planetary Science*, 28, 391–417. doi: 10.1146/annurev. Earth.28.1.391.
- Nataf, H. C., & VanDecar, J. (1993). Seismological detection of a mantle plume? *Nature*, 364, 115–120.
- Neele, F., de Regt, H., & VanDecar, J. (1997). Gross errors in upper-mantle discontinuity topography from underside reflection data. *Geophysical Journal International*, 129, 194–204.
- Nelson, P. L., & Grand, S. P. (2018). Lower-mantle plume beneath the Yellowstone hotspot revealed by core waves. *Nature Geoscience* 11, 280–284. <https://doi.org/10.1038/s41561-018-0075-y>
- Niu, F., Solomon, S. C., Silver, P. G., Suetsugu, D., & Inoue, H. (2002). Mantle transition-zone structure beneath the south Pacific superswell and evidence for a mantle plume underlying the Society Hotspot. *Earth and Planetary Science Letters*, 198, 371–380. [https://doi.org/10.1016/S0012-821X\(02\)00523-X](https://doi.org/10.1016/S0012-821X(02)00523-X)
- Nolet, G., & Dahlen, F. A. (2000). Wavefront healing and the evolution of seismic delay times. *Journal of Geophysical Research*, 105, 19,043–19,054.
- Nolet, G., Karato, S., & Montelli, R. (2006). Plume fluxes from seismic tomography. *Earth and Planetary Science Letters*, 248, 685–699.
- Nolet, G., Hello, Y., van der Lee, S., Bonnieux, S., Ruiz, M. C., Pazmino, N. A., et al. (2019). Imaging the Galapagos mantle plume with an unconventional application of floating seismometers. *Scientific Reports*, 9, 1326. <https://www.nature.com/articles/s41598-018-36835-w>.
- Olson, P., Schubert, G., & Anderson, C. (1993). Structure of axisymmetric mantle plumes. *Journal of Geophysical Research – Solid Earth*, 98 (B4), 6829–6844.
- Olson, P., Schubert, G., Anderson, C., & Goldman, P. (1988). Plume formation and lithosphere erosion: A comparison of laboratory and numerical experiments. *Journal of Geophysical Research – Solid Earth*, 93 (B12), 15,065–15,084.
- Pham, T.-S., Tkalčić, H., Sambridge, M., & Kennett, B. L. N. (2018). Earth’s correlation wavefield: Late coda correlation. *Geophysical Research Letters*, 45, 3035–3042. <https://doi.org/10.1002/2018GL07724>.
- Phipps Morgan, J., Morgan, W. J., & Price, E. (1995). Hotspot melting generates both hotspot volcanism and a hotspot swell?. *Journal of Geophysical Research – Solid Earth*, 100 (B5), 8045–8062.
- Poli, P., Campillo, M., Pedersen, H., & LAPNET Working Group. (2012). Body-wave imaging of Earth’s mantle discontinuities from ambient seismic noise. *Science*, 338, 1063–1065. doi: 10.1126/science.1228194.

- Reed, C. A., Gao, S. S., Liu, K. H., & Yu, Y. (2016). The mantle transition zone beneath the Afar Depression and adjacent regions: implications for mantle plumes and hydration. *Geophysical Journal International*, 205, 1756–1766. <https://doi.org/10.1093/gji/ggw116>
- Ribe, N., Davaille, A., & Christensen, U. R. (2007). Fluid dynamics of mantle plumes. in Ritter J., Christensen U. R., (Eds), *Mantle Plumes – A Multidisciplinary Approach*. Berlin Springer.
- Ribe, N. M., & Christensen, U. R. (1994). Three-dimensional modelling of plume – lithosphere interaction. *Journal of Geophysical Research*, 99, 669–682.
- Ribe, N. M., & Christensen, U. R. (1999). The dynamical origin of Hawaiian volcanism. *Earth and Planetary Science Letters*, 17, 517–531, 1999.
- Richards, M. A., Duncan, R. A., & Courtillot, V. E. (1989). Flood basalts and hotspot tracks: Plume heads and tails. *Science*, 246, 103–107.
- Richards, M. A., & Griffiths, R. W. (1989). Thermal entrainment by deflected mantle plumes. *Nature*, 342 (6252), 900.
- Rickers, F., Fichtner, A., & Trampert, J. (2012). Imaging mantle plumes with instantaneous phase measurements of diffracted waves. *Geophysical Journal International*, 190, 650–664. <https://doi.org/10.1111/j.1365-246X.2012.05515.x>.
- Rickers, F., Fichtner, A., & Trampert, J. (2013). The Iceland–Jan Mayen plume system and its impact on mantle dynamics in the North Atlantic region: Evidence from full-waveform inversion. *Earth and Planetary Science Letters*, 367, 39–51. <https://doi.org/10.1016/j.epsl.2013.02.022>
- Ritsema, J., & Allen, R. M. (2003). The elusive mantle plume. *Earth and Planetary Science Letters*, 207, 1–12.
- Ritsema, J., van Heijst H. J., Woodhouse J. H., & Deuss A. (2009). Long-period body-wave traveltimes through the crust: Implication for crustal corrections and seismic tomography. *Geophysical Journal International*, 179, 1255–1261. <https://doi.org/10.1111/j.1365-246X.2009.04365.x>
- Ritsema, J., Deuss, A. A., Van Heijst, H. J., & Woodhouse, J. H. (2011). S40RTS: a degree-40 shear-velocity model for the mantle from new Rayleigh wave dispersion, teleseismic travel-time and normal-mode splitting function measurements. *Geophysical Journal International*, 184 (3), 1223–1236.
- Rost, S., & Thomas, C. (2009). Improving seismic resolution through array processing techniques. *Surveys in Geophysics*, 30, 271–299. <https://doi.org/10.1007/s10712-009-9070-6>
- Saki, M., Thomas C., Stuart E. J. Nippres, S. E. J., & Lessing S. (2015). Topography of upper mantle seismic discontinuities beneath the North Atlantic: The Azores, Canary and Cape Verde plumes. *Earth and Planetary Science Letters*, 409, 193–202. <https://doi.org/10.1016/j.epsl.2014.10.052>.
- Samuel, H., & Bercovici, D. (2006). Oscillating and stagnating plumes in the Earth’s lower mantle. *Earth and Planetary Science Letters*, 248, 90–105. <https://doi.org/10.1016/j.epsl.2006.04.037>
- Schmandt, B., Dueker, K., Humphreys, E., & Hansen, S. (2012). Hot mantle upwelling across the 660 beneath Yellowstone. *Earth and Planetary Science Letters*, 331–332, 224–236. <https://doi.org/10.1016/j.epsl.2012.03.025>.
- Schmerr, N., Garnero, E., & McNamara, A. (2010). Deep mantle plumes and convective upwelling beneath the Pacific Ocean. *Earth and Planetary Science Letters*, 294, 143–151. <https://doi.org/10.1016/j.epsl.2010.03.014>.
- Schulze, K., Marquardt, H., Kawazoe, T., Boffa Ballaran, T., McCammon, C., Koch-Müller, M., et al. (2018). Seismically invisible water in Earth’s transition zone? *Earth and Planetary Science Letters*, 498, 9–16. <https://doi.org/10.1016/j.epsl.2018.06.021>.
- Schumacher, L., & Thomas, C. (2016). Detecting lower-mantle slabs beneath Asia and the Aleutians. *Geophysical Journal International*, 205, 1512–1524. <https://doi.org/10.1093/gji/ggw098>.
- Shearer, P. M. (1991). Constraints on upper mantle discontinuities from observations of long-period reflected and converted phases. *Journal of Geophysical Research: Solid Earth*, 96 (B11), 18,147–18,182.
- Simmons, N. A., Forte, A. M., Boschi, L., & Grand, S. P. (2010). GyPSuM: A joint tomographic model of mantle density and seismic wave speeds. *Journal of Geophysical Research*, 115, B12310. doi:10.1029/2010JB007631.
- Skilbeck, J. N., & Whitehead Jr, J. A. (1978). Formation of discrete islands in linear island chains. *Nature*, 272 (5653), 499.
- Sleep, N. H. (1997). Lateral flow and ponding of starting plume material. *Journal of Geophysical Research – Solid Earth*, 102 (B5), 10001–10012.
- Sobolev, A. V., Hofmann, A. W., Kuzmin, D. V., Yaxley, G. M., Arndt, N. T., Chung, S.-L., et al. (2007). The amount of recycled crust in sources of mantle-derived melts. *Science*, 316, 412–417.
- Song, T. R. A., Helmlinger, D. V., & Grand, S. P. (2004). Low-velocity zone atop the 410-km seismic discontinuity in the northwestern United States. *Nature*, 427 (6974), 530–533. doi:10.1038/nature02231
- Spica, Z., Perton, M., & Beroza, G. C. (2017). Lateral heterogeneity imaged by small-aperture ScS retrieval from the ambient seismic field. *Geophysical Research Letters*, 44, 8276–8284. doi:10.1002/2017GL073230.
- Stähler, C., Sigloch, K., & Nissen-Meyer, T. (2012). Triplicated P-wave measurements for waveform tomography of the mantle transition zone. *Solid Earth*, 3, 339–354. doi:10.5194/se-3-339-2012.
- Steinberger, B., & O’Connell, R. J. (1998). Advection of plumes in mantle flow; implications for hot spot motion, mantle viscosity and plume distribution. *Geophysical Journal International*, 132, 412–434. <https://doi.org/10.1046/j.1365-246x.1998.00447.x>
- Stixrude, L., & Lithgow-Bertelloni, C. (2011). Thermodynamics of mantle minerals — II Phase equilibria. *Geophysical Journal International*, 184, 1180–1213. <https://doi.org/10.1111/j.1365-246X.2010.04890.x>
- Stockmann, F., Cobden, L., Deschamps, F., Fichtner, A., & Thomas, C. (2019). Investigating the seismic structure and visibility of dynamic plume models with seismic array methods. *Geophysical Journal International*, 219, S167–S197, <https://doi.org/10.1093/gji/ggz334>.
- Styles, E., Goes, S., van Keken, P. E., Ritsema, J., & Smith, H. (2011). Synthetic images of dynamically predicted plumes and comparison with a global tomographic model. *Earth and Planetary Science Letters*, 311, 351–363. <https://doi.org/10.1016/j.epsl.2011.09.012>.

- Suetsugu, D., Isse, T., Tanaka, S., Obayashi, M., Shiobara, H., Sugioka, H., et al. (2009). South Pacific mantle plumes imaged by seismic observation on islands and seafloor. *Geochemistry, Geophysics, Geosystems* 10, Q11014. doi:10.1029/2009GC002533.
- Suetsugu, D., & Shiobara, H. (2014). Broadband ocean-bottom seismology. *Annual Reviews Earth Planetary Sciences*, 42, 27–43. doi:10.1146/annurev-earth-060313-054818.
- Sukhovich, A., Bonnieux, S., Hello, Y., Irissou, J.-O., Simons, F. J., & Nolet, G. (2015). Seismic monitoring in the oceans by autonomous floats. *Nature Communications*, 6 (8027). <http://dx.doi.org/10.1038/ncomms9027>.
- Takeuchi, N. (2007). Whole mantle SH velocity model constrained by waveform inversion based on three-dimensional Born kernels. *Geophysical Journal International*, 169, 1153–1163.
- Tauzin, B., Debayle, E., & Wittlinger, G. (2008). The mantle transition zone as seen by global Pds phases: no clear evidence for a thin transition zone beneath hotspots. *Journal of Geophysical Research*, 113, B08309. doi:10.1029/2007JB005364.
- Thio, V., Cobden, L., & Trampert, J. (2016). Seismic signature of a hydrous mantle transition zone. *Physics of the Earth Planetary Interiors*, 250, 46–63. <https://doi.org/10.1016/j.pepi.2015.11.005>.
- Thompson, D. A., J. O. S. Hammond, J.-M. Kendall, G. W. Stuart, G. R. Helffrich, D. Keir, et al. (2015). Hydrous upwelling across the mantle transition zone beneath the Afar Triple Junction. *Geochemistry, Geophysics, Geosystems*, 16, 834846, doi:10.1002/2014GC005648.
- Thorne, M. S., Garnero, E., Jahnke, G., Igel, H., & McNamara, A. K. (2013). Mega ultra low velocity zone and mantle flow. *Earth and Planetary Science Letters*, 364, 59–67. <https://doi.org/10.1016/j.epsl.2012.12.034>
- To, A., Capdeville, Y., & Romanowicz, B. (2016). Anomalously low amplitude of S waves produced by the 3D structures in the lower mantle. *Physics of the Earth Planetary Interiors*, 256, 26–36. <https://doi.org/10.1016/j.pepi.2016.04.001>
- Tilmann, F. J., McKenzie, D., & Priestley, K. F. (1998). P and S wave scattering from mantle plumes. *Journal of Geophysical Research*, 103, 21,145–21,163.
- Trampert, J., & Spetzler, J. (2006). Surface wave tomography: finite-frequency effects lost in the null space. *Geophysical Journal International*, 164, 394–400. <https://doi.org/10.1111/j.1365-246X.2006.02864.x>
- van der Hilst, R. D., & de Hoop, M. V. (2005). Banana-doughnut kernels and mantle tomography. *Geophysical Journal International*, 163, 956–961. <https://doi.org/10.1111/j.1365-246X.2005.02817.x>
- van Hunen, J., & Zhong, S. (2003). New insight in the Hawaiian plume swell dynamics from scaling laws. *Geophysical Research Letters*, 30 (15), 1785. doi:10.1029/2003GL017646.
- Vinnik, L. P. (1977). Detection of waves converted from P to SV in the mantle. *Physics of the Earth Planetary Interiors*, 15(1), 39–45. [https://doi.org/10.1016/0031-9201\(77\)90008-5](https://doi.org/10.1016/0031-9201(77)90008-5)
- Wei, S. S., & Shearer, P. M. (2017). A sporadic low-velocity layer atop the 410 km discontinuity beneath the Pacific Ocean. *Journal of Geophysical Research – Solid Earth* 122 (7), 5144–5159. <https://doi.org/10.1002/2017JB014100>
- Wen, L., Silver, P., James, D., & Kuehnel, R. (2001). Seismic evidence for a thermo-chemical boundary layer at the base of the Earth's mantle. *Earth and Planetary Science Letters*, 189, 141–153. [https://doi.org/10.1016/S0012-821X\(01\)00365-X](https://doi.org/10.1016/S0012-821X(01)00365-X)
- Whitehead Jr, J. A., & Luther, D. S. (1975). Dynamics of laboratory diapir and plume models. *Journal of Geophysical Research*, 80 (5), 705–717.
- Wilson, J. T. (1963). A possible origin of the Hawaiian Islands. *Canadian Journal of Physics*, 41, 863–870.
- Wolfe, C., Solomon, S. C., Laske, G., Collins, J. A., Detrick, J., Orcutt, J. A., et al. (2009). Mantle shear-wave velocity structure beneath the Hawaiian hot spot. *Science*, 326, 1388–1390. <https://doi.org/10.1126/science.1180165>
- Workman, R. K., & Hart, S. R. (2005). Major and trace element composition of the depleted MORB mantle (DMM). *Earth and Planetary Science Letters*, 231, 53–72. <https://doi.org/10.1016/j.epsl.2004.12.005>.
- Xu, W., Lithgow-Bertelloni, C., Stixrude, L., & Ritsema, J. (2008). The effect of bulk composition and temperature on mantle seismic structure. *Earth and Planetary Science Letters*, 275, 70–79. doi:10.1016/j.epsl.2008.08.012.
- Xue, J., Zhou, Y., & Chen, Y. J. (2015). Tomographic resolution of plume anomalies in the lowermost mantle. *Geophysical Journal International*, 201, 979–995. <https://doi.org/10.1093/gji/ggv067>.
- Yu, C., Day, E. A., de Hoop, M. V., Campillo, M., & van der Hilst, R. D. (2017). Mapping mantle transition zone discontinuities beneath the Central Pacific with array processing of SS precursors. *Journal of Geophysical Research*, 122, 10,364–10,378. <https://doi.org/10.1002/2017JB014327>
- Yu, C., Day, E. A., de Hoop, M. V., Campillo, M., Goes, S., Blythe, R. A., & van der Hilst, R. D. (2018). Compositional heterogeneity near the base of the mantle transition zone beneath Hawaii. *Nature Communications*, 9. <https://dx.doi.org/10.1038/s41467-018-03654-6>
- Yuan K., & Romanowicz, B. (2017). Seismic evidence for partial melting at the root of major hot spot plumes. *Science*, 357, 393–397. doi: 10.1126/science.aan0760
- Zhou, Y. (2018). Anomalous mantle transition zone beneath the Yellowstone hotspot track. *Nature Geoscience* 11, 449–453. doi:10.1038/s41561-018-0126-4.
- Zhao, D. (2015). Hotspots and mantle plumes. In *Multiscale Seismic Tomography*, 139–184. Springer. doi:10.1007/978-4-431-55360-1_5
- Zhao, L., & Chevrot, S. (2003). SS-wave sensitivity to upper mantle structure: implications for the mapping of transition zone discontinuity topographies. *Geophysical Research Letters*, 30. <https://doi.org/10.1029/2003GL017223>.
- Zheng, Z., Ventosa, S., & Romanowicz, B. (2015). High resolution upper mantle discontinuity images across the Pacific Ocean from SS precursors using local slant stack filters. *Geophysical Journal International*, 202, 175–189. <https://doi.org/10.1093/gji/ggv118>.
- Zhong, S. (2006). Constraints on thermochemical convection of the mantle from plume heat flux, plume excess temperature, and upper mantle temperature. *Journal Geophysical Research*, 111, B04409. doi:10.1029/2005JB003972.

Part III

Surface Expressions: Mantle Controls on Planetary Evolution and Habitability

Observational Estimates of Dynamic Topography Through Space and Time

Mark Hoggard^{1,2}, Jacqueline Austermann², Cody Randel², and Simon Stephenson³

ABSTRACT

Earth's mantle undergoes convection on million-year timescales as heat is transferred from depth to the surface. While this flow has long been linked to the large-scale horizontal forces that drive plate tectonics and supercontinent cycles, geologists are increasingly recognizing the signature of convection through transient vertical motions in the rock record, known as *dynamic topography*. A significant component of topography is supported by lithospheric isostasy, and changes in lithospheric thermal structure are sometimes included in the definition of dynamic topography. An additional component arises from active flow within the underlying convecting mantle, and this process causes dynamic topography that has lengthscales varying from 10,000 km down to 500 km and typical amplitudes of ± 1 km. Transient uplift and subsidence events are often slow, but might evolve at rates as fast as 500 m Myr^{-1} over cycles as short as ~ 3 Myr, leading to periodic overwriting of the geological record that results in complex interpretational challenges. Despite these difficulties, a growing number of observational and computational studies have highlighted the important role of dynamic topography in fields as diverse as intraplate magmatism, sedimentary stratigraphy, landscape evolution, paleo-shorelines, oceanic circulation patterns, and the stability of ice sheets. This review provides a brief overview of our current understanding of the topic and explores some basic insights that can be gained from simple three-dimensional (3D) numerical simulations of mantle convection under different convective regimes. We then summarize a suite of observational techniques used to estimate dynamic topography, and finish by laying out some key unanswered questions to stimulate debate and inspire future studies.

15.1. INTRODUCTION

The generation and movement of heat through the mantle gives rise to lateral density heterogeneity and convective flow. These buoyancy anomalies and their motion

act to push Earth's surface up or pull it down, resulting in an evolving pattern of vertical deflections known as *dynamic topography*. Over the last decade, there has been growing recognition of the influence of dynamic topography on surface processes, including landscape evolution, stratigraphic development of sedimentary basins, oceanic circulation, paleo-shoreline deformation, and ice sheet dynamics (Braun et al., 2013; Petersen et al., 2010; Spasojević & Gurnis, 2012; Poore et al., 2006; Rovere et al., 2014; Austermann et al., 2015). In turn, identification of the fingerprint of dynamic topography within the rock

¹Department of Earth & Planetary Sciences, Harvard University, Cambridge, MA, USA

²Lamont-Doherty Earth Observatory, Columbia University, New York, NY, USA

³Department of Earth Sciences, University of Oxford, Oxford, UK

record can be used to gain insights into the structure and dynamics of the Earth's mantle (Hager et al., 1985; Gurnis et al., 2000; Flament, 2019). The potential relevance of dynamic topography to such a diverse range of fields has led to a proliferation of studies investigating this important topic using theoretical, observational, and computational approaches (Ghelichkhan & Bunge, 2016; Hoggard et al., 2016; Arnould et al., 2018). Despite considerable advances arising from this work, several controversies remain that are the focus of considerable ongoing investigation. Examples include how best to define dynamic topography, the length scales and rates over which it changes, the driving mechanisms primarily responsible for its temporal evolution, and which geological observations are appropriate for constraining this behavior.

In this chapter, we first provide a brief overview of convective regimes within the mantle and their variable signature in Earth's dynamic topography. This genetic link between the surface and deep interior constitutes the most fundamental motivation for studying dynamic topography, and therefore provides important context. Next, we review observational constraints that can be used to infer dynamic topography, both its present-day spatial pattern and its temporal evolution. We finish by outlining several important outstanding challenges in this research area.

15.2. CONVECTIVE REGIMES AND THEIR SURFACE EXPRESSION

The Earth acts as a giant heat engine, with transfer of thermal energy between various sources and sinks giving rise to many of the geological processes that have sculpted its surface. Heat is simultaneously generated in the interior of the mantle (primarily from the decay of radioactive nuclides) and supplied from below by the core (Lay et al., 2008). This heat is transferred to the surface of the mantle, where it continuously escapes by conduction through the lithosphere.

15.2.1. Thermal Convection of the Mantle

On geological timescales, the mantle deforms as a fluid and can be modeled using the principles of conservation of mass, momentum, and energy. Some basic insights into its first-order behavior have been obtained from simple fluid dynamical analysis. Deformation of mantle rocks is often treated as a Newtonian process, where the rate of strain is linearly related to the driving deviatoric stress, and the effects of inertia can be neglected. The resulting balance between pressure, gravitational, and viscous forces in such a fluid leads to the Stokes equation, which depends on a dimensionless parameter known as the *Rayleigh number*. Its magnitude quantifies the timescale of conductive heat transport over that of convective transport across the

mantle, and gives an indication of convective vigor. Thus, systems with low Rayleigh numbers efficiently transfer heat by conduction, whilst high Rayleigh numbers correspond to vigorous thermal convection. For a simple isoviscous layer heated from below, the Rayleigh number, Ra_B , is given by

$$Ra_B = \frac{\rho g \alpha \Delta T d^3}{\kappa \eta} \quad (15.1)$$

where ρ is the density of material at surface conditions, g the gravitational acceleration, α the coefficient of thermal expansion, ΔT the temperature difference between upper and lower boundaries, d the layer depth, κ the thermal diffusivity, and η the kinematic viscosity (Turcotte & Schubert, 2002). In the case of a purely internally heated fluid, the Rayleigh number, Ra_H , is instead evaluated using

$$Ra_H = \frac{\rho^2 g \alpha H d^5}{\kappa \eta k} \quad (15.2)$$

where H is the rate of internal heat generation per unit mass and k is the thermal conductivity. Analysis of the stability of small temperature perturbations within a fluid reveals that a critical transition occurs at $Ra \approx 10^3$ in either heating scenario, above which the layer begins to undergo thermal convection (Rayleigh, 1916).

There is considerable ongoing debate over the relative magnitude of internal heat generation within the mantle versus basal heating from the core (Lay et al., 2008; Nimmo, 2015). However, adopting approximate estimates of the various parameters in Equations (15.1) and (15.2), either definition yields Rayleigh numbers for the mantle from 10^6 up to 10^9 , depending on whether layer depth is taken to be only the upper 670 km or the whole depth of the mantle (e.g., Knopoff, 1964). Thus, variations in temperature within the mantle give rise to buoyancy variations that drive vigorous flow. Although this analysis is predicated on a simple system with several approximations and assumptions, the order of magnitude is thought to be valid for more realistic mantle rheologies that include the pressure and temperature dependence of parameters such as viscosity and thermal expansivity, resulting in spatial variation of the Rayleigh number (e.g., Parmentier et al., 1976).

Both computational simulations and laboratory experiments on analog systems show that at these Rayleigh numbers, convection is vigorous, can develop multiple layers, and exhibits a strongly time-dependent planform (Busse, 1978; Machetel & Yuen, 1986; Weinstein & Olson, 1990; Yuen et al., 1994; Davies & Davies, 2009). Convection cells develop that have isothermal cores bounded by thin layers where conductive heat transfer dominates (Turcotte & Oxburgh, 1967). These *thermal boundary*

layers form at the top of the mantle as hot material rises to the surface and spreads horizontally, gradually cooling to generate progressively thicker oceanic lithosphere (McKenzie, 1967). When the thickness exceeds a critical value, the thermal boundary layer destabilizes and begins to participate in convection (Huang & Zhong, 2005). On Earth, these downwellings are thought to be dominated by sinking slabs, although smaller-scale convective rolls and drips have also been suggested (Richter, 1973; McKenzie et al., 1974; Balachandar et al., 1992; Parmentier et al., 1994). Importantly, some regions of thick continental lithosphere are anomalously buoyant and viscous due to chemical depletion, so do not destabilize in this manner (Jordan, 1975). Buoyant instabilities within the lower thermal boundary layer at the core-mantle boundary are expected to generate isolated upwelling plumes and sheets (e.g., Olson et al., 1987). The planform of these various features is expressed in dynamic topography on the overlying surface.

15.2.2. Dynamic Topography: A Definition

Lateral density variations in the mantle and convective flow produce temporally evolving radial stresses, $\sigma_{rr}(t)$, that act on Earth's surface. These radial stresses are balanced by vertical deflections of the surface, which are generally referred to as dynamic topography. The magnitude of these radial stresses depends on the viscosity of the mantle and the depth, wavelength, and size of the buoyancy anomaly (Parsons & Daly, 1983; Forte & Peltier, 1991). The amplitude of resulting dynamic topography, $\delta a(t)$, depends on the buoyancy of the fluid displaced at the surface (i.e., air- versus water-loaded) according to

$$\delta a(t) = \frac{\sigma_{rr}(t)}{g\Delta\rho} \quad (15.3)$$

where $g = 9.8 \text{ m s}^{-2}$ is the acceleration due to gravity at the Earth's surface, and $\Delta\rho$ is the density difference between mantle and displaced surface fluid. The existence of these surface deflections was first alluded to by Pekeris (1935) and is generated by three interwoven processes. Firstly, buoyancy associated with variations in the thickness and thermal structure of the upper boundary layer (lithosphere) is isostatically compensated at the surface (Figure 15.1a). This process is particularly well-expressed in oceanic regions, whereby average water-loaded basement depths subside by ~ 3.5 km as the plate ages, conductively cools, and increases in density (Richards et al., 2018). This first-order behavior of oceanic lithosphere has been comprehensively studied and is well-understood (e.g. McKenzie, 1967; Parsons & Sclater, 1977; Stein & Stein, 1992). However, the contribution of lithospheric isostasy in continental regions is an area of considerable ongoing research (e.g., Guerri et al., 2015; Ball et al., 2019; Davies et al., 2019; Klöcking et al., 2020; Lamb

et al., 2020). In particular, treatment of cratonic lithosphere is complicated by the fact that some of its buoyancy arises from chemical depletion, which may be sufficiently extensive that its high intrinsic buoyancy and viscosity only allows it to passively affect convective flow without participating in it (Jordan, 1978; Jain et al., 2019). The second process arises from variations in temperature and chemical composition within the asthenosphere and deeper mantle. This lateral heterogeneity causes density anomalies that can, even in the absence of vertical flow, be isostatically compensated at the surface (Figure 15.1b). Third, the flow field itself produces pressure gradients and vertical deviatoric stresses that exert tractions on the overlying plate (Figure 15.1c). A standard assumption in mantle convection modeling is that inertial forces are negligible, such that the flow field is entirely driven by buoyancy anomalies. This assumption inextricably links these second and third processes.

There is general consensus that crustal isostasy should not be considered part of dynamic topography, but definitions in the literature beyond this starting point tend to diverge, including and excluding various of the aforementioned processes (Flament et al., 2013). Some studies treat dynamic topography as the deflections caused by buoyancy in the lower mantle, whilst others include shallower features up to a depth of ~ 200 km, or even all sublithospheric structure (e.g., Hager et al., 1985; Ricard et al., 1993; Conrad & Husson, 2009; Steinberger, 2016). Lithospheric isostasy (process *a* in Figure 15.1) is commonly excluded from the definition, as it tends to dominate contributions from other processes and is difficult to model accurately due to the complex density structure of continental lithosphere. Nevertheless, several studies do incorporate lithospheric isostasy in the definition (e.g., Forte et al., 1993; Moucha et al., 2008; Glišović & Forte, 2016). Finally, it is also possible to subtract all isostatic contributions and consider flow induced topography in isolation (only process *c* in Figure 15.1; e.g., Molnar et al., 2015). Although these alternative definitions have resulted in significant confusion in the literature, none of them is necessarily incorrect, but rather, they aim to understand and explain different processes (e.g., isostatic effects arising from the lithosphere versus deeper mantle flow). The salient point is that a consistent definition of dynamic topography should be used when comparing model predictions either with one another or against observational constraints.

A consequence of dynamic topography arising from these three processes is that evolving vertical motions can be a result of changes in any of the individual components:

1. *As the lithospheric plate translates laterally over temperature anomalies in the convecting mantle, any point at the surface undergoes alternating cycles of uplift and subsidence* (Figure 15.1d; Sandiford, 2007;

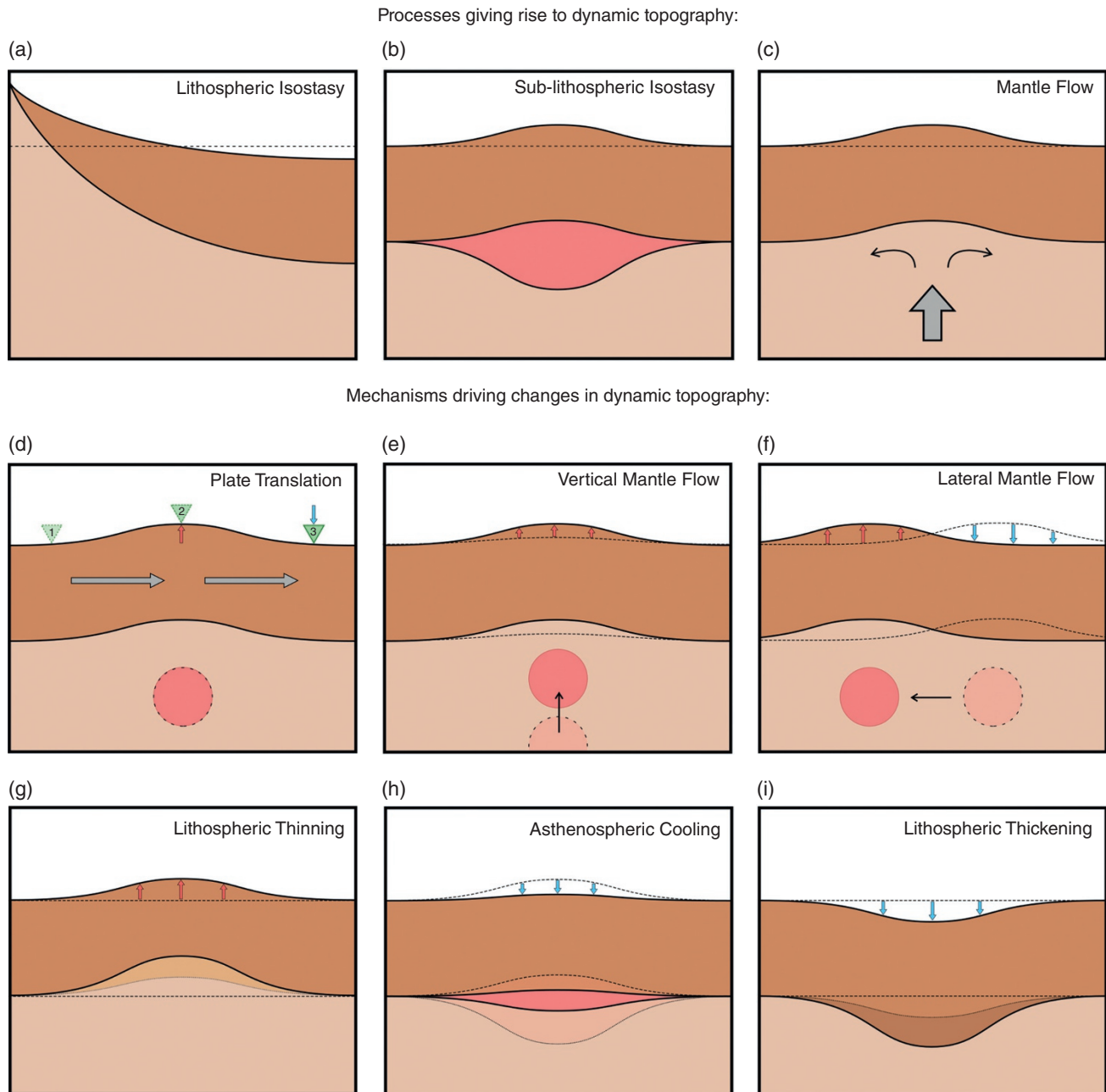


Figure 15.1 Processes producing dynamic topography and mechanisms causing evolving vertical motion. Top row = three processes causing dynamic topography: (a) lithospheric isostasy (both oceans and continents); (b) isostasy within the convecting mantle (asthenosphere and deeper); (c) mantle flow. Lower panels = mechanisms causing changing vertical motion at the surface: (d) lateral translation of plate across underlying convective plume; (e) evolving vertical flow field; (f) lateral advection of convecting mantle; (g) lithospheric thinning (e.g., by thermal erosion); (h) cooling of temperature anomalies; (i) lithospheric thickening (e.g., during oceanic spreading or following horizontal extension).

Czarnota et al., 2013). The greatest rates of change associated with this mechanism will occur when short-wavelength temperature anomalies are located beneath fast-moving plates, such as in Australia or the Pacific Ocean.

2. *The amplitude and spatial extent of dynamic topography changes as vertical mantle flow progresses.* This occurs, for example, above a subducting slab or upwelling plume head (Figure 15.1e; Gurnis et al., 2000; Spasojević et al., 2009; Eakin et al., 2014).

3. *Temperature anomalies flow laterally beneath the plate*, producing a progressing wave of uplift and subsidence (Figure 15.1f). This lateral advection mechanism is thought to be particularly prevalent where plume heads impact the base of the plate and subsequently spread horizontally within a low-viscosity asthenospheric channel (Vogt, 1971; Hartley et al., 2011).
4. *Excess heat can thermally erode and thin the lithospheric mantle*. This produces uplift of the overlying surface (Figure 15.1g; Klöcking et al., 2020).
5. *Over time, the layer of hot plume head material can cool by conduction*. This causes subsidence (Figure 15.1h; Anderson, 1982).
6. *Conductive cooling of the lithosphere causes it to thicken and increase in density, driving subsidence of the overlying surface* (Figure 15.1i; McKenzie, 1978).

It should be noted that an additional seventh mechanism also operates, whereby convection-induced changes in the gravity field generate relative vertical motions in the geological record (Austermann & Mitrovica, 2015). However, this effect is generally very small (particularly at shorter wavelengths) and is highly correlated with the pattern of solid Earth deformation driven by the first six mechanisms.

These mechanisms can act simultaneously or in isolation to produce complex patterns of vertical motion. Spatial length scales can be highly variable, and are limited at short wavelengths by the flexural rigidity of the lithosphere (Colli et al., 2016; Arnould et al., 2018; Golle et al., 2012; Sembroni et al., 2017). There is also an interplay between timescales of these different mechanisms. The rate of dynamic topography change due to plate translation is controlled by plate speed, the two evolving flow mechanisms depend on convective flow velocity and therefore mantle viscosity, while cooling asthenosphere and lithospheric modification depend on warming and cooling of shallow material and therefore evolve over conduction timescales. Some of the fastest rates of inferred vertical motion are up to 0.5 mm yr^{-1} and appear to be associated with lateral mantle flow within the asthenosphere (mechanism *f* in Figure 15.1; Hartley et al., 2011), whilst conductive cooling at lithospheric scales occurs on 10s Myr timescales and produces rates as slow as 0.01 mm yr^{-1} (mechanisms *h* and *i* in Figure 15.1; Parsons & Sclater, 1977). Furthermore, there is a complicated interaction between differential plate translation (mechanism *d* in Figure 15.1) and the other five mechanisms. For example, the plate is mechanically coherent and so sites of lithospheric thinning and thickening travel horizontally with the plate, in a fixed position with respect to the overlying surface. In a similar manner, downwellings are generated by instabilities within the thermal boundary layer at the top of the mantle, and are therefore

more likely to track horizontally with the plate than upwellings, which are sourced from depth and are less likely to be directly coupled to surface plate motion.

15.2.3. Simple Convection Simulations

Here, we illustrate in Figure 15.2 the effect of varying the convective vigour of the mantle on the resulting pattern of dynamic topography, where all three processes causing surface deflections have been included. The purpose of these simulations is to demonstrate that global patterns of dynamic topography are strongly sensitive to convective regime, and to provide a first-order understanding of this relationship. The simulations are intentionally kept simple to convey these key points and more complex rheologies and thermal properties would be required to make them more Earth-like.

Our finite element simulations are performed using the ASPECT code (version 2.2.0-pre) where we adopt a 3D spherical shell that is heated from below (Kronbichler et al., 2012; Heister et al., 2017). We perform five incompressible simulations at a range of Rayleigh numbers using different radial viscosity profiles. Three are isoviscous, a fourth includes a lower viscosity upper mantle, and a fifth also incorporates a high viscosity lithospheric lid (see caption of Figure 15.2). Free-slip boundary conditions are applied at the top and bottom of the domain, and net rotation is removed. Models are initialized with minor density perturbations around a constant mantle temperature profile and run forward through time until they reach steady state, which is achieved when the root-mean-squared (r.m.s.) surface velocities stabilize. Runs take between 0.5–15 Gyr to reach steady state and use adaptive mesh refinement in the upper boundary layers (uppermost 200 km) and at grid cells with large thermal gradients, such that the most well-resolved features have a resolution of $\sim 10 \text{ km}$. While this resolution limits the degree to which boundary layer dynamics are resolved, we believe that it is sufficient to correctly simulate first-order differences in convective regimes. Dynamic topography is calculated based on Equation (15.3) using the consistent boundary flux method to calculate radial stresses at the surface (Zhong et al., 1993). This definition therefore includes the contributions from flow field, lithospheric and asthenospheric isostasy (all three processes *a*, *b* and *c* in Figure 15.1). All parameter files are included in the associated OSF database.

At $Ra_B = 10^5$, convection is relatively sluggish and produces long-wavelength, plume-like swells surrounded by lows above downwelling sheets that are stationary through time (Figure 15.2a). The r.m.s. amplitude of air-loaded dynamic topography is 6.9 km, with peak amplitudes of -17 km and $+32 \text{ km}$. Figures 15.2b–2c show that increasing to $Ra_B = 10^6$ yields an r.m.s. amplitude of 2.8 km (peak amplitudes of $\pm 13 \text{ km}$), whilst at $Ra_B = 10^7$

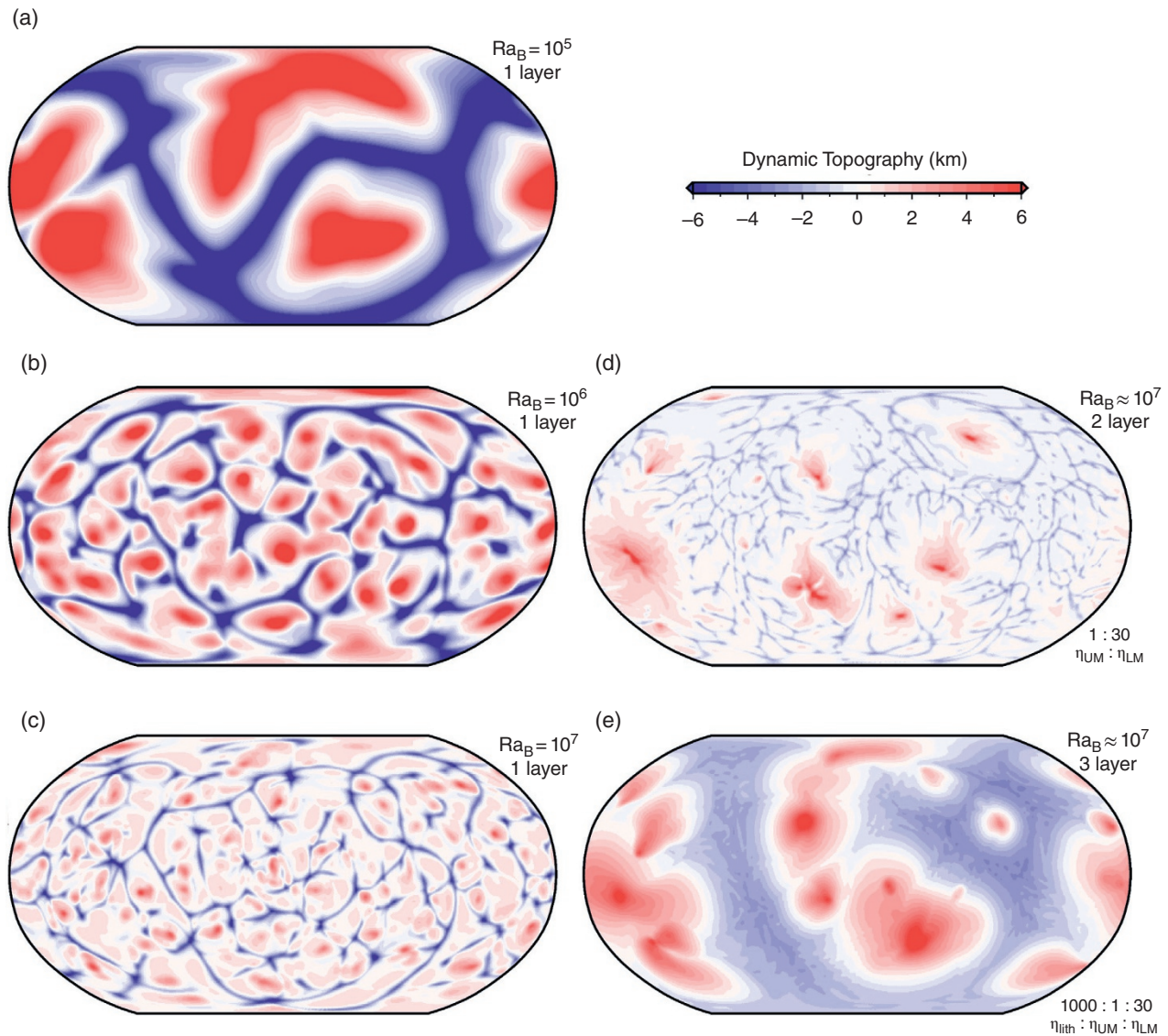


Figure 15.2 Synthetic dynamic topography fields for simple convection simulations within ASPECT using a 3D mantle shell. Dynamic topography is calculated using Equation (15.3) assuming an air-load and includes the contributions from flow field, lithospheric, and asthenospheric isostasy (processes *a*, *b*, and *c* in Figure 15.1). (a) Isoviscous run with $Ra_B = 10^5$. (b) Isoviscous run with $Ra_B = 10^6$. (c) Isoviscous run with $Ra_B = 10^7$. (d) Run with factor of 30 viscosity jump across 670 km between the upper mantle, η_{UM} , and lower mantle, η_{LM} , at $Ra_B \approx 10^7$. (e) Same as *d*, but also including a 100 km-thick lithosphere, η_{lith} , that is 1000 times more viscous than the underlying upper mantle. All grids and parameter files are included in the associated OSF database.

the r.m.s. drops to 1.3 km (−7.5 km to +5.5 km). Thus, by raising the Rayleigh number, the increasingly vigorous flow results in lower amplitude, shorter-wavelength dynamic topography.

These first three runs are isoviscous. Introducing a viscosity increase of a factor of 30 across the 670 km discontinuity causes a further drop in the r.m.s. amplitude to 0.84 km (Figure 15.2d). This also causes the upwellings, which initiate in the thermal boundary layer at the base of the lower mantle, to become more widely spaced and

have more localized, higher amplitude peaks than the more elongated lows above downwellings (peaks of +8.4 km versus lows of −3.5 km), as previously found by Bunge et al. (1996). Finally, introducing a high viscosity lithosphere causes the downwellings to concentrate into wide bands separated by more closely spaced upwellings with broader swells (Figure 15.2e).

These simple examples illustrate that the potential impacts of mantle convection on vertical motions of Earth's surface are highly diverse and likely to be variable

through time. An important corollary is that making accurate observations of dynamic topography can provide unique insights into the structure and dynamics of Earth's interior. Parallel advances between numerical modeling, the quantity and accuracy of observational constraints, and the efficiency at which they can be assimilated, are key for better reconstructions of dynamic topography. Several excellent review papers in the last decade have highlighted various improvements from a modeling perspective (e.g., Braun, 2010; Flament et al., 2013; Coltice et al., 2017). Here, we briefly revisit these advances, but mainly choose to focus on providing a complementary overview of the methods that are used to reconstruct dynamic topography from observational constraints in the geological record.

15.3. EARLY OBSERVATIONAL CONSTRAINTS ON LARGE-SCALE MANTLE FLOW AND THEIR ROLE IN PAST AND PRESENT GEODYNAMIC MODELING

Our knowledge of Earth's present-day dynamic topography has undergone several major developments over the past 80 years as powerful new datasets have become available. The late 1950s saw the first measurements of the long-wavelength component of Earth's gravity field, derived from orbit-tracking of rockets and satellites (Kaula, 1963). One common representation of this field is to map variations in the height of the equipotential surface that coincides with mean sea level, known as the *geoid*. The primary component of the observed field is stronger gravity near the equator compared to the poles, which is caused by excess flattening of the Earth due to its rotation (Nakiboglu, 1982). Once this hydrostatic component is removed, there remains a dominant *spherical harmonic degree-2* pattern. Two major geoid highs of approximately +100 m are centered over Africa and the western Pacific Ocean, encircled by a ring of -100 m lows above the sites of Mesozoic and Cenozoic subduction zones. These anomalies were soon interpreted as being caused by flow within the mantle, and are generated by a combination of two competing effects (Runcorn, 1965). In the case of a buoyant upwelling, a negative gravity contribution arises from the hot, lower density thermal anomaly within the mantle, which is opposite in sign to the positive contribution generated by upward deflection of the surface and core-mantle boundary (Pekeris, 1935; McKenzie, 1968; McKenzie et al., 1973). The reverse occurs for a dense, downwelling structure. Which of these two effects is the strongest (i.e., geoid contributions from driving mass anomalies versus boundary deflections) depends on the size of the buoyancy anomaly, its depth and the viscosity of the mantle (Parsons & Daly, 1983; Colli et al., 2016).

In the late 1970s, the first global seismic tomographic images were produced, mapping variations in shear-wave and bulk-sound velocities throughout the Earth's mantle (Dziewonski & Anderson, 1984). In particular, underlying the geoid highs, two large, spherical harmonic degree-2 patches of slower than average shear wave velocities were observed in the lower mantle, now termed *large, low-velocity provinces* or LLVPs (Garnero et al., 2016). The simplest interpretation of these features is that they represent hotter-than-ambient, buoyant material that is rising, causing corresponding upward deflections of the surface and core-mantle boundary (CMB) and generating the observed non-hydrostatic geoid anomalies (Figure 15.3). In a seminal paper, Hager et al. (1985) tested this hypothesis using a spectral approach to calculate the solution of the instantaneous mantle flow field. A series of depth-varying sensitivity kernels, based on Green's functions, are derived for the surface topography, CMB deflections, and geoid undulations that depend on the magnitude of relative jumps within a radial viscosity profile, but not the absolute viscosity (Forte & Peltier, 1991). These kernels vary as a function of wavelength (or spherical harmonic degree) of the density anomaly that is driving

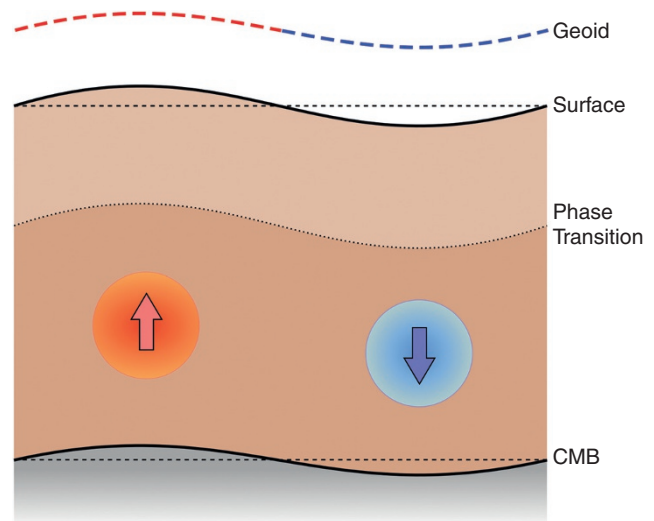


Figure 15.3 Schematic cartoon of lower mantle flow and associated boundary deflections. Vertical deflections of the geoid, surface, mantle phase transitions, and core-mantle boundary (CMB) are driven by a hot, buoyant, upwelling anomaly (red) and a cold, dense, sinking anomaly (blue). Note that mass anomalies associated with these internal buoyancy variations and with the flow-driven boundary deflections are opposite in sign. Competition between these sources results in the amplitude and sign of geoid height deflections depending on the buoyancy anomaly magnitude, its wavelength and burial depth, and the viscosity of the mantle. Sources: Parsons & Daly (1983); Hager et al., (1985).

viscous flow. As a general rule, short-wavelength dynamic topography kernels have sensitivity to density structure within the asthenosphere and upper mantle, whilst the longest wavelengths also show sensitivity to features in the lower mantle. For their density structure, Hager et al. (1985) used an early lower mantle *P*-wave tomography model that was linearly scaled into density variations. For any input radial viscosity profile, the resulting sensitivity kernels are convolved with this density model to predict geoid height variations. A satisfactory fit to geoid observations was obtained by adjusting the radial viscosity profile to have a factor of 10 increase at 670 km from the upper into the lower mantle, which simultaneously yielded the first predictions of dynamic topography and CMB deflections arising from lower mantle flow (Figure 15.4). The predicted dynamic topography exhibits

a dominant spherical harmonic degree-2 structure, with ~ 1 km highs over Africa and the Pacific Ocean, ringed by -1 km lows.

Many important theoretical advances have been made since this initial study. Mantle density models have been constructed based on updated seismic tomography models and conversion factors, assimilation of slab subduction histories from plate reconstructions, or a combination of both (e.g., Ricard et al., 1993; Conrad & Husson, 2009; Spasojević & Gurnis, 2012). The spectral instantaneous flow methodology has been improved to include the effects of self-gravitation and compressibility (Corrieu et al., 1995; Forte, 2007). Switching to fully numerical, time-dependent codes has allowed lateral variations in viscosity to be incorporated into the flow field (Zhong & Davies, 1999). This move has also allowed the temporal

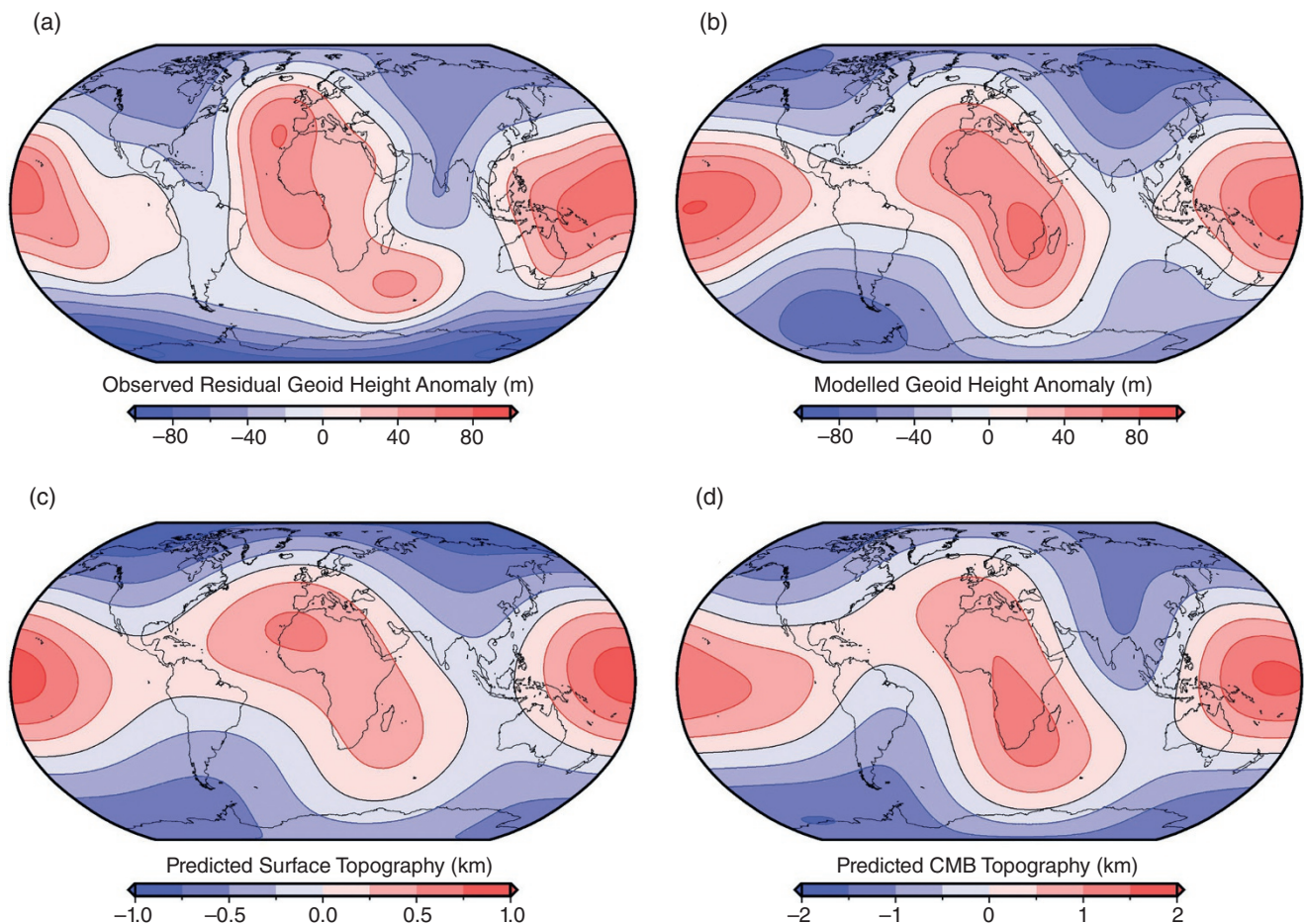


Figure 15.4 Results of present-day instantaneous flow calculations from Hager et al. (1985). (a) Observed geoid height anomaly, corrected for the effects of hydrostatic flattening due to Earth rotation and the presence of downwelling slabs beneath subduction zones (Hager, 1984); contoured every 20 m. (b) Modeled geoid height anomaly using a lower mantle density structure derived from seismic tomography and a radial viscosity profile with a factor 10 increase across the 670 km discontinuity. (c) Predicted dynamic topography at the Earth's surface assuming a global water-load; contoured every 250 m. (d) Predicted vertical deflections of the core-mantle boundary (CMB); contoured every 500 m. Source: (a–d) Hager et al. (1985).

evolution of mantle convection to be explored using forward, backward, and adjoint approaches (e.g., Gurnis et al., 1998; Conrad & Gurnis, 2003; Bunge et al., 2003; Glišović & Forte, 2014; Li et al., 2017; Colli et al., 2018). This development has the added bonus of allowing reconstructed plate velocities to be built in as boundary conditions, providing sensitivity to values of absolute mantle viscosity (Lithgow-Bertelloni & Richards, 1998; Gurnis et al., 2000; Bower et al., 2015; Glišović & Forte, 2015). As a consequence, predictive models of present-day dynamic topography have steadily evolved. Although the shape of the dominant spherical harmonic degree-2 pattern is fixed by the requirement to fit the observed geoid, predicted peak amplitudes vary between $\pm 1\text{--}3$ km between different models (Flament et al., 2013). One corollary of this long-wavelength pattern is that, as plates translate across the surface or the planform of convection evolves, predicted rates of vertical motion are slow (typically ~ 0.01 mm yr⁻¹; Lithgow-Bertelloni & Gurnis, 1997). However, despite these various computational and theoretical advances, there remains considerable non-uniqueness in model solutions that arises from trade-offs between parameters controlling buoyancy sources and those that govern rheological properties. These uncertainties emphasise the necessity of obtaining additional observational constraints to test predictive models.

15.4. ESTIMATING PRESENT-DAY DYNAMIC TOPOGRAPHY

The majority of predictive flow models of global dynamic topography are driven by convection in the sub-lithospheric mantle (processes *b* and *c* in Figure 15.1). In order to test them, observational constraints on present-day dynamic topography are required. A significant challenge in making these estimates arises from the requirement to remove the effects of lithospheric isostasy (process *a* in Figure 15.1) from the observed topography. Given that this process often dominates surface topography, accurate and detailed knowledge of crustal and lithospheric density structure is required to successfully remove it (Guerra et al., 2015). Efforts to isolate isostatic topography from onshore elevations are hampered by the long-lived and complex geological histories of continents, which have resulted in complicated lithospheric architectures. For example, chemical depletion arising from melt extraction early in the Earth's history increased the buoyancy of residual lithospheric mantle (Jordan, 1978). To date, attempts to observe the pattern of present-day dynamic topography in the oceanic realm have proven more fruitful due to its relative geological youthfulness and simpler lithospheric density structure.

15.4.1. Oceanic Residual Depth Anomalies

The first-order control on oceanic bathymetry is the pattern of subsidence with increasing age as plates spread laterally away from mid-ocean ridges. Many studies have focused on this behavior, and it is generally accepted to be driven by the progressive growth of a thermal boundary layer (Turcotte & Oxburgh, 1967; McKenzie, 1967). As two plates separate at a mid-ocean ridge, hot asthenospheric material passively upwells and spreads laterally through time. Conductive heat loss through the surface steadily cools this material, increasing its density and thickening the lithosphere, which drives subsidence (Parsons & Sclater, 1977). This process (panel *a* in Figure 15.1) is clearly a consequence of mantle convection and this topographic component driven by thickening of oceanic lithosphere is therefore sometimes included in dynamic topography maps (e.g., Forte et al., 1993). However, it tends to dominate over bathymetric expressions caused by sub-lithospheric buoyancy and flow (processes *b* and *c* in Figure 15.1), so many maps of dynamic topography remove the average age-depth subsidence trend in order to isolate *residual* topographic anomalies (e.g., Cazenave et al., 1988; Panasyuk & Hager, 2000).

We will focus on these sub-plate contributions to dynamic topography throughout the rest of Section 15.4.1, although a couple of important caveats should be noted. First, the age-depth subsidence correction typically approximates local lithospheric isostasy with that expected for average oceanic lithosphere of equivalent age obtained from a thermal evolution model. Topography caused by regional lithospheric thickness variations away from this average background trend, such as thinning above a hot upwelling or thickening above a cold downwelling, will therefore still be present within residual depth estimates. Thus, residual bathymetry is likely to represent a maximum bound on the amplitude of deflections arising from deeper mantle flow (Hoggard et al., 2017). Second, there are multiple options for the choice of lithospheric cooling model, including half-space, plate cooling, and thermal boundary layer instability models, which predominantly differ in whether and by what mechanism heat is resupplied to the base of the lithosphere as it ages (Korenaga & Korenaga, 2008; Richards et al., 2020a; Crosby et al., 2006). These models yield similar results in lithosphere younger than ~ 70 Ma, but residual depth anomalies can deviate by up to ~ 1 km in the oldest parts of ocean basins (Zhong et al., 2007; Hoggard et al., 2016).

Notwithstanding these issues, Menard (1965) was the first to link anomalous bathymetric variations in the oceans to the vertical deflections expected from mantle convection. He identified several prominent mid-plate rises as likely surface expressions of sub-plate convection cells (Menard, 1969). In addition to age-depth subsidence,

a component of oceanic bathymetry is controlled by flexural and isostatic responses to sedimentary loading, crustal thickness variations, and subduction zones. Correcting bathymetric data for these processes yields a map of *residual depth anomalies* that can be regarded as a proxy for present-day dynamic topography (Menard, 1973). Early attempts to map these anomalies were focused on central areas of large ocean basins where sediments are generally thinner, reducing uncertainty in sedimentary loading corrections (Cochran & Talwani, 1977). The largest limitation on the accuracy of residual depth maps for many years was the absence of a correction for variable crustal isostasy, primarily due to the lack of accurate global grids of oceanic crustal thickness. However, a shift in focus from global grids to spot measurements at the sites of marine seismic experiments, where crustal thickness can be mapped in high resolution, has significantly reduced this uncertainty (Winterbourne et al., 2009, 2014).

The latest compilations include ~2000 seismic experiments of varying ages from a mixture of hydrocarbon industry and academic sources (Hoggard et al., 2017). There is good coverage on most passive margins and along active subduction zones, with scarcer spot measurements in central portions of the major basins due to a paucity of distal experiments. Fortunately, the generally thinner sedimentary cover in these regions results in lower uncertainty in global grids of sedimentary thickness in comparison to passive margins and major river deltas. Therefore, the most accurate spot measurements are usually supplemented in distal settings with gridded residual depth estimates derived from these global compilations. Uncertainty arising from the absence of a correction for variable crustal isostasy in these grids has been partially mitigated by removing oceanic lithosphere that is clearly anomalous, such as at major fracture zones and seamounts, using high resolution bathymetry and gravity anomaly maps. Resulting sediment and crustal-corrected observations measure the difference in the observed depth of basement below the sea surface, compared to its expected depth from age-depth subsidence curves. However, an additional factor to consider is that the sea surface follows the geoid, which is also deflected by mantle convection. Therefore a final correction for height of the local geoid with respect to its hydrostatic equilibrium figure is applied, which is typically on the order of 100 m (Hoggard et al., 2017).

Our latest maps of oceanic residual topography with age-depth subsidence trends removed reveal striking patterns, particularly along passive margins with good data coverage (Figure 15.5). Rather than the spherical harmonic degree-2 pattern anticipated from predictive flow models of dynamic topography (e.g., Figure 15.4c), the residual anomalies are significantly more variable, often changing over ~1000 km wavelengths. The highest

water-loaded amplitudes reach +2 km in the vicinity of major magmatic hotspots such as Iceland, Afar, and Cape Verde. The deepest drawdowns of -2 km are generally, but not exclusively, associated with backarc settings above subducting slabs, such as the Banda Sea, western Gulf of Mexico, and Argentine abyssal plain. Away from these areas, residual depth anomalies exhibit typical amplitudes of ± 1 km. A particularly noteworthy example comes from the southwestern margin of Africa, where spot measurements capture at least two coherently varying ± 1 km cycles with 1500 km wavelengths along strike of the margin (Winterbourne et al., 2009; Hoggard et al., 2017).

The broad characteristics of these anomalies were evident even in the earliest studies of oceanic residual topography (Menard, 1973; Cochran & Talwani, 1977; Cazenave et al., 1988). However, the steady inclusion of higher accuracy measurements of sedimentary and crustal thickness, in combination with more formalized error propagation, has greatly improved resolution and reduced the associated uncertainties. At present, for the spot observations of Hoggard et al. (2017), the median size of the water-loaded crustal correction is ~200 m, which has propagated uncertainties of ± 70 m, but can locally be as large as 800 ± 150 m in regions of very thick oceanic crust such as around Iceland. The median water-loaded sedimentary correction is ~1.25 km, with uncertainty of ± 50 m for data obtained from seismic reflection profiles collected in two-way traveltimes (when uncertainty in porosity compaction parameters is minimized). The sedimentary loading correction is therefore typically larger than the crustal correction, but can vary from zero in sites with no sediment cover right up to 6.0 ± 0.5 km on the most heavily sedimented passive margins, where it dominates uncertainty estimates of oceanic residual topography.

15.4.2. Continental Residual Topography

Removal of isostatic topography arising from continental lithosphere (process *a* in Figure 15.1) requires constraints on its density structure that have largely been obtained from seismology. Active source experiments such as reflection or wide-angle refraction profiles yield information on the local sub-surface velocity structure and major boundary depths, including the sediment-basement interface and Moho (Mooney, 2015). Passive seismological methods are also widely used. For example, receiver function studies provide layer thicknesses and V_p/V_s ratios beneath the site of seismometers, and combined inversion with surface wave data mitigates some of the trade-offs between these parameters (e.g., Julià et al., 2009). On a more regional scale, seismic tomography can constrain the broad velocity structure of the lithosphere. Higher resolution studies often combine body-wave arrivals with

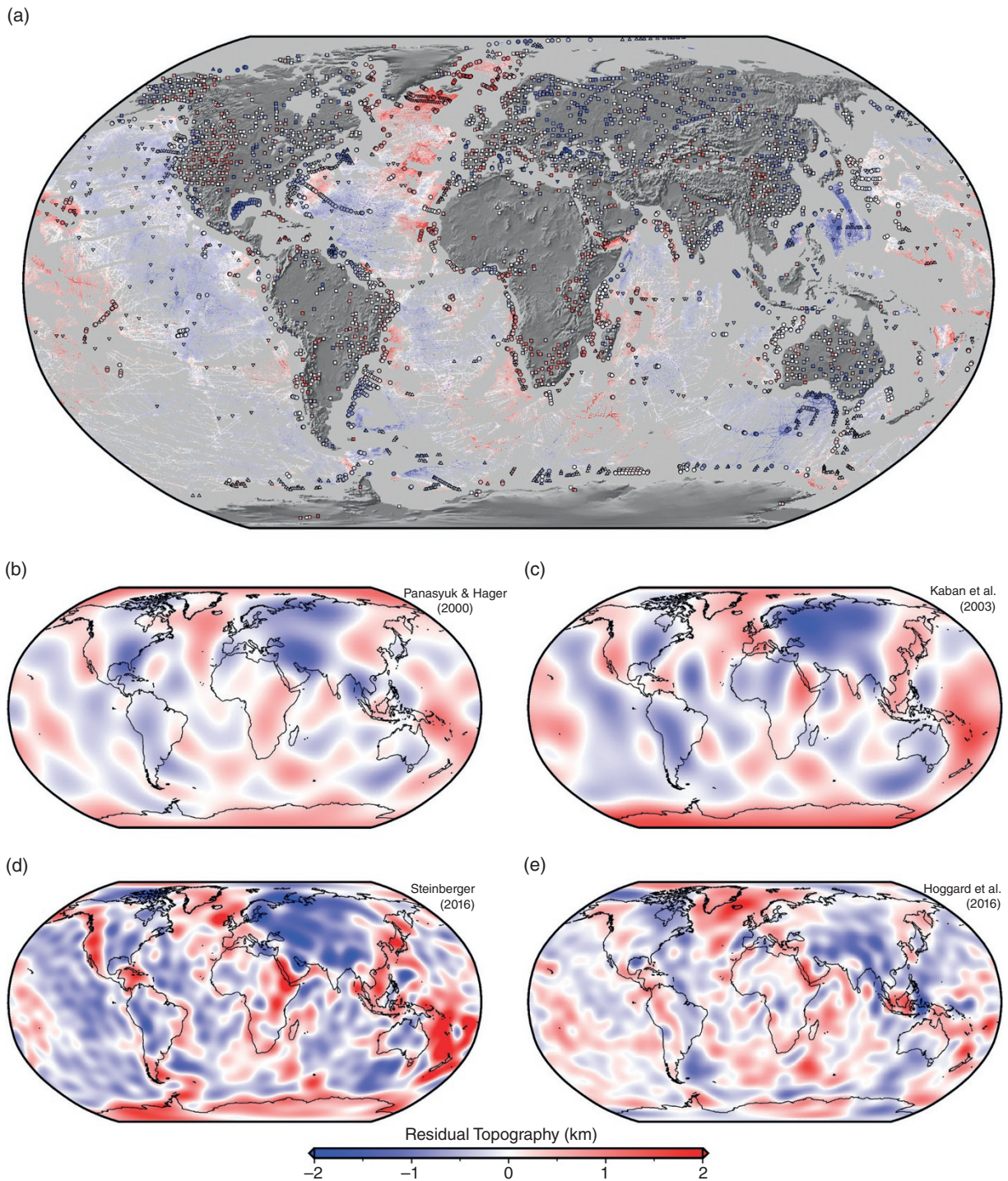


Figure 15.5 Estimates of present-day residual topography. All maps are air-loaded in the continents and water-loaded in the oceans, where the correction for age-depth subsidence assumes a plate or plate-like cooling model (i.e., flattening at old ages). These residuals are considered a proxy for dynamic topography caused by convection in the sub-lithospheric mantle (processes *b* and *c* in Figure 15.1). However, inaccurate removal of lithospheric isostasy (process *a* in Figure 15.1) may also be present, alongside any other data errors. (a) Oceanic data from Hoggard et al. (2017), updated using the RHCW18 plate cooling curve and oceanic age model (Richards et al., 2018); circles = spot measurements with geoid height, sedimentary and crustal corrections; upward/downward pointing triangles = minimum/maximum spot measurements where no crustal correction has been made but its sign is estimated from nearby crustal thickness measurements; grid = shiptrack-derived measurements with no crustal correction. Squares = 1915 new onshore spot estimates derived from seismic experiments and corrected for crustal and lithospheric isostasy (Section 15.4.2); (b) Panasyuk & Hager (2000), expanded to a maximum spherical harmonic degree, l_{\max} , of 12 (Steinberger 2007); (c) Kaban et al. (2003), expanded to $l_{\max} = 12$ (Steinberger, 2007); (d) Steinberger (2016), expanded to $l_{\max} = 31$; (e) Hoggard et al. (2016), expanded to $l_{\max} = 30$. Sources: (a) Hoggard et al., (2017), (b) Panasyuk & Hager (2000), Steinberger (2007), (c) Kaban et al. (2003), Steinberger (2007), (d) Steinberger (2016), (e) Hoggard et al. (2016).

fundamental and higher modes of surface waves, which are particularly sensitive to upper mantle structure (e.g., Schaeffer & Lebedev, 2013). Resultant maps of seismic velocity are subsequently converted into density using a variety of laboratory-based calibrations, although these conversions are subject to considerable uncertainty arising from factors including the effect of minor phases such as water or melt on velocities, anisotropic fabrics, anelasticity, and the frequency content of seismic sources (e.g., Brocher, 2005; Jackson & Faul, 2010; Yamauchi & Takei, 2016). Final density maps can be calibrated using observed gravity anomalies, although the high non-uniqueness of this technique means that it is of limited use in isolation (Cowie et al., 2015; Afonso et al., 2019).

Some studies have used global grids of crustal thickness and density compiled from local spot measurements to generate continuous maps of continental residual topography (e.g., Pari & Peltier, 2000; Panasyuk & Hager, 2000; Steinberger et al., 2019). Here, however, we deliberately return to the original spot measurements in order to avoid using areas in the global grids that are poorly constrained due to a lack of input data (following Davis et al., 2012). We adopt a simple isostatic approach to calculating continental residual topography using a global compilation of 11,062 local crustal thickness estimates derived from a mixture of active and passive seismic experiments (Szwilius et al., 2019, and other sources). The isostatically corrected elevation, e_{corr} , at each location is given by

$$e_{corr} = e_{obs} - \left(\frac{\rho_a - \bar{\rho}_c}{\rho_a} \right) z_c - \left(\frac{\rho_a - \bar{\rho}_l}{\rho_a} \right) z_l \quad (15.4)$$

where e_{obs} is the observed elevation, $\rho_a = 3200 \text{ kg m}^{-3}$ is the density of asthenospheric mantle, $\bar{\rho}_c$ is the bulk density of crust with thickness z_c , and $\bar{\rho}_l$ is the bulk density of lithospheric mantle with thickness z_l . The bulk crustal density is obtained by integrating the interval density profile of Christensen & Mooney (1995), extended beyond 40 km up to 50 km depth using a constant value of 3100 kg m^{-3} . Crustal thickness measurements above 50 km have been rejected due to growing uncertainty in this crustal density. Lithospheric thickness is taken from the global grid of Hoggard et al. (2020), which is derived from the SL2013SV surface wave tomography model (Schaeffer & Lebedev, 2013). The bulk lithospheric density is given by

$$\bar{\rho}_l = \begin{cases} 3250 \text{ kg m}^{-3} & \text{for } [z_c + z_l] \leq 100 \text{ km} \\ 3280 - 0.0003 [z_c + z_l] \text{ kg m}^{-3} & \text{for } 100 \text{ km} < [z_c + z_l] < 300 \text{ km} \\ 3190 \text{ kg m}^{-3} & \text{for } [z_c + z_l] \geq 300 \text{ km} \end{cases} \quad (15.5)$$

which approximates the effect of temperature-dependent density variations and increasing chemical depletion in thick lithosphere (Jordan, 1978). We convert corrected

elevation to residual topography by subtracting the median value of the entire dataset, which assumes that the sub-lithospheric components of dynamic topography (processes b and c in Figure 15.1) average to zero in the continents, and spatially average the results by taking the median value within $2^\circ \times 2^\circ$ bins. Finally, we add the correction for non-hydrostatic geoid deflections introduced in Section 15.4.1.

The resulting dataset of 1915 onshore points is shown in Figure 15.5a and has typical air-loaded amplitudes of $\pm 2 \text{ km}$. It is substantially noisier than the oceanic residual depths, which is a direct result of the larger uncertainties in crustal and lithospheric thickness and density structure, particularly for measurements obtained from receiver functions. The sensitivity of results to each of these parameters can be tested by propagating a realistic range of uncertainties through Equation (15.4). Random 10% errors in crustal thickness produce typical residual topography changes of approximately $\pm 400 \text{ m}$, while the same errors in lithospheric thickness produce $\pm 150 \text{ m}$. Crustal densities probably vary by at least $\sim 100 \text{ kg m}^{-3}$ (Guerri et al., 2015), which introduces $\pm 1.1 \text{ km}$ residual topography changes, while 30 kg m^{-3} local variations in the density of the lithospheric mantle yield $\pm 1.3 \text{ km}$ changes. Thus, it seems that continental residual topography results are particularly sensitive to the choice of densities for the crust and lithospheric mantle, and a more time consuming yet improved approach could exploit additional information, such as the local seismic velocity structure, to estimate these parameters (e.g., Brocher, 2005).

These overly simplistic continental residual topography estimates are less robust than their oceanic counterparts because they are severely hampered by uncertainty in the corrections for crustal and lithospheric isostasy (Guerri et al., 2015). Furthermore, they do not account for flexural loading effects that may occur around sites of volcanic emplacement or erosion and removal of crustal material (Sembroni et al., 2016). However, they do illustrate the great value of local seismic experiments and reveal that the current spatial coverage is fairly good, except for in Africa and in the vicinity of major ice caps (Figure 15.5).

15.5. OBSERVATIONAL ESTIMATES OF TIME-EVOLVING DYNAMIC TOPOGRAPHY

In addition to constraining the absolute amplitude of dynamic topography at the present day, accurate measurements of its rate of change provide important insights into the dynamics of convection and rheological properties of the mantle. We can illustrate this phenomenon using the simple convection simulations from Section 15.2.3. For isoviscous runs, increasing the

Rayleigh number causes higher rates of vertical motion that are dominated by increasingly shorter wavelengths (higher spherical harmonic degrees; Figures 15.6a and 15.6b). Introducing a low-viscosity upper mantle over a higher-viscosity lower mantle has a similar effect, with rates

of vertical motion increasing (Figures 15.6c and 15.6d). In contrast, when a high viscosity lithospheric lid is also added, the rate of change of dynamic topography is reduced and the spectral properties flatten significantly. Thus, inferring rates of dynamic topography from

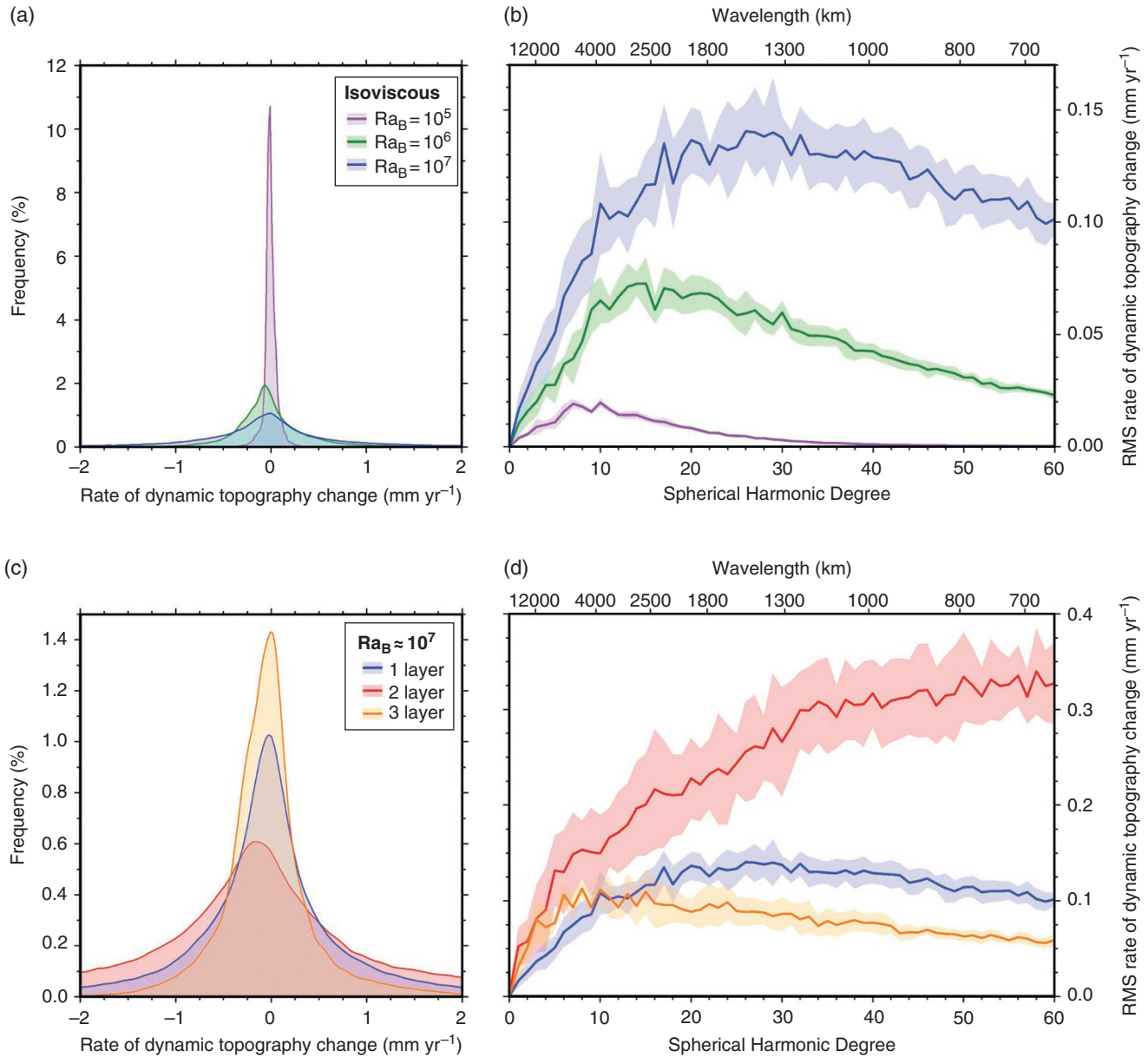


Figure 15.6 Rates of air-loaded dynamic topography change from simple convection simulations shown in Figure 15.2. Rates are calculated as changes in dynamic topography using Equation (15.3) between timesteps, which includes all five mechanisms $e-i$ from Figure 15.1. Note that these simulations do not include mechanism d of Figure 15.1, since the reference frame is external to the mantle such that observation points are fixed in space and do not track across the surface at plate velocities. (a) Histogram of area-normalized rate of change of dynamic topography in the spatial domain for isoviscous runs at $Ra_B = 10^5$, 10^6 , and 10^7 (Figures 15.2a–2c). (b) Spectral decomposition of field of evolving dynamic topography, labeled with equivalent wavelengths at the surface. (c) and (d) Same for runs with $Ra_B \approx 10^7$ for isoviscous mantle, two-layer mantle with factor of 30 viscosity jump across 670 km boundary, and a three-layer mantle, including a 100 km lithospheric lid that is 1000 times more viscous than the underlying upper mantle (Figures 15.2c–2e). Data are included in the associated OSF database.

observational constraints is an important problem in geodynamics that yields information concerning the fluid dynamical properties of Earth's interior.

Investigating the temporal evolution of dynamic topography requires identification of markers that can track changes in elevation. Despite the difficulty in isolating absolute amplitudes of present-day dynamic topography in continental areas, the onshore geological record does contain many useful recorders of changing vertical motion, provided that sufficiently accurate dating can be carried out (Figure 15.7). However, a significant interpretational challenge involves isolating the desired signal from other geological processes. Relative changes between local sea-level and the solid Earth can also result from active tectonics, volcanic emplacement, sedimentation, eustatic sea level variations, and ongoing glacial isostatic adjustment (GIA). Careful analysis of the total amplitude, rate, duration, and spatial extent of uplift and subsidence events yields insights into the relative

contributions of these different driving mechanisms (Miller et al., 2005; Lovell, 2010).

15.5.1. Satellite Observations

The advent of the satellite-era has led to two promising new avenues for constraining present-day changes in dynamic topography. First, the earliest satellites for the Global Positioning System (GPS) were launched in the late 1970s, and the system became widely available for civilian use in the 1990s (Bock & Melgar, 2016). GPS allows for the direct measurement of both horizontal and vertical ground motion with respect to the Earth's center of mass. Decadal rates of motion have been obtained from stations that are either continuously recording or are repeatedly visited as part of campaigns (e.g., Feigl et al., 1993). Hunting for signals associated with dynamic topography is aided by avoiding locations

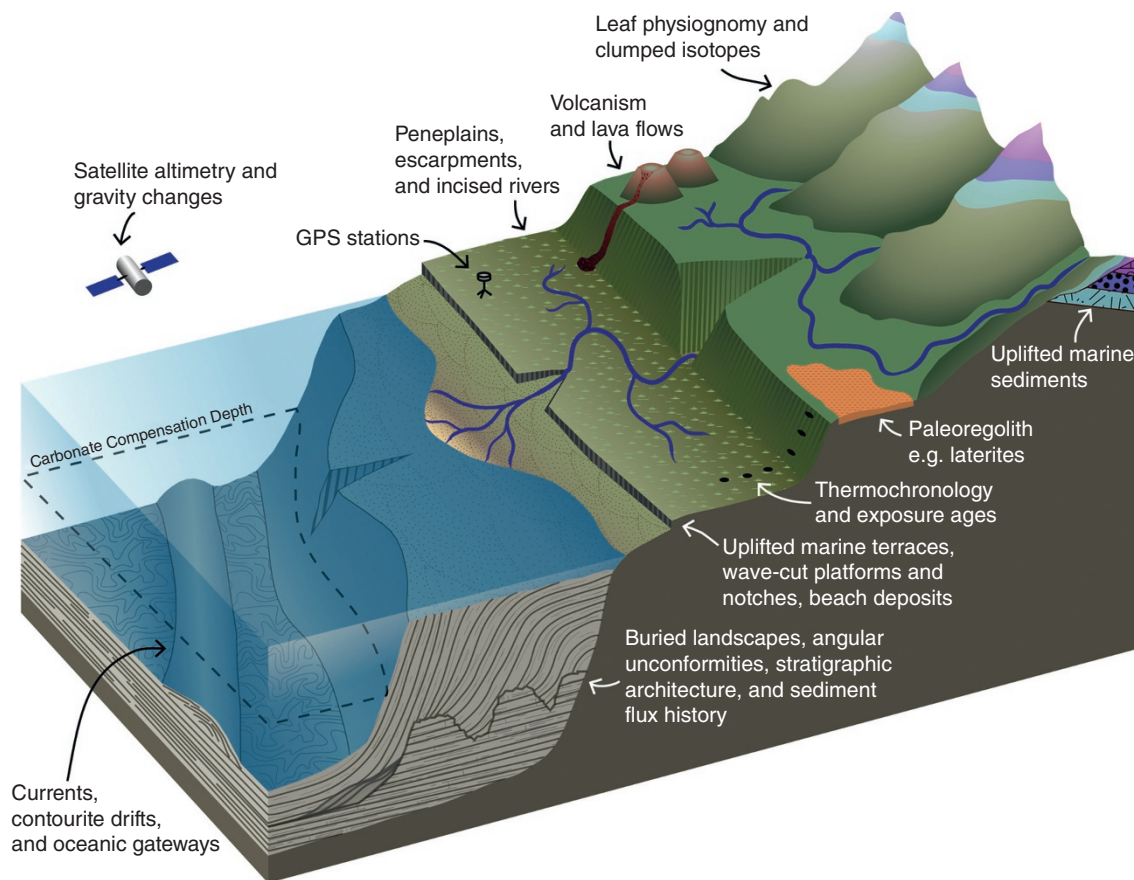


Figure 15.7 Geological observations recording a history of evolving relative vertical motion. This is a passive margin setting, but some of these techniques are applicable on active margins, in continental interiors, and in deep ocean basins. These features generally record relative changes between elevation of the land surface and sea level, except for GPS, which measures solid Earth deformation alone. Care must be taken to separate eustatic variations in sea-level height from uplift and subsidence of the solid Earth. Cartoon is not drawn to scale.

where other processes are likely to dominate, including regions that are actively deforming via earthquakes and faulting, such as at plate boundaries, or locations that are near obvious local loading changes, such as in the vicinity of volcanoes, river deltas, and groundwater reservoirs (Bock & Melgar, 2016). However, ongoing viscoelastic deformation of the solid Earth in response to the evolving ice-water loads of glacial cycles is a global phenomenon and unfortunately cannot be avoided in this manner (Farrell & Clark, 1976). Although the most significant GIA-induced changes occur in the vicinity of glaciated regions, modeled present-day rates of vertical motion from the last glacial period are still $\pm 0.5 \text{ mm yr}^{-1}$ at far-field sites, which is an order of magnitude larger than typical rates expected for dynamic topography (Milne et al., 2001; Mitrović & Milne, 2002). Thankfully, the spatial pattern of GIA motions is well-understood and quite distinct from expectations for dynamic topography. Nevertheless, GIA models with highly accurate ice histories and viscoelastic mantle structure are essential before secondary signals associated with mantle convection might be reliably extracted. Obtaining such models is an area of considerable ongoing research (e.g., Whitehouse, 2018), and so GPS rates are yet to be exploited to constrain Earth's dynamic topography.

The second relevant satellite-derived observation is temporal evolution of the gravity field, which has been recorded by the GRACE mission over the period 2002–2017. This dataset has been successfully used to quantify mass changes associated with ice melting, hydrological cycles, and post-seismic deformation following large earthquakes (e.g., Shepherd et al., 2012; Crowley et al., 2006; Han et al., 2006; Chao & Liao, 2019). Mantle convection simulations predict associated long-wavelength changes in geoid height to occur at rates of $\sim 0.005 \text{ mm yr}^{-1}$, which is close to, but unfortunately just below the threshold of detection for GRACE (Ghelichkhan et al., 2018). Future gravity missions in the coming decade should lower this measurement threshold and potentially allow investigation of evolving dynamic topography, again provided that these signals can be successfully isolated from larger contributions associated with GIA and hydrology.

The great value of obtaining signals associated with evolving mantle convection from GPS and satellite-gravity is the high resolution spatial coverage afforded by these datasets. The limit for GPS comes down to on-the-ground station spacing, which in continental areas is easily shorter than the $\sim 500 \text{ km}$ length scales associated with dynamic topography. The horizontal resolution of satellite gravity depends both on flight path spacing and the orbital elevation, as short-wavelength signals attenuate more quickly with measurement height (Wahr et al., 1998). The $\sim 500 \text{ km}$ orbit height for GRACE and its follow-on missions should be sufficient for observing expected mantle

convection signals. However, the principal issue to date with both of these datasets is the short duration of their observation windows. Thus, long-term dynamic topography signals operating on million-year timescales are dwarfed by faster, shorter duration processes such as GIA and hydrologic cycles. In order to isolate changes caused by mantle convection, we must turn to longer-duration markers of vertical motion from the geological record.

15.5.2. Sea-Level Markers

The clearest elevation marker in the geological record is sea level, which marks a transition between the broadly erosive onshore regime and the predominantly depositional offshore environment. Morphological features such as wave-cut platforms, sea cliffs, marine terraces, and beach deposits form in a narrow palaeo-elevation band (Lyell, 1830). The same is true for biological markers such as coral reefs and other marine fauna that grow in shallow water (Darwin, 1842). Post-formation uplift or subsidence therefore yield measurements of the relative change of sea level with respect to land, and can be converted into rates of relative vertical motion providing that these features can be dated.

Some of the earliest and best constraints on long-term vertical motion of the continents have come from observations of exposed marine sediments. In a seminal paper, Bond (1978b) used the position of several Cretaceous, Eocene, and Miocene shorelines in different continents to constrain the extent of continental flooding at these times. In combination with the present-day distribution of topography within each continent (known as *hypsometry*), they were able to separate global variations in relative sea level seen simultaneously on all continents from local changes arising from differential vertical motions. Distinct subsidence and uplift events were indicated for Europe, Australia, North America, and Africa (Bond, 1978a, 1979). This approach was extended by Sahagian (1988), who considered nearshore or low-elevation sediments in addition to purely shoreline deposits in an attempt to reconstruct the full two-dimensional surface representing Cenomanian ($\sim 95 \text{ Ma}$) sea level in Africa. This surface is now locally warped by up to 3 km of topography, including a series of $\sim 800 \text{ km}$ diameter amagmatic and magmatic domes that are located far from recognized plate boundaries.

The first-order features of these global flooding and uplift histories have been successfully modeled using mantle convection simulations, as well as higher-level details in specific locations such as Australia, southeast Asia, and north Africa (Gurnis, 1993; Lithgow-Bertelloni & Gurnis, 1977; Heine et al., 2010; Matthews et al., 2011; Zahirovic et al., 2016; Barnett-Moore et al., 2017; Cao et al., 2019). One of the most iconic examples of dynamic topography controlling the distribution of stranded marine rocks occurs in North America. Here, $\sim 3 \text{ km}$ of

Late Cretaceous subsidence caused westward tilting of a 1400 km wide region and produced a marine depocenter, known as the Western Interior Seaway, that subsequently rebounded in Cenozoic times (Sloss, 1963; Bond, 1976). The gradual lateral thickening and widespread nature of these sediments rules out standard basin forming processes alone, such as rifting or flexural loading, instead necessitating dynamic drawdown above the eastward-subducting Farallon slab (Cross & Pilger, 1978; Mitrovica et al., 1989). The subsequent rebound is attributed to passage of North America over the shallower parts of the slab and eventually its rear edge, and the broad pattern and timing of sedimentation has been successfully matched by models of mantle flow (Mitrovica et al., 1989; Burgess et al., 1977; Liu et al., 2008; Spasojević et al., 2009).

It is important to consider a couple of significant caveats in interpretation of sea-level markers. One complication is that each marker only constrains the integrated uplift or subsidence since its time of formation. For example, a Cretaceous marine limestone found 500 m above modern sea level indicates a minimum of 500 m of cumulative uplift has occurred since Cretaceous times. The actual history of vertical motion may be substantially more complicated, consisting of a non-uniform uplift rate or even multiple cycles of uplift and subsidence (Roberts et al., 2018; Conway-Jones et al., 2019). For this reason, to place tighter constraints on the temporal evolution of vertical motion at a given location, a series of sea-level markers are desirable that have various ages and therefore cover a range of durations (e.g., Fernandes et al., 2019; Fernandes & Roberts, 2021).

A further issue is that there are variations in global mean sea level that are driven by changes in the volume of ocean basins and the mass of ice sheets through time. These processes will generate changes in eustatic sea level of up to ~300 m, even in locations where the solid Earth undergoes no vertical motion. For example, estimated eustatic variations resulting from variable sea-floor spreading rates and associated ocean volume changes are controversial but are believed to have amplitudes on the order of ± 100 m, based on analysis of both sea-floor age distributions and passive margin stratigraphy from ice-free periods such as the mid-Cretaceous (e.g., Rowley, 2002; Miller et al., 2005; Müller et al., 2008). Meanwhile, the total eustatic sea-level rise associated with ice melt between the last glacial maximum and today is ~130 m (e.g., Austermann et al., 2013). This is in addition to remaining present-day ice that is thought to have a volume equivalent to ~74 m of further eustatic sea-level rise when spread uniformly over the area of present-day oceans (Peltier et al., 2015). In the absence of tight constraints on sea level at time of formation, large-amplitude, long-duration recorders of relative vertical motion therefore yield dynamic topography rates that are the least affected by these eustatic uncertainties.

Over short timescales (durations less than ~3 Myr), the typical amplitude of dynamic topography change is expected to be outweighed by glacial isostatic effects. Despite this issue, however, the relative ubiquity and enhanced preservation of recent sea-level markers from Quaternary and Neogene interglacial periods has led to several attempts to extract elevation components associated with evolving dynamic topography. For example, dynamic topographic signals act in addition to GIA effects in warping Pliocene shorelines on the eastern US, southern African, and southern Australian coastlines (Moucha et al., 2008; Müller et al., 2008; Rowley et al., 2013; Flament et al., 2013; Rovere et al., 2014, 2015). In a global analysis, Austermann et al. (2017) found that this signal can also be detected in the elevations of shorelines from the last interglacial period (~125 ka), as has recently been confirmed in a local study from northern Madagascar (Stephenson et al., 2019). Concentrated investigation of continental margins exhibiting flights of marine terraces of variable age should greatly elucidate the temporal resolution and reduce uncertainties on uplift rate histories.

15.5.3. Sedimentary Flux and Stratal Architecture of Basins

Relative sea-level changes also influence the supply of clastic material into the offshore and the large-scale stratal architecture of sediments in basins. Pulses of high sedimentary flux occur at times of increased uplift, while topographic quiescence suppresses the supply of clastic material to river deltas, promoting the growth of carbonates (Lavie et al., 2001; Walford et al., 2005; Richards et al., 2016). Provided that the rules governing stratigraphic relationships can be understood, sedimentation patterns can be further used to investigate long-term vertical motion and infer evolving dynamic topography at sites of sediment deposition (e.g., Eakin & Lithgow-Bertelloni, 2018). Diagnostic stratigraphic patterns develop primarily in response to a competition between changes in the available accommodation space versus the rate at which sediment is supplied to infill (Beelen et al., 2019). This latter component leads to slightly different behavior in settings that are dominated by deposition of siliciclastic versus carbonate sediments.

In clastic systems, sedimentation is controlled by the external supply of material eroded onshore and transported by rivers. When influx is high, such as at large deltas, sediments infill available accommodation space up to wave base. If accommodation space remains constant, this results in *progradation*, as new material can only be deposited on the leading edge of the delta and the sedimentary packages build outward into more distal areas (Catuneanu, 2006). A relative drop in sea level also causes sediment depocenters to move further out into deeper

water, accompanied by erosion of older topset material that is now above wave base, and the development of unconformities with missing section. These features can be highly angular and often cover large areas of the basin or shelf. Significant examples from uplifting passive margins have been found off Angola, South Africa, and west India (Al-Hajri et al., 2009; Baby et al., 2018; Richards et al., 2016). Conversely, a relative sea-level rise increases accommodation space and produces *aggradation* as sediments build upward. The difference in sediment-starved settings is that insufficient material is available to infill this new space, resulting in a proximal shift of the depocenter known as *retrogradation*. Analysis of these cyclical sedimentation patterns is called *sequence stratigraphy* and has been used to produce histories of relative sea-level change at various passive margins (Vail et al., 1977; Haq et al., 1987; Miller et al., 2005).

The principal difference in carbonate settings is that sedimentary material is grown in situ by various marine organisms rather than supplied externally (N.B. influx of clastic material generally tends to inhibit carbonate production). Euphotic and oligophotic biota (e.g., corals, stromatolites, foraminifera, algae) create flat-topped shelves because they grow in the photic zone, with their depth extent depending on the penetration of sunlight (Pomar, 2001). In these settings, sediment supply rate is usually governed by the surface area of the shelf that occupies this photic zone. Stratal architectures associated with either constant or falling relative sea level are similar to clastic systems (Sarg, 1988). However, during increases in accommodation space, if growth rates cannot keep up with relative sea-level rise, entire carbonate platforms can become drowned (Kendall & Schlager, 1981). Such a process has been documented to have occurred at ~ 9 Ma across the entire Northwest Shelf of Australia (Czarnota et al., 2013). These sudden increases in accommodation space are sometimes associated with highstand carbonate shedding, whereby significant erosional channeling develops due to rapid vertical growth of platforms and reefs, as organisms try to keep up with the photic zone, leading to oversteepening and gravitational instability (Schlager et al., 2003). This is in contrast to clastic systems, where the formation of erosional gullies predominantly occurs during periods of low sea level.

One of the most striking manifestations of transient vertical motion occurs when shallow marine settings are uplifted above sea level and exposed to subaerial erosion, before subsiding back beneath the waves. This cycle results in ephemeral landscapes, whereby the initial marine sediments are often dissected by river channels, whose bases and deltas can contain terrestrial deposits such as coarse siliciclastics and coals, before a marine depositional setting is gradually restored. The height of any resulting valley incision places minimum bounds on

the amplitude of uplift, whilst biostratigraphic dating of fossils either side of the unconformity places tight book-ends on the event duration. Candidates for these landscapes have been observed in stratigraphy of the Grand Canyon in western USA, Bass Strait of Australia, and all across the North Atlantic region in the vicinity of the Icelandic plume (Billingsley & Beus, 1999; Holdgate et al., 2003; Underhill, 2001; Smallwood & Gill, 2002; Millett et al., 2016; Stucky de Quay et al., 2017). The most impressive of these occurs in the Faroe-Shetland Basin, where an Eocene uplift and subsidence event generated and infilled a fluvial landscape with ~ 1 km of topography over a period of only 3 Myr (Hartley et al., 2011). The amplitude of this event is significantly larger than glacial-eustatic sea-level cycles, whilst its transient nature rules out other geological mechanisms that would result in permanent uplift, such as crustal thickening or magmatic underplating. The inferred vertical motion rates of ~ 0.5 mm yr⁻¹ mark this landscape as one of the fastest examples of dynamic topography inferred from observational constraints. Furthermore, the rapidity of the subsidence phase rules out driving mechanisms involving the cooling of an asthenospheric temperature anomaly or thermal growth of the lithosphere (mechanisms *h* or *i* in Figure 15.1), as these processes operate on conductive timescales (at least 30 Myr for a 100 km thick layer of lithosphere or asthenosphere; McKenzie, 1978). Lateral advection of an asthenospheric temperature anomaly from the proto-Icelandic plume beneath the basin is most compatible with these constraints (mechanism *f* in Figure 15.1; Rudge et al., 2008). Observations of V-shaped ridges of thickened crust down the Reykjanes oceanic spreading center provide independent support for this Poiseuille-type flow within the Icelandic plume head (Vogt, 1971; Parnell-Turner et al., 2017).

15.5.4. Peneplanation and Palaeosurfaces

A distinct advantage of reconstructing vertical motions to infer changes in dynamic topography in regions of drawdown is that they tend to be dominated by sediment deposition, often leading to continuous subsidence records. Conversely, constraining histories of vertical motion in locations of dynamic uplift is often challenging, as subaerial erosion acts to destroy the geological record. Nevertheless, when early geomorphologists explored the interiors of supposedly tectonically quiescent continents such as Africa, they found evidence for 1000 km-scale doming of ancient erosional surfaces that appeared to be surprisingly youthful, based in part on the ages of overlying marine strata (e.g., King, 1942). Whilst controversial at the time, it is now generally accepted that this *basin-and-swell* morphology can be directly attributed to convective circulation of the underlying mantle, with

the clearest example of this expression occurring on the African continent (Burke & Gunnell, 2008; Moucha & Forte, 2011).

Stable continental interiors in both glaciated and non-glaciated areas often contain large, low relief surfaces that can be identified and mapped over large distances. These features are variably referred to as peneplains or pediplains and are attributed to former base levels at which erosion becomes negligible. Initially, the conceptual model of their formation involved a steady, simultaneous erosion of all hillslopes in a process analogous to diffusion (e.g., Davis, 1899, 1930). However, observed preservation of older relict surfaces in stepped terraces or isolated remnants, known as inselbergs and monadnocks, suggested that the dominant process is actually advective retreat of scarps, whereby erosion is concentrated in locations of steepest hillslope that backwear into the landscape (King, 1953).

The simplest interpretation is that these former base levels were in the vicinity of sea level at the time of their formation and were subsequently uplifted (King, 1962). At sea level, the potential energy of water is at a minimum and sediment transportation and deposition dominate, inhibiting further vertical erosion and promoting lateral mobility of river channels (Schumm, 1993). An important corollary is that the relative height above sea level or the elevation difference between two surfaces represents a discrete uplift event of this magnitude, from which a rate can be calculated if the surfaces can be dated.

In reality, understanding erosional surfaces can be substantially more complicated and the resulting interpretations more controversial (e.g., Pelletier, 2010). For example, obtaining absolute age measurements requires careful consideration of the geological processes involved. An erosional surface will cut across rocks of various ages, the youngest of which provides a maximum age for peneplanation. Volcanic material is often suitable for radiometric dating and so can be used in this way if it is eroded as part of the surface (e.g., Stanley & Flowers, 2016). Alternatively, lava flows can yield a minimum age if deposited unconformably on top of the erosion surface. The same is true for sedimentary rocks containing marker fossils that yield biostratigraphic ages. Some surfaces subsequently undergo intense chemical weathering, whereby all but the most immobile elements are leached away by groundwater to leave thick lateritic or bauxitic soils (e.g., Chowdhury et al., 1965). Associated precipitation of potassium-manganese oxides, such as cryptomelane, enables $^{40}\text{Ar}/^{39}\text{Ar}$ dating of these weathering events (e.g., Vasconcelos et al., 1992). Thus, a variety of measurements may be available that pre- and post-date the formation of erosional surfaces and thereby bracket their age. An added complication is that the escarpment retreat mechanism can generate diachronous dates across the surface (e.g., Stanley et al., 2015). Indeed, a second

uplift event may result in simultaneous erosion of two distinct elevation surfaces as their respective escarpments continue to back-wear. Finally, there is also significant debate over the mechanism of planation, including whether the postulated base level is sea level or whether surfaces can form *in situ* at higher elevations (e.g., Phillips, 2002; Clark et al., 2006; Yang et al., 2015; Chardon et al., 2016; Guillocheau et al., 2018). It is worth emphasizing that rock uplift can be driven by dynamic or tectonic uplift, but is amplified by any erosion and associated isostatic rebound (England & Molnar, 1990). Thus, care is required when using rock uplift rates to infer changes in dynamic topography (e.g., Richards et al., 2016).

Notwithstanding these complex issues, there are prominent planation surfaces bounded by great escarpments on most continents. Where these occur in the vicinity of coastlines, the approximation of base level representing sea level is likely to be valid and uplift histories can be inferred. The classic example is the so-called *African Surface*, which had formed as a result of erosion and extensive weathering by Oligocene times (~30 Ma), and has since been warped upward to form topographic domes and downward to form basins infilled with sediments (King, 1953; Burke & Gunnell, 2008). In northwest Africa, radiometric dating of laterites suggests that a series of stepped erosional surfaces were formed in discrete peneplanation events that have since been warped during growth of the Hoggar Dome (Chardon et al., 2006, 2016). Reinterpretation of the African surface by Guillocheau et al. (2018) suggests that there is actually a staircase of composite surfaces, dated using cross-cutting relationships, which document epeirogenic uplift of the basin and swell topography of central Africa since 30 Ma. Sembroni et al. (2016) reconstructed the basal and surface topography of flood basalts erupted from 40–20 Ma in Ethiopia to show that large-scale doming above the upwelling Afar plume both partially predated basalt emplacement, but has also continued to grow since.

A couple of important examples from other continents include a series of K-Mn oxides that reside on the coastal planation surface of western peninsular India and have been dated to Mid Eocene – Miocene times, (Beauvais et al., 2016; Bonnet et al., 2016). In light of independent evidence from margin stratigraphy, sea-level markers, and thermochronology, these ages have been interpreted by Richards et al. (2016) to indicate Neogene uplift and denudation of the Western Ghats escarpment. A set of three striking paleosurfaces in Greenland, which cut across a range of underlying formations, have been interpreted to represent discrete, kilometer-scale uplift events at ~60 Ma, 33 ± 3 Ma and 10–4 Ma, using a combination of thermochronologic and stratigraphic constraints (Japsen et al., 2006). The most important factor to bear in mind when interpreting the age of incision events is that erosion occurs

in response to uplift. As a result, the oldest geological evidence for incision dissecting an uplifted surface places a limit on the youngest possible age of the onset of uplift.

15.5.5. Landscape Denudation and Thermochronology

Prominent erosional surfaces are limited in spatial extent, and determining their absolute ages can be challenging. In the absence of these large-scale features, local constraints on the timing and magnitude of *denudation* (the amount of overburden stripped off) are still valuable for inferring changes in dynamic topography, as erosion is isostatically related to the amplitude of tectonic or dynamic uplift (England & Molnar, 1990; Brodie & White, 1994; Japsen et al., 2006; Łuszczak et al., 2018; Jess et al., 2018). In order to extract quantitative estimates of denudation, the last few decades have seen a proliferation of geochronologic techniques that exploit radioactive decay, either induced by bombardment of atoms by cosmogenic radiation or from spontaneous alpha, beta, and fission decay of radionuclides. Here, we briefly outline the principal techniques that are commonly used to constrain the temporal history of erosion and exposure on the 100 kyr to million-year timescales relevant to the study of dynamic topography.

Low-temperature thermochronology exploits temperature-dependent processes operating as a result of radioactive decay (Wagner, 1968; Gallagher et al., 1988; Reiners et al., 2005; Reiners & Brandon, 2006). First, parent radionuclides within a mineral undergo alpha- or beta-decay to produce a daughter according to a decay chain with a known half-life. The decay products subsequently diffuse through and out of the crystal lattice at a rate governed by the absolute temperature, which is commonly represented using an Arrhenius relationship, and effectively drops to zero below the *closure temperature* (e.g., Wolf et al., 1998; Farley, 2000; Harrison et al., 2009). Thus, the observed concentration of parent and daughter isotopes within the crystal volume is affected by the cooling history experienced by the host mineral. Techniques that exploit this effect include the (U-Th-Sm)/He system in apatite and zircon, $^{40}\text{Ar}/^{39}\text{Ar}$ in mica and feldspar, and the U-Pb system in a range of minerals (e.g., Farley, 2000; Harrison et al., 2009; Godin et al., 2001). Second, the much rarer spontaneous fission of naturally occurring heavy radionuclides (nearly exclusively ^{238}U) results in energetic ejection of two daughter nuclides, causing damage to the crystal lattice (fission tracks) that steadily anneal through time (Wagner, 1968). The healing rate of these fission tracks is temperature-dependent, such that the damage trails shorten as a function of both temperature and time following an empirically derived relationship (e.g., Green et al., 1985, 1986; Laslett et al., 1987; Ketcham et al., 1999, 2007). *Fission track analysis* therefore exploits

the distribution of track lengths, in combination with the absolute concentrations of fission tracks and parent isotopes, to constrain a mineral's thermal history (e.g., Gallagher, 1995; Ketcham, 2005; Gallagher, 2012).

Two commonly exploited low-temperature thermochronometers are the apatite fission track (AFT) system, which is sensitive to temperatures between 60–110 °C, and the apatite helium system (AHe or apatite (U-Th-Sm)/He), which is sensitive to temperatures between 40–70 °C (Wagner, 1968; Gleadow & Duddy, 1981; Gallagher et al., 1988; Farley, 2000, 2002; Reiners & Brandon, 2006; Ketcham et al., 2007). Inverse modeling of these thermochronologic data can approximate the thermal history experienced by a rock sample, which can be turned into an equivalent burial depth beneath the surface through time by applying an assumed geothermal gradient (e.g., Ketcham et al., 2007; Gallagher & Brown, 1999; Gallagher, 2012; Braun et al., 2013). The temperature sensitivity ranges of these two thermochronologic systems are such that, given standard continental geothermal gradients, they are able to constrain the burial and exhumation histories of the uppermost ~2–7 km of the crust. Application of such analyses to the problem of landscape denudation can bracket the timing of the onset of incision, peneplanation episodes, burial by sedimentary deposition, or active tectonic processes, all of which may be associated with regional epeirogenic uplift (e.g., Japsen et al., 2006; Stanley et al., 2015; Łuszczak et al., 2018; Wildman et al., 2016; Guillaume et al., 2013). Landscape evolution models indicate that the maximum magnitudes of denudation associated with dynamic topographic motions should be on the order of 2–3 km (e.g., Braun et al., 2013). In locations with typical geothermal profiles of 15–25 °C km⁻¹, these amplitudes place the AHe and AFT closure temperatures at the limits of resolution for samples found at the surface today. Current research is focused on exploiting alternative systems with lower closure temperatures, which should elucidate cooling histories and therefore denudation to within a few hundred meters of the surface. Such approaches include $^4\text{He}/^3\text{He}$ thermochronology, with a closure temperature around 30–40 °C (Shuster & Farley, 2004; Flowers & Farley, 2012).

Over shorter timescales, a widely used method to reconstruct recent rates of denudation is *cosmogenic exposure dating*. The Earth is continuously bombarded by cosmic rays sourced from the sun and outside the solar system, the majority of which are stopped in the atmosphere. The radiation that reaches the land surface is primarily composed of neutrons, which collide with atoms within the top ~2 m to produce cosmogenic isotopes, some of which undergo radioactive decay (Davis & Schaeffer, 1955; Lal & Peters, 1967). Provided that the production rate and half-life of these radionuclides is known, the

observed isotopic composition within a surficial sample can be inverted to estimate the time elapsed since its exposure. As well as depth-dependence, the production rate is also a function of latitude, elevation, geometry of surrounding topography, and mineral composition, which are the source of the principal uncertainties in these techniques. Due to high abundance of their parent nuclides in silicate minerals, the two most commonly exploited isotopes are ^{10}Be (produced from ^{16}O) and ^{26}Al (produced from ^{28}Si), with half-lives suitable for investigating landscape incision on hundred-thousand year timescales (Nishiizumi et al., 1993). Cosmogenic exposure dating has been widely used to obtain spot measurements of local incision rate, but can also be applied to estimate integrated erosion across an entire drainage catchment by analyzing the sediments carried within its rivers, provided that incision localization and hillslope processes are also carefully considered (Bierman & Steig, 1996; Codilean et al., 2018; Tofelde et al., 2018; Riley et al., 2019).

A final related technique that is commonly used in landscape evolution analysis is *optically stimulated luminescence*. In contrast to cosmogenic exposure dating, which constrains erosion rates, this approach can be used to date the time of sample burial and therefore age of landscape features. The method exploits the fact that the decay of radionuclides generates ionising radiation that causes a build up of charge within a feldspar or quartz crystal. This charge can either be released by heating the sample, or more commonly by exposure to solar radiation at the surface (Huntley et al., 1985). When sediments that were exposed to sunlight become buried by overlying material, this charge begins to accumulate, and can therefore be used to measure the time elapsed up to a maximum age of ~ 100 ka for quartz, beyond which charge traps become saturated (Aitken, 1998; Wallinga, 2002; Duller & Wintle, 2012). Sand deposited in fluvial or marine terraces is a common target for these studies. For example, terraces along the Angolan coast have been dated using this approach and indicate rapid Quaternary uplift rates of up to ~ 1.4 mm yr $^{-1}$ associated with growth of the Bié dome (Walker et al., 2016). Age overestimation is the principal issue in fluvial environments, where inadequate exposure to sunlight during transport can cause incomplete resetting of the accumulated charge (Wallinga, 2002).

A longstanding problem that inhibits our understanding of landscape denudation is the significant time gap between the 10^3 – 10^5 -year sensitivity of optically stimulated luminescence in quartz and cosmogenic exposure techniques, and the $>10^6$ -year sensitivity of existing thermochronologic approaches. Furthermore, the low amplitude of denudation in response to epeirogenic uplift requires sensitivity to low, upper crustal temperatures. Exciting new research is attempting to bridge these gaps by exploiting multi-optically stimulated luminescence

on feldspar and electron spin resonance as thermochronometers. These systems are potentially sensitive to ages back to ~ 1 Ma and to temperatures as low as 25°C , making them ideal for investigating shallow burial and exhumation histories (Guralnik et al., 2015; King et al., 2016; Bartz et al., 2018).

15.5.6. Drainage Analysis

The elevations of peneplains, paleosurfaces, marine rocks, and sea-level markers yield constraints on time-integrated uplift or subsidence since their formation, providing spot estimates of dynamic topography changes over specific time frames. Higher resolution spatio-temporal reconstructions are desirable, and require a more continuous record of evolving vertical motion. Drainage networks are a ubiquitous feature of terrestrial landscapes, and the elevation of river profiles along their lengths has long been known to record the interplay of uplift and erosion (Howard et al., 1994). Recent spectral analyses of African drainage patterns indicate that river elevation changes are dominated by power at wavelengths $\gtrsim 100$ km, suggesting that large coherent signals, such as regional uplift caused by dynamic topography, are potentially recoverable despite overprinting by shorter wavelength complexities, such as variations in lithology, precipitation and biota (Roberts, 2019; Roberts et al., 2019; Faccenna et al., 2019).

In order to extract quantitative information about the spatio-temporal history of vertical motions from fluvial landscapes, it is necessary to understand and parameterise the processes of erosion responsible for sculpting the observed remnant features. The early qualitative descriptions of peneplanation, river incision, and escarpment retreat have steadily transformed into mathematical formulations. Most models of fluvial erosion take the form of kinematic wave equations, and some also consider erosional *diffusion* (e.g., Luke, 1972; Howard & Kerby, 1983; Rosenbloom & Anderson, 1994; Whipple & Tucker, 1999). The phenomenological stream power erosional model, for example, relates the incision rate at any point on a river to its local slope, $\frac{\partial z}{\partial x}$, and upstream drainage area, A , which is a proxy for the water flux or stream discharge (Howard & Kerby, 1983). By parameterizing erosional processes, the change in elevation of any point on a river through time, $\frac{\partial z}{\partial t}$, can be written as a competition between the local uplift rate and erosion rate. Thus,

$$\frac{\partial z}{\partial t} = U - vA^m \left[\frac{\partial z}{\partial x} \right]^n + \kappa \frac{\partial^2 z}{\partial x^2} \quad (15.6)$$

where U is the rock uplift rate and v , m , n , and κ are erosional coefficients that include the effects of bedrock erodibility, precipitation, sediment cover, catchment shape, and channel geometry (Stock & Montgomery, 1999). All parameters could potentially vary as a function of

space and time. The advective erosional term (second on the righthand side) represents the back-wearing velocity of concavities known as *knickzones* as they retreat upstream, whilst the third term acts to smooth sharp changes in river slope in a process analogous to diffusion (Howard & Kerby, 1983; Rosenbloom & Anderson, 1994; Whipple & Tucker, 2002; Dietrich et al., 2003). In a simple sense, the river can be thought of as a tape recorder, where information about the history of regional uplift becomes stored within the fluvial landscape and can be extracted, provided that the erosion history can be reconstructed with sufficient accuracy (Pritchard et al., 2009).

Three main approaches have been developed to extract quantitative information about rock uplift histories using Equation (15.6) and the shape of observed river profiles. Each method has its own assumptions and limitations, and is variously championed or vilified within the geomorphological community. The first approach is *slope-area analysis*, which has been typically applied in small catchments draining across faults (e.g., Whipple, 2001; Schoenbohm et al., 2004). The key assumptions of this method are that each river is in steady state, such that uplift is balanced by erosion at all locations at any given time (i.e., $\frac{\partial z}{\partial t} = 0$), and that the diffusional term is negligible ($\kappa \frac{\partial^2 z}{\partial x^2} \rightarrow 0$ for a *detachment-limited* channel with little to no basal sediment cover). Incorporating these assumptions into Equation (15.6) and rearranging yields

$$\log \left[\frac{\partial z}{\partial x} \right] = -\frac{m}{n} \log [A] + \frac{1}{n} \log \left[\frac{U}{v} \right] \quad (15.7)$$

This formulation means that a logarithmic plot of local slope versus upstream drainage area for multiple points along the profile should have a slope of $-\frac{m}{n}$ and intercept of $\frac{1}{n} \log \left[\frac{U}{v} \right]$. In reality, these points often define multiple sets of linear arrays. Provided that v , m and n can be considered invariant for each linear trend, differences in the intercept can therefore be interpreted as variations in uplift rate along the river. The value of $\left(\frac{U}{v} \right)^{\frac{1}{n}}$ is referred to as the *channel steepness index*, k_s , which is a common proxy for uplift rate (e.g., Kirby & Whipple, 2001). Problematically, uplift rates that vary as a function of space and time can violate the steady-state assumption, resulting in transient changes in slope that do not reflect the value of U (e.g., Whittaker, 2012). The timing and spatial location of the formation of these transient knick-points trade-off, such that prior information on the spatial pattern of uplift (such as the locations of faults) is required for successful interpretation (Whipple &

Tucker, 2002; Whittaker et al., 2008; Pritchard et al., 2009; Whittaker, 2012). Furthermore, this approach involves differentiating profile elevation with respect to distance, and is therefore susceptible to amplification of noise present in the digital elevation model used to extract the river profile (e.g., Roberts et al., 2012b).

This noise issue can be suppressed by solving Equation (15.6) using an integrative approach (Luke, 1972; Weissel & Seidl, 1988; Pritchard et al., 2009). The most widely applied methodology was described by Perron & Royden (2013) and is known as *chi analysis*. Making the same assumptions concerning elevation steady state and absence of diffusional erosion, Equation (15.6) can be rearranged and integrated to give

$$z = z_{bl} + \left(\frac{U}{vA_0^m} \right)^{\frac{1}{n}} \int_{x_{bl}}^x \left(\frac{A_0}{A} \right)^{\frac{m}{n}} dx \quad (15.8)$$

where z_{bl} is the elevation of local base level, x_{bl} is the distance upstream that this base level extends from the river mouth, and A_0 is a reference drainage area introduced to force the integral term (referred to as χ) to have dimensions of length. By choosing values of m and n , χ can be calculated along the length of the river. Plots of elevation

as a function of χ should therefore have a slope of $\left(\frac{U}{vA_0^m} \right)^{\frac{1}{n}}$ (equivalent to the channel steepness index when $A_0 = 1 \text{ m}^2$), which yields values for uplift rate if v is independently known and upstream drainage area is assumed not to have varied through time (Perron & Royden, 2013; Willett et al., 2014; Yang et al., 2015). In addition to suppressing noise, another clear advantage of this approach over slope-area analysis is that this procedure of normalizing by the upstream drainage area makes transient uplift signals appear as discontinuities in elevation that stack at the same value of χ across multiple tributaries, thereby placing minimum constraints on how far downstream uplift signals must have been inserted. However, whilst transient uplift events that violate the steady-state elevation assumption can be identified using this approach, it remains challenging to extract continuous uplift histories at the regional to continental scales that are driven by dynamic topography.

A third, alternative methodology has been demonstrated by Roberts & White (2010), whereby Equation (15.6) is directly solved numerically in a forward sense, in response to a given uplift history. The observed shape of any real river profile can then be matched by inversion to find a best-fitting history of uplift. This approach avoids the steady-state elevation assumption and can include the term associated with diffusional erosion, but is substantially more computationally expensive. While v , m , n , κ and A could all potentially be varied through space and time, as with previous approaches, it

is necessary to fix these parameters to extract a unique history of uplift. Application of this method to individual African rivers suggests much of the continent's basin-and-swell topography grew during the Neogene period (Roberts & White, 2010). This initial study also assumed that the uplift rate was spatially invariant, with uplift events generating knickzones at the river mouth that propagate upstream. This setup is only applicable when the length of a river is small in comparison to the wavelength of uplift signals.

When uplift is also allowed to vary with distance along the profile, the trade-off returns between the location a signal is inserted on the river versus the time it has taken to retreat upstream. This issue has been tackled in two ways. First, damping parameters are applied that force the uplift history to be smooth as a function of space and time, consistent with expectations for uplift signals caused by dynamic topography. Second, multiple rivers in the region are simultaneously inverted. This step has the added bonus of emphasising signals that are coherent between different channels and catchments, therefore reducing the impact of local stream-capture events, lithological variation and fault-induced knickzones. The first such regional-scale spatio-temporal uplift history was obtained for Madagascar, where ~ 1.5 km of uplift was inferred to have occurred since 20 Ma at rates of $0.2\text{--}0.4$ mm yr⁻¹ (Roberts et al., 2012a). Importantly, summing up incision rates across catchments also yields simple estimates of the sedimentary flux carried by rivers into deltas. Observed histories of solid clastic flux into both the Gulf of Mexico and Amazon Cone have been successfully predicted by this methodology, suggesting that regional uplift is a primary control on sedimentation in major deltas (Stephenson et al., 2014; Rodríguez Trialdos et al., 2017).

It is important to note that these continental-scale histories of uplift depend fundamentally on the erosion parameters assumed in Equation (15.6), requiring careful calibration against independent constraints on uplift and incision, such as the aforementioned sea-level markers, denudation estimates, and sedimentary flux histories. One of the tightest examples of calibration comes from the Snowy Mountains of southeast Australia, where a series of basaltic lavas flowed down river valleys and recorded the shape of the profiles at 20 Ma, yielding measurements of total incision over the intervening period by comparison to the modern channel elevation (Young & McDougall, 1993). These data have been modeled using Equation (15.6) to constrain the best-fitting local erosion parameters and explore their trade-offs, before being extended to drainage analysis of the full Australian continent (Stock & Montgomery, 1999; Czarnota et al., 2014).

This Australian example illustrates the great benefit of drainage analysis, in that disparate and diverse spot

observations of uplift and incision are interpolated through space and time within a self-consistent framework. However, several major issues remain that must be considered when interpreting the validity of inferred uplift histories. For example, the computational efficiency and number of river profiles analyzed can be significantly increased by assuming that $\kappa = 0$ and $n = 1$, allowing Equation (15.6) to be linearized (Goren et al., 2014; Fox et al., 2014; Rudge et al., 2015). However, considerable debate surrounds these assumptions and the possibility of spatio-temporal variability of erosional parameters in response to variations in climate and bedrock lithology. The methods outlined so far generally assume that the locations of drainage basins are static and that there are minimal changes in upstream drainage area arising from capture events and stream piracy. They also ignore the effects of subsidence and sedimentation, assume channels have fixed locations, and are highly dependent on water discharge and sedimentary flux, both of which can vary by more than an order of magnitude (e.g., Sklar & Dietrich, 2001; Bufe et al., 2016). Furthermore, although river profiles can provide an important continuous record of uplift, they constitute only a small proportion of the landscape. The majority of the land surface resides on hillslopes, interfluves, and plateaux, and it is increasingly being recognized that the interplay of these settings and the fluvial channels in response to long-wavelength uplift is important in controlling erosional processes (e.g., Fernandes & Dietrich, 1997; Tucker & Hancock, 2010; Braun et al., 2013).

Naturalistic full-landscape evolution simulations are able to calculate erosion rates across whole landscapes in response to a given uplift history, not just within the fluvial channels, by solving Equation (15.6) in two dimensions (e.g., Tucker et al., 2001; Salles & Hardiman, 2016; Hobbey et al., 2017). Unfortunately, significant trade-offs exist between erosional parameters, such that inverse modeling of entire landscapes including hillslope processes, drainage capture, and both channel and divide migration remains challenging. Nevertheless, a number of studies have hinted at the new information such simulations can provide about continental-scale uplift and sedimentation patterns (e.g., Ruetenik et al., 2016; Salles et al., 2017; Chang & Liu, 2019; Ding et al., 2019). For example, simulations have suggested that uplift histories recovered from inverse modeling river profiles are consistent with observed regional erosional histories (Fernandes et al., 2019). The effects of climatic variations on the ability of river profiles to recover long-wavelength uplift histories are also being investigated (O'Malley et al., 2021, in review). The complex and relatively underexplored series of trade-offs between different erosional parameters and the choice of damping coefficients used in inverse schemes has also been tested (Croissant & Braun 2014; McNab

et al., 2018). Thus, suites of independent measurements of uplift and incision constrained with available morphologic and stratigraphic observations are essential for advancing these promising early results and inferring the temporal evolution of continental dynamic topography.

15.5.7. Paleoaltimetry

Many inferences of the temporal evolution of dynamic topography rely on sea level as a geological marker to reconstruct relative vertical motions. There are, however, a couple of alternative techniques that exploit physical or biological processes that change as a function of increasing elevation. Although these approaches remain underutilized from the perspective of dynamic topography, they are being actively explored and represent promising avenues for future studies.

First, it has long been recognized that temperature influences the fractionation of isotopes in some near-surface geological processes (Urey, 1947; McCrea, 1950). Since the temperature of the atmosphere steadily decreases with increasing elevation, variations in the isotopic composition of a sample can be converted into a paleo-temperature history and therefore used as a proxy for paleo-elevation (e.g., Poage & Chamberlain, 2001; Rowley & Garzzone, 2007; Eiler, 2007). For example, during formation of a calcium carbonate shell (CaCO_3), the ratio of ^{18}O to ^{16}O (often presented as $\delta^{18}\text{O}$) depends both on the temperature at time of mineral precipitation and the isotopic composition of the solution from which it forms (Emiliani, 1950). If the composition of the mineralizing fluid can be independently constrained, the inferred temperature can be converted into a paleo-elevation at formation using an assumed vertical temperature gradient. This technique relies on accurate reconstruction of the average atmospheric temperature gradient, which has a present-day global average reduction of ~ 5.5 °C per kilometer of increasing elevation, but can locally vary from $3\text{--}8$ °C km^{-1} (Meyer, 2007).

Unfortunately, changes in global ice volume, seawater salinity, and hydrological cycles lead to significant uncertainty in reconstructing original fluid compositions that limit the accuracy of inferred paleo-elevations. It is, therefore, desirable to use an approach that is independent of fluid composition, allowing this major weakness to be circumvented. To this end, Ghosh et al. (2006a) developed a method that exploits the small thermodynamic inclination for the rarer heavier isotopes to clump preferentially together with each other, rather than bond with the lighter isotopes. Given their relative isotopic abundances, the number of $^{13}\text{C}\text{--}^{18}\text{O}$ bonds will be higher than expected from a stochastic (random) distribution of C–O bonds,

and the amount of this “clumping” increases at lower temperature. This process is independent of $\delta^{18}\text{O}$ and $\delta^{13}\text{C}$ (^{13}C to ^{12}C) values, and so does not depend on original fluid compositions. The technique is known as *clumped isotope paleothermometry*, has an accuracy of approximately ± 2 °C, and has been most successfully applied to study uplift histories of mountain belts that have undergone large elevation changes, where the uncertainty introduced by natural variability in the vertical temperature gradient is minimized. For example, analysis of paleosol carbonates in the Bolivian Andes records a series of discrete ~ 1 km Miocene uplift events that have been independently predicted using drainage analysis (Ghosh et al., 2006b; Garzzone et al., 2014; Rodríguez Tribaldos et al., 2017).

Despite some success, paleoaltimetric estimates derived from analysis of clumped isotopes remain controversial for a variety of reasons. Care must be taken in cases where carbonate precipitation did not occur at thermodynamic equilibrium, or where the original isotopic signal has been modified by diagenetic alteration and mineral reprecipitation (Affek, 2012). Furthermore, lateral temperature differences and climate variability introduce significant uncertainty into the temperature–elevation relationships (Huntington & Lechler, 2015).

A second branch of paleoaltimetric techniques exploit the impact of increasing elevation on biological systems. For example, there is a systematic reduction in the partial pressure of CO_2 ($p\text{CO}_2$) with height in the atmosphere, which is thought to place a physiological limit on photosynthesis in plants. Various elevation proxies have been suggested that involve interpreting compensating changes in leaf shape, and have been applied to fossil assemblages to infer uplift histories (e.g., Gregory & Chase, 1992; Wolfe et al., 1997). Another promising approach takes advantage of the increasing number and density of stomata on leaves, with particular emphasis on the black oak species *Quercus kelloggii*, which is expected to yield some of the smallest paleo-elevation uncertainties of ± 300 m (McElwain, 2004). Since the elevation versus stomatal density relationship varies between different species, application to paleoaltimetric studies requires calibration on living examples and is therefore limited to Eocene and younger fossil leaves that are represented by extant flora today. Additional limitations of the method include the possibility of saturation of stomatal density at high values of $p\text{CO}_2$, and the narrow elevation range of most species that reduces calibration accuracy and the magnitude of uplift events that can be reconstructed. Nevertheless, paleoaltimetric techniques have the potential to yield inferences of changing dynamic topography at sites that have not been directly influenced by sea level, such as in mountain belts and deep continental interiors (e.g. Huyghe et al., 2020).

Table 15.1 Summary of techniques available for inferring changes in dynamic topography, including approximate timescales for which they yield information, key benefits, and important limitations.

Technique	Timescale (yr)	Benefits	Limitations
GPS	Present day	Measures absolute vertical motion of surface w.r.t. center of mass, rather than relative sea-level change	Decadal duration means convection signals swamped by glacial isostatic adjustment, hydrology, active tectonics
Satellite gravity	Present day	Complete, time-evolving global coverage	Decadal duration means convection signals swamped by glacial isostatic adjustment, hydrology, active tectonics
Sea-level markers	10^4 – 10^8 +	Direct evidence of relative vertical motion, narrow paleoelevation range	Dating limitations, restricted spatial extent and poor preservation potential, yields only time-integrated vertical motion histories
Sedimentary flux and provenance	10^6 – 10^9 +	Timing of major exhumation events and drainage reorganizations	Poor constraint on magnitude of uplift, causes can also be other tectonic and climatic processes
Stratigraphic architecture	10^5 – 10^8 +	Deep time records, widespread, well preserved	Requires amplitudes of relative motion greater than paleowater depth uncertainties, borehole samples necessary for horizon dating
Paleosurfaces	10^6 – 10^8 +	Extensive coverage of continental interiors	Challenging to date, base levels may not represent sea level
Thermochronology	10^6 – 10^8 +	Continuous, quantitative histories of sample temperature	Depends on mineralogy/lithology, uncertainty over kinetics, paleogeothermal gradients, and how to infer uplift from denudation, currently insensitive to temperatures $<60^\circ\text{C}$
Cosmogenic exposure dating	10^4 – 10^5	Dates precise time of sample exposure	Production rate of radionuclides poorly constrained as depends on several unknowns, uncertainty in relating exposure to history of vertical motions, currently limited to $\sim 10^5$ yr timescales
Optically stimulated luminescence	10^4 – 10^5	Dates sample burial and age of landscape features, useful where no biological material for radiometric dating	Potentially incomplete resetting during exposure, saturation of charge traps beyond ~ 100 ka for quartz
Drainage analysis	10^5 – 10^7 +	Nearly ubiquitous in the continents, continuous temporal record of relative vertical motion	Erosion parameterizations require independent data for calibration, trade-offs between location and timing of uplift events, duration limited by river lengths, sensitive to climatic variations and potential drainage capture events, subsidence poorly constrained
Clumped isotopes	10^5 – 10^8 +	Sensitive to relative changes in sea level even away from coastal areas, such as in mountainous regions and continental interiors	Uncertainty over paleoatmospheric temperature gradient necessitates high amplitude of relative vertical motion change, diagenetic alteration of isotopic ratios
Leaf physiognomy	10^6 – 10^7 +	Sensitive to relative changes in sea level even away from coastal areas, such as in mountainous regions and continental interiors	Limited preservation potential, requires calibration on extant fauna (limits to Eocene or younger), sensitive to climatic factors, high paleoelevation uncertainties
Carbonate compensation depth	10^6 – 10^8	Sensitive to relative sea-level changes in the deep ocean basins	Also affected by sediment accumulation rates and the chemistry of deep ocean waters, limited by deep sea borehole locations and age of ocean floor
Contourites and ocean circulation	10^5 – 10^7 +	Sensitive to relative sea-level changes in the ocean basins	Difficulty fingerprinting water masses, accurately reconstructing sedimentation rates, and ruling out other climatic causes

15.5.8. Bathymetric Indicators

Given that it covers more than two-thirds of the Earth's surface, it would be highly desirable to obtain reconstructions of evolving vertical motion in the oceanic realm. Transient ~ 1 km uplift and subsidence events associated with dynamic topography might be expected to have little to no visible record on old ocean floor, the majority of which resides at depths of 4–7 km. However, it has recently been suggested that such signals may be preserved in the style of sedimentation, as seafloor rises above and sinks below a paleobathymetric marker known as the *carbonate compensation depth* (CCD; Campbell et al., 2018). The existence of the CCD was first postulated based on the general decrease in the quantity of carbonate observed in seafloor sediments as a function of increasing water depth (Murray & Renard, 1891). Above the CCD, seawater is oversaturated with carbonate such that biological material (such as dead plankton) can sink to the seafloor and become preserved, whereas below this level, seawater is undersaturated and any sinking carbonate is redissolved (Ben-Yaakov et al., 1974). Temporal variations in the carbonate content of sediments returned from deep-sea drill cores can therefore potentially be used to infer bathymetric evolution. However, the absolute depth of the CCD also varies as a function of factors affecting both carbonate accumulation rates (e.g., primary productivity in surface waters) and the chemistry of deep ocean waters (e.g., concentration of dissolved carbon dioxide), making the isolation of dynamic topography signals a significant ongoing challenge (Campbell et al., 2018).

Elsewhere, it has been suggested that uplift and subsidence of oceanic gateways can impact the pattern of oceanic circulation, with deep water currents shifting their location or even becoming blocked. The type example comes from the North Atlantic region, where periodic Neogene uplift of the Greenland-Scotland Ridge by temperature anomalies within the Icelandic plume is believed to have prevented overflow of Northern Component Water from the Arctic Ocean (Wright & Miller, 1996). Analysis of carbon isotopes in benthic foraminifera indicates up to two cycles of waxing and waning overflow within the last 10 Ma, subject to significant uncertainties related to site selection and variations in the location and composition of water masses through time (Poore et al., 2006). The latter of these cycles has been partially corroborated by careful reconstruction of sedimentation rates in the contourite drifts deposited by these currents (Parnell-Turner et al., 2015).

Despite these advances, there remains a paucity of constraints on the temporal evolution of dynamic topography in oceanic settings in comparison to continental observations. This situation is in marked contrast to information regarding the amplitude of present-day dynamic topography, which is comparatively well-constrained in the

oceanic realm but remains highly uncertain for the continents. This discrepancy highlights the importance of passive margins to studies of dynamic topography (e.g., Moucha et al., 2008). In these locations, the benefits of observations made in both marine and terrestrial settings can be interwoven to reconstruct both the present amplitude and history of vertical motions.

15.6. FRONTIERS AND OUTSTANDING CHALLENGES

It is clear that the geological record contains abundant recorders of evolving dynamic topography, but a significant challenge remains in extracting the necessary measurements with associated uncertainties, integrating diverse observational datasets, and interpreting the results. This review is focused on providing brief overviews of some of the most widely used techniques for estimating vertical motions and discussing some of their limitations (see Table 15.1 for summary). It is by no means an exhaustive list, and there are many excellent preexisting and exciting upcoming studies that provide complimentary constraints (e.g., Friedrich et al., 2018; Vibe et al., 2018; Hayek et al., 2020). In order to motivate future research and promote interdisciplinary discussions, we finish by outlining some outstanding methodological issues that need to be tackled, as well as some of the big open questions that remain in the field of dynamic topography.

15.6.1. Continental Residual Topography

As illustrated by our simplistic approach in Section 15.4.2, the complex lithospheric architecture of continental regions and active margins significantly hampers attempts to constrain the present-day amplitude of dynamic topography (Guerra et al., 2016). Dynamic topography arising from density anomalies and flow within the convecting mantle (processes *b* and *c* in Figure 15.1) should be relatively insensitive to whether the overlying plate is composed of oceanic or continental lithosphere. Thus, peak water-loaded amplitudes of ± 2 km in the oceans might be expected to roughly translate into ± 1.4 km when air-loaded in the continents. However, this conversion does not include dynamic topography arising from lithospheric isostasy (process *a* in Figure 15.1), which may be substantially larger than in oceanic regions due to the generally greater thickness and age of continental lithosphere, and is certainly harder to determine. Regional seismic experiments are key to constraining the local lithospheric structure, and understanding the effects of buoyancy arising from variable chemical depletion in the mantle requires integration of these datasets with geochemical observations on mantle

xenoliths and melt products (e.g., Afonso et al., 2016; Plank & Forsyth, 2016; Klöcking et al., 2018; Celli et al., 2020; Klöcking et al., 2020). Furthermore, the filtering effect of the lithosphere on the expression of deeper buoyancy remains poorly understood (Golle et al., 2012; Sembroni et al., 2017).

15.6.2. Integrated Landscape Evolution Analysis

In Section 15.5, we outline the great wealth of information from disparate sources pertaining to the uplift and erosion of landscapes. A substantial challenge involves integrating these datasets into a single coherent history of rock uplift and incision, which must also account for thermal evolution of the sub-surface if thermochronological data are to be included (e.g., Glotzbach, 2015). The development of thermochronometric systems that are sensitive to lower temperatures is expected to enable detection of denudation related to low-amplitude dynamic topography. This work will be aided by improved understanding of the dominant erosional processes, their mathematical formulation, and sensitivity analysis to test how well they are represented by the relatively simplistic vertical incision laws currently used to invert fluvial systems for a history of regional uplift (Section 15.5.6).

15.6.3. Spectral Properties of Dynamic Topography

Many predictive models driven by sub-lithospheric flow, such as Figure 15.4c, indicate that dynamic topography is dominated by spherical harmonic degree-2 structure that varies on 10,000 km lengthscales. However, residual topography suggests dynamic topography can vary on lengthscales down to 1000 km (Figure 15.5; Hoggard et al., 2016). These shorter-wavelength features must be sourced from shallow buoyancy structure, either within the convecting asthenospheric mantle or from variations in lithospheric thickness, and disentangling these two sources is the focus on ongoing research (e.g., Ball et al., 2019; Davies et al., 2019; Richards et al., 2020b; Lamb et al., 2020). Nevertheless, this discovery has important ramifications for the rates of change of dynamic topography. While lithospheric isostasy will travel with the plates, surface deflections arising from short-wavelength buoyancy variations in the convecting mantle (processes *b* and *c* in Figure 15.1) will uplift and subside significantly faster than previously expected as the planform of convection evolves or plates translate across the surface. Recent numerical simulations of Earth-like convection have also begun to reproduce this behavior (Arnould et al., 2018). Attempts to link inferred observations of dynamic topography to our latest images of mantle structure obtained from modern seismic tomography methods are proving fruitful (e.g., Steinberger, 2016). Higher-resolution tomography models combined

with improved experimental constraints on how to map seismic velocities into temperature and density should help to further illuminate this issue (e.g., Priestley & McKenzie, 2013; Yamauchi & Takei, 2016; Richards et al., 2020b).

A more controversial topic concerns the amplitude of dynamic topography caused by sub-plate buoyancy at long wavelengths (processes *b* and *c* in Figure 15.1). The earliest predictive flow models had peak amplitudes of ± 0.9 km at spherical harmonic degrees 0–3 (wavelengths $\gtrsim 10,000$ km; Figure 15.4c; Hager et al., 1985; Ricard et al., 1993). Notably, predictions of this amplitude generally increased over the following 20 years (e.g., ± 2.0 km in Steinberger, 2007; ± 2.2 km in Spasojević & Gurnis, 2012; ± 1.7 km in Flament et al., 2013). However, Hoggard et al. (2016) suggested that spot estimates of residual topography, water-loaded in the oceans and air-loaded in the continents, infer only ± 0.5 km of this dynamic topography at degrees 0–3. Sparse data coverage means that this exact value depends on the choice of continental constraints and how the spherical harmonic fitting procedure is regularized (Hoggard et al., 2016; Yang & Gurnis, 2016; Hoggard et al., 2017; Yang et al., 2017). Inclusion of a previously missing residual topography correction that accounts for deflections of the sea surface by the non-hydrostatic geoid increases peak amplitudes by ~ 100 m (Hoggard et al., 2017). Applying a more advanced regularization procedure to only the oceanic constraints has yielded the most robust observationally inferred value to date of ± 0.7 km, although this amplitude assumes a global water-load such that continental values have been amplified in comparison to other residual topography studies (Davies et al., 2019). Amplitudes of ± 0.5 km at long wavelengths have also been shown to be consistent with patterns of asymmetric subsidence either side of Atlantic and Pacific mid-ocean ridge spreading centers (Watkins & Conard, 2018). Thus, there appears to remain an intriguing mismatch between observational inferences and flow predictions of long-wavelength dynamic topography caused by sub-plate buoyancy, requiring further exploration of seismic tomography to density scalings, phase boundary topography, thermochemical heterogeneity and viscosity variations in the mantle, as well as theoretical assumptions in convection simulations (Steinberger et al., 2019; Flament, 2019).

15.6.4. Flow Regime in the Asthenosphere

Considerable uncertainty surrounds the degree of coupling between plate motions and horizontal flow in the underlying asthenosphere. In one endmember scenario known as *Couette flow*, translation of the plate shears the asthenosphere, which therefore travels in the same

direction with a velocity profile that decreases from the plate speed at the top to zero at some base. The other end member is *Poiseuille flow*, whereby lateral pressure gradients in an asthenospheric channel drive horizontal flow that is significantly faster and can be highly oblique to velocities of the overriding plate. Numerical experiments have shown that these behaviors are strongly dependent on the rheology of the lithosphere and asthenosphere, as well as the wavelength of convection (e.g., Höink & Lenardic, 2010; Osei Tutu et al., 2018). The fact that convection simulations using mantle density anomalies derived from either seismic tomography or slab subduction histories can successfully reproduce the first-order characteristics of surface plate motions implies a degree of coupling between deep mantle flow and plates (Hager & Connell, 1981; Lithgow-Bertelloni & Richards, 1998; Conrad et al., 2013; Stotz et al., 2018). However, observational evidence, particularly in the vicinity of plumes such as the V-shaped ridges south of Iceland, indicate flow can locally be strongly decoupled, with asthenospheric velocities an order of magnitude faster than plate spreading (Vogt, 1971; Conder et al., 2002; Hartley et al., 2011; Ballmer et al., 2013; Lin et al., 2016; Bredow et al., 2017).

Flow regimes are highly sensitive to the rheology of mantle rocks, and these somewhat contrasting observations may potentially be reconciled if viscosity is strongly controlled by temperature, such that hot plume head material in the asthenosphere produces more decoupling than the longer-wavelength, cold downwellings. A further consideration is that these flow regimes interact with basal topography of the lithosphere, which can lead to small-scale circulation across lithospheric steps through edge-driven convection and shear-driven upwelling (Elder, 1976; King & Anderson, 1998; Conrad et al., 2010; Ballmer et al., 2015).

One approach for investigating the role of these different flow regimes in generating dynamic topography involves comparing and contrasting patterns and rates of change in vertical motion on fast- versus slow-moving plates. Africa is relatively stationary with respect to the underlying mantle, whereas Australia is traveling rapidly northward and transits across the top of the mantle flow field (Burke & Gunnell, 2008; Sandiford, 2007). The former should therefore predominantly record temporal evolution of the underlying convective planform, whilst the latter will also be sensitive to differential plate translation (mechanism *d* in Figure 15.1) and variations in edge-related flow on the leading and trailing portions of thick lithosphere (e.g., Davies & Rawlinson, 2014). An important caveat to consider in these analyses is that numerical models and laboratory convection experiments have shown that the surface expression of basal stresses caused by mantle flow is strongly modulated by the rheology of the lithosphere, including its effective elastic

thickness and any viscosity layering (Burov & Gerya, 2014; Sembroni et al., 2017).

15.6.5. Numerical Convection Models and Rheology of the Upper Mantle

New insights into dynamic topography and subsurface processes will come from high-resolution numerical experiments that can incorporate realistic physical processes, such as plate-like behavior, by introducing additional model complexity. Examples of such properties include the highly heterogeneous composition of the mantle, viscoelastic rheologies, temporal evolution of grain size, the effects of latent heat, porous flow, full compressibility, and inclusion of thermodynamically self-consistent mineralogical properties, all of which must be captured at the necessary spatial resolution using techniques such as adaptive mesh refinement (e.g., Burstedde et al., 2013; Wilson et al., 2017; Heister et al., 2017; Dannberg et al., 2017; Patočka et al., 2019; Flament, 2019). Uncertainties in input rheological parameters in particular remain a major challenge in predictive flow models.

One approach to overcoming this limitation is improving rheological constraints on mantle materials using laboratory experiments. The dominant mechanism of crystal lattice deformation varies strongly as a function of properties such as the strain rate, temperature, and grain size. Effects of polycrystalline materials, anisotropic viscosity, and the time-dependent accumulation of damage and healing are underexplored (Zhao et al., 2018; Wheeler, 2010; Bercovici & Ricard, 2014). Furthermore, applying the results of lab experiments to mantle conditions necessarily requires extrapolation across many orders of magnitude for properties such as the strain rate or grain size, and associated uncertainties need to be carefully considered (Jackson & Faul, 2010; Yamauchi & Takei, 2016; Richards et al., 2018).

A second approach to improving our understanding of mantle rheology is to use observational inferences of dynamic topography as constraints in numerical convection simulations. Data assimilation methods that have been explored include machine-learning schemes (Atkins et al., 2016; Shahnas et al., 2018), adjoint-based inversions (Liu et al., 2008; Worthen et al., 2014; Ratnaswamy et al., 2015; Li et al., 2017), and conjugate direction misfit minimization (Yang & Gurnis, 2016). Studies vary not only in inversion scheme but also in model complexity and choice of surface observations. In general, inversions for realistic Earth-like properties remain computationally expensive and non-unique due to trade-offs between parameters (e.g., rheology versus buoyancy). This problem highlights the immense value of placing observational constraints on the amplitude and rate of change of dynamic topography, necessitating a thorough

assessment of the geological record and its associated uncertainties using techniques outlined in this review.

15.7. SUMMARY

In summary, observational estimates of present-day dynamic topography and its evolution through space and time provide a unique window into processes operating in the Earth's interior. In turn, convection simulations that can accurately satisfy available constraints on dynamic topography will yield predictive insights into previous Earth states. This interdisciplinary review reflects our increasing understanding of the influence of dynamic topography in shaping the rock record, which has important implications for volcanic systems, oceanic circulation, ice sheet dynamics, and interpretation of paleoclimatic records (e.g., Mitrovica et al., 2020). Improving observational, computational, and theoretical constraints on mantle convection is therefore a fundamental goal of our community, with important ramifications for many areas of Earth sciences.

ACKNOWLEDGMENTS

Acknowledgment is made to the Donors of the American Chemical Society Petroleum Research Fund (59062-DNI8) for partial support of this research. We thank editor Maxim Ballmer for his patience and comments, Bernhard Steinberger and Walter Mooney for sharing datasets, and Terry Plank for inspiring Figure 15.1. Aaron Bufe, Karol Czarnota, Tyler Mackey, Fergus McNab, Dorothy Peteet, Evelyn Powell, Fred Richards, and Gareth Roberts generously read early versions of the manuscript and provided feedback. Nicolas Flament and an anonymous reviewer wrote detailed and comprehensive reviews. We thank the Computational Infrastructure for Geodynamics (geodynamics.org), which is funded by the National Science Foundation under award EAR-0949446 and EAR-1550901, for supporting the development of ASPECT. We acknowledge computing resources from Columbia University's Shared Research Computing Facility project, which is supported by NIH Research Facility Improvement Grant 1G20RR030893-01, and associated funds from the New York State Empire State Development, Division of Science Technology and Innovation (NYSTAR) Contract C090171, both awarded April 15th, 2010. Digital copies of the dynamic topography simulations and ASPECT initialisation files are available on the accompanying OSF database (<https://osf.io/u86ny>).

REFERENCES

Affek, H. P. (2012). Clumped isotope paleothermometry: Principles, applications, and challenges. *The Paleontological Society Papers*, 18, 101–114.

Afonso, J. C., N. Rawlinson, Y. Yang, D. L. Schutt, A. G. Jones, J. Fulla, & W. L. Griffin (2016). 3-D multiobservable probabilistic inversion for the compositional and thermal structure of the lithosphere and upper mantle: III. Thermochemical tomography in the Western-Central U.S. *Journal of Geophysical Research: Solid Earth*, 121, 7337–7370.

Afonso, J. C., F. Salajegheh, W. Szwilius, J. Ebbing, & C. Gaina (2019). A global reference model of the lithosphere and upper mantle from joint inversion and analysis of multiple data sets. *Geophysical Journal International*, 217, 1602–1628.

Aitken, M. J. (1998). *An introduction to optical dating: The dating of Quaternary sediments by the use of photon-stimulated luminescence*. Oxford University Press, Oxford.

Al-Hajri, Y., N. J. White, & S. Fishwick (2009). Scales of transient convective support beneath Africa. *Geology*, 37 (10), 883–886.

Anderson, D. L. (1982). Hotspots, polar wander, Mesozoic convection and the geoid. *Nature*, 297, 391–393.

Arnould, M., N. Coltice, N. Flament, V. Seigneur, & R. D. Müller (2018). On the scales of dynamic topography in whole-mantle convection models. *Geochemistry, Geophysics, Geosystems*, 19, 3140–3163.

Atkins, S., A. P. Valentine, P. J. Tackley, & J. Trampert (2016). Using pattern recognition to infer parameters governing mantle convection. *Physics of the Earth and Planetary Interiors*, 257, 171–186.

Austermann, J. & J. X. Mitrovica (2015). Calculating gravitationally self-consistent sea level changes driven by dynamic topography. *Geophysical Journal International*, 203, 1909–1922.

Austermann, J., J. X. Mitrovica, P. Huybers, & A. Rovere (2017). Detection of a dynamic topography signal in last interglacial sea-level records. *Science Advances*, 3 (7).

Austermann, J., J. X. Mitrovica, K. Latychev, & G. A. Milne (2013). Barbados-based estimate of ice volume at Last Glacial Maximum affected by subducted plate. *Nature Geoscience*, 6, 553–557.

Austermann, J., D. Pollard, J. X. Mitrovica, R. Moucha, A. M. Forte, R. M. DeConto, D. B. Rowley, & M. E. Raymo (2015). The impact of dynamic topography change on Antarctic ice sheet stability during the mid-Pliocene warm period. *Geology*, 43 (10), 927–930.

Baby, G., F. Guillocheau, J. Morin, J. Ressonche, C. Robin, O. Broucke, & M. Dall'Asta (2018). Post-rift stratigraphic evolution of the Atlantic margin of Namibia and South Africa: Implications for the vertical movements of the margin and the uplift history of the South African Plateau. *Marine and Petroleum Geology*, 97, 169–191.

Balachandar, S., D. A. Yuen, & D. Reuteler (1992). Time-dependent three dimensional compressible convection with depth-dependent properties. *Geophysical Research Letters*, 19 (22), 2247–2250.

Ball, P. W., N. J. White, A. Masoud, S. Nixon, et al. (2019). Quantifying asthenospheric and lithospheric controls on mafic magmatism across North Africa. *Geochemistry, Geophysics, Geosystems*, 20, 3520–3555.

Ballmer, M. D., C. P. Conrad, E. I. Smith, & N. Harmon (2013). Non-hotspot volcano chains produced by migration of shear-driven upwelling toward the East Pacific Rise. *Geology*, 41 (4), 479–482.

- Ballmer, M. D., C. P. Conrad, E. I. Smith, & R. Johnsen (2015). Intraplate volcanism at the edges of the Colorado Plateau sustained by a combination of triggered edge-driven convection and shear-driven upwelling. *Geochemistry Geophysics Geosystems*, 16, 366–379.
- Barnett-Moore, N., R. Hassan, R. D. Müller, S. E. Williams, & N. Flament (2017). Dynamic topography and eustasy controlled the paleogeographic evolution of northern Africa since the mid-Cretaceous. *Tectonics*, 36 (5), 929–944.
- Bartz, M., G. Rixhon, M. Duval, G. E. King, C. Álvarez Posada, J. M. Parés, & H. Brückner (2018). Successful combination of electron spin resonance, luminescence and palaeomagnetic dating methods allows reconstruction of the Pleistocene evolution of the lower Moulouya river (NE Morocco). *Quaternary Science Reviews*, 185, 153–171.
- Beauvais, A., N. J. Bonnet, D. Chardon, N. Arnaud, & M. Jayananda (2016). Very long-term stability of passive margin escarpment constrained by $^{40}\text{Ar}/^{39}\text{Ar}$ dating of K-Mn oxides. *Geology*, 44 (4), 299–302.
- Beelen, D., C. A.-L. Jackson, S. Patruno, D. M. Hodgson, & J. P. Trabucho Alexandre (2019). The effects of differential compaction on clinothem geometries and shelf-edge trajectories. *Geology*, 47 (11), 1011–1014.
- Ben-Yaakov, S., E. Ruth, & I. R. Kaplan (1974). Carbonate compensation depth: Relation to carbonate solubility in ocean waters. *Science*, 184, 982–984.
- Bercovici, D. & Y. Ricard (2014). Plate tectonics, damage and inheritance. *Nature*, 508, 513–516.
- Bierman, P. & E. J. Steig (1996). Estimating rates of denudation using cosmogenic isotope abundances in sediment. *Earth Surface Processes and Landforms*, 21, 125–139.
- Billingsley, G. H. & S. S. Beus (1999). *Geology of the Surprise Canyon Formation of the Grand Canyon, Arizona*. Museum of Northern Arizona, Flagstaff, Arizona.
- Bock, Y. & D. Melgar (2016). Physical applications of GPS geodesy: A review. *Reports on Progress in Physics*, 79 (106801).
- Bond, G. C. (1976). Evidence for continental subsidence in North America during the Late Cretaceous global submergence. *Geology*, 4, 557–560.
- Bond, G. C. (1978a). Evidence for Late Tertiary uplift of Africa relative to North America, South America, Australia and Europe. *The Journal of Geology*, 86 (1), 47–65.
- Bond, G. C. (1978b). Speculations on real sea-level changes and vertical motions of continents at selected times in the Cretaceous and Tertiary Periods. *Geology*, 6, 247–250.
- Bond, G. C. (1979). Evidence for some uplifts of large magnitude in continental platforms. *Tectonophysics*, 61, 285–305.
- Bonnet, N. J., A. Beauvais, N. Arnaud, D. Chardon, & M. Jayananda (2016). Cenozoic lateritic weathering and erosion history of Peninsular India from $^{40}\text{Ar}/^{39}\text{Ar}$ dating of supergene K-Mn oxides. *Chemical Geology*, 446, 33–53.
- Bower, D. J., M. Gurnis, & N. Flament (2015). Assimilating lithosphere and slab history in 4-D Earth models. *Physics of the Earth and Planetary Interiors*, 238, 8–22.
- Braun, J. (2010). The many surface expressions of mantle dynamics. *Nature Geoscience*, 3 (12), 825–833.
- Braun, J., X. Robert, & T. Simon-Labric (2013). Eroding dynamic topography. *Geophysical Research Letters*, 40, 1494–1499.
- Bredow, E., B. Steinberger, R. Gassmüller, & J. Dannberg (2017). How plume-ridge interaction shapes the crustal thickness pattern of the Réunion hotspot track. *Geochemistry, Geophysics, Geosystems*, 18 (8), 2930–2948.
- Brocher, T. M. (2005). Empirical relations between elastic wave speeds and density in the Earth's crust. *Bulletin of the Seismological Society of America*, 95 (6), 2081–2092.
- Brodie, J. & N. J. White (1994). Sedimentary basin inversion caused by igneous underplating: Northwest European continental shelf. *Geology*, 22 (2), 147–150.
- Bufe, A., C. Paola, & D. W. Burbank (2016). Fluvial bevelling of topography controlled by lateral channel mobility and uplift rate. *Nature Geoscience*, 9 (9), 706–710.
- Bunge, H.-P., C. R. Hagelberg, & B. J. Travis (2003). Mantle circulation models with variational data assimilation: Inferring past mantle flow and structure from plate motion histories and seismic tomography. *Geophysical Journal International*, 152, 280–301.
- Bunge, H.-P., M. A. Richards, & J. R. Baumgardner (1996). Effect of depth-dependent viscosity on the planform of mantle convection. *Nature*, 379 (6564), 436–438.
- Burgess, P. M., M. Gurnis, & L. Moresi (1997). Formation of sequences in the cratonic interior of North America by interaction between mantle, eustatic, and stratigraphic processes. *Bulletin of the Geological Society of America*, 109 (12), 1515–1535.
- Burke, K. & Y. Gunnell (2008). The African erosion surface: A continental-scale synthesis of geomorphology, tectonics, and environmental change over the past 180 million years. *Geological Society of America Memoirs*, 201, 1–66.
- Burov, E. & T. Gerya (2014). Asymmetric three-dimensional topography over mantle plumes. *Nature*, 513, 85–89.
- Burstedde, C., G. Stadler, L. Alisic, L. C. Wilcox, E. Tan, M. Gurnis, & O. Ghattas (2013). Large-scale adaptive mantle convection simulation. *Geophysical Journal International*, 192, 889–906.
- Busse, F. H. (1978). Non-linear properties of thermal convection. *Reports on Progress in Physics*, 41, 1929–1967.
- Campbell, S. M., R. Moucha, L. A. Derry, & M. E. Raymo (2018). Effects of dynamic topography on the Cenozoic carbonate compensation depth. *Geochemistry, Geophysics, Geosystems*, 19, 1025–1034.
- Cao, W., N. Flament, S. Zahirovic, S. Williams, & R. D. Müller (2019). The interplay of dynamic topography and eustasy on continental flooding in the late Paleozoic. *Tectonophysics*, 761, 108–121.
- Catuneanu, O. (2006). *Principles of sequence stratigraphy*. Elsevier, Amsterdam.
- Cazenave, A., K. Dominh, M. Rabinowicz, & G. Ceuleneer (1988). Geoid and depth anomalies over ocean swells and troughs: Evidence of an increasing trend of the geoid to depth ratio with age of plate. *Journal of Geophysical Research*, 93 (B7), 8064–8077.
- Celli, N. L., S. Lebedev, A. J. Schaeffer, & C. Gaina (2020). African cratonic lithosphere carved by mantle plumes. *Nature Communications*, 11, 92.
- Chang, C. & L. Liu (2019). Distinct responses of intraplate sedimentation to different subsidence mechanisms: Insights from forward landscape evolution

- simulations. *Journal of Geophysical Research: Earth Surface*, 124, 1139–1159.
- Chao, B. F. & J. R. Liao (2019). Gravity changes due to large earthquakes detected in GRACE satellite data via empirical orthogonal function analysis. *Journal of Geophysical Research: Solid Earth*, 3, 3024–3035.
- Chardon, D., V. Chevillotte, A. Beauvais, G. Grandin, & B. Boulangé (2006). Planation, bauxites and epeirogeny: One or two paleosurfaces on the West African margin? *Geomorphology*, 82, 273–282.
- Chardon, D., J.-L. Grimaud, D. Rouby, A. Beauvais, & F. Christophoul (2016). Stabilization of large drainage basins over geological time scales: Cenozoic West Africa, hot spot swell growth, and the Niger River. *Geochemistry, Geophysics, Geosystems*, 17, 1164–1181.
- Chowdhury, M. K. R., V. Venkatesh, M. A. Anandalwar, & D. K. Paul (1965). Recent concepts on the origin of Indian laterite. *Memoirs of the Geological Survey of India*, 31 A (6), 547–558.
- Christensen, N. I. & W. D. Mooney (1995). Seismic velocity structure and composition of the continental crust: A global view. *Journal of Geophysical Research*, 100 (B7), 9761–9788.
- Clark, M. K., L. H. Royden, K. X. Whipple, B. C. Burchfiel, X. Zhang, & W. Tang (2006). Use of a regional, relict landscape to measure vertical deformation of the eastern Tibetan Plateau. *Journal of Geophysical Research*, 111 (F03002).
- Cochran, J. R. & M. Talwani (1977). Free-air gravity anomalies in the world's oceans and their relationship to residual elevation. *Geophysical Journal of the Royal Astronomical Society*, 50, 495–552.
- Codilean, A. T., H. Munack, T. J. Cohen, W. M. Saktura, A. Gray, & S. M. Mudd (2018). OCTOPUS: An open cosmogenic isotope and luminescence database. *Earth System Science Data*, 10 (4), 2123–2139.
- Colli, L., S. Ghelichkhan, & H.-P. Bunge (2016). On the ratio of dynamic topography and gravity anomalies in a dynamic Earth. *Geophysical Research Letters*, 43, 2510–2516.
- Colli, L., S. Ghelichkhan, H. P. Bunge, & J. Oeser (2018). Retrodictions of Mid Paleogene mantle flow and dynamic topography in the Atlantic region from compressible high resolution adjoint mantle convection models: Sensitivity to deep mantle viscosity and tomographic input model. *Gondwana Research*, 53, 252–272.
- Coltice, N., M. Gérault, & M. Ulvrová (2017). A mantle convection perspective on global tectonics. *Earth-Science Reviews*, 165, 120–150.
- Conder, J. A., D. W. Forsyth, & E. M. Parmentier (2002). Asthenospheric flow and asymmetry of the East Pacific Rise, MELT area. *Journal of Geophysical Research: Solid Earth*, 107 (B12), 2344.
- Conrad, C. P. & M. Gurnis (2003). Seismic tomography, surface uplift, and the breakup of Gondwanaland: Integrating mantle convection backwards in time. *Geochemistry, Geophysics, Geosystems*, 4 (3).
- Conrad, C. P. & L. Husson (2009). Influence of dynamic topography on sea level and its rate of change. *Lithosphere*, 1 (2), 110–120.
- Conrad, C. P., B. Steinberger, & T. H. Torsvik (2013). Stability of active mantle upwelling revealed by net characteristics of plate tectonics. *Nature*, 498, 479–482.
- Conrad, C. P., B. Wu, E. I. Smith, T. A. Bianco, & A. Tibbetts (2010). Shear-driven upwelling induced by lateral viscosity variations and asthenospheric shear: A mechanism for intraplate volcanism. *Physics of the Earth and Planetary Interiors*, 178, 162–175.
- Conway-Jones, B. W., G. G. Roberts, A. Fichtner, & M. J. Hoggard (2019). Neogene epeirogeny of Iberia. *Geochemistry, Geophysics, Geosystems*, 20, 1138–1163.
- Corrieu, V., C. Thoraval, & Y. Ricard (1995). Mantle dynamics and geoid Green functions. *Geophysical Journal International*, 120, 516–523.
- Cowie, L., N. Kusznir, & G. Manatschal (2015). Determining the COB location along the Iberian margin and Galicia Bank from gravity anomaly inversion, residual depth anomaly and subsidence analysis. *Geophysical Journal International*, 203, 1355–1372.
- Croissant, T. & J. Braun (2014). Constraining the stream power law: A novel approach combining a landscape evolution model and an inversion method. *Earth Surface Dynamics*, 2, 155–166.
- Crosby, A. G., D. P. McKenzie, & J. G. Sclater (2006). The relationship between depth, age and gravity in the oceans. *Geophysical Journal International*, 166, 553–573.
- Cross, T. A. & R. H. Pilger (1978). Tectonic controls of late Cretaceous sedimentation, western interior, USA. *Nature*, 274, 653–657.
- Crowley, J. W., J. X. Mitrovica, R. C. Bailey, M. E. Tamisiea, & J. L. Davis (2006). Land water storage within the Congo Basin inferred from GRACE satellite gravity data. *Geophysical Research Letters*, 33 (19), 2–5.
- Czarnota, K., M. J. Hoggard, N. J. White, & J. Winterbourne (2013). Spatial and temporal patterns of Cenozoic dynamic topography around Australia. *Geochemistry, Geophysics, Geosystems*, 14, 634–658.
- Czarnota, K., G. G. Roberts, N. J. White, & S. Fishwick (2014). Spatial and temporal patterns of Australian dynamic topography from river profile modeling. *Journal of Geophysical Research: Solid Earth*, 119, 1384–1424.
- Dannberg, J., Z. Eilon, U. Faul, R. Gassmüller, P. Moulik, & R. Myhill (2017). The importance of grain size to mantle dynamics and seismological observations. *Geochemistry, Geophysics, Geosystems*, 18, 3034–3061.
- Darwin, C. R. (1842). *The structure and distribution of coral reefs. Being the first part of the geology of the voyage of the Beagle, under the command of Capt. Fitzroy, R.N. during the years 1832 to 1836.* Smith Elder and Co, London.
- Davies, D. R. & J. H. Davies (2009). Thermally-driven mantle plumes reconcile multiple hot-spot observations. *Earth and Planetary Science Letters*, 278, 50–54.
- Davies, D. R. & N. Rawlinson (2014). On the origin of recent intraplate volcanism in Australia. *Geology*, 42 (12), 1031–1034.
- Davies, D. R., A. P. Valentine, S. C. Kramer, N. Rawlinson, M. J. Hoggard, C. M. Eakin, & C. R. Wilson (2019). Earth's multi-scale topographic response to global mantle flow. *Nature Geoscience*, 12, 845–850.

- Davis, M. W., N. J. White, K. F. Priestley, B. J. Baptie, & F. J. Tilmann (2012). Crustal structure of the British Isles and its epeirogenic consequences. *Geophysical Journal International*, 190, 705–725.
- Davis, R. & O. A. Schaeffer (1955). Chlorine-36 in nature. *Annals of the New York Academy of Sciences*, 62, 107–121.
- Davis, W. M. (1899). The geographical cycle. *The Geographical Journal*, 14 (5), 481–504.
- Davis, W. M. (1930). Rock floors in arid and in humid climates. I. *The Journal of Geology*, 38 (1), 1–27.
- Dietrich, W. E., D. G. Bellugi, L. S. Sklar, J. D. Stock, A. M. Heimsath, & J. J. Roering (2003). Geomorphic transport laws for predicting landscape form and dynamics. In: *Geophysical Monograph Series: Prediction in Geomorphology* (edited by P. R. Wilcock & R. M. Iverson), vol. 135, pp. 103–132. American Geophysical Union.
- Ding, X., T. Salles, N. Flament, C. Mallard, & P. F. Rey (2019). Drainage and sedimentary responses to dynamic topography. *Geophysical Research Letters*, 46, 14,385–14,394.
- Duller, G. A. T. & A. G. Wintle (2012). A review of the thermally transferred optically stimulated luminescence signal from quartz for dating sediments. *Quaternary Geochronology*, 7, 6–20.
- Dziewonski, A. M. & D. L. Anderson (1984). Seismic tomography of the Earth's interior: The first three-dimensional models of the Earth's structure promise to answer some basic questions of geodynamics and signify a revolution in Earth science. *American Scientist*, 72 (5), 483–494.
- Eakin, C. M. & C. Lithgow-Bertelloni (2018). An overview of dynamic topography: The influence of mantle circulation on surface topography and landscape. In: *Mountains, Climate, and Biodiversity* (edited by C. Hoorn, A. Perrigo, & A. Antonelli), chap. 3, pp. 37–50. John Wiley and Sons Ltd, 1 edn.
- Eakin, C. M., C. Lithgow-Bertelloni, & F. M. Dávila (2014). Influence of Peruvian flat-subduction dynamics on the evolution of western Amazonia. *Earth and Planetary Science Letters*, 404, 250–260.
- Eiler, J. M. (2007). “Clumped-isotope” geochemistry – The study of naturally-occurring, multiply-substituted isotopologues. *Earth and Planetary Science Letters*, 262, 309–327.
- Elder, J. (1976). *The bowels of the Earth*. Oxford University Press, Glasgow.
- Emiliani, C. (1950). Isotopic paleotemperatures. *Science*, 154 (3751), 851–857.
- England, P. & P. Molnar (1990). Surface uplift, uplift of rocks, and exhumation of rocks. *Geology*, 18, 1173–1177.
- Farley, K. A. (2000). Helium diffusion from apatite: General behavior as illustrated by Durango fluorapatite. *Journal of Geophysical Research: Solid Earth*, 105 (B2), 2903–2914.
- Faccenna, C., P. Glišović, A. Forte, T. W. Becker, E. Garzanti, A. Sembroni, & Z. Gvirtzman (2019). Role of dynamic topography in sustaining the Nile River over 30 million years. *Nature Geoscience*, 12, 1012–1017.
- Farley, K. A. (2002). (U-Th)/He dating: Techniques, calibrations, and applications. *Reviews in Mineralogy and Geochemistry*, 47, 819–844.
- Farrell, W. E. & J. A. Clark (1976). On postglacial sea level. *Geophysical Journal of the Royal Astronomical Society*, 46, 647–667.
- Feigl, K. L., D. C. Agnew, Y. Bock, D. Dong, et al. (1993). Space geodetic measurement of crustal deformation in central and southern California, 1984–1992. *Journal of Geophysical Research*, 98 (B12), 21,677–21,712.
- Fernandes, N. F. & W. E. Dietrich (1997). Hillslope evolution by diffusive processes: The timescale for equilibrium adjustments. *Water Resources Research*, 33 (6), 1307–1318.
- Fernandes, V. M. & G. G. Roberts (2021). Cretaceous to Recent net continental uplift from paleobiological data: Insights into sub-plate support. *Geological Society of America Bulletin*, 133.
- Fernandes, V. M., G. G. Roberts, N. White, & A. C. Whittaker (2019). Continental-scale landscape evolution: A history of North American topography. *Journal of Geophysical Research: Earth Surface*, 124, 2689–2722.
- Flament, N. (2019). Present-day dynamic topography and lower-mantle structure from palaeogeographically constrained mantle flow models. *Geophysical Journal International*, 216, 2158–2182.
- Flament, N., M. Gurnis, & R. D. Müller (2013). A review of observations and models of dynamic topography. *Lithosphere*, 5 (2), 189–210.
- Flowers, R. M. & K. A. Farley (2012). Apatite $^4\text{He}/^3\text{He}$ and (U-Th)/He evidence for an ancient Grand Canyon. *Science*, 338, 1616–1619.
- Forte, A. M. (2007). Constraints on seismic models from other disciplines – Implications for mantle dynamics and composition. *Treatise on Geophysics*, pp. 805–858.
- Forte, A. M. & R. Peltier (1991). Viscous flow models of global geophysical observables 1. Forward problems. *Journal of Geophysical Research*, 96 (B12), 20,131–20,159.
- Forte, A. M., W. R. Peltier, A. M. Dziewonski, & R. L. Woodward (1993). Dynamic surface topography: A new interpretation based upon mantle flow models derived from seismic tomography. *Geophysical Research Letters*, 20 (3), 225–228.
- Fox, M., L. Goren, D. A. May, & S. D. Willett (2014). Inversion of fluvial channels for paleorock uplift rates in Taiwan. *Journal of Geophysical Research: Earth Surface*, 119, 1853–1875.
- Friedrich, A. M., H.-P. Bunge, S. M. Rieger, L. Colli, S. Ghelichkhan, & R. Nerlich (2018). Stratigraphic framework for the plume mode of mantle convection and the analysis of interregional unconformities on geological maps. *Gondwana Research*, 53, 159–188.
- Gallagher, K. (1995). Evolving temperature histories from apatite fission-track data. *Earth and Planetary Science Letters*, 136, 421–435.
- Gallagher, K. (2012). Transdimensional inverse thermal history modeling for quantitative thermochronology. *Journal of Geophysical Research: Solid Earth*, 117 (B02408).
- Gallagher, K. & R. Brown (1999). Denudation and uplift at passive margins: The record on the Atlantic Margin of southern Africa. *Philosophical Transactions of the Royal Society A*, 357, 835–859.
- Gallagher, K., R. Brown, & C. Johnson (1998). Fission track analysis and its applications to geological problems. *Annual Review of Earth and Planetary Sciences*, 26, 519–572.

- Garnero, E. J., A. K. McNamara, & S.-H. Shim (2016). Continent-sized anomalous zones with low seismic velocity at the base of Earth's mantle. *Nature Geoscience*, 9 (7), 481–489.
- Garzzone, C. N., D. J. Auerbach, J. Jin-Sook Smith, J. J. Rosario, B. H. Passey, T. E. Jordan, & J. M. Eiler (2014). Clumped isotope evidence for diachronous surface cooling of the Altiplano and pulsed surface uplift of the Central Andes. *Earth and Planetary Science Letters*, 393, 173–181.
- Ghelichkhan, S. & H.-P. Bunge (2016). The compressible adjoint equations in geodynamics: Derivation and numerical assessment. *International Journal on Geomathematics*, 7, 1–30.
- Ghelichkhan, S., M. Murböck, L. Colli, R. Pail, & H. P. Bunge (2018). On the observability of epeirogenic movement in current and future gravity missions. *Gondwana Research*, 53, 273–284.
- Ghosh, P., J. Adkins, H. P. Affek, B. Balta, W. Guo, E. A. Schauble, D. Schrag, & J. M. Eiler (2006a). ^{13}C – ^{18}O bonds in carbonate minerals: A new kind of paleothermometer. *Geochimica et Cosmochimica Acta*, 70, 1439–1456.
- Ghosh, P., C. N. Garzzone, & J. M. Eiler (2006b). Rapid uplift of the Altiplano revealed through ^{13}C – ^{18}O bonds in paleosol carbonates. *Science*, 311, 511–515.
- Gleadow, A. J. & I. R. Duddy (1981). A natural long-term track annealing experiment for apatite. *Nuclear Tracks and Radiation Measurements*, 5, 169–174.
- Glišović, P. & A. M. Forte (2014). Reconstructing the Cenozoic evolution of the mantle: Implications for mantle plume dynamics under the Pacific and Indian plates. *Earth and Planetary Science Letters*, 390, 146–156.
- Glišović, P. & A. M. Forte (2015). Importance of initial buoyancy field on evolution of mantle thermal structure: Implications of surface boundary conditions. *Geoscience Frontiers*, 6, 3–22.
- Glišović, P. & A. M. Forte (2016). A new back-and-forth iterative method for time-reversed convection modeling: Implications for the Cenozoic evolution of 3-D structure and dynamics of the mantle. *Journal of Geophysical Research: Solid Earth*, 121 (6), 4067–4084.
- Glotzbach, C. (2015). Deriving rock uplift histories from data-driven inversion of river profiles. *Geology*, 43 (6), 467–470.
- Godin, L., R. R. Parrish, R. L. Brown, & K. V. Hodges (2001). Crustal thickening leading to exhumation of the Himalayan metamorphic core of central Nepal: Insight from U–Pb Geochronology and $^{40}\text{Ar}/^{39}\text{Ar}$ Thermochronology. *Tectonics*, 20 (5), 729–747.
- Golle, O., C. Dumoulin, G. Choblet, & O. Cadec (2012). Topography and geoid induced by a convecting mantle beneath an elastic lithosphere. *Geophysical Journal International*, 189, 55–72.
- Goren, L., M. Fox, & S. D. Willett (2014). Tectonics from fluvial topography using formal linear inversion: Theory and applications to the Inyo Mountains, California. *Journal of Geophysical Research F: Earth Surface*, 119 (8), 1651–1681.
- Green, P. F., I. R. Duddy, A. J. Gleadow, P. R. Tingate, & G. M. Laslett (1985). Fission-track annealing in apatite: Track length measurements and the form of the Arrhenius plot. *Nuclear Tracks and Radiation Measurements*, 10 (3), 323–328.
- Green, P. F., I. R. Duddy, A. J. Gleadow, P. R. Tingate, & G. M. Laslett (1986). Thermal annealing of fission tracks in apatite 1. *A qualitative description. Chemical Geology: Isotope Geoscience Section*, 59, 237–253.
- Gregory, K. M. & C. G. Chase (1992). Tectonic significance of paleobotanically estimated climate and altitude of the late Eocene erosion surface, Colorado. *Geology*, 20 (7), 581–585.
- Guerri, M., F. Cammarano, & J. A. D. Connolly (2015). Effects of chemical composition, water and temperature on physical properties of continental crust. *Geochemistry Geophysics Geosystems*, 16, 2431–2449.
- Guerri, M., F. Cammarano, & P. J. Tackley (2016). Modelling Earth's surface topography: Decomposition of the static and dynamic components. *Physics of the Earth and Planetary Interiors*, 261, 172–186.
- Guillaume, B., C. Gautheron, T. Simon-Labric, J. Martinod, M. Roddaz, & E. Douville (2013). Dynamic topography control on Patagonian relief evolution as inferred from low temperature thermochronology. *Earth and Planetary Science Letters*, 364, 157–167.
- Guillocheau, F., B. Simon, G. Baby, P. Bessin, C. Robin, & O. Dauteuil (2018). Planation surfaces as a record of mantle dynamics: The case example of Africa. *Gondwana Research*, 53, 82–98.
- Guralnik, B., M. Jain, F. Herman, C. Ankjærgaard, et al. (2015). OSL-thermochronometry of feldspar from the KTB borehole, Germany. *Earth and Planetary Science Letters*, 423, 232–243.
- Gurnis, M. (1993). Phanerozoic marine inundation of continents driven by dynamic topography above subducting slabs. *Nature*, 364, 589–593.
- Gurnis, M., J. X. Mitrovica, J. Ritsema, & H.-J. van Heijst (2000). Constraining mantle density structure using geological evidence of surface uplift rates: The case of the African Superplume. *Geochemistry, Geophysics, Geosystems*, 1 (1020).
- Gurnis, M., R. D. Müller, & L. Moresi (1998). Cretaceous vertical motion of Australia and the Australian-Antarctic Discordance. *Science*, 279, 1499–1504.
- Hager, B. H. (1984). Subducted slabs and the geoid: Constraints on mantle rheology and flow. *Journal of Geophysical Research*, 89 (B7), 6003–6015.
- Hager, B. H., R. W. Clayton, & M. A. Richards (1985). Lower mantle heterogeneity, dynamic topography and the geoid. *Nature*, 313, 541–545.
- Hager, B. H. & R. J. O. Connell (1981). A simple global model of plate dynamics and mantle convection. *Journal of Geophysical Research*, 86 (B6), 4843–4867.
- Han, S.-C., C. K. Shum, M. Bevis, C. Ji, & C.-Y. Kuo (2006). Crustal dilatation observed by GRACE after the 2004 Sumatra-Andaman earthquake. *Science*, 313, 658–662.
- Haq, B. U., J. Hardenbol, & P. R. Vail (1987). Chronology of fluctuating sea levels since the Triassic. *Science*, 235, 1156–1167.
- Harrison, T. M., J. Célérier, A. B. Aikman, J. Hermann, & M. T. Heizler (2009). Diffusion of ^{40}Ar in muscovite. *Geochimica et Cosmochimica Acta*, 73, 1039–1051.
- Hartley, R. A., G. G. Roberts, N. White, & C. Richardson (2011). Transient convective uplift of an ancient buried landscape. *Nature Geoscience*, 4, 562–565.
- Hayek, J. N., B. Vilacis, H.-P. Bunge, A. M. Friedrich, S. Carena, & Y. Vibe (2020). Continent-scale hiatus maps for the

- Atlantic realm and Australia since the Upper Jurassic and links to mantle flow-induced dynamic topography. *Proceedings of the Royal Society A*, 476, 20200390.
- Heine, C., R. D. Müller, B. Steinberger, & L. DiCaprio (2010). Integrating deep Earth dynamics in paleogeographic reconstructions of Australia. *Tectonophysics*, 483, 135–150.
- Heister, T., J. Dannberg, R. Gassmöller, & W. Bangerth (2017). High accuracy mantle convection simulation through modern numerical methods - II: Realistic models and problems. *Geophysical Journal International*, 210, 833–851.
- Hobley, D. E., J. M. Adams, S. Siddhartha Nudurupati, E. W. Hutton, N. M. Gasparini, E. Istanbuloglu, & G. E. Tucker (2017). Creative computing with Landlab: An open-source toolkit for building, coupling, and exploring two-dimensional numerical models of Earth-surface dynamics. *Earth Surface Dynamics*, 5, 21–46.
- Hoggard, M. J., K. Czarnota, F. D. Richards, D. L. Huston, A. L. Jaques, & S. Ghelichkhan (2020). Global distribution of sediment-hosted metals controlled by craton edge stability. *Nature Geoscience*, 13, 504–510.
- Hoggard, M. J., N. J. White, & D. Al-Attar (2016). Global dynamic topography observations reveal limited influence of large-scale mantle flow. *Nature Geoscience*, 9 (6), 456–463.
- Hoggard, M. J., J. Winterbourne, K. Czarnota, & N. White (2017). Oceanic residual depth measurements, the plate cooling model, and global dynamic topography. *Journal of Geophysical Research: Solid Earth*, 122, 2328–2372.
- Höink, T. & A. Lenardic (2010). Long wavelength convection, Poiseuille-Couette flow in the low-viscosity asthenosphere and the strength of plate margins. *Geophysical Journal International*, 180, 23–33.
- Holdgate, G., C. Rodriguez, E. Johnstone, M. Wallace, & S. Gallagher (2003). The Gippsland Basin Top Latrobe unconformity, and its expression in other SE Australia basins. *The APPEA Journal*, 43 (1), 149–173.
- Howard, A. D., W. E. Dietrich, & M. A. Seidl (1994). Modeling fluvial erosion on regional to continental scales. *Journal of Geophysical Research*, 99 (B7), 13,971–13,986.
- Howard, A. D. & G. Kerby (1983). Channel changes in badlands. *Geological Society of America Bulletin*, 94, 739–752.
- Huang, J. & S. Zhong (2005). Sublithospheric small-scale convection and its implications for the residual topography at old ocean basins and the plate model. *Journal of Geophysical Research: Solid Earth*, 110 (B05404).
- Huntington, K. W. & A. R. Lechler (2015). Carbonate clumped isotope thermometry in continental tectonics. *Tectonophysics*, 647–648, 1–20.
- Huntley, D. J., D. I. Godfrey-Smith, & M. L. Thewalt (1985). Optical dating of sediments. *Nature*, 313, 105–107.
- Huyghe, D., F. Mouthereau, L. Ségalen, & M. Furió (2020). Long-term dynamic topographic support during post-orogenic crustal thinning revealed by stable isotope ($\delta^{18}\text{O}$) paleo-altimetry in eastern Pyrenees. *Scientific Reports*, 10, 2267.
- Jackson, I. & U. H. Faul (2010). Grainsize-sensitive viscoelastic relaxation in olivine: Towards a robust laboratory-based model for seismological application. *Physics of the Earth and Planetary Interiors*, 183, 151–163.
- Jain, C., A. B. Rozel, & P. J. Tackley (2019). Quantifying the correlation between mobile continents and elevated temperatures in the subcontinental mantle. *Geochemistry, Geophysics, Geosystems*, 20, 1358–1386.
- Japsen, P., J. M. Bonow, P. F. Green, J. A. Chalmers, & K. Lidmar-Bergström (2006). Elevated, passive continental margins: Long-term highs or Neogene uplifts? New evidence from West Greenland. *Earth and Planetary Science Letters*, 248, 315–324.
- Jess, S., S. Randell, & R. Brown (2018). Evolution of the central West Greenland margin and the Nuussuaq Basin: Localised basin uplift along a stable continental margin proposed from thermochronological data. *Basin Research*, 30, 1230–1246.
- Jordan, T. H. (1975). The continental tectosphere. *Reviews of Geophysics*, 13 (3), 1–12.
- Jordan, T. H. (1978). Composition and development of the continental tectosphere. *Nature*, 274, 544–548.
- Julià, J., S. Jagadeesh, S. S. Rai, & T. J. Owens (2009). Deep crustal structure of the Indian shield from joint inversion of P wave receiver functions and Rayleigh wave group velocities: Implications for Precambrian crustal evolution. *Journal of Geophysical Research*, 114 (B10313).
- Kaban, M. K., P. Schwintzer, I. M. Artemieva, & W. D. Mooney (2003). Density of the continental roots: Compositional and thermal contributions. *Earth and Planetary Science Letters*, 209, 53–69.
- Kaula, W. M. (1963). Improved geodetic results from camera observations of satellites. *Journal of Geophysical Research*, 68 (18), 5183–5190.
- Kendall, C. G. S. C. & W. Schlager (1981). Carbonates and relative changes in sea level. *Marine Geology*, 44, 181–212.
- Ketcham, R. A. (2005). Forward and inverse modeling of low-temperature thermochronometry data. *Reviews in Mineralogy and Geochemistry*, 58, 275–314.
- Ketcham, R. A., A. Carter, R. A. Donelick, J. Barbarand, & A. J. Hurford (2007). Improved modeling of fission-track annealing in apatite. *American Mineralogist*, 92, 799–810.
- Ketcham, R. A., R. A. Donelick, & W. D. Carlson (1999). Variability of apatite fission-track annealing kinetics: III. Extrapolation to geological time scales. *American Mineralogist*, 84, 1235–1255.
- King, G. E., F. Herman, R. Lambert, P. G. Valla, & B. Guralnik (2016). Multi-OSL-thermochronometry of feldspar. *Quaternary Geochronology*, 33, 76–87.
- King, L. C. (1942). *South African scenery: A textbook of geomorphology*. Oliver and Boyd, Edinburgh, 1 edn.
- King, L. C. (1953). Canons of landscape evolution. *Bulletin of the Geological Society of America*, 64, 721–752.
- King, L. C. (1962). *The morphology of the Earth: A study and synthesis of world scenery*. Oliver and Boyd, Edinburgh.
- King, S. D. & D. L. Anderson (1998). Edge-driven convection. *Earth and Planetary Science Letters*, 160, 289–296.
- Kirby, E. & K. Whipple (2001). Quantifying differential rock-uplift rates via stream profile analysis. *Geology*, 29 (5), 415–418.
- Klöcking, M., M. J. Hoggard, V. Rodríguez Tribaldos, F. D. Richards, A. R. Guimarães, J. Maclennan, & N. J. White (2020). A tale of two domes: Neogene to recent volcanism

- and dynamic uplift of northeast Brazil and southwest Africa. *Earth and Planetary Science Letters*, 547, 116464.
- Klöcking, M., N. J. White, J. Maclennan, D. McKenzie, & J. G. Fitton (2018). Quantitative relationships between basalt geochemistry, shear wave velocity, and asthenospheric temperature beneath western North America. *Geochemistry, Geophysics, Geosystems*, 19, 3376–3404.
- Knopoff, L. (1964). The convection current hypothesis. *Reviews of Geophysics*, 2 (1), 89–122.
- Korenaga, T. & J. Korenaga (2008). Subsidence of normal oceanic lithosphere, apparent thermal expansivity, and seafloor flattening. *Earth and Planetary Science Letters*, 268, 41–51.
- Kronbichler, M., T. Heister, & W. Bangerth (2012). High accuracy mantle convection simulation through modern numerical methods. *Geophysical Journal International*, 191, 12–29.
- Lal, D. & B. Peters (1967). Cosmic ray produced radioactivity on the Earth. In: *Cosmic Rays II (edited by K. Sitte)*, pp. 551–612. Springer Berlin Heidelberg, Berlin.
- Lamb, S., J. D. P. Moore, M. Perez-Gussinye, & T. Stern (2020). Global whole lithosphere isostasy: Implications for surface elevations, structure, strength, and densities of the continental lithosphere. *Geochemistry, Geophysics, Geosystems*, 21, e2020GC009150.
- Laslett, G. M., P. F. Green, I. R. Duddy, & A. J. Gleadow (1987). Thermal annealing of fission tracks in apatite 2. A quantitative analysis. *Chemical Geology: Isotope Geoscience Section*, 65, 1–13.
- Lavier, L. L., M. S. Steckler, & F. Brigaud (2001). Climatic and tectonic control on the Cenozoic evolution of the West African margin. *Marine Geology*, 178, 63–80.
- Lay, T., J. Hernlund, & B. Buffett (2008). Core-mantle boundary heat flow. *Nature Geoscience*, 1 (1), 25–32.
- Li, D., M. Gurnis, & G. Stadler (2017). Towards adjoint-based inversion of time-dependent mantle convection with nonlinear viscosity. *Geophysical Journal International*, 209, 86–105.
- Lin, P. Y. P., J. B. Gaherty, G. Jin, J. A. Collins, D. Lizarralde, R. L. Evans, & G. Hirth (2016). High-resolution seismic constraints on flow dynamics in the oceanic asthenosphere. *Nature*, 535, 538–541.
- Lithgow-Bertelloni, C. & M. A. Richards (1998). The dynamics of Cenozoic and Mesozoic plate motions. *Reviews of Geophysics*, 36 (1), 27–78.
- Lithgow-Bertelloni, C. R. & M. Gurnis (1997). Cenozoic subsidence and uplift of continents from time-varying dynamic topography. *Geology*, 25 (8), 735–738.
- Liu, L., S. Spasojevic, & M. Gurnis (2008). Reconstructing Farallon Plate subduction beneath North America back to the Late Cretaceous. *Science*, 322, 934–938.
- Lovell, B. (2010). A pulse in the planet: Regional control of high-frequency changes in relative sea level by mantle convection. *Journal of the Geological Society, London*, 167, 637–648.
- Luke, J. C. (1972). Mathematical models for landform evolution. *Journal of Geophysical Research*, 77 (14), 2460–2464.
- Łuszczak, K., C. Persano, & F. M. Stuart (2018). Early Cenozoic denudation of central west Britain in response to transient and permanent uplift above a mantle plume. *Tectonics*, 37, 914–934.
- Lyell, C. (1830). *Principles of geology, being an attempt to explain the former changes of the Earth's surface, by reference to causes now in operation*. John Murray, London.
- Machel, P. & D. A. Yuen (1986). The onset of time-dependent convection in spherical shells as a clue to chaotic convection in the Earth's mantle. *Geophysical Research Letters*, 13 (13), 1470–1473.
- Matthews, K. J., A. J. Hale, M. Gurnis, R. D. Müller, & L. DiCapprio (2011). Dynamic subsidence of Eastern Australia during the Cretaceous. *Gondwana Research*, 19, 372–383.
- McCrea, J. M. (1950). On the isotopic chemistry of carbonates and a paleotemperature scale. *The Journal of Chemical Physics*, 18 (6), 849–857.
- McElwain, J. C. (2004). Climate-independent paleoaltimetry using stomatal density in fossil leaves as a proxy for CO₂ partial pressure. *Geology*, 32 (12), 1017–1020.
- McKenzie, D. P. (1967). Some remarks on heat flow and gravity anomalies. *Journal of Geophysical Research*, 72 (24), 6261–6273.
- McKenzie, D. P. (1968). The influence of the boundary conditions and rotation on convection in the Earth's mantle. *Geophysical Journal of the Royal Astronomical Society*, 15, 457–500.
- McKenzie, D. P. (1978). Some remarks on the development of sedimentary basins. *Earth and Planetary Science Letters*, 40, 25–32.
- McKenzie, D. P., J. Roberts, & N. Weiss (1973). Numerical models of convection in the Earth's mantle. *Tectonophysics*, 19, 89–103.
- McKenzie, D. P., J. M. Roberts, & N. O. Weiss (1974). Convection in the Earth's mantle: Towards a numerical simulation. *Journal of Fluid Mechanics*, 62 (3), 465–538.
- McNab, F., P. W. Ball, M. J. Hoggard, & N. J. White (2018). Neogene uplift and magmatism of Anatolia: Insights from drainage analysis and basaltic geochemistry. *Geochemistry, Geophysics, Geosystems*, 19, 175–213.
- Menard, H. W. (1965). Sea floor relief and mantle convection. *Physics and Chemistry of the Earth*, 6, 315–364.
- Menard, H. W. (1969). Elevation and subsidence of oceanic crust. *Earth and Planetary Science Letters*, 6, 275–284.
- Menard, H. W. (1973). Depth anomalies and the bobbing motion of drifting islands. *Journal of Geophysical Research*, 78 (23), 5128–5137.
- Meyer, H. W. (2007). A review of paleotemperature lapse rate methods for estimating paleoelevation from fossil floras. *Reviews in Mineralogy and Geochemistry*, 66, 155–171.
- Miller, K. G., M. A. Kominz, J. V. Browning, J. D. Wright, et al. (2005). The Phanerozoic record of global sea-level change. *Science*, 310, 1293–8.
- Millett, J. M., M. J. Hole, D. W. Jolley, N. Schofield, & E. Campbell (2016). Frontier exploration and the North Atlantic Igneous Province: New insights from a 2.6 km offshore volcanic sequence in the NE Faroe-Shetland Basin. *Journal of the Geological Society*, 173 (2), 320–336.
- Milne, G. A., J. L. Davis, J. X. Mitrovica, H. G. Scherneck, J. M. Johansson, M. Vermeer, & H. Koivula (2001). Space-geodetic constraints on glacial isostatic adjustment in Fennoscandia. *Science*, 291, 2381–2385.
- Mitrovica, J. X., J. Austermann, S. Coulson, J. R. Creveling, M. J. Hoggard, G. T. Jarvis, & F. D. Richards (2020). Dynamic topography and ice age paleoclimate. *Annual Review of Earth and Planetary Sciences*, 48.
- Mitrovica, J. X., C. Beaumont, & G. T. Jarvis (1989). Tilting of continental interiors by the dynamical effects of subduction. *Tectonics*, 8 (5), 1079–1094.

- Mitrovica, J. X. & G. A. Milne (2002). On the origin of late Holocene sea-level highstands within equatorial ocean basins. *Quaternary Science Reviews*, 21, 2179–2190.
- Molnar, P., P. C. England, & C. H. Jones (2015). Mantle dynamics, isostasy, and the support of high terrain. *Journal of Geophysical Research: Solid Earth*, 120, 1932–1957.
- Mooney, W. D. (2015). Crust and lithospheric structure – Global crustal structure. In: *Treatise on Geophysics*, vol. 1, pp. 339–390. Elsevier Inc., 2nd edn.
- Moucha, R. & A. M. Forte (2011). Changes in African topography driven by mantle convection. *Nature Geoscience*, 4 (10), 707–712.
- Moucha, R., A. M. Forte, J. X. Mitrovica, D. B. Rowley, S. Quéré, N. A. Simmons, & S. P. Grand (2008). Dynamic topography and long-term sea-level variations: There is no such thing as a stable continental platform. *Earth and Planetary Science Letters*, 271, 101–108.
- Müller, R. D., M. Sdrolias, C. Gaina, B. Steinberger, & C. Heine (2008). Long-term sea-level fluctuations driven by ocean basin dynamics. *Science*, 319, 1357–1362.
- Murray, J. & A. F. Renard (1891). Report on deep-sea deposits based on the specimens collected during the voyage of H.M.S. Challenger in the years 1872 to 1876. In: *Report on the scientific results of the voyage of H.M.S. Challenger during the years 1873–76*, p. 688. Eyre & Spottiswoode, London.
- Nakiboglu, S. M. (1982). Hydrostatic theory of the Earth and its mechanical implications. *Physics of the Earth and Planetary Interiors*, 28, 302–311.
- Nimmo, F. (2015). Energetics of the core. In: *Treatise on Geophysics* (edited by G. Schubert), vol. 8, chap. 2. Elsevier, Amsterdam, 2 edn.
- Nishiizumi, K., C. P. Kohl, J. R. Arnold, R. Dorn, J. Klein, D. Fink, R. Middleton, & D. Lal (1993). Role of in situ cosmogenic nuclides ^{10}Be and ^{26}Al in the study of diverse geomorphic processes. *Earth Surface Processes and Landforms*, 18, 407–425.
- Olson, P., G. Schubert, & C. Anderson (1987). Plume formation in the “D”-layer and the roughness of the core-mantle boundary. *Nature*, 327, 409–413.
- O’Malley, C. P. B., N. J. White, G. G. Roberts, & S. N. Stephenson (2021). Large-scale tectonic forcing of the African landscape and its drainage patterns. *Journal of Geophysical Research: Earth Surface*.
- Osei Tutu, A., S. V. Sobolev, B. Steinberger, A. A. Popov, & I. Rogozhina (2018). Evaluating the influence of plate boundary friction and mantle viscosity on plate velocities. *Geochemistry, Geophysics, Geosystems*, 19, 642–666.
- Panasyuk, S. V. & B. H. Hager (2000). Models of isostatic and dynamic topography, geoid anomalies, and their uncertainties. *Journal of Geophysical Research: Solid Earth*, 105 (B12), 28,199–28,209.
- Pari, G. & W. R. Peltier (2000). Subcontinental mantle dynamics: A further analysis based on the joint constraints of dynamic surface topography and free-air gravity. *Journal of Geophysical Research*, 105 (B3), 5635–5662.
- Parmentier, E. M., C. Sotin, & B. J. Travis (1994). Turbulent 3-D thermal convection in an infinite Prandtl number, volumetrically heated fluid: Implications for mantle dynamics. *Geophysical Journal International*, 116, 241–251.
- Parmentier, E. M., D. L. Turcotte, & K. E. Torrance (1976). Studies of finite amplitude non-Newtonian thermal convection with application to convection in the Earth’s mantle. *Journal of Geophysical Research*, 81 (11), 1839–1846.
- Parnell-Turner, R., N. White, T. J. Henstock, S. M. Jones, J. Maclennan, & B. J. Murton (2017). Causes and consequences of diachronous V-shaped ridges in the North Atlantic Ocean. *Journal of Geophysical Research: Solid Earth*, 122, 8675–8708.
- Parnell-Turner, R. E., N. J. White, N. McCave, T. J. Henstock, B. J. Murton, & S. M. Jones (2015). Architecture of North Atlantic contourite drifts modified by transient circulation of the Icelandic mantle plume. *Geochemistry, Geophysics, Geosystems*, 16, 3414–3435.
- Parsons, B. & S. Daly (1983). The relationship between surface topography, gravity anomalies, and temperature structure of convection. *Journal of Geophysical Research*, 88 (B2), 1129–1144.
- Parsons, B. & J. G. Sclater (1977). An analysis of the variation of ocean floor bathymetry and heat flow with age. *Journal of Geophysical Research*, 82 (5), 803–827.
- Patocka, V., H. Cížková, & P. J. Tackley (2019). Do elasticity and a free surface affect lithospheric stresses caused by upper-mantle convection? *Geophysical Journal International*, 216, 1740–1760.
- Pekeris, C. L. (1935). Thermal convection in the interior of the Earth. *Geophysical Supplements to the Monthly Notices of the Royal Astronomical Society*, 3 (8), 343–367.
- Pelletier, J. D. (2010). How do pediments form?: A numerical modeling investigation with comparison to pediments in southern Arizona, USA. *Bulletin of the Geological Society of America*, 122, 1815–1829.
- Peltier, W. R., D. F. Argus, & R. Drummond (2015). Space geodesy constrains ice age terminal deglaciation: The global ICE-6G_C (VM5a) model. *Journal of Geophysical Research: Solid Earth*, 120, 450–487.
- Perron, J. T. & L. Royden (2013). An integral approach to bedrock river profile analysis. *Earth Surface Processes and Landforms*, 38, 570–576.
- Petersen, K. D., S. B. Nielsen, O. R. Clausen, R. Stephenson, & T. Gerya (2010). Small-scale mantle convection produces stratigraphic sequences in sedimentary basins. *Science*, 329, 827–830.
- Phillips, J. D. (2002). Erosion, isostatic response, and the missing peneplains. *Geomorphology*, 45, 225–241.
- Plank, T. & D. W. Forsyth (2016). Thermal structure and melting conditions in the mantle beneath the Basin and Range province from seismology and petrology. *Geochemistry, Geophysics, Geosystems*, 17 (4), 1312–1338.
- Poage, M. A. & C. P. Chamberlain (2001). Empirical relationships between elevation and the stable isotope composition of precipitation and surface waters: Considerations for studies of paleoelevation change. *American Journal of Science*, 301, 1–15.
- Pomar, L. (2001). Types of carbonate platforms: A genetic approach. *Basin Research*, 13, 313–334.
- Poore, H. R., R. Samworth, N. J. White, S. M. Jones, & I. N. McCave (2006). Neogene overflow of Northern Component

- Water at the Greenland-Scotland Ridge. *Geochemistry, Geophysics, Geosystems*, 7 (6).
- Priestley, K. & D. P. McKenzie (2013). The relationship between shear wave velocity, temperature, attenuation and viscosity in the shallow part of the mantle. *Earth and Planetary Science Letters*, 381, 78–91.
- Pritchard, D., G. G. Roberts, N. J. White, & C. N. Richardson (2009). Uplift histories from river profiles. *Geophysical Research Letters*, 36 (L24301).
- Ratnaswamy, V., G. Stadler, & M. Gurnis (2015). Adjoint-based estimation of plate coupling in a non-linear mantle flow model: Theory and examples. *Geophysical Journal International*, 202, 768–786.
- Rayleigh, L. (1916). LIX. On convection currents in a horizontal layer of fluid, when the higher temperature is on the under side. *The London, Edinburgh, and Dublin Philosophical Magazine and Journal of Science*, 32 (192), 529–546.
- Reiners, P. W. & M. T. Brandon (2006). Using thermochronology to understand orogenic erosion. *Annual Review of Earth and Planetary Sciences*, 34, 419–466.
- Reiners, P. W., T. A. Ehlers, & P. K. Zeitler (2005). Past, present, and future of thermochronology. *Reviews in Mineralogy and Geochemistry*, 58, 1–18.
- Ricard, Y., M. A. Richards, C. Lithgow-Bertelloni, & Y. Le Stunff (1993). A geodynamic model of mantle density heterogeneity. *Journal of Geophysical Research*, 98 (B12), 21,895–21,909.
- Richards, F. D., M. J. Hoggard, L. R. Cowton, & N. J. White (2018). Reassessing the thermal structure of oceanic lithosphere with revised global inventories of basement depths and heat flow measurements. *Journal of Geophysical Research: Solid Earth*, 123, 9136–9161.
- Richards, F. D., M. J. Hoggard, A. Crosby, S. Ghelichkhan, & N. J. White (2020a). Structure and dynamics of the oceanic lithosphere-asthenosphere system. *Physics of the Earth and Planetary Interiors*, 309, 106559.
- Richards, F. D., M. J. Hoggard, & N. J. White (2016). Cenozoic epeirogeny of the Indian peninsula. *Geochemistry, Geophysics, Geosystems*, 17, 4920–4954.
- Richards, F. D., M. J. Hoggard, N. J. White, & S. Ghelichkhan (2020b). Quantifying the relationship between short-wavelength dynamic topography and thermomechanical structure of the upper mantle using calibrated parameterization of anelasticity. *Journal of Geophysical Research: Solid Earth*, 125, e2019JB019062.
- Richter, F. M. (1973). Convection and the large-scale circulation of the mantle. *Journal of Geophysical Research*, 78 (35), 8735–8745.
- Riley, K. E., T. M. Rittenour, J. L. Pederson, & P. Belmont (2019). Erosion rates and patterns in a transient landscape, Grand Staircase, southern Utah, USA. *Geology*, 47 (9), 811–814.
- Roberts, G. G. (2019). Scales of similarity and disparity between drainage networks. *Geophysical Research Letters*, 46, 3781–3790.
- Roberts, G. G., J. D. Paul, N. White, & J. Winterbourne (2012a). Temporal and spatial evolution of dynamic support from river profiles: A framework for Madagascar. *Geochemistry, Geophysics, Geosystems*, 13 (4).
- Roberts, G. G., N. White, M. J. Hoggard, P. W. Ball, & C. Meehan (2018). A Neogene history of mantle convective support beneath Borneo. *Earth and Planetary Science Letters*, 496, 142–158.
- Roberts, G. G., N. White, & B. H. Lodhia (2019). The generation and scaling of longitudinal river profiles. *Journal of Geophysical Research: Earth Surface*, 124, 137–153.
- Roberts, G. G. & N. J. White (2010). Estimating uplift rate histories from river profiles using African examples. *Journal of Geophysical Research*, 115 (B02406).
- Roberts, G. G., N. J. White, G. L. Martin-Brandis, & A. G. Crosby (2012b). An uplift history of the Colorado Plateau and its surroundings from inverse modeling of longitudinal river profiles. *Tectonics*, 31 (TC4022).
- Rodríguez Tribaldos, V., N. J. White, G. G. Roberts, & M. J. Hoggard (2017). Spatial and temporal uplift history of South America from calibrated drainage analysis. *Geochemistry, Geophysics, Geosystems*, 18, 2321–2353.
- Rosenbloom, N. A. & R. S. Anderson (1994). Hillslope and channel evolution in a marine terraced landscape, Santa Cruz, California. *Journal of Geophysical Research*, 99 (B7), 14,013–14,029.
- Rovere, A., P. J. Hearty, J. Austermann, J. X. Mitrovica, J. Gale, R. Moucha, A. M. Forte, & M. E. Raymo (2015). Mid-Pliocene shorelines of the US Atlantic coastal plain – An improved elevation database with comparison to Earth model predictions. *Earth-Science Reviews*, 145, 117–131.
- Rovere, A., M. E. Raymo, J. X. Mitrovica, P. J. Hearty, M. J. O’Leary, & J. D. Inglis (2014). The Mid-Pliocene sea-level conundrum: Glacial isostasy, eustasy and dynamic topography. *Earth and Planetary Science Letters*, 387, 27–33.
- Rowley, D. B. (2002). Rate of plate creation and destruction: 180 Ma to present. *Bulletin of the Geological Society of America*, 114 (8), 927–933.
- Rowley, D. B., A. M. Forte, R. Moucha, J. X. Mitrovica, N. A. Simmons, & S. P. Grand (2013). Dynamic topography change of the eastern United States since 3 million years ago. *Science*, 340, 1560–1564.
- Rowley, D. B. & C. N. Garzione (2007). Stable isotope-based paleoaltimetry. *Annual Review of Earth and Planetary Sciences*, 35, 463–508.
- Rudge, J. F., G. G. Roberts, N. J. White, & C. N. Richardson (2015). Uplift histories of Africa and Australia from linear inverse modeling of drainage inventories. *Journal of Geophysical Research: Earth Surface*, 120, 894–914.
- Rudge, J. F., M. E. Shaw Champion, N. White, D. P. McKenzie, & B. Lovell (2008). A plume model of transient diachronous uplift at the Earth’s surface. *Earth and Planetary Science Letters*, 267, 146–160.
- Ruetenik, G. A., R. Moucha, & G. D. Hoke (2016). Landscape response to changes in dynamic topography. *Terra Nova*, 28, 289–296.
- Runcorn, S. K. (1965). Changes in the convection pattern in the Earth’s mantle and continental drift: Evidence for a cold origin of the Earth. *Philosophical Transactions of the Royal Society A*, 258, 228–251.

- Sahagian, D. L. (1988). Epeirogenic motions of Africa as inferred from Cretaceous shoreline deposits. *Tectonics*, 7 (1), 125–138.
- Salles, T., N. Flament, & R. D. Muller (2017). Influence of mantle flow on the drainage of eastern Australia since the Jurassic Period. *Geochemistry Geophysics Geosystems*, 18, 280–305.
- Salles, T. & L. Hardiman (2016). Badlands: An open-source, flexible and parallel framework to study landscape dynamics. *Computers and Geosciences*, 91, 77–89.
- Sandiford, M. (2007). The tilting continent: A new constraint on the dynamic topographic field from Australia. *Earth and Planetary Science Letters*, 261, 152–163.
- Sarg, J. F. (1988). Carbonate sequence stratigraphy. *SEPM Special Publications*, 42, 155–181.
- Schaeffer, A. J. & S. Lebedev (2013). Global shear speed structure of the upper mantle and transition zone. *Geophysical Journal International*, 194, 417–449.
- Schlager, W., J. J. G. Reijmer, & A. Droxler (2003). Highstand shedding of carbonate platforms. *Journal of Sedimentary Research*, B64 (3), 270–281.
- Schoenbohm, L. M., K. X. Whipple, B. C. Burchfiel, & L. Chen (2004). Geomorphic constraints on surface uplift, exhumation, and plateau growth in the Red River region, Yunnan Province, China. *Bulletin of the Geological Society of America*, 116 (7–8), 895–909.
- Schumm, S. A. (1993). River response to baselevel change: Implications for sequence stratigraphy. *The Journal of Geology*, 101 (2), 279–294.
- Sembroni, A., C. Faccenna, T. W. Becker, P. Molin, & B. Abebe (2016). Long-term, deep-mantle support of the Ethiopia-Yemen Plateau. *Tectonics*, 35 (2), 469–488.
- Sembroni, A., A. Kiraly, C. Faccenna, F. Funiciello, T. W. Becker, J. Globig, & M. Fernandez (2017). Impact of the lithosphere on dynamic topography: Insights from analogue modeling. *Geophysical Research Letters*, 44 (6), 2693–2702.
- Shahnas, M. H., D. A. Yuen, & R. N. Pysklywec (2018). Inverse problems in geodynamics using machine learning algorithms. *Journal of Geophysical Research: Solid Earth*, 123, 296–310.
- Shepherd, A., E. R. Ivins, A. Geruo, V. R. Barletta, et al. (2012). A reconciled estimate of ice-sheet mass balance. *Science*, 338, 1183–1189.
- Shuster, D. L. & K. A. Farley (2004). $^4\text{He}/^3\text{He}$ thermochronometry. *Earth and Planetary Science Letters*, 217, 1–17.
- Sklar, L. S. & W. E. Dietrich (2001). Sediment and rock strength controls on river incision into bedrock. *Geology*, 29 (12), 1087–1090.
- Sloss, L. L. (1963). Sequences in the cratonic interior of North America. *Bulletin of the Geological Society of America*, 74 (2), 93–114.
- Smallwood, J. R. & C. E. Gill (2002). The rise and fall of the Faroe-Shetland Basin: Evidence from seismic mapping of the Balder Formation. *Journal of the Geological Society*, 159, 627–630.
- Spasojevic, S. & M. Gurnis (2012). Sea level and vertical motion of continents from dynamic Earth models since the Late Cretaceous. *AAPG Bulletin*, 96 (11), 2037–2064.
- Spasojevic, S., L. Liu, & M. Gurnis (2009). Adjoint models of mantle convection with seismic, plate motion, and stratigraphic constraints: North America since the Late Cretaceous. *Geochemistry, Geophysics, Geosystems*, 10 (5).
- Stanley, J. R. & R. M. Flowers (2016). Dating kimberlite emplacement with zircon and perovskite (U-Th)/He geochronology. *Geochemistry, Geophysics, Geosystems*, 17 (11), 4517–4533.
- Stanley, J. R., R. M. Flowers, & D. R. Bell (2015). Erosion patterns and mantle sources of topographic change across the southern African Plateau derived from the shallow and deep records of kimberlites. *Geochemistry, Geophysics, Geosystems*, 16, 3235–3256.
- Stein, C. & S. Stein (1992). A model for the global variation in oceanic depth and heat flow with lithospheric age. *Nature*, 359 (9), 123–139.
- Steinberger, B. (2007). Effects of latent heat release at phase boundaries on flow in the Earth's mantle, phase boundary topography and dynamic topography at the Earth's surface. *Physics of the Earth and Planetary Interiors*, 164, 2–20.
- Steinberger, B. (2016). Topography caused by mantle density variations: Observation-based estimates and models derived from tomography and lithosphere thickness. *Geophysical Journal International*, 205, 604–621.
- Steinberger, B., C. P. Conrad, A. Osei Tutu, & M. J. Hoggard (2019). On the amplitude of dynamic topography at spherical harmonic degree two. *Tectonophysics*, 760, 221–228.
- Stephenson, S. N., G. G. Roberts, M. J. Hoggard, & A. C. Whitaker (2014). A Cenozoic uplift history of Mexico and its surroundings from longitudinal river profiles. *Geochemistry, Geophysics, Geosystems*, 15, 4734–4758.
- Stephenson, S. N., N. J. White, T. Li, & L. T. Robinson (2019). Disentangling interglacial sea level and global dynamic topography: Analysis of Madagascar. *Earth and Planetary Science Letters*, 519, 61–69.
- Stock, J. D. & D. R. Montgomery (1999). Geologic constraints on bedrock river incision using the stream power law. *Journal of Geophysical Research: Solid Earth*, 104 (B3), 4983–4993.
- Stotz, I. L., G. Iaffaldano, & D. R. Davies (2018). Pressure-driven Poiseuille flow: A major component of the torque-balance governing Pacific plate motion. *Geophysical Research Letters*, 45, 117–125.
- Stucky de Quay, G., G. G. Roberts, J. S. Watson, & C. A.-L. Jackson (2017). Incipient mantle plume evolution: Constraints from ancient landscapes buried beneath the North Sea. *Geochemistry Geophysics Geosystems*, 18, 973–993.
- Szwillus, W., J. C. Afonso, J. Ebbing, & W. D. Mooney (2019). Global crustal thickness and velocity structure from geostatistical analysis of seismic data. *Journal of Geophysical Research: Solid Earth*, 124, 1626–1652.
- Tofelde, S., W. Duesing, T. F. Schildgen, A. D. Wickert, H. Wittmann, R. N. Alonso, & M. Strecker (2018). Effects of deep-seated versus shallow hillslope processes on cosmogenic ^{10}Be concentrations in fluvial sand and gravel. *Earth Surface Processes and Landforms*, 43, 3086–3098.
- Tucker, G. E. & G. R. Hancock (2010). Modelling landscape evolution. *Earth Surface Processes and Landforms*, 35, 28–50.
- Tucker, G. E., S. Lancaster, N. Gasparini, & R. Bras (2001). The channel-hillslope integrated landscape development model

- (CHILD). In: *Landscape Erosion and Evolution Modeling* (edited by R. S. Harmon & W. W. Doe), chap. 12, pp. 349–388. Kluwer Academic/Plenum Publishers, New York.
- Turcotte, D. L. & E. R. Oxburgh (1967). Finite amplitude convective cells and continental drift. *Journal of Fluid Mechanics*, 28 (1), 29–42.
- Turcotte, D. L. & G. Schubert (2002). *Geodynamics*. Cambridge University Press, Cambridge, 2nd edn.
- Underhill, J. R. (2001). Controls on the genesis and prospectivity of Paleogene palaeogeomorphic traps, East Shetland Platform, UK North Sea. *Marine and Petroleum Geology*, 18, 259–281.
- Urey, H. C. (1947). The thermodynamic properties of isotopic substances. *Journal of the Chemical Society*, pp. 562–581.
- Vail, P. R., R. M. Mitchum, & S. Thompson (1977). Seismic stratigraphy and global changes of sea level, Part 4: Global cycles of relative changes of sea level. *American Association of Petroleum Geologists*, 26, 83–97.
- Vasconcelos, P. M., T. A. Becker, P. R. Renne, & G. H. Brimhall (1992). Age and duration of weathering by K-Ar and Ar/Ar analysis of potassium-manganese oxides. *Science*, 258, 451–455.
- Vibe, Y., A. M. Friedrich, H. Bunge, & S. R. Clark (2018). Correlations of oceanic spreading rates and hiatus surface area in the North Atlantic realm. *Lithosphere*, 10 (5), 677–684.
- Vogt, P. R. (1971). Asthenosphere motion recorded by the ocean floor south of Iceland. *Earth and Planetary Science Letters*, 13, 153–160.
- Wagner, G. A. (1968). Fission track dating of apatites. *Earth and Planetary Science Letters*, 4, 411–415.
- Wahr, J., M. Molenaar, & F. Bryan (1998). Time variability of the Earth's gravity field: Hydrological and oceanic effects and their possible detection using GRACE. *Journal of Geophysical Research: Solid Earth*, 103 (B12), 30,205–30,229.
- Walford, H. L., N. J. White, & J. C. Sydow (2005). Solid sediment load history of the Zambezi Delta. *Earth and Planetary Science Letters*, 238, 49–63.
- Walker, R. T., M. Telfer, R. L. Kahle, M. W. Dee, B. Kahle, J.-L. Schwenninger, R. A. Sloan, & A. B. Watts (2016). Rapid mantle-driven uplift along the Angolan margin in the late Quaternary. *Nature Geoscience*, 9 (11), 909–914.
- Wallinga, J. (2002). Optically stimulated luminescence dating of fluvial deposits: A review. *Boreas*, 31, 303–322.
- Watkins, C. E. & C. P. Conrad (2018). Constraints on dynamic topography from asymmetric subsidence of the mid-ocean ridges. *Earth and Planetary Science Letters*, 484, 264–275.
- Weinstein, S. A. & P. Olson (1990). Planforms in thermal convection with internal heat sources at large Rayleigh and Prandtl numbers. *Geophysical Research Letters*, 17 (3), 239–242.
- Weissel, J. K. & M. A. Seidl (1998). Inland propagation of erosional escarpments and river profile evolution across the southeast Australian passive continental margin. *Geophysical Monograph Series*, 107, 189–206.
- Wheeler, J. (2010). Anisotropic rheology during grain boundary diffusion creep and its relation to grain rotation, grain boundary sliding and superplasticity. *Philosophical Magazine*, 90 (21), 2841–2864.
- Whipple, K. X. (2001). Fluvial landscape response time: How plausible is steady-state denudation? *American Journal of Science*, 301, 313–325.
- Whipple, K. X. & G. E. Tucker (1999). Dynamics of the stream-power river incision model: Implications for height limits of mountain ranges, landscape response timescales, and research needs. *Journal of Geophysical Research*, 104 (B8), 17,661–17,674.
- Whipple, K. X. & G. E. Tucker (2002). Implications of sediment-flux-dependent river incision models for landscape evolution. *Journal of Geophysical Research*, 107 (B2-2039).
- Whitehouse, P. L. (2018). Glacial isostatic adjustment modeling: Historical perspectives, recent advances, and future directions. *Earth Surface Dynamics*, 6, 401–429.
- Whittaker, A. C. (2012). How do landscapes record tectonics and climate? *Lithosphere*, 4 (2), 160–164.
- Whittaker, A. C., M. Attal, P. A. Cowie, G. E. Tucker, & G. Roberts (2008). Decoding temporal and spatial patterns of fault uplift using transient river long profiles. *Geomorphology*, 100, 506–526.
- Wildman, M., R. Brown, R. Beucher, C. Persano, F. Stuart, K. Gallagher, J. Schwanethal, & A. Carter (2016). The chronology and tectonic style of landscape evolution along the elevated Atlantic continental margin of South Africa resolved by joint apatite fission track and (U-Th-Sm)/He thermochronology. *Tectonics*, 35, 511–545.
- Willett, S. D., S. W. McCoy, J. Taylor Perron, L. Goren, & C. Y. Chen (2014). Dynamic reorganization of river basins. *Science*, 343 (6175).
- Wilson, C. R., M. Spiegelman, & P. E. van Keken (2017). TerraFERMA: The transparent finite element rapid model assembler for multiphysics problems in Earth sciences. *Geochemistry, Geophysics, Geosystems*, 18, 769–810.
- Winterbourne, J. R., A. G. Crosby, & N. J. White (2009). Depth, age and dynamic topography of oceanic lithosphere beneath heavily sedimented Atlantic margins. *Earth and Planetary Science Letters*, 287, 137–151.
- Winterbourne, J. R., N. J. White, & A. G. Crosby (2014). Accurate measurements of residual topography from the oceanic realm. *Tectonics*, 33.
- Wolf, R. A., K. A. Farley, & D. M. Kass (1998). Modeling of the temperature sensitivity of the apatite (U-Th)/He thermochronometer. *Chemical Geology*, 148, 105–114.
- Wolfe, J. A., H. E. Schorn, C. E. Forest, & P. Molnar (1997). Paleobotanical evidence for high altitudes in Nevada during the Miocene. *Science*, 276, 1672–1675.
- Worthen, J., G. Stadler, N. Petra, M. Gurnis, & O. Ghattas (2014). Towards adjoint-based inversion for rheological parameters in nonlinear viscous mantle flow. *Physics of the Earth and Planetary Interiors*, 234, 23–34.
- Wright, J. D. & K. G. Miller (1996). Control of North Atlantic Deep Water circulation by the Greenland-Scotland Ridge. *Paleoceanography*, 11 (2), 157–170.
- Yamauchi, H. & Y. Takei (2016). Polycrystal anelasticity at near-solidus temperatures. *Journal of Geophysical Research: Solid Earth*, 121 (11), 7790–7820.

- Yang, R., S. D. Willett, & L. Goren (2015). In situ low-relief landscape formation as a result of river network disruption. *Nature*, *520*, 526–529.
- Yang, T. & M. Gurnis (2016). Dynamic topography, gravity and the role of lateral viscosity variations from inversion of global mantle flow. *Geophysical Journal International*, *207* (2), 1186–1202.
- Yang, T., L. Moresi, R. D. Müller, & M. Gurnis (2017). Oceanic residual topography agrees with mantle flow predictions at long wavelengths. *Geophysical Research Letters*, *44*, 10,896–10,906.
- Young, R. & I. McDougall (1993). Long-term landscape evolution: Early Miocene and modern rivers in southern New South Wales, Australia. *The Journal of Geology*, *101*, 35–49.
- Yuen, D. A., D. M. Reuteler, S. Balachandar, V. Steinbach, A. V. Malevsky, & J. J. Smedsmo (1994). Various influences on three-dimensional mantle convection with phase transitions. *Physics of the Earth and Planetary Interiors*, *86*, 185–203.
- Zahirovic, S., N. Flament, R. D. Müller, M. Seton, & M. Gurnis (2016). Large fluctuations of shallow seas in low-lying Southeast Asia driven by mantle flow. *Geochemistry, Geophysics, Geosystems*, *17* (9), 3589–3607.
- Zhao, N., G. Hirth, R. F. Cooper, S. C. Kruckenberg, & J. Cukjati (2018). Low viscosity of mantle rocks link to enhanced phase boundary kinetics. *Earth and Planetary Science Letters*, *517*, 83–94.
- Zhong, S. & G. F. Davies (1999). Effects of plate and slab viscosities on the geoid. *Earth and Planetary Science Letters*, *170*, 487–496.
- Zhong, S., M. Gurnis, & G. Hulbert (1993). Accurate determination of surface normal stress in viscous flow from a consistent boundary flux method. *Physics of the Earth and Planetary Interiors*, *78*, 1–8.
- Zhong, S., M. Ritzwoller, N. Shapiro, W. Landuyt, J. Huang, & P. Wessel (2007). Bathymetry of the Pacific plate and its implications for thermal evolution of lithosphere and mantle dynamics. *Journal of Geophysical Research*, *112* (B06412).

16

Connecting the Deep Earth and the Atmosphere

Trond H. Torsvik^{1,2}, Henrik H. Svensen¹, Bernhard Steinberger^{1,3},
Dana L. Royer⁴, Dougal A. Jerram^{1,5,6}, Morgan T. Jones¹, and Mathew Domeier¹

ABSTRACT

Most hotspots, kimberlites, and large igneous provinces (LIPs) are sourced by plumes that rise from the margins of two large low shear-wave velocity provinces in the lowermost mantle. These thermochemical provinces have been quasi-stable for hundreds of millions years and plume heads rise through the mantle in about 30 Myr or less. LIPs provide a direct link between the deep Earth and the atmosphere but environmental consequences depend on both their volumes and the composition of the crustal rocks they are emplaced through. LIP activity can alter the plate tectonic setting by creating and modifying plate boundaries and hence changing the paleogeography and its long-term forcing on climate. Extensive blankets of LIP-lava on the Earth's surface can also enhance silicate weathering and potentially lead to CO₂ drawdown, but we find no clear relationship between LIPs and post-emplacment variation in atmospheric CO₂ proxies on very long (>10 Myrs) time-scales. Subduction flux estimates correlate well with zircon age frequency distributions through time. This suggest that continental arc activity may have played an important role in regulating long-term climate change (greenhouse vs. icehouse conditions) but only the Permo-Carboniferous icehouse show a clear correlation with the zircon record.

16.1. INTRODUCTION

The Earth's surface is ever changing as a reflection of how the deep Earth interacts with its crust and atmosphere. By controlling the distribution of continents and oceans,

construction of mountains, arc-volcanism, topography, and weathering, the process of plate tectonics plays an intricate role in shaping the climate on geological timescales. On shorter timescales, large igneous provinces (LIPs) can directly perturb the climate system through the massive release of gases to the atmosphere (Figure 16.1a), either from lavas and shallow intrusions, or remobilized from sedimentary rocks subjected to metamorphism in contact with subvolcanic sills, dykes, and igneous centers (Svensen et al. 2004). LIPs mark punctuated periods in Earth's history characterized by an initial onset phase followed by a large volume flux ("acme"; generally over geologically short timescales), and a waning phase (e.g., Jerram & Widdowson 2005). This main acme phase that sees the largest volumes of melt emplaced/erupted is often about one million years (Myr) or shorter in duration (e.g., Ernst 2014).

¹Centre for Earth Evolution and Dynamics, University of Oslo, Oslo, Norway

²School of Geosciences, University of Witwatersrand, Johannesburg, South Africa

³Helmholtz Centre Potsdam, GFZ German Research Centre for Geosciences, Potsdam, Germany

⁴Department of Earth and Environmental Sciences, Wesleyan University, Middletown, CT, USA

⁵DougalEARTH Ltd., Solihull, UK

⁶Earth, Environmental and Biological Sciences, Queensland University of Technology, Brisbane, Queensland, Australia

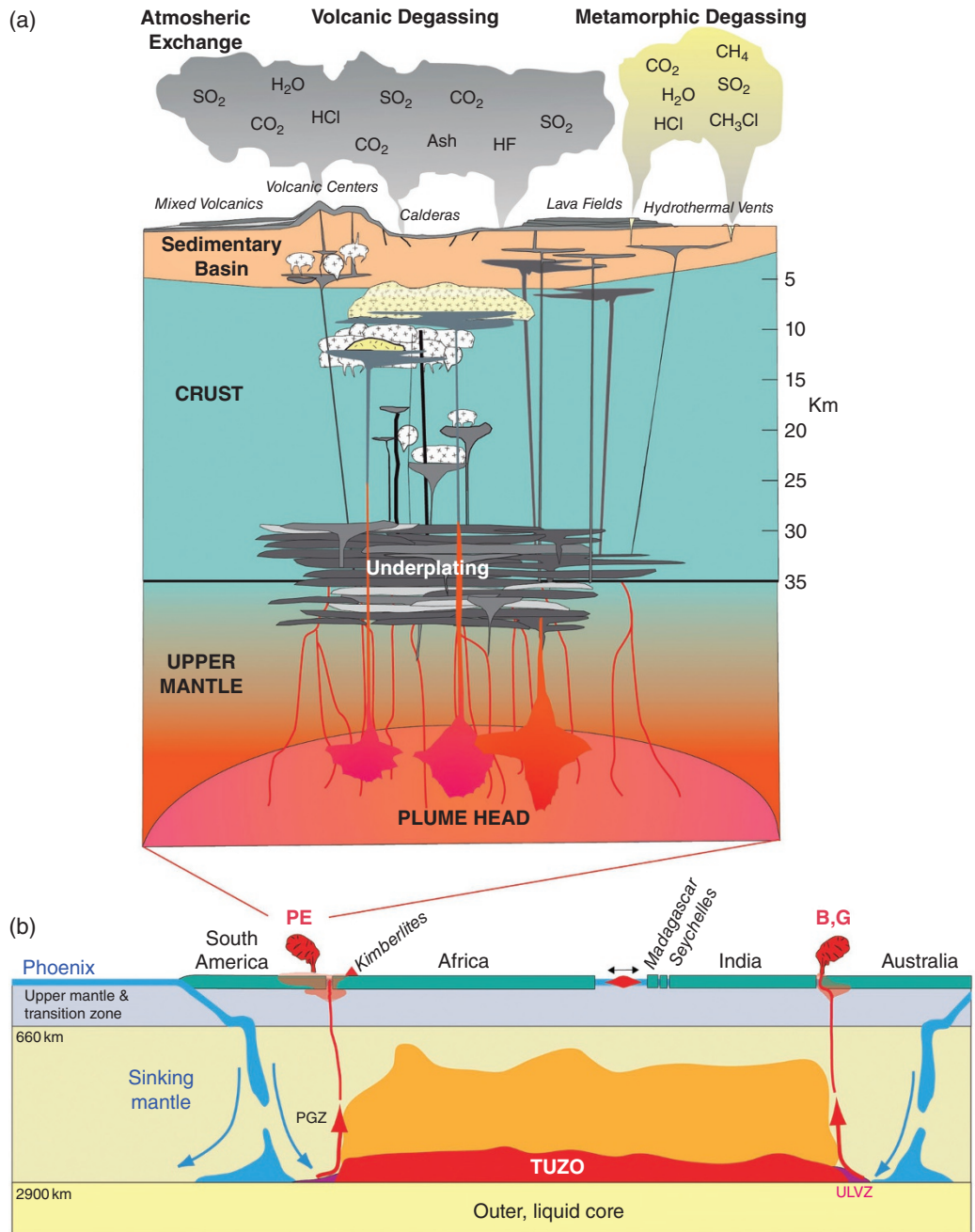


Figure 16.1 The dynamic exchanges from the core to atmosphere. (a) The internal pluming system, eruption and degassing during LIP emplacement. Melt can be emplaced at various levels within the crust and the mix of volcanic and metamorphic degassing exchanges gases into the Earth’s atmosphere (e.g., Svensen & Jamtveit 2010; Jones et al. 2016). (b) A cartoon profile approximately through the reconstructed Paraná-Etendeka (PE) LIP, North Madagascar-Seychelles, India and Australia at ~135 Ma. The slabs that influenced the formation of plumes sourcing the Paraná-Etendeka LIP, and contemporaneous kimberlites in South Africa and Namibia, were probably linked to an old subduction zone along the western margin of South America. The South Atlantic opened shortly after the Paraná-Etendeka LIP. Conversely, the Gascoyne (G) and Bunbury (B) LIPs were linked to old subduction systems along eastern Australia. Earth today is a degree-2 planet dominated by the two antipodal large low-shear-wave velocity provinces in the lower mantle (Figures 16.4b, 5) beneath Africa (TUZO) and the Pacific (JASON), which are warmer but probably also denser and stiffer than the ambient mantle in its lowermost few hundred kilometres. Here we only show TUZO, and the orange color is shown to indicate that the area above TUZO is also warmer than the background mantle. PGZ, plume generation zone; ULVZ, Ultra Low Velocity Zone. Source: (a) Adapted from Bryan et al. 2010; Jerram & Bryan 2015; Jerram et al. 2018, (b) Svensen et al. 2018; Torsvik 2018.

Such short-lived events have had a profound influence on the shaping of the Earth's surface and directly contribute to the Earth's atmosphere and biosphere. Therefore, a causal link between LIPs and mass extinctions has long been postulated (e.g., Wignall 2001). The LIPs themselves are manifest on the Earth's surface in the form of giant "traps," i.e., lava sequences, sill and dyke complexes, and large igneous centers, with preservation dependant on age, style of emplacement, and erosional/tectonic circumstances (field examples of preserved parts of various LIPs through time are shown in Figure 16.2). The rapid reshaping of the Earth's surface with aerially extensive blankets of lava can lead to large areas of juvenile volcanics undergoing weathering and erosion, thereby contributing to the sedimentary budget (Jones et al. 2016).

In the case of lava and magma degassing, the volatiles are ultimately sourced from the mantle and include carbon dioxide (CO₂), sulphur dioxide (SO₂), and hydrogen chloride (HCl). The emplacement of melts into sedimentary basins (Figure 16.1a) generates additional volatiles during prograde heating of the surrounding sedimentary rocks. Such reactions involve the release of methane (CH₄), CO₂, SO₂, HCl, and halocarbons from vast, volatile-rich reservoirs such as shale, coal, carbonates, and evaporites. Depending on the melt fluxes during the evolution of LIPs, the released gases may cause a range of environmental and climatic effects on various timescales (e.g., Jones et al. 2016). Aerosol-generating SO₂ may trigger initial global cooling on very short timescales (years), CH₄ and CO₂ can lead to global warming over longer timescales (10²–10⁵ years), whereas HCl and halocarbons perturb the atmospheric chemistry and can destabilize the ozone layer (Svensen et al. 2009; Black et al. 2012). The large volume of magma input into the Earth's surface system also leads to a marked increase in mercury (Hg) released into the environment, eventually deposited in sedimentary archives (e.g., Sanei et al. 2012). High-resolution stratigraphic studies and new proxies (such as Hg) have strengthened the view that LIPs may have played an important role in triggering key events such as mass extinctions and oceanic anoxia through rapid climate perturbations. Examples include the end-Permian (~252 Ma; Siberian Traps) and end-Triassic events (~201 Ma; Central Atlantic Magmatic Province, CAMP), the early Toarcian (~183 Ma; Karoo-Ferrar LIP), and the Paleocene-Eocene Thermal Maximum (North Atlantic Igneous Province, NAIP) at around 56 Ma (Figures 16.3b–e).

LIP emplacement (Figure 16.4a) highlights a direct link between plume generation processes in the deep mantle (Figure 16.1b), dynamic interactions within the Earth's crust, and changes within the atmosphere-hydrosphere-

biosphere system. Mantle plumes preferentially rise from the margins of two thermochemical anomalies in the deepest mantle (Burke & Torsvik 2004; Burke et al. 2008; Torsvik et al. 2006, 2010a, 2014, 2016). These regions (Figure 16.4b) are known as large low shear-wave velocity provinces (LLSVPs; Garnero et al. 2007, 2016), or simply dubbed TUZO (The Unmoved Zone Of Earth's deep mantle) and JASON (Just As Stable ON the opposite meridian), beneath Africa and the Pacific, respectively (Burke 2011), to honor the pioneering works of Tuzo Wilson (e.g., Wilson 1963) and Jason Morgan (e.g., Morgan 1971).

A simple model of surface–mantle interaction has emerged after the recognition of a remarkable correlation, not only between active hotspot volcanoes and present day deep mantle structures (Figure 16.5a), but also reconstructed kimberlites and LIPs (Figure 16.4b) for the past 300 Myrs. Numerical models of mantle convection made to investigate the stability of TUZO and JASON have shown that it is possible to maintain stability for hundreds of millions years (Steinberger & Torsvik 2012; Bower et al. 2013; Bull et al. 2014) and their continued existence for billions of years (Mulyukova et al. 2015a). However, the long-term stability of TUZO and JASON with plumes sourced from their margins is debated (e.g., Auermann et al. 2014; Davies et al. 2015; Zhong et al. 2007; Zhang et al. 2010; Zhong & Rudolph 2015; Doubrovine et al. 2016; Torsvik et al. 2016; Hassan et al. 2016; Flament et al. 2017; Tegner et al. 2019), some LIPs may not have been originating from plumes (e.g., Coltice et al. 2007), and some question the very existence of mantle plumes (e.g., Julian et al. 2015). We therefore briefly review the *observational* evidence for the existence of specific plume generation zones and LLSVP stability (Section 16.2), before moving on to estimates for how long plumes take to travel from the core–mantle boundary (CMB) to the base of the lithosphere (Section 16.3). Catastrophic melting at the base of the lithosphere can lead to the formation of LIPs at the surface and consequent atmospheric perturbations that are temporally linked to abrupt climate changes and mass extinctions (Section 16.4).

The long-term role of LIPs in the Earth system include a reduction in atmospheric CO₂ (cooling) on long timescales (10⁵ to 10⁶ years) through enhanced silicate weathering. The chemical weathering of silicates sequesters atmospheric CO₂ by providing alkalinity and dissolved cations (Ca, Mg) to the oceans, which promotes carbonate formation (Walker et al. 1981). Moreover, the supply of nutrients and reactive Fe causes the enhanced burial of organic carbon (Hawley et al. 2017). Combined, these effects work to lower atmospheric CO₂ on a range of timescales from seasonally (organic carbon) to >10,000 years

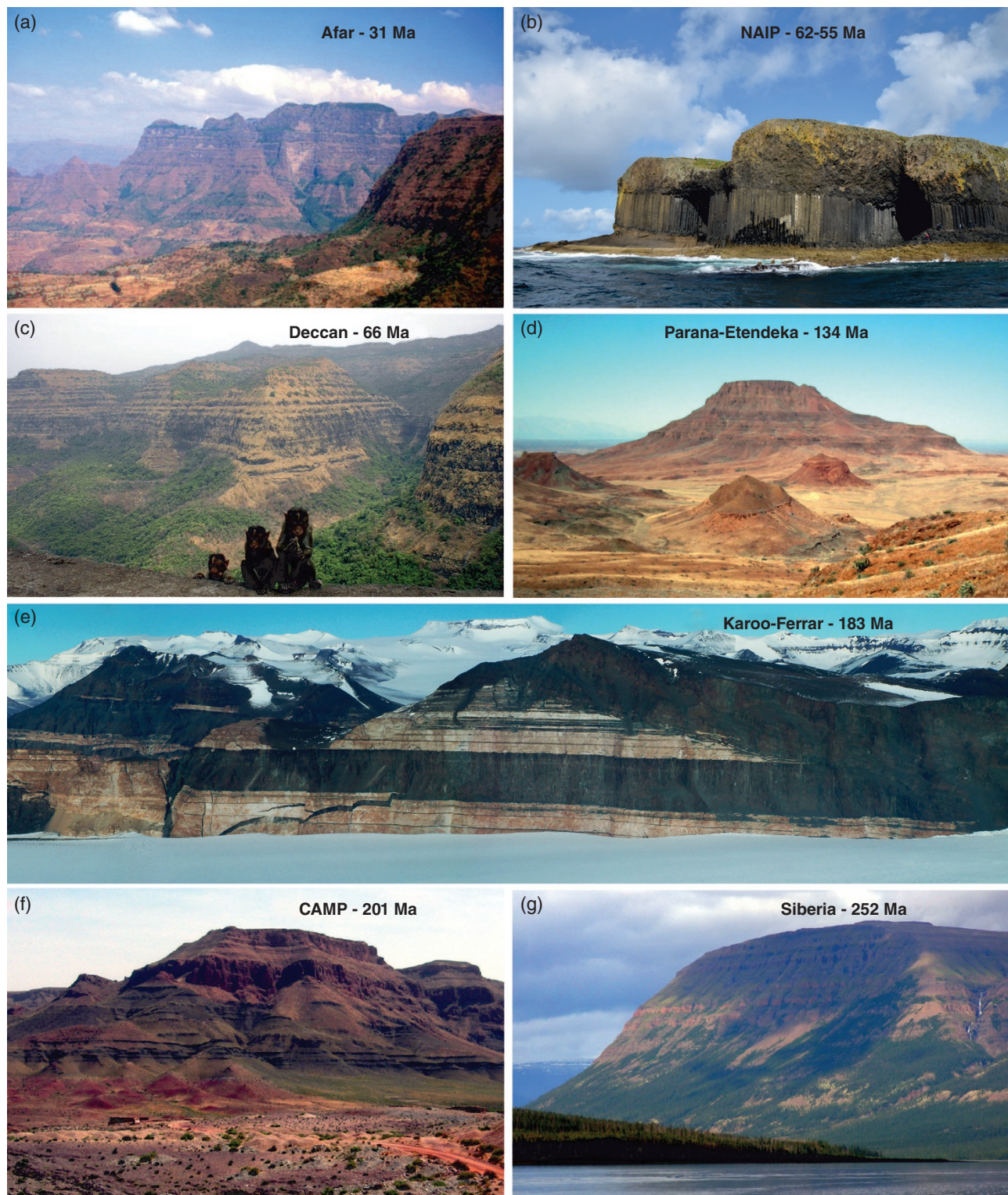


Figure 16.2 The expression of LIPs on the Earth's surface with key examples through time. (a) Ethiopian plateau, Afar (Ethiopia-Yemen province); (b) Fingal's cave, North Atlantic Igneous Province (NAIP), Scotland; (c) Deccan Traps, India; (d) Etendeka lava sequences in Namibia, Parana-Etendeka Province; (e) Giant sill complexes in Antarctica, Karoo-Ferrar Province; (f) Rare lava flow examples in Morocco, Central Atlantic Magmatic Province (CAMP); (g) Siberian Traps in Russia. Source: (a-e) Photographs by Dougal Jerram, (f) Courtesy of Sara Callegaro, (g) Photographs by Dougal Jerram.

(carbonate formation). The denudation of basaltic terrains is a particularly important component of silicate weathering, with modern estimates predicting that such terrains contribute 30–35% of the terrestrial silicate flux, despite comprising only ~5% of the continental surface area (Dessert et al. 2003). Projected subaerial extents of LIPs are a similar order of magnitude to the modern aerial extent of basaltic terrains ($6.85 \times 10^6 \text{ km}^2$), indicating that the arrival of abundant lavas and volcanic products at the Earth surface may have a strong impact on global silicate weathering rates.

Weathering is largely controlled by relief and climate, where LIPs in cold and dry climates weather slowly, and warm and wet environments lead to rapid weathering. A striking example is the difference between the CAMP emplaced at 201 Ma and the Siberian Traps erupted at 252 Ma. The CAMP (Figure 16.2f) was emplaced in the tropics (Figure 16.3d) and most of the flood basalts are argued to have eroded rapidly (Marzoli et al. 2018), which makes it very challenging to reconstruct the original LIP volumes, including melt fluxes and volatile release (Svensen et al. 2018). The present-day volume of the CAMP *flood basalts* is estimated to be about $0.1 \times 10^6 \text{ km}^3$, with an original volume on the order of $1.5 \times 10^6 \text{ km}^3$; this represents a preservation of ~7% (cf. Marzoli et al. 2018). In contrast, the Siberian Traps, located at ~60° North (Figure 16.3d) since the Triassic, still have about 22% of the original flood basalt volume remaining (cf. Vasiliev et al. 2000; $0.651 \times 10^6 \text{ km}^3$ of present day flood basalts versus an assumed original volume of $3 \times 10^6 \text{ km}^3$). Although the original volume of the Siberian Traps flood basalts is poorly constrained, it would need to be $8.6 \times 10^6 \text{ km}^3$ in order to obtain the same percentage of preservation as that for the CAMP. In Section 16.5 we consider such long-term effects stemming from the complex interplay of LIP emplacement, paleogeography, weathering, atmospheric CO₂ fluctuations and climate.

16.2. OBSERVED LINKS BETWEEN DEEP EARTH AND SURFACE VOLCANISM

There are three distinct kinds of volcanic systems that are interpreted to be related to the deep mantle: LIPs (Figure 16.4b), kimberlites, and hotspot volcanoes (Figure 16.5a). Almost all of these features laid, at the time of their original eruption, vertically or nearly vertically above the margins of TUZO and JASON. By comparing restored LIPs with global tomographic shear-wave models (Torsvik et al. 2006; Doubrovine et al. 2016), it becomes apparent that most reconstructed LIPs overlie a contour of constant velocity which corresponds to the largest horizontal velocity gradient in the lowermost mantle. That is

the 1% slow contour in the *smean* model (Becker & Boschi 2002), or the 0.9% slow contour in the *s10mean* model (Doubrovine et al. 2016), both at 2800 km depth. This contour was originally dubbed the faster/slower boundary (Torsvik et al. 2006) and later the plume generation zone (PGZ; Burke et al. 2008; red lines in Figures 16.4b, 16.5). Global shear-wave-velocity models provide broadly similar characteristics near the CMB (e.g., Torsvik et al. 2008a, 2014; Doubrovine et al. 2016; Garnero et al. 2016), the choice of tomographic model is therefore not critical to our analysis below, but leads to slightly different statistical correlations. Also note that *smean* (Becker & Boschi 2002) and *s10mean* (Doubrovine et al. 2016) are averaged from 3 and 10 global shear-wave-velocity models, respectively. Around 30 global tomography models can be visualized and compared at <http://submachine.earth.ox.ac.uk> (Hossenli et al. 2018).

Hotspots are commonly referred to as volcanism unrelated to plate boundaries and some define linear chains of seamounts and volcanoes with a clear age progression (e.g., the Hawaiian Chain). A few hotspots also lie at the ends of volcano chains connected to a starting LIP, e.g., the Tristan (Paraná–Etendeka) and Réunion (Deccan) hotspots, while the New England hotspot (Doubrovine et al. 2012) lies at the end of a trail that was connected with Jurassic kimberlite volcanism in continental north–east America (e.g., Zurevinski et al. 2011). Numerous catalogues of hotspots have been compiled and published (e.g., Richards et al. 1988; Sleep 1990; Steinberger 2000, Courtillot et al. 2003; Torsvik et al. 2006; Morgan & Morgan 2007), but many hotspots in these lists may not have a deep plume origin. Consequently, we here only analyze 27 hotspots (Figure 16.5a, Table 16.1) classified as being sourced by deep-rooted plumes from seismic tomography (French & Romanowicz 2015). Most are today located near-vertically above the margins of TUZO and JASON and plot on average $5.9 \pm 4.4^\circ$ (great-circle distance, the shortest distance on a sphere, and reported with standard deviation) from the PGZ (0.9% slow contour in the *s10mean* model). Eruptions of kimberlites (ultrabasic magmas) were exceptionally rare in the past 50 Myrs (Figure 16.3f; Torsvik et al. 2010a), but the youngest known kimberlite volcanoes – the Igwisi Hills volcanoes in Tanzania (Dawson 1994) – erupted near-vertically above the eastern margin of TUZO (Figure 16.5a) at around 12,000 years ago (Brown et al. 2012). This young kimberlite and all hotspots in the Indo-Atlantic realm are located directly above the margins of TUZO while a few of the deeply sourced Pacific hotspots (e.g., Tahiti) are displaced toward the interior of JASON (Torsvik et al. 2016).

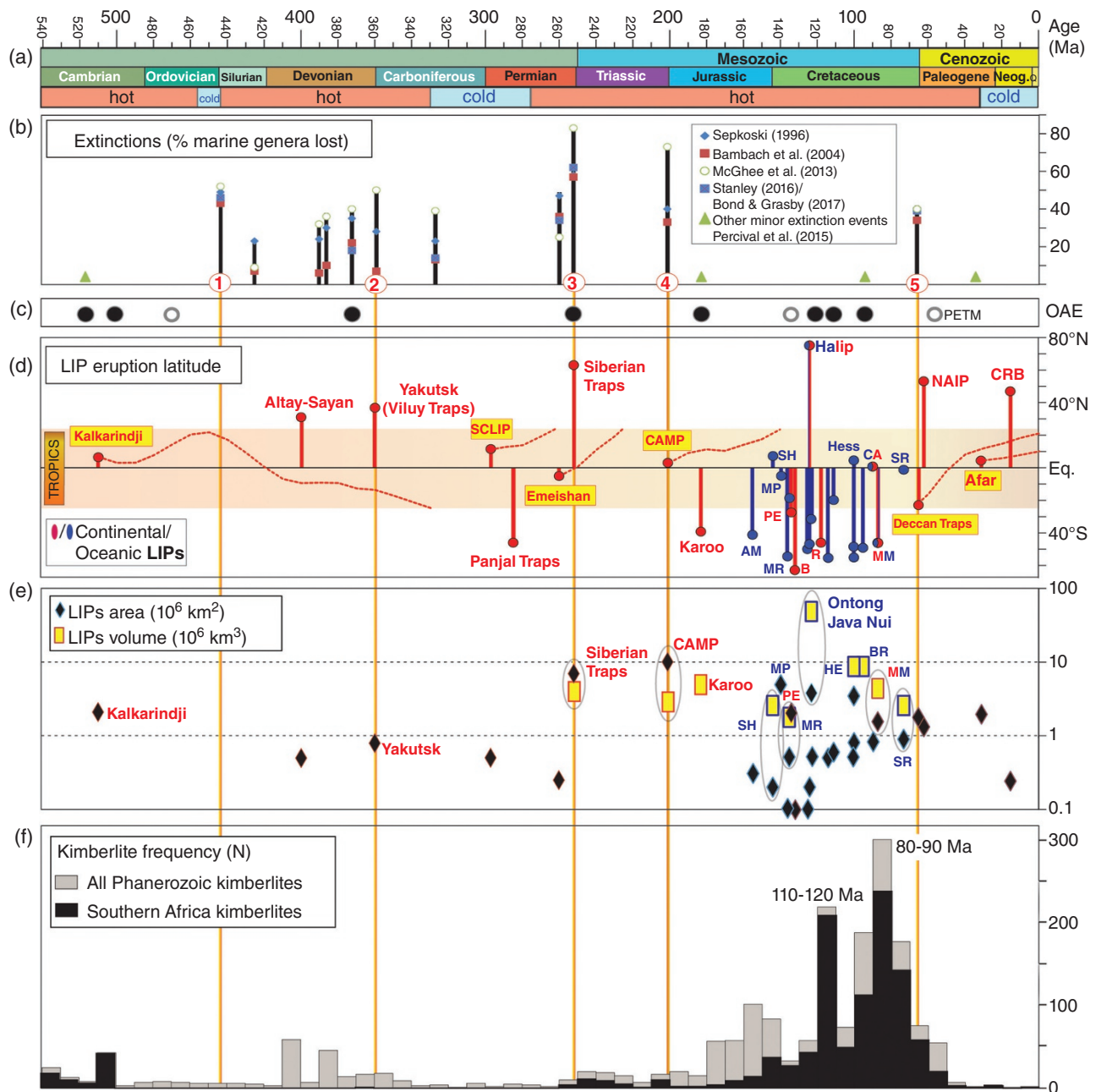


Figure 16.3 (a) Phanerozoic timescale with greenhouse (hot) versus icehouse (cold) conditions. (b) Major extinction events (% marine genera lost) and other minor extinction events. The “Big Five” mass extinctions are labeled 1 to 5 (see also Table 16.2). (c) Ocean Anoxic Events (OAEs, black filled circles) and carbon-isotope excursion/or black shale development not formally classified as OAEs (open white circles, e.g., PETM, Paleocene-Eocene thermal maximum at ~56 Ma). (d) LIP eruption latitudes calculated from paleomagnetic data (i.e., relative to the spin-axis) for the past 510 Myrs. We have reconstructed the estimated latitudinal centers through time (red dashed lines) for those LIPs that remained within the tropics for considerable times. Note that CAMP (Central Atlantic Magmatic Province) is reconstructed for North America and CAMP volcanics in NW Africa and South America will essentially stay within the tropics until present times. AM, Argo Margin; B, Bunbury; BR, Broken Ridge; CA, Caribbean; CAMP, Central Atlantic Magmatic Province; CRB, Columbia River Basalt; HALIP, High Arctic LIP; HE, Hess Rise; MR, Maud Rise; MR, Mid-Pacific Mountains; MM, Madagascar-Marion; NAIP, North Atlantic Igneous Province; PE, Paraná-Etendeka; SCLIP, Skagerrak Centred LIP; SH, Shatsky Rise; SR, Sierra Leone Rise; R, Rajmahal. (e) Estimated area extent and volumes for Phanerozoic LIPs (logarithmic scale). (f) Kimberlite frequency plot ($N = 1918$) for the Phanerozoic (gray bars in 10 Myr bins). Also shown the frequency distribution separately for southern African kimberlites ($N = 867$) as black bars. Globally, two main peaks are identified for the Phanerozoic – between 80–90 Ma and 110–120 Ma – but both Cretaceous peaks are dominated by kimberlite eruptions in southern Africa. Ages based on a combination of *in-house* CEED-industry sources and Tappe et al. (2018; only kimberlites and not related rocks also listed in this compilation; e.g., lamprophyres). Source: (a) Torsvik & Cocks 2017, (b) Bond & Grasby 2017, (Percival et al. 2015) (e) Ernst & Buchan 2001; Ernst 2014, (f) Torsvik et al. 2010a, 2014; Torsvik & Cocks 2017.

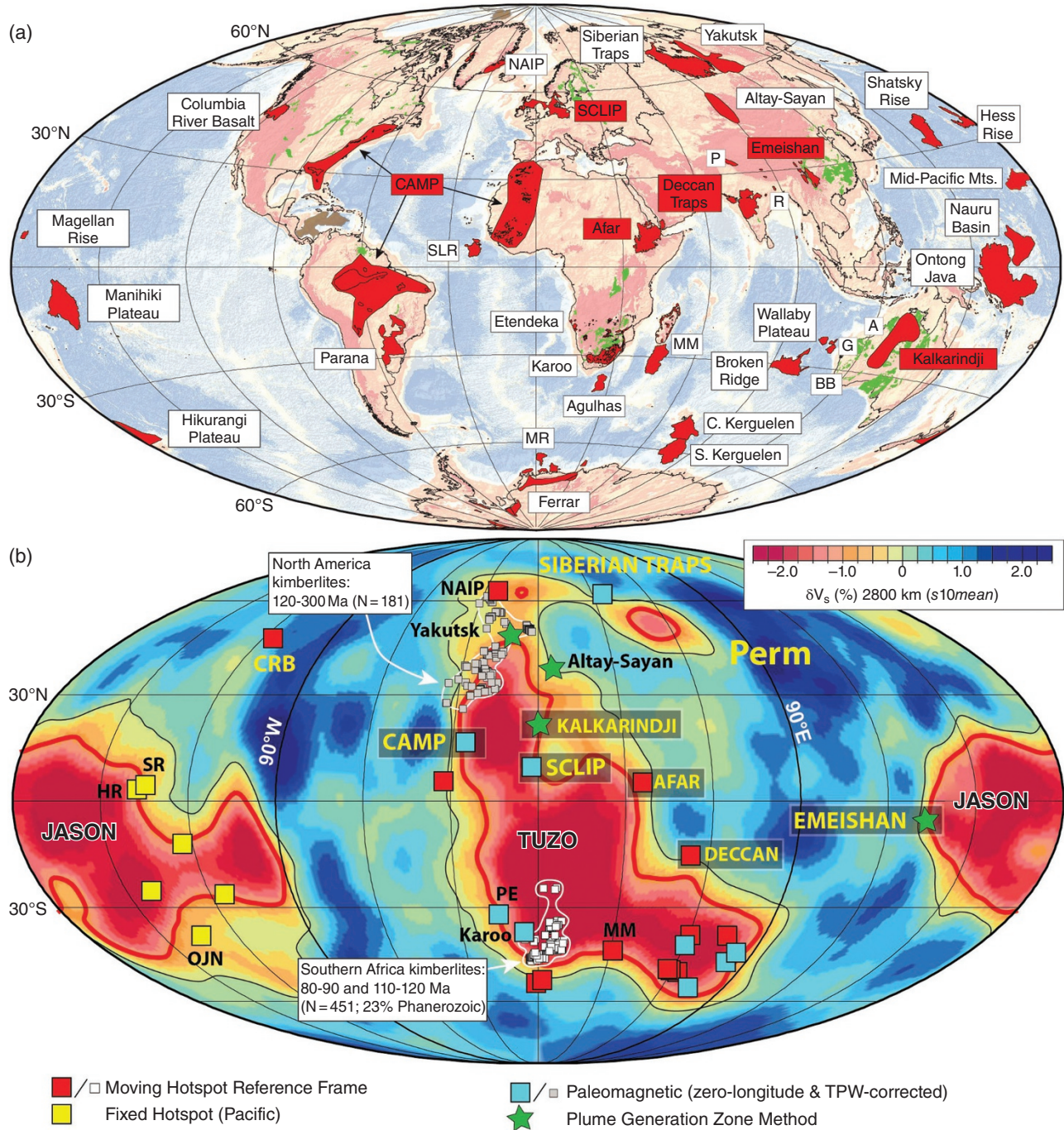


Figure 16.4 (a) The location of 32 Phanerozoic large igneous provinces (LIPs; 15–510 Myr old) which we can reconstruct with varying confidence back to their eruption time (panel b). These are shown with red polygon fills whilst two others that we do not reconstruct (Caribbean and the High Arctic LIPs) are shown with brown polygon fills. Precambrian/Early Cambrian rocks argued to be LIP-related are shown with green polygon fills. The areal extent of the Central Atlantic Magmatic Province (CAMP) is liberal in the inclusion of ~201 Myr basalts, sills and dykes. (b) Reconstructed estimated LIP centers (based on panel a) using four different reconstruction methods. After 83.5 Ma we use a global moving hotspot frame. In the Indo-Atlantic realm this is extended by a moving hotspot frame to 120 Ma (red squared symbols) and a paleomagnetic frame corrected for true polar wander 120–320 Ma (blue squared symbols). The Pacific-Panthalassic can only be extended from 83.5 Ma to ~150 Ma with a fixed hotspot frame (yellow squared symbols). Before Pangea we can use the plume generation zone (PGZ) method (green triangles) (see text for details). Reconstructed LIPs are draped on

In contrast to hotspots, LIPs (Figure 16.4a, Table 16.2) and kimberlites (except the young Igwisi Hills) must be reconstructed in a mantle reference frame in order to explore their links to present day deep-Earth mantle structures. Figure 16.4b summarizes our latest reconstructions of 32 Phanerozoic LIPs between 510 and 15 Ma. We use a global moving hotspot reference frame back to 83.5 Ma, which has been extended by a separate Indo-Atlantic moving hotspot reference frame back to 120 Ma (Dobrovine et al. 2012) and – except for the young and relatively small Colombia River Basalt – the restored LIPs fall near-vertically above the plume generation zones of an assumed fixed TUZO ($5.0 \pm 2.7^\circ$, $N = 10$ LIPs, red-colored squared symbols in Figure 16.4b). About 80% of all kimberlites that occurred since Pangea formed (Torsvik et al. 2010a) show a close link to the margins of TUZO – and as an example – reconstructed kimberlites from southern Africa (South Africa, Botswana, Angola and Lesotho) with ages between 80–90 Ma and 110–120 Ma (dominating the two peaks in global kimberlite occurrences; Figure 16.3f) plot $12.8 \pm 1.0^\circ$ ($N = 451$ kimberlites) from the PGZ (white-colored squared symbols in Figure 16.4b).

The Pacific Plate can only be linked through plate-circuits to the Indo-Atlantic realm for the last 83.5 Ma, and before that, the Pacific Plate must be referenced directly to the mantle using a fixed hotspot scheme. Here we use a new hotspot model of Torsvik et al. (2019) to reconstruct Pacific LIPs between 100 Ma (Hess Rise) and 144 Ma (Shatsky Rise). The new model shows similarities to that of Wessel and Kroenke (2008), but net lithosphere rotation and Pacific Plate velocities are much lower, and a total of six reconstructed Pacific LIPs (yellow squared symbols in Figure 16.4b) fall near-vertically above the PGZ of JASON ($3.2 \pm 2.8^\circ$, $N = 6$ LIPs). No kimberlites are related to JASON for the past 320 Ma since kimberlites are mostly derived from great depths in continental lithosphere and no continents have overlain

JASON since Pangea formed. In the Indo-Atlantic domain, LIPs older than 120 Ma are reconstructed with true polar wander (TPW) corrected paleomagnetic data (Torsvik et al. 2012; Dobrovine et al. 2016; Torsvik 2018), and reconstructed LIPs between 120 Ma and 297 Ma (Figure 16.4b) also closely correlate with the PGZs of TUZO ($4.1 \pm 3.1^\circ$, $N = 11$ LIPs). This is also the case for most kimberlites before 120 Ma, and as an example, reconstructed North American kimberlites (USA, Canada) with ages between 120 and 300 Ma cluster along the northwest PGZ margin of TUZO ($4 \pm 4^\circ$, $N = 181$ kimberlites, gray-colored squared symbols in Figure 16.4b).

Austermann et al. (2014) and Davies et al. (2015) have argued that the observed correlation between the reconstructed LIPs and the margins of TUZO and JASON (Figure 16.4b) can be equally well or even better explained by deep plumes forming randomly over the entire area associated with the LLSVPs. This criticism was addressed statistically in Dobrovine et al. (2016), and although the hypothesis proposing that LIP-sourcing plumes form randomly over the entire area of TUZO and JASON cannot be ruled out, probability models assuming plumes rising from their margins provide a much better fit to the observed distribution of reconstructed LIPs.

The striking spatial correlation between reconstructed LIPs and the PGZs of TUZO and JASON for the past 300 Ma (also the case for kimberlites and TUZO PGZs) implies that TUZO and JASON have remained quasi-stable since Pangea formed. Taking a step further, if we assume that TUZO and JASON were likewise stable in earlier time (before 300 Ma), we can calibrate continental longitudes in such a way that LIPs and kimberlites erupted above the edges of TUZO and JASON (Torsvik et al. 2014). This is known as the plume generation zone reconstruction method; there are ~300 kimberlites but only three Paleozoic LIPs to be reconstructed in this manner, i.e., the ~360 Ma Yakutsk LIP (Siberia), the

Figure 16.4 (Continued) the *s10mean* tomography model (2800 km depth). The lowermost mantle is dominated by two antipodal large low shear-wave velocity provinces (LLSVPs) beneath Africa (TUZO) and the Pacific (JASON). Most LIPs are formed near their margins – the plume generation zones (PGZs) – which are approximated by the 0.9% slow contour (thick red line) in *s10mean*. The Columbia River Basalt (CRB) is an exception as it erupted above an area of high shear-wave velocities (blue regions) in the lowermost mantle and the Siberian Traps may overlie a smaller and perhaps separate anomaly, named Perm. Abbreviated LIPs include: A, Argo; BB, Bunbury; CAMP, Central Atlantic Magmatic Province; G, Gascoyne; HR, Hess Rise; MM, Madagascar-Marion; MR, Maud Rise; NAIP, North Atlantic Igneous Province; OJN, Ontong Java Nui; P, Panjal; PE, Parana-Etendeka; R, Rajmahal; SCLIP, Skagerrak Centred LIP; SLR, Sierra Leone Rise; SR, Shatsky Rise. We have highlighted six continental LIPs that erupted at low latitudes (e.g., CAMP). We have also included two examples of reconstructed kimberlites, (i) reconstruction of 451 Southern African (South Africa, Botswana, Angola & Lesotho) kimberlites between 80–90 Ma and 110–120 Ma (dominating the two global kimberlite frequency peaks in Figure 16.3f), and (ii) reconstruction of 181 North American (USA, Canada) kimberlites with ages 120–300 Ma. Source: (a) Modified after Ernst (2014), (b) Torsvik et al. (2019), Dobrovine et al. (2016), Garnero et al. (2007), Lekic et al. (2012).

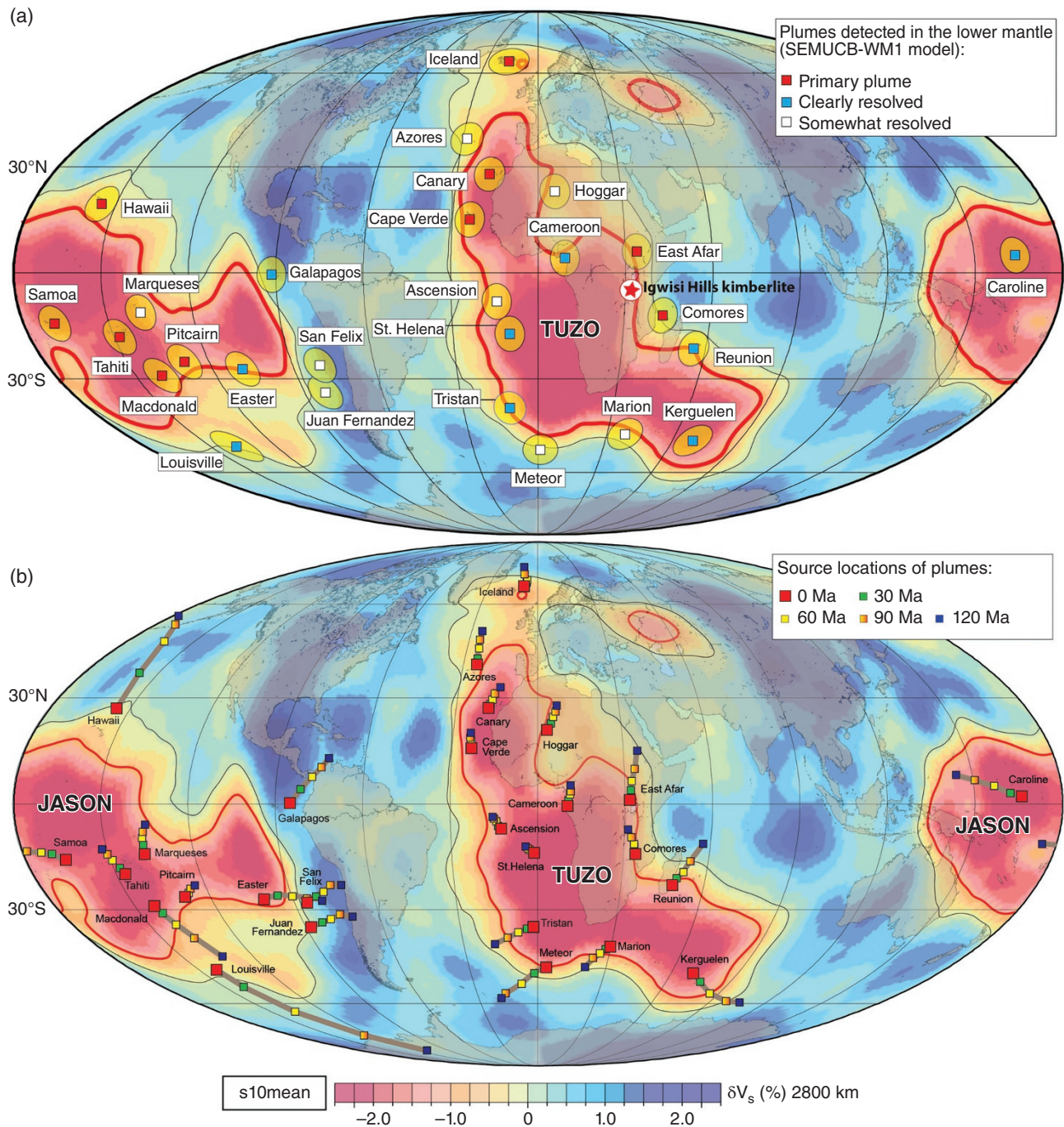


Figure 16.5 (a) Seismic tomographic $s10_{mean}$ model (δV_s %) at 2800 km depth (Dubrovine et al. 2016). The thick red line is the 0.9% slow contour and approximates the plume generation zones (PGZs; largest horizontal gradients in $s10_{mean}$). The thin black lines are the zero contours. The location of 27 inferred deep-rooted plumes (French & Romanowicz 2015) are shown with 5° ovals which are close to the average great-circle distance to the PGZ ($5.8 \pm 4.4^\circ$). We also show the location of the youngest kimberlite on Earth (Igwisi Hills kimberlite in Tanzania), only 12,000 years and can therefore be shown on the map without reconstructing it. (b) Computed plume source locations in the lowermost mantle for plume head rise times 0–120 Myr, for time-dependent mantle flow based on $s10_{mean}$ tomography, and considering the LLSVPs to be chemically dense piles (see text and Appendix 16.1).

Table 16.1 List of 27 hotspots that we analyse (Figure 16.5) and which are those considered to be potentially sourced by deep plumes from the core–mantle boundary (French & Romanowicz 2015). We largely adopted hotspot ages, anomalous mass (buoyancy) fluxes and hotspot locations from Steinberger (2000, *Table 1*). For plumes included in Steinberger & Antretter (2006) we adopted locations from Table 1 of that paper (the first one, if several are given). We here use ages 31 Ma for East Africa (Afar), 62 Ma for Iceland and 135 Ma for Tristan, and for Hawaii, Kerguelen, Louisville, Marion, Reunion and Samoa we adopt ages from Steinberger & Antretter (2006), based in part on newer and better age constraints of the associated flood basalts. For Ascension, which is not included in either of these papers, the location (14.3°W, 7.9°S) corresponds to Ascension Island, an age of 20 Ma is inferred from the location of the further one of two seamounts, ~500 km west of the island, and local South America plate motion in a hotspot reference frame (Dubrovine et al., 2012). Anomalous mass flux $0.7 \cdot 10^3 \text{kg/s}$ is inferred from averaging over the same sources as in Steinberger (2000).

Hotspot	Long (°)	Lat (°)	Age (Ma)	Anomalous mass flux (10^3kg/s)	Category*
Ascension	-14.3	-7.9	20	0.7	3
Azores	-28.4	38.5	100	1.2	3
Cameroon	9.2	4.2	31	0.5	2
Canary	-18	28	65	1	1
Cape Verde	-24	15	20	1.1	1
Caroline	164	5	80	1.6	2
Comores	43.3	-11.8	63	0.5	1
East Africa (<i>Afar</i>)	34	6	31	1.1	1
Easter	-109.3	-27.1	100	2.1	2
Galapagos	-91.5	-0.4	85	1.4	2
Hawaii	-155.3	19.4	120	6.5	1
Hoggar	6	23	20	0.6	3
Iceland	-17	64.4	62	1.2	1
Juan Fernandez	-82	-34	30	1.7	3
Kerguelen	69	-49	118	0.9	2
Louisville	-138.1	-50.9	121	2	2
Macdonald	-140.2	-29	120	3.6	1
Marion (<i>Crozet</i>)	37.8	-46.9	182	0.5	3
Marquesas	-138	-11	9	3.9	1
Meteor (<i>Bouvet</i>)	1	-52	120	0.5	3
Pitcairn	-129	-25	8	2.5	1
Reunion	55.7	-21.2	65	1.4	2
Samoa	-169.1	-14.1	40	1.6	1
San Felix	-80	-26	30	1.9	3
St Helena	-10	-17	100	0.4	2
Tahiti	-148.1	-17.9	5	4.5	1
Tristan	-11.3	-38.7	135	1	2

*Follows classification of French & Romanowicz (2015): (1) Primary, (2) clearly resolved, and (3) somewhat resolved.

~400 Ma Altay-Sayan LIP (South Siberia) and the ~510 Ma Kalkarindji LIP in Western Australia. All three of these LIPs erupted in the Northern Hemisphere (Figure 16.3d), and in a mantle frame (i.e., corrected for TPW) modeled to be sourced by plumes from the northeast margin of TUZO (green stars in Figure 16.4b). We have also restored a younger LIP, the ~260 Ma Emeishan LIP, to the western margin of JASON using this method (Figure 16.4b). The longitude of south China is otherwise unknown as it cannot be tied to the Indo-Atlantic reference frame through plate circuits because it was not an integrated part of Pangea in the late Paleozoic (Torsvik et al. 2008a, 2014; Jerram et al. 2016a; Torsvik & Domeier 2017).

There is also a High Arctic LIP (HALIP), originally considered to include only upper Cretaceous volcanics, on Axel Heiberg Island in the Canadian Arctic (Tarduno et al. 1998), but extended to be grouped with magmatism in many other places in the High Arctic (e.g., Svalbard, Franz Josef Land and the Barents Sea). Because radiometric ages for HALIP show a wide range (130–180 Ma) and a plume center is not readily defined, HALIP is not shown in our reconstructions of LIPs (Figure 16.4b). However, assuming that peak activity occurred around 124 Ma (based on U/Pb data on sills; Corfu et al. 2013) and a tentative plume center just to the north of Ellesmere, we estimate an eruption latitude of ~60°N (paleomagnetic frame; Figure 16.3d,

Table 16.2 Large igneous provinces (LIPs, Figure 16.4a), eruption latitude with respect to the Earth's spin axis (i.e., paleomagnetic latitude), mass extinctions (1–5), Oceanic Anoxic Events (OAEs; black shaded rows) and carbon-isotope excursion or black shale development not formally classified as OAEs (gray-shaded rows; see Figure 16.3b–d). Reconstruction of the LIPs with respect to the mantle is shown in Figure 16.4b. LIP type: CLIP, continental; OLIP, Oceanic. ^{#1}Peak magmatic activity around 55–56 Ma, near the PETM, and just prior to opening of the Northeast Atlantic (Torsvik et al. 2015); ^{#2}Magmatic activity occurred from 92 to 84 Ma with peak magmatic activity around 87 Ma and just a few million year before India/Seychelles drifted off Madagascar (Torsvik et al. 2001). ^{#3, #4}Uncertain to reconstruct in an absolute reference frame (not reconstructed in Figure 16.4b); ^{#5}Ernst (2014) assumed an emplacement age of 130 Ma (oldest known date is 128 Ma) whilst Madrigal et al. (2016) used an initial LIP age of 140 Ma (magnetic anomaly age) for the main volcanic constructs. ^{#6}Most preserved parts are allochthonous and thus there are considerable reconstruction uncertainties.

Age (Ma)	Large igneous province	Eruption latitude	Mass extinction/Anoxia events	LIP type
15	Columbia River Basalt	46.8°N		CLIP
31	Afar	4.2°N		CLIP
56			PETM	
62	North Atlantic Igneous Province ^{#1}	52.9°N		CLIP
66	Deccan	22.7°S	#5	CLIP
73	Sierra Leone Rise	1.4°S		OLIP
87	Madagascar ^{#2}	46°S		CLIP/OLIP
90	Caribbean ^{#3}	~ 0°N		CLIP/OLIP
94			OAE2	
95	Broken Ridge	49.3°S		OLIP
100	Hess Rise	4.3°N		OLIP
100	Central Kerguelen	48.7°S		OLIP
100	Agulhas Plateau	55.2°S		OLIP
111	Nauru Basin	20°S	OAE1b	OLIP
114	South Kerguelen	55.3°S		OLIP
118	Rajmahal	46.1°S		CLIP
121			OAE1a	
123	Ontong Java Nui mega-LIP (Ontong Java, Manihiki & Hikurangi Plateaus)	31.4°S		OLIP
124	High Arctic LIP ^{#4}	~ 60°N		CLIP/OLIP
124	Wallaby Plateau	47.2°S		OLIP
125	Maud Rise	49.9°S		OLIP
132	Bunbury	62.7°S		CLIP
134	Paraná-Etendeka	27.7°S		CLIP
135	Magellan Rise	18.6°S		OLIP
136	Gascoyne	54.5°S		OLIP
140	Mid-Pacific Mountains ^{#5}	6.1°S		OLPI
144	Shatsky Rise	7°N		OLIP
155	Argo Margin	41.3°S		OLIP
183	Karoo-Ferrar	39.5°S	OAE	CLIP
201	Central Atlantic Magmatic Province	2.8°N	#4	CLIP
252	Siberian Traps	62.4°N	#3	CLIP
260	Emeishan	5.1°S		CLIP
285	Panjal Traps (Tethyan Plume) ^{#6}	46.2°S		CLIP
297	Skagerrak Centred LIP	11.3°N		CLIP
360	Yakutsk	36.6°N	#2	CLIP
372			OAE	
400	Altay-Sayan	30.9°N		CLIP
470				
445			#1	
501			OAE	
510	Kalkarindji	6.5°N		CLIP
517			OAE	

Table 16.2) – and sourced by a mantle plume from the northernmost areas of TUZO. The Cretaceous Caribbean LIP is also not included in our analysis (Figure 16.4b) because of plate reconstruction uncertainties and an unknown plume center. But using an age of ~90 Ma and a tentative plume center near the western margin of central Americas, we estimate an eruption latitude near the Equator (Figure 16.3d, Table 16.2), and sourced by a plume from the eastern margin of TUZO.

16.3. PLUME ASCENT SCENARIOS

Over the past decade considerable effort has been dedicated to estimating the sinking rate of subducted slabs through the lower mantle. On a global scale, van der Meer et al. (2010) determined an average lower-mantle slab sinking rate of ~1.2 cm/yr, but on the basis of a larger subduction dataset this sinking rate was later refined and determined to be nonlinear (van der Meer et al. 2018). Interpretation of lower mantle slab ages critically depend on their upper mantle history (Figure 16.6a): some slabs may directly penetrate the base of the transition zone (660 km), while others flatten and may stagnate for tens of million years (e.g., Goes et al. 2017). Nevertheless, a first-order estimate of whole mantle slab sinking rates will prove useful for our purposes here. Assuming sinking rates in the upper mantle of ~5 cm/yr, possible delays in the transition zone, and 1–2 cm/yr sinking rates in the lower mantle (van der Meer et al. 2010, 2018; Domeier et al. 2016), the estimated time for slabs to reach the lowermost mantle above the core–mantle boundary (CMB) is about 200–240 Myrs (Figure 16.6a). This is approximately twice as long as predictions derived from geodynamic models (Steinberger et al. 2012), although some convection models show such timing when viscosity increases with depth and thermal expansivity decreases too (Cizková et al. 2012).

Subducting slabs impose global flow, which influences the formation of instabilities and mantle plumes along the margins of TUZO and JASON (Figures 16.1b, 16.6a). As sinking slabs approach the CMB, they push material, including the hot thermal boundary layer above the CMB, ahead of them. Once these hot, displaced materials reach the boundary with the hot, but chemically dense LLSVPs, they are forced upward, and may start to rise in the form of plumes (Steinberger & Torsvik 2012). We therefore have a consistent picture of how and where plumes may start their protracted journey from the deep Earth – but a key question is, how long does a plume take to travel from the CMB to the base of the lithosphere? This could be estimated analytically for a Stokes sphere, and numerical model results also exist (e.g., Lin & Van Keken 2006), but these results are unreliable, due to large

uncertainties, especially in mantle rheology and the composition of plume material. Here we therefore take an alternative approach and investigate this question by finding plume ascent times from source locations in the lowermost mantle that most closely coincide with the edges of the LLSVPs, following the assumption that their margins should act as PGZs.

Plume source locations are determined by using an extension of an existing method: Steinberger and O’Connell (1998) initiated their computation with a vertical conduit at the time of plume head eruption. This approximation corresponds to a plume head that rises very fast, such that the conduit, which trails the head, is not much distorted during ascent of the head. They computed how, subsequent to eruption of the plume head, the conduit gets distorted and the surface hotspot moves accordingly. Here we extend this computation by taking a finite ascent time of the plume head into account, during which the motion and distortion of the conduit is already considered. Our aim, then, is to determine an ascent time that will restore a plume from its present-day surface location (which we know) to an original source location in the lowermost mantle that is proximal to a PGZ. We make the simplifying assumption that plume head rising speed is inversely proportional to ambient mantle viscosity at that depth, and absolute values are chosen such that a specified total ascent time results. Because viscosity reaches its maximum in the lower part of the lower mantle, plume heads rise most slowly in that depth range, and their lateral advection is therefore dominated by the horizontal flow component at those depths. In general, because that flow is dominated by a degree-2 pattern with horizontal flow converging toward the two LLSVPs (Figure 16.6a), the rate at which a plume ascends controls the computed location of its source and specifically its distance from a PGZ: the slower a plume ascends, the farther its original source location must lie from the edge of the nearest LLSVP. The question to be addressed, hence, is whether there is a single ascent time, or a range of times, for which the computed plume source locations match the PGZs comparatively well. This could then be seen as an indication for the realistic time it takes a plume to rise. Obviously, one simplification of this approach is the assumption that, for a given model case, all plumes take the same time to rise through the mantle. *In reality, plume heads may have different sizes and hence rise at different speeds through the mantle.* Furthermore, a plume head may ascend faster or slower because of rising or sinking ambient mantle flow. A second implicit assumption of this approach is that all plumes should have nucleated along a PGZ (see Appendix 16.1 for method details).

Figure 16.5b shows the computed plume head source locations in the lowermost mantle. Present-day hotspot locations (Figure 16.5a) tend to be near the

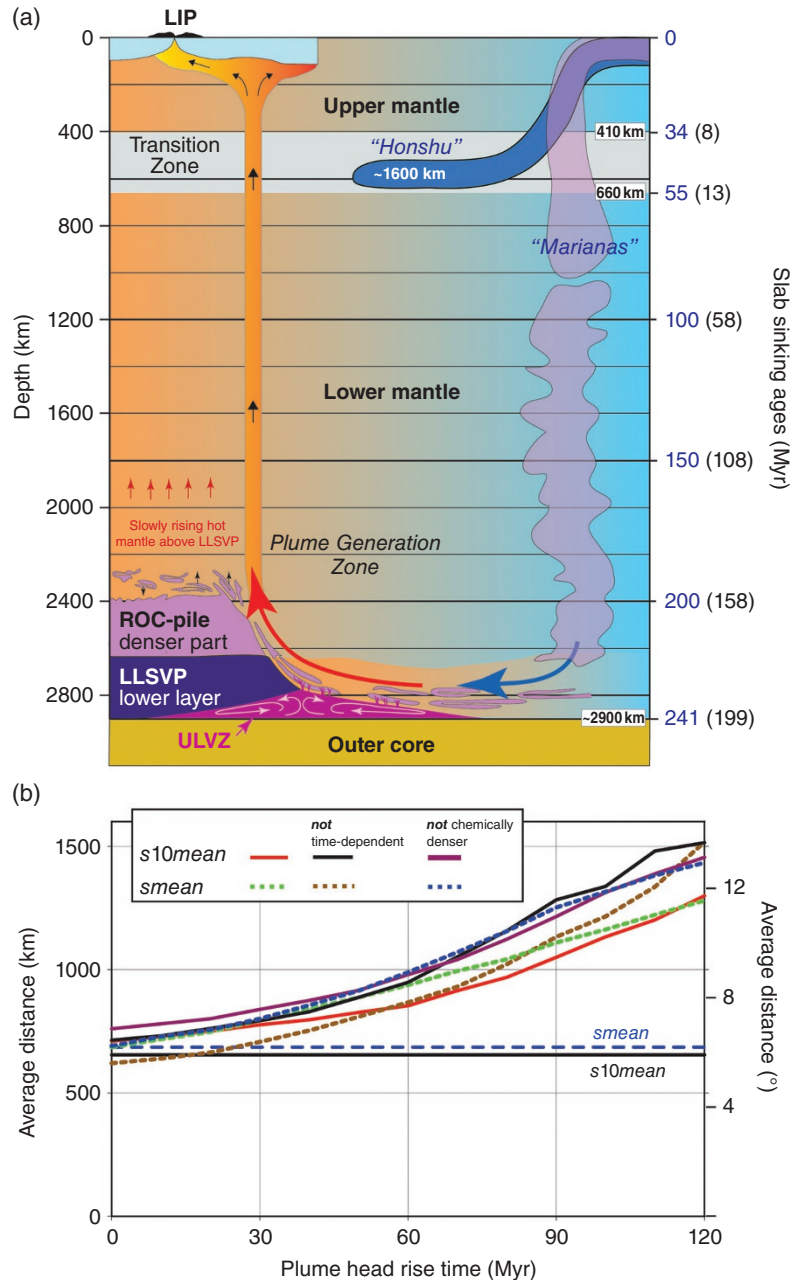


Figure 16.6 (a) Schematic representations of present-day sinking slabs (based on fast seismic anomalies; Goes et al. 2016) in the northwest and west Pacific illustrating a slab that has flattened and stagnated (Honshu with a flattened slab length of ~1600 km) and the Marianas slab that directly penetrated the base of the transition zone (660 km). Interpretation of lower mantle slab ages therefore critically depends on their upper mantle history: Black colored sinking ages (in brackets) assume sinking rates of 5 cm/yr in the upper mantle and 1.2 cm/yr in the lower mantle, and approximately represent slabs directly penetrating the transition zone and then sinking slower in the lower mantle. Blue colored slab sinking ages assume constant sinking rates (1.2 cm/yr) for the entire mantle; this is unrealistically low for the upper mantle but can be regarded as a proxy for slabs with a long residence time in the transition zone (tens of million years). This time could be longer if basaltic materials (ROC; recycled oceanic crust) first get incorporated into the thermochemical piles (LLSVPs), before they become entrained into plumes. The ROC (recycled oceanic crust) stockpile, indicated here, and forming the upper parts of the LLSVPs, might be continuously replenished in relatively stagnant regions between plumes, concurrently with erosion near plumes rooted along the LLSVP margins (Torsvik et al. 2016; Trønnes et al. 2019). Some plumes may directly penetrate the lithosphere and in the process create new plate boundaries, but “upside-down

surface-projected PGZs, but occur both inside (over the LLSVP) and outside the boundary itself. Our computed hotspot surface positions through time, in the case with initially vertical plume conduits (Steinberger & O'Connell 1998; Steinberger 2000; Steinberger et al. 2004), tend to remain near the margins, as there is no clear trend, in this case, whether the hotspot moves toward or away from the LLSVPs. This is because the advection of the plume conduit, and hence the hotspot surface motion, is influenced by both flow in the upper half of the mantle, which tends to be *away from* LLSVPs and the lower half *toward* LLSVPs. As the initially vertical plume conduits get distorted, the hotspot position initially tends to move with upper-mantle flow. Later on, segments of the tilted conduit buoyantly rise to the surface and thus the motion of older plumes rather tends to be in the direction of lower mantle flow. This is also the case for flow that is not time-dependent, i.e., it is not necessary to have time-dependent flow in order to obtain time-dependent hotspot motion. Hence, for younger plumes, the motion *away from* LLSVPs tends to dominate and for older ones the motions *toward*, but because of compensating effects the overall hotspot motion is rather slow – leading to the concept of fixed hotspots (Morgan 1971) – and the total amount of motion is rather small and not preferentially directed toward or away from the LLSVPs. Hence, the modeled initial plume positions required to match present-day hotspot positions, and the initial plume source locations, which in this case are vertically below (red squares in Figure 16.5b), are near the margins at a similar average distance to the PGZs as present-day hotspots.

Because flow in the lowermost mantle is directed toward the LLSVPs, a finite plume head rise time will be associated with a trade-off between that ascent time and the distance between the plume's source location and an LLSVP margin. The longer a plume head takes to rise to the surface, the further away from the LLSVP margins (and also from their interiors) it must have started in the lowermost mantle in order to reach the surface location observed at present day (near the projected PGZs). This clear trend can be seen both in Figure 16.5b and in

Figure 16.6b, which also shows that this trend holds for two tested tomography models, and regardless of whether time-dependence of flow, and the thermochemical excess density of LLSVPs is considered (see Appendix 16.1). It also shows that the slope of the mean distance vs. rise time curve generally gets steeper with increasing rise time. That is, increasing the rise time e.g., from 0 to 30 Myr has less of an effect – the predicted plume source locations tend to remain near the LLSVP margins – than increasing the rise time from e.g., 60 to 90 Myr (Figure 16.6b). Backward-advection of density anomalies leads to increasing stratification of the density field back in time, leading to decreasing flow velocities. Therefore, the average distance increases less strongly with plume head rise time in this case; however, the stronger increase without backward-advection (black and brown lines in Figure 16.6b) may actually be more appropriate. The observed trend, though, holds independent of the uncertain backward-advection. Also, disregarding thermochemical excess densities in LLSVPs corresponds to stronger density anomalies causing stronger flow, hence a stronger dependence of average distance on plume head rise time (violet and blue lines in Figure 16.6b). Another reason that speaks against slow rising of plume heads is that for rise times of ~80 Myr and more, an increasing number of cases occurs where the present-day hotspot position cannot be matched – which also slightly affects the results shown in Figure 16.6b.

Our approach favors that plume heads rise through the mantle in ~30 Myr or less – rather fast compared to what could be inferred from simple geodynamic considerations: Using Stokes formula and a density contrast of 30 kg/m^3 , which corresponds to realistic values of temperature and thermal expansivity for a thermal plume vs. the surrounding mantle (Steinberger & Antretter 2006), a plume rise time of 60 Myr corresponds to a plume head with a very large diameter of ~1600 km. The head radius inferred from Stokes' formula is inversely proportional to the square root of rise time; hence a more realistic diameter of 1000 km (Campbell 2007) would correspond to a rise time of more than 150 Myrs, which is incompatible with our results. There are several ways to resolve this apparent

Figure 16.6 (Continued) drainage" (Sleep 1997) provides an explanation of how LIPs may have erupted into pre-existing rifts or active spreading centres. This is exemplified here by an oceanic LIP that initially may have erupted into an active spreading ridge. (b) Average distances of plume source locations (great-circle distances in km or degrees) from the plume generation zone (PGZ). Apart from the reference case (red line, corresponding to Figure 16.5b), based on s10mean tomographic model (Dobrovine et al. 2016), we also include results with constant (not time-dependent) flow (black line), results without considering that the LLSVPs (TUZO and JASON) are chemically denser (violet line) and results based on the smean (Becker & Boschi 2002) tomography model, both for computing mantle flow and plume sources (see Appendix 16.1), and for defining the PGZ (stippled green, brown, and blue lines corresponding to red, black, and violet lines, respectively). Horizontal lines show the average distance of surface hotspot locations, for comparison, from PGZ's based on s10mean (black) and smean (stippled blue; -1% contour).

discrepancy: First, plume heads could be much larger than often assumed, although this would imply much lower melting rates than commonly assumed to explain the volume of flood basalts (Richards et al. 1989), or that melting only occurs in a small part of the plume head. Second, it is plausible that plume heads encounter a lower-than-average ambient mantle viscosity, as they rise through the mantle above the LLSVPs, where the mantle may, on average, be hotter and hence less viscous. They may also be aided by large-scale flow, which tends to be upward above the LLSVPs (Conrad et al. 2013). In addition, if viscosity is stress-dependent, effective mantle viscosity may be reduced in the surroundings of the plume head, further reducing rise times. The inferred rather fast plume ascent speeds contrast with the slabs, which appear to sink only about half as fast as geodynamic models would predict (van der Meer et al. 2010, 2018; Domeier et al. 2016).

Combining plume ascent times of ~ 30 Myr and slab sinking times ~ 200 Myr with the time that basaltic material remains near the CMB (also ~ 30 Myr, if we assume an average horizontal flow speed of ~ 10 cm/yr, and a typical distance from where slabs reach the lowermost mantle to the PGZs of about 3000 km), we estimate that ~ 260 Myr must elapse from the subduction of oceanic crustal materials until eruption of recycled crustal components in hotspot lavas, whereby the most time is spent on the way down. This time could be much longer, if basaltic materials get first incorporated into the thermochemical piles (Figure 16.6a), before they become entrained into plumes. Numerical models of Mulyukova et al. (2015b) show that a large fraction of basaltic material is effectively immediately recycled, entrained by plumes, i.e., the age versus frequency of occurrence plot tends to show a maximum at a young age, but there is also a long tail toward older ages, i.e., material can linger near the CMB for a billion years and longer, and there is considerable variability in the age distribution between individual plumes. In contrast, the time from when a slab starts sinking (i.e., a new subduction zone is formed) until a plume rises to the surface in response to the sinking of that slab can also be considerably shorter than the ~ 260 Myrs estimated for material transport – perhaps only about half as long – as the slab pushes material ahead it and therefore influences the formation of instabilities and plumes long before it has even reached the lowermost mantle (Steinberger & Torsvik 2012).

16.4. VOLCANISM AND ENVIRONMENTAL EFFECTS ON VARIOUS TIMESCALES

We estimate that plumes rise through the mantle in ~ 30 Myr or less and the surface manifestations are hotspots,

kimberlites, and LIPs. In terms of environmental effects, hotspot and subduction related volcanoes can be significant sources of climate-sensitive gases such as halogens, carbon, and sulphur species that can disturb the climate on a wide range of timescales (Jones et al. 2016). While stochastic in nature, global volcanism is fairly constant on a millennial timescale. Large individual eruptions can lead to climate disturbances such as a sulphate aerosol cloud inducing a net cooling of the Earth's surface (e.g., Robock 2000; Thordarson et al. 2001; Thompson et al. 2009, Toohey et al. 2016), but these impacts are temporally restricted to a few years and are therefore limited as a long-term climate forcing (Schmidt et al. 2012). The radiative effects of volcanic aerosols produced by short-lived explosive hotspot and kimberlite volcanoes generally have relatively small climate effects compared with that of LIPs due to the volumetric and flux differences. In order to further discuss the environmental effects of plume-related volcanism, we start by addressing kimberlite eruptions before moving on to LIPs.

16.4.1. Kimberlites

Hotspot observations are known from present-day examples (e.g., from Hawaii and Iceland), whereas kimberlite eruptions have not been witnessed in modern times. It can be shown that the majority of late Paleozoic-recent kimberlites are related to TUZO (Torsvik et al. 2010a), and clearly linked with the mantle, as they are derived from great depths (>150 km; Wyllie 1980; Mitchell 1986), entraining host rocks from the mantle upward during rapid ascent, as witnessed by the fragmental content of the erupted products (e.g., Jerram et al. 2009). Around 75% of all known Mesozoic-Cenozoic kimberlites are of Cretaceous age (~ 1100 known pipes), and they have intruded many cratonic areas (North America, Brazil, Australia, east Antarctica and India) – but the vast majority of these ($\sim 77\%$) intruded the Kalahari and Congo cratons in southern Africa at intermediate southerly latitudes (e.g., Figure 16.7a, b).

Kimberlite magmas are almost exclusively associated with old cratons, and the ascent of kimberlites is considered to be anomalously fast, even though they carry substantial mantle-derived payloads, i.e., xenoliths and xenocrysts (including diamonds). The exsolution of dissolved volatiles (primarily CO_2 and H_2O) is considered essential for providing adequate buoyancy for the high ascent rates of dense crystal-rich magmas, as well as the cone-like kimberlite shape caused by explosive eruptions (Russel et al. 2012). Kimberlites provide direct conduits between the deep mantle and the atmosphere. Kimberlite magmas with very high carbonate contents ($\text{CO}_2 \sim 20$ wt. %) are estimated to rise to the surface in a matter of hours from great depths, and eruption durations are probably

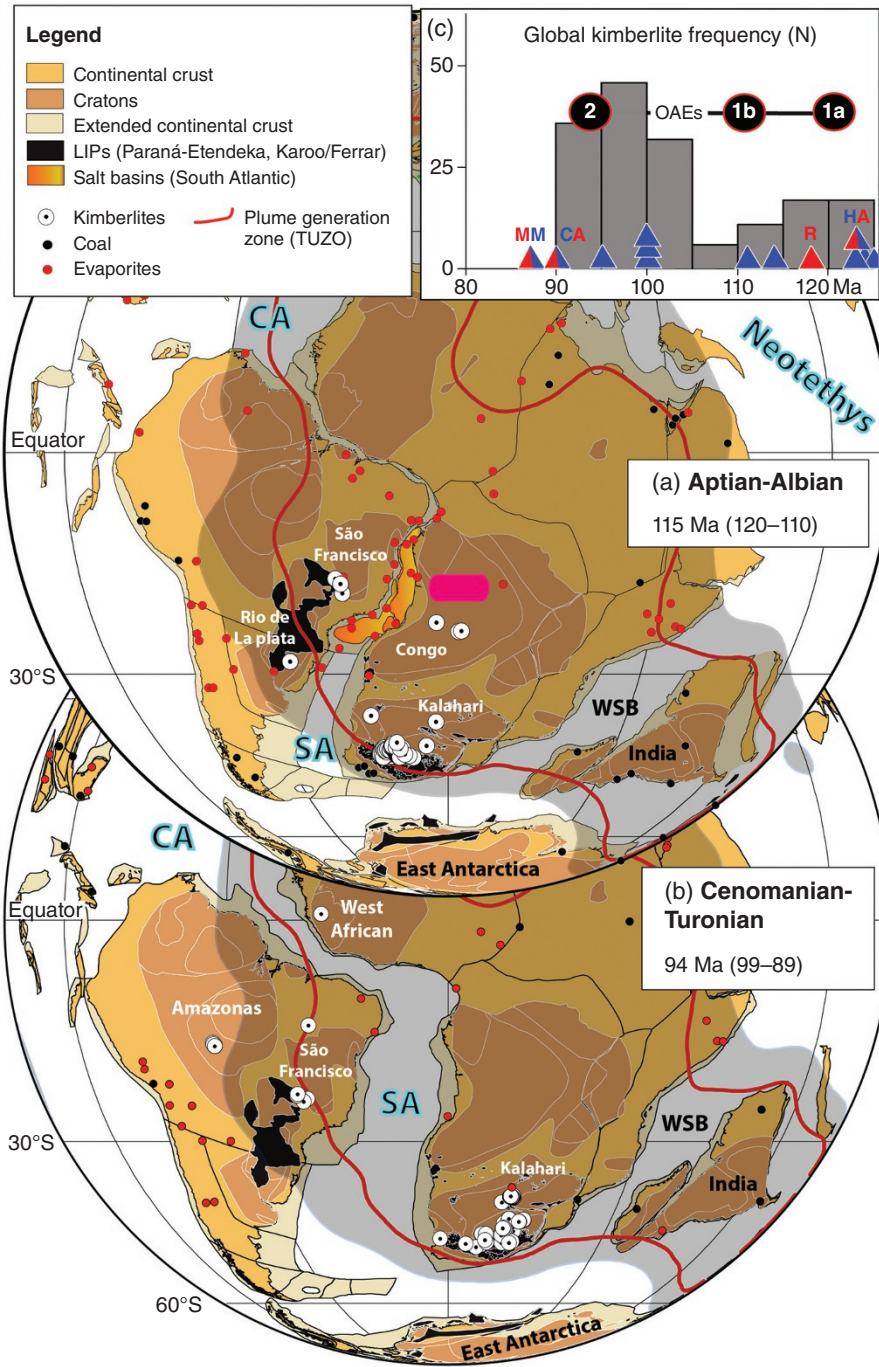


Figure 16.7 (a) Cretaceous (Aptian-Albian) paleomagnetic reconstruction (~115 Ma) with occurrences of kimberlite (large white shaded circles with a central black dot), evaporite (red shaded circles and salt basins in the South Atlantic; Torsvik et al. 2009) and coal (black/white shaded circles). Symbols may represent multiple occurrences (e.g., 213 kimberlite pipes averaging to 118 ± 2 Ma are found within the Kalahari and Congo cratons). For comparison with the areal extent of kimberlite pipes we show the LIP outlines of Paraná-Etendeka (Brazil, Namibia) and Karoo-Ferrar in southern Africa and east Antarctica. Precambrian craton outlines after Gubanov & Mooney (2009). CA, central Atlantic (early opening at around 195 Ma shortly after CAMP erupted); SA, south Atlantic (seafloor spreading south of Walvis Ridge started at ~130 Ma and shortly after Parana-Etendeka LIP erupted). WSB, West Somalian Basin (early opening at around 170 Ma and soon after Karoo-Ferrar LIP; Gaina et al. 2013). (b) Cretaceous (Cenomanian-Turonian) paleomagnetic reconstruction (~94 Ma) with occurrences of kimberlite (127 kimberlite pipes in Kalahari craton between 89 and 99 Ma),

on the order of weeks, and substantial volumes of CO₂ can therefore be released at high rates (Patterson & Don Francis 2013).

Oceanic anoxic events (OAEs) witness short interludes (< 1 Myrs) where parts of the seas were markedly exhausted in oxygen (e.g., Jenkyns 2010), and these are often viewed as the Earth's response to the injection of huge volumes of CO₂ into the atmosphere and hydrosphere (e.g., Percival et al. 2015). LIP volcanism has been linked to several OAEs (Section 16.4.2), but peak Phanerozoic kimberlite activity during the Cretaceous (Figure 16.3c,f) clearly overlaps with OAE1 (~121 Ma and ~111 Ma) and OAE2 (~94 Ma), and at times with limited continental LIP activity (Figure 16.7c). At least 850 kimberlites with ages between 80 and 130 Ma are known. Some kimberlite ages are based on Rb-Sr and K-Ar methods, and some are not directly dated but inferred from neighboring kimberlite ages; if we only analyze kimberlites dated by U/Pb (zircon/perovskite) between 80 and 125 Ma, we notice clear age peaks that overlap with OAE1 and OAE2 (Figure 16.7c). The largest concentration of kimberlites in Earth history – mostly in southern Africa and erupted at intermediate southerly latitudes (Figure 16.7a,b) – is therefore temporally coincident with Cretaceous OAEs. The role of kimberlites in triggering OAEs is uncertain as kimberlites are restricted in volume and occurrence, but the eruption of large kimberlite clusters could potentially deliver enough CO₂ to the atmosphere to trigger sudden global warming events. Patterson & Don Francis (2013), for example, have estimated that a kimberlite cluster of ~50 pipes could produce about 1000 Gt of carbon in a few years.

16.4.2. Large Igneous Provinces and Global Changes

Continental LIPs are generally defined as predominantly mafic volcanic provinces that were emplaced in a short time period (1–5 Myr) covering at least 100,000 km² with a volume of more than 100,000 km³ (Ernst 2014). They are often characterized by extensive flood basalt sequences commonly termed *traps* (Svensen et al. 2019) comprising thick lava sequences (Self et al. 1998), by explosive/fragmented volcanic deposits (both

from mafic and silicic eruptions; e.g., Bryan et al. 2002), and by sheet-like or plutonic intrusions in sedimentary basins and other crustal settings (e.g., Jerram et al. 2010; Svensen et al. 2018; see examples in Figure 16.2). Clearly such events, driven by upwelling from the mantle below, have impacts on the topography at a regional to continental scale, and on the biosphere and atmosphere, not only due to the sheer volume of igneous material added to the crust but due to volcanic and metamorphic degassing (Figure 16.1a) during the LIP evolution.

The potential environmental impact of any LIP is governed by numerous processes, chief among them: the amounts and degree of magmatic degassing, the composition of the crust heated by the igneous plumbing system and the fate of subsequent metamorphic generated gases (crustal storage vs. seepage vs. rapid venting to the atmosphere), the particular state of the climate and tectonic configurations at the time of LIP formation, and the paleolatitude of the emplacement. LIPs themselves can be rather mixed in terms of the relative volumes of intrusions vs. lava flows vs. explosive eruptive products (Bryan et al. 2010; Jerram et al. 2016b). This is why the climatic response to LIP emplacement must have varied through the geological record, with no clear correlation between the estimated volume of a LIP and the severity of the related environmental disturbance (e.g., Wignall 2001; Jones et al. 2016) (Figure 16.3b–e). Volume estimates and rates of LIP emplacement are also challenging to derive due to few field-based volume estimates of individual flows or sills, buried/offshore parts of LIPs (Figure 16.8a) being inaccessible or poorly known, and due to geochronological limitations. Recent estimates from the Karoo-Ferrar LIP, for example, suggest emplacement rates of 0.78 km³/yr, calculated from the present-day sill volume assuming a steady state emplacement over 0.47 Myr (derived using U-Pb zircon ages and Monte Carlo age modeling; Svensen et al. 2012). Other Karoo-Ferrar LIP estimates are based on melt extraction rates from the mantle during a 6 Myr period, giving results of 0.3 km³/yr (Jourdan et al. 2005).

There are five big Phanerozoic mass extinctions. The first one (end-Ordovician) is not linked to any known LIP (Figure 16.3b–e), but three of the big five have been

Figure 16.7 (*Continued*) evaporite and coal. We also show the plume generation zones (red thick lines), which have been counter-rotated +10° (panel a) and +4° (panel b) around 0°N and 11°E to account for true polar wander at these times. (c) Global distribution of kimberlites (5 Myr bins) but only the most reliable dated kimberlites (U/Pb zircon and perovskite age) between 80 and 125 Ma ($N = 172$). The majority of the kimberlites are from southern Africa and many statistically overlap with the Cretaceous Oceanic anoxia events OAE1 (subdivided into 1a and 1b) and OAE2. This is also the time of the most widespread occurrences of LIPs (blue and red triangles), mostly oceanic LIPs (blue triangles) except for the small Rajmahal (R) LIP in India, and the partly continental/oceanic High Arctic (HA), Caribbean (CA) and Madagascar (MM) LIPs, which mostly erupted before or after these Cretaceous OAEs events.

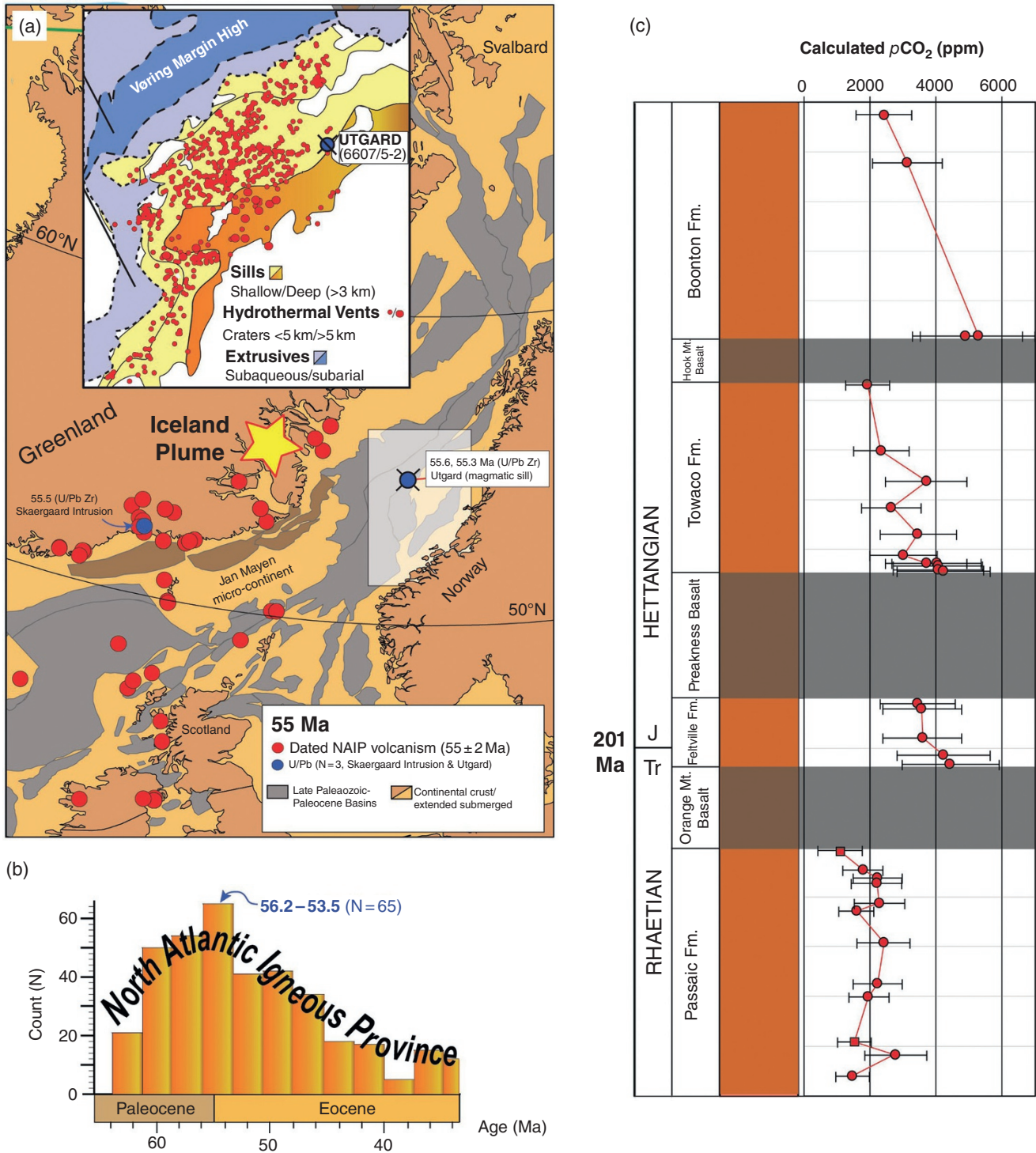


Figure 16.8 (a) Reconstruction of the Northeast Atlantic at 55 ± 2 Ma with the distribution of dated onshore and offshore sample locations (red/blue filled circles) for the North Atlantic Igneous Province (NAIP), the location of the Iceland plume (yellow star) with respect to Greenland (Torsvik et al. 2015; Torsvik & Cocks 2017), and rift basins developed from the late Paleozoic to the Paleocene (Faleide et al. 2010). Peak NAIP volcanic activity overlapped with the Paleocene Eocene Thermal Maximum (PETM) at ~56 Ma. The inset map demonstrates the extensive sill and hydrothermal vent complexes in the Vøring Basin offshore Norway (see white box in main map), and location of the Utgard borehole, where magmatic sills intruding organic-rich sediments are dated to 55.6 and 55.3 Ma (U/Pb Zircon; Svensen et al. 2010). (b) Histogram of 383 isotope ages from NAIP (Torsvik et al. 2015), mainly ⁴⁰Ar/³⁹Ar

linked to LIP emplacement; i.e., the Yakutsk-Vilyui LIP (Devonian Extinction), the Siberian Traps (End-Permian, Figure 16.2g) located in the Siberian Craton and the central Atlantic (CAMP – Triassic-Jurassic Extinction, Figure 16.2f). The fifth mass extinction (Cretaceous-Tertiary Extinction) has also been linked to a LIP in India (Deccan Traps, Figure 16.2c), as highlighted in Figure 16.3 and Table 16.2, but it was likely the combination of the toxicity caused by the Deccan Traps and the effects of an asteroid together that were responsible for the mass extinction (Alvarez et al. 1980). Moreover, LIPs coincide in time with climate change and several OAEs (Figure 16.3c–d), an observation for which numerous authors have assigned a causal relationship. Examples include the Toarcian event (linked to the Karoo-Ferrar LIP) and the Paleocene-Eocene Thermal Maximum (PETM) linked to the Northeast Atlantic Igneous Province (Svensen et al. 2004; Jones et al. 2019; Figure 16.8a,b). PETM is associated with global disturbances in carbon isotopes and dissolution of CaCO₃ sediments. The origin of the PETM at around 56 Ma is still debated. In addition to the proposed link to volcanic activity in the northeast Atlantic, explanations for the PETM include methane hydrate dissociation (Dickens et al. 1995), comet impact (Kent 2003), global wildfires (Kurz et al. 2003), or kimberlite eruptions in Canada (Patterson & Francis 2013).

LIPs release massive volumes of greenhouse gases quickly to the atmosphere. These can be in the form of direct volcanic degassing and from gases escaping from intrusions and their contact metamorphosed host rocks (e.g., Svensen et al. 2004, 2009; Heimdal et al. 2018; Ganino & Arndt 2009; Jones et al. 2016). Such rapid degassing can explain how LIPs can trigger global climate change and mass extinctions (Vogt 1972; Courtillot & Renne 2003; Wignall 2001; Bond & Wignall, 2014; Figure 16.3b–d). Voluminous degassing from magmatic and organic-rich metamorphic sources alone could be in excess of 30,000 Gt CO₂ for LIPs such as the Siberian Traps (Beerling et al. 2007; Courtillot & Renne 2003; Sobolev et al. 2011; Svensen et al. 2009) and 80,000 Gt CO₂ for the CAMP (Heimdal et al. 2018), which, combined with other associated volcanic emissions, would be sufficient to cause sustained global warming on the

order of >100,000 years. The eruption of halogens and halocarbons, in particular HCl, HF, and CH₃Cl, are predicted to cause widespread ozone depletion and acid rain, damaging global ecosystems (Visscher et al. 2004; Svensen et al. 2009; Black et al. 2012). LIP eruptions may also emit considerable SO₂, leading to “volcanic winters” that remain while volcanism is ongoing (Rampino et al. 1988).

In the case of LIPs that rise beneath oceanic crust and form submarine basaltic plateaus, the amount of degassing is more limited. They are limited in terms of the production of volatiles through contact metamorphism and/or crustal contamination, and volcanic degassing can be inhibited due to the depth of emplacement. Silicate weathering of LIP products is diminished due to a lack of sub-aerial exposure, limiting interactions to hydrothermal processes. As such, the environmental impacts of oceanic LIPs appear to be more restricted and less severe than their continental counterparts. Examples of oceanic LIPs include the Ontong Java, Manihiki, and Hikurangi Plateaus (Figure 16.4a), which have been considered as a single vast and voluminous LIP (~50 × 10⁶ km³) – the Ontong Java Nui (Taylor 2006) – which erupted at ~123 Ma.

16.5. LIPs AND PALEO GEOGRAPHY: LONG-TERM EFFECTS

On geological timescales, atmospheric CO₂ is mainly controlled by plate tectonic forcing, both via *sources* (volcanic emissions and metamorphic decarbonation in continental arcs) and *sinks* (silicate weathering and organic and inorganic carbon burial) (Walker et al. 1981; Berner et al. 1983; Marshall et al. 1988; Worsley & Kidder 1991; Bluth & Kump 1991; Otto-Bliesner 1995; Raymo et al. 1988; Gibbs et al. 1999; Berner 2004; Nardin et al. 2011; Godd ris et al. 2012, 2014). The long-term role of LIP generation is twofold. First, it includes a reduction in atmospheric CO₂ on long timescales through enhanced silicate weathering. Second, LIPs punctuate plate tectonics by creating new plate boundaries, thereby changing paleogeography and plate kinematics, and thus plate tectonic forcing.

Silicate weathering can be affected by the rate of erosion of material and the chemistry of the substrate. LIP

Figure 16.8 (Continued) and K/Ar ages, with 3% high-precision U/Pb ages (Torsvik & Cocks 2017), 62.6 Ma (Antrim basalt in Ireland) to 55.5 Ma (Skaergaard intrusion, East Greenland), 55.6 and 56.3 Ma (magmatic sills in the V ring area, offshore mid-Norway). (c) Stratigraphy and lithology of the upper Newark Basin, eastern North America (part of the ~201 Ma Central Atlantic Magmatic Province, CAMP) and calculated *p*CO₂ from stable isotopic values of pedogenic carbonates (Schaller et al. 2011). Increased *p*CO₂ values above each volcanic unit (gray rectangles) interpreted as a response to magmatic activity while decreases in *p*CO₂ after each magmatic episode are argued to reflect rapid consumption of atmospheric CO₂ by silicate weathering of fresh CAMP volcanics.

emplacements can have a large impact on silicate weathering as many of the constituent minerals that comprise basalt are inherently unstable in hydrous, oxygen-rich conditions. For example, basaltic material is an order of magnitude more weatherable than granitic material (Dessert et al. 2003; Gaillardet et al. 1999). Therefore, the extrusion of continental flood basalts would provide a significant increase in fresh, weatherable substrate that can then consume atmospheric CO₂ through silicate weathering and related carbon burial. Erosion rates are intrinsically linked to topography, with juvenile and mountainous regions contributing a disproportionately high dissolved and suspended fluvial flux compared to their surface area (Milliman & Farnsworth 2011). If an area affected by a LIP is elevated, either through the emplacement of km-thick flood basalts and/or regional uplift due to thermal buoyancy effects, then the subsequent erosion of that elevated region would considerably enhance atmospheric CO₂ drawdown for thousands to millions of years following its “uplift” (Jones et al. 2016). Erosion is also enhanced by deforestation (applicable since Devonian times), which could be extensive during, and for some time following, the emplacement of a LIP.

Sulphuric acid is also a key component of chemical weathering, as evidenced by numerous modern catchments (e.g., Liu et al. 2016; Spence & Telmer 2005). This increases the total weathering of both carbonate and silicate materials, but also replaces some of the weathering done by carbonic acid. This means that if large fluxes of SO₂ are emitted to the atmosphere, then sulphuric acid weathering may either diminish the efficiency of silicate weathering as an atmospheric CO₂ sink, and/or may increase the total weathering of surface silicates. These processes are poorly quantified at present, but are worthy of consideration as the range of volatiles produced by LIP emplacements could have a wide range of both positive and negative feedbacks affecting the long-term carbon cycle.

16.5.1. Plate Tectonic Configurations and Their Modifications by LIPs

The early Phanerozoic is exceptional because nearly all the continents were located in the southern hemisphere and the latitudinal distribution is readily seen from a *heat map* (Figure 16.9a), which shows how the continental paleolatitude has changed through the Phanerozoic. A key observation to be taken from this heat map (but also evident from a curve showing the average continental paleolatitude through time; Figure 16.9b) is that the continents were effectively restricted to the Southern Hemisphere during the early and middle Paleozoic, but progressively drifted northward in the late Paleozoic

and early Mesozoic until the break-up of Pangea at ~195 Ma (early Jurassic). From then on, the average paleolatitude of the continents has remained largely stable while the latitudinal spread continued to increase substantially (i.e., compare the latitudinal spread of light areas of the heat map between times before and after Pangea; Figure 16.9a).

The Paleozoic paleogeography was dominated by Gondwana, which amalgamated during Ediacaran-Cambrian times, and stretched from the South Pole to the Equator (western Australia) during most of the Paleozoic (Figure 16.10d). An important ocean (the Iapetus) largely closed during the Ordovician and disappeared entirely during the Silurian (430-420 Ma) when Baltica and Avalonia collided with Laurentia to form Laurussia. Another significant ocean (the Rheic) opened at ~480 Ma (early Ordovician) between Gondwana and the Avalonia terranes and remained an important ocean until ~320 Ma when Gondwana, Laurussia and intervening terranes collided to form Pangea (Torsvik & Trench 1992; Torsvik & Rehnström 2003; Cocks & Torsvik 2002; Domeier & Torsvik 2014; Domeier 2015; Torsvik & Cocks 2004, 2017). Some tectonic blocks were never attached to Pangea, and thus, the term Paleotethys is used for the ocean once separating the China blocks from Pangea (Figure 16.10c). The Panthalassic Ocean (the predecessor of the Pacific Ocean) is best known as the vast ocean that once surrounded the supercontinent Pangea, but *Panthalassic* also refers to the ocean that dominated more than half the globe (effectively the entire Northern Hemisphere) in the early Paleozoic (Figure 16.10d).

The distribution of continents and oceans varied immensely before Pangea and its break-up, which mostly occurred along former sutures (Buitter & Torsvik 2014) and was clearly assisted by extensive LIP volcanism. Early Pangea break-up was witnessed by the opening of the Neotethys Ocean (Figure 16.11), starting already at ~275 Ma, which was possibly linked to a Tethyan plume that sourced the ~285 Ma Panjal Traps in the western Himalaya (Shellnutt et al. 2011) and igneous remnants now preserved in Oman (Arabia). There is an exhaustive list of examples of how LIP activity can change the surface paleogeography by creating and modifying plate boundaries (Torsvik & Cocks 2013; Buitter & Torsvik 2013; Svensen et al. 2018); this as best exemplified among the Atlantic bordering continents: The opening of the central Atlantic at ~195 Ma (Labails et al. 2010; Gaina et al. 2013) led to the definite break between north and south Pangea and was preceded by the emplacement of the CAMP (201 Ma; Figure 16.11b). The Paraná-Etendeka (134 Ma) heralded the early opening of the south Atlantic (~130 Ma) south of the Walvis ridge (Figure 16.7a), and finally, the NAIP assisted the opening of the northeast Atlantic (~54 Ma). NAIP activity started around

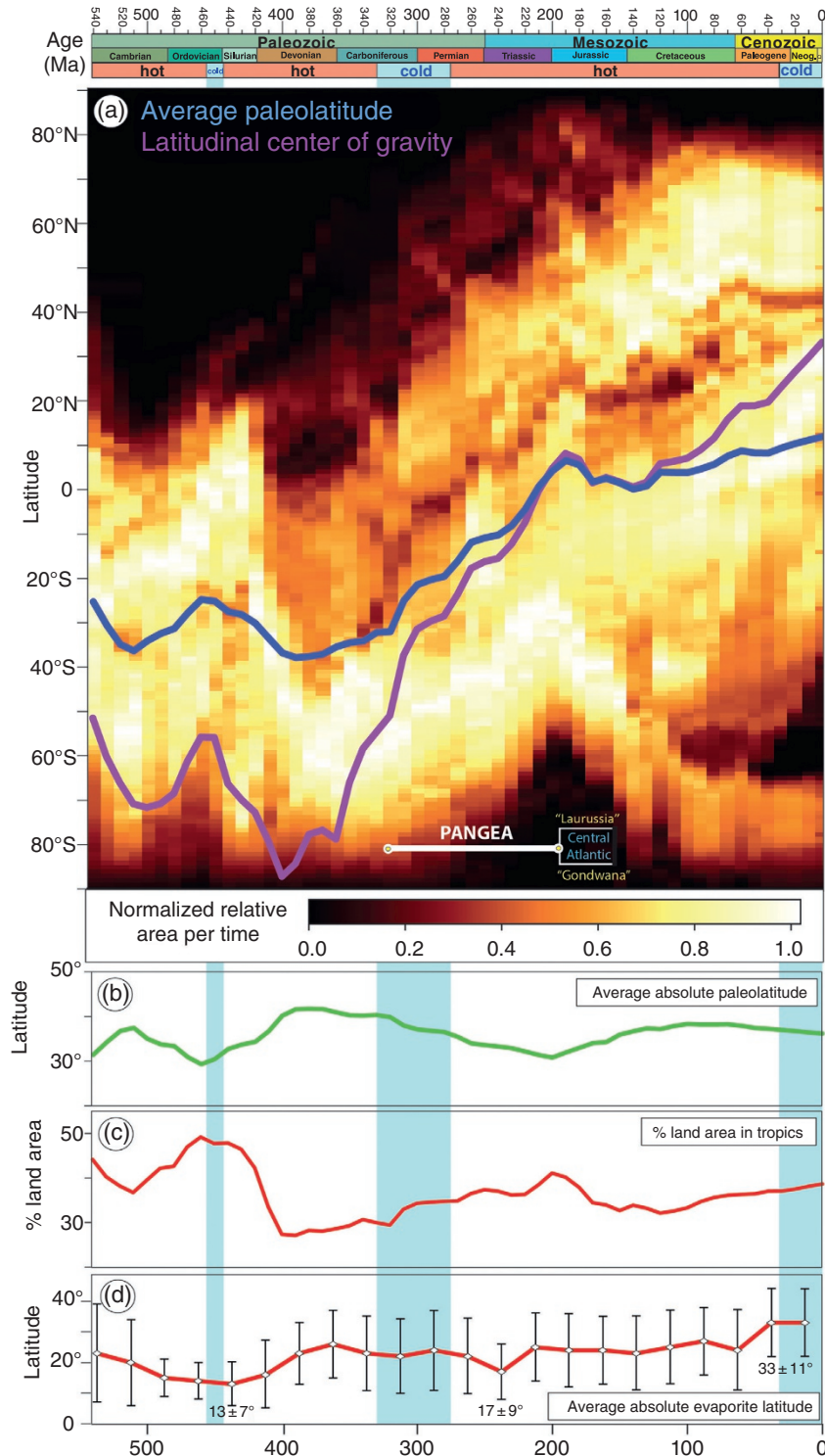


Figure 16.9 Phanerozoic timescale with greenhouse (hot) versus icehouse (cold) conditions and (a) Continental paleolatitude through the Phanerozoic, according to continental polygons and total reconstruction poles taken from Torsvik et al. (2014). Only continental blocks that are defined (both as a polygon and by rotation history) through the entire 541 to 0 Ma interval are used, which amounts to a constant area of ~27% of Earth's surface. The distribution of continental paleolatitudes was calculated in 10 Myr steps across the Phanerozoic, wherein for each step the relative area in each 1° latitudinal band (90°S to 90°N) was determined and normalized such that the band with the largest absolute area was set equal to 1. The heat map shows how the latitudinal

62 Ma (linked to the Iceland plume), and covered vast areas in Baffin Island, Greenland, the United Kingdom, Ireland, the Faroe Islands, and offshore regions, but peak volcanic activity probably occurred at around 56 Ma (coinciding with the PETM event; Figure 16.8a,b).

Not all LIPs cause or contribute to changes in plate boundaries (e.g., Kalkarindji, Skagerrak Centred LIP, Siberian Traps; Figures 16.10c–d, Figure 16.11a), but many conjugate margins are linked to LIPs with break-up occurring almost concurrent with LIP emplacement. In many margins rifting began before the main phase of volcanism, which suggests that rifting was initiated by tectonic forces and that mantle plume material was guided toward the thinned rifted lithosphere to help trigger final continental break-up (Buiter & Torsvik 2013). Continental break-up has fragmented many LIPs shortly after emplacement, with LIP rocks now located on opposed passive margins. Prime examples include CAMP (now mostly located on North America, Northwest Africa, and South America; Figures 16.4a, 16.10a,b), Parana–Etendeka (Brazil and Namibia; Figures 16.4a, 16.7a,b), NAIP (Greenland/North America and Eurasian margin; Figure 16.8a), Karoo–Ferrar (South Africa and East Antarctica; Figures 16.4a, 16.7a,b) and Deccan (India and Seychelles). The coastal onshore parts of passive margins may have formed mountainous escarpments of variable height during continental break-up, thus affecting weathering processes. But it is highly disputed whether passive margin uplift is a transient, long-lived, or even permanent phenomenon, as many passive continental margins today (and long after initial break-up) are characterized by elevated plateaux of several kilometers height (e.g., Japsen

et al. 2011; Osmundsen & Redfield 2011; Redfield & Osmundsen 2012; Steinberger et al. 2015).

Plumes impinging the oceanic lithosphere also influence the plate tectonic configuration, e.g., by relocating plate boundaries (ridge jumps) and generating micro-continents, or making entirely new plates such as with the eruption of the ~123 Ma Ontong Java Nui “mega-LIP” (Ontong Java, Manihiki & Hikurangi Plateaus), which probably led to the break-up of the Phoenix Plate into four new plates at ~120 Ma (Chandler et al. 2010; Seton et al. 2012; Torsvik et al. 2019). The oldest known *in-situ* oceanic LIP is late Jurassic in age, but most preserved oceanic LIPs were emplaced during the Cretaceous (Figure 16.3d; Table 16.2). The total number of oceanic LIPs will remain unknown as the oceanic crust and the LIPs embedded within it can be recycled back into the Earth’s mantle via subduction (e.g., Liu et al. 2010; Sigloch & Mihalynuk 2013). Examples of LIPs being recycled today include the ongoing subduction of Ontong Java and Hikurangi Plateau.

16.5.2. Paleoclimate and Atmospheric CO₂

The Phanerozoic was dominated by a greenhouse climate with high atmospheric CO₂ levels (Figure 16.12e), interrupted by three main periods of cold (icehouse) conditions, in the End-Ordovician (Hirnantian), Permian–Carboniferous, and the second half of the Cenozoic. Low atmospheric CO₂ is a principal variable in controlling continental-scale glaciations (Royer 2006), but the short-lived Hirnantian cooling event (~445 Ma) is paradoxical because of its apparent association with very high

Figure 16.9 (*Continued*) distribution of continental area changes as a function of time according to this definition. Note that the South Polar region remains dark, even though it was occupied by continents at several times in the past (including at present-day), because the area of the polar regions is small compared to the area of lower latitudes (the pole itself has no area); so the heat map does not necessarily show the position of the continents directly, but how their area is latitudinally distributed. The blue curve shows the average continental paleolatitude, weighted by area. The purple curve shows the latitude component of the 3D continental center of gravity vector, which is the vector sum of area-weighted continental position vectors (defined by both latitude and longitude). The latitude component of this vector can reach much higher latitudes than the average latitude weighted by area (e.g., a continental cap balanced over the South Pole will have a center of gravity at the South Pole, whereas the average latitude weighted by area will give a lower latitude value). Pangea formed at ~320 Ma, it had begun to break up before the Paleozoic had ended (e.g., opening of the Neotethys Ocean, Figure 16.11a) but most of Pangea was united until the central Atlantic Ocean started to open between North America (Laurussia) and Africa–South America (Gondwana) at ~195 Ma and shortly after the emplacement of the CAMP (201 Ma). Note that the latitudinal component of the continental center of mass drifted slowly northward with approximately the same velocity from 320 to 195 Ma, and thus unaffected by the formation of Pangea (see text). (b) Average absolute continental paleolatitude weighted by area (i.e., North and South values collapsed together). (c) Percent of the total continental area that lies in the tropics (between 23.5° N and S) as a function of time. (d) Average absolute evaporite latitudes (i.e., North and South values collapsed together). The mean evaporite latitude for the past 50 Myrs is $33 \pm 11^\circ$ (standard deviation; 25 Myr bin averages) but in deeper time mean latitudes are considerably lower. All calculations are based on a paleomagnetic reference frame. Source: (a) Torsvik et al. (2014), (d) Torsvik et al. 2014; Torsvik & Cocks 2017.

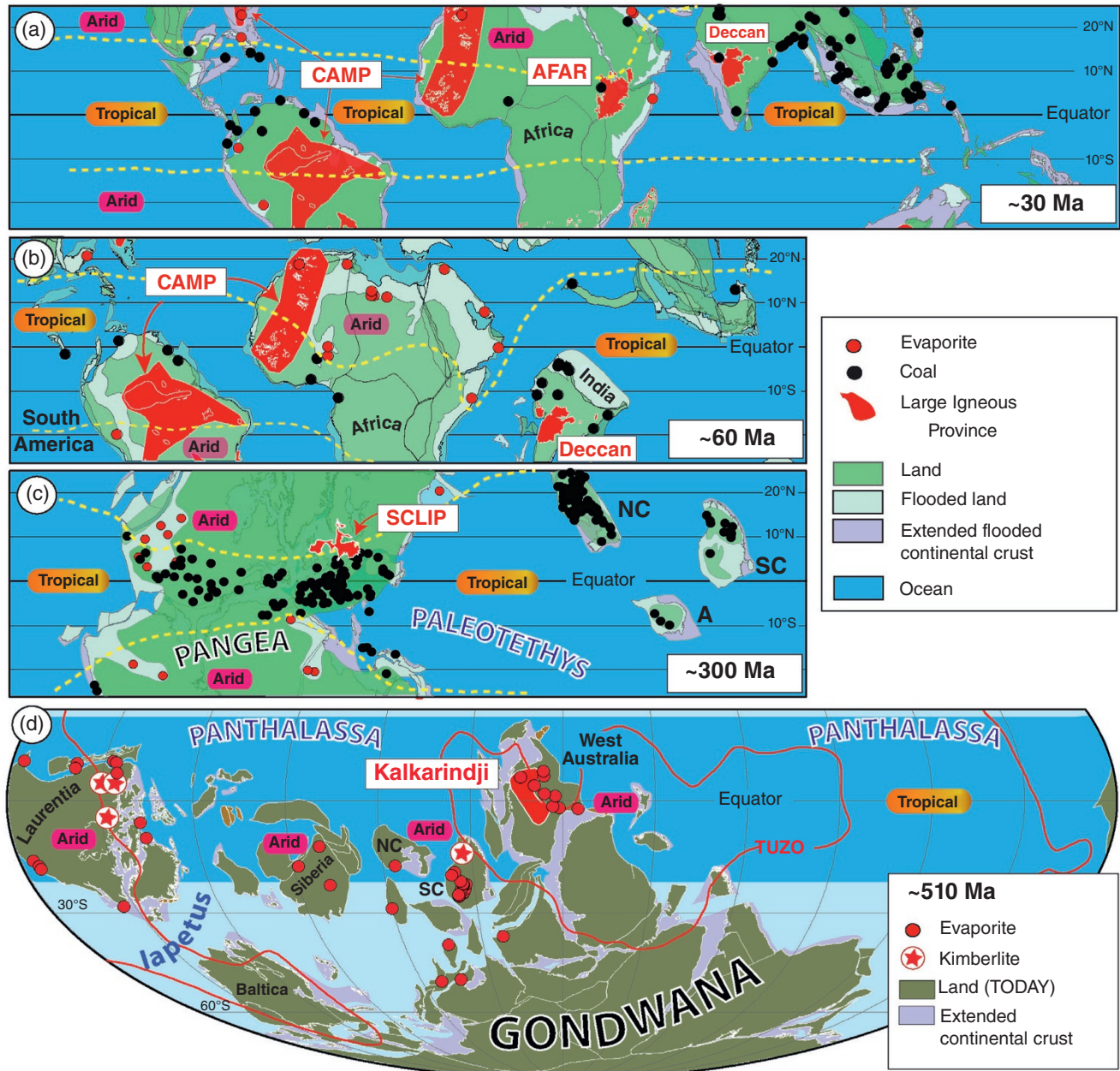


Figure 16.10 Reconstructed tropical belts at (a) 30 Ma; (b) 60 Ma; and (c) 300 Ma along with occurrences of evaporite and coal, tentative outlines (yellow lines) of tropical climate, and the outlines of the Central Atlantic Magmatic Province (CAMP), Deccan Traps, Afar (panels a, b), and the Skagerrak Centred LIP (SCLIP, panel c). We also indicate the areas of flooded land. (d) Earth geography in the Cambrian (~510 Ma) with restored occurrences of evaporites and the outline of the Kalkarindji LIP. All reconstructions in a paleomagnetic frame and in panel d we also show the PGZs which have been counter-rotated (-49° around 0°N and 11°E) to account for estimated true polar wander at this time. A, Annamia (Indo-China); NC, North China; SC, South China. Source: (a-c) Torsvik & Cocks 2017; Boucot et al. 2013, (d) Torsvik et al. 2014, Torsvik & Cocks 2017.

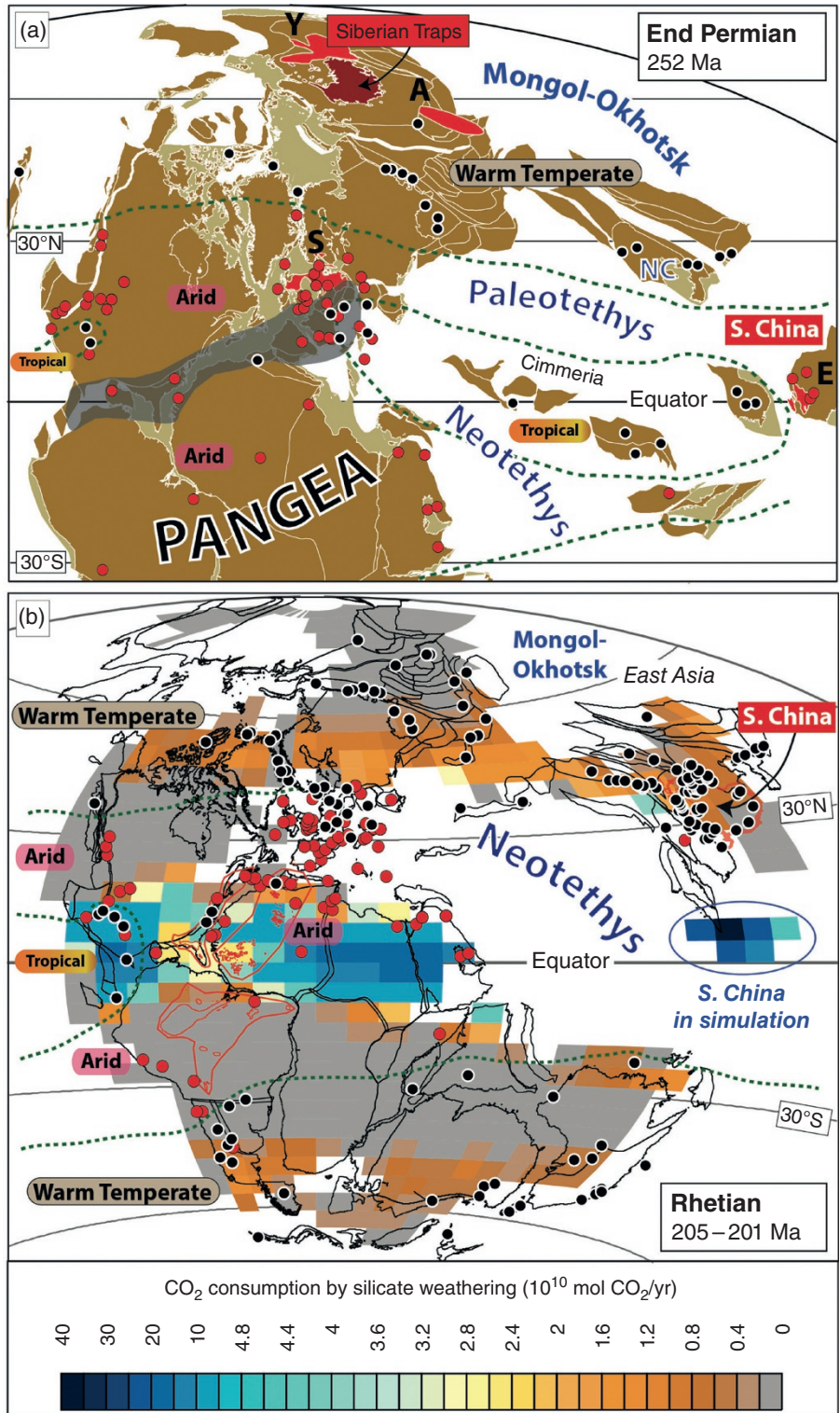


Figure 16.11 (a) End-Permian paleomagnetic reconstruction (252 Ma) and occurrences of evaporite (red shaded circles) and coal (black/white shaded circles), tentative climate-zone boundaries (green stippled lines) and outline of the areas affected by the Variscan and Alleghanian orogenies (dark shading) during Pangea formation. We also show the extent of the Siberian Traps (linked to mass extinction #3) but also the location of the Altay-Sayan (A), Emeishan (E); Skagerrak Centred LIP (S) and the Yakutsk (Y, linked to mass extinction #2) LIPs at this time. NC, North China. (b) Rhetian paleomagnetic reconstruction (205–201 Ma) with occurrences of evaporite (red shaded circles)

modeled atmospheric CO₂ levels. However, the solar luminosity was lower (by 3–5%) and the CO₂ threshold for nucleating ice sheets at that time could have been four to eight times (1120–2240 ppm) higher than pre-industrial levels of ~280 ppm (Gibbs et al. 2000; Herrmann et al. 2003; Royer 2006; Lowry et al. 2014).

Atmospheric CO₂ concentrations can be estimated from proxies, and the most robust proxies include $\delta^{13}\text{C}$ of paleosols, stomatal densities, and indices in plants, $\delta^{13}\text{C}$ of long-chained alkenones in haptophytic algae, $\delta^{11}\text{B}$ of marine carbonate and $\delta^{13}\text{C}$ of liverworts (Royer 2006). The averaging of these proxy systems in 10 Myr bins (Figure 16.12e) suggests that atmospheric CO₂ values were high between 420 and 400 Ma (~2000 ppm), followed by a pronounced decline to about 500 ppm at ~340 Ma. This shift was probably greatly enhanced by the origin and expansion of forests in the Devonian (Bernier 1997) – leading to a situation favoring glacial conditions – but continental arc-activity and plate tectonic degassing (sourcing) were also reduced during late Devonian-Carboniferous times (Figure 16.12d; Section 16.5.4). Pangea assembly also culminated with the Alleghenian-Variscan Orogeny, which resulted in a low-latitude (equatorial) orogenic belt of ~7500 km in length across the heart of Pangea (Figure 16.11a), and that may also have accelerated weathering and removed more CO₂ out of the atmosphere. It has also been argued that arc-continent collisions contributed to cooling through exhumation and erosion of mafic and ultramafic rocks in the warm, wet tropics during the Permo-Carboniferous (Macdonald et al. 2019).

During most of the Carboniferous and Permian, CO₂ proxies average about 500 ppm, but with a sharp increase in the early Triassic (between 240 and 230 Ma) to values of more than 2000 ppm, followed by a decline to values near 1000 ppm by the early Jurassic (Figure 16.12e). Through the rest of the Mesozoic and into the Cenozoic the atmospheric CO₂ fluctuated around 1000 ppm (peaking in the Aptian), followed by a decline to near pre-industrial levels in recent times. Cenozoic glaciations are recorded in Antarctica at ~34 Ma (e.g., Kennett 1977; Zachos et al. 2001; Katz et al. 2008), but it was during the Pliocene at ~2.7 Ma

that the first phase of the Plio-Pleistocene glaciations started (Jansen et al. 2000; Thiede et al. 2011; Bailey et al. 2013; De Schepper et al. 2014; Bierman et al. 2014). A pronounced decline in atmospheric CO₂ played a central role in preconditioning the climate for the Plio-Pleistocene glaciation (Figure 16.12e).

The Earth's atmosphere circulates as three cells in each hemisphere, i.e., between the intertropical convergence zone (near the Equator) and the subtropical highs at ~30 °N/S (Hadley cells), between 30 °N/S and ~40°–60 °N/S, depending on the season (Ferrell cells), and the Polar cells above ~40°–60 °N/S (see Hay et al. 2018). On geological timescales it has commonly been assumed that climate gradients have remained broadly similar to today, with a stable Hadley circulation, and even on an Earth free of polar ice the subtropical highs should be close to where they are today (~30 °N/S). Past climate gradients can be assessed from paleogeographic biome maps. Coals (since the early Devonian) are commonly confined to near the Equator (humid conditions) or the northerly/southerly wet belts and indicate a prolonged excess of precipitation over evaporation. Conversely, evaporites are mostly found in the subtropics at mean latitudes of 33 °(N/S) for the past 50 Myrs (Figure 16.9d) – but mean evaporite latitudes become strikingly lower back in time (Torsvik & Cocks 2017). This is witnessed by absolute mean values of ~24° stretching from the early Paleocene back to Devonian times – except for a pronounced minimum ($17 \pm 9^\circ$) in the Triassic – and then a second shift to even lower mean latitudes before 400 Ma. Thus, the tropics appear increasingly more arid back in time (Figure 16.9d). This is perhaps unexpected, given that the Hadley Cell is currently expanding (e.g., Northern Hemisphere desert zones spreading and migrating northward; DeMeo 1989) with global warming, but there are suggestions that Hadley circulation shrank to ~20 °N/S latitude during the middle Cretaceous super-greenhouse (Aptian through early Coniacian; Hasegawa et al. 2012; Hay et al. 2018). Lower mean evaporite latitudes of the past may partly reflect the slowing down of Earth: A faster-spinning Earth displaces the subtropics equatorward and Christiansen and Stouge (1999) have estimated

Figure 16.11 (Continued) and coal (black/white shaded circles), and tentative outlines of climate gradients. We also show the possible original extent of the Central Atlantic Magmatic Province (linked to mass extinction #4) at around 201 Ma (red lines). The estimated plume center is near the southern tip of Florida. The reconstruction is compared with a Rhetian GEOCLIM simulation (Goddéris et al. 2014) with estimated CO₂ consumption from silicate weathering. The continental distribution (defined by the colored and gray regions of continental weatherability) broadly matches our reconstruction (black lines). CO₂ consumption in the tropical parts of central Pangea is typically calculated to 10–20' 10¹⁰ mol CO₂/yr while the warm temperate belts range between 1.4–1.8' 10¹⁰ mol CO₂/yr. South China in the simulation is located near the Equator in the Neotethys – with CO₂ consumption estimates peaking at 40' 10¹⁰ mol CO₂/yr.

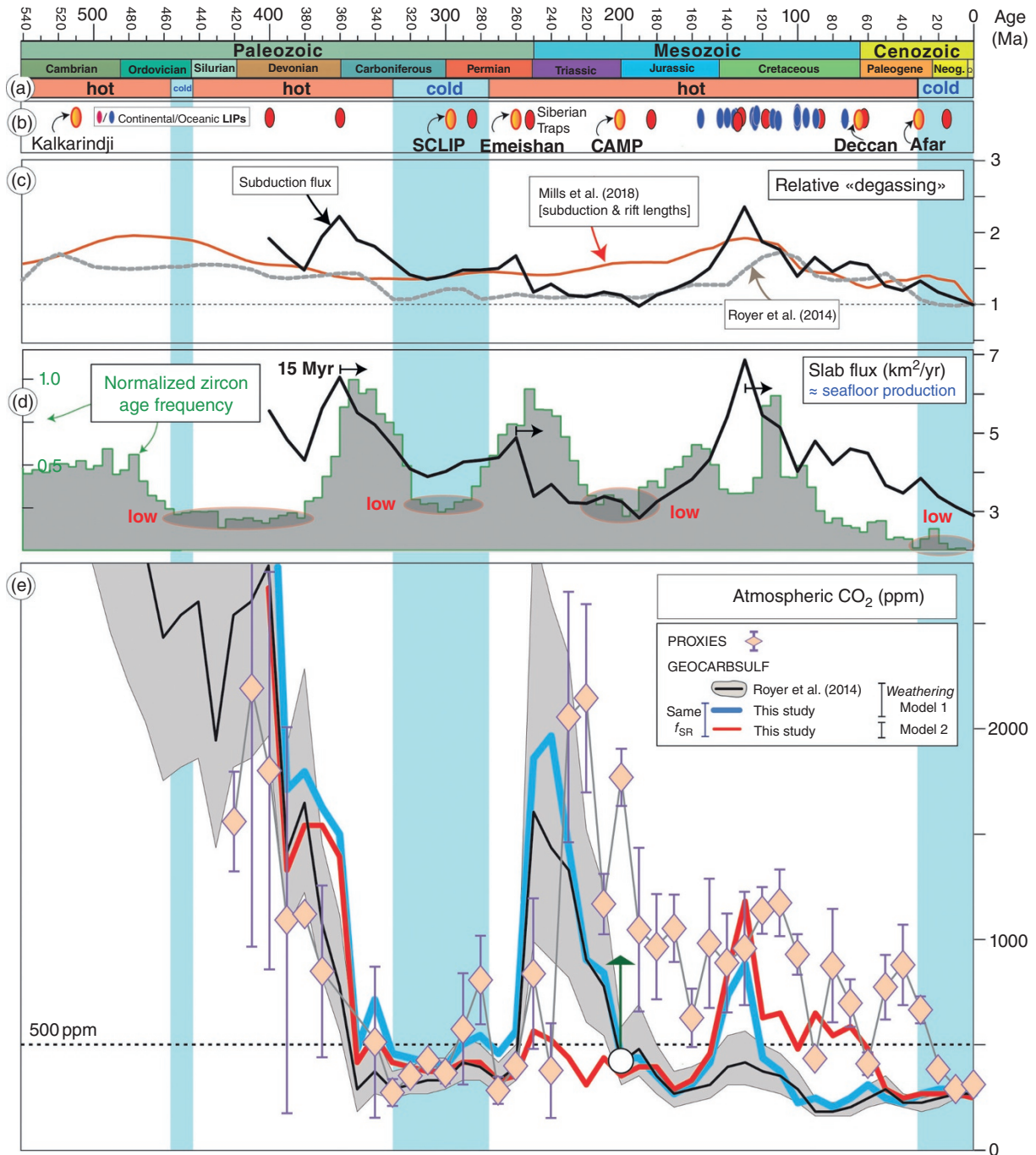


Figure 16.12 (a) Phanerozoic timescale with greenhouse (hot) versus icehouse (cold) conditions. (b) LIPs where Kalkarindji, Skagerrak Centred LIP (SCLIP), Emeishan (E), Central Atlantic Magmatic Province (CAMP), Deccan and Afar LIPs were emplaced at low latitudes (ST, Siberian Traps). Also indicated are the two kimberlite frequency peaks between 110–120 and 80–90 Ma (see Figure 16.3f). (c) Relative CO₂ degassing (red curve, Mills et al. 2018) based on a combination of subduction [from seismic tomography for the past 200 Myrs (van der Meer et al. 2014) and a plate model before that time (Mills et al. 2017)] and continental rift lengths (Brune et al. 2017). Mills et al. (2018) assumed 37% (63%) of tectonic CO₂ contribution from continental rifts (ridges and arcs) and assumed constant rift input before 200 Ma. We also show relative degassing based on the global subduction flux (black curve) back to 400 Ma based on full-plate models (see Table 16.3 for details), and the standard GEOCARBSULF curve (f_{SR}) back to 541 Ma (gray curve; Royer et al. 2014). (d) Age frequency of detrital zircons from arc environments (frequency lows indicated with red ellipses) and subduction flux (black line; Table 16.3). Globally, the main peaks in the detrital

that the subtropical high was displaced 5° equatorward in Ordovician times (see also Torsvik & Rehnström 2002).

16.5.3. Paleolatitude of LIP Emplacement

Low continental latitudes (and their associated warm and wet climates) promote CO₂ consumption by silicate weathering, and are theoretically associated with low CO₂ periods (Goddéris et al. 2014). Enhanced silicate weathering due to LIP emplacement is dependent on many factors, including relief, the area of subaerial exposure, and the latitudinal location of the LIP. Six major Phanerozoic continental LIPs (i.e., Kalkarindji, SCLIP, Emeishan, CAMP, Deccan and Afar) were emplaced within present-day tropical latitudes (Figure 16.3d), although the wet belts may have been narrower or even absent in the past. With the exception of the Emeishan LIP (Jerram et al. 2016a), they were sourced from the margins of TUZO (Figure 16.4b). There are, of course, also continental Precambrian LIPs (Figure 16.4a) undergoing weathering today but their areal extent today is less than 10% of the total preserved LIP areas, and exposed basalt substrates become significantly less weatherable with time (Porder et al. 2007).

Theoretical silicate weatherability and cooling have been explored by estimating the average continental paleolatitude or average absolute paleolatitude weighted by area (i.e., north and south values collapsed together; Figure 16.9a, b), but a better approach is to calculate the fraction of the total continental area that is located in the tropics (currently around $\pm 23.5^\circ$; present axial tilt of the Earth), i.e., subjected to potentially warm and wet climates with high weatherability (Figure 16.9c). We notice, however, peaks during both the end-Ordovician glaciation (~50%) and the Triassic-Jurassic greenhouse world (40%). Due to substantial changes in global sea level (peaking in Ordovician and Cretaceous times, and perhaps 200 m higher sea level than present day; Haq & Al-Qahtani 2005; Haq & Shutter 2008) and continental

flooding, the *effective* weatherability at tropical latitudes would peak in the late Triassic, at a time with no evidence for ice. This may suggest, to a first order, that enhanced silicate weathering in the tropics is not fundamentally important in triggering glaciations, but one should keep in mind that the equatorial region of Pangea was dominated by arid conditions in the late Paleozoic and early Mesozoic.

Evaporite localities within a single continent can certainly reflect seasonal and local conditions rather than global climatic conditions, but there is ample evidence that Laurentia, Siberia, north and south China and western Australia defined an extensive, arid, low-latitude evaporite belt in the early Paleozoic (Figure 16.10d). In the Cambrian, Gondwana stretched from the South Pole (northwest Africa) to the Equator and the ~510 Ma Kalkarindji LIP (Figure 16.4a) – sourced from the northeast margin of TUZO (Figure 16.4b) – was emplaced over a vast tropical area (>2 million km²) in western Australia. However, the widespread evaporite occurrences in western Australia suggest low weatherability during the late Cambrian and most of the Ordovician. Western Australia, however, appears less arid in late Ordovician and early Silurian times (Torsvik & Cocks 2017), which may have resulted in higher weatherability in the low-latitude regions of Gondwana. The end-Ordovician (Hirnantian glaciation) was followed by widespread extinctions near the Ordovician–Silurian boundary (~445 Ma), the first of the “Big Five” Phanerozoic extinctions, which is *not* temporally linked to any known LIP.

The second low-latitude Phanerozoic LIP is the ~300 Ma Skagerrak centered LIP (SCLIP; Torsvik et al. 2008), perhaps affecting an area of ~500,000 km² in Scandinavia, Scotland, and northern Germany (Figure 16.4a). SCLIP was sourced by a plume from the northeast margin of TUZO (Figure 16.4b) and erupted at low latitudes when central Pangea – including North America and Europe – was located near the Equator (Figure 16.10c) and covered by humid tropical rainforest. Latitudinal

Figure 16.12 (Continued) zircon frequency distribution are shifted by ~15 Myrs (Domeier et al. 2018), i.e., zircons trailing subduction. (e) Atmospheric CO₂ proxies (binned in 10 Myr intervals with 95% confidence standard errors when N ≥ 2) since the early Devonian (based on data used in Foster et al. 2017). GEOCARBSULF modeling (Royer et al. 2014) shown with 95% confidence area (shaded in gray) using the standard relative degassing curve (panel c) or CO₂ modeling (since 400 Ma) based on use of the subduction flux as a proxy for plate tectonic degassing (f_{SR}). The latter has been calculated using two different silicate weathering feedback models, i.e., Royer et al. (2014; blue line) and Berner (2006; red line). Weathering-related inputs in Royer et al. (2014) is based on Goddéris et al. (2012, 2014) but in the global runoff/weathering model South China was *misplaced* near the equator at 200 Ma and accounting for about 17% of the global CO₂ consumption by silicate weathering (see text and Figure 16.11b). If the large “cooling” contribution from South China is removed, then modeled CO₂ would increase by around 500 ppm and better match the CO₂ proxies (green arrow at 200 Ma).

temperature gradients during the early phase of the Permo-Carboniferous icehouse (~330–275 Ma) were much higher than during the earlier greenhouse periods and perhaps not dissimilar to the present day (Torsvik & Cocks 2017). As the climate aridified, the rain forests collapsed and were eventually replaced by seasonally dry biomes in the early Permian (Sahney et al. 2010). The areas that were affected by SCLIP aridified quickly during the Permian, thus weakening the silicate weathering efficiency, and extensive salt basins (Zechstein) covered northwest Europe in late Permian–Triassic times (Figure 16.10a). The middle–late Permian was dominated by an expansive arid region that extended across much of Pangea, spanning both northern and southern latitudes, and crossing both the Americas and Europe (Boucot et al. 2013; Torsvik & Cocks 2017). Low global climatic gradients and a low latitude arid region traversing most of central Pangea broadly characterized the Triassic and Jurassic, but the arid realm shifted southward as Pangea moved systematically northward until the middle Jurassic (Figure 16.9a), when the opening of the central Atlantic initiated the break-up of the supercontinent. Interestingly, from the early Devonian (~400 Ma) to the early Jurassic (~190 Ma), the latitudinal component of the continental center of mass (with respect to the spin axis) has drifted slowly northward (Figure 16.9a) with approximately the same velocity ($0.44^\circ/\text{Ma}$ or $\sim 50 \text{ km}/\text{Ma}$) – and was seemingly unaffected by the formation of Pangea.

The next low-latitude LIP, the Emeishan LIP (ELIP), erupted ~260 Ma (Jerram et al. 2016a) and a tropical humid condition at eruption time is evidenced by shallow marine carbonates and widespread coal-measures derived from marine mangrove-like plants (Shao et al. 1998). Most of the Emeishan lavas, however, were emplaced at or below sea level, and terrestrial lava flows only developed in the later stages (Ukstins Peate & Bryan 2008; Jerram et al. 2016a). South China drifted northward after the ELIP eruptions; it aridified during the early Triassic (Figure 16.11a), and since the mid-Triassic it has essentially remained in the northern temperate zone. Early Triassic evaporites in South China are clearly anomalous (Boucot et al. 2013) as most of the low latitude continental blocks and terranes bordering the Panthalassic Ocean during late Paleozoic and early Mesozoic times are characterized by coal deposits, suggesting tropical conditions (e.g., Figures 16.10c, 16.11a).

High atmospheric CO_2 levels (~2000 ppm) are indicated from the proxy record from about 230 Ma, declining to ~1000 ppm by about 190 Ma (early Jurassic) (Figure 16.12e). The 201 Ma CAMP was emplaced during this greenhouse period, at low latitudes (Figure 16.3d), and it covered a vast area (Figure 16.11b), perhaps more than 10 million km^2 . Its emplacement in tropical latitudes should theoretically have led to extensive post-

emplacement silicate weathering and reduced CO_2 levels (cooling). However, biome maps suggest that the equatorial region of Pangea was dominated by an arid or at least seasonally dry environment at end-Triassic times, with limited evidence for tropical conditions (e.g., coal is found in the southernmost Newark Basin; Smoot 1991) (Figure 16.11b). The end-Triassic and early Jurassic climate was characterized by low climate gradients with a Pangean low-latitude arid region in southernmost North America, north Africa, and South America, except a humid realm facing the Panthalassic Ocean along the west coast of central Pangea (Figure 16.11b). As with all LIPs, it is difficult to determine the timing or the rate of weathering. In contrast to the biome maps, which suggest extensive low-latitude arid regions in central Pangea, many argue that huge amounts of the CAMP were removed by chemical weathering within a few million years. This is based on observed trends in seawater Sr- and Os-isotope compositions (Cohen & Coe 2007), and carbon-cycle variations in the Newark Basin (Figure 16.8c; see below).

The ~66 Ma Deccan Traps, with an estimated subaerial extent of $\sim 1.8 \times 10^6 \text{ km}^2$, were emplaced at low southerly latitudes (centered on $\sim 20^\circ\text{S}$) in tropical humid conditions (widespread coal-measures) and subsequently drifted across the Equator to $\sim 20^\circ\text{N}$ (Figure 16.3d) while India also collided with Asia in the process to produce the Himalayan orogeny. Finally, Afar was emplaced at low latitudes at 31 Ma (Figure 16.3d), and the combined weathering (cooling) effects of the Afar, Deccan and remnants of CAMP (notably in western Africa and northern South America) may have decreased CO_2 levels in the late Cenozoic (Figure 16.10a). However, declining late Cenozoic CO_2 levels can also be attributed to accelerated continental weathering due to Himalayan mountain building (Raymo et al. 1988) and/or increased weathering due to tropical ophiolite obduction over the past 30 Myrs (Macdonald et al. 2019).

Elevated silicate weathering associated with the weathering of LIP lavas has been argued for both CAMP and the Deccan Traps. Schaller et al. (2011) found that pre-CAMP CO_2 background values of ~2000 ppm approximately doubled in response to magmatic activity but decreased toward pre-CAMP levels in just a few hundred thousand years after each magmatic episode (Figure 16.8c), which they interpreted to reflect rapid weathering of fresh CAMP volcanics. Similarly, Dessert et al. (2001) modeled an increase in atmospheric CO_2 levels by ~1000 ppm for Deccan, which subsequently was reduced to pre-Deccan levels in about one Myr. Such short-time perturbations are not recognized in the long-term GEOCARBSULF carbon and sulphur cycle model, which estimates atmospheric CO_2 levels in 10 Myr intervals (Royer et al. 2014).

CO₂ proxies in Figure 16.12e are averaged in 10 Myrs bins and there are two notable CO₂ peaks at 250 Ma ($N = 5$ proxies) and 200 Ma ($N = 105$) that may reflect the influence of the Siberian Traps and the CAMP, respectively. But the most pronounced increase in long-term atmospheric CO₂ is observed between 240 and 230 Ma (early Triassic). Johansson et al. (2017) argued for a strong correlation between the weathering of CAMP and CO₂ proxies from 200 Ma to 100 Ma, but there is no systematic decrease in CO₂ (*cooling*) between 190 and 100 Ma (i.e., proxy values, except 160 Ma, statistically overlap at the 95% confidence level; Figure 16.12e). We therefore do not see any clear statistical relationship between CAMP – presumably one of the largest LIPs in Earth history – and very long-term (>10 million years) weathering and potential CO₂ drawdown and cooling.

16.5.4. GEOCARBSULF: Proxy-Model CO₂ Mismatches

The proxy-record and atmospheric CO₂ modeled with GEOCARBSULF fits well for the late Paleozoic (correlation coefficient = 0.96; 400–260 Ma) but modeled CO₂ levels from about 200 Ma to 30 Ma (Figure 16.12e; black curve with gray confidence envelope) are consistently lower than the proxy record (Royer et al. 2014), and thus the correlation coefficient calculated for the past 400 Myrs is low (~0.5). Mismatches can partly be reduced by increased seafloor production rates – an important time-dependent plate tectonic degassing parameter (f_{SR}) in the GEOCARBSULF model. Variations in seafloor production (e.g., Coltice et al. 2013) can be calculated with sufficient confidence for the last 83 Myrs (after the Cretaceous Normal Superchron) from oceanic lithospheric age-grids estimated from marine magnetic anomalies. Before that time this approach has much larger uncertainties, but because the subduction flux must equal the seafloor production rate (to first order), we can use estimates of the subduction flux derived from full-plate models as a proxy for plate tectonic degassing. van der Meer et al. (2014) pursued an even simpler approach: assuming a constant average rate of convergence for subduction zones, globally (specifically 6 cm/yr, the present-day average; Schellart et al. 2007), they used normalized subduction lengths through time (estimated back to 235 Ma from seismic tomography) as a proxy for plate tectonic degassing (f_{SR}). This approach was also used by Mills et al. (2018), where they used subduction lengths for the past 200 Myr from van der Meer et al. (2014), extended backward with subduction lengths estimated from a plate model (Mills et al. 2017), but also combined with normalized rift lengths (Brune et al. 2017), assuming that degassing from continental rifts is about one third of that from ridges and arcs. The combined forcing from CO₂ degassing generally yields higher relative

degassing than the standard GEOCARBSULF curve (Figure 16.12c), but enhanced relative forcing is inadequate to significantly reduce proxy-model discrepancies between 200 and 30 Ma (Mills et al. 2018).

The use of subduction lengths as a proxy for the subduction flux requires that the average rate of subduction remains constant through time, but Mesozoic-Cenozoic full-plate models (e.g., Torsvik et al. 2010b; Seton et al. 2012; Matthews et al. 2016) show that high subduction fluxes are often linked to higher average subduction rates rather than to longer global subduction lengths (Domeier & Torsvik 2017; Hounslow et al. 2018). Zircons track past continental arc systems since zircon-ferrous rocks are primarily produced along continental subduction zones. From analyses of zircon ages in the context of full-plate tectonic models (back to 410 Ma), we observe that subduction fluxes provide a stronger statistical correlation to zircon age frequency distributions than subduction lengths do, implying that convergence rates play a significant role in regulating the volume of melting in subduction-related magmatic systems (Domeier et al. 2018). Zircon age peaks correspond well to intervals of high subduction flux with a ~15 Ma time lag (zircons trailing subduction), and icehouse conditions are associated with lows in zircon age frequency (Figure 16.12d). Continental arc-activity has been argued to have played an important role in regulating long-term climate changes (McKenzie et al. 2016), i.e., high continental arc activity is linked to warm climate (greenhouses) and reduced arc activity explains icehouse climates. But only the Permo-Carboniferous icehouse shows a clear relation to the zircon record, the end-Cenozoic icehouse occurs long after a major reduction in zircon-age frequencies (starting in the late Cretaceous), and the end-Ordovician Hirnantian icehouse was followed by ~120 Myrs of low zircon age frequencies when the climate was generally warm, although there are some rocks of glacial origin in the latest Devonian and earliest Carboniferous of South America (Torsvik & Cocks 2017). A minimum in zircon age frequencies is also noticed in Triassic–Jurassic times during greenhouse conditions. The *continental arc magmatic hypothesis* (McKenzie et al. 2016), attempting to explain all icehouses by reduced continental arc activity, is partly founded on the idea that arc-related magmatism along continental-margin subduction zones may have contributed three to five times more CO₂ to the atmosphere than island arcs because of decarbonation of the continental crust of the overriding plate (e.g., Lee et al. 2013; Lee & Lackey 2015; Cao et al. 2017).

Modeling atmospheric CO₂ levels for the past 400 Myrs using normalized subduction flux (Table 16.3) as a time-variable input for f_{SR} in the GEOCARBSULF model reduces model-proxy mismatches in the middle Triassic and early Cretaceous (blue curve in Figure 16.12e). But

Table 16.3 Estimated subduction flux for the past 400 Myrs that we use to define the time-dependent (normalized) f_{SR} parameter (i.e., 1.00 = today) in the GEOCARBSULF model (Figure 16.12c). Subduction flux calculated dynamically from the Paleozoic full-plate model of Domeier & Torsvik (2014) and a revised Mesozoic–Cenozoic full-plate model (250–0 Ma; Torsvik et al. 2019), which is originally based on Matthews et al. (2016). Using the latest GEOCARBSULF model (Royer et al. 2014) but with our revised estimates for plate tectonic degassing (f_{SR}) we have modeled the atmospheric CO₂ for the past 400 Myrs with two different weathering models (WM). The GEOCARB R code was ran with the *resampleN* parameter set to 1 and the two different weathering models are selected by the *Godderis* parameter set to TRUE (WM-1; Godderis et al. 2012) or FALSE (WM-2; Berner 2006). The model code and original input files from Royer et al. (2014) are available at: https://figshare.com/articles/code_to_run_GEOCARBSULF_model/902207

Age (Ma)	Subduction flux (km ² /year)	f_{SR}	WM-1	WM-2
			CO ₂ (ppm)	CO ₂ (ppm)
400	5.56	1.92	3825	2680.6
390	4.83	1.67	1711	1331.6
380	4.30	1.48	1798	1551.0
370	5.63	1.94	1621	1539.7
360	6.42	2.21	1506	1398.6
350	5.52	1.90	485	415.4
340	5.21	1.80	709	545.1
330	4.69	1.62	460	407.9
320	4.09	1.41	439	393.3
310	3.90	1.34	411	370.4
300	4.02	1.39	401	368.8
290	4.27	1.47	500	418.9
280	4.30	1.48	552	410.2
270	4.38	1.51	467	332.9
260	4.88	1.68	575	362.9
250	3.38	1.17	1872	565.9
240	3.70	1.28	1966	517.8
230	3.24	1.12	1436	445.0
220	3.20	1.10	908	318.7
210	3.38	1.17	836	437.7
200	3.26	1.12	444	354.9
190	2.84	0.98	429	388.1
180	3.25	1.12	353	388.3
170	3.54	1.22	275	294.6
160	3.83	1.32	314	339.6
150	4.34	1.50	417	454.5
140	5.41	1.87	733	852.3
130	6.85	2.36	879	1191.7
120	5.45	1.88	436	631.2
110	5.14	1.77	373	652.9
100	4.02	1.39	232	486.5
90	4.80	1.66	244	659.0
80	4.20	1.45	211	540.1
70	4.60	1.59	255	578.5
60	4.48	1.54	301	477.8
50	3.68	1.27	241	279.9
40	3.48	1.20	227	246.1
30	3.84	1.32	261	265.2
20	3.38	1.17	279	263.9
10	3.12	1.08	295	266.1
0	2.90	1.00	270	243.0

large offsets, averaging to 510 ± 458 ppm for the past 400 Myrs, still exist and a distinct peak at 250 Ma (~ 1900 ppm) is at odds with the proxy record. This modeling peak is coeval with a pronounced zircon age peak, and is close to the smallest of three peaks in the input subduction flux curve (~ 360 , 260, and 130 Ma), but it is apparently controlled by the strength of the silicate weathering feedback. GEOCARBSULF has been revised several times, and an important change in the current version (Royer et al. 2014) was the inclusion of new weathering-related inputs based on coupled climate and carbon cycle models (Godd ris et al. 2012, 2014). These time-dependent inputs included the land mean surface temperature (GEOG), land area (f_A), fraction of land area undergoing chemical weathering (f_{Aw}/f_A), and global river runoff (f_D). Interestingly, if we revert to the original GEOCARBSULF inputs for these parameters (Berner 2006), modeled CO_2 (red curve in Figure 16.12e) correlates better with proxy data at 250 Ma and the Cretaceous–early Paleogene, and the magnitude of the modeled carbon CO_2 spikes correlate more linearly to the subduction flux input curve (Figure 16.12d,e). Using the original weathering parameters of Berner (2006), however, results in uniformly low modeled CO_2 levels (around 500 ppm) during the early Mesozoic (240–170 Ma) and therefore does not capture the much higher CO_2 greenhouse levels suggested from proxies. Average model-proxy mismatches since the early Devonian are somewhat reduced (415 ppm) using the old weathering parameters, but the correlation coefficient is lower (0.35) and statistically insignificant.

Runoff is a first-order controlling factor of silicate weathering, and the global runoff model of Berner (1994; 2006) was based on an assumed correlation between temperature and runoff, modulated by a *continental* factor that accounted for the effect of paleogeography. In the current GEOCARBSULF version (Royer et al. 2014), Phanerozoic silicate weathering parameterizations are derived from 3D climate and carbon-cycle GEOCLIM simulations (Godd ris et al. 2014). The only forcing functions in these simulations are the energy input from the Sun (dimmer in the past) and paleogeography taken from many sources (Vrielynck & Bouysse 2003; Blakey 2003, 2008; Sewall et al. 2007; Herold et al. 2008), but we note that these are much generalized and sometime outdated. As an example, we compare our end-Triassic paleogeography (Torsvik & Cocks 2017) with that used in the Godd ris et al. (2014) simulations, and at a time when both weathering models yield much lower modeled CO_2 than proxy values (Figure 16.12e). The bulk of Pangea matches our reconstruction, but the location of South China is very different; it should be centered on 35°N and not near the Equator as in the GEOCLIM simulation (Figure 16.11b). Because it was probably *incorrectly* located in the humid tropical area (as in the late Paleozoic;

Figure 16.11a), south China accounted for $\sim 17\%$ of the global CO_2 consumption by silicate weathering at this time. If this added cooling effect is corrected, modeled CO_2 would increase significantly (~ 500 ppm; Yves Godd ris, pers. comm. 2019) and much better match the late Triassic to early Jurassic proxies (Figure 16.12e). This single example stresses the importance of accurate paleogeography because it is a prime factor controlling runoff and therefore silicate weathering (Godd ris et al. 2014).

16.6. CONCLUDING REMARKS AND CHALLENGES

The connections between the Earth’s interior and its surface are manifold, and defined by processes of material transfer: from the deep Earth to lithosphere, through the crust and into the interconnected systems of the atmosphere-hydrosphere-biosphere, and back again. One of the most spectacular surface expressions of such a process, with origins extending into the deep mantle, is the emplacement of LIPs, which have led to rapid climate changes and mass extinctions, but also to moments of transformation with respect to Earth’s evolving paleogeography. But equally critical are those process that involve material fluxes going the other way—as best exemplified by subduction, a key driving force behind plate tectonics, but also a key driver for long-term climate evolution through arc volcanism and degassing of CO_2 . Below we summarize some of the key aspects among the complex systems and processes that we have addressed.

- Plumes are sourced from specific regions in the deep Earth and mostly from the edges of two quasi-stable thermochemical piles (TUZO and JASON) and they travel from the core–mantle boundary to the base of the lithosphere in about 30 Myrs or less, if the spatial correlation between plume source and the margins of the piles is to be maintained.
- Plumes take us to sub-lithospheric levels where significant partial melting occurs, and to the surface, where hot-spot lavas are erupting today, and where episodic kimberlite and especially LIP activity have led to major climate perturbations and Earth crises on very short time-scales. The degree of climate perturbations and mass extinctions probably reflects a combination of LIP-emplacement environment and magma volume, and a key challenge in understanding the short-term LIP-environment connection is the lack of reliable estimates of magma and gas volumes, and their fluxes.
- Hotspot and kimberlite volcanoes generally have relatively small climate effects compared with that of LIPs (because of volumetric and flux differences), but the eruption of large kimberlite clusters, notably in the

Cretaceous, could be capable of delivering enough CO₂ to the atmosphere (1000 Gt or more) to trigger sudden global warming events.

- LIPs are episodic but there is a notable concentration in the Cretaceous (145–66 Ma) when also 75% of all known Mesozoic–Cenozoic kimberlites erupted. Considering slab sinking rates, the time basaltic material may remain near the core–mantle boundary and plume ascent rates, we estimate that material transfer through the entire system (i.e., from subduction of crustal materials until their re-eruption at a hotspot via a plume) should take at least 260 Myr. If so, the vast amount of kimberlites and LIPs that surfaced in the Cretaceous therefore contain material derived from Rheic and Panthalassic oceanic lithosphere, which was subducted before Pangea formed. However, the formation of plumes may also be influenced by mantle flow caused by much younger slabs of perhaps only half that age, which have only sunk to the mid-mantle, without containing any material derived from them.

- LIP activity affects plate tectonics by creating and modifying plate boundaries, best exemplified by the Atlantic bordering continents where LIP activity was followed by continental break-up and seafloor spreading within a few million years. This resulted in LIP fragmentation: for example, CAMP-related magmatism is now scattered across several different plates.

- The long-term climate is largely controlled by plate tectonic forcing, both via sources and sinks – e.g., silicate weathering – which can be enhanced by extensive blankets of LIP-lava on short (<1 Myr) and potentially much longer timescales (not well documented). A key challenge in understanding the rate and timing of LIP weathering lies in securing reliable estimates of the original subaerial lava-areas, and improved paleogeographic biome maps to evaluate climate gradients and weatherability in deep time.

- Subduction fluxes derived from full-plate models provide a powerful means of estimating plate tectonic CO₂ degassing (sourcing) through time. These correlate well with zircon age frequency distributions and zircon age peaks clearly correspond to intervals of high subduction flux associated with greenhouse conditions. Lows in zircon age frequency are more variable with links to both icehouse and greenhouse conditions, and only the Permo-Carboniferous icehouse is clearly related to the zircon and subduction flux record. A key challenge is to develop reliable full-plate models before the Devonian in order to consider the subduction flux during the end-Ordovician Hirnantian glaciations, but we also expect refinements in subduction fluxes for Mesozoic–Cenozoic times as more advanced ocean-basin models with intra-oceanic subduction are being developed and implemented in full-plate models.

- The Permo-Carboniferous and end-Cenozoic icehouses correspond to periods of low CO₂ levels and low plate tectonic degassing. Elevated CO₂ values in the early Triassic may have resulted from a combination of increased plate tectonic degassing (sourcing) and reduced weatherability due to a low latitude arid region running across most of central Pangea.

- Relative degassing estimates based on subduction flux rates are too low to match proxy CO₂ levels for parts of the Mesozoic and notably the early Cenozoic. Implementing intra-oceanic subduction histories, adding fluxes from continental rifts and/or explicitly considering the intersection of continental magmatic arcs with carbonate-filled basins through time would almost certainly increase plate tectonic degassing and further minimize existing model-proxy CO₂ mismatches. But there are many other parameters to consider – including the silicate weathering parametrization – which can be improved by better global paleogeographies to estimate theoretical weatherability, and confirmed by biome maps.

ACKNOWLEDGMENTS

We acknowledge financial support from the Research Council of Norway (RCN), through its Centres of Excellence funding scheme, project number 223272 (CEED), through RCN project 263000 to M.T.J., and through RCN project 250111 to M.D., and from the innovation pool of the Helmholtz Association through the “Advanced Earth System Modelling Capacity (ESM)” activity to B.S. We thank Maxim Ballmer for inviting us to write this chapter, and Nicolas Coltice and an anonymous reviewer for constructive comments and suggestions.

REFERENCES

- Alvarez, L.W., Alvarez, W., Asaro, F. & Michel, H.V. (1980). Extra-terrestrial cause for the Cretaceous–Tertiary extinction: experimental results and theoretical interpretation. *Science*, 208, 1095–1108.
- Austermann, J., Kaye, B.T., Mitrovica, J.X. & Huybers, P. (2014). A statistical analysis of the correlation between Large Igneous Provinces and lower mantle seismic structure. *Geophysical Journal International*, 197, 1–9. doi:10.1093/gji/ggt500.
- Bailey, I., Hole, G.M., Foster, G.L., Wilson, P.A., Storey, C., Trueman, C.N., & Raymo, M.E. (2013). An alternative suggestion for the Pliocene onset of major Northern Hemisphere glaciation based the geochemical provenance of North Atlantic Ocean ice-rafted debris. *Quaternary Science Reviews*, 75, 181–194.
- Bambach, R.K., Knoll, A.H., & Wang, S.C. (2004). Origination, extinction, and mass depletions of marine diversity. *Paleobiology*, 30, 522–542.
- Becker, T.W., & Boschi, L. (2002). A comparison of tomographic and geodynamic mantle models. *Geochemistry Geophysics Geosystems*, 3, 1003. doi:10.1029/2001GC000168.

- Beerling, D.J., Harfoot, M., Lomax, B., & Pyle, J.A. (2007). The stability of the stratospheric ozone layer during the end-Permian eruption of the Siberian Traps. *Philosophical Transactions Royal Society*, 365, 1843–1866.
- Berner, R.A. (1997). The rise of plants and their effect on weathering and atmospheric CO₂. *Science* 276, 544–546.
- Berner, R.A. (2004). *The Phanerozoic Carbon Cycle: CO₂ and O₂*. Oxford University Press, New York.
- Berner, R.A. (2006). Inclusion of the weathering of volcanic rocks in the GEOCARBSULF model. *American Journal Science*, 306, 295–302.
- Berner, R.A., Lasaga, A.C., & Garrels, R.M. (1983). The carbonate silicate geochemical cycle and its effect on atmospheric carbon dioxide over the past 100 million years. *American Journal Science*, 283, 641–683.
- Bierman, P.R., Corbett, L.B., Graly, J.A., Neumann, T.A., Lini, A., Crosby, B.T., & Rood, D.H. (2014). Preservation of a preglacial landscape under the center of the Greenland Ice Sheet. *Science*, 344, 402–405.
- Black, B.A., Elkins-Tanton, L.T., Rowe, M.C., & Peate, I.U. (2012). Magnitude and consequences of volatile release from the Siberian traps. *Earth and Planetary Science Letters*, 317, 363–373.
- Blakey, R.C. (2003). Carboniferous-Permian Paleogeography of the Assembly of Pangea. In: Wong, T.E. (Ed.), *Fifteenth International Congress on Carboniferous and Permian Stratigraphy* (pp. 443–465). Royal Netherlands Academy of Arts and Sciences, Utrecht, the Netherlands.
- Blakey, R.C. (2008). Gondwana paleogeography from assembly to breakup – a 500 m.y. odyssey. *Geological Society America Special Paper*, 441, 1–28.
- Boucot, A.J., Xu, C., & Scotese, C.R. (2013). Phanerozoic Paleoclimate: An Atlas of Lithologic Indicators of Climate. *SEPM Concepts in Sedimentology and Paleontology*, 11.
- Bryan S.E., Peate I.U., Peate D.W., Jerram D.A., Mawby M.R., Marsh J.S., & Miller J.A. (2010). The largest volcanic eruptions on Earth. *Earth-Science Reviews*, 102 (3–4), 207–229.
- Bryan S.E., Riley, T.R., Jerram D.A., Philip T. Leat, P.T., & Stephens, C.J. (2002) Silicic volcanism: an undervalued component of large igneous provinces/volcanic rifted margins. In Menzies, M.A., Klemperer, S.L., Ebinger, C.J. & Baker, J. (Eds.), *Volcanic Rifted Margins* (Vol. 362, pp. 99–120). Geological Society of America Special Paper.
- Bluth, G.J.D., & Kump, L.R. (1991). Phanerozoic paleogeology. *American Journal Science*, 291, 284–308.
- Bond, D.P.G., & Wignall, P.B. (2014). Large igneous provinces and mass extinctions: An update. *Geological Society of America Special Paper*, 505, 29–55.
- Bond, D.P.G., & Grasby, S.E. (2017). On the causes of mass extinctions. *Palaeogeography, Palaeoclimatology, Palaeoecology*, 478, 3–29.
- Bower, D.J., Gurnis, M., & Seton, M. (2013). Lower mantle structure from paleogeographically constrained dynamic Earth models. *Geochemistry, Geophysics, Geosystems*, 14, 44–63.
- Brown R.J., Manya, S., Buisman, I., Fontana, G., Field, M., Mac Niocaill, C., Sparks, R.S.J., & Stuart, F.M. (2012). Eruption of kimberlite magmas: physical volcanology, geomorphology and age of the youngest kimberlitic volcanoes known on earth (the Upper Pleistocene/Holocene Igwisi Hills volcanoes, Tanzania). *Bulletin of Volcanology*, 74, 1621–1643. doi:10.1007/s00445-012-0619-8
- Brune, S., Williams, S.E., & Müller, R.D. (2017). Potential links between continental rifting, CO₂ degassing and climate change through time. *Nature Geoscience*, 10, 941–946.
- Bull, A.L., Domeier, M., & Torsvik, T.H. (2014). The effect of plate motion history on the longevity of deep mantle heterogeneities. *Earth and Planetary Science Letters*, 401, 172–182.
- Buiter, S.J.H., & Torsvik, T.H. (2014). A review of Wilson Cycle plate margins: a role for mantle plumes in continental breakup along sutures? *Gondwana Research*, 26, 627–653, doi:10.1016/j.gr.2014.02.007.
- Burke, K. (2011). Plate Tectonics, the Wilson Cycle, and Mantle Plumes: Geodynamics from the Top. *Annual Review of Earth and Planetary Sciences*, 39, 1–29. doi:10.1146/annurev-earth-040809-152521.
- Burke, K., & Torsvik, T.H. (2004). Derivation of large igneous provinces of the past 200 million years from long-term heterogeneities in the deep mantle. *Earth and Planetary Science Letters*, 227, 531–538.
- Burke, K., Steinberger, B., Torsvik, T.H., & Smethurst, M.A. (2008). Plume Generation Zones at the margins of Large Low Shear Velocity Provinces on the Core–Mantle Boundary. *Earth and Planetary Science Letters*, 265, 49–60. doi:10.1016/j.epsl.2007.09.042.
- Campbell, I.H. (2007). Testing the plume theory. *Chemical Geology*, 241, 153–176.
- Cao, W., Lee, Cin-Ty A., & Lackey, J.S. (2017). Episodic nature of continental arc activity since 750 Ma: A global compilation. *Earth and Planetary Science Letters*, 462, 85–95.
- Chandler, M.T., Wessel, P., Taylor, B., Seton, M., Kim, S.-S., & Hyeong, K. (2012). Reconstructing Ontong Java Nui: Implications for Pacific absolute plate motion, hotspot drift and true polar wander. *Earth and Planetary Science Letters*, 331–332, 140–151. doi:10.1016/j.epsl.2012.03.017.
- Christiansen, J.L., & Stouge, S. (1999). Oceanic circulation as an element in palaeogeographical reconstructions: the Arenig (early Ordovician) as an example. *Terra Nova*, 11, 73–78.
- Cizková, H., van den Berg, A.P., Spakman, W. & Matyska, C. (2012). The viscosity of Earth's lower mantle inferred from sinking speed of subducted lithosphere. *Physics of the Earth and Planetary Interiors*, 200–201, 56–62.
- Cocks, L.R.M., & Torsvik, T.H. (2002). Earth Geography from 500 to 400 million years ago: a faunal and palaeomagnetic review. *Journal Geological Society London*, 159, 631–644.
- Cohen A.S., & Coe A.L. (2007). The impact of the Central Atlantic Magmatic Province on climate and on the Sr- and Os-isotope evolution of seawater. *Palaeogeography Palaeoclimatology Palaeoecology*, 244, 374–390.
- Coltice, N., Bertrand, H., Rey, P., Jourdan, F., Phillips, B.R. & Ricard, Y. (2009). Global warming of the mantle beneath continents back to the Archaean. *Gondwana Research*, 15, 254–266.
- Coltice, N., Seton, M., Rolf, T., Müller, R.D., & Tackley, P.J. (2013). Convergence of tectonic reconstructions and mantle

- convection models for significant fluctuations in seafloor spreading. *Earth and Planetary Science Letters*, *383*, 92–100.
- Conrad, C.P., Steinberger, B., & Torsvik, T.H. (2013). Stability of active mantle upwelling revealed by net characteristics of plate tectonics. *Nature*, *498*, 479–482. doi:10.1038/nature12203.
- Corfu, F., Polteau, S., Planke, S., Faleide, J.I., Svensen, H., Zayoncheck, A., & Stolbov, N. (2013). U-Pb geochronology of Cretaceous magmatism on Svalbard and Franz Josef Land, Barents Sea large igneous province. *Geological Magazine*, *150*, 1127–1135. doi:10.1017/S0016756813000162.
- Courtillot, V.E., & Renne, P.R. (2003). On the ages of flood basalt events. *Comptes Rendus Geoscience*, *335*, 113–140.
- Courtillot, V., Davaille, A., Besse, J., & Stock, J. (2003). Three distinct types of hotspots in the Earth's mantle. *Earth and Planetary Science Letters*, *205*, 295–308. doi:10.1016/S0012-821X(02)01048-8.
- Davies, D.R., Goes, S., & Sambridge, M. (2015). On the relationship between volcanic hotspot locations, the reconstructed eruption sites of large igneous provinces and deep seismic structure. *Earth and Planetary Science Letters*, *411*, 121–130. doi:10.1016/j.epsl.2014.11.052.
- Dawson J.B. (1994). Quaternary kimberlitic volcanism on the Tanzania craton. *Contributions to Mineral and Petrology*, *116*, 473–485.
- DeMeo J. (1989). Desert expansion and drought: environmental crisis, Part I. *Journal of Arid Environments*, *23*, 15–26.
- De Schepper, S., Gibbard, P.L., Salzmann, U., & Ehlers, J. (2014). A global synthesis of the marine and terrestrial evidence for glaciation during the Pliocene Epoch. *Earth-Science Reviews*, *135*, 83–102.
- Dessert, C., Dupré, B., François, L.M., Schott, J., Gaillardet, J., Chakrapani, G., & Bajpai, S. (2001). Erosion of Deccan Traps determined by river geochemistry: impact on the global climate and the $^{87}\text{Sr}/^{86}\text{Sr}$ ratio of seawater. *Earth and Planetary Science Letters*, *188* (3–4), 459–474.
- Dessert, C., Dupré, B., Gaillardet, J., François, L.M., & Allègre, C.J. (2003). Basalt weathering laws and the impact of basalt weathering on the global carbon cycle. *Chemical Geology*, *202*, 257–273.
- Dickens G.R., J.R. O'Neil, D.K. Rea & R.M. Owen (1995). Dissociation of oceanic methane hydrate as a cause of the carbon isotope excursion at the end of the Paleocene. *Paleoceanography*, *10*, 965–971.
- Domeier, M. (2015). A plate tectonic scenario for the Iapetus and Rheic oceans. *Gondwana Research*, *36*, 275–295. doi:10.1016/j.gr.2015.08.003.
- Domeier, M., & Torsvik, T.H. (2014). Plate tectonics in the late Paleozoic. *Geoscience Frontiers*, *5*, 303–350.
- Domeier, M., & Torsvik, T.H. (2017). Full-plate modelling in pre-Jurassic time. *Geological Magazine Special Issue*. doi:10.1017/S0016756817001005.
- Domeier, M., Doubrovine, P.V., Torsvik, T.H. Spakman, W., & Bull, A.L. (2016). Global correlation of lower mantle structure and past subduction. *Geophysical Research Letters*, *43*, 4945–4953. doi:10.1002/2016GL068827.
- Domeier, M., Magni, V., Hounslow, M.W., & Torsvik, T.H. (2018). Episodic zircon age spectra reflect true fluctuations in global subduction. *Scientific Reports*, *8*, 17471, doi:10.1038/s41598-018-35040-z.
- Doubrovine, P.V., Steinberger, B., & Torsvik, T.H. (2012). Absolute plate motions in a reference frame defined by moving hotspots in the Pacific, Atlantic and Indian oceans. *Journal of Geophysical Research*, *117*, B09101. doi:10.1029/2011JB009072.
- Doubrovine, P.V., Steinberger, B., & Torsvik, T.H. (2016). A failure to reject: Testing the correlation between large igneous provinces and deep mantle structures with EDF statistics. *Geochemistry Geophysics Geosystems*, *17*, 1130–1163. doi:10.1002/2015GC006044.
- Dziewonski, A.M., & Anderson, D.L. (1981). Preliminary Reference Earth Model. *Physics of the Earth and Planetary Interior*, *25*, 297–356.
- Ernst R.E. (2014). *Large Igneous Provinces*. Cambridge University Press, London.
- Ernst, R.E., & Buchan, K.L. (2001). Large mafic magmatic events through time and links to mantle plume-heads. In R.E. Ernst and K.L. Buchan (Eds.), *Mantle Plumes: Their Identification Through Time* (Vol. 352, Chapter 19). Geological Society of America Special Paper.
- Faleide, J.I., Bjørlykke, K., & Gabrielsen, R.H. (2010). Geology of the Norwegian Continental Shelf. In K. Bjørlykke (Ed.), *Petroleum Geoscience: From Sedimentary Environments to Rock Physics* (pp. 467–499). Springer Science Business Media.
- Flament, N., Williams, S., Müller, R.D., Gurnis, M., & Bower, D.J. (2017). Origin and evolution of the deep thermochemical structure beneath Eurasia. *Nature Communications*, *8*, 14164. doi:10.1038/ncomms14164.
- Foster, G.L., Royer, D.L., & Lunt, D.J. (2017). Future climate forcing potentially without precedent in the last 420 million years: *Nature Communications*, *8*, 14845, doi:10.1038/ncomms14845.
- French, S.W., & Romanowicz, B. (2015). Broad plumes rooted at the base of the Earth's mantle beneath major hotspots. *Nature*, *525*, 95–99.
- Gaillardet, J., Dupré, B., Louvat, P., & Allègre, C.J. (1999). Global silicate weathering and CO₂ consumption rates deduced from the chemistry of large rivers. *Chemical Geology*, *159*, 3–30.
- Gaina, C., Torsvik, T.H., van Hinsbergen, D.J.J., Medvedev, S., Werner, S.C., & Labails, C. (2013). The African Plate: a history of oceanic crust accretion and subduction since the Jurassic. *Tectonophysics*, *604*, 4–25.
- Ganino, C., & Arndt, N.T. (2009). Climate changes caused by degassing of sediments during the emplacement of large igneous provinces. *Geology*, *37*, 323–326.
- Garnero, E.J., Lay, T., & McNamara, A. (2007). Implications of lower mantle structural heterogeneity for existence and nature of whole mantle plumes. *Geological Society of America Special Paper*, *430*, 79–102. doi:10.1130/2007.2430(05).
- Garnero, E.J., McNamara, A.K. & Shim, S.H. (2016). Continent-sized anomalous zones with low seismic velocity at the base of Earth's mantle. *Nature Geoscience*, *9*, 481–489.
- Gibbs, M.T., Bluth, G.J.S., Fawcett, P.J., & Kump, L.R. (1999). Global chemical erosion over the last 250 My: variations due

- to changes in paleogeography, paleoclimate, and paleogeology. *American Journal of Science*, 299, 611–651.
- Gibbs, M.T., Bice, K.L., Barron, E.J., & Kump, L.R. (2000). Glaciation in the early Paleozoic ‘greenhouse’: the roles of paleogeography and atmospheric CO₂. In Huber, B.T., MacLeod, K. G., & Wing, S.L. (Eds.), *Warm Climates in Earth History* (pp. 386–422). Cambridge, Cambridge University Press.
- Goddéris, Y., Donnadieu, Y., Lefebvre, V., Le Hir, G., & Nardin, E. (2012). Tectonic control of continental weathering, atmospheric CO₂, and climate over Phanerozoic times: *Comptes Rendus Geoscience*, 344, 652–662.
- Goddéris, Y., Donnadieu, Y., Le Hir, G., Lefebvre, V., & Nardin, E. (2014). The role of palaeogeography in the Phanerozoic history of atmospheric CO₂ and climate. *Earth-Science Reviews*, 128, 122–138.
- Goes, S., Agrusta, R., van Hunen, J. & Garel, F. 2017. Subduction-transition zone interaction: A review. *Geosphere*, 13 (3), 644–664.
- Gubanov, A.P., & Mooney, W.D. (2009). New global maps of crustal basement age. Eos Transactions. *American Geophysical Union*, 90 (Fall Meeting Supplement, Abstract T53B-1583).
- Hager, B. H., & O’Connell, R.J. (1979). Kinematic models of large-scale mantle flow. *Journal of Geophysical Research*, 84, 1031–1048.
- Hager, B. H., & O’Connell, R.J. (1981). A simple global model of plate dynamics and mantle convection. *Journal of Geophysical Research*, 86, 4843–4867.
- Hasegawa, H., Tada, R., Jiang, X., Sukanuma, Y., Imsamut, S., Charusiri, P., Ichinnorov, N., & Khand Y. (2012). Drastic shrinking of the Hadley circulation during the mid-Cretaceous Supergreenhouse. *Climate of the Past*, 8, 1323–1337.
- Haq, B.U. & Al-Qahtani, A.M. (2005). Phanerozoic cycles of sea-level change on the Arabian Platform. *GeoArabia*, 10, 127–160.
- Haq, B.U. & Shutter, S.R. (2008). A chronology of Paleozoic sea-level changes. *Science*, 322, 64–68.
- Hassan, R., Müller, R.D., Gurnis, M., Williams, S.E., & Flament, N.A (2016). Rapid burst in hotspot motion through the interaction of tectonics and deep mantle flow. *Nature*, 533, 239–241.
- Hawley, S.M., Pogge von Strandmann, P.A.E., Burton, K.W., Williams, H.M., & Gislason, S.R. (2017). Continental weathering and terrestrial (oxyhydr)oxide export: Comparing glacial and non-glacial catchments in Iceland. *Chemical Geology*, 462, 55–66.
- Hay, W.W., DeConto, R.M., de Boer, P.L., Flögel, S., Song, Y., & Stepashk, A. (2018). Possible solutions to several enigmas of Cretaceous climate. *International Journal of Earth Sciences*. doi:10.1007/S0053101816702
- Heimdal, T.H., Callegaro, S., Svensen, H.H., Jones, M.T., Pereira, E., & Planke, S. (2019). Evidence for magma–evaporite interactions during the emplacement of the Central Atlantic Magmatic Province (CAMP) in Brazil. *Earth and Planetary Science Letters*, 506, 476–492.
- Herold, N., Seton, M., Müller, R.D., You, Y., & Huber, M. (2008). Middle Miocene tectonic boundary conditions for use in climate models. *Geochemistry, Geophysics, Geosystems*, 9, Q10009.
- Herrmann, A. D., Patzkowsky, M. E., & Pollard, D. 2003. Obliquity forcing with 8-12 times preindustrial levels of atmospheric pCO₂ during the late Ordovician glaciation. *Geology*, 31, 485–488.
- Hounslow, M., Domeier, M., & Biggin, A.J. (2018). Subduction flux modulates the geomagnetic polarity reversal rate. *Tectonophysics*, 742–743, 34–49.
- Hosseini, K., Matthews, K.J., Sigloch, K., Shephard, G.E., Domeier, M. & Tsekhmistrenko, M. (2018). SubMachine: Web-Based tools for exploring seismic tomography and other models of Earth’s deep interior. *Geochemistry, Geophysics, Geosystems*, 19, 1464–1483.
- Jansen, E., Fronval, T., Rack, F., & Channell, J.E.T. (2000). Pliocene-Pleistocene ice rafting history and cyclicity in the Nordic Seas during the last 3.5 Myr. *Paleoceanography*, 15, 709–721.
- Japsen, P., Chalmers, J.A., Green, P.F., & Bonow, J.M. (2011). Elevated, passive continental margins: Not rift shoulders, but expressions of episodic, post-rift burial and exhumation. *Global and Planetary Change*, 90–91, 73–86. doi:10.1016/j.gloplacha.2011.05.004.
- Jerram D.A., Dobson, K.J., Morgan, D.J., & Pankhurst, M.J. 2018. The Petrogenesis of Magmatic Systems: Using Igneous Textures to Understand Magmatic Processes. In S. Burchardt (Ed.), *Volcanic and Igneous Plumbing Systems* (pp. 191–229). Elsevier. ISBN 9780128097496, https://doi:10.1016/B9780128097496.00008X.
- Jerram D.A., Widdowson, M., Wignall, P.B., Sun, Y., Lai, X., Bond, D.P.G., & Torsvik, T.H. (2016a). Submarine palaeoenvironments during Emeishan flood basalt volcanism, SW China: Implications for plume–lithosphere interaction during the Capitanian, middle Permian (‘end Guadalupian’) extinction event. *Palaeogeography, Palaeoclimatology, Palaeoecology*, 441 (1), 65–73.
- Jerram D.A., Svensen, H.H., Planke, S., Polozov, A.G., & Torsvik, T.H. (2016b). The onset of flood volcanism in the north-western part of the Siberian Traps: Explosive volcanism versus effusive lava flows. *Palaeogeography, Palaeoclimatology, Palaeoecology*, 441 (1), 38–50.
- Jerram D.A., Mock, A., Davis, G.R., Field, M., & Brown, R.J. (2009). 3D crystal size distributions: A case study on quantifying olivine populations in kimberlites. *Lithos*, 112, 223–235.
- Jerram D.A., & Widdowson, M. (2005). The anatomy of Continental Flood Basalt Provinces: Geological constraints on the processes and products of flood volcanism. *Lithos*, 79, 385–405.
- Jerram D.A., Davis, G.R., Mock, A., Charrier, A., & Marsh, B. D. (2010). Quantifying 3D crystal populations, packing and layering in shallow intrusions: a case study from the Basement Sill, Dry Valleys, Antarctica. *Geosphere*, 6 (5), 537–548.
- Johansson, L., Zahirovic, S., & Müller, R.D. (2017). The interplay between the eruption of large igneous provinces and the deep-time carbon cycle. *Geophysical Research Letters*, 45, 5380–5389.
- Jones, M.T., Jerram, D.A., Svensen, H.H., & Grove, C. (2016). The effects of large igneous provinces on the global carbon

- and sulphur cycles. *Palaeogeography Palaeoclimatology Palaeoecology*, 441, 4–21.
- Jones, M.T., Percival, L.M.E., Stokke, E.W., Frieling, J., Mather, T.A., Riber, L., Schubert, B.A., Schultz, B., Tegner, C., Planke, S., & Svensen, H.H. (2019). Mercury anomalies across the Palaeocene-Eocene Thermal Maximum. *Climate of the Past*, 15, 217–236.
- Jourdan, F., Féraud, G., Bertrand, H., Kampunzu, A.B., Tshoso, G., Watkeys, M.K., & Le Gall, B. (2005). Karoo large igneous province: brevity, origin, and relation to mass extinction questioned by new $^{40}\text{Ar}/^{39}\text{Ar}$ age data. *Geology*, 33, 745–748.
- Julian, B., Foulger, G., Hatfield, O., Jackson, S., Simpson, E., Einbeck, J., & Moore, A. (2015). Hotspots in Hindsight. *Geological Society of America Special Paper*, 514, 105–121. doi:10.1130/2015.2514(08).
- Katz, M.E., Miller, K.G., Wright, J.D., Wade, B.S., Browning, J.V., Cramer, B.S., & Rosenthal, Y. (2008). Stepwise transition from the Eocene greenhouse to the Oligocene icehouse. *Nature Geoscience*, 1, 329–334.
- Kennett, J.P. (1977). Cenozoic evolution of Antarctic glaciations, the circum-Antarctic ocean and their impact on global paleoceanography. *Journal of Geophysical Research*, 82, 3843–3860.
- Kent D.V. (2003). A case for a comet impact trigger for the Paleocene/Eocene thermal maximum and carbon isotope excursion. *Earth and Planetary Science Letters*, 211, 13–26.
- Kurtz A.C., L.R. Kump, M.A. Arthur, J.C. Zachos & A. Paytan (2003). Early Cenozoic decoupling of the global carbon and sulfur cycles. *Paleoceanography*, 18 (4), 1090.
- Labails, C., Olivet, J.L., Aslanian, D., & Roest, W.R. (2010). An alternative early opening scenario for the Central Atlantic Ocean. *Earth and Planetary Science Letters*, 297, 355–368.
- Lee, C.-T. A., & Lackey, J.S. (2015). Global Continental Arc Flare-ups and Their Relation to Long-Term Greenhouse Conditions. *Elements*, 11, 125–130.
- Lee, C.-T. A., Shen, B., Slotnick, B.S., Liao, K., Dickens, G.R., Yokoyama, Y., Lenardic, A., Dasgupta, R., Jellinek, M., Lackey, J.S., Schneider, T., & Tice, M.M. (2013). Continental arc–island arc fluctuations, growth of crustal carbonates, and long-term climate change. *Geosphere*, 9, 21–36.
- Lin, S.C., & van Keken, P.E. (2006). Dynamics of thermochemical plumes: 2. Complexity of plume structures and its implications for mapping mantle plumes, *Geochemistry Geophysics Geosystems*, 7, Q03003, doi:10.1029/2005GC001072.
- Liu, L., Gurnis, M., Seton, M., Saleeby, J., Müller, R.D., & Jackson J.M. (2010). The role of oceanic plateau subduction in the Laramide orogeny. *Nature Geoscience*, 3, 353–357, doi:10.1038/NGE0829.
- Liu, W., Shi, C., Xu, Z., Zhao, T., Jiang, H., Liang, C., Zhang, X., Zhou, L., & Yu, C. (2016). Water geochemistry of the Qiantangjiang River, East China: Chemical weathering and CO₂ consumption in a basin affected by severe acid deposition. *Journal of Asian Earth Sciences*, 127, 246–256.
- Lowry, D.P., Poulsen, C.J., Horton, D.E., Torsvik, T.H., & Pollard, D. (2014). Thresholds for Paleozoic ice sheet initiation. *Geology*, 42, 627–630.
- Macdonald, F.A., Swanson-Hysell, N.L., Park, Y., Lisiecki, L. & Jagoutz, O. (2019). Arc-continent collisions in the tropics set Earth’s climate state. *Science*, 364, 181–184.
- Madrigal, P., Gazel, E., Flores, K., Bizimis, M. & Jicha, B. (2016). Record of massive upwellings from the Pacific large low shear velocity province. *Nature Communications*, 7, 13309.
- Marshall, H.G., Walker, J.C.G., & Kuhn, W.R. (1988). Long-term climate change and the geochemical cycle of carbon. *Journal of Geophysical Research*, 93, 791–801.
- Marzoli, A., Callegaro, S., Dal Corso, J., Davies, J.H.F.L., Chiaradia, M., Youbi, N., Bertrand, H., Reisberg, L., Merle, R., & Jourdan, F. (2018). The Central Atlantic Magmatic Province (CAMP): A Review. In: Tanner L. (Ed.), *The Late Triassic World. Topics in Geobiology* (Vol. 46). Springer, Cham.
- Matthews, K., Maloney, K.T., Zahirovic, S., Williams, S.E., Seton, M., & Müller, R.D. (2016). Global plate boundary evolution and kinematics since the late Paleozoic. *Global and Planetary Change*, 146, 226–250.
- McGhee, G.R., Clapham, M.E., Sheehan, P.M., Bottjer, D.J., & Droser, M.L. (2013). A new ecological-severity ranking of major Phanerozoic biodiversity crises. *Palaeogeography Palaeoclimatology Palaeoecology*, 370, 260–270.
- McKenzie, N.R., Horton, B.K., Loomis, S.E., Stockli, D.F., Planavsky, N.J., & Lee, C.-T. (2016). Continental arc volcanism as the principal driver of icehouse-greenhouse variability. *Science*, 352, 444–447.
- Mills, B.J.W., Scotese, C.R., Walding, N.G., Shields, G.A., & Lenton, T.M. (2017). Elevated CO₂ degassing rates prevented the return of Snowball Earth during the Phanerozoic. *Nature Communications*. doi:10.1038/s41467-017-01456-w
- Mills, B.J.W., Krause, A.J., Scotese, C.R., Hill, D.J., Shields, G. A., & Lenton, T.M. (2019). Modelling the long-term carbon cycle, atmospheric CO₂, and Earthsurface temperature from late Neoproterozoic to present day. *Gondwana Research*, 67, 172–186.
- Mitchell, R.H. (1986). *Kimberlites: Mineralogy, Geochemistry and Petrology* (Plenum).
- Milliman, J., & Farnsworth, K.L. (2011). *River Discharge to the Coastal Ocean: A Global Synthesis*. Cambridge University Press.
- Morgan, W.J. (1971). Convection plumes in the lower mantle. *Nature*, 230, 42–43. doi:10.1038/230042a0.
- Morgan, W.J., & Morgan, J.P. (2007). Plate velocities in the hot-spot reference frame. In Foulger, G.R., & Jurdy, D.M. (Eds.), *Plates, Plumes, and Planetary Processes* (Vol. 430, pp. 65–78). Geological Society of America Special Paper. doi:10.1130/2007.2430(04).
- Mulyukova, E., Steinberger, B., Dabrowski, M., & Sobolev, S.V. (2015a). Survival of LLSVPs for billions of years in a vigorously convecting mantle: replenishment and destruction of chemical anomaly. *Journal of Geophysical Research – Solid Earth*, 120, 3824–3847. doi:10.1002/2014JB011688.
- Mulyukova, E., Steinberger, B., Dabrowski, M., & Sobolev, S. V. (2015b). *Residence time of oceanic crust in the deep mantle*.

- GRC – Gordon Research Conferences, South Hadley, MA, USA.
- Nardin, E., Godd eris, Y., Donnadiou, Y., Le Hir, G., & Blakey, R.C. (2011). Modeling the early Paleozoic long-term climatic trend. *Geological Society of America Bulletin*. doi:10.1130/B30364.1
- Osmundsen, P.T. & Redfield, T.F. (2011). Crustal taper and topography at passive continental margins. *Terra Nova*, 23 (6).
- Otto-Bliesner, B.L. (1995). Continental drift, runoff, and weathering feedbacks: Implications from climate model experiments. *Journal of Geophysical Research*, 100, 11,537–11,548.
- Panasjuk, S.V., Hager, B.H., & Forte, A.M. (1996). Understanding the effects of mantle compressibility on geoid kernels. *Geophysical Journal International*, 124, 121–133. doi:10.1111/j.1365-246X.1996.tb06357.x
- Patterson M.V. & Francis, D. (2013). Kimberlite eruptions as triggers for early Cenozoic hyperthermals. *Geochemistry Geophysics Geosystems*, 14, 448–456. doi:10.1002/ggge.20054.
- Percival, L.M.E., Witt, M.L.I., Mather, T.A., Hermoso, M., Jenkyns, H.C., Hesselbo, S.P., Al-Suwaidi, A.H., Storm, M. S., Xu, W. & Ruhl, M. (2015). Globally enhanced mercury deposition during the end-Pliensbachian extinction and Toarcian OAE: a link to the Karoo-Ferrar Large Igneous Province. *Earth and Planetary Science Letters*, 428, 267–280.
- Porder, S., Hilley, G.E., & Chadwick, O.A. (2007). Chemical weathering, mass loss, and dust inputs across a climate by time matrix in the Hawaiian Islands. *Earth and Planetary Science Letters*, 258, 414–427.
- Rampino, M.R., Self, S., & Stothers, R.B. (1988). Volcanic winters. *Annual Review of Earth and Planetary Sciences*, 16, 73–99.
- Raymo, M.E., Ruddiman, W.F., & Froelich, P.N. 1988. Influence of late Cenozoic mountain building on ocean geochemical cycles. *Geology*, 16, 649–653.
- Redfield, T.F. & Osmundsen, P.T. (2012). The long-term topographic response of a continent adjacent to a hyperextended margin: A case study from Scandinavia. *Geological Society of America Bulletin*, 125 (1–2).
- Richards, M.A., & Griffiths, R.W. (1988). Deflection of plumes by mantle shear flow: experimental results and a simple theory. *Geophysical Journal International*, 94, 367–376.
- Richards, M.A., Hager, B.H., & Sleep, N.H. (1988). Dynamically supported geoid highs over hotspots: Observations and theory: *Journal of Geophysical Research*, 93, 7690–7708. doi:10.1029/JB093iB07p07690.
- Richards, M.A., Duncan R.A., & Courtillot V.E. (1989). Flood basalts and hot-spot tracks: plume heads and tails. *Science*, 246, 103–107.
- Robock, A. (2000). Volcanic eruptions and climate. *Reviews of Geophysics*, 38 (2), 191–219.
- Ronov, A.B. (1994). Phanerozoic transgressions and regressions on the continents; a quantitative approach based on areas flooded by the sea and areas of marine and continental deposition. *American Journal of Science*, 294, 777–801. doi:10.2475/ajs.294.7.777
- Royer D.L. (2006). CO₂-forced climate thresholds during the Phanerozoic. *Geochimica et Cosmochimica Acta*, 70, 5665–5675.
- Royer, D.L., Donnadiou Y., Park, J., Kowalczyk, J., & Godd eris Y. (2014). Atmospheric CO₂ and O₂ during the Phanerozoic: Tools, Patterns, and Impacts. *Treatise on Geochemistry* 251–266.
- Russell, J.K. Porritt, L.A., Lavall e, Y., Dingwell, D.B. (2012). Kimberlite ascent by assimilation-fuelled buoyancy. *Nature*, 481, 352–356.
- Sahney, S., Benton, M.J., & Falcon-Lang, H.J. (2010). Rainforest collapse triggered Carboniferous tetrapod diversification in Euramerica. *Geology*, 38, 1079–1082.
- Sanei, H., Grasby, S., & Beauchamp, B. (2012). Latest Permian mercury anomalies. *Geology*, 40, 63–66.
- Seton, M., M uller, R.D., Zahirovic, S., Gaina, C., Torsvik, T. H., Shephard, G., Talsma, A., Gurnis, M., Turner, M., Maus, S., & Chandler, M. (2012). Global continental and ocean basin reconstructions since 200 Ma. *Earth-Science Reviews*, 113, 212–270.
- Sewall, J.O., van deWal, R.S.W., Zwan, K.V.D., Oosterhout, C. V., Dijkstra, H.A., & Scotese, C.R. (2007). Climate model boundary conditions for four Cretaceous time slices. *Climate Past*, 3, 647–657.
- Schaller, M.F., Wright, J.D., & Kent, D.V. (2011). Atmospheric PCO₂ Perturbations Associated with the Central Atlantic Magmatic Province. *Science*, 331, 1404–1409.
- Schellart, W., Stegman, D., & Freeman, J. (2008). Global trench migration velocities and slab migration induced upper mantle volume fluxes: constraints to find an Earth reference frame based on minimizing viscous dissipation. *Earth-Science Reviews*, 88, 118–144.
- Schmidt, A., Carslaw, K.S., Mann, G.W., Rap, A., Pringle, K. J., Spracklen, D.V., Wilson, M., & Forster, P.M. (2012). Importance of tropospheric volcanic aerosol for indirect radiative forcing of climate. *Atmospheric Chemistry and Physics*, 12, 7321–7339.
- Scotese, C.R., & Golonka, J. (1992). Paleogeographic Atlas, *PALEOMAP Progress Report 20–0692*, Department of Geology, University of Texas at Arlington, Texas (34 pp.).
- Self, S., Keszthelyi, L., & Thordarson, T. (1998). The importance of pahoehoe. *Annual Review of Earth Planetary Sciences*, 26, 81–110.
- Sepkoski Jr., J.J. (1996). Patterns of Phanerozoic extinction: a perspective from global data bases. In: Walliser, O.H. (Ed.), *Global Events and Event Stratigraphy in the Phanerozoic*. Springer-Verlag, Berlin, pp. 35–51.
- Shao, L., Zhang, P., Ren, D., & Lei, J. (1998). Late Permian coal-bearing carbonate successions in southern China: coal accumulation on carbonate platforms. *International Journal of Coal Geology*, 37, 235–256.
- Shellnutt, J.G., Bhat, G.M., Brookfield, M.E., & Jahn, B-M. (2011). No link between the Panjal Traps (Kashmir) and the late Permian mass extinctions. *Geophysical Research Letters*, 38, L19308, doi:10.1029/2011GL049032.
- Sigloch, K., & Mihalynuk, M.G. (2013). Intra-oceanic subduction shaped the assembly of Cordilleran North America. *Nature*, 496, 50–56. doi:10.1038/nature12019.

- Sleep, N.H. (1990). Hotspots and mantle plumes: Some phenomenology: *Journal of Geophysical Research*, *95*, 6715–6736. doi:10.1029/JB095iB05p06715.
- Sleep, N.H. (1997). Lateral flow and ponding of starting plume material. *Journal of Geophysical Research*, *102*, 10001–10012.
- Smoot, J.P. (1991). Sedimentary facies and depositional environments of early Mesozoic Newark Supergroup basins, eastern North America. *Paleogeography, Paleoclimatology, and Paleocology*, *84*, 369–423.
- Sobolev, S.V., Sobolev, A.V., Kuzmin, D.V., Krivolutsкая, N. A., Petrunin, A.G., Arndt, N.T., Radko, V.A., & Vasiliev, Y. R. (2011). Linking mantle plumes, large igneous provinces and environmental catastrophes. *Nature*, *477*, 312–316.
- Spence, J., & Telmer, K. (2005). The role of sulphur in chemical weathering and atmospheric CO₂ fluxes: Evidence from major ions, δ¹³C_{DIC}, and δ³⁴S_{SO₄} in rivers of the Canadian Cordillera. *Geochimica et Cosmochimica Acta*, *69* (23), 5441–5458.
- Stanley, S.M. (2016). Estimates of the magnitudes of major marine mass extinctions in earth history. *Proceedings of the National Academy of the United States of Sciences USA*, *113*, E6325–E6334.
- Steinberger, B. (2000). Plumes in a convecting mantle: Models and observations for individual hotspots. *Journal of Geophysical Research: Solid Earth*, *105*, 11127–11152. doi:10.1029/1999JB900398.
- Steinberger, B. (2007). Effect of latent heat release at phase boundaries on flow in the Earth's mantle, phase boundary topography and dynamic topography at the Earth's surface. *Physics of the Earth and Planetary Interiors*, *164*, 2–20.
- Steinberger, B., & O'Connell, R.J. (1998). Advection of plumes in mantle flow: implications on hotspot motion, mantle viscosity and plume distribution. *Geophysical Journal International*, *132*, 412–434. doi:10.1046/j.1365-246x.1998.00447.x.
- Steinberger, B., & Antretter, M. (2006). Conduit diameter and buoyant rising speed of mantle plumes: Implications for the motion of hotspots and shape of plume conduits. *Geochemistry Geophysics Geosystems*, *7*(1), Q11018, doi:10.1029/2006GC001409
- Steinberger, B., & Calderwood, A. (2006). Models of large-scale viscous flow in the Earth's mantle with constraints from mineral physics and surface observations. *Geophysical Journal International*, *167*, 1461–1481.
- Steinberger, B., & Holme, R. (2008). Mantle flow models with core–mantle boundary constraints and chemical heterogeneities in the lowermost mantle. *Journal of Geophysical Research*, *113*, B05403, doi:10.1029/2007JB005080.
- Steinberger, B., & Torsvik, T.H. (2012). A geodynamic models of plumes from the margins of Large Low Shear Velocity Provinces. *Geochemistry Geophysics Geosystems*, *13*, Q01W09. doi:10.1029/2011GC003808.
- Steinberger, B., Sutherland, R., & O'Connell, R.J. (2004). Prediction of Emperor-Hawaii seamount locations from a revised model of global plate motion and mantle flow. *Nature*, *430*, 167–173. doi:10.1038/nature02660. PMID:15241405.
- Steinberger, B., Torsvik, T.H. & Becker, T.W., 2012. Subduction to the lower mantle – a comparison between geodynamic and tomographic models. *Solid Earth*, *3*, 415–432.
- Steinberger, B., Spakman, W., Japsen, P., & Torsvik, T.H. (2015). The key role of global solid-Earth processes in preconditioning Greenland's glaciation since the Pliocene. *Terra Nova*, *27*, 1–8.
- Svensen, H., Planke, S. & Malthe-Sørensen, A. (2004). Release of methane from a volcanic basin as a mechanism for initial Eocene global warming. *Nature*, *429* (6991), 542–545.
- Svensen, H., & Jamtveit, B. (2010). Metamorphic fluids and global environmental changes. *Elements*, *6*, 179–182.
- Svensen, H., Planke, S., & Corfu, F. (2010). Zircon dating ties NE Atlantic sill emplacement to initial Eocene global warming. *Journal of the Geological Society London*, *167*, 433–436.
- Svensen, H., Corfu, F., Polteau, S., Hammer, Ø. & Planke, S. (2012). Rapid magma emplacement in the Karoo Large Igneous Province. *Earth and Planetary Science Letters*, *325–326*, 1–9.
- Svensen, H., Jamtveit, B., Planke, S., & Chevallier, L. (2006). Structure and evolution of hydrothermal vent complexes in the Karoo Basin, South Africa. *Journal of the Geological Society London*, *163*, 671–682.
- Svensen, H.H., Jerram, D.A., Polozov, A.G., Planke, S., Neal, C.R., Augland, L.E., & Emeleus, H.C. (2019) Thinking about LIPs: A brief history of ideas in Large igneous province research. *Tectonophysics* (Vol. 760, pp. 229–251). doi:10.1016/j.tecto.2018.12.008.
- Svensen, H. et al. (2009). Siberian gas venting and the end-Permian environmental crisis. *Earth and Planetary Science Letters*, *277* (3), 490–500.
- Svensen, H., Aarnes, I., Podladchikov, Y.Y., Jettestuen, E., Harstad, C.H., & Planke, S. (2010). Sandstone dikes in dolerite sills: evidence for high-pressure gradients and sediment mobilization during solidification of magmatic sheet intrusions in sedimentary basins. *Geosphere*, *6* (3), 211–224.
- Svensen, H.H., Torsvik, T.H., Callegaro, S., Augland, L., Heimdal, T.H., Jerram, D.A., Planke, S., & Pereira, E. (2018). Gondwana LIPs: plate reconstructions, volcanic basins and sill volumes. In Sensarma, S., Storey, B.C. (Eds.), *Large Igneous Provinces from Gondwana and Adjacent Regions* (Vol. 463, pp. 17–40). The Geological Society of London Special Publications.
- Tappe, S., Smart, K.A., Torsvik, T.H., Massuyeau, M., & de Wit, M. (2018). Geodynamics of kimberlites on a cooling Earth: Clues to plate tectonic evolution and deep volatile cycles. *Earth and Planetary Science Letters*, *484*, 1–14.
- Tarduno, J.A., Brinkman, D.B., Renne, P.R. (1998). Late Cretaceous Arctic volcanism: tectonic and climatic connections. In American Geophysical Union Spring Meeting Abstracts, Washington, DC: American Geophysical Union.
- Taylor, B. (2006). The single largest oceanic plateau: Ontong Java–Manihiki–Hikurangi. *Earth and Planetary Science Letters*, *241*, 372–380.
- Tegner, C., Andersen, T.B., Kjøl, H.J., Brown, E.L., Hagen-Peter, G., Corfu, F. (2019). A mantle plume origin for the Scandinavian Dyke Complex: A “piercing point” for 615 Ma plate reconstruction of Baltica? *Geochemistry, Geophysics, Geosystems*, *20*. doi:10.1029/2018GC007941.
- Thiede, J., Jessen, C., Knutz, P. (2011). Millions of Years of Greenland Ice Sheet History Recorded in Ocean Sediments. *Polarforschung*, *80*, 141–159.

- Thompson, D.W.J., Wallace, J.M., Jones, P.D., & Kennedy, J.J. (2009). Identifying signatures of natural climate variability in time series of global-mean surface temperature: Methodology and Insights. *Journal of Climate*, 22, 6120–6141.
- Thordarson, T., Miller, D.J., Larsen, G., Self, S., & Sigurdsson, H. (2001). New estimates of sulfur degassing and atmospheric mass-loading by the 934 AD Eldgjá eruption, Iceland. *Journal of Volcanology Geothermal Research*, 108, 33–54.
- Toohey, M., Krüger, K., Sigl, M., Stordal, F., & Svensen H.H. (2016). Climatic and societal impacts of a volcanic double event at the dawn of the Middle Ages. *Climatic Change*, 136, 401–412. doi:10.1007/s10584-016-1648-7.
- Torsvik, T.H., & Trench, A. (1991). The Ordovician history of the Iapetus Ocean in Britain: New palaeomagnetic constraints. *Journal of the Geological Society London*, 148, 423–425.
- Torsvik, T.H., & Cocks, L.R.M. (2017). *Earth History and Palaeogeography*. Cambridge University Press.
- Torsvik, T.H., & Domeier, M. (2017). Correspondence: Numerical modelling of the PERM anomaly and the Emeishan Large Igneous Province. *Nature Communications*, 8. doi:10.1038/s41467-017-00125-2.
- Torsvik, T. H. et al. (2001). Late Cretaceous India-Madagascar fit and timing of break-up related magmatism. *Terra Nova*, 12, 220–224.
- Torsvik, T.H., Steinberger, B., Cocks, L.R.M. & Burke, K. (2008a). Longitude: Linking Earth's ancient surface to its deep interior. *Earth and the Planetary Science Letters*, 276, 273–283.
- Torsvik, T.H., & Rehnström, E.F. (2003). The Tornquist Sea and Baltica-Avalonia docking. *Tectonophysics*, 362, 67–82.
- Torsvik, T.H., & Cocks, L.R.M. (2004). Earth geography from 400 to 250 million years: a palaeomagnetic, faunal and facies review. *Journal of the Geological Society London*, 161, 555–572.
- Torsvik, T.H., Smethurst, M.A., Burke, K., & Steinberger, B. (2008b). Long term stability in Deep Mantle structure: Evidence from the ca. 300 Ma Skagerrak-Centered Large Igneous Province (the SCLIP). *Earth and Planetary Science Letters*, 267, 444–452. doi:10.1016/j.epsl.2007.12.004.
- Torsvik, T.H., Burke, K., Steinberger, B., Webb, S.J., & Ashwal, L.D. (2010a). Diamonds sampled by plumes from the core–mantle boundary. *Nature*, 466, 352–355. doi:10.1038/nature09216.
- Torsvik, T. H., Steinberger, B., Gurnis, M., & Gaina, C. (2010b). Plate tectonics and net lithosphere rotation over the past 150 My. *Earth and Planetary Science Letters*, 291, 106–112.
- Torsvik, T.H., Smethurst, M.A., Burke, K., & Steinberger, B. (2006). Large Igneous Provinces generated from the margins of the Large Low-Velocity Provinces in the deep mantle. *Geophysical Journal International*, 167, 1447–1460. doi:10.1111/j.1365-246X.2006.03158.x.
- Torsvik, T.H., Rousse, S., Labails, C., & Smethurst, M.A. (2009). A new scheme for the opening of the South Atlantic Ocean and dissection of an Aptian Salt Basin. *Geophysical Journal International*, 177, 1315–1333.
- Torsvik, T. H., Van der Voo, R., Preeden, U., Mac Niocaill, C., Steinberger, B., Doubrovine, P.V., et al. (2012). Phanerozoic polar wander, paleogeography and dynamics. *Earth-Science Reviews*, 114, 325–368.
- Torsvik, T.H., van der Voo, R., Doubrovine, P.V., Burke, K., Steinberger, B., Ashwal, L.D., et al. (2014). Deep mantle structure as a reference frame for movements in and on the Earth. *Proceedings of the National Academy of Sciences USA*, 111 (24): 8735–8740 doi:10.1073/pnas.1318135111.
- Torsvik, T. H., Amundsen, H.E.F., Trønnes, R.G., Doubrovine, P.V., Gaina, C., Kuszniir, N., et al. (2015). Continental crust beneath southeast Iceland. *Proceedings of the National Academy of Sciences USA*, 112, E1818–E1827.
- Torsvik, T.H., Steinberger, B., Ashwal, L.D., Doubrovine, P.V., & Trønnes, R.G. (2016). Earth evolution and dynamics – a tribute to Kevin Burke. *Canadian Journal of Earth Sciences*, 53 (11), 1073–1087. https://doi.org/10.1139/cjes-2015-0228.
- Torsvik, T.H., Steinberger, B., Shephard, G.E., Doubrovine, P. V., Gaina, C., Domeier, M., et al. (2019). Pacific-Panthalassic reconstructions: Overview, errata and the way forward. *Geochemistry, Geophysics, Geosystems* (20, 3659–3689).
- Trønnes, R.G., Baron, M.A., Eigenmann, K.R., Guren, M.G., Heyn, B.H., Løken, A. & Mohn, C.E. (2019). Review: Core formation, mantle differentiation and core–mantle interaction within Earth and the terrestrial planets. *Tectonophysics*, 760, 165–198. doi:10.1016/j.tecto.2018.10.021.
- Ukstins Peate, I., & Bryan, S.E. (2008). Re-evaluating plume-induced uplift in the Emeishan large igneous province. *Nature Geoscience*, 1, 625–629. doi:10.1038/ngeo281.
- van der Meer, D., Spakman, W., van Hinsbergen, D.J.J., Amaru, M.L., & Torsvik, T.H. (2010). Absolute plate motions since the Permian inferred from lower mantle subduction remnants. *Nature Geoscience*, 3, 36–40. doi:10.1038/NNGEO708.
- van der Meer, D.G., Zeebe, R., van Hinsbergen, D.J.J., Sluijs, A., Spakman, W., & Torsvik, T.H. (2014). Plate tectonic controls on atmospheric CO₂ levels since the Triassic. *Proceedings of the National Academy of Sciences USA*. doi:10.1073/pnas.1315657111.
- van der Meer, D.G., van Hinsbergen, D.J.J. & Spakman, W. (2018). Atlas of the Underworld: subduction remnants in the mantle, their sinking history, and a new outlook on lower mantle viscosity. *Tectonophysics*, 723, 309–448.
- Vasilev, Y.R., Zolotukhin, V.V., Feoktistov, G.D., & Prusskaya, S.N. (2000). Evaluation of the volumes and genesis of Permo-Triassic trap magmatism on the Siberian Platform. *Geol. Geofiz.*, 41, pp. 1696–1705. (in Russian).
- Visscher, H., Looy, C.V., Collinson, M.E., Brinkhuis, H., Cittert, J., Kurschner, W.M., et al., (2004). Environmental mutagenesis during the end-Permian ecological crisis. *Proceedings of the National Academy of Sciences USA*, 101, 12952–12956.
- Vogt, P.R. (1972). Evidence for global synchronism in mantle plume convection, and possible significance for geology. *Nature*, 240, 338–342.
- Vrielynck, B., & Bouysse, P. (2003). The Changing Face of the Earth. The Break-Up of Pangaea and Continental Drift over the Past 250 Million Years in Ten Steps. Earth Sciences Series. UNESCO Publishing/Commission for the Geological Map of the World (CGMW).

- Walker, J.C.G., Hays, P.B., & Kasting, J.F. (1981). A negative feedback mechanism for the long-term stabilization of Earth's surface temperature. *Journal of Geophysical Research*, *86*, 9776–9782.
- Wignall, P.B. (2001). Large igneous provinces and mass extinctions. *Earth-Science Reviews*, *53*, 1–33.
- Wilson, J.T. (1963). A possible origin of the Hawaiian islands. *Canadian Journal of Physics*, *41*, 863–870. doi:10.1139/p63-094.
- Worsley, T.R. & Kidder D.L. (1991). First-order coupling of paleogeography and CO₂, with global surface temperature and its latitudinal contrast. *Geology*, *19*, 1161–1164.
- Wyllie, P.J. (1980). The origin of kimberlites. *Journal of Geophysical Research*, *85*, 6902–6910.
- Zachos, J., Pagani, M., Sloan, L., Thomas, E., & Billups, K. (2001). Trends, rhythms, and aberrations in global climate 65 Ma to present. *Science*, *292*, 686–693.
- Zhang, N., Zhong, S.J., Leng, W., & Li, Z.X. (2010). A model for the evolution of the Earth's mantle structure since the Early Paleozoic. *Journal of Geophysical Research – Solid Earth*, *115*: B06401. doi:10.1029/2009JB006896.
- Zhong, S., & Rudolph, M.L. (2015). On the temporal evolution of long-wavelength mantle structure of the earth since the early Paleozoic. *Geochemistry Geophysics Geosystems*, *16*, 1599–1615.
- Zhong, S., Zhang, N., Li, Z.-X., & Roberts, J.H. (2007). Supercontinent cycles, true polar wander, and very long-wavelength mantle convection. *Earth and Planetary Science Letters*, *261*, 551–564.
- Zurevinski, S.E., Heaman, L.M., & Creaser, R.A. (2011). The origin of Triassic/Jurassic kimberlite magmatism, Canada: Two mantle sources revealed from the Sr–Nd isotopic composition of groundmass perovskite. *Geochemistry Geophysics Geosystems*, *12*, Q09005. doi:10.1029/2011GC003659.

APPENDIX 16.1

COMPUTING PLUME ASCENT TIME Both for the plume conduit and the plume head, lateral advection is computed from the ambient mantle flow field. Radial motion of plume conduit elements is computed as the sum of ambient mantle flow and rising speed, whereas for the plume head, buoyant rising is dominant and the ambient vertical flow component is disregarded. Also, if the contribution of ambient flow on plume head rising were considered, it would not be possible to prescribe total ascent time, and hence match the hotspot age (Table 16.1) for a specified time when the plume head starts rising from the lowermost mantle, as it could only be determined after the modeling. To compute mantle flow, mantle density structure is derived from a seismic tomography model. Here we use *s10mean* (Dubrovine et al. 2016), but we also report results using *smean* (Becker & Boschi 2002) for comparison. For most of the mantle, we use a thermal scaling of seismic velocity to density anomalies (Model 2 of Steinberger & Calderwood 2006), but we also consider that LLSVPs are probably chemically distinct, by adding a “chemical” density anomaly (1.2%) to those regions below a certain depth (2600 km, i.e., in the lowermost 300 km of the mantle) where the seismic velocity anomaly is more negative than a specified value (–0.9% for *s10mean*, –1% for *smean*). The LLSVPs were outlined in this way because steep horizontal gradients in seismic velocity tend to be most frequent near those values of shear-wave anomaly, and both seismic velocity anomalies themselves and steep horizontal gradients are most pronounced in the lowermost 300 km (Torsvik et al. 2006; Burke et al. 2008). Adding a chemical density anomaly of 1.2% makes the piles overall slightly negatively buoyant, despite being hotter, approximately consistent with their long-term stability

and cross-sectional shape (Mulyukova et al. 2015a) and CMB topography constraints (Steinberger & Holme 2008). Regardless of whether this chemical anomaly is added, LLSVPs are overlain by buoyant, rising material. Hence, large-scale flow structure and inferred plume source locations do not strongly depend on whether the chemical anomaly is considered.

In the uppermost 220 km, density anomalies are reduced by a factor 0.5 because strong positive seismic velocity anomalies in the continental lithosphere would otherwise be interpreted as unrealistically strong density anomalies. This simplified treatment is justified because density anomalies in the upper 220 km have almost no effect at all on the results. We use the preferred mantle viscosity model 2b of Steinberger & Calderwood (2006), which features a strong increase of viscosity with depth, from $\sim 3 \times 10^{20}$ Pas below the lithosphere to nearly 10^{23} Pas in the lower part of the lower mantle. A similar viscosity structure was previously found to yield sufficiently slow hotspot motion compatible with observed tracks (Steinberger & O'Connell, 1998): A rather high viscosity in the lowermost mantle is required such that mantle flow, and hence advection of plume conduits, is sufficiently slow. A low viscosity just below the lithosphere helps to largely decouple mantle flow from plate motions, which are imposed as boundary conditions to flow, and hence prevents plume conduits from becoming strongly tilted (incompatible with observations) by moving plates. Results strongly depend on which mantle viscosity structure is used (Steinberger & O'Connell 1998), however for those viscosity structures that yield amounts of hotspot motion compatible with observations, and moderate plume conduits tilts typically not exceeding 60°, and that also match other constraints (geoid, heat flux, postglacial rebound), results tend to be overall similar. Hence, we do not vary mantle viscosity here.

Based on the viscosity and density structure, and time-dependent plate motions (Torsvik et al. 2010b) prescribed as surface boundary conditions, large-scale mantle flow is computed with the method of Hager & O'Connell (1979, 1981), extended to consider compressibility (Panasyuk et al. 1996) and the effect of phase boundary deflection but disregarding latent heat release and absorption at phase boundaries, as this was found to play a minor role (Steinberger 2007). At the core–mantle boundary, we use a free-slip boundary condition, except for spherical harmonic degree-1 toroidal flow (the net rotation component) where we use no-slip, such that it is possible to apply a net rotation of the lithosphere without causing a net rotation in the deep mantle. Radial density structure is adopted from PREM (Dziewonski & Anderson 1981), and a constant gravity 10 m/s^2 is used. The flow field is also used to backward-advect density heterogeneities,

which are hence time-dependent. Before 68 Ma, a constant density structure is used, as backward-advection becomes increasingly unreliable further back in time (Steinberger & O'Connell 1998). Considering time-dependence of flow is not crucial, and results remain qualitatively similar even if constant present-day flow is used. To model the motion of the plume conduit we use hotspot ages, buoyancy fluxes, and locations as listed Table 16.1, and with these parameters and viscosity structure, the plume conduit rising speed through the surrounding mantle is computed as in Steinberger et al. (2004) based on a modified Stokes formula (Richards & Griffiths 1988). The hotspot ages correspond to the time when the plume reaches the surface. The time when the plume head detaches from the source depth (taken as 2620 km depth, at the top of a low-viscosity D'' layer) is accordingly earlier by an amount equal to the plume head rise time.

17

Mercury, Moon, Mars: Surface Expressions of Mantle Convection and Interior Evolution of Stagnant-Lid Bodies

Nicola Tosi¹ and Sebastiano Padovan^{1,2}

ABSTRACT

The evolution of the interior of stagnant-lid bodies is comparatively easier to model and predict with respect to the Earth's due to the absence of the large uncertainties associated with the physics of plate tectonics, its onset time and efficiency over the planet's history. Yet, the observational record for these bodies is both scarcer and sparser with respect to the Earth's. It is restricted to a limited number of samples and a variety of remote-sensing measurements of billions-of-years-old surfaces whose actual age is difficult to determine precisely. Combining these observations into a coherent picture of the thermal and convective evolution of the planetary interior represents thus a major challenge. In this chapter, we review key processes and (mostly geophysical) observational constraints that can be used to infer the global characteristics of mantle convection and thermal evolution of the interior of Mercury, the Moon, and Mars, the three major terrestrial bodies where a stagnant lid has likely been present throughout most of their history.

17.1. INTRODUCTION

In contrast to the Earth whose evolution is controlled by plate tectonics and surface recycling, the other rocky bodies of the solar system operate today in a stagnant-lid mode. While Venus has and had a complex and rather poorly understood tectonics, Mercury, the Moon, and Mars are the paradigm of stagnant-lid bodies. They possess a single, continuous lithosphere, not fragmented into

tectonic plates, which undergoes deformation to a much lower extent than the Earth's, and below which solid-state mantle convection takes (or took) place (Breuer & Moore, 2015). With the possible exception of Mars, which could have experienced a brief episode of surface mobilization in its earliest history (Nimmo & Stevenson, 2000; Tosi, Plesa, & Breuer, 2013; Plesa et al., 2014), the three bodies have been characterized by stagnant-lid convection over the largest part of their evolution as their old and highly cratered surfaces testify.

While Earth's plate tectonics allows for continuous arc, mid-ocean-ridge, and hot-spot volcanism, stagnant-lid bodies experience only the latter form, which causes mantle melting and the production of secondary crust to be largely concentrated during the early evolution and to fade rapidly

¹*Deutsches Zentrum für Luft- und Raumfahrt, Institute of Planetary Research, Berlin, Germany*

²*WGS, Flight Dynamics, EUMETSAT, Darmstadt, Germany*

as the mantle begins to cool and the stagnant lid to thicken. Sinking of cold tectonic plates on Earth causes efficient cooling of the mantle and core. It promotes core convection and associated solidification of an inner core, resulting in the generation of a magnetic field. The presence of a stagnant lid tends to prevent heat loss, maintaining the interior warm with fundamental consequences for the mode and timing of magnetic field generation.

The absence of a recycling mechanism in stagnant-lid bodies makes the surface record of billions of years of evolution shaped by impacts and volcanism available to remote or in-situ inspection (Fassett, 2016). Measurements by orbiting spacecrafts of gravity, topography, surface composition, and magnetic field, combined with surface imaging and analysis of samples and meteorites (available for the Moon and Mars, but not for Mercury) provide a set of observational constraints that can be combined to investigate the thermal history of the interior and how mantle convection shaped it.

Venus shows a uniformly young surface (Hauck et al., 1998) as indicated by the random distribution of impact craters (Herrick, 1994). It does not show signs of Earth-like plate tectonics. Sites of potential subduction (Schubert & Sandwell, 1995), possibly induced by mantle plumes (Davaille et al., 2017), suggest that Venus is neither in a plate-tectonic nor in a classical stagnant-lid regime. The additional lack of a global magnetic field and the extreme paucity of observational constraints on the interior structure (e.g., Venus's moment of inertia is not known, preventing any meaningful estimate of its core size) strongly limit the possibility to infer the convective evolution of the planet as opposed to pure stagnant-lid bodies such as Mercury, the Moon, and Mars, to which we limit the present work. Besides Venus, we will also omit discussing Jupiter's moon Io. Although strictly speaking Io is also a stagnant-lid body, its interior dynamics (e.g., Tackey et al., 2001; Moore & Schubert, 2003) and surface tectonics (e.g., Bland & McKinnon, 2016) are largely controlled by tidal dissipation (e.g., Peale et al., 1979; Segatz et al., 1988). The associated heat production is at the origin of Io's massive volcanic activity, which controls heat loss via the so-called heat piping mechanism (e.g., O'Reilly & Davies, 1981; Moore & Webb, 2013) and sets this body apart from those whose evolution is governed by solid-state convection driven by radiogenic heating and secular cooling.

The chapter is divided in largely self-contained sections according to physical processes and, loosely, on their temporal extent. Accordingly, Section 17.2 discusses some developments in the understanding of the earliest stages of the evolution characterized by the solidification of magma oceans and its potential consequences for the creation of a primary crust and the onset of mantle convection. Following magma ocean solidification, the mantle will remove heat through convection and associated

decompression melting, which contributes to the creation of a secondary crust, a topic discussed in Section 17.3. Large impacts were common during the first phases of the solar system, sometimes with important implications for the overall evolution of the body. We describe the potential interaction of the impact-delivered energy with mantle convection in Section 17.4. The evidence for the presence of ancient magnetic fields on all the three bodies and a present magnetic field on Mercury provides insights into the cooling of the core, as discussed in Section 17.5. Section 17.6 describes a set of additional, though somewhat more indirect, constraints on the thermal evolution provided by evidences for global contraction and expansion, measurements of the heat flux, and inferences on the lithospheric thickness based on analysis of gravity and topography. We conclude in Section 17.7 with a summary comparing the evolution of Mercury, the Moon, and Mars in light of the constraints discussed throughout the chapter.

17.2. MAGMA OCEAN SOLIDIFICATION AND ONSET OF SOLID-STATE MANTLE CONVECTION

During the early stages of the solar system, accretionary impacts of planetesimals, high rates of radiogenic heat production, core-mantle differentiation, and giant collisions involving planetary embryos and protoplanets all contribute to store vast amounts of thermal energy into forming bodies. The accompanying temperatures can easily exceed the liquidus of silicates, leading to the formation of magma oceans, which can extend to great depths, possibly over the entire mantle (e.g., Elkins-Tanton, 2012; Solomatov, 2015). The crystallization of a magma ocean sets the stage for the subsequent long-term evolution of the planet: it controls the initial silicate differentiation of the mantle and the generation of the first (primordial) crust (e.g., Wood et al., 1970; Warren, 1985; Elkins-Tanton et al., 2005; Vander Kaaden & McCubbin, 2015), affects the volatile budget of the interior and atmosphere (e.g., Abe & Matsui, 1986; Elkins-Tanton, 2008; Lebrun et al., 2013; Hier-Majumder & Hirschmann, 2017; Nikolaou et al., 2019), and determines the earliest forms of mantle convection and surface tectonics (Tosi, Plesa, & Breuer, 2013; Maurice et al., 2017; Ballmer et al., 2017; Boukaré et al., 2018; Morison et al., 2019).

Because of the low viscosity of silicate liquids (e.g., Karki & Stixrude, 2010), turbulent convection initially controls the dynamics of magma oceans, which are expected to be well mixed and adiabatic (e.g., Solomatov, 2015). For relatively small bodies like Mercury, the Moon and Mars, the mantle melting temperature increases with pressure more rapidly than the convective adiabat. Upon cooling, solidification proceeds thus from the base of the

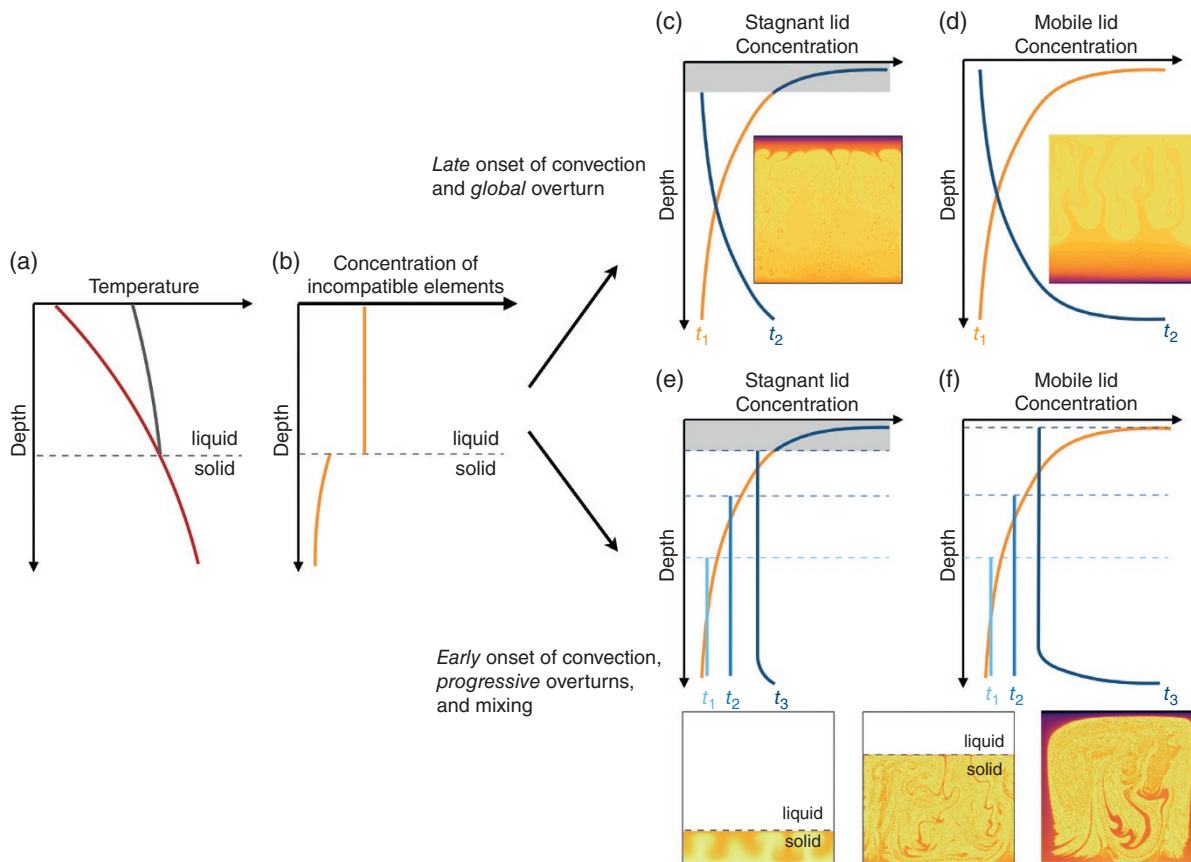


Figure 17.1 Different scenarios for the consequences of the fractional crystallization of a magma ocean. (a) Bottom up solidification due to the steeper slope of the liquid adiabat (gray line) with respect to the melting temperature (red line). (b) Enrichment of incompatible elements in the liquid phase. (c, d) Complete fractional crystallization before the onset of mantle convection. FeO and HPEs are more and more enriched at shallow depths (orange lines at time t_1). The formation of a stagnant lid (gray area in panel c) can prevent late-stage cumulates from sinking. The overturn takes place beneath the lid (blue line at time t_2 and contour plot in panel c). If the uppermost cumulates are mobilized, a global-scale overturn takes place (blue line at time t_2 and contour plot in panel d). The contour plots schematically describe the concentration of FeO and HPEs in the solid mantle, with low and high values in light yellow and black, respectively. (e, f) As in panels c and d, but for the case of solid-state convection beginning during solidification. Times t_1 to t_3 refer to subsequent stages. An early onset of convection can cause mixing of newly formed cumulates beneath the magma ocean. The formation of a stagnant lid leaves a largely mixed mantle depleted in incompatible elements (blue line at time t_3 in panel e). Surface mobilization causes the formation of a dense primordial layer, overlaid by a compositionally homogeneous mantle (blue line at time t_3 in panel f). Snapshots in panels c and d are derived from simulations similar to those of Tosi, Plesa, and Breuer (2013); snapshots beneath panels e and f are obtained following the approach of Maurice et al. (2017).

magma ocean upwards (Figure 17.1a). Given the shape of the relevant high-pressure melting curves (Fiquet et al., 2010; Andraut et al., 2011), this scenario likely applies also to the Earth, although the possibility exists for solidification starting at mid-mantle depths (Stixrude et al., 2009), ultimately leading to the formation of a basal magma ocean (see Labrosse et al., 2015, for a review). For simplicity, here we do not distinguish between solidus and liquidus and simply consider the mantle melting temperature as the temperature corresponding to the so-called rheologically-critical melt fraction. Above this threshold, which is usually set around 30–40% (e.g., Costa et al.,

2009), the crystal-melt mixture exhibits a liquid-like behavior; below it, crystals tend to form a stress-supporting interconnected network with partially molten rocks effectively deforming as a solid (e.g., Solomatov & Stevenson, 1993).

Depending on whether newly-formed crystals settle or are suspended by the turbulent flow, the magma ocean can undergo fractional or equilibrium (batch) crystallization. In the first case, liquid and crystals effectively separate without equilibrating. The composition of the liquid evolves continuously through the removal of solidified materials, ultimately leading to the silicate differentiation

of the solid mantle (Figure 17.1b). In the second case, crystals and liquid remain in equilibrium resulting in a compositionally-homogeneous mantle. The conditions determining whether settling or entrainment occurs are still poorly understood. The density difference between liquid and solids, the size of crystals, the vigour of convection, the effects of planetary rotation, and the cooling rate of the magma ocean, all of which evolve in complex ways during solidification, may play a role in controlling whether fractional or equilibrium crystallization occurs (e.g., Tonks & Melosh, 1990; Solomatov & Stevenson, 1993; Solomatov et al., 1993; Suckale et al., 2012; Solomatov, 2015; Maas & Hansen, 2015, 2019; Cassanelli & Head, 2016;).

The Moon represents the paradigm of terrestrial body that likely experienced a global-scale magma ocean that underwent fractional crystallization (e.g., Warren, 1985). The analysis of *Apollo* samples and lunar meteorites, as well as remote-sensing measurements revealed that the ancient lunar highlands largely consist of anorthosites composed of plagioclase feldspar, building a 30–40 km thick crust as inferred from the inversion of gravity and topography data from the GRAIL mission (Wieczorek et al., 2013). In a lunar magma ocean that fractionally solidifies from the bottom up, plagioclase begins to crystallize at a pressure of around 1 GPa, when 70–80% of the magma ocean is solid (e.g., Snyder et al., 1992; Elkins-Tanton et al., 2011; Charlier et al., 2018). At these conditions, the residual liquid is denser than plagioclase crystals. These float to the top of the magma ocean forming the bulk of the Moon’s anorthositic crust, which dramatically reduces the heat loss at the surface and retards magma ocean solidification (Elkins-Tanton et al., 2011) (see also Sections 17.2.2 and 17.3.1). Plagioclase flotation is thought to work efficiently only on the Moon or smaller bodies; for larger bodies like Mars, the more rapid increase of pressure with depth causes plagioclase to become stable at shallow depths where the magma ocean has reached a degree of crystallinity high-enough to prevent flotation (Brown & Elkins-Tanton, 2009; Elkins-Tanton, 2012).

Mercury’s surface is unusually dark (e.g., Robinson et al., 2008). Spectral measurements (Murchie et al., 2015; Peplowski et al., 2016) indicate that graphite is the material responsible for this characteristic. Indeed, Vander Kaaden and McCubbin (2015) showed that for Mercury’s melts, graphite is the only mineral that could form a flotation crust in a crystallizing magma ocean. Yet, the composition of Mercury’s surface is largely the product of secondary volcanism (Section 17.3.2). Widespread lava flows buried over time the primary graphite crust, which seems to have been exposed in some craters. Similar to Mercury, the surface of Mars is also largely volcanic but lacks evidence for primordial materials

generated through the fractional crystallization of a magma ocean (Section 17.3.2).

From the perspective of the convective dynamics and evolution of the solid mantle, the fractional crystallization of a magma ocean can have fundamental consequences beyond the formation of a primordial crust. As solids are removed, incompatible elements tend to be progressively enriched in the remaining liquid phase. These include wüstite (FeO) and long-lived heat-producing elements (HPEs) Uranium (U), Thorium (Th), and potassium (K) in addition to volatiles such as water (H₂O) and carbon dioxide (CO₂). The concentration C_{sol} of incompatible elements at a given radius r of the solidified cumulates can be expressed as follows (e.g., Boukaré et al., 2018; Morison et al., 2019):

$$C_{\text{sol}}(r) = DC_{\text{liq}}^0 \left(\frac{R_p^3 - R_b^3}{R_p^3 - r^3} \right)^{1-D}, \quad (17.1)$$

where C_{liq}^0 is the initial concentration in the liquid magma ocean, R_p and R_b are the top and bottom radii of the magma ocean (corresponding to the planet radius and, in the case of a global magma ocean, to the core radius), and D is a partition coefficient, typically $\ll 1$. The concentration of incompatible elements in solidified cumulates tends thus to follow a power-law profile (Figure 17.1b).

17.2.1. Late Onset of Mantle Convection and Global Overturn

If fractional crystallization proceeds fast compared to the timescale for the onset of solid-state convection (see below), the progressive enrichment of FeO in the residual liquid ultimately causes the formation of dense, FeO-rich layers at shallow depths overlying deep, FeO-poor layers (Elkins-Tanton et al., 2003, 2005; Tosi, Plesa, & Breuer, 2013; Plesa et al., 2014; Scheinberg et al., 2014). This configuration is gravitationally unstable and prone to overturn (Figures 17.1c and 17.1d). The scenario of fractional crystallization followed by a global-scale overturn has been proposed for Mercury (Brown & Elkins-Tanton, 2009), Mars (Elkins-Tanton et al., 2003, 2005; Elkins-Tanton et al., 2005), the Earth (Elkins-Tanton, 2008; Foley et al., 2014), and the Moon, although in the latter case, the overturn only involves a dense layer forming beneath the plagioclase crust (Zhong et al., 2000; Zhang et al., 2017; Li et al., 2019; Yu et al., 2019; Zhao et al., 2019) (see also Section 17.3).

Flotation crusts or solid cumulates that crystallize at shallow depth and relatively low temperature have a high viscosity that prevents deformation. Late-stage cumulates enriched in FeO and HPEs tend to remain locked in the stagnant lid with the overturn involving only the

sub-lithospheric mantle (Figure 17.1c). Thus, a stagnant lid with primordial composition forms, overlying a mantle with a moderately stable compositional stratification. Alternatively, the viscosity of the near-surface mantle may remain relatively low due to the presence of interstitial melt or to a high surface temperature, allowing for sluggish mobilization (e.g., Scheinberg et al., 2014). Alternatively, the stresses induced by the first upwellings impinging at the base of the lithosphere may locally exceed its yield strength, inducing an early episode of plate-tectonics-like surface mobilization (Tosi, Plesa, & Breuer, 2013). In both cases, a whole-mantle overturn takes place, resulting in a highly-stable compositional gradient due to increasing FeO-enrichment of the overturned materials from the surface to the base of the mantle (Figure 17.1c).

The global-scale overturn of a fractionally crystallized magma ocean – beneath the stagnant lid or involving the lid itself – has been studied in particular in the framework of the early evolution of Mars as it provides a suitable explanation for the generation of an early magnetic field (Elkins-Tanton et al., 2005; Plesa et al., 2014; Scheinberg et al., 2014) (see Section 17.5), for the rapid formation of secondary crust caused by upwelling cumulates undergoing partial melting upon overturning (Elkins-Tanton et al., 2005) (see Section 17.3), and for the generation of compositionally distinct domains in the silicate mantle (e.g., Elkins-Tanton et al., 2003; Debaille et al., 2009). The latter constraint is derived from the analysis of Martian meteorites whose isotopic heterogeneity requires the formation of distinct source-reservoirs within the first ~ 100 Myr of the solar system that remained unmixed throughout the planet's evolution (Mezger et al., 2013).

Albeit successful, a global-scale overturn of the above kind poses a problem for the long-term evolution of the Martian mantle. As discussed in Section 17.3, surface evidence indicates that Mars has been volcanically active throughout its history (Hartmann et al., 1999; Werner, 2009). Long-lived volcanism in a stagnant lid body like Mars is only possible in the presence of a convective mantle where hot plumes rising from the core-mantle boundary (CMB) undergo decompression melting (Plesa et al., 2018). Using the crystallization sequence proposed by Elkins-Tanton et al. (2005), Plesa et al. (2014) performed numerical simulations of global-scale overturn in the Martian mantle in the presence of either a stagnant or a mobile lid. They showed that in both cases the compositional gradient following the overturn (Figure 17.1c and 17.1d) is stable enough to largely prevent the subsequent onset of thermal convection and partial melting, at odds with the evidence that volcanism lasted over most of Mars' history, until as recently as few million years ago (Neukum et al., 2004).

The reason for the above behavior is to be sought in the large buoyancy ratio associated with the overturned mantle. The buoyancy ratio (B) is defined as

$$B = \frac{\Delta\rho_C}{\Delta\rho_T} = \frac{\Delta\rho_C}{\rho_0\alpha\Delta T}, \quad (17.2)$$

where $\Delta\rho_C$ is the compositional density difference between shallow, FeO-poor cumulates and deep, FeO-rich cumulates that hinders convection, and $\Delta\rho_T$ is the density difference due to thermal expansion between cold shallow cumulates and deep hot cumulates that drives convection (ρ_0 is a reference density, α the coefficient of thermal expansion, and ΔT the temperature difference between the surface and the base of the mantle). For a mantle that underwent a bottom-up solidification, $\Delta\rho_T$ in Equation 17.2 can be well determined assuming that the initial core temperature corresponds to the melting temperature of the silicate mantle at CMB conditions. Much more uncertain is the value of $\Delta\rho_C$, which can range from 0 for the (unlikely) case of a complete equilibrium crystallization up to several hundreds of kg/m^3 in the case of a purely fractional crystallization. The crystallization sequence obtained by Elkins-Tanton et al. (2005) assuming pure fractionation and used by Plesa et al. (2014) results in a buoyancy ratio of ~ 3 , sufficiently large to suppress thermal buoyancy and solid-state convection in the overturned mantle. As shown by Tosi, Plesa, and Breuer (2013), post-overturn thermo-chemical convection begins to be possible (at least in the upper mantle) for values of B lower than ~ 2 .

In addition, the dense, FeO-rich cumulates that sink to the CMB are also highly enriched in HPEs. In the presence of a high value of B preventing the deep mantle from convecting, such cumulates will tend to heat up. The accompanying temperatures can then exceed the solidus, leading to the formation of partial melt, or even the liquidus, leading to the formation of a basal magma ocean (Plesa et al., 2014; Scheinberg et al., 2018), whose consequences for Mars are yet to be explored.

17.2.2. Early Onset of Mantle Convection and Progressive Mixing

Convective mixing acting while the magma ocean is still solidifying provides a viable way to reduce the effective buoyancy ratio of a solid mantle formed via fractional crystallization. The scenarios described above apply whenever the timescale of magma ocean solidification is shorter than the timescale of convective mobilization of newly formed cumulates. The presence of a growing atmosphere on top of a crystallising magma ocean has been widely recognized as capable to exert a fundamental control on the magma ocean lifetime (Abe & Matsui, 1986; Elkins-Tanton, 2008; Lebrun et al., 2013; Hamano

et al., 2013; Nikolaou et al., 2019). Similar to FeO and HPEs, volatiles are enriched in the liquid phase as the magma ocean cools and solidifies, with their concentration that can increase until reaching saturation in the magma. In this context, H₂O and CO₂ are the two gases that have been studied most extensively. The amount of gas in excess of saturation is generally assumed to form bubbles that efficiently rise to the surface and escape from the magma ocean forming a secondary atmosphere. This slows down the solidification due to the ability of H₂O and CO₂ to act as greenhouse gases absorbing infrared radiation. The solidification timescale depends on several poorly constrained parameters (Nikolaou et al., 2019). Above all, it is influenced by the initial bulk abundance of volatiles and by the incoming stellar radiation (e.g., Hamano et al., 2013; Lebrun et al., 2013). For the Earth, for example, model calculations show that a volatile-depleted, whole-mantle magma ocean would solidify in only $\sim 10^3$ years (e.g., Monteux et al., 2016). By contrast, the presence of an outgassed steam atmosphere corresponding to a bulk water inventory of one Earth's ocean would extend the solidification to more than 1 Myr (e.g., Elkins-Tanton, 2008; Lebrun et al., 2013; Salvador et al., 2017; Nikolaou et al., 2019). Besides the presence of a thick outgassed atmosphere, the formation of a solid flotation crust can slow down magma ocean solidification even more significantly. In the case of the Moon, a growing flotation crust forming a solid conductive lid on top of the crystallizing magma ocean extends its solidification timescale to at least few tens of millions of years (Meyer et al., 2010; Elkins-Tanton et al., 2011; Perera et al., 2018). For Mercury, the idea of a graphite flotation crust is relatively new, the thickness of such crust highly uncertain (Vander Kaaden & McCubbin, 2015), and dynamic models of Mercury's convection accounting for the effects of magma ocean solidification still absent. Therefore, it remains unclear what its effect would be.

At any rate, a slowly solidifying magma ocean opens the possibility for convection to set in during solidification. Newly formed solid cumulates can overturn and start to be mixed by convection while being overlaid by a liquid magma ocean (Figures 17.1e and 17.1f). If mixing is efficient, two end-member configurations at the end of solidification are possible, similar to the previous case of a global overturn. The latest, highly enriched cumulates can remain locked in the stagnant lid, while the underlying mantle has been largely homogenized by an early onset of convection (Figure 17.1e). Alternatively, if the lid can be mobilized, the uppermost cumulates can sink to the CMB, forming a basal layer of materials enriched in incompatible elements (Figure 17.1f).

Whether or not the solid mantle begins overturning before the end of magma ocean crystallization largely depends on a competition between the timescale of

solidification (τ_{MO}) and the timescale of convective destabilization of the mantle (τ_{conv}) due to the unstable compositional stratification (Maurice et al., 2017; Ballmer et al., 2017; Boukaré et al., 2018). To quantify the relation between the two timescales, Boukaré et al. (2018) introduced a nondimensional number (R_C) defined as

$$R_C = \frac{\tau_{\text{MO}}}{\tau_{\text{conv}}} = \tau_{\text{MO}} \frac{\Delta\rho_C g D}{\eta}, \quad (17.3)$$

where τ_{MO} is the magma ocean solidification time, η the dynamic viscosity of the solid mantle, $\Delta\rho_C$ the density difference between FeO-rich and FeO-poor cumulates (as in Equation (17.2)), g the gravity acceleration, and D the thickness of the solidified mantle. The larger R_C is, the more likely it is that convection will start mixing the mantle during its solidification. As shown by Boukaré et al. (2018) in the framework of isoviscous models, the critical value of R_C that separates the two scenarios of late onset of convection and global overturn (Figure 17.1c and 17.1d) as opposed to an early onset characterized by progressive overturns (Figure 17.1e and 1f) is between 10^4 and 10^5 . Figure 17.2 (which reproduces Figure 3b of Boukaré et al. (2018)), shows the boundary separating the two regimes assuming $R_C = 5 \times 10^4$, $\Delta\rho = 1000 \text{ kg/m}^3$, and for g and H the gravity acceleration and mantle thickness of the corresponding body. As shown by Equation (17.3), an early onset is facilitated by long solidification times, a thick mantle and a low viscosity.

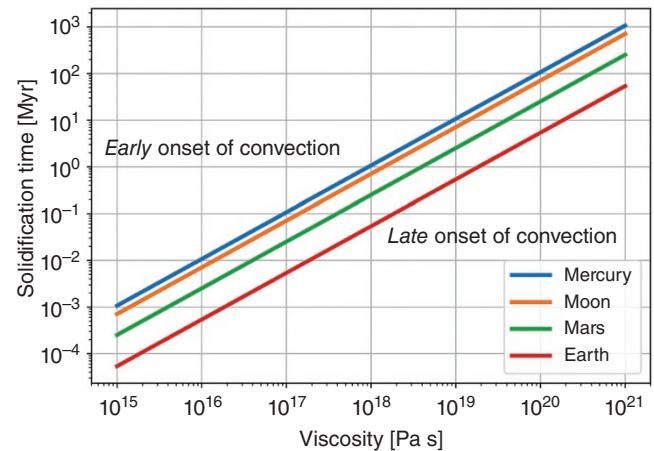


Figure 17.2 Boundary separating the regime of early onset of convection (above the curve) and late onset of convection (below the curve) for different bodies according to magma ocean solidification time and viscosity of the solid mantle. For a given value of the viscosity, the solidification time allowing for an early onset of convection is longest for Mercury and shortest for the Earth. Similarly, for a given solidification time, the viscosity making an early onset possible is lowest for Mercury and largest for the Earth. The diagram is based on Equation (17.3) and calculated assuming $R_C = 5 \times 10^4$.

The presence of residual melts as well as volatiles renders low values of the viscosity (10^{17} Pa s or even lower) fully plausible (see, e.g., Maurice et al., 2017). For these viscosities, an early onset of convection and mixing (Figures 17.1e and 17.1f) becomes likely for Mars (Maurice et al., 2017) in the presence of an outgassed atmosphere retarding magma ocean solidification (Lebrun et al., 2013) – a scenario that Ballmer et al. (2017) have proposed also for the Earth – and inevitable for the Moon (Boukaré et al., 2018) because of the strong insulating effect of the flotation crust, which remained part of the stagnant lid. Furthermore, recent works that considers the effects of a semipermeable boundary at the solid–liquid interface via a melting-freezing boundary condition (Labrosse et al., 2018; Morison et al., 2019) suggests that the critical Rayleigh number for the onset of solid-state mantle convection can be significantly lower and the heat transfer efficiency significantly higher than for non-penetrative boundaries as assumed in the works of Maurice et al. (2017), Ballmer et al. (2017) and Boukaré et al. (2018). In such a case, an early onset of convection would be facilitated and its effects strengthened. Although a flotation crust was probably present also on Mercury (see also Section 17.3), the low convective vigor due to the planet’s thin mantle makes the hypothesis of an early onset of convection unlikely and the possibility of a global overturn beneath the stagnant lid and flotation crust (Brown & Elkins-Tanton, 2009) more plausible (Figure 17.1c). The inferred lack of a highly enriched primary crust on Mars (Section 17.3) suggests that an early episode of surface mobilization accompanied by the subduction of the latest cumulates (Figure 17.1f) may have characterized the final stages of magma ocean solidification.

17.3. CRUSTAL MANIFESTATIONS

Being their geologic evolution largely the result of interior processes, planetary crusts contain important clues on the nature and temporal variations of such processes. The focus here is on three aspects of the crust: type, volume, and age of emplacement. Typically, three types of crust are identified according to a temporal criterion, which also discriminates the different processes associated with their production (Taylor & McLennan, 2009). As anticipated in Section 17.2, primary crusts are the result of magma ocean solidification and are emplaced very early in the history of an object; secondary crusts are the result of partial melting of the mantle, which can occur throughout the solar system history; and tertiary crusts are the results of, e.g., remelting of the secondary crust, and at present the only concrete evidence for tertiary crust is the continental crust of the Earth, possibly because plate

tectonics is required to produce it (Taylor & McLennan, 2009).

Characterizing the type of crust(s) present in a given body has important implications for models of its thermal evolution, since the crust is chemically different from the bulk composition, most importantly in its content of the long-lived HPEs. Thus, crustal production effectively decreases the value of H , the specific (i.e., volumetric) rate of internal heat generation appearing in the Rayleigh number for internally heated convection (Turcotte & Schubert, 2002):

$$\text{Ra}_H = \frac{\rho g \alpha D^5 H}{\eta k \kappa}. \quad (17.4)$$

In this expression ρ and D are the density and thickness of the mantle, g the gravitational acceleration; α , k , and κ are the thermal expansivity, conductivity, and diffusivity; η is the dynamic viscosity. In the case of an early emplaced primary crust, the effect on the internal evolution can be treated as an initial boundary condition on the value of H (Laneuville et al., 2013; Rolf et al., 2016). In the case of a secondary crust, which in general is created over an extended period of time, the value of H has to be time-dependent, consistent with the secondary crust produced (Morschhauser et al., 2011; Padovan et al., 2017). The absolute amount of heat sources that are extracted in creating crustal material depends critically on the volume of this material and its enrichment with respect to the mantle. These two parameters should be characterized for each crustal type and, at least for the secondary crust, which is emplaced over an extended period of time, for its different units.

The bulk volume of the crust can be investigated using a combination of gravity and topography data. The basic idea is that the non-central components of the gravitational field of a planet contain the contribution of the mass associated with the topography and with any internal non-radially symmetric mass distribution. By ascribing the Bouguer anomaly – the gravitational signal left after the removal of the topographical signal – to subsurface interfaces or loading, models for the thickness of the crust can be obtained. This is usually done either by assuming a given compensation mechanism (Wieczorek & Phillips, 1997; Padovan et al., 2015), or by globally minimizing the anomalies using an anchor point obtained, e.g., by imposing an average thickness of the crust or by requiring the thickness to be larger than zero everywhere (see, e.g., the review by Wieczorek, 2015). In addition to the bulk volume, it is important to identify the volumes of different units that are associated with different crustal types and/or different time of emplacement. As a case in point, the lunar maria are dark basaltic provinces located mostly on the near-side of the Moon. They represent the extruded component of

magmatic events associated with secondary crustal production, and thus HPEs mantle depletion. In principle, surficial units can be dated through crater counting (Section 17.4) and their volumes can be estimated by taking advantage of additional stratigraphical, compositional, and geological analyses (Ernst et al., 2015; Whitten et al., 2011).

The enrichment is typically defined with respect to some model for the bulk abundance of heat-producing elements. The availability of lunar and martian meteorites greatly improves estimates of the bulk abundances of these bodies (Taylor, 2013; Taylor & Wieczorek, 2014). In the case of Mercury, the bulk composition of the silicate part is obtained from a combination of geochemical and geophysical considerations informed by experiments, analysis of the surface composition, and formation and early evolution scenarios (see Nittler et al., 2018, for a recent review). The enrichment of the primary crust depends on a number of physical parameters both extensive – e.g., pressure profile of the body and bulk composition of the magma ocean – and intensive – e.g., density and composition of the last cumulates to solidify. For the secondary crust, which results from the accumulation of melt produced at different times and different locations in the mantle, the enrichment is better defined as a function of local thermodynamic conditions (pressure, temperature, composition, melt fraction) – which, in turn, are a function of the overall evolution of the body.

17.3.1. Primary Crusts

Primary crusts are formed as a result of the late-stage solidification of a magma ocean (Section 17.2). While it is expected that bodies at least as large as Vesta (i.e., with an equivalent diameter larger than about 500 km) go through a magma ocean phase (Elkins-Tanton, 2012), thus possibly producing a primary crust, for bodies larger than Mercury this primary crust is likely overturned and thus, it is not directly observable at present time. The best known, and possibly only certain, example of a primary crust is represented by the lunar anorthositic crust (Wood et al., 1970), which is enriched in HPEs (Taylor & Wieczorek, 2014). In a sense, the lunar primary crust is also an exception, since it represents a flotation crust, created by the upward accumulation of light crystals during the last phases of solidification of the lunar magma ocean. It is generally accepted that also Mercury underwent an initial hot phase characterized by the presence of a global magma ocean (Brown & Elkins-Tanton, 2009). In the case of Mercury, the only mineral that could float and thus originate a lunar-like, gravitationally-stable primordial crust is graphite, a very dark mineral (Vander Kaaden & McCubbin, 2015). Overall, the crust of Mercury as observed today is interpreted as being for the most

part secondary (Denevi et al., 2013), with its oldest units having been emplaced in a period consistent with the timing of the late heavy bombardment (LHB) (Marchi et al., 2013). These findings indicate that any primary crust would be difficult to identify. However, the general dark appearance of the Mercurian surface and the existence of extensive dark units, the so-called low reflectance material (Murchie et al., 2015), may represent the sign of a dark, graphitic primary crust subsequently covered by volcanic material and in turn reworked by the intense period of bombardments typical of LHB scenarios (Ernst et al., 2015; Peplowski et al., 2016). The possible volume of the primary crust depends on the unknown bulk carbon content of Mercury. If the carbon content of Mercury lies anywhere between the carbon-poor silicate portion of the Moon and the carbon-rich CI meteorites, then the thickness of the Mercurian primary crust can be anywhere between 1 cm and 10 km (Vander Kaaden & McCubbin, 2015).

The lunar anorthositic crust and the putative graphite primary crust of Mercury are easy to label as primary crusts, since they result from floatating, chemically well-defined minerals. However, the definition of what constitutes a primary crust is both wider and not necessarily unique. What is commonly accepted is that an initial magma ocean phase characterizes all planetary-sized bodies, and the evolving composition of these solidifying magma oceans results in FeO- and HPE-rich late cumulates. Under the simplifying assumption that no convection operates in the solid mantle while the magma ocean is still present (but see Section 17.2.2), the resulting radial density profile in the solid mantle is gravitationally unstable (Brown & Elkins-Tanton, 2009; Elkins-Tanton et al., 2011). Apart from the light components, as in the case of the Moon and probably Mercury, this primary heavy crust is likely to be overturned, i.e., to sink at larger depths until a gravitationally stable profile is reached. Indeed, crystallization models for the lunar magma ocean predict the formation of a dense ilmenite-rich layer (Elkins-Tanton et al., 2011), which is overlain by the floatation crust (or explicitly, by the *floatating component* of the primary crust). The chemical signature of this layer would make it part of the primary crust. However, its high density and possibly low viscosity would make it sink in the mantle possibly reaching all the way to the core-mantle boundary (Parmentier et al., 2002; Yu et al., 2019). Depending on its geometry, this overturn could explain the asymmetric nature of the lunar secondary crust (Section 17.3.2 below).

The rapid accretion of Mars indicates that it sustained a global magma ocean (Dauphas & Pourmand, 2011). Models for the radial density profiles resulting from the solidification of a Martian magma ocean do not predict the formation of a floatation crust and show a strongly

gravitationally unstable profile, which would likely rapidly overturn through a Rayleigh-Taylor instability (Elkins-Tanton et al., 2003). As shown in Section 17.2, since these heavy components of the primary crusts are rich in HPE, their overturn may segregate part of the heat-sources at the bottom of the mantle, as also proposed – but as of yet lacking observational verification – for the Moon, the Earth, and Mars (Labrosse et al., 2007; Zhang et al., 2013a; Plesa et al., 2014; Yu et al., 2019; Li et al., 2019).

17.3.2. Volume and Time of Emplacement of the Secondary Crust

Contrary to the case of the Earth, where plate tectonics operates, melting activity in one-plate bodies is associated only with decompression melting in mantle upwellings (Baratoux et al., 2013). The melt, if buoyant, contributes to the formation and thickening of the so-called secondary crust through eruptions and/or intrusions. Thus, the volume of the secondary crust as observed today represents the cumulative amount of melt produced in the mantle during the 4.5 Gyr of evolution of the solar system. The thermal state of the mantle largely controls the secondary crustal production (Laneuville et al., 2013; Grott et al., 2013; Padovan et al., 2017), so putting constraints on the temporal evolution of secondary crustal building would indirectly provide insight on the thermal evolution of the mantle. This approach rests on the possibility of dating the various surface units, typically through crater counting (Section 17.4), and of interpreting them in terms of interior processes.

The surface of the Earth is continuously reworked by plate tectonics and erosion, and the dating of geological events gets more difficult with older ages, in particular in the Precambrian era, which ended about 600 Ma (Press & Siever, 1978). Similarly, Venus has a surface younger than about a billion years (Hauck et al., 1998), which is interpreted as being the result of episodic catastrophic overturns (Rolf et al., 2018) or continuous volcanic resurfacing (King, 2018). It is therefore difficult to reconstruct the ancient volcanic history of these two bodies. On the contrary, the geological record of the Moon and Mercury, airless bodies with no plate tectonics, potentially holds the signs of events that occurred during the entire solar system evolution. Mars does not have plate tectonics, unless perhaps for a short time early after its formation (e.g., Nimmo & Stevenson, 2000) (see also Sections 17.2 and 17.5), but early in its evolution its surface has been altered by aeolian, fluvial, glacial, and possibly lacustrine – i.e., exogenic – processes (Craddock & Howard, 2002; Bibring et al., 2006) and the interpretation of its geological record is significantly more complicated than for Mercury and the Moon (Carr, 2006).

As described above, the crust of the Moon is for the most part primary in nature. The dark patches that can be observed with the naked eye on the near side of the full Moon represent the surficial manifestations of magmatic events associated with the relatively minor secondary lunar crust production. Overall they account for only about 0.7% of the volume of the crust (Head & Wilson, 1992). Typically, every surficial – or extrusive – volcanic event is associated with a subsurface reservoir of magma, its intrusive counterpart. The amount of intrusive volcanism is difficult if not impossible to assess remotely, and on Earth, where a lot of data are available, the variability of the intrusive-to-extrusive ratio is large (White et al., 2006). Typically, a value of 10 times the extruded component can be used as a very rough rule of thumb. Accordingly, the crust of the Moon has a secondary component corresponding to about 7% of its volume. This secondary component, as inferred from crater counting and analysis of samples returned during the *Apollo* program, shows that the vast majority of the lunar secondary crust has been emplaced in the first 1.5 billions of years of evolution (e.g., Fig. 18 of Hiesinger et al., 2011).

The secondary crust of the Moon is peculiar in its highly asymmetrical distribution. Almost the entire majority of secondary crustal units are located in the near side, mostly within large impact basins (Hiesinger et al., 2011). The location of the secondary crust coincides with a region of the surface rich in incompatible elements like Th and U (Lawrence et al., 1998; Lawrence et al., 2003), which encompasses the Procellarum and Imbrium basins and is commonly referred to as Procellarum KREEP Terrane (PKT), because of its strong enrichment in potassium (K), rare-earth elements (REE) and phosphorous (P) (Jolliff et al., 2000). Additionally, recent magnetic data obtained by the Lunar Prospector and Kaguya missions (Tsunakawa et al., 2015), show a region of weak crustal magnetization roughly corresponding to the PKT (Wieczorek, 2018). The high crustal temperatures associated with a higher abundance of heat-producing elements in the PKT region could have prevented retention of a magnetic signature (Wieczorek, 2018). The above set of observations have been interpreted as indicating the presence of material enriched in HPE in the crust or below the crust in the PKT region (Laneuville et al., 2013; Laneuville et al., 2018). In addition to being compatible with the measurements listed above, this scenario can explain a number of additional observations, including asymmetric lunar impact basin morphologies (Miljković et al., 2013) and heat flux variations as directly measured at the *Apollo 15* and *Apollo 17* landing sites and as remotely inferred at one location using the Lunar radiometer experiment onboard the Lunar Reconnaissance Orbiter (Langseth et al., 1976; Warren & Rasmussen, 1987; Paige & Siegler, 2016). While a fully satisfactory

explanation for the creation of an enriched layer localized in the near side is currently lacking, several mechanisms have been proposed, both endogenous and exogenous.

Volcanism that is localized on a single lunar hemisphere may be indicative of an early phase of degree-1 convection in the Moon, i.e., convection where buoyant material rises in a single upwelling (Zhong et al., 2000). This scenario may arise if the late dense cumulates resulting from the solidification of the lunar magma ocean and forming beneath the flotation crust would sink to the CMB. For some combination of the rheological properties of the mantle, this material would induce a single mantle upwelling (Zhang et al., 2013a). In addition, part of these heavy cumulates would remain at the CMB up to the present day (Zhang et al., 2017; Zhao et al., 2019), potentially providing a mechanism to explain the presence of partial melt there, as inferred from the *Apollo* seismic data (Weber et al., 2011). As initial conditions these models typically assume a post-overturn scenario, where the heavy late cumulates resulting from the solidification of the lunar magma ocean have already sunk to the CMB. However, as described in Section 17.2.2, the mechanism of the overturn is debated, and accordingly, its role in the asymmetrical nature of the lunar evolution is an open question.

Alternatively, the dichotomy has been ascribed to the effect of an impact. Jutzi and Asphaug (2011) investigated the slow-velocity accretion of a companion moon with a mass about 4% of the lunar mass and a diameter of 1270 km, formed in the same protolunar disk and thus, with a composition similar to the Moon. Such a slow-velocity impact on the current far side would explain the thickening of the far-side lunar crust and the displacement of a residual, KREEP-rich magma ocean in the near side. This scenario, while possible, would require the correct timing of the impact with respect to the magma ocean solidification. Some authors have speculated that the compositional and topographical properties of the lunar near side are compatible with an ancient mega-basin (Cadogan, 1974; Whitaker, 1981). Building on this hypothesis, Zhu et al. (2019) explained the observed crustal dichotomy in thickness and composition as the result of an impact of an object with a diameter of about 750 km on the current near-side on an already solidified Moon. The ejecta distribution would explain the crustal thickness dichotomy, and since the excavated KREEP-rich cumulates located below the preimpact primordial crust would flow back in the resulting giant basin, this model would provide an explanation for the exposure of KREEP-rich material in the near side. However, gravity gradiometry obtained from the GRAIL mission indicates that the subsurface structure in the near side is the result of endogenous magmatic-tectonic structures, likely not compatible with a large impact (Andrews-Hanna

et al., 2014). Furthermore, the composition of the far side crust as predicted with the giant impact scenario does not match the observed composition (Zhu et al., 2019).

Similar to the Moon, the secondary crust of Mars has a striking asymmetry. There is a hemispheric difference of about 5 km in surface elevation between the ancient southern highlands and the younger northern lowlands. This difference is recognized as one of the oldest features of Mars and is reflected in the so-called crustal dichotomy, where, based on gravity and topography data, the crust has an average thickness of about 45 km in the northern lowlands, but is about 25 km thicker under the Southern Hemisphere (Neumann et al., 2004; Wieczorek & Zuber, 2004; Plesa et al., 2016). The origin of this difference is the subject of a vast literature. Several mechanisms have been investigated, including exogenous processes involving a giant impact (Andrews-Hanna, Zuber, & Banerdt, 2008; Marinova et al., 2008) and endogenous ones associated with the formation – as proposed for the Moon – of a hemispherical (i.e., degree-1) upwelling (Roberts & Zhong, 2006; Keller & Tackley, 2009; Šrámek & Zhong, 2012). Additional hypotheses include a hemispherical overturn of a crystallized magma ocean (Elkins-Tanton et al., 2003) as proposed for the Moon (Parmentier et al., 2002), or a combined exogenous-endogenous scenario, with a giant impact triggering a degree-1 convection planform (Golabek et al., 2011; Citron et al., 2018).

Irrespective of the mechanism responsible for the generation of the dichotomy, analysis of Martian meteorites indicates that the crust of Mars is secondary, the bulk of which has been emplaced very early on, likely within 100 Myr of the planet formation (Nimmo & Tanaka, 2005), and certainly no later than the early Noachian about 4.2 Ga (Grott et al., 2013). Based on the estimated volume of extruded volcanic units (Greeley & Schneid, 1991), and using a similar intrusive-to-extrusive ratio as for the Moon above, observations can account for about 7% of the volume of the crust, assuming its average thickness is 62 km (Wieczorek & Zuber, 2004; Plesa et al., 2018). While Mars shows signs of very recent volcanic activity (Hartmann et al., 1999; Werner, 2009), possibly extending to the present day (Neukum et al., 2004), the bulk of the secondary crust has been emplaced during the first two billions of years of evolution (Greeley & Schneid, 1991), and mostly very early on, as testified by the geological record in the Valles Marineris, which shows that Mars underwent voluminous volcanism during its first billion of years (McEwen et al., 1999).

The analysis of the data returned by the spacecraft *MESSENGER*, which orbited Mercury between March 2011 and April 2015, indicates that the surface of the innermost planet likely represents the prototype of a secondary crust, since it is interpreted as being largely the result of volcanic events (Denevi et al., 2013). By dating

the different geological units of the surface of the planet, Marchi et al. (2013) showed that the oldest surficial units have been emplaced between 4.0 and 4.1 Ga. This range of ages corresponds roughly with the period of the LHB, and it has been suggested that corresponding to this time any record of older units would have been erased due to the combined effect of impacts and possibly related volcanism (Fassett et al., 2012; Marchi et al., 2013). However, the observational framework supporting the LHB scenario has been recently put into question (Michael et al., 2018; Morbidelli et al., 2018). Independent of the chosen impactor flux, for which several functional shapes have been proposed (Neukum & Ivanov, 1994; Marchi et al., 2009; Morbidelli et al., 2012), the oldest crust of Mercury is younger than the oldest Lunar crust. Given the secondary nature of the crust, a straightforward explanation is that early on, the hot post-formation mantle produced massive amounts of melt and associated volcanic events that simply kept obliterating older units. However, through melt-induced depletion of heat sources, the mantle cooled (see discussion on the time-dependent H above) and gradually melt-production decreased. Using similar techniques to those of Marchi et al. (2013), Byrne et al. (2016) inferred that the youngest large volcanic provinces date back to 3.5 Ga. These timings are compatible with recent thermal evolution models of the planet (Tosi et al., 2013; Padovan et al., 2017).

Figure 17.3 condenses the present understanding on the composition, origin, and associated volume of the primary and secondary crusts of Mercury, the Moon, and Mars. For Mercury, the secondary crustal volume is based on the central value of Padovan et al. (2015) for the thickness of the crust, 35 ± 18 km. For the thickness of a potential primary crust we use the value of 10 m, based on the possible range between 1 cm and 10 km obtained by Vander Kaaden and McCubbin (2015). The lower end member corresponds to the lower measured lunar carbon content, while the upper-end member corresponds to the carbon content of the carbon-rich CI meteorites (Section 17.3.1). In calculating the volumes, a total silicate thickness of 419 km is assumed, based on the results of Hauck et al. (2013) for the radius of the core and of Perry et al. (2015) for the planetary radius. The thickness of the lunar crust comes from Wiczorek et al. (2013), while the volume of secondary crustal material assumes a total magmatic reservoir that is ten times the volume of the extruded volcanic material as estimated in Head and Wilson (1992). Values for the volumes are based on a lunar radius of 1737 km (Wiczorek et al., 2006) and a core radius of 330 km (Weber et al., 2011). The Martian crustal thickness range comes from Plesa et al. (2018), and volumes are based on a core radius of 1850 km (Plesa et al., 2018) and a planetary radius of 3390 km (Seidelmann et al., 2007). Interestingly,

independent of the particular sources used in creating Figure 17.3, Mercury, the Moon, and Mars, despite their different sizes, thickness of the mantles, and dominant crustal type, have roughly 7–10% of their total silicates contained in the crust.

17.4. IMPACTS

Craters are created from an impactor population, which has a power-law size distribution comprising relatively few very large objects (Strom et al., 2015). These large members are responsible for creating some of the largest impact structures observed on the surface of the terrestrial planets, such as the Caloris basin on Mercury (basin diameter $D_b \sim 1550$ km, Fassett et al., 2012), the South-Pole Aitken basin on the Moon ($D_b \sim 2200$ km, Garrick-Bethell & Zuber, 2009), and the Hellas basin on Mars ($D_b \sim 2070$ km Frey, 2008). Most impacts occur early on, and the cumulative number of impacts occurring on a given surface unit will grow in time, thus potentially providing a way to date the unit based on the statistics of the crater population. Indeed, crater statistics is the most powerful tool to date the surfaces of solid solar system objects (see Fassett, 2016, for a recent review). Comparison of crater statistics for different units of the same object provides relative ages. In the case of the Moon, absolute ages can be obtained through calibration with *Apollo* samples (Stöffler & Ryder, 2001). Then, the scaling of the impactor population to different parts of the solar system provides an indirect way to assess the absolute age of surficial units for planets where only crater statistics is available (Marchi et al., 2009).

Outside of the limited range of impact parameters available in a laboratory setting, the details of impact processes can be simulated using smoothed particle hydrodynamic codes (Monaghan, 1992), shock-physics codes like iSALE¹ (e.g., Wünnemann et al., 2006), or simple scaling laws (Pierazzo et al., 1997). Here, we focus on basin-forming impacts, energetic events that have the potential of interacting with the temperature field of the mantle modifying locally its convective vigor (Elkins-Tanton et al., 2004; Ghods & Arkani-Hamed, 2007; Padovan et al., 2017). These are smaller than planetary-scale events like the Moon-forming impact, but larger than the events that create the smaller classes of impact craters observed on the surfaces of airless rocky bodies (e.g. Moon, Mercury, large asteroids). As a rule of thumb, impacts where the size of the impactor is small with respect to the size of the target (i.e., the planet) and that result in the formation

¹ Access to the code can be obtained from <https://isale-code.github.io/access.html>

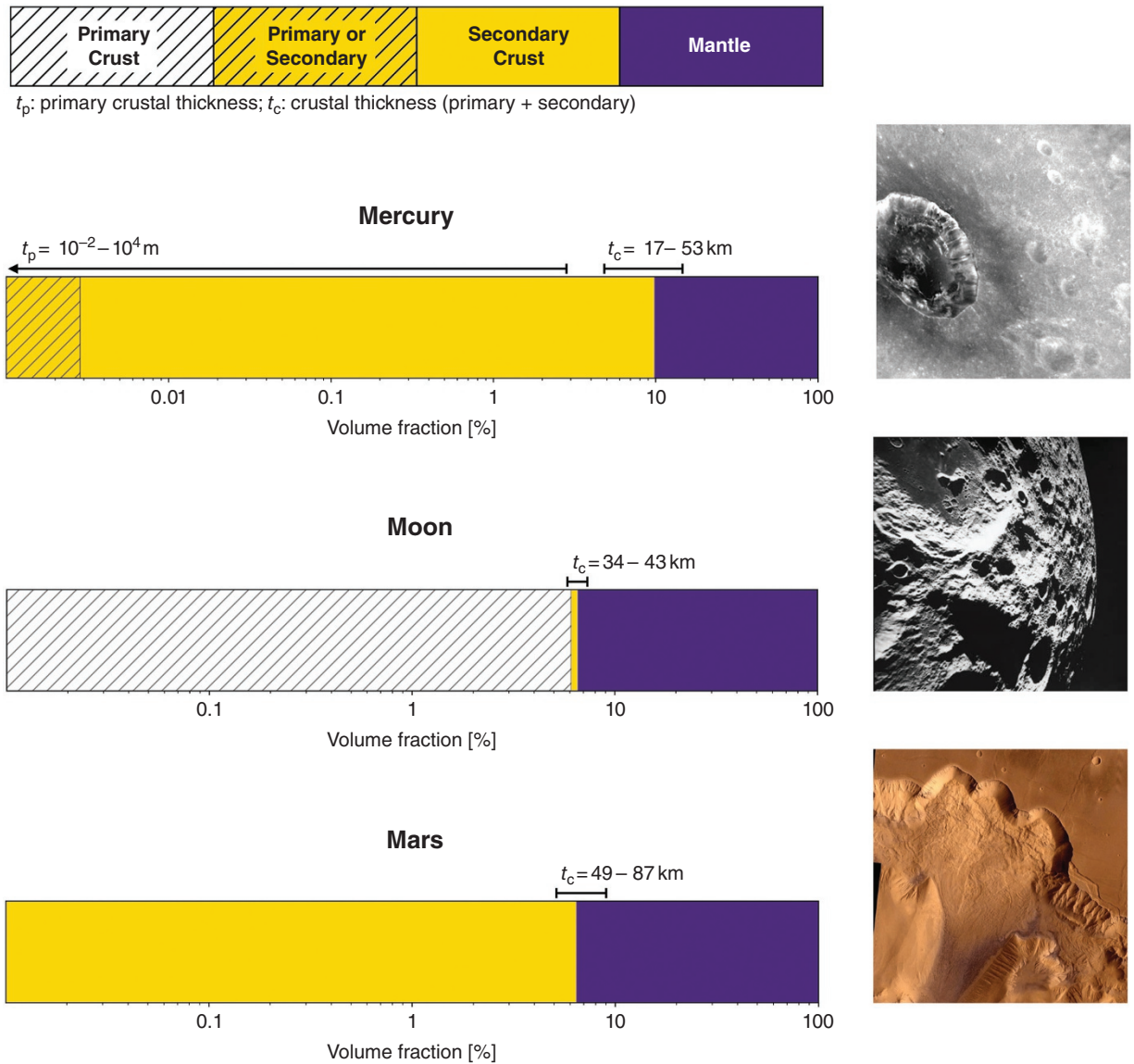


Figure 17.3 Left column: Volumetric composition of the different silicate reservoirs of Mercury, the Moon, and Mars. Colors indicate composition, according to the legend on top. Note that the scale is logarithmic. The black bars indicate the range of values for the volume fractions, with the labels expressing the corresponding range of thicknesses. Sources for the data are described in the text. Right column: example of the surfaces of each body. Mercury: Berkel crater (diameter $D = 21$ km), image obtained by the *MESSENGER* mission. The background represents secondary crust, while the crater is a typical example of exposure of dark material, which has been ascribed to the planet's primary graphite crust. Moon: the crater on the top left is Aitken ($D = 135$ km) on the far side of the Moon, in an image obtained by the *Apollo 17* mission. The crater is infilled with dark volcanic material (i.e., secondary lunar crust). The light-colored surrounding area is the primary anorthositic crust. Mars: Ophir Chasma, a valley connected to Valles Marineris, in an image obtained by the *Viking 1* mission. This region is associated with massive volcanism early in the history of Mars. The large crater in the lower right corner is 30 km wide. Image credits: Mercury: NASA/Johns Hopkins University APL/Carnegie Institution of Washington Image 5770878 (<https://tinyurl.com/yy96rrkr>); Moon: NASA Image AS17-M-0831, hosted on the LPI website (<https://tinyurl.com/y6mhp7p>); Mars: NASA/JPL/USGS Image PIA00425 (<https://tinyurl.com/yxnp1fw>).

of basins (large, multi-ring craters) have the potential of interacting with mantle convection.

The potential effects of impacts on surface magnetization and dynamo action in the core are described in Section 17.5. Here we discuss the connection between impacts and the thermal state of the mantle, with a focus on the potential surface signatures of this interaction. In so doing, we are explicitly making a qualitative distinction between impacts as a dating tool (Fassett, 2016), which is key in deciphering the history of crustal building (Section 17.3.2), and (large) impacts as a potential energy source of mantle dynamics.

17.4.1. Basin Formation

The formation of an impact basin is a relatively fast process taking place on timescales of a few hours, even for the largest basins (e.g., Potter et al., 2012). Schematically, an object hits the surface of a planet at hypervelocity, creating a so-called transient cavity, which then collapses to form a shallower basin (Melosh, 1989, 2011). In this process, shock waves are produced that travel in the interior, whose energy is released as thermal energy (Bjorkman & Holsapple, 1987) that increases the temperature in a volume roughly centered along the vertical axis of the contact point, possibly causing large scale melting events. The most widely used code for the accurate simulation of large impacts, events that cannot be reproduced in a laboratory setting, is the iSALE hydrocode (Wünnemann et al., 2006). Scaling laws aim at condensing in analytical expressions the main effects of impacts as observed in laboratory and numerical experiments. They represent a relatively simple way to describe how the properties of the impactor (size, speed, composition) and of the target (composition, gravity) control a number of physical quantities that are key in the description of the impact process. In this section, the goal is to elucidate the connections of large impacts with the interior dynamics, which occurs through the deposition of the impact shock energy in the subsurface. Accordingly, we focus on the properties of the thermal anomaly that forms in the subsurface as a result of the release of the energy of the shock wave.

The computation of the impact-induced thermal anomaly occurs through the following steps. First, a connection is established between the size of the observed basin and the diameter and velocity of the impactor, according to the following scheme, where each arrow indicates a connection through a scaling law: basin diameter \rightarrow transient cavity diameter \rightarrow diameter and velocity of the impactor. Estimates for the velocity of the impactor are based on statistical models of the impactors population for the body of interest (Le Feuvre & Wicczorek, 2008; Marchi

et al., 2009). The combination of these estimates with the size of the observed basin provides the diameter of the impactor. From the velocity and diameter of the impactor, additional scaling laws provide the distribution of the shock pressure in the subsurface, whose release is responsible for the impact heating, i.e., for the release of energy to the target (e.g., Watters et al., 2009). The following equation highlights the key dependencies in the expression of H_{imp} , the energy release associated to a given impact:

$$H_{\text{imp}} = F(\rho_{\text{P}}, \rho_{\text{T}}, g, D_{\text{P}}, v_i), \quad (17.5)$$

where the gravity g and density ρ_{T} of the target are known. The projectile (i.e., impactor) density ρ_{P} is unknown, while its diameter D_{P} and impact velocity v_i are related to the basin diameter as described above. To compute H_{imp} , a number of assumptions are usually made. First, despite impacts occurs preferentially at 45° from the vertical (Le Feuvre & Wicczorek, 2008), only the vertical component of the velocity is considered, since it accounts for the majority of the impact-related effects (Shoemaker, 1962, 1983). Second, it is often assumed that the impactor has the same composition of the target (i.e., rocky), which can be justified on the basis that objects from the asteroid belt are the main current contributors to the Earth impactors population (e.g., Morbidelli et al., 2002). Both assumptions can be relaxed, and studies exist on the effects of composition and obliquity on the impact processes (Elbeshhausen & Wünnemann, 2011; Ruedas & Breuer, 2018). A recent and clear description of the computation of the energy release for a given impact can be found in, e.g., Roberts and Arkani-Hamed (2017), which accounts for the crater scaling laws (Schmidt & Housen, 1987; Melosh, 1989; Holsapple, 1993), the shock-pressure scaling of Pierazzo et al. (1997), and the foundering shock-heating method of Watters et al. (2009). Care should be taken in using scaling laws appropriate for the problem at hand. For example, the pressure scaling of Pierazzo et al. (1997) should only be used for impactor velocities $\gtrsim 10$ km/s. The scalings of Monteux et al. (2015), based on iSALE-2D simulations, cover the slow impactor range ($v_i \gtrsim 4$ km/s).

Given the very different timescales of basin formation processes (few hours) and mantle convection (millions of years), the use of scaling laws represented, until recently, the only viable approach to investigate the interplay of these two processes (Roberts & Barnouin, 2012; Roberts & Arkani-Hamed, 2017). However, the increase in the computational power available allows one to use outputs of the short timescales simulations (such as those of iSALE) within the long timescales of convection simulations (Rolf et al., 2016; Golabek et al., 2018).

17.4.2. Impact-Induced Melting

There are three types of melting processes that can be induced by a large impact. First, the release of the impact shock energy increases the temperature of a volume of the target around the impact location, possibly melting it completely (Roberts & Barnouin, 2012). This process results in what is commonly referred to in the literature as a melt pond or melt sheet (Cassanelli & Head, 2016). Second, during the formation of a basin a transient crater is excavated, whose maximum depth is larger than the depth of the final basin (Melosh, 1989). For very large events this transient crater can reach depths of tens of kilometers, thus locally depressing the solidus and potentially inducing massive in-situ decompression melting. This possibility was initially suggested by Ronca (1966) – the seminal work on the connection of impacts and volcanism – and was subsequently discussed several times in relation to the potential connection of impact events with the generation of large igneous provinces (Rogers, 1982; Rampino, 1987; Elkins-Tanton & Hager, 2005). Third, the positive thermal anomaly resulting from a large impact event locally warps the isotherms producing dynamical currents in the mantle under the newly formed basin, which could lead to additional post-impact convective decompression melting (Grieve, 1980).

The solidification of the melt sheet could occur through equilibrium crystallization, which preserves the bulk composition of the melt, or through igneous differentiation, which would induce a compositional gradient in the solidified melt sheet (Cassanelli & Head, 2016) (see Section 17.2). According to the model of Cassanelli and Head (2016), the discrimination between the two possibilities is controlled by the size of the crystals that form in the cooling pond, while the bulk size of the melt sheet plays a minor influence. However, the crystal size is difficult to determine a priori. On the Moon, there are indications for igneous differentiation in the Orientale basin (Spudis et al., 2014) and in the South-Pole Aitken basin (Vaughan & Head, 2014).

The process of in-situ decompression melting is predicated on the assumption that in the short timescales of transient crater formation rocks at depth undergo melting due to the rapid removal of lithostatic pressure. However, Ivanov and Melosh (2003) argue that a more appropriate estimate is based on the profile of the final crater, which, being shallower than the transient crater, would induce significantly less melting. Independent of the feasibility of the in-situ decompression melting process, it is important to note that both the solidification of the melt sheet and the eruption of the in-situ decompressed melt would occur on geologically short timescales (Reese & Solomtov, 2006; Elkins-Tanton et al., 2004; Elkins-Tanton & Hager, 2005). Thus, dating of units related to the first

two processes would coincide with the age of the basin itself.

17.4.3. Impact-Related Effects on Global Mantle Dynamics

The observations that most basaltic units on the near side of the Moon are located within large impact basins and have been emplaced from several tens to up to hundreds of millions of years after the basins formation, hinted at a possible causal connection between impacts and subsequent volcanism. This process would result from the interaction of the impact-induced thermal anomaly with the mantle temperature field, the process referred to above as post-impact convective decompression melting. While a qualitative assessment of post-impact convective decompression melting has been published early on (Grieve, 1980), more quantitative work has appeared only in the last 20 years.

Reese et al. (2002, 2004) showed that a thermal anomaly induced by a very ancient impact event can explain the long-term volcanism observed in the Tharsis province on Mars (Hartmann et al., 1999; Werner, 2009). However, conventional thermal evolution models do not require a large impact to justify the long-term volcanism on Tharsis, and are also compatible with several additional constraints (Plesa et al., 2018). More recently, Roberts and Arkani-Hamed (2012, 2017) investigated the role of large impacts on the dynamics of the mantle and energetics of the core of Mars. While large impacts can focus upwellings under the impact locations (Roberts & Arkani-Hamed, 2012), a confirmation of the results of Reese et al. (2004), and can temporarily frustrate dynamo action in the core, the duration of a Martian dynamo is controlled by the rheological properties of the lower mantle (Roberts & Arkani-Hamed, 2017). Similar models for Mercury, where the largest confirmed impact basin is the relatively small Caloris basin, with a diameter of about 1500 km (Fassett et al., 2009), show that the effects on the energetics of the core are minor, while inducing a modification of the convection planform under the basin location (Roberts & Barnouin, 2012). Rolf et al. (2016) investigated the effects of the lunar impact history on the long-term evolution of the body, concluding that the full sequence of large impacts may influence the present-day heat flux and the initial expansion of the Moon, two parameters that could be measured and thus, provide additional constraint for thermal evolution models (Section 17.6). However, Miljković et al. (2013) proved that the different morphologies of the lunar impact basins between the near-side and the far-side can be explained by the asymmetric distribution of heat producing elements in the interior before the basins formed (Laneuville et al., 2013; Laneuville et al., 2018). Accordingly, it seems

plausible, at least for the Moon, that while large impacts may induce effects that are still measurable today (Rolf et al., 2016; Ruedas & Breuer, 2019), it is the initial distribution of heat-producing elements that largely controls the overall evolution.

17.4.4. Local Signatures of Impact-Related Effects

The studies described in the previous section all dealt with the potential global consequences of one or more large impacts. However, the creation of an impact basin is by definition a local process, which ejects or melts pre-existing crust (Potter et al., 2012), thus modifying the local surficial composition and topography. Often, large basins on the Moon and Mercury are associated with the presence of positive gravity anomalies (or mascons, for mass concentrations) and volcanic infillings, which on the Moon are called *maria* (Melosh et al., 2013; James et al., 2015).

Elkins-Tanton et al. (2004) investigated the potential causal connection of impact processes with subsequent localized enhanced volcanism. They developed a model for the magmatic effects of large impacts, which takes into account the in-situ decompression melting and the post-impact convective decompression melting (see Section 17.4.2 for definitions). By adjusting the pre-impact lunar mantle temperature profile, Elkins-Tanton et al. (2004) were able to reproduce the source depth and volume of the maria. However, it was difficult to match the interval observed between the formation of the basin and the later emplacement of the volcanic material. The authors recognize that a potential shortcoming of the model lies in their assumption that the mantle, before an impact, is not convecting. Accordingly, any post-impact convective decompression melting is only due to the limited convection activity induced by the warping of the isotherms – and related horizontal temperature gradient – induced by the impact itself.

Using thermal evolution models that include two-phase flow, Ghods and Arkani-Hamed (2007) investigated convective long-term magmatic activity induced by lunar impact basins using as background temperature field a set of models evolved for 500 Myr, when the largest impacts are assumed to occur. This model is able to reproduce the timing of volcanic activity within Imbrium-sized basins and, for certain combination of parameters, the observed volume of volcanic material. As for the case of Elkins-Tanton et al. (2004), the model predicts a large amount of volcanic activity within the large SPA basin, which is not observed.

Padovan et al. (2017) investigated the magmatic effects of the formation of large impact basins on Mercury using as background temperature and velocity field a reference model selected from a large suite of 2D dynamical models.

The reference model was selected based on its compatibility with the observed thickness of the crust (as inferred by geoid-to-topography ratios, Padovan et al., 2015), the duration of volcanic activity (as inferred by crater statistics, Byrne et al., 2016), and the depth of the lithospheric thickness at two different epochs (as inferred by petrologic experiments, Namur et al., 2016). Figure 17.4 illustrates how the formation of a Caloris-sized basin produces a large thermal anomaly in the mantle, which locally alters the magmatic activity for a geologically long timescale. By tracking the amount of melt produced under a basin, Padovan et al. (2017) were able to reproduce the volume and time of emplacement of the volcanic materials within the Caloris and Rembrandt basins on Mercury. This result critically depends on the thermal state of the mantle at the time of the basin formation, thus indicating how basin-specific datasets (namely, volume and time of emplacement of volcanic material) provide information on the global evolution of the body.

17.5. MANTLE COOLING AND MAGNETIC FIELD GENERATION

Besides the Earth, among the solid planets and satellites of the solar system only Mercury and Ganymede possess today a self-sustained magnetic field. In addition, the surfaces of Mercury, the Moon, and Mars exhibit a remnant magnetization due to the presence of magnetic minerals in their crust and lithosphere. On the one hand, an active magnetic field requires organized, large-scale motion of an electrically conducting fluid, generally thought to be the liquid core. On the other hand, a remnant magnetization, detected via remote sensing or measured by direct sample analysis, indicates that a dynamo was active in the past so that the accompanying magnetic field left its imprint in surface and shallow rocks when these formed. The possibility to generate a magnetic dynamo is tightly related to the way mantle convection operates by cooling the core (Stevenson et al., 1983). Therefore, the existence of an internally-generated magnetic field, at present or in the past, can be used as an indicator of convection and cooling of the mantle and as a constraint for its thermal evolution.

Ferromagnetic minerals present in crustal rocks acquire a so-called thermoremanent magnetization (TRM) if cooled from above their Curie temperature (T_C) in the presence of an ambient magnetic field. Melts that erupt on a planetary surface or are intruded at depth typically have temperatures largely in excess of T_C and, in the presence of a background magnetic field, acquire a strong TRM upon cooling below T_C . If the age of the magnetized rocks is also known – from radiometric techniques or from dating of surface units – it is possible to infer the

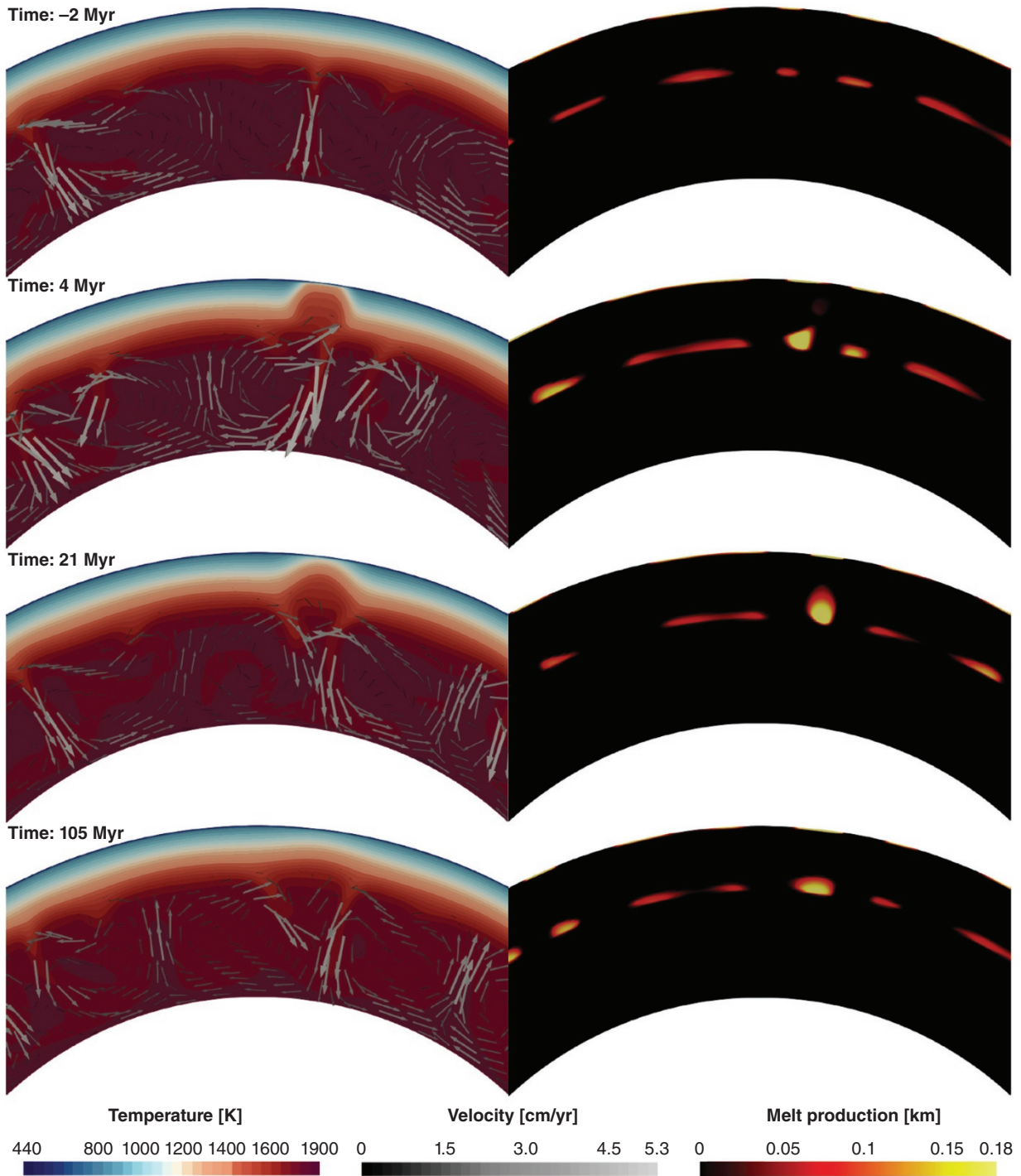


Figure 17.4 Formation of a Caloris-sized basin on Mercury. Each panel indicates the timing with respect to the basin-forming impact. Left column: Temporal evolution of the temperature field (background) and of the magnitude of the velocity field (arrows). Right column: temporal evolution of the melt production, which is expressed in equivalent crustal thickness. The thermal anomaly warps the isotherms and convective currents, which generate melt, develop in the region close to the impact, but with a certain delay with respect to the impact event. Redrawn after Padovan et al. (2017).

lifetime of an ancient magnetic field and place constraints on the thermal history of the body.

The generation of a planetary-scale magnetic field is possible in the presence of a large volume of electrically conducting fluid whose motion is driven by an energy source – thermal, compositional, and/or mechanical – and structurally organized through rotation, which provides the positive feedback necessary for the field to be self-sustained (Olson, 2008). Although promising advances in theory and experiments indicate that core motion and turbulence can be excited by periodic forcing induced by tides, precession, and libration (Le Bars, 2016), buoyancy-driven flows of thermal and/or chemical origin provide today the standard model of core convection and dynamo action (see, e.g., the review by Breuer et al., 2010).

Thermal and compositional convection in a liquid core are driven by mantle cooling. From a global-scale perspective, thermal convection requires that the average heat flux at the base of the mantle (F_{CMB}) exceeds the heat flux conducted along the adiabat of the convective core (F_{ad}), i.e.,

$$F_{\text{CMB}} = k_m \frac{dT_{\text{CMB}}}{dr} \geq F_{\text{ad}} = k_c \frac{\alpha_c g_c T_{\text{CMB}}}{c_c}, \quad (17.6)$$

where r is the radial coordinate, k_m and k_c the thermal conductivities of the mantle and core, α_c the coefficient of thermal expansion of the liquid core, g_c the gravity acceleration at the CMB, T_{CMB} the temperature at the CMB, and c_c the core specific heat capacity. A large temperature gradient at the base of the mantle helps satisfying this condition. On Earth, the subduction of tectonic plates favors cooling of the interior; it leads to a large temperature difference between the mantle and core and in turn to a high heat flux at the base of the mantle, which facilitates core convection and cooling over Earth’s history (e.g., Nakagawa & Tackley, 2015). In contrast, on stagnant lid bodies, the interior is cooled less efficiently; the mantle tends to remain hotter and the temperature gradient at the CMB smaller, with the consequence that driving thermal convection in the core is generally possible only during the early stages of evolution if the process of core formation left the core largely superheated with respect to the mantle (e.g., Breuer & Spohn, 2003; Williams & Nimmo, 2004) and/or upon the first mantle overturn corresponding to onset of thermal (and possibly compositional) mantle convection (Elkins-Tanton et al., 2005; Plesa et al., 2014). In addition, the presence of heat-producing elements such as K, as well as the release of latent heat upon core freezing (see below) can also contribute to drive thermal convection in the core.

For compositional convection to occur, the core must be (1) composed of a mixture of Fe and one or more light alloying elements – S being the best-studied candidate –

and (2) cooled sufficiently to start local freezing. The presence of light elements reduces the density of the core alloy and its melting temperature with respect to those of a core with a pure Fe composition.

Let us consider a standard model of freezing of a Fe-S core. If the pressure slope of the core melting temperature is larger than that of the core adiabat as in the case of the Earth, upon cooling of a fully liquid core, the temperature drops below the liquidus first at the center of the planet, causing the core to freeze from the bottom up in a similar way as a magma ocean would freeze (Figure 17.1a). As cooling and crystallization continue, the liquid outer core becomes more and more depleted in Fe and enriched in S. Atop of the solidified core, a sulphur-rich layer forms. Being lighter than the overlying fluid, this layer buoyantly rises driving compositional convection that tends to homogenize the remaining fluid and can potentially power a dynamo.

In the framework of the Fe-S system, a different crystallization scenario is also possible. Melting experiments indicate that at pressures smaller than ~ 14 GPa – relevant for the cores of Mercury, the Moon, and Mars – the pressure slope of the core melting temperature is negative (Chen et al., 2008; Buono & Walker, 2011). As a consequence, the adiabatic temperature of a cooling core would first drop below the liquidus at the CMB rather than at the center. Fe crystals would then form at the CMB and precipitate, generating an “iron-snow” (see e.g., Breuer et al., 2015, for a review). Since the melting temperature of an Fe-S liquid is lower than that of pure Fe, newly formed Fe crystals would rapidly remelt, enriching the remaining fluid in Fe. Dense, Fe-rich fluid atop lighter Fe-FeS fluid creates a gravitationally unstable configuration that triggers compositional convection and possibly dynamo action (e.g., Rückriemen et al., 2018).

17.5.1. Mercury’s Present-Day and Early Magnetic Field

The current knowledge of Mercury’s magnetic field is largely the result of more than four years spent by the *MESSENGER* spacecraft orbiting the planet (see Johnson et al., 2018, for a recent review). The field is weak, axisymmetric, dipolar, and characterized by a large quadrupolar component corresponding to a northward offset of the magnetic equator with respect to the geographic equator of about 20% of the planetary radius (Anderson et al., 2012). Taken together, these features pose a significant challenge for numerical dynamo models (Wicht & Heyner, 2014). On the one hand, standard models of core flow driven by compositional convection associated with an Earth-like growth of the inner core can produce under certain conditions a weak magnetic field, but not other key characteristics such as the small amplitude of harmonic components greater than 2 and the large

northward offset of the dipole (Heimpel et al., 2005; Stanley et al., 2005; Takahashi & Matsushima, 2006). On the other hand, models involving a stably stratified (i.e., non-convecting) layer at the top of the liquid core, with convection and dynamo action taking place beneath it, successfully predict a low-amplitude field with large dipolar and quadrupolar components (Christensen, 2006; Christensen & Wicht, 2008; Takahashi et al., 2019).

Core flow driven by a laterally variable heat flux extracted at the base of the mantle has been identified as a potentially important ingredient to induce a stable dipolar field with a large quadrupolar component (Cao et al., 2014; Tian et al., 2015). Because of its 3:2 spin-orbit resonance, Mercury experiences an uneven insolation that results in large-scale differences of its surface temperature with cold poles at 0° and 180° latitude, and equatorial hot and warm poles at 0° and 180° and $\pm 90^\circ$ longitude, respectively. Such pattern diffuses through the mantle leading to a high CMB heat flux at the poles (where the mantle is cooler) and a low heat flux in the equatorial regions (where the mantle is hotter) (Tosi et al., 2015). Cao et al. (2014), however, found that the characteristics of Mercury's magnetic field are best reproduced when assuming the highest heat flux to be at the equator. Although such distribution could be important to constrain the planform of mantle convection, no obvious mechanism seems to be able to generate it and it is at odds with the heat flow pattern expected on the base of the surface temperature. The same holds for the degree-2 pattern postulated by Tian et al. (2015). The authors obtained a Mercury-like magnetic field assuming a high heat flux in the Northern Hemisphere, which they posited to be a remnant of the mantle activity that produced the northern volcanic plains 3.7–3.8 Ga (see Section 17.3). However, no mechanism has so far been proposed to generate hemispherical volcanism on Mercury and, at any rate, maintaining the required heat flux throughout Mercury's evolution seems unlikely. Overall, a conclusive dynamo theory for Mercury and its link to the cooling mantle are yet to be established.

A low-altitude observation campaign carried out between 2014 and 2015 during the final phase of the mission, allowed *MESSENGER* to probe small-scale, low-amplitude magnetic fields of crustal origin. Johnson et al. (2015) identified a field with a peak intensity of about 20 nT in the Suisei Planitia region, consistent with the TRM of the underlying crust (Figure 17.5a). The analyzed region encompasses different geological units and, in particular, smooth volcanic plains emplaced between 3.9 and 3.7 Ga. Subsequent analyses revealed crustal magnetization associated with the Caloris and circum-Caloris region, which is of similar age (Hood, 2016). Overall, these observations indicate that a dynamo-generated field, most likely with a strength between that of the

present-day field and up to a factor hundred higher (i.e., similar to the Earth's) was active on Mercury at least until 3.7 Ga (Johnson et al., 2018). Models of the interior evolution of Mercury need thus to be compatible with an ancient dynamo active around 3.7 Ga as well as with the present-day one.

Whether or not a dynamo was active continuously throughout the planet's history is unknown and represents a major source of uncertainty. Thermal evolution models of the interior of Mercury predict an initial phase of efficient crust production where the mantle heats up because of radiogenic heating (e.g., Tosi et al., 2013; Padovan et al., 2017; Hauck et al., 2018). During this phase, the temperature difference between the mantle and core decreases and so does the heat flux at the CMB, which rapidly drops below the critical adiabatic value. A sub-adiabatic heat flux at the CMB – a common feature throughout most of the evolution of one-plate bodies – causes the top of the liquid core to become thermally stratified and suggests that thermal convection driven by mantle cooling alone cannot be responsible for maintaining a dynamo over long time spans.

As for the cores of the other terrestrial planets, the composition of Mercury's core is not well known. Dumberry and Rivoldini (2015) showed that under the assumption of a Fe-S composition, a present-day magnetic field together with geodetic constraints on Mercury's moment of inertia and rotation state can be best accounted for if the inner core is relatively small (≤ 650 km) and operates in the Fe-snow crystallization regime. However, a Fe-Si composition is thought to be more relevant for Mercury than a Fe-S one (Knibbe & van Westrenen, 2018). The low FeO content of the surface (Nittler et al., 2011) hints at reducing conditions for the mantle (Zolotov et al., 2013), which, during planet formation and core segregation, may have favored the fractionation of Si rather than S in the core (e.g., Malavergne et al., 2010). In a crystallizing Fe-Si core, the amount of Si fractionating between solid and liquid is small (Kuwayama & Hirose, 2004). Upon freezing, negligible compositional buoyancy is generated, which thus cannot drive core convection and dynamo action. In contrast to previous efforts largely based on the assumption of a Fe-S composition (Grott et al., 2011; Tosi et al., 2013; Dumberry & Rivoldini, 2015), Knibbe and van Westrenen (2018) developed a model of Mercury's interior evolution including the crystallization of a Fe-Si core and, importantly, the self-consistent formation of a thermally-stratified layer at the top of the liquid core caused by the expected drop of the mantle heat flux at the CMB in the early evolution. The authors showed that under these circumstances, core convection and an accompanying magnetic field can be powered by the release of latent heat (higher for a Fe-Si core than for a Fe-S one) within a thin liquid shell located

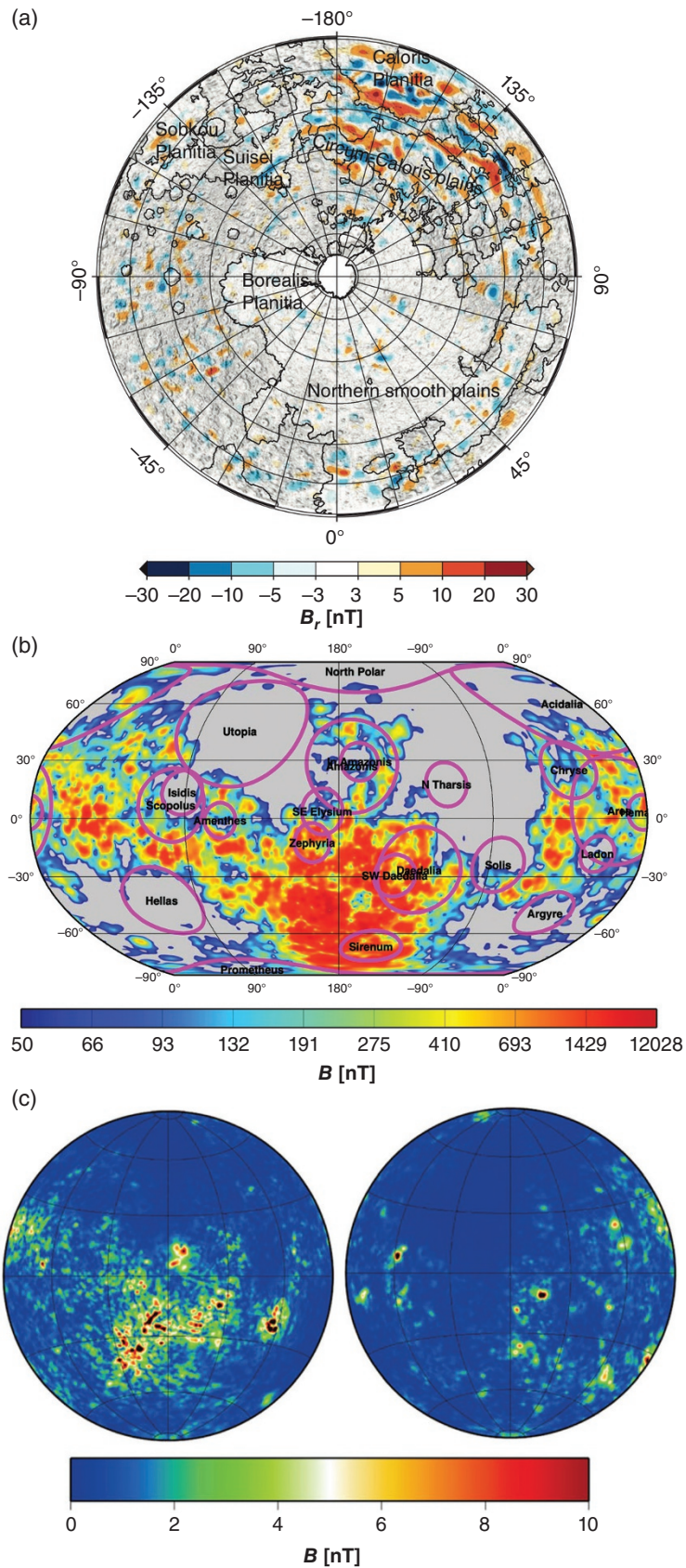


Figure 17.5 (a) Map of the radial component of Mercury's magnetic field at 30 km altitude based on a model of lithospheric magnetization. (b) Total intensity of the lithospheric magnetic field of Mars evaluated at the mean planetary radius of 3393.5 km. Thick purple circles indicate major impact basins. (c) Total intensity of the lithospheric magnetic field of the lunar nearside (left) and farside (right) at 30 km altitude. Source: (a) Johnson et al. (2018), Figure 5.19; (b) Morschuser (2016), Figure 10.8; (c) Tsunakawa et al. (2015), Figure 2.

between a liquid, but thermally-stratified, upper core, and a growing solid inner core. In agreement with the evidence of remnant crustal magnetization (Johnson et al., 2015), the model of Knibbe and van Westrenen (2018) also predicts an early onset of magnetic field generation, which is expected to continue until present due to the slow growth of the inner core.

17.5.2. Mars's Early Magnetic Field

At present, Mars does not possess a global-scale magnetic field of internal origin, but exhibits a strong, small-scale crustal magnetization largely associated with the old, heavily cratered southern highlands (Acuna et al., 1999) (Figure 17.5b). Therefore, a dynamo-generated field must have existed in the past. The lack of significant magnetization within large impact basins can be used to infer the time at which the Martian dynamo stopped operating. Impacts can reset the surface age as well as surface and crust magnetization over an area roughly corresponding to the size of the resulting crater (e.g., Mohit & Arkani-Hamed, 2004). The age of weakly or non-magnetized basins thus provides an upper bound on the age of the dynamo and in turn a constraint for the thermal evolution of the interior. Analyses of the distribution of magnetization (or the lack thereof) of large basins, together with the corresponding ages, indicate that a dynamo stopped being active on Mars before 4.0 – 4.1 Ga (e.g., Acuna et al., 1999; Lillis et al., 2008, 2013).

Most models of the thermal evolution of Mars's interior, which can satisfy the above requirement of an early dynamo, consider this to be of thermal origin, i.e., powered by thermal convection in the core driven by a super-adiabatic CMB heat flux (e.g., Schubert & Spohn, 1990; Hauck & Phillips, 2002; Breuer & Spohn, 2003; Williams & Nimmo, 2004; Morschhauser et al., 2011; Samuel et al., 2019), although more speculative hypotheses such as that of a tidally driven dynamo also exist (Arkani-Hamed, 2009). The required heat flux in excess of the core adiabatic gradient, as shown in Equation (17.6), is easily obtained during the early evolution – for Mars as well as for other bodies – by simply considering the core to be initially superheated with respect to the mantle, an expected outcome of core segregation (Solomon, 1979). This simple scenario is particularly plausible for Mars, which accreted and differentiated within the first few million years of the solar system (e.g., Nimmo & Kleine, 2007; Dauphas & Pourmand, 2011), a compressed timescale that likely prevented the interior from achieving thermal equilibration and favored instead a large temperature difference between core and mantle.

Building on an early hypothesis of Sleep (1994), Nimmo and Stevenson (2000) argued that a strong heat flux at the

CMB may have also been caused by cooling of the core due to plate tectonics operating during the first ~500 Myr of Mars's history and followed by a stagnant-lid regime that persisted until present. The reported discovery from Mars Global Surveyor data of alternating magnetic lineations in the Southern Hemisphere resembling those that characterize spreading oceanic ridges on Earth (Connerney et al., 2005) provided some observational ground to the hypothesis of early plate tectonics. However, the efficient mantle cooling initially caused by sinking plates tends to delay the subsequent production of crust once the stagnant lid regime is established because the sub-lithospheric mantle needs a relatively long time (1–2 Gyr) to heat up and produce partial melt (Breuer & Spohn, 2003). A delayed crust production is at odds with the evidence that volcanism and crust production on Mars were concentrated in the Noachian period (about 4.5–3.7 Ga) and declined since its end (see Section 17.3), thus making the plate tectonics hypothesis somewhat problematic.

While the generation of a thermal dynamo necessarily requires a sufficiently high CMB heat flux, its cessation may also be the result of large impacts (Roberts et al., 2009; Roberts & Arkani-Hamed, 2012, 2017; Monteux et al., 2015). The release of shock-pressure associated with impacts locally raises the mantle temperature and promotes the formation of upwellings beneath the impact region (see Section 17.4). As a consequence, the average heat flux at the base of the mantle tends to decrease. Several giant impacts likely occurred on Mars within a narrow time window (~100 Myr), around the time at which Mars' global magnetic field disappeared (Frey, 2008; Frey & Mannoia, 2013). Simulations of mantle convection including the (cumulative) thermal effects of impacts have shown that for events generating basins larger than 2500 km, the accompanying decrease of the CMB heat flux can be sufficient to stop the dynamo (Roberts & Arkani-Hamed, 2012). However, whether the dynamo is halted only temporarily or permanently, ultimately depends on the thermal state of the mantle preceding the impact as well as on its viscosity and thermal conductivity (Roberts & Arkani-Hamed, 2012, 2017), thus making it difficult to robustly evaluate this hypothesis.

17.5.3. The Long-Lived Lunar Magnetic Field

Like Mars, the Moon lacks a present-day magnetic field, but it has been known since the *Apollo* era that lunar rocks and crust are magnetized (see, e.g., Fuller & Cisowski, 1987). Laboratory analyses of numerous *Apollo* samples show evidence of a paleomagnetic field from 4.25 Ga until possibly as recently as 200 Ma (see Weiss & Tikoo, 2014, for a review). However, the inferred field intensity varies widely among samples of different ages.

Until 3.56 Ga, samples show a mean paleointensity of several tens of μT (e.g., Garrick-Bethell et al., 2009; Shea et al., 2012; Suavet et al., 2013). The intensity declines abruptly by about one order of magnitude around 3.2–3.3 Ga and remains at the level of few μT for younger samples. It has been recognized that due to the limited accuracy associated with the retrieval of the TRM of weakly magnetized samples, the low intensities inferred for samples younger than 3.3 Ga are actually compatible with a vanishingly small field (Tikoo et al., 2014; Buz et al., 2015). However, the recent measurements by Tikoo et al. (2017) appear sufficiently robust to indicate that a weak field of 5 μT was indeed present at least 2.5 Ga, more likely around 1 Ga, firmly extending the lifetime of the lunar dynamo by about 1.0–2.5 billion years (based on the previous idea that 3.56 Ga was the youngest robust age of the dynamo). The actual time at which the dynamo ceased to operate remains unclear.

Accounting for a long-lived magnetic field of widely variable intensity poses a severe challenge for dynamo models. No single mechanism is able to account for an early, intense, and relatively short-lived dynamo between 4.25 and 3.56 Ga and a weak, long-lived one operating until (at least) 2.5 Ga and possibly longer. Several authors studied the conditions required to generate a magnetic dynamo on the Moon in the framework of coupled models of core–mantle evolution (e.g., Konrad & Spohn, 1997; Stegman et al., 2003; Evans et al., 2014; Laneuville et al., 2014; Scheinberg et al., 2015; Evans et al., 2018). A simple thermal dynamo induced by the cooling of a superheated core is generally possible only during the first few hundred million years of evolution for a chemically homogeneous mantle (e.g., Konrad & Spohn, 1997; Laneuville et al., 2014). A heat flux at the base of the mantle in excess of the core adiabatic heat flux can be maintained for a much longer time, even up to 2.5 Ga, in the presence of a compositionally-stratified mantle following the overturn of a crystallized magma ocean, particularly for a hydrous lower mantle where, upon overturn, water, behaving as incompatible, is sequestered within the deepest cumulates (Evans et al., 2014) (see Section 17.2). In addition to thermal buoyancy, the compositional buoyancy associated with the release of S upon core freezing (S is so far the only light alloying element considered in detail) easily extends the dynamo lifetime to billions of years (Laneuville et al., 2014; Scheinberg et al., 2015). A dynamo powered by core crystallization could even persist until present day unless a change in the regime of core crystallization from bottom-up to top-down takes place due to the progressive increase of S in the outer core (Laneuville et al., 2014; Rückriemen et al., 2018).

Overall, these models show that the generation of a long-lived lunar dynamo can be explained in terms of the well-known mechanisms of thermal and

compositional buoyancy in the core induced by convective mantle cooling. However, accounting for the inferred intensity of the resulting magnetic field – both for the early and the late dynamo – is much more difficult. This is usually computed on the base of scaling laws derived from numerical simulations that express the intensity of a dynamo-generated magnetic field at a planetary surface in terms of, among other parameters, the heat flux at the CMB (Christensen, 2010). As discussed by Evans et al. (2018), in principle, thermo-compositional convection in the core could power until a recent past a weak field of $\leq 1.9 \mu\text{T}$, not exactly as high as the 5 μT inferred by Tikoo et al. (2017). However, it cannot provide enough energy to generate a magnetic field of tens of μT until 3.56 Ga, even under the most optimistic assumptions on poorly known parameters. Nonconvective dynamos generated via mechanical stirring of the liquid core induced by precession of the Moon's spin axis (Dwyer et al., 2011) or other instabilities associated with precession, librations, or tides that could be triggered by large impacts (Le Bars et al., 2011) also fall short by about one order of magnitude in predicting the surface intensity of the lunar magnetic field. A higher intensity of up to a few tens of μT and hence close to the observed values, as well as a long-lived field could be accounted for by a *silicate dynamo* (Ziegler & Stegman, 2013) generated in a basal magma ocean atop the lunar core (Scheinberg et al., 2018). As discussed in Section 17.2, upon overturn of a crystallized magma ocean, dense cumulates enriched in incompatible HPEs may sink at the base of the mantle (e.g., Yu et al., 2019) and heat up (Stegman et al., 2003; Zhang et al., 2013a). If their density and heat sources content are sufficiently large, a basal magma ocean can form (see e.g., Plesa et al., 2014, for a description of this process in the context of early Mars). Provided that the poorly known, high-temperature electrical conductivity of the overturned silicates is sufficiently large, Scheinberg et al. (2018) showed that the surface intensity of a magnetic field generated in a thick basal magma ocean could be marginally compatible with the observations, largely because the surface strength of the magnetic field is positively affected by the vicinity and large size of the convective region.

In synthesis, observational constraints provide a relatively clear picture of the evolution of the lunar magnetic field. Its interpretation, however, is nontrivial. No single mechanism of magnetic field generation is able to account for both the amplitude and the timing of the dynamo. A combination of different mechanisms such as thermal convection (in the core or in a magma ocean), compositional convection, or mechanically driven instabilities acting at different times and possibly in concert could be key to explain the history of the lunar magnetic field in its entirety.

17.6. ADDITIONAL SURFICIAL MANIFESTATION

We devote this section to a brief discussion of additional constraints that can be placed on the interior evolution of stagnant-lid bodies. These constraints are both heavily model-dependent and their bearing on the interior evolution is somewhat indirect. They include planetary contraction and expansion, surface heat flux, and thickness of the elastic lithosphere.

17.6.1. Global Contraction and Expansion

The thermal evolution of terrestrial bodies can be manifest in the geological record through extensional and contractional features such as grabens and thrust faults, which, if interpreted as a global response to the changes in the overall thermal state of the body, testify to periods of warming and cooling, respectively. In fact, the radius change ΔR of a planet due to thermal expansion and contraction can be expressed as (Solomon & Chaiken, 1976):

$$\Delta R = \frac{1}{R_p^2} \int_0^{R_p} \alpha \Delta T(r) r^2 dr, \quad (17.7)$$

where R_p is the planet radius, r the radial coordinate, α the coefficient of thermal expansion, and $\Delta T(r)$ the laterally averaged temperature variation over a given time interval. In addition, internal differentiation can also contribute to global variations in the planetary radius. On the one hand, melting associated with the production of secondary crust can cause radial expansion because of the lower density of the residual mantle material depleted in the incompatible elements that are enriched in the crust. On the other hand, freezing of an inner core can cause additional contraction due to the higher density of the solid part of the core that is progressively depleted in light alloying elements (e.g., Grott et al., 2011; Tosi et al., 2013).

The interpretation of compressive tectonic features in terms of global planetary contraction is well established. It consists in mapping such features over the entire surface and using displacement–length scaling properties of faults to estimate the amount of radial shortening experienced by a given body (e.g., Watters et al., 2004; Byrne et al., 2014; Nahm & Schultz, 2011; Watters et al., 2010). With a surface dominated by compressive tectonic landforms (Strom et al., 1975) – lobate scarps and wrinkle ridges – Mercury is the body for which this approach has been used most extensively. Current estimates based on *MESSENGER* images suggest an overall contraction of up to 7 km (Byrne et al., 2014), with up to two additional kilometers that could be accommodated by elastic deformation prior to the formation of the observed faults

(Klimczak, 2015). Furthermore, cross-cutting relationships between faults and impact craters indicate that global contraction on Mercury started early, about 3.9 Ga, and continued until present at a decreasing rate (Crane & Klimczak, 2017). Models of the thermal evolution of Mercury typically predict a short initial phase of mantle heating and expansion lasting ~ 1 Gyr, followed by cooling leading to a cumulative amount of radial contraction that compares well with the available observations, although the onset time of contraction tends to be slightly overestimated and the contraction rate to be constant rather than declining (Tosi et al., 2013; Knibbe & van Westrenen, 2018; Hauck et al., 2018).

Similar compilations of compressional features at a global scale have been obtained for Mars (Knapmeyer et al., 2006). When considering all contractional structures regardless of their age, Nahm and Schultz (2011) inferred a maximum radial shortening of up to 3.77 km, although, as for Mercury, the expected rate of contraction would not be constant with time when taking into account the ages of the tectonic features. As discussed by Nahm and Schultz (2011), the overall cooling predicted by thermal evolution models of Mars (Andrews-Hanna, Zuber, & Hauck, 2008) significantly overestimates the inferred amount of global contraction. However, the extensive volcanic resurfacing underwent by the planet during the Hesperian epoch (about 3.7–3.0 Ga) (Greeley & Schneid, 1991) may have buried older faults generated by contraction, which renders a direct comparison with thermal evolution models nontrivial. Indeed, in contrast to Mercury, for which global contraction is traditionally used as one of the primary observations to constrain the interior evolution of the planet, models of Mars generally rely on different sets of observables (Plesa et al., 2018; Samuel et al., 2019).

On the Moon, the exceptional quality of the gravity experiment of the GRAIL mission revealed ancient igneous intrusions, indicative of an early phase of expansion of few km (Andrews-Hanna et al., 2013; Elkins-Tanton & Bercovici, 2014). Apart from tectonic structures observed within the lunar maria and associated with loading of mare basalts, compressional lobate scarps are the most common features present on the farside. Their length and surface relief, however, are much smaller than those of Mercury and Mars, implying an amount of global contraction of less than 1 km (Watters & Johnson, 2010; Watters et al., 2010). Early (and strongly simplified) models starting from a cold, accretion-like interior underlying a shallow magma ocean could meet this tight constraint (Solomon & Chaiken, 1976). More recent and sophisticated ones based on 3D thermal convection predict at least 2–3 km of shortening after an initial expansion phase (Zhang et al., 2013b; Rolf et al., 2016), which could be

marginally compatible with the observations if additional contraction – up to 1.4 km according to Klimczak (2015) – was accumulated elastically without surface manifestation.

17.6.2. Heat Flux and Elastic Lithosphere Thickness

The heat flowing through the surface from the interior provides the most direct way to probe the thermal state of a planetary body. However, heat flux measurements on an extraterrestrial body currently exist only for the Moon (Langseth et al., 1976). Taken as part of the *Apollo 15* and *Apollo 17* missions, these measurements were conducted near the margins of the anomalous PKT region (Section 17.3). Even if they cannot be considered to be representative of the average lunar heat flux, they can still be used as a direct constraint for the global evolution of the interior (Laneuville et al., 2013; Laneuville et al., 2018).

As part of the *InSight* mission to Mars (Banerdt & Russell, 2017), the Heat Flow and Physical Properties Package (HP³), consisting of a self-hammering probe designed to measure the thermal conductivity and temperature gradient – hence the heat flux – across up to 5 m of Martian ground, was deployed on the surface of Mars on February 2019. Unfortunately the experiment has not been successful and did not provide new constraints on the martian heat flux.

In the absence of direct measurements, the heat flux at a specific location can be inferred by estimating the effective thickness of the elastic lithosphere (T_e) using gravity and topography data. Topographic features associated with observed gravity anomalies can either be compensated and hence in isostatic equilibrium in the presence of a strengthless lithosphere (Padovan et al., 2015), or supported, partly or fully, by a lithosphere of finite strength. Although the crust-lithosphere system is characterized by a complex rheology, its flexural behavior can be approximated with that of an elastic plate overlying a strengthless interior. By making (rather strong) assumptions on the rheological properties of the crust and lithosphere and under the approximation of small plate curvature, T_e can be derived (McNutt, 1984) and further identified with the depth of a characteristic isotherm, thereby providing clues on the thermal gradient at specific locations. Furthermore, if the age of the topographic feature responsible for lithospheric flexure is also known, for example, through crater counting, an attempt can be made to reconstruct the cooling history of the mantle by estimating T_e for features of different ages. Upon mantle cooling, the depth of the isotherm corresponding to T_e will increase and so the elastic thickness, thus indicating a heat flux that progressively decreases over the evolution.

In addition to the above inferences based on the use of gravity and topography data, the thickness of the elastic lithosphere beneath impact basins can be determined

from loading and flexure models constrained by the distribution of tectonic structures within the basin (Comer et al., 1979; Solomon & Head, 1980), or from models of viscous or viscoelastic relaxation of the basin's topographic relief (Solomon et al., 1982; Mohit & Phillips, 2006; Kamata et al., 2015), two approaches that have been extensively applied to the Moon.

For Mercury, only few estimates of the elastic thickness pertaining the early evolution are available (Melosh & McKinnon, 1988; Nimmo & Watters, 2004; Tosi et al., 2015; James et al., 2016). However, these are highly discordant, with values ranging from ~30–35 km (Nimmo & Watters, 2004; James et al., 2016) to ~80–100 km (Melosh & McKinnon, 1988; Tosi et al., 2015) around 3.9 – 3.8 Ga. The reasons of the discrepancy are not fully clear (Phillips et al., 2018), but possibly due to the different methods employed and approximations used to relate T_e with the internal temperature.

For the Moon, a variety of estimates have been made, mostly associated with impact basins. Values of T_e of less than 30 km have been suggested for basins older than 3.9 Ga (Kamata et al., 2015), possibly as small as 12 km (Crosby & McKenzie, 2005), suggesting an initially thin lithosphere and hot interior as expected for a mantle that crystallized from a magma ocean. For younger basins such as Crisium and Imbrium, a T_e of up to 75 km has been proposed (Solomon & Head, 1980), in line with the idea of rapidly thickening lithosphere in a cooling mantle.

From the analysis of gravity and topography associated with a variety of structures across Mars' surface (see e.g., Grott et al., 2013, for a thorough discussion of the evolution of T_e on Mars), a consistent scenario emerges with $T_e < 25$ km during the Noachian epoch (4.5–3.7 Ga), between ~50 and 150 km during the Hesperian (3.7–3.0 Ga) and Amazonian (age ≤ 3 Ga), though with very large temporal uncertainties, and as large as 300 km at present-day beneath the northern polar cap (Phillips et al., 2008). Recently, Plesa et al. (2018) presented 3D models of Mars's interior evolution using, among others, constraints on the elastic thickness. These models agree generally well with the above estimates. In particular, the requirement of a large T_e at present-day beneath the North Pole poses a tight constraint, limiting the set of admissible models to those characterized by a mantle highly-depleted in HPEs. In fact, a limited amount of heat sources causes the mantle to cool over the evolution to generate a sufficiently large lithosphere thickness at present.

17.7. SUMMARY AND OUTLOOK

Combining the various constraints and models described in the previous sections, it is possible to outline likely scenarios for the evolution of Mercury, the Moon,

and Mars. Of course the picture is far from being complete, and this outlook provides a summary and indicates potential avenues for future improvements of our understanding of the evolution of stagnant-lid bodies.

All three bodies likely had a magma ocean phase followed by fractional crystallization of the mantle, which set the stage for the subsequent evolution. The primary crust on the Moon and its traces on Mercury provide direct support to this hypothesis. A rapid formation within the first few million years of the solar system and isotopic evidence from meteorites favor a magma ocean also for Mars. A global-scale overturn of the solid mantle – beneath the stagnant lid or involving the lid – due to the gravitational instability of FeO-rich cumulates is a direct consequence of fractional crystallization and the most widely explored scenario. However, for a slowly solidifying magma ocean, as is possibly the case for Mars and most likely for the Moon, convection and mixing can start during solidification. Existing models of the long-term evolution of these bodies constrained by observations mostly rely on the assumption of a homogeneous mantle. The long-term consequences of the complex processes associated with magma ocean crystallization are receiving more and more attention but are yet to be explored in detail for each planet.

The presence of the stagnant lid early on in the evolution (possibly following a brief episode of surface mobilization at the end of the magma ocean phase) causes inefficient heat loss, and hence heating and expansion of the mantle (Figure 17.6a), and crust formation (Figure 17.6b). The segregation of HPEs due to the formation of the primary crust of the Moon left the mantle largely depleted, which strongly limited the production of large volumes of secondary crust, but not of volcanism in general, as the lunar maria clearly show. The crusts of Mercury and Mars are instead mostly volcanic (i.e., secondary) and grew to the thickness inferred at present day from gravity and topography data within the first few hundred million years of evolution due to the production of partial melt, implying that a substantial amount of HPEs remained available to drive mantle convection and decompression melting after magma ocean solidification.

The phase of mantle heating and crust production is followed by secular cooling (Figure 17.6a), radial contraction, and by the increase of the thickness of the lithosphere and its elastic part. Surficial evidence is provided by the extent and number of compressive tectonic features, which allow the amount of radial contraction accumulated through a planet's history to be estimated. Such features are present on all the three bodies, particularly on Mercury, whose estimated contraction of about 7 km can be matched by evolution models. The smaller global contraction of Mars (<4 km) and the Moon (<1 km) are generally difficult to match by evolution

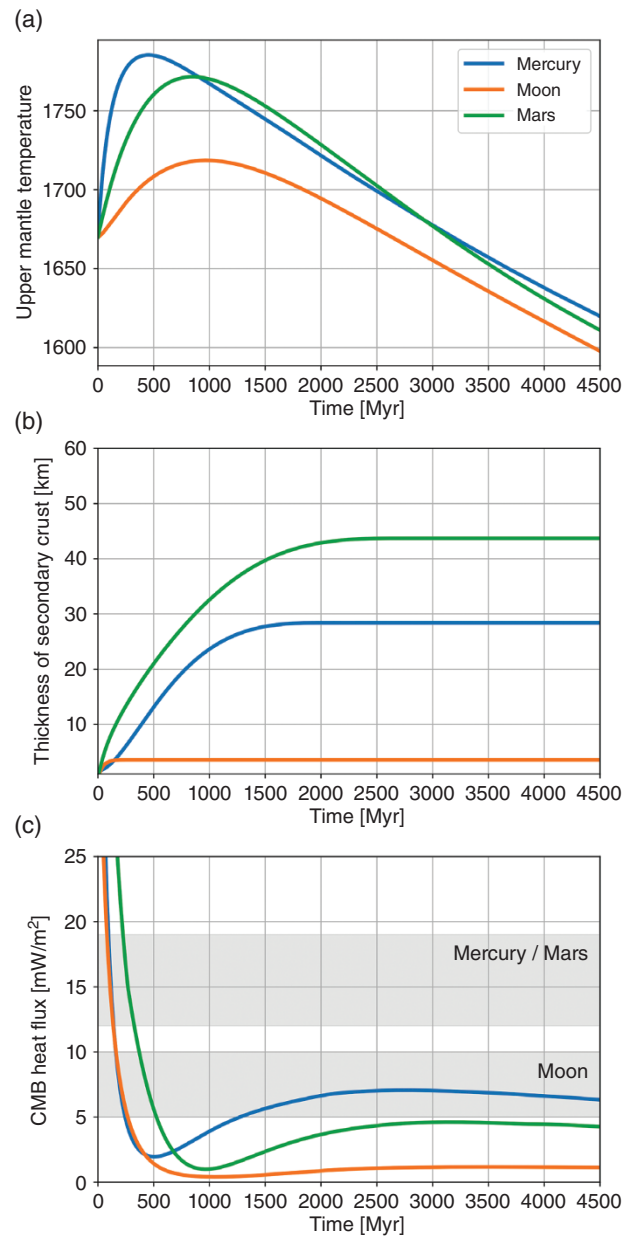


Figure 17.6 Possible evolution of the (a) upper mantle temperature (i.e., the temperature beneath the stagnant lid); (b) thickness of the secondary crust (which would sum up to an existing primary crust); and (c) heat flux at the CMB for Mercury (blue lines), the Moon (orange lines), and Mars (green lines). (c) The two gray areas indicate a possible range of core adiabatic heat flux for Mercury and Mars (upper area between 12 and 19 mW/m²), and for the Moon (lower area between 5 and 10 mW/m²). The curves are obtained using parameterized thermal evolution models similar to those of Grott et al. (2013) and Tosi et al. (2013), to which we refer for a complete description. Model parameters for Mercury are taken from Hauck et al. (2018), for Mars from Grott et al. (2013), and for the Moon from Laneuville et al. (2018).

models, which instead predict larger values, thus suggesting that part of the accumulated contraction may have been stored elastically with no surface expression. The effective elastic lithosphere thickness, estimated at specific locations by combining gravity and topography data with flexure modeling, increases with time due to mantle cooling. This behavior has been mostly recognized for Mars and is confirmed by numerical models. Large uncertainties associated with dating of the corresponding surface units somehow limit the use of this constraint.

In the early phases of the solar system many large objects collided with the newly formed planets, and the history of this tumultuous past is manifest in the battered surfaces of Mercury, the Moon, and to a somewhat lesser extent, Mars. The energies involved in this kind of events are extremely large, enough to interact with mantle convection, thus affecting the overall evolution, with melting activity, thus affecting the secondary crust production, and possibly with the core heat flux, thus affecting dynamo action. The most energetic events occur early on, and their dating is often quite uncertain, making the connection between these exogenous events and the interior processes they may interact with not straightforward to assess. However, it is clear that the mutual interaction depends on the interior thermal state, and, as such, large impact basins provide a window into the interior processes at the time of impact. There is evidence that the formation of the several large Martian basins did temporally stop dynamo action in the mantle, and that the properties of large lunar basins confirm the existence of large scale compositional heterogeneities in the mantle of the Moon. Compared to Mars and the Moon, data for Mercury are relatively sparse. However, as in the case of the Moon, the properties of its large basins are compatible with the overall evolution of the planet, as inferred from the entire set of available constraints (Figure 17.6).

Although at present-day only Mercury possesses a global magnetic field, an early one was active on all the three bodies, as the magnetization of their crust and lithosphere demonstrates (Figure 17.5). Thermal dynamos driven by a super-adiabatic heat flux extracted from the core by the convecting mantle are short-lived (Figure 17.6c). A thermal dynamo on Mercury would have likely stopped before 3.7 Ga (the age of the observed magnetized region). Furthermore, it is not known whether or not Mercury's magnetic field operated continuously from this age until present. Evolution models considering a core with Fe-Si composition and accounting for the effects of its crystallization seem to suggest so. An early episode of strong mantle and core cooling due to surface mobilization or to an initially hot core may have been responsible for the Martian dynamo, which ceased to operate ~ 4 Ga. This mechanism is not sufficient to power the lunar dynamo, which survived until 2.5 Ga, possibly much longer, and

generated ~ 4 Ga a magnetic field of high intensity, which no single mechanism can account for.

The global evolutions of Mercury, the Moon, and Mars illustrated in Figure 17.6 are valid for a specific model with a specific set of parameters. Yet, the figure shows that overall the evolution of the three bodies, as constrained by the observations described in this chapter, which are different for each body, is largely similar. Thus, one could surmise that thermal evolution models do capture the most important physical processes relevant to the thermo-chemical evolution of stagnant-lid bodies. However, given the large number of parameters that are required to run these kind of models (typically in excess of about 20), it is fair to admit that there is often enough room to adjust them in order to match the observations. A better leverage on the predictive and inference powers of these models would require major advances along two main avenues: material properties and observational constraints. In terms of material properties, we take viscosity as the most relevant example, since it represents a parameter that has a huge effect on the thermal evolution, but for which only very broad constraints exist. Viscosity is difficult to measure both in the laboratory and with theoretical calculations. Furthermore, in a planetary setting, it is affected by several poorly known and difficult to constrain factors, such as presence of melt, presence of volatiles, grain size, and dominant creep mechanism. These unavoidable obstacles imply that improvements in observational constraints are the most likely way to refine our understanding of the evolution of stagnant-lid bodies. With their potential ability of inferring interior structure, heat flux, crustal structure, and possibly density and temperature structures of the mantle, geophysical stations, such as the InSight lander currently located on the surface of Mars, are poised to provide a big step forward in our understanding of the detailed evolution history of the stagnant-lid bodies of the inner solar system. Complementary refinements of the dating of the surficial units, possible by direct analysis of samples, which will be facilitated by future sample-return missions, will also improve the information content of a large set of additional constraints, from large basins properties to lid thickness estimates, which critically depend on the age of the associated crustal units.

It is somewhat self-evident that the level of complexity of a given model must depend on the detail, amount, and variety of the observations that the model is trying to explain. Future missions will provide new data, and evolution models will obviously need to be expanded and possibly adapted and tailored specifically for the different bodies. This future development will necessarily make the straightforward and informative comparison of the evolution of the different bodies, as presented in Figure 17.6, not possible. But this will only indicate that

the field will have matured, which is only to be welcomed as long as modelers will not attempt to reach the level of exactitude of the ancient Art of Cartography (Borges, 1999).

ACKNOWLEDGMENTS

We thank Maxim Ballmer for inviting us to write this manuscript and two anonymous reviewers for their comments that helped improve it. We also thank Maxime Maurice for his assistance in setting up the model used to generate Figure 17.1. N.T. acknowledges support by the Helmholtz Association (project VH-NG-1017) and S.P. by the DFG (Research Unit FOR 2440 Matter under planetary interior conditions).

REFERENCES

- Abe, Y., & Matsui, T. (1986). Early evolution of the Earth: Accretion, atmosphere formation, and thermal history. *J. Geophys. Res. Planets*, 91 (B13), E291–E302. doi: 10.1029/JB091iB13p0E291
- Acuna, M., Connerney, J., Lin, R., Mitchell, D., Carlson, C., McFadden, J., et al. (1999). Global distribution of crustal magnetization discovered by the Mars Global Surveyor MAG/ER experiment. *Science*, 284 (5415), 790–793.
- Anderson, B. J., Johnson, C. L., Korth, H., Winslow, R. M., Borovsky, J. E., Purucker, M. E., et al. (2012). Low-degree structure in Mercury's planetary magnetic field. *J. Geophys. Res. Planets*, 117. doi: 10.1029/2012JE004159
- Andraut, D., Bolfan-Casanova, N., Nigro, G. L., Bouhifd, M. A., Garbarino, G., & Mezouar, M. (2011). Solidus and liquidus profiles of chondritic mantle: Implication for melting of the Earth across its history. *Earth Planet. Sci. Lett.*, 304 (1–2), 251–259. doi: 10.1016/j.epsl.2011.02.006
- Andrews-Hanna, J. C., Besserer, J., Head, J. W., Howett, C. J. A., Kiefer, W. S., Lucey, P. J. et al. (2014). Structure and evolution of the lunar Procellarum region as revealed by GRAIL gravity data. *Nature*, 514 (7520), 68–71. doi: 10.1038/nature13697
- Andrews-Hanna, J. C., Zuber, M. T., & Banerdt, W. B. (2008). The Borealis basin and the origin of the martian crustal dichotomy. *Nature*, 453, 1212–1215. doi: 10.1038/nature07011
- Andrews-Hanna, J. C., Zuber, M. T., & Hauck, S. A. (2008). Strike-slip faults on Mars: Observations and implications for global tectonics and geodynamics. *J. Geophys. Res. Planets*, 113(E8), E08002. doi: 10.1029/2007JE002980
- Andrews-Hanna, J. C., Asmar, S. W., Head, J. W., Kiefer, W. S., Konopliv, A. S., Lemoine, F. G., et al. (2013). Ancient igneous intrusions and early expansion of the Moon revealed by GRAIL gravity gradiometry. *Science*, 339(6120), 675–678.
- Arkani-Hamed, J. (2009). Did tidal deformation power the core dynamo of Mars? *Icarus*, 201 (1), 31–43. doi: 10.1016/j.icarus.2009.01.005
- Ballmer, M. D., Lourenço, D. L., Hirose, K., Caracas, R., & Nomura, R. (2017). Reconciling magma-ocean crystallization models with the present-day structure of the Earth's mantle. *Geochem. Geophys. Geosyst.*, 18(7), 2785–2806. doi: 10.1002/2017GC006917
- Banerdt, W., & Russell, C. (2017). Editorial on: Topical collection on InSight mission to Mars. *Space Sci. Rev.*, 211 (1–4), 1–3.
- Baratoux, D., Toplis, M., Monnereau, M., & Sautter, V. (2013). The petrological expression of early Mars volcanism. *J. Geophys. Res. Planets*, 118(1), 59–64.
- Bibring, J.-P., Langevin, Y., Mustard, J. F., Poulet, F., Arvidson, R., Gendrin, A., et al. (2006). Global Mineralogical and Aqueous Mars History Derived from OMEGA/Mars Express Data. *Science*, 312, 400–404. doi: 10.1126/science.1122659
- Bjorkman, M. D., & Holsapple, K. A. (1987). Velocity scaling impact melt volume. *Intern. J. Impact Engin.*, 5, 155–163.
- Bland, M. T., & McKinnon, W. B. (2016). Mountain building on Io driven by deep faulting. *Nature Geosci.*, 9, 429–432. doi: 10.1038/ngeo2711.
- Borges, J. L. (1999). *On Exactitude in Science*. In *Collected Fictions*. The Penguin Press. kvarc.info/teaching/TDM/Borges.pdf.
- Boukaré, C. E., Parmentier, E. M., & Parman, S. W. (2018). Timing of mantle overturn during magma ocean solidification. *Earth Planet. Sci. Lett.*, 491, 216–225. doi: 10.1016/j.epsl.2018.03.037
- Breuer, D., Labrosse, S., & Spohn, T. (2010). Thermal evolution and magnetic field generation in terrestrial planets and satellites. *Space Sci. Rev.*, 152(1–4), 449–500.
- Breuer, D., & Moore, W. B. (2015). Dynamics and thermal history of the terrestrial planets, the Moon, and Io. In J. Schubert (Ed.), *Planets and moons* edited by T. Spohn, *Treatise on Geophysics*, vol. 10 (2nd ed.). Elsevier, Amsterdam, The Netherlands.
- Breuer, D., Rueckriemen, T., & Spohn, T. (2015). Iron snow, crystal floats, and inner-core growth: modes of core solidification and implications for dynamos in terrestrial planets and moons. *Prog. Earth Planet. Sci.*, 2, 39. doi: 10.1186/s40645-015-0069-y
- Breuer, D., & Spohn, T. (2003). Early plate tectonics versus single-plate tectonics on Mars: Evidence from magnetic field history and crust evolution. *J. Geophys. Res.*, 108(E7), 5072. doi: 10.1029/2002JE001999
- Brown, S. M., & Elkins-Tanton, L. T. (2009). Compositions of Mercury's earliest crust from magma ocean models. *Earth Planet. Sc. Lett.*, 286, 446–455. doi: 10.1016/j.epsl.2009.07.010
- Buono, A. S., & Walker, D. (2011). The Fe-rich liquidus in the Fe-FeS system from 1 bar to 10 GPa. *Geochim. Cosmochim. Acta*, 75(8), 2072–2087. doi: 10.1016/j.gca.2011.01.030
- Buz, J., Weiss, B. P., Tikoo, S. M., Shuster, D. L., Gattacceca, J., & Grove, T. L. (2015). Magnetism of a very young lunar glass. *J. Geophys. Res. Planets*, 120(10), 1720–1735. doi: 10.1002/2015JE004878
- Byrne, P. K., Klimczak, C., Celâl Sengör, A. M., Solomon, S. C., Watters, T. R., & Hauck, S. A., II. (2014). Mercury's global contraction much greater than earlier estimates. *Nat. Geosci.*, 7, 301–307. doi: 10.1038/ngeo2097

- Byrne, P. K., Ostrach, L. R., Fassett, C. I., Chapman, C. R., Denevi, B. W., Evans, A. J., et al. (2016). Widespread effusive volcanism on Mercury likely ended by about 3.5 Ga. *Geophys. Res. Lett.*, *43*, 7408–7416. doi: 10.1002/2016GL069412
- Cadogan, P. H. (1974, Jul). Oldest and largest lunar basin? *Nature*, *250*(5464), 315–316. doi: 10.1038/250315a0
- Cao, H., Aurnou, J. M., Wicht, J., Dietrich, W., Soderlund, K. M., & Russell, C. T. (2014). A dynamo explanation for Mercury's anomalous magnetic field. *Geophys. Res. Lett.*, *41* (12), 4127–4134. doi: 10.1002/2014GL060196
- Carr, M. H. (2006). *The Surface of Mars*. Cambridge, UK: Cambridge University Press.
- Cassanelli, J. P., & Head, J. W. (2016). Did the Orientale impact melt sheet undergo large-scale igneous differentiation by crystal settling? *Geophys. Res. Lett.*, *43*, 11. doi: 10.1002/2016GL070425
- Charlier, B., Grove, T. L., Namur, O., & Holtz, F. (2018). Crystallization of the lunar magma ocean and the primordial mantle-crust differentiation of the Moon. *Geochim. Cosmochim. Acta*, *234*, 50–69. doi: 10.1016/j.gca.2018.05.006
- Chen, B., Li, J., & Hauck, S. A. (2008). Non-ideal liquidus curve in the Fe-S system and Mercury's snowing core. *Geophys. Res. Lett.*, *35*(7), L07201. doi: 10.1029/2008GL033311
- Christensen, U. R. (2006). A deep dynamo generating Mercury's magnetic field. *Nature*, *444* (7122), 1056–1058. doi: 10.1038/nature05342
- Christensen, U. R. (2010). Dynamo Scaling Laws and Applications to the Planets. *Space Sci. Rev.*, *152*(1–4), 565–590. doi: 10.1007/s11214-009-9553-2
- Christensen, U. R., & Wicht, J. (2008). Models of magnetic field generation in partly stable planetary cores: Applications to Mercury and Saturn. *Icarus*, *196*(1), 16–34. doi: 10.1016/j.icarus.2008.02.013
- Citron, R. I., Manga, M., & Tan, E. (2018). A hybrid origin of the Martian crustal dichotomy: Degree-1 convection antipodal to a giant impact. *Earth Planet. Sci. Lett.*, *491*, 58–66. doi: 10.1016/j.epsl.2018.03.031
- Comer, R. P., Solomon, S. C., & Head, J. W. (1979). Elastic lithosphere thickness on the Moon from mare tectonic features: a formal inversion. *Lun. Planet. Sci. Conf. Proc.*, *3*, 2441–2463.
- Connerney, J. E. P., Acuña, M. H., Ness, N. F., Kletetschka, G., Mitchell, D. L., Lin, R. P., & Reme, H. (2005). Tectonic implications of Mars crustal magnetism. *Proc. Nat. Acad. Sci.*, *102*(42), 14970–14975. doi: 10.1073/pnas.0507469102
- Costa, A., Caricchi, L., & Bagdassarov, N. (2009). A model for the rheology of particle-bearing suspensions and partially molten rocks. *Geochem. Geophys. Geosyst.*, *10*(3). doi: 10.1029/2008GC002138
- Craddock, R. A., & Howard, A. D. (2002). The case for rainfall on a warm, wet early Mars. *J. Geophys. Res.*, *107*, 5111. doi: 10.1029/2001JE001505
- Crane, K. T., & Klimczak, C. (2017). Timing and rate of global contraction on Mercury. *Geophys. Res. Lett.*, *44* (7), 3082–3089. doi: 10.1002/2017GL072711
- Crosby, A., & McKenzie, D. (2005). Measurements of the elastic thickness under ancient lunar terrain. *Icarus*, *173*(1), 100–107. doi: 10.1016/j.icarus.2004.07.017
- Dauphas, N., & Pourmand, A. (2011). Hf-W-Th evidence for rapid growth of Mars and its status as a planetary embryo. *Nature*, *473*(7348), 489–492. doi: 10.1038/nature10077
- Davaille, A., Smrekar, S. E., & Tomlinson, S. (2017). Experimental and observational evidence for plume-induced subduction on Venus. *Nature Geosci.*, *10*(5), 349–355. doi: 10.1038/ngeo2928
- Debaille, V., Brandon, A. D., O'Neill, C., Yin, Q. Z., & Jacobsen, B. (2009). Early martian mantle overturn inferred from isotopic composition of nakhlite meteorites. *Nat. Geosci.*, *2* (8), 548–552. doi: 10.1038/ngeo579
- Denevi, B. W., Ernst, C. M., Meyer, H. M., Robinson, M. S., Murchie, S. L., Whitten, J. L., et al. (2013). The distribution and origin of smooth plains on Mercury. *J. Geophys. Res. Planets*, *118*, 891–907. doi: 10.1002/jgre.20075
- Dumberry, M., & Rivoldini, A. (2015). Mercury's inner core size and core-crystallization regime. *Icarus*, *248*, 254–268. doi: 10.1016/j.icarus.2014.10.038
- Dwyer, C., Stevenson, D., & Nimmo, F. (2011). A long-lived lunar dynamo driven by continuous mechanical stirring. *Nature*, *479*(7372), 212.
- Elbeshausen, D., & Wünnemann, K. (2011). iSALE-3D: A three-dimensional, multi-material, multi-rheology hydrocode and its applications to large-scale geodynamic processes. In F. Schäfer & S. Hiermaier (Eds.), *Proceedings of the 11th hypervelocity impact symposium 2010*. Fraunhofer Verlag.
- Elkins-Tanton, L. T. (2008). Linked magma ocean solidification and atmospheric growth for Earth and Mars. *Earth Planet. Sci. Lett.*, *271* (1–4), 181–191. doi: 10.1016/j.epsl.2008.03.062
- Elkins-Tanton, L. T. (2012). Magma Oceans in the Inner Solar System. *Ann. Rev. Earth Pl. Sc.*, *40*, 113–139. doi: 10.1146/annurev-earth-042711-105503
- Elkins-Tanton, L. T., & Bercovici, D. (2014). Contraction or expansion of the Moon's crust during magma ocean freezing? *Phil. Trans. Royal Soc. London Series A*, *372*(2024), 20130240–20130240. doi: 10.1098/rsta.2013.0240
- Elkins-Tanton, L. T., Burgess, S., & Yin, Q.-Z. (2011). The lunar magma ocean: Reconciling the solidification process with lunar petrology and geochronology. *Earth Planet. Sci. Lett.*, *304* (3–4), 326–336. doi: 10.1016/j.epsl.2011.02.004
- Elkins-Tanton, L. T., & Hager, B. H. (2005). Giant meteoroid impacts can cause volcanism. *Earth Planet. Sci. Lett.*, *239*, 219–232. doi: 10.1016/j.epsl.2005.07.029
- Elkins-Tanton, L. T., Hager, B. H., & Grove, T. L. (2004). Magmatic effects of the lunar late heavy bombardment. *Earth Planet. Sci. Lett.*, *222*, 17–27. doi: 10.1016/j.epsl.2004.02.017
- Elkins-Tanton, L. T., Zarnek, S. E., Parmentier, E. M., & Hess, P. C. (2005). Early magnetic field and magmatic activity on Mars from magma ocean cumulate overturn. *Earth Planet. Sci. Lett.*, *236*(1–2), 1–12. doi: 10.1016/j.epsl.2005.04.044
- Elkins-Tanton, L. T., Hess, P. C., & Parmentier, E. M. (2005). Possible formation of ancient crust on Mars through magma ocean processes. *J. Geophys. Res.*, *110*(E12). doi: 10.1029/2005JE002480
- Elkins-Tanton, L. T., Parmentier, E., & Hess, P. (2003). Magma ocean fractional crystallization and cumulate overturn in terrestrial planets: Implications for Mars. *Meteorit. Planet. Sci.*, *38*(12), 1753–1771.
- Ernst, C. M., Denevi, B. W., Barnouin, O. S., Klimczak, C., Chabot, N. L., Head, J. W., et al. (2015). Stratigraphy of the Caloris basin, Mercury: Implications for volcanic history

- and basin impact melt. *Icarus*, 250, 413–429. doi: 10.1016/j.icarus.2014.11.003
- Evans, A. J., Tikoo, S. M., & Andrews-Hanna, J. C. (2018). The Case Against an Early Lunar Dynamo Powered by Core Convection. *Geophys. Res. Lett.*, 45(1), 98–107. doi: 10.1002/2017GL075441
- Evans, A. J., Zuber, M. T., Weiss, B. P., & Tikoo, S. M. (2014). A wet, heterogeneous lunar interior: Lower mantle and core dynamo evolution. *J. Geophys. Res. Planets*, 119(5), 1061–1077. doi: 10.1002/2013JE004494
- Fassett, C. I. (2016). Analysis of impact crater populations and the geochronology of planetary surfaces in the inner solar system. *J. Geophys. Res. Planets*, 121, 1900–1926. doi: 10.1002/2016JE005094
- Fassett, C. I., Head, J. W., Baker, D. M. H., Zuber, M. T., Smith, D. E., Neumann, G. A., et al. (2012). Large impact basins on Mercury: Global distribution, characteristics, and modification history from *MESSENGER* orbital data. *J. Geophys. Res. Planets*, 117. doi: 10.1029/2012JE004154
- Fassett, C. I., Head, J. W., Blewett, D. T., Chapman, C. R., Dickson, J. L., Murchie, S. L., et al. (2009). Caloris impact basin: Exterior geomorphology, stratigraphy, morphometry, radial sculpture, and smooth plains deposits. *Earth Planet. Sci. Lett.*, 285, 297–308. doi: 10.1016/j.epsl.2009.05.022
- Fiquet, G., Auzende, A. L., Siebert, J., Corgne, A., Bureau, H., Ozawa, H., & Garbarino, G. (2010). Melting of Peridotite to 140 Gigapascals. *Science*, 329(5998), 1516. doi: 10.1126/science.1192448
- Foley, B. J., Bercovici, D., & Elkins-Tanton, L. T. (2014). Initiation of plate tectonics from post-magma ocean thermochemical convection. *J. Geophys. Res. Solid Earth*, 119(11), 8538–8561. doi: 10.1002/2014JB011121
- Frey, H. (2008). Ages of very large impact basins on Mars: Implications for the late heavy bombardment in the inner solar system. *Geophys. Res. Lett.*, 35(13).
- Frey, H., & Mannoia, L. (2013). A revised, rated and dated inventory of very large candidate impact basins on Mars. In *Lun. planet. sci. conf.* (Vol. 44, p. 2501).
- Fuller, M., & Cisowski, S. M. (1987). Lunar paleomagnetism. In J. A. Jacobs (Ed.), *Geomagnetism*. Orlando: Academic Press.
- Garrick-Bethell, I., Weiss, B. P., Shuster, D. L., & Buz, J. (2009). *Early Lunar Magnetism*. *Science*, 323(5912), 356. doi: 10.1126/science.1166804
- Garrick-Bethell, I., & Zuber, M. T. (2009). Elliptical structure of the lunar South Pole-Aitken basin. *Icarus*, 204 (2), 399–408. doi: 10.1016/j.icarus.2009.05.032
- Ghods, A., & Arkani-Hamed, J. (2007). Impact-induced convection as the main mechanism for formation of lunar mare basalts. *J. Geophys. Res. Planets*, 112, E03005. doi: 10.1029/2006JE002709
- Golabek, G. J., Emsenhuber, A., Jutzi, M., Asphaug, E. I., & Gerya, T. V. (2018). Coupling SPH and thermochemical models of planets: Methodology and example of a Mars-sized body. *Icarus*, 301, 235–246. doi: 10.1016/j.icarus.2017.10.003
- Golabek, G. J., Keller, T., Gerya, T. V., Zhu, G., Tackley, P. J., & Connolly, J. A. D. (2011). Origin of the martian dichotomy and Tharsis from a giant impact causing massive magmatism. *Icarus*, 215(1), 346–357. doi: 10.1016/j.icarus.2011.06.012
- Greeley, R., & Schneid, B. D. (1991). Magma Generation on Mars: Amounts, Rates, and Comparisons with Earth, Moon, and Venus. *Science*, 254 (5034), 996–998. doi: 10.1126/science.254.5034.996
- Grieve, R. A. (1980). Impact bombardment and its role in proto-continental growth on the early Earth. *Precamb. Res.*, 10, 217–247. doi: https://doi.org/10.1016/0301-9268(80)90013-3
- Grott, M., Baratoux, D., Hauber, E., Sautter, V., Mustard, J., Gasnault, O., et al. (2013). Long-Term Evolution of the Martian Crust-Mantle System. *Space Sci. Rev.*, 174 (1–4), 49–111. doi: 10.1007/s11214-012-9948-3
- Grott, M., Breuer, D., & Laneuville, M. (2011). Thermochemical evolution and global contraction of Mercury. *Earth Planet. Sci. Lett.*, 307, 135–146. doi: 10.1016/j.epsl.2011.04.040
- Hamano, K., Abe, Y., & Genda, H. (2013). Emergence of two types of terrestrial planet on solidification of magma ocean. *Nature*, 497(7451), 607–610. doi: 10.1038/nature12163
- Hartmann, W. K., Malin, M., McEwen, A., Carr, M., Soderblom, L., Thomas, P., et al. (1999). Evidence for recent volcanism on Mars from crater counts. *Nature*, 397, 586–589. doi: 10.1038/17545
- Hauck, S. A., Grott, B. P. K., M., W., D. B., S., S., & J., M. T. (2018). Mercury's global evolution. In S. C. Solomon, B. J. Anderson, & L. R. Nittler (Eds.), *Mercury, the View after MESSENGER*. Cambridge, UK: Cambridge University Press.
- Hauck, S. A., & Phillips, R. J. (2002). Thermal and crustal evolution of Mars. *J. Geophys. Res. Planets*, 107(E7), 5052. doi: 10.1029/2001JE001801
- Hauck, S. A., Phillips, R. J., & Price, M. H. (1998). Venus: Crater distribution and plains resurfacing models. *J. Geophys. Res.*, 103(E6), 13635–13642. doi: 10.1029/98JE00400
- Hauck, S. A., II, Margot, J.-L., Solomon, S. C., Phillips, R. J., Johnson, C. L., Lemoine, F. G., et al. (2013). The curious case of Mercury's internal structure. *J. Geophys. Res. Planets*, 118, 1204–1220. doi: 10.1002/jgre.20091
- Head, J. W., & Wilson, L. (1992). Lunar mare volcanism: Stratigraphy, eruption conditions, and the evolution of secondary crusts. *Geochim. Cosmochim. Acta*, 56(6), 2155–2175.
- Heimpel, M. H., Aurnou, J. M., Al-Shamali, F. M., & Gomez Perez, N. (2005). A numerical study of dynamo action as a function of spherical shell geometry. *Earth Planet. Sci. Lett.*, 236(1–2), 542–557. doi: 10.1016/j.epsl.2005.04.032
- Herrick, R. R. (1994). Resurfacing history of Venus. *Geology*, 22 (8), 703. doi: 10.1130/0091-7613
- Hier-Majumder, S., & Hirschmann, M. M. (2017). The origin of volatiles in the Earth's mantle. *Geochem. Geophys. Geosyst.*, 18(8), 3078–3092. doi: 10.1002/2017GC006937
- Hiesinger, H., Head, J., Wolf, U., Jaumann, R., & Neukum, G. (2011). Ages and stratigraphy of lunar mare basalts: A synthesis. *Recent Advances and Current Research Issues in Lunar Stratigraphy*, 477, 1–51.
- Holsapple, K. A. (1993). The Scaling of Impact Processes in Planetary Sciences. *Ann. Rev. Earth Planet. Sci.*, 21, 333–373. doi: 10.1146/annurev.ea.21.050193.002001
- Hood, L. L. (2016). Magnetic anomalies concentrated near and within Mercury's impact basins: Early mapping and

- interpretation. *J. Geophys. Res. Planets*, 121 (6), 1016–1025. doi: 10.1002/2016JE005048
- Ivanov, B. A., & Melosh, H. J. (2003). Impacts do not initiate volcanic eruptions: Eruptions close to the crater. *Geology*, 31, 869. doi: 10.1130/G19669.1
- James, P. B., Phillips, R. J., Grott, M., Hauck, S. A., & Solomon, S. C. (2016). The Thickness of Mercury's Lithosphere Inferred from MESSENGER Gravity and Topography. In *Lun. planet. sci. conf.* (p. 1992).
- James, P. B., Zuber, M. T., Phillips, R. J., & Solomon, S. C. (2015). Support of long-wavelength topography on Mercury inferred from MESSENGER measurements of gravity and topography. *J. Geophys. Res. Planets*, 120, 287–310.
- Johnson, C. L., Anderson, B. J., Korth, H., Phillips, R. J., & Philipott, L. C. (2018). Mercury's internal magnetic field. In S. C. Solomon, B. J. Anderson, & L. R. Nittler (Eds.), *Mercury, the View after MESSENGER*. Cambridge, UK: Cambridge University Press.
- Johnson, C. L., Phillips, R. J., Purucker, M. E., Anderson, B. J., Byrne, P. K., Denevi, B. W., et al. (2015). Low-altitude magnetic field measurements by MESSENGER reveal Mercury's ancient crustal field. *Science*, 348, 892–895. doi: 10.1126/science.aaa8720
- Jolliff, B. L., Gillis, J. J., Haskin, L. A., Korotev, R. L., & Wieczorek, M. A. (2000). Major lunar crustal terranes: Surface expressions and crust-mantle origins. *J. Geophys. Res. Planets*, 105(E2), 4197–4216.
- Jutzi, M., & Asphaug, E. (2011, Aug). Forming the lunar farside highlands by accretion of a companion moon. *Nature*, 476 (7358), 69–72. doi: 10.1038/nature10289
- Kamata, S., Sugita, S., Abe, Y., Ishihara, Y., Harada, Y., Morota, T., et al. (2015). The relative timing of Lunar Magma Ocean solidification and the Late Heavy Bombardment inferred from highly degraded impact basin structures. *Icarus*, 250, 492–503. doi: 10.1016/j.icarus.2014.12.025
- Karki, B. B., & Stixrude, L. P. (2010). Viscosity of MgSiO₃ Liquid at Earth's Mantle Conditions: Implications for an Early Magma Ocean. *Science*, 328(5979), 740. doi: 10.1126/science.1188327
- Keller, T., & Tackley, P. J. (2009). Towards self-consistent modeling of the martian dichotomy: The influence of one-ridge convection on crustal thickness distribution. *Icarus*, 202(2), 429–443. doi: 10.1016/j.icarus.2009.03.029
- King, S. D. (2018). Venus Resurfacing Constrained by Geoid and Topography. *J. Geophys. Res. Planets*, 123(5), 1041–1060. doi: 10.1002/2017JE005475
- Klimczak, C. (2015). Limits on the brittle strength of planetary lithospheres undergoing global contraction. *J. Geophys. Res. Planets*, 120, 2135–2151. doi: 10.1002/2015JE004851
- Knapmeyer, M., Oberst, J., Hauber, E., Wählisch, M., Deuchler, C., & Wagner, R. (2006). Working models for spatial distribution and level of Mars' seismicity. *J. Geophys. Res.*, 111 (E11), E11006. doi: 10.1029/2006JE002708
- Knibbe, J. S., & van Westrenen, W. (2018). The thermal evolution of Mercury's Fe-Si core. *Earth Planet. Sci. Lett.*, 482, 147–159. doi: 10.1016/j.epsl.2017.11.006
- Konrad, W., & Spohn, T. (1997). Thermal history of the Moon: implications for an early core dynamo and post-accretionary magmatism. *Adv. Space Res.*, 19(10), 1511–1521. doi: 10.1016/S0273-1177(97)00364-5
- Kuwayama, Y., & Hirose, K. (2004). Phase relations in the system Fe-FeSi at 21 GPa. *Am. Mineral.*, 89(2–3), 273–276. doi: 10.2138/am-2004-2-303
- Labrosse, S., Hernlund, J. W., & Coltice, N. (2007). A crystallizing dense magma ocean at the base of the Earth's mantle. *Nature*, 450, 866–869. doi: 10.1038/nature06355
- Labrosse, S., Hernlund, J. W., & Hirose, K. (2015). Fractional melting and freezing in the deep mantle and implications for the formation of a basal magma ocean. In J. Badro & M. Walter (Eds.), *The early Earth* (Vol. 212, p. 123–142). Wiley. doi: 10.1002/9781118860359.ch7
- Labrosse, S., Morison, A., Deguen, R., & Alboussière, T. (2018). Rayleigh-Bénard convection in a creeping solid with melting and freezing at either or both its horizontal boundaries. *J. Fluid. Mech.*, 846, 5–36. doi: 10.1017/jfm.2018.258
- Laneuville, M., Taylor, J., & Wieczorek, M. A. (2018). Distribution of Radioactive Heat Sources and Thermal History of the Moon. *J. Geophys. Res. Planets*, 123(12), 3144–3166. doi: 10.1029/2018JE005742
- Laneuville, M., Wieczorek, M., Breuer, D., Aubert, J., Morard, G., & Rückriemen, T. (2014). A long-lived lunar dynamo powered by core crystallization. *Earth Planet. Sci. Lett.*, 401, 251–260.
- Laneuville, M., Wieczorek, M., Breuer, D., & Tosi, N. (2013). Asymmetric thermal evolution of the moon. *J. Geophys. Res. Planets*, 118(7), 1435–1452.
- Langseth, M. G., Keihm, S. J., & Peters, K. (1976). Revised lunar heat-flow values. In *Lunar planet. sci. conf.* (Vol. 7, p. 3143–3171).
- Lawrence, D., Elphic, R., Feldman, W., Prettyman, T., Gagnault, O., & Maurice, S. (2003). Small-area thorium features on the lunar surface. *J. Geophys. Res.*, 108 (E9).
- Lawrence, D. J., Feldman, W. C., Barraclough, B. L., Binder, A. B., Elphic, R. C., Maurice, S., & Thomsen, D. R. (1998). Global Elemental Maps of the Moon: The Lunar Prospector Gamma-Ray Spectrometer. *Science*, 281, 1484. doi: 10.1126/science.281.5382.1484
- Le Bars, M. (2016). Flows driven by libration, precession, and tides in planetary cores. *Phys. Rev. Fluids*, 1 (6), 060505. doi: 10.1103/PhysRevFluids.1.060505
- Le Bars, M., Wieczorek, M. A., Karatekin, Ö., Cébron, D., & Laneuville, M. (2011). An impact-driven dynamo for the early Moon. *Nature*, 479(7372), 215.
- Le Feuvre, M., & Wieczorek, M. A. (2008). Nonuniform cratering of the terrestrial planets. *Icarus*, 197, 291–306. doi: 10.1016/j.icarus.2008.04.011
- Lebrun, T., Massol, H., Chassefière, E., Davaille, A., Marcq, E., Sarda, P., et al. (2013). Thermal evolution of an early magma ocean in interaction with the atmosphere. *J. Geophys. Res. Planets*, 118(6), 1155–1176. doi: 10.1002/jgre.20068
- Li, H., Zhang, N., Liang, Y., Wu, B., Dygert, N. J., Huang, J., & Parmentier, E. (2019). Lunar cumulate mantle overturn: A model constrained by ilmenite rheology. *J. Geophys. Res. Planets*.
- Lillis, R. J., Frey, H. V., & Manga, M. (2008). Rapid decrease in Martian crustal magnetization in the Noachian era:

- Implications for the dynamo and climate of early Mars. *Geophys. Res. Lett.*, 35(14), L14203. doi: 10.1029/2008GL034338
- Lillis, R. J., Robbins, S., Manga, M., Halekas, J. S., & Frey, H. V. (2013). Time history of the Martian dynamo from crater magnetic field analysis. *J. Geophys. Res. Planets*, 118(7), 1488–1511. doi: 10.1002/jgre.20105
- Maas, C., & Hansen, U. (2015). Effects of Earth's rotation on the early differentiation of a terrestrial magma ocean. *J. Geophys. Res. Solid Earth*, 120(11), 7508–7525. doi: 10.1002/2015JB012053
- Maas, C., & Hansen, U. (2019). Dynamics of a terrestrial magma ocean under planetary rotation: A study in spherical geometry. *Earth Planet. Sci. Lett.*, 513, 81–94. doi: 10.1016/j.epsl.2019.02.016
- Malavergne, V., Toplis, M. J., Berthet, S., & Jones, J. (2010). Highly reducing conditions during core formation on Mercury: Implications for internal structure and the origin of a magnetic field. *Icarus*, 206, 199–209. doi: 10.1016/j.icarus.2009.09.001
- Marchi, S., Chapman, C. R., Fassett, C. I., Head, J. W., Bottke, W. F., & Strom, R. G. (2013). Global resurfacing of Mercury 4.0–4.1 billion years ago by heavy bombardment and volcanism. *Nature*, 499, 59–61. doi: 10.1038/nature12280
- Marchi, S., Mottola, S., Cremonese, G., Massironi, M., & Martellato, E. (2009). A New Chronology for the Moon and Mercury. *Astrophys. J.*, 137, 4936–4948. doi: 10.1088/0004-6256/137/6/4936
- Marinova, M. M., Aharonson, O., & Asphaug, E. (2008). Mega-impact formation of the Mars hemispheric dichotomy. *Nature*, 453(7199), 1216–1219. doi: 10.1038/nature07070
- Maurice, M., Tosi, N., Samuel, H., Plesa, A.-C., Hüttig, C., & Breuer, D. (2017). Onset of solid-state mantle convection and mixing during magma ocean solidification. *J. Geophys. Res. Planets*, 122(3), 577–598. doi: 10.1002/2016JE005250
- McEwen, A. S., Malin, M. C., Carr, M. H., & Hartmann, W. K. (1999). Volcanic volcanism on early Mars revealed in Valles Marineris. *Nature*, 397, 584–586. doi: 10.1038/17539
- McNutt, M. K. (1984). Lithospheric flexure and thermal anomalies. *J. Geophys. Res.*, 89, 11180–11194. doi: 10.1029/JB089iB13p11180
- Melosh, H. J. (1989). *Impact Cratering: A Geologic Process*. Oxford University Press (Oxford Monographs on Geology and Geophysics, No. 11), 1989, 253 p.
- Melosh, H. J. (2011). *Planetary Surface Processes*. Cambridge University Press.
- Melosh, H. J., Freed, A. M., Johnson, B. C., Blair, D. M., Andrews-Hanna, J. C., Neumann, G. A., et al. (2013). The Origin of Lunar Mascon Basins. *Science*, 340, 1552–1555. doi: 10.1126/science.1235768
- Melosh, H. J., & McKinnon, W. B. (1988). The tectonics of Mercury. In Vilas, F., Chapman, C. R., & Matthews, M. S. (Ed.), *Mercury* (pp. 374–400). University of Arizona Press.
- Meyer, J., Elkins-Tanton, L., & Wisdom, J. (2010). Coupled thermal-orbital evolution of the early Moon. *Icarus*, 208(1), 1–10. doi: 10.1016/j.icarus.2010.01.029
- Mezger, K., Debaille, V., & Kleine, T. (2013). Core Formation and Mantle Differentiation on Mars. *Space Sci. Rev.*, 174 (1–4), 27–48. doi: 10.1007/s11214-012-9935-8
- Michael, G., Basilevsky, A., & Neukum, G. (2018). On the history of the early meteoritic bombardment of the Moon: Was there a terminal lunar cataclysm? *Icarus*, 302, 80–103. doi: https://doi.org/10.1016/j.icarus.2017.10.046
- Miljković, K., Wieczorek, M. A., Collins, G. S., Laneuville, M., Neumann, G. A., Melosh, H. J., et al. (2013). Asymmetric distribution of lunar impact basins caused by variations in target properties. *Science*, 342, 724–726. doi: 10.1126/science.1243224
- Mohit, P. S., & Arkani-Hamed, J. (2004). Impact demagnetization of the martian crust. *Icarus*, 168(2), 305–317. doi: 10.1016/j.icarus.2003.12.005
- Mohit, P. S., & Phillips, R. J. (2006). Viscoelastic evolution of lunar multiring basins. *J. Geophys. Res. Planets*, 111 (E12), E12001. doi: 10.1029/2005JE002654
- Monaghan, J. J. (1992). Smoothed particle hydrodynamics. *Ann. Rev. Astron. Astrophys.*, 30, 543–574. doi: 10.1146/annurev.aa.30.090192.002551
- Monteux, J., Amit, H., Choblet, G., Langlais, B., & Tobie, G. (2015). Giant impacts, heterogeneous mantle heating and a past hemispheric dynamo on Mars. *Phys. Earth Planet. Int.*, 240, 114–124. doi: 10.1016/j.pepi.2014.12.005
- Monteux, J., Andraut, D., & Samuel, H. (2016). On the cooling of a deep terrestrial magma ocean. *Earth Planet. Sci. Lett.*, 448, 140–149. doi: 10.1016/j.epsl.2016.05.010
- Moore, W. B., & Schubert, G. (2003). The tidal response of Ganymede and Callisto with and without liquid water oceans. *Icarus*, 166, 223–226. doi: 10.1016/j.icarus.2003.07.001
- Moore, W. B., & Webb, A. A. G. (2013). Heat-pipe Earth. *Nature*, 501 (7468), 501–505. doi: 10.1038/nature12473
- Morbidelli, A., Bottke, W. F., Jr., Froeschlé, C., & Michel, P. (2002). Origin and Evolution of Near-Earth Objects. In W. F. Bottke Jr., A. Cellino, P. Paolicchi, & R. P. Binzel (Eds.), *Asteroids III* (p. 409–422). University of Arizona Press.
- Morbidelli, A., Marchi, S., Bottke, W. F., & Kring, D. A. (2012). A sawtooth-like timeline for the first billion years of lunar bombardment. *Earth Planet. Sci. Lett.*, 355, 144–151. doi: 10.1016/j.epsl.2012.07.037
- Morbidelli, A., Nesvorný, D., Laurenz, V., Marchi, S., Rubie, D. C., Elkins-Tanton, L., et al. (2018). The timeline of the lunar bombardment: Revisited. *Icarus*, 305, 262–276. doi: 10.1016/j.icarus.2017.12.046
- Morison, A., Labrosse, S., Deguen, R., & Alboussière, T. (2019). Timescale of overturn in a magma ocean cumulate. *Earth Planet. Sci. Lett.*, 516, 25–36. doi: 10.1016/j.epsl.2019.03.037
- Morschhauser, A. (2016). *A model of the crustal magnetic field of mars* (Doctoral dissertation: http://nbn-resolving.de/urn:nbn:de:hbz:6-62269665189). Westfälischen Wilhelms-Universität Münster, Münster. (187 pp.)
- Morschhauser, A., Grott, M., & Breuer, D. (2011). Crustal recycling, mantle dehydration, and the thermal evolution of Mars. *Icarus*, 212, 541–558. doi: 10.1016/j.icarus.2010.12.028
- Murchie, S. L., Klima, R. L., Denevi, B. W., Ernst, C. M., Keller, M. R., Domingue, D. L., et al. (2015). Orbital multispectral mapping of Mercury with the MESSENGER Mercury Dual Imaging System: Evidence for the origins of plains units

- and low-reflectance material. *Icarus*, 254, 287–305. doi: 10.1016/j.icarus.2015.03.027
- Nahm, A. L., & Schultz, R. A. (2011). Magnitude of global contraction on Mars from analysis of surface faults: Implications for martian thermal history. *Icarus*, 211 (1), 389–400.
- Nakagawa, T., & Tackley, P. J. (2015). Influence of plate tectonic mode on the coupled thermochemical evolution of Earth's mantle and core. *Geochim. Geophys. Geosyst.*, 16 (10), 3400–3413. doi: 10.1002/2015GC005996
- Namur, O., Collinet, M., Charlier, B., Grove, T. L., Holtz, F., & McCammon, C. (2016). Melting processes and mantle sources of lavas on Mercury. *Earth Planet. Sci. Lett.*, 439, 117–128. doi: 10.1016/j.epsl.2016.01.030
- Neukum, G., & Ivanov, B. A. (1994). Crater size distributions and impact probabilities on earth from lunar, terrestrial-planet, and asteroid cratering data. In T. Gehrels (Ed.), *Hazards Due to Comets and Asteroids* (p. 359–416). University of Arizona Press.
- Neukum, G., Jaumann, R., Hoffmann, H., Hauber, E., Head, J. W., Basilevsky, A. T., et al. (2004). Recent and episodic volcanic and glacial activity on Mars revealed by the High Resolution Stereo Camera. *Nature*, 432(7020), 971–979. doi: 10.1038/nature03231
- Neumann, G. A., Zuber, M. T., Wieczorek, M. A., McGovern, P. J., Lemoine, F. G., & Smith, D. E. (2004). Crustal structure of Mars from gravity and topography. *J. Geophys. Res. Planets*, 109(E8), E08002. doi: 10.1029/2004JE002262
- Nikolaou, A., Katyal, N., Tosi, N., Godolt, M., Grenfell, J. L., & Rauer, H. (2019). What Factors Affect the Duration and Outgassing of the Terrestrial Magma Ocean? *Astrophys. J.*, 875(1). doi: 10.3847/1538-4357/ab08ed
- Nimmo, F., & Kleine, T. (2007). How rapidly did Mars accrete? Uncertainties in the Hf/W timing of core formation. *Icarus*, 191 (2), 497–504. doi: 10.1016/j.icarus.2007.05.002
- Nimmo, F., & Stevenson, D. (2000). Influence of early plate tectonics on the thermal evolution and magnetic field of Mars. *J. Geophys. Res.*, 105(E5), 11969–11979.
- Nimmo, F., & Tanaka, K. (2005). Early crustal evolution of Mars. *Annu. Rev. Earth Planet. Sci.*, 33, 133–161.
- Nimmo, F., & Watters, T. R. (2004). Depth of faulting on Mercury: Implications for heat flux and crustal and effective elastic thickness. *Geophys. Res. Lett.*, 31, 2701. doi: 10.1029/2003GL018847
- Nittler, L. R., Chabot, N. L., Grove, T. L., & Peplowski, P. N. (2018). The Chemical Composition of Mercury. In S. C. Solomon, B. J. Anderson, & L. R. Nittler (Eds.), *Mercury, the View after MESSENGER*. Cambridge, UK: Cambridge University Press.
- Nittler, L. R., Starr, R. D., Weider, S. Z., McCoy, T. J., Boynton, W. V., Ebel, D. S., et al. (2011). The major-element composition of Mercury's surface from MESSENGER X-ray spectrometry. *Science*, 333, 1847–1850. doi: 10.1126/science.1211567
- Olson, P. (2008). Planetary magnetism. In P. Cardin & L. Cugliandolo (Eds.), *Dynamos – lecture notes of the les houches summer school 2007* (p. 137–249). Elsevier.
- O'Reilly, T. C., & Davies, G. F. (1981). Magma transport of heat on Io: A mechanism allowing a thick lithosphere. *Geophys. Res. Lett.*, 8(4), 313–316. doi: 10.1029/GL008i004p00313
- Padovan, S., Tosi, N., Plesa, A.-C., & Ruedas, T. (2017). Impact-induced changes in source depth and volume of magmatism on Mercury and their observational signatures. *Nature Comm.*, 8, 1945. doi: 10.1038/s41467-017-01692-0
- Padovan, S., Wieczorek, M. A., Margot, J.-L., Tosi, N., & Solomon, S. C. (2015). Thickness of the crust of Mercury from geoid-to-topography ratios. *Geophys. Res. Lett.*, 42(4), 1029–1038. doi: 10.1002/2014GL062487
- Paige, D., & Siegler, M. (2016). New constraints on lunar heat flow rates from Iro diviner lunar radiometer experiment polar observations. In *Lunar planet. sci. conf.* (Vol. 47, p. 2753).
- Parmentier, E., Zhong, S., & Zuber, M. (2002). Gravitational differentiation due to initial chemical stratification: origin of lunar asymmetry by the creep of dense KREEP. *Earth Planet. Sci. Lett.*, 201 (3–4), 473–480.
- Peale, S. J., Cassen, P., & Reynolds, R. T. (1979). Melting of Io by tidal dissipation. *Science*, 203, 892–894. doi: 10.1126/science.203.4383.892
- Peplowski, P. N., Klima, R. L., Lawrence, D. J., Ernst, C. M., Denevi, B. W., Frank, E. A., et al. (2016). Remote sensing evidence for an ancient carbon-bearing crust on Mercury. *Nature Geosci.*, 9(4), 273–276. doi: 10.1038/ngeo2669
- Perera, V., Jackson, A. P., Elkins-Tanton, L. T., & Asphaug, E. (2018). Effect of reimpacting debris on the solidification of the lunar magma ocean. *J. Geophys. Res. Planets*, 123(5), 1168–1191.
- Perry, M. E., Neumann, G. A., Phillips, R. J., Barnouin, O. S., Ernst, C. M., Kahan, D. S., et al. (2015). The low-degree shape of Mercury. *Geophys. Res. Lett.*, 42, 6951–6958. doi: 10.1002/2015GL065101
- Phillips, R. J., Byrne, P. K., James, P. B., Mazarico, E., Neumann, G. A., & Perry, M. E. (2018). Mercury's crust and lithosphere: Structure and mechanics. In S. C. Solomon, B. J. Anderson, & L. R. Nittler (Eds.), *Mercury, the View after MESSENGER*. Cambridge, UK: Cambridge University Press.
- Phillips, R. J., Zuber, M. T., Smrekar, S. E., Mellon, M. T., Head, J. W., Tanaka, K. L., et al. (2008). Mars North Polar Deposits: Stratigraphy, Age, and Geodynamical Response. *Science*, 320(5880), 1182. doi: 10.1126/science.1157546
- Pierazzo, E., Vickery, A. M., & Melosh, H. J. (1997). A reevaluation of impact melt production. *Icarus*, 127, 408–423. doi: 10.1006/icar.1997.5713
- Plesa, A.-C., Grott, M., Tosi, N., Breuer, D., Spohn, T., & Wieczorek, M. (2016). How large are present-day heat flux variations across the surface of Mars? *J. Geophys. Res. Planets*, 121 (12), 2386–2403.
- Plesa, A.-C., Padovan, S., Tosi, N., Breuer, D., Grott, M., Wieczorek, M. A., et al. (2018). The Thermal State and Interior Structure of Mars. *Geophys. Res. Lett.*, 45, 12. doi: 10.1029/2018GL080728
- Plesa, A.-C., Tosi, N., & Breuer, D. (2014). Can a fractionally crystallized magma ocean explain the thermo-chemical evolution of Mars? *Earth Planet. Sci. Lett.*, 403, 225–235. doi: 10.1016/j.epsl.2014.06.034

- Potter, R. W. K., Collins, G. S., Kiefer, W. S., McGovern, P. J., & Kring, D. A. (2012). Constraining the size of the South Pole-Aitken basin impact. *Icarus*, *220*, 730–743. doi: 10.1016/j.icarus.2012.05.032
- Press, F., & Siever, R. (1978). *Earth*. San Francisco: Freeman and Company.
- Rampino, M. R. (1987). Impact cratering and flood basalt volcanism. *Nature*, *327*(6122), 468.
- Reese, C. C., & Solomatov, V. S. (2006). Fluid dynamics of local martian magma oceans. *Icarus*, *184*, 102–120. doi: 10.1016/j.icarus.2006.04.008
- Reese, C. C., Solomatov, V. S., & Baumgardner, J. R. (2002). Survival of impact-induced thermal anomalies in the Martian mantle. *J. Geophys. Res.*, *107*, 5082. doi: 10.1029/2000JE001474
- Reese, C. C., Solomatov, V. S., Baumgardner, J. R., Stegman, D. R., & Veizolainen, A. V. (2004). Magmatic evolution of impact-induced Martian mantle plumes and the origin of Tharsis. *J. Geophys. Res.*, *109*, E08009. doi: 10.1029/2003JE002222
- Roberts, J. H., & Arkani-Hamed, J. (2012). Impact-induced mantle dynamics on Mars. *Icarus*, *218*, 278–289. doi: 10.1016/j.icarus.2011.11.038
- Roberts, J. H., & Arkani-Hamed, J. (2017). Effects of basin-forming impacts on the thermal evolution and magnetic field of Mars. *Earth Planet. Sci. Lett.*, *478*, 192–202. doi: 10.1016/j.epsl.2017.08.031
- Roberts, J. H., & Barnouin, O. S. (2012). The effect of the Caloris impact on the mantle dynamics and volcanism of Mercury. *J. Geophys. Res. Planets*, *117*, 2007. doi: 10.1029/2011JE003876
- Roberts, J. H., Lillis, R. J., & Manga, M. (2009). Giant impacts on early Mars and the cessation of the Martian dynamo. *J. Geophys. Res. Planets*, *114* (E4), E04009. doi: 10.1029/2008JE003287
- Roberts, J. H., & Zhong, S. (2006). Degree-1 convection in the Martian mantle and the origin of the hemispheric dichotomy. *J. Geophys. Res. Planets*, *111* (E6), E06013. doi: 10.1029/2005JE002668
- Robinson, M. S., Murchie, S. L., Blewett, D. T., Domingue, D. L., Hawkins, S. E., Head, J. W., et al. (2008). Reflectance and color variations on Mercury: Regolith processes and compositional heterogeneity. *Science*, *321* (5885), 66. doi: 10.1126/science.1160080
- Rogers, G. C. (1982). Oceanic plateaus as meteorite impact signatures. *Nature*, *299*, 341–342. doi: 10.1038/299341a0
- Rolf, T., Steinberger, B., Sruthi, U., & Werner, S. C. (2018). Inferences on the mantle viscosity structure and the post-overturn evolutionary state of Venus. *Icarus*, *313*, 107–123. doi: 10.1016/j.icarus.2018.05.014
- Rolf, T., Zhu, M.-H., Wünnemann, K., & Werner, S. C. (2016). The role of impact bombardment history in lunar evolution. *Icarus*, *286*, 138–152. doi: 10.1016/j.icarus.2016.0.007
- Ronca, L. B. (1966). Meteoritic impact and volcanism. *Icarus*, *5*, 515–520. doi: 10.1016/0019-1035(66)90063-7
- Rückriemen, T., Breuer, D., & Spohn, T. (2018). Top-down freezing in a Fe-FeS core and Ganymede's present-day magnetic field. *Icarus*, *307*, 172–196. doi: 10.1016/j.icarus.2018.02.021
- Ruedas, T., & Breuer, D. (2018). “Isocrater” impacts: Conditions and mantle dynamical responses for different impactor types. *Icarus*, *306*, 94–115. doi: 10.1016/j.icarus.2018.02.005
- Ruedas, T., & Breuer, D. (2019). Dynamical effects of multiple impacts: Large impacts on a Mars-like planet. *Phys. Earth Planet. Int.*, *287*, 76–92.
- Salvador, A., Massol, H., Davaille, A., Marcq, E., Sarda, P., & Chassefiere, E. (2017). The relative influence of H₂O and CO₂ on the primitive surface conditions and evolution of rocky planets. *J. Geophys. Res. Planets*, *122*(7), 1458–1486. doi: 10.1002/2017JE005286
- Samuel, H., Lognonné, P., Panning, M., & Lainey, V. (2019). The rheology and thermal history of Mars revealed by the orbital evolution of Phobos. *Nature*, *569*(7757), 523–527. doi: 10.1038/s41586-019-1202-7
- Scheinberg, A., Elkins-Tanton, L. T., & Zhong, S. J. (2014). Timescale and morphology of Martian mantle overturn immediately following magma ocean solidification. *J. Geophys. Res. Planets*, *119*(3), 454–467. doi: 10.1002/2013JE004496
- Scheinberg, A., Soderlund, K. M., & Schubert, G. (2015). Magnetic field generation in the lunar core: The role of inner core growth. *Icarus*, *254*, 62–71. doi: 10.1016/j.icarus.2015.03.013
- Scheinberg, A. L., Soderlund, K. M., & Elkins-Tanton, L. T. (2018). A basal magma ocean dynamo to explain the early lunar magnetic field. *Earth Planet. Sci. Lett.*, *492*, 144–151.
- Schmidt, R. M., & Housen, K. R. (1987). Some recent advances in the scaling of impact and explosion cratering. *Int. J. Impact Engin.*, *5*(1), 543–560. doi: 10.1016/0734-743X(87)90069-8
- Schubert, G., & Sandwell, D. T. (1995). A global survey of possible subduction sites on Venus. *Icarus*, *117*(1), 173–196. doi: 10.1006/icar.1995.1150
- Schubert, G., & Spohn, T. (1990). Thermal history of Mars and the sulfur content of its core. *J. Geophys. Res.*, *95*, 14095–14104. doi: 10.1029/JB095iB09p14095
- Segatz, M., Spohn, T., Ross, M. N., & Schubert, G. (1988). Tidal dissipation, surface heat flow, and figure of viscoelastic models of Io. *Icarus*, *75*, 187–206. doi: 10.1016/0019-1035(88)90001-2
- Seidelmann, P. K., Archinal, B. A., A'Hearn, M. F., Conrad, A., Consolmagno, G. J., Hestroffer, D., et al. (2007). Report of the IAU/IAG Working Group on cartographic coordinates and rotational elements: 2006. *Celestial Mech. Dynam. Ast.*, *98*(3), 155–180. doi: 10.1007/s10569-007-9072-y
- Shea, E. K., Weiss, B. P., Cassata, W. S., Shuster, D. L., Tikoo, S. M., Gattacceca, J., et al. (2012). A long-lived lunar core dynamo. *Science*, *335*(6067), 453. doi: 10.1126/science.1215359
- Shoemaker, E. M. (1962). Interpretation of lunar craters. In Z. Kopal (Ed.), *Physics and Astronomy of the Moon*. New York and London: Academic Press.
- Shoemaker, E. M. (1983). Asteroid and Comet Bombardment of the Earth. *Ann. Rev. Earth Planet. Sci.*, *11*, 461. doi: 10.1146/annurev.ea.11.050183.002333
- Sleep, N. H. (1994). Martian plate tectonics. *J. Geophys. Research*, *99*(E3), 5639–5655.

- Snyder, G. A., Taylor, L. A., & Neal, C. R. (1992). A chemical model for generating the sources of mare basalts: Combined equilibrium and fractional crystallization of the lunar magma-sphere. *Geochim. Cosmochim. Acta*, *56*(10), 3809–3823. doi: 10.1016/0016-7037(92)90172-F
- Solomatov, S. (2015). Magma ocean and primordial mantle differentiation. In G. Schubert (Ed.), *Treatise on geophysics* (p. 81–104). Elsevier.
- Solomatov, V. S., Olson, P., & Stevenson, D. J. (1993). Entrainment from a bed of particles by thermal convection. *Earth and Planetary Science Letters*, *120* (3–4), 387–393. doi: 10.1016/0012-821X(93)90252-5
- Solomatov, V. S., & Stevenson, D. J. (1993). Suspension in convective layers and style of differentiation of a terrestrial magma ocean. *J. Geophys. Res.*, *98*(E3), 5375–5390. doi: 10.1029/92JE02948
- Solomon, S. C. (1979). Formation, history and energetics of cores in the terrestrial planets. *Phys. Earth. Planet. Inter.*, *19*(2), 168–182. doi: 10.1016/0031-9201(79)90081-5
- Solomon, S. C., & Chaiken, J. (1976). Thermal expansion and thermal stress in the Moon and terrestrial planets: clues to early thermal history. *Lun. Planet. Sci. Conf. Proc.*, *3*, 3229–3243.
- Solomon, S. C., Comer, R. P., & Head, J. W. (1982). The evolution of impact basins: viscous relaxation of topographic relief. *J. Geophys. Res.*, *87*, 3975–3992. doi: 10.1029/JB087iB05p03975
- Solomon, S. C., & Head, J. W. (1980). Lunar mascon basin: lava filling, tectonics, and evolution of the lithosphere. *Rev. Geophys. Space Phys.*, *18*, 107–141. doi: 10.1029/RG018i001p0107
- Spudis, P. D., Martin, D. J. P., & Kramer, G. (2014). Geology and composition of the Orientale Basin impact melt sheet. *J. Geophys. Res. Planets*, *119*, 19–29. doi: 10.1002/2013JE004521
- Stanley, S., Bloxham, J., Hutchison, W. E., & Zuber, M. T. (2005). Thin shell dynamo models consistent with Mercury's weak observed magnetic field. *Earth Planet. Sci. Lett.*, *234* (1–2), 27–38. doi: 10.1016/j.epsl.2005.02.040
- Stegman, D. R., Jellinek, A. M., Zatman, S. A., Baumgardner, J. R., & Richards, M. A. (2003). An early lunar core dynamo driven by thermochemical mantle convection. *Nature*, *421* (6919), 143–146. doi: 10.1038/nature01267
- Stevenson, D. J., Spohn, T., & Schubert, G. (1983). Magnetism and thermal evolution of the terrestrial planets. *Icarus*, *54*, 466–489. doi: 10.1016/0019-1035(83)90241-5
- Stixrude, L., de Koker, N., Sun, N., Mookherjee, M., & Karki, B. B. (2009). Thermodynamics of silicate liquids in the deep Earth. *Earth Planet. Sci. Lett.*, *278*(3–4), 226–232. doi: 10.1016/j.epsl.2008.12.006
- Stöffler, D., & Ryder, G. (2001). Stratigraphy and Isotope Ages of Lunar Geologic Units: Chronological Standard for the Inner Solar System. *Space Sci. Rev.*, *96*, 9–54.
- Strom, R. G., Malhotra, R., Zhi-Yong, X., Takashi, I., Fumi, Y., et al. (2015). The inner solar system cratering record and the evolution of impactor populations. *Res. Ast. Astrophys.*, *15*(3), 407.
- Strom, R. G., Trask, N. J., & Guest, J. E. (1975). Tectonism and volcanism on Mercury. *J. Geophys. Res.*, *80*, 2478–2507. doi: 10.1029/JB080i017p02478
- Suavet, C., Weiss, B. P., Cassata, W. S., Shuster, D. L., Gattaccecchia, J., Chan, L., et al. (2013). Persistence and origin of the lunar core dynamo. *Proc. Nat. Acad. Sci.*, *110*(21), 8453–8458. doi: 10.1073/pnas.1300341110
- Suckale, J., Sethian, J. A., Yu, J.-d., & Elkins-Tanton, L. T. (2012). Crystals stirred up: 1. Direct numerical simulations of crystal settling in nondilute magmatic suspensions. *J. Geophys. Res. Planets*, *117*(E8), E08004. doi: 10.1029/2012JE004066
- Tackley, P. J., Schubert, G., Glatzmaier, G. A., Schenk, P., Ratcliff, J. T., & Matas, J. P. (2001). Three-Dimensional Simulations of Mantle Convection in Io. *Icarus*, *149*(1), 79–93. doi: 10.1006/icar.2000.6536
- Takahashi, F., & Matsushima, M. (2006). Dipolar and non-dipolar dynamos in a thin shell geometry with implications for the magnetic field of Mercury. *Geophys. Res. Lett.*, *33* (10), L10202. doi: 10.1029/2006GL025792
- Takahashi, F., Shimizu, H., & Tsunakawa, H. (2019). Mercury's anomalous magnetic field caused by a symmetry-breaking self-regulating dynamo. *Nature Comm.*, *10*, 208. doi: 10.1038/s41467-018-08213-7
- Taylor, G. J. (2013). The bulk composition of Mars. *Chemie der Erde / Geochemistry*, *73*(4), 401–420. doi: 10.1016/j.chemer.2013.09.006
- Taylor, G. J., & Wieczorek, M. A. (2014). Lunar bulk chemical composition: a postgravity recovery and interior laboratory reassessment. *Phil. Trans. R. Soc. A*, *372*(2024), 20130242.
- Taylor, S. R., & McLennan, S. M. (2009). *Planetary Crusts: Their Composition, Origin and Evolution*. Cambridge University Press, Cambridge, UK.
- Tian, Z., Zuber, M. T., & Stanley, S. (2015). Magnetic field modeling for Mercury using dynamo models with a stable layer and laterally variable heat flux. *Icarus*, *260*, 263–268. doi: 10.1016/j.icarus.2015.07.019
- Tikoo, S. M., Weiss, B. P., Cassata, W. S., Shuster, D. L., Gattaccecchia, J., Lima, E. A., et al. (2014). Decline of the lunar core dynamo. *Earth Planet. Sci. Lett.*, *404*, 89–97. doi: 10.1016/j.epsl.2014.07.010
- Tikoo, S. M., Weiss, B. P., Shuster, D. L., Suavet, C., Wang, H., & Grove, T. L. (2017). A two-billion-year history for the lunar dynamo. *Sci. Adv.*, *3*(8), e1700207. doi: 10.1126/sciadv.1700207
- Tonks, W. B., & Melosh, H. J. (1990). The physics of crystal settling and suspension in a turbulent magma ocean. In H. E. Newsom & J. H. Jones (Eds.), *Origin of the Earth* (p. 151–174). Oxford University Press.
- Tosi, N., Grott, M., Plesa, A.-C., & Breuer, D. (2013). Thermochemical evolution of Mercury's interior. *J. Geophys. Res. Planets*, *118*, 2474–2487. doi: 10.1002/jgre.20168
- Tosi, N., Plesa, A. C., & Breuer, D. (2013). Overturn and evolution of a crystallized magma ocean: A numerical parameter study for Mars. *J. Geophys. Res. Planets*, *118*(7), 1512–1528. doi: 10.1002/jgre.20109
- Tosi, N., Čadek, O., Běhouňková, Káňová, M., Plesa, A.-C., Grott, M., Breuer, D., Padovan, S. and Wieczorek, M. A. (2015).

- Mercury's low-degree geoid and topography controlled by insolation-driven elastic deformation. *Geophys. Res. Lett.*, *42*, 7327–7335. doi: 10.1002/2015GL065314
- Tsunakawa, H., Takahashi, F., Shimizu, H., Shibuya, H., & Matsushima, M. (2015). Surface vector mapping of magnetic anomalies over the Moon using Kaguya and Lunar Prospector observations. *J. Geophys. Res. Planets*, *120*(6), 1160–1185. doi: 10.1002/2014JE004785
- Turcotte, D. L., & Schubert, G. (2002). *Geodynamics* (2nd ed.). Cambridge University Press, Cambridge, UK. doi: 10.2277/0521661862
- Vander Kaaden, K. E., & McCubbin, F. M. (2015). Exotic crust formation on Mercury: Consequences of a shallow, FeO-poor mantle. *J. Geophys. Res. Planets*, *120*(2), 195–209. doi: 10.1002/2014JE004733
- Vaughan, W. M., & Head, J. W. (2014). Impact melt differentiation in the South Pole-Aitken basin: Some observations and speculations. *Planet. Space Sci.*, *91*, 101–106. doi: 10.1016/j.pss.2013.11.010
- Šrámek, O., & Zhong, S. (2012). Martian crustal dichotomy and Tharsis formation by partial melting coupled to early plume migration. *J. Geophys. Res. Planets*, *117*(E1), E01005. doi: 10.1029/2011JE003867
- Warren, P. H. (1985). The magma ocean concept and lunar evolution. *Ann. Rev. Earth Planet. Sci.*, *13*, 201–240. doi: 10.1146/annurev.earth.13.050185.001221
- Warren, P. H., & Rasmussen, K. L. (1987). Megaregolith insulation, internal temperatures, and bulk uranium content of the moon. *J. Geophys. Res.*, *92*, 3453–3465. doi: 10.1029/JB092iB05p03453
- Watters, T. R., & Johnson, C. L. (2010). Lunar tectonics. In T. R. Watters & R. A. Schulz (Eds.), *Planetary Tectonics* (p. 121–182). Cambridge Univ. Press.
- Watters, T. R., Robinson, M. S., Beyer, R. A., Banks, M. E., Bell, J. F., Pritchard, M. E., et al. (2010). Evidence of recent thrust faulting on the Moon revealed by the lunar reconnaissance orbiter camera. *Science*, *329*(5994), 936–940.
- Watters, T. R., Robinson, M. S., Bina, C. R., & Spudis, P. D. (2004). Thrust faults and the global contraction of Mercury. *Geophys. Res. Lett.*, *31* (4), L04701. doi: 10.1029/2003GL019171
- Watters, W. A., Zuber, M. T., & Hager, B. H. (2009). Thermal perturbations caused by large impacts and consequences for mantle convection. *J. Geophys. Res. Planets*, *114*, 2001. doi: 10.1029/2007JE002964
- Weber, R. C., Lin, P.-Y., Garnero, E. J., Williams, Q., & Lognonné, P. (2011). Seismic detection of the lunar core. *Science*, *331*, 309–312. doi: 10.1126/science.1199375
- Weiss, B. P., & Tikoo, S. M. (2014). The lunar dynamo. *Science*, *346*(6214), 1246753.
- Werner, S. C. (2009). The global martian volcanic evolutionary history. *Icarus*, *201* (1), 44–68.
- Whitaker, E. A. (1981). The lunar Procellarum basin. In R. B. Merrill & P. H. Schultz (Eds.), *Multi-ring basins: Formation and evolution* (p. 105–111).
- White, S. M., Crisp, J. A., & Spera, F. J. (2006). Long-term volumetric eruption rates and magma budgets. *Geochem. Geophys. Geosys.*, *7*, Q03010. doi: 10.1029/2005GC001002
- Whitten, J., Head, J. W., Staid, M., Pieters, C. M., Mustard, J., Clark, R., et al. (2011). Lunar mare deposits associated with the Orientale impact basin: New insights into mineralogy, history, mode of emplacement, and relation to Orientale Basin evolution from Moon Mineralogy Mapper (M³) data from Chandrayaan-1. *Journal of Geophysical Research (Planets)*, *116*, E00G09. doi: 10.1029/2010JE003736
- Wicht, J., & Heyner, D. (2014). Mercury's magnetic field in the MESSENGER era. In J. Shuanggen (Ed.), *Planetary Geodesy and Remote Sensing*. CRC Press.
- Wieczorek, M. A. (2015). Gravity and topography of the terrestrial planets. In J. Schubert (Ed.), *Planets and moons* edited by T. Spohn, *Treatise on Geophysics*, vol. 10 (2nd ed.). Elsevier, Amsterdam, The Netherlands.
- Wieczorek, M. A. (2018). Strength, depth, and geometry of magnetic sources in the crust of the moon from localized power spectrum analysis. *J. Geophys. Res. Planets*, *123*(1), 291–316.
- Wieczorek, M. A., Jolliff, B. L., Khan, A., Pritchard, M. E., Weiss, B. P., Williams, J. G., et al. (2006). The constitution and structure of the lunar interior. *Rev. Mineral. Geochem.*, *60*, 221–364. doi: 10.2138/rmg.2006.60.3
- Wieczorek, M. A., Neumann, G. A., Nimmo, F., Kiefer, W. S., Taylor, G. J., Melosh, H. J., et al. (2013). The Crust of the Moon as Seen by GRAIL. *Science*, *339*, 671–675. doi: 10.1126/science.1231530
- Wieczorek, M. A., & Phillips, R. J. (1997). The structure and compensation of the lunar highland crust. *J. Geophys. Res.*, *102*, 10933–10944. doi: 10.1029/97JE00666
- Wieczorek, M. A., & Zuber, M. T. (2004). Thickness of the Martian crust: Improved constraints from geoid-to-topography ratios. *J. Geophys. Res. Planets*, *109*, 1009. doi: 10.1029/2003JE002153
- Williams, J.-P., & Nimmo, F. (2004). Thermal evolution of the Martian core: Implications for an early dynamo. *Geology*, *32* (2), 97. doi: 10.1130/G19975.1
- Wood, J. A., Dickey Jr, J., Marvin, U. B., & Powell, B. (1970). Lunar anorthosites and a geophysical model of the Moon. *Geochim. Cosmochim. Acta Suppl.*, *1*, 965.
- Wünnemann, K., Collins, G. S., & Melosh, H. J. (2006). A strain-based porosity model for use in hydrocode simulations of impacts and implications for transient crater growth in porous targets. *Icarus*, *180*, 514–527. doi: 10.1016/j.icarus.2005.10.013
- Yu, S., Tosi, N., Schwinger, S., Maurice, M., Breuer, D., & Xiao, L. (2019). Overturn of ilmenite-bearing cumulates in a rheologically weak lunar mantle. *J. Geophys. Res. Planets*, *124* (2), 418–436.
- Zhang, N., Dygert, N., Liang, Y., & Parmentier, E. M. (2017). The effect of ilmenite viscosity on the dynamics and evolution of an overturned lunar cumulate mantle. *Geophys. Res. Lett.*, *44* (13), 6543–6552. doi: 10.1002/2017GL073702
- Zhang, N., Parmentier, E. M., & Liang, Y. (2013a). A 3-D numerical study of the thermal evolution of the Moon after cumulate mantle overturn: The importance of rheology and core solidification. *J. Geophys. Res. Planets*, *118*, 1789–1804. doi: 10.1002/jgre.20121
- Zhang, N., Parmentier, E. M., & Liang, Y. (2013b). Effects of lunar cumulate mantle overturn and megaregolith on the

- expansion and contraction history of the Moon. *Geophys. Res. Lett.*, *40*(19), 5019–5023. doi: 10.1002/grl.50988
- Zhao, Y., de Vries, J., van den Berg, A. P., Jacobs, M. H. G., & van Westrenen, W. (2019). The participation of ilmenite-bearing cumulates in lunar mantle overturn. *Earth Planet. Sci. Lett.*, *511*, 1–11. doi: 10.1016/j.epsl.2019.01.022
- Zhong, S., Parmentier, E. M., & Zuber, M. T. (2000). A dynamic origin for the global asymmetry of lunar mare basalts. *Earth Planet. Sci. Lett.*, *177*(3–4), 131–140. doi: 10.1016/S0012-821X(00)00041-8
- Zhu, M.-H., Wünnemann, K., Potter, R. W., Kleine, T., & Morbidelli, A. (2019). Are the Moon's Nearside-Farside Asymmetries the Result of a Giant Impact? *J. Geophys. Res. Planets*, *124* (0), 1–24. doi: 10.1029/2018JE005826
- Ziegler, L. B., & Stegman, D. R. (2013). Implications of a long-lived basal magma ocean in generating Earth's ancient magnetic field. *Geochem. Geophys. Geosyst.*, *14* (11), 4735–4742. doi: 10.1002/2013GC005001
- Zolotov, M. Y., Sprague, A. L., Hauck, S. A., II, Nittler, L. R., Solomon, S. C., & Weider, S. Z. (2013). The redox state, FeO content, and origin of sulfur-rich magmas on Mercury. *J. Geophys. Res. Planets*, *118*, 138–146. doi: 10.1029/2012JE004274

INDEX

- 410 km. *see* Discontinuities
660 km. *see* Discontinuities
- Absolute Plate Motion, 265–269, 292, 295
- Anelasticity, 102–114, 384
- Anharmonic effects, 59–60, 101–102, 105, 108–111, 114
- Anisotropy
Elastic, 28, 41, 54, 61, 76, 82, 209, 211, 262, 265, 339
Plastic, 28, 39, 42
Seismic. *see* Seismic anisotropy
Mechanical or viscous, 273
- APM. *see* Absolute Plate Motion
- Asthenosphere, Viscosity, 270
- Accretion, 462, 464
- Afar. *see* Plume, Afar
- Arc. *see* Magmatic Arc
- Asthenosphere, 5, 15, 398, 399
- Atmosphere, 414, 429, 437, 460, 461
- Atmospheric Circulation, 437
- Attenuation, seismic, 105–109, 111, 113–114, 201, 217, 270, 287, 356, 359
- Basal Magma Ocean. *see* Magma Ocean, Basal
- Basalt
mid-ocean ridge. *see* Mid-Ocean Ridge
Basalt
flood, 354
in the mantle, 358, 359
ocean island. *see* Ocean Island Basalt
- Basins. *see* Sedimentary Basins
- Bathymetry, 381, 382, 397
- Body waves
diffracted S waves, 362
PcP phase, 232–235
PKP/PKKP precursors, 232–233
Pn waves, 260, 286
PnKP phases, 232–235
PP and SS precursors, 359, 360
receiver functions, 360
scattered waves, 354, 362
S-ScS splitting, 330, 332, 338, 340
SKKS-SKS splitting, 332, 338–345
Sdiff splitting, 332, 338, 340, 342–343
- Boundary layer
anisotropy, 268–269, 329
thermal. *see* Thermal boundary layer
- Breyite, 180, 184
- Bridgmanite, 17, 22, 30, 32, 33, 40, 42, 52, 60, 65, 71, 73, 74, 180, 195, 202, 204, 211, 213, 247, 307, 313, 335, 354
- Brillouin Spectroscopy, 55–56, 79, 102
- Bulk modulus, 53–54, 58, 67, 69–70, 74, 77, 79, 108, 201
- Buoyancy, 315–317, 375, 379, 381, 398, 432, 459, 472, 475
- Buoyancy Flux. *see* Plume
- Buoyancy Number, 315, 316, 453, 459
- C-component, 127
- CAMP. *see* Large Igneous Province, Central Atlantic
Magmatic Province
- Calcium Silicate Perovskite, 22, 29–30, 32–33, 57, 72–75, 180–182, 184–185, 210–211, 213, 218, 337
- Carbon Cycle, deep, 181, 432, 440, 443
- Carbon Compensation Depth, 396, 397
- Carbon Dioxide, 395, 414, 415, 431, 434, 436–443, 460
- Carbonatitic melt, 130, 132, 182, 188
- CaSiO₃ perovskite. *see* Calcium Silicate Perovskite
- CDM. *see* Mantle Composition, Dense Chondrites, CI, 462, 465
- Central Atlantic Magmatic Province. *see* Large Igneous Province, Central Atlantic Magmatic Province
- CI Chondrites. *see* Chondrites, CI
- Circulation, Atmosphere. *see* Atmospheric Circulation
- Circulation, Mantle. *see* Mantle Circulation Model
- Circulation, Ocean. *see* Oceanic Circulation
- Clapeyron slope, 358
- Climate, 395, 417, 427, 431, 434–437, 439–441, 443
- CMB. *see* Core-mantle boundary
- CO₂. *see* Carbon Dioxide
- Compositionally Dense Materials. *see* Mantle Composition, Dense
- Composition. *see* Mantle Composition, source
- Convection, Mantle. *see* Mantle Convection
- Convection, Core. *see* Core Convection
- Core, 414, 465, 468, 469, 471–472, 474–476
- Core Convection, 471, 472
- Core-mantle boundary, 9, 81, 199, 210, 310, 313, 314, 379, 415, 424, 427, 459, 464, 471, 472, 474, 478
- ellipticity, 237
heat flux through, 354
thermal boundary layer, 354
topography, 379
body wave models of, 235–236, 238, 242, 246
dynamic predictions of, 239, 243–245
normal mode models of, 235–238, 242, 246
peak-to-peak amplitudes, 233–234, 237, 245–247
- Cosmogenic Exposure Dating. *see* Dating, Cosmogenic Exposure
- CPO. *see* Crystal Preferred Orientation
- Creep
Diffusion, 17, 22–23, 27, 42, 270, 284, 335, 338
(Non-)Newtonian, 22–23, 36, 374
- Critical Resolved Shear Stress, 27
- CRSS. *see* Critically Resolved Shear Stress
- Crust, 414, 425, 428–430, 435, 461
Oceanic. *see* Oceanic Crust
Primary, 461, 462, 466, 478
Secondary, 461–466, 478
- Crystal Preferred Orientation, 333, 335–337. *see also* Lattice Preferred Orientation
- Cumulates, 457–462, 464, 475
- Crystallization, 457–459, 471, 472, 475, 478
- D" Layer, 41, 72, 181, 193–194, 197, 199–201, 203–204, 453
- DAC. *see* Diamond anvil cell
- Dating, Cosmogenic Exposure, 391, 392, 396
- Debye model, 53, 61, 64
- Deccan Traps. *see* Large Igneous Province, Deccan
- Deep mantle plumes, 353–358
- Deep Water Cycle, 183

- Deformation
 Experimental Devices, 24
 Diamond-anvil cell, 23
 Large-Volume, 25
 Plastic, 21, 23, 26
 Polyphase, 36, 37, 40, 337
- Degassing, 431, 438, 441, 444, 460, 461
- Dense Hydrous Magnesium Silicates, 183, 186, 188–189
- Density Functional Theory, 58–59, 82
- Depleted, 75, 122, 124, 126–130, 134, 136, 137, 160, 164, 305–306, 457, 460, 476
- DFT. *see* Density Functional Theory
- DHMS. *see* Dense Hydrous Magnesium Silicates
- Diamond
 Super-deep, 180, 186, 188
 Inclusions, 132, 305
 CLIPPIR, 180–181, 185–189
 Sublithospheric, 179–180, 182, 185–186, 188
- Diamond anvil cell, 23–24, 55, 57–58, 81–82, 169, 335
- Differentiation, Planetary, 456, 468, 476
- Differentiation, Magmatic. *see* Fractionation
- Diffusion creep. *see* Creep
- Discontinuities
 core-mantle boundary. *see* Core-mantle boundary
 410, km, 358–360
 660, km, 358–360
- Dislocation glide, 22–23, 26–27, 335–337
 lower mantle, 335–337
 olivine, 272
- DM, 122, 127–128. *see also* DMM
- DMM, 75–76, 78, 153
- Dynamic Topography. *see* Topography, Dynamic
- Early Earth, 313
- Eclogite, 127–130, 133–134, 140, 153, 155, 161–162, 318
- Elasticity
 Constants. *see* Tensor
 Measurements, 56
 Moduli, 54–61, 70–71, 82–83, 101–102, 106, 108, 218, 284
 Tensor, 53, 55, 209–210, 265, 294, 330, 333–334, 337–338, 340, 345
- Equation of State, 55, 57, 66, 101, 105, 307, 359
- Elasto-Visco-Plastic Self-Consistent Model, 26–28
- Elasto-Plastic Self-Consistent Model, 26–28
- EM1, 123–129, 132–135, 137–139
- EM2, 123–126, 130, 135, 137–139
- Enriched, 121–122, 124, 127–128, 132–133, 136, 137, 152, 158, 160, 163, 167, 304, 476
- Entrainment. *see also* Mantle Composition, Entrainment of, 355
- Erosion, 376, 389–394, 396, 425, 432
- Evaporite, 428, 433–437, 439
- Evolution, Landscape, 398
- Evolution, Thermal, 304, 461, 463, 465, 468, 469, 474, 476, 478, 479
- E(V)PSC. *see* Elasto-(Visco-)Plastic Self-Consistent Model
- Exchange coefficients (Fe-Mg) 72–73, 77–79, 81
- Extinction. *see* Mass Extinction
- Ferropicoclase, 17, 22, 28, 29, 32, 40, 52, 58, 67, 70, 79, 180, 183, 209, 211, 218, 336
- Finite Strain
 Theory, 52–55, 59–70, 81–82
 Parameters, 74
- Fractionation, 81, 122, 125, 133–134, 136, 155, 158–160, 163, 167, 395, 459, 472
- Fresnel zones, 356, 360
- FOZO, 123, 126–127
- Garnet, 307, 358
- Generation Zone, Plume. *see* Plume Generation Zone
- Geochemical Component, 3, 122–128, 130, 132–137, 139, 161, 163
- Geoid, 8, 9, 11, 17, 233, 237, 379, 380, 383, 384, 398, 452
- GIA. *see* Isostatic Adjustment, Global
- Glaciation, 437, 439, 489
- Global Isostatic Adjustment. *see* Isostatic Adjustment, Global
- Global Positioning System, 386, 396
- GPS. *see* Global Positioning System
- Gravity, 234, 237, 379, 387, 396, 433, 434, 458, 460, 461, 464, 467, 471, 476, 477
- Greenhouse, 433, 438–441
- Harzburgite, 73, 75–81, 157, 305–312, 358–360
- Heat Flux, 463, 468, 471, 472, 474, 475, 477, 478
- Heating, Impact. *see* Impact Heating
- Heating, Radiogenic. *see* Radiogenic Heating
- HIMU, 123, 125–132, 134–139
- Hotspot, 5, 24–25, 126, 194, 206–209, 254, 289, 293, 353–355, 358, 417, 419, 420, 422, 426, 427, 452
- Icehouse, 418, 433, 434, 438, 439, 441
- Icelandic Plume. *see* Plume, Icelandic
- Ice Sheets, 388, 437
- Igneous Provinces, Large. *see* Large Igneous Provinces
- Impact(s), 456, 464–469, 479
- Impact Basins, 463, 466, 467, 473, 474, 477, 479
- Impact Heating, 467
- Inertia, Moment of. *see* Moment of Inertia
- InSight mission, 477, 479
- Interconnected Weak Layer, 36, 37, 336
- Internal Heating. *see* Radiogenic Heating
- Intraplate Volcanism. *see* Magmatism, Intraplate; Volcanism, Intraplate
- Isostasy, 381–383
- Isostatic Topography. *see* Topography, Isostatic
- Isostatic Adjustment, Global, 386–388, 396
- Isostatic Topography. *see* Topography, Isostatic
- IWL, *see* Interconnected Weak Layer
- Jeffbenite, 180
- Karoo-Ferrar. *see* Large Igneous Province, Karoo-Ferrar
- Kimberlites, 417, 427–429
- Landau Theory, 67, 75, 79, 83
- Landscape Evolution. *see* Evolution, Landscape
- Large Igneous Provinces, 414, 417–420, 422–426, 428, 429, 431, 432, 435, 436, 438–440, 468
 Central Atlantic Magmatic Province, 416–419, 423, 428, 431, 435, 440, 441
 Deccan, 416, 418, 419, 423, 431, 435, 438, 440
 Karoo-Ferrar, 416, 418, 419, 423, 428
 Parana-Etendeka, 414, 416, 418, 419, 423, 428
 Siberian, 416, 418–420, 423, 431, 435, 436, 438
- Large Low (Shear) Velocity Provinces, 3–5, 11, 41, 209, 217, 230, 304–305, 338, 415, 420, 424–427, 452
 African, 248, 419, 420
 Anisotropy at boundary, 330, 333, 346
 Bulk sound velocity, 230
 Composition, 304, 305, 310, 415
 Density, 11, 230–232, 234, 236, 238–241, 247–248, 426
 Pacific, 248, 419, 420
 Shear Velocity, 304, 421
 Stability, 5, 13, 305, 415
- Large Volume Press, 24–26, 30–31, 33–34, 38, 335
- Lattice Preferred Orientation, 264–269, 271–273, 284
 Olivine, 264–269, 271–273, 288–289
- Lattice Strain, 26, 37
- LBF. *see* Load Bearing Framework
- Length-of-day variations, 237, 239
- LIP. *see* Large Igneous Provinces
- Lithology, 80, 127–129, 137, 152, 162, 392, 394, 396, 431
- Lithosphere, 264–266, 317, 318, 320, 375–377, 381, 434, 452, 469, 473, 476, 477
 continental, 271, 297

- oceanic, 264–266, 297
 LL(S)VP. *see* Large Low (Shear) Velocity Provinces
 Load Bearing Framework, 36, 37
 Love waves. *see* Surface waves
 Lowermost Mantle, 5–6, 11, 15–16, 27, 40–42, 81–82, 194–195, 320, 329–330, 332–340, 421, 452
 Density, 234, 236, 238–241, 243, 247–248
 Dynamics of, 239
 P wave velocity of, 231
 Shear wave velocity, 231, 304, 305
 Structure, 16
 LPO. *see* Lattice Preferred Orientation
 Magma, 415, 417, 427
 Magma Ocean, 446–458, 460–462, 464–466, 478
 Magma Ocean, Basal, 475
 Magmatic Arc, 441
 Magmatic Underplating. *see* Underplating
 Magmatism, 422, 423, 440, 463, 469
 Magnetic Field, 456, 469, 471–475, 479
 Mantle Circulation Model, 8, 98–104, 109, 258, 264–268, 362. *see also* Mantle Convection
 Mantle Convection, 312, 374, 381, 383, 386, 399, 456–461, 468–472, 478
 Models of, 8–10, 16, 308, 309, 311, 312, 314, 316, 318, 374, 377, 378, 385, 399, 424
 Onset of, 457, 460, 461
 Mantle Composition, 466
 Dense, 315, 316, 318, 320
 Entrainment of, 315, 316, 425, 458
 Segregation of, 306–309
 Source, 122–124, 127–134, 136–140, 151–152, 154, 158, 160–165, 168–169, 303–304, 320–321, 353–354, 362, 459
 Mantle Overturn, 457–460, 462–464, 475, 478
 Mantle Structure, 11–16
 Density, 11, 16, 452
 Shear Velocity, 13–15
 Mantle Transition Zone, 5–6, 11–16, 18, 60–61, 66, 100, 132, 182–184, 186–188, 260–261, 304–310, 317–318, 320–321, 354, 358–359, 424–425
 Mantle Viscosity, 21–22, 40–41, 80, 101–102, 113, 215–216, 239–240, 246, 267–268, 307, 379, 385, 399, 460, 461, 479
 Mantle Viscosity, Profile, 9, 10, 13, 16, 17, 380, 452
 Mars, 456, 458–461, 463–466, 468, 473, 474, 476–479
 Mass Extinction, 418, 423, 431, 436, 437, 439
 Melting, 17, 304, 305, 415, 427, 441, 456, 457, 459, 461, 463, 468, 471, 476
 partial, 122, 124, 126–128, 130–132, 134, 136, 151–152, 155, 157, 160–169
 Mercury, 456, 458, 460, 462, 463, 465, 466, 469, 471–473, 478, 479
 Mg#, 152, 158–161, 163–164, 166, 168
 Mid-Ocean Ridge, 381
 Mid-Ocean Ridge Basalt, 40, 121–122, 158, 165–166, 195, 205, 209, 304
 Moment of Inertia, 456, 472
 Moon, 456, 458, 460, 462–466, 468, 469, 474–479
 MORB. *see* Mid-Ocean Ridge Basalt
 MTZ. *see* Mantle Transition Zone
 Multi-anvil Apparatus, 57–58, 81–82. *see also* Large Volume Press
 Normal modes
 CMB Stoneley modes, 234, 240
 frequency spectra, 234–235, 248
 self-coupling approximation, 240–241, 248
 splitting function measurements, 240–241, 248–249
 Ocean-bottom seismometers, 357, 363
 Oceanic Circulation, 396, 397, 400
 Oceanic Crust, 303–314, 317–321, 384, 425, 427
 Ocean Island Basalts, 304
 OIB. *see* Ocean Island Basalts
 Olivine, 358–359
 anisotropy, 264, 267, 269, 272, 288–289
 Outgassing. *see* Degassing
 P wave velocity. *see* Velocity models
 Paleomagnetism, 395
 Paleoclimate, 400, 434, 435, 437, 440, 443
 Paleoelevation, 395, 396
 Paleogeography, 431, 432, 443
 Paleolatitude, 432–434, 439
 Paleomagnetism, 418, 419, 428, 474
 Paleosurfaces, 389, 390
 Paleo Shorelines. *see* Shorelines, Paleo
 Paleozoic, 420, 422, 427, 430, 432–434, 438
 Parana-Etendeka. *see* Large Igneous Province, Parana-Etendeka
 Peridotite, 121–122, 124, 126, 128–132, 134, 151–158, 160–166, 168, 170–177, 186, 187, 258, 262, 272, 337
 PGZ. *see* Plume Generation Zone
 Phanerozoic, 432, 433, 438, 439
 Phase Transition, 9, 16–17, 51–52, 66–67, 75, 78–79, 83, 230, 305–307, 317, 358, 379
 Clapeyron slope, 202, 336
 Kinetics of, 202
 olivine-wadsleyite, 61, 358–359
 ringwoodite dissociation, 358
 post-perovskite, 22, 41, 195, 201–202, 205–206, 336, 346, 349
 PHEM, 126–127
 Peierls Stress, 22, 335
 Plate
 Motion, 398, 399, 422
 Motions, Patterns of, 14–16
 Oceanic, 264–266, 270–271
 Reconstructions, 418–423, 428, 430, 433, 435–437
 Tectonics, 310, 431, 432, 434, 441, 459, 463, 474
 Plume, 314, 316–319
 Afar, 390, 416, 419, 421, 423, 435, 438
 Buoyancy Flux, 422
 Deep mantle, 353–358
 Generation Zone, 414, 417, 419–421, 424, 426, 435
 Hawaii, 355, 357
 Head, 316, 377, 421, 424–427
 Icelandic, 389, 397
 Samoa, 355
 Thermochemical, 317, 318
 Plastic Deformation. *see* Deformation
 Polarity, of seismic waves, 197, 200–203, 333
 Post-perovskite, 30–32, 35, 195, 201–202, 209–211, 217, 235, 239, 245–247, 313, 316, 332, 334–338, 346, 356
 Precursors
 PKP, PKKP, 232–233
 PP, SS, 359, 360
 Preliminary Reference Earth Model, 247, 356–357
 PREM. *see* Preliminary Reference Earth Model
 Primary magma, 151–152, 158–170
 Pyrolite, 65, 73–81, 102, 205, 305–307, 358–359
 Pyroxenite, 121, 126, 128–132, 134, 137, 151–156, 160–164, 167, 168
 Quality factor, seismic, 106–109
 Radiogenic Heating, 313, 456, 461, 476
 Radiogenic Isotope, 121–128, 130–133, 136–137
 Rayleigh Number, 310–312, 374, 461
 Rayleigh waves. *see* Surface waves
 Receiver functions, 360
 Recycling, 80, 122, 125–126, 132–134, 136–137, 140, 169, 186, 188
 Residual Topography. *see* Topography, Residual
 Rheology, 17, 22–23, 36–37, 194, 271, 336, 399, 477
 Reuss bound, 54–55, 60–61, 65–66, 78, 82, 210
 Ringwoodite, 17, 30, 34, 60–63, 66, 180–185, 188, 354, 358–359
 ROC. *see* Oceanic Crust
 Scattered waves, 354, 362
 Sea Level, 387–389, 396, 437
 Sedimentation, 388, 389, 394, 396
 Sedimentary Basins, 373, 413

- Seismic anisotropy
 azimuthal, 260–274, 284–297
 modeling of, 266–269, 337–338
 radial, 262–263, 265, 267–269, 272, 284–289
 radial in lowermost mantle, 330–333
 Pn waves, 260, 286
 shear wave splitting, 261, 294
 surface waves, 262–264, 293–294
 synthetic analysis, 340–345
- Seismic Scatters, 305
- Shear modulus, 22, 54, 69, 74, 77, 83, 101, 106
- Shear wave splitting, 261, 294, 330, 332, 338–345
- Shear wave velocity. *see* Velocity models
- Shorelines, Paleo, 387, 388
- Siberian Traps. *see* Large Igneous Province, Siberian
- Silicate Weathering. *see* Weathering, Silicate
- SPO. *see* Shape Preferred Orientation
- Shape Preferred Orientation, 284, 333
- Slip systems, 22, 26–27, 32–34, 39, 265, 267, 270, 335–338
- SO₂. *see* Sulphur Dioxide
- Source. *see* Mantle Composition, Source
- Spin crossover. *see* Spin transition
- Spin transition, 52, 58–59, 67–73, 77–80, 83, 210–211
- Stable Isotope, 121–122, 132–133, 136, 140
- Stagnant Lid, 455–461, 471, 474, 476, 478, 479
- Stagnant Slabs. *see* Slabs, Stagnant
- Stokes Equation, 311, 312, 426, 453
- Stokes Flow, 101
- Strain Partitioning, 36, 38
- Strain tensor, 53
- Stratigraphy, 388, 389, 396, 430, 431
- Strength
 Flow, 26, 28–31
 Yield, 24, 28, 32, 36, 459
- Stress tensor, 53
- Subduction, 15–18, 305, 438, 441, 456, 471
- Subduction Flux, 438, 439, 441–443
- Subduction Zones, 287–293, 303, 380, 382, 414, 441
- Subsidence, 377, 381, 383, 386–389, 396, 397
- Sulphur, 471, 472, 475
- Sulphur Dioxide, 414, 415
- Surface waves
 Anisotropy, 262–264, 293–294
 Love waves, 262–264
 Rayleigh waves, 262–264
- Synchrotron, 23, 25, 39, 57–58, 185
- Tethys, 432–434, 436, 437
- Thermal Boundary Layer, 311, 334, 354, 424
- Thermal Evolution. *see* Evolution, Thermal
- Thermochemical Piles, 245–246
- Thermochemical Plumes. *see* Plumes, Thermochemical
- Thermochronology, 386, 391, 392, 396, 398
- Thermodynamic model, 52, 73, 81, 99, 359
- Texture, 21, 26, 31, 42, 160, 194, 262, 268, 271, 336, 338, 345. *see also* CPO, LPO
- Tomographic Filter, 99
- Tomographic models. *see* Velocity models
- Tomography
 adjoint, 362–363
 azimuthal anisotropy, 286
 radial anisotropy, 286
 shear wave splitting, 294
 tidal, 241
 travel-time, 356–358
- Topography
 Dynamic, 375–387
 Dynamic, Spectra of, 398
 Isostatic, 381, 382
 On core-mantle boundary. *see* Core-mantle boundary
 Residual, 381–384
- Transition Zone. *see* Mantle Transition Zone
- Tropics, 418, 433–435, 437, 439, 440
- ULVZ. *see* Ultra-Low Velocity Zone
- Ultra-Low Velocity Zone, 81, 193–194, 196, 206–211, 213–217, 305, 334, 362, 414, 425
- Ultrasonics, 56–57, 79, 81, 102
- Underplating, 389, 414
- Uplift, 386–396
- Velocity models
 Azimuthal anisotropy, 264–266, 287–293
 P wave lower mantle, 5, 231
 Radial Correlation, 7, 12, 16
 Shear Velocity
 Spectra of, 11–13, 15
 Surface wave anisotropy, 293–294
 S wave, 7, 8, 16, 231, 355, 358, 417–419, 426
- Venus, 456
- Visco-Plastic Self-Consistent Model, 26–28, 42, 335, 338
- Viscosity. *see* Mantle Viscosity
- Voigt bound, 6, 8, 11, 13, 54–55, 60–61, 65–66, 78, 82, 210, 340
- Voigt-Reuss-Hill average, 28, 54–55, 60–61, 65–66, 356
- Volatile, 121–122, 125, 129, 133, 136–139, 141, 155, 163–164, 166, 169, 188, 194, 265, 268, 270–271, 345, 415, 417, 427, 431, 432, 456, 458, 460–461
- Volcanism, 386, 427, 458.459.464–466, 468, 469, 472, 474, 478
- Volcanism, Intraplate. *see* Hotspots
- Vote map, 231, 241, 243–244, 331
- VPSC. *see* Visco-Plastic Self-Consistent Model
- Wadsleyite, 60–63, 66, 183–184, 358–359
- Wavefront healing, 354, 356, 360, 361
- Weathering, 390, 417, 432, 436–439, 441–443
 Silicate, 432, 436, 437, 439, 440, 443
- X-ray
 diffraction, 23–24, 55, 57–58, 184
 diffraction in radial geometry, 24, 26, 335
 scattering, 57, 210
 radiography, 57, 169
- X-ray diffraction (XRD), 23, 26, 29, 30, 55, 57, 58, 184, 335